SynerCrete'18: Interdisciplinary Approaches for Cement-based Materials and Structural Concrete: Synergizing Expertise and Bridging Scales of Space and Time
Vol. 2

SynerCrete'18 International Conference on Interdisciplinary Approaches
for Cement-based Materials and Structural Concrete

24-26 October 2018, Funchal, Madeira Island, Portugal

Published by RILEM Publications S.A.R.L.
4 avenue du Recteur Poincaré 75016 Paris - France
Tel : + 33 1 42 24 64 46 Fax : + 33 9 70 29 51 20
http://www.rilem.net E-mail: dg@rilem.net

ISBN Vol. 1:978-2-35158-211-4 ISBN Vol. 2: 978-2-35158-212-1
ISBN Vol. 1&2: 978-2-35158-202-2 e-ISBN Vol. 1&2: 978-2-35158-203-9
DOI: 10.5281/zenodo.1405563 Legal deposit n. (Portugal):
Printed by Canto Redondo / VASP DPS http://www.cantoredondo.eu
Cover design by: Boutik Studio http://boutik.pt/

RILEM, The International Union of Laboratories and Experts in Construction Materials, Systems and Structures, is a non-profit-making, non-governmental technical association whose vocation is to contribute to progress in the construction sciences, techniques and industries, essentially by means of the communication it fosters between research and practice. RILEM's activity therefore aims at developing the knowledge of properties of materials and performance of structures, at defining the means for their assessment in laboratory and service conditions and at unifying measurement and testing methods used with this objective.

RILEM was founded in 1947, and has a membership of over 900 in some 70 countries. It forms an institutional framework for co-operation by experts to:

- optimise and harmonise test methods for measuring properties and performance of building and civil engineering materials and structures under laboratory and service environments,
- prepare technical recommendations for testing methods,
- prepare state-of-the-art reports to identify further research needs,
- collaborate with national or international associations in realising these objectives.

RILEM members include the leading building research and testing laboratories around the world, industrial research, manufacturing and contracting interests, as well as a significant number of individual members from industry and universities. RILEM's focus is on construction materials and their use in building and civil engineering structures, covering all phases of the building process from manufacture to use and recycling of materials.

RILEM meets these objectives through the work of its technical committees. Symposia, workshops and seminars are organised to facilitate the exchange of information and dissemination of knowledge. RILEM's primary output consists of technical recommendations. RILEM also publishes the journal *Materials and Structures* which provides a further avenue for reporting the work of its committees. Many other publications, in the form of reports, monographs, symposia and workshop proceedings are produced.

SynerCrete'18: Interdisciplinary Approaches for Cement-based Materials and Structural Concrete: Synergizing Expertise and Bridging Scales of Space and Time
Vol. 2

Funchal, Madeira, Portugal
24-26 October 2018

Edited by
Miguel Azenha
Dirk Schlicke
Farid Benboudjema
Agnieszka Jędrzejewska

RILEM Publications S.A.R.L.

National Support (Portugal)

International Support

Sponsors

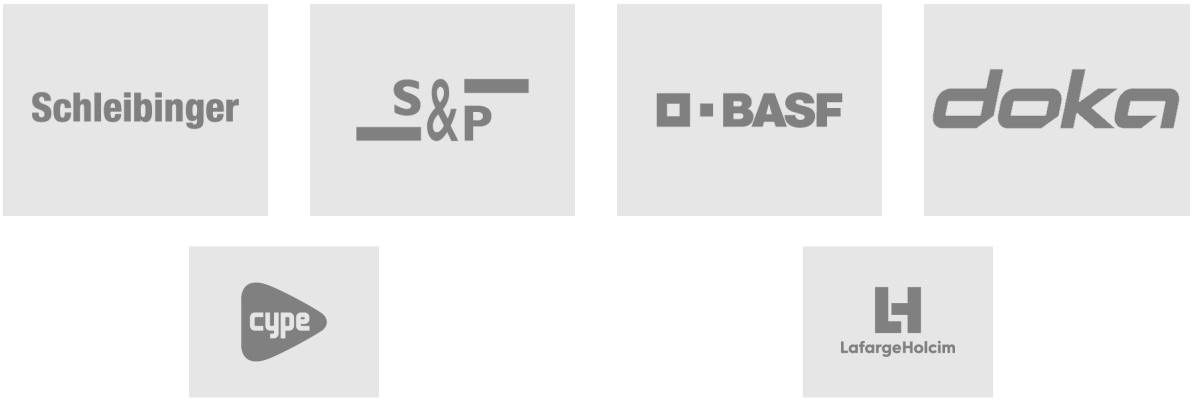

RILEM Publications

The following list is presenting the global offer of RILEM Publications, sorted by series. Each publication is available in printed version and/or in online version.

RILEM PROCEEDINGS (PRO)

PRO 1: Durability of High Performance Concrete (ISBN: 2-912143-03-9); *Ed. H. Sommer*

PRO 2: Chloride Penetration into Concrete (ISBN: 2-912143-00-04); *Eds. L.-O. Nilsson and J.-P. Ollivier*

PRO 3: Evaluation and Strengthening of Existing Masonry Structures (ISBN: 2-912143-02-0); *Eds. L. Binda and C. Modena*

PRO 4: Concrete: From Material to Structure (ISBN: 2-912143-04-7); *Eds. J.-P. Bournazel and Y. Malier*

PRO 5: The Role of Admixtures in High Performance Concrete (ISBN: 2-912143-05-5); *Eds. J. G. Cabrera and R. Rivera-Villarreal*

PRO 6: High Performance Fiber Reinforced Cement Composites - HPFRCC 3 (ISBN: 2-912143-06-3); *Eds. H. W. Reinhardt and A. E. Naaman*

PRO 7: 1st International RILEM Symposium on Self-Compacting Concrete (ISBN: 2-912143-09-8); *Eds. Å. Skarendahl and Ö. Petersson*

PRO 8: International RILEM Symposium on Timber Engineering (ISBN: 2-912143-10-1); *Ed. L. Boström*

PRO 9: 2nd International RILEM Symposium on Adhesion between Polymers and Concrete ISAP '99 (ISBN: 2-912143-11-X); *Eds. Y. Ohama and M. Puterman*

PRO 10: 3rd International RILEM Symposium on Durability of Building and Construction Sealants (ISBN: 2-912143-13-6); *Eds. A. T. Wolf*

PRO 11: 4th International RILEM Conference on Reflective Cracking in Pavements (ISBN: 2-912143-14-4); *Eds. A. O. Abd El Halim, D. A. Taylor and El H. H. Mohamed*

PRO 12: International RILEM Workshop on Historic Mortars: Characteristics and Tests (ISBN: 2-912143-15-2); *Eds. P. Bartos, C. Groot and J. J. Hughes*

PRO 13: 2nd International RILEM Symposium on Hydration and Setting (ISBN: 2-912143-16-0); *Ed. A. Nonat*

PRO 14: Integrated Life-Cycle Design of Materials and Structures - ILCDES 2000 (ISBN: 951-758-408-3); (ISSN: 0356-9403); *Ed. S. Sarja*

PRO 15: Fifth RILEM Symposium on Fibre-Reinforced Concretes (FRC) - BEFIB'2000 (ISBN: 2-912143-18-7); *Eds. P. Rossi and G. Chanvillard*

PRO 16: Life Prediction and Management of Concrete Structures (ISBN: 2-912143-19-5); *Ed. D. Naus*

PRO 17: Shrinkage of Concrete – Shrinkage 2000 (ISBN: 2-912143-20-9); *Eds. V. Baroghel-Bouny and P.-C. Aïtcin*

PRO 18: Measurement and Interpretation of the On-Site Corrosion Rate (ISBN: 2-912143-21-7); *Eds. C. Andrade, C. Alonso, J. Fullea, J. Polimon and J. Rodriguez*

PRO 19: Testing and Modelling the Chloride Ingress into Concrete (ISBN: 2-912143-22-5); *Eds. C. Andrade and J. Kropp*

PRO 20: 1st International RILEM Workshop on Microbial Impacts on Building Materials (CD 02) (e-ISBN 978-2-35158-013-4); *Ed. M. Ribas Silva*

PRO 21: International RILEM Symposium on Connections between Steel and Concrete (ISBN: 2-912143-25-X); *Ed. R. Eligehausen*

PRO 22: International RILEM Symposium on Joints in Timber Structures (ISBN: 2-912143-28-4); *Eds. S. Aicher and H.-W. Reinhardt*

PRO 23: International RILEM Conference on Early Age Cracking in Cementitious Systems (ISBN: 2-912143-29-2); *Eds. K. Kovler and A. Bentur*

PRO 24: 2nd International RILEM Workshop on Frost Resistance of Concrete (ISBN: 2-912143-30-6); *Eds. M. J. Setzer, R. Auberg and H.-J. Keck*

PRO 25: International RILEM Workshop on Frost Damage in Concrete (ISBN: 2-912143-31-4); *Eds. D. J. Janssen, M. J. Setzer and M. B. Snyder*

PRO 26: International RILEM Workshop on On-Site Control and Evaluation of Masonry Structures (ISBN: 2-912143-34-9); *Eds. L. Binda and R. C. de Vekey*

PRO 27: International RILEM Symposium on Building Joint Sealants (CD03); *Ed. A. T. Wolf*

PRO 28: 6th International RILEM Symposium on Performance Testing and Evaluation of Bituminous Materials - PTEBM'03 (ISBN: 2-912143-35-7; e-ISBN: 978-2-912143-77-8); *Ed. M. N. Partl*

PRO 29: 2nd International RILEM Workshop on Life Prediction and Ageing Management of Concrete Structures (ISBN: 2-912143-36-5); *Ed. D. J. Naus*

PRO 30: 4th International RILEM Workshop on High Performance Fiber Reinforced Cement Composites - HPFRCC 4 (ISBN: 2-912143-37-3); *Eds. A. E. Naaman and H. W. Reinhardt*

PRO 31: International RILEM Workshop on Test and Design Methods for Steel Fibre Reinforced Concrete: Background and Experiences (ISBN: 2-912143-38-1); *Eds. B. Schnütgen and L. Vandewalle*

PRO 32: International Conference on Advances in Concrete and Structures 2 vol. (ISBN (set): 2-912143-41-1); *Eds. Ying-shu Yuan, Surendra P. Shah and Heng-lin Lü*

PRO 33: 3rd International Symposium on Self-Compacting Concrete (ISBN: 2-912143-42-X); *Eds. Ó. Wallevik and I. Níelsson*

PRO 34: International RILEM Conference on Microbial Impact on Building Materials (ISBN: 2-912143-43-8); *Ed. M. Ribas Silva*

PRO 35: International RILEM TC 186-ISA on Internal Sulfate Attack and Delayed Ettringite Formation (ISBN: 2-912143-44-6); *Eds. K. Scrivener and J. Skalny*

PRO 36: International RILEM Symposium on Concrete Science and Engineering – A Tribute to Arnon Bentur (ISBN: 2-912143-46-2); *Eds. K. Kovler, J. Marchand, S. Mindess and J. Weiss*

PRO 37: 5th International RILEM Conference on Cracking in Pavements – Mitigation, Risk Assessment and Prevention (ISBN: 2-912143-47-0); *Eds. C. Petit, I. Al-Qadi and A. Millien*

PRO 38: 3rd International RILEM Workshop on Testing and Modelling the Chloride Ingress into Concrete (ISBN: 2-912143-48-9); *Eds. C. Andrade and J. Kropp*

PRO 39: 6th International RILEM Symposium on Fibre-Reinforced Concretes - BEFIB 2004 (ISBN: 2-912143-51-9); *Eds. M. Di Prisco, R. Felicetti and G. A. Plizzari*

PRO 40: International RILEM Conference on the Use of Recycled Materials in Buildings and Structures (ISBN: 2-912143-52-7); *Eds. E. Vázquez, Ch. F. Hendriks and G. M. T. Janssen*

PRO 41: RILEM International Symposium on Environment-Conscious Materials and Systems for Sustainable Development (ISBN: 2-912143-55-1); *Eds. N. Kashino and Y. Ohama*

PRO 42: SCC'2005 - China: 1st International Symposium on Design, Performance and Use of Self-Consolidating Concrete (ISBN: 2-912143-61-6); *Eds. Zhiwu Yu, Caijun Shi, Kamal Henri Khayat and Youjun Xie*

PRO 43: International RILEM Workshop on Bonded Concrete Overlays (e-ISBN: 2-912143-83-7); *Eds. J. L. Granju and J. Silfwerbrand*

PRO 44: 2nd International RILEM Workshop on Microbial Impacts on Building Materials (CD11) (e-ISBN: 2-912143-84-5); *Ed. M. Ribas Silva*

PRO 45: 2nd International Symposium on Nanotechnology in Construction, Bilbao (ISBN: 2-912143-87-X); *Eds. Peter J. M. Bartos, Yolanda de Miguel and Antonio Porro*

PRO 46: ConcreteLife'06 - International RILEM-JCI Seminar on Concrete Durability and Service Life Planning: Curing, Crack Control, Performance in Harsh Environments (ISBN: 2-912143-89-6); *Ed. K. Kovler*

PRO 47: International RILEM Workshop on Performance Based Evaluation and Indicators for Concrete Durability (ISBN: 978-2-912143-95-2); *Eds. V. Baroghel-Bouny, C. Andrade, R. Torrent and K. Scrivener*

PRO 48: 1st International RILEM Symposium on Advances in Concrete through Science and Engineering (e-ISBN: 2-912143-92-6); *Eds. J. Weiss, K. Kovler, J. Marchand, and S. Mindess*

PRO 49: International RILEM Workshop on High Performance Fiber Reinforced Cementitious Composites in Structural Applications (ISBN: 2-912143-93-4); *Eds. G. Fischer and V.C. Li*

PRO 50: 1st International RILEM Symposium on Textile Reinforced Concrete (ISBN: 2-912143-97-7); *Eds. Josef Hegger, Wolfgang Brameshuber and Norbert Will*

PRO 51: 2nd International Symposium on Advances in Concrete through Science and Engineering (ISBN: 2-35158-003-6; e-ISBN: 2-35158-002-8); *Eds. J. Marchand, B. Bissonnette, R. Gagné, M. Jolin and F. Paradis*

PRO 52: Volume Changes of Hardening Concrete: Testing and Mitigation (ISBN: 2-35158-004-4; e-ISBN: 2-35158-005-2); *Eds. O. M. Jensen, P. Lura and K. Kovler*

PRO 53: High Performance Fiber Reinforced Cement Composites - HPFRCC5 (ISBN: 978-2-35158-046-2); *Eds. H. W. Reinhardt and A. E. Naaman*

PRO 54: 5th International RILEM Symposium on Self-Compacting Concrete (ISBN: 978-2-35158-047-9); *Eds. G. De Schutter and V. Boel*

PRO 55: International RILEM Symposium Photocatalysis, Environment and Construction Materials (ISBN: 978-2-35158-056-1); *Eds. P. Baglioni and L. Cassar*

PRO56: International RILEM Workshop on Integral Service Life Modelling of Concrete Structures (ISBN 978-2-35158-058-5); *Eds. R. M. Ferreira, J. Gulikers and C. Andrade*

PRO57: RILEM Workshop on Performance of cement-based materials in aggressive aqueous environments (e-ISBN: 978-2-35158-059-2); *Ed. N. De Belie*

PRO58: International RILEM Symposium on Concrete Modelling - CONMOD'08 (ISBN: 978-2-35158-060-8); *Eds. E. Schlangen and G. De Schutter*

PRO 59: International RILEM Conference on On Site Assessment of Concrete, Masonry and Timber Structures - SACoMaTiS 2008 (ISBN set: 978-2-35158-061-5); *Eds. L. Binda, M. di Prisco and R. Felicetti*

PRO 60: Seventh RILEM International Symposium on Fibre Reinforced Concrete: Design and Applications - BEFIB 2008 (ISBN: 978-2-35158-064-6); *Ed. R. Gettu*

PRO 61: 1st International Conference on Microstructure Related Durability of Cementitious Composites 2 vol., (ISBN: 978-2-35158-065-3); *Eds. W. Sun, K. van Breugel, C. Miao, G. Ye and H. Chen*

PRO 62: NSF/ RILEM Workshop: In-situ Evaluation of Historic Wood and Masonry Structures (e-ISBN: 978-2-35158-068-4); *Eds. B. Kasal, R. Anthony and M. Drdácký*

PRO 63: Concrete in Aggressive Aqueous Environments: Performance, Testing and Modelling, 2 vol., (ISBN: 978-2-35158-071-4); *Eds. M. G. Alexander and A. Bertron*

PRO 64: Long Term Performance of Cementitious Barriers and Reinforced Concrete in Nuclear Power Plants and Waste Management - NUCPERF 2009 (ISBN: 978-2-35158-072-1); *Eds. V. L'Hostis, R. Gens, C. Gallé*

PRO 65: Design Performance and Use of Self-consolidating Concrete - SCC'2009 (ISBN: 978-2-35158-073-8); *Eds. C. Shi, Z. Yu, K. H. Khayat and P. Yan*

PRO 66: 2nd International RILEM Workshop on Concrete Durability and Service Life Planning - ConcreteLife'09 (ISBN: 978-2-35158-074-5); *Ed. K. Kovler*

PRO 67: Repairs Mortars for Historic Masonry (e-ISBN: 978-2-35158-083-7); *Ed. C. Groot*

PRO 68: Proceedings of the 3rd International RILEM Symposium on 'Rheology of Cement Suspensions such as Fresh Concrete (ISBN 978-2-35158-091-2); *Eds. O. H. Wallevik, S. Kubens and S. Oesterheld*

PRO 69: 3rd International PhD Student Workshop on 'Modelling the Durability of Reinforced Concrete (ISBN: 978-2-35158-095-0); *Eds. R. M. Ferreira, J. Gulikers and C. Andrade*

PRO 70: 2nd International Conference on 'Service Life Design for Infrastructure' (ISBN set: 978-2-35158-096-7, e-ISBN: 978-2-35158-097-4); *Ed. K. van Breugel, G. Ye and Y. Yuan*

PRO 71: Advances in Civil Engineering Materials - The 50-year Teaching Anniversary of Prof. Sun Wei' (ISBN: 978-2-35158-098-1; e-ISBN: 978-2-35158-099-8); *Eds. C. Miao, G. Ye, and H. Chen*

PRO 72: First International Conference on 'Advances in Chemically-Activated Materials – CAM'2010' (2010), 264 pp, ISBN: 978-2-35158-101-8; e-ISBN: 978-2-35158-115-5, *Eds. Caijun Shi and Xiaodong Shen*

PRO 73: 2nd International Conference on 'Waste Engineering and Management - ICWEM 2010' (2010), 894 pp, ISBN: 978-2-35158-102-5; e-ISBN: 978-2-35158-103-2, *Eds. J. Zh. Xiao, Y. Zhang, M. S. Cheung and R. Chu*

PRO 74: International RILEM Conference on 'Use of Superabsorsorbent Polymers and Other New Addditives in Concrete' (2010) 374 pp., ISBN: 978-2-35158-104-9; e-ISBN: 978-2-35158-105-6;
Eds. O.M. Jensen, M.T. Hasholt, and S. Laustsen

PRO 75: International Conference on 'Material Science - 2nd ICTRC - Textile Reinforced Concrete - Theme 1' (2010) 436 pp., ISBN: 978-2-35158-106-3; e-ISBN: 978-2-35158-107-0; *Ed. W. Brameshuber*

PRO 76: International Conference on 'Material Science - HetMat - Modelling of Heterogeneous Materials - Theme 2' (2010) 255 pp., ISBN: 978-2-35158-108-7; e-ISBN: 978-2-35158-109-4; *Ed. W. Brameshuber*

PRO 77: International Conference on 'Material Science - AdIPoC - Additions Improving Properties of Concrete - Theme 3' (2010) 459 pp., ISBN: 978-2-35158-110-0; e-ISBN: 978-2-35158-111-7; *Ed. W. Brameshuber*

PRO 78: 2nd Historic Mortars Conference and RILEM TC 203-RHM Final Workshop – HMC2010 (2010) 1416 pp., e-ISBN: 978-2-35158-112-4; *Eds J. Válek, C. Groot, and J. J. Hughes*

PRO 79: International RILEM Conference on Advances in Construction Materials Through Science and Engineering (2011) 213 pp., e-ISBN: 978-2-35158-117-9; *Eds Christopher Leung and K.T. Wan*

PRO 80: 2nd International RILEM Conference on Concrete Spalling due to Fire Exposure (2011) 453 pp., ISBN: 978-2-35158-118-6, e-ISBN: 978-2-35158-119-3; *Eds E.A.B. Koenders and F. Dehn*

PRO 81: 2nd International RILEM Conference on Strain Hardening Cementitious Composites (SHCC2-Rio) (2011) 451 pp., ISBN: 978-2-35158-120-9, e-ISBN: 978-2-35158-121-6; *Eds R.D. Toledo Filho, F.A. Silva, E.A.B. Koenders and E.M.R. Fairbairn*

PRO 82: 2nd International RILEM Conference on Progress of Recycling in the Built Environment (2011) 507 pp., e-ISBN: 978-2-35158-122-3; *Eds V.M. John, E. Vazquez, S.C. Angulo and C. Ulsen*

PRO 83: 2nd International Conference on Microstructural-related Durability of Cementitious Composites (2012) 250 pp., ISBN: 978-2-35158-129-2; e-ISBN: 978-2-35158-123-0; *Eds G. Ye, K. van Breugel, W. Sun and C. Miao*

PRO 85: RILEM-JCI International Workshop on Crack Control of Mass Concrete and Related issues concerning Early-Age of Concrete Structures – ConCrack 3 – Control of Cracking in Concrete Structures 3 (2012) 237 pp., ISBN: 978-2-35158-125-4; e-ISBN: 978-2-35158-126-1; *Eds F. Toutlemonde and J.-M. Torrenti*

PRO 86: International Symposium on Life Cycle Assessment and Construction (2012) 414 pp., ISBN: 978-2-35158-127-8, e-ISBN: 978-2-35158-128-5; *Eds A. Ventura and C. de la Roche*

PRO 87: UHPFRC 2013 – RILEM-fib-AFGC International Symposium on Ultra-High Performance Fibre-Reinforced Concrete (2013), ISBN: 978-2-35158-130-8, e-ISBN: 978-2-35158-131-5; *Eds F. Toutlemonde*

PRO 88: 8th RILEM International Symposium on Fibre Reinforced Concrete (2012) 344 pp., ISBN: 978-2-35158-132-2, e-ISBN: 978-2-35158-133-9; *Eds Joaquim A.O. Barros*

PRO 89: RILEM International workshop on performance-based specification and control of concrete durability (2014) 678 pp, ISBN: 978-2-35158-135-3, e-ISBN: 978-2-35158-136-0; *Eds. D. Bjegović, H. Beushausen and M. Serdar*

PRO 90: 7th RILEM International Conference on Self-Compacting Concrete and of the 1st RILEM International Conference on Rheology and Processing of Construction Materials (2013) 396 pp, ISBN: 978-2-35158-137-7, e-ISBN: 978-2-35158-138-4; *Eds. Nicolas Roussel and Hela Bessaies-Bey*

PRO 91: CONMOD 2014 - RILEM International Symposium on Concrete Modelling (2014), ISBN: 978-2-35158-139-1; e-ISBN: 978-2-35158-140-7; *Eds. Kefei Li, Peiyu Yan and Rongwei Yang*

PRO 92: CAM 2014 - 2nd International Conference on advances in chemically-activated materials (2014) 392 pp., ISBN: 978-2-35158-141-4; e-ISBN: 978-2-35158-142-1; *Eds. Caijun Shi and Xiadong Shen*

PRO 93: SCC 2014 - 3rd International Symposium on Design, Performance and Use of Self-Consolidating Concrete (2014) 438 pp., ISBN: 978-2-35158-143-8; e-ISBN: 978-2-35158-144-5; *Eds. Caijun Shi, Zhihua Ou, Kamal H. Khayat*

PRO 94 (online version): HPFRCC-7 - 7th RILEM conference on High performance fiber reinforced cement composites (2015), e-ISBN: 978-2-35158-146-9; *Eds. H.W. Reinhardt, G.J. Parra-Montesinos, H. Garrecht*

PRO 95: International RILEM Conference on Application of superabsorbent polymers and other new admixtures in concrete construction (2014), ISBN: 978-2-35158-147-6; e-ISBN: 978-2-35158-148-3; *Eds. Viktor Mechtcherine, Christof Schroefl*

PRO 96 (online version): XIII DBMC: XIII International Conference on Durability of Building Materials and Components (2015), e-ISBN: 978-2-35158-149-0; *Eds. M. Quattrone, V.M. John*

PRO 97: SHCC3 – 3rd International RILEM Conference on Strain Hardening Cementitious Composites (2014), ISBN: 978-2-35158-150-6; e-ISBN: 978-2-35158-151-3; *Eds. E. Schlangen, M.G. Sierra Beltran, M. Lukovic, G. Ye*

PRO 98: FERRO-11 – 11th International Symposium on Ferrocement and 3rd ICTRC - International Conference on Textile Reinforced Concrete (2015), ISBN: 978-2-35158-152-0; e-ISBN: 978-2-35158-153-7; *Ed. W. Brameshuber*

PRO 99 (online version): ICBBM 2015 - 1st International Conference on Bio-Based Building Materials (2015), e-ISBN: 978-2-35158-154-4; *Eds. S. Amziane, M. Sonebi*

PRO 100: SCC16 - RILEM Self-Consolidating Concrete Conference (2016)**,** ISBN: 978-2-35158-156-8; e-ISBN: 978-2-35158-157-5

PRO 101 (online version): III Progress of Recycling in the Built Environment (2015), e-ISBN: 978-2-35158-158-2; *Eds I. Martins, C. Ulsen and S. C. Angulo*

PRO 102 (online version): RILEM Conference on Microorganisms-Cementitious Materials Interactions (2016), e-ISBN: 978-2-35158-160-5; *Eds. Alexandra Bertron, Henk Jonkers, Virginie Wiktor*

PRO 103 (online version): ACESC'16 - Advances in Civil Engineering and Sustainable Construction (2016), e-ISBN: 978-2-35158-161-2

PRO 104 (online version): SSCS'2015 - Numerical Modeling - Strategies for Sustainable Concrete Structures (2015), e-ISBN: 978-2-35158-162-9

PRO 105: 1st International Conference on UHPC Materials and Structures (2016), ISBN: 978-2-35158-164-3, e-ISBN: 978-2-35158-165-0

PRO 106: AFGC-ACI-fib-RILEM International Conference on Ultra-High-Performance Fibre-Reinforced Concrete – UHPFRC 2017 (2017), ISBN: 978-2-35158-166-7, e-ISBN: 978-2-35158-167-4; *Eds. François Toutlemonde & Jacques Resplendino*

PRO 107 (online version): XIV DBMC – 14th International Conference on Durability of Building Materials and Components (2017), e-ISBN: 978-2-35158-159-9; *Eds. Geert De Schutter, Nele De Belie, Arnold Janssens, Nathan Van Den Bossche*

PRO 108: MSSCE 2016 - Innovation of Teaching in Materials and Structures (2016), ISBN: 978-2-35158-178-0, e-ISBN: 978-2-35158-179-7; *Ed. Per Goltermann*

PRO 109 (two volumes): MSSCE 2016 - Service Life of Cement-Based Materials and Structures (2016), ISBN Vol. 1: 978-2-35158-170-4, Vol. 2: 978-2-35158-171-4, Set Vol. 1&2: 978-2-35158-172-8, e-ISBN : 978-2-35158-173-5; *Eds. Miguel Azenha, Ivan Gabrijel, Dirk Schlicke, Terje Kanstad and Ole Mejlhede Jensen*

PRO 110: MSSCE 2016 - Historical Masonry (2016), ISBN: 978-2-35158-178-0, e-ISBN: 978-2-35158-179-7; *Eds. Inge Rörig-Dalgaard and Ioannis Ioannou*

PRO 111: MSSCE 2016 - Electrochemistry in Civil Engineering (2016), ISBN: 978-2-35158-176-6, e-ISBN: 978-2-35158-177-3; *Ed. Lisbeth M. Ottosen*

PRO 112: MSSCE 2016 - Moisture in Materials and Structures (2016), ISBN: 978-2-35158-178-0, e-ISBN: 978-2-35158-179-7; *Eds. Kurt Kielsgaard Hansen, Carsten Rode and Lars-Olof Nilsson*

PRO 113: MSSCE 2016 - Concrete with Supplementary Cementitious Materials (2016), ISBN: 978-2-35158-178-0, e-ISBN: 978-2-35158-179-7; *Eds. Ole Mejlhede Jensen, Konstantin Kovler and Nele De Belie*

PRO 114: MSSCE 2016 - Frost Action in Concrete (2016), ISBN: 978-2-35158-182-7, e-ISBN: 978-2-35158-183-4; *Eds. Marianne Tange Hasholt, Katja Fridh and R. Doug Hooton*

PRO 115: MSSCE 2016 - Fresh Concrete (2016), ISBN: 978-2-35158-184-1, e-ISBN: 978-2-35158-185-8; *Eds. Lars N. Thrane, Claus Pade, Oldrich Svec and Nicolas Roussel*

PRO 116: BEFIB 2016 – 9th RILEM International Symposium on Fiber Reinforced Concrete (2016), ISBN: 978-2-35158-187-2, e-ISBN: 978-2-35158-186-5;

PRO 117: 3rd International RILEM Conference on Microstructure Related Durability of Cementitious Composites (2016), ISBN: 978-2-35158-188-9, e-ISBN: 978-2-35158-189-6; *Eds. Changwen Miao, Wei Sun, Jiaping Liu, Huisu Chen, Guang Ye and Klaas van Breugel*

PRO 118 (4 volumes): International Conference on Advances in Construction Materials and Systems (2017), ISBN Set: 978-2-35158-190-2, Vol. 1: 978-2-35158-193-3, Vol. 2: 978-2-35158-194-0, Vol. 3: ISBN:978-2-35158-195-7, Vol. 4: ISBN:978-2-35158-196-4, e-ISBN: 978-2-35158-191-9; *Ed. Manu Santhanam*

PRO 119 (online version): ICBBM 2017 - Second International RILEM Conference on Bio-based Building Materials, (2017), e-ISBN: 978-2-35158-192-6; *Ed. Sofiane Amziane*

PRO 120 (2 volumes): EAC-02 - 2nd International RILEM/COST Conference on Early Age Cracking and Serviceability in Cement-based Materials and Structures, (2017), Vol. 1: 978-2-35158-199-5, Vol. 2: 978-2-35158-200-8, Set: 978-2-35158-197-1, e-ISBN: 978-2-35158-198-8; *Eds. Stéphanie Staquet and Dimitrios Aggelis*

RILEM REPORTS (REP)

Report 19: Considerations for Use in Managing the Aging of Nuclear Power Plant Concrete Structures (ISBN: 2-912143-07-1); *Ed. D. J. Naus*

Report 20: Engineering and Transport Properties of the Interfacial Transition Zone in Cementitious Composites (ISBN: 2-912143-08-X); *Eds. M. G. Alexander, G. Arliguie, G. Ballivy, A. Bentur and J. Marchand*

Report 21: Durability of Building Sealants (ISBN: 2-912143-12-8); *Ed. A. T. Wolf*

Report 22: Sustainable Raw Materials - Construction and Demolition Waste (ISBN: 2-912143-17-9); *Eds. C. F. Hendriks and H. S. Pietersen*

Report 23: Self-Compacting Concrete state-of-the-art report (ISBN: 2-912143-23-3); *Eds. Å. Skarendahl and Ö. Petersson*

Report 24: Workability and Rheology of Fresh Concrete: Compendium of Tests (ISBN: 2-912143-32-2); *Eds. P. J. M. Bartos, M. Sonebi and A. K. Tamimi*

Report 25: Early Age Cracking in Cementitious Systems (ISBN: 2-912143-33-0); *Ed. A. Bentur*

Report 26: Towards Sustainable Roofing (Joint Committee CIB/RILEM) (CD 07) (e-ISBN 978-2-912143-65-5); *Eds. Thomas W. Hutchinson and Keith Roberts*

Report 27: Condition Assessment of Roofs (Joint Committee CIB/RILEM) (CD 08) (e-ISBN 978-2-912143-66-2); *Ed. CIB W 83/RILEM TC166-RMS*

Report 28: Final report of RILEM TC 167-COM 'Characterisation of Old Mortars with Respect to Their Repair (ISBN: 978-2-912143-56-3); *Eds. C. Groot, G. Ashall and J. Hughes*

Report 29: Pavement Performance Prediction and Evaluation (PPPE): Interlaboratory Tests (e-ISBN: 2-912143-68-3); *Eds. M. Partl and H. Piber*

Report 30: Final Report of RILEM TC 198-URM 'Use of Recycled Materials' (ISBN: 2-912143-82-9; e-ISBN: 2-912143-69-1); *Eds. Ch. F. Hendriks, G. M. T. Janssen and E. Vázquez*

Report 31: Final Report of RILEM TC 185-ATC 'Advanced testing of cement-based materials during setting and hardening' (ISBN: 2-912143-81-0; e-ISBN: 2-912143-70-5); *Eds. H. W. Reinhardt and C. U. Grosse*

Report 32: Probabilistic Assessment of Existing Structures. A JCSS publication (ISBN 2-912143-24-1); *Ed. D. Diamantidis*

Report 33: State-of-the-Art Report of RILEM Technical Committee TC 184-IFE 'Industrial Floors' (ISBN 2-35158-006-0); *Ed. P. Seidler*

Report 34: Report of RILEM Technical Committee TC 147-FMB 'Fracture mechanics applications to anchorage and bond' Tension of Reinforced Concrete Prisms – Round Robin Analysis and Tests on Bond (e-ISBN 2-912143-91-8); *Eds. L. Elfgren and K. Noghabai*

Report 35: Final Report of RILEM Technical Committee TC 188-CSC 'Casting of Self Compacting Concrete' (ISBN 2-35158-001-X; e-ISBN: 2-912143-98-5); *Eds. Å. Skarendahl and P. Billberg*

Report 36: State-of-the-Art Report of RILEM Technical Committee TC 201-TRC 'Textile Reinforced Concrete' (ISBN 2-912143-99-3); *Ed. W. Brameshuber*

Report 37: State-of-the-Art Report of RILEM Technical Committee TC 192-ECM 'Environment-conscious construction materials and systems' (ISBN: 978-2-35158-053-0); *Eds. N. Kashino, D. Van Gemert and K. Imamoto*

Report 38: State-of-the-Art Report of RILEM Technical Committee TC 205-DSC 'Durability of Self-Compacting Concrete' (ISBN: 978-2-35158-048-6); *Eds. G. De Schutter and K. Audenaert*

Report 39: Final Report of RILEM Technical Committee TC 187-SOC 'Experimental determination of the stress-crack opening curve for concrete in tension' (ISBN 978-2-35158-049-3); *Ed. J. Planas*

Report 40: State-of-the-Art Report of RILEM Technical Committee TC 189-NEC 'Non-Destructive Evaluation of the Penetrability and Thickness of the Concrete Cover' (ISBN 978-2-35158-054-7);
Eds. R. Torrent and L. Fernández Luco

Report 41: State-of-the-Art Report of RILEM Technical Committee TC 196-ICC 'Internal Curing of Concrete' (ISBN 978-2-35158-009-7); *Eds. K. Kovler and O. M. Jensen*

Report 42: 'Acoustic Emission and Related Non-destructive Evaluation Techniques for Crack Detection and Damage Evaluation in Concrete' - Final Report of RILEM Technical Committee 212-ACD (e-ISBN: 978-2-35158-100-1); *Ed. M. Ohtsu*

Report 45: Repair Mortars for Historic Masonry - State-of-the-Art Report of RILEM Technical Committee TC 203-RHM (e-ISBN: 978-2-35158-163-6); *Eds. Paul Maurenbrecher and Caspar Groot*

Report 46: Surface delamination of concrete industrial floors and other durability related aspects guide - Report of RILEM Technical Committee TC 268-SIF (e-ISBN: 978-2-35158-201-5); *Ed. Valérie Pollet*

Conference Chairs

Miguel Azenha, Dirk Schlicke

Scientific Committee Chairs

Farid Benboudjema, Agnieszka Jędrzejewska

National Organizing Committee

Paulo Lobo, José Sena Cruz, Eduardo Júlio, Rui Faria, Manuel Pipa, Romeu Vicente

COST Organizing Committee

Violeta Bokan-Bosiljkov, Laurie Lacarrière, Terje Kanstad, Sreejith Nanukuttan, Emmanuel Rozière, Marijana Serdar, Stéphanie Staquet, François Toutlemonde, Mateusz Wyrzykowski

Scientific Committee

Farid Benboudjema (Chair)
Agnieszka Jędrzejewska (Chair)
Ouali Amiri
Sofiane Amziane
Shingo Asamoto
Miguel Azenha
Nele de Belie
Violeta Bokan Bosiljkov
Alexandra Bourdot
Matthieu Briffaut
Tomo Cerovšek
Özlem Cizer
Gianluca Cusatis
Aveline Darquennes
Szymon Dawczyński
Eduardo Fairbairn
Rui Faria
Ivan Gabrijel
Erez Gal
Dariusz Gawin
Ole Jensen
Joachim Juhart
Terje Kanstad
Eduardus Koenders
Barbara Klemczak
Laurie Lacarrière
Paulo B. Lourenço
Ippei Maruyama
Kyuichi Maruyama
Enrico Masoero
Hadi Mazaheripour
Sreejith Nanukuttan
Małgorzata Pająk
Arnaud Perrot
Bernhard Pichler
Manuel Pipa
John Provis
Vlastimir Radonjanin
Marta Roig
Emmanuel Rozière
Mercedes Sanchez Moreno
Ryoichi Sato
José Sena-Cruz
Dirk Schlicke
Geert De Schutter
Giuseppe Sciumè
Marijana Serdar
Carlos Serra
Ioannis Sfikas
Paulo Silva Lobo
Mohammed Sonebi
Carlos Sousa
Tayfun Altuğ Söylev
Maria Stefanidou
Stéphanie Staquet
Aljoša Šajna
Vít Šmilauer
Luping Tang
Katrin Turner
Jean-Michel Torrenti
François Toutlemonde
Jörg F. Unger
Neven Ukrainczyk
Mateusz Wyrzykowski
Guang Ye
Ismail Yurtdas
Xiangming Zhou
Mariusz Zych

Preface

The focus of the conference is set to communicating, discussing and arousing progress in research, development and application of Cement-based Materials and Structural Concrete, which have been attained through combination of expertise from distinct fields of knowledge. Indeed, in the words of Federico Capasso, a renowned Physicist who was one of the inventors of the quantum cascade laser:

> "*... we must not think of science in a disciplinary way, by making boxes. Nature does not know what physics, chemistry or biology is! It is a question of putting an end to the positivist philosophy of Auguste Comte, fortunately in decline of speed, which classified the disciplines and despised the experimental activity.*"

The intent of this conference was therefore to provide added value through collaboration and by bringing together researchers and practitioners with similar views in regard to interdisciplinary approaches in the fields of Cement-based Materials and Structural Concrete: it is about **Syner**gizing expertise on the ultimate goal of Structural Conc**Crete**, hence the acronym **SynerCrete**, was chosen for the conference. Exciting fields of research such as performance-based design, 3D modelling for analysis/design, Building Information Modelling and even robotics (e.g. digital fabrication or robotics design) were included, while retaining focus on multi-scale approaches at time and spatial levels.

SynerCrete'18 also marks the end of COST Action TU1404 "Towards the next generation of standards for service life of cement-based materials and structures" (www.tu1404.eu), offering a final forum to the discussions raised during the funded period of the Action, that started 4 years ago in 2014. The conference is an opportunity for the 304 COST Action members to deepen their collaboration and to focus on activities that allow the continuation of the networking which was established by the Action. A sense of accomplishment is felt by all the members of the Action, in the view of the important achievements of networking tools that were brought about by the extended Round Robin Testing Programme (RRT+), the Numerical Benchmarking Activities and 24 Short Term Scientific Missions (STSMs). Indeed, a remarkable number of papers that have been published in the two volumes of these Conference Proceedings are directly a result of one of the aforementioned networking tools.

The conference has consisted of 8 key-note speakers and 180 regular papers presented over 3 days. It is also relevant to emphasize the collaboration of another COST Action in SynerCrete: COST Action CA15202 "Self-healing As preventive Repair of COncrete Structures – SARCOS", which has an important contribution to the purposes of COST TU1404.

A further remark in regard to the wide international institutional support that this conference attained, is about the direct support of RILEM, fib, JCI and ACI. Specifically, with regard to the Japanese Concrete Institute, a mention is given to the special session dedicated to the most recent version of "JCI Guidelines for Control of Cracking of Mass Concrete", as it was indeed one of the most inspiring documents that influenced the genesis of COST Action TU1404.

A final word is given in regard to the location of the conference which combines implicit symbolisms. Firstly, this is the only event of COST Action TU1404 taking place in Portugal, which is the home country of the Grant Holder and Chairman of the Action. Secondly, the conference venue is the island of Madeira, therefore not in mainland Portugal, putting attention to one of the remotest regions of Europe, officially classified as one of the eight ultra-peripheral regions of the European Union.

Miguel Azenha **Dirk Schlicke** **Farid Benboudjema** **Agnieszka Jędrzejewska**

October 2018, Funchal, Portugal

Acknowledgements

This publication is based upon work from COST Action TU1404 'Towards the next generation of standards for service life of cement-based materials and structures', supported by COST (European Cooperation in Science and Technology).

COST (European Cooperation in Science and Technology) is a pan-European intergovernmental framework. Its mission is to enable break-through scientific and technological developments leading to new concepts and products and thereby contribute to strengthening Europe's research and innovation capacities. It allows researchers, engineers and scholars to jointly develop their own ideas and take new initiatives across all fields of science and technology, while promoting multi- and interdisciplinary approaches. COST aims at fostering a better integration of less research intensive countries to the knowledge hubs of the European Research Area. The COST Association, an International not-for-profit Association under Belgian Law, integrates all management, governing and administrative functions necessary for the operation of the framework. The COST Association has currently 37 Member Countries.

Funded by the Horizon 2020 Framework Programme
of the European Union

www.tu1404.eu
www.cost.eu

VOLUME 1

KEYNOTE LECTURES

COST ACTION TU1404 - RRT+, NUMERICAL BENCHMARKING AND RECOMMENDATIONS

CONCRETE TECHNOLOGY AND ADVANCED MATERIAL TESTING

FIBRE-REINFORCED CONCRETE AND NON-METALLIC REINFORCEMENT

SELF-HEALING AND REPAIR OF CONCRETE STRUCTURES (COST CA15202 - SARCOS)

MULTI-PHYSICS SIMULATION

AND

STRUCTURAL DESIGN

SynerCrete'18 International Conference on Interdisciplinary Approaches
for Cement-based Materials and Structural Concrete
24-26 October 2018, Funchal, Madeira Island, Portugal

CONCRETE CASTING AND LIFETIME CONDITIONS IMPACT ON HIGH TEMPERATURE RESISTANCE

Giuseppe Sciumè [(1)], Stefano Dal Pont [(2)], Dorjan Dauti [(2)]

(1) I2M – Institut de Mécanique et d'Ingénierie, Université de Bordeaux, France
(2) 3SR – Laboratoire Sols, Solides, Structures, Risques, Université Grenoble Alpes, France

Abstract
In this paper the impact of early age and service-life conditions on high temperature behaviour is analysed and shown for a 60-cm heated wall. Numerical experiments are performed using a porous media model, coupling dependencies of material parameters on hydration advancement degree. Concrete hydration at early age and dehydration/degradation due to high temperature exposure are here treated by means of an original unified approach.
The mathematical model is based on general conservation equations of mass, energy and linear momentum. The explicit introduction of the stoichiometric model of Powers allows deriving some of the needed closure relationship. A new constitutive model is also proposed for the desorption isotherms.

1. Introduction

Despite two thousand years of history, concrete is yet among the most complex materials to be understood and modelled. Advances in concrete mixtures (current concretes may include non-conventional binders, additives, low weight aggregates, polymer fibres, etc.) are certainly one cause of such complexity. However the main reason resides in the mesoscale and microscopic structure of concrete: the connection between coarse aggregates and cement paste strongly affects the material behaviour and often constitutes the "weak link" where failure initiates. Furthermore cement paste has a porous and chemically active nature with capillary and adsorbed water strongly affecting its global behaviour (shrinkage, creep, etc.).
The presence of water and moisture transport within the pores give to the time dimension a critical importance for prediction of concrete performance; hence, the knowledge of casting and environmental conditions during service-life of the structure is needed for a predictive

simulation of concrete response when submitted to extreme loads and/or hard environmental conditions.
While the awareness of early age and curing conditions is often not important, it becomes critical point for massive structures. Cement hydration is a thermo-activated reaction and therefore the rise of temperature, not well dissipated in mass concrete, increases the rate of reaction which may become very important inducing a temperature gradient up to 40-60 °C (see [1]). The positive thermal strain associated with heating is very often restrained by an existing substrate, or self-restrained due to the cast geometry, leading to compressive stresses. Then, during the subsequent cooling phase the volume of concrete decreases progressively and also this compressive stress decreases. However, due to the increased stiffness of the material with hydration, the stress in certain parts of the structure is transformed to traction and may induce diffuse cracking or traversing localized cracks. These phenomena are well known and concern civil engineering structures of safety and strategical relevance such as concrete dams, reactor's containments in nuclear power plants and tunnels.
In this work, it is shown that state-of-the-art models ([2,3]), can be further formally improved introducing stoichiometric relations of Powers and treating hydration and high-temperature degradation in a unified way. The resulting mathematical model has been implemented in the finite element software Cast3M (http://www-cast3m.cea.fr) and allows to naturally compute solutions about high temperature resistance accounting for concrete history: early age and aging.

2. The multiphase model

Concrete is here modelled as a multiphase material consisting of the solid phase, *s*, the liquid phase, *l*, and the gaseous phase, *g*. The solid phase consists of fine and coarse aggregates and cement paste, the liquid phase is liquid water whereas the gaseous phase is a binary mixture of water vapour and dry air.
At each macroscopic point the three phases coexist and their volume fractions, indicated as ϕ^{α} ($\alpha = s, l, g$) have to satisfy the following constraint:

$$\phi^{s} + \phi^{l} + \phi^{g} = 1 \tag{1}$$

2.1 The unified hydration de-hydration model

Cement hydration is a thermo-activated process. In other words, hydration's rate of reaction increases as temperature increases during concrete hardening. On the other hand, during a fire accident when temperature increases over a certain threshold, hydrated products release the chemically bound water and the cement paste loses gradually mechanical properties attained with hydration. Such process is concrete dehydration induced by high temperature exposure. To take into account the effect of high temperature an internal variable, here indicated as *F* (for fire dehydration), is considered. The equivalent degree of reaction, is then given as:

$$\tilde{\Gamma} = \Gamma(1 - F) \tag{2}$$

where Γ is the advancement of hydration degree. Most of parameters of the computational model (porosity, permeability, Young's modulus, etc.) depends on $\tilde{\Gamma}$. *F*(T) is a continuous function growing from 0 to 1 with temperature [2]. Deriving Eq. (2) with time gives:

$$\frac{D^s\tilde{\Gamma}}{Dt} = (1-F)\frac{D^s\Gamma}{Dt} - \Gamma\frac{D^s\mathrm{F}}{Dt} \tag{3}$$

Considering that fire damaging is irreversible, a non-negative increment of F(T) is imposed.

2.2 Concrete stoichiometry

The adoption of Powers model allows estimating the amount of water chemically combined after the complete hydration of cement in the mix. In particular simple calculations give:

$$m_\infty = 0.228 c \xi_\infty \tag{4}$$

where *c* is the cement content in the mix, and ξ_∞ is the fraction of cement hydrated when at the end (ξ_∞ depends on the water-to-cement ratio) [4].
Powers model allows also obtaining the evolution of porosity, ϕ, which reads:

$$\phi = \phi_\infty + a_\phi\left(1-\tilde{\Gamma}\right) \tag{5}$$

with ϕ_∞ the final porosity, and a_ϕ a constant coefficient; both parameters can be calculated from data about the concrete mix as explained in [1].

2.3 Conservation equations

The mathematical model is governed by mass, momentum and energy conservation equations of considered phases and gas species. From these, introducing some assumptions as detailed in [2] a system of four independent equations is derived and then solved numerically:

- the mass conservation equation of dry air;
- the mass conservation equation of water species (liquid water + water vapour);
- the enthalpy conservation equation;
- the momentum conservation equation for the multiphase system.

It can be shown that Eq. (4) and (5) allow deriving naturally and explicitly some of terms of the reference formulation [2]; these terms must otherwise be identified experimentally or assumed from literature.

2.4 The pressure-saturation relationship

A new equation is also proposed for the desorption isotherm. This equation accounts for modifications of concrete microstructure and evolution of water surface tension due to temperature. Differently from equation proposed in [2], this law is less intricate, and allows describing in a unified way effect of hydration/dehydration. Furthermore, effect of fire-induced dehydration on retention curve is properly accounted as irreversible since depending on $\tilde{\Gamma}$ (and not on T as in [2]). The developed relationship is an extension to high temperature of the constitutive model proposed in [1, 5] by the first author for young concrete.

3. Low rate heating (2 K/min) for a 60-cm wall

A 1-dimensional case is simulated numerically to analyse and quantify the impact of age on the computed results. A 60-cm wall exposed from both sides to heating is modelled. Due to symmetry only one half of the wall is considered and discretized in the FE code.
The concrete is the OC adopted for the COST Action TU1404 benchmark [6], its water to cement ratio is of 0.45 (other details about the composition are available in [6]). Data provided by benchmark organisers are assumed to identify most of model parameters; the remaining ones are assumed from literature [2] and author previous works on similar concretes [3, 5, 7].

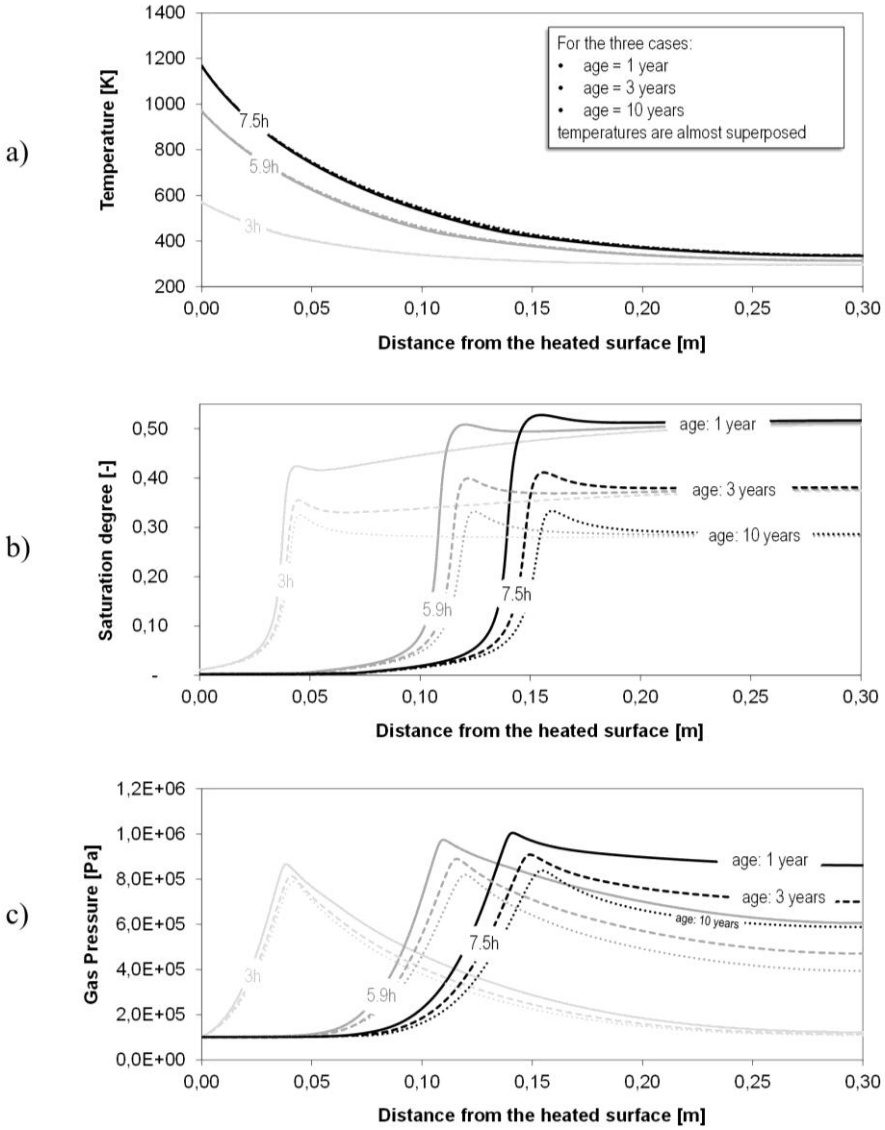

Figure 1: a) Temperature, b) saturation and c) gas pressure in a concrete wall for 3 different heat exposure times (3h, 5.9h, 7.5h) highlighting the impact of the concrete age (1 year, 3 years, 10 years).

3.1 Test description and assumed boundary conditions

The assumed heating conditions are the same as in [2]. However this time the test is more complex as the wall history, early age and aging, is also considered.
Three phases are modelled:

- Phase 1, *very early age* – from casting to 3 days: the adiabatic calorimetry test provided in [6] is used to identify hydration parameters. The wall is assumed sealed (no mass exchange) while a convective model is assumed for thermal exchange (h_t = 10 W/(m^{2}K)). Initial and external temperatures are assumed of 22°C.

- Phase 2, *drying-aging* – from 3 days to considered "age time": at 3 days the wall starts drying (*e.g.* due to formwork removing) assuming the following convective model:

$$\mathbf{q}^l = \beta_c\left(\rho_{surf}^{wg} - \rho_{ext}^{wg}\right)\mathbf{n} \tag{6}$$

  with ρ_{surf}^{wg} and ρ_{ext}^{wg} surface and external density of the water vapour respectively, and β_c = 0.002 m/s; the external relative humidity is assumed constant and equal to 50%. Thermal exchange is also convective with the same convective coefficient of phase 1. Three aging times are considered: case-1) one year; case-2) three years; case-3) 10 years.

- Phase 3, *fire accident* – 8 hours of heating from "age time": results of the three cases of phase 2 ("age time" = 1, 3 and 10 years), are assumed as starting condition for simulation of high temperature heating. External temperature is imposed as a linear function of time with a heating rate of 2 K/min: so external temperature change from 295.15 K (22°C) to 1255.15 K (982°C) after 8 hours of heating.
  Surface thermal exchange is convective-radiative with convection coefficient equal to h_t = 20 W/(m^{2}K) and emissivity ε = 0.9 .
  Moisture exchange at the heated surface is assumed convective as in phase 2 but this time the convection coefficient is ten times higher (β_c = 0.02 m/s), and the partial pressure of vapour is imposed, p^{gw} = 1300 Pa, instead of prescribing the relative humidity.

3.2 Numerical results

Results for temperature, saturation degree and gas pressure are plotted in Fig. 1 for the three modelled cases: the graphs represent spatial evolution of such variables after 3 hours, 5.9 hours and 7.5 hours of heating. The chosen time stations are the same as in the numerical analyses of [2]; indeed their numerical results have been compared with the shown ones. Actually, such comparison is only qualitative due to the fact the simulations deal with different concrete mixes. Nevertheless, it has been useful to assess the impact of the modification introduced in the constitutive laws.
As one can observe in Fig. 1.a, age has no impact on temperature in the wall, i.e. the lines corresponding to the three cases are almost superposed. Nevertheless, age has a significative impact on the saturation profiles and desaturation fronts, as shown in Fig. 1.b. When heating starts, initial condition in term of saturation degree is very different depending on the concrete

age: after 10 years of drying the hygral equilibrium is reached while at 1 year the saturation degree varies from 0.5 (in the centre) to 0.28 (at the drying surface) following a typical parabolic drying profile. Even if initial pressure field is the same, gas pressure results are different for the three considered concrete ages (see Fig. 1.c). In particular it is observed that the "younger" the concrete, the higher will be gas pressure peaks. This is due to previous commented differences on saturation degree which influence gas permeability and gas pressure. A difference of almost 20% can be observed after 7.5 hours between peaks obtained for the 1-year concrete and the 10-year one.

4. Conclusions

A thermo-hydro-mechanical model describing concrete behaviour from casting until accident conditions has been implemented and used in this study for the investigation of the impact of concrete age on the high temperature behaviour of the material. A novel approach expressing the constitutive laws at high temperature such as porosity, permeability and sorption isotherms with respect to the hydration degree is presented. The results have shown that different concrete age induces different conditions, notably a different saturation field, when the high temperature load is initiated. This has a direct influence on the saturation and gas pressure fields developing during the fire incident. The combined "early age – high temperature" model is a powerful tool for investigating and shedding light on the often-random behaviour of concrete samples at high temperature observed experimentally. Such behaviour could be linked with the varying saturation field when concrete is exposed to heat.

References

[1] Sciumè, G., Thermo-hygro-chemo-mechanical model of concrete at early ages and its extension to tumor growth numerical analysis, PhD Thesis, École normale supérieure de Cachan - ENS Cachan (2013)
[2] Gawin, D. et al, What physical phenomena can be neglected when modelling concrete at high temperature? A comparative study. Part 1: Physical phenomena and mathematical model, International Journal of Solids and Structures, 48 (2011), 1927-1944
[3] Dal Pont, S. et al, A multiphase thermo-hydro-mechanical model for concrete at high temperatures - finite element implementation and validation under LOCA load. Nuclear Eng. and Design 237(20) (2007), 2137-2150
[4] Mills, R.H., Factors Influencing Cessation of Hydration in Water Cured Cement Pastes, (1966), 406-424
[5] Sciumè, G. et al, A multiphysics model for concrete at early age applied to repairs problems, Engineering Structures 57 (2013), 374-387
[6] Jędrzejewska, A. et al, COST TU1404 benchmark on macroscopic modelling of concrete and concrete structures at early age: Proof-of-concept stage, Constr Build Mater 174 (2018) 173-189
[7] Dauti, D. et al, Modelling Concrete Exposed to High Temperature: Impact of Dehydration and Retention Curves on Moisture Migration, International Journal for Numerical and Analytical Methods in Geomechanics 42(13) (2018) 1516-1530

SynerCrete'18 International Conference on Interdisciplinary Approaches
for Cement-based Materials and Structural Concrete
24-26 October 2018, Funchal, Madeira Island, Portugal

DAMAGE INVESTIGATION AND ANALYTICAL INVESTIGATION OF PILOTIS-TYPE RC BUILDING IN THE 2016 KUMAMOTO EARTHQUAKE

Masaru Shimazu [(1)]

(1) Sojo University, Kumamoto, Japan

Abstract
This research carried out a static elastoplastic analysis of a Pilotis-type reinforced concrete building that collapsed in the 2016 Kumamoto earthquake. It examined the usability of these types of analyses. Also, it conducted a damage survey and executed a static three-dimensional frame analysis with the aim of unravelling the collapse mechanism of the damaged building. It turned out that the analysis is actually effective.

1. Introduction

The Pilotis structure is widespread as a way to utilize space effectively. This type of structure is expected to be used for a number of buildings also in the future. But the Pilotis floor has a low inter-story stiffness since it is made of independent columns. In the event of a severe earthquake, therefore, the damage is likely to concentrate on this type of building, causing it to fall apart. Many RC-made Pilotis structures are reported to have fallen to pieces or been devastated in the wake of the 2016 Mw 7.0 Kumamoto earthquake [1]. These reports effectively warned against the danger of RC-made Pilotis structures.
This research reports on the results of a survey of Pilotis-type RC-made structures that sustained damage in the 2016 Kumamoto earthquake. The research also carries out an elastoplastic analysis of destroyed buildings and compares the damage status with the analysis results. It examines the usability of a static three-dimensional frame analysis as a way to evaluate the seismic capacity of conventional buildings and check the mechanism of damaged buildings falling down.

2. The overview and damage of buildings

2.1 The overview and buildings

The main target of the survey in this research was the Pilotis-type 7-story RC-made building that served as a middle scale dwelling complex in Kumamoto, which collapsed to pieces in the Kumamoto earthquake during the early hours of April 16, 2016. By the way, the building was constructed in 1974.

Figure 1 shows the first-floor plan view while Fig. 2 gives the second-floor plan view. The third to sixth floors carry the same plan views as the second floor. The seventh-floor plan view is unknown. Hereafter, the column and beam positions are shown by codes as in respective floor plans. For example, the No.4 column on aisle C on the first floor is described as 1C4. The height of the second floor is 3,000 millimeters while that of the third to seventh floor is 2,700 millimeters. The building takes on a planar shape that looks like the alphabetic character L. The first floor includes the staircase, retail stores, and parking lots. The second to seventh floors are used for dwelling.

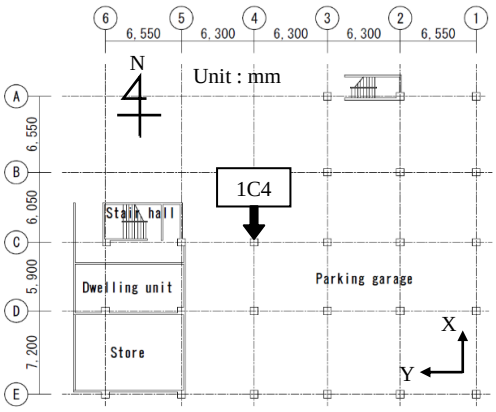

Figure 1: 1F.

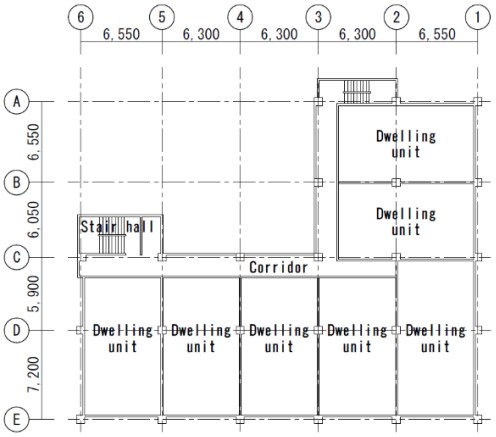

Figure 2: 2F.

Figure 3 shows cross-sectional views of the first-floor columns and the second-floor beams. The column bar is 8-D29 and the column stirrup is ϕ12@100mm. The section size and the location of the reinforcement in the column are measured by convex rule. Since the measurement is taken from damaged components, they differ from the figures taken in the perfect status before the earthquake.

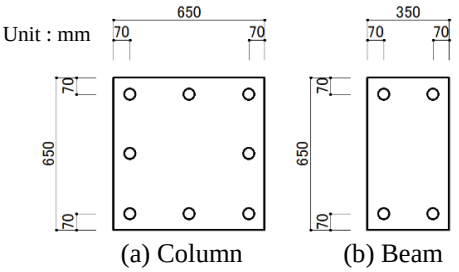

(a) Column (b) Beam

Figure 3: Cross section of member.

Concrete strength. The concrete strength of the 1C4 column, photo 5, is measured with the use of a rebound hammer. The concrete compressive strength is determined to be 27.3 N/mm^2, which is the average of 25 measured data. The measurement took place in June 2016, two months after the earthquake. No cracks were found on the measurement point.

Mechanical property of the reinforcing bar. Tensile tests show the yield strength of the D29 column rebar to be 357 N/mm^2 and its elastic modulus to be 207 kN/mm^2. The yield strength of the ϕ12 stirrup is identified to be 206kN/mm^2. The rebars used as test pieces were free of any deformation from buckling and squeezing. Chances are, however, that the test pieces actually yielded.

2.2 The overview of the damage

Photo 1 shows the building after the earthquake from respective directions. Photo 2 to 4 respectively show the 1A1, 1A3, and 1C3 columns. Many of these Pilotis columns show severe damage. By comparison, photo 2 and 3 confirms severe damage on the columns whose heads slipped off to the east face. The fracture pattern is unknown, however. Photo 5 shows the 1C4 column. It is presumed that flexural fracture first occurred on its head and base, causing the rebar to bend severely in vibrations. As a result, the swelling of the rebar probably drove the head concrete to a fall. The shear-margin Q_{su}/Q_{mu} is calculated from the measurement results to be 1.53. The calculations of the ultimate shear strength Q_{su} and the ultimate bending-moment strength Q_{mu} are based on the Arakawa mean method [2] and the AIJ standard formula [3]. The member length is defined to be 2,350 millimeters in the inner measurement.

Figure 4 shows side views of the 3A to 3C axes and the C3 to C5 axes. The post-quake beam positions on the respective floors are marked by red lines in respective charts. It is obvious from the illustration that the 3A to 3C aisle beams sank deep into the south face while the C34 beam deformed deep into the east face. The 1C34 beam, in particular, sank by a maximum 2,050 millimeters. In this research, a measurement survey of the building was carried out in October 2017. So, the results of measurement include deformity in aftershocks.

(a) East face

(b) West face

Photo 1: Full view.

Photo 4: 1C3 column.

(c) South face

(d) North face

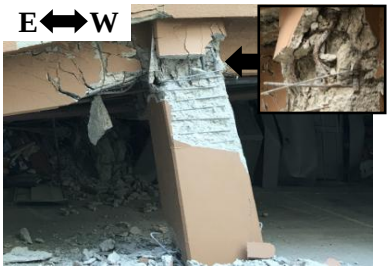

Photo 5: 1C4 column.

Photo 2: 1A1 column.

Photo 3: 1A3 column.

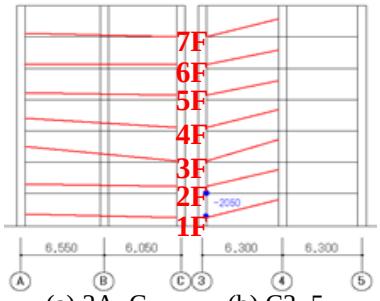

(a) 3A~C (b) C3~5

Figure 4: Side view.

3. The elastoplastic analysis

3.1 The analysis method

Figure 5 shows the analysis model. The static elastoplastic analysis uses the finite element analysis program, FPHM v4.01 [4]. This analysis method is a one-dimensional complex non-linear finite element method that can evaluate the load-bearing capacity at high accuracy in the collapse analysis of reinforced concrete one-story frame [5]. The model is generated with beam elements. The model is constructed on the basis of one element per member. Walls and floors constitute an elastic structure subject to brace replacement. In the brace replacement method, the walls are replaced with braces with equivalent shear stiffness. Walls containing openings and the terrace are not modeled. Based on the actual measurement, the compression strength, tensile strength, and elastic modulus of concrete are set to be 27.3 N/mm^2, 2.73 kN/mm^2, 24 kN/mm^2 respectively. Also, the yield strength and elastic modulus of the column rebar are set at the standard values of 300 N/mm^2 and 206 kN/mm^2 respectively. The elastic modulus of the brace members used for the modeling of walls and floors are 20kN/mm^2 and 1,000kN/mm^2 respectively. The configuration rule on the reinforcing bar is the bilinear type with the strain hardening exponent of 0.01. The constitutive law on the compression stress of the concrete is to be elastic-perfectly plastic and that on the tension stress is to become zero after the tensile strength is achieved.

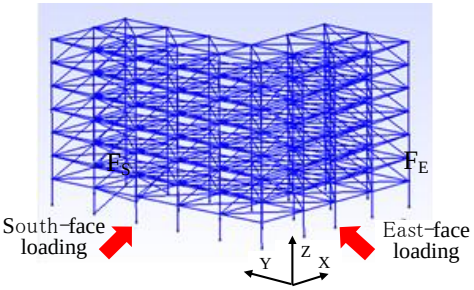

Figure 5: 3D analysis model.

Table 1: Values of W_i, ΣW_i and A_i

Story i	W_i [kN]	ΣW_i [kN]	A_i
7	5180	5180	1.92
6	5502	10682	1.58
5	5502	16184	1.40
4	5502	21686	1.27
3	5502	27188	1.17
2	5502	32690	1.08
1	5538	38228	1.00

Table 1 shows the values of W_i, ΣW_i and A_i. In the table, W_i is defined as the sum of the fixed and movable loads on the respective floors, and ΣW_i is the sum of the loads on the top to the i floors. Used in the calculation are the reinforced concrete unit weight of 24 kN/m^3 and the movable weight on the residential zone. The column weight is calculated separately for the upper and lower floors. In the analysis, the horizontal force is increased on the respective floors under the influence of the vertical load, or the sum of the fixed and movable loads, on the floor center in the incremental load displacement control method following the A_i distribution [6]. The analysis ends when the maximum strength point is reached. Vibrations were three-dimensional in the real earthquake. So, this analysis examines the mechanical properties of the building faced with the in-plane loading.

3.2 The analysis results

Figure 6 shows the relationship between the shear force coefficient and the inter-story drift angle. The downward triangle in the illustration shows the maximum strength point on the first floor and the figure gives the shear force coefficient at those points. The inter-story drift angle is expressed as the value at the representative point. Also, the dashed line in Fig. 6 (b) shows the data on the south-face first-floor load in the event of the brace stiffness being reduced by half. Figure 6 (b) shows a rapid increase in the first-floor inter-story drift angle both on the east- and south-face loading. Comparison between the maximum story-shearing

force coefficients on both faces shows a greater coefficient on the south face. This is because the first-floor wall resists the south to north directional horizontal force with its in-plane force. In addition, data on the south-face loading as in Fig. 6 (b) shows no major disparity in the results in the event that there is a change in the stiffness of the bracing member used for the wall modeling.

Figure 7 shows the fracture status of column members on the first and second floors. In this analysis, the column is found to have yielded at the time part of the column cross-section fractures, in other words, at the moment part of the concrete reaches compression strength or tensile strength or a reinforcement bar reaches yield strength. No. 1 to 10 in the illustration shows the order of the occurrence of the yield. The point of the 10th yield is marked by a red dot in Fig. 6. At the time the 10th yield occurs, no yield is underway in the beam member.

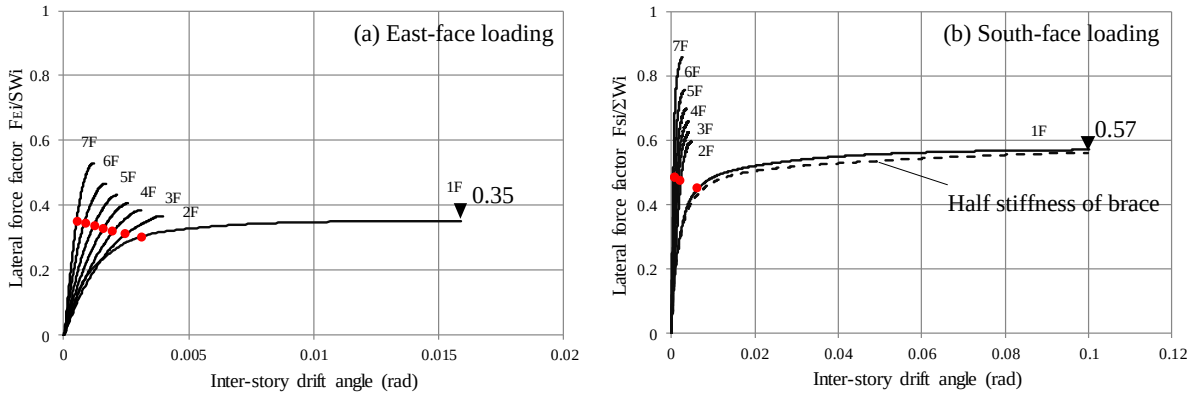

Figure 6: Relationship between lateral force factor and inter-story drift angle.

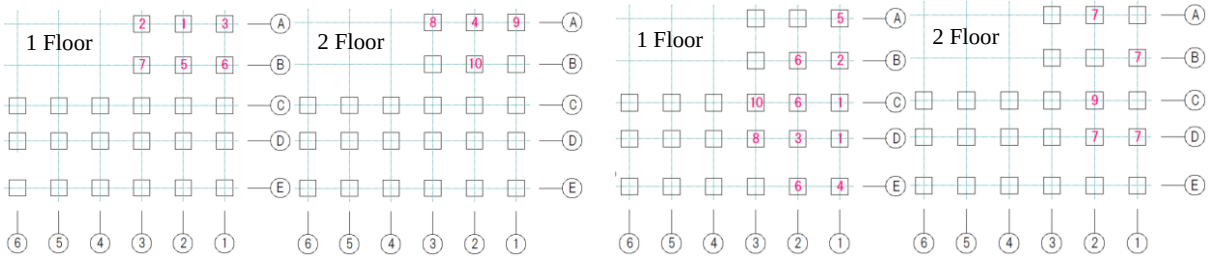

(a) East-face loading (b) South-face loading

Figure 7: Fracture status of column members.

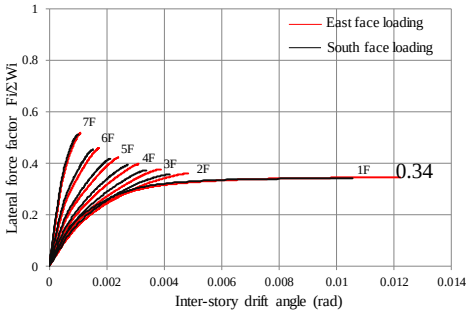

Figure 8: Relationship between lateral force factor and inter-story drift angle.

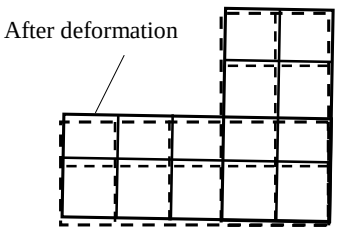

Figure 9: Deformation diagram.

In all loading directions, Fig. 7 shows, first-floor columns yielded in their bases first, followed by surrounding columns. It also shows that damage spreads onto the second floor. Also indicated is the fact that the yield strength reaches about 80 percent of the maximum level at the time the 10th column yields. This means damage does not spread onto the entire building, but that the frame collapses because the damage concentrates on the first-floor columns. Since the beam ends do not yield, this type of collapse can be said to be triggered by fractured columns.
For comparison, Fig. 8 shows the relationship between the lateral force factor and the inter-story drift angle in the modeled case in which all walls are disregarded. Fig. 9 shows the deformation diagram of the second floor with a load on the south surface at a red dot in Fig. 6.

3.3 Comparison between the damage status of the real building and the analysis results

The maximum acceleration measured at a location in Ohe, Chuo Ward, Kumamoto, about 3 kilometers away from the building was 298.8gal in the east to west direction and 363.5gal in the north to south direction on April 14, 2016, and 478.2gal in the east to west direction and 626.8gal in the north to south direction on April 16, 2016 [7]. These values were not measured at the building in question. Therefore, they are likely to differ from the maximum acceleration actually inputted into that affected building. Since there is no other indicator for comparison, however, these values are used as the benchmark for the examination.
The building in question collapsed to pieces in the April 16 earthquake. It is presumed to have been destroyed by a seismic force equivalent to about 0.48 in the east to west direction and 0.63 in the north to south direction in the lateral force factor. Based on this assumption, the actual damage status of the real building is compared with the analysis results.

4. Conclusion

An elastoplastic analysis using the results of actual measurement can generally help figure out the fracture mode of construction components and the horizontal load-bearing capacity of the frame. It should be noted, however, that the exclusion of walls in the process of modeling can lead to an underestimated load-bearing capacity.

References

[1] Hideo, A., Kumamoto Earthquake damage survey report, http://saigai.aij.or.jp/ (in Japanese)
[2] Arakawa, T., Ultimate shear strength and transvers reinforcement of reinforced concrete beams, Transactions of the Japan Concrete Institute 8 (1970), 11-20 (in Japanese)
[3] AIJ Standard for Structural Calculation of Reinforced Concrete Structures, Architectural Institute of Japan, (1991), 615-616 (in Japanese)
[4] FPHM v.4.01., http://naosite.lb.nagasaki-u.ac.jp/dspace/handle/10069/37150
[5] Shimazu, M., Elastoplastic analysis of reinforced concrete frames by the fibered plastic hinge model, Proceedings of the Japan Concrete Institute 31 (2009) (in Japanese)
[6] Enforcement Ordinance of Construction Standard Law, the 88 amendment (in Japanese)
[7] Japan Meteorological Agency, Strong-motion earthquake record, Ohe, Kumamoto, Japan http://www.data.jma.go.jp/svd/eqev/data/kyoshin/jishin (in Japanese)

SynerCrete'18 International Conference on Interdisciplinary Approaches
for Cement-based Materials and Structural Concrete
24-26 October 2018, Funchal, Madeira Island, Portugal

EFFECT OF HUMIDITY AND ELEVATED TEMPERATURE ON THE MECHANICAL BEHAVIOR OF CONCRETE

Laurie Lacarrière [(1)], Ponleu Chhun [(1)], Alain Sellier [(1)]

(1) Université de Toulouse, UPS, INSA, LMDC (Laboratoire Matériaux et Durabilité des Constructions), 135, avenue de Rangueil, 31 077 Toulouse Cedex 04, France

Abstract
This paper deals with the prediction of the evolution of mechanical behaviour of concrete when it is subjected to high humidity and temperatures. a non linear creep-damage model to assess the mechanical response of the concrete to such solicitations. This model was previously developed for the prediction of concrete behaviour at ambient or moderate temperature. But the effect of combined high humidity and elevated temperature was not investigated up to now.
In this paper, laws are proposed to reproduce the evolution of strengths according to the saturation degree and temperature of concrete. A thermal damage is also introduced in addition to the thermo-activation of creep by temperature. The complete THCM model is validated using tests performed, at different temperatures and relative humidity, on lab specimens and on structural members.

1. Introduction

In French nuclear power plants, the prestressed reinforced concrete containment vessel plays a major role to limit the radionuclide dispersion in the environment in case of failure of the first two barriers (the fuel cladding and the primary cooling system). It is thus of primary importance to master the containment building tightness during all the duration of a severe accident. In the scenario of a severe accident, the internal pressure (0.5 MPa) and temperature (180 °C) on the inner face of the concrete containment structure are maintained constant during two weeks.
During this accident scenario, the high temperature level, the high relative humidity and the loading duration are going to affect the mechanical behaviour of concrete and steel. The aim of the work done in the framework of the program MACENA (Tightness assessment of

confinement vessels during an accident) was thus to assess the behaviour of concrete when it is subjected to high humidity and temperature. Based on results obtained by some partners in the project [1], the evolution of mechanical behaviour of concrete in such environmental conditions is modelled.

2. General principle of non-linear mechanical model for concrete

The mechanical model used and adapted to carry out the couplings with the physico-chemical evolutions presented here is the result of work carried out at the LMDC in the recent years. It is based on a non-linear behaviour law taking into account concrete damage, plasticity and delayed behaviour [2,3]. The total stress is defined from the effective stress on the sound material by considering two kinds of damages (more details in [2]) (Eq. (1)):

- Isotropic damages due to microcracks: This is the case of the compressive damage D^{shear} induced by the compressive loadings (shear damage at microlevel which induced isotropic distribution) and of the thermal damage D^{TH} which is induced (as it will be explained in section 3) by the incompatibilities of strains at the mesoscale.
- Anisotropic damages characterizing an oriented cracking: This is the case of the post-pic tensile damage D^t that is evaluated from the opening of oriented cracks under the effect of tensile stresses and of the crack closure damage D^r applied to compressive stresses to reproduce the transmission loss of compressive stresses when the previously opened crack is not closed.

For both damages, an energetic regularisation based on Hillerborg theory is made [2].

$$\sigma_{ij} = (1 - D^{TH}).(1 - D^{shear}).\left[(1 - D^t)_{ijkl}.\tilde{\sigma}_{kl}^{+} + (1 - D^r)_{ijkl}.\tilde{\sigma}_{kl}^{-}\right] \quad (1)$$

The effective stress (in terms of damage) is calculated from a rheological model reproducing the delayed behaviour of concrete as the sum of the elastic stress applied to the solid skeleton and the stress induced by capillary depression σ^W (Eq. (2)). The following creep model has been validated on several tests under constant temperature in [3].

$$\begin{aligned} \tilde{\sigma}_{kl} &= S_{klmn}.\varepsilon_{mn}^{el} - \sigma_{kl}^{W} \\ \varepsilon_{mn}^{el} &= \varepsilon_{mn} - \varepsilon_{mn}^{pl} - \varepsilon_{mn}^{th} - \varepsilon_{mn}^{KV} - \varepsilon_{mn}^{M} \end{aligned} \quad (2)$$

- S_{klmn} is the material stiffness tensor (fct° of E and υ);
- ε_{mn} is the total strain;
- ε_{mn}^{el} is the elastic strain and ε_{mn}^{th} is the thermal strain;
- ε_{mn}^{pl} is the plastic strain (resulting from the application of the plastic criteria [2]);
- ε_{mn}^{KV} and ε_{mn}^{M} are the strain of Kelvin-Voigt reversible viscoelastic creep modulus and Maxwel consolidating viscous creep level (more details in [3]).

3. Effect of saturation degree on concrete mechanical behaviour

The degree of saturation first influences the creep rate. Indeed, at the microscopic scale, creep is linked to water movements or to variations in disjunction pressure, and it will be affected by a decrease of saturation of the material (leading to a lower creep rate). For simplification it

is assumed that the characteristic time of both Kelvin and Maxwel levels in the creep model are both affected by the variation of water content:

$$\tau^K = \frac{\tau^K_{ref}}{Sr}.f^K(T) \text{ and } \tau^M = \frac{\tau^M_{ref}}{Sr}.f^M(T) \quad (3)$$

In this equation the functions $f^K(T)$ and $f^{KM}(T)$ reproduce the effect of temperature on creep rate and will be presented in the next section (Eq. (7).

The preponderant effect of the saturation state of a concrete on its mechanical behaviour is of course the application of a capillary pressure on the solid skeleton leading to a strain.

In the modelling approach adopted here, this effect is directly taken into account by introducing the effect of capillary pressure in the law of behaviour (through σ^W in Eq. (2)).

In addition to this poro-mechanical effect, the capillary depression also has indirect effects on the mechanical properties. As in the case of thermal strains, the shrinkage of the paste can lead to a micro-cracking by incompatibility of paste-aggregates strain. However, recent results, obtained by tests performed at LMDC in the framework of Mosaic project [4], show an increase in tensile strength when the degree of saturation decreases (Fig. 1). This increase is explained by the fact that the application of capillary depression on the skeleton prestresses the paste [5], and this effect is greater than the micro-cracking effect. On Fig. 1 it can also be noticed that the tests conducted at SIAME within the framework of Macena [1], on concretes subjected to varying (but controlled) temperatures and degrees of saturation, confirm this increase in resistance but with a decreasing effect with temperature.

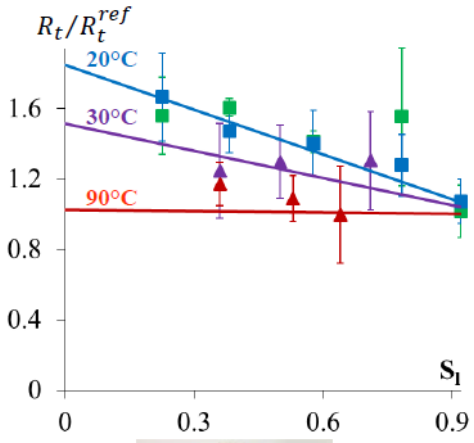

Figure 1: Evolution of tensile strength according to temperature and saturation degree (experimental results issued from [4,1] and proposed law for Rt)

As these tests also showed that the effect of the degree of saturation on the Young's modulus (macroscopic indicator of damage) was rather limited [1], it seems consistent to neglect the effect at the macroscopic level of micro-cracking induced by aggregates. The consolidation effect of the material by the degree of saturation is therefore only considered, by proposing a law of tensile strength evolution as a function of the degree of saturation (Eq. (4)). The decrease of the effect of Sr when the temperature increases is attributed to the effect of temperature on the desorption isotherm [6]. Indeed if the temperature increases the capillary depression will be reduced for the same degree of saturation. This effect is therefore modelled by the exponential term of Eq. (4).

$$\frac{Rt}{Rt_{ref}} = 1 - K^W . exp\left(-\frac{T - T_{ref}}{T_{kW} - T_{ref}}\right).\left(Sr - Sr_{ref}\right) \quad (4)$$

- Rt_{ref} is the reference resistance measured at T_{ref} and Sr_{ref};
- K^W is a material parameter identified at T_{ref} (0.85 if $T_{ref} = 20°C$).

4. Effect of temperature on concrete mechanical behaviour

First of all, temperature variations within the material can lead to concrete damage. Our approach decouples the effect on the mechanical properties of very high temperatures (leading to dehydration of the paste) from the more moderate temperature effect for which variations in mechanical properties are attributable more to the consequences of incompatibility strains at the material scale (leading to micro-cracking or to the creation of micro-defects). This effect is thus reproduced by the introduction of an isotropic damage variable D^{TH} in the equation (1). This damage is determined with the equation (5) from the coefficient $C^{T,D}$. The function presented in Eq. (5) has been developed and validated for saturated concrete in [7] and has been adapted to other saturation states in this study by introducing a calibration function A^{TH} to control the level of damage at a given temperature that depends on saturation degree. Indeed, as the incompatibilities of thermal strains are related to the differences of thermal expansion coefficient, a dry paste will have a lower expansion coefficient and thus a potential of incompatibility of strains lower.

$$D^{TH} = 1 - \frac{1}{A^{TH}(C^{T,D} - 1) + 1} \text{ and } C^{T,D} = exp\left(-\frac{E_a^W}{R}\left(\frac{1}{T} - \frac{1}{T_{thr}}\right)^{+}\right) \quad (5)$$

- E_a^W/R is the associated activation energy (approx. 3000K^{-1} according to [7]);
- T_{thr} is the threshold temperature at which thermal damage occurs (45°C [7]).

$$A^{TH} = \frac{1}{C^{T,D}(80°C) - 1}.\frac{Sr.D_{80}^{TH}}{1 - Sr.D_{80}^{TH}} \quad (6)$$

- E_a^W/R is the associated activation energy (approx. 3000K^{-1} according to [7]);
- T_{thr} is the threshold temperature at which thermal damage occurs (45°C [7]);
- $C^{T,D}(80°C)$ is calculated for T=80°C;
- D_{80}^{TH} is the thermal damage determined experimentally at 80°C for Sr=1.

This parameter is identified using the experimental results from [7] and it can be noticed in Fig. 2 that the identified value (0.15) allows reproducing the damage obtained in [1] for a higher temperature (without refitting of the law). Fig. 2 also gives the evolution of D^{TH} as a function of temperature for several degrees of saturation to illustrate the decrease of thermal damage with drying.

Temperature has also a physical effect on the creep rate because it changes the viscosity of the water. The creep rate of the Kelvin and Maxwell levels are therefore both affected by this effect modelled by an exponential function depending on T (Eq. (7)). For the viscous level (linked to consolidation and to C-S-H behaviour) the thermal damage identified previously will lead to an increase in the non-linear creep rate. This effect is modelled by also affecting the characteristic time of the Maxwell viscous creep level by the $C^{T,D}$ coefficient defined in Eq. (6).

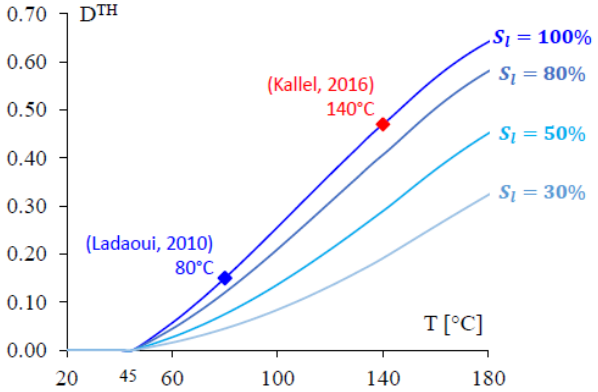

Figure 2: Evolution of thermal damage according to temperature and saturation degree

$$\begin{cases} f^K(T) = exp\left(-\frac{E_a^W}{R}\left(\frac{1}{T}-\frac{1}{T_{ref}}\right)\right) \\ f^M(T) = exp\left(-\frac{E_a^W}{R}\left(\frac{1}{T}-\frac{1}{T_{ref}}\right)\right) \times C^{T,D} \end{cases} \quad (7)$$

5. Validation of the proposed laws on lab tests

The laws of evolution of mechanical properties and damage as a function of temperature and humidity have been tested on the tests performed under the ANR Macena at SIAME [8] for instantaneous tests and at CERIB [9] for creep tests (Fig. 3).

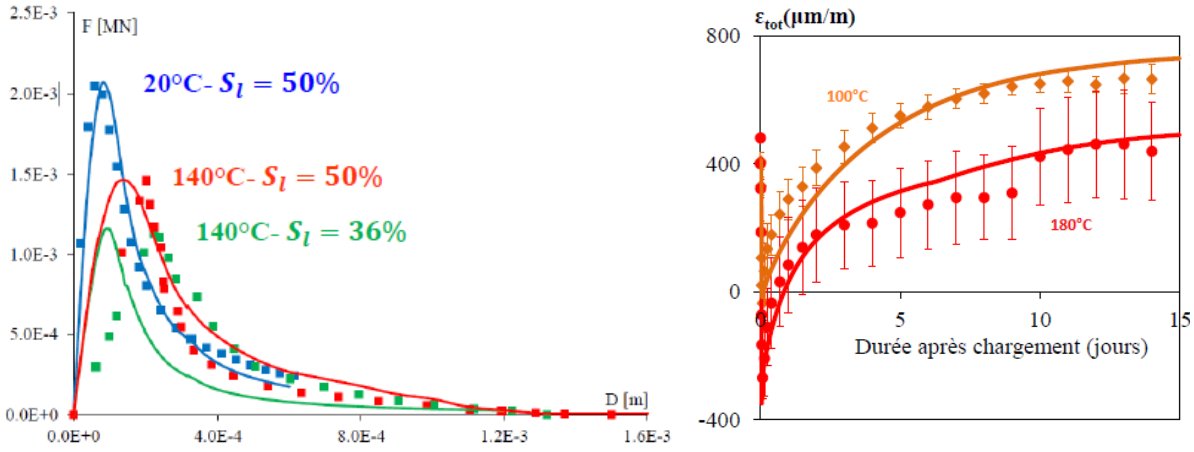

Figure 3: Modelling of DCT tensile test (left) and compressive creep test (right) at different temperature and saturation degree (experimental results from [8,9]).

The DCT tests were developed at SIAME laboratory to maintain both temperature and relative humidity constant in the sample during the test and are therefore performed on small notched discs (15 cm diameter, 5 cm thickness and 5.5 cm long notch) (see [8] for details). The possible uncertainty on the control of the displacements, of the real relative humidity at the bottom of notch led us to consider that the model could be considered as valid even if it

does not reproduce perfectly the pre-pic part for the tests at high temperature. For creep tests (see [9] for more details), the relative humidity was not controlled so the specimens were subjected to drying concomitantly with temperature rise and loading. This effect was taken into account in by modelling the drying and the associated desiccation creep strains which allows a good reproduction of the strains during the test.

6. Conclusions

The paper dealt with the prediction of the mechanical behaviour on concrete in severe environmental conditions corresponding to high temperature (up to 200°C) and high variation of humidity. In these conditions the non-linear behaviour of concrete is affected, creep rate are increased and a diffuse damage is induced by the temperature evolution (and the associated incompatibilities of paste and aggregate strains). The originality of the work was to proposed a way to model these effects that take into account the concomitant effects of temperature and saturation. Indeed, it was shown that the temperature effect is reduced by a decrease of saturation degree. The proposed evolution laws, implemented in a non-linear mechanical model for concrete were successfully applied to the simulation of mechanical tests performed at high temperature and for different saturation degrees.

Acknowledgements
The investigations and results reported here were supported by the French National Research Agency (ANR-PIA) under the MACENA research program 11-RSNR-0012 (Control of nuclear vessel in accident conditions). We are also grateful to CEA/DEN/DM2S/SEMT for providing the finite element code CASTEM.

References

[1] Kallel H., Carré H., Laborderie C., Masson B., Tran NC., (2016) Effect of temperature and moisture on the instantaneous behaviour of concrete, Cem. Concr. Compos. 80, 326-332
[2] Sellier A., Cazaux-Ginestet G., Buffo-Lacarrière L., Bourbon X. (2013) Orthotropic damage coupled with localised crack reclosure processing. Part I: Constitutive laws. Engineering Fracture Mechanics 97(1), 148-167
[3] Sellier A., Multon S., Buffo-Lacarrière L., Vidal T., Bourbon X., Camps G. (2016) Concrete creep modelling for structural applications: non-linearity, multi-axiality, hydration, temperature and drying effects. Cem. Concr. Research, 79(1); 301-315
[4] Bucher, R., Vidal, T., Sellier, A., and Verdier, J. (2017). Effet du séchage sur les propriétés mécaniques des matériaux cimentaires, Rapport intermédiaire ANR Mosaic (LMDC), *in French*
[5] Burlion, N., Bourgeois, F., and Shao, J.-F. (2005). Effects of desiccation on mechanical behaviour of concrete. Cem. Concr. Compos. 27, 367–379
[6] Chhun P. (2017). Modélisation du comportement thermo-hydro-chemomécanique des enceintes de confinement nucléaire en béton armé-précontraint. phd. Université de Toulouse, Université Toulouse III - Paul Sabatier, in French
[7] Ladaoui, W., Vidal, T., Sellier, A., Bourbon, X. (2013). Analysis of interactions between damage and basic creep of HPC and HPFRC heated between 20 and 80 °C. Mater. Struct. 46, 13–23
[8] Kallel H., Carré H., Laborderie C., Masson B., Tran NC., (2016) Effects of the Hygrothermal Conditions on the Fracture Energy of the Concrete, Key Engineering Materials 711, 397-403
[9] Daval C., 2016, Rapport intermédiaire ANR Macena: Compression et module élastique à 20°C, 100°C et 180°C – Fluage à 100°C (CERIB), *in French*

SynerCrete'18 International Conference on Interdisciplinary Approaches
for Cement-based Materials and Structural Concrete
24-26 October 2018, Funchal, Madeira Island, Portugal

EFFECT OF PARTIAL RESTRAINING CONDITIONS AND POISSON'S RATIO IN BOTTOM-RESTRAINED WALLS

Dirk Schlicke [(1)], Lýdia Matiašková [(2)], Július Šoltész [(2)]

(1) Institute of Structural Concrete, Graz University of Technology, Graz, Austria
(2) Department of Concrete Structures and Bridges, Slovak University of Technology in Bratislava, Bratislava, Slovakia

Abstract

The stress distribution in bottom-restrained walls is a desired information for an efficient design of wall-like concrete members which are eccentrically restrained at the bottom. Practical examples are retaining walls or bridge abutment walls where the results were used in order to assess the risk and intensity of harmful separating cracks over the wall height. The stress distributions of common design tasks are usually estimated with graphical solutions in form of diagrams or determined on basis of analytical solutions. In general, all these solutions provide straightforward results, whereby effort and complexity is usually limited by generally approved simplifications within these solutions. This contribution provides detailed background on the effect of common simplifications, namely (i) assuming complete restraint at the wall bottom, or respectively, (ii) separate determination of axial and bending restraint in order to consider partial restraining conditions, and (iii) neglect of Poisson's effect. The significance of these simplifications is outlined by comparative studies with an illustrative shell model. Overall, recommendations for the consideration of the outlined effects in practical design were given on basis of these results.

1. Introduction

Bottom-restrained walls are wall-like concrete members whose deformation behavior is eccentrically restrained at the wall bottom. This contribution defines a wall-like concrete member as any concrete member with a height of at least five times the width ($H/B > 5$) and a length of at least 2 times the height ($L/H > 2$). As soon as the deformation behavior of such wall-like members is restrained at the bottom, e.g. because they are cast on a foundation or slab, a distinct stress distribution from imposed thermal and moisture induced deformations occurs over the width, length and height of the wall. Main parameters on the size and shape of

these stress distributions are the imposed deformation in the wall, stiffness ratios between wall and foundation (axial and bending stiffness) as well as length to height-ratio of the wall (L/H). Neglecting at first the stress distribution over the width, the resulting stresses can be estimated at the decisive center section by the product of the imposed strain $\bar{\varepsilon}$, the effective modulus of elasticity $E_{c,eff}$ and the degree of restraint over the height $a(x)$. Various solutions for the estimation of the degree of restraint can be found in the literature, e.g. [1] - [6]. Fig. 1 exemplarily shows two engineering solutions which are often used in practice. The diagram in Fig. 1a) is a simplified graphical solution derived from shell models with complete axial and bending restraint at the wall bottom but taking into account the effect of L/H, whereas Fig. 1b) presents a combined solution with regard to the influence of L/H by the factor $K_R(x)$ as well as the influence of decreasing restraint due to the real axial stiffness ratio between the wall and restraining foundation by the factor $K_F = [1+(A_W E_W)/(A_F E_F)]^{-1}$.

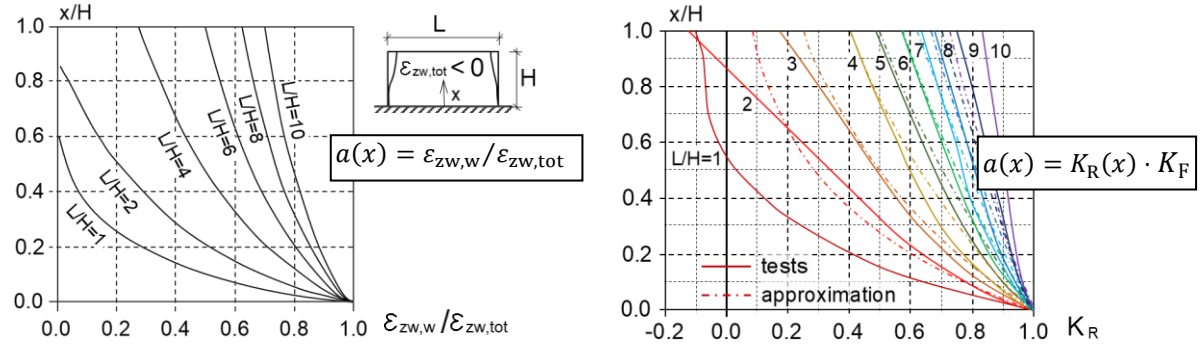

a) acc. to [1] *b) acc. to [2] taken from [7]*

Figure 1: Diagrams for the degree of restraint in the center section of walls

Besides the shown solutions in Fig. 1, solutions of different nature are available in the literature, e.g. empirical restraint factors of [3] and [4], restraint factors derived from a comprehensive 3D-FEM study [5] or other simplified methods according to [6]. These may allow the consideration of additional effects such as slip at the free wall corner, asymmetric location of the wall on the foundation, etc., but they are not further described in this paper. Another possibility for stress calculation in walls is the analytical solution given in [8] and [9]. Hereby, the restraint stresses due to an imposed strain $\bar{\varepsilon}$ were determined by superposition of stress resultants due to cross section compatibility and additional bending due to uplift of the whole wall-foundation-system according to L/H, (see Fig. 2). A general overview and further details of all these solutions can be found in [10].

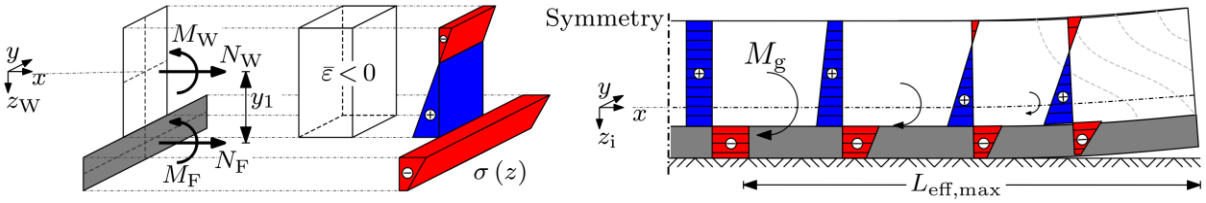

a) inner restraint forces and stress distribution due to cross section compatibility *b) resulting stress distribution with regard of an outer bending moment due to uplift of the whole system*

Figure 2: Stress distribution in bottom-restrained walls acc. to [8] and [9]

The stress distribution can also be determined by thermo-(chemo)-mechanical Finite Element Analysis, see e.g. [6], [7], [8], [10] or [11]. Although, numerical models enable a significantly better consideration of the real temperature distribution, shrinkage, the effect of maturity and viscoelasticity, implicit consideration of the restraining condition, etc., these solutions require also expertise and experience, see e.g. [12]. On the contrary, engineering solutions are gaining more importance in practical design. Although as outlined before, the available graphical and analytical solutions come along with some simplifications, which are expected to provide results on the safe side. With the aim of optimized design, the significance of these simplifications is discussed in the following by means of a parametric study.

2. Parametric study

2.1. Calculation Model

The study was conducted with the deliberately simple linear-elastic FE shell models of a wall on a foundation shown in Fig. 3. The models use symmetry in length direction and enable the consideration of two axial restraining conditions at the bottom of the wall (fully and partially restrained) as well as two restraining conditions of the uplift (fully and partially restrained according to the self-weight activation).

In case of full bottom restraint (Fig. 3a), the shell model comprises only the wall with bottom support conditions fully constraining displacements in horizontal and vertical directions. In case of partial axial restraint but full restraint of uplift (Fig. 3b), a foundation was included at the wall bottom with shell elements. The supports were kept at the wall bottom but set for only constraining vertical displacements. Thus, contribution of the stiffness ratio between the wall and the adjacent foundation as well as the full vertical restraint to the enforced uplift from the shortening of the wall could be examined. In case of partial restraint of both (axial deformation and uplift (Fig. 3c), springs with very high stiffness in vertical compression ($k = 10^6 \mathrm{kN/m^3}$) that fail in tension were introduced at the bottom of the wall, allowing for uplift of edges with the subsequent activation of self-weight.

In these models, the wall was imposed with a uniformly distributed unit deformation of $\Delta T = -10$ °C and the degree of restraint over the height in the center section of the wall was determined from the resulting course of calculated stresses in length direction with $a(x) = -\sigma_{calc} / (E_W \times \alpha_T \times \Delta T)$. Thus, the result of this study is independent from the entering values of thermal loading ΔT, thermal expansion α_T and the elastic modulus E_W. Moreover, an uncracked cross section of the walls was assumed, hence Poisson's effect on stresses was taken into account with the Poisons ratio of $\mu = 0.2$.

2.2. Studied scenarios

The parametric study covers eight different *L/H* ratios starting from 2 until 10 with steps of 1 which were all considered with full and partial axial restraint at the wall bottom as well as full and partial restraining of the uplift due to self-weight activation.

Presuming that the resulting stresses are determined from the inner forces of the ideal cross section including both the wall and foundation, the changing position of the center of gravity (CoG) was of interest as well. For this reason, the study was conducted for two types of wall and foundation cross-section geometries with CoG located above and below the wall bottom. Geometrical data for the analyzed walls is summarized in the Tab. 1 and illustrated in Fig. 3.

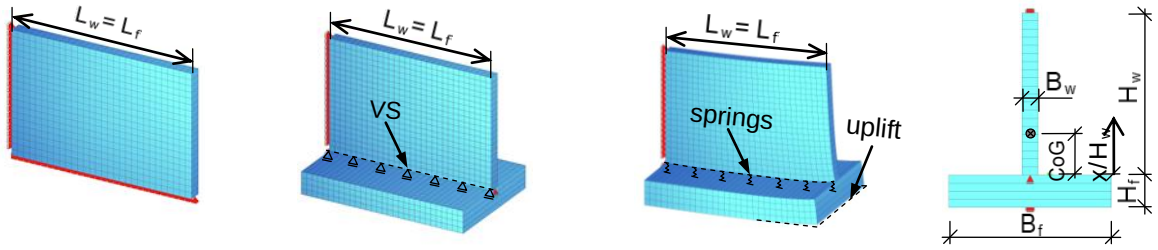

a) full bottom restraint *b) partial axial restraint but full restraint of uplift* *c) partial axial restraint and partial restraint of uplift* *d) definition of dimensions*

Figure 3: Models of the parametric study

Table 1: Geometrical data of the analysis

Wall					Foundation					$\frac{EA_w}{EA_f}$
L/H	L_w=L_f (m)	B_w (m)	H_w (m)	A_w (m²)	No.	CoG (m)	B_f (m)	H_f (m)	A_f (m²)	
2 - 10	8 – 32, 40 (incr. 4)	0.4	4	1.6	1	0.4	4	0.8	3.2	0.5
					2	-0.4	1	3.2	3.2	0.5

2.3. Results

The following figures, Fig. 4 – Fig. 6, depict the distribution of the degree of restraint over the height of analyzed walls for the different restraining conditions. Hereby, the proportional height above base complies with *x*/*H* as in Fig. 1. At first, Fig. 4 gives the results of the full bottom restraint with regard to the consideration, or respectively, the neglect of Poisson's ratio. In general, the results agree with the expectation that the degree of restraint gradually decreases over the height and increases with higher *L*/*H* ratios.

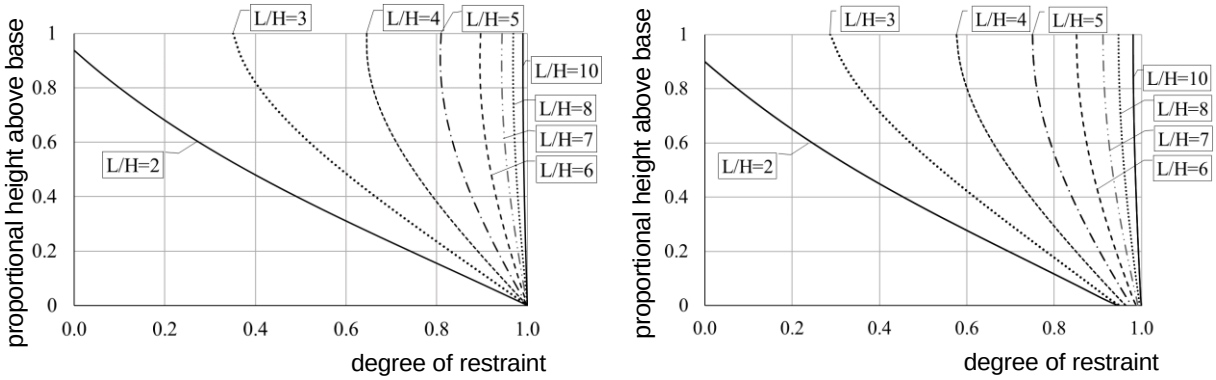

a) μ = 0 *b) μ = 0.2*

Figure 4: Degree of restraint for full bottom restraint

It can further be seen in Fig. 4 that the consideration of Poisson's effect in the present FE model decreases the degree of restraint for shorter walls by 5 - 10%. This is most obvious at the wall bottom, where the determined values approach 100 % restraint only in case of $\mu = 0$. The reason can be found by abstracting the stress distribution in the wall with a strut and tie model. In such model, the restraint force in the center section is in equilibrium with a diagonal tie starting at the bottom of the free edge and progressing to half height of the wall with increasing distance from the free edge. And this diagonal tie is in turn in equilibrium with a

vertical strut at the end of the introduction length which causes beneficial compressive stresses in horizontal direction in case of $\mu \neq 0$.
In contrast, consideration of a partial axial restraint causes an overall decrease of restraint, as shown in Fig. 5. However, the degree of restraint is also significantly influenced by the location of the CoG of the ideal wall-foundation cross section. In case CoG is placed above the wall bottom (Fig. 5a), short walls show higher degree of restraint at the bottom as long walls, whereas cases with CoG below the wall bottom (Fig. 5b) show an obvious decrease of this effect as well as a slight decrease of restraint over the whole height. The reason can be found in the positive global bending moment caused by vertically restrained uplift of edges, as illustrated in Fig. 2. As already shown in [8], this global bending moment creates beneficial compression at the wall bottom in case the CoG is located above the wall bottom. However, resulting compressive stresses in short walls gain lower values due to the lower activation of self-weight compared to longer walls. Hence, tensile stresses, and accordingly the degrees of restraint, at the bottom of short walls increase compared to long walls.

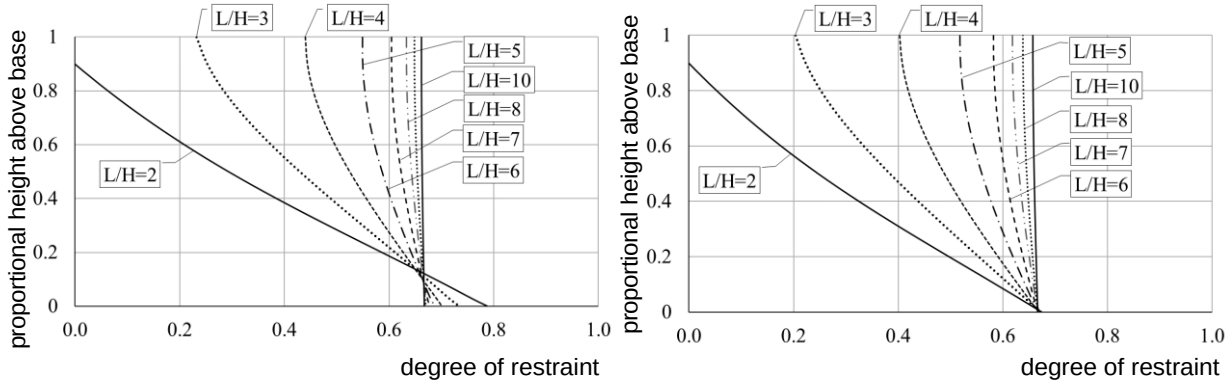

a) CoG located 0.4m above the wall bottom *b) CoG located 0.4m below the wall bottom*

Figure 5: Degree of restraint for partial axial restraint but full restraint of uplift, $\mu = 0.2$

Another important effect is the realistic consideration of uplift of edges shown in Fig. 6.

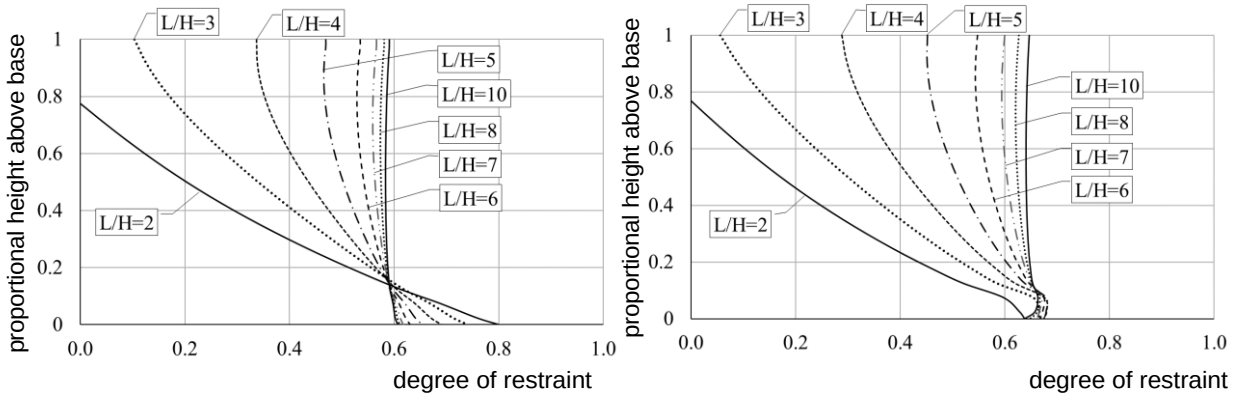

a) CoG located 0.4m above the wall bottom *b) CoG located 0.4m below the wall bottom*

Figure 6: Degree of restraint for partial axial restraint and partial restraint of uplift, $\mu = 0.2$

The uplift of edges generally shows a stress releasing effect over the height of the wall. However, in short walls with CoG located above the wall bottom (Fig. 6a), the degrees of

restraint exceed even the ones from the previous case. The reason can again be found in the effect of the global bending moment due to self-weight activation. This positive effect was overestimated in the previous case since more beneficial compressive stresses were induced due to the full restraint of uplift.

3. Conclusion

Restraint stresses in bottom-restrained walls are determined on the safe side when presuming full restraint at the wall bottom and $\mu = 0$. Consideration of partial restraint results in lower stresses, however, this numerical study indicates in accordance with the analytical solution of [8] that a representative consideration of the CoG of the whole cross section is required. In fact, a simple reduction of the degree of restraint on basis of the axial stiffness ratio, as proposed by [2] or [4], can only be seen as a pragmatic solution without a mechanically consistent background. In short walls with CoG located above the foundation, this approach would even give results on the unsafe side. Altogether, it is recommended to determine the degree of restraint in bottom-restrained walls with an explicit consideration of the bending stiffness ratio as well as the real restraining condition of uplift due to self-weight activation.

Acknowledgements
This contribution was completed with the support of COST Action TU1404 together with the support of the Scientific Grant Agency VEGA under the contract No. VEGA 1/0456/17.

References

[1] König, G. and Tue, N.V.: Grundlagen und Bemessungshilfen für die Rissbreitenbeschränkung im Stahlbeton und Spannbeton. DAfStb Heft 466. Beuth-Verlag, (1996)
[2] ACI 207.2R-07: Report on thermal and volume change effects on cracking of mass concrete (2007)
[3] EN 1992-3: Design of concrete structures, Part 3: Liquid retaining and containment structures (2006)
[4] CIRIA C766: Control of Cracking caused by restrained deformation in concrete (2017)
[5] JSCE: Guidelines for concrete, 15: Standard specifications for concrete structures. Design (2007)
[6] COIN Project report 31, Basis for and practical approaches to stress calculations and crack risk estimation in hardening concrete structures (2011)
[7] Knoppik-Wróbel, A.: Analysis of early-age thermal–shrinkage stresses in reinforced concrete walls. Ph.D. Thesis. Silesian University of Technology, Gliwice, Poland (2015)
[8] Schlicke, D., Minimum reinforcement for restrained concrete, PhD thesis, Graz University of Technology, Austria (2014), ISBN: 978-3-85125-473-0 (revised edition)
[9] ÖBV Bulletin: Analytical design of watertight structures with optimized concrete (in German), Austrian society for constructuion technology, Vienna, Austria (2018)
[10] Fairbairn, E. M.R. and Azenha, M.: Thermal Cracking of Massive Concrete Structures. State of the Art Report of the RILEM TC 254-CMS, Springer (2018), DOI: 10.1007/978-3-319-76617-1
[11] Matiašková, L. and Šoltész, J.: Macroscopic calculation model for simulating early age behavior of concrete members. In: Early Age Cracking and Serviceability in Cement-based Materials and Structures. Vol. 2, RILEM Publications, Brussels, Belgium (2017)
[12] Jędrzejewska, A. et.al: COST TU1404 benchmark on macroscopic modelling of concrete and concrete structures at early age: Proof-of-concept stage, Construction and Building Materials, Volume 174 (2018), ISSN 0950-0618

SynerCrete'18 International Conference on Interdisciplinary Approaches
for Cement-based Materials and Structural Concrete
24-26 October 2018, Funchal, Madeira Island, Portugal

GAMMA AND X RADIATION ABSORPTION CHARACTERISTICS OF SPECIALLY SELECTED TYPES OF CONCRETE

Srboljub Stankovic [(1)], Ksenija Jankovic [(2)]

(1) Institute of nuclear sciences VINCA, Belgrade, Serbia
(2) IMS Institute, Belgrade, Serbia

Abstract

Medical institutions with linear accelerators, cyclotrons as installations for particles acceleration, nuclear facilities as nuclear power stations and nuclear research reactors using concrete in building construction. In cost-benefit analysis the question is what are the radiation characteristics of different types of concrete, which could be used to protect against gamma and X rays. In this paper, computer code XCOM was used for the calculation of the total mass attenuation coefficients, which is an important factor for determination of the photon attenuation, as well as during research and testing of radiation protection properties for concrete with components of different type materials. Thereby, the basic absorption radiation characteristics of ordinary and barite concretes, as well as specially selected type of concrete with magnetite and steel and concrete UHPC with barite and nanosilica as specific material composition, were considered. The results of this research point to the conclusion that before the concrete production of certain mechanical properties is approached, it is reasonable to apply the appropriate methodology with the numerical calculation of the basic absorption characteristic of the concrete for protection against gamma and X radiation.

1. Introduction

Medical institutions with linear accelerators, cyclotrons as installations for particles acceleration, nuclear facilities as nuclear power stations and nuclear research reactors using concrete in building construction. Barite aggregate is used to produce heavyweight concrete which application concerns radiation shielding in hospitals and nuclear facilities. The basic characteristics of ordinary concrete and heavy-weight concrete with barite were studied for the case of their use for shielding from gamma radiation [1, 5, 6]. In cost-benefit analysis the question is what are the radiation characteristics of different types of concrete, which could be

used to protect against gamma and X rays [2, 3, 4]. The energy deposited the transmission factor and the mass attenuation coefficients in ordinary and barite concretes have been calculated with the photon transport Monte Carlo software. The numerical simulations results show that using barite as an aggregate in the concrete is one of the solutions for gamma ray shielding. Thereat, it is shown non-destructive method for determining the gamma radiation absorption characteristics of concrete [9]. In references [10, 11], one of the goals is to implement appropriate numerical calculations for obtaining the value of the total mass attenuation coefficient in the energy range 10 keV - 150 MeV of gamma and X radiation, and their dependence in the content of barite and nano-silica in UHPC concrete with specially defined mechanical properties. Nanosilica has a dominant influence on the improvement of the mechanical properties, and barite has a dominant influence on the characteristics that increase the absorption of ionizing radiation, i.e., improves the characteristics for protection against ionizing radiation. Investigations in these references [10, 11] is designed to, by simultaneously using different portions of the two materials, nano-silica and barite, in the composition of various types of concrete conduct tests on the ability to improve the mechanical properties and properties for the radiation protection of concrete.

In this paper, computer code XCOM [8] was used for the calculation of the total mass attenuation coefficients $(\mu/\rho)_{tot}$, which is an important factor for determination of the photon attenuation, as well as during research and testing of radiation protection properties [1-6] for different content of aggregates in concrete. Computer code XCOM operates on a method of combining the values of the existing database for effective cross section of physical processes accompanying the transport of photons through different materials. This means that there is a possibility to use data bases for coherent and incoherent scattering, photoelectric absorption, and pair production cross-sections for the different chemical structure of materials which enter into the composition of the concrete.

2. Numerical methods

One of the most important characteristics of the concrete for protection against gamma and X radiation is its Total Mass Attenuation Coefficient $(\mu/\rho)_{tot}$.

Basic relations for engineering calculations the attenuation of exposure dose rate of ionizing radiation, which passes through the wall of concrete, can be displayed as:

$$X = X_0 \cdot \exp\left[-\left(\frac{\mu}{\rho}\right)_{tot} \cdot \rho d\right] \tag{1}$$

where X (C/kg s) and X_0 are intensity exposure rates behind and in front of the wall, where the wall thickness is d (m) and the density is ρ (kg/m^3). This Eq. (1) is consistent with the application of Bouguer-Lambert-Beer law for attenuation of the intensity of mono energetic photon radiation for the cases of penetration of the narrow beam of radiation through a concrete wall as a protective barrier.

The definition of Total Mass Attenuation Coefficient for mixture or compound is given by:

$$\left(\frac{\mu}{\rho}\right)_{tot} = \sum_j w_j \cdot \left(\frac{\mu}{\rho}\right)_j \tag{2}$$

where w_j and $(\mu/\rho)_j$ are the weight fraction and mass attenuation coefficient of the constituent element j.

The numerical calculations included two steps: 1. For each type of concrete from Tab. 1 its composition was determined in accordance with the nomenclature of chemical elements and chemical compounds, 2. Interactive use of the program XCOM [8], where the known composition of individual types of concrete determines the total mass attenuation coefficient depending on the change of energy photon radiation.

XCOM program enables to calculate interaction coefficients for the following processes: Compton (incoherent) and Rayleigh (coherent) scattering, photoelectric absorption, and pair production in the field of the atomic nucleus and in the field of the atomic electrons. The mean free paths between scatterings, between photo-electric absorption events, or between pair production events are the reciprocals of partial interaction coefficients. The total attenuation coefficient is equal to the sum of the interaction coefficients for the individual processes.

3. Results and discussion

In our work, computer code XCOM was used for the calculation of the total mass attenuation coefficients for four different concrete types, which is specified in Table 1.

Table 1: Types of concrete for numerical calculations of the total mass attenuation coefficients with software code XCOM [8].

Mark	**Type of concrete**	**Density (g cm^{-3})**	**Material composition data in [reference]**
CB	Concrete, Barite (Type BA)	3.350	[7]
CMS	Concrete, Magnetite and Steel	4.640	[7]
COR	Concrete, Ordinary (NBS 04)	2.350	[7]
B5n	Concrete, UHPC barite nanosilica 5%	2.830	[11]

The dependence of values total mass attenuation coefficients on energy photon radiation is shown in the figure Fig. 1.

On the graphs Fig. 1, one can see, that total mass attenuation coefficients $(\mu/\rho)_{tot}$ has dependence of the photon energy (E): a) in three ranges for concrete types CMS and COR,

decreasing sharply at low energies (E<0.15 MeV), decreasing slightly in the middle range (0.15 MeV<E<6 MeV) and increasing slightly at high energies (E>6 MeV); b) in three ranges for concrete types CB and B5n, decreasing sharply in bottom range (10 keV<E<400 keV) with the sharp discontinuity around 30 keV, decreasing slightly in the middle range (0.4 MeV<E<6 MeV) and increasing slightly at high energies (E>6 MeV); c) in the energy range of 400 keV to 6 MeV values for the total mass attenuation coefficients are approximately the same for four different types of concrete. The results, which we have pointed out, are tied to different photon absorption mechanism for different energy range. The sharp discontinuities in energy dependence for total mass absorption coefficient are connected with the processes of the photoelectric absorption.

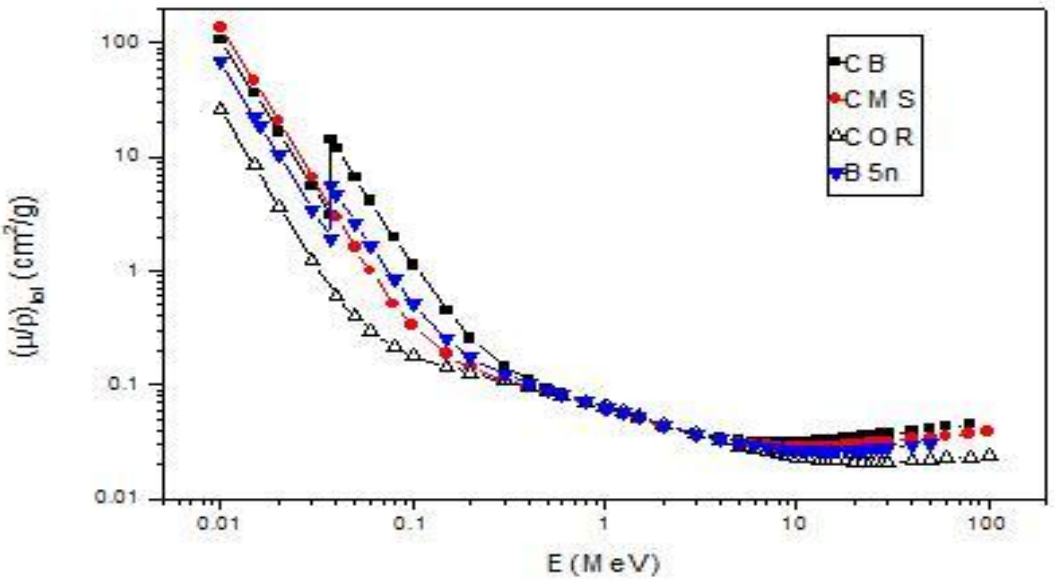

Figure 1: Total mass attenuation coefficients for four different concrete types.

4. Conclusion

In this investigation, based on the results of the corresponding graphs for Total Mass Attenuation Coefficient $(\mu/\rho)_{tot}$ it can be concluded that in the range of energy of gamma and X radiation from 30 keV to 300 keV, concrete types CB and B5n with barite sand has greater protective power than concrete types CMS or COR. Concrete type CMS with magnetite and steel has greater protective power than other three concrete types for the energy of gamma and X radiation E < 30 keV, while the concrete type CB is with better characteristics than other types of concrete for the attenuation of the radiation beam for photon energies greater than 30 keV. The results of this research point to the conclusion that before the concrete production of certain mechanical properties is approached, it is reasonable to apply the appropriate

methodology with the numerical calculation of the basic absorption characteristic of the concrete for protection against gamma and X radiation.

Acknowledgements
The work presented in this paper is a part of the investigation conducted within the research projects TR 36017 and III 43009 supported by the Ministry of Education, Science and Technological Development, Republic of Serbia. This support is gratefully acknowledged.

References
[1] Yılmaz, E. et al, Gamma ray and neutron shielding properties of some concrete materials, Annals of Nuclear Energy 38 (2011), 2204–2212
[2] Ling, T.C. et al, X-ray radiation shielding properties of cement mortar prepared with different types of aggregate, Materials and Structures (2013), DOI 10.1617/s11527-012-9959-2
[3] Bashter, I.I. et al, Magnetite ores with steel or basalt for concrete radiation shelding, Jpn. J. Appl. Phys. Vol. 36, Part 1, No.6A (1997), 3692-3696
[4] Sarkawi, M.S. et al, Radiation shielding properties of ferro-boron concrete, IOP Conf. Series: Materials Science and Engineering 298 (2018), doi:10.1088/1757-899X/298/1/012037
[5] Juniora, T.A.A. et al, Mass attenuation coefficients of X-rays in different barite concrete used in radiation protection as shielding against ionizing radiation, Radiation Physics and Chemistry 140 (2017), 349-354
[6] Ouda, A.S., Development of high-performance heavy density concrete using different aggregate for gamma-rey shilding, Progress in Nuclear Energy 79 (2015), 48-55
[7] Shultis J.K. and Faw, R.E., Radiation Shielding, Prentice Hall, Englewood Cliffs, New Jersey, (1996)
[8] Berger, M.J. et al, XCOM: Photon Cross Section Database (version 3.1). http://www.nist.gov/pml/data/xcom/index.cfm, NBSIR 87-3597. National Institute of Standards and Technology, Gaithersburg, MD (2010)
[9] Stankovic et al, Gamma Radiation Absorption Charcteristics of Concrete with Components of Different Type Materials, Acta Physica Polonica A, Vol. 117, (2010), 812-816
[10] Jankovic et al, Effect of nano-silica and aggregate type on properties of ultra high performance concrete, Proceedings of the 9th International Concrete Conference 2016 "Environment, Efficiency and Economic Challenges Challenges for Concrete", Dundee, Scotland, UK (2016), 839-846
[11] Jankovic et al, The influence of nano-silica and barite aggregate on properties of ultra high performance concrete, Construction and Building Materials 126 (2016), 147-156

SynerCrete'18 International Conference on Interdisciplinary Approaches
for Cement-based Materials and Structural Concrete
24-26 October 2018, Funchal, Madeira Island, Portugal

HYDRO-MECHANICAL MODELLING OF SELF INDUCED STRESSES: IMPACT OF DRYING GRADIENTS ON DAMAGE

François Soleilhet [(1)], Farid Benboudjema [(1)], Xavier Jourdain [(1)], Fabrice Gatuingt [(1)]

(1) LMT, ENS Cachan, CNRS, University Paris-Saclay, 94230 Cachan, France

Abstract

The prediction of the concrete structure durability is closely linked to the prediction of cracking in the long-term. Initially saturated cementitious materials are the seat of water movements that are responsible for mechanisms such as drying shrinkage, creep or changes in mechanical properties. For instance, the differential drying between the surface and the core of the structure leads to a heterogeneous state of stresses and can induce significant micro-cracking at the surface [1]. Those micro-cracks will impact not only the mechanical properties but also the permeability of the structure [2]. In this study, a sequential analysis is proposed to represent the drying evolution and the corresponding cracking pattern. First, calculations are performed to model the drying process and drying gradients. Then relative shrinkage strains are computed through shrinkage model proportional to water content. The impact of the initially determined water fields is investigated both in terms of drying shrinkage and damage generated by the different drying shrinkage models. The influence on the damage fields of the initial drying gradients is thus highlighted. Depending on the hydric fields determined, the damage is not similar. This finding illustrates the importance of precise characterization of drying gradients.

1. Introduction

Cementitious materials are the most widely used in civil engineering works. They are heavily used to face a various or aggressive environments in the fields of housing, transport or energy. Today, the durability of buildings is a major challenge. To address this problem it is necessary, among other things, to predict the long-term behaviour of the structures. Nevertheless, this task remains difficult. The great heterogeneity of the material combined with multiple origins of stresses (thermal, chemical, drying, mechanical) make the work complex.

The objective of the work presented is to study the impact of the determination of hydric fields resulting from concrete drying on the prediction of drying shrinkage and induced damage. To answer this question a sequential analysis integrating the prediction of the drying of 7x7x28 cm concrete test pieces and the development of the drying shrinkage is studied. The mechanical model used is based on a damage model. The state of induced damage is then determined. The impact of hydric prediction is thus studied by comparing two hydric modelling with the same macroscopic results (same relative mass variation).

2. Hydro-mechanical modelling

As part of the proposed work, some simplifying assumptions were made. The material is considered mature (final material properties) and hydration is not taken into account. All the mechanisms are considered in a decoupled way [3] which makes it possible to consider them one after the other.

2.1 Drying modelling

The drying of cement-based materials is a complex phenomenon. Several, more-or-less coupled, mechanisms are involved: permeation, diffusion, adsorption-desorption and condensation-evaporation. Drying can be analysed through the resolution of liquid water, vapour and dry air mass balance equations. The use of several hypotheses [4,5] allows for considering only the mass balance equation of liquid water:

$$\frac{dS_l}{dP_c}\frac{dP_c}{dt} = div\left(k_{rl}(S_l)\frac{K}{\mu_l \phi}grad(P_c)\right) \quad (1)$$

where S_l, Pc, ϕ, K, k_{rl} and μ_l are, respectively, the saturation degree, the capillary pressure, the porosity, the intrinsic permeability, the relative permeability and the viscosity of the liquid water. It is shown [6,7] that this equation is sufficient for an accurate prediction of the drying of ordinary and high-performance concretes at 20°C with a relative humidity greater than 50%. The capillary pressure and the relative permeability are related to the degree of saturation through van Genuchten's relations [8]:

$$S_l = \left(1 + \frac{P_c}{P_0}\right)^{1-\gamma} \quad (2)$$

$$k_{rl}(S_l) = S_l^{nk}\left(1 - \left(1 - S_l^{\frac{1}{\beta}}\right)^{\beta}\right)^2 \quad (3)$$

where n_k, P_0 and β are materials parameters. Drying at surfaces was modelled using a convection-type approach with a convection coefficient equal to 50 (m^3.s).

2.2 Shrinkage modelling

There are different ways to model drying shrinkage. Some of these are based on the theory of porous media mechanics. The development of this kind of modelling could be easily found in literature [6]. Other models are based on phenomenological observations. Indeed, following experimental results [7,9] it was found a proportional relation between water content variation and drying shrinkage rate. These observations lead to the equation (5).

$$\underline{\underline{\dot{\epsilon}}}_{ds} = k_{ds}\,\dot{w}\,\underline{\underline{1}} \tag{5}$$

where k_{ds} is a constant hydrous compressibility factor and $\underline{\underline{1}}$ is the unit matrix. It is possible to find alternative approaches but in this present work this modelling approach was chosen. It is easy to implement and gives satisfactory results.

2.3 Mechanical Modelling

This study is based on 3D modelling. It involves non-explicit modelling of concrete cracking using a damage theory. The variable D, a scalar damage variable ranging from 0 to 1, is considered in the stress-strain relation:

$$\sigma_{ij} = (1 - D)C_{ijkl}\epsilon_{kl}^{elas} \tag{6}$$

where σ_{ij}, C_{ijkl}, ϵ_{kl}^{elas}, are respectively stress, elastic stiffness and elastic strains. The evolution of the damage relies on an equivalent strain criterion, calculated from the equivalent strain ϵ_{eq} introduced by Mazars [10]. It was shown [11] that the evolution of damage in tension could be taken as an exponentially decreasing:

$$D = 1 - \frac{\epsilon_{d0}}{\epsilon_{eq}}.\exp\left(-B_t\left(\epsilon_{eq} - \epsilon_{d0}\right)\right) \tag{7}$$

where $\epsilon_{d0} = f_t/E_c$, with f_t the tensile strength, E_c the Young modulus and B_t a parameter controlling the softening behaviour of the concrete.

Softening behaviour of concrete may lead to non-unicity of solutions and mesh dependency. Energetic regularization prevents these difficulties [12]. Regularization is then based on the parameter B_t, which is a function of h, the characteristic size of the finite element, f_t the tensile strength, G_f the fracture energy and a parameter for the initiation of the damage ϵ_{d0} as described above.

$$B_t = \frac{h.f_t}{G_f - \frac{h.\epsilon_{d0}.f_t}{2}} \tag{8}$$

3. Results

In this section, the numerical results of the different studies are presented. These are based on experimental results of standard concretes carried out within the LMT Cachan over a period of 440 days and which has been kept under conditions of 45% relative humidity and 21.5°C. The experimental results will not be detailed; only the relative mass variation and drying shrinkage curves will serve as a basis for numerical tests.

3.1 Hydric fields

The various simulations are carried out using three-dimensional modelling of one eighth of the total section. The elements, numbering of 2187, are linear. The specimens are subjected on their exposed sides to storage conditions. After identifying the model parameters presented in Tab. 1, the hydric fields are simulated. The reader will notice that at time "0" on Figure 1 and 2 the concrete had already 28 days of age.

Table 1: Water solutions.

Set of parameters	**β [-]**	**P_0 [MPa]**	**n_k [-]**	**K [m^2]**	**Φ [-]**	**ρ [$kg.m^{-3}$]**
1	0.45	11.4	-1.42	$5.81.10^{-21}$	0.16	2400
2	0.48	24.2	-0.46	$4.35.10^{-21}$	0.17	2366

The comparison with the evolution of the experimental relative mass variation presented in Figure 1, shows a good similarity of the numerical results with both sets of parameters.

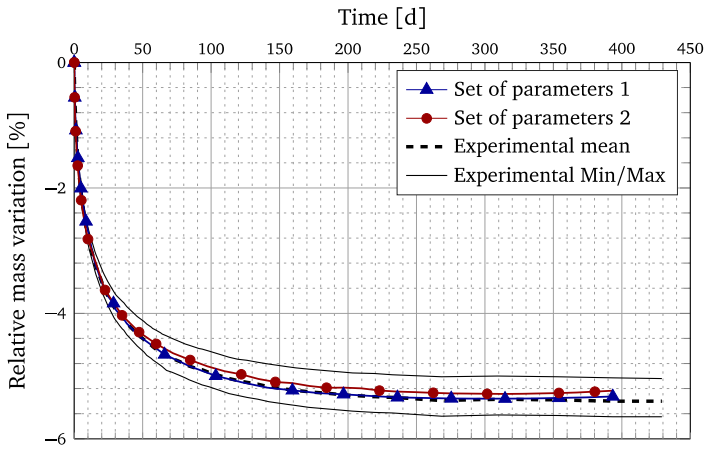

Figure 1: Evolution of relative mass variation after 440 days of drying

Although the evolution of relative mass variation is the same for both modelling, we notice that the hydric fields are not equal. Figure 2 shows major difference between both simulations. First of all, after 440 days of drying, the two profiles are not yet in equilibrium with the environment. Moreover, the field from the first parameter set is much less dry than the second. The drying is more concentrated on the first centimetres of the sample while the second model shows a drying that seems more homogeneous. This difference is mainly explained by different isotherms.

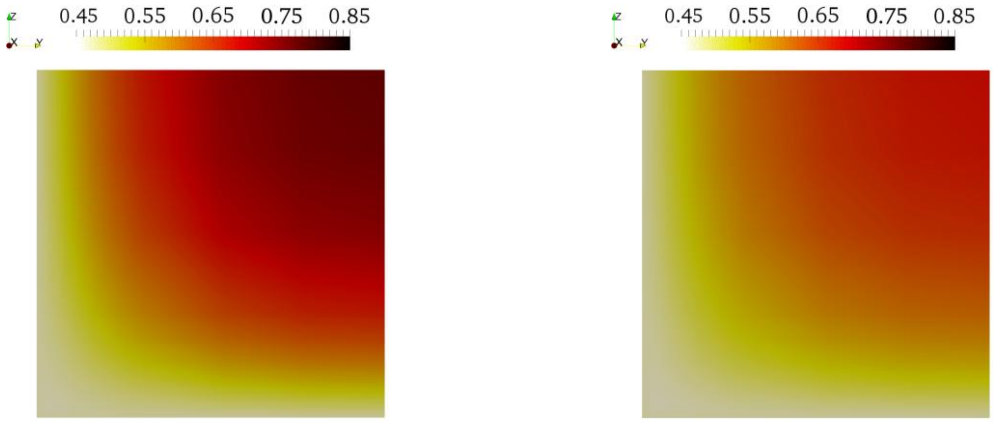

(a) Set of parameters 1 (b) Set of parameters 2

Figure 2: Relative humidity fields within the sample in the mid-section (eighth of section)

3.2 Damage induced by shrinkage

Once the hydric state is set, it is then possible to simulate the evolution of the drying shrinkage using equation (5). The mesh size data are similar to the previous hydric problem. Figure 3 shows the drying shrinkage trend after 440 days of drying. It can be seen that by adapting the k_{ds} coefficient it is possible to represent the shrinkage over this period of time in almost the same way. Moreover, the coefficients are close to each other.

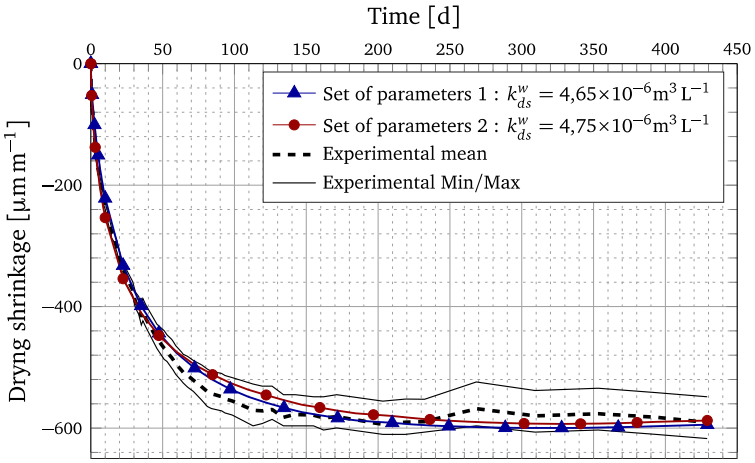

Figure 3: Evolution of drying shrinkage after 440 days

Although a good similarity is observed at the macroscopic level if we now place ourselves at the cracking scale when the shrinkage reaches a plateau, which is here around 220 days, we see in Figure 4 that the damage profiles differ. With almost similar shrinkage, the damage to profile 1 is greater than the second. This observation seems logical at the sight of the model used; the first hydric profile is the one which presents the strongest gradients which generates a more important damage. All this suggests that it is necessary to define the hydric state and more particularly the saturation degree precisely.

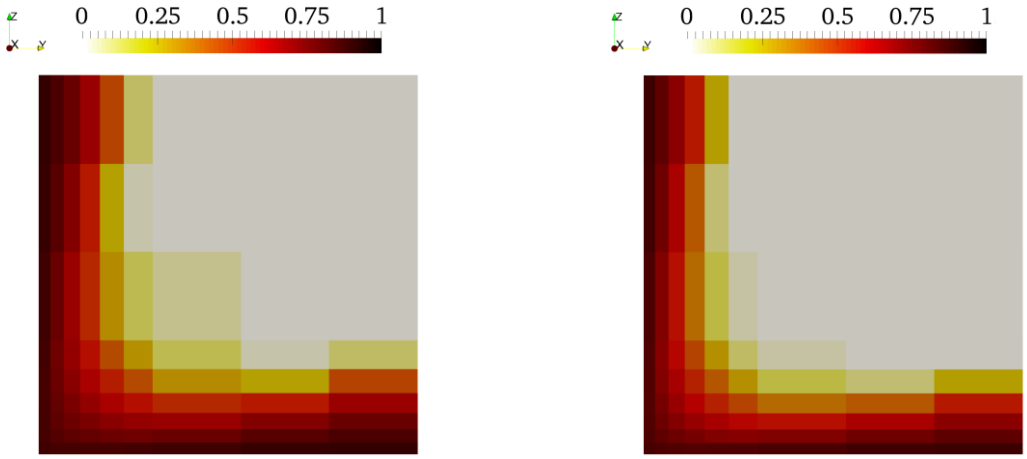

(a) Set of parameters 1 (b) Set of parameters 2

Figure 4: Comparison of damage fields between the two sets of parameters after 220 days

4. Conclusion

In this communication, the impact of the determination of hydric fields was investigated. After defining hydric state, drying shrinkage was simulated using a phenomenological model proportional to water content. We note:

- Macroscopically the relative mass variation is similar but we notice that at the cracking scale the hydric fields are very different. This difference is mainly explained by the difference in desorption isotherms.
- It can be seen that by adapting the proportionality coefficient, the two hydric fields make it possible to determine the apparent drying shrinkage; nevertheless the corresponding damage fields are not similar. This observation leads the modeller to define precisely the hydric state of the material so as not to over- or underestimate the cracking of the material.

References

[1] Bisschop, J. and van Mier, JGM., How to study drying shrinkage microcracking in cement-based materials using optical and scanning electron microscopy. Cement and Concrete Res, 32 (2002), 279–287.
[2] Yurtdas, I., Peng, H., Burlion, N. and Skoczylas, F., Influences of water by cement ratio on mechanical properties of mortars submitted to drying. Materials and Structures, 36 (2006), 1286–1293.
[3] Granger L. Comportement différé du béton dans les enceintes de centrales nucléaires : analyse et modélisation, PhD Thesis from Ecole Nationale des Ponts et Chaussees (1995).
[4] Bažant ZP, Sener S, Kim JK, Effect of cracking on drying permeability and diffusivity of concrete. ACI Materials Journal 84 (1986), 351-357
[5] Hansen TC, Creep of concrete: the influence of variations in the humidity of ambient atmosphere, Proceedings 6th Congress of the International Association of Bridge and Structural Engineering, Stockholm (1960), 57-65
[6] Thiery M, Baroghel-Bouny V, Bourneton N, Villain G, Stefani C, Modélisation du séchage des bétons : analyse des différents modes de transfert hydrique, Revue Européenne de Génie Civil 11(5) (2007), 541-577
[7] Goltermann P, Mechanical predictions of concrete deterioration – Part 2: classification of crack patterns, ACI Materials Journals 92(1) (1995), 58-63
[8] Lassabatère T, Torrenti J-M, Granger L, Sur le couplage entre séchage du béton et contrainte appliqué, Proceedings Actes du Symposium Saint-Venant, Paris (1997), 331-338
[9] Baroghel-Bouny V and al., Characterization and identification of equilibrium and transfer moisture properties for ordinary and high-performance cementitious materials, Cement and Concrete Research 29 (1999), 1225-1238
[10] Mazars J. A description of micro-and macro scale damage of concrete structures. Eng Fract Mech 25(5) (1986), 729–37
[11] Feenstra PH. Computational aspects of biaxial stress in plain and reinforced concrete, PhD thesis Technical University of Delft (1993)
[12] Hillerborg A, Modéer M, Petersson P-E. Analysis of crack formation and crack growth in concrete by means of fracture mechanics and finite elements. Cem Concr Res 6(6) (1976), 773–81

SynerCrete'18 International Conference on Interdisciplinary Approaches
for Cement-based Materials and Structural Concrete
24-26 October 2018, Funchal, Madeira Island, Portugal

NUMERICAL MODELING OF POROUS MEDIA FREEZING PROCESS BY MEANS OF A NON-EQUILIBRIUM APPROACH

Dariusz Gawin [(1)], Francesco Pesavento [(2)]

(1) Lodz University of Technology, Lodz, Poland
(2) University of Padova, Padova, Italy

Abstract

Freezing-thawing cycles are one of the most significant causes of durability problems for concrete structures in cold climate countries. Water freezing in a porous material is a very complex physicochemical process, difficult to model numerically due to the interactions between different phases/components, the inner microstructure of the material and phase changes taking place in a confined environment, what leads to an alteration of the standard freezing and fusion points of water.

In this work, we present a coupled model for the numerical modelling of heat and mass transport and their mechanical effects in partially saturated porous media, exposed to freezing – thawing processes. Phase changes are modelled by means of a kinetic, non-equilibrium approach derived from the Thermodynamics of porous media. It is able to reproduce the cryo-suction, supercooling and undercooling phenomena considering in such a way the hysteresis of ice content vs. temperature during the phase change, what results also in hysteresis of material strains. The latter ones are calculated here by means of appropriately formulated effective stress principle considering crystallization pressure in partially saturated materials. Some relevant numerical cases will be presented to show the effectiveness of the formulated model in the simulation of freezing-thawing process.

1. Introduction

In this work we present a new numerical model for the simulation of the behaviour of porous materials under cooling, with particular regard to cementitious materials. The latter ones are characterized by a fine inner microstructure, formed of C–S–H gels, mineral crystals of various compositions and pores of different sizes which can be fully or partially saturated with water. Due to this complex microstructure and the mutual interactions between various

phases/components at micro level, the formulation of a mathematical/numerical model able to take into account all the most important phenomena is particularly difficult, especially in the case of partially saturated states, i.e. when all the phases of water (solid, liquid and vapour) are simultaneously present.
Unlike most of the models in literature, which are based on an approach at equilibrium (see [1] for example), here the water freezing/melting processes for the porous material are modelled far from equilibrium. Their kinetics are governed by a first order evolution law, obtained from the second law of Thermodynamics with capillary pressure as main physical variable used for the definition of the thermodynamic imbalance during the process evolution.
Pore water freezing is initiated by heterogeneous nucleation and then followed by a progressive penetration of the ice front from larger to smaller pores. With the formulation here proposed, it is possible to observe the so-called supercooling phenomenon, i.e. the delayed first freezing of water at temperature below zero, due to the uncertainties of nucleation. The liquid water can flow through a thin film of physically adsorbed water between the skeleton and ice crystal, hence water pressure does not increase during freezing in a partially saturated material.
The model takes also into consideration the freezing point depression due to the confinement of the water phases in the pores' network and their mutual interactions. This phenomenon is known as undercooling process and leads to a sort of hysteresis between the freezing and the melting stages (because of the different curvatures of the ice-water interface we can observe during freezing and melting [2]).
The model defined in this way, is able to take into account several phenomena leading to the deformation of the porous material and to the internal microcracking: (*i*) the expulsion of unfrozen water from the freezing sites towards the airvoids, which is usually related to the 9% expansion of water upon freezing, (*ii*) the crystallization process which is strictly related to the formation of ice crystals and their growth; (*iii*) the transfer of liquid water from the unfrozen pores to already frozen sites (i.e. cryo-suction process); (*iv*) the thermo-mechanical interactions between the solid skeleton and the water in its various forms (liquid, gaseous, solid).
A comparison between experimental results (obtained from a DSC test) and numerical ones, are shown for the validation of the model proposed. Furthermore, some additional numerical examples are presented to show its effectiveness.

2. Kinetics of water freezing in porous materials

Here the water freezing/melting in a capillary-porous material is modelled as a non-equilibrium process, the kinetics of which is governed by a linear evolution law, obtained from the second law of Thermodynamics in the following form [3],

$$\dot{s}_i = A_{fr}\dot{\Gamma}_{fr} \tag{1}$$

where $\dot{s}_i$ is the rate of internal production of molar entropy due to the freezing, $\dot{\Gamma}_{fr}$ the rate of freezing, and the process affinity is $A_{fr} = \mu_w\left(T, p^w\right) - \mu_{ice}\left(T, p^{ice}\right)$, with μ_w and μ_{ice} being chemical potentials of liquid water and ice (solid water), respectively.

By considering:

i) the definition of the chemical potentials and equilibrium condition for the transition of bulk phases at temperature T_0 and pressure p_0;
ii) that in porous materials, due to curved interfaces between the phases and interaction of pore walls, the water and ice pressures are different;
iii) a simplified form of the affinity Afr;
iv) the relationships at equilibrium;

it is possible to formulate the equations describing the kinetics of the freezing/melting processes taking place in the pores of the material (see [3] for further details). These evolution equations have the form described in the following.

Water freezing process

The evolution equation of the ice mass source due to freezing of liquid water, $\dot{m}_{fr/w}$, can be described through the following law (T_m^* is the melting temperature):

$$\text{if } p_{fr}^c < p_{fr,eq}^c\left(T\right) \text{ and } T < T_m^*: \quad \dot{m}_{fr/w} = -n\rho^w S_w \frac{v_w}{RT}\frac{p_{fr}^c - p_{fr,eq}^c}{\tau_{fr}}; \qquad \text{otherwise}: \quad \dot{m}_{fr/w} = 0. \tag{2}$$

where n is the porosity of the material, ρ^w and v_w are the density and the molar volume of the water respectively, R is the universal gas constant and, finally, τ_{fr} is the characteristic time of freezing which is related to the affinity of the process and to its reaction rate. Moreover in eq. (3) p_{fr}^c is the actual value of the capillary pressure during freezing process (far from equilibrium) and $p_{fr,eq}^c$ is the corresponding value of capillary pressure under equilibrium. From eq. (3) it is clear that it is possible to have freezing of liquid water only if the current value of capillary pressure is lower than the value of the same quantity at equilibrium.

Ice melting process

Ice melting can be treated in a similar manner. In such a case, it is needed to consider the different shape of the liquid water-ice interface respect to the case of freezing. At this aim, a parameter $\bar{\lambda}(S_w)$ is introduced in the evolution model. This parameter is the ratio of the curvature of the meniscus during freezing and melting. Thus, the ice mass source during melting process can be expressed as follows:

$$\text{if } p_{fr}^c > p_{m,eq}^c(T) \text{ and } \dot{T} > 0: \quad \dot{m}_{fr/w} = -n\rho^w S_w \bar{\lambda}\left(S_w\right)\frac{v_w}{RT}\frac{p_{fr}^c - p_{m,eq}^c}{\tau_m}; \qquad \text{otherwise}: \quad \dot{m}_{fr/w} = 0. \tag{3}$$

where τ_m is the characteristic time of melting, and $p_{m,eq}^c(T)$ is the capillary pressure at equilibrium during the melting process (different than the one during freezing). One can observe melting only if the actual value of capillary pressure p_{fr}^c is higher than the value

under equilibrium conditions $p^c_{m,eq}(T)$. The latter one, is related to the capillary pressure at equilibrium during the freezing process according to the following relationship: $p^c_{m,eq} = p^c_{fr,eq} / \bar{\lambda}(S_w)$.

The constitutive law for $\bar{\lambda}(S_w)$ can be identified by means of experimental tests conducted with a calorimeter or by supposing a spherical and a cylindrical shape for the water-ice interface during freezing and melting respectively. In such a case $\bar{\lambda}(S_w)$ assumes a constant value equal to 0.5.

This evolution model for freezing was introduced in a more general model which treats concrete as multiphase porous material. It takes into account the bulk phases, the interfaces and their thermo-chemical and mechanical interactions, as well as, phase changes and chemical reactions for the components/species considered. The reader can refer to [4] for further details.

3. Validation of the model

In the following some results of a DSC (Differential Scanning Calorimetry) test, are compared with the numerical ones in order to validate the model proposed in this work. The material is a silicate whose main properties are depicted in Table 1.

Table 1: Main properties of the material used in DSC test.

Property	**Value**
Density	1792 kg/m^3
Young's Modulus	9 GPa
Compressive Strength	26 MPa
Thermal Conductivity	0.78 W/mK
Specific Heat	880 J/kgK
Porosity	30.1 %

For the identification of the suction curve (i.e. the main isotherm of the porous material) some results of a MIP (Mercury Intrusion Porosimetry) test have been used in order to characterize the inner microstructure. Fig. 1 shows a comparison between the MIP experimental results and the theoretical isotherm adopted in the range of interest for the capillary pressure. The initial saturation of the material was 35% corresponding to a relative humidity of 96.4%. For the sake of simplicity, the coefficient $\bar{\lambda}(S_w)$ was assumed constant equal to 0.5 in the numerical simulation of the DSC test, while the same value of the characteristic time for freezing and melting processes was adopted (15 sec). The temperature history during the DSC test is shown in Fig. 2. In Fig. 3 one can observe a comparison between experimental and numerical results in terms of ice saturation degree (in the domain of temperature). We can identify a maximum level of ice content corresponding to the instants at which the

temperature reaches the lowest value and then increase, and an intermediate level corresponding to the central part of the temperature evolution. The overall agreement is good: the differences are mainly due to the form of the isotherm adopted, which represents the hygral behavior of the material only in a short (central) range of capillary pressure. Furthermore, we can notice as the peculiar approach adopted here (i.e. far from equilibrium) helps in capturing the first-freezing phase which is often characterized by a sudden release of energy.

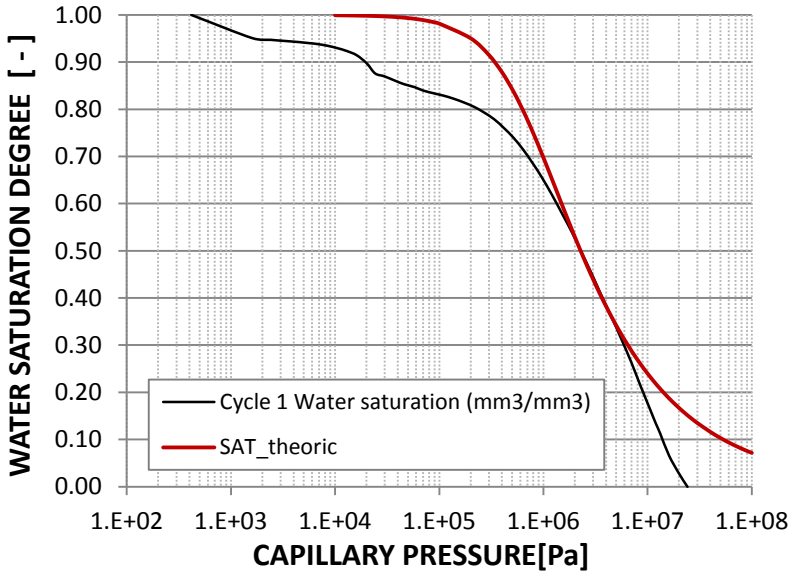

Figure 1: Isotherm of the silicate used for the validation: comparison between MIP test results and the theoretical formulation used in the model.

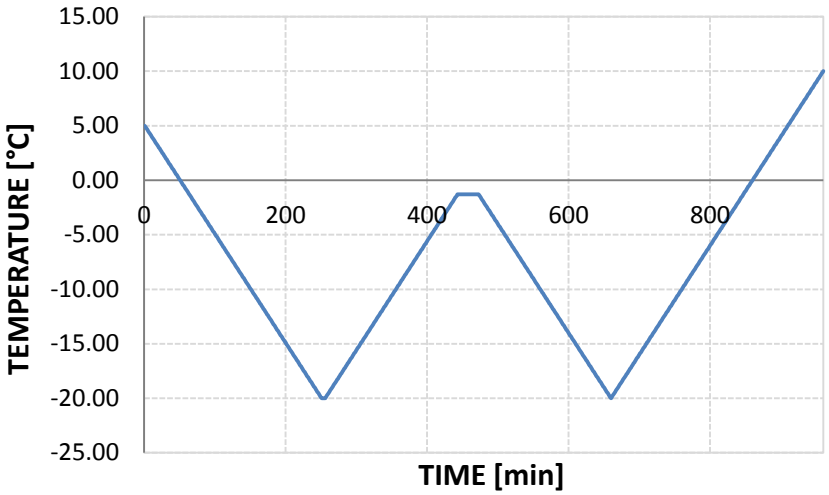

Figure 2: Thermal cycle applied to the specimen during the experimental tests.

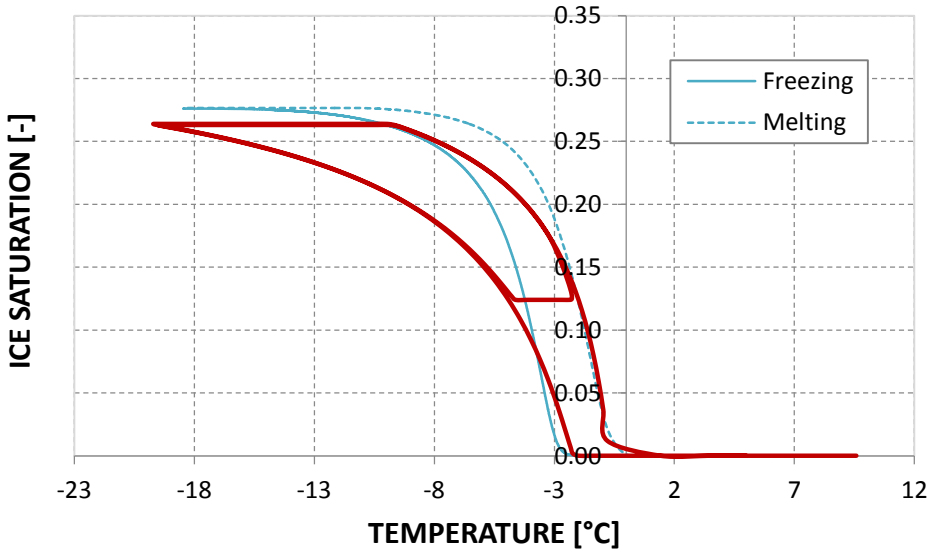

Figure 3: Comparison between experimental (thin lines) and numerical (bold line) results in terms of ice saturation degree S_{ice}.

4. Conclusions

In this work, we have shown a coupled model for the numerical simulation of freezing-melting processes in partially saturated porous media. The model is able to catch the heat and mass transfer phenomena taking place in the material and also the related mechanical effects. It is based on a non-equilibrium approach derived from the Thermodynamics of Phase Changes (considering all the phases of water simultaneously present in the pores of the material). By means of such a kind of approach, it is possible to reproduce numerically the cryo-suction, supercooling and undercooling phenomena as well as the associated hysteresis in the ice content and material strains evolution.

References

[1] Coussy, O and Monteiro, P.J.M., Poroelastic model for concrete exposed to freezing temperatures, Cem Concr Res 38 (2008), 40-48
[2] Sun, Z. and Scherer, G.W., Measurement and simulation of dendritic growth of ice in cement paste, Cem Concr Res 40 (2010), 1393-1402
[3] Gawin, D., Pesavento, F., Schrefler, B.A, Non-equilibrium modeling of water freezing-thawing with hysteresis in partially saturated porous media., submitted to Transport in Porous Media
[4] Gawin, D., Pesavento, F., Schrefler, B.A., Hygro-thermo-chemo-mechanical modelling of concrete at early ages and beyond. Part I. Hydration and hygro-thermal phenomena, Int J for Num Meth in Eng 67(3) (2006), 299-331

SynerCrete'18 International Conference on Interdisciplinary Approaches
for Cement-based Materials and Structural Concrete
24-26 October 2018, Funchal, Madeira Island, Portugal

NUMERICAL SIMULATION OF EARLY-AGE CONCRETE BEHAVIOUR OF AN ARCH DAM

Noemi Schclar Leitão [(1)], Eloísa Castilho [(1)]

(1) Laboratório Nacional de Engenharia Civil, Lisbon, Portugal

Abstract
This paper reports a case study of the chemo-thermal-mechanical analysis of a concrete arch dam during its construction and first reservoir filling phases. The hydration kinetics model is formulated in the framework of thermodynamics of chemically reactive porous media based in the model presented by Ulm and Coussy. The structural response of the dam is assessed by a viscoelastic model. The parameters of the normalized affinity and the double power creep law are defined based on laboratory tests performed on samples extracted during construction. The predicted temperatures and stresses are compared with the monitoring system values.

1. Introduction

In dam engineering, the analysis of the observed behaviour and assessment of security conditions is performed by comparing the values measured by the monitoring system installed in the dam with the values predicted by mathematical models representing the structural behaviour, the material properties and the loads. Instrumentation provides data for monitoring the safe performance during the various phases of the dam's life including design, construction, first filling of the reservoir, evaluation of long-term, in service performance (normal operation), and to manage or predict unsatisfactory performance. Installation of instrumentation typically occurs 1) during constructions, and 2) during the life of the dam to address new or changing conditions [1].
The purpose of this paper is to describe the main issues concerning the chemo-thermal-mechanical modelling necessary to obtain a representative simulation of early-age concrete behaviour of an arch dam. The general description of the dam as well as the finite element mesh, material properties and loads adopted to simulate the first filling of the reservoir can be

seen in [2]. This paper will be focused on the definition of the hydration kinetics and the viscoelastic models which allow the simulation of the dam behaviour since its construction.

2. Determination of the normalized affinity

The hydration kinetics model is formulated in the framework of thermodynamics of chemically reactive porous media based in the model presented by Ulm and Coussy [3]. Among the different empirical relationships used to represent the normalized affinity $\tilde{A}(\xi)$ [4] [5] [6], the one presented by Cervera *et al.* [6] is used:

$$\tilde{A}(\xi) = \frac{k_\xi}{\eta_{\xi o}} \left(\frac{A_{\xi o}}{k_\xi \xi_\infty} + \xi \right) (\xi_\infty - \xi) \exp\left(-\bar{\eta} \, \frac{\xi}{\xi_\infty} \right) \tag{1}$$

where ξ is the hydration degree, ξ_∞ is the asymptotic degree of hydration and k_ξ, $A_{\xi o}$, $\eta_{\xi 0}$ and $\bar{\eta}$ are material properties. According to [6] the material properties involved in expression (1) can be determined experimentally, by an adiabatic calorimetric test, considering:

$$\tilde{A}(\xi) = \frac{\xi_\infty \, \dot{T}^{ad}}{T_\infty^{ad} - T_o} \exp\left(\frac{E_a}{RT} \right) \qquad \text{and} \qquad \xi = \xi_\infty \frac{T^{ad} - T_o}{T_\infty^{ad} - T_o} \tag{2}$$

where T^{ad} is the measured temperature of concrete during the experiment, $\dot{T}^{ad}$ is the measured temperature rate, T_∞^{ad} is the final reached temperature, T_o is the initial temperature, E_a is the activation energy of the reaction and R is the ideal gas constant. In many cases, however, the available data of heat of hydration is restricted to a few points. Thus, in order to represent the whole course of the adiabatic hydration process, an analytical expression has to be fitted to the data points. For example, adopting an S-shape function of the form [7]:

$$Q = Q_\infty \exp\left(-(\tau/t)^\beta \right) \tag{3}$$

where Q_∞ is the liberated heat when hydration has practically ceased, t is the time and τ and β model the shape of the function. Adopting $\beta = 1$ and taking into account that $T^{ad} = Q/(\rho c)$, where ρc is the volumetric specific heat of concrete, the normalized affinity function (2) is as follows:

$$\tilde{A}(\xi) = \frac{\xi_\infty}{T_\infty^{ad} - T_o} \exp\left(\frac{E_a}{RT} \right) \frac{Q_\infty \tau}{\rho c \, t^2} \exp(-(\tau/t)) \tag{4}$$

Finally, the analytical expression (1) is determined by calibrating the three material properties $k_\xi/\eta_{\xi o}$, $A_{\xi o}/k_\xi$ and $\bar{\eta}$ with expression (4). Although the analytical expression (4) can be used directly to model the affinity, it was decided to approximate it to the Cervera *et al.* [6] function form, in order to preserve the meaning of the different terms involved in the empirical relationship, as described in [8]. In the case under analysis, as part of the *Concrete Quality Assurance*, three samples of cement were tested to determine the heat of hydration at the ages of 3, 7 and 28 days. These results and the best fitting curve (3) adopting $\beta = 1$ are presented in Fig. 1.

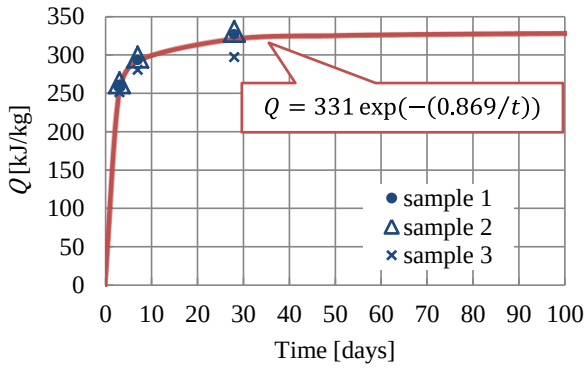

Figure 1: Cement heat of hydration development.

To consider the reduction in the total heat of hydration produced by the replacement of a portion of the Portland cement with fly ash, the results obtained by EDP [9] for the mass concrete of the Portuguese dams was taken into account. This study shows that for 50% of fly ash, the decrease in heat of hydration is of approximately one third.

To the composition of the concrete used in the body of the dam characterized by a cementitious content of 260 kg/m^3 with 55% of fly ash and a ratio w/c = 0.55 and considering a decrease in heat of hydration is approximately of 1/3 [9], the following parameters (to be used in Eq. (1)) were determined ξ_∞ = 0.77; $k_\xi/\eta_{\xi o}$ = 4x10^5 h^{-1}; $A_{\xi o}/k_\xi$ = 1.04×10^{-2} and $\bar{\eta}$ = 5.59. The adiabatic temperature rise and the normalized affinity obtained are illustrated in Fig. 2. Fig. 2 (b) shows the comparison of the estimated normalized affinity of Eq. (4) and the Cervera *et al.* analytical expression (1) evaluated with the parameters defined above.

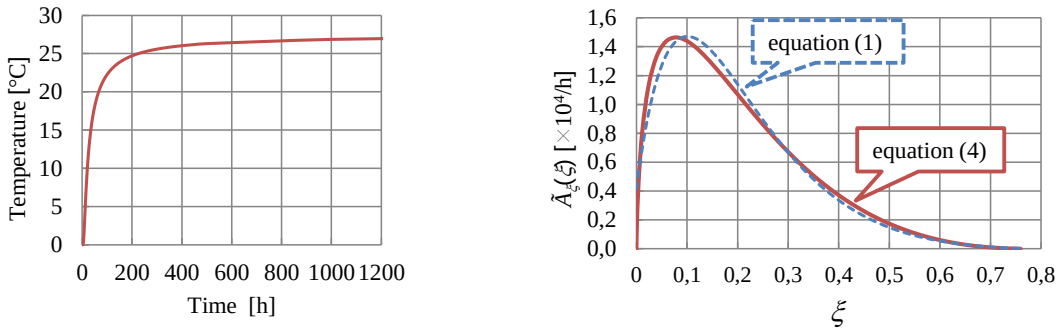

(a) (b)

Figure 2: (a) Adiabatic temperature rise, (b) normalized affinity

3. Concrete creep law

Following the normal procedure utilized by the National Laboratory for Civil Engineering for the monitoring of the Portuguese dams, the double power law [10] was adopted as the concrete creep prediction model:

$$J(t-t') = \frac{1}{E_o} + \frac{\varphi_1}{E_o}\,(t'^{-m} + \alpha)(t-t')^n \qquad (5)$$

in which $J(t-t')$ is the compliance function (or the creep function), *i.e.* the strain at age t caused by a unit uniaxial constant stress acting since age t'; E_o is the asymptotic modulus; n, m, α and φ_1 are material parameters. The static modulus as function of age may be expressed also from the double power law, setting $t-t'$ = 0.1 day in Eq. (5):

$$\frac{1}{E(t')} = \frac{1}{E_o} + \frac{\varphi_1}{E_o}\, 10^{-n}(t'^{-m} + \alpha) \tag{6}$$

Figure 3 shows the fit of Eq. (5) and (6) to the results obtained in laboratory for creep in samples at ages 28 and 32 days and for the modulus of elasticity at ages 28, 32, 90 and 365 days for E_o = 35 GPa, n = 0.12, m = 0.51, α = 0.043 and φ_1 = 4.

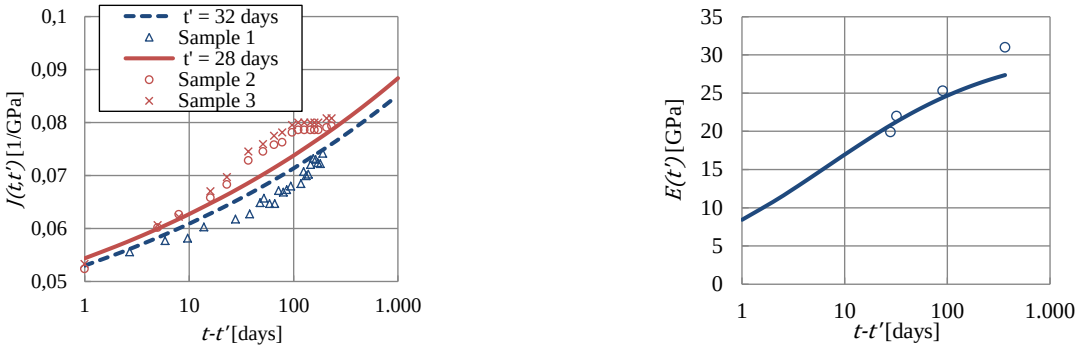

(a) (b)

Figure 3: (a) Fits of creep test, (b) fits of modulus of elasticity

4. Results and discussion

The analysed dam is a concrete double curvature arch dam with artificial gravity abutments. The total height above the foundation is 41 m, the crest length is 100 m, and the crest elevation is 668.50 m. Its shape definition is based on parabolic arches, which increase in thickness towards the abutments; the central cross section has a theoretical thickness of 2 m at the crest and 5.5 m at the base. The dam is divided in six blocks along its axes, the two central blocks have 16 m in width and the laterals blocks have 17 m in width.

The simulation starts with the beginning of the construction on June 22, 2011. The finite element model of the dam was updated for every construction stage by applying the birth and death methods. At this stage, all the contraction joints, simulated by zero thickness interface elements, were considered open, *i.e.* no interaction between blocks was allowed. On May 1, 2013 the interface elements were activated in order to simulate the grouting of the contraction joints. The first filling of the reservoir began on June 28, 2013 and by July 8 the water level reached the first stage at elevation 642.00 m and was maintained during the summer. At the end of September the hold point at elevation 649.00 m was achieved and it was maintained for several weeks. Finally, the period of severe rainstorms that occurred during late 2013 and early 2014 led to an uncontrollable rising of the reservoir, being reached the second stage at elevation 658.50 m on January 9, the third stage at elevation 664.00 m on February 4 and the last stage at elevation 665.40 m on February 11, 2014.

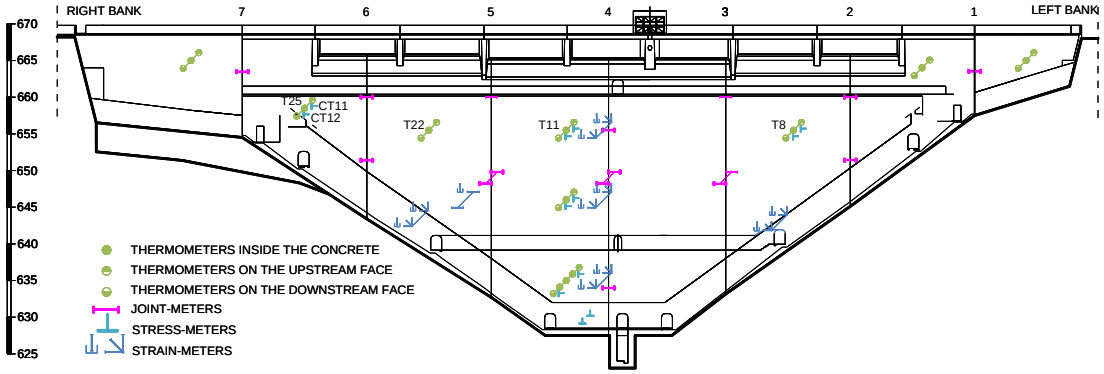

Figure 4: Monitoring electrical devices embedded into the concrete

Fig.4 shows the instrumentation embedded into the concrete based on electrical devices: strain-meters, stress-meters, joint-meters and thermometers. This figure also includes the name of the electrical devices mentioned in Fig. 5.

Fig. 5 shows the comparison between the recorded and calculated values of temperatures at elevation 655.50 m (thermometers T8, T11 and T22) and temperatures and arch stresses at elevation 658.50 m (thermometer T25 and stress-meters CT11 and CT12).

Considering the uncertainties associated with air and water temperatures and solar radiation, the variability in concrete composition and the approximation involved in the finite element mesh, mainly during the construction stage, the results obtained in the chemo-thermal-mechanical analysis are very encouraging. Additional work remains to be done on modelling the concrete properties evolution as result of cement hydration.

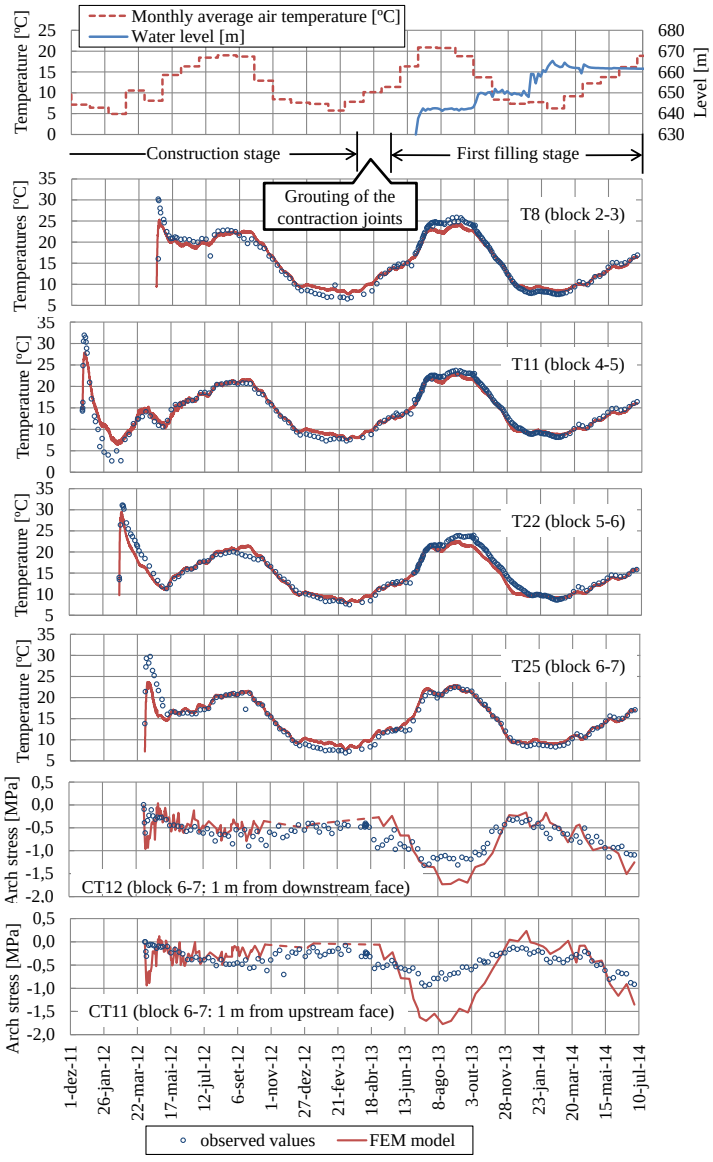

Figure 5: Comparison of monitored and numerical results

References

[1] Leitão, N.S. et al, Analysis of the observed behavior of Alto Ceira II dam during the first filling of the reservoir, Second International Dam World Conference, Portugal (2015)
[2] USSD, Development of a dam safety instrumentation program, United States Society of Dams (2013)
[3] Ulm, F.J. and Coussy, O., Modeling of thermochemomechanical couplings of concrete at early ages, J. Engrg. Mech., ASCE, 121(7) (1995), 185-794
[4] Hellmich, C. et al, Consistent linearization in Finite Element analysis of coupled chemo-thermal problems with exo- or endothermal reactions, Computational Mechanics 24 (1999), 238-244
[5] Lackner, R. and Mang, H., Chemoplastic material model for the simulation of early-age cracking: From the constitutive law to numerical analyses of massive concrete structures, Cement & Concrete Composites 26 (2004), 551-562
[6] Cervera, M. et al, Thermo-chemo-mechanical model for concrete. Part I: Hydration and aging, Journal of Engineering Mechanics 125(9) (1999), 1018-1027
[7] Van Breugel, K., Prediction of temperature development in hardening concrete, Prevention of thermal cracking in concrete at early ages, RILEM Report 15 (1998)
[8] Cervera, M. et al, Numerical modelling of concrete curing, regarding hydration and temperature phenomena, Computer & Structures 80 (2002), 1511-1521
[9] Camelo, A., Durabilidade e vida útil das estruturas hidráulicas de betão e de betão armado, JMC2011 Proceedings from 1as Jornadas de materiais na construção, Portugal (2011), 149-169
[10] Bazant, Z.P. and Panula, L., Practical Prediction of Time-Dependent Deformation of Concrete, Materials and Structures, Part I and II: 11(65) (1978), 307-328; Parts III and IV: 11,(66) (1978), 415-434; Parts V and VI: 12(69) (1979), 169-173

SynerCrete'18 International Conference on Interdisciplinary Approaches
for Cement-based Materials and Structural Concrete
24-26 October 2018, Funchal, Madeira Island, Portugal

NUMERICAL STUDY OF CHLORIDE INGRESS IN CONCRETE: EFFECT OF EXPOSURE CONCENTRATION

Mohamad Achour [1,2], Ouali Amiri [2], François Bignonnet [2], Emmanuel Rozière [1], Mahdi Haidar [2]

(1) Centrale Nantes, Nantes, France
(2) University of Nantes, Nantes, France

Abstract
The corrosion process is usually described into two periods that model the service life of the reinforced concrete structures such as bridges and other structures exposed to marine environments: 1) the initiation period and 2) the propagation period. The initiation period is the time required for aggressive substances (e.g., carbon dioxide, chlorides, etc.) to penetrate from the environment into the cover concrete until critical chloride ion concentration is reached at the bar reinforcement to initiate the corrosion process. In the present paper, a numerical model is developed to study the effect of the exposed concentration of chloride on the initiation period of the corrosion. This initiation period is modelled by considering physico-chemical interactions between the ions and the solid components of the concrete. Several examples of application of the model are presented to show the interest of studying the influence of the exposure concentration of chloride ions on the penetration depth in the concrete. The effects of chloride binding, chemical activity of the pore solution and electrostatic interactions are also presented.

1. Introduction

The corrosion of reinforcement concrete structures due to the penetration of chloride ions is an important problem in civil engineering. When the concentration of chloride ions is critical, the corrosion of the steel will start and the service life of the concrete structure will reduce. In United Kingdom, this pathology of concrete is the first cause of degradation of bridges. This degradation depends on the exhibition class [1]. According to the norm NF EN 206-1 there are 18 exhibition classes. These classes depend on the exposure weather and on the concentration of chloride ions which penetrate in the concrete structure such as sea water

attack (XS class) and de-icing salt (XD class). When concrete is submerged totally in water, chloride ions will penetrate by diffusion only such as in the submerged bridge pier. When concrete is partially saturated and exposed to wetting and drying cycles chloride ions will penetrate by diffusion and convection.

The transport of chloride ions is well studied in the literature and many models are available for the simulation of chloride ions in saturated [2-3] and unsaturated concrete [4-5]. The ingress of chloride ions is significant in a marine environment and also when using salt spray. For this reason, this paper aim to enhance the signification of the penetration depth of chloride ions taking into account the exposure weather and the exposure concentration of chloride ions. This study will show us the effect of the initial concentration of chloride ions on the service life of concrete structure and on the initiation of corrosion of reinforced concrete. In order to study the unsaturated case, this work could be considered as an extension or a continuation of the Benchmark WG2.4 "Macroscopic model to predict chloride content in saturated concrete" carried out in the framework of Cost action.

After this introduction, the used numerical model is presented in section 2. It considers the physico-chemical mechanisms of the penetration of chloride ions. The influence of the exposure concentration of chloride ions on the service life of concrete and on the penetration depth of chloride ions are shown in section 3. The conclusion of this work follows in section 4.

2. Model of chloride transport in unsaturated concrete

The chloride penetration is a complex physical and chemical process. In our model, this process is divided into four parts: transport of chloride by 1) diffusion, 2) convection, 3) ions interaction and 4) chemical activity of ions. The flowchart of the model is illustrated in Fig.1. The governing equations can be given by:

$$J_i = -D_i\left[\mathrm{grad}C_i + \frac{z_i F}{RT}C_i \mathrm{grad}\Psi + C_i \mathrm{grad}(\ln Y_i)\right] + C_i V \quad (1)$$

Where D_i, C_i, z_i and Y_i are respectively the effective coefficient of diffusion (m^2/s), the concentration ($mol.m^{-3}$), the valence and the coefficient of activity of the ion i. F the Faraday constant (96485,309 $C.mol^{-1}$), R the ideal gas constant (8,3143 $J.mol^{-1}.K^{-1}$), T the temperature (K), Ψ the electrostatic potential (V) and V the velocity of water (m/s).

To take into account the effect of water content, the coefficient of diffusion of ions is assessed by Buchwald's work [6] for the ions in the pore solution. D_i depends on the evolution of the porosity ε and on the saturation degree S_e which is linked to water content volume W. The equation is expressed as follows:

$$D_i = D_i^{sat}\left(\frac{W}{\varepsilon}\right)^{\lambda} \quad (2)$$

Where D_i^{sat} is the coefficient of diffusion of ions in saturated concrete (m^2/s) and $\lambda = 6$.

The model adopted for the humidity transport can be derived as follows:

$$\frac{\partial S_e}{\partial t} = -\frac{K_e K_{re}}{\varepsilon \mu_e}\frac{\partial P_c}{\partial S_e}\mathrm{grad}S_e + \frac{R_a D_{va}}{\rho_e}\frac{\partial \rho_v}{\partial S_e}\mathrm{grad}S_e - \frac{M_{H_2O}}{\rho_e}\frac{\partial S_{CaOH_2}}{\partial t} \quad (3)$$

Where D_{va}, μ_e, M_{H_2O} and ρ_e are, respectively, the coefficient of diffusion of water vapor, the viscosity, the molar mass and the density of water. S_{CaOH_2} is the solid content of Portlandite during the transport of chloride ions. P_c is the capillary pressure (atm) calculated from φ(W), which describes sorption and desorption isotherms which relate the water content to the humidity. The isotherms can be derived from experimental results depending on the type of concrete and on wetting-drying cycles

$$P_c = -\rho_e \frac{RT}{M_v} \ln\varphi(W) \quad (4)$$

K_e is the intrinsic permeability (m^2). It depends on the microstructure of concrete and it was assessed from its initial porosity ε_0 through Genuchten's equation [7] and K_{re} is the relative permeability (m^2) [8]. R_a is the resistance to the air (Thiery's work [9] based on Millington's study [10])

$$K_e = K_e^0 \left(\frac{\varepsilon}{\varepsilon_0}\right)^2 \left(\frac{1-\varepsilon_0}{1-\varepsilon}\right)^2 \quad (5)$$

$$K_{re} = (S_e)^{0.5}[1-(1-(S_e)^{1/0.34})^{0.34}]^2 \quad (6)$$

$$R_a = (\varepsilon)^{2.74}(1-S_e)^{4.8} \quad (7)$$

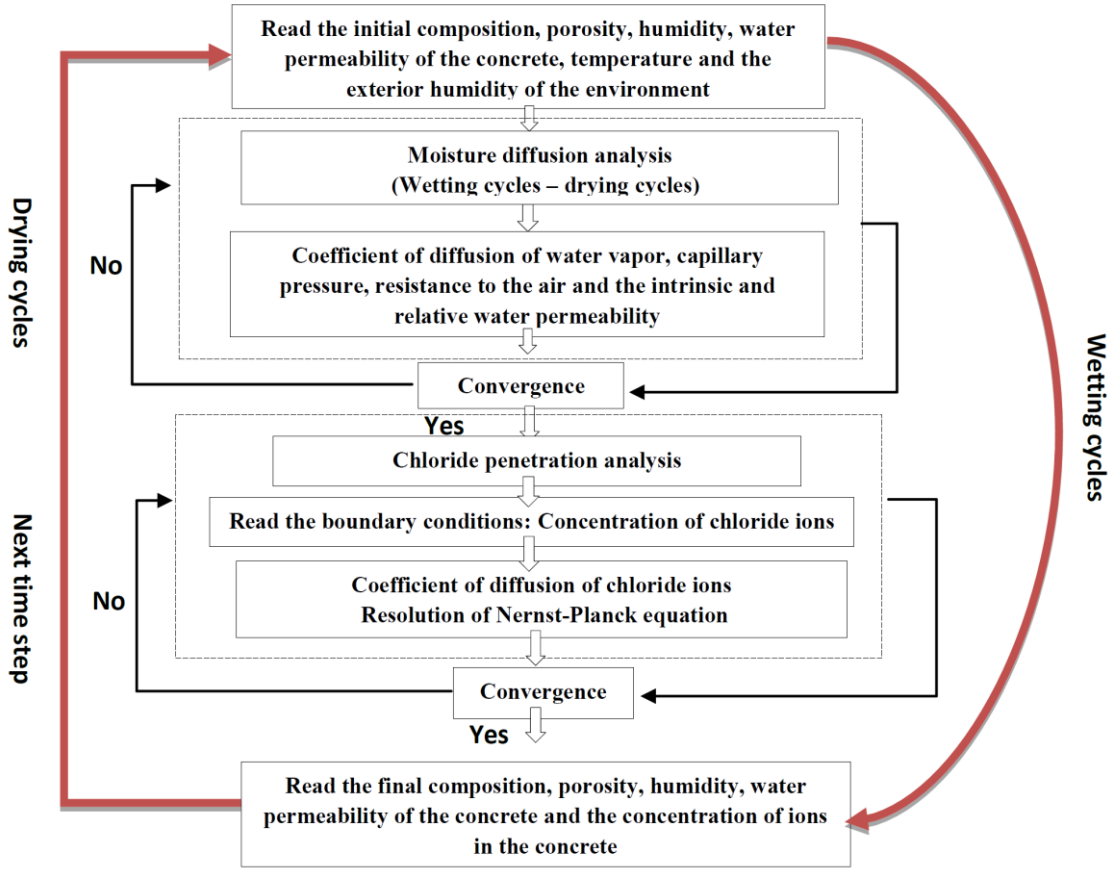

Figure 1: Flowchart of the numerical model.

3. Results and discussion

The discretization approach for 1D domain had been to model the ionic transport process of concrete. The finite difference method is used to solve the above equations (1-7).

3.1 Concrete composition, input data and boundary conditions

The concrete mixture used in this study has the composition described in Tab.1 [11].

Table 1: Composition of the concrete specimen.

Concrete M30CV	**Value**
Gravel 5/12.5	565 Kg/m^3
Sand 0/5	864 Kg/m^3
Cement	436 Kg/m^3
Fly Ash	223 Kg/m^3
Silica fume	95 Kg/m^3
Water/Binder	0.74

This concrete is selected from the literature because the input data and the parameters needed in the model are available. The concrete properties and the input data needed for the model are listed in Tab.2. The sorption and desorption isotherms are presented in the Bouny's works [11].

Table 2: Input data of the numerical model.

	Value
Water porosity	0.128
Density of concrete	2349 Kg/m^3
Effective coefficient of diffusion of chloride ions	2.17 E-13 m^2/s
Water permeability	4 E-21 m^2

In order to take into consideration the interaction between chloride ions and the cement paste of the concrete, binding isotherms were measured. The results show that a Langmuir isotherm can be used to link free and bound chlorides:

$$C_{cl,b}\ (mol/m^3) = \frac{0.000025 C_{cl,f}}{1+0.0006 C_{cl,f}} \quad (8)$$

The concrete specimen (50 mm) is initially partially saturated (S_e^0= 80%) and then exposed to chloride attack (0.5 mol/L) under 6h/6h of wetting and drying cycles ($S_e^{t>0}$ = 92% wetting, $S_e^{t>0}$ = 60% drying, T=23^{o}C).

3.2 Chloride transport validation in concrete under cyclic drying-wetting conditions

Fig. 2 shows the profile of chloride ions after an exposure period of 10 years with 6h/6h of wetting and drying conditions. It is clear from the results that the model can predict well the penetration of chloride ions obtained experimentally. We can also note the convection zone is identified. This profile is the result of eq.1 considering chloride ions.

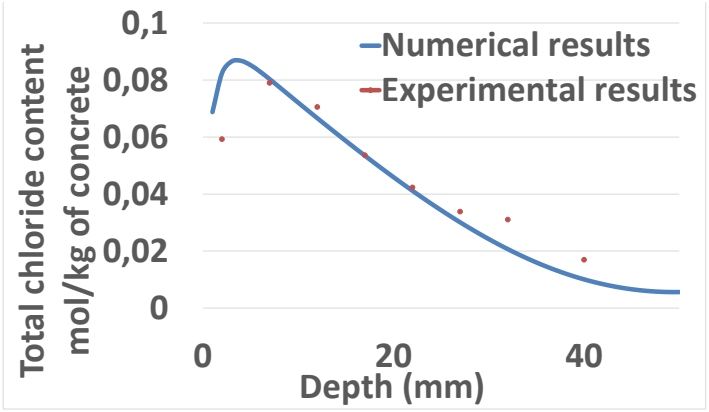

Figure 2: Validation of the model to predict the penetration of chloride ions in the concrete.

3.3 Influence of the exposure concentration on the chloride penetration and on the service life of concrete

In order to show the influence of the exposure concentration (0.5-1-2-3 mol/L) on total chloride concentration, a number of simulations are presented in Fig.3 and Fig.4. The numerical model simulates the profile of chloride ions fixing all the parameters and changing only the exposure concentration. These figures show clearly that when the concentration of chloride ions on the surface increases, the penetration depth of chloride increases also due to the high amount of chloride ions. We have to note that the convection zone occurs whatever the chloride concentration. This is due to the convection effect which accelerates the penetration of chloride ions.

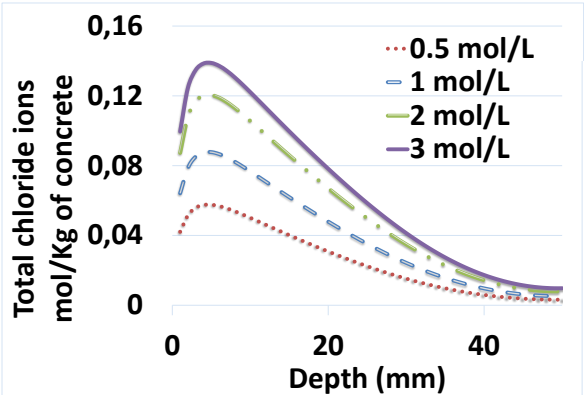

Figure 3: Influence of the exposure concentration on the chloride penetration into concrete.

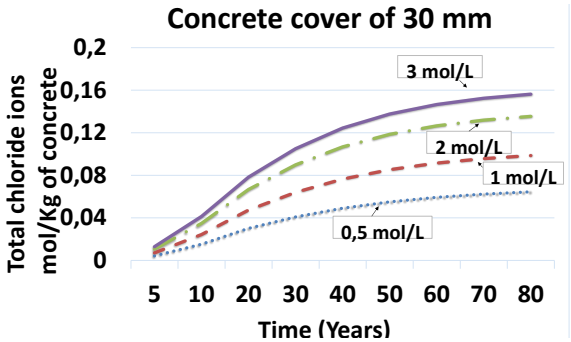

Figure 4: Influence of the exposure concentration on the initiation stage of corrosion.

The numerical model simulates the profile of chloride ions after 80 years of time exposure. For every 10 years the concentration of chloride ions at x=30 mm is plotted in Fig.4 shows clearly that for a concrete cover of 30 mm and after 50-80 years, the initiation stage of corrosion is accelerated when the exposure concentration increases. Finally, as expected, when the chloride content is important (de-icing salt) the corrosion initiation is accelerated.

4. Conclusion

This study is focussed on the study of the effect of exposure concentration on chloride ingress in concrete. The main conclusions that can we drawn are;

1- To highlight the convection zone, the coupling of chloride and humidity ingress is required.
2- When the concentration of chloride ions is more important on the surface, the initiation time of corrosion is increased.
3- The numerical predictions of the penetration of chloride ions are compared with a set of experimental results for unsaturated concrete. It was clear that the experimental results support the validity of the model.

References

[1] NF EN 197-1 Ciment-Partie 1: Composition, spécification et critères de conformité des ciments courants. 2001.
[2] Tang, L., Lindvall, A., Validation of models for prediction of chloride ingress in concrete exposed in de-icing salt road environment, Int. J. of Structural Engineering 4 (2013), 86-99.
[3] Li, L., Page, C., Finite element modelling of chloride removal from concrete by an electrochemical method, Corrosion Science 42 (2000), 2145–2165.
[4] Achour M., Amiri O., Bignonnet F., Rozière E., Influence of carbonation on ionic transport in unsaturated concrete: evolution of porosity and prediction of service life. European Journal of Environmental and Civil Engineering 0 (2018), 1–16.
[5] Nguyen P., Amiri O., Study of the chloride transport in unsaturated concrete: Highlighting of electrical double layer, temperature and hysteresis effects. Constr. Build. Mater 122 (2016), 284–293.
[6] Buchwald, A.: Determination of the Ion Diffusion Coefficient in Moisture and Salt Loaded Masonry Materials by Impedance Spectroscopy. In 3rd International Symposium Vienna (2000), 475–482.
[7] Van Genuchten, M. T., A Closed-form Equation for Predicting the Hydraulic Conductivity of Unsaturated Soils1. Soil Science Society of America Journal 44 (1980), 892-897.
[8] Mualem, Y., A new model for predicting the hydraulic conductivity of unsaturated porous media. Water Resour. Res. 12 (1976), 513–522.
[9] Thiery, M., Dangla, P., Villain ,G., Platret, G. : Modélisation du processus physico -chimique de carbonatation des bétons. Acte des Journées des Sci. L'Ingénieur du réseau des LPC (2003), 403–408.
[10] Millington, R., Gas diffusion in porous media. In Science 130 (1959),100–102.
[11] Baroghel-Bouny, V., Dierkens, M., Wang, X., Soive, A., Saillio, M., Thiery, M., Thauvin, B.: Ageing and durability of concrete in lab and in field conditions: investigation of chloride penetration. Journal of Sustainable Cement-Based Materials. 2 (2014), 67-110.

SynerCrete'18 International Conference on Interdisciplinary Approaches
for Cement-based Materials and Structural Concrete
24-26 October 2018, Funchal, Madeira Island, Portugal

PARAMETRIC STUDY OF THE MINIMUM REQUIRED REINFORCEMENT FOR CRACKING CONTROL IN THICK RESTRAINED RC MEMBERS BASED ON THERMO-HYGRO-MECHANICAL FE ANALYSES

Carlos Sousa [(1)], Miguel Azenha [(2)], Cláudio Ferreira [(1)], Rui Faria [(1)]

(1) CONSTRUCT, University of Porto, Porto, Portugal
(2) ISISE, University of Minho, Guimarães, Portugal

Abstract
This paper discusses the structural behaviour of walls or slab-like reinforced concrete (RC) elements fully restrained at their ends, considering the effects of self-induced deformations due to the heat of hydration and concrete shrinkage. It focuses on the formation and propagation of cracks in thick ties. The analysed thicknesses are 500 mm and 1000 mm. The ultimate objective of the analyses presented in the paper is the rational calculation of the minimum required area of reinforcement to control cracking. For that purpose, thermo-hygro-mechanical analyses are conducted, so that the non-uniform cross-sectional distribution of self-induced deformations is conveniently simulated, and the crack propagation process can be studied. A staggered analysis approach is followed: an uncoupled thermo-hygral analysis is firstly conducted to calculate the self-induced deformation, in each location throughout the structure thickness, for each instant of time. Then, this deformation field is used as input for the mechanical analysis, where the relevant features of the mechanical concrete behaviour are simulated: maturity; creep; softening behaviour after cracking; and nonlinear bond stress-slip relationship at the steel-concrete interface. The results are discussed in view of the regulatory framework of Eurocode 2 for minimum reinforcement for adequate crack width control.

1. Introduction

The definition of the reinforcement for thick RC slabs or walls is frequently governed by cracking control criteria, particularly in situations where the deformation of such members is externally restrained. Design codes, such as the Eurocode 2 [1], provide simple design procedures for calculation of the required reinforcement. These procedures are simple to use,

but involve very important simplifications of the actual structural and material behaviour. One of the most important is the adoption of a simple correction factor, *k*, to take into account the effect of self-induced stresses which vary nonlinearly throughout the member thickness. This factor is set as a function of a single variable, the member thickness. This simplification is very convenient for a rapid estimate of the required reinforcement. However, the simplicity comes with a price: the calculated amount of reinforcement may give rise to crack openings significantly higher or smaller than the specified crack limit (to meet durability, water tightness or other conditions). In view of these limitations of the design rules, alternative methodologies have been proposed for crack width control, namely the deformation compatibility approach [2].

In this context, this paper shows the experience gained with the application of a thermo-hygro-mechanical framework to the calculation of minimum required reinforcement in thick restrained RC members (slabs or walls). The temperature and shrinkage deformations of concrete are completely hindered at the member extremities, thus creating a case of full end restraint. No additional action is considered.

An uncoupled analysis strategy is followed. The local concrete deformations due to temperature variations during the cement hydration and drying shrinkage are calculated for unidirectional fluxes of temperature and humidity (perpendicular to the middle plane of the studied member). The evolution along time of the temperature and humidity fields, as well as the relationship between humidity and local shrinkage, are determined for a concrete mix and exposure conditions previously characterized in laboratory. Thermo-hygral analyses are carried out using the modelling framework described in [3, 4]. Their output is used as input for the mechanical model. In the mechanical analyses, concrete is discretized using plane stress finite elements (FEs). The constitutive model for concrete is based on a total strain approach with rotating cracks. A Kelvin chain approach is used to simulate creep and the time variation of the concrete modulus of elasticity. The reinforcement is discretized using truss elements. The bond action between steel and concrete is explicitly modelled. The mechanical analyses are made with recourse to the FE package DIANA [5].

The discussion of the analysis results focuses on the mechanical response of the structure in terms of crack propagation, crack openings and steel stresses.

2. Structures under analysis

2.1 Geometry and loading

The analysed structures are RC tie elements, 500 mm and 1000 mm thick. The longitudinal deformation of each tie is fully restrained at its extremities, since the instant of casting. The ties are assumed to be moulded and cured for a period of 7 days after casting. No additional load is considered besides the self-induced deformations due to the heat of hydration and the shrinkage of concrete.

The concrete cover to the longitudinal reinforcement is 50 mm (measured from the concrete surface to the reinforcement axis). For each concrete geometry, two different amounts of reinforcement are considered in the analyses shown in this paper:

- The minimum amount of reinforcement which, according to the Eurocode 2 [1] is required to avoid yielding of the reinforcement, herein labelled as $a_{s,min}$. It is equal to 24.9 cm^2/m for the 0.5 m thick slab and 37,3 cm^2/m for the one with a thickness of

1 m. Note that this is, according to the code, the minimum amount to avoid yielding. The reinforcement which ensures, according to the code, that a certain limit crack opening (e.g. 0.3 mm) is not exceeded is much higher.

- An amount of reinforcement 30% higher than $a_{s,min}$, labelled as 1.3 $a_{s,min}$.

The bar diameter is determined, for all of the analysed geometries, by considering that the bar spacing is equal to 100 mm. The diameter is, therefore, 13.4 mm and 15.4 mm for the 500 mm structure reinforced with $a_{s,min}$ and 1.3 $a_{s,min}$, respectively. For the 1000 mm thick member, the diameters are 16.7 mm and 19.3 mm. The fact that these diameters are not available in the reality does not impair the validity of this study.

2.2 Finite element modelling

Eight-node plane stress quadrilateral FEs, with 25 mm edges, are adopted to discretize the concrete elements. The plane stress FE thickness is taken as 1 m. Compatible interface FEs and truss FEs were used to model the bond action and the steel behaviour, respectively. The model length, (*L* in Fig. 1) is 4 m for the 1 m thick slab. For the 0.5 m thick one, different *L* values were considered (4 m and 2 m), in order to assess the influence of this variable. Only half of the thickness was discretized owing to symmetry.

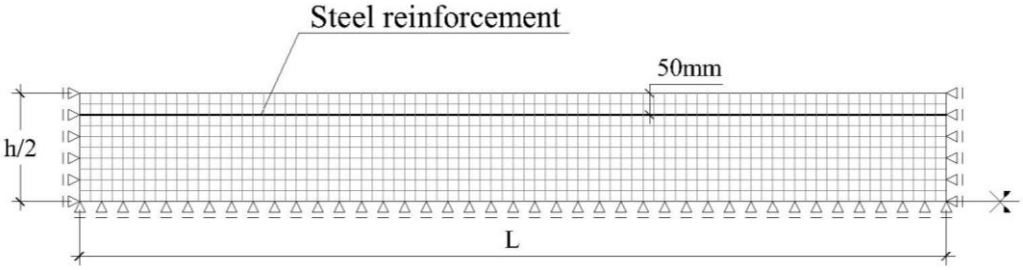

Figure 1: FE mesh for 500 mm thick RC ties

2.3 Material and boundary properties

The parameters to define the concrete properties, the environment and the boundaries take the values previously characterized and experimentally validated [6]. The most relevant parameters are shown in Tab. 1. A full characterization can be found in reference [6]. Note that, to make it concise, no information about the heat generation function is shown in Tab. 1. The adopted concrete mix can be considered as a relatively typical mixture for applications with normal strength requirements. It includes 280 kg/m^3 of CEM II 42.5R, 40 kg/m^3 of fly ash, 143 kg/m^3 of water, 6 kg/m^3 of water reducing admixture and granitic aggregates. The local relationship between the relative humidity in concrete and the local concrete shrinkage strain is given by the equation proposed by Kwak [7], with a shrinkage strain of 539 μ when the concrete humidity reaches 60%. The kelvin chain model to describe the viscoelastic concrete behaviour is fitted to the fib Model Code [8] creep and modulus of elasticity models, considering that the mechanical properties start developing in concrete at the end of the dormant period. The tension softening model adopted for concrete is the one proposed by the fib Model Code [8].

A linear elastic-perfectly plastic behaviour is assumed for steel, with a modulus of elasticity of 200 GPa and a yield stress equal to 500 MPa. The steel-concrete interface behaviour is

modelled according to the cubic function by Dörr [9] up to a slip value of 0.06 mm. For higher slip values, the bond-stress is kept constant and equal to 1.9 times the concrete tensile strength ($1.9 \times 2.9 = 5.51$ MPa).

Table 1: Material and boundary properties.

Analysis	**Property**	**Value**
Thermal	volumetric specific heat	2400 $kJm^{-3}K^{-1}$
	thermal conductivity	2.6 $Wm^{-1}K^{-1}$
	convection/radiation coefficient for free surfaces	10.0 $Wm^{-2}K^{-1}$
	convection/radiation coefficient before demoulding	5.0 $Wm^{-2}K^{-1}$
	environmental temperature	20 ºC
Hygral	diffusivity for H=1, D_1	3.08×10^{-10} m^2s^{-1}
	diffusivity for H=0, D_0	0.0967 D_1
	H for $D_H = 0.5\ D_1$	0.8
	material parameter n	2
	moisture emissivity coefficient	4.81×10^{-8} ms^{-1}
	environmental relative humidity	60 %.
Mechanical	average tensile strength	2.9 MPa
	average compressive strength	38 MPa
	fracture energy	0.140 kNm/m^2
	thermal dilation coefficient	10^{-5} $ºC^{-1}$

3. Results and discussion

As mentioned before, the discussion focuses on the results of the mechanical analyses. It was found that the adopted analysis strategy to model cracking and bond action is robust. Converged results were always reached. Preliminary parametric analyses (considering linear or, alternatively, bilinear tension softening models; different structure lengths; and one or, alternatively, three structure spots with 5% lower tensile strength to induce the first crack localizations) showed that the most significant analysis variables (maximum crack openings and steel stresses) are not significantly affected by these variations. This conclusion shows that the analysis results are meaningful.

Figs. 2 and 3 show the deformed meshes, for the two concrete thicknesses, for two instants of time: before the formation of the second crack, which is the instant when the highest steel stresses and crack openings are reached; at the end of the analysis. The crack propagation sequence followed the expected behaviour for thick RC elements: initially, micro-cracks were formed throughout all the surface region of the member; then, closely spaced cracks were formed from the surface; later, through cracks were formed, gradually along time. The time

variation of steel stresses at the location of the first through crack (the position where the highest stresses occur) is shown in Fig. 4.

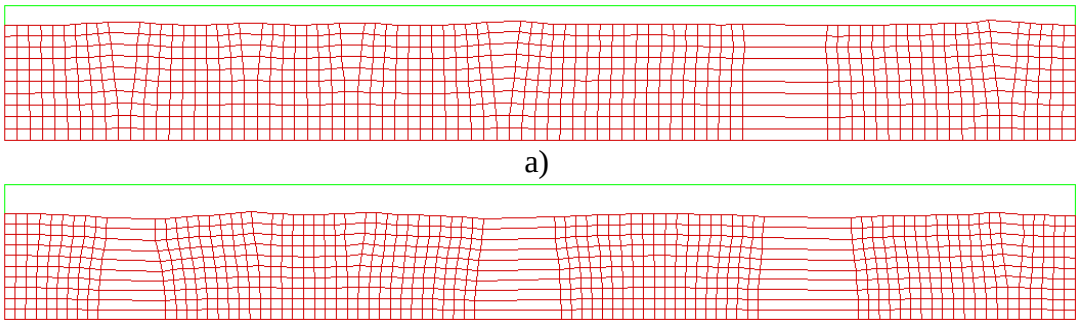

a)

b)

Figure 2: Deformed mesh for 500 mm thick RC ties with reinforcement $a_{s,min}$: a) 3 years after casting; b) at 50 years

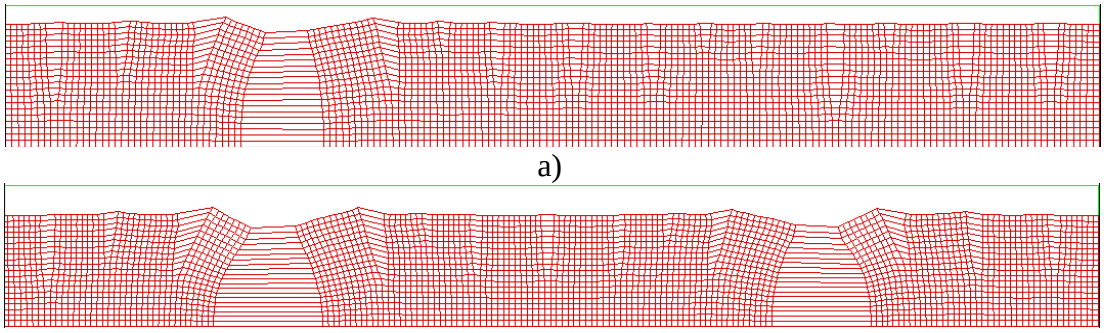

a)

b)

Figure 3: Deformed mesh for 1000 mm thick RC ties with reinforcement $a_{s,min}$: a) 10 years after casting; b) at 50 years

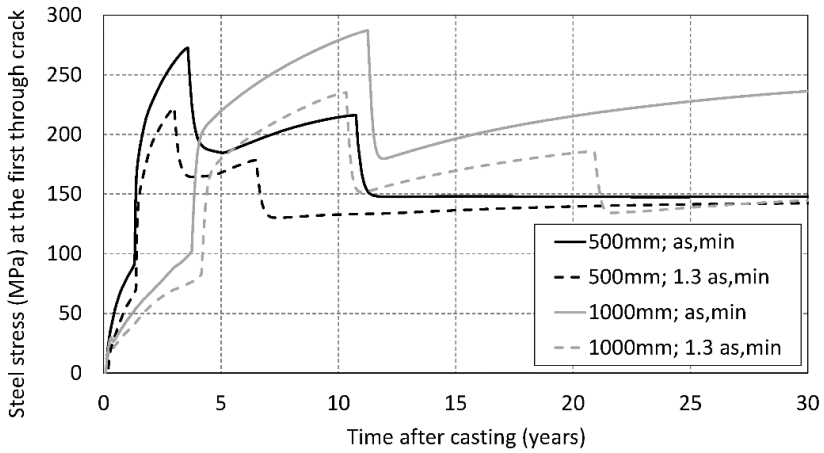

Figure 4: Steel stresses at the most critical position

4. Final remarks

Three relevant conclusions are summarized: (*i*) The analysis results revealed, for the studied cases, that the rules in Eurocode 2 for calculation of the minimum reinforcement to avoid yielding are conservative. The maximum steel stress in the analysed ties was always lower than 300 MPa, a value considerably inferior to the yield limit (500 MPa in this case); (*ii*) In the studied cases, by adopting an amount of reinforcement 30% higher than $a_{s,min}$, the maximum crack opening was approximately equal to 0.30 mm. According to the Eurocode 2, the required area of reinforcement to reach such limit crack opening is much higher (~ twice $a_{s,min}$); (*iii*) the adopted analysis strategy can be a useful tool to study the cracking behaviour of thick RC members, however, further analyses and validations are required to confirm the applicability of the reached conclusions.

Acknowledgements
This work was financially supported by: Project POCI-01-0145-FEDER-007457 (CONSTRUCT - Institute of R&D in Structures and Construction) and by project POCI-01-0145-FEDER-007633 (ISISE), funded by FEDER funds through COMPETE2020 - Programa Operacional Competitividade e Internacionalização (POCI), and by national funds through FCT - Fundação para a Ciência e a Tecnologia. FCT and FEDER (COMPETE2020) are also acknowledged for the funding of the research project IntegraCrete PTDC/ECM-EST/1056/2014 (POCI-01-0145-FEDER-016841). The financial support of COST Action TU1404 through its several networking instruments is also gratefully acknowledged.

References

[1] EN 1992-1-1, Eurocode 2: Design of Concrete Structures – Part 1-1: General Rules and Rules for Buildings, CEN (2004)
[2] Schlicke, D. and Vie Tue, N., Minimum reinforcement for crack width control in restrained concrete members considering the deformation compatibility, Structural Conrete 2 (2015), 221-232
[3] Azenha, M., Numerical Simulation of the Structural Behaviour of Concrete since its Early Ages, PhD thesis, University of Porto – Faculty of Engineering (2009)
[4] Azenha, M., Sousa, C., Faria, R. and Neves, A., Thermo-hygro-mechanical modelling of self-induced stresses during the service life of RC structures, Eng Struct 33 (2011), 3442-3453
[5] DIANA, Finite Element Analysis, release 10.2, DIANA FEA BV, Delft (2017)
[6] Azenha, M., Leitão, L., Granja, J., Sousa, C., Faria, R. and Barros, J., Experimental validation of a framework for hygro-mechanical simulation of self-induced stresses in concrete, Cem Concr Compos 80 (2017), 41-54
[7] Kwak, H., Ha, S. and Kim, J., Non-structural cracking in RC walls: Part 1, finite element formulation, Cem Concr Res 36 (2006), 749-760
[8] fib, Model Code for Concrete Structures 2010, Ernst & Sohn (2013)
[9] Dörr, K., Ein Beitrag zur Berechnung von Stahlbetonscheiben unter besonderer Berücksichtigung des Verbundverhaltens, PhD thesis, University of Darmstadt (1980)

SynerCrete'18 International Conference on Interdisciplinary Approaches
for Cement-based Materials and Structural Concrete

24-26 October 2018, Funchal, Madeira Island, Portugal

PARAMETRIC STUDY ON DAMAGES AND STRENGTH BEHAVIOUR OF POST-TENSIONED GIRDERS IN DECHATIWONG BRIDGES

Nat Hanwiboonwat[(1)], Tidarut Jirawattanasomkul [(1)], Songpol Charuvisit [(1)], Nattamet Wuttiwannasak [(1)], Nuttapong Kongwang [(1)], Chinapat Banluelap [(1)], Tawan Norsakul [(1)]

(1) Kasetsart University, Department of Civil Engineering, Faculty of Engineering, Thailand

Abstract

The Dechatiwong bridges located on Nakhon Sawan province, Thailand, are in the part of national highways as well as Asian Highways, connecting between Bangkok and the northern part of the country. To date, horizontal cracks have been observed at the ledge's corner of the end girders in these bridges. This research, therefore, aims to indicate causes of such cracks and investigate their behaviour using 2D non-linear finite element method by ATENA program. The vehicle loads and load patterns were evaluated based on AASHTO LRFD-2012 standards. The analysed Post-tensioned Concrete (PC) girder is 11.75 m long with a cantilever fixed-end support. The analysis is focused on influences of prestressing sequences and losses in prestress which are varied from 0-50%. From the analytical results, severe cracks at the end of girders are caused by the losses in prestress.

1. Introduction

The Dechatiwong Bridges are located in the national highways no.1 as well as Asian Highways (AH1). Therefore, this research is essential for Asian transportation and can contribute to Thailand's economic growth. This research focuses on investigation of the horizontal crack at re-entrant corner of Post-tensioned Concrete (PC) girders in the extension part of Dechatiwong Bridge No.2 and No.3 (see Fig. 1). This project is aimed to evaluate behavior of bridge's superstructure using Finite Element Method (FEM) by 2D ATENA program. The vehicle loads and load patterns were followed AASHTO LRFD-2012 standard. The analysed Post-tensioned Concrete (PC) girder has 11.75 meters long with a cantilever fixed-end support at pier. The models could simulate I-girders in 2D which material properties of the girders were based on the previous researches [1-5]. In this research, there are two possible assumptions for causes of the horizontal cracks which are prestressing

sequences and losses in prestress. From the analytical results, prestressing sequences may not be a cause of the cracks since crack did not occur. When losses in presstress are reached to 20%, cracks appeared in the analysis. Therefore, this may be one of the most possible causes for the current horizontal cracks.

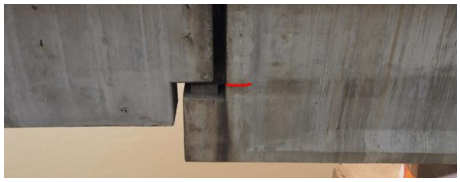


a) Cracks at Dechatiwong Bridge No.2 b) Cracks at Dechatiwong Bridge No.3

Figure 1: Ledge girders and horizontal crack at reentrant corner in Dechatiwong Bridge.

2. Detail of girders

The extension girders of Dechatiwong Bridge No.2 and No.3 were designed as the Prestressed Concrete (PC) girders in box-shape section based on AASSHTO LRFD standards. However, only exterior I-girders were analysed because cracks were observed. In this research, cantilever girders have a span length of 11.75 m and the maximum height of 3.50 m. The effective width of flange is 1.72 m. Details of targeted cantilever girders are shown in Fig 2.

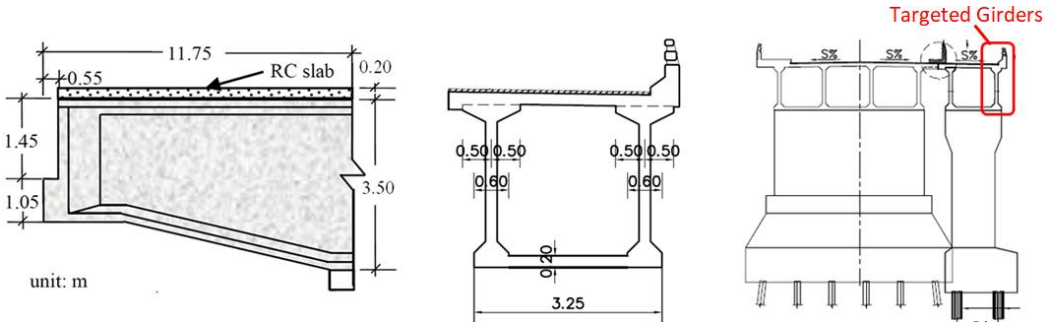

a) Size view of girders b) Section of girders c) Location of girders

Figure 2: Details of targeted cantilever girders.

3. Finite Element Analysis

The 2D Finite Element Method (2D-FEM) by ATENA program is used to analyse crack patterns and behaviours at the re-entrant corner of ledge girders in Dechatiwong Bridge. In the analysis, the material properties and models were followed previous researchers [1-5].

3.1 Materials

Concrete. The compressive strength of concrete is 30 MPa for PC girder. In compression, the stress-strain relationship of concrete is based on the uniaxial behaviour of concrete proposed by CEB-FIB Model Code 2010 [5], as shown in Fig. 3a. In tension, the stress-strain

relationship of concrete is based on the bilinear softening behaviour of concrete proposed by Hordijik [3], as shown in Fig. 3b.

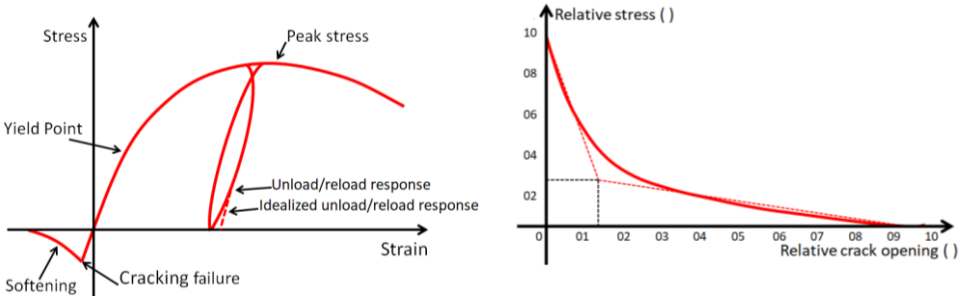

a) Compression b) Tension

Figure 3: Uniaxial behaviour of concrete.

Reinforcement and Prestressed Tendon. There are 10 post-tensioned tendons in the girder with profiles as shown in Fig. 4a and sectional area of each tendon is 416.8 mm^2 with a yield strength of 1,356 MPa and an ultimate strength of 1,600 MPa. For the steel reinforcement, the deformed bar with a diameter of 12 mm and spacing of 200 mm is used to prevent shear crack and lateral buckling with details as shown in Fig. 4b. A yield strength of steel reinforcement is 400 MPa and an ultimate strength is 435 MPa. The modulus of elasticity of tendons and reinforcement are 2.0×10^5 MPa with poison ratio of 0.3.

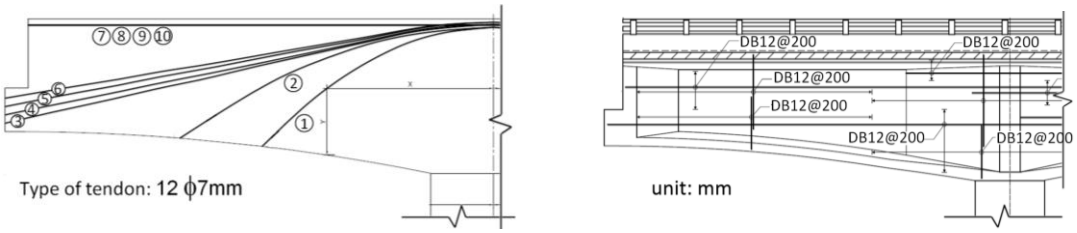

a) Profile of prestressed tendons b) Detail of steel reinforcement

Figure 4: Detail of prestressed tendons and steel reinforcement.

Connection and Element Type. In analytical models, the connections in steel reinforcement-concrete and prestressed tendons-concrete are assumed as the perfect connections and defined as a discrete reinforcement. Therefore, prestressing forces are constant along the tendons length. The concrete element is modelled as 4-node quadrilateral plane. The element size at free-ended ledge is 50 mm based on a maximum aggregate size of concrete. For the other parts of model, the element is defined with a size of 100 mm as shown in Fig. 5.

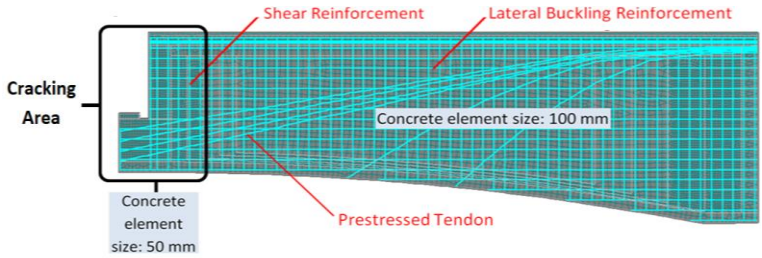

Figure 5: Detail of discrete reinforcement in analytical model and element size of concrete.

3.2 Boundary condition

From the designed detail, the support of extension-cantilevered girders is designed as a fixed support as shown in Fig. 6a. Therefore, at the pier-end, the support of girder's models was assumed as a fixed support. At the free end, the displacement control is applied to increase 0.25 mm in each step as shown in Fig. 6b. Types and locations of monitoring points in the models are also shown in Fig. 6b.

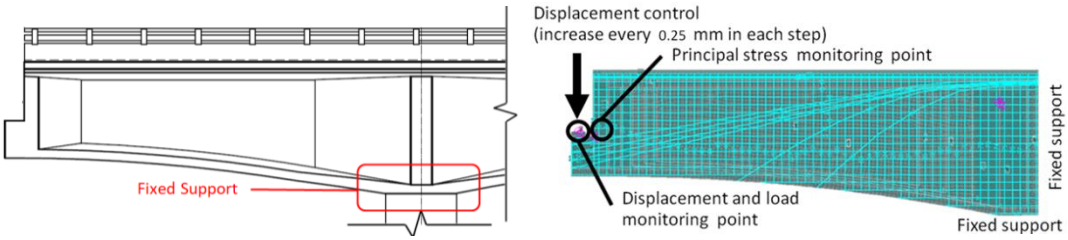

a) Design detail of girder's support b) Boundary condition of model

Figure 6: Design detail of girder's support and boundary condition of model.

3.3 Analytical cases

In this research, there are 2 assumptions of the causes of horizontal cracks at re-entrant corner which are 1) prestressing sequences and 2) losses in prestress. Therefore, analytical models were created in 2 types; 1) Type 1-analysis of horizontal cracks caused by different prestressing sequences, and 2) Type 2-analysis of horizontal cracks caused by losses in prestress.

Effect of prestressing sequences. Initial prestressing or bursting forces at anchorage zones were defined as forces from the design details. The size of steel plate is 200×200 mm and prestressing sequences of analytical models are assumed into 3 pulled out steps as shown in Fig. 7. Note that Steps 1–3 are prestressing sequences in the analytical models, whereas tendon No. (1) – (10) are prestressing forces in the actual design details. As a result, prestressing sequences in the actual construction were different from that in the design details.

Figure 7: Sequences of prestressing in analytical models and prestressed forces defined in actual design details.

Effect of losses in prestress. From calculation based on ACI-423, the actual immediate losses are between 5 - 25% and time dependent losses are between 15 - 25%. Therefore, to analyse the cracks caused by losses in prestress, losses in prestress are assumed as 0, 10, 20, 25, 30, 40, and 50% of prestressed force as stated in design details.

4. Analytical results

4.1 Effect of prestressing sequences

From the analytical models, the horizontal cracks do not occur at re-entrant corner after all of tendons are pulled out as assumed steps. This is because the principal stress at that re-entrant corner is still in compression after pulling out all of tendons. The contour of the principal stress is shown in Fig. 8.

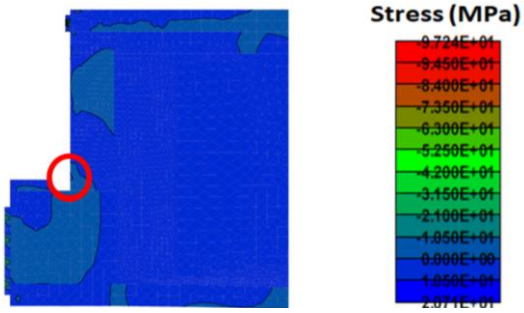

Figure 8: Principal stress for analytical model of girder after analysis.

4.2 Effect of losses in prestress

From the analysis, the first cracking load at re-entrant corner of ledge is significantly depended on the losses in prestress as shown in Table 1. It can be seen that the higher losses in prestress are applied, the less girder's first cracking load is observed. If losses in prestress are increased more than 20% of the designed prestressed forces, the analytical first cracking load is less than 809 kN which is a minimum required load based on AASHTO LRFD 2012 standard. In summary, the predicted cracks may occur when losses are more than 20%.

Table 1: Analytical results and cracks prediction by 2D-FEM analysis.

Losses in prestress (%)	Analytical first cracking load (kN)	Minimum required load AASHTO LRFD (kN)	Predicted crack
0	865	809	Not occur
10	835	809	Not occur
20	772	809	Occur
25	741	809	Occur
30	710	809	Occur
40	678	809	Occur
50	615	809	Occur

The graphics of crack patterns from 2D-FEM are shown in Fig. 9a. In addition, the cracks analysed by 2D-FEM model show the same direction and pattern as the cracks observed in visual inspection. In Fig.9b, the stress at re-entrant corner and the load is shown with varied losses in prestress from 0 to 50%. The tensile stress at re-entrant corner depends on vertical compressive force. If the vertical force is increased, the tensile stress is also increased. From the analysis, this area is subjected to tensile stress which is increased step by step until

reaching the tensile strength of concrete (+2.4 MPa). After that the horizontal cracks occur at the re-entrant corner of the ledge. In addition, the curves indicate that the stress is depended on the losses in prestress. If the losses in prestress are increased, the tensile stress is higher and reaches to tensile strength of concrete earlier, leading to the horizontal cracks in this area.

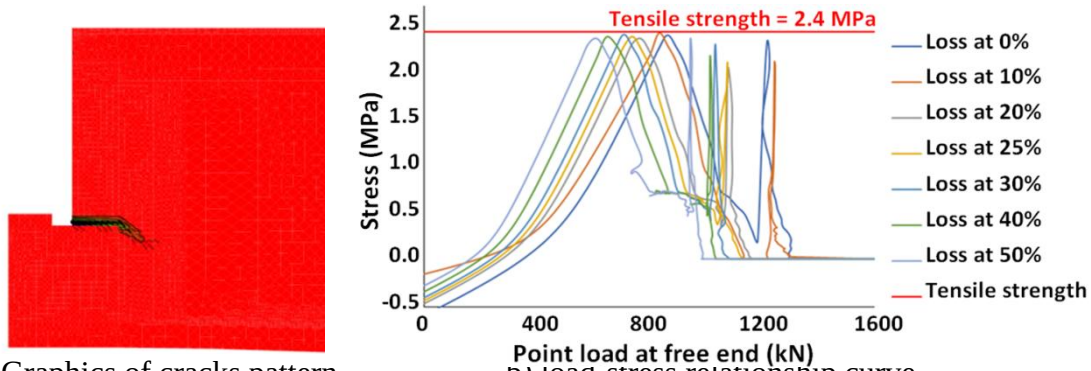

a) Graphics of cracks pattern b) load-stress relationship curve

Figure 9: Graphics of cracks pattern at re-entrant corner and load-stress relationship curve.

5. Conclusions

1) From the analytical models, the horizontal crack occurred at the re-entrant corner of PC ledge girders agrees well with the cracks observed by visual inspection.
2) From the analytical models, the cracks may be caused by the tensile stress at that re-entrant corner which is a result from perpendicular compressive force.
3) In the analysis, losses in prestress significantly affect to first cracking load of girders.
4) The horizontal cracks occur at re-entrant corner when the prestressed losses are increased more than 20% of designed prestressed forces. This is because girders cannot carry the loads which are required by AASHTO LRFD 2012 standards (809 kN).

Acknowledgement

The authors would like to acknowledge Dr. Rajwanlop Kumpoopong and Dr. Sukit Yindeesuk from Department of Highway, Ministry of Transport, Thailand, for providing information of the Dechatiwong Bridge and invaluable guidance. The authors would also like to acknowledge AUN-Seed Net for research funding under project titles “Development of Upgrade Systems for Structural Performances of Existing Concrete Bridges in Thailand”.

References

[1] Wu, X.-H. et al, Tendon Model for Nonlinear Analysis of Prestressed Concrete Structures, J Struct Eng 127(4) (2001) 398-405
[2] Hognestad, E., Study of combined bending and axial load in reinforced concrete members. University of Illinois at Urbana Champaign, USA (1951)
[3] Hordijk, D.A., Local approach to fatigue of concrete. PhD Thesis, Delft University of Technology, The Netherlands (1991)
[4] Timoshenko S.P., Strength of materials, 3rd Ed, Van Nostrand, Princeton, USA (1956)
[5] FIB Bulletin 55, CEB-FIB Model Code 2010

SynerCrete'18 International Conference on Interdisciplinary Approaches
for Cement-based Materials and Structural Concrete
24-26 October 2018, Funchal, Madeira Island, Portugal

PARAMETRIC STUDY ON DAPPED-END OF PRESTRESSED CONCRETE GIRDER IN DECHATIWONG BRIDGE USING FINITE ELEMENT ANALYSIS

Nuttapong Kongwang [(1)], Tidarut Jirawattanasomkul [(1)], Wanakorn Prayoonwet [(2)], Songpol Charuvisit [(1)]

(1) Department of Civil Engineering, Kasetsart University, Bangkok, Thailand
(2) Division of Engineering and Policy for Sustainable Environment, Hokkaido University, Sapporo, Japan

Abstract

End parts of concrete bridge girders in Thailand are usually dapped-end connections, particularly in a suspended span of bridges. However, the diagonal cracks in the dapped-end zone were found in a 40-meter suspended span in Dechatiwong Bridge due to insufficient reinforcement in the dapped-end region compared to that in PCI Design 2010. Hence, the aim of this research is to analyze the influence of different dapped reinforcement and effect of the tendon in the nib portion of the dapped-end on the failure modes and strength of dapped-end girders using 2D nonlinear finite element modeling in ATENA program. The result of nonlinear finite element analysis indicated that the hanger reinforcement is significant because it can change the failure mode from shear compression at the nib region to flexure shear in the full-depth section, and the models with tendon in nib portion can significantly increase the structural strength compared to that without tendon in the nib portion model. It was also found that the strength of the dapped-end girder predicted by the PCI design agrees well with that of girders without prestressing in nib portion. Therefore, the design equations proposed by PCI is still reliable and accurate for the structure without prestressing in the nib portion.

1. Introduction

Currently, precast girder is widely used, especially in bridge structures with long span~~,~~ because of its convenience for quality control and construction. Girder's lateral stability is increased when its depth at end support, a dapped-end connection, is reduced~~.~~ When placed it on to supporting structures, this can help to decrease the overall height of bridges. Nevertheless, this part is characterized by a high concentration of stress at the end of the beam

due to discontinuity. The dapped-end connection is also implemented in Dechatiwong Bridge, Nakornsawan, Thailand. This bridge consists of 40 meters suspended span of post-tensioned Prestressed Concrete (PC) girder; however, the dapped-end region is very sensitive to loads if dapped-end reinforcement is insufficiently used or improperly placed. These may cause severe cracks, leading to a sudden failure [1]. It is also evident that the cracks have already occurred at the dapped-end of Dechatiwong Bridge. Thus, this research focuses on the behavior and characteristics or failure patterns of dapped-end PC girder using the non-linear Finite Element Method (FEM) by 2D ATENA program to construct analytical models for that bridge under static loading.

2. Bridge's Details

This research focuses on Dechatiwong Bridge No.3 in which the cracks were observed at the dapped-end region. Only 40 meters suspended span post-tensioned PC girder with an I-shape cross section is studied which is supported by cantilever beams with lower nibs at both sides.

2.1 Details of a 40 meters Suspended Span

The 40 meters suspended span girder has an I cross-section with depth 2.50 m (Fig. 1b); the cast-in-place Reinforced Concrete (RC) top flange slab of thickness (t) 0.18 m; the effective flange width (b_e) of 2.75 m; a dapped-end connection of girder with a nib depth of 1.40 m, and recession length of 0.55 m (Fig. 1a).

2.2 Material Properties

According to the as-built drawing of the bridge, the compressive strength of concrete cylinder is 35 MPa and 25 MPa for the PC girder and the RC slab, respectively.

The PC girder had 17 tendons, the end region of the girder had 11 tendons (Fig. 1a), and the position of tendons as shown in Fig. 1b. Each tendon contained 12 wires with a diameter of 7 mm. In addition, the tensile strength (f_{py}) and the ultimate tensile strength (f_{pu}) of the wires were 1,377 MPa and 1,632 MPa respectively. The prestressing forces were assumed to apply with 25% prestress losses [2], in all case of the analysis. In the dapped-end area, the deformed bar of 10 mm (DB10) with SD40 grade was placed with a spacing of 150 mm. The DB10 had the tensile strength (f_y) of 400 MPa and the ultimate tensile strength (f_u) of 435.4 MPa.

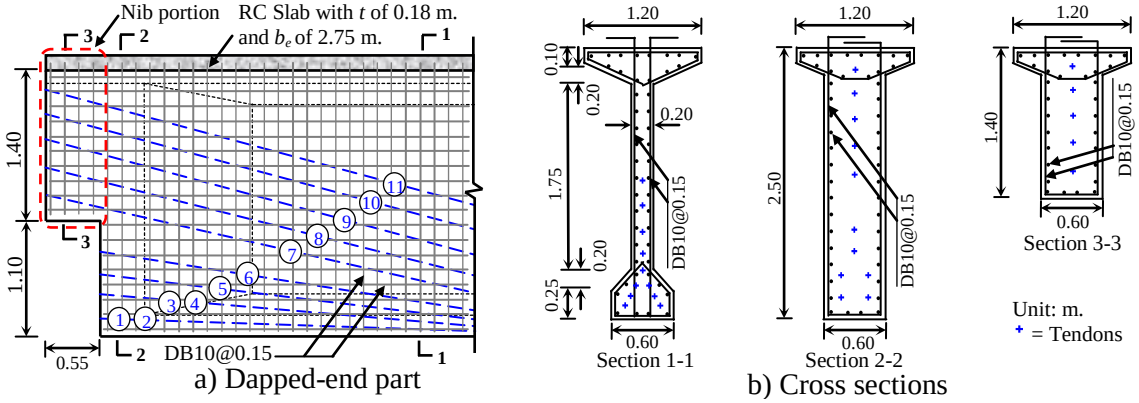

a) Dapped-end part b) Cross sections

Figure 1: Dapped-end details of a 40 meter suspended span girder

3. Design Code for Dapped-End Connection

Dapped-end connection can be designed based on the Precast/Prestressed Concrete Institute (PCI) Design Handbook [3] in which five potential modes of failure are proposed (Fig. 2a). Each mode of failure are prevented by dapped reinforcement as shown in Fig. 2b. The amount of dapped reinforcement can be calculated with equations proposed in PCI 2010 [3].

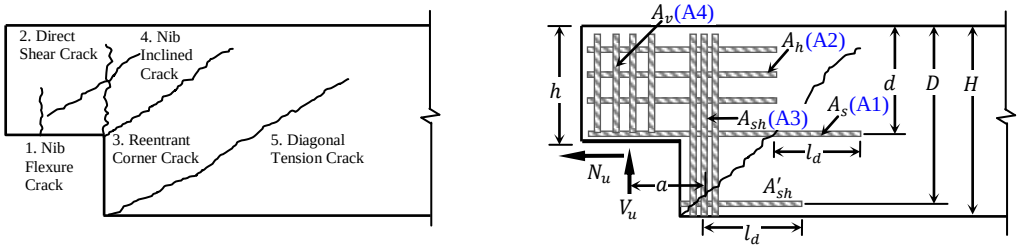

a) Potential Failure Modes b) Required Reinforcement

Figure 2: Failure modes and required reinforcement in dapped-end connection

3.1 Dapped-End Reinforcement in Actual Girder

The actual amount of dapped-end reinforcement in Dechatiwong's PC girder was compared with the design equations recommended in the PCI design; the applied load is calculated based on a factored load combination with HL-93 truck [4], which is approximately 1,896 kN. These reinforcement are summarized in Table 1. It can be seen that all of the actual dapped-end reinforcement is less than the calculated from the PCI equations.

Table 1: Reinforcement in dapped-end

Type of Reinforcement	Reinforcement Area (mm^2)		% Ratio Actual/PCI
	Actual	PCI Requirement	
Flexure Reinforcement, A_s	314	2,935	11%
Shear Friction Reinforcement, A_h	628	1,233	51%
Hanger Reinforcement, A_{sh}	471	6,320	7%
Vertical Reinforcement, A_v	628	2,255	28%

* % Ratio between Actual and PCI is calculated from ($Area_{actual}/Area_{PCI}$)×100.

4. Finite Element Analysis

The 2D-FEM in this study were constructed using the ATENA program to analyze the behavior and failure modes of the dapped-end of the 40 meters suspended span.

4.1 Material Models

The concrete models can be classified into compression and tension. The former–is recommended by the CEB-FIP Model Code 90 [5], with compressive strain at peak (ε_c) of 0.002 and a Poisson's ratio of 0.2; whereas, the latter, assumed linear elastic, the tension behavior after cracking is an exponential function, experimentally derived by Hordijk [6], with fracture energy of 71.6 N/m.

For reinforcing steel, the bilinear stress-strain curve with an elastic-perfectly plastic behavior is used. For tendon, the stress-strain curve proposed by Ramberg and Osgood [7] is used. Additionally, the modulus of elasticity (E_{ps}) is 2.0×10^5 MPa and a Poisson's ratio of 0.3 is used in both curves.

4.2 Boundary Conditions and Element types

In 2D-FE modeling, the load was applied at 6 m from the end support with simple support boundary condition. The displacement was monitored under the loading point, as shown in Fig. 4a. Two element types (Fig. 4b): 1) a 2-node truss element for reinforcing and prestressing steels, and 2) a plane quadrilateral element for concrete are used and are bonded perfectly.

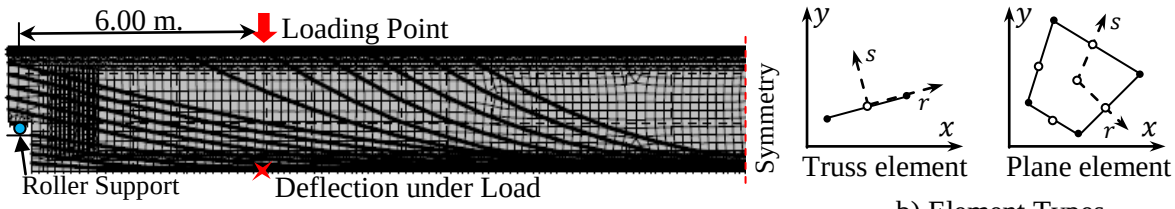

a) Boundary Condition of FEM Models

b) Element Types

Figure 4: Boundary condition and element types in FEM

4.3 Analytical Cases

In this research, the analytical cases are categorized into 2 cases, and the summary is presented in Table 2. In Case 1, in order to evaluate the effect of different types of the dapped-end reinforcement, 5 analytical models were performed with varied reinforcement details (A_s, A_{sh}, A_h, and A_v), denoted as A0-A4. A0 represents the actual girder with actual reinforcement from the existing drawing, whereas A1-A4, only one reinforcement detail such as A_s, A_{sh}, A_h, and A_v changes based on the PCI design. The rest of the reinforcement details such as the number of tendons (T) and spacing of the hanger reinforcement (S) are based on the actual drawing. In Case 2, in order to evaluate the effect of the prestressing steel in the nib portion, 6 analytical models were analyzed with different number of tendons, denoted as T0-T5. T0 represents a model without tendon, and T5, the most prestressing steel of 5 tendons. In this case, A3 with A_{sh} of 12-DB28 from PCI design and the spacing of hanger reinforcement 50 mm (S50) was used to prevent cracks at a re-entrant corner.

Table 2: Summary of analytical cases

Case No.	Models	Dapped-End Reinforcement (mm^2)				No. of Tendon, T	Spacing of Hanger Bars, S (mm)
		A_s	A_h	A_{sh}	A_v		
1	A0-T5-S150	314	628	471	628	5	150
	A1-T5-S150	3,142	628	471	628	5	150
	A2-T5-S150	314	1,257	471	628	5	150
	A3-T5-S50	314	628	7,389	628	5	50
	A4-T5-S150	314	628	471	2,513	5	150
2	A3-T0-S50	314	628	7,389	628	No	50
	A3-T1-S50	314	628	7,389	628	1	50
	A3-T2-S50	314	628	7,389	628	2	50
	A3-T3-S50	314	628	7,389	628	3	50
	A3-T4-S50	314	628	7,389	628	4	50
	A3-T5-S50	314	628	7,389	628	5	50

Note: A0 = Actual dapped-end reinforcement, A1 = Flexure reinforcement (A_s), A2 = Shear friction reinforcement (A_h), A3 = Hanger Reinforcement (A_{sh}), A4 = Vertical reinforcement (A_v), T = Number of tendon in a nib portion, S = Spacing of hanger reinforcement.

5. Analytical results

In both cases, the first crack width of all models are less than limited crack width which is 0.43 mm. [4], so PC dapped-end girders can be used in the crucial condition. However, the crack propagation increasing when the vertical compressive force was increased.

5.1 Sensitivity of Dapped-End Reinforcement in Case 1

From FEM results, A3-T5-S50 show the highest load capacity with the increase in the amount of hanger reinforcement based on PCI code (Fig. 5a). This is because the mode of failure changes from compression shear (Fig. 6a) to flexure-shear (Fig. 6b). In the grey zone, compressive strain is greater than 0.002 resulting the concrete failure. This criterion was used by Hassan et al. [8]. However, the Dechatwong's PC girder remains safely operated under HL-93 according to the ASSHTO LRFD 2012, because the actual girder's strength from FEM (A0-T5-S150) is2,784kN, whereas $V_u$is 1,896 kN.

5.2 Effect of Prestressing Steel in Nib Portion for Case 2

Most of the failures in the 2D-FEM of case 2 are flexure shear (Fig. 6b), except that A3-T0-S50 showing direct shear combined with flexure shear (Fig. 6c). This failure is attributed by the absence of tendon in the nib portion. Therefore, it indicates that the prestressing steel can impact the dapped-end structural behavior. In addition, the strength predicted by PCI agrees well with case A3-T0-S50 as shown in Fig. 5b, illustrating the accurate prediction of PCI design.

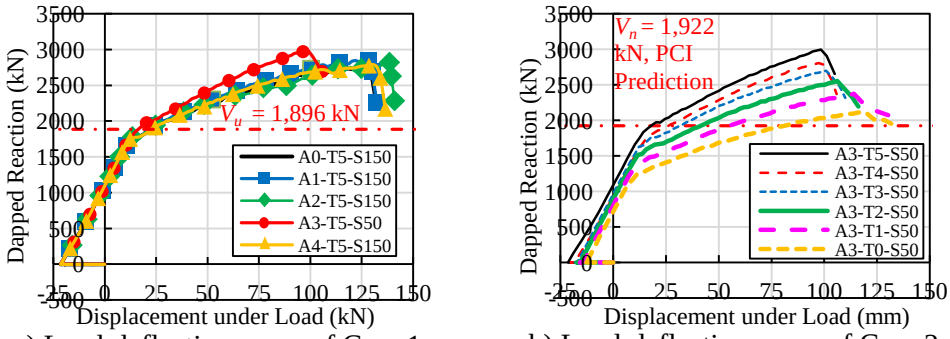

a) Load-deflection curve of Case 1 b) Load-deflection curve of Case 2

Figure 5: Load-deflection curves

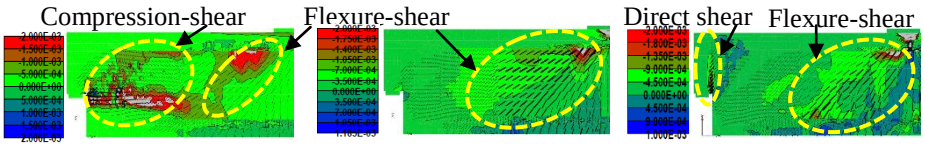

a) Typical failure of Case 1 b) A3-T5-S50 c) A3-T0-S50

Figure 6: Failure modes

6. Conclusions

1) The sensitivity study of dapped-end reinforcement in each type shows that hanger reinforcement is significant because it can change the failure mode from shear compression at the nib region to flexure shear in the full-depth section.
2) The Dechatwong's PC girder remains safely operated because the actual girder's strength from FEM is 2,784 kN while the ultimate load calculated by ASSHTO is only 1,896 kN.
3) Predicted strength from PCI design agrees well with girders without prestressing in nib portion, so PCI equations are suitable for structures without prestressing steel in nib portion.

Acknowledgement
The authors would like to acknowledge Dr. Rajwanlop Kumpoopong and Dr. Sukit Yindeesuk from Department of Highway, Ministry of Transport, Thailand, for guidance and information of the Dechatiwong Bridge, and AUN-Seed Net for research funding under the project title "Development of Upgrade Systems for Structural Performances of Existing Concrete Bridges in Thailand". The last author is thankful for the Master's scholarship granted by Faculty of Engineering, Kasetsart University, Thailand.

References

[1] Mitchell, D. et al, Concorde overpass collapse: structural aspects, Journal of Performance of Constructed Facilities (2011), 545-553
[2] Branson, D.E. and Kripanarayanan, K.M., Loss of prestress, camber and deflection of non-composite and composite prestressed concrete structures. PCI Journal (1970), 22-52
[3] Precast/Prestressed Concrete Institute, PCI Design Handbook 7th ed, Chicago (2010).
[4] AASHTO, LRFD., Bridge design specifications 2012 Washington, DC, USA American Association of State Highway and Transportation Officials (2012)
[5] CEB-FIP Model Code 1990, First Draft, Comittee Euro-International du Beton, Bulletin information No. 195,196, Mars (1990)
[6] Hordijk, D.A., Local Approach to Fatigue of Concrete, Doctor Dissertation, Delft University of Technology, the Netherlands (1991)
[7] Ramberg, W. and Osgood, W.R, Description of stress-strain curves by three parameters, (1943)
[8] Hassan, T. et al., Modeling of L-shaped, precast, prestressed concrete spandrels, PCI journal (2007), 78

SynerCrete'18 International Conference on Interdisciplinary Approaches
for Cement-based Materials and Structural Concrete
24-26 October 2018, Funchal, Madeira Island, Portugal

PREDICTION OF THE IMPACT OF SHRINKAGE ON CONCRETE STRENGTH WITH THE BEAM-PARTICLE APPROACH

Nicolas Chan [(1)], Cécile Oliver-Leblond [(1)], Farid Benboudjema [(1)], Frédéric Ragueneau [(1)], François Soleilhet [(1)]

(1) LMT, ENS Cachan, CNRS, Université Paris-Saclay, Cachan, France

Abstract

Durability is a relevant criterion for preserving a safe structure and avoiding the renewal of costs. However, several phenomena – such as delayed deformation, corrosion, leading to cracking – can severely affect the service life. Not only cracks opening have an influence on concrete performance, but also the crack pattern. In the case of drying shrinkage, due to the low rate of gas and water transfers, stress that may lead to a network of micro-cracks Mechanical and hydric properties are directly impacted by those cracks.

Therefore, it seems essential to consider shrinkage when studying cracking of cementitious materials. This study focuses on a beam-particle model in order to investigate the formation and impact of drying shrinkage cracks. The cohesion of the material is obtained with a lattice of Euler-Bernoulli brittle beams. When a crack occurs, cohesion disappears. To capture the crack closure, a contact law with friction is considered between the polygonal particles. 2D simulations on three points bending test with or without considering drying shrinkage are performed. The finite element method is used to obtain the drying shrinkage strain field. Then, a reanalysis method – inspired from [1]– is used to obtain the cracking patterns caused by drying. The parameters of the numerical models are identified on the results of an experimental campaign carried out by Soleilhet [2]. This same campaign is then used to validate the pertinence of an explicit representation of cracking.

1. Introduction

In this paper, the beam particle model and the hydric transport model are presented. Then, three points bending modelling is achieved in two cases: with and without considering previous drying.

Moreover, the beam-particle model generates a random mesh which represents material's heterogeneity. It reproduces the experiment variability.

2. Beam-particle model

This model is constituted by a set of polygons. It is generated in four steps [3] with a Voronoi's tessellation and Delaunay's triangulation. Each rigid particle has a centroid which is randomly placed, to represent the material's heterogeneity. They are connected to each neighbour with Euler-Bernoulli brittle beam to represent cohesion between particles (Figure 1). E, α, A_b, l_b respectively represent beam young modulus, the inertia, the cross-section area and the length. $\overrightarrow{U_i}, \overrightarrow{U_j}, \theta$ are the three degrees of freedom: 2 translations, 1 rotation. Otherwise, a contact law with friction is introduced to represent particles interaction such as cracks closure.

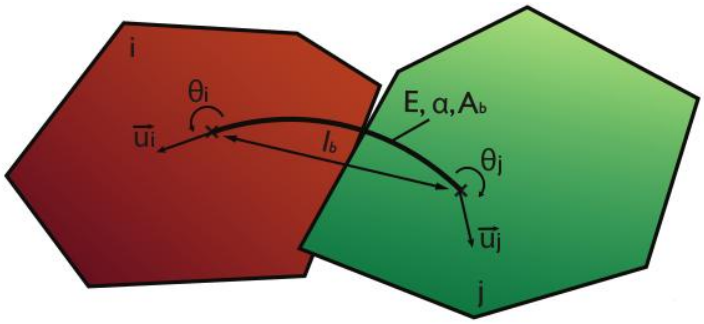

Figure 1: Linked particles [3].

These mechanisms permit to capture the elastic and softening behaviour. Indeed, for a mechanical or a hydric loading, a breaking criterion based on Mohr Coulomb is considered [3] with deformation and beam's rotation, which represent particles displacement. When the criterion threshold is reached the beam is deleted. The link between two particles disappears and it permits to obtain an explicit crack opening.
Furthermore, due to random mesh, each simulation gives different results. Experiment variability is represented. Contrary to an experiment campaign, virtual testing permit to generated more than 3 specimens which is generally considered in an experiment campaign. A statistic model is taken account with the normal distribution. Properties such as flexural strength average seem to convert with more than 20 tests.

2. Hydric transport model

In this study, two steps are needed to obtain a hydric strain field. A simulation is realised on Cast3m which is a finite element program. Then a reanalysed method is used [1]. This method acts as a bridge between continuum and discrete models.
The hydric transport model is based on a non-stationary transport equation with Eq. (1). It is supervised with initial intern and extern moisture. In this equation, liquid transfer is supposed.

$$\phi \frac{\partial S}{\partial P_c} \frac{\partial P_c}{\partial t} = \left(\frac{K.k_r}{\mu} grad(P_c) \right) \quad (1)$$

ϕ is material's porosity, S the degree of saturation, P_c the capillarity suction, k_r the relative permeability, K the permeability and $\mu$the water viscosity. These parameters are identified with van Genuchten model which is basically developed for soil [4] It is also supposed that liquid moisture transport is predominant compared to gas transport in a considered interval of moisture [5]. Otherwise, relative permeability is determined with Eq. (2), with the parameter m.

$$k_r = \sqrt{S} \left(1 - \left(1 - S^{\frac{1}{m}} \right)^m \right)^2 \quad (2)$$

Degree of saturation is obtained with Eq. (3). Then, Kelvin-Laplace equation Eq. (4) permits to create a link between capillary suction and relative humidity with ideal gas hypothesis.

$$S(P_c) = \left(1 + \left(\frac{|P_c|}{a} \right)^{\frac{1}{1-m}} \right)^{-m} \quad (3)$$

ρ bulk weight, $R = 8.314$ Jmol^{-1}K^{-1}, T temperature, M molar mass, HR relative humidity.

$$P_c = \frac{\rho RT}{M} ln\,(HR) \quad (4)$$

Once the finite element analysis is realised, a hydric strain field is obtained. The reanalysis method [1] permits to project nodes or gauss points of this strain field on the beam-particle discretisation. The shrinkage induces a force which is locally estimated on each beam. Then, the discrete model converges to a steady state which induces cracks due to the breaking criterion. Results represent explicit cracks' expansion and trajectory [6].

3. Three points bending modelling

In this part, 2D three points bending simulations are performed to determine the impact of drying shrinkage on an 84x10cm specimen Figure 2. 21 000 nodes are generated in the random mesh, which is equivalent to 63 000 degrees of freedom. Concerning boundary conditions, an isostatic case is considered. The mechanical and hydric parameters correspond to Soleilhet [5] concrete. Then, beam-particle model's parameters are identified. 26 simulations are performed with or without modelling shrinkage. Experimentally [5], drying specimens are conserved in a controlled room at temperature 25°C (±1°C) and 36% RH (±5). Beam-particle parameters permit to characterise quasi-brittle material's behaviour. Then, drying simulations are realised with the same set of parameters to predict the drying impact on strength resistance.

Figure 2: Cracking pattern.

In Figure 3 numerical and experimental forces-displacements curves are represented. The identification reveals a difference of 2.7%.

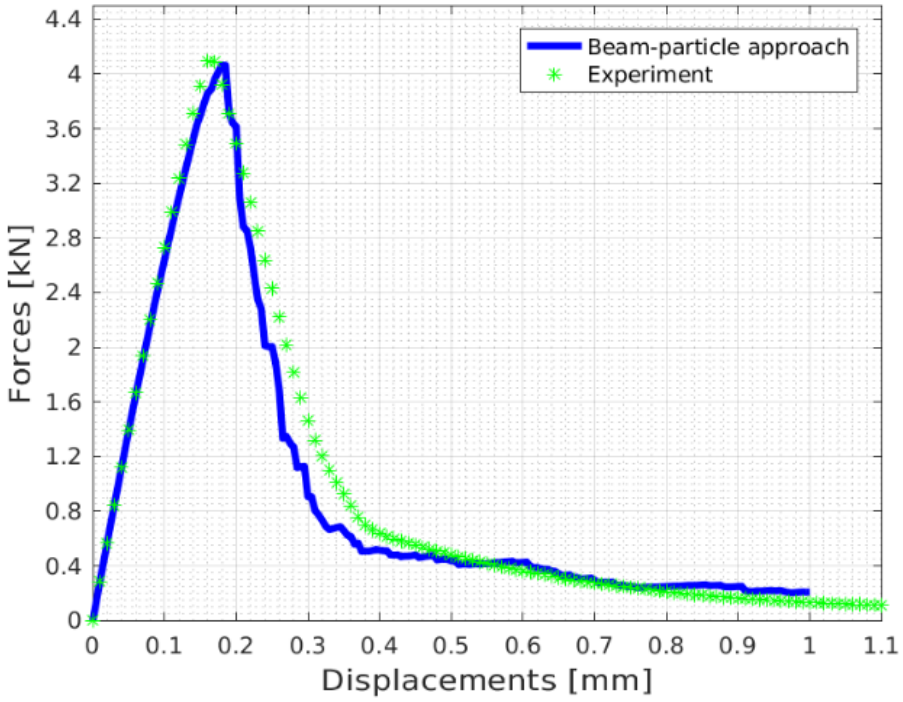

Figure 3: Three points bending forces-displacements average curves without shrinkage.

For non-drying case, the results are given in Figure 3 and for drying case results are given is Figure 4. It demonstrates a reduction of 12% of the maximum flexural strength due to initial strains at the peak, in the numerical model. Furthermore, in the elastic part, Young modulus decreases slightly due to previous micro-cracks formed during shrinkage. The cracks opening is in the order of 10 µm.

In drying case, because of three points bending, the upper part of the beam is compressed, previous shrinkage cracks are closed, and particles are interacted to model the unilateral effect and the stiffness' recovering, whereas on the down side, the beam is in tensile state and cracks are still opened.

Otherwise, contact law, between particles, has an impact on post peak behaviour. Indeed, with contact law between each particle the drop is less significant because cracks closure is considered.

In Figure 4 the beam-particle model's prediction underestimates the experimental curves. Indeed, it has to consider complementary phenomena. The comparison between numerical and experimental results reveals a difference of 12% at the peak. The average of 26 virtual

testing drying specimen is represented on the force-displacement curve. Standard deviation reveals that the maximal and minimal strength force is respectively included between 20% and 14% of the average value.

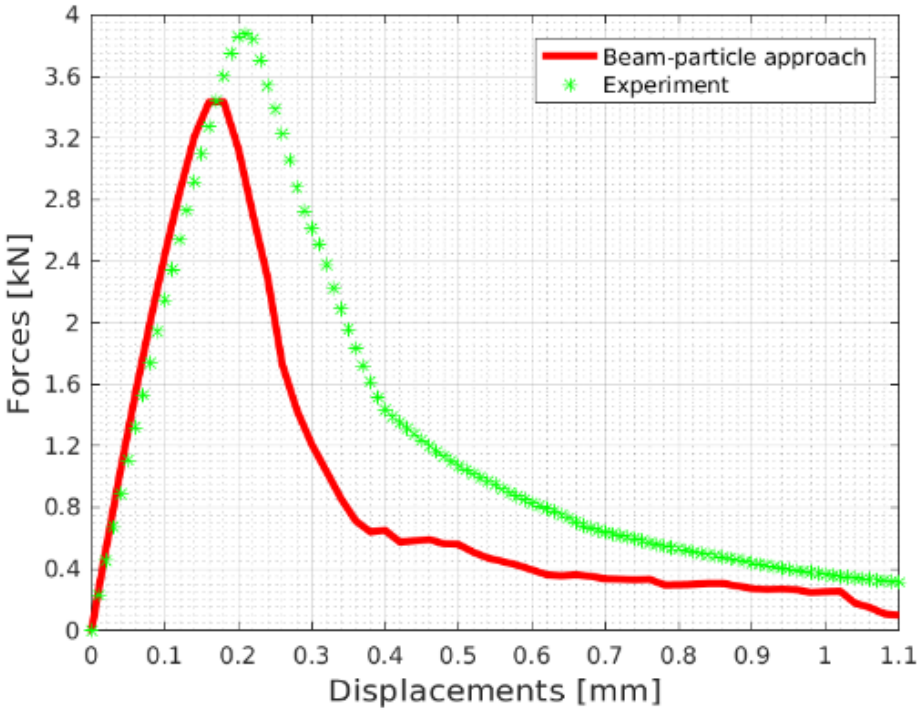

Figure 4 : Three points bending forces-displacements average curves with shrinkage.

It is important to emphasize that experimentally, there's generally not enough considered specimens to represent reality with certainty.
It is noticed that the main crack caused by mechanical loading is often initiated on a shrinkage crack. It is not possible to claim that shrinkage cracks directly impact the specimen force-strain, with certainty. Indeed, in Euler-Bernoulli beam's theory, three points bending test induces a maximal moment at the middle of the beam. However, numerical crack appears around this zone.
So therefore, to examine only the macroscopic crack openings without forcing the initiation in the middle of the beam, four points bending tests are achieved. As a matter of fact, moment is both maximal and constant between the two points of loading.
Besides, the prediction of decrease of flexural strength and Young modulus are lower (and thus closer to experimental values) than the ones obtained with a macroscopic damage approach [2]. This may be due to the explicit considered cracking and cracks closure. The consideration of additional phenomenon such as creep should also improve the numerical results.

5. Conclusion

In this study, the impact of shrinkage on concrete's strength is examined with a beam-particle approach. It indicates that natural shrinkage due to a gradient of moisture, induces a decrease of concrete's strength. Then, this decrease depends on crack initiation. Indeed, in case of mechanical crack initiation on a previous shrinkage crack, a drop of 12% of the flexural strength is observed.
Variability is also highlighted. Maximal force strength depends on material heterogeneity, which is represented by Voronoi polygons' mesh. The model's confidence interval seems to be excessive to represent the reality.

References

[1] Oliver-Leblond, C. et al, 3D Global/Local Analysis of Cracking of Reinforced Concrete. The third International Conference on Computational Modeling of Fracture and Failure of Materials and Structures (CFRAC2013), Prague, Czech Republic (2013)
[2] Soleilhet, F. et al, Hygro-mechanical modelling of self-induced stresses during the service life of concrete, 2nd International RILEM/COST Conference on Early Age Cracking and Serviceability in Cement-based Materials and Structures – EAC02, Vol. 2, Brussels, Belgium (2017)
[3] Vassaux, V. et al, Beam-particle approach to model cracking and energy dissipation in concrete: Identification strategy and validation, Cement and Concrete Composites 70 (2016), 1-14
[4] Van Genuchten, M.Th., A closed form equation for predicting the hydraulic conductivity of unsaturated soils, Soil Sci Soc Am J 44(5) (1980), 892-898
[5] Soleilhet, F., Experimental and numerical investigations of cementitious materials under hydro-mechanical loadings, PhD thesis, Ecole normale superieure Paris-Saclay (2018)
[6] Oliver-Leblond. C., Two scale description of local mechanisms: application to reinforced concrete, PhD thesis, Ecole normale superieure Paris-Saclay (2013)

SynerCrete'18 International Conference on Interdisciplinary Approaches
for Cement-based Materials and Structural Concrete
24-26 October 2018, Funchal, Madeira Island, Portugal

THERMOMECHANICAL MODELLING FOR THE ESTABLISHMENT OF A NEW BUILDING METHOD FOR BASEMENTS OF CONVENTIONAL HOUSINGS

Dirk Schlicke [(1)], Thomas Hochgatterer [(2)], Martin Zabern [(2)], Alexander Glebe [(2)], Alexander Reinisch [(2)]

(1) Institute of Structural Concrete, Graz University of Technology, Graz, Austria
(2) Doka GmbH, Amstetten, Austria

Abstract

This paper presents an interdisciplinary cooperation between structural engineering, concrete technology and formwork technology aiming at the establishment of an innovative building method for basements of conventional housings, named *DokaBase*. Its innovation consists of an integrative application of the external insulation as formwork already with the main benefits of (i) an simplified and accelerated construction process; (ii) a defined and precise mounting of the insulation; and (iii) the achievement of enhanced concrete quality at the outer surface of the concrete members providing watertightness without additional measures.
However, the establishment of this solution in practice requires also targeted investigations on the effect of the presence of the insulation during the hydration and hardening of the concrete. In detail, the one-sided insulation is expected to cause higher temperature increases in the members as well as temperature gradients over the thickness of the slab and the wall. Therefore, detailed thermomechanical modelling was conducted on macroscopic level. This contribution presents this thermomechanical modelling with special regard to interdisciplinary aspects of this cooperation in order to achieve best possible acceptance of the results and conclusions for practical application.

1. Introduction

DokaBase is a new building method for basements of conventional housings. In this solution, the external insulation of the basement serves already as formwork, as illustrated in Fig. 1. The insulation itself is XPS with a ca. 5 mm thick cement-based coating of the surface in order to enable a durable bond between XPS and fresh concrete without additional measures.

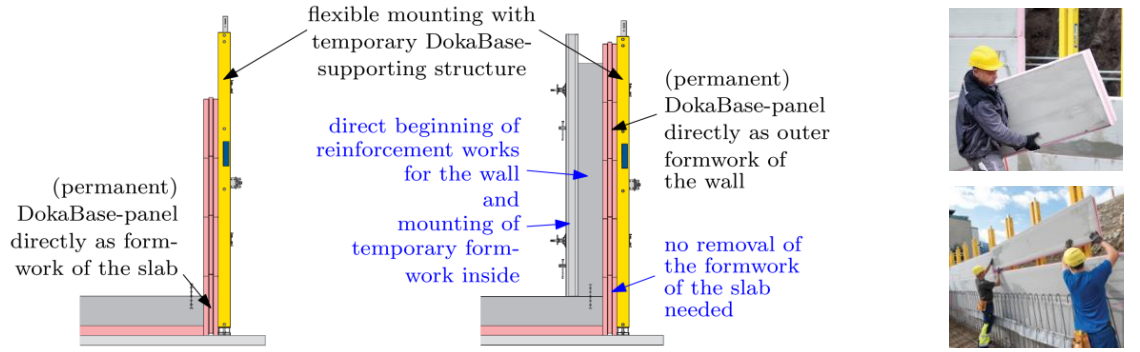

a) working step 'ground slab' *b) working step 'wall'* *c) mounting on-site*

Figure 1: *DokaBase* system taken from [1].

On the one hand, this solution simplifies and accelerates the construction process; and on the other hand, the continuous treatment with XPS ($\lambda = 0.036$ W/m°C, closed-cell content ≥ 95 %) reduces temperature and moist gradients at the outer surface with a beneficial effect on the concrete quality. As outlined in [1], detailed investigations on material level showed that the finally achieved concrete quality will limit the water penetration to a depth < 25 mm for high water pressure up to 10 m water pressure height. Thus, adequate watertightness can be provided without additional measures in the present basements.
Nevertheless, using insulation material as formwork reduces the outflow of hydration heat. And even if the thicknesses of the present members are rather small and the insulation exists only on one side, higher temperature increases in the member as well as higher temperature gradients between the outer surface with insulation and the inner surface without insulation are to be expected. Aiming at a profound understanding of the temperature field and stress development in one-sided insulated members as well as for a quantification of this effect in the present case, detailed thermomechanical modelling was conducted on macroscopic level. Altogether, a comprehensive parametric study was accomplished with regard to the influence of different concretes, changing areal dimensions, fresh concrete temperature and climatic conditions, seasonal climatic conditions, different stripping times and treatments at the inner surface as well as delays in the construction process.
This contribution presents this thermomechanical modelling on basis of the reference case with special regard to interdisciplinary aspects of this cooperation in order to achieve best possible acceptance of the results and conclusions for practical application.

2. Reference case

2.1 Geometry and dimensions

The reference case was defined by a basement with a room height of 2.7 m and areal dimensions at the inside of 13 × 13 m. The dimensions of the basement at the outside amount 13.8 × 13.8 m taking into account 2 × 15 cm insulation and 2 × 25 cm wall thickness. The overall height of this basement is 3.15 m taking into account a 10 cm subbase concrete layer, 10 cm insulation layer, 25 cm concrete ground slab and 2.7 m high walls. Fig. 2 illustrates this reference case in detail. The *L*/*H*-ratio of the wall is 5.0.

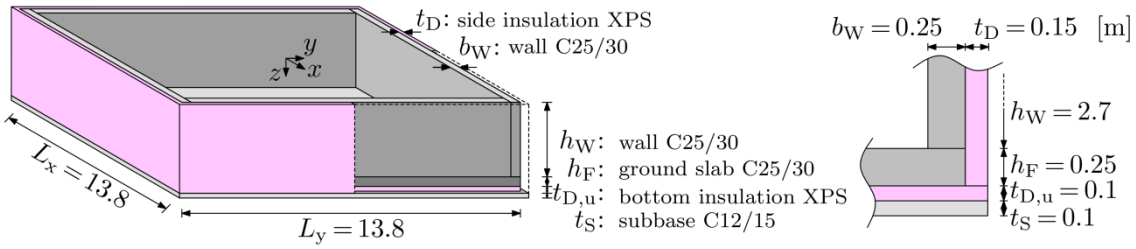

Figure 2: Dimensions of the reference case.

2.2 Concrete used

The concrete mix for the reference case in the investigations is shown in Tab. 1. This mix is based on a conventional Austrian concrete with strength class C25/30 and durability requirements of XC3/XD2/XF1/XA1 according to [2]. Further information on the hydration heat development as well as evolution of mechanical properties was determined with targeted material testing according to [2]. The results are given in Tab. 2.

Table 1: Mix properties for the reference concrete.

	specification	**Amount**
aggregates	0-4 / 4-8 / 8-16 / 16-32	1092 / 356 / 559 / 544 kg/m³
cement	CEM II/A-M (S-L) 42,5 N Kirchdorfer	330 kg / m³
superplasticizer	Master Glenium Sky676MONO BASF	2,8 kg / m³ (0,6 %)
water	[-]	180 kg / m³

Table 2: Evolution of hydration heat and mechanical properties.

effective age [h]	**Hydration heat [J/g]**	**Elastic modulus [N/mm²]**	**Tensile strength [N/mm²]**
24 h	160	[-]	[-]
48 h	250	23 062	1.44
72 h	283	[-]	[-]
672 h	340	31 000	2.60
Activation energy:		33 500 J/mol	

2.3 Initial temperatures and climatic conditions

The reference case represents a moderate summer scenario. Initial temperatures were set with 15 °C for the ground, 17.5 °C for the subbase, 20 °C for the insulation and 25 °C for fresh concrete. And the ambient air was considered with an average temperature of 20 °C and a daily sinusoidal variation of ± 10 °C. In this scenario the effect of solar radiation and radiation losses was not considered explicitly.

3. Calculation Model

3.1 Geometric idealization

The basement was idealized with a 3D Finite Element calculation model using volumetric elements for the hardening concrete members, but also for insulation elements, the subbase and the soil in order to represent their heat storage effect, as shown in Fig. 3 with additional information on the used symmetry for minimization of computational efforts.

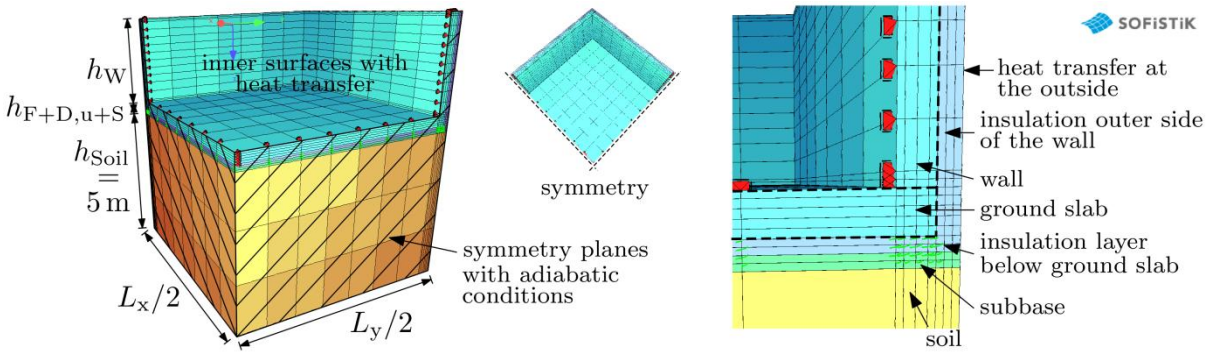

a) view *b) cross-sectional structure*

Figure 3: Calculation model.

Apart from that, the model is generated according to the modelling assumptions presented in [3] with special regard to realistic horizontal restraint and self-weight activation due to uplift.

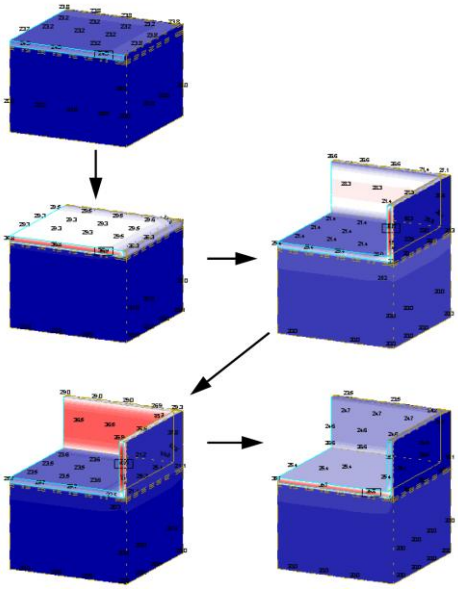

- t = 0 h (1st day; 4:00 pm):
  - casting ground slab
  - no thermal treatment at the top surface of the slab; heat transfer α = 20 W / °Cm²
- t = 24 h (2nd day; 4:00 pm):
  - casting wall
    - » safe side assumption of casting "all in once", formwork α = 5.5 W / °Cm²
  - no thermal treatment at the top surface of the wall, α = 20 W / °Cm²
- t = 40 h (3rd day; 8:00 am):
  - one-sided removal of the formwork at the inner surface of the wall
  - no thermal treatment at the inner side of the wall, α = 20 W / °Cm²

Figure 4: Considered stages to represent the construction process.

3.2 Material model

The hydration was simulated with a thermo-mechanically coupled material model for aging concrete with regard to heat release and heat flow under transient conditions, maturity, evolution of elastic modulus, shrinkage and viscoelasticity. The model was implemented for each element independently enabling a time- and localization-discrete consideration of the several thermal and mechanical properties. Special attention was hereby given to the viscoelastic behaviour with regard to each elements own stress history. Further information can be found in [3] and [4].

3.3 Time control of the calculation with special regard to the construction process

The model represents the construction process with the considered stages shown in Fig. 4. It is on the safe side assumed, that the wall is casted all in once around the corner.

4. Typical results and expected insights

4.1 Temperature and stress history in slab and wall

The temperature and stress history in the slab and in the wall was analysed on basis of the timely development of temperature and stresses in selected points with extreme values. Fig. 5 shows the results for the slab of the reference case (areal location of the analysed points is at $L_x/2$ and $L_y/2$); and Fig. 6 shows the results for the wall (areal location of the analysed points is in the symmetry of the wall in length direction).

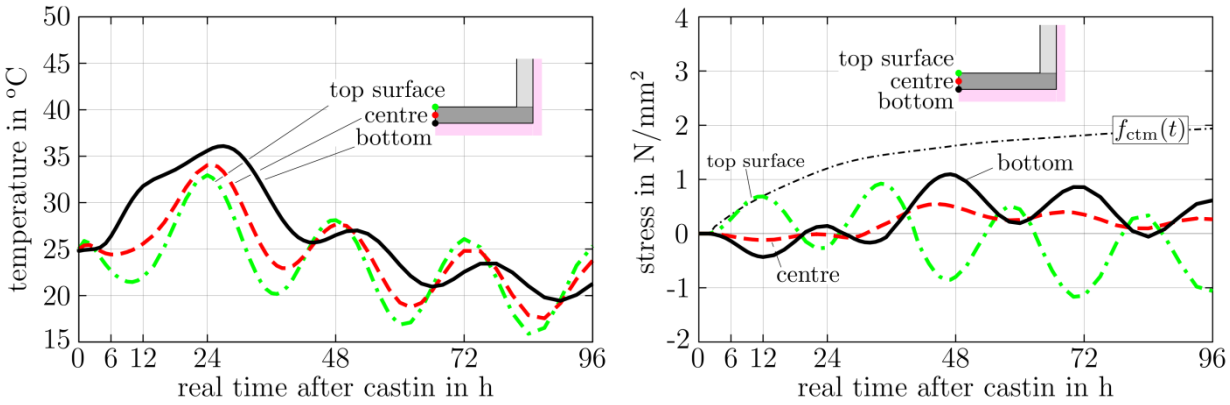

a) temperature history *b) stress history*

Figure 5: Typical nodal results for the ground slab exemplified for the reference case.

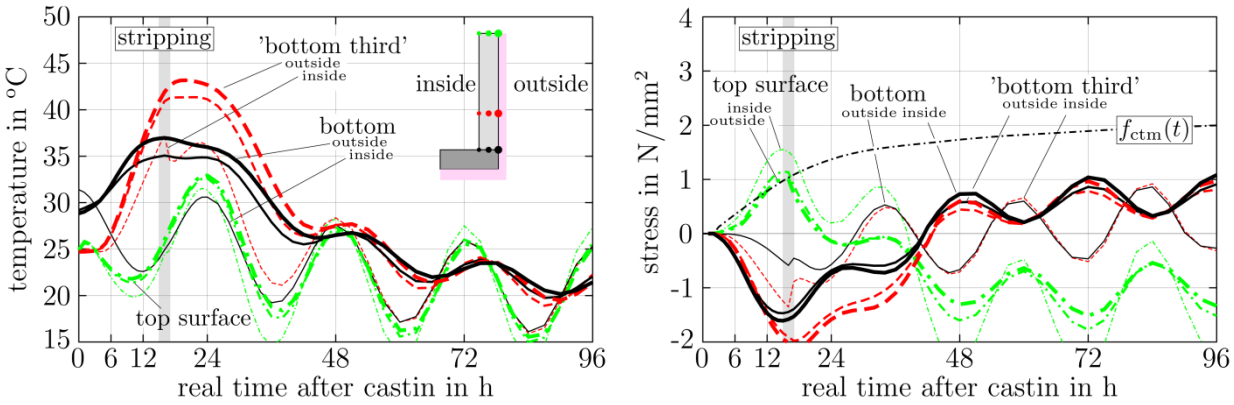

a) temperature history *b) stress history*

Figure 6: Typical nodal results for the wall exemplified for the reference case.

In addition to the nodal results, the stress field was further analysed regarding uniformly and linearly distributed parts corresponding with a restraint force and restraint moments. This was done by removal of the self-balanced non-linear part of the stress distribution, see Fig. 7.

4.2 Assessment of cracking risk

The cracking risk was assessed by the two-stage procedure proposed in [3]: Firstly, the general risk of cracking is assessed by a comparison of maximum stresses in the material point or element with 80 % of $f_{ctk;0.05}(t)$. If this is fulfilled, cracking can be safely excluded at

all. If not, micro-cracking with reduction of Eigenstresses is to be expected, so that the uniformly and linearly distributed parts have to be assessed in the second step. These stresses correspond with restraint forces and moments and will cause macrocracks when the cracking forces and moments are exceeded. Thus, the stresses were now compared with the mean-value $f_{\mathrm{ctm}}(t)$ of the actual tensile-strength; see also [5]. Fig. 7 illustrates this procedure.

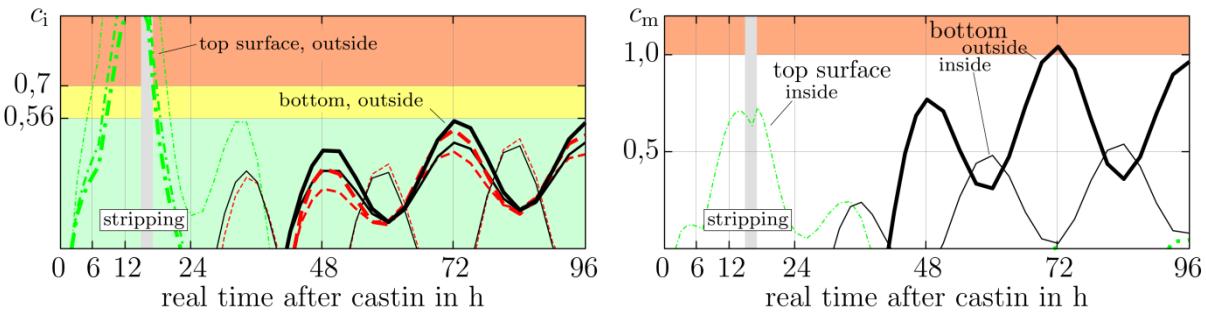

$$c_{\mathrm{i}} = \frac{\sigma_{c,i}(x,y,z,t)}{f_{\mathrm{ctm},i}(x,y,z,t)} < 0{,}56 \qquad (1)$$

a) general risk of cracking

$$c_{\mathrm{m}} = \frac{\sigma_{c,N+M}(t)}{f_{\mathrm{ctm}}(t)} = \frac{\frac{N_{\mathrm{rest}}(t)}{A_{\mathrm{c}}} \pm \frac{M_{\mathrm{rest}}(t)}{W}}{f_{\mathrm{ctm}}(t)} < 1{,}0 \qquad (2)$$

b) risk of macrocracking

Figure 7: Crack assessment exemplified for the wall of the reference case.

5. Conclusion

This contribution presents the thermomechanical modelling for the establishment of the building method *DokaBase* aiming at a simplified and fastened construction for watertight basements of conventional housings. In fact, it exemplifies an interdisciplinary cooperation between structural engineering, concrete technology and formwork technology, whereby all the different aspects and demands of the three stakeholders were adequately addressed and suitably combined. The result is a robust tool for comprehensive analysis of the building method with regard to the influences of different concretes, changing areal dimensions, fresh concrete temperature and climatic conditions, seasonal climatic conditions, different stripping times and treatments at the inner surface as well as delays in the construction process.

References

[1] DokaBase, application information 999810001 - 07/2017, Doka GmbH (in German)
[2] EN 206-1:2017 + AC:2018 (ÖNORM B 4710-1): Concrete – Part 1: Specification, performance, production and conformity
[3] Schlicke, D. and Tue, N.V., Minimum reinforcement for crack width control in restrained concrete members, Structural Concrete 16 (2014), 221-232
[4] Schlicke, D., Minimum reinforcement for restrained concrete, PhD thesis (revised edition), Graz University of Technology (2014)
[5] ÖBV Bulletin, Analytical design of watertight structures with optimized concrete (in German), Austrian society for Construction Technology, Vienna, Austria (2018).

MULTI-SCALE IN TIME AND SPACE MODELLING

AND

EXPERIMENTS

SynerCrete'18 International Conference on Interdisciplinary Approaches
for Cement-based Materials and Structural Concrete
24-26 October 2018, Funchal, Madeira Island, Portugal

A NEW CREEP TEST METHOD FOR REINFORCED CONCRETE TENSION MEMBERS UNDER CONSTANT LOADING

Eugenijus Gudonis [(1*)], Pui-Lam Ng [(1,2)], Shao-Hua Chu [(2)], Aleksandr Sokolov [(1)]

(1) Vilnius Gediminas Technical University, Vilnius, Lithuania
(2) The University of Hong Kong, Hong Kong, China

Abstract
This paper reports the experimental study on creep behaviour of reinforced concrete (RC) tension members subjected to long-term constant loading. An innovative testing rig was designed and four replicates were fabricated for concurrent testing of multiple specimens under the same temperature and humidity conditions. Four direct tension specimens were produced and tested under sustained loading up to beyond 300 days. The test results indicated the augmentation of deformation due to concrete creep in RC member. The creep strain of specimens became practically steady after 300 days, and the creep half-time was obtained as approximately two weeks.

1. Introduction

Creep of concrete is a major component of time-dependent deformation that affects the serviceability of concrete structures. Experimental investigation of concrete creep behaviour has been attempted by many researchers [1-5]. From previous research findings, when the sustained tensile or compressive load does not exceed approximately 40% of the respective concrete tensile or compressive strength, the creep can be treated as linear creep, where the creep strain is linearly dependent on the sustained stress, and the principle of superposition is applicable for evaluating the creep strain subject to variable stress history [6,7].
There are issues in connection with concrete creep experiment that require particular attention. First is the environmental condition: The experiment normally would span over prolonged durations. There might be difficulty in maintaining constant environmental conditions even in laboratories with controlled indoor environment. This might introduce errors and undulations in the measured creep deformations. Second is presence of embedded reinforcement: Whilst the creep of plain concrete is regarded as a fundamental property of

concrete, the creep deformation of reinforced concrete is subject to the influence by reinforcement. The interaction between creeping concrete and reinforcing bars is complicated and cannot be reflected in the creep test of plain concrete [8].

To tackle the first issue, the fluctuations of environmental condition can be minimised by providing active control of the indoor temperature and relative humidity. On the other hand, to tackle the second issue, creep test of reinforced concrete that requires tailored loading mechanism is necessary. This calls for a new concept of experiment design. A bespoke testing rig for creep test of RC tension members has been innovated in this research. The long-term tension loading was constantly exerted via a double lever system with adjustable fixities to ensure verticality, which is an improved version of lever type testing rig described in the literature [8]. Four RC direct tension specimens were tested under constant loading up to beyond 300 days using the new test set-up.

2. Test set-up of creep test

The scheme design of the double lever system test set-up is shown in Fig. 1. It has double tiers of lever mechanisms. The external load is applied by placing pre-defined weights in the tray container. The gross weight of the loaded container would be transmitted via the first-tier lever of ratio close to 4:1 (the actual measured ratio is 3.93:1, with respect to the projected length of loaded lever arm), to become a downward load on the second lever. This downward load would be transmitted via the second-tier lever of ratio 4:1, to become an upward load at the opposite side of the pivot. Through the double lever mechanism, the resulting upward load would be magnified to approximately 16 times the gravity loading at the tray container, and it would act on the upper end of the vertically oriented direct tension specimen. The lower end of the specimen is connected to the ground beam of the testing rig and restrained from any vertical movement. To ensure verticality of the specimen, the connection from the lower end of specimen to the ground beam is adjustable with a horizontal slot. By this arrangement, the testing rig would be self-equilibrating and the specimen would be subjected to pure axial tension loading.
The overall height of the testing rig is close to 2.35 m, and its internal headroom has been designed to accommodate 1.5 m long vertically-placed specimen, with sufficient vertical clearance allowed for the connection components and instrumentation. Four replicated testing rigs have been fabricated for concurrent testing in the same environment. Before usage, each testing rig has been calibrated by placing standard weights in the tray container and recording the resultant force transmitted through the double lever system. To conduct the creep test, initially, the designated load should be applied to the test specimen in a sequential manner. Standard weight blocks are placed into the tray container one by one. This process is done manually and gently to maintain the balanced position of the container hung from the hanging point using metal chains. A short pause should be given after placing each weight block to stabilise the load and to record the load and deformation readings. After the load addition, the weight blocks are undisturbed as sustained loading.

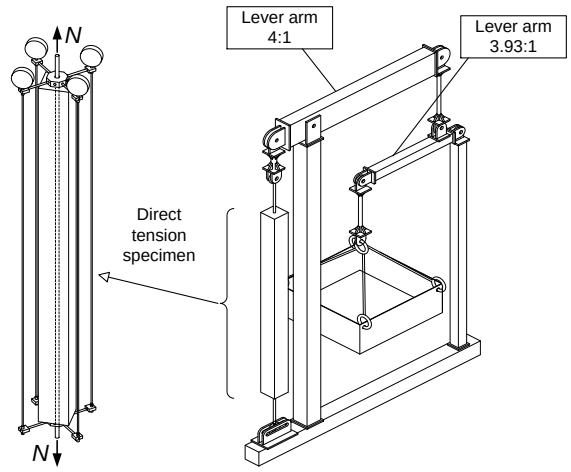

Figure 1: Schematic diagram of test set-up.

The RC tension specimen has uniform 100 mm square cross-section and is of 1500 mm long. A steel bar is embedded at the centre, and protruded 50 mm from each of the two ends. The protruded parts of steel bar were connected to the testing rig via hexagonal coupling bolts and steel rods. The long-term deformation of the specimen was measured using 4 mechanical gauges installed at diagonal positions of the specimen. The gauges have resolution of 0.001 mm and the gauge length of measurement is 1520 mm. The measured values from the 4 mechanical gauges can be averaged for better reliability of experimental results. Fig. 2 depicts a photograph of the creep test.

Figure 2: Photograph of ongoing creep test.

3. Testing programme

Four RC tension specimens (labelled DT-12, DT-13, DT-14 and DT-15) have been fabricated and tested. Each specimen was reinforced with 12 mm diameter high-strength deformed steel bar. The corresponding reinforcement ratio p was 1.1%. The specimens were cast from the same concrete mix, with water/cement ratio of 0.45 and fine to total aggregate ratio of 0.49 by mass. The 28-day mean cylinder compressive strength f_{cm} was 33.6 MPa and the elastic

modulus E_{cm} was 35.9 GPa. Subsequent to casting, the specimens were demoulded at 2 days and cured under moist condition until loading at age t_0 of 52 days. Regarding reinforcing bar, the nominal yield stress f_y and the elastic modulus E_s averaged from test samples were 945 MPa and 190 GPa, respectively.

With regard to the determination of loading magnitude, the ultimate capacity of specimen N_{ult} is taken as the nominal yield stress of reinforcement f_y multiplied by the area of reinforcement A_s. Then, for specimens DT-12 and DT-13, the applied tension load was designated as 38% of the ultimate capacity of specimen (load magnitude of 40 kN); whereas for specimens DT-14 and DT-15, the applied tension load was designated as 33% of the ultimate capacity of specimen (load magnitude of 35 kN). The test was conducted in a laboratory room with controlled temperature and humidity without natural ventilation. The creep test was conducted over a period of 315 days (concrete age of 367 days). Throughout the test duration, the average temperature and average relative humidity were respectively 19°C and 64%.

4. Test results and discussion

At any time, the deformation measurement can be converted to strain with respect to the specimen length. Theoretically, the long-term deformation comprises of the short-term deformation in response to the load application and the time-dependent creep deformation. To reveal the creep behaviour, the instantaneous deformation recorded upon the completion of load application prior to the creep effect can be deducted from the measured time-dependent deformation. In other words, the creep strain $\Delta\varepsilon_m(t,t_0)$ can be obtained by subtracting the instantaneous strain $\varepsilon_m(t_0)$ from the total strain $\varepsilon_m(t,t_0)$. Fig. 3 presents the variation of creep strain results with time in days. It can be seen that the creep strain increased more rapidly initially and then at a gradually diminishing rate. Beyond 300 days, the creep strains became approximately steady. Therefore, the strain values subsequent to 300-day duration of constant loading can be regarded as the final creep strain.

The respective strain values of the specimens are tabulated in second to fourth columns of Tab. 1. Among the specimens, the total strains were ranging from 1620 to 1920 με, whereas the instantaneous strains were ranging from 1290 to 1680 με. As expected, the more heavily-loaded specimens DT-12 and DT-13 exhibited larger total and instantaneous strains than specimens DT-14 and DT-15. To indicate the proportional augmentation of deformation under sustained loading, the ratio of creep strain to instantaneous strain is computed, which is found to be ranging from 0.145 to 0.257 as listed in the fifth column of Tab. 1. It can be seen that under the restraining effect of reinforcement, the creep of concrete would increase the deformation by approximately 15% to more than 25%. This is not small and should be properly considered in designing concrete structures.

From the experimental results, the creep half-time $t_{0.5}$ (which means the time required for half of the ultimate creep strain to take place) is evaluated. The creep half-time is useful information for construction planning and control. It allows engineers to assess the time to compensate certain amount of creep deformation and anticipate the remaining creep deformation during construction [9,10]. In the present study, as the creep strain was practically steady beyond 300 days, the final creep strain is treated as the ultimate creep strain. For the 4 specimens, the creep half-time was ranging from 13.8 to 14.8 days as reported in the last column of Tab. 1. Therefore, although creep is a long-term process, half of

the ultimate creep deformation would occur approximately in the first two weeks after loading.

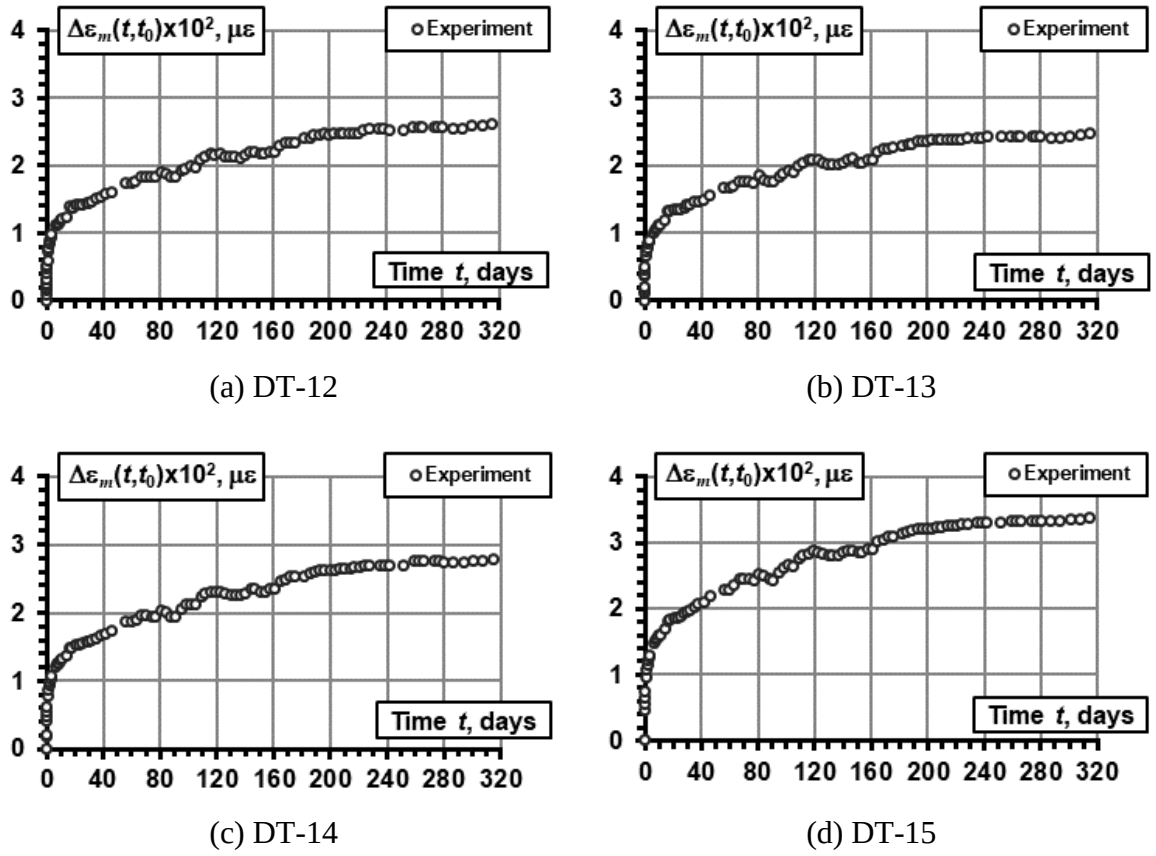

(a) DT-12 (b) DT-13

(c) DT-14 (d) DT-15

Figure 3: Variations of creep strain with time.

Table 1: Results of creep test.

Specimen	Total strain, $\varepsilon_m(t,t_0)\times10^{-6}$	Instantaneous strain, $\varepsilon_m(t_0)\times10^{-6}$	Creep strain, $\Delta\varepsilon_m(t,t_0)\times10^{-6}$	Ratio of creep strain to instantaneous strain	Creep half-time, $t_{0.5}$ (days)
DT-12	1740	1480	255	0.172	14.8
DT-13	1920	1680	243	0.145	14.7
DT-14	1690	1420	271	0.191	14.2
DT-15	1620	1290	332	0.257	13.8

5. Conclusions

A new test method of the creep behaviour of reinforced concrete (RC) tension members has been developed. A bespoke testing rig with double-tier lever system for load application was innovated. In this paper, the principles and details of the test set-up have been explicated. Four RC direct tension specimens were fabricated for undergoing the creep test up to beyond 300 days. The test results have revealed approximately 15% to more than 25% augmentation of short-term deformation in RC member due to long-term creep effect. The creep half-time (the time for half of the ultimate creep to take place) of specimens has been found as equal to approximately two weeks.

Acknowledgements

The authors gratefully acknowledge the financial support provided by the Research Council of Lithuania (Project No. MIP-093/2015). The second author wishes to express his gratitude for the support provided by the European Commission Research Executive Agency under the Marie Skłodowska-Curie Actions (Project no.: 751461).

References

[1] L'Hermite, R., Déformation du béton, Bâtir 27 (1952), 18-22
[2] Troxell, G. E., Raphael, J. M. and Davis, R. E., Long-time creep and shrinkage tests of plain and reinforced concrete, ASTM Proc 58 (1958), 1101-1120
[3] Neville, A. M., The influence of cement on creep of concrete and mortar, PCI J 2(1) (1958), 12-18
[4] Tamtsia, B. T. and Beaudoin, J. J., Basic creep of hardened cement paste: a re-examination of the role of water, Cem Concr Res 30(9) (2000), 1465-1475
[5] Persson, B., Correlating laboratory and field tests of creep in high-performance concrete, Cem Concr Res 31(3) (2001), 389-395
[6] Comité Euro-International du Béton, Structural effects of time-dependent behaviour of concrete, CEB Bulletin 142, Lausanne (1984)
[7] Balevicius, R. and Marciukaitis, G., Linear and non-linear creep models for a multi-layered concrete composite, Archives Civ Mech Engin 13(4) (2013), 472-490
[8] Scott, R. H. and Beeby, A. W., Test rigs for long-term tension tests, Strain 41 (2005), 151-155
[9] Ng, P. L., Lam, J. Y. K. and Kwan, A. K. H., Multi-layer visco-elastic creep model for time-dependent analysis of concrete structures, Proceedings of the Eleventh International Conference on Civil, Structural and Environmental Engineering Computing, Malta (2007)
[10] Ng, P. L., Kwan, A. K. H., Fung, W. W. S. and Du, J. S., Prediction of concrete creep by multi-layer visco-elastic model, Proceedings of the 7th International Conference on Tall Buildings, Hong Kong (2009), 677-688

SynerCrete'18 International Conference on Interdisciplinary Approaches
for Cement-based Materials and Structural Concrete
24-26 October 2018, Funchal, Madeira Island, Portugal

AN EXPERIMENT-BASED FE APPROACH TO ANALYZE EARLY-AGE TEMPERATURE AND STRAIN DISTRIBUTION IN LARGE-DIMENSION CONCRETE WALL

Yan Geng [(1)], Suduo Xue [(1)], Xiongyan Li [(1)], Jinguang Li [(2)]

(1) Beijing University of Technology, Beijing, China
(2) China Huanqiu Contracting and Engineering Co. Ltd., Beijing, China

Abstract

Hydration heat and thermal cracking is a main concern for large-dimension concrete structures. In order to investigate the early-age properties of concrete under research, a set of time-varying experiments were conducted, namely the hydration experiment, standard thermal and mechanical tests. Then a finite-element (FE) method based on the material experiments was proposed with User Subroutine UMATHT, USDFLD and UEXPAN. In order to verify the accuracy of the proposed FE method and investigate the temperature distribution and strain development of large-dimension concrete structures, an experimental wall of 3.6m×0.8m×3.6m in dimension was constructed. According to the temperature measurement, the highest temperature reached a maximum of 52.3℃ at the central point after 36 hours of pouring. The maximum temperature difference between the core and ambient environment was 41.5℃, with a maximum cooling rate of 9.0℃ per day. Compared with the FE analysis results, the average temperature difference at the peak was only 3.6%. As for the strain results, the computed curves reflected the trend of measured strain development with a maximum difference of 9.5% despite some local deviations. Overall, the computed results agreed well with test data, indicating the effectiveness of the proposed FE approach.

1. Introduction

Hydration heat and thermal cracking is a main concern for large-dimension concrete structures, which experience rapid temperature rise in the core and manifest distinct temperature difference between centre and surface at very early age [1]. Micro thermal cracks may consequently occur [2] and gradually develop into obvious cracking through structures, severely reducing the service life of structures or even resulting in structure failures.

Therefore, it is significant to make accurate prediction of structural thermal stress and strain development and to take appropriate measurements to prevent concrete cracking.
Thermo-mechanical analysis has been applied to concrete structures for decades. Zreiki *et al*. [3] developed a thermo-chemo-mechanical model based on a set of mechanical characterization experiments. Xiang *et al*. [4] presented a thermal-mechanical sequential coupling analysis of a newly cast concrete wall in the construction of a subway station structure and provided suggestions for prediction and control of early age concrete cracking. De Schutter [5] performed a finite element simulation on temperature fields and the resulting stresses at any time during hardening of a non-reinforced massive concrete wall. However, some complexities still exist particularly in the current reinforced concrete structure embedded with corrugated pipes.
In this research, a FE approach was proposed with User Subroutine UMATHT, USDFLD and UEXPAN on the basis of complete time-dependant material experiments, namely hydration heat test, standard thermal tests of thermal conductivity, thermal expansion and specific heat, and standard mechanical tests for *E*-modulus, compressive strength and shrinkage. Moreover, an experimental wall of 3.6m×0.8m×3.6m in dimension was constructed to investigate temperature distribution and strain development and validate the accuracy of the proposed FE method.

2. Material and method

Adiabatic temperature rise experiment and standard thermal and mechanical tests at totally thirteen sets of casting ages (namely 1day(d), 2d, 3d, 5d, 7d, 10d, 14d, 20d, 28d, 45d, 60d, 90d and 120d) were carried out with the designed concrete mix proportion (as listed in Tab.1). The adiabatic temperature rise experiment was performed using a concrete adiabatic temperature measuring instrument with an accuracy of 0.02ºC. A hydration model based on hydration degree $\alpha(t_e)$ (see Eq.1) was utilized in this study. The cumulative heat of hydration $Q_c(t_e)$ with $\alpha(t_e)$ was expressed as Eq.2 based on the improved exponential function formula proposed by Zhu B.F.[6]. Equivalent time t_e (in day) was expressed according to Arrhenius equation as Eq.3. The hydration degree-dependant equation was then written in the subroutine UMATHT to define heat generation of the concrete.

$$\alpha(t_e) = (1 - e^{-0.75{t_e}^{0.87}}) \quad (1)$$

$$Q_c(t_e) = 1.72 \times 10^5 \times \alpha(t_e) \quad (2)$$

$$t_e = \int_0^t \exp\left[\frac{E_A}{R}\left(\frac{1}{T_r} - \frac{1}{T}\right)\right] dt \quad (3)$$

Table 1: Mix proportion of concrete (mass in kg/m^3).

Water	Cement	Slag powder	Fine aggregate	Coarse aggregate	Super-plasticiser	W/B
140	310	142	759	1006	9.04	0.31

As for thermal tests, thermal conductivity λ and specific heat c were obtained according to Code GB/T 10294-2008 and SL 352-2006, respectively, and the results of λ and c are shown in Fig.1. In general, the values of c remained within empirical value range, while the values of λ were slightly smaller, considering the component of slag in the concrete proportion and relative humidity conditions of the test samples. Since the values of λ and c both varied relatively greatly during the first 7days, they were directly written into Subroutine UMATHT.

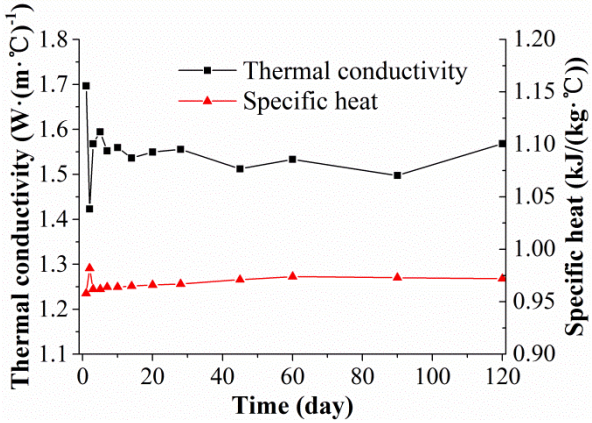

Figure 1: Test results of λ and c.

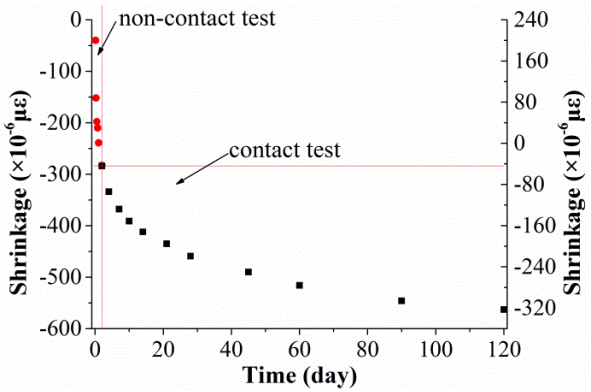

Figure 2: Measured shrinkage.

Besides, mechanical characterization of compressive strength f_c, tensile splitting strength f_{ts} and elastic modulus E_c were also conducted and the results are fitted to Eq.4, Eq.5 and Eq.6,

$$f_c(t_e) = 64.3 \times (1 - (1 - \alpha(t_e))^{0.47}) \text{ MPa} \quad (4)$$

$$f_{ts}(t_e) = 0.075 \times f_c(t_e) \text{ MPa} \quad (5)$$

$$E_c(t_e) = 39.5 \times (1 - e^{-0.9 \times \ln^{0.64}(1-\alpha(t_e))}) \text{GPa} \quad (6)$$

Moreover, free shrinkage tests were carried out with non-contact method at 20°C and RH=68% for the first two days and with contact method from the third day till the 120d after demoulding according to GB/T 50082-2009. The results of the tested shrinkage were depicted in Fig.2. The results of non-contact test were mainly autogenous shrinkage for high performance concrete, while those of contact test were mainly drying shringkage [7]. The contact shrinkage results were in accordance with the values calculated with CEB/FIP 2010 Model, while the non-contact shrinkage results was much larger, which may be accounted for slag replacement and low water to binder ratio(w/b) of the concrete. Based on the tests illustrated above, subroutine USDFLD and UEXPAN was developed to describe the hydration degree-dependent mechanical and shrinkage properties.

3. Case study

3.1 General description

In order to validate the effectiveness of the proposed FE approach, four experimental walls of 3.6m×0.8m×3.6m in dimension was constructed, the original design of which derived from a practical project to be constructed in China. A reinforced concrete base of 10.8m×7m×1m and

columns of 1.5m×1.2m×4m were previously constructed to provide fixed boundaries to the wall. Six PT100 temperature sensors and four vibration wire(VW) sensors were appropriately fixed onto rebars and embedded in each concrete wall to obtain the temperature and strain variations at the specified test points, as shown in Fig.3(a). Meanwhile, a FE model was established to perform a thermo-mechanical coupling analysis, as shown in Fig.3(b). The convection coefficients for wall surfaces was estimated to be 6.8 W/(m^2·K) and 23W/(m^2·K) before and after formwork removal (at 5th day after casting), respectively, abiding by the third type of boundary condition. Ambient temperature was taken from in situ record.

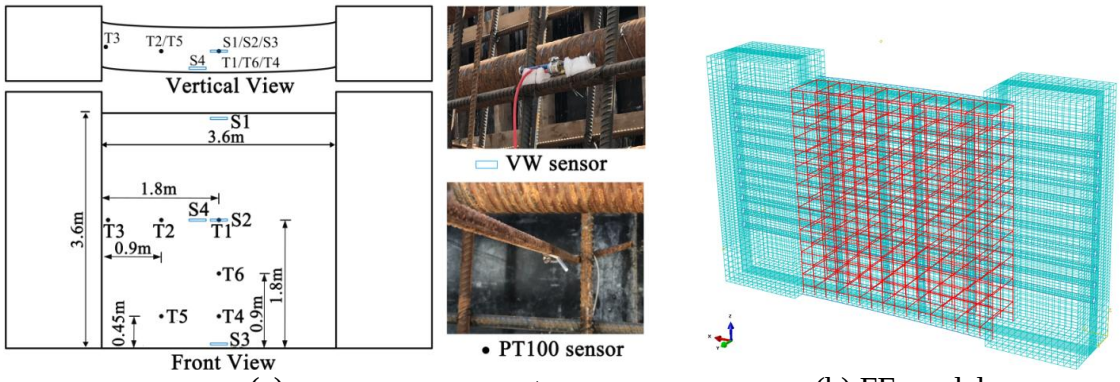

(a) sensor arrangement (b) FE model

Figure 3 : Sensor arrangement and FE model.

3.2 Temperature comparison

The first 14 days of temperature data are shown in Fig.4. It is noticed that the highest temperature reached a maximum of 52.3℃ at the central point (Point T1) after 36 hours of pouring. The maximum temperature difference between the core and ambient environment was 41.5℃, with a maximum cooling rate of 9.0℃ per day. Compared with the calculated results, the average temperature difference at the temperature peak of all the 6 test points was only 3.6%, among which the minimum deviation occured in the central part of the wall (Point T1 and T6) and the maximum deivation (1.2℃) occured in the boundary part adjacent to the column (Point T3). It may be accounted for the heat conduction between the wall and column.

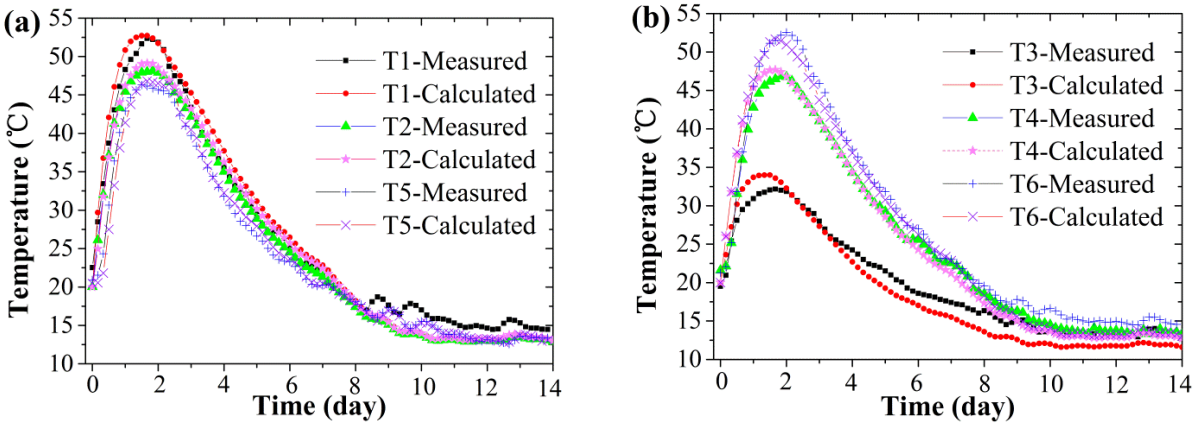

Figure 4: Temperature comparison between calculated and tested data.

3.3 Strain comparison

Internal strain variations of concrete were monitored and compared with the results obtained from thermo-mechanical coupling analysis, as shown in Fig.5. It is observed that the core concrete firstly experienced a sharp rise of tensile strain due to hydration heat and thermal expansion. With concrete hardening and temperature decline, tensile strain instantly decreased and turned to compressive strain, reaching a maximum of -369με after 800hours. Besides, both the tensile and the compressive strain were larger on the upper surface than those on the lower surface, owing to the stronger constraint at the bottom. Compared with the test strain results, the computed curves reflected the overall trend of strain development with a maximum difference of 9.5% despite some local deviations.

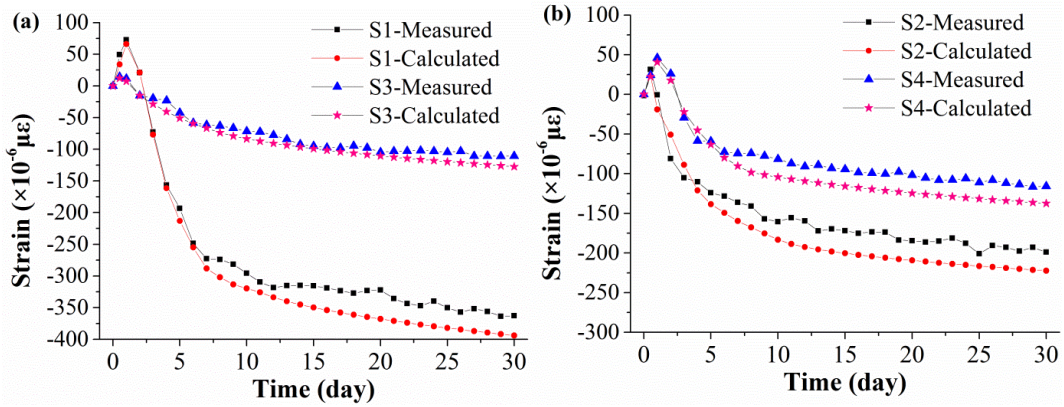

Figure 5: Strain developments at specified points.

3.4 Cracking risk

The first principle thermal stress σ_1 was obtained from coupled simulation considering variation of E_c with time and compared with tensile stength, as is shown in Fig.6. It is noticed that the stress was compressive during the first 5 days till tensile stress occurred then and remained stable after the 8th day. The ratio of σ_1 to f_{ts} was 0.637 at the 8th day, indicating that the cracking risk is relatively high according to the cracking criterion proposed by Sule [8]. In fact, one surface crack did occur at the 7th day after concrete pouring, which belonged to the type of base-restrained crack, as is shown in Fig.7. Therefore, it implies that the proposed FE subroutine can effectively predict the occurrence of surface cracking.

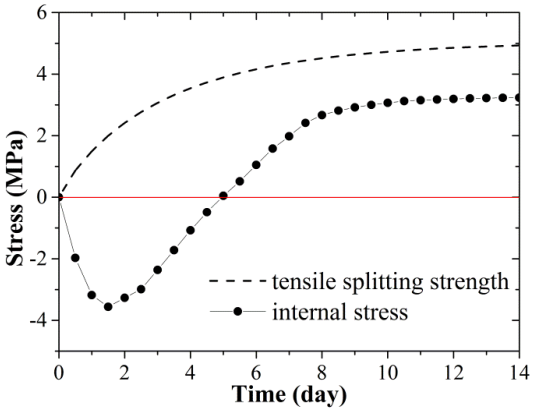

Figure 6: First principle stress of internal concrete.

Figure 7: Surface cracking.

4. Conclusion

An experimented-based FE method was proposed for early-age thermo-mechnical analysis with redevelopment of user subroutine UMATHT, USDFLD and UEXPAN, based on complete thermal and mechnical characterization of concrete. Moreover, an experimental wall was constructed to validate the effectiveness of the proposed FE approach. According to the comparison results, the calculated results in temperature and strain field both agreed well with test data, indicating the effectiveness of the proposed FE approach. Moreover, the occurrence of surface cracking can be effectively predicted with the proposed method by considering the cracking risk index. It can provide a sufficient way to perform more parametric analysis of the experiment wall under difficient ambient conditions and air cooling through corrugated pipes, as well as to predict temperatrue and strain development of similar massive reinforced concrete structures.

References

[1] Geng, Y. et al, Early-age thermal analysis and strain monitoring of massive concrete structures, Comp Concr 21(3) (2018), 279-289
[2] Knoppik, A. et al, Cracking risk and regulations, in: Eduardo M R Fairbairn, Miguel Azenha (Eds), Thermal cracking of massive concrete structure, Springer International Publishing, Cham, Switzerland (2019), 257-304
[3] Zreiki, J. et al, Early-age behaviour of concrete in massive structures, experimentation and modelling, Nucl Eng Des 240 (2010), 2643-2654
[4] Xiang, Y.Y. et al, Thermal–mechanical analysis of a newly cast concrete wall of a subway structure, Tunn Undergr Space Technol 20 (2005), 442-451
[5] De Schutter, G., Vuylsteke, M., Minimisation of early age thermal cracking in a J-shaped non-reinforced massive concrete quay wall, Eng Struct 26 (2004), 801-808
[6] Zhu B.F., Thermal Stresses and Temperature Control of Mass Concrete. Butterworth-Heinemann: Waltham (2014)
[7] Wu L.M. et al, Autogenous shrinkage of high performance concrete: A review, Constr Build Mater 149 (2017), 62-75
[8] Sule M. S., Effect of reinforcement on early-age cracking in high strength concrete, Ph.D. Thesis, Delft University of Technology (2003)

SynerCrete'18 International Conference on Interdisciplinary Approaches
for Cement-based Materials and Structural Concrete
24-26 October 2018, Funchal, Madeira Island, Portugal

ASSESSING THE CO_2-BINDING OF CONCRETE DURING ITS SERVICE LIFE

Andreas Leemann [(1)], Fritz Hunkeler [(2)], Heiner Widmer [(3)]

(1) Empa, Dübendorf, Switzerland
(2) TFB AG, Wildegg, Switzerland
(3) cemsuisse, Bern, Switzerland

Abstract
In order to assess the impact of cement production on the atmospheric CO_2 concentration and with it on the global warming, not only the CO_2 emissions but also the CO_2 capture by carbonation of cementitious products during their service life needs to be considered. The key parameter for a reasonably accurate estimation is the carbonation coefficient that allows to calculate the temporal evolution of carbonation depth and the CO_2 adsorption by the cement hydrates. Current approaches use a strength-based concept linking carbonation coefficient and compressive strength. This approach has proven to be valid for Portland cement-based concrete, but appears to be questionable in the case of concrete produced with blended cements, which are prevalent nowadays. Based on recent scientific findings showing an excellent correlation between the CO_2 binding capacity of concrete and the carbonation coefficient, an alternative approach is proposed.

1. Introduction

The increasing CO_2 concentration in the atmosphere is regarded as a governing factor for the observed global temperature increase. The important contribution of cement production to anthropogenic CO_2 emission with 5-6 % is indisputable [1]. However, due to carbonation of cement hydrates, part of the emitted CO_2 is recaptured. Calcium-silicate-hydrate (C-S-H) is decalcified, leading to the formation of a phase with a lower Ca/Si-ratio and $CaCO_3$ and portlandite is transformed into $CaCO_3$. [2]. Only if CO_2 binding by carbonation of cementitious products during their service life is considered as well, the environmental impact of cement can thoroughly be assessed.

Carbonation starts at the surface of mortar or concrete components. The carbonation depth as a function of the square root of time is described by the carbonation coefficient K_N. It depends on various parameters like water-to-cement-ratio (w/c) of the mortar or concrete and relative humidity (RH) [3]. Therefore, an assessment of the carbonation coefficient K_N is mandatory to calculate CO_2 uptake by cementitious materials during their service life. This has been the subject of several studies, in which the carbonation coefficient K_N was assessed based on concrete strength [4-7]. In addition to CO_2 adsorption during its service life, a substantial amount of CO_2 is bound during the recycling phase of concrete [4-7]. This aspect is not considered in this study, as it solely focuses on service life.
A major drawback of the majority of studies dealing with CO_2 adsorption of cementitious materials is that the assessment of the carbonation coefficient K_N is based on concrete strength or that attempts are made to link the obtained experimental values only with strength-based concepts. Currently, CEN TC 229 WG 5 is following this path. However, mortar and concrete produced with blended cements do not show the same relation between carbonation coefficient K_N and compressive strength as mortar and concrete produced with Portland cement [8-10]. The share of blended cement used worldwide is steadily increasing in an attempt to decrease CO_2 emissions. Therefore, alternative approaches to assess the carbonation coefficient of mortar and concrete should be considered. In this paper, the CO_2 binding capacity of mortar and concrete as a tool to assess carbonation coefficient K_N of mortar and concrete is explored.

2. CO_2 binding capacity of mortar and concrete

The scientific background of the presented approach was published in Leemann et al. [9] and Leemann and Moro [10]. In these studies mortar and concrete mixtures containing various mineral additions were exposed both to accelerated and natural carbonation in sheltered and unsheltered conditions. They showed that it is possible to assess carbonation coefficient K_N based on the water-to-CaO-ratio (*w/CaO*) in concrete (Fig. 1). Hereby, only CaO present in clinker and reactive mineral additions like fly ash or slag but not in unreactive ones like limestone powder are taken into account. The *w/CaO* can easily be calculated, if the cement composition is known. It expresses the CO_2 binding capacity per volume of cement paste and, as it is a mass ratio between water and solid, it additionally contains information about porosity and microstructure. It shows a considerably better correlation with the carbonation coefficient K_N determined in sheltered (R^2 = 0.90) and unsheltered (R^2 = 0.83) outdoor exposure (Fig. 1) than the compressive strength. Based on these findings, the following empirical equations can be approximated for sheltered and unsheltered exposure [21]:

$$K_{N,S} = C \cdot (8.3 \cdot w/CaO - 4.7) \qquad C = 1.00 \qquad (1)$$

$$K_{N,US} = C \cdot (8.3 \cdot w/CaO - 4.7) \qquad C = 0.47 \qquad (2)$$

Of course, these equations are representative for the environmental conditions at the specific exposure site. In this case, yearly averages of temperature, RH and precipitation were 11.4 °C, 78 % and 1200 l/m^2, respectively. The slope of the linear regression is mainly dependent on the moisture state of the concrete. The value of C can be adapted to different humidity conditions dependent on the exposure site. Assessing carbonation coefficient K_N and

carbonation depth d_c based on the *w/CaO* is advantageous compared to a strength-based concept, because it is chemistry-based and as such takes into account cement composition and with it the cement-specific carbonation resistance.

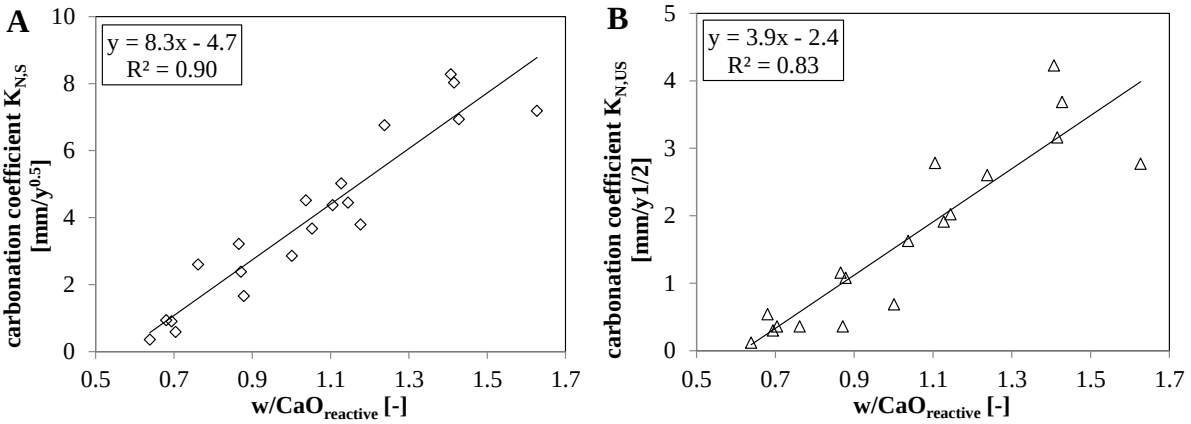

Figure 1: Carbonation coefficient $K_{N,S}$ in sheltered (A) and carbonation coefficient $K_{N,US}$ in unsheltered (B) outdoor exposure as a function of the $w/CaO_{reactive}$ according to [10].

3. Calculation of CO_2-binding

As calculation examples, Swiss cements as described in Environmental Product Declarations (EPD) [11] are used, representing the average composition of the specific cement types (CEM I, CEM II/A, CEM II/B, CH-total). The key figures for the model calculation assumed typical Swiss concrete compositions used for house building. This type of concrete represents about 35 % of the concrete produced in Switzerland. For other types of concrete used for different types of structures, the input parameters like cement type and w/c leading to different values of *w/CaO* can easily be adapted using software as basic as an excel spreadsheet. The following comments provide additional information on some of the parameters used in the exemplified calculation shown in Table 1:

- The empirical value for the degree of carbonation a_c corresponds to the relative amount of carbonated CaO in concrete under natural conditions (1= CaO fully carbonated, 0= no CaO carbonated). It has been reported to be about 0.50 in [12].
- The content of the reactive CaO in Swiss cements has been determined in [9]. Only the CaO reacting during cement hydration is taken into account. Limestone powder for example is not included.
- Carbonation coefficients in sheltered ($K_{N,S}$) and unsheltered ($K_{N,US}$) conditions have been calculated according to Eq. 1 and Eq. 2, respectively. In the exemplified calculation, the ratio of sheltered to unsheltered surfaces has been assumed to be 1. This ratio has to be adapted for individual cases. The sum of sheltered and unsheltered carbonation depth is finally represented by $d_{c,tot}$.
- A service life of 100 years is used for this calculation corresponding to EN 16757 [13].
- The implications of carbonation on reinforcement corrosion are not elaborated in this publication, as it is focusing on CO_2-binding. Possible implications between carbonation and corrosion have to be considered in the structural design.

- The thickness of the concrete element is assumed to be 200 mm. This value refers to 1 m^3 of concrete, allowing to derive the surface area exposed to carbonation.
- The ratio of CO_2-uptake to emission of concrete (U/E_{conc}) is calculated using the carbonation depth $d_{c,tot}$, the degree of carbonation a_c and the thickness of the concrete x.
- The CO_2 emission resulting from calcination (kg CO_2/kg cement) was published in the EPD for Swiss cements (www.cemsuisse.ch) following SN EN 15804+A1 [14].
- The final CO_2 uptake by concrete is calculated in kg CO_2/t of concrete.

Table 1: Exemplified calculation of CO_2-binding in concrete used for housing during its service life applied for Swiss cements (average composition corresponding to [11]).

parameter	abbr.	units	**CEM I**	**CEM II/A**	**CEM II/B**	**CH-total**	**source / calculation**
degree of carbonation (abs)	a_c	%	0.50	0.50	0.50	0.50	Thiery et al., 2013
water-cement ratio	w/c	-	0.60	0.60	0.60	0.60	typical Swiss value
cement content	c	kg/m^3	280	280	280	280	typical Swiss value
water content	w	kg/m^3	168	168	168	168	typical Swiss value
CaO content of cement	$CaO_{reactive}$	mass-%	0.61	0.53	0.44	0.53	Leemann et al., 2015
CaO content of concrete	$CaO_{reactive}$	kg/m^3	171	147	123	149	$CaO_{reactiv} \cdot c$
water/CaO-ratio	$w/CaO_{reactive}$	-	0.98	1.14	1.36	1.13	$w/CaO_{reactive}$
carbonation coefficient shelterd	$K_{N,S}$	mm/$y^{0.5}$	3.46	4.77	6.63	4.66	Eq. 1
carbonation coefficient unshelterd	$K_{N,US}$	mm/$y^{0.5}$	1.63	2.24	3.12	2.19	Eq. 2
reference service life	RSL	y	100	100	100	100	see EN 16757 [25]
carbonation depth sheltered at end of service life	$d_{c,S}$	mm	34.6	47.7	66.3	46.6	$K_{N,S} \cdot y^{0.5}$
carbonation depth unsheltered at end of service life	$d_{c,US}$	mm	16.3	22.4	31.2	21.9	$K_{N,US} \cdot y^{0.5}$
sum of carbonation depth	$d_{c,tot}$	mm	50.9	70.1	97.4	68.5	$d_{c,S} + d_{c,US}$
thickness of concrete element	x	mm	200	200	200	200	related to 1 m^3 of concrete
CO_2 emission from calcination of cement	E_{cem}	kg CO_2/kg of cement	0.474	0.413	0.357	0.422	EPD cemsuisse, 2015
ratio of CO_2 uptake-to-emission of concrete	$\boldsymbol{U/E_{conc}}$	-	**0.127**	**0.175**	**0.244**	**0.171**	$\boldsymbol{d_{c,tot} \cdot a_c / x}$ **(Eq. 3)**
density of concrete	ϱ_{conc}	t/m^3	2.4	2.4	2.4	2.4	
CO_2-uptake per volume of concrete	U	kg/m^3	16.9	20.3	24.3	20.2	$c \cdot E_{cem} \cdot (U/E_{conc})$
CO_2-uptake per mass of concrete	$\boldsymbol{U}$	**kg CO_2/t of concrete**	**7.0**	**8.4**	**10.1**	**8.4**	U/ϱ_{conc}

As shown in Table 1, the ratio of CO_2 uptake to CO_2 emission (U/E_{conc}) per volume of concrete can be calculated according to Eq. 3:

$$U/E_{conc} = (CO_2 \text{ uptake})/(CO_2 \text{ emission}) = (d_{C,tot} \cdot a_c)/x \quad (3)$$

The ratio U/E_{conc} increases with decreasing thickness of the concrete element as its surface-to-volume-ratio increases (Fig. 2). The higher $d_{c,tot}$ and a_c are, the higher is the ratio U/E_{conc}. The ratio U/E_{conc} was calculated for the three different cement types and the average of cement

types used in Switzerland as presented in Table 1 using Eq. 3. Concrete mix design (cement type, cement content, w/c) and dimensions of the concrete elements can easily be adapted in the model calculation. Fig. 2 shows how the ratio U/E_{conc} changes as a function of the thickness of a given concrete element.

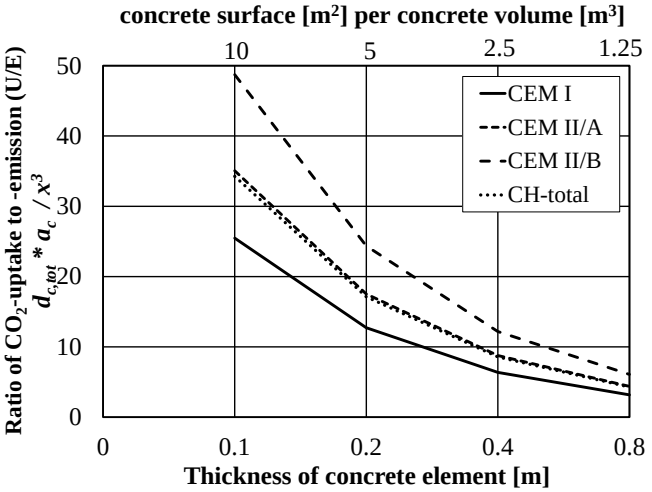

Fig. 2: Ratio of CO_2 uptake to CO_2 emission of concrete (U/E_{conc}) as a function of thickness of concrete element.

4. Limitations of assessing CO_2-binding

Any calculation of CO_2-binding has its limitations, as simplifications have to be made in order to achieve a manageable degree of complexity. This applies on the approach presented in this paper, as it does for strength-based concepts as well. One key question is the role of RH. Progress of carbonation shows a non-linear response to changes in RH [3,10]. Moreover, both porosity and RH change with concrete depth [15,16]. This point has to be studied further, because the carbonation depth as calculated in this study may be overestimated and therefore, an adaptation of the carbonation coefficients $K_{N,US}$ and $K_{N,S}$ used to calculate long-term CO_2-binding may be required.

5. Summary

CO_2-binding of concrete during its service life is an important point to be taken into account, when the impact of cement production on atmospheric CO_2 concentration and global warming is considered. It can be calculated by assessing the carbonation coefficient K_N and the carbonation depth d_c. This paper presents an approach based on the *w/CaO* of concrete, as this parameter governs the carbonation coefficient K_N. Examples for the implementation of this approach are given using boundary conditions of cement and concrete as used for housing in Switzerland. The two key parameters for the *w/CaO* are cement composition and w/c. They can easily be adapted for specific concrete compositions, climatic conditions and service life.
The presented approach seems to be especially advantageous when the increasing use of blended cements is considered. In this scenario, the strength-based concept has clear limitations. Therefore, it is proposed that the presented approach is used instead of or in addition to existing strength-based concepts. This approach was not incorporated into EN

16757 [25], but it is currently under consideration to be included into the Technical Report "Carbonation" by CEN TC 104 SC1 TG20.
As shown in this paper, the amount of CO_2 bound by concrete during its service life is substantial compared to the emission of geogenic CO_2 during cement production. A comprehensible assessment of recaptured CO_2 is paramount for a realistic life cycle assessment.

References

[1] Le Quéré, C., Andrew, R. M., Canadell, J. G., Sitch, S., … and Keeling, R. F., Global carbon budget 2016. Earth System Science Data, 8(2) (2016), 605-649
[2] Groves, G.W., Brough, A., … and Dobson, C.M., Progressive changes in the structure of hardened C_3S cement pastes due to carbonation, J Am Ceram Soc 74 (1991), 2891-2896
[3] Wierig, H.J., Longtime studies on the carbonation of concrete under normal outdoor exposure. In: Proceedings of the RILEM Seminar on the Durability of Concrete Structures under Normal Outdoor Exposure (1984), 239-249
[4] Lagerblad, B., Carbon dioxide uptake during concrete life cycle–state of the art. Swedish Cement and Concrete Research Institute CBI, Stockholm (2005)
[5] Pade, C. and Guimaraes, M., The CO_2 uptake of concrete in a 100 year perspective, Cem Conc Res 37(9) (2007), 1348-1356
[6] Nygaard, P. and Leemann A., Kohlendioxidaufnahme von Stahlbeton durch Karbonatisierung, Cemsuisse Projekt 201106, Bern (in German) (2012)
[7] Andersson, R., Fridh, K., Stripple, H. and Häglund, M., Calculating CO_2 uptake for existing concrete structures during and after service life, Envir Sc Tech, 47(20) (2013), 11625-11633
[8] Papadakis, V. G., Effect of supplementary cementing materials on concrete resistance against carbonation and chloride ingress, Cem Conc Res 30(2) (2000), 291-299
[9] Leemann, A., Nygaard, P., Kaufmann, J. and Loser, R., Relation between carbonation resistance, mix design and exposure of mortar and concrete, Cem Conc Comp 62 (2015), 33-43
[10] Leemann, A., Moro, F., Carbonation of concrete: the role of CO_2 concentration, relative humidity and CO_2 buffer capacity, Mat Struct 50 (2017), 30.
[11] cemsuisse, EPD for four types of Swiss cements. http://www.cemsuisse.ch/cemsuisse/ueberuns/publikationen/epd/index.html?lang=de (2016)
[12] Thiery, M., Dangla, P., Belin, P., Habert, G., Roussel, N., Carbonation kinetics of a bed of recycled concrete aggregates: A laboratory study on model materials, Cem Conc Res 46 (2013), 50-65
[13] EN 16757, Sustainability of construction works - Environmental product declarations - Product Category Rules for concrete and concrete elements (2017)
[14] EN 15804+A1, Sustainability of construction works - Environmental product declarations - Core rules for the product category of construction products, 2013.
[15] Parrott, L.J., Influence of cement type and curing on the drying and air permeability of cover concrete, Mag Concr Res 47 (1995), 103-111
[16] Parrot L.J., Factors influencing relative humidity in concrete, Mag Concr Res 43 (1991), 45-52

SynerCrete'18 International Conference on Interdisciplinary Approaches
for Cement-based Materials and Structural Concrete
24-26 October 2018, Funchal, Madeira Island, Portugal

CREEP PROPERTIES OF POLYMER PARTICLES IN POLYMER-MODIFIED CEMENT PASTES, QUANTIFIED BY MEANS OF MULTISCALE MODELING

Luise Göbel [1,2], Markus Königsberger [2,3], Andrea Osburg [1], Bernhard Pichler [2]

(1) Bauhaus-Universität Weimar, F.A. Finger-Institute for Building Material Engineering, Germany
(2) TU Wien – Vienna University of Technology, Institute for Mechanics of Materials and Structures, Austria
(3) Université libre de Bruxelles (ULB), BATir Department, Belgium

Abstract
Polymer-modified mortars and concretes are more creep active than conventional cement-based materials. The present contribution studies the effects of the polymer particles at microscopic observation scales and quantifies their viscoelastic properties during cement hydration. To this end, two different polymer-modified cement pastes were characterized in the context of a comprehensive early-age creep testing campaign. Experimental results are exploited by means of multiscale modeling, carried out using methods of continuum micromechanics. Scale-transition relations are used for downscaling macroscopic experimental results, referring to the material scale of cement pastes, to the microscopic creep behavior of the cementitious hydrates and the polymer particles. In order to study the creep-magnifying effect of the polymers, three different modeling approaches are investigated. The microscopic polymer particles are considered as (i) pores, exhibiting vanishing elastic stiffness, (ii) an elastic phase without creep activity, or (iii) a viscoelastic material phase. The modeled creep curves obtained from the latter approach agree well with the experimental results. This corroborates that polymers act as viscoelastic phases in the cement microstructure and, thus, magnify the macroscopic creep behavior of polymer-modified cement-based materials.

1. Introduction

Polymer-modified mortars and concretes (PCC) have been successfully used for repair and overlays [1,2]. The materials are used to extend the service life of structures and bridge decks

by providing increased adhesion strength, improved chemical resistance, and reduced permeability. However, the polymer modification entails a lowered elastic stiffness of the mortars and concretes, accompanied by a larger creep activity [3,4]. The present contribution investigates whether or not the more pronounced creep behavior of PCC can be explained by considering that both the cementitious hydration products *and* the polymers contribute to the creep strains. Thereby, three different modeling approaches are used: (i) polymers are considered as pores, without viscoelastic stiffness; (ii) polymers are considered as an elastic material phase, without creep activity; (iii) polymers are considered as a viscoelastic material phase, whereby an isochoric power-law creep function is considered and the creep parameters are obtained from downscaling the aforementioned macroscopic creep tests.
The homogenized (upscaled) creep behavior is compared with experimental results from an early-age creep testing campaign on two different polymer-modified cement pastes [3]. As for the required scale transitions (creep up- and downscaling), we rely on a recently proposed continuum micromechanics model for polymer-modified cement-based materials [3–5]. This provides the relation between the micromechanical properties of the polymer particles and the hydration products, on the one hand, and the macroscopic creep strains of polymer-modified cement pastes subjected to short-term compressive loads, on the other hand.
The paper is structured as follows. In Section 2, the continuum micromechanics model for homogenization of the viscoelastic properties of polymer-modified cement pastes is presented. Then, the predictive capability of the multiscale model is assessed by comparing the modeling results to the measured creep strains (Section 3). This comparison allows for conclusions on the role of the polymers in hydrating cement pastes (Section 4).

2. Modeling of the non-aging creep properties of polymer-modified cement pastes

2.1 Micromechanical representation and viscoelastic phase behavior

The hierarchically organized microstructure of polymer-modified cement pastes can be represented by two scale-separated representative volume elements (RVEs) [3–5]. The RVE of cement paste is envisaged as a matrix-inclusion type composite of a polycrystalline hydrate foam matrix [6,7], spherical clinker inclusions, and entrapped air voids. The latter result from polymer-cement interactions during the mixing of the raw materials [8]. The hydrate foam is resolved at the scale of a few microns and consists of spherical polymer particles, capillary pores, and isotropically oriented needle-shaped hydrates [6,7], see Fig. 1.
During the hydration process, the phase volume fractions can be described by means of the Powers hydration model [9], as functions of the hydration degree and the initial water-to-cement mass ratio. This was extended to include the volume fractions of the polymers and the entrapped air porosity at the scales of the hydrate foam and the cement paste, respectively [3].
As for the mechanical phase properties, the bulk and shear moduli of the purely elastic clinker phase amount to 116.7 GPa and 53.8 GPa. The water- and air-filled pores exhibit vanishing elastic stiffness. Ultrasonic tests on solid polymer specimens provided access to their elastic bulk and shear modulus as 4.0 GPa and 0.9 GPa [3], their creep behavior is identified from macroscopic experiments in Section 3. The hydrate creep function $\boldsymbol{J}_{hyd}$ is isochoric [10]:

$$\boldsymbol{J}_{hyd}(t-\tau) = \frac{1}{3k_{hyd}}\boldsymbol{I}^{vol} + \frac{1}{2}\left[\frac{1}{\mu_{hyd}} + \frac{1}{\mu_{c,hyd}}\left(\frac{t-\tau}{t_{ref}}\right)^{\beta_{hyd}}\right]\boldsymbol{I}^{dev} \tag{1}$$

$\boldsymbol{I}^{vol}$ and $\boldsymbol{I}^{dev}$ are the volumetric and deviatoric parts of the symmetric fourth-order identity tensor $\boldsymbol{I}$. t and τ, respectively, are the chronological time and the time instant of loading. t_{ref} = 86400 s is a fixed reference time. In Eq. (1), $k_{hyd} = 18.7$ GPa and $\mu_{hyd} = 11.8$ GPa [7], and $\mu_{c,hyd}$ and β_{hyd} denote the shear creep modulus and the power-law creep exponent of the hydrates. Based on 500 early-age short-term creep tests, they were identified as [10] $\mu_{c,hyd} = 20.93$ GPa and $\beta_{hyd} = 0.251$.

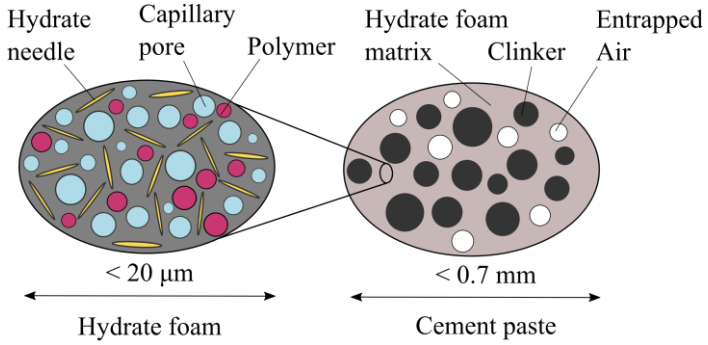

Figure 1: Two-scale representation of polymer-modified cement pastes: material organogram according to [4]. The 2D sketches illustrate qualitative properties of 3D RVEs.

2.2 Homogenization of the viscoelastic behavior of polymer-modified cement pastes

Homogenization of the viscoelastic properties is carried out based on the correspondence principle [11]. Accordingly, the elastic and viscoelastic behavior of the material phases is transformed from the time domain to the Laplace-Carson (LC) domain. There, upscaling of the creep behavior of the microscopic phases, via the scale of the hydrate foam, up to the cement paste scale can be performed as quasi-elastic homogenization. As for the polycrystalline RVE of hydrate foam, the self-consistent scheme is employed [12]. As for the matrix-inclusion RVE of cement paste, homogenization is performed by means of the Mori-Tanaka scheme. Computational details about the upscaling procedure and the analytical formulae for the LC-transformed creep properties of the cement pastes are given in [4,10]. The obtained creep tensor function of cement paste in the LC domain is numerically back-transformed to the time domain, applying the Gaver-Wynn-Rho algorithm [13].

3. Top-down identification of the viscoelastic polymer behavior

In the following, it is investigated whether or not the polymer phase contributes to the viscoelastic behavior of polymer-modified cement pastes. To this end, the mechanical properties of the polymers are introduced according to the three different approaches described in Section 1. The performance of the model is checked by comparing the modeled creep strains to experiments which are described next.

3.1 Early-age creep testing of polymer-modified cement pastes

Hourly repeated ultra-short creep tests were performed to characterize the creep behavior of one ordinary Portland cement paste and two different polymer-modified pastes, see [3] for details. Polymer-modified paste P1 was mixed with a polymer dispersion containing styrene

acrylate copolymers. Paste P2, in turn, contained a dispersion with styrene butadiene copolymers. The initial water-to-cement mass ratio for all pastes amounted to 0.40 and the initial polymer-to-cement mass ratio to 0.10.
A series of 168 uniaxial compressive creep tests was performed on every specimen during ongoing hydration of the pastes, whereby each individual test lasted for three minutes. The material ages ranged from 21 hours up to eight days. The load levels were restricted to 7.5 % of the estimated uniaxial compressive strength at the time instant of loading, in order to avoid damage of the specimens and to get access to the linear creep behavior.
It was observed that the neat reference paste exhibits a creep activity which is approximately three times smaller than that of the polymer-modified specimens. Paste P2 shows a smaller elastic stiffness and a slightly more pronounced creep activity than paste P1. This is particularly related to the entrapped air porosity of paste P2, amounting to 4.8 %. Paste P1, in turn, does not contain entrapped air porosity [3].

3.2 Modeling results and comparison with experimental data

The goodness-of-fit between modeled and experimentally determined viscous part of the uniaxial creep functions $J_{v,cp}$ is assessed via the mean error, which is defined as $\epsilon = \frac{1}{n_\zeta n_t} \sum_{i=1}^{n_\zeta} \sum_{j=1}^{n_t} \left| J_{v,cp}^{mod}(t_j) - J_{v,cp}^{exp}(t_j) \right|$. The sum over n_ζ refers to the 168 varying material ages of the cement pastes, n_t refers to a temporal resolution of the individual three-minutes-long creep tests in 180 steps. For details concerning the determination of $J_{v,cp}^{mod}$ and $J_{v,cp}^{exp}$, see [4,10]. Scenario 1 envisages that the polymers act as pores, without any stiffness. The resulting model underestimates the experimentally observed creep strains, see Fig. 2 (a) and (d). The mean errors amount to 3.59×10^{-6}/MPa for paste P1 and to 1.53×10^{-6}/MPa for paste P2. Scenario 2 envisages that the polymers act as elastic phases with (non-zero) experimentally determined stiffness properties given in [3]. The resulting model underestimates the experimental creep strains considerably, see Fig. 2 (b) and (e). The mean errors amount to 5.78×10^{-6}/MPa for paste P1 and to 4.74×10^{-6}/MPa for paste P2.
Scenario 3 envisages that the polymers act as a viscoelastic phase. An isochoric creep tensor function is used to model the polymers. As for quantification of the related creep properties, a top-down identification process is carried out, starting with results from ultra-short creep tests on polymer-modified cement pastes, see [4] for all details. It was found that the creep activity of the polymer particles decreases significantly as a function of the material age of the cement pastes. The shear creep modulus increases rapidly within the first 40 h. It is almost constant between 40 h and 110 h and amounts to 80 MPa for paste P1 and to 110 MPa for paste P2. Afterwards, it increases rapidly again up to values of 600 MPa and 400 MPa, respectively. The related creep strain evolutions, obtained from the multiscale model, re-produce the experimental observation very reliably, see Fig. 2 (c) and (f). The residual mean errors are as small as 1.98×10^{-7}/MPa for paste P1 and 2.23×10^{-7}/MPa for paste P2.

3.3 Discussion of the results shown in Fig. 2

The micromechanical origin of the macrostrain differences between the three modeled scenarios is discussed next. Notably, the strains depicted in Fig. 2 are the time-dependent viscous macrostrains, obtained from subtracting the instantaneous elastic macrostrains from the total macrostrains. When considering the polymers as pores, the hydrates are the only solid constituent of the hydrate foam, see Fig. 1. Thus, they take over significant stresses upon

macroscopic loading. Their viscous behavior results in a stress-transfer to the cement grains, but this is not very effective, because the hydrates and the cement grains refer to *different* scales of observation (Fig. 1). When considering the polymers as a purely elastic solid phase, they do also take over stresses upon macroscopic loading. Thus, the hydrates experience smaller stresses as in the previously discussed scenario. In addition, the viscous behavior of the hydrates results in a stress-transfer both to the polymer particles and the cement grains. The stress transfer to the polymers is quite effective, because the hydrates and the polymers refer to the *same* scale of observation. Thus, modeling polymers as elastic solid phases results in smaller stress levels in the hydrates and, thus, in smaller viscous macrostrains compared to the case where polymers are considered as pores. When considering the polymers as a viscoelastic solid phase, the initial microstress distribution is the same as in the previously discussed scenario. Given that both the hydrates and the polymers are viscous, the stress transfer from the hydrates to the polymers and vice versa is not very effective. Also, the stress transfer to the cement grains is not very effective, see above. Thus, the largest macroscopic creep activity is obtained, provided that polymers are modeled as a viscoelastic solid phase. Finally, it is worth mentioning that modeling the polymers as pores results in a significantly larger spontaneous elastic deformation of cement paste compared to the alternative of modeling polymers as solids, but this is not shown in Fig. 2, see above.

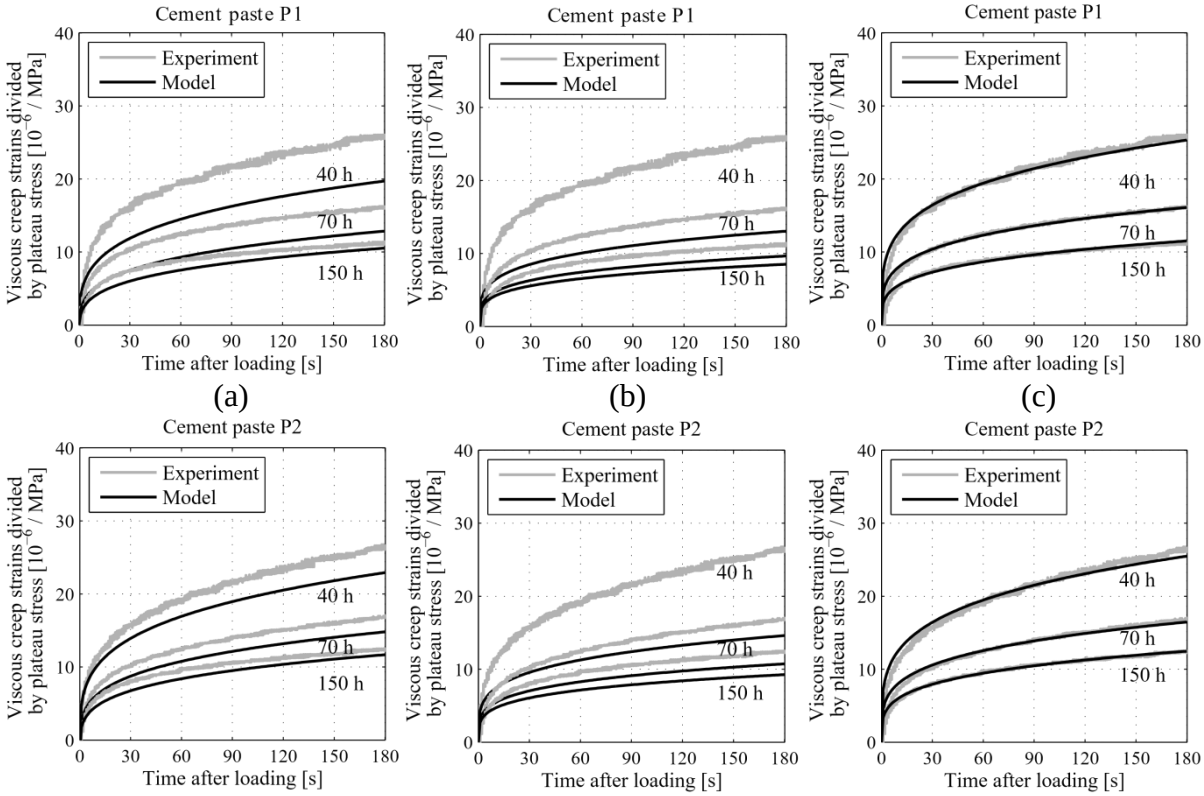

Figure 2: Measured vs. modeled evolutions of viscous strains: (a) and (d) refer to polymers acting as pores; (b) and (e) refer to polymers acting as elastic phases; (c) and (f) refer to polymers acting as viscoelastic phases; see also the discussion in Section 3.3.

5. Conclusions

The present contribution studied the viscoelastic characteristics of polymer particles at microscopic scales. Based on an early-age creep testing campaign and multiscale modeling, the following conclusions can be drawn:

- Considering polymer particles as elastic phases without creep activity considerably underestimates the creep activity of polymer-modified cement pastes.
- The situation can be significantly improved provided that modeling accounts for the viscoelastic behavior of the polymer particles. Their creep properties were identified by means of a top-down identification approach, based on results of an early-age creep testing campaign on polymer-modified cement pastes.

References

[1] R. Wang, Z. Yang (Eds.), Progress in Polymers in Concrete, Trans Tech Publications, Zürich, 2013.
[2] Y. Ohama, D. van Gemert, M. Ota, Introducing process technology and applications of polymer-modified mortar and concrete in construction, International Journal for Restoration of Buildings and Monuments 19 (2013) 369–392.
[3] L. Göbel, B. Pichler, A. Osburg, The mechanical performance of polymer-modified cement pastes at early ages: ultra-short non-aging creep tests and multiscale homogenization, Construction and Building Materials 173 (2018) 495–507.
[4] L. Göbel, M. Königsberger, A. Osburg, B. Pichler, Viscoelastic Behavior of Polymer-modified Cement Pastes: Insight From Downscaling Short-term Macroscopic Creep Tests by Means of Multiscale Modeling, Applied Sciences 8 (2018) 487.
[5] L. Göbel, C. Bos, R. Schwaiger, A. Flohr, A. Osburg, Micromechanics-based prediction of the elastic properties of polymer-modified cementitious materials using nanoindentation and semi-analytical modeling, Cement and Concrete Composites 88 (2018) 100–114.
[6] B. Pichler, C. Hellmich, J. Eberhardsteiner, Spherical and acicular representation of hydrates in a micromechanical model for cement paste: prediction of early-age elasticity and strength, Acta Mech 203 (2009) 137–162.
[7] B. Pichler, C. Hellmich, Upscaling quasi-brittle strength of cement paste and mortar: A multi-scale engineering mechanics model, Cement and Concrete Research 41 (2011) 467–476.
[8] D.A. Silva, John, V.M., Ribeiro, J.L.D., H.R. Roman, Pore size distribution of hydrated cement pastes modified with polymers, Cement and Concrete Research 31 (2001) 1177–1184.
[9] T.C. Powers, T.L. Brownyard, Studies of the Physical Properties of Hardened Portland Cement Paste, Research Laboratories of the Portland Cement Association Bulletin 43 (1948) 101–132.
[10] M. Königsberger, M. Irfan-ul-Hassan, B. Pichler, C. Hellmich, Downscaling Based Identification of Nonaging Power-Law Creep of Cement Hydrates, Journal of Engineering Mechanics 142 (2016) 4016106.
[11] N. Laws, R. McLaughlin, Self-Consistent Estimates for the Viscoelastic Creep Compliances of Composite Materials, Proceedings of the Royal Society of London A: Mathematical, Physical and Engineering Sciences 359 (1978) 251–273.
[12] A.V. Hershey, The elasticity of an isotropic aggregate of anisotropic cubic crystals, Journal of Applied Mechanics 21 (1954) 236.
[13] J. Abate, P.P. Valkó, Multi-precision Laplace transform inversion, International Journal for Numerical Methods in Engineering 60 (2004) 979–993.

SynerCrete'18 International Conference on Interdisciplinary Approaches
for Cement-based Materials and Structural Concrete
24-26 October 2018, Funchal, Madeira Island, Portugal

DEVELOPMENT OF PORE-SCALE MODEL FOR INGRESS OF CO_2 BRINE THROUGH CEMENT PASTE

Ravi A. Patel [(1)], Nikolaos I. Prasianakis [(1)]

(1) Laboratory for waste management (LES), Paul Scherrer institute, Villigen CH 5232, Switzerland

Abstract

Carbonation of cementitious materials is of relevance for a wide range of practical applications. It leads to dissolution of calcium bearing phases in cementitious materials and subsequent precipitation of calcite. This process alters the properties of the material itself. The progression of carbonation and its effect on the microstructure of cementitious materials depends on a variety of parameters. Therefore, a pore-scale modelling approach capable of capturing changes in microstructure under external boundary conditions, can be a useful tool in developing mechanistic understanding. With this aim, a pore-scale modelling approach is presented for carbonation under saturated conditions, and is applied to a stylized pore structure consisting solely of portlandite and open pores. Evolution of this pore structure under different boundary conditions is investigated. Preliminary simulations illustrate that the model is able to capture qualitatively the main trends that are reported in the literature. These simulations also effectively demonstrate that a very small volume fraction of precipitating mineral can have a large effect on transport pathways, inhibiting or slowing down the dissolution.

1. Introduction

Carbonation of cementitious materials refers to the interaction of cement with CO_2. CO_2 as a gas, dissolves in the pore water of cement paste forming carbonic acid (H_2CO_3) which further reacts with calcium bearing cement paste chemical phases leading to calcite precipitation. Carbonation is of practical relevance in the context of several practical applications such as service life predictions of reinforced concrete structures, improving recycled aggregates quality, capturing CO_2 in cementitious materials, self-healing of concrete structures through carbonation, long-term integrity of geological nuclear waste disposal system, etc [1].

Therefore, it is important to understand the underlying mechanisms and to be able to model changes in cement paste micro structure due to carbonation. This eventually allows to also predict the progression of carbonation.
Carbonation models developed at continuum scale, require as input a wide range of parameters. The evolution of these parameters due to microstructural changes during carbonation are difficult if not impossible to measure directly [2]. Therefore, such models can only provide qualitative understanding, and can be hardly used for predictive purposes. Similarly, most of the service life models for carbonation, are based on the square root time approach and are highly empirical [3,4]. A "bottom up" approach in which the pore-scale model which simulates changes in the pore-space due to carbonation can be used for upscaling can prove to be a valuable tool. With this aim, a pore-scale model is developed to simulate changes in a saturated cement paste micro-structure due to ingress of CO_2 brine. While, in reality natural carbonation occurs under unsaturated conditions, this model setup is relevant within the context of clay rock-concrete interfaces which is of significant for deep geological disposal of nuclear waste [5,6] and well-bore cement interaction with CO_2 brine in context of CO_2 sequestration [7]. Further details on modelling approach for carbonation is given in section 2. In section 3 we discuss the simulation results for different boundary composition of CO_2 brine ingression through a stylized portlandite pore-structure. Finally, conclusions are presented in section 4.

2. Pore-scale modelling approach

A lattice Boltzmann method (LBM) based pore scale reactive transport modelling tool, *Yantra*, is used for the modelling and simulations [8,9]. It also has a special implementation for multilevel porous systems where continuum media and pores co-exist. Such treatment is essential for cementitious systems which has wide range of pore size distribution. In *Yantra*, the LBM solver for simulating mass transport, has been coupled with the geochemical solver *IPhreeqC*, to account for complex reaction networks using appropriate thermodynamic databases [10]. Its reactive transport solver can track microstructure evolution which occurs due to dissolution, and precipitation process. For further details on algorithms implemented in readers are referred to [8]. Previously, the application of this scheme has been successfully demonstrated to simulate calcium leaching through cementitious systems [11,12].

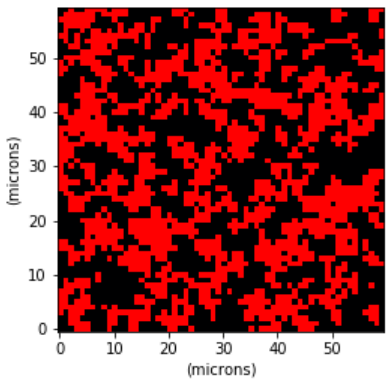

Figure 1: Stylized porous media used for simulation. Portlandite is represented in red and pores in black.

In this preliminary study, a simplified porous system consisting of portlandite and pores, is considered as shown in Figure 1. The volume fraction of portlandite is 45% and correspondingly, the initial porosity of the domain is 0.55. The simulation domain consists of 60 µm × 60 µm with 1 µm discretization. The diffusion coefficient of all primary species is taken as 2.2×10^{-9} m^2/s corresponding to diffusion of calcium ions [11]. Simulations are carried out using different boundary solutions at left hand boundary as summarized in Table 1, and all other boundaries are set as zero flux boundary. Case 1 refers to the system subject to left-boundary concentration of primary carbon species (C) 0.01 M and primary sodium species (Na) 0.082 M with pH maintained at 7. For Case 2, the concentration is reduced to 0.001 M and pH is maintained at 7 by reducing Na concentration to 0.00081 M. For Case 3, Na is not added to system with C concentration 0.01 M, which correspond to a pH= 4.192. Finally, for Case 4, instead of Na, the primary calcium species (Ca) concentration is equal to 0.00414 and is added in order to keep the pH of the solution at the boundary equal to 7. For all the cases, the boundary solution is undersaturated with respect to portlandite which leads to its dissolution. Moreover, for Cases 1-3, the boundary solution is undersaturated with respect to calcite which might lead to dissolution of precipitated calcite whereas for Case 4 boundary solution is oversaturated with respect to calcite. These different cases have been inspired from the experimental observations reported by Schwotzer et al. [13]. They reported that in case calcium is supplied from pore-water for calcite precipitation it triggers chemical degradation of solid phases in cement paste. However, if calcium is supplied from external boundary a dense protective layer of calcite can build up. The developed simulation example aims to reproduce this observation. The dissolution of portlandite and precipitation of calcite is modelled under the assumption of thermodynamic equilibrium. For simplification, it is assumed that calcite only nucleates heterogeneously on the surface of portlandite phase. The results of the simulations are discussed in next section.

Table 1: Boundary solution composition used for different cases in simulation.

	Ca [M]	Na [M]	C[M]	pH
Case 1	-	0.00821	0.01	7
Case 2	-	0.00081	0.001	7
Case 3	-	-	0.01	4.192
Case 4	0.00414	-	0.01	7

3. Results

Figure 2 shows the evolution of microstructure at different times for the four cases described in previous section. For Case 1 and Case 3 the calcite precipitation front is dynamic, with its location varying with time. This is due to fact that boundary solution is unsaturated with respect to calcite. However, for Case 2 precipitation of calcite only occurs near the boundary during the time span of simulation, and the calcite front does not penetrate into the portlandite structure. For Case 4 calcite is precipitating in a fast pace, initially clogging the surface, while only slight dissolution of portlandite is observed near the surface. Evolution of average volume fractions of portlandite and calcite with respect to time are plotted in Figure 3. It shows that for case 3, the portlandite dissolution is fastest, followed by case 2 and case 1. For case 4 after initial clogging at the boundary portlandite dissolution is stopped. In case 3, a

continuous dissolution and reprecipitation occurs whereas in case 1 the precipitation of calcite slows down dissolution of portlandite and further dissolution of calcite reinitiates dissolution of portlandite. As a result, dissolution of portlandite for case 3 is much slower.

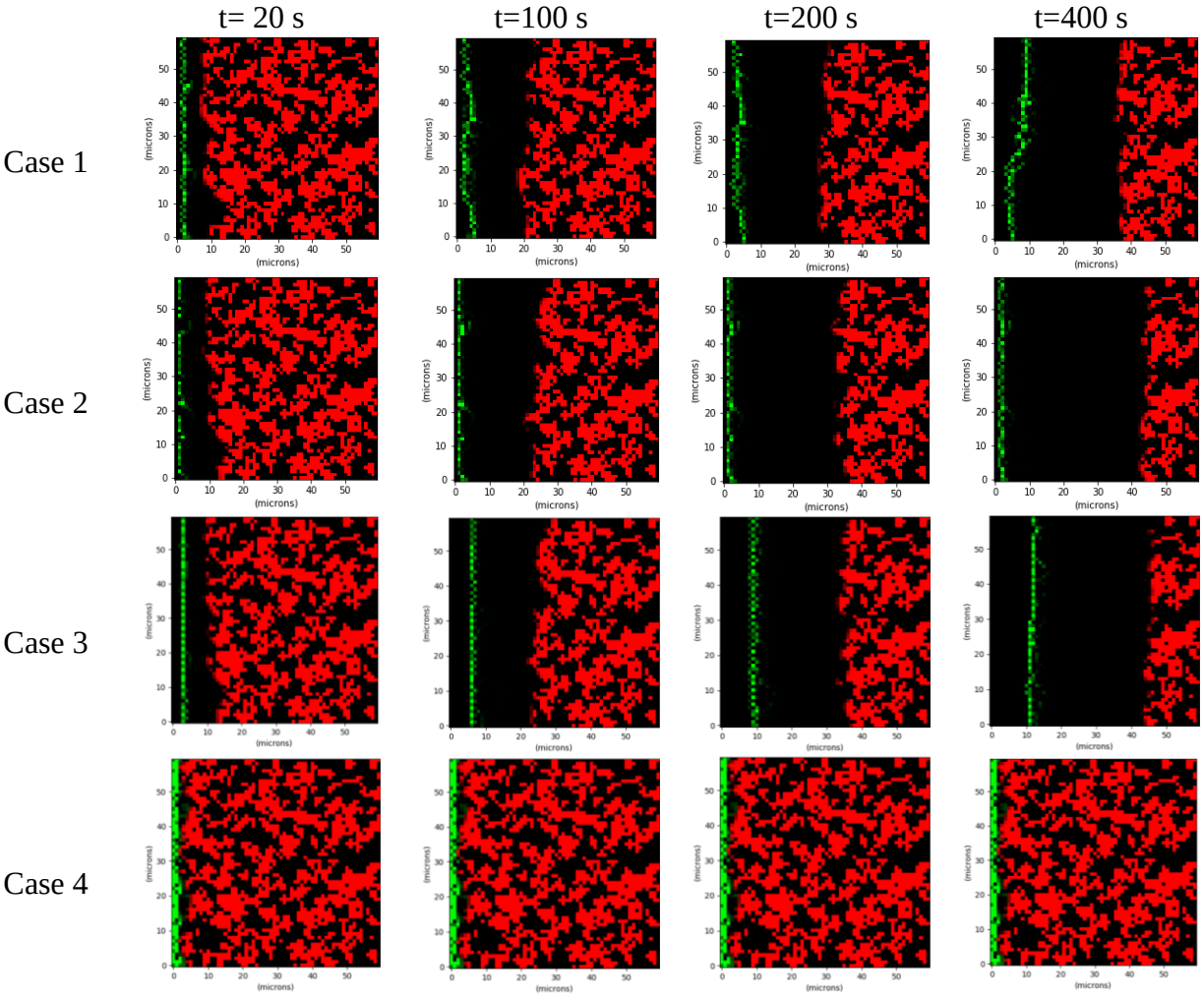

Figure 2: Evolution of pore-structure at different timesteps. Calcite, portlandite and pores are represented in green, red and black respectively (for colour figure refer to the online version). Shading of colour is proportional to the volume fraction of the phase.

In case 2, due to low carbon species concentration at the boundary, the precipitation of calcite is slower and initially less compared to case 3 and case 1. These simulations reveal the rich physics and complexity of the effect of chemical concentrations on the pore structure evolution. The simulations are able to capture the essence of the observations reported by Schwozter et al [13] and as summarized in previous section. It should be noted the total volume of solid phases in the domain is less than one and the volume fraction of precipitating mineral ranges from 1 to 3% at the end of simulation. It demonstrates that the process of clogging (case 4) can occur much earlier, compared to the standard assumption of continuum scale models, which stipulates that clogging occurs when the control volume is filled

completely with solid. Similarly, a small volume of precipitating mineral can have a large effect on dissolution process. Therefore, it is important to understand how the precipitating mineral affects transport pathways at lower scales, which can be readily captured by pore-scale modelling. This example highlights the importance of pore-scale modelling in context of carbonation of cementitious materials.

4. Conclusions

A pore-scale reactive transport model has been developed, to simulate carbonation under saturated conditions in a cementitious system. Preliminary simulations on stylized pore-structure, illustrate the distinct evolution paths due to carbonation, which strongly depend on the solution concentrations. The simulation reveals the complexity as well as the effect of different boundary conditions, and their influence on pore structure evolution. The simulations are able to qualitatively capture the observations reported in literature. We also stress and demonstrate that even a small volume fraction of precipitating mineral can affect transport pathways inhibiting or slow down the dissolution pores, highlighting the need for pore-scale modelling. In the future, simulations considering realistic cement pore-structure and more detailed precipitation mechanisms [14] are planned, which will provide new insights into the process of carbonation.

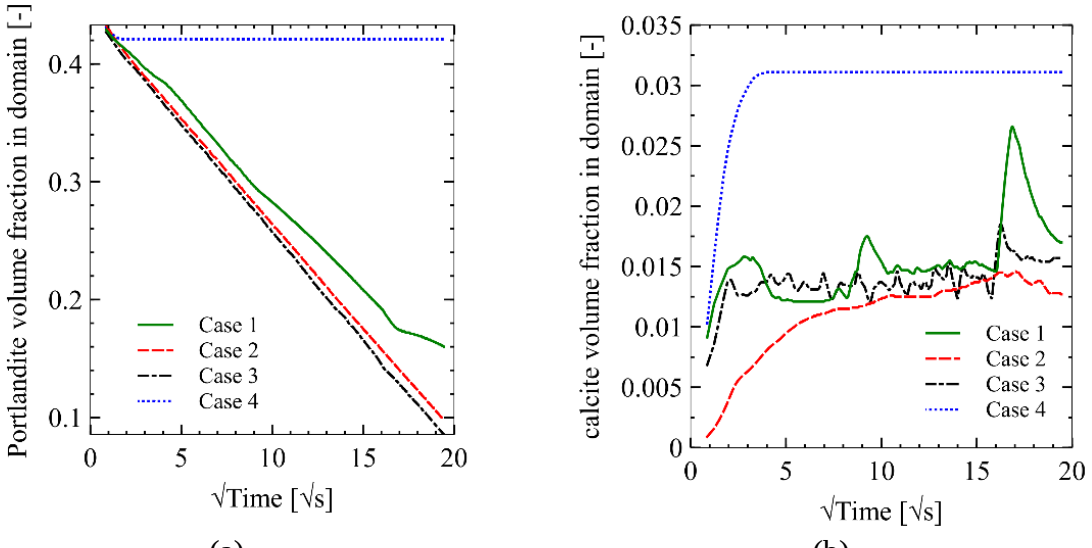

(a) (b)

Figure 3: Time evolution of (a) portlandite and (b) calcite volume fraction (averaged over simulation domain).

Acknowledgements
This project has received funding from the European union's Horizon 2020 research and innovation programme under the Marie Sklodowska-Curie grant agreement No 701647.

References

[1] B. Šavija, M. Luković, Carbonation of cement paste: Understanding, challenges, and opportunities, Constr. Build. Mater. 117 (2016) 285–301.
[2] Q.T. Phung, N. Maes, D. Jacques, G. De Schutter, G. Ye, J. Perko, Modelling the carbonation of cement pastes under a CO2 pressure gradient considering both diffusive and convective transport, Constr. Build. Mater. 114 (2016) 333–351.
[3] S.O. Ekolu, Model for practical prediction of natural carbonation in reinforced concrete: Part 1-formulation, Cem. Concr. Compos. 86 (2018) 40–56.
[4] V.-L. Ta, S. Bonnet, T. Senga Kiesse, A. Ventura, A new meta-model to calculate carbonation front depth within concrete structures, Constr. Build. Mater. 129 (2016) 172–181.
[5] E.C. Gaucher, P. Blanc, Cement/clay interactions – A review: Experiments, natural analogues, and modeling, Waste Manag. 26 (2006) 776–788.
[6] U. Mäder, A. Jenni, C. Lerouge, S. Gaboreau, S. Miyoshi, Y. Kimura, V. Cloet, M. Fukaya, F. Claret, T. Otake, M. Shibata, B. Lothenbach, 5-year chemico-physical evolution of concrete–claystone interfaces, Mont Terri rock laboratory (Switzerland), Swiss J. Geosci. 110 (2017) 307–327.
[7] B.G. Kutchko, B.R. Strazisar, D.A. Dzombak, G. V. Lowry, N. Thauiow, Degradation of well cement by CO2 under geologic sequestration conditions, Environ. Sci. Technol. 41 (2007) 4787–4792.
[8] R. Patel, Lattice Boltzmann Method Based Framework for Simulating Physico-Chemical Processes in Heterogeneous Porous Media and Its Application to Cement Paste, Ghent university, 2016.
[9] R.A. Patel, https://bitbucket.org/yantralbm/yantra, (2016).
[10] R.A. Patel, J. Perko, D. Jacques, G. De Schutter, K. Van Breugel, G. Ye, A versatile pore-scale multicomponent reactive transport approach based on lattice Boltzmann method: Application to portlandite dissolution, Phys. Chem. Earth. 70–71 (2014) 127–137.
[11] R.A. Patel, J. Perko, D. Jacques, G. De Schutter, G. Ye, K. Van Breugel, A three-dimensional lattice Boltzmann method based reactive transport model to simulate changes in cement paste microstructure due to calcium leaching, Constr. Build. Mater. 166 (2018).
[12] S.C. Seetharam, R.A. Patel, J. Perko, D. Jacques, Quantification of leaching kinetics in OPC mortars via a mesoscale model, Constr. Build. Mater. 180 (2018) 614–628.
[13] M. Schwotzer, T. Scherer, A. Gerdes, Protective or damage promoting effect of calcium carbonate layers on the surface of cement based materials in aqueous environments, Cem. Concr. Res. 40 (2010) 1410–1418.
[14] N.I. Prasianakis, E. Curti, G. Kosakowski, J. Poonoosamy, S. V. Churakov, Deciphering pore-level precipitation mechanisms, Sci. Rep. 7 (2017) 13765.

SynerCrete'18 International Conference on Interdisciplinary Approaches
for Cement-based Materials and Structural Concrete
24-26 October 2018, Funchal, Madeira Island, Portugal

EARLY AGE MECHANICAL PROPERTIES AND SHRINKAGE OF BLENDED CEMENT CONCRETE CONTAINING SLAG

Tahsin Alper Yikici[(1)], Egemen Kesler [(2)], Yilmaz Akkaya [(2)]

(1) MEF University, Istanbul, Turkey
(2) Istanbul Technical University, Istanbul, Turkey

Abstract

Slag cement concrete is usually preferred for the design of mass concrete structures exposed to the marine environment, due to chloride binding capacity and low heat of hydration properties. However, the early age property development of slag cement concrete is comparatively slower than Portland cement concrete (PCC). Therefore, longer curing might be essential to prevent early age cracks. In general, early age cracking potential of concrete mixtures depend on the stresses induced by shrinkage strains caused by hydration of cement, drying, and thermal contraction. Depending on the development of rigidity and modulus of elasticity of the concrete, such strains cause stresses that result in cracking when they exceed the tensile strength capacity of concrete. Thus, early-age shrinkage, mechanical strength and elasticity modulus development of slag cement concrete are essential parameters in early age cracking risk calculations. This study investigates the adiabatic heat development of slag cement concrete and its relation to the development of compressive strength, tensile strength, modulus of elasticity, and early-age shrinkage. Concrete mixtures containing 380-440 kg/m3 CEMIIIB 32.5N were cast with water to cement ratio of 0.32-0.40. Additionally, the effect of aggregate size and aggregate type was investigated by using limestone aggregates, and sandstone. The microstructure of the cement paste, investigated by thin sections, provided valuable information to distinguish the relationship between adiabatic heat, early-age shrinkage, and mechanical properties. The distance between particles and differences in particle size distribution of binders and aggregates were essential parameters in understanding the differences in performance of the concrete mixtures.

1. Introduction

Blast-furnace slag (BFS) is being used as a cement substitute to produce high performance concrete for structural applications such as anchorage blocks and caissons of bridges due to

slower rate of heat generation and chloride ingress. Additionally, when used in higher levels (>70%) it provides more economic and environmental friendly solution compared with PCC [1]. However, BFS concrete with low water to cement ratio (<0.40) and relatively fine pore structure exhibits larger early-age shrinkage. If not properly accounted for, such rapid deformations may cause cracking under restrained conditions since concrete has very low strain capacity thereby very sensitive to internal stresses at early ages [2,3,4,5].
In this study early-age shrinkage behavior of high early strength BFS concrete was investigated in accordance with development of degree of hydration. Early-age shrinkage was measured as the length change occurring from the time of concrete solidification to the age of 28 days. Degree of hydration of the concrete mixtures was calculated from the heat development obtained experimentally from semi-adiabatic calorimeter tests [6,7]. Moreover, development of compressive strength, tensile strength and modulus of elasticity of concrete specimens was determined. The relationship between early-age shrinkage, mechanical properties and degree of hydration was presented by means of mix design parameters.

2. Experimental Study

For this study eight different concrete mixtures were investigated with different types of cement and cementitious materials, and equivalent water to cement ratios ranging from 0.32 to 0.40. Compressive strength class and the workability class of all mixtures were C50/70 and S5, respectively. Each concrete mixture design was specifically developed to satisfy structural service life requirement of minimum 100 years, by using CEM III B cement or combining CEM I cement with Class F fly ash, (FA) micro silica (MS) and BFS as mineral admixtures. Natural sand and crushed sand were used as fine aggregates, and two crushed aggregates with nominal maximum sizes of 12.5 mm (No1) and 22 mm (No2) were used as coarse aggregates. Concrete mixture design proportions are given in Table 1.

Table 1: Concrete Mix Designs per m^3.

Mix design	**Mix 1***	**Mix 2***	**Mix 3***	**Mix 4***	**Mix 5$^+$**	**Mix 6$^+$**	**Mix 7***	**Mix 8***
w/c	0.37	0.37	0.40	0.37	0.37	0.37	0.38	0.32
$D_{max,}$ mm	22.0	12.5	12.5	22.0	22.0	22.0	22.0	22.0
CEM IIIB, kg	390	380	380	390	390	390		
CEM I, kg	-	-	-	-	-	-	285	146
GGBS, kg	-	-	-	-	-	-	-	294
Class F FA, kg	-	-	-	-	-	-	50	-
MS, kg	-	-	-	-	-	-	12	-
Water, kg	144	141	152	144	144	144	123	141
Natural Sand, kg	508	486	479	458	540	540	386	470
Crushed Sand, kg	414	398	392	434	415	415	456	373
No1, kg	472	910	897	493	440	450	498	542
No2, kg	401	-	-	423	380	385	479	469

*Limestone aggregate +Sandstone aggregate

Ready-mix concrete was delivered to the laboratory from the plant. Fresh concrete properties including slump, flow diameter and air content were tested and results are given in Table 2. Specimens were prepared for compressive strength, tensile strength, modulus of elasticity,

shrinkage and microstructural evaluations. The evaluation of the early-age shrinkage and mechanical properties will be discussed by means of degree of hydration. Moreover, semi-adiabatic calorimetry tests were conducted in accordance with NT BUILT 388 [7].

Table 2: Fresh concrete properties.

Mix design	Slump [cm]	Flow [cm]	Air Content [%]	Unit Weight [kg/m^3]	Ambient Temp [°C]	Concrete Temp [°C]
Mix1	20	50	6.5	2350	16.7	21.2
Mix2	24	-	3.0	2450	21.0	25.0
Mix3	20	47	4.7	2450	14.5	19.7
Mix4	19	48	4.0	2400	19.2	25.1
Mix5	18	50	5.4	2350	19.0	24.8
Mix6	18	41	4.6	2400	9.7	16.5
Mix7	21	-	-	2450	20.4	22.2
Mix8	23	50	1.3	2500	13.2	11.0

2.1 Semi-Adiabatic Calorimetry

The concrete for semi-adiabatic calorimetry was mixed in the laboratory and samples were immediately placed in heat insulated drums. The temperature increase in the sample was measured during hydration. The total heat produced from the hydration and the rate of heat of hydration of the concrete mixtures were calculated based on the heat capacity and activation energy of the sample in addition to the heat losses through the insulated drum [7]. The results of semi-adiabatic calorimeter test are given in Figure 1.

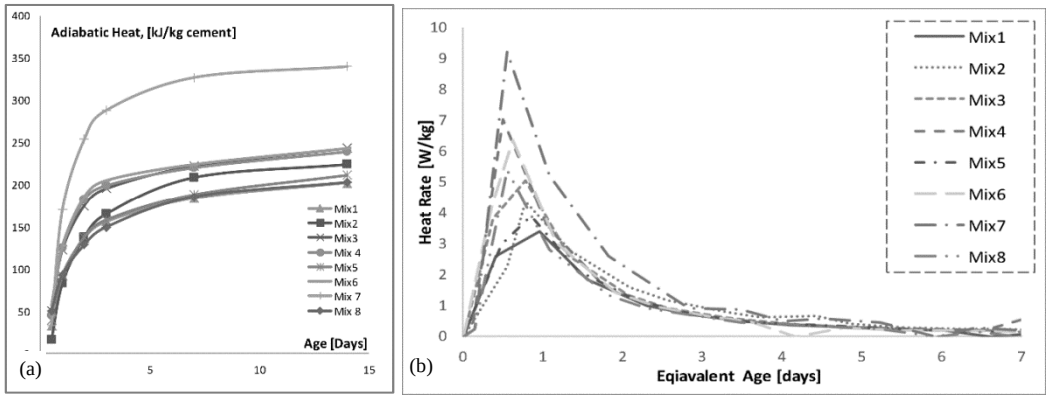

Figure 1: Semi-adiabatic test results (a) Total heat generated (b) Rate of heat generation.

3. Results and Discussion

Early-age shrinkage and mechanical properties of the hardening concrete was evaluated as a function of degree of hydration (α). Consequently, degree of hydration $\alpha(t)$ was calculated as the ratio of the heat generated by the mixture $Q(t)$ to the total heat available in the mixture referred to as Q_{ult} [6].

$$\alpha(t) = \frac{Q(t)}{Q_{ult}} \quad (1)$$

3.1 Evaluation of Mechanical Properties

Compressive strength, tensile strength and modulus of elasticity of the samples were determined testing three 150 by 300 mm cylinder specimens at 12 hours, 1, 2, 3, 7, 14 and 28 days of age. Average test results are presented in Figure 3a, 3b and 3c, respectively. The mechanical properties increase as a function of hydration degree.

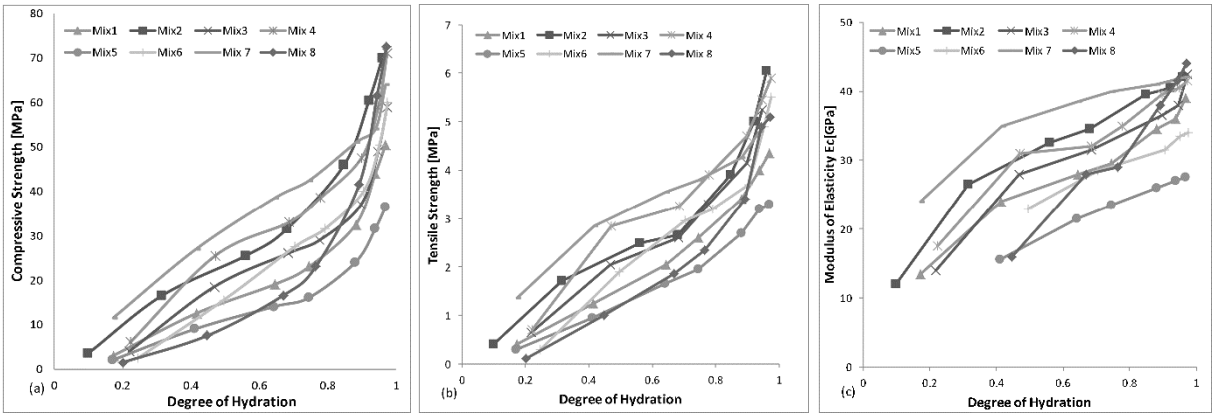

Figure 2: Evolution of (a) compressive strength (b) tensile strength (c) modulus of elasticity.

It can be observed from Figure 2, the relative rate of development of compressive and tensile strength is much lower compared to the relative rate of development of modulus of elasticity. Similar behavior of low water to cement ratio and high early age strength concrete was demonstrated in earlier studies as well [8].

Table 3: Development of mechanical properties, %

Mix#	$\sigma_{c,2d/28d}$	$\sigma_{t,2d/28d}$	$E_{2d/28d}$
Mix1	38	47	72
Mix2	36	41	77
Mix4	44	50	74
Mix5	36	45	73
Mix6	46	54	84
Mix7	60	74	92
Mix8	23	36	64

In general mixtures containing CEMIIIB cement show slower mechanical property development compared to CEMI cement mixtures. Especially, development of modulus of elasticity of Mix5 and Mix6 is much slower. This can be related to the use of sand stone aggregates instead of limestone (Figure 2c). Furthermore, the effect of maximum nominal size of aggregates is observed between Mix1 and Mix2. Eventually, use of smaller size of aggregates resulted in higher mechanical properties. Table 3 represents the percentage of the achieved mechanical properties of the concrete mixtures at two days. According to the results, Mix7 containing large amount of CEMI cement with fly ash and micro silica gains its mechanical properties much faster than the mixtures containing GGBS.

3.2 Evaluation of Early-Age Shrinkage

Early age shrinkage deformations are determined using two 130 by 700 mm cylinder specimens as a function of the age of the concrete starting after final set for a period of 28 days [9]. Specimens are kept in a temperature controlled environment under sealed conditions. Figure 3 shows shrinkage strains up to 28 days.

The shrinkage strain ε_s is determined as the measured concrete strain in the specimen corrected for contributions from the temperature deformations of the concrete:

$$\varepsilon_s = \varepsilon_{m,s} + \alpha_c(T_c - T_{c0}) \quad (2)$$

where $\varepsilon_{m,s}$ is the concrete strain, α_c is the thermal expansion coefficient, T_c and T_{c0} are two consecutive temperature readings from the specimens.

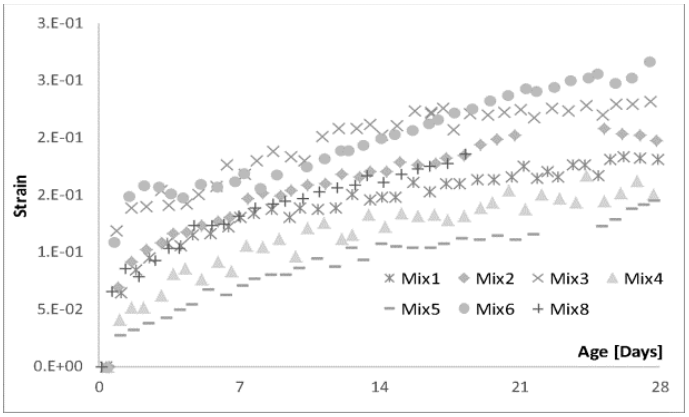

Figure 3: Early-age shrinkage deformations.

Mix2 and Mix3 has relatively higher early-age shrinkage deformation which can be related to the smaller maximum nominal size of aggregate. Although Mix4, 5 and 6 have similar concrete compositions, Mix6 shows the largest shrinkage strain development (Figure 3). In order to investigate this behavior microstructural analysis on thin sections were performed.

3.3. Evaluation of Microstructure

Concrete microstructure, was investigated via fluorescent optical microscopy. Thin sections of approximately 30 microns thickness were produced according to DS.423.4 [10] and images were taken by a UV-light polarization microscope where aggregate particles appear in dark, voids and cracks appear in light color, and cement paste can be observed in between, depending on the volume of capillary porosity. The smaller white spots which can be recognized on the images are the GBFS particles. Thin section images of Mix1, Mix4, Mix5 and Mix6 are presented in Figure 4a, 4b,4c and 4d, respectively.

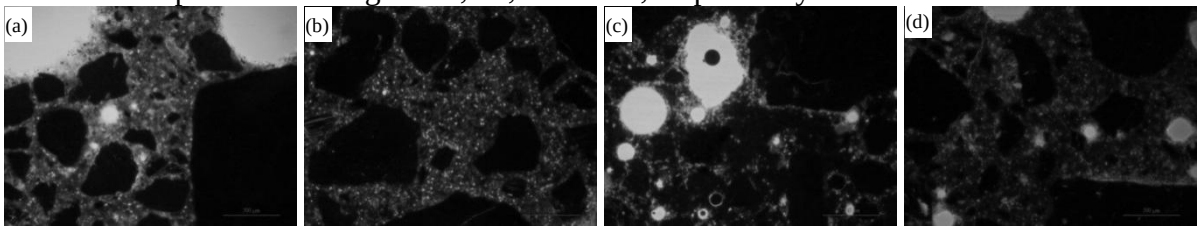

Figure 4: Microstructure of concrete samples (a) Mix1 (b) Mix4 (c) Mix5 (d) Mix6

4. Summary and Conclusion

Adiabatic heat development of slag cement concrete and its relation to development of compressive strength, tensile strength, modulus of elasticity, and early-age shrinkage. Concrete mixtures with CEMIIIB 32,5N were cast with water to cement ratios of 0,32 to 0,40. The maximum size of the aggregates varied from 12,5 mm to 22 mm. Effect of aggregate type was investigated by using limestone aggregates, and sand stone. Results showed that the early age property development of CEMIIIB cement concrete is comparatively slower than CEMI cement concrete. In an attempt to analyze this matter further, microstructure of the cement paste was investigated by thin section analysis and results provided valuable information to distinguish the development of mechanical properties, adiabatic heat and early-age shrinkage deformations of different concrete mixtures. In conclusion, differences in particle size distribution of binders and aggregates as well as the homogeneity of the cement paste and cement-aggregate interface needs to be investigated to identify the differences in performance of the concrete mixtures.

References

[1] Osborne, G. J., Durability of Portland blast-furnace slag cement concrete, Cem Concr Comp 21 (1) (1999), 11-21
[2] Lura P., Van Breugel K. and Maruyama I., Effect of curing temperature and type of cement on early-age shrinkage of high-performance concrete, Cem Concr Res, 31 (2001), 1867-1872
[3] Lee, K. M., H. K. Lee, S. H. Lee, and G. Y. Kim, Autogenous shrinkage of concrete containing granulated blast-furnace slag, Cem Concr Res, 36 (7) (2006), 1279-1285
[4] Bentz D. P., and Jensen O. M., Mitigation strategies for autogenous shrinkage cracking, Cem Concr Comp, 26(6) (2004), 677-685
[5] Darquennes, A., Staquet, S., Delplancke-Ogletree and M.P. and Espion, B., Effect of autogenous deformation on the cracking risk of slag cement concretes. Cem Concr Comp, 33(3) (2011), 368-379
[6] De Schutter, G., Hydration and temperature development of concrete made with blast-furnace slag cement. Cem Conc Res 29.1 (1999), 143-149
[7] NT BUILD 388, Concrete: Heat Development. Nordtest, Finland, (1992)
[8] Bisschop, J., Evolution of solid behavior, RILEM REPORT (2003), 27-36
[9] TI-B 102 (15), Testing and Sampling Method Concrete: Stress from Shrinkage and Contraction at an Early Age, Danish Technological Institute, Denmark (2015)
[10] DS 423.40 Testing of concrete - Hardened concrete - Producing fluorescence impregnated thin sections, Danish Standard, Denmark, (2002)

SynerCrete'18 International Conference on Interdisciplinary Approaches
for Cement-based Materials and Structural Concrete
24-26 October 2018, Funchal, Madeira Island, Portugal

EARLY-AGE EVOLUTION OF ELASTIC STIFFNESS AND COMPRESSIVE STRENGTH OF RECYCLED CONCRETE: INSIGHTS FROM MULTISCALE MICROMECHANICS MODELING

Markus Königsberger [(1)], Stéphanie Staquet [(1)]

(1) Université libre de Bruxelles, Belgium

Abstract

Recycled concrete, i.e. concrete which contains aggregates that are obtained from crushing waste concrete, typically exhibits a smaller elastic stiffness and a smaller compressive strength than conventional concretes. Based on a continuum micromechanics multiscale model, the mechanical origin and the extent of the reduction are studied herein. Therefore, recycled aggregates are considered as a mix of old cement paste and old aggregates, and they are considered to be embedded in a cement paste matrix at the scale of centimeters. Both, the old and the new cement paste are resolved at micrometer-sized observation scales. The multiscale representation allows for stiffness homogenization (micro-to-macro upscaling) as well as stress concentration (macro-to-micro downscaling), and the latter allows for strength predictions by considering that failure in most unfavorably loaded cement hydrates triggers macroscopic failure. The model suggests that the stiffness of recycled concrete significantly decreases with increasing replacement of natural by recycled aggregates. The strength reduction is less pronounced, in particular at early age, except if the old source concrete is significantly weaker than the targeted new concrete.

1. Introduction

Recycled concrete, i.e. concrete which contains aggregates that are obtained from crushing waste concrete, typically exhibits a smaller elastic stiffness and a smaller compressive strength than conventional concretes [1, 2]. The reduction of the mechanical properties originates from the (old) cement paste which typically comprises 20-40% of the volume of recycled aggregates. Recycled aggregates are less stiff than their natural counterparts, given that the old cement paste is typically less stiff than the natural aggregates. Moreover, recycled aggregates induce additional potential "weak links" in the microstructural interfaces. Such

weaknesses occur, by analogy to conventional concrete, between aggregates and the (new) cement paste, but also between the old and the new cement paste and even "within" the recycled aggregate, i.e. between the old aggregate and the old cement paste. Failure of recycled concrete is triggered by failure of either of the interfaces [3].
Herein, we aim for quantifying the extend of the reduction of elastic stiffness and uniaxial compressive strength at early and late material ages by means of micromechanics-based modeling. Therefore, we use a recently developed multiscale model [3]. Recycled concrete is represented across four scales of observation ranging from micrometer-sized hydration products to centimeter-sized natural aggregates, see Section 2 for details. Combining homogenization techniques with a quasi-brittle failure criterion for the hydration products, we upscale the intrinsic stiffness and failure behavior of the constituents of concrete (such as hydrates, clinker, and aggregates) to predict the macroscopic stiffness and strength of recycled concrete. The model is evaluated for different composition and different maturity states of both old and new cement paste (Section 3). This paper is closed by micromechanics-inspired conclusions on extend and origin of the stiffness and strength reduction as compared to conventional concrete (Section 4).

2. Multiscale Modelling

2.1 Multiscale representation of recycled concrete including ITZs

Recycled aggregates are separated into three classes to capture their morphology [4]: (I) plain aggregates without attached old mortar or paste, (II) old mortar aggregates which consist – at a smaller observation scale – of aggregates embedded in an old cement paste matrix, and (III) old aggregates covered by a layer of old cement paste, see Fig. 1. The microstructural features of old/new cement paste, both for the bulk material and for the ITZs are millimeter-to-micrometer scales, and are built up by elongated hydration products, capillary pores, and unhydrated clinker grains, following the extensively validated model of Pichler and Hellmich [5].

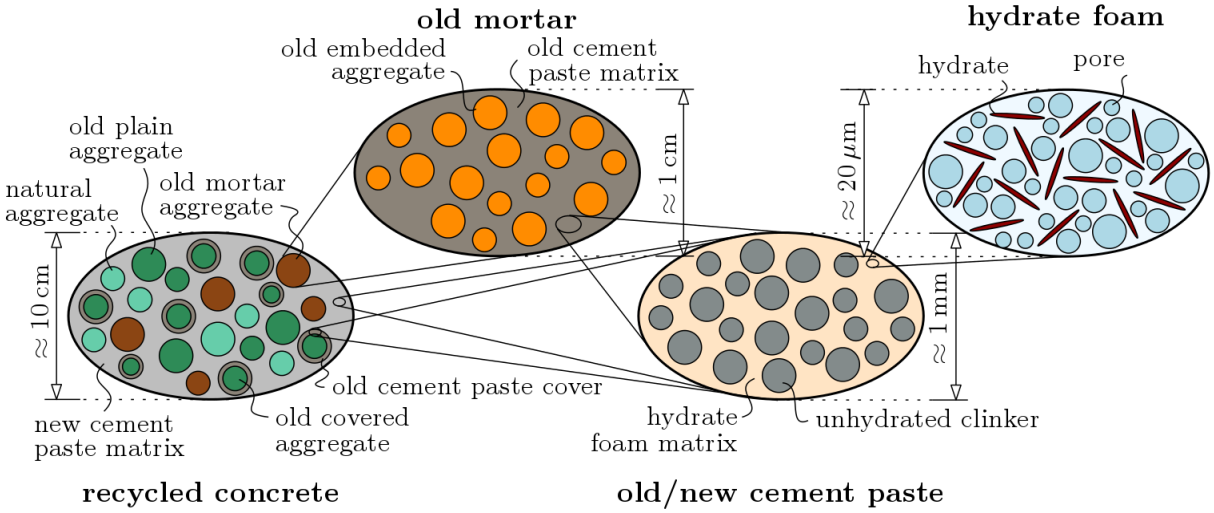

Figure 1: Hierarchical micromechanical representation of recycled concrete across four observation scales from [3].

Interfacial transition zones (ITZs) occur between old aggregates and old cement paste, old aggregates and new cement paste, new aggregates and new cement paste, as well as between old and new cement pastes. We consider that the ITZs are thin enough to be represented as two-dimensional, perfectly bonded interfaces at the scale of concrete and mortar, but that the three-dimensional nature of their microstructure is resolved only at scales which are one order of magnitude smaller than the concrete and mortar scales. The ITZ microstructure is considered to be identical to the microstructure of the adjacent cement paste matrix, either the old or the new one.

2.2 Model input: elastic phase constants and volume evolution

We consider that all constituents exhibit isotropic elastic phase constants. The Young's moduli for aggregates (old and new ones), clinker and hydrates amount to 70.0, 139.9, 29.2 GPa and the Poisson's ratio amount to 0.17, 0.3, 0.24, respectively; by analogy to the [6].
While we consider that all constituents exhibit invariant mechanical properties, their volume dosage changes (i) according to the initial composition and (ii) during the hydration of cement with water. We apply Powers' model [6] to get access to the volume fraction of hydrates in new and old pastes with respect to their water-to-cement ratios $(w/c)_{ocp}$ and $(w/c)_{ncp}$ and their hydration degrees ξ_{ncp} and ξ_{ocp}. Moreover, we consider that all three recycled aggregate classes are equally represented, that the old cement paste content in recycled aggregates as well as the new cement paste content in the recycled concrete amount to 35%, and that the old cement paste is fully hydrated, see [4] for corresponding expressions of the scale-specific volume fractions.

2.3 Stiffness and strength homogenization

In order to obtain the macroscopic stiffness of recycled concrete, we apply mean-field homogenization techniques to upscale the phase stiffness constituents to the macroscopic ("homogenized") stiffness of concrete. Thereby, we consider the self-consistent scheme for homogenization of the polycrystalline hydrate foam, and the Mori-Tanaka scheme for homogenization of the other three matrix-inclusion-type volume elements.
As for strength predictions, we apply a brittle failure upscaling approach, which has been successfully validated for cement paste [5] as well as for mortar/concrete [7]. Failure of the most unfavorably loaded hydration product, located in the most unfavorable ITZs, is considered to trigger concrete failure. The macro-to-micro stress concentration is realized stepwise:

i. First, the volume averages of aggregate stresses are derived by applying mean field-based micromechanics stress concentration laws as function of the macroscopic loads at the concrete level.

ii. Next, ITZ stress states prevailing in the immediate vicinity of the aggregate-to-cement paste interface follow from stress and strain compatibility relations at the aggregate-to-cement paste interface.

iii. Finally, we derive second-order stress averages of the volumetric and the deviatoric stress scalars of the needle-shaped hydrates, which qualify as stress measures to determine microscopic failure.

Failure of micrometer-sized hydrates is considered by means of a Drucker-Prager failure criterion [4], with intrinsic strength properties obtain from limit state analysis of nanoindentation data [8].

3. Results and discussion

The model is first exploited in order to predict the reduction of the mechanical properties of recycled concrete with respect to conventional concrete. Therefore, the sensitivity of the elastic modulus and of the compressive strength of recycled concrete, respectively, is studied regarding changes of the aggregate replacement ratios Γ in the interval from zero (only natural aggregates) to one (only recycled aggregates). We focus on recycled concrete with $(w/c)_{ocp} = (w/c)_{ncp} = 0.5$. The Young's modulus and the compressive strength naturally decrease with increasing replacement ratio, see Fig. 2. The decrease at early ages is much less pronounced than at late ages, because the "weakness" of the recycled aggregate due to the attached old paste is less critical as long as the new cement paste matrix is still very soft. In other words, at early ages, the potential of the stiff natural aggregates can be less exploited. The model also shows that the stiffness reduction is much larger (approximately 25% at full hydration) than the strength reduction (approximately 12% at full hydration), which is also in line with related experimental findings [2]. Notably, the presented stiffness reduction refers to similar elastic properties of old and new aggregates. In case of old aggregates being softer than the new aggregates, the resulting reduction would be even more pronounced. The amount of strength reduction, in turn, crucially depends on the ITZ properties, as discussed in [4]. Interestingly, there is a discontinuity (a change in slope) in the strength evolution of fully hydrated recycled concrete at $\Gamma = 0.8$, see Fig. 2(b), resulting from a change in the failure mode from ITZ failure around plain or natural aggregates to ITZ failure around old embedded aggregates, see [4] for more in-depth discussions on the critical ITZ for various compositions.

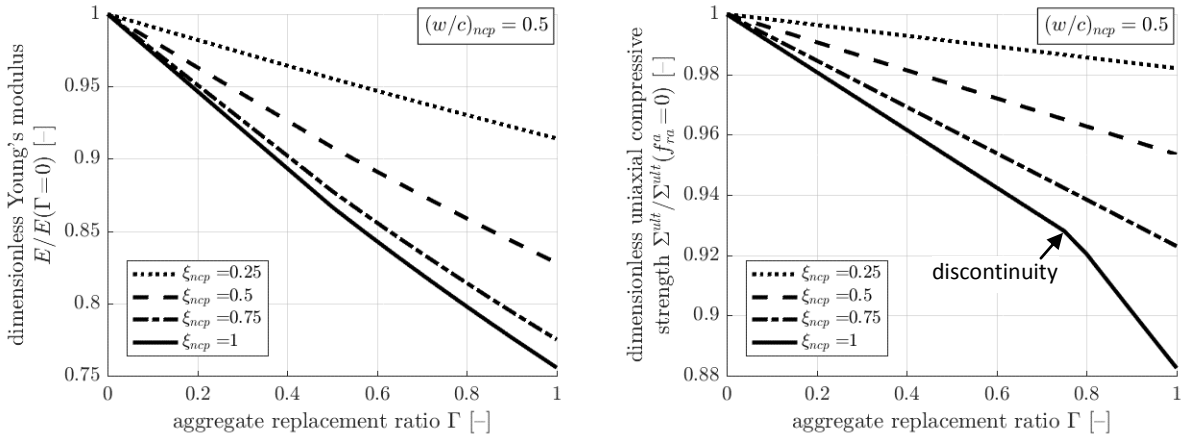

(a) (b)

Figure 2: Model-predicted (normalized) Young's moduli and (normalized) uniaxial compressive strength as function of the aggregate replacement ratio for $(w/c)_{ocp} = (w/c)_{ncp} = 0.5$; $\xi_{ncp} = \{0.25,0.5,0.75,1\}$; $\xi_{ocp} = 1$

Next, we study the evolution of the elastic properties with respect to the hydration degree of the new cement paste. The model is evaluated for a recycled concrete with recycled aggregates only ($\Gamma = 1$), but several combinations of water-to-cement ratios of the old and new cement paste are studied. The stiffness is higher if water-to-cement ratio (of both old and new paste) is smaller and if the hydration degree is higher, see Fig. 3(a). The stiffness loss by using a less quality (high-w/c-ratio) old paste is less significant at early age, but more significant at late ages.
The strength for recycled concrete progressively increases with increasing hydration degree (of the new cement paste) and increasing w/c ratio (of the new cement paste), see Fig. 3(b). However, the sensitivity towards varying w/c ratios of the old paste is quite remarkable. The model suggests that for high-w/c-new pastes, the strength is virtually independent on the w/c ratio of the old cement paste. For low-w/c-new pastes, the strength evolution is virtually identical up to a certain hydration degree. Thereafter, however, the strength does not significantly increase, even when hydration proceeds, if the old cement paste is not strong enough. The weakest link in the microstructure then becomes the ITZ around old cement paste. This shows that a high strength recycled concrete requires the use of a high strength recycled aggregate (obtained from crushing low w/c ratio parent concretes). This demonstrates the importance of quality control when selecting recycled aggregates.

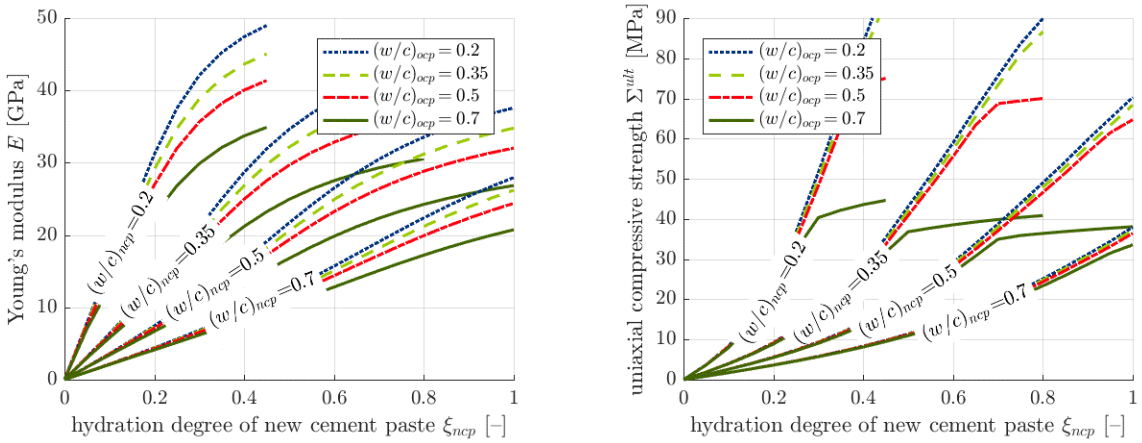

(a) (b)

Figure 3: Model-predicted Young's moduli and uniaxial compressive stresses as function of the degree of hydration of the new paste for $(w/c)_{ocp} = \{0.2,0.35,0.5,0.7\}$; $(w/c)_{ncp} = \{0.2,0.35,0.5,0.7\}$; $\xi_{ocp} = \min\{(w/c)_{ocp}/0.42,1\}$; and 100% recycled aggregates.

4. Conclusions

This micromechanics approach provides some unique insights into the origin of the reduction of the mechanical properties when recycled aggregates are used instead of natural aggregates. It allows to quantify the reduction for any combination of mixture parameters, and therefore might be very helpful for the design of recycled concrete compositions. The model suggests that the stiffness of recycled concrete significantly decreases with increasing replacement of natural by recycled aggregates. The strength reduction is less pronounced, in particular at

early age. Furthermore, the model also shows that if high-strength recycled concretes are targeted, the old source concrete must exhibit a high strength, otherwise the ITZs between old aggregate and old cement paste are prone to failure and the potential of a high-quality new cement paste cannot be exploited.

References

[1] Poon, C. S., Shui, Z. H. and Lam, L. Effect of microstructure of ITZ on compressive strength of concrete prepared with recycled aggregates. Construction and Building Materials, 18(6),461-468, 2004.
[2] Omary, S., Ghorbel, E., Wardeh, G. and Nguyen, M. D. Mix Design and Recycled Aggregates Effects on the Concrete's Properties. International Journal of Civil Engineering, DOI 10.1007/s40999-017-0247-y, 2017.
[3] Otsuki, N., Miyazato, S. and Yodsudjai, W. Influence of recycled aggregate on interfacial transition zone, strength, chloride penetration and carbonation of concrete. Journal of Materials in Civil Engineering, 15(5),443-451, 2003.
[4] Königsberger, M. and Staquet, S. Micromechanical Multiscale Modeling of ITZ-driven Failure of Recycled Concrete: Effects of Composition and Maturity on the Material Strength. Applied Sciences, 8(6), 976, 2018.
[5] Pichler, B. and Hellmich, C. Upscaling quasi-brittle strength of cement paste and mortar: A multi-scale engineering mechanics model, Cement and Concrete Research, 41(5),467-476, 2011.
[6] Königsberger, M., Hlobil, M., Delsaute, B., Staquet, S., Hellmich, C. and Pichler, B. Hydrate failure in ITZ governs concrete strength: A micro-to-macro validated engineering mechanics model. Cement and Concrete Research, 103,77-94, 2018.
[7] Powers, T. C. and Brownyard, T. L. Studies of the physical properties of hardened Portland cement paste. American Concrete Institute Journal Proceedings, 18(2-8),101-992, 1946-1947.
[8] Sarris, E. and Constantinides, G. Finite element modeling of nanoindentation on C-S-H: Effect of pile-up and contact friction. Cement and Concrete Composites, 36,78-84, 2013.

SynerCrete'18 International Conference on Interdisciplinary Approaches
for Cement-based Materials and Structural Concrete
24-26 October 2018, Funchal, Madeira Island, Portugal

EFFECT OF HIGH TEMPERATURE AT EARLY AGE ON INTERFACIAL TRANSITION ZONE AND MATERIAL PROPERTIES OF CONCRETE

Shingo Asamoto [(1)], Ryosuke Yuguchi [(1)], Isao Kurashige [(2)], Pang-Jo Chun [(3)]

(1) Saitama University, Saitama, Japan
(2) Central Research Institute of Electric Power Industry (CRIEPI), Abiko, Japan
(3) Ehime University, Matsuyama, Japan

Abstract

In this study, we investigated the damage risk at interfacial transition zone of concrete exposed to 65°C at early age assuming steam curing and the influence of the damage on material properties of concrete such as dynamic elastic modulus, permeability and shrinkage. When the concrete was exposed to the high temperature at early age, the dynamic elastic modulus was reduced and air permeability was increased comparing to concrete without high temperature history. The modulus reduction and permeability increase of the concrete subjected to 65°C with ground granulated blast furnace slag were larger than those of the concrete without the slag. It can be attributed to larger coefficient of thermal expansion and larger shrinkage of cement paste with the slag to form microcracks around the aggregate. The impregnated fluorescent resin also indicated more microcracks in concrete having the slag when 65°C was induced at early age. Although it is reported that the drying shrinkage was generally reduced after curing at high temperature, the drying shrinkage of concrete with the slag was increased when the concrete was cured in water after 65°C exposure and then dried.

1. Introduction

In Japan, the application of precast concrete to members of civil infrastructures is expected to increase in order to improve the productivity and quality of concrete structures. The precast concrete is generally subjected to the steam curing with high temperature to achieve earlier strength development than the concrete cured at normal ambient temperature. The maximum temperature of steam curing should be less than 65°C according to JSCE specification [1] but it was reported that the high curing temperature can increase volume of coarse pores to

increase the permeability [2]. In addition, the previous studies [3] suggested that the high-temperature history at early age can cause microcracking between mortar and coarse aggregate during temperature decline period due to the different coefficient of thermal expansion between the cement paste and the aggregate. It is important to comprehend the damage the risk at interfacial transition zone due to the high temperature history leading to material properties change for precast concrete.
In this paper, the influence of high temperature at early age on the material properties of concrete such as dynamic elastic modulus, air permeability and drying shrinkage was studied The damage at interfacial transition zone due to the high temperature was also examined using the florescent resin to discuss the relation to the properties. Two types of cements were used to investigate the different coefficients of thermal expansion.

Table 1: Mix proportion of concrete

Cement type	W/C	Water [kg/m^3]	Cement [kg/m^3]	Fine aggregate [kg/m^3]	Coarse aggregate [kg/m^3]	AE agent [kg/m^3]	AE water reducing agent [ml/m^3]	Air	Slump
OPC	0.50	175	350	831	959	0.021	875	5.3%	16 cm
BB	0.50	175	350	825	953	0.021	875	4.6%	19 cm

2. Experimental program

2.1 Materials and specimens

The concrete with W/C = 0.5 was used for all tests. Two types of cement were studied to compare the different coefficients of thermal expansion: Ordinary Portland cement (OPC) and blast furnace slag cement type B (BB). The fine and coarse aggregates are river sand and limestone, respectively. The maximum coarse aggregate size was 20 mm. AE agent and AE water reducing agent are the alkyl ether type surface acting agent and the mix of lignosulfonic acids compound and polyol, respectively. The mix proportion, air content and slump values are given in Tab. 1.

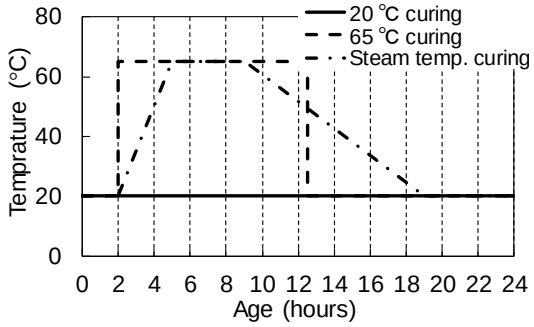

Figure 1: Intial curing tempetaure

ø100 x 200 mm cylinder specimens were used for dynamic elastic modulus and cut to be slices when air permeability and fluorescent impregnation tests were carried out while drying shrinkage was measured using 100 × 100 × 400 mm prismatic specimens. Three initial curing temperature conditions for 24 hours after casting were set up under sealed conditions to investigate the temperature effect at early age: keeping constant 20°C (20°C curing) and 65°C (65°C curing) and simulating steam curing temperature (steam temp. curing) based on JSCE specification even though it was sealed condition as shown in Fig .1. The accumulated temperature of 65°C curing was set to be the same as that of steam temp. curing to investigate the effect of temperature rise and drop rates on concrete properties. After the initial curing for 24 hours, all specimens were submerged into water at 20°C till an age of 7 days to be saturated with water regardless of curing conditions. Then, the prismatic specimens were dried to measure drying shrinkage while the cylinder specimens were cured under sealed curing until air permeability and fluorescent impregnation tests at about 50 days age.

2.2 Dynamic elastic modulus, drying shrinkage and air permeability tests

The first resonance frequency was measured at an age of 7 days after water curing and at about 50 days age using cylinder and dried prismatic specimens to calculate the dynamic elastic modulus based on Japan industrial standard (JIS). The frequency was measured twice for the same specimens and three specimens for each condition were used. The dynamics elastic modulus was obtained by averaging total 6 values of three specimens.

The cylinder specimens under sealed condition were cut to be slices with 40 mm thickness for air permeability test at about 50 days of age. Before the test, the sliced specimens were dried at 50°C for 48 hours to remove water in capillary pores. The air pressure of 0.5 MPa by nitrogen was applied to the specimen sealed by rubber in the air flow cell for about 1 hour to be steady by checking air flow amount several times. Then, air flow amount was measured per a minute for three minutes. The results were obtained by averaging values for three specimens. The permeability was calculated as below:

$$K = \frac{2LP_2\gamma_N}{P_1^2 - P_2^2} \times \frac{Q}{A} \tag{1}$$

where, K is air permeability, L is thickness of specimen, P_1 and P_2 are air pressure and pressure at vent (atmospheric pressure), γ_N is unit volume weight of nitrogen, Q is air flow amount and A is cross section area of specimen.

The longitudinal length change of about 200 mm spans in the drying shrinkage specimens was measured under drying at a relative humidity of 60±10% and 20±1°C from 7 days of age by using a contact strain gauge with an accuracy of 0.001mm. The weights of specimens were also measured with a resolution of 10 g.

2.3 Fluorescent impregnation method by epoxy resin

The both sides of the sliced specimens with 40 mm thickness for the air permeability test were cut into two 10 mm sliced samples to be used for fluorescent impregnation. The both surfaces were polished with water to remove the damage by concrete cutter. After polishing, the samples were dried at 50°C for 24 hours to remove the water near surface. Then, they were impregnated by fluorescent epoxy resin under vacuum condition. The fluorescent resin impregnated in the microcracks was observed by ultraviolet light. The impregnated area was distinguished by the image analysis. The brightness in the image can be approximately classified into 4 parts: air, the mortar area impregnated by the resin, mortar without impregnation and coarse aggregate. In order to distinguish the 4 parts, the threshold selection method proposed by Otsu et al. [4] was applied. One pixel corresponds to about 3 μm.

3. Results and discussion

3.1 Dynamic elastic modulus

The dynamic elastic modulus of longitudinal and flexural oscillation is shown in Fig. 2. At an age of 7 days after water curing, the dynamic elastic modulus of concrete subjected to 65°C at early age for both longitudinal and flexural oscillations of OPC and BB was reduced comparing to that of the concrete cured at 20 °C. It is suggested that the different coefficient

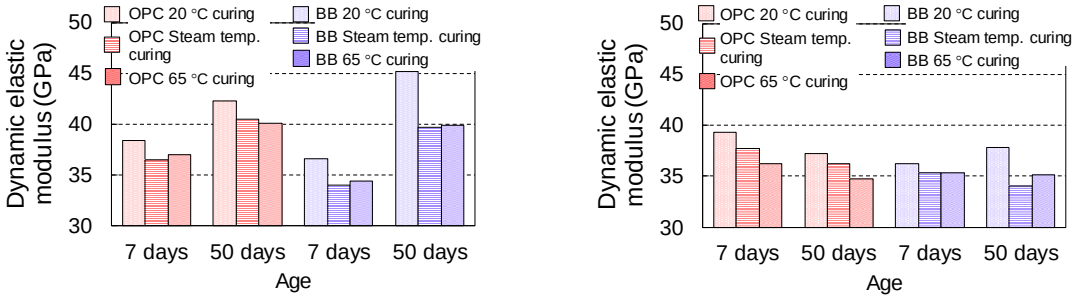

Cylinder specimen(under water by 7 days age and sealing by about 50 days age)

Prismatic specimen(under water by 7 days age and drying by about 50 days age)

Figure 2: Dynamic elastic modulus (longitudinal and flexural oscillation for cylinder and prismatic specimens).

of thermal expansion between cement paste and aggregate can cause the damage in concrete during high temperature exposure to reduce the modulus as reported in the previous study [3]. In addition, large autogenous shrinkage of concrete with the slag during heating may also induce cracking. The modulus reduction of flexural oscillation for BB concrete with high temperature after drying at about 50 days of age was greater than that at an age of 7 days. It may be ascribed to the shrinkage of cement paste during curing and drying as discussed later. The effect of temperature rise and drop rates was not clarified in this experiment as the dynamic elastic modulus between steam temp. curing and 65°C curing was not so different.

3.2 Air permeability

The result of air permeability test was shown in Fig. 3. The air permeability of BB concrete with high temperature at early age was much larger than that of BB concrete cured at 20°C while the air permeability of OPC concrete with high temperature is slightly increased comparing to that of OPC concrete without high temperature. The dynamic modulus of longitudinal oscillation was greatly reduced at about 50 days age when BB concrete was exposed to high temperature as shown in Fig. 2. It is deduced that the air permeability was increased because the damage at interfacial transition zone arising from larger coefficient of thermal expansion and larger autogenous shrinkage of BB cement paste may be more significant with aging under sealing condition comparing to that in OPC concrete with smaller coefficient of the cement paste.

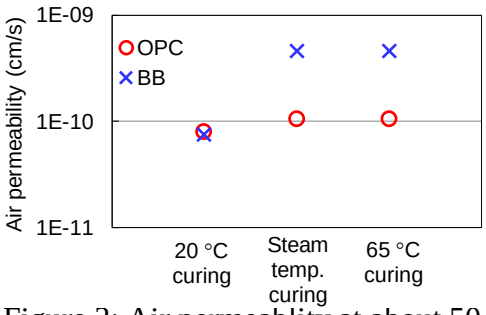

Figure 3: Air permeablity at about 50 days age

3.3 Image analysis of fluorescent impregnation

The examples of image analysis for 20°C and steam temp. curing are given in Fig. 4. The red colour in the images represents the bright part in mortar by ultraviolet light to indicate the microcracks where the fluorescent resin was impregnated. The results of concrete cured at 65°C show similar tendency to those of both OPC and BB concrete with steam temp. curing. As shown in Fig. 4, the red area of BB concrete with high temperature is likely to be more significant especially around the coarse aggregate than that of BB concrete cured at 20°C. It is suggested that microcracks arising from the large coefficient of expansion of BB cement paste

as discussed above were severely formed in the BB concrete with high temperature to make air permeability larger. It is also possible that larger shrinkage of BB cement paste was confined by aggregate to cause microcracks around aggregate. The microcracks around the coarse aggregate were also visually confirmed by digital microscope. On the other hand, the difference between curing at 20 °C and with high temperature was small in the case of OPC concrete. It is speculated that the microcracks during the temperature rise and drop may be too small in the OPC concrete to be impregnated by the resin but slightly reduce the dynamic elastic modulus. The brightness of the samples, however, was not stable even though the camera and light were fixed at the same position and the calculated area by the analysis was scattered for the same condition although the tendency of all samples is the same as discussed above. Hence, further improvement of fluorescent impregnation method is necessary for more quantitative discussion.

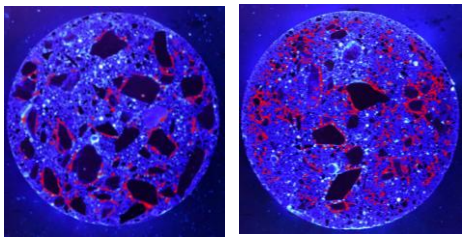

OPC concrete BB concrete
20°C curing

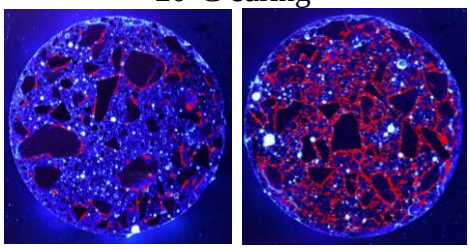

OPC concrete BB concrete
Steam temp. curing

Figure 4: Results of image analysis

3.4 Drying shrinkage

Mass loss and drying shrinkage of concrete dried at an age of 7 days is represented in Fig. 5. The mass loss of OPC concrete with high temperature increased while the drying shrinkage is smaller comparing to the concrete cured at 20°C. Thomas and Jennings reported the same tendency using cement paste and explained that the coarsened capillary pores due to the densification of the C-S-H gel phase by high temperature increase the mass loss and reduce

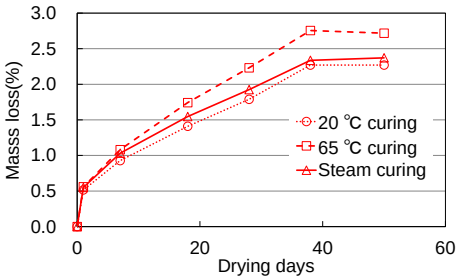

Mass loss of OPC concrete

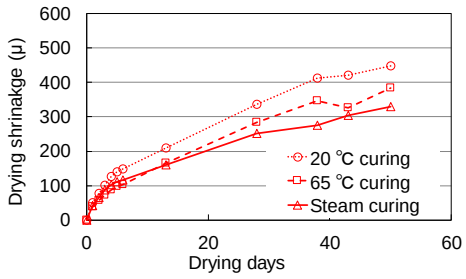

Drying shrinkage of OPC concrete

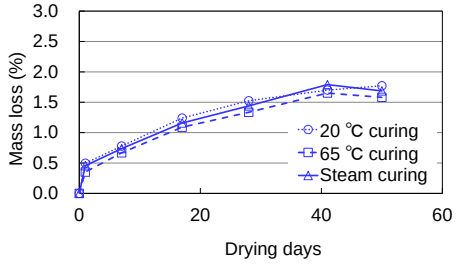

Mass loss of BB concrete

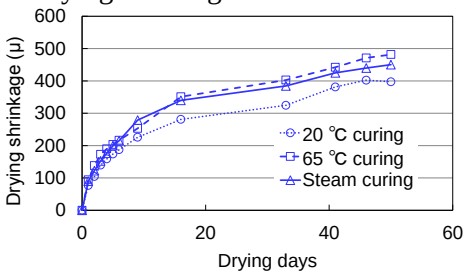

Drying shrinkage of BB concrete

Figure 5: Mass loss and drying shrinkage of concrete dried at 7 days of age.

the shrinkage [5]. In this experiment, it is suggested that the effect of the coarsened pore structure in the cement paste is dominant even in concrete with OPC. On the other hand, in the case of BB concrete, the mass loss was almost independent of curing temperature while the shrinkage of concrete with high temperature is larger than that of concrete cured at 20 ºC. It is reported that Portland cement with blast furnace slag can precipitate hydration products with different morphology from OPC [6]. It is speculated that the larger shrinkage of BB cement paste with different amorphous phase can promote the microcracks around the aggregate leading to larger dynamic elastic modulus reduction after 50 days of drying than OPC concrete as shown in Fig 2.

4. Conclusion

The findings in the paper are summarized below.

- The dynamic elastic modulus was reduced and the air permeability increased when the concrete was cured at 20 °C by about 50 days age after exposing to 65 °C at early age, especially using the slag, comparing to the concrete cured at constant 20 °C.
- The image analysis of the impregnated florescent resin in concrete suggests that more microcracks around the coarse aggregate can be formed in the concrete with the slag subjected to 65 °C.
- The drying shrinkage of concrete with the slag was increased when the concrete was submerged in water after 65 °C exposure and then dried comparing to the concrete cured at 20 °C. The large shrinkage may promote microcracks around aggregate.

Acknowledgement
This study was supported by the JSPS Grant-in-Aid for Scientific Research (B) No. 17H03285 and by JSPS Core-to-Core Program B. Asia-Africa Science Platforms.

References

[1] Japan Society of Civil Engineering, Standard Specifications for Concrete Structures 2007, Materials and Construction, No. 16 (2007), 484-485
[2] Goto, S. and Roy, D.M., The effect of w/c ratio and curing temperature on the permeability of hardened cement paste, Cem Concr Res 11 (1981), 575-579
[3] Son, H. N. and Hosoda, A., Detection of microcracking in concrete subjected to elevated temperature at very early age by acoustic emission, J Adv Concr Tech 8 (2010), 201-211
[4] Otsu, N., A threshold selection method from gray-level histograms, IEEE transactions on systems, man, and cybernetics 9(1) (1979), 62-66
[5] Thomas, J.J. and Jennings, H.M., Effect of heat treatment on the pore structure and drying shrinkage behavior of hydrated cement paste, J Am Ceram Soc 85 (2002) 2293-98
[6] Richardson, I. G., Tobermorite/jennite- and tobermorite/calcium hydroxide-based models for the structure of C-S-H: applicability to hardened pastes of tricalcium silicate, h-dicalcium silicate, Portland cement, and blends of Portland cement with blast-furnace slag, metakaolin, or silica fume, Cem Concr Res 34 (2004), 1733-1777

SynerCrete'18 International Conference on Interdisciplinary Approaches
for Cement-based Materials and Structural Concrete
24-26 October 2018, Funchal, Madeira Island, Portugal

EFFECT OF THE MATURATION PRESSURE ON MECHANICAL AND HYDRAULIC PROPERTIES OF OILWELL CEMENT PASTE

Issam Takla [(1)], Nicolas Burlion [(1)], Jian-Fu Shao [(1)], Thomas Rougelot [(1)]

(1) University of Lille, LaMcube, F-59000 Lille, France

Abstract
Oilwell cement (G class) is commonly used for the cementing works in the boring operations. The cementing aims to place a ring of cement paste between the wall of the drilled hole and the tubing.
The maturation of oilwell cement takes place at high temperatures and under pressures higher than the pressure at the surface. Within the framework of a general project for the sequestration of CO_2 in oil reservoirs developed by Total Exploration and Production (E&P), this study aims to investigate the effects of pressure during the maturation of G class cement on its mechanical and hydraulic properties.
All tests were performed at a temperature of 90°C (real temperature of the well) for two different maturations of the cement paste: under atmospheric pressure or under a pressure of 3000 psi (20.7 MPa) usually reached in oilwells. Porosity, permeability and mechanical strength were measured and analysed. A very slight difference between the two types of maturation was observed: the kinetic effect of curing pressure at early age seems to be concealed on the long term if a sufficient hydration time is guaranteed.

1. Introduction

The curing pressure is an important factor when studying oilwell cement since maturation of the cement paste takes place usually under a pressure higher than atmospheric pressure.
In literature, most studies were dedicated to the effect of curing pressure on hydration products and on the microstructure of hardened cement. According to Le Saout et al [1] the increase in pressure and temperature of oilwell cement paste leads to more polymerised C–S–H. Scherer et al [2], by treating the hydration of H class cement as a simply activated process, found that the increase in pressure and temperature only change the rate of hydration but not

the nature of the process. Le Saout et al [3] found also that the effect of temperature and pressure on the hydration of cement paste seems to be only kinetic.
The effect of the pressure on the hydration kinetic could be explained by an increase in the amount of water passing into the gel coating and thus an increase in the hydrolysis at the clinker grain surface [4]. More recently, Zhou and Beaudoin [5] found by using SEM examination that micro-cracking only appears on samples hydrated under pressure which in turn facilitates the migration of water into the protective layers around cement grains and thus accelerating the reaction with the unreacted cores of the particles.
Most studies on the effect of curing pressure on mechanical properties were often performed on concrete (autoclaved concrete); it would be important now to verify the effect of curing pressure on mechanical and hydraulic properties of G class cement paste.
The value of this pressure is variable according to the depth and the location of the cement paste in the well. The cement paste is subjected also to an additional pressure coming from its self-weight.
In order to study the possible effect of curing pressure on mechanical and hydraulic behaviour of oilwell cement G class, two groups of samples were prepared:

- first group: samples matured under atmospheric pressure at a temperature of 90°C in the Laboratory of Mechanics, Multi-physics, Multi-scale (LaMcube).
- second group: samples matured under a pressure of 3000 psi (20.7 MPa) at a temperature of 90°C. The pressure value of 3000 psi was adopted by Total to match the requirements of API (American Petroleum Institute) as a maximal value which might be found in the well for the G class cement paste. These samples were prepared by Total and a part of them were transmitted to LaMcube to perform the mechanical and hydraulic tests.

2. Fabrication protocol

The present study was performed with classic cement "G class" used in the petroleum domain. The composition of the cement paste is detailed in Tab. 1.

Table 1: Composition of the cement paste

Component	Quantity (kg/m3)
Cement G class	1308.3
Water	578.5
D175 (antifoaming)	5.2
D 80 (dispersant)	8.1
Water/Cement ratio	0.44

Two additives, an antifoaming and a dispersant (supplied by Total) were added when preparing the cement paste.
Samples (Ø36, H = 100 mm) were obtained by using stainless steel moulds, from which other samples (Ø20, H = 22 mm) were later derived to perform the tests.
The cement paste was mixed at ambient temperature, then the moulds were kept for 72 h in lime saturated water at 90°C. This temperature was adopted to simulate the real conditions in the wells. Samples were kept after demoulding in lime saturated water at 90°C for one month.

The mass evolution during this period was monitored and shows a stabilization before the age of one month, ensuring a quasi-complete hydration of samples and that mechanical properties of sample may only slightly evolve after this age. The same protocol has been adopted for the fabrication of the second type of samples. These ones have been kept immediately after mixing in a pressurized oven regulated at a temperature of 90°C and a pressure of 3000 psi.

3. Porosity

The test of water porosity was performed on sound samples of G class cement paste matured under atmospheric pressure or under a pressure of 3000 psi at a temperature of 90°C (one sample for each type of maturation). The porosity was measured at 90°C then at 105°C for both cases (Tab. 2). Saturated samples (kept in lime saturated water during maturation) were first dried in an oven at 90°C until the mass stabilization. Then, the temperature was raised to 105°C and the porosity was measured once more in the same manner. This rise of temperature up to 105°C aims to quantify the change of porosity due to the partial removal of water (mainly from C-S-H and ettringite), which could slightly modify the microstructure of these hydrates.

Table 2: Values of the porosity obtained for sound samples of G class cement paste matured under atmospheric pressure and under a pressure of 3000 psi.

	Porosity 90°C (%)	**Porosity 105°C (%)**
Atmospheric pressure	35.4	36.3
Pressure of 3000 psi	35.1	36

No real change in porosity was detected, the curing pressure seems not to have an influence on the void ratio.
After one month of maturation at 90°C, the two types of samples in this study might have the same hydration products and nearly the same pore size distribution, although some difference could have existed at a very early age.
The results of the porosity show a priori that the microstructure of the cement paste was not changed by raising the curing pressure when a sufficient period of hydration is guaranteed. This conclusion has to be confirmed according to the results of permeability and triaxial tests.

4. Triaxial tests and permeability measurement

4.1 Experimental devices

A triaxial cell has been used and was placed in an oven in order to perform the tests at 90°C. Three Gilson® pumps connected to the cell were necessary to apply confining and deviatoric pressure and also for the injection of interstitial fluid (distilled water). A data acquisition system has been used to record axial strain measured by two displacement transducers (LVDTs) and lateral deformation measured by a circumferential collar.

4.2 Water permeability at 90°C

The test of permeability was performed at 90°C on samples of G class cement paste matured under atmospheric pressure or under a pressure of 3000 psi for a confining pressure of 3MPa and an interstitial pressure of 2.5 MPa.
Results of the permeability for the two types of samples are presented in Tab. 3.

Table 3: Values of the permeability obtained for sound samples of G class cement paste matured under atmospheric pressure and under a pressure of 3000 psi for a confining pressure of 3MPa and an interstitial pressure of 2.5 MPa.

	Pc=3MPa
Atmospheric pressure	K=3.7 E-18 m²
Pressure of 3000 psi	K=1E-18 m²

The permeability slightly changes between the two cases. The curing pressure does not affect the connectivity rate of the pores which is in accordance with the results of the porosity. In fact, the permeability of a cement paste is influenced by the development of hydration ratio; the permeability decreases rapidly along with the progress of the hydration because the volume of the gel becomes bigger, so that it fills gradually a part of the space which was occupied initially by mixing water [6]. Although the curing pressure affects the hydration ratio at early ages, this effect is still less significant than the effect of the temperature in this study, as all tests were realized at 90°C. Curing temperature has a much stronger effect on cement hydration rate than curing pressure [7].

4.3 Triaxial tests at 90°C

For the two types of samples (matured under atmospheric pressure and under a pressure of 3000 psi), four trixial tests were performed at a temperature of 90°C. The confining pressure for the four tests was Pc= 0, 3, 10 and 20 MPa and the interstitial pressure was Pi=2.5 MPa when Pc≠0.
Fig. 1 shows a comparison of triaxial results between the two types of samples under different confining pressures. For the four values of confining pressure, the two types of cement paste have nearly the same stress-strain behaviour. The post-peak behaviour is widely dependent on the confining pressure; the material is rather brittle when confining pressure is low, the post-peak behaviour becomes more and more ductile with the increase of the confining pressure, the failure of the two types of samples takes places nearly at the same ratio of strain for each value of confining pressure. The tests at Pc= 20 MPa have been stopped when the axial strain reaches a value of about 7%, in order to avoid to damage the two LVDTs. The real peak was not reached in this case.
Fig. 2 recapitulates the evolution of failure strength in function of the confining pressure.
Mechanical tests for the four values of confining pressure show very close results between the two types of samples. The curing pressure does not have a significant influence on mechanical behaviour of studied cement paste. This seems somehow logical and in accordance with the previous tests as the two types of sample have nearly the same values of porosity and permeability.
In general, the development of the strength of cementitious materials depends on the duration of maturation even when cured under a pressure higher than the atmospheric pressure.

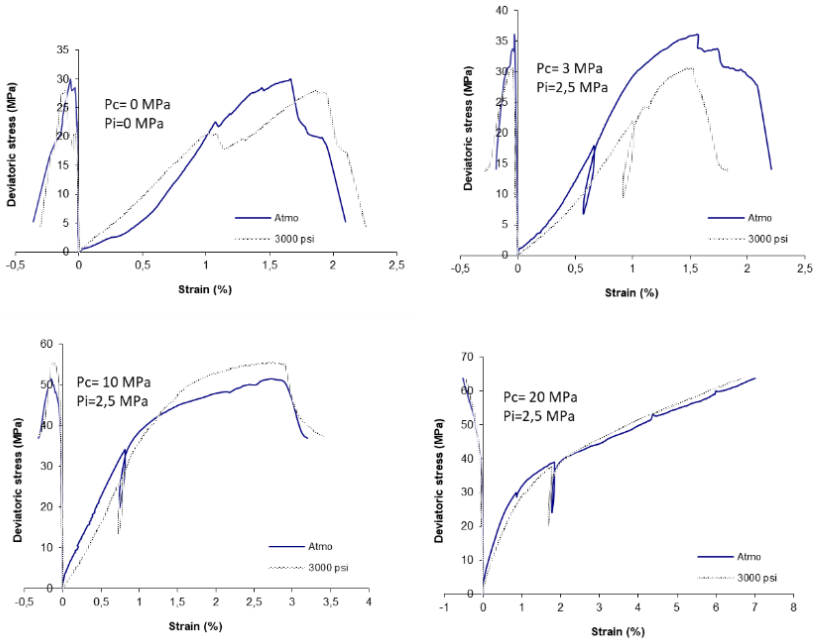

Figure 1: Evolution of axial and lateral deformations at 90°C of samples matured under atmospheric pressure and under a pressure of 3000 psi for Pc=(0,3, 10, 20) MPa and Pi=2.5 MPa

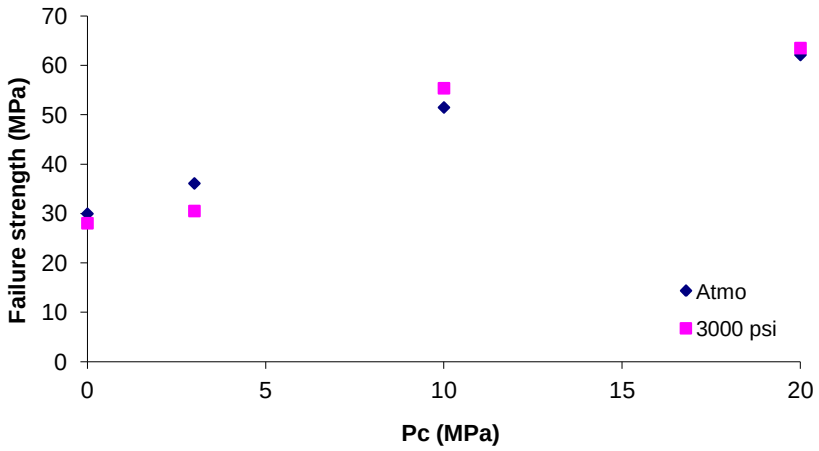

Figure 2: Failure strength obtained at 90°C of samples matured under atmospheric pressure and under a pressure of 3000 psi in function of confining pressure

The acceleration of the chemical reactions of hydration process due to the curing temperature of 90°C has positively affected the mechanical strength at early age, as the duration of dormant (induction) has been reduced because of this hot curing, thus the global structure of hydrated cement paste was established very soon. At the age of one month, the two types of samples have mostly the same hydration rate, regardless of the curing pressure. Hence a similar mechanical behaviour has been obtained.

5. Conclusions

This study has been realized on two types of samples of G class cement paste: the first one was matured under atmospheric pressure at a temperature of 90°C and the second one was matured under a pressure of 3000 psi (20.7 MPa) at the same temperature.
After one month of maturation the two types of sample have nearly the same pore size distribution and the same pore connectivity, values of porosity and permeability being very close.
Triaxial mechanical tests show that the two types of samples have a similar stress-strain behaviour for the four values of confining pressure and that the failure strength slightly varies between these two types.
The obtained results prove that the effect of curing pressure was only kinetic; microstructure and hydration products might be the same when a sufficient period of maturation is guaranteed.
This conclusion has enabled us to perform all other tests in this project, in term of carbonation and leaching, on samples cured under atmospheric pressure, which is simpler for laboratory work conditions, and thus to extrapolate the results of these tests to cement paste in the oilwell for minimum error rate.

Acknowledgments
The authors gratefully acknowledge Total for entrusting this study to the Couplages Thermo-Hydro-Mechanical-Chemical (THMC) team of the Laboratory of Mechanics, Multi-physics, Multi-scale (LaMcube), Lille - France, and for the permission to publish these results.

References

[1] Gwenn Le Saout, Eric Lécolier, Alain Rivereau, Hélène Zanni. Study of oilwell cements by solid-state NMR. C. R. Chimie 7 (2004) 383–388.
[2] George W. Scherer , Gary P. Funkhouser , S. Peethamparan. Effect of pressure on early hydration of class H and white cement. Cement and Concrete Research 40 (2010) 845–850.
[3] Gwenn Le Saout, Eric Lécolier, Alain Rivereau, Hélène Zanni. Chemical structure of cement aged at normal and elevated temperatures and pressures Part I. Class G oilwell cement. Cement and Concrete Research 36 (2006) 71–78.
[4] A.A. Rahman and D.D Double. Dilatation of Portland cement grains during early hydration and the effect of applied hydrostatic pressure on hydration. Cement and Concrete Research 12 (1982) 33–38.
[5] Zhou, Q.; Beaudoin, J.J. Effect of Applied Hydrostatic Stress on the Hydration of Portland Cement and C3S. Advances in Cement Research 15 (2003) 9–16.
[6] Adam M.Neville (2000). "*Propriétés des bétons*" CRIB, Sherbrooke- Laval pp. 12-57, 345-358.
[7] Pang X, Meyer C, Darbe R, Funkhouser GP. Modeling the effect of curing temperature and pressure on cement hydration kinetics. ACI Mater J 110 (2013)137–48.

SynerCrete'18 International Conference on Interdisciplinary Approaches
for Cement-based Materials and Structural Concrete
24-26 October 2018, Funchal, Madeira Island, Portugal

ESTIMATION OF SETTING TIME IN CONCRETE THROUGH MODELLING OF ULTRASONIC PARAMETERS

Ivan Gabrijel [(1)], Mario Pintar [(1)]

(1) University of Zagreb, Faculty of Civil Engineering, Zagreb, Croatia

Abstract
In a standardized procedure initial and final setting in mortar or concrete is determined from penetration resistance test. A wide variety of different test methods has been explored which are sensitive to the transformation of cement composites from a fluid to solid state. Different suggestions on how to determine initial and final setting from these measurements were given by their authors but up today there is no method which would be generally accepted and which would serve as a new standard for setting time measurement. In this paper a methodology of estimating setting time from ultrasonic measurements is given. Ultrasonic data for two concrete mixtures is modelled with exponential model using a curve fitting procedure. Model parameters representing time/age are compared with setting time determined by penetration resistance test.

1. Introduction

The point at which initial setting occurs represents a beginning of the transformation process of cement based material from fluid-like to a solid material. Initial setting indicates that the connectivity between particles has started to develop. From a practical point of view all activities involving placing of concrete should finish before initial setting. The point at which final set occurs in concrete is important since it provides an estimate when the development of concrete strength and stiffness starts.

Standardized method for measuring setting time of concrete (ASTM C403/C403M-16) gives the procedure for initial and final setting determination on mortar sieved from the concrete mixture by measuring resistance (in MPa) to penetration of needles with specified bearing areas. The purpose of penetration resistance test is to optimize concrete mixtures with respect to setting. The drawback of standard method is that measurements are limited to small

number of discrete points in time, measurement is semi-destructive and sample is disturbed each time a new penetration is made and penetration resistance is not measured directly on concrete material itself but on mortar obtained by sieving concrete.

To improve understanding of the relationship between hydration process and setting times alternative methods are investigated. Ultrasonic transmission [1, 2] and reflection [3, 4] methods can provide a finer representation of the fluid-solid transformation process. However, ultrasonic measurement results do not show distinct points in time which could be unambiguously recognized as initial and final setting. This lead to different criterions for setting times that have been proposed based on measurement of ultrasonic parameters. It has been reported that final setting of cement paste determined according to standard EN 196-3 arise at the longitudinal wave velocity of about 1500 m/s [2, 5]. Initial setting of mortar and concrete determined according to standard ASTM C 403 appears in the vicinity of the first inflection point of the curve which describes changes in the wave velocity over time [6, 7]. Making parallel measurements of P-wave (Primary wave) and S-wave (Secondary wave, shear wave) it was found that in mortar the peak of the S-wave velocity derivative corresponds to the initial setting time and the peak of the dynamic elastic modulus derivative occurs at the final setting time [8]. Trtnik and Gams successfully applied frequency spectrum analysis of the waveform transmitted through the specimen for setting time evaluation [9]

In this paper a methodology of estimating setting time from transmission measurements of ultrasonic P-waves is given. Curve fitting procedure is applied to the ultrasonic pulse velocity (UPV) and frequency centroid (FC) obtained during first few days of hydration in concrete. Model parameters representing time/age are compared with setting time determined by penetration resistance test according to ASTM C403/C403M-16.

2. Experimental work

Experimental work is made on two concrete mixtures. Each mixture is prepared two times and measurement was repeated. Mix composition is presented in Table 1. All components were preconditioned at a temperature of 20±2°C before mixing. From 1 batch for each mixture initial and final setting time was determined by standardized penetration method

Table 1: Mix composition.

Material	**Type of the material**	**OC**	**MOC**
Cement [kg]	CEM I 52.5 N N-SR3 CE PM-CP2 NF HRC	320	439
Sand [kg]	0-4 mm	830	772
Gravel [kg]	4-11mm (rounded silicate and limestone)	449	525
	8-16 mm (rounded silicate and limestone)	564	424
Admix. [kg]	Plasticizer SIKAPLAST Techno 80	1.44	3.73
Water [kg]		166.4	175.6
w/c		0.52	0.40

Ultrasonic measurements started when mixture was in the fresh state. Dimension of the concrete specimens in the mould are 15×15×10 cm. The distance between sending and receiving sensors was 10 cm. Compaction of specimens was made by hand and specimens were stored in a temperature controlled room with temperature 19 ± 2°C. In the specimen under test type K thermocouple was embedded and temperature was recorded at an interval of 5 minutes. From each batch 3 samples for ultrasonic measurements were made and tested simultaneously. UPV was measured on 1 specimen and acousto-ultrasonic (AU) measurement was made on 2 samples (Fig. 1a). UPV was measured using Pundit instrument from CNS Farnell with 54 kHz transducers. UPV was recorded every 120 seconds during measurement. Equipment for AU measurements consisted of Physical Acoustics Corporation (PAC) components: PAC 1220 preamplifiers with selectable gain of 0/20/40 dB, 16 bit PCI-8 data acquisition system and piezoelectric transducers type R6 which are sensitive in the range 20-120 kHz. Waveforms were recorded at a sampling rate of 1 MHz. Arbitrary waveform generator was used to pulse R6 sensors with repetition frequency of 0,01 Hz.

Frequency centroid (FC) is parameter calculated from the frequency domain of a waveform recorded by receiving sensor. It is also known as a first moment of inertia calculated from Eq. 1. In Fig. 1b magnitude of frequency spectrum is plotted for two waveforms recorded at concrete age of 10 h and 72 h. Position of FC for these two waveforms is also plotted.

$$\mathrm{FC} = \frac{\sum(magnitude \times frequency)}{\sum magnitude} \tag{1}$$

a)

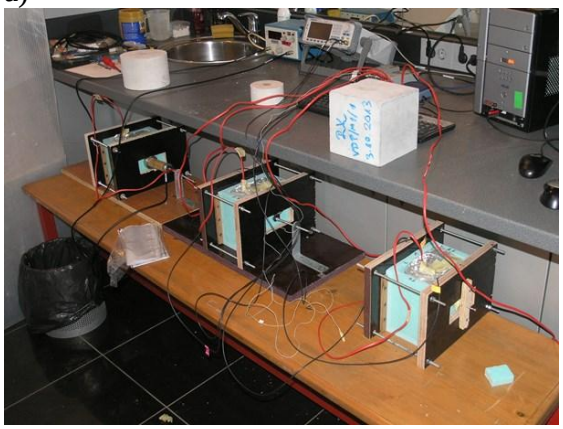

b)

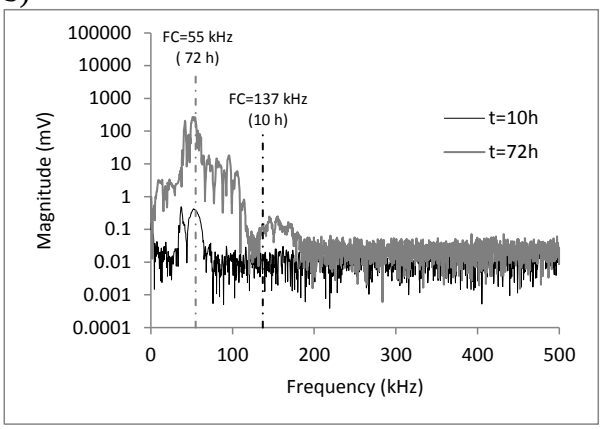

Figure 1: a) Samples during ultrasonic test; b) comparison of magnitude of the frequency spectrum and FC for waveforms recorded at 10 h and 72 h after mixing (from OC mix)

3. Results

In Fig. 2 development of UPV (Fig. 2a) and FC (Fig. 2b) during first 72 hours is presented. In Fig. 2 numbers 1 and 2 represent batch from which sample was taken and letters a and b represent two samples from one batch tested with AU method.

a) b)

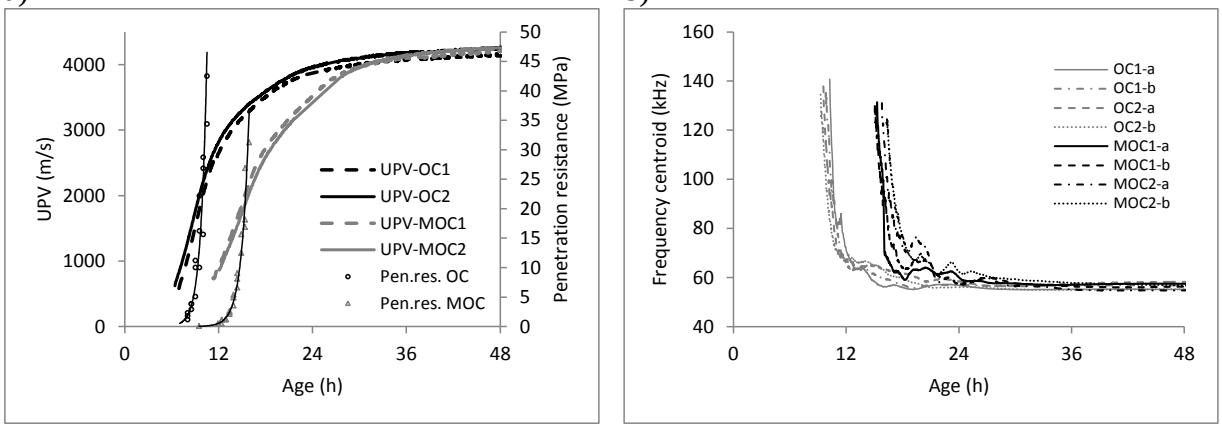

Figure 2: Ultrasonic data on samples from mixtures OC and MOC: a) UPV and penetration resistance; b) FC

Changes in UPV and FC can be accurately described by 3-parameter exponential model (Fig. 3). Model for UPV data is presented in Eq. 2. In this model V_u is ultimate velocity, τV is time parameter and βV is shape parameter. Since FC has a decreasing trend it is modelled with exponential model given in Eq. 3. In this model F_u is ultimate frequency, τF is time parameter and βF is shape parameter.

$$\mathrm{UPV}(t) = V_u \cdot e^{-\left(\frac{\tau V}{t}\right)^{\beta V}} \tag{2}$$

$$\mathrm{FC}(t) = F_u \cdot e^{\left(\frac{\tau F}{t}\right)^{\beta F}} \tag{3}$$

a) b)

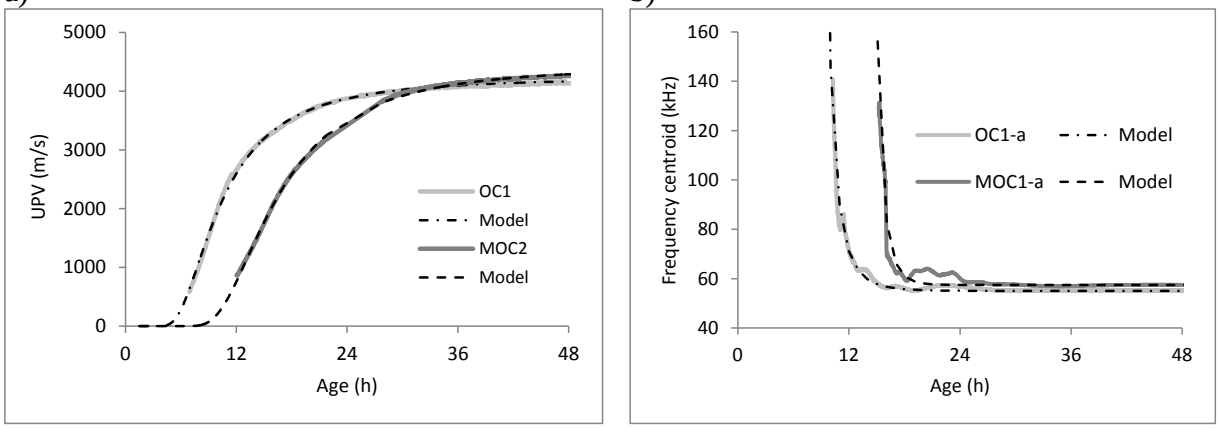

Figure 3: Modelling of measured ultrasonic parameters: a) UPV; b) FC

Model parameters calculated by a curve fitting procedure are given in tables 2 and 3. Values of time parameter τV and τF are close to initial and final setting time value obtained by penetration resistance test.

Table 2: Curve fitting parameters for UPV measurements and setting time determined by penetration test

	Parameter				Penetration resistance test	
Measurement	**V_u (m/s)**	**τV (h)**	**βV**	**R^2**	**Initial setting (h)**	**Final setting (h)**
OC1	4233	9,0	2,5	0,998	8,6 (± 0,4)	10,2 (± 0,4)
OC2	4316	8,5	2,4	0,999	average (± st.dev.)	average (± st.dev.)
MOC1	4332	14,1	3,0	0,999	13,8 (± 0,1)	15,6 (± 0,3)
MOC2	4418	14,6	2,9	0,999		

Table 3: Curve fitting parameters for FC measurement results

	Parameter				
Measurement	**F_u (m/s)**	**τF (h)**	**βF**	**R^2**	**Average value of τF (h)**
OC1-a	55	10,0	7,3	0,967	
OC1-b	56	9,7	7,2	0,982	9,5 (± 0,5)
OC2-a	58	9,3	7,7	0,960	average (± st.dev.)
OC2-b	56	8,9	5,1	0,944	
MOC1-a	57	15,1	15,8	0,902	
MOC1-b	57	14,6	8,2	0,960	15,1 (± 0,4)
MOC2-a	55	15,0	5,9	0,951	average (± st.dev.)
MOC2-b	57	15,6	7,3	0,950	

Additional calculation is made where all parameters are expressed as a function of maturity. Maturity is calculated from the measured temperature history in the samples. Evaluation of maturity is made through *temperature-time factor* maturity function defined in the standard ASTM C1074-04. In evaluation of maturity assumption was made that datum temperature is 0°C. Comparison of initial and final setting time obtained by penetration resistance test with time parameters calculated from UPV and FC measurements are presented in Fig. 4. From Fig. 4 it can be noticed that values of time parameters are better related to the values of initial setting time. For two mixtures analysed average value of τF gave a better estimate of initial setting time than average value of τV.

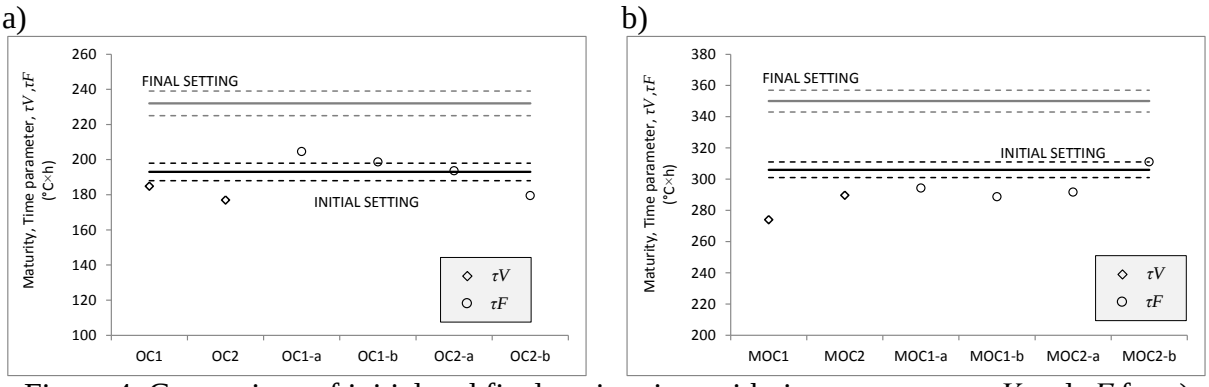

Figure 4: Comparison of initial and final setting time with time parameters τV and τF for a) OC mixture; b) MOC mixture (all parameters expressed as a function of maturity)

4. Conclusion

Ability of concrete to support transmission of acoustic waves of different frequencies is highly dependent on the connectivity of the structure. Parameter called frequency centroid which can be calculated from the frequency spectrum shows a rapid decrease during the transformation of concrete from fluid to solid state. Changes of the frequency centroid during hydration can be accurately described by 3-parameter exponential model. For two mixtures analysed in this work average value of time parameter τF was closely related to initial setting time obtained by penetration resistance test.

References

[1] Reinhardt, H.W. and Grosse, C.U. Continuous monitoring of setting and hardening of mortar and concrete, Construction and building materials, Vol. 18, (2004), pp 145-154.
[2] Trtnik, G., Turk, G., Kavčič, F., Bokan Bosiljkov, V. Possibilities of using the ultrasonic wave transmission method to estimate initial setting time of cement paste, Cement and Concrete Research V. 38 (2008), pp 1336–1342
[3] Valič, M. I. Hydration of cementitious materials by pulse echo USWR: Method, apparatus and application examples, Cement and Concrete Research, Vol. 30, Issue 10, (2000), pp 1633-1640
[4] Voigt, T. and Shah, S.P. Properties of early age Portland cement mortar monitored with shear wave reflection method, ACI Materials Journal, Vol.101, No. 6, (2004), pp 473-482
[5] Kamada, T., Uchida, S., Rokugo, K. Non-destructive evaluation of Setting and Hardening of Cement Paste Based on Ultrasonic Propagation Characteristics, Journal of Advanced Concrete Technology, V. 3(3) (2005), pp 343-353
[6] Grosse, C. U., Reinhardt, H. W., Krüger, M. Beutel, R. Ultrasound trough-transmission techniques for quality control of concrete during setting and hardening // Workshop: Advanced testing of fresh cementitious materials / ed. Reinhardt, H. W, Stuttgart, Germany, 2006. pp 1-11
[7] Mikulić, D., Sekulić, D., Štirmer, N., Bjegović, D. Application of ultrasonic methods for early age concrete characterisation. // International Journal of Microstructure and Materials Properties V. 1(3/4) (2006), pp 297-309
[8] Carette, J., Staquet, S. Monitoring the setting process of mortars by ultrasonic P and S-wave transmission velocity measurement, Construction and Building Materials 94(2015), pp 196-208
[9] Trtnik, G., Gams, M. The use of frequency spectrum of ultrasonic P-waves to monitor the setting process of cement pastes, Cement and Concrete Research 43 (2013) pp 1–11

SynerCrete'18 International Conference on Interdisciplinary Approaches
for Cement-based Materials and Structural Concrete
24-26 October 2018, Funchal, Madeira Island, Portugal

EULERIAN TWO-PHASE COMPUTATIONAL FLUID DYNAMICS MODEL OF A CONCRETE SCREW MIXER

Nicolò Beccati [(1)], Cristian Ferrari [(1)]

(1) Institute for Agricultural and Earthmoving Machinery of the Italian National Research Council (CNR - IMAMOTER), Ferrara, Italy

Abstract
The state-of-art in computational fluid dynamics (CFD) simulations of fresh concrete mostly focuses on gravitational based physics, like Abrams cone test or L-box test. Focus of this work is the Eulerian-Eulerian two-phase CFD model of the working cycle of a continuous concrete screw mixer, useful for a simulation of the machine and a characterization of its performances. Screw mixers are used in the concrete industry to produce and convey fresh concrete directly in the moulds, starting from segregated materials put directly into the machine. The work focuses mainly on the calibration of the numerical fresh concrete fluid model, simplified as a homogenous and continuous liquid as mainly reported in scientific literature. Another task is the review of the critical in applying this simplified fluid model into a real industrial machine cycle, with centrifugal based physics applied. The calibration of the fresh concrete behaviour is obtained through a parameterization of the viscosity models. The results show how the numerical rheology of the fluid has to be corrected as a function of the simulated physics applied, and how the CFD model can be used to study the performances or compare a new design of the studied machine.

1. Introduction

From scientific literature, the CFD applied on fresh concrete flow is mainly used for simple geometries, such as Slump test or L-box test, for a correct calibration of physical and rheological properties of the material [1][2]. The correction of the numerical viscosity model applied to the material is the main parameter to calibrate, so the hypothesis of the fresh concrete described as an homogeneous fluid is applied in the screw simulations, as found for a mixer drum [3], a Slump test [4][5][6] or a L-box test [5][7]. This simplification permits to reduce the physical uncertainty only to a rheological calibration. In previous works of the

authors, a study of the working process of a self-loading mixer drum was performed using a CFD model, in which the discharge process and the Slump test have been calibrated using different viscosity models for the fresh concrete simulated as an homogeneous and Newtonian fluid. The same model for the fluid will be applied in the screw simulations for a calibration of the dynamic viscosity value, related to the experimental tests realized.

2. Geometry Analysed

The screw mixer is a machine capable to mix and convey in short time fresh concrete from the feeding to the moulds. The helicoid screw auger is welded to a centre shaft and inserted into a U-shape trough with a wear-resistant rubber bottom. The trough has an outlet spout at one end and two end plates at each through end, while the inlet spot is larger in order to gather the segregated components. The production cycle starts with the feeding of the segregated materials, water, cement and solid aggregates, into the conveyor. The auger is designed to fulfil a satisfying mixing in the first envelope of the screw and, at the same time, to convey the material in the last development towards the discharge, without any change in its speed direction. The analysed mixer (Fig. 1) can be inclined up to 35° from the horizontal plane and the auger can reach a rotational speed up to 200 rpm. The machine is employed directly in the building site, but the following considerations can be made also for simple screw conveyors. The geometry is then prepared from 3D CAD to a finite element discretization. The volume is split into two defined regions, a stationary and a rotating domain. The stationary domain collects the inlet hopper, the trough and the discharge tank, while the rotating domain includes the screw auger and the shaft; between the two domains a rotor-stator interface is set, in order to define the separation of the finite volumes that are rotating or not. The final mesh adopted after a grid sensibility analysis is a hybrid unstructured mesh, made of prismatic, hexahedral and tetrahedral elements, of globally $2.5 \cdot 10^6$ elements (Fig. 2).

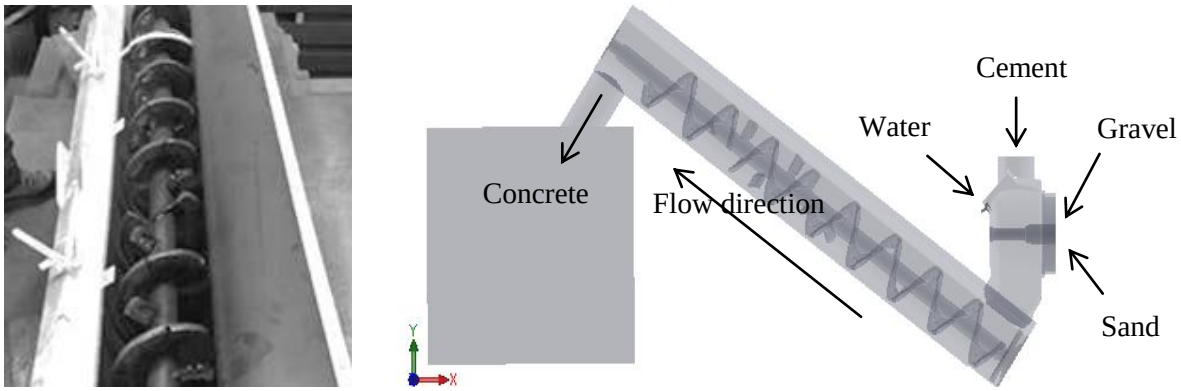

Figure 1: Screw mixer analysed, real geometry (left) and 3D CAD geometry (right).

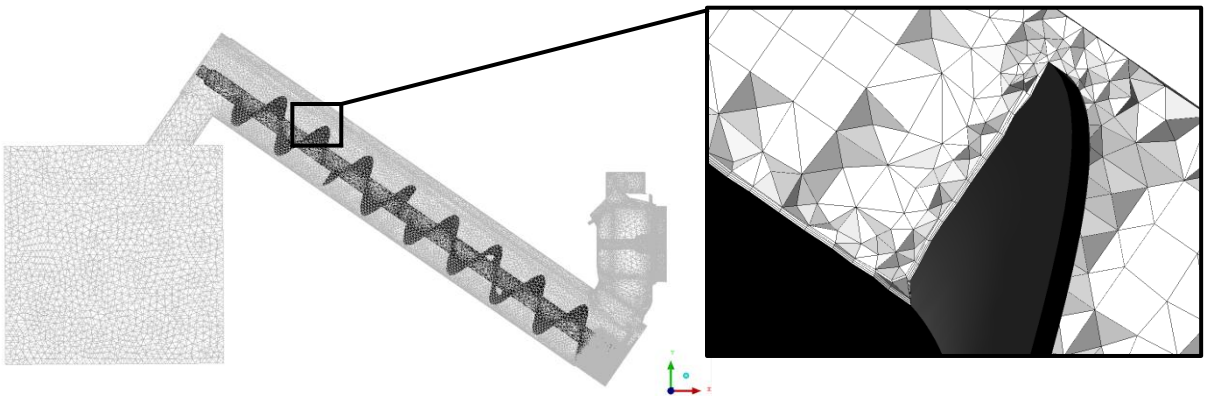

Figure 2: Finite element mesh used for simulations.
The different colours identify the stationary (light) and the rotating (dark) walls.

3. Numerical Model

The numerical simulations are carried out with the commercial CFD code ANSYS CFX, Release 17. The code solves the 3D Reynolds averaged form of the Navier–Stokes equations by using a finite element based finite-volume method. The Eulerian-Eulerian approach, based on the principle of interpenetrating continua, is the most generally used to solve a multiphase flow [8]. The phases, which are each described by its physical properties and its own velocity, pressure, concentration and temperature field, share the same volume and penetrate each other in space exchanging mass, momentum and energy. Two distinct models are available for Eulerian-Eulerian multiphase flow: homogeneous model and inhomogeneous model. In the homogeneous model, the fluids share common fields for flow, temperature and turbulence. In the inhomogeneous model each fluid possesses its own flow field and the fluids interact via interphase transfer terms. This last model is chosen for the following work because of the expected differences between the flows of air and concrete. The main equations in fluid mechanics, for a generic phase α, are derived from conservation of mass (Eq. 1), momentum (Eq. 2) and energy, not simulated for the isothermal hypothesis applied. For every volume element simulated, the sum of the volume fractions of the phases (α, β) has to equal 1 (Eq. 3). The numerical computation involves a discretization in both space and time of the properties of the fluid. The calculated variables are related to the velocity and pressure fields and the materials volume fractions for every discrete element [9].

$$\frac{\partial}{\partial t}\rho_i + \ div(\rho_i \boldsymbol{u}_i) = 0 \tag{1}$$

$$\frac{\partial}{\partial t}(\rho_i \boldsymbol{u}_i) + \ \boldsymbol{u}_i \cdot div(\rho_i \boldsymbol{u}_i) = -\nabla p_i + \ \nabla \overline{\overline{\tau_i}} + \boldsymbol{F}_i \tag{2}$$

$$\sum_{i=\alpha,\beta} r_i = 1 \tag{3}$$

The gravitational field is set, with a buoyancy model based on density difference between air and concrete. For the transient simulation of 45 s total time, a discretization for time stepping

occurs. The time step is set as an adaptive iteration in order to maintain the RMS Courant number below 1 [10]. With these settings, the time step sets around $2.5 \cdot 10^{-3}$ s, resulting in circa $2 \cdot 10^{4}$ time iterations. The following tables (Tab. 1, 2, 3) resume the material properties and the numerical settings implemented as boundary conditions in the simulation. For an analysis of the screw performances, three different inlet flow rates of concrete are simulated: 14, 18 and 22 m^3/h. The inlet flow of the fresh concrete is divided into the surfaces that simulate the real inlets of the different components, water, cement, sand and gravel, into the machine. On the upper surface of the inlet hopper it has been placed an opening, named degassing condition surface. The degassing condition permits the out flow only to the air phase, in order to avoid a pressurization of the domain. The calculation of the Reynolds number gives the laminar flow regime, in which the viscous forces are dominant.

Table 1: Materials properties.

	ρ (kg/m^3)	**μ (Pa s)**	**Thermodynamic State**
Air (Standard)	1.185	$1.831 \cdot 10^{-5}$	Gas
Fresh concrete	2403	150	Liquid

Table 2: Numerical schemes adopted.

Setting	**Value**	**Setting**	**Value**
Advection scheme	High Resolution	Transient scheme	Second Order Backward Euler
Turbulence model	Laminar	Interphase transfer	Mixture Model
Convergence max. coefficient loops	10	Convergence criteria	$5 \cdot 10^{-4}$

Table 3: Constant parameters implemented.

Setting	**Value**	**Setting**	**Value**
Screw rotational speed	200 rpm	Surface tension coefficient	66 mN/m [11]

4. Conclusions and perspectives

The constitutive equation for the simulated fresh concrete is calibrated in relation to the experimental tests of the machine. The tested screw, with a constant inlet bulk flow rate of 18 m^3/h, starts to discharge fresh concrete after approximately 20 s from the insertion of the raw materials. The first result was the correction of the viscosity parameter for the simulated concrete, by measuring the discharge starting time. The model adopted for the concrete viscosity is the Newtonian model. The calibration of the viscosity for the fresh gives satisfying results with a viscosity value of 150 Pa s concrete (Fig. 3). With the calibrated material, the numerical model can simulate the machine performances at different flow rates

of concrete inserted. The following Fig. 4 shows the performances of the machine, by plotting the volume of concrete discharged versus time.

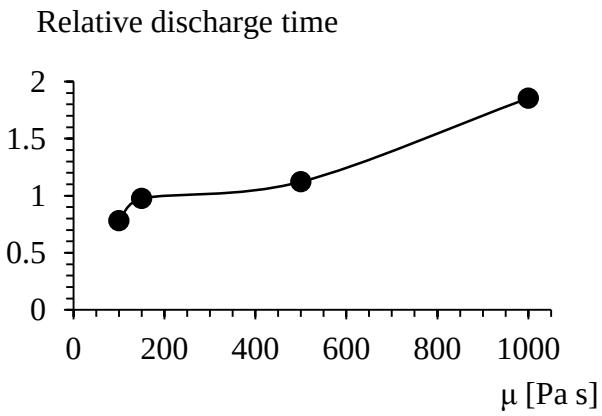

Figure 3: Correction of the viscosity with the starting discharge time, related to the experimental.

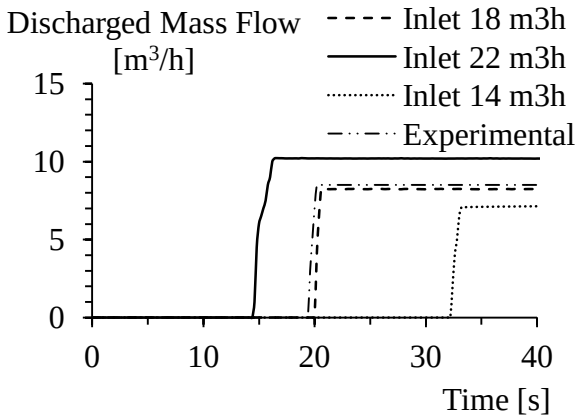

Figure 4: Concrete discharge flow rate versus time.

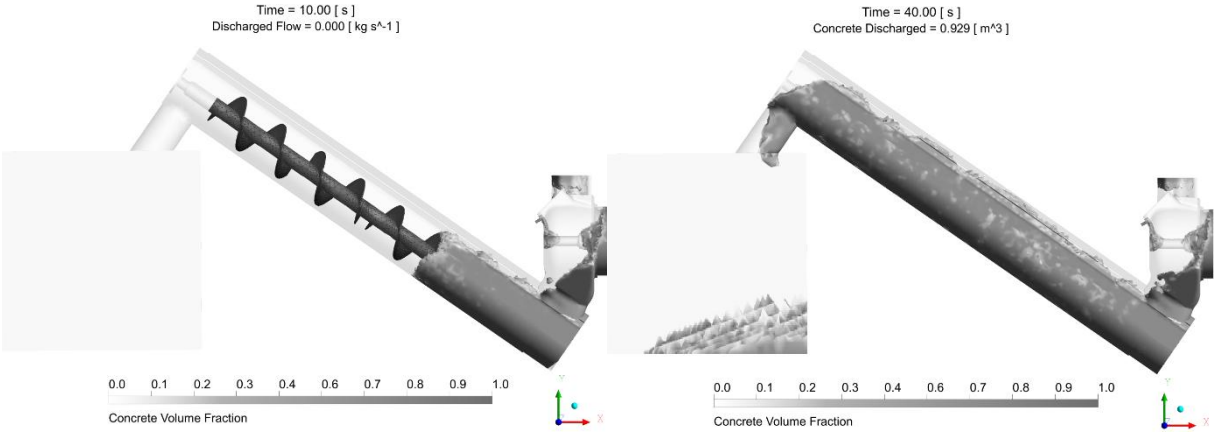

Figure 5: 3D plot of the elaborated concrete in different time steps.

A further improvement of the numerical model will regard the application of a Non-Newtonian Bingham's viscosity model (Eq. 4) to the simulated fluid, as mainly related to the fresh concrete behaviour in the listed references.

$$\tau = \tau_0 + K\dot{\gamma} \tag{4}$$

The difficulties in applying the model is the two-parameter calibration that has to be made with more experimental data available, different from the classical Slump test results, with an iterative calibration on both the yield stress and the plastic viscosity values. For this reason, there is the need to develop a new experimental test method for the characterization of the fresh concrete. The new method should take in account at the same time the centrifugal and the gravitational forces applied on the material, in order to better calibrate the numerical

properties and apply the Bingham's model for future applications of the CFD on industrial machinery for fresh concrete production.

List of symbols

Variable	Description	Variable	Description
α, β	Analysed phase	r_i	Phase volume fraction
ρ_i	Phase density	μ	Newtonian viscosity
$\boldsymbol{u}_i$	Flow velocity	τ	Shear stress
p_i	Pressure	τ_0	Yield stress
$\bar{\bar{\tau}}_i$	Deviatoric stress tensor	K	Bingham plastic viscosity
$\boldsymbol{F}_i$	Total specific energy	$\dot{\gamma}$	Shear rate

References

[1] Patzak, B. et al, Modeling of fresh concrete flow, Computers and Structures 87 (2009), 962-969
[2] Roussel, N. et al, Simulation of fresh concrete flow, RILEM State-of-the-Art Reports 15, Springer (2014)
[3] Wallewik, J. E. et al, Analysis of shear rate inside a concrete truck mixer, Cement and Concrete Research 95 (2017), 9-17
[4] Saak, A. W. et al, A generalized approach for the determination of yield stress by slump and slump flow, Cement and Concrete Research 34 (2004), 363-371
[5] Dufour, F. et al, Numerical modelling of concrete flow: homogeneous approach, Int. J. Numer. Anal. Meth. Geomech. 29 (2005), 395-416
[6] Roussel, N., Correlation between yield stress and slump: Comparison between numerical simulations and concrete rheometers results, Materials and Structures 39 (2006), 501-509
[7] Cremonesi, M. et al, Simulation of the flow of fresh cement suspensions by a Lagrangian finite element approach, J. Non-Newtonian Fluid Mech. 165 (2010), 1555-1563
[8] Enwald, H. et al, Eulerian Two-Phase Flow Theory Applied to Fluidization, Int. J. Multiphase Flow 22 (1996), 21-66
[9] Hiltunen, K. et al, Multiphase Flow Dynamics Theory and Numerics, VTT Publications 722, Edita Prima Oy, Helsinki (2009)
[10] Courant, R. et al, On the Partial Difference Equations of Mathematical Physics, IBM Journal of Research and Development 11 (1967), 215-234
[11] Sahin, Y. et al, Characterization of air entraining admixtures in concrete using surface tension measurements, Cement and Concrete Composites 82 (2017), 95-104

SynerCrete'18 International Conference on Interdisciplinary Approaches
for Cement-based Materials and Structural Concrete
24-26 October 2018, Funchal, Madeira Island, Portugal

FROM DISORDERED TO ORDERED PACKINGS: A NEW PACKING MODEL FOR UHPC?

Gerard Roquier (1)

(1) Laboratoire Navier, France

Abstract

A high efficiency packing model constitutes a key concept in a wide range of concrete. In a binary mixture, the peak shape at the optimum of a packing fraction curve represented as a function of the volume fraction of the fine class does not really exist, due to the compaction which is not optimal: the Compressible Packing Model (CPM) was developed with the introduction of a compaction index *K*. The latter is representative of the packing process efficiency and is one of the three parameters which are taken into account in the original CPM. The two other parameters are the wall effect parameter and the loosening effect parameter. Concerning this last geometrical effect, the cavity size ratio at which the loosening effect appears significantly depends of the coarse particle shape and of their surface roughness. By the introduction of a critical cavity size ratio as the fourth parameter, the CPM has evolved into the 4-parameter CPM. Herein, this model is validated both for application to disordered ternary mixtures of spherical, round aggregate and crushed aggregate particles (from *K=4.7* to *K=15*) and for application to binary crystalline structures of alloys (*K=100*). The 4-parameter CPM appears to be a useful tool for predicting the packing fraction of the granular skeleton in all circumstances. The microstructure of UHPC could be thus optimized by precise gradation of all particles in the mix to yield minimum void ratio.

1. Introduction

Particle packings of many different sizes are often used as structural models for a wide range of concrete. These models usually generalize the case of binary particle packings. Herein, the 4-parameter Compressible Packing Model (CPM), originally developed for predicting the packing fraction of binary mixtures, is validated for ternary mixtures from literature test results for different shape of particles. However, the efficient arrangement of particles inside a packing concerns many sectors in science and industry. One of them is the crystallography. In

this experimental science, many efforts have been made to identify the densest binary sphere packings. In the quest of the highest performance concrete, we wanted to know if the 4-parameter CPM was also efficient in the field of high packing fractions by applying it on binary crystalline structures of alloys.

2. The 4-parameter for binary mixtures

The 4-parameter CPM was originally developed for binary mixtures of spherical particles [1] and crushed aggregate particles [2]. Firstly, the packing fraction is calculated in a virtual reference frame where each particle is placed in its ideal location: this is the virtual packing fraction that characterizes the material. Secondly, the real packing fraction is determined by involving the compaction index *K* that characterizes the packing process efficiency. Let us consider a binary mixture composed of two monosized classes: size classes 1, 2 with diameters d_1, d_2 ($d_1 \geq d_2$). Their volume fractions by reference of the total solid volume are denoted by y_1, y_2 ($y_1 + y_2 = 1$), their real and virtual packing fractions are respectively denoted by α_1, α_2 and β_1, β_2. Let us consider x as the size ratio d_2/d_1. The virtual packing fraction of the binary mixture when size classes 1, 2 are dominant are given by:

$$\gamma_1 = \frac{\beta_1}{1 - \left(1 - \frac{\beta_1}{\beta_2}\, a_{12}\right) y_2} \; ; \; \gamma_2 = \frac{\beta_2}{1 - \left(1 - \beta_2 + b_{21}\, \beta_2 \left(1 - \frac{1}{\beta_1}\right)\right) y_1} \tag{1}$$

where b_{21} is the wall effect parameter and a_{12} the loosening effect parameter.

2.1 Theory about wall effect and loosening effect for spheres

In the virtual reference frame, the wall effect and the loosening effect theory [1] is elaborated on the basis of a coarse or a fine spherical particle belonging to the dominated class and surrounded by dominant class neighbours (Figure 1). A spherical reference cell concentric to the central spherical particle is used for quantifying the two geometrical interactions.

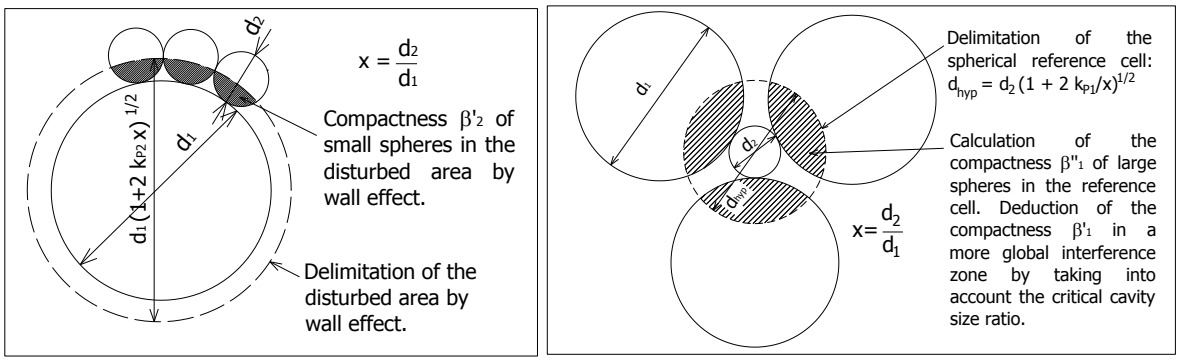

Figure 1: Definition of the spherical reference cells for studying the wall effect (left) and the loosening effect (right)

The packing fraction of the fine particles inside the disturbed volume by the wall effect $\beta'_2(x)$ and the packing fraction of the coarse particles inside the reference cell affected by the loosening effect $\beta''_1(x)$ are calculated on the basis of geometrical considerations by calling

upon the coordination number. The latter is determined by an original method. As part of the dense virtual packings [1], the Spherical Square Model (SSM) highlights two remarkable achievements in the field of crystalline packings of spherical particles. Indeed, for the loosening effect theory, the number of coarse spherical particles against a small one is deduced from the following mathematical expression:

$$N_{21,SSM}^{dense}(x) = \frac{\pi(1+x)}{arcsin\left(\frac{1}{(1+x)}\right)} \quad (2)$$

Firstly, $N_{21,SSM}^{dense}(1) = 12$: it means that 12 spherical particles can touch a central spherical particle with the same diameter. It corresponds to the answer of the famous kissing number problem in three dimensions. Secondly, $N_{21,SSM}^{dense}(0.222) = 4$: it means that 4 coarse spherical particles, whose centers constitute the vertex corners of a regular tetrahedron, can be in contact with a small central particle with a size ratio of 0.222. This value is in very close agreement with the tetrahedral cavern theory $\left(x_0 = \frac{(\sqrt{3}-\sqrt{2})}{\sqrt{2}} \approx 0.2247\right)$ [2]. The critical cavity size ratio x_0 has been introduced as the fourth parameter in the present theory to study all types of aggregate particles. When $x \leq x_0$: the loosening effect does not occur. When $x > x_0$, the loosening effect occurs.

2.2 Influence of the compaction index *K*

The real packing fraction ϕ^* of aggregate particles directly depends of the packing process. In the 4-parameter CPM, to reach the maximum packing fraction value, each particle should be placed one by one in a determined manner: it corresponds to the virtual packing fraction. The latter takes into account the intrinsic characteristics of the material: state of particle surfaces and morphology. The link between the virtual packing fraction and the real packing fraction of the mixture is provided through the compaction index *K*. This scalar value is of the following form to guarantee the self-consistency of the model:

$$K = \frac{\frac{y_1}{\beta_1}}{\frac{1}{\phi^*} - \frac{1}{\gamma_1}} + \frac{\frac{y_2}{\beta_2}}{\frac{1}{\phi^*} - \frac{1}{\gamma_2}} \quad (3)$$

K has been calibrated from the analysis of 654 packing fractions [1,2] measured on binary mixtures under different packing process conditions (Table 1).

Table 1: Compaction index *K*

Packing process	Pouring	Vibration or compaction	Vibration + compression	Optimized filling + vibration + compression	Crystalline structures
K	**4.7**	**5.6**	**9**	**15**	**100**

Let us consider a monodisperse system with $\alpha_1 = \alpha_2 = \alpha = 0.64$. The influence of K on the packing fraction of a binary mixture is represented in Figure 2 for a size ratio $x = 0.2$ and, for example, for a critical cavity size ratio $x_0 = 0.1$.When K tends to infinity, the representative

curve reveals a peak shape at the optimum. In contrast, the peak shape reduces significantly as the packing process becomes less efficient.

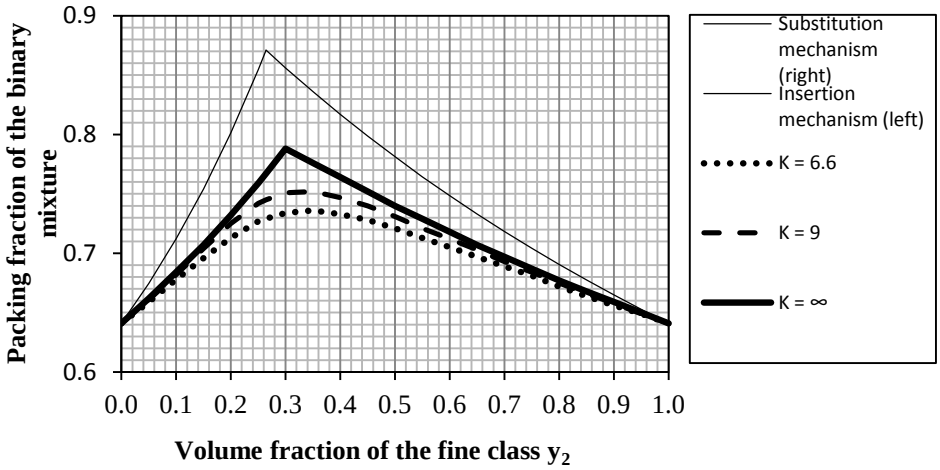

Figure 2: 4-parameter CPM – Influence of the compaction index *K* on the packing fraction - $\alpha_1=\alpha_2=0.64 - x = 0.2 - x_0 = 0.1$

2.3 Influence of the critical cavity size ratio x_0

Experimental results show that the cavity size ratio at which the loosening effect occurs depends of the coarse particle shape and of their surface roughness [2]. The chosen way consists in calibrating only one parameter, the critical cavity size ratio x_0: from $x_0 = 0$ for irregular particles with strong surface roughness to $x_0 = 0.2$ for frictionless spherical particles. In Figure 3, the theoretical influence of x_0 on the packing fraction of binary mixtures is represented for a size ratio $x = 0.2$.

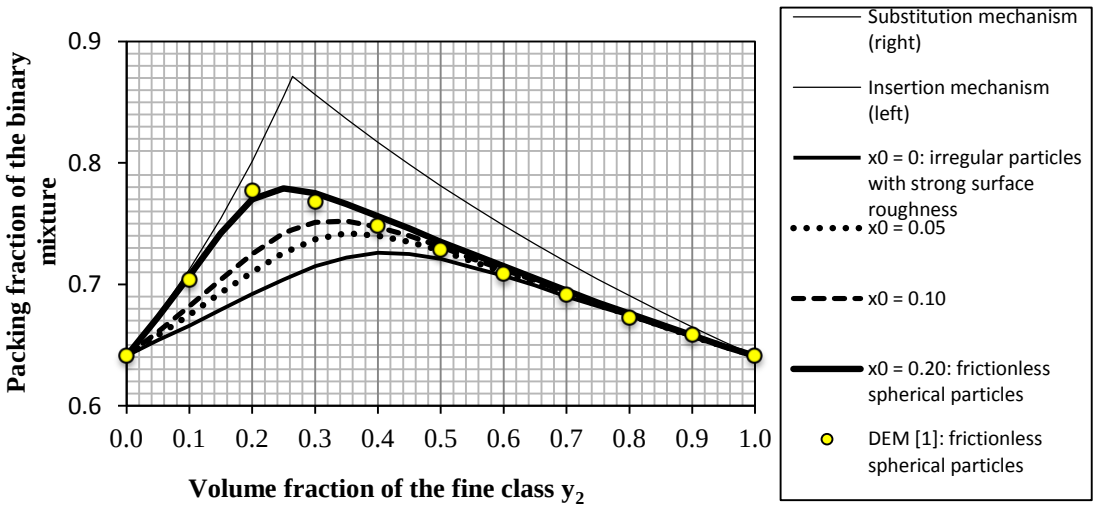

Figure 3: 4-parameter CPM – Influence of the critical cavity size ratio x_0 on the packing fraction - $\alpha_1=\alpha_2=0.64 - x = 0.2 - K = 9$

3. Packing fraction: from non-crystalline to crystalline binary structures

In the 4-parameter CPM, ordered and very packed piles of spherical particles are used as the virtual reference frame. This suggests the opportunity of studying various particle structures thanks to the compaction index K: from non-crystalline to crystalline ones. For a high value of K, the 4-parameter CPM is expected to be valid for the structures of alloys: the densest binary sphere packings, as A.B. Hopkins *et al.* called them [3]. Let us examine the predictions of the 4-parameter CPM for $K = 100$ and $\beta = 0.711$ at the optimum of each packing fraction curve for a wide range of size ratios: from 0.217 to 0.497, including 0.225 which corresponds to the tetrahedral cavern theory.

Table 2: Comparison between the 4-parameter CPM predictions for $\beta=0.711$, $K=100$ and the selected densest binary alloy packing fractions (AAPE: Average Absolute Prediction Error)

Binary Alloy	(11-1)	(10-1)	(6-1)$_{10}$	(6-1)$_{4,6,8}$	(6-6)	(7-3)	(5-2)	(4-2)	(2-2)	**Overall**
Size ratio x	**0.217 to 0.220**	**0.225 to 0.270**	**0.264 to 0.292**	**0.295 to 0.352**	**0.414 to 0.457**	**0.468 to 0.480**	**0.480 to 0.483**	**0.480 to 0.488**	**0.480 to 0.497**	
Number of values	**2**	**14**	**11**	**21**	**16**	**5**	**2**	**4**	**7**	**82**
AAPE	**0.93%**	**2.03%**	**1.89%**	**0.72%**	**1.42%**	**0.15%**	**0.60%**	**0.45%**	**0.46%**	**1.17%**

Let us compare them with those of [3] (Table 2): the agreement is good, the Average Absolute Prediction Error (AAPE) being 1.17% for 82 packing fraction values. Further validations are required but the field of binary sphere packings is so complex that the development of a packing fraction model able to provide accurate predictions for both disordered assemblies of particles and crystalline structures appears to be well launched.

4. Packing fraction for ternary mixtures

Table 3: Average Prediction Error (APE) and Average Absolute Prediction Error (AAPE) characterizing the three models tested on packing fractions obtained on ternary mixtures

Types of particles	**Packing fractions data**	**Statistical indicators**	***PAL model***	***3PPM***	***4-parameter CPM***
Spherical particles (117 data)	**Ridgway, Tarbuck [4]: 30 data**	*APE*	-0.38%	-1.62%	***-0.10%***
		AAPE	***0.52%***	1.62%	***0.52%***
	Jeschar et al. [5]: 66 data	*APE*	1.73%	-0.63%	***-0.11%***
		AAPE	2.27%	0.78%	***0.73%***
	Standish, Borger [6]: 21 data	*APE*	-3.32%	-4.34%	***-1.17%***
		AAPE	3.32%	4.34%	***1.22%***
Round aggregate particles (66 data)	**Westman, Hugill [7]: 66 data**	*APE*	5.58%	-0.34%	***0.19%***
		AAPE	5.60%	1.05%	***1.03%***
Crushed aggregate particles (66 data)	**Goltermann et al. [8]: 66 data**	*APE*		-1.13%	***-0.07%***
		AAPE		1.51%	***1.16%***

The 4-parameter CPM is now going to be evaluated from 249 packing fraction results obtained on ternary mixtures. The compaction index K has been adjusted to the different packing processes involved. The critical size ratio x_0 has been optimized for each set of aggregate data. The 4-parameter CPM predictions are compared with those of the 3-parameter Particle Packing Model (3PPM) elaborated by V. Wong, A.K.H. Kwan [9] and those of the PAL (J.M.V. Prior, I. Almeida, J.M. Loureiro) model [10]. The 4-parameter CPM provides the most consistent predictions (APE range from -1.17% to -0.10%) for the spherical particles with a single value of the critical cavity size ratio x_0 ($x_0 = 0.2$), is really accurate for the round aggregate particles ($APE = 0.19\%$), and is very efficient for the tested crushed aggregate particles ($APE = -0.07\%$).

5. Conclusion

With the incorporation of the compaction index and the critical cavity size ratio, it is found that the 4-parameter CPM can predict the packing fraction of both binary crystalline structures and ternary mixtures of mono-sized spherical particles, round and crushed aggregate particles. The open way in the field of high packing fractions and in the field of ternary mixtures suggests the possibility of studying the high packing fraction polydisperse mixtures. Thus, the 4-parameter CPM could be employed in optimization algorithms for the design of UHPC.

References

[1] Roquier, G., The 4-parameter Compressible Packing Model (CPM) including a new theory about wall effect and loosening effect for spheres, Powder Technol. 302 (2016) 247-253
[2] Roquier, G., The 4-parameter Compressible Packing Model (CPM) for crushed aggregate particles, Powder Technol. 320 (2017) 133-142
[3] Hopkins, A.B., Stillinger, F.H., Torquato, S., Densest binary sphere packings, Phys. Rev. E, 85(2) (2012) 021130
[4] Ridgway, K., Tarbuck, K.J., Particulate mixture bulk densities, Chem. Process Eng. , 49(2) (1968) 103
[5] Jeschar, R., Potke, W., Petersen, V., Polthier, K., Blast Furnace Aerodynamics, In: Proceedings of the symposium on blast furnace aerodynamics (1975) 25-27
[6] Standish, N., Borger, D.E., The porosity of particulate mixtures, Powder Technol. 22(1) (1979) 121-125
[7] Westman, A.E.R., Hugill, H.R., The packing of particles, J. Am. Ceram. Soc. 13.10 (1930) 767-779
[8] Goltermann, P., Johansen, V., Palbøl, L., Packing of aggregates: an alternative tool to determine the optimal aggregate mix, Materials Journal 94(5) (1997) 435-443
[9] Wong, V., Kwan, A.K.H., A 3-parameter model for packing density prediction of ternary mixes of spherical particles, Powder Technol. 268 (2014) 357-367
[10] Prior, J.M.V., Almeida, I., Loureiro, J.M., Prediction of the packing porosity of mixtures of spherical and non-spherical particles with a geometric model, Powder Technol. 249 (2013) 482-496

SynerCrete'18 International Conference on Interdisciplinary Approaches
for Cement-based Materials and Structural Concrete
24-26 October 2018, Funchal, Madeira Island, Portugal

HOW DOES THE SIZE OF AGGREGATES AFFECT PERMEABILITY OF DAMAGED CONCRETE?

Marta Choinska [(1)], Stéphanie Bonnet [(1)], Aurélie Fabien [(1, 2)], Hayder Al-Khazraji [(1, 3)], Abdelhafid Khelidj [(1)]

(1) Institut de Recherche en Génie Civil et Mécanique GeM, Université Bretagne Loire, Université de Nantes, Saint-Nazaire, France
(2) ESITC Caen, Épron, France
(3) Missan University, Engineering College, Iraq

Abstract
This experimental study concerns impact of aggregate size on mechanical behavior and gas permeability of concrete. The work has been carried out using three types of materials: a microconcrete, a concrete and a macroconcrete, all with the same water-to-cement ratio, as well as the same aggregate volume fraction. Specimens of the formulated materials have been submitted to controlled uniaxial compression cycles or to indirect tensile in the Brazilian splitting test, till certain damage levels. Gas permeability have then been measured on damaged specimens, after unloading for specimens loaded in compression, and during loading for specimens loaded in indirect tension. For the latter, a special lab-made device has been developed to control tensile loading in the pre-peak and the post-peak phases and to measure gas transfer during loading. For all the tested materials, the results emphasize that compressive and tensile strengths decrease and gas permeability increases, when aggregate size increases, independently on the cement type, CEM I or CEM III. Moreover, the obtained results highlight that the effects of tensile or compressive damage on permeability may be separated from the effects of aggregate size by two distinct functions. This behaviour, independent on cement type, represents a strong advantage for concrete modelling.

1. Introduction

In quasi-brittle materials, like concrete, fracture exhibits a finite size process zone. The size of this zone is not dependent on the structural size, but is controlled by local heterogeneity parameter (aggregate size) and concrete behaviour yields therefore size effects [1, 2]. It is

important to characterise these effects in order to correlate laboratory test results with structural behaviour. In fact, two approaches may be employed to investigate this issue: the first one, based on the change of the specimen size for the same material, and the second one, based on the change of the aggregate size for the same specimen size. The authors of this work propose to study the effects of the aggregate size on concrete mechanical and mass transfer behaviour, as far as the literature review presents important scatter concerning this issue. Indeed, the remark of Wolinski et al. [3] is still relevant: « Obviously, the test data with respect to the influence of the aggregate size on the tensile behaviour of concrete are conflicting ». Let's mention, for example, the work of Hillerborg [4] who concluded that there is a tendency for fracture energy to increase, while the maximum aggregate size increases. The same tendency was noticed by Bazant and Oh [5]. However, Petersson [6] reported that the fracture energy does not seem to be affected by the maximum particle size. Bisschop and van Mier [7] observed drying shrinkage microcracking increase in cement-based composites with spherical glass aggregates size and with volume percentage increases. Szczesniak et al. [8] noticed a great correlation between spherical glass aggregate diameter and compressive strength: the latter decreases when aggregate size increases. However, Rao and Prassad [9] observed the opposite effect for tensile behavior. Currently, opinions still differ on outcomes because many parameters must be taken into account. Besides, there are very few results in the literature review regarding the effects of the aggregate size on the concrete mass transfer. Grassl et al. [10] pointed out that the concrete permeability increases with the increasing of crack width and with the aggregate diameter. Moreover, permeability increase with cracking appears to be amplified under loading [11].
In view of these results, this work has therefore two main objectives: the first one concerns the effects of aggregate size on mechanical behavior and permeability and the second one is focused on the evolution of permeability with mechanical compressive and tensile loading. The authors use experimental methods to investigate these issues.

2. Experimental program

2.1 Materials

For the sake of simplicity, experimental study has been restricted to dry materials with mix proportions given in Tab. 1. All the materials have the same water-to-cement ratio, equal to 0,48, as well as the same aggregate volume fraction, equal to 66% of the total volume. All the aggregates are crushed limestone. In order to investigate aggregate size effect on mechanical and transport properties, three types of formulations have been proposed: microconcrete, concrete and macroconrete. Microconcrete contains sand and medium size aggregates, two concretes contain sand, medium and coarse size aggregates and macroconcrete contains sand and coarse size aggregates only, following to the grading curves of aggregate mixes presented by Fabien et al. [12].
Cylindrical specimens (diameter of 11 cm, length of 22 cm) of microconcrete, concrete and macroconcrete have been prepared from single batches and cast in PVC rigid moulds. 24 h after casting, they have been stored in a room maintained at 20°C with a 95% relative humidity, and then cured in water at 20°C for at least 4 weeks for the CEM I materials and 3 months for the CEM III ones, what permit to stabilise mechanical strengths. After the storage in water, a part of the cylinders have been damaged in compressive tests, then all the cylinders

have been cut using a diamond blade saw in order to obtain "disc" specimens (diameter of 11 cm, length of 5 cm) within each cylinder. "Disc" specimens have been dried at 80°C over 2 weeks, then at 105°C down to constant mass to permit permeability tests. The latter have been performed on the sound and on the compressive-damaged materials, as well as at the tensile-damaged materials under loading, using a specially developed set-up.

Table 1: Microconcrete, concrete and macroconcrete constituents and mix proportions.

Ingredients	**Quantity (kg/m^3)**		
	Microconcrete	**Concrete**	**Macroconcrete**
Cement CEM I 52.5 PM ES or CEM III/A 52.5 PM ES	350	350	350
Sand 0-4mm	868	868	868
Medium aggregate 4-12mm	1009	432	-
Coarse aggregate 12-20m	-	561	981
Water	168	168	168
Superplasticizer (solid content 20%)	1.71	1.71	1.71

2.2 Compressive damage and permeability test methods

A part of the specimens have been loaded using cyclic uniaxial compression test. This method permits to generate uniform damage as already shown by other researchers [13]. The tests were performed under load control with a hydraulic loading frame. The loading and unloading rate was kept constant and equal to 2 kN/s. The specimens have been instrumented using three axial and one circumferential extensometers. Three levels of loading, corresponding to 30%, 60% and 80% of the compressive strength have been applied to the specimens. At 30 and 60%, six loading-unloading cycles were applied to the specimen, and at 80%, only three cycles were applied in order to avoid any damage of extensometer equipment.

In order to evaluate the intrinsic permeability of a concrete specimen, a gas permeability device was used. It was equipped with a permeability cell based on the Cembureau one [12]. The tests have been performed using an inert gas (dry nitrogen, N2). In order to ensure a uniaxial flow of the gas and to prevent any gas leakage, the lateral face of each cylindrical specimen has been protected by an aluminum film and a specimen is placed in a fitted collar and then confined during the tests (0,5 MPa). A gas was injected at the lower surface of a specimen at a pressure ranging between 0,3 and 0,1 MPa (relative values), the upper side of a specimen being at the atmospheric pressure. The injection pressure has been applied and maintained until gas flow stabilization. Apparent permeability value for each injection pressure was determined following to French standards XP P18-463 and the intrinsic permeability was calculated using Klinkenberg's regression of the apparent permeabilities.

2.3 Tensile loading-permeability test method

For many years, our lab (GeM) has been working and developing coupled mechanical and permeability tests. The authors developed [14] a tensile loading - gas permeability set-up, based on indirect tension in the Brazilian splitting test (compression in the diameter plane). The principle of this test is to perform gas permeability measurements during loading, for different levels of controlled cracking in the pre-peak and post-peak phases, using a "disc"

specimen loaded in the Brazilian splitting test. This test presents the advantage of forming a single crack, parallel to the loading direction, where openings may be measured at one or two sides of a specimen, using f.ex. a CMOD sensor (crack-mouth opening displacement) as a feedback signal during the test. The new modified "double" device is presented in Fig. 1. It includes two aluminium cells: one placed on the up-stream side and the second one on the down-stream side, each one fitted with a CMOD sensor, called COD 1 and COD 2. The 250 kN MTS loading cell is employed within a hydraulic loading frame CFM / MTS 1000 kN. Gas pressure and flow rates are measured at the up-stream and at the down-stream and the feedback signal of the tensile test corresponds to the mean COD value between COD 1 and COD 2, in the pre-peak and in the post-peak phases.

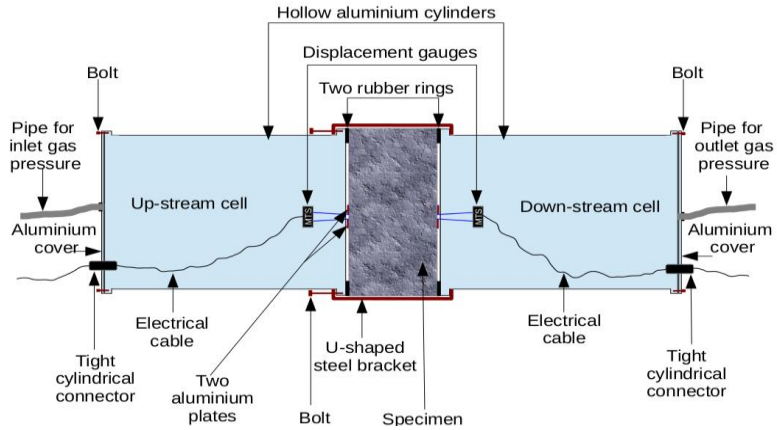

Figure 1. Upper section view of the "double" loading-permeability device (GeM).

3. Results and discussion

Results emphasized a general tendency: compressive and tensile strengths slightly decrease with aggregate size increase. The opposite is noticed for the permeabilites of the sound materials. The competition between the specific surface effects and the restrained shrinkage effects, acting in the opposite ways, lead to the observed tendencies, independent on the cement type, CEM I or CEM III.

Following the analysis proposed by Picandet et al. [15], it is more consistent, in the pre-peak phase, to record the evolution of the permeability with compressive damage instead of the strain or stress. We follow here this procedure and compressive damage is determined as an initial elastic modulus loss for each loading level. The obtained results highlight higher damage for the boths macroconcretes (CEM I and CEM III) in comparison to the microconcretes and concretes (see Fig. 2 (a)). The evolution of a relative permeability (the measured permeability divided by the initial permeability of the sound material) versus compressive damage of the specimens, presented in Fig. 2 (b), exhibits a non-linear increase, common to all the specimens tested. One may therefore imagine that the contributions of the damage on concrete permeability evolution may be therefore separated from the effects of the aggregate size.

Concerning the tensile loading-permeability tests, the study was restricted to 4 materials: the microconcrete, the concrete and the macroconcrete CEM I and the concrete CEM III. Fig. 3

(a) plots the experimental results obtained on the CEM I materials during tensile cracking. Here, permeabilities are reported to the permeability of the CEM I concrete (equal to 3,6.10-17m²). Moreover, one may observe that permeability increase with cracking is amplified by the aggregate size. Fig. 3 (b) plots a relative permeability evolution for all the tested specimens and materials (with 2 different cements) during tensile cracking. Once again, one may observe that all the results fall on the same master curve, function of the permeability reported to the initial one of each material, and to the COD reported to the peak COD at the failure side. These results assume that a relative permeability evolution follows a single sigmoid law, independently to other parameters. Therefore, one may say that the permeability increase due to tensile cracking may be separated from the aggregate size effect.

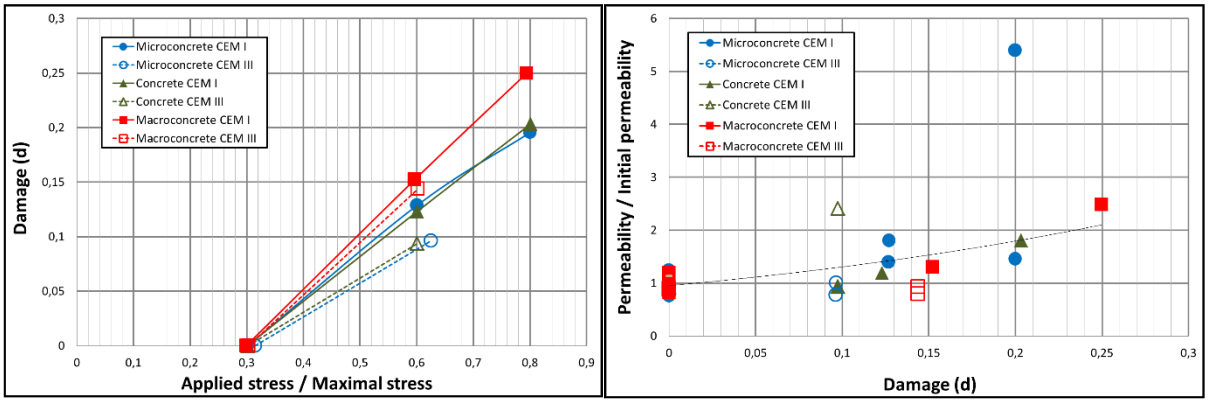

Figure 2: (a) Compressive damage evolution with loading level. (b) Relative permeability evolution with compressive damage.

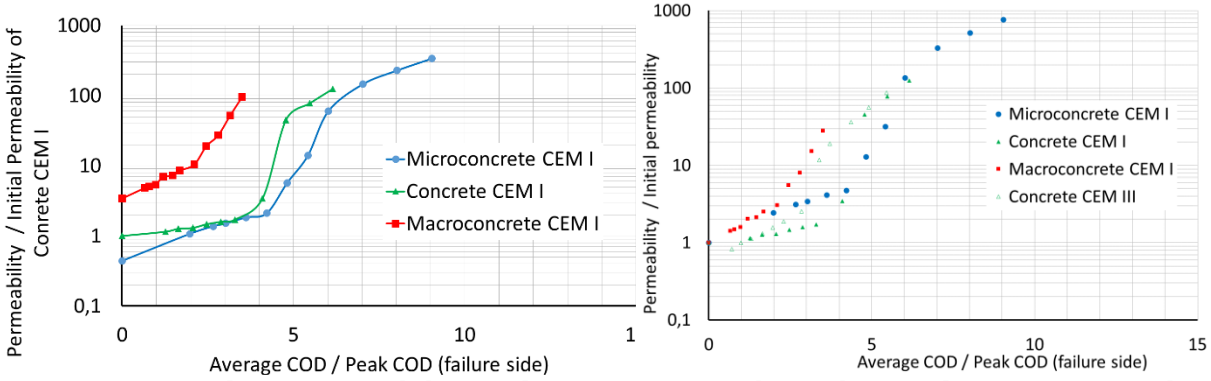

Figure 3: (a) Relative permeability evolution versus tensile cracking and aggregate size. (b) Another relative permeability evolution versus tensile cracking.

4. Concluding Remarks

The results reported in this study can be summarised as follows:

- The developed testing methods and materials permit to highlight the effects of aggregate size on concrete mechanical behaviour and its gas permeability. An original device has been developed to evaluate crack opening simultaneously to gas permeability.
- Permeability increases not only with the compressive or tensile damage, but also with the aggregate size, independently on the cement nature.

- Permeability increase versus tensile cracking, represented by a crack-mouth opening displacement, follows a sigmoid curve, already observed for the compressive tests [11]. Three regimes with different rates may be distinguished for this sigmoidal evolution, depending on crack connectivity and geometry.
- Results highlight that the overall evolution of a relative permeability versus compressive or tensile damage follows a single law for all the materials tested. The effects of cracking and of aggregate size may therefore be separated by two distinct functions.

References

[1] Bazant, Z., Introduction aux effets d'échelle sur la résistance des structures, Lavoisier, Paris (2004)
[2] Pijaudier-Cabot, G. et al, Non local damage models with evolving internal length: motivations and applications to coupled problems, FraMCos 5 (2004), 531-538
[3] Wolinski, S. et al, Influence of aggregate size on fracture mechanics parameters of concrete, Int. J. of Cem. Comp. and Lightweight Concrete 9(2) (1987), 95-103
[4] Hillerborg, A. A., Results of three comparative test series for determining the fracture energy G_f of concrete, Materials and Structures 18 (1985), 33-39
[5] Bazant, Z. P. and Oh, B. H., Crack Band theory for fracture of concrete, Materials and Structures 16 (1983), 155-177
[6] Petersson, P.E., Fracture energy of concrete: practical performance and experimental result, Cem. Concr. Res. 10 (1980), 91-101
[7] Bisschop, J. and Van Mier, J.G.M., Effect of aggregates on drying shrinkage microcracking in cement-based composites, Materials and Structures 35 (2002), 453-461
[8] Szczesniak, M. et al, Compressive strength of cement-based composites: Roles of aggregate diameter and water saturation degree, Cem. Concr. Compos. 37 (2013), 249-258
[9] Rao, G. A. and Prasad, B. R., Fracture energy and softening behavior of high-strength concrete, Cem Concr Res. 32 (2002), 247-252
[10] Grassl, P. et al, Influence of aggregate size and volume fraction on shrinkage induced micro-cracking of concrete and mortar, Cem. Concr. Res. 40(1) (2010), 85-93
[11] Choinska M. et al, Effects and interactions of temperature and stress-level related damage on permeability of concrete, Cem. Concr. Res. 37 (2007), 79-88
[12] Fabien, A. et al, Experimental Study of Aggregates Size Effect on Strain, Damage and Permeability of Concrete, Key Engineering Materials 729 (2017), 115-121
[13] Saito, M. and Ishimori, H., Chloride permeability of concrete under static and repeated compressive loading, Cem. Concr. Res. 25(4) (1995), 803-808
[14] Choinska, M. et al, How to extract a crack opening from a continuous damage finite element computation? Application for the estimation of permeability, ISTE – Wiley, GeoProc 2008, Lille, France (2008)
[15] Picandet, V. et al, Effect of axial compressive damage on gas permeability of ordinary and high-performance concrete, Cem. Concr. Res. 31(11) (2001), 1525-1532

SynerCrete'18 International Conference on Interdisciplinary Approaches
for Cement-based Materials and Structural Concrete
24-26 October 2018, Funchal, Madeira Island, Portugal

IMPACT OF DRYING RATE ON DELAYED STRAINS IN CEMENT-BASED MATERIALS

Justin Kinda [1,2], Laurent Charpin [1], Jean-Luc Adia [1], Farid Benboudjema [2], Sylvie Michel-Ponnelle [3]

(1) EDF R&D MMC, France
(2) LMT, ENS Paris-Saclay, France
(3) EDF R&D ERMES, France

Abstract
A part of the concrete containment buildings (CBB) in French nuclear power plants operated by EDF are double-walled CBBs. The concrete of the post-tensioned inner containment building plays a major role as a barrier against radiological release during a hypothetical accident. The leak-tightness of the inner CCB depends vastly on the pre-stress. If it is too low due to pre-stressing cable relaxation or concrete creep and shrinkage, some parts of the concrete might experience tension during the integrated leak rate test (performed every 10 years) or an accident, inducing cracking and an increased leakage.
Therefore, EDF builds simulation tools dedicated to the prediction of strains in CCBs, which requires properly calibrated models.
Most of the time models are calibrated on laboratory test on rather small samples, while CCBs are very large structures. These different concrete thicknesses induce vastly different drying kinetics. Thus, the concrete constitutive laws should be able to correctly take into account the effect of the rate of drying on the delayed strains (creep, shrinkage) of concrete.
As an introduction to this subject, it has been decided to work on the experimental data provided by literature.
The set of experimental data is first simulated with a delayed strains law used at EDF R&D [2]. Second, the microprestress-solidification law [3] (which was implemented for this purpose) is used.
It is shown that both these constitutive laws can reproduce the main features of the shrinkage and creep tests, but also that the experimental program lacks some information to be truly discriminant. This motivates further experimental developments which will be undergone in the future.

1. Introduction

In the present paper, two delayed strain models are used to simulate the experimental data by Day [1], in which mass loss, shrinkage and creep strains were measured on thin cement paste samples for two drying rates.- The final goal is to verify if those models are able to reproduce the creep and shrinkage for these different experimental conditions. -
To do so, for each model, we used the same set of parameters to reproduce the experimental curves, regardless of the rate of drying.
First the models are briefly presented. Then, the experimental set up is explained. Finally the simulation results are shown and conclusions are drawn.

2. Delayed strain model description

2.1 EDF model

The model was originally developed for EDF R&D by F. Benboudjema [4]. It was later modified to better reproduce basic creep in long term following ideas from [5] and [6]. The material was assumed to be viscoelastic. Under such assumption, the total strain is considered as the sum of four main contributions: elastic strain, drying shrinkage, basic creep and drying creep. A detailed description of the model can be found in [2]. The basic creep compliance is based on a Burgers unit as show on Figure 1, left.

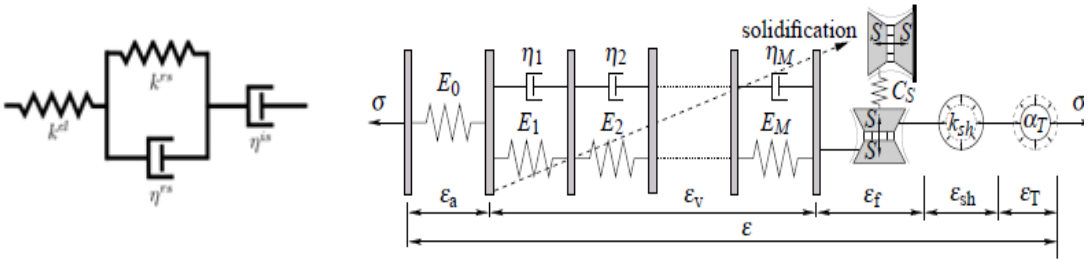

Figure 1– Left: Burgers unit of EDF model (spherical part)[2]. Right: Rheological scheme of the complete hygro-thermo-mechanical MPS model [3].

2.2 Microprestress-solidification (MPS) model

The second model (Figure 1 right) was published in [3]. The model was formulated within the framework of viscoelasticity, hence the principle of superposition is applied and the behavior of is captured by compliance function J (strain under unit stress). The model is based on three main phenomena: aging of concrete (short term chemical aging, long term aging), drying creep effect and transitional thermal creep. For more details, refer to [3].
The model was recently implemented in MFront (tfel.sourceforge.net), and coupled with Code_aster, the finite element simulation tool used developed at EDF R&D (www.code-aster.org).

3. Experimental Data

Results from tests performed by Day [1], on thin cement paste specimen are used here. The experiments were conducted on S-shaped thin specimens, to avoid cracking induced by drying. The S-shaped specimens are 1.9 mm thick (see Figure 2).

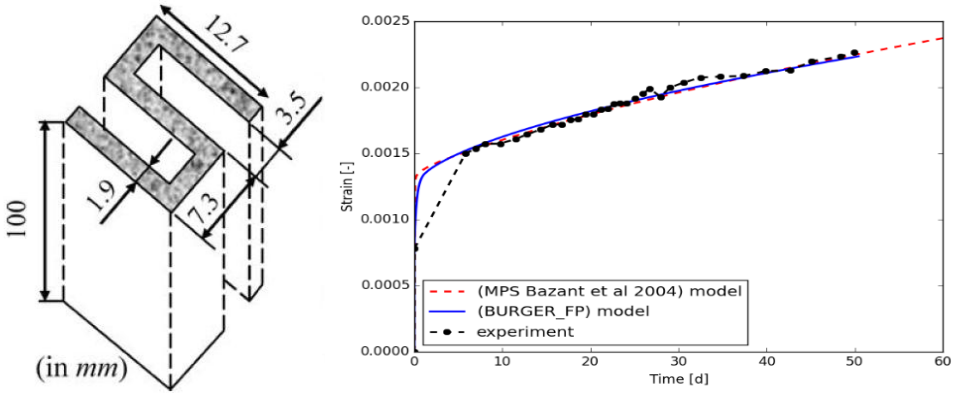

Figure 2: Left: S-shaped specimen [1], Right: Basic creep.

The specimens were loaded by means of miniature, hydraulically controlled, creep rigs. A compressive load of 11.6 MPa was applied, 75 days after casting. The specimens were exposed to two different drying rate. The humidity reduction starts 7 days after loading; it was made between 100% and 53% RH (See Figure. 3). by using saturated magnesium nitrate. For more details, refer to [1].

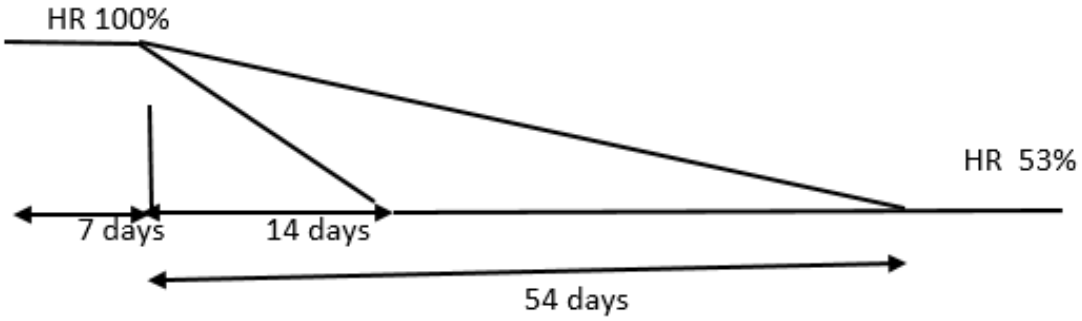

Figure 3: Humidity control, two rates of drying.

4. Simulations

The basic creep parameters have been identified first. In the case of drying, a full water transport analysis is necessary. In this study, the water content evolution was supposed to be homogenous in the specimen, due to lack of sufficient information on the imposed relative humidity and on the desorption isotherm of the material. Under this assumption, which will be

discussed later, the parameters identification have been performed by a least square method implemented thanks to the Python function scipy.optimize.fmin.
The parameters associated to the identification using the EDF model on the slow rate test are: for basic creep, κ^{rd} = 1.946 10^{10} Pa, η^{id} = 1.050 10^{14} (Pa.s), η^{rd} =3.677 10^{14} (Pa.s), α = 0.423, κ^{shr} =1.617 10^{-5} m^3/Kg for drying shrinkage and η^{fdd} = 1.071 10^{9} (Pa.s) for drying creep. For MPS model, fits have been obtained using the following optimum values of the parameters: $q_1 = 9.482998\ \ 10^{-5}$/MPa, $q_2 = 2.747752\ \ 10^{-4}$/MPa, $\alpha = 1.601378\ \ 10^{-3}$, $c = 1.164680\ \ 10^{-9}$/ (MPa.day).

The simulation results are presented below for both models, first for basic creep, secondly for drying shrinkage (slow and fast rate) and finally for drying creep. The parameters calibration for basic creep went well (see Figure 2), but in case of drying, the parameters calibrated on slow drying rate, could not be used to fit fast rate drying experimental data (see Figures 4,5). Was the assumption on homogenous water content in the specimen valid? Apparently not. The difference between the experimental and calculated results might come from this assumption.

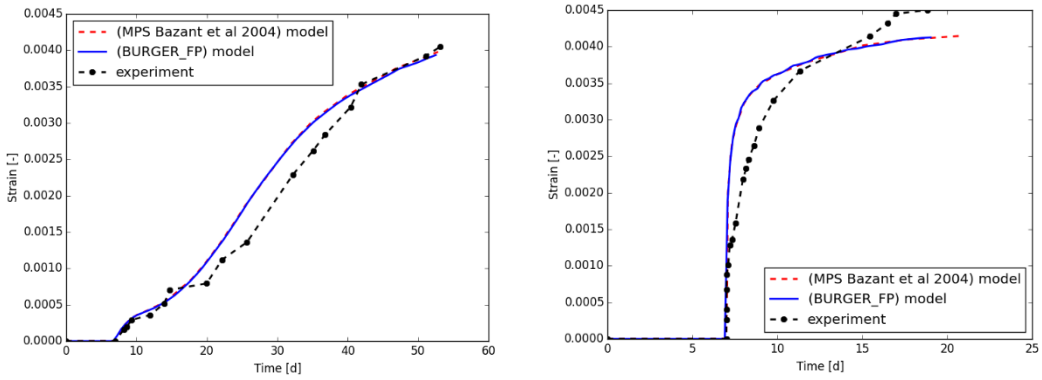

Figure 3 - Left: slow drying shrinkage calibration, Right: Fast drying shrinkage simulation.

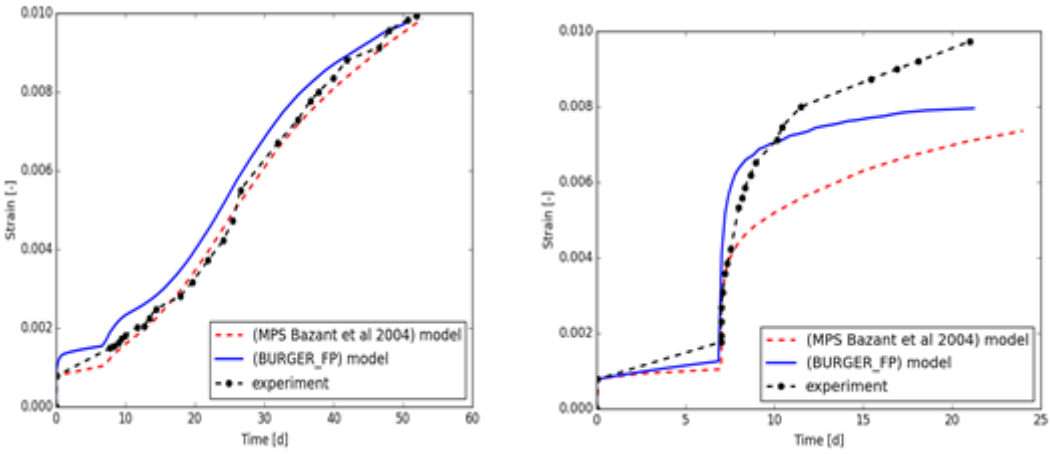

Figure 4- Left: slow drying creep calibration, Right: fast drying creep simulation.

Figures 4, 5 show how strongly, the rate of drying affects the delayed response of the material, but does the final value of drying creep still the same regardless of the rate of drying? That still is an open question.

5. Conclusions

The prediction of delayed strains in large structures such as CCB, requires models that correctly take into account the rate of drying. In this work, It is shown that both constitutive laws can reproduce the main features of the shrinkage and creep tests. The MPS model seems to underestimate drying creep in the case of fast drying. The experimental program is also shown to lack some information to be truly discriminant. This motivates further experimental developments which will be undergone in the future. Then, more calculations combining different RH/water content related to creep coefficient, shrinkage and cracking would be performed, to understand this phenomenon.

Acknowledgements
This work has been funded by EDF R&D, France

References

[1] Day, R.L., Cuffaro, P., and Illston, J.M., The effect of rate of drying on the drying creep of hardened cement paste. *Cement and Concrete Research*, 14(3): 329–338, 1984.
[2] Charpin, L., Sow, T.O., d'Estève de Pradel, X.; Hamon, F., and Mathieu, J.-P., Numerical simulation of 12 years long biaxial creep tests. Efficiency of assuming a constant Poisson's ratio, *Proceedings of the VIth Biot conference on poromechanics*, Champs-sur Marne, France, 2017
[3] Bažant, Z.P., Cusatis, G., and Cedolin, L., Temperature effect on concrete creep modeled by microprestress-solidification theory. *Journal of engineering mechanics*, 130(6): 691–699, 2004
[4] Benboudjema, F. (2002). Modélisation des déformations différées du béton sous sollicitations biaxiales. Application aux enceintes de confinement de bâtiments réacteurs des centrales nucléaires (Doctoral dissertation, Université de Marne la Vallée).
[5] Sellier, A., & Buffo-Lacarrière, L. (2009). Vers une modélisation simple et unifiée du fluage propre, du retrait et du fluage en dessiccation du béton. European Journal of Environmental and Civil Engineering, 13(10), 1161-1182.
[6] Foucault, S. Michel-Ponnelle, E. Galenne. A new creep model for NPP containment behavior prediction. Proceedings of the 1st SSCS (Strategies for Sustainable Concrete Strategies) Conference, Aix-en-Provence, France, May 29th – June 1st, 2012.

SynerCrete'18 International Conference on Interdisciplinary Approaches
for Cement-based Materials and Structural Concrete
24-26 October 2018, Funchal, Madeira Island, Portugal

INFLUENCE OF THE FLEXIBILITY OF CALCIUM SILICATE HYDRATES LAYERS ON THE MESOTEXTURE: COARSE GRAINED SIMULATIONS ACCOUNTING FOR THREE-BODY INTERACTIONS

Tulio Honorio [(1,2)]

(1) Laboratoire Modélisation et Simulation Multi Echelle, Université Paris-Est Créteil, Créteil, France
(2) *Present address*: LMT-Cachan/ENS-Cachan/CNRS/Université Paris Saclay, Cachan, France

Abstract
Calcium silicate hydrates exhibit various mesotextures, composed of fundamental pieces presenting with different morphologies. The structuration of nanolayer (2D) and nanofibrillar (1D) materials is a result of the interplay between intermolecular forces involving the fundamental pieces (layers or fibrils) and the pore fluid as well as the flexibility of each piece. In this paper, coarse-grained simulations are performed to simulate the differences in the mesotexture of crystalline calcium silicate hydrate with a fibril morphology taking into account the flexibility of these fibrils. The resulting pore size distributions of the gel are computed and exhibit a dependence on the size of the fibril. These results are a contribution to a better understating of C-S-H nanostructuration.

1. Introduction

Calcium silicate hydrates exhibit a variety of morphologies, such as isotropic grains, 1D fibrils and 2D foils as well as in-plane dimensions, ranging from few tens of manometers up to several micrometers [1]. For layers with large aspect ratio, the flexibility of the layers might play a role in the structuration of the material with important repercussion in the hygro-mechanical response of the material [2]. However, the effects of flexibility (or three body interactions) are not generally taken into account in simulations of the mesotexture of calcium silicate hydrates [3–5]. The structuration of nanolayered or nanofibrillar materials is a result of the interplay between intermolecular forces involving the fundamental "pieces" (layers of fibrils) and the pore fluid as well as the flexibility of piece. These intermolecular forces, or

potential of mean force, can be computed by means of grand canonical simulations (c.f. the paper "Interactions between crystalline calcium silicate hydrates: grand canonical simulation of pressure and temperature effects" presented by the author also in this conference). The flexibility of single layers of tobermorite (Hamid's 11 Å tobermorite with Ca/Si=1 [6]) have been previously computed by the author [2]. The bending moduli in each orthogonal in-plane direction of the pseudo-orthorhombic cell are, respectively (4.68 ± 1.74) x 10^{-17} J and (1.42 ± 0.91) x 10^{-17} J [2]. These values are few orders of magnitude larger than (flexible) polymeric layers (~ x 10^{-20} J) and on the same order than other phyllosilicates such as clays [7]. With this bending modulus, tobermorite layers with more than few nanometers in one of the in-plane dimensions may potentially exhibit a bent configuration [2].

The flexibility of clays layers is recognized to play a major role on the structuration of the nanolayered materials. The reasoning can be, of course extended to nanofibrillar materials. Two limit cases can be compared [8]: (a) flexible or long layers or fibrils that are not prone to stack leads to entangled or spaghetti-like mesotextures, whilst (b) rigid or short layers or fibrils that are prone to stack leads to brick-like mesotextures. The resulting microstructure in (a) presents smaller pores (less permeable, therefore) and cohesion due to entanglement of a layer in different ordered domains, which may lead to a more ductile macroscopic behaviour. The resulting microstructure in (b) presents larger pores (more permeable) and granular behaviour, which may translate in a brittle macroscopic behaviour.

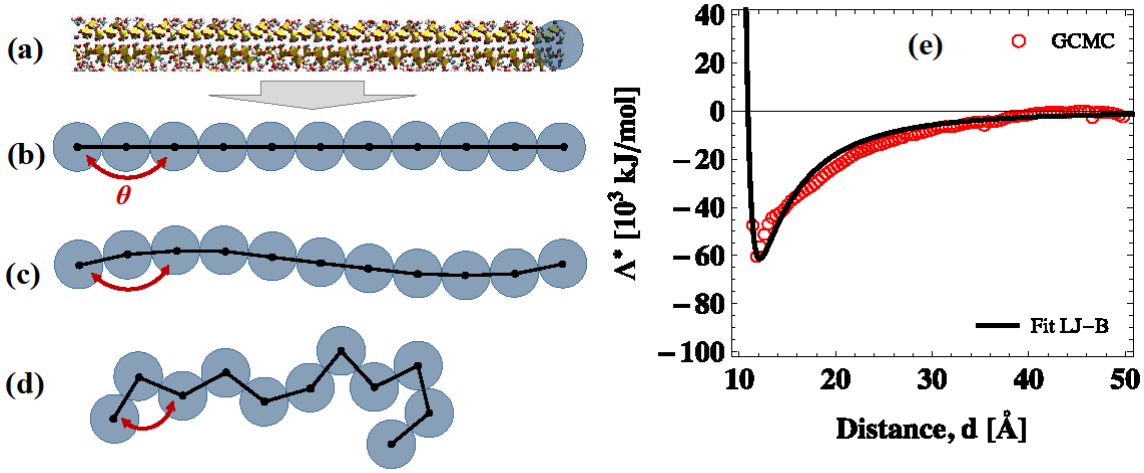

Figure 1. *At left*, Representation of a solid layer by a chain of spherical grains: (**a**) snapshot of the atomic structure of Hamid's [6] 11 Å tobermorite with Ca/Si = 1; fibril representation with (**b**) large bending modulus (**c**) intermediary bending modulus (persistence length larger than the grain sizes) and (**d**) small bending modulus (the persistence length smaller than the grain size). At right, (**e**) potential of mean force obtained from grand canonical Monte Carlo simulation [9] and fitted LJ-B potential from a previous study.

In this paper, coarse-grained simulations are performed to simulate these differences in the mesotexture of calcium silicate hydrates. The potential of mean force and flexibility of a crystalline calcium silicate hydrate are considered. Three fibrils sizes and their propensity to stack are explicitly taken into account. The resulting pore size distributions for each scenario

are compared. These results are a contribution to a better understating of C-S-H nanostructuration.

2. Models and simulations

The atomic structure of Hamid's 11 Å tobermorite [6] with molar Ca/Si ratio of 1 is considered ($Ca_6[Si_6O_{18}].2H_2O$). This same structure was also studied by other authors interests in the meso-structuration of calcium silicates (e.g. [10, 11]). Figure 1 (a) shows the replicated monoclinic cell (a = 6.69 Å, b = 7.39 Å, c = 22.77 Å and γ = 123.49°) along a-axis, as proposed by Hamid [6]. The atoms in tobermorite are interacting via CSHFF [12], which is a force field based only in non-bonded Lennard-Jones interactions for metal and metalloids while harmonic bonds are only defined for water molecules and hydroxyls. This force field has been extensively used in the computation mechanical, thermal and interfacial properties of crystalline and disordered calcium silicates [13].The surface change density of the tobermorite layer is -0.55 $C.m^{-2}$, which is close to the experimental value of -0.5 $C.m^{-2}$ [14].

2.2 Coarse-grained simulations accounting for two- and three-body interactions

The tobermorite solid layer is represented by a chain of spherical grain interacting *via* non-bonded forces (derived from the potential of mean force), two-body forces (derived from the in-plane elasticity of the solid layer) and three-body forces (derived from the bending modulus of the solid layer). The interaction between solid tobermorite layers and the fluid in drained conditions are detailed in another study [9]. These interactions are fitted by a generalized Lennard-Jones (LJ) potential combined with the Buckingham potential, as reported in Fig. 2, for all distances smaller than the cut-off distance $d_c = 50$ Å:

$$U_{LJ-B}(d) = 4\epsilon\left[\left(\frac{\sigma}{d}\right)^{2\alpha} - \left(\frac{\sigma}{d}\right)^{\alpha}\right] + A\exp\left(-\frac{d}{\beta}\right) - \frac{C}{d^6} \qquad \forall\, d < d_c \tag{1}$$

with σ = 5.907 Å, $\epsilon = 151.85 \times 10^3$ kJ/mol and $\alpha = 2.85$, for the LJ potential and $A = 1.213 \times 10^{12}$ kJ/mol, β = 0.4670 Å and $C = 0$, for the Buckingham potential.

Bonds or two-body interaction are described by an harmonic bond:

$$U_{2-b}(d) = k_{2-b}(d - d_0)^2 \tag{2}$$

with force constant k_{2-b}= 939 kJ/(mol $Å^2$) computed from the elastic moduli according to the in-plane direction of the solid layer; and the equilibrium bond length distance d_0, corresponding to the effective thickness of the solid layer. In this study, the in-plane elastic moduli computed by first principles simulations [15], in Hamid 11 Å tobermorite with Ca/Si = 1, are used (i.e. 148.25 and 138.35 GPa). The equilibrium bond length adopted is d_0= 11.81 Å.

Angles or three-body interaction described by a harmonic bond:

$$U_{3-b}(d) = k_{3-b}(\theta - \theta_0)^2 \tag{2}$$

where k_{3-b} = 11.44 kJ/(mol rad^2), is the bending modulus of the solid fibril and θ_0 is the equilibrium angle (180° for a flat solid fibril). According to their flexibility and persistence length (parameter depending on the bending modulus), the fibril can assume different configurations (Fig. 1 right): from a flat surface (large bending modulus) to a crumpled configuration (small bending modulus).

The molecular dynamics simulations are performed with LAMMPS [16]. The fibrils are generated in a grid with a dilute concentration so that the distance between the fibrils is much larger than the cut-off of the non-bonded interactions. Circa 40000 grain are considered in each scenario. A velocity corresponding to 5000 K is randomly attributed to each individual grain. A 0.5 ns run in NVT ensemble is performed so that the fibril may assume random orientations. Then, the temperature is decreased to 300 K during 0.1 ns and equilibrated in this temperature during 0.2 ns. Next, the system is subjected to a pressure of 1 atm; an equilibration run of 0.5 ns is followed by the sampling of the configurations to be considered in pore size distribution analysis. The pore size distribution of the resulting mesotexture is assessed by means of the method developed by Bhattacharya et al. [17]. Three fibril size are considered N = 5, 10, and 20 grains, where $N = L/d_0$ is the ratio between the largest dimension L of the fibril divided by the diameter of the grain $d_g = d_0$.

3. Results and discussion

Figure 2 displays the mesotextures obtained for the three fibril sizes considered. It is possible to identify only slightly bent configurations in all cases. In the cases treated here, the fibrils can be fairly approximated by rigid rods. This aspect highlights the importance of considering bending rigidity in modelling C-S-H.

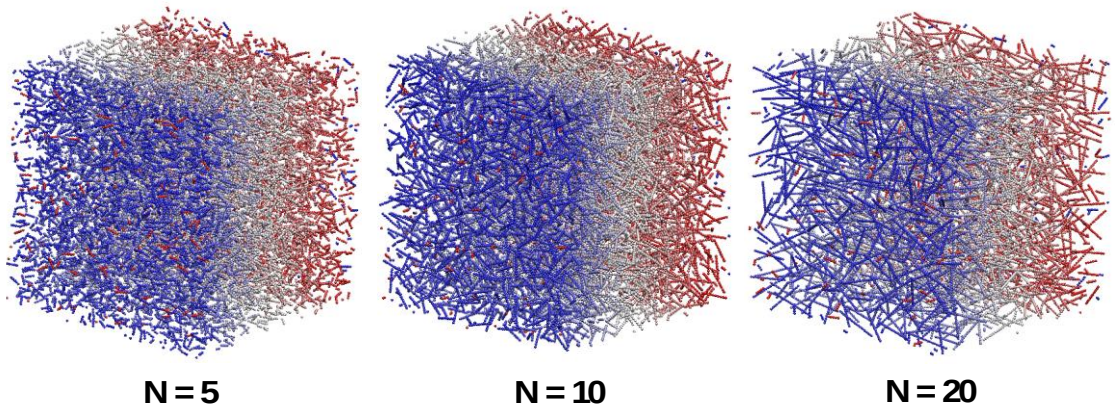

Figure 2. Mesotexture according to the size of the fibril: systems with 8000 (N = 5), 4096 (N = 10) and 1728 (N = 20) fibrils, respectively (i.e. circa 40000 grains in each case).

The corresponding pore size distributions of the mesotextures are compared in Fig. 3. The range of pore sizes covered by the numerical samples corresponds to gel pores (0.5-10 nm) and medium capillary pores (10-50 nm). The probability density function follows a normal

distribution with average (± standard deviation) pore diameter of 7.6±1.8 nm (N = 5), 9.0±1.9 nm (N = 10) and 9.1±2.2 nm (N = 20), respectively. For moderately flexible fibrils as tobermorite, increasing the fibril size leads to an increase in the average pore size and the standard deviation of the pore size distribution.

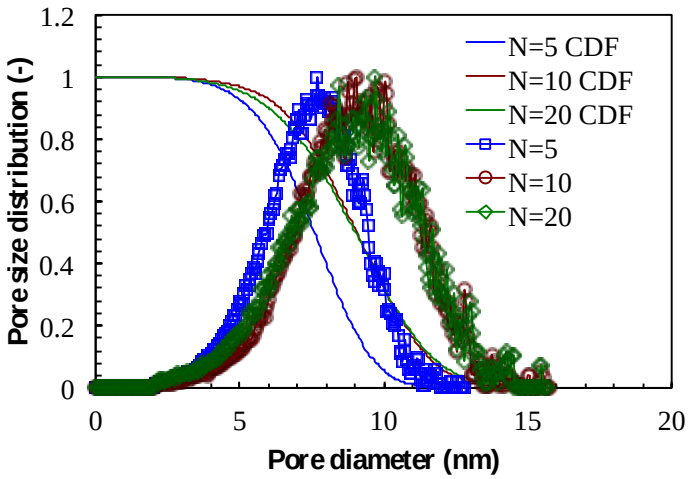

Figure 3 Differential and cumulative pore size distributions according to the size of the fibril (considering the bending modulus of tobermorite layer).

4. Conclusion

In this paper, the effect of considering the flexibility (or three-body interaction) of solid fibrils on the mesotexture of calcium silicate hydrates is studied. Fibrils of tobermorite are moderately flexible in the sense that they can show some bent configurations for moderate loads on the order of the kPa up to the MPa [2], which can easily be found in cement-based materials [18]. The increase of fibril size translates in the increase of the probability of finding bent fibrils in the equilibrium configurations. In this study, only slightly bent configurations were observed even for the scenarios with the longest fibril (N = 20). An increase in the fibril size, for a fixed bending modulus, leads to changes in the meso-structuration of calcium silicate hydrates: both the average pore size and the standard deviation of the pore size distribution increase with the size of the fibril. Future investigations will tackle with the structuration of 2D layers as well as combination of fibrils of different sizes.

References

[1] Richardson IG. Tobermorite/jennite- and tobermorite/calcium hydroxide-based models for the structure of C-S-H: applicability to hardened pastes of tricalcium silicate, β-dicalcium silicate, Portland cement, and blends of Portland cement with blast-furnace slag, metakaolin, or silica fume. Cem Concr Res 34 (2004), 1733–1777

[2] Honorio T, Brochard L. Flexibility of C-S-H sheets and stacks from molecular simulations. Second International RILEM/COST Conferene on Early Age Cracking and Serviceability in Cement-Based Materials and Structures, Belgium (2017)

[3] Masoero E, Del Gado E, Pellenq RJ-M, et al. Nanostructure and Nanomechanics of

Cement: Polydisperse Colloidal Packing. Phys Rev Lett 109 (2012), 155503
[4] Ioannidou K, Krakowiak KJ, Bauchy M, et al. Mesoscale texture of cement hydrates. Proc Natl Acad Sci (2016) 201520487
[5] Yu Z, Zhou A, Lau D Mesoscopic packing of disk-like building blocks in calcium silicate hydrate. Sci Rep 6 (2016)
[6] Hamid SA. The crystal structure of the 11 Ä natural tobermorite Ca2.25[Si3O7.5(OH)1.5]·1H2O. Z Für Krist - Cryst Mater 154 (1981), 189–198
[7] Suter JL, Coveney PV, Greenwell HC, Thyveetil M-A. Large-Scale Molecular Dynamics Study of Montmorillonite Clay: Emergence of Undulatory Fluctuations and Determination of Material Properties. J Phys Chem C 111 (2007), 8248–8259
[8] Zabat M, Vayer-Besançon M, Harba R, et al. Surface topography and mechanical properties of smectite films. In: Rosenholm JB, Lindman B, Stenius P (eds) Trends in Colloid and Interface Science XI. Steinkopff, (1997) pp 96–102
[9] Honorio T. Interactions between crystalline calcium silicate hydrates: grand canonical simulation of pressure and temperature effects. Funchal, Madeira Island, Portugal (2018)
[10] Masoumi S, Valipour H, Abdolhosseini Qomi MJ. Intermolecular Forces between Nanolayers of Crystalline Calcium-Silicate-Hydrates in Aqueous Medium. J Phys Chem C 121 (2017), 5565–5572
[11] Masoumi S, Valipour H, Abdolhosseini Qomi MJ. Interparticle Interactions in Colloidal Systems: Toward a Comprehensive Mesoscale Model. ACS Appl Mater Interfaces 9 (2017), 27338–27349
[12] Shahsavari R, Pellenq RJ-M, Ulm F-J. Empirical force fields for complex hydrated calcio-silicate layered materials. Phys Chem Chem Phys 13 (2010), 1002–1011
[13] Mishra R, Kunhi A, Geissbühler D, et al. cemff: A force field database for cementitious materials including validations, applications and opportunities. Cem Concr Res. (2017)
[14] Allen AJ, Thomas JJ, Jennings HM. Composition and density of nanoscale calcium–silicate–hydrate in cement. Nat Mater 6 (2007), 311–316
[15] Shahsavari R, Buehler MJ, Pellenq RJ-M, Ulm F-J. First-Principles Study of Elastic Constants and Interlayer Interactions of Complex Hydrated Oxides: Case Study of Tobermorite and Jennite. J Am Ceram Soc 92 (2009), 2323–2330
[16] Plimpton S. Fast Parallel Algorithms for Short-Range Molecular Dynamics. J Comput Phys 117 (1995),1–19
[17] Bhattacharya S, Gubbins KE. Fast Method for Computing Pore Size Distributions of Model Materials. Langmuir 22 (2006) 7726–7731
[18] Honorio, T, Brochard, L, Bary, B. Statistical variability of mechanical fields in thermo-poro-elasticity: multiscale analytical estimations applied to cement-based materials at early-age. Cem. Concr. Res 110 (2018) 24-41

SynerCrete'18 International Conference on Interdisciplinary Approaches
for Cement-based Materials and Structural Concrete
24-26 October 2018, Funchal, Madeira Island, Portugal

INTERACTIONS BETWEEN CRYSTALLINE CALCIUM SILICATE HYDRATES: GRAND CANONICAL SIMULATION OF PRESSURE AND TEMPERATURE EFFECTS

Tulio Honorio [(1,2)]

(1) Laboratoire Modélisation et Simulation Multi Echelle, Université Paris-Est Créteil, Créteil, France
(2) *Present address*: LMT-Cachan/ENS-Cachan/CNRS/Université Paris Saclay, Cachan, France

Abstract
The interactions between calcium silicate hydrates and pore solution at the nanoscale are crucial in physical phenomena related to the thermo-hydro-mechanical behaviour of cement-based materials. In this paper, these interactions are studied using grand canonical Monte Carlo simulations according to various temperatures and pressures. A nanocrystalline structure of calcium silicate hydrate (tobermorite) is considered. Micro-instabilities of snap-through type are identified. The corresponding potential of mean force, accounting for the interactions of the solid layers in drained conditions, is provided, which leaves rooms to upscale the behaviour of calcium silicate hydrates to the mesoscale.

1. Introduction

Adsorption related phenomena is reported to be at the heart of important features of cement-based materials behaviour such as drying shrinkage and hysteresis [1], creep [2], thermal expansion [3] and transmission of stresses between solid and liquids phases [4]. Adsorption takes place at the molecular scale and is recognized to be pressure and temperature dependent. The main product of cement hydration processes is calcium silicate hydrates, a microporous adsorbing material. Cement-based materials are generally subjected to variations of temperatures during their service life. Under temperature rise, fluid molecules are expected to desorb whereas the entire system is expected to show thermal expansion.
Simulations at the molecular scale are well suited to investigate adsorption phenomena in details. These simulations allow assessing water structuration as a function of confinement

and the presence of ions in microporous materials [5]. Such approach have been use to evaluate the intermolecular forces between solids layers of calcium silicate hydrates in drained conditions [6, 7]. Even if a macroscopically a nanoporous material, as calcium silicate hydrates, is not under drained conditions, at the nanoscale, due to the exchange of fluids between interlayer pores and gel pores the former class of pores can be seen as in drained conditions with respect to the fluid reservoir in gel pores. Experimental evidence [8] showing instantaneous changes in water population in these pores under temperature change corroborates this assumption regarding the internal migration of water. In this context, the thermodynamic ensemble adapted to study adsorption phenomenon is the grand canonical ensemble for the fluid combined with canonical ensemble for the solid layers: the total volume V and temperature T are fixed (while the total pressure P and entropy fluctuate), the chemical potential of the fluid μ_w is fixed (while the number of fluid molecules N_w fluctuates) and the number of atoms in the solid as well as counterions are fixed. This ensemble minimises the mixed thermodynamic potential $\Lambda(V,T,\mu_w)$. For a layered materials, the confinement pressure (in the direction orthogonal to the basal plane) $P = -\frac{\partial \lambda}{\partial d}\Big|_{T,\mu_w}$ can de defined in terms of Λ per unit area $\lambda(d,T,\mu_w) \equiv \Lambda(V,T,\mu_w)/A$, where d is the basal spacing. The energy profile for a system controlled by the volume is $\lambda = \lambda_0(d_0,T,\mu_w) - \int_{d_0}^{d} P\, d(d)$. The convex hull of λ, resulting from the integration of λ over a Representative Volume Element (RVE) represents the energy associated with all stable states of stacks under displacement control. The corresponding energy profile for a system controlled by the confining pressure is the Legendre transform of λ:

$$\lambda^* = \lambda + P\, d = \Lambda^*(P,T,\mu_w)/A \tag{2}$$

This is what is called the free energy of swelling in clay science [5, 9]. This energy profile informs on the prevalence and stability of specific basal spacings.

In this paper, the dependence of adsorption, disjoining pressure isotherms and free energy of swelling on temperature and pressure is investigated by means of grand canonical Monte Carlo molecular simulations (GCMC).

2. Molecular simulation of crystalline calcium silicate hydrates

Classical Monte Carlo simulations in grand canonical ensemble are run as a function of the confinement (i.e. for different centre-to-centre or basal distance with respect to solid layers) and temperature. Interactions between the species are described by CSHFF force field [10] and SPC water model. The chemical potential of SPC water as a function of the temperature is obtained by means of thermodynamic integration of Gibbs-Duhem equation. Calcium counterions are added to the interlayer space in order to ensure the electroneutrality of the system. For each temperature and basal spacing, a simulation is run with Towhee [11] package using configuration bias methods. Each simulation is run during 30 million Monte Carlo steps (10 million steps for equilibration and 20 million for sampling). The convergence criterion adopted is a stable energy system (with the standard deviation of the total energy

below 0.02 % of the mean value). The atomic structure of calcium silicate hydrate is derived from Hamid's [12] structure of tobermorite 11 Å with molar Ca/Si ratio of 1: $Ca_6[Si_6O_{18}].2H_2O$. The cell parameters of the resulting monoclinic cell are a = 6.69 Å, b = 7.39 Å, c = 22.77 Å and $\gamma = 123.49°$ [12]. Figure 1 shows snapshots of configurations at equilibrium associated to three basal spacings.

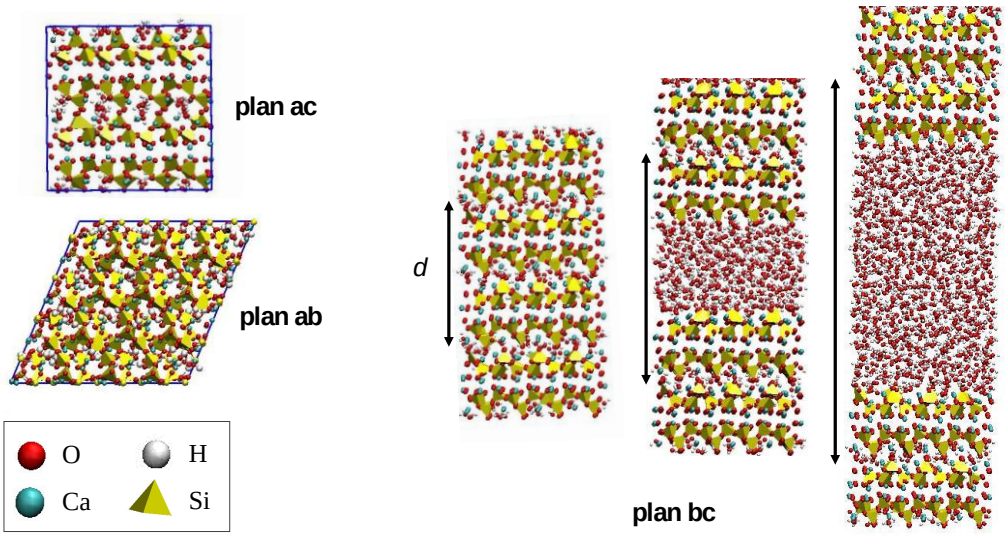

Figure 1: Snapshots of the (monoclinic) structure of Hamid's 11 Å tobermorite with Ca/Si = 1 and equilibrium configurations at three basal spacings *d*.

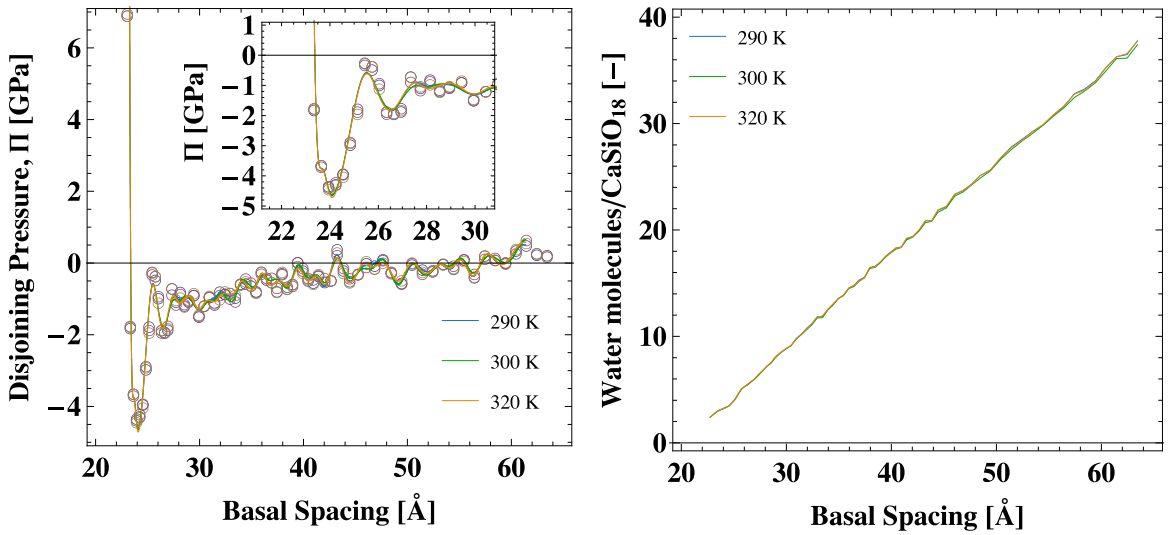

Figure 2: *At left*, disjoining pressure isotherms as a function of basal spacing for three temperatures. The inset shows the details of oscillation corresponding to the first hydration states. *At right*, adsorption isotherms as a function of basal spacing for the same temperatures.

4. Results and discussion

Figure 2 (left) shows the disjoining pressure isotherms according to the three temperatures. The disjoining pressure is the difference between the confining pressure and the fluid pressure $\Pi = P - P_w$. The effects of the temperature, in the temperature range considered, is not very pronounced. The confining pressure isotherms at 300 K are in agreement with other pressure isotherms reported in the literature [6, 7]. For small basal spacings, it is possible to identify the quasi-dehydrated (some water molecules remains trapped in the calcium silicate pores even for small basal spacings), in which the confining pressure strongly increases with the decrease in *d* as a result of the steric repulsion between the solid layers, counterions and the remaining water molecules. The oscillations corresponds to the various possible hydration states *nW* with water structuring in discrete *n* layers up to the state of pore water ∞W. The 1W hydration state can be clearly distinguished, as can be seen in the inset of Fig. 2. The distance between the oscillations (taking, for example, the minimum values in the inset of Fig. 2 as reference) is circa 3 Å, which roughly corresponds to the Lennard-Jones diameter of the oxygen in SPC water model. The portions of the curve in which the pressure increases with the basal spacing are instable. Therefore, the system is subjected to micro- or snap-through instabilities [13], which are reported to be at the heart of important phenomena in nanoporous materials such as shrinkage and creep. Figure 2 (right) reports the adsorption isotherms for the three temperatures. Again, the effect of the temperature in the range considered is not very pronounced.

Some key physical properties can be computed from the pressure isotherms. This information can be used to validate the output of the simulation [6]. Table 1 shows the out-of-plane elastic modulus $E_{zz} = -d_{eq}\frac{\partial\lambda}{\partial d}\Big|_{d_{eq}}$, surface energy $\gamma_s = -\frac{1}{2}\int_{d_{eq}}^{\infty}\lambda\, d(d)$ and cohesive pressure $P_{cohesive}$ (i.e. the pressure needed to disjoin two solid layers, which corresponds to the minimum in the pressure isotherms) computed at different temperatures. The estimates are compared against results from experiments and simulations reported in the literature and a fair agreement is observed.

Table 1: Physical properties computed from the confining pressure isotherms: validation against experimental and simulation results from the literature.

	Out-of Plane elastic modulus, E_{zz} (GPa)	**Surface energy, γ_s (J/m^2)**	**Cohesive pressure, $P_{cohesive}$ (GPa)**
This work:	79.7 (290 K) 77.7 (300 K) 79.9 (310 K)	1.07 (290 K) 1.07 (300 K) 1.05 (310 K)	4.18 (290 K) 4.16 (300 K) 4.22 (310 K)
Others	77.6 [6]; 61 [14] 89 [15]; 68.4 [16]	0.67 [6]; 1.15 [19] 0.32-0.4 [17, 18]	6.5 [6] 5.0 [20]

Figure 3 shows the free energy of swelling as a function of the basal spacing: according to the temperature (left) and control pressure (right). The effect of temperature, in the range considered, is minor. The control pressure affects the depth of the potential well, or the total

surface energy. The energy barriers associated with hydrate state transitions can be measured directly on these energy profiles. The energy profile concerning the system at 300 K was fitted using the of generalized Lennard-Jones potential: $U_i(d) = 4\epsilon\left[\left(\frac{\sigma}{d}\right)^{2\alpha} - \left(\frac{\sigma}{d}\right)^{\alpha}\right]$, with σ = 21.81 Å, $\epsilon = 60.1 \times 10^3$ kJ/mol and $\alpha = 7.01$. This potential can be used to upscale calcium silicate hydrates behaviour at the mesoscale.

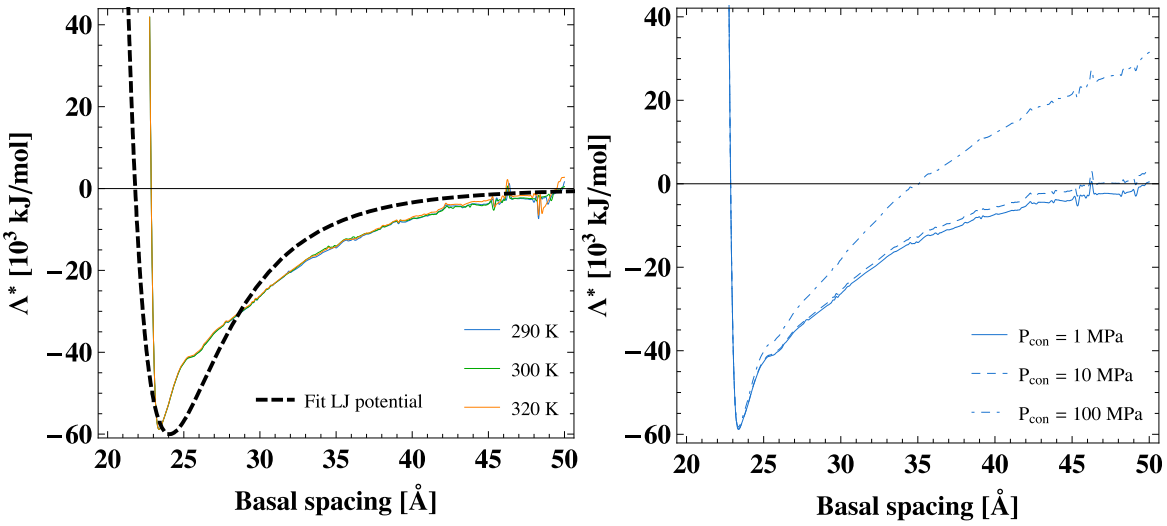

Figure 3: Free energy of swelling as a function of the basal spacing: according to the temperature (*left*) and control pressure (*right*). At left, the energy profile at 300K is fitted using the generalized Lennard-Jones potential.

4. Conclusion

In this article, the intermolecular interactions between crystalline calcium silicate hydrates were reported. These interactions result from the interplay between steric repulsion, attractive forces and depletion forces or entropic solvation, which lead to an oscillatory (non-convex) energy profile susceptible to manifest (snap-through) micro-instabilities. Here, these interactions were presented in terms of disjoining pressure isotherms and free energy of swelling. The convexification of the energy profile leads to the mesoscopic energy profile of a stack of solid layers in drained conditions. These results leave room to a better understating of the nature of water confined in calcium silicate hydrates nanopores (i.e. interlayer and gel pores). The derived energy profiles can be used to compute the interparticle interactions at a mesoscale (gel scale).

References

[1] Pinson MB, Masoero E, Bonnaud PA, et al. Hysteresis from Multiscale Porosity: Modeling Water Sorption and Shrinkage in Cement Paste. Phys Rev Appl 3 (2015), 064
[2] Acker P Swelling, shrinkage and creep: a mechanical approach to cement hydration. Mater Struct 37 (2004), 237–243

[3] Sellevold EJ, Bjøntegaard Ø. Coefficient of thermal expansion of cement paste and concrete: Mechanisms of moisture interaction. Mater Struct 39 (2006), 809–815
[4] Honorio T, Brochard L, Vandamme M. Effective stresses and estimations of the apparent Biot coefficient in stacked clay nanolayers. Géotechnique Lett (2018)
[5] Honorio T, Brochard L, Vandamme M (2017) Hydration Phase Diagram of Clay Particles from Molecular Simulations. Langmuir 33 (2017), 12766–12776
[6] Masoumi S, Valipour H, Abdolhosseini Qomi MJ. Intermolecular Forces between Nanolayers of Crystalline Calcium-Silicate-Hydrates in Aqueous Medium. J Phys Chem C 121 (2017), 5565–5572
[7] Bonnaud PA, Labbez C, Miura R, et al. Interaction grand potential between calcium–silicate–hydrate nanoparticles at the molecular level. Nanoscale 8 (2016), 4160–4172
[8] Wyrzykowski M, Mcdonald PJ, Scrivener K, Lura P. Water Redistribution within the Microstructure of Cementitious Materials Due to Temperature Changes Studied with 1H NMR. J Phys Chem C (2017)
[9] Tambach TJ, Bolhuis PG, Hensen EJM, Smit B. Hysteresis in Clay Swelling Induced by Hydrogen Bonding: Accurate Prediction of Swelling States. Langmuir 22(2006), 1223–1234
[10] Shahsavari R, Pellenq RJ-M, Ulm F-J. Empirical force fields for complex hydrated calcio-silicate layered materials. Phys Chem Chem Phys 13 (2010), 1002–1011
[11] Martin MG. MCCCS Towhee: a tool for Monte Carlo molecular simulation. Mol Simul 39 (2013), 1212–1222
[12] Hamid SA. The crystal structure of the 11 Ä natural tobermorite Ca2.25[Si3O7.5(OH)1.5]·1H2O. Z Für Krist - Cryst Mater 154 (1981), 189–198
[13] Bazant ZP, Bazant MZ. Theory of sorption hysteresis in nanoporous solids: Part I. Snap-through instabilities. J Mech Phys Solids 60 (2012), 1644–1659
[14] Oh JE, Clark SM, Monteiro PJM. Does the Al substitution in C–S–H(I) change its mechanical property? Cem Concr Res 41 (2011), 102–106
[15] Oh JE, Clark SM, Wenk H-R, Monteiro PJM. Experimental determination of bulk modulus of 14 Å tobermorite using high pressure synchrotron X-ray diffraction. Cem Concr Res 42 (2012), 397–403
[16] Shahsavari R, Buehler MJ, Pellenq RJ-M, Ulm F-J. First-Principles Study of Elastic Constants and Interlayer Interactions of Complex Hydrated Oxides: Case Study of Tobermorite and Jennite. J Am Ceram Soc 92 (2009), 2323–2330
[17] Brunauer S. Surfaces of solids. Pure Appl Chem 10 (1965), 293–308
[18] Brunauer S, Kantro DL, Weise CH. The Surface Energy of Tobermorite. Can J Chem 37 (1959), 714–724
[19] Bauchy M, Laubie H, Qomi MJA, et al. Fracture toughness of calcium–silicate–hydrate from molecular dynamics simulations. J Non-Cryst Solids 419 (2015), 58–64
[20] Pellenq RJ-M, Lequeux N, van Damme H. Engineering the bonding scheme in C–S–H: The iono-covalent framework. Cem Concr Res 38 (2008), 159–174

SynerCrete'18 International Conference on Interdisciplinary Approaches
for Cement-based Materials and Structural Concrete
24-26 October 2018, Funchal, Madeira Island, Portugal

MICROSTRUCTURAL CHARACTERISATION OF CEMENT-BASED MATERIALS (CBM) USING THE NUMERICAL SIMULATION OF ULTRASONIC PROPAGATION

José Vicente Fuente [(1)], Sreejith Nanukuttan [(2)], Jorge Gosalbez [(3)], Neil Campbell [(4)]

(1) Geozone Asesores SL, Paterna, Valencia, Spain
(2) Queens University of Belfast, Northern Ireland, United Kingdom.
(3) iTEAM, Universitat Politècnica de València, Valencia, Spain
(4) Amphora NDT, Northern Ireland, United Kingdom, United Kingdom

Abstract
This article reports the developments made during a short term scientific mission (STSM) funded by COST Action TU1404. The aim was to develop a refined methodology for the microstructural characterisation of cement-based materials (CBM) using the numerical simulation of ultrasonic propagation. Images that represent the microstructure of cement paste and mortars were created using the uniform and gaussian functions.
Further the attenuation-dependence of the ultrasonic pulse for the wide range of microstructures has been tested since from a set of Images of Microstructure (IoM) as an output of the image generation process. This IoM were the input for the ultrasonic modelling to obtain some ultrasonic parameters that they characterise each microstructure. This theoretical procedure has been used to simulation a wide range of CBM microstructures. The microstructural parameters considered in the analysis were the porosity (two size ranges), grain number and size and interfacial zone modelling.
Finally, it is planned to integrate the findings from the previous objectives to develop a refined methodology for microstructural characterization of CBM using ultrasonic pulse. This study has been funded by COST Action through a Scientific Short Time Mission (STSM), numbered by 38439, being supported the main author of this paper for the Congress and being part of the dissemination activities of this STSM.

1. Introduction

It is well-known the phenomena (scattering, absorption, reflection …) of the ultrasonic pulse along a porous media and including the cement microstructures [1]. For the conventional tests at the concrete technology, the ultrasonic testing is commonly used. Most authors have worked in an extended model for the strength behaviour using combined NDT as ultrasounds and sclerometer (Schmidt hammer). Ultrasonic velocity [2] and its amplitude [3] in some cases reveal as some good estimation parameters in certain conditions. Many efforts and contribution have been performed in the experimental research side, with large testing campaign and intensive ultrasonic measurements [4].
One of the weak points that we have detected is the limited control of the microstructure that it can be generated in the manufacturing process at real scale (on-site) mainly for concrete mixtures. In other words, there are some restrictions in the process of production the cement matrix and the final microstructure with specific microstructural parameters by using the standard raw materials and mixing methods. It is very difficult to maintain porosity and move in a wide range their sizes, tortuosity and the distribution of aggregates. Definitively, you cannot vary a single parameter remaining constant others. This effect can be reduced and overcome with numerical simulation. Therefore, we have focused in the theoretical side of this research and using simulation tools for developing a wide range of microstructure building a set of images where test the simulation procedure.
The objectives of this research were the following: a) to generate microstructure of cement paste and mortars by simulation tools using Matlab© uniform and gaussian functions. The output was some IoM., b) to develop a set of the numerical simulation using different kinds of ultrasonic pulse to analysis the attenuation-dependence of the pulse for the wide range of microstructures, c) to analysis the most relevant parameters in time and spectral domain and d) to integrate the findings from the previous objectives to develop a refined methodology for microstructural characterization of CBM using ultrasonic pulse.

2. Research workplan

The work plan was implemented by 4 different tasks which were repeated for cement pastes as well as for mortar. Results of cement pastes matrix were used as an input in the numerical simulation of mortars.

2.1 Microstructure generation

It was implemented to different matlab script to generate the cement paste matrix as a 2-phases grey-scale image reproducing the capillary porosity and small air bubbles that it simulates the real situation during the mix performing. The porosity under 1 micron was not generated in this procedure dur to the required high cost computation and it was considered as part of the elastic cement matrix. The matlab scripts consist of some brief instructions to set the desirable amount of the circular porous with gaussian diameter size distribution, uniformed distributed in a 2000 x 2001 pixeled image. Each pixel corresponds to a 1 nm therefore the representative IoM were 2 mm-sized. A total of 12 cement paste microstructures were generated by using the above scripts from 16.7% until 39.0%. The IoM were a composition of two images, first one for capillary porosity from 1 to 10 microns and the

second for macropores from 10 to 100 microns. Next figure shows images and pore values of the IoM.

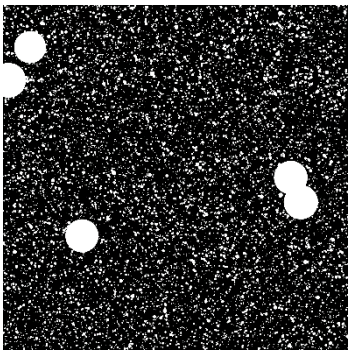

16.7% (13.7% + 3.4 %)

Table 1. Porosity values

Capillary porosity	Macropore 3.4	5.4	6.7
13.7	16.7	18	19.6
19.2	22.0	23.5	24.6
27.2	28.0	29.5	30.5
34.6	36.7	38.1	39.0

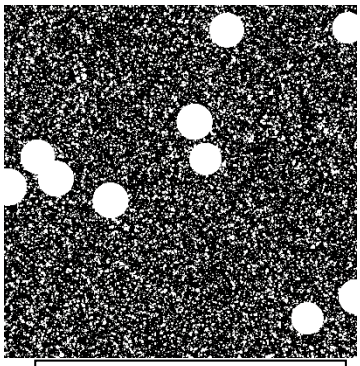

39.0% (34.6 %+ 6.7%)

Figure 1. Images of porous cement matrix by using gaussian and uniform functions.

The mortar image generation has obtained by using 2D-concrete builder programme (developed by IZPF Fraunhofer of Dresden). The input parameters allow to generate an output image with specific features that can be varied to range were the following:

```
xmax = 40.0e-03
ymax = 40.0e-03
grain_fraction = 0.5 ⟶ 0.75, 0.66, 0.5
mingrain = 0.125e-03
maxgrain = 4e-03
grading_curve_coefficient = 0.2 ⟶ 0.6, 0.37, 0.2
aspectratio_min = 1.0
aspectratio_max = 2.5
ngrain = 50000
matint = 2
random = 1782

xpixel = 2000
periodic_boundary = on
```

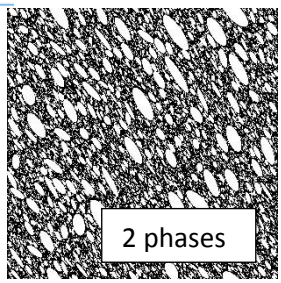

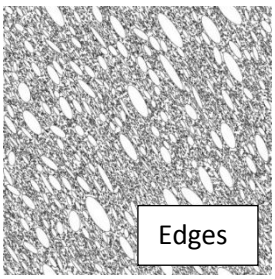

Figure 2. Input parameters, specification ranges and intermediate mortar images.

In order to reproduce the Interfacial Zone (ITZ) it was performed a digital image processing algorithm to select edges of the white scatters that represents the sand grands while cement matrix (including capillary porous and macropores) remains in a black colour. The n-index reflect the grading curve of the particle distribution of scatters (sand particles) and it is considered the different values, the considered values were 0.2 (German DIN grading curve B); 0.37 (optimal compacity factor) and the binder an the 0.7 value (DIN grading curve A), all above following the grading curve that it can be mathematically described by:

$$A_{d_{min}/d} = \frac{100}{1-\left(\frac{d_{min}}{D}\right)^n} \cdot \left[\left(\frac{d}{D}\right)^n - \left(\frac{d_{min}}{D}\right)^n\right] \quad (1)$$

It gives the volume fraction (in %) of grains with diameters between d_{min} (fixed to 0.125 mm) and d as a function of the maximum grain size D (fixed to 4 mm), the minimum grain size d_{min} and the grading curve coefficient n. After that, adding both images it can be obtained the 9 different microstructures for CP. Higher values of n-index represent lower sand filler contain. The task is completed using intermediate images capillary and macropore 2D-phases (sand and cement matrix) and edges images for mortars.

2.2 Ultrasonic simulations

This task concerns with the ultrasonic propagation through the above images. It was used the Wave2000-Plus software from Cyberlogic© where output image can be loaded as basis media where a range of ultrasonic pulse were propagated. Following Tab.2 shows the different frequencies applied to the IoM.

Table 2: Set of numerical simulation for cement pastes and mortars.

Cement Pastes Simulations

Frec. (MHz)	0.35	1	3.5	5	10	20
16.7	X	X	X	X	X	X
18.4	X	X	X	X	X	X
19.6	X	X	X	X	X	X
22.0	X	X	X	X	X	X
23.5	X	X	X	X	X	X
24.6	X	X	X	X	X	X
28.0	X	X	X	X	X	X
29.5	X	X	X	X	X	X
30.5	X	X	X	X	X	X
36.9	X	X	X	X	X	X
38.1	X	X	X	X	X	X
39.0	X	X	X	X	X	X

Mortar Simulations

Cement Porosity	Matrix	Frec. (MHz)	0.35	1	3.5	5
24.6		1/1-0.20	X	X	X	X
		1/1-0.37	X	X	X	X
		1/1-0.70	X	X	X	X
		2/1-0.20	X	X	X	X
		2/1-0.37	X	X	X	X
		2/1-0.70	X	X	X	X
		3/1-0.20	X	X	X	X
		3/1-0.37	X	X	X	X
		3/1-0.70	X	X	X	X
39.0		1/1-0.2	X	X	X	X
		1/1-0.37	X	X	X	X
		1/1-0.70	X	X	X	X
		2/1-0.20	X	X	X	X
		2/1-0.37	X	X	X	X
		2/1-0.70	X	X	X	X
		3/1-0.20	X	X	X	X
		3/1-0.37	X	X	X	X
		3/1-0.70	X	X	X	X

An amount of 144 numerical simulations for the cement pastes and mortars have been performed. Also, it is considering 140 as valid regarding the acquired waveforms from the P-wave and S-Wave velocity. The instability reasons can occur in the process of solving the differential wave propagation equation in every matrix. Each time the discrete wave propagation equation must be solved for each matrix cell and boundary conditions but in certain cases the solving algorithms cannot converge to concrete solutions. In order to manage a reasonable number of simulations it was selected low different range of the cement pastes porosity matrix to perform since from them the mortar simulations.

3. Signal processing and ultrasonic parameters

Reference values for the different phases are shown in the Tab. 3. The parameters were: Vp/Vs longitudinal/ shear wave velocities, λ/μ were the lame constants, ρ the apparent

density, ν (Poisson ratio), E (Young Modulus), α (attenuation and η/ϕ that were the scattering parameters.

Table 3. Ultrasonic parameters and elastic constants.

	Vp (m/s)	Vs (m/s)	λ (MPa)	μ (MPa)	ρ (kg/m3)	σ [0-0.5] Poisson ratio	E (Mpa) Young Modulus	α (dB/cm) - Long Wave	α (dB/cm) - Shear wave	η (Pa s) at 1 Mhz	ϕ (Pa s) at 1 MHz
Sand	5044	3018	15900	20040	2200	0.22	49.98	0.0318	0.106	3.75	0.25
IZT	2835	1823	2270	5482	1650	0.15	12.50	4.72	1.71	10	90
Cement Paste											
39.0	2867	1307	3429	9636	2007	0.36	9.45	3.5	2.18	5.70	89.00
24.6	3455	1835	16657	9636	2244	0.32	19.97	0.39	0.14	1.64	30.55
0.0	4004	2606	6500	18000	2650	0.13	40.03	0.00	0.00	0.00	0.00

The blue values have been changed for the different used frequencies in order to reflect the changes on the attenuation coefficient for both cement pastes matrix (including porosity effect 24.6/39.0 %). Digital signal processing involves the output parameters estimation. After that, it was performed the correlation with the microstructural features controlled by the IoM. Ultrasonic parameters were the P-wave and S-wave velocity, attenuation coefficient for full wave and P and S independent waves, centroid frequency calculated at transmitted and reflected signal. These parameters are selected to characterize the viscoelastic and the scattering effect of ultrasonic energy on each IoM and the subsequent matching with the ranged microstructural features involved in this theoretical study. Last stage involves the correlationship of the extracted parameters and the analysis of them in the range of microstructures will provide relevant information to assess the referred microstructures (respect of the IoM) using frequency-variation of ultrasonic testing.

4. Results

Regarding the simulations on the CP-Matrix, it can be extracted the following results:
- The different evolution of the attenuation coefficient from the pulse frequencies allows establishing some kind of estimation of porosity typology and range. Some missed points in the Figure 3 are related to unstable simulation and the scattered relationship could be observed in some porous range causes by the reduced size of IoM and the limited portion interaction between the propagation inside the considered IoM.
- Higher porosity range (35%-39%) show a rapid increasing of attenuation and a saturation effect from 5 MHz of central frequency.
- Lower (16%-20%) and intermediate (22%-31%) porosity ranges show linear increasing with different slopes. For the lower porosity range it is shown slops lower than 1.5 dB/MHz, intermediate porosity ranges show slops higher than 2 dB/MHz.

Regarding the simulations on the Mortar matrix, it can be extracted the following results:
Finding edges of the IoM at the 2-phases images, it can be simulated the interfacial zone of 50 um of width by using 1000x1000 pixels (6% of total area will be assigned to ITZ). This new phase represents a better approach to the real microstructural composition. The ITZ has been simulated as a higher porosity CP-matrix, so that low density and elastic values are assigned (Tab. 3). This is a novel contribution of the STSM of the Cost Action TU1404.

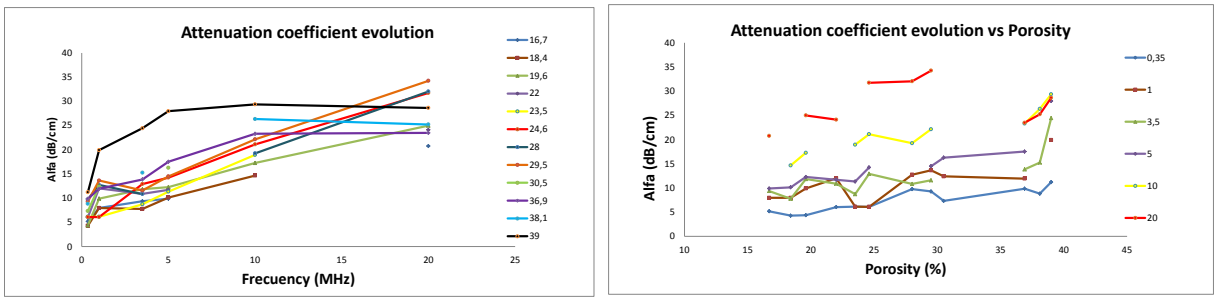

Figure 3. Correlation attenuation, porosity and ultrasonic frequencies (cement pastes).

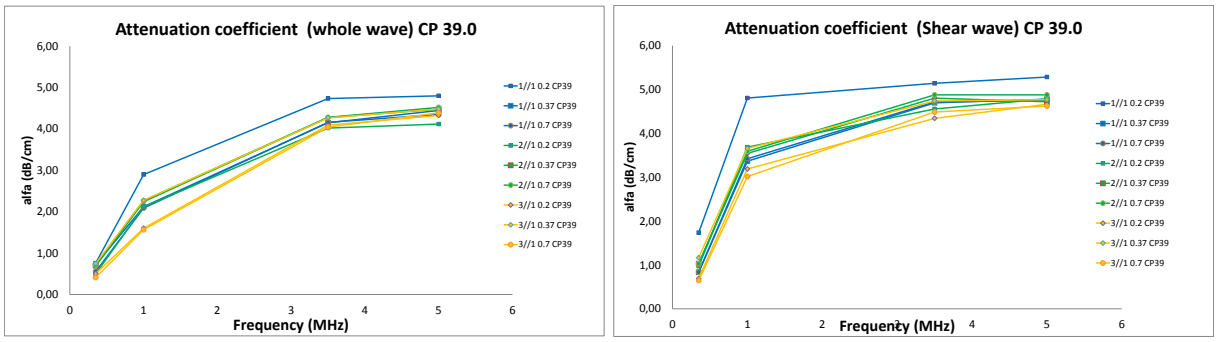

Figure 4. Correlation ultrasonic attenuation, porosity and ultrasonic frequencies (mortars).

5. Conclusions

This study explores the feasibility of using the frequency-attenuation dependence of the ultrasonic attenuation for a wide range of microstructures. A limited of set of images has been obtained in this research. Some reasonable matching of expected trends for ultrasonic parameters has been obtained for the low elastic constant of the interfacial zone or region in the mortar simulation regarding the output values for IZT in the Tab 3.

Acknowledgements

The Spanish Ministry of Economy, Industry and Competitiveness supported this research under grants numbers BIA-2014-55311 OndaTest.

References

[1] Jens Becker; Laurence J. Jacobs and J. Qu. Characterization of cement-based materials using diffuse ultrasound, Journal of Engineering Mechanics 129 (2013), 1478-1484.
[2] M. Molero, I. Segura, S. Aparicio, J.V. Fuente, Influence of aggregates and air voids on ultrasonic, velocity and attenuation in cementitious materials, European Journal of Environmental and Civil Engineering, Vol. 15, Issue 4 (2011), 501-517.
[3] Ivan Gabrijel, Dunja Mikulić and Bojan Milovanović, Application of Ultrasonic Measurements for Determination of Setting and Hardening in Cement Paste, Journal of Civil Engineering and Architecture Volume 5, No. 3 (2011), 278-283.
[4] G. Ye, K. van Breugel, A.L.A. Fraaij, Experimental study on ultrasonic pulse velocity evaluation of the microstructure of cementitiuos material at early page, Delft University of Technology, HERON, vol. 46, nº 3, (2001).

SynerCrete'18 International Conference on Interdisciplinary Approaches
for Cement-based Materials and Structural Concrete
24-26 October 2018, Funchal, Madeira Island, Portugal

MICROSTRUCTURE-BASED PREDICTION OF THERMAL PROPERTIES OF CEMENT PASTE AT EARLY AGES

Hadi Mazaheripour [(1)], Amin Abrishambaf [(1)], Rui Faria [(1)], Miguel Azenha [(2)], Guang Ye [(3)]

(1) Faculty of Engineering, University of Porto (FEUP), Porto, Portugal
(2) School of Engineering, University of Minho, Guimarães, Portugal
(3) Microlab, Delft University of Technology, Delft, The Netherlands

Abstract
The time-dependent process of cement hydration affects many physical and mechanical properties of the cement-based materials, particularly at early ages. To estimate the thermomechanical response of cementitious composites, such as concrete, determination of thermal properties, including heat capacity, thermal conductivity and coefficient of thermal expansion, are necessary. An effort is made in the present study to predict the thermal behaviour of cement pastes by simulating the development of the microstructure during the hydration progress. The model deals with the thermal properties of main cement hydration products, Calcium-Silicate-Hydrate (C-S-H) and Calcium Hydroxide CH, and the change in their volume fraction in the microstructure. The paper discusses the results of thermal conductivity and the specific heat capacity from the model, and they are compared to some recent experimental data from the literature.

1. Introduction

The prediction of the thermomechanical behaviour of concrete depends on adequate knowledge of its thermal properties. Heat capacity, thermal conductivity and coefficient of thermal expansion are the properties that play important roles in the structural behaviour of concrete structures (RC) at early ages, especially the massive ones [1], which are particularly prone to significant thermal stress development. At early ages, these thermal properties evolve with the changes in the microstructure due to cement hydration processes. Therefore, an understanding of the thermal properties of cement paste can contribute to the prediction of such properties for concrete. The evolution of thermal properties in cement paste during hydration is mainly due to the difference between the thermal properties of the hydration product (i.e. Calcium-Silicate-Hydrate (C-S-H)) and those of the corresponding reactants. In

this paper, a microstructural modelling strategy is proposed to estimate the thermal properties of cement paste at early age in respect with the change in the volume fraction of the cement paste components in the microstructure. The thermal properties of cement paste are simulated by modelling its microstructure on a cubic representative elementary volume (REV) with a periodic boundary condition. The REV is obtained through application of the HYMOSTRUC3D hydration model. The method and some primary results in terms of the effective thermal conductivity and the specific heat capacity per unit mass are presented in the present herein.

2. Cement paste: properties and simulations of nano-micro structural features

This study focuses on CEM II 42.5R, as marketed in Portugal. The mineral composition of this cement, expressed in mass percentage, is: 63.2% C3S, 2.6% C2S, 7.6% C3A, 11.6% C4AF, and 11.3% limestone. The cumulative particle distribution size (PSD) of cement was measured by using Laser Diffraction Spectrometry (LDS). The PSD curves can be fairly defined as a Rosin-Rammler function, i.e. $f(D)=1-e^{-bDn}$, where D is the diameter of the cement particle, and b and n are coefficients. By employing a curve fitting analysis, the values of 0.052 and 1.00 were calculated for, respectively, b and n. The thermal properties of individual components of cement clinker and limestone, as well as the hydration product adopted from the literature, and written in Table 1.

Table 1: Some thermal properties of cement paste components used for the simulation.

Compound		**Thermal conductivity** W/m.K	**Specific heat capacity** J/(kg.K)	**Density** g/cm^3
Clinker phases	C3S	3.45 [2]	0.69 [2]	3.13 [2]
	C2S	3.35 [2]	0.68 [2]	3.31 [2]
	Average	3.29	0.73	3.15
Limestone (saturated)		2.95 [3]	0.92 [3]	2.50 [3]
CH		1.32 [2]	1.15 [2]	2.17 [2]
C-S-H globules (Ca/Si=1.75)		0.98 [2]	0.84 [2]	2.6 [2]
Inner C-S-H – saturated *		0.870 [2] (0.883)	0.86-0.97 [2] (0.88)	2.18
Outer C-S-H– saturated *		0.825 [2] (0.830)	0.86-0.97 [2] (0.90)	1.99
Water in gel pores		0.607 [4]	1.13 [5]	1.0
Water in capillary pores		0.607 [4]	4.18	1.0

* the values in the parenthesis obtained from the nanostructure model in the present study.

2.1 Simulation of the nanostructure of C-S-H

The thermal conductivity and the specific heat capacity of the inner and outer C-S-H is estimated by simulating the nanostructure of these products. The nanostructure of outer C-S-H is constructed by assuming the random close packing of mono-sized (5 nm) C-S-H sphere globules (Figure 1a). The random close packing of mono-sized is equivalent to "*the maximum density that a large, random collection of spheres can attain and this density is a universal quantity*" [6]. This packing density of mono-sized sphere is about 0.64, which is very close to the packing density reported for the outer C-S-H globules [2]. In this study, the code from Skoge *et al.* [7] is used to generate the nanostructure of outer C-S-H, which is based on molecular dynamics mechanism. The nanostructure of the inner C-S-H is also simulated by

the close packing of mono-sized (5 nm) C-S-H globules (Figure 1b). For the case of the inner C-S-H, the close packing of mono-sized spheres is arranged in a lattice, and not as a random form. The packing density is approximate 0.74, which is higher than that of the random close packing, and it is very close to the density reported for the inner C-S-H in the literature [2].

2.2 Simulation of the microstructure of cement paste

The latest version of HYMOSTRUC3D software [8] is used for constructing the cement paste microstructure during hydration. This simulation is implemented in a cubic REV volume of the cement paste where the cement particles are modelled as spheres randomly distributed. The initial number and diameter of the particles are built in accordance with PSD curve. The main cement hydration products are the Calcium-Silicate-Hydrate (C-S-H) and the Calcium Hydroxide (CH). C-S-H is formed as two layers of inner and outer products, which are the result of the inward and outward radial growing of the cement spheres. The important parameters to be defined in HYMOSTRUC3D for modelling cement hydration are minimum and maximum size of the cement particles, REV size, temperature, *w/c*, and two reaction factors that control the speed and progress of hydration. For further details on fundamental aspects of the model parameters, the reader is addressed to the studies in [8, 9]. The hydration analysis was performed for *w/c* = 0.3, 0.4, 0.5 and 0.6. The curing temperature was set at 20°C. An image of the microstructure can be seen in Fig. 1c.

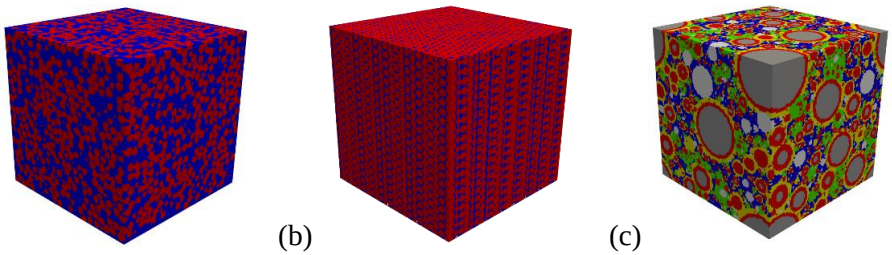

(a) (b) (c)

Figure 1: The nanostructure of (a) the outer CSH, and (b) the inner CSH (blue: gel water, red: CSH globules); (c) the microstructure of a hydrated cement paste (grey: unreacted cement, red: inner CSH, yellow: outer CSH, white: limestone, blue: capillary water, green: CH).

3. Estimation of the effective thermal properties

The REV microstructure obtained from HYMOSTRUC3D is digitalized by means of voxels of 1.0×1.0×1.0 μm^3. A single material phase is assigned for each voxel based on the greatest volume fraction of the material that the voxel is representing. For example, if the voxel is in the boundary of two material phases (e.g. inner and outer C-S-H), the voxel represents the material with the higher volume fraction. The whole REV is totally discretized to 10^6 voxels of six different material phases including: unreacted cement, inner and outer C-S-H, CH, limestone, and pore/water phases. The simulations assume saturated conditions (simplifying assumption at the present stage), hence the pore phases are filled by water, and they are simulated as solid-like behaviour elements with the relevant thermal conductivity. The simplification of solely considering thermal conduction effects for water is backed by previous studies, which have shown that the other contributions such as thermal convection and radiative conductivity in the pore phases (both capillary and gel pores) can be neglected at the microstructural scale [10]. The size of the pores is an effective parameter to address the

thermal properties of water. Two types of water phases are assumed: 1) water in gel pores (being presented only in gel porosity in the nanostructure of C-S-H), and 2) water in capillary pores (being presented in the microstructure of cement paste. The thermal properties of these two types of confined water are given in the last rows in Table 1, based on [2, 4]. The same strategy is followed for discretization of the nanostructure of the inner and outer C-S-H. In this case, the nanostructure includes only two material phases: 1) C-S-H globules; 2) gel pores.

The thermal conductivity: the thermal conductivity of C-S-H is estimated by simulating the discretised REV nanostructure of the outer and inner C-S-H under a steady state condition of temperature field. By imposing unit degree of temperature difference at two sides of the REV, the effective thermal conductivity simply is

$$\lambda_{eff} = -\left\langle q_z^r \right\rangle \Delta z = -\left\langle q_z^r \right\rangle L \tag{1}$$

where q_z^r is the heat flux of phase *r* flowing through the REV in *z* direction from the outer surface with higher temperature to another surface with lower temperature. The operator $\langle . \rangle$ denotes volume averaging. *L* is the length of the REV, in correspondence to the distance between the two surfaces with a unit degree of temperature difference. The discretised REV is imported to DIANA FEA software. The voxels are considered as eight-node isoparametric solid elements for general three-dimensional potential flow analysis.

The specific heat capacity: according to the thermoelacticity, the elastic properties, the heat capacity, and thermal expansion coefficient are correlated [10]. However, for C-S-H hydration product, the contribution of heat energy to its elastic behaviour can be neglected, meaning that the specific heat at constant volume (C_v) can be assumed equal to the specific heat capacity per unit volume (C_p) [2, 10]. Therefore, the effective heat capacity per unit volume (C_p^{eff}) can be derived by

$$C_p^{eff} = \left\langle C_p^r \right\rangle \approx C_v^{eff} \tag{2}$$

where C_p^r is the specific heat capacity of phase *r* in the nanostructure of the C-S-H. The calculated results of the effective thermal conductivity and specific heat capacity of the inner and outer C-S-H are also given in Table 1 (values in the parenthesis). The results are in good agreement with the previous results reported in [2]. Eqs. (1) and (2) can be also used for calculation of the effective thermal properties of the cement paste microstructure. The thermal properties of C-S-H phases (inner and outer) are taken from the analysis on the nanostructure of C-S-H as described earlier. The thermal properties of other phases are written in Table 1.

4. Experimental *vs* numerical results

An example of the results from the model for *w/c* = 0.3 at 0.65 degree of reaction in terms of temperature gradient and the heat flux gradient is shown, respectively, in Figure 2a and b. In Figure 3, the obtained results in terms of the effective thermal conductivity are compared to

the results from recent studies in the literature [11-15] for *w/c* ratios of 0.3 and 0.4 at different hydration time. It should be noted that the experimental results are collected only for saturated cement paste samples, and that the data is not necessarily correspondent to the same type of cement. Despite the observable scatter in the data obtained from the literature, the simulation lies within acceptable margins in regard to experimental data. In the same figure, a comparison is also made between the simulation results and some few data in the literature [12, 13, 16] in terms of the specific heat capacity per mass unit of cement paste. The specific heat capacity per unit mass is calculated in accordance with the calculated density by the model using the discretized REV microstructure. The measurement of thermal properties of the exact cement type simulated in the present paper is still an ongoing process, and cannot yet be communicated herein.

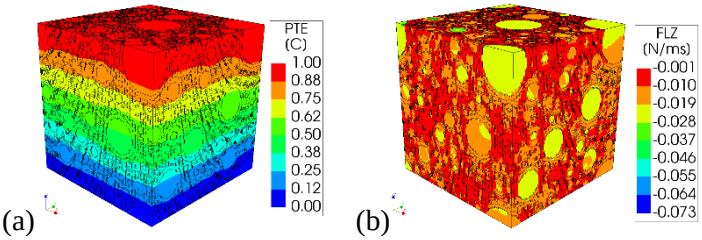

Figure 2: (a) nodal temperature gradient (PTE), (b) heat flux gradient in z direction (FLZ).

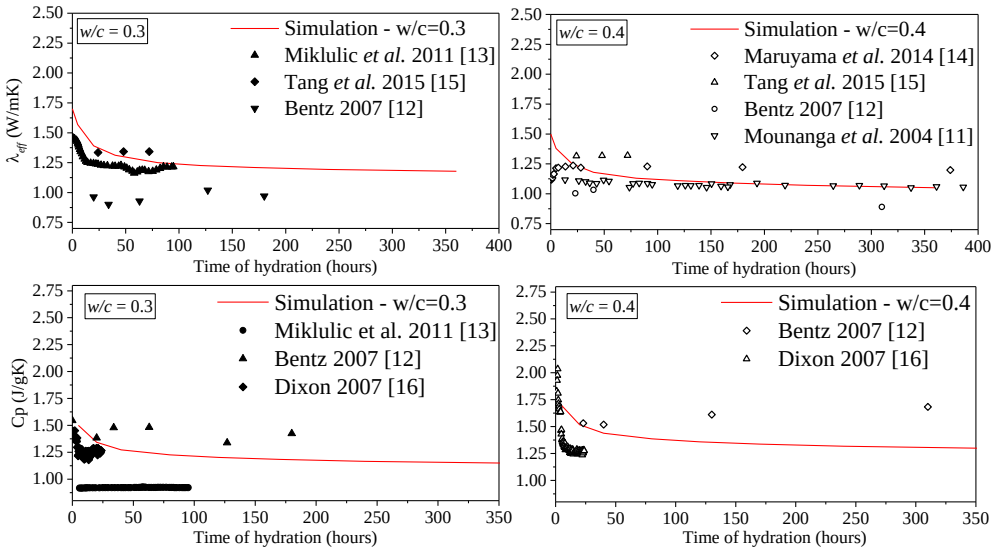

Figure 3: Comparison between the experimental and numerical results.

5. Conclusion

The primary focus was on the evolution of the thermal conductivity and the specific heat capacity. The thermal properties obtained based on the nanostructure of C-S-H (both inner and outer) are in good agreement with the results in the literature. Despite the experimental results from the literature for cement paste being highly scattered, the obtained results are in an acceptable margin, providing grounds to the feasibility of the proposed methodology.

Acknowledgements
This work was financially supported by: Project POCI-01-0145-FEDER-007457 (CONSTRUCT - Institute of R&D in Structures and Construction) and by project POCI-01-0145-FEDER-007633 (ISISE), funded by FEDER funds through COMPETE2020 - Programa Operacional Competitividade e Internacionalização (POCI), and by national funds through FCT - Fundação para a Ciência e a Tecnologia. FCT and FEDER (COMPETE2020) are also acknowledged for the funding of the research project IntegraCrete PTDC/ECM-EST/1056/2014 (POCI-01-0145-FEDER-016841). The financial support of COST Action TU1404 through its several networking instruments is also gratefully acknowledged.

References
[1] Azenha, M. et al, Application of air cooled pipes for reduction of early age cracking risk in a massive RC wall. Engineering Structures 62-63 (2014), 148-163
[2] Abdolhosseini Qomi, M.J. et al, Physical Origins of Thermal Properties of Cement Paste. Physical Review Applied 3(6) (2015), 064010
[3] Thomas Jr, J. et al, Thermal conductivity of carbonate rocks. Engineering Geology 7(1) (1973), 3-12
[4] Etzler, F.M. and White, P.J., The heat capacity of water in silica pores. Journal of Colloid and Interface Science 120(1) (1987), 94-99
[5] Bonnaud, P.A. et al, Temperature dependence of nanoconfined water properties: application to cementitious materials. The Journal of Physical Chemistry C 120(21) (2016), 11465-11480
[6] Torquato, S. et al, Is random close packing of spheres well defined? Physical review letters 84(10) (2000), 2064
[7] Skoge, M. et al, Packing hyperspheres in high-dimensional Euclidean spaces. Physical Review E 74(4) (2006), 041127
[8] Ye, G., Experimental study and numerical simulation of the development of the microstructure and permeability of cementitious materials, PhD Thesis, Delft University of Technology (2003)
[9] Van Breugel, K., Simulation of hydration and formation of structure in hardening cement-based materials, PhD Thesis, Delft University of Technology (1991)
[10] Honorio, T. et al, Thermal properties of cement-based materials: Multiscale estimations at early-age. Cement and Concrete Composites 87 (2018), 205-219
[11] Mounanga, P. et al, Experimental study and modelling approaches for the thermal conductivity evolution of hydrating cement paste. Advances in Cement Research 16(3) (2004), 95-103
[12] Bentz, D.P., Transient plane source measurements of the thermal properties of hydrating cement pastes. Materials and Structures 40(10) (2007), 1073
[13] Mikulić, D. et al, Analysis of thermal properties of cement paste during setting and hardening, Nondestructive Testing of Materials and Structures, Springer (2013), 465-471
[14] Maruyama, I. and Igarashi, G. Cement reaction and resultant physical properties of cement paste. Journal of Advanced Concrete Technology 12(6) (2014), 200-213
[15] Tang, S.W. et al, A fractal approach to determine thermal conductivity in cement pastes. Construction and Building Materials 74 (2015), 73-82
[16] Dixon, J.C., The shock absorber handbook, John Wiley & Sons (2008)

SynerCrete'18 International Conference on Interdisciplinary Approaches
for Cement-based Materials and Structural Concrete
24-26 October 2018, Funchal, Madeira Island, Portugal

MULTI-SCALE MODELING AND NON DESTRUCTIVE TESTING: ASSESSING WATER CONTENT OF CONCRETE

Vincent Guihard [1,2], Jean-Luc Adia [3], Julien Sanahuja [3]

(1) LMDC, Toulouse, France
(2) EDF lab PRISME department, Chatou, France
(3) EDF lab MMC department, Moret sur Loing, France

Abstract
Concrete delayed behavior (shrinkage, creep, etc...) prediction can be significantly improved by monitoring the amount and spatial distribution of water within a concrete structure over time. Electromagnetic properties, such as dielectric permittivity, of heterogeneous and porous materials are closely linked to water content. Measurement of these properties is thus a common non destructive technique to assess the moisture content. A calibration curve is then required to relate the measured permittivity to the saturation degree. This curve can be classically determined experimentally, or from empirical models. However, the first approach is tedious and time consuming, and the second one is not taylored to the specific concrete at stake. This contribution thus proposes an alternative route, relying on an explicit description of liquid and gas phases in the pore domain, and on upscaling techniques. This approach is presented and validated on unsaturated sand for the sake of simplicity. Then, an application to cement pastes is described.

1. Introduction: industrial context

Both concrete delayed mechanical behavior and durability properties depend on its moisture content. Assessing the latter is thus of paramount importance for long term operation of civil engineering structures. While direct measurements are possible, they are by nature destructive, which may not be feasible depending on the structure of interest. Non destructive testing procedures are thus of great importance. These techniques take advantage of the sensitivity to water content of an easily measurable physical property. Due to the relative contrast between liquid (around 80), gas (1) and solids (about 3-10) properties, dielectric permittivity represents an appealing property. It is straightforward to measure, either from

embedded sensors or from the surface using a hand-held probe [1]. A calibration curve is then required to relate permittivity to moisture content.
Such a calibration curve is often obtained experimentally, point per point [2, 3]. This requires to successively equilibrate a concrete sample with various relative humidities. At each step, once equilibrium has been reached, permittivity is measured. A large enough sample must be considered, to be representative of concrete, but the larger the sample, the longer the moisture equilibration process. Obtaining such an experimental calibration curve can thus be tedious and time consuming, and this process has to be repeated for each different concrete. On the other hand, classical empirical relations tend to lack accuracy as they are not taylored to the uniqueness of each concrete. Multi-scale modeling then represents an interesting alternative, as it could allow to break down concrete into individual phases whose elementary permittivity is expected to be a unique property from one concrete to another.
The main originality of this contribution lies in the proposed multidisciplinary approach, combining signal processing, multi-scale microstructure representation, fluids repartition modeling in pore domain, and permittivity homogenization. The process is first validated on a model material: unsaturated sand. Then, a multiscale morphological model of mature cement paste is designed, going down to elementary solid phases, liquid, and gas. Finally, a first validation is performed with respect to several cement pastes.

2. Dielectric constant measurement with an open-ended coaxial probe

Dielectric constant of materials can be derived from the analysis of transmission and reflection of electromagnetic waves through a sample inserted into a coaxial structure [4] or placed at the end of this structure in the case of reflection-only based devices. In this particular case, reflection phenomena are induced by the impedance discontinuity caused by the sample located at the end of the coaxial structure. Open-ended coaxial probes are one of these methods. They present simple implementation and a broad frequency range driven by the network analyzer used to synthesize the RF signal. The non-destructive and non-invasive characteristics of such tools have enabled investigations of various kinds of media, including soils [2] and stems of mature trees [3]. Measurements have also been performed to validate models for coupled heat and moisture transport in building materials [5].
In the present contribution, a specially designed large probe (figure 1 left) was built in order to investigate heterogeneous materials. Appropriate signal processing yields the complex permittivity of the material as a function of frequency.

3. Relating permittivity to saturation degree: principle and validation on sand

A model material is first considered: unsaturated sand. Indeed, the solid phase (sand grains) can be considered as homogeneous. From density measurements on the dry sand in a natural state and on the bulk rock (characteristic of the solid phase), porosity is estimated as $\phi = 37 \pm 0.2$ %. For each target saturation degree S_r, the volume of water to be added is deduced. After mixing this water with dry sand, the sample is compressed to reach the reference volume of dry sand. Porosity is thus maintained equal for each saturation degree. Permittivity measurement is then performed over the frequency range 200 - 800 MHz

(figure 1 right). The average over this range will be considered for subsequent comparisons. The modeling process is first briefly described in the next three subsections.

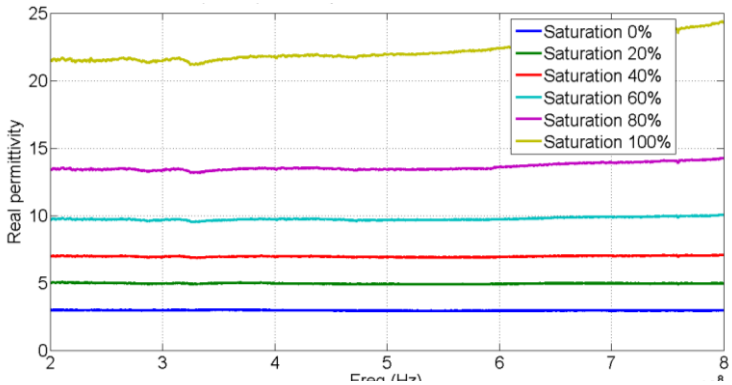

Figure 1: Left: coaxial probe and vector network analyser (VNA) used in this contribution. Right: real part of permittivity of sand for saturation degrees S_r = 0, 20, 40, 60, 80, 100 %.

3.1 Microstructure generation

First, a representative elementary volume (REV) of dry sand has to be generated. In the pore domain (complementary to the solid grains), liquid and gas phases are not yet distinguished. To later optimize convergence with respect to the REV size, microstructure is built as periodic. Sand grains are obviously non overlapping, and represented as spheres. The size distribution is assumed to be monodisperse. The diameter of particles is 2 mm while the REV size is 10 mm. The solid volume fraction, 63 %, being around the random close packing of monodisperse spheres, the Random Sequential Adsorption algorithm cannot be used as it is far from being able to reach such a high volume fraction. The Lubachevsky and Stillinger algorithm [6] is more suitable, as it considers particles growing up to the required volume fraction.

The microstructure generation process is more detailed in [7]. The geometrical representation of the microstructure is obtained as a list of spheres. For subsequent operations, a sampled version is generated, as a 3D image made up of voxels (figure 2 left).

3.2 Liquid and gas repartition

Second, a realistic repartition of liquid and gas at equilibrium in the pore domain of the sand REV has to be generated. It can be derived from multiphase fluid flow modeling. The macroscopic approach, using computational fluid dynamics, can be tedious due to the specific treatments required to track the interfaces between liquid and gas phases. The microscopic approach, based on molecular dynamics, is highly time and memory consuming: current computers cannot cope with large volumes such as realistic pore domains. Therefore, a mesoscopic description based on kinetic theory is considered as a compromise. The Lattice Boltzmann Method (LBM) [8] is indeed an appealing numerical tool, particularly for multiphase flows. Liquid and gas interfaces emerge from the physical nature of the interactions between fluid molecules at the microscopic level, which are described by a mean-field interaction potential.

For the interested reader, more details about theory, implementation and validation of the LBM method used in this contribution can be found in [9]. Sample repartitions of liquid and gas in pore domain of sand are represented on figure 2 right.

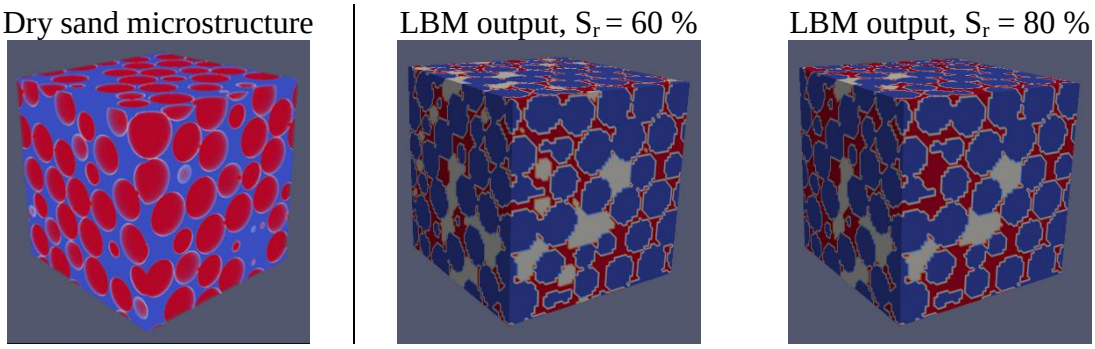

Figure 2: Generated periodic microstructure of dry sand (red: sand grains; blue: pore domain), and liquid/gas repartitions from LBM computations (blue: sand grains; red: liquid; gray: gas).

3.3 Numerical homogenization of permittivity

Third, the effective permittivity of a 3D image of unsaturated porous material is estimated using numerical homogenization. Taking advantage of the equivalence between an electrostatics boundary value problem and a heat conduction one, a numerical code initially developed for heat transfer [10] is reused. The latter is based on finite differences and implements a multigrid solver, relying on the PETSc library [11]. Periodic boundary conditions are considered to optimize convergence with respect to the REV size [12]. The permittivities of elementary phases are respectively 4.5, 1 and 80 for sand grains, gas and liquid. Once the boundary value problem is solved, the effective permittivity is computed from volume averages of local fields.

3.4 Comparison to experimental measurements and alternative analytical estimates

For each saturation degree, calculation processes are repeated from five different random geometries, in order to investigate results deviation. A very good agreement between experimental and numerical permittivities is observed (figure 3).

As computation time may prevent the broad use of numerical homogenization processes, analytical estimates can be appealing. Both the empirical Topp equation [2] and the symmetric Bruggeman upscaling model [13] (also known as the self-consistent scheme in the elasticity framework) provide a reasonable estimate of the effective permittivity, see figure 3.

4. Application to cement paste

This first application to cementitious materials uses mean-field homogenization, as microstructure is highly complex to describe comprehensively. A morphological model of mature cement paste is proposed (figure 4), going down to elementary solid phases, liquid and gas. It is inspired by the morphologies designed to upscale mechanical behavior, such as [14, 15]. The main differences rely in the pore space representation and liquid/gas repartition in the latter. A specific procedure is conducted to identify the permittivity of the elementary solid phases.

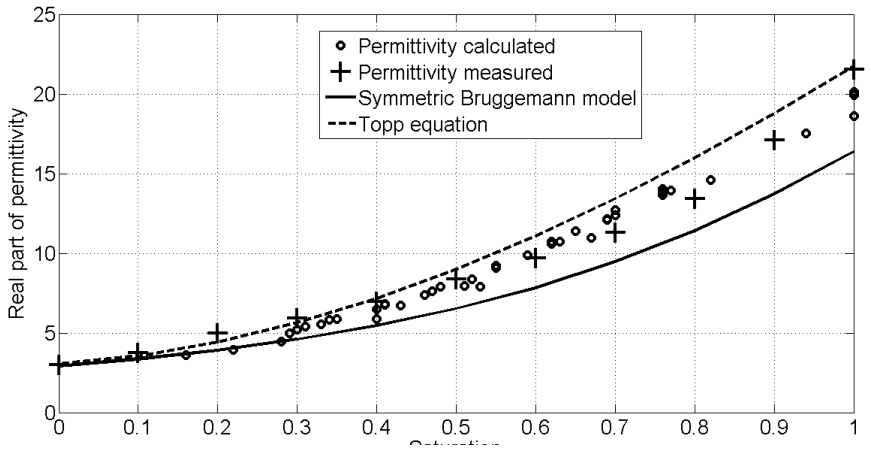

Figure 3: Comparison between measured and numerically or analytically estimated effective permittivity of unsaturated sand.

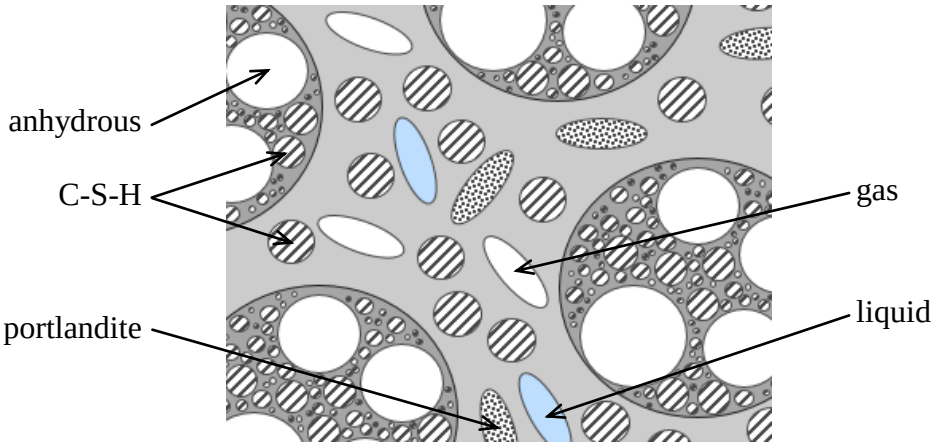

Figure 4: Simplified morphological model of cement paste.

The global approach is then validated on two different cement pastes. The saturation degree dependence of permittivity is reasonably predicted (figure 5).

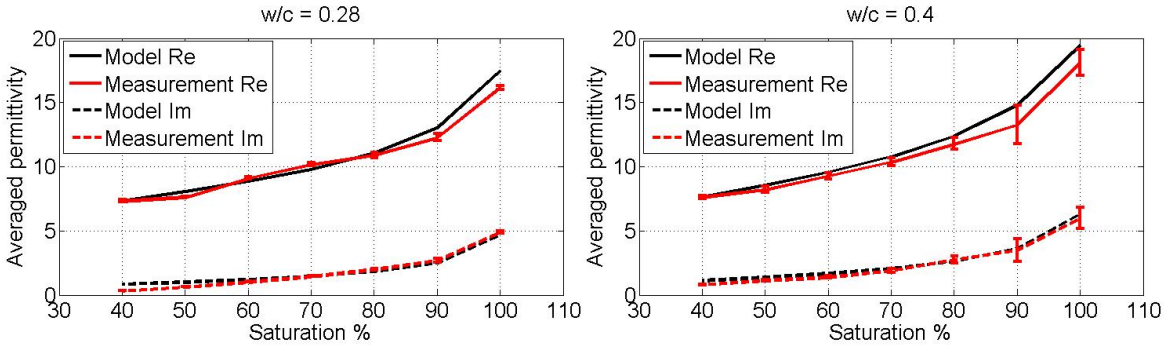

Figure 5: Average (over 750 - 1000 MHz range) real and imaginary permittivities, measured and modeled for cement pastes at w/c = 0.28 and 0.4.

Prospects include refinements of the morphological model and extensions to concrete. Direct application to drying structures would yield an average moisture content, over a depth roughly equivalent to the probe diameter. Measuring the moisture profile requires further investigations. Moreover, classical homogenization techniques consider a homogeneous moisture content across the REV, so that structures with high moisture gradients need more developments.

References

[1] Guihard, V., Taillade, F., Balayssac, J.-P., Steck, B., Sanahuja, J., and Deby, F. Modelling the behaviour of an open-ended coaxial probe to assess the permittivity of heterogeneous dielectrics solids. In Progress In Electromagnetics Research Symposium, St. Petersburg, Russia, may 2017.

[2] Topp, G., Davis, J., and Annan, A. Electromagnetic determination of soil water content: Measurements in coaxial transmission lines. Water Resources Res., 16(3):574-582, 1980.

[3] Irvine, J. and Grace, J. Non-destructive measurement of stem water content by time domain reflectometry using short probes. Journal of Experimental Botany, 48(308):813-818, 1997.

[4] Chen, L. F., Ong, C. K., Neo, C. P., Varadan, V. V., and Varadan, V. K. Microwave Electronics Measurement and Materials Characterization. Chapter 3, Reflection Methods. Johan Wiley and Sons, Inc., 2004.

[5] Gawin, D. and Klemm, P. Coupled heat and moisture transfer with phase changes in porous building materials. Archives of Civil Engineering, 40:89-103, 1994.

[6] Lubachevsky, B. and Stillinger, F. Geometric properties of random disk packings. J. Stat. Phys., 60:561-583, 1990.

[7] Lavergne, F., Sab, K., Sanahuja, J., Bornert, M., and Toulemonde, C. Investigation of the effect of aggregates' morphology on concrete creep properties by numerical simulations. Cement and Concrete Research, 71(0):14-28, 2015.

[8] Shan, X. and Chen, H. Lattice Boltzmann model for simulating flows with multiple phases and components. Physical Review E, 47(3):1815-1819, 1993.

[9] Adia, J.-L. Multi-scale modelling of the shrinkage and creep phenomena of cementitious materials: a combined Finite Elements-Lattice Boltzmann-numerical approach. PhD, 2017.

[10] Sanahuja, J. and Toulemonde, C. Numerical homogenization of concrete microstructures without explicit meshes. Cement and Concrete Research, 41(12):1320-1329, 2011.

[11] Balay, S., Abhyankar, S., Adams, M. F., Brown, J., Brune, P., Buschelman, K., Dalcin, L., Eijkhout, V., Gropp, W. D., Kaushik, D., Knepley, M. G., May, D. A., McInnes, L. C., Mills, R. T., Munson, T., Rupp, K., Sanan, P., Smith, B. F., Zampini, S., Zhang, H., and Zhang, H. PETSc Web page. http://www.mcs.anl.gov/petsc, 2018.

[12] Kanit, T., Forest, S., Galliet, I., Mounoury, V., and Jeulin, D. Determination of the size of the representative volume element for random composites: statistical and numerical approach. International Journal of Solids and Structures, 40:3647-3679, 2003.

[13] Bruggeman, D. A. G. Berechnung verschiedener physikalischer konstanten von heterogenen substanzen. i. dielektrizitätskonstanten und leitfÃ¤higkeiten der mischkörper aus isotropen substanzen. Annalen der Physik, 416(7):636-664, 1935.

[14] Bernard, O., Ulm, F.-J., and Lemarchand, E. A multiscale micromechanics-hydration model for the early-age elastic properties of cement-based materials. Cement and Concrete Research, 33(9):1293-1309, 2003.

[15] Sanahuja, J., Dormieux, L., and Chanvillard, G. Modelling elasticity of a hydrating cement paste. Cement and Concrete Research, 37(10):1427-1439, 2007.

SynerCrete'18 International Conference on Interdisciplinary Approaches
for Cement-based Materials and Structural Concrete
24-26 October 2018, Funchal, Madeira Island, Portugal

NUMERICAL ANALYSIS OF THE DRYING KINETICS IN 3D CONCRETE SPECIMENS OF DIFFERENT SIZE

Benoit Bary [(1)], Stéphane Poyet [(1)]

(1) Den-Service d'Etude du Comportement des Radionucléides (SECR), CEA, Université Paris-Saclay, F-91191, Gif-sur-Yvette, France

Abstract

We propose in this study to investigate numerically the variability of water permeability in unsaturated conditions through the simulation of drying on concrete specimens of different size. Numerical simulations on 3D reconstructed cylindrical concrete samples are performed and analyzed so as to investigate the effects of their thickness on the overall drying kinetics. Water transfer is modelled via a classical approach involving a single mass balance equation associated with the matrix phase corresponding to mortar. Besides the 'structural' variability related to the random process of aggregate placement, another source of variability is introduced through a distribution on the porosity. The results obtained in terms of drying kinetics and saturation degree profiles are analyzed and discussed, with a special regard to the effects of the thickness of the concrete specimens. Comparisons with simulations on the same specimens with homogeneous parameters for the drying model are made macroscopically.

1. Introduction

An accurate description of water exchange between concrete material and its surrounding environment is of major importance for durability assessment of concrete structures. In this regard, permeability is a key parameter as it characterizes the ability of a fluid to transport through concrete porosity due to pressure gradients. As such, permeability is generally viewed as a relevant durability index for service-life prediction. Its experimental characterization is usually performed using specimens prepared in laboratory conditions. However this procedure may not appear totally satisfactory since the obtained properties often differ from the ones of concrete prepared onsite. Indeed, while 'labcrete' specimens are commonly prepared carefully with batches of limited volume in controlled environmental conditions, 'fieldcrete' is prepared in much larger batches in concrete plants with variable conditions,

before being cast onsite. In this context it has been shown recently that fieldcretes exhibit lower general performance and more variability regarding permeability properties than labcretes [1].
In this study we investigate numerically the water permeability and its variability in unsaturated conditions via the simplified simulation of drying on concrete specimens of different sizes. Computations on 3D reconstructed cylindrical concrete samples are then performed and analyzed to examine the effects of their thickness on the overall drying kinetics. The specimens are generated by randomly dispersing polyhedral aggregates of various shapes and sizes in a cube, from which cylinders of specified diameter and various thicknesses are cored. Water transport is modelled via a standard approach involving a single mass balance equation for the matrix phase corresponding to mortar. Besides the 'structural' variability related to the random process of aggregate placement, another source of variability consisting in a spatial distribution on the porosity is introduced in the simulations. The results obtained in terms of drying kinetics, overall saturation degree and mass loss profiles are analyzed and discussed, with a special regard to the effects of the thickness of the concrete specimens. Comparisons between simulations on the same specimens with homogeneous parameters for the drying model are also made macroscopically.

2. Model

Water transport in unsaturated concrete is described here via a simplified approach accounting only for liquid water permeation. The contribution of overall gas permeation and vapor diffusion is assumed as negligible with respect to the liquid transport [2]. The problem is then formulated with a single equation in the form:

$$\phi\left(\frac{\partial S}{\partial P}\right)\frac{\partial P}{\partial t} = \mathrm{div}\left[\frac{K k_r}{\eta}\mathrm{grad}(P)\right] \tag{1}$$

with ϕ the concrete porosity, S the saturation degree, P the water pressure, η the water viscosity, K the intrinsic permeability and k_r the relative permeability to water. The intrinsic permeability of the concrete was evaluated previously using classical inverse analysis [2]. The classical relation proposed by van Genuchten [3] is further used to describe the water retention curve:

$$S = \left[1 + \left(\frac{P}{P_0}\right)^{\frac{1}{1-m}}\right]^{-m} \tag{2}$$

where m and P_0 are two positive parameters that have been identified in [1] to the following values corresponding to a fieldcrete: $m = 0.532$ and $P_0 = 59.05\,\mathrm{MPa}$. Finally, Mualem's model [4] is used to express the relative permeability to water k_r:

$$k_r = \left[1 + \left(\frac{P}{P_0}\right)^{\frac{1}{1-m}}\right]^{-m\alpha}\left\{1 - \left(\frac{P}{P_0}\right)^{-\frac{m}{1-m}}\left[1 + \left(\frac{P}{P_0}\right)^{\frac{1}{1-m}}\right]^{-m}\right\}^2 \tag{3}$$

where α is the pore-interaction factor that characterizes the connectivity and tortuosity of the pore network, and is set to the value -1.2 (see [1] for details). Eq. (1) is solved by means of the finite element code Cast3m (http://www-cast3m.cea.fr/).

3. Numerical procedure

3.1 Specimens generation

The procedure for generating the numerical specimens is described in e.g. [1], [5]. It takes advantage of the functionalities of the CAD code Salome (www.salome-platform.org), and consists in constructed samples by randomly distributing inclusions of given shape and size in a parallelepipedic box. In this study, mesoscopic numerical samples of concrete material are obtained from cubic volumes with dimensions 15×15×15 cm, from which cylindrical samples of diameter 60 mm and different heights ranging from 8 to 110 mm are extracted. The aggregate dimensions are set to conform to an actual grading curve. They consist of convex polyhedrons obtained by a Voronoi space decomposition, further modified to comply with an aspect ratio selected between 1 and 4, so as to resemble real shapes as closely as possible. Note that the actual aggregate volume fraction calculated in the specimens ranges between 0.354 and 0.383, which is higher than the value 0.35 imposed in the initial cubic volumes, see [1]. Figure 1 presents the matrix of 3 generated specimens with thickness of 8, 20 and 55 mm. In this preliminary study, the number of generated specimens is 4, 4, 9 and 15 for the thicknesses of 110, 55, 20 and 8 mm, respectively, which is deemed to be sufficient to get basic statistical information.

Figure 1: examples of specimens with thickness of 8 (left), 20 (middle) and 55 (right) mm.

3.2 Porosity variability

As mentioned above, in this paper we are concerned with the effects of the porosity variability on the drying kinetics and permeability properties. To this aim, simulations are performed with porosity field randomly generated conforming to a Gaussian distribution with mean 0.2 and standard deviation 0.04. Such probability distribution is considered to be close to that of the mortar tested in [6].

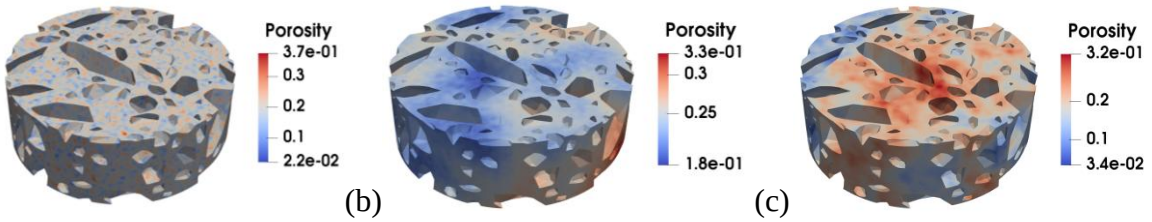

(a) (b) (c)

Figure 2: randomly generated porosity field in a 20 mm-thick specimen: uncorrelated (a), correlation length of 10 mm (b) and of 50 mm (c).

To further analyze the impact of the porosity variability, spatially uncorrelated field and spatially correlated ones with 2 different correlation lengths are generated and the results are compared with constant porosity. Figure 2 illustrates the obtained random fields in the case of a 20 mm-thick specimen for uncorrelated distribution (a), correlated one with correlation

length of 10 mm (b) and of 50 mm (c). Due to the lack of experimental data, the chosen values for these lengths are somewhat arbitrary; this point would deserve further investigations. We observe important differences between the porosity fields obtained with uncorrelated and correlated distributions; the extrema values may be as high as 0.37 and as low as 0.022 in the case of the uncorrelated distribution. Note that, besides being explicitly involved in Eq. (1), the porosity also enters in the expression of the intrinsic permeability through the following Kozeny-Carman relation [7]:

$$K = K_0 \left(\frac{\phi}{\phi_0}\right)^3 \left(\frac{1-\phi_0}{1-\phi}\right)^2 \quad (4)$$

where K_0 is the mean permeability value set to 2.1×10^{-22} m^2, and ϕ_0 is the corresponding mean porosity of 0.2.

4. Results: drying simulations

The drying simulations consist in imposing a relative humidity of 55% at the lateral surfaces of the initially saturated specimens. Figure 3 presents the numerical results in terms of mass loss and average saturation degree evolutions with time, for the 110 (left) and 55 (right) mm-thick specimens, for the different considered porosity distributions.

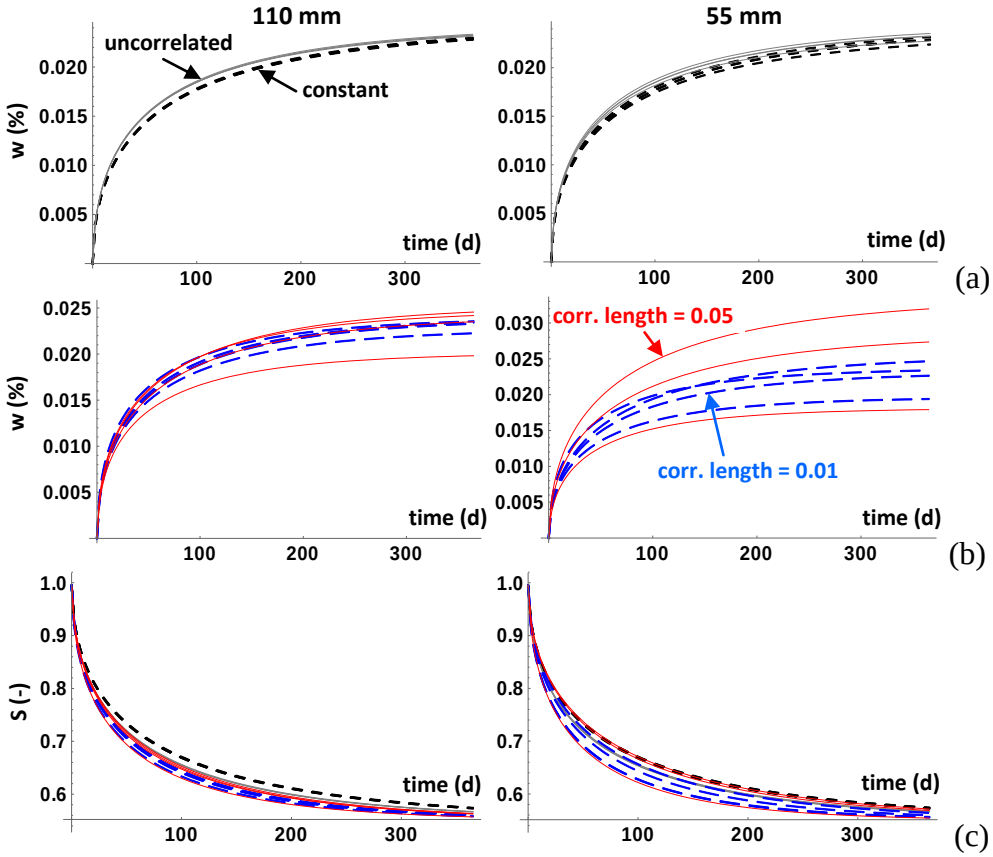

Figure 3: mass loss for the 110 mm (left) and 55 mm-thick specimens (right), for constant and uncorrelated (a), and correlated distributions (b); corresponding saturation evolution (c).

Figure 4 shows the same curves for the 20 (left) and 8 (right) mm-thick specimens. The water mass loss is determined assuming a solid phase density estimated to 2.37 and accounting for the local variable porosity. Note that the isotherm sorption curve is kept constant in the simulations, which is likely an oversimplifying assumption in the case of varying porosity.

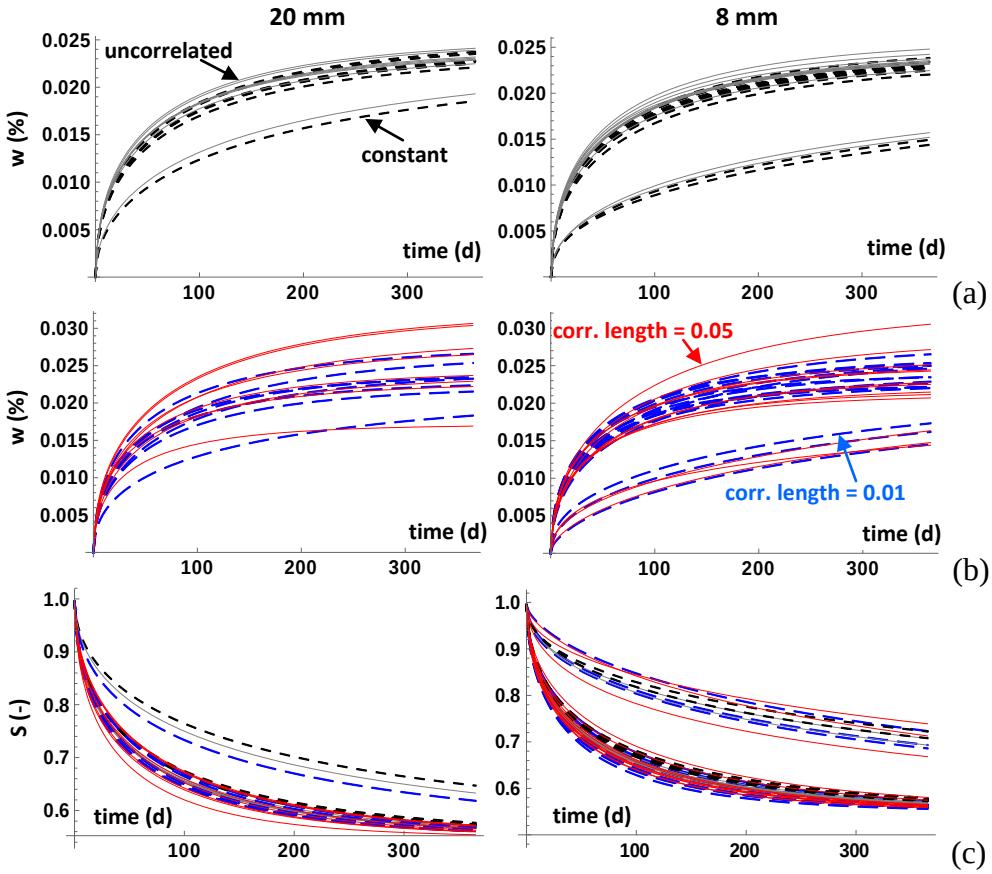

Figure 4: mass loss for the 20 mm (left) and 8 mm-thick specimens (right), for constant and uncorrelated (a), and correlated distributions (b); corresponding saturation evolution (c).

The legend of curves is as follows: black lines and black dashed curves correspond to uncorrelated and constant porosity, blue long-dashed curves and red lines to a correlation length of 10 and 50 mm, respectively. From these curves, we observe that, as expected, reducing the specimen thickness leads to increase the results dispersion. This is particularly visible when comparing the results with constant porosity for 110 and 8 (or 20) mm-thick specimens. Thus, for a sufficiently important specimen size, the variability related to random aggregate size and placement does not appear to explain the dispersion observed experimentally. Another aspect is the moderate effect of the uncorrelated Gaussian distribution on the results, which are very close to the ones obtained with constant porosity. By contrast, introducing correlation lengths in the distribution results in greater dispersion, all the more than the length is high. As mentioned, this aspect would deserve to be more thoroughly examined, as it appears to be very influential. We also note that the results in terms of macroscopic saturation degree evolutions are much less dispersed than their counterparts expressed in mass loss. This is because the saturation degree is defined through a pore volume ratio and does not explicitly integrate the (local) porosity value, contrary to the

mass loss. Finally, we observe on the 20 mm and 8 mm-thick curves that some specimens exhibit a different response, corresponding to a slower drying kinetics. It may be explained by a significantly lower surface exposed to drying.

5. Conclusion

This paper presents first simulation results regarding drying of cylindrical concrete samples of different thicknesses. The 3D specimens are generated numerically by randomly distributing polyhedral aggregates of various shape and size. Water transport is modelled classically via a single mass balance equation involving only liquid water permeation. A variability is introduced in the porosity through uncorrelated and correlated Gaussian distributions. The results are analyzed in terms of time evolutions of mass loss and saturation degree. The main conclusions are that as expected the greater the thickness of the specimens, the lower the dispersion in the mass loss, independently of the porosity variability. The results with constant porosity report a negligible dispersion for the 110 mm-thick specimens, while they exhibit a slight scatter for the 55 mm-thick ones, which signifies that the size of a representative volume may range between these 2 values. Further, the curves obtained with the uncorrelated distribution are close to the ones with constant porosity, indicating that such distributions have very limited effects. By contrast, distributions with correlation lengths may affect significantly the results, depending on the length value. It is then important that this parameter be accurately identified and characterized experimentally.
Among the aspects that would deserve further investigations in the future, besides the characterization of the porosity variability, its links with the isotherm desorption curve dispersion would also be of importance as this curve is known to have a great impact on drying. Confrontation of drying simulation results with experimental data obtained on specimens of same microgeometry (characterized for instance by tomography and numerically reconstructed for the simulations) would be helpful to validate the whole procedure. Finally, possible microcracking, which affects considerably the drying kinetics, should also be accurately described and characterized.

References

[1] S. Poyet and B. Bary, "Analysis of water transport in unsaturated conditions: comparison between labcrete and fieldcrete," *Submitted in Constr. Build. Mater.*, 2018.
[2] M. Mainguy, O. Coussy, and V. Baroghel-Bouny, "Role of air pressure in drying of weakly permeable materials," *J. Eng. Mech. ASCE*, vol. 127, no. 6, pp. 592–592, 2001.
[3] M. T. van Genuchten, "A Closed-form Equation for Predicting the Hydraulic Conductivity of Unsaturated Soils," *Soil Sci. Soc. Am. J.*, vol. 44, no. 5, pp. 892–898, 1980.
[4] Y. Mualem, "A new model for predicting the hydraulic conductivity of unsaturated porous media," *Water Resour. Res.*, vol. 12, no. 3, pp. 513–522, 1976.
[5] T. de Larrard, B. Bary, E. Adam, and F. Kloss, "Influence of aggregate shapes on drying and carbonation phenomena in 3D concrete numerical samples," *Comput. Mater. Sci.*, vol. 72, 2013.
[6] J. Jeong, P. Sardini, H. Ramézani, M. Siitari-Kauppi, and H. Steeb, "Modeling of the induced chemo-mechanical stress through porous cement mortar subjected to CO2: Enhanced micro-dilatation theory and 14C-PMMA method," *Comput. Mater. Sci.*, vol. 69, pp. 466–480, Mar. 2013.
[7] W. D. Carrier III, "Goodbye, hazen; hello, kozeny-carman," *J. Geotech. Geoenvironmental Eng.*, vol. 129, no. 11, pp. 1054–1056, 2003.

SynerCrete'18 International Conference on Interdisciplinary Approaches
for Cement-based Materials and Structural Concrete
24-26 October 2018, Funchal, Madeira Island, Portugal

NUMERICALLY ACCELERATED CHEMICAL EVOLUTION IN CEMENTITIOUS SYSTEMS

Janez Perko [(1)], Diederik Jacques[(1)]

(1) Belgian Nuclear Research Centre SCK·CEN

Abstract
This paper describes the approach for numerical acceleration of reactive transport pore-scale models where transport dominates dissolution/precipitation processes. Chemical changes in cementitious systems are typically transport dominated because of slow chemical reaction rates. The conditions under which the acceleration is possible and the level of acceleration are analysed. For this purpose we derive a new dimensionless number. On this basis the applicability of the approach is demonstrated on a simple system as well as on complex systems and applied to dissolution processes. The result demonstrate that, in the case of calcium leaching from hardened cement paste the dissolution can be accelerated for 50 times.

1. Introduction

Cement-based materials are known as materials with large resistance to some chemical detrimental processes such as calcium leaching because it combines slow transport processes with high buffer properties in a high solid-to-liquid ratio. This high resistance of cementitious materials poses challenges to experimental studies aiming to understand cement behaviour or to optimize cement compositions to increase durability; chemical alterations take a lot of time under natural conditions. To alleviate the problems of slow chemical processes, experimental approaches use so-called accelerated conditions where the chemical processes are accelerated, for example by increasing the solubility of Ca. The shortcoming of accelerated conditions is that the resulting chemical evolution may differ chemically form the evolution obtained under natural conditions. Another approach to alleviate long chemical processes is by numerical modelling. In numerical modelling, the processes are represented by a conceptual and numerical model that are solve by computers which is believed to be faster. When modelling complex problems also numerical models face practical limitations linked to computational resources. In recent years, pore-scale approaches became an attractive method to simulate

durability [1]. However, in order to capture the critical features at that scale, such as the presence of capillary pores or heterogeneity in mineral phases, geometrically information with high resolution is needed in a sufficiently large volume to assure a representative elementary volume (REV). This leads to a very high number of unknowns with substantial memory and computational costs, especially in three-dimensional simulations. Moreover, in diffusion-controlled systems any numerical method should obey Neumann criteria to correctly asses the chemical degradation. This inevitably leads to a huge amount of time steps and cannot be treated with parallelization of computational processes. In this work, we present a new approach, which allows for considerable accelerations of the simulation of the chemical evolutions of cementitious systems. The idea is that the number of iterations can be reduced if the chemical buffering is sufficient to bring transport to a steady state. If this condition is satisfied, then it is possible to reduce physical (and thus also computational) time by adjusting the chemical system appropriately. The process is in fact similar to chemically accelerated experiments, but without the risk of influencing the chemical evolutionary path.
In this paper we first define the theoretical background and reasoning for the acceleration. The derivation is based on the diffusive transport process, because this process is usually the main transport process in cementitious materials. The theoretical assumptions are tested on a simple regular material and on a real cementitious system. The analysis shows that the pore structure resulting from the dissolution process remains invariant with respect to certain ratio between solid and equilibrium concentration.

2. Theoretical background

Consider a chemical system which involves a dissolution of solid. For the purpose of presentation we define the concentration in solid C_{solid} and the equilibrium concentration C_{eq} in solute. We further assume that diffusive transport defines the rate of dissolution. When solid mass at the solid surface decreases below the equilibrium concentration, this solid becomes liquid and solid geometry changes. Every time the geometry changes, there is some time required to establish new equilibrium. We can distinguish between two different situations depicted in Fig. 1. The situation (a) represents the system when the geometry changes before the transport equilibrium is established (i.e. when the diffusion process in steady-state). This means that fluxes at time t_1 and time t_2 ($t_2 > t_1$) are not the same. In other words, this system is not buffered enough to be accelerated. On the other hand, Figure 1b represents the situation where there is a steady state at t_3 achieved without the change of geometry. Any time larger than t_3 the specie flux remains constant until t_4 when the geometry changes. The time between t_4 and t_3 is the time which could be accelerated.
In order to determine whether the buffering is sufficient or not, we define the reference distance between the boundaries between two solids (or between a solid and the boundary as shown in Fig. 1) L. The time during which the aqueous solution is close to a steady-state can be determined from the amount of mass which is distributed within the length L, the so-called length patch or root-mean-square displacement [L]. For pure diffusion processes, the amount of mass that is distributed within the interval L at time t can be expressed in terms of standard deviation of mass in the domain $\sigma = 2\,D\,t$. The length of mass patch at time t is then defined by the confidence interval $\psi \times \sigma$ or

$$L=\psi\sqrt{2Dt} \tag{1}$$

where ψ is an arbitrary constant defining how many σ of mass is in the patch of length L and D is diffusion coefficients.

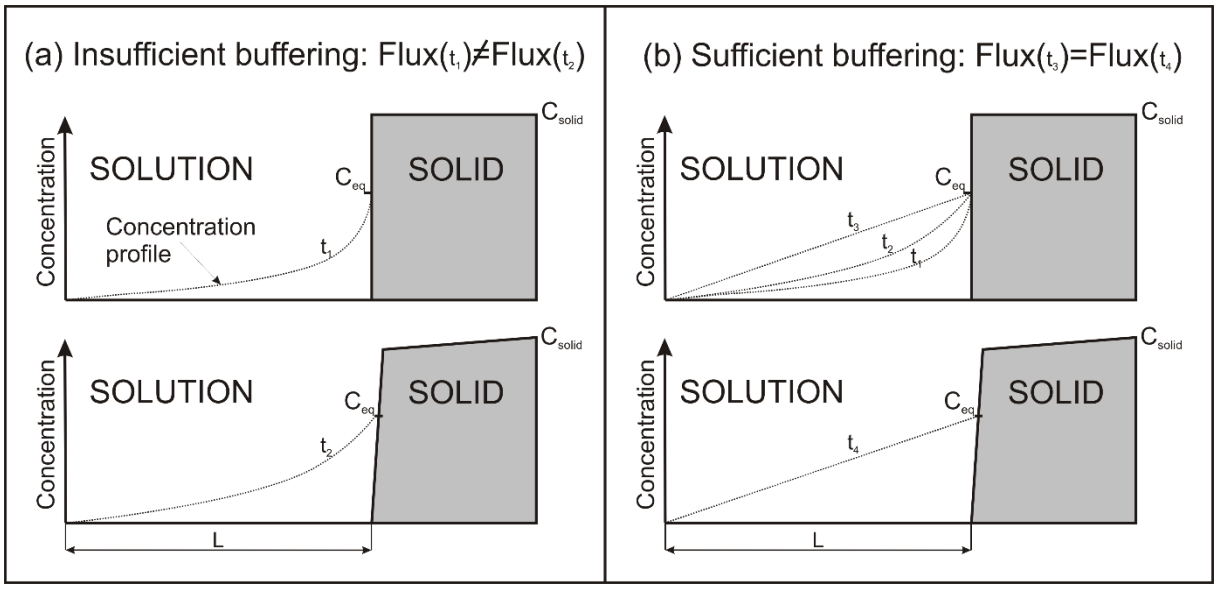

Figure 1: Graphical representation of sufficiently buffered system.

At time t the concentration is distributed as a function from the distance from the solid as

$$C(x,t)=C_{eq}\left[1+\mathrm{erf}\frac{x}{\sqrt{4Dt}}\right] \tag{2}$$

From these two relations we can define the minimal time until the steady-state is achieved. Further derivation [2] leads to a final dimensionless number, which we call *Buffering number* which is denoted as *Bu* number. Bu number obtains a simple form in Eq.(3)

$$\mathrm{Bu}=\frac{V_{total}C_{eq}}{V_{solid}C_{solid}}, \tag{3}$$

where V_{total} and V_{solid} are a total volume and volume of solid, respectively. The volumes represent initial volumes in this case. The ratio between V_{total} and V_{solid} does not change considerably with time as long as REV is respected (e.g. that the volume is large enough) because V_{total} also reduces with time in completely leached domain. Hence we assume that *Bu* number remains constant during calculations.

We demonstrated that the physical time, and thus the number of iterations, required to dissolve the solid can be scaled by *Bu*. For example, if time t_1 is required to fully dissolve a solid phase in a system with Bu_1 number, the time can be, according to Eq.(3), reduced by reducing either V_{solid}, C_{solid} or increasing C_{eq}. In a real chemical system only V_{solid} can be changed. However the intention of this numerical analysis is to leave the pore geometry

(V_{solid}) intact and change either C_{solid} (solid grain density) or C_{eq} in order to numerically accelerate dissolution.

the time t_2 to dissolve the same volume of solid with other C_{solid} or C_{eq} (other *Bu* number – Bu_2) would be

$$t_2 = t_1 \frac{\mathrm{Bu}_2}{\mathrm{Bu}_1} \tag{4}$$

Expanding this relation with Eq. (3) we get

$$t_2 = t_1 \frac{C_{eq,2} \times C_{solid,1}}{C_{solid,2} \times C_{eq,1}} \tag{5}$$

This means that in order to reduce the final time t_2 at given original solid concentration $C_{solid,1}$ and given equilibrium concentration $C_{eq,1}$ we can either decrease solid concentration $C_{solid,2}$ or increase the equilibrium concentration $C_{eq,1}$. The latter is typically done in accelerated experiments where the solubility is increased in order to accelerate the dissolution [3].

3. Numerical examples

To support our assumptions described in the previous section the dissolution will be made on a regular configuration of solid within a solute. The pattern tested here is made out of solid blocks of size 3 voxels which is surrounded by 3 voxels space (3×3 space block configuration). The ratio V_{solid}/V_{total} for this configuration is 11%. By changing either C_{solid} or C_{eq} we can adapt the *Bu* number.

The dissolution profile at the final time for different Bu numbers for the 3x3 configuration is shown in Fig. 2 The dissolution front progresses faster with higher Bu numbers because the solute concentration profiles are not in equilibrium and mass fluxes from the solid are higher. Visually, there is only a small difference between Bu=0.9 and Bu=0.2,which indicates that even with Bu around 1 the results are within the order of few percent difference if Bu doubles. With Bu around 0.2-0.5 the system has less than 1% differece and even less when the V_{solid}/V_{total} is larger than in this system

A cementitious system is a typically examples of a system for which a significant numerical acceleration can be obtained; V_{solid}/V_{total} and C_{solid}/C_{eq} are high. Therefore, Ca-leaching is therefore a slow process which requires a lot of time steps to simulate. To illustrate the gain in numerical application, we take an example from [4] which describes leaching of a mortar. The model consists of random spherical particles (i.e. cement clinkers) between two hypothetical aggregate surfaces, respecting initial water-to-cement (W/C) ratio of mortar as well as particle size distribution of the cement type. Particle size distribution represents CEM I 42.5 N cement with Blaine fineness of 430 cm^2/g with W/C=0.35. The domain is of size 2.5×5×5 mm3. Volume fraction of aggregates in the presented case is V_{agg}=0.2. Volumetric fraction of portlandite (CH) is V_{CH}=0.154 and of C-S-H is V_{CSH}=0.476. Diffusion coefficient in cement paste is $2.22\times10^{-12} m^2/s$.

The initial *Bu* numbers for CH, Ca in C-S-H and Si in C-S-H are 1.05×10^{-2}, 6.63×10^{-3} and 1.73×10^{-5}, respectively. According to our previous discussion the acceleration of dissolution process can be at least 20-50 times without any visible difference in a dissolution front. The limiting phase is portlandite (CH) because *Bu* number is the highest. Other phases and species are even less limited and could be accelerated more than that.

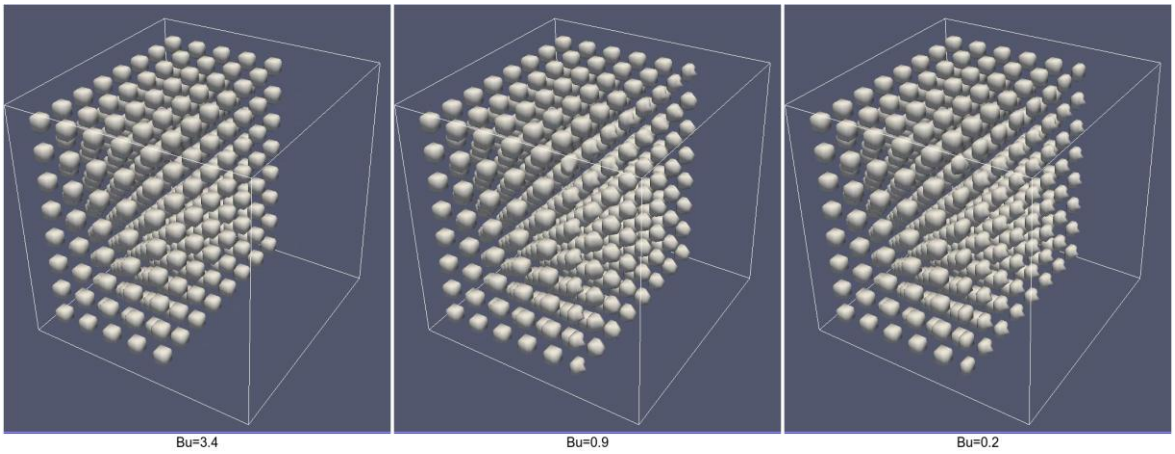

Figure 2: Final position of dissolution front at the same time for the example of 3×3 configurations for Bu=3.4 left, Bu=0.9 middle, and Bu=0.02 right.

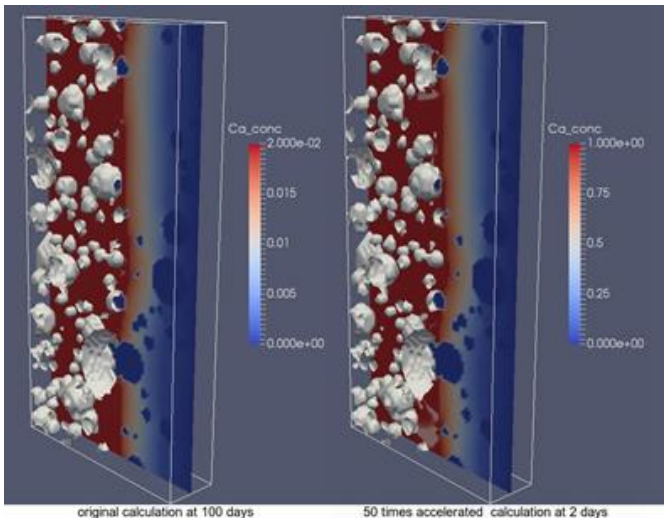

Figure 3: Dissolution front in mortar at 100 days for the original system (left and at 2 days for system with 50 times higher Bu number (right). Dissolved Ca concentration is given in mol/dm^3. Dark blue spots are aggregates (zero concentration).

The acceleration solved the problem in a few hours which is significantly faster than without acceleration requiring a simulation time of about. This enables analysis of larger systems or to perform a parameter sensitivity or uncertainty analysis in the same time. The figure below shows that the dissolution front (white represents portlandite) obtained with the proposed

approach is virtually the same at the original system and at 50 times accelerated system (right). For this particular example, we shortened the real calculation time from one month to less than a half day on desktop workstation.

4. Conclusions

In this text we summarized and illustrated an approach to reduce calculation time when dealing with equilibrium geochemical systems. The approach is based on the evaluation of real chemical system in terms of *Bu* number and reduction of time steps by the increase of *Bu* number to the critical value either by the decrease of C_{solid} or increase of C_{eq}. The latter approach is similar to the experimental techniques where solubility is increased which in fact increases *Bu* number in a similar way as we showed in this work. A significant advantage of numerical approach compared to the experimental one; in experiments the reaction rate might change because of higher ion strength while in numerical approach the same chemistry and activity correction approach can be used when C_{solid} is decreased. In other words, the acceleration can represent natural conditions with high fidelity. For the difference in remaining solid mass to be below 1% if the concentration in solid doubles Bu number is around 0.2, but can be higher when V_{solid}/V_{total} is high. The analysis showed that for mortar the acceleration can be until Bu=0.5 which resulted in 50 times acceleration.

References

[1] Patel, R.A., Perko, J., Jacques, D., Schutter, G.D., Ye, G., Breugel, K.V.: A three-dimensional lattice Boltzmann method based reactive transport model to simulate changes in cement paste microstructure due to calcium leaching. Construction & Building Materials 166, 158–170 (2018)
[2] Perko, J., Jacques, D.: Numerically accelerated pore-scale equilibrium dissolution, In preparation
[3] Phung, Q.T., Maes, N., Jacques, D., Perko, J., Schutter, G.D., Ye, G.: Modelling the evolution of microstructure and transport properties of cement pastes under conditions of accelerated leaching. Construction and Building Materials 115, 179 – 192 (2016).
[4] Seetharam, S., Patel, R.A., Perko, J., Jacques, D.: Quantification of leaching kinetics in OPC mortars via a mesoscale model. Construction & Building Materials Accepted, n/a–n/a (2018)

SynerCrete'18 International Conference on Interdisciplinary Approaches
for Cement-based Materials and Structural Concrete
24-26 October 2018, Funchal, Madeira Island, Portugal

PARTICLE MODEL FOR THE PREDICTION OF LONG-TERM DEFORMABILITY PROPERTIES OF DAM CONCRETE

Carlos Serra [(1)], Nuno Monteiro Azevedo [(1)], António Lopes Batista [(1)]

(1) National Laboratory for Civil Engineering, Lisboa, Portugal

Abstract
This paper presents a methodology for the prediction of dam concrete instantaneous and long-term deformability properties using discrete element method (DEM) based on particle models (PM). The concrete mix, namely the content, size and distribution of the aggregates is explicitly taken into account. This type of concrete has large aggregate size and fraction volume. Due to the computational cost of the analysis of a large number of particles, dam concrete specimen is represented by an arrangement of mortar particles and of coarse aggregates particles. The overall behaviour is determined by the micro properties at each contact type, i.e., mortar-mortar, aggregate-aggregate, and aggregate-mortar which defines the interfacial transition zone (ITZ).
The proposed approach is to characterize and model both the mortar and the coarse aggregates separately and study their interaction in the heterogeneous model of concrete. For the mortar, a long-term analysis is required for modelling the aging viscoelastic properties. For the aggregates, an elastic analysis defines the contact micro properties in order to obtain the macro properties of the intact rock. The numerical results obtained from the dam concrete particle model using DEM show a good agreement with the available experimental results for several loading ages.

1. Introduction

Mesoscale analyses are being used to study of the behaviour of concrete focusing on the interactions between coarse or fine aggregates and the maturing mortar or cement paste in order to evaluate the main mechanical properties and their evolution over time [1], [2].
The discrete or distinct element method (DEM) is especially suited for the analysis of quasi-brittle behaviour of some heterogeneous materials, such as concrete, since it is easier to consider the material microstruture and the randomness of material heterogeneity [3].

For modelling of concrete, main heterogeneity is due to the aggregates, mainly because the rock used for the aggregates and the cement paste have very different mechanical properties and due to the weaker properties of the interfacial transition zone (ITZ). The long-term behaviour of cementitious materials has an important role on the development of stresses inside concrete and it should be taken into account for the prediction of the behaviour over time, including complex deterioration scenarios that can occur relatively slow over a large period of time.
This paper presents the methodology for the prediction of dam concrete mechanical properties using particle models. The contact micro properties are calibrated using small homogeneous numerical specimens.

2. Discrete element method based on particle models

2.1 General aspects

The discrete element method (DEM) can be described as a numerical method for solving structural systems of individual elements, blocks (polygons) or particles (circular or spherical) interacting with each other at contact points or interfaces. The Newton's second law of motion defines the differential equation that governs the kinematics of the elements, which is solved using explicit methods. The interaction law determines the interaction forces between elements at the contact point, according with their relative displacement. In the DEM particle model, the elements interacting with each other are circular rigid particles defined by a position in space and a given radius. The normal and shear contact force increments, ΔF_n^C and $\Delta \boldsymbol{F}_s^C$, are obtained from an incremental linear constitutive law of the contact,

$$\Delta F_n^C = -k_n \Delta x_n^C, \qquad \Delta \boldsymbol{F}_s^C = -k_s \Delta x_s^C \tag{1}$$

where Δx_n^C and $\Delta \boldsymbol{x}_s^C$ are the normal and shear contact displacement increments, respectively, and k_n and k_s are the normal and shear contact stiffnesses.
The mechanical critical time step, related to the maximum frequency and required for explicit time integration schemes, is usually very small, which can be time consuming and computationally demanding. In order to avoid overshooting of the solution, an adaptive dynamic relaxation algorithm (ADR) can be used in which the global damping coefficient is updated at each time increment [4]. At each step, the scaled masses and inertias need to be updated for stability purposes whenever there is an increase in the model stiffness, for example due to the constitutive law or if new contacts are found to occur during numerical simulation.

2.2 Aging viscoelastic contact model based on the solidification theory

The aging viscoelastic model used is based on Bažant's solidification theory [5]. The model considers viscoelastic strain, ε^v, a consequence of the volume fraction growth associated to the viscoelastic behaviour, $v(t)$, and viscous strain, ε^f, a consequence of the volume fraction growth associated with the viscous behaviour, $h(t)$, and has a consistent mathematical formulation [5].
One can write the quasi-elastic incremental contact normal force, ΔF_n,

$$\Delta F_n = k_n''(\Delta x_n - \Delta x_n'') \tag{2}$$

$$\frac{1}{k_n''} = q_{1,n} + \frac{1}{v_n(t_i^*)}\sum_{\mu=0}^{N}\left(\frac{1-\lambda_{\mu,n}}{k_{\mu,n}}\right), \Delta x_n'' = \frac{\Delta\gamma_n''}{v_n(t_i^*)} + \frac{q_{4,n}F_n(t_i^*)\Delta t_i}{t_i^*} \quad (3)$$

$$v_n(t) = \left(\frac{1}{t}\right)^m + \frac{q_{3,n}}{q_{2,n}} \quad (4)$$

The shear contact behaviour follows the same formulation as the one previously described for normal direction.

To simulate creep behaviour of structural systems, such as rock or concrete, total calculation time can be expensive. A fast numerical procedure for the long-term behaviour was adapted from [6] for cementitious materials and makes use of both the adaptive dynamic relaxation method to obtain a fast equilibrium without overshooting and the aging viscoelastic contact model [7]. The effect of temperature can be taken into account by converting both the loading age and the time under loading into equivalent values, based on the measured temperature and maturity concepts. Higher temperatures increases the mechanical property rate of development, decreasing the creep rate and it increases the movement of water inside the cement structure and the rate of bond breakage and, therefore, increasing the creep strains [8].

3. Prediction of dam concrete deformability properties using particle models

3.1 Definition of particle model properties

The goal of this type of analysis is to explicitly take into account the deformability and strength properties of each component of concrete. Therefore, the particle model definitions should reflect, as much as possible, the internal structure of the different types of concrete. Table 1 presents the macro parameters used for the behaviour simulation of each type of contact: aggregate, mortar and ITZ. The modulus of elasticity of the aggregate was obtained directly from experimental testing of the rock used in the production. The aging viscoelastic parameters of the mortar were calculated using the available experimental results of concrete, a calibrated composite model and B3 model fitting [9]. The behaviour of ITZ is taken into account using a serial model of the elastic properties of the aggregate (E_{agg}) and the aging viscoelastic properties of the ITZ ($q_{i,ITZ}$). Since the aggregates only have elastic behaviour, the asymptotic elastic part of the aging viscoelastic model of ITZ, $q_{1,ITZ}$, is affected by the aggregate's stiffness and the other aging coefficients, $q_{2,ITZ}$, $q_{3,ITZ}$ and $q_{4,ITZ}$, remain equal to the ones considered for the mortar properties.

The size of the particles has to take into consideration the size of the smallest coarse aggregate. On the other hand, the model refinement is constraint to the computational costs, especially when testing large specimens of dam concrete. In order to reproduce the testing conditions, the particle model includes two rigid boundary walls, at the top and bottom of the specimen, which represent the rigid platens of the testing equipment and sets the same loading conditions for each boundary particle (Fig. 1).

3.2 Model validation using wet-screened concrete test results obtained in creep cells

The *in situ* characterization of dam concrete relies, among others, on a specific experimental setup based on creep cells [10], in which compressive creep tests can be done. The creep cells are subjected to the same thermohygrometric conditions as the structural concrete since its top face is connected to the dam concrete and are cast and completely covered with the surrounding lift. A typical temperature profile includes a sharp temperature increase in the first days, followed by a slow decrease which can last several months.

Table 1: Macro deformability properties of each concrete component.

Type of contacts	**E (GPa)**	**q_1 (1×10^{-6}/MPa)**	**q_2 (1×10^{-6}/MPa)**	**q_3 (1×10^{-6}/MPa)**	**q_4 (1×10^{-6}/MPa)**
Aggregate	46.3	-	-	-	-
Mortar	-	27.2	164.7	26.0	11.6
ITZ	-	13.6	164.7	26.0	11.6

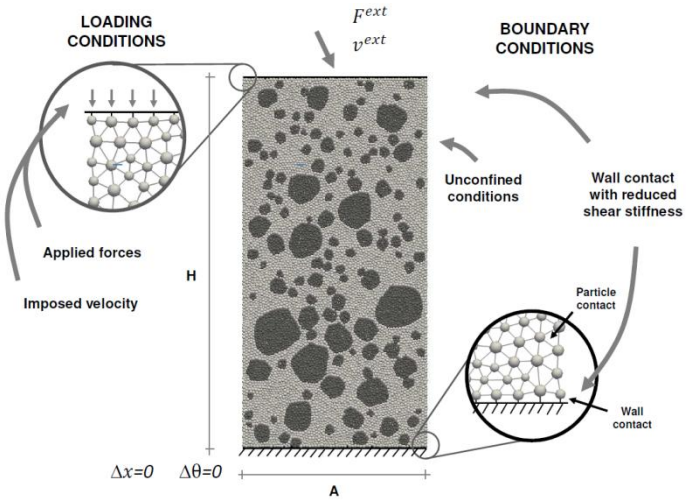

Figure 1: Representation of the loading conditions and the boundary conditions.

As it would be expected, the high initial temperatures accelerate the hydration processes and yield an increase of the modulus of elasticity. The grey area in the left plot of Fig. 2 is the particle model prediction which is in agreement with the measured modulus of elasticity in creep cells (diamond points). This effect is also present in the development of the creep strains, since its initial values are lower mainly due to higher modulus of elasticity at loading age (right plot in Fig. 2). The creep strain development over time has a misfit for the younger ages after loading, especially for the loading age of 28 days. The results show that this type of model is capable of accurately simulate the concrete deformability including not only the internal mesostructure of concrete but also the effect of temperature. The typical high temperatures in the early ages and rapid temperature variations, besides introducing differential imposed strains are known to increase the concrete stiffness and, therefore, influence the development of stresses over time.

3.3 Prediction of dam concrete test results obtained in creep cells

Using the same contact micro properties as the ones used for the wet-screened prediction, the dam concrete particle model gives a prediction for the experimental *in situ* results obtained *in situ* in dam concrete creep cells. As previously stated, the prediction of dam concrete deformability properties is greatly related to the aggregate's modulus of elasticity. Due to the its large scatter, the presented numerical results include three scenarios, considering the mean value of the aggregate's modulus of elasticity, an upper bound value of the aggregate's modulus of elasticity and, a lower bound value of the aggregate's modulus of elasticity.

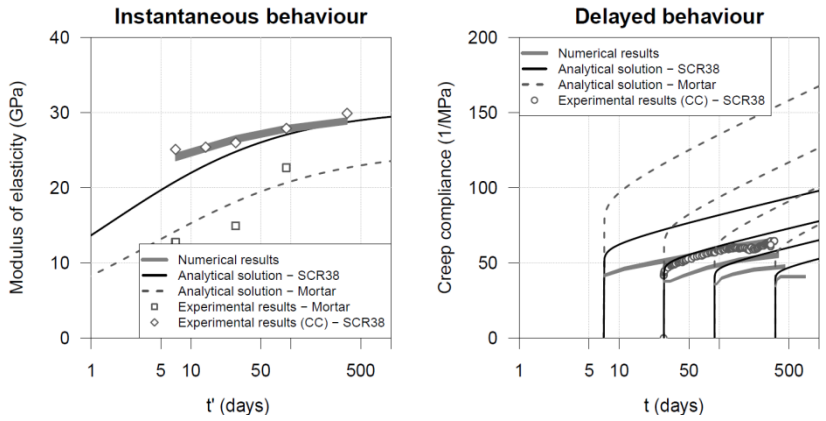

Figure 2: Results of wet-screened concrete (SCR38) particle model and comparison with creep cell results.

The difference between the prediction of the composite model at reference constant temperature (continuous black line in Fig. 3) is partially due to the acceleration of hydration processes, which is very significant at the younger ages. For the latter ages, the deviation between the numerical results and the experimental results can be due to the variability of the aggregate's modulus of elasticity. The large percentage deviation of the creep strain for the loading age of 28 days can be due to the difficulty of the maturity concepts under heating and cooling conditions applied to the creep rate. Some studies indicate that creep increases under cooling while other show the opposite effect [8].

4. Conclusions

This paper presents an aging viscoelastic contact model based on the solidification theory and a DEM particle model for the prediction of long-term dam concrete behaviour, considering the different types of contacts between each material, namely the mortar, the aggregates and the ITZ. The effect of temperature on the strain development is also considered in the model.
Firstly, the model is validated for instantaneous and long-term properties of wet-screened concrete and, then, a prediction of dam concrete behaviour is obtained using the same contact micro properties. The model results show that the large stiffness of dam concrete, obtained *in situ*, can be partially explained by the elevated temperatures at early age and by the large scatter of the aggregate. The effect of temperature on creep development is well captured with the DEM particle model.

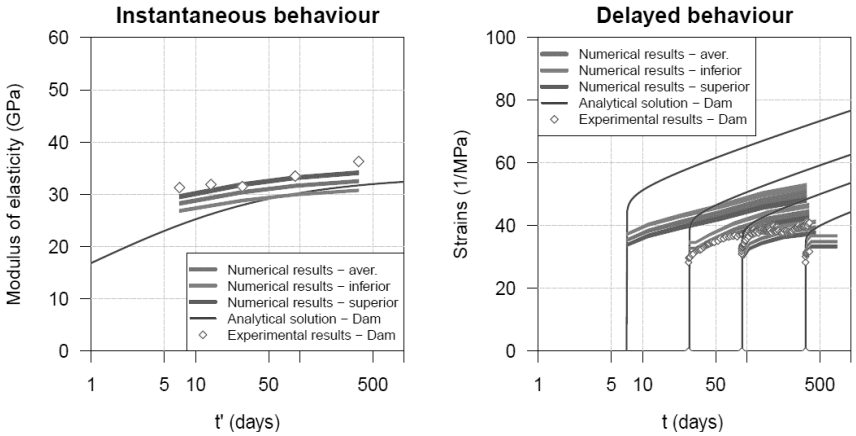

Figure 3: Results of dam concrete particle model and comparison with creep cell results.

Acknowledgements
Thanks to EDP for permission to publish data related to monitoring of Baixo Sabor dam.

References

[1] M. Alnaggar, G. Cusatis, and G. Di Luzio, "Lattice Discrete Particle Modeling (LDPM) of Alkali Silica Reaction (ASR) deterioration of concrete structures" Cem. Concr. Compos., vol. 41, August, pp. 45–59, Aug. 2013.
[2] Y. Pan, A. Prado, R. Porras, O. Hafez, and J. Bolander, "Lattice Modeling of Early-Age Behavior of Structural Concrete" Materials (Basel)., vol. 10, no. 3, p. 231, Feb. 2017.
[3] N. Monteiro Azevedo, J. Vieira de Lemos, and J. R. de Almeida, "Influence of aggregate deformation and contact behaviour on discrete particle modelling of fracture of concrete" Eng. Fract. Mech., vol. 75, no. 6, pp. 1569–1586, Apr. 2008.
[4] P. Underwood, "Dynamic Relaxation" in Computational Methods for Transient Analysis, Oxford, United Kingdom: Elsevier Science Publishers B.V., 1983, pp. 245–265.
[5] Z. P. Bažant and S. Prasannan, "Solidification theory for concrete creep. I: Formulation" J. Eng. Mech., vol. 115, no. 8, pp. 1691–1703, Aug. 1989.
[6] J. Feng, Z. Chuhan, W. Gang, and W. Guanglun, "Creep Modeling in Excavation Analysis of a High Rock Slope" J. Geotech. Geoenvironmental Eng., vol. 129, no. 9, pp. 849–857, 2003.
[7] C. Serra, N. Monteiro Azevedo, A. L. Batista, and N. Schclar, "Discrete Element Method for Modeling the Long-Term Aging Viscoelastic Behavior of Concrete Considering Its Mesostructure" J. Eng. Mech., vol. 144, no. 5, May 2018.
[8] Z. P. Bažant and S. Baweja, "Creep and shrinkage prediction model for analysis and design of concrete structures - model B3" in Adam Neville Symposium: Creep and Shrinkage - Structural Design Effects, 2000, vol. 28, no. 6, pp. 1–83.
[9] C. Serra, "Prediction of dam concrete structural properties based on wet-screened test results and mesoscale modelling", PhD. Thesis, Universidade Nova de Lisboa, 2018.
[10] C. Serra, A. L. Batista, and N. Monteiro Azevedo, "Dam and wet-screened concrete creep in compression: in situ experimental results and creep strains prediction using model B3 and composite models" Mater. Struct., vol. 49, no. 11, pp. 4831–4851, Nov. 2016.

SynerCrete'18 International Conference on Interdisciplinary Approaches
for Cement-based Materials and Structural Concrete
24-26 October 2018, Funchal, Madeira Island, Portugal

SCALE EFFECT ON ALKALI-SILICA REACTION

Jacques Jabbour [(1) (2) (3)], Aveline Darquennes [(2)], Loic Divet [(3)], Rachid Bennacer [(2)], Jean-Michel Torrenti [(3)], Georges Nahas [(1)]

(1) IRSN, Fontenay-aux-Roses, France
(2) LMT ENS-Paris-Saclay, CNRS, University Paris-Saclay, Cachan, France
(3) University Paris-Est, Materials and Structures Department, IFSTTAR, Marne la Vallée, France

Abstract

Many laboratory studies of internal swelling reactions are realized on relatively small size samples. Those laboratory samples do not allow to reproduce real conditions to which is submitted the real concrete in its environment, in terms of kinetics, volume/surface ratio, thermal and mechanical conditions especially in massive structures. Therefore, an experimental protocol to accelerate internal swelling reactions of concrete on a structural scale has been developed to allow better observation and understanding of swelling reactions at structure scale. A representative massive concrete structure (2.4 x 1.4 x 1 m^3) was realized under controlled and optimized conditions for the development of alkali silica reaction (ASR). The scale effect on swelling kinetics is demonstrated by an experimental study comparing the evolution of swelling reaction in the massive sample with the evolution in reconstituted concrete laboratory specimens as well as coring specimens. Results show different swelling kinetics and amplitude in function of sample type, size and boundary conditions.

1. Introduction

Alkali-silica reaction (ASR) is a chemical reaction between amorphous silica mineral from the aggregates and the alkali hydroxides (Na, K – OH) dissolved in the concrete pore solution [1]. This reaction generates a secondary alkali-silica gel which expands and induces overpressure within the reacting aggregate material and the adjacent cement paste upon moisture uptake from its surrounding environment, thus causing micro-cracking, loss of material's integrity (mechanical/durability). It's known that swelling pathologies act at different scales: microscopic, mesoscopic and macroscopic. Thus, multi-scale approaches are

necessary in order to fill the gap between conventional laboratory samples and the behavior of real scale massive structures.
The experimental laboratory investigations about the scale effect on swelling reactions have been carried out on concrete specimens, using cement with a high alkali-content combined with reactive aggregates. It aims to quantify the expansion magnitudes and kinetics in different specimen types and sizes. Three sample geometries are considered: first, the massive structure mock-up (2.4 x 1.4 x 1 m^3). The second and third specimens geometry studied are concrete cylinders cast in the laboratory and subjected to conservation conditions equivalent to those of the mock-up. The concrete cylinders dimensions are 16 cm (diameter)/32 cm (height), and 11 cm (diameter)/22 cm (height) respectively. In addition to that, three cores were extracted from the massive structure and subjected to conventional test procedures in order to determine the structure's residual swelling. The cores dimensions are equally 11 cm (diameter)/22 cm (height). This article, presents the results of expansion for the different concrete samples. The swelling behaviour of the massive structure and the impact of boundary conditions are discussed. Then the swelling characteristics (magnitude and kinetics) of the different concrete specimens are quantified using a mathematical relation. The impact of conservation conditions is thus demonstrated. Finally, the impact of specimen's size on the swelling magnitude and kinetic parameters is discussed.

2. Materials

The concrete used in this study is made with calcareous non-reactive sand (0/5), reactive siliceous coarse aggregates (5/12.5 – 12.5/20), and a W/C=0.57. This combination was chosen based on the works of Guedon-Dubied [2], hence the same quarry provides the reactive aggregates. These aggregates are rich in carbonals which, from a mineralogical point of view, is a microcrystalline silica deemed to have a significant alkali reactivity [2]. Furthermore, Monnin showed that the kinetics of alkali consumption increases when the aggregate diameter decreases [3]. This causes a rapid drop in the alkali concentration of the interstitial solution which may limit the final swelling of the concrete. Therefore, by opting for non-reactive sand, the final swelling due to the alkali-granulate reaction is maximized. The binder used is a Portland cement CEM II/A-LL 42.5 R. It contains 1.06% of Na_2eq (by mass), hence providing a total of 4.24 Kg/m^3 of alkalis in the mix. As a result, this concrete mix is highly ASR-prone.

3. Multi-scale experimental study

3.1 Structural scale

The monitoring of swelling in the structure is ensured by 9 vibrating wire extensometers embedded within the concrete at three levels (Fig. 1b): 0.25 H, 0.5 H and 0.75 H, where H is the mock-up height (140 cm). At each level, three strain sensors are oriented in the three directions (X, Y, Z) respectively making it possible to continuously follow the deformations over time with an accuracy of the order of 2 μm/m.

Special measures were taken in order to keep the concrete temperature at the early age below 65°C in order to avoid delayed ettringite formation. The mock-up is conserved fully

submerged in a pool constantly maintained at 38°C (Fig 1a). The pool is emptied monthly in order to perform a follow up of the structure's surface. Tap water is used to fill the pools.

(a) 

(b) 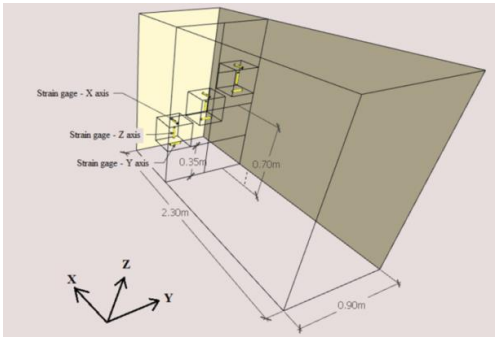

Figure 1: (a) Photo of the structure's mock-up (b) Strain sensors placement in the structure (dimensions not including concrete cover)

3.2 Specimen scale

Six cylindrical concrete specimens (three Ø11H22 and three Ø16H32) were prepared according to the standards NF P 18-400 and NF P 18-422. After casting, the concrete specimens were heat treated. The heat treatment applied is identical to the temperature profile measured in the structure mock-up at the early age. It was performed in a climatic chamber regulated at 100% relative humidity. The maximum temperature reaches a value of 62°C. Afterwards, the specimens are stored in 20°C water until 28 days age, then they are placed at 38°C in a volume of water respecting the same ratio (Water Volume)/(Exposed Surface) as the structure in the pool and respecting the same renewal cycles as well. Therefore, the specimens have an identical heat profile and an equivalent conservation environment.

In addition to that, three Ø11H22 core samples were extracted from the structure at 0.25 H along the Y axis. They are subjected to the *LPC N44 test method*, in which the cores are conserved at 38°C and 100% relative humidity [4]. For each sample, the length variation is measured along three longitudinal lines located at 120° from each other in the circumference using an extensometer. The length base used for strain measures is 10 cm for Ø11H22 specimens (cast and coring) and 20 cm for Ø16H32 specimens.

4. Results

Results show different expansion behaviour in the massive structure in comparison with unrestrained laboratory specimens.

4.1 The effect of boundary conditions on swelling mechanism in massive structures

Fig. 2 shows the swelling in the mock-up as recorded by the strain sensors. Until the time 235 days, the massive structure is conserved in water at ambient temperature. This phase corresponds to the time required to finalize the construction of the experimental platform and install the temperature regulation system. There's hardly no swelling at this stage. Once the temperature rose to 38°C, swelling in the mock-up started increasing in a similar manner to accelerated tests on laboratory specimens. Fig. 2 shows the swelling in the structure and that thermo-activation is a valid method to accelerate ASR on a massive scale.

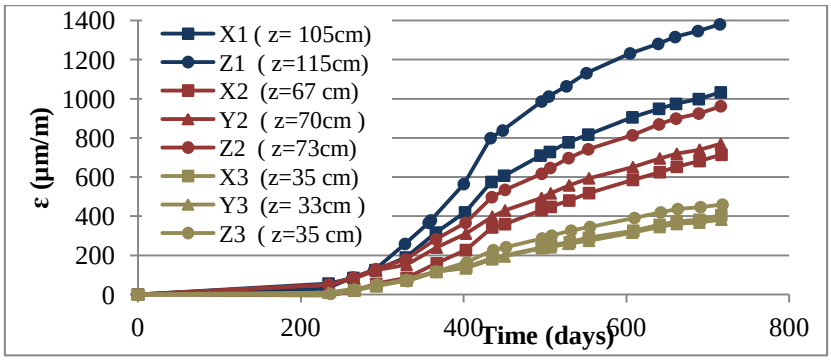

Figure 2: Swelling evolution in the massive structure mock-up.

After 700 days of follow-up, swelling in the structure seems to reach the second inflection point. The maximum amplitude recorded at this stage is about 1400 µm/m. However this value varies according to the position of the sensor and its orientation. As a general rule, the swelling decreases as we approach the base of the structure regardless of the orientation of the sensor. Thus, a $\Delta\varepsilon$ of approximately 900 µm/m is measured between the sensors Z1(z =115 cm) and Z3 (z = 35 cm). Simulations showed that this behavior is actually due to the stress generated by the restraint effect due to the metal support on which the structure was cast. The upper part of the mock-up can expand freely whereas the lower part is hindered by the boundary conditions. However, at lower heights, the swellings measured in the horizontal plane parallel to the support (along X and Y) are hindered more than the swelling measured vertically (along Z). Another approach to analyze this behavior would be to consider that the expansion, which is prevented along the directions of the metal support, is compensated by a greater expansion in the unstressed direction (Z). This effect decrease as we approach the upper part of the mock-up. As a matter of fact, the experimental campaign conducted by Larive, has shown that the mean volume swelling remains generally constant when the value of the uni-axial stress applied to the specimens remains below 10 Mpa [1].

4.2 Scale-effect on swelling kinetics and magnitude

Fig. 3 shows the swelling in the small scale concrete specimens in comparison to that of the structure. A correction was applied to the expansion results of the mock-up taking into account the temperature shift at 235 day and the difference in maturity conditions.

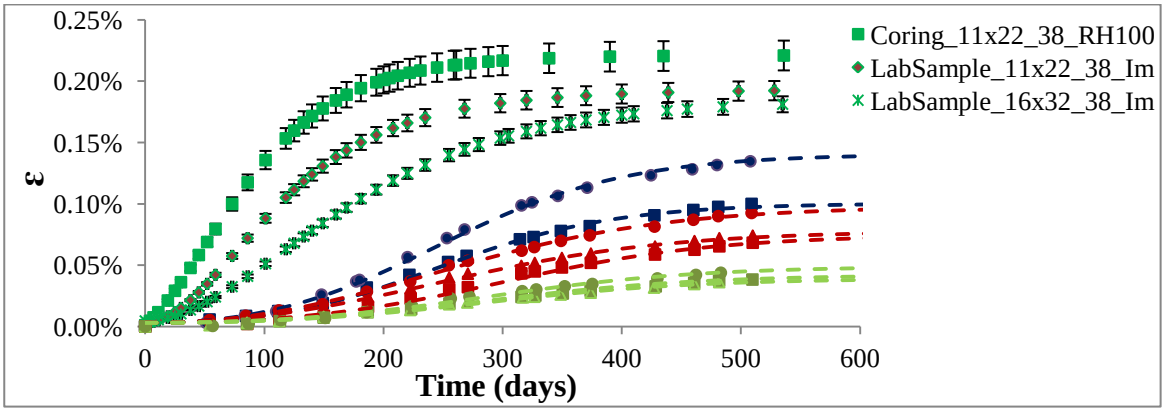

Figure 3: Comparison of the swelling evolution between the laboratory scale specimens and the massive structure behavior

The cores subjected to the *LPC N°44 test method* (Coring_11x22_38_RH100) yield a residual swelling of 0.22% whereas the cast concrete specimens of the same dimensions (LabSample_11x22_38_Im) yield a swelling of 0.19%. This difference is most probably due to the conservation environment: the immersed specimens are subject to a higher alkali-leaching than the cores conserved at 100% relative humidity. This reduces the final volume of gel formed. Similar results were obtained by Martin [5].
However, if we consider the series LabSample_11x22_38_Im, LabSample_16x32_38_Im and the mock-up, we notice different swelling behaviours knowing that we have the same concrete composition and conservation environment but different sample sizes. Hence, the swelling characteristics (magnitude and kinetics) are quantified using Kchakech's law (a mathematical relation). Tab. 2 recapitulates Kchakech's swelling parameters obtained for the different specimens' series by minimizing the differences between the curve and the experimental points using the least squares method where $\boldsymbol{\varepsilon}^{\infty}$ is the final magnitude of expansion, $\boldsymbol{\tau_L}$ and $\boldsymbol{\tau_C}$ are respectively the latency and the characteristic times [6].
Sensors in the upper part of the mock-up are considered for this comparison knowing that this part of the structure expands "freely".

Table 2: Parameters of Kchakech's model.

	Coring	**LabSample _11x22**	**LabSample _16x32**	**Z1 (z= 115cm)**	**X1 (z= 105 cm)**
$\boldsymbol{\varepsilon}^{\infty}$	0.22%	0.19%	0.18%	0.1375%	0.0975%
$\boldsymbol{\tau_L}$	0	18	32	240	240
$\boldsymbol{\tau_C}$	55	53	105	80	75

We notice that the latency and characteristic times increase and that the final swelling decrease as the sample size increase. By assuming that the swelling in the concrete generates a tensile solicitation, then the decrease in the final swelling can be explained by the Weibull's effect [7]. Rossi's research in scale effects on the mechanical behavior of concrete suggests that tensile strength of the concrete decreases as the volume of the specimen increase [7]. From another perspective, given that the ASR kinetics can be assimilated to a diffusive phenomenon, Fig. 4 shows a normalized evolution of the swelling in the different specimens function of $(\sqrt{t})/r$, where t stands for time (days) and r is the radius of the specimen (m). An equivalent radius was computed for the massive structure taking into account the shape factor (parallelepiped vs cylinder) and yielding the same cross-section area ($r_{mock\text{-}up}$ = 0.668 m).

Fig. 4 reveals different swelling slopes in the normalized graph. This suggests different reaction kinetics and swelling mechanisms. If we consider that we have the same chemical advancement in the three specimen sizes (same pore distribution, same aggregate-cement paste interface…); then a possible explanation is the following: as the sample size increase, crack occurrence increase hence creating stress release points and additional space for gel permutation thus slowing down the over-all expansion mechanism. However this point ought to be clarified by further research considering additional intermediate geometries and microscopic observations.

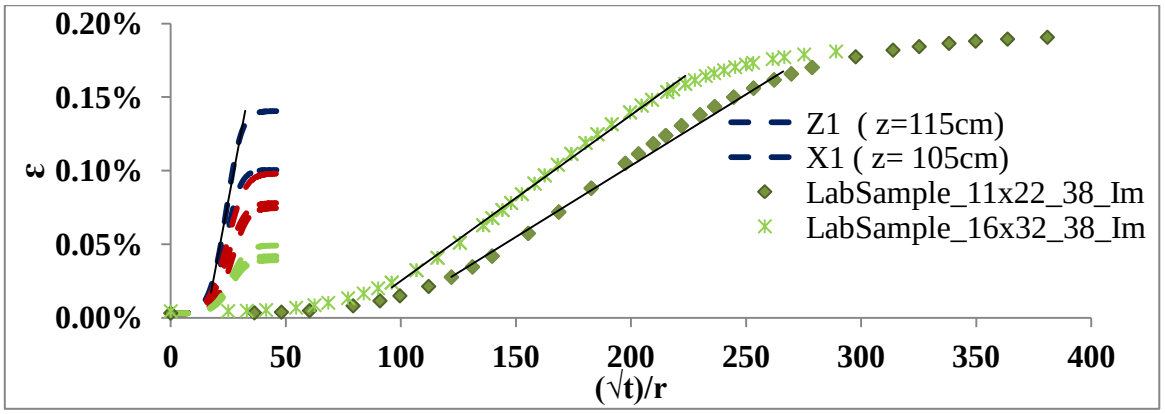

Figure 4: Normalized evolution of the swelling in the different specimens sizes

5. Conclusions

We show in this paper that thermo-activation can be used to accelerate ASR in a massive structure. However, expansion in massive structures varies greatly from analogous laboratory samples. Boundary conditions could hinder expansion along certain directions thus compensated by a higher expansion along unstressed directions which leads to an anisotropic behaviour in the material. The most important observation is that we identified the existence of a scale effect on internal swelling reactions. By comparing the strain evolution in different samples sizes subject to analogous concrete composition, thermal history and conservation environment, we found that the final swelling amplitude and the swelling kinetics are reduced by increasing the specimen's size.

It ought to be mentioned that similar results were obtained in a parallel study investigating two similar pathologies: Delayed Ettringite Formation (DEF) and the concomitance of ASR and DEF.

References

[1] Larive, C., Apports combinés de l'expérimentation et de la modélisation à la compréhension de l'alcali-réaction et de ses effets mécaniques. PhD thesis, Ecole Nationale des Ponts et Chaussées. (1997).

[2] Guédon-Dubied, J-S., Etude du calcaire tournaisien de la carrière Cimescaut à Antoing (Belgique). Bulletin des Laboratoires des Ponts et Chaussées 226 (2000), 57-66.

[3] Monnin, Y., Méthodologie pour décrire le gonflement multi-échelle de calcaires siliceux soumis à la réaction alcali-silice dans le matériau béton. PhD thesis, Université de l'Artois, (2005).

[4] Fasseu, P., Alcali-réaction du béton : Essai d'expansion résiduelle sur béton durci. Méthode d'essai LPC n° 44, Techniques et méthodes des laboratoires des ponts et chaussées, 1997.

[5] Martin, R-P., Analyse sur structures modèles des effets mécaniques de la réaction sulfatique interne du béton. PhD thesis, Université Paris-Est, (2010).

[6] Kchakech, B., Etude de l'influence de l'échauffement subi par un beton sur le risque d'expansions associées à la Réaction Sulfatique Interne. PhD thesis, Université Paris-Est, (2015).

[7] Rossi, P. et al., Scale effect on concrete in tension, Materials and Structures 27 (1994), 437-444

SynerCrete'18 International Conference on Interdisciplinary Approaches
for Cement-based Materials and Structural Concrete
24-26 October 2018, Funchal, Madeira Island, Portugal

SMALL SCALE FRACTURE PROPERTIES OF CEMENT PASTE AND ALKALI-ACTIVATED FLY ASH

J. Němeček [(1)], J. Němečková [(1)], J. Němeček [(1)], J. Maňák [(2)]

(1) Czech Technical University in Prague, Faculty of Civil Engineering, Prague, Czech Republic
(2) Institute of Physics, Academy of Sciences, Prague, Czech Republic

Abstract
The paper shows novel methodology and quantitative results of small scale elastic and fracture properties of cement paste and alkali-activated fly ash constituents at the level of micrometers. Local Young's moduli, tensile strengths and fracture energies are derived from nanoindentation and micro-beam bending on microscale specimens prepared with focused ion beam milling. It is shown that the main cement hydration products (inner and outer products) that are rich of C-S-H gel reach tensile strength of 260-700 MPa. N-A-S-H gel in alkali-activated fly ash is characterized with the mean strength of 340 MPa. The values are several orders of magnitude higher compared to their macroscopic counterparts. Supremum fracture energies were found in the range 4-20 J/m^2 on individual microstructural components.

1. Introduction

Composites based on cement of alkali-activated fly ash matrix are highly heterogeneous multi-scale materials. Usual engineering properties vary with the level of observation as the representative volume element contains different amount of heterogeneities or inclusions at individual scales. Among others, tensile strength and fracture energy are crucial material properties that vary significantly starting from C-S-H globules in cement paste [1] to concrete level [2]. Mutual similarities between C-S-H in cement paste and N-A-S-H gels in alkali-activated fly ash (AAFA) exist [3,4]. In this paper, we introduce a unique experimental method that allows cutting out a micrometer sized cantilever beams using the Focused Ion Beam (FIB) milling technique [5] from a heterogeneous composition of hydrated cement or alkali-activated fly ash pastes. High precision geometry of the beams is reached with FIB at micrometer scale. The beam is loaded in bending with the help of a nanoindenter and

mechanical response is determined. Careful selection of homogeneous-like regions allows assigning results to dominant micro-mechanical phases, particularly C-S-H rich inner and outer products and Portlandite regions in cement paste and N-A-S-H gel areas in AAFA. From these tests, it is possible to determine tensile strengths of the individual phases in micrometer scale and, in some extent, fracture energy needed to break the cantilever.

2. Experiments

In order to study small scale material properties on individual phases of cement pastes and AAFA several micro-machined samples were prepared by FIB milling in the form of cantilever beams laying in a specific material phase. Samples were scanned in electron microscope (SEM) to assess local beam positions based on the morphology of individual phases. The morphologically detectable and mechanically significant phases have been selected. The beams were subsequently loaded by the nanoindenter and local elastic and fracture properties deduced.

2.1 Cement paste samples

Samples were prepared from Portland cement CEM-I 42.5R with water to binder ratio 0.4 and cast into small plastic moulds. After 24 hours, samples were stored in water for a long period of 8 years, thus fully hydrated. Then, samples were taken out of water, cut into ~5 mm thick slices and prepared with a metallographic procedure [3,5] to get a flat and smooth surface with small roughness of several tens of nm suitable for microscopy and micromechanical testing.

Microstructure of cement paste composes mainly of C-S-H rich phases [6]. Two morphologies are distinguished. Inner product surrounding unhydrated clinkers is described with higher density and forms less portion of the sample volume (~28%) while more porous outer product forms majority of the sample volume (~50%). Large Portlandite crystals (CH) appear in the microstructure (~10%). The rest of the volume is occupied by unhydrated clinkers (3%) and capillary porosity (12%), see [5] for details. The situation is illustrated in Fig. 1a.

2.2 Alkali activated fly ash samples

Raw fly ash from brown coal power plant Opatovice (Czech Republic) was used as a binder precursor for preparation of AAFA samples. The fly ash was mixed with an alkali-activator which was prepared by dissolving NaOH pellets in tap water and by adding sodium silicate (water glass). Resulting mixture was characterized by mass oxide ratio of an activator and activator-to-solid mass ratio as: $Na_2O/SiO=0.881$, $H_2O/Na_2O=3.068$, activator/solid=0.456. After mixing, samples were cured at 80°C for 12 h and then stored in laboratory conditions (~22°C) until testing. Before SEM and nanoindentation samples were mechanically polished with equal polishing procedure as cement paste samples.

Microstructure of AAFA samples is more complex. It consists of the main reaction product, the N-A-S-H gels, non-reacted and partly reacted slag grains, non-reacted glass particles and multi-level porosity [4]. Typical microstructure with a N-A-S-H region used for preparation of micro-beams is shown in Fig. 1b.

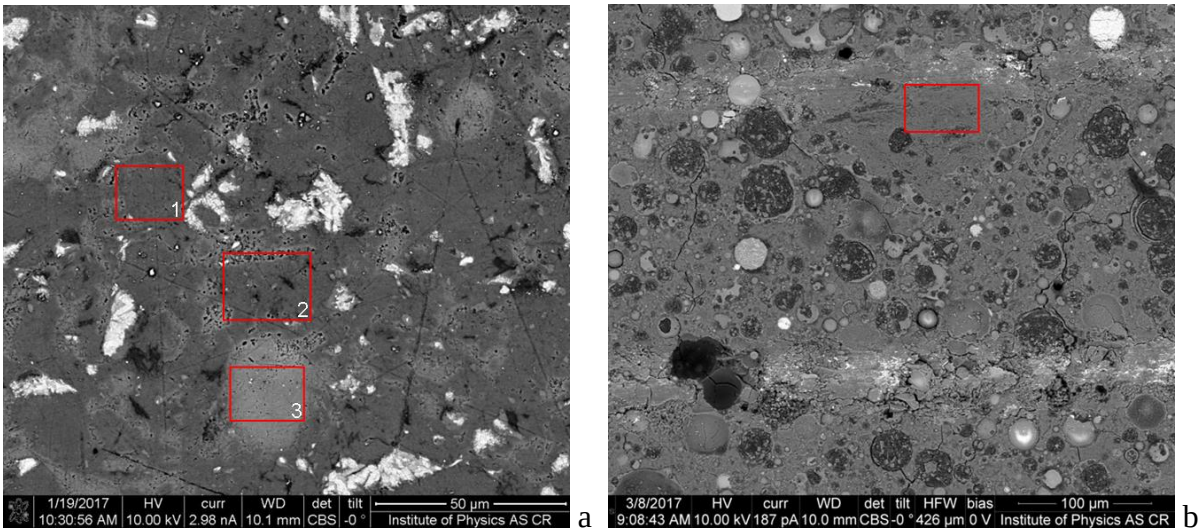

a b

Figure 1: Examples of (a) cement paste (1=inner product, 2=outer product, 3=CH) and (b) AAFA (rectangle shows a N-A-S-H gel region).

2.3 FIB

Micro-beams were prepared with FEI Quanta 3D FEG dual beam instrument combining SEM and FIB was used for fabrication of all samples. The FIB technique uses a finely focused beam of gallium ions for precise milling of microscopic samples. The sample geometry was chosen to be a cantilever beam of 15-20 um length and triangular cross-section with approximate dimensions of 3-4 um in height and width. FIB works similar to scanning electron microscope (SEM) with working conditions of accelerating voltage between 10 and 50 kV and current in the interval between 1 pA and 30 nA. FIB milling procedure was optimized to suppress the redeposition of sputtered material on the micro-beam surface and the final milling step was done at an accelerating voltage of 30 kV and low current of 1 nA [5] on cement samples and 0.1 nA on AAFA samples. Milling of a single beam takes a few hours. After FIB milling, the micro-beams were observed by SEM to scan their actual dimensions and position in a particular microscopic phase. An example of the milled beam is shown in Fig. 2.

2.4 Nanoindentation

Nanoindentation was employed to derive elastic properties of a specific material phase measured with standard indentation technique [7] and as a loading tool for bending micro-beams [5]. Force-deflection diagrams were recorded in the displacement controlled regime and tensile strength, f_t, and fracture energy, G_f, calculated using beam theory as

$$f_t = \frac{F_{\max} L}{W_h}, \tag{1}$$

$$G_f^{\sup} = \frac{1}{A_f} \int_0^{w_{\max}} F dw, \tag{2}$$

where F_{max} is the maximum measured force, L is the beam length and W_h is the section modulus, w_{max} is the peak deflection and A_f is the nominal fracture area (i.e. $A_f = ½bd$ for the triangle $b \times d$). Note that the fracture energy was computed as the supremum estimate based on the assumption that the micro-beam behavior shows neither snap-back nor softening and that the maximum force corresponds to the maximum energy release rate with a limiting stable crack propagation. Such assumption is not fully correct since some of the loading diagrams show stable softening. Unfortunately, stable softening can be captured only in very limited cases with the current instrument even in depth controlled regime. Therefore, only supremum energies are calculated here.

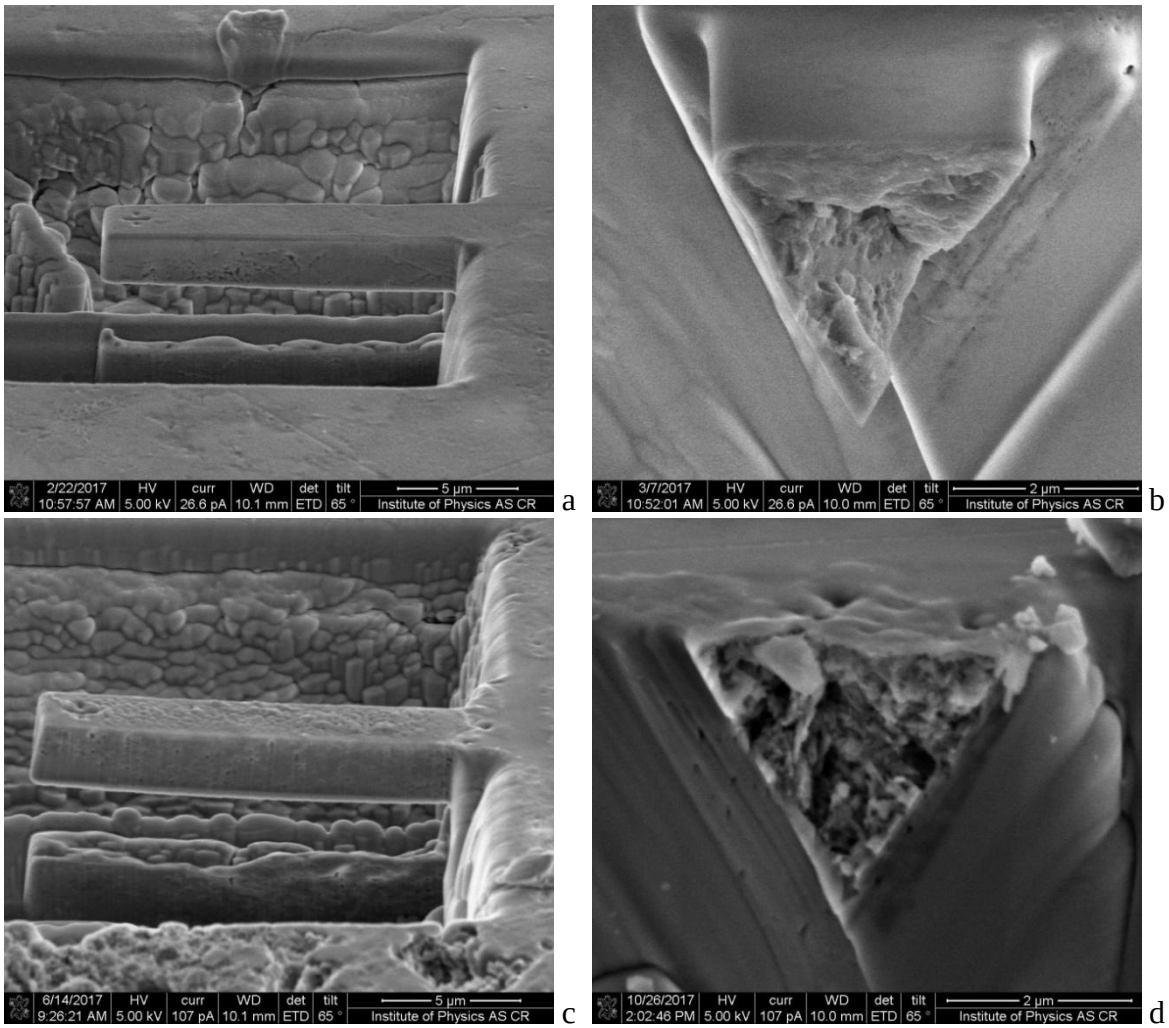

Figure 2: Examples of micro-beam geometry before and after fracture (a,b=outer product in cement paste; c,d=AAFA).

3. Results and discussion

Results of material parameters collected from bending of about 10 beams for each phase is summarized in Tab. 1. Typical load-deflection curves normalized with respect to the

microbeam length are shown in Fig. 1. The micro-beams in bending behave approximately linearly up to the break which suggests that no or small microcracking appears before the rupture. Then, sudden failure characterized with steep brittle fracture on unloading branch is a demonstration of release of elastic energy stored in the beam. Although, in some cases also stable descending (softening) branch has been recorded (as seen in Fig. 1 for AAFA sample), usually unstable behavior was encountered (most cement samples). Thus, the post-peak is not well maintained even in the depth controlled regime in the nanoindenter and must be treated only as approximate.

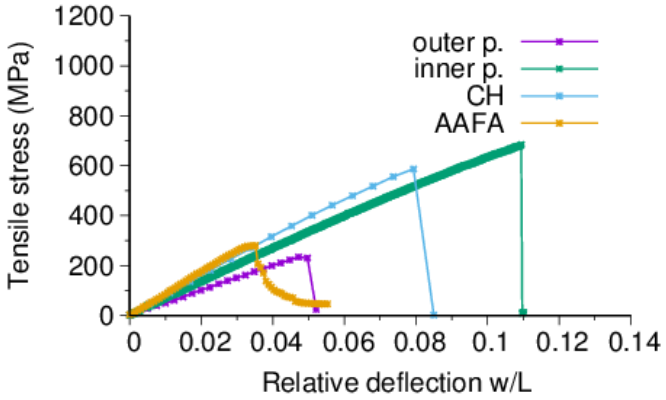

Figure 1: Examples of micro-beam stress vs. relative deflection curves.

Table 1: Results of nanoindentation and micro-beam bending.

	Outer product	**Inner product**	**CH**	**N-A-S-H**
E (GPa)	24.9 ± 1.3	33.6±2.0	39.0±7.1	25.5±4.24
f_t (MPa)	264.1 ± 73.4	700.2±198.5	655.1±258.3	340.8±124.1
G_f^{sup} (J/m^2)	4.4±1.9	19.7±3.8	19.9±14.4	4.5±1.8

The results of strengths in Tab. 1 are several orders of magnitude higher compared to macroscopically obtained characteristics where the tensile strengths on mm/cm sized samples are a few MPa. The reason lies in the defects that are present on higher composite scales and lead to strength reduction [8].

The results are in good agreement with previously obtained results of elastic and strength properties of individual cement paste constituents [3,5] and AAFA [4]. Strength calculation at C-S-H level are provided e.g. by molecular dynamics models which yield tensile strength for low density and high density C-S-H as 550-720 MPa [9], AFM measurements as 930 MPa [10]. Those values are comparable with microbending tests in Tab. 1. MD simulations give fracture energies in the range of 0.4-3 J/m^2 [11,12] which is slightly less than our results suggesting that our supremum energies are slightly above the real values.

So far, no particular data on strength and fracture energy were known for N-A-S-H gel at micrometer scale. This measurement gives first experimental estimates (Tab. 1). It seems that the values are mechanically comparable with outer product of cement paste which also has similar density [4,5].

4. Conclusions

The paper provides quantitative results of low level micromechanical properties (strength and fracture energy) of individual components of hydrated cement paste and AAFA with the aid on FIB and nanoindentation. It was found that the strength in micrometer scale is in the order of hundreds of MPa and the specific fracture energy lies in the range of units of J/m^2. N-A-S-H gel mechanical response was found to be similar to outer product in cement paste.

Acknowledgement
Financial support of the Czech Science Foundation (project 17-18652S) is gratefully acknowledged.

References

[1] Jennings, H. M., A model for the microstructure of calcium silicate hydrate in cement paste, Cement and Concrete Research 30 (1) (2000), 101-116
[2] Bažant, Z. P., Scaling of Structural Strength, 2nd ed., Elsevier Ltd. (2005)
[3] Němeček, J. et al, Micromechanical analysis of heterogeneous structural materials. Cement and Concrete Composites 36 (2013), 85-92
[4] Němeček, J. et al, Nanoindentation characteristics of alkali-activated aluminosilicate materials, Cem Concr Comp 33 (2011) 163-170
[5] Němeček, J. et al, Tensile strength of hydrated cement paste phases assessed by microbending tests and nanoindentation, Cem Concr Comp 73 (2016), 164-173
[6] Scrivener, K.L., Backscattered electron imaging of cementitious microstructures: understanding and quantification. Cem Concr Comp 26(8) (2004), 935-945
[7] Oliver, W. and Pharr, G., An Improved Technique for Determining Hardness and Elastic-Modulus using Load and Displacement Sensing Indentation Experiments, J. Mater. Res. 7 (1992), 1564-1583
[8] Němeček, J. et al, Fracture properties of cement hydrates determined from microbending tests and multiscale modeling, Proceedings of EURO-C 2018
[9] Davie, C. and Masoero, E., Modelling damage from the nano-scale up. In 10th International Conference on Mechanics and Physics of Creep, Shrinkage, and Durability of Concrete and Concrete Structures (2015)
[10] Plassard, C. et al, Nanoscale experimental investigation of particle interactions at the origin of the cohesion of cement. Langmuir 21(16) (2005), 7263–7270
[11] Ghebrab, T. and Soroushian, P. Mechanical properties of hydrated cement paste: development of structure-property relationships, J. Concr. Struct. Mater. 7(4) (2010), 37-43
[12] Bauchy, M. et al, Fracture toughness of calcium-silicate-hydrate from molecular dynamics simulations, J. Non Cryst. Solids 419 (2015), 58-64

SynerCrete'18 International Conference on Interdisciplinary Approaches
for Cement-based Materials and Structural Concrete
24-26 October 2018, Funchal, Madeira Island, Portugal

STRUCTURAL PERFORMANCE OF REINFORCED CONCRETE SLAB SUBJECTED TO FIRE AND EXPLOSION

Jiangpeng Shu[(1)], Terje Kanstad[(1)], Max Hendriks[(1) (2)], Jan A. Øverli[(1)], Assis Barenys[(1)]

(1) NTNU Norwegian University of Science and Technology, Trondheim, Norway
(2) Delft University of Technology, Delft, the Netherlands

Abstract

This study was conducted as part of the submerged floating tunnel (SFT) for the "Ferry-free coastal route E39" project by the Norwegian Public Roads Administration (NPRA). The aim of the project is to represent the condition, the concrete shell of SFT under a combination of fire and explosive loads, and for the calibration of the developed numerical model for the analysis of SFT. A laboratory experiment was designed by using shock tube to apply blast load to a series of RC slabs, after heated in a burner according to ISO 834 fire curve. A numerical simulation was conducted to develop modelling strategy for RC structures under such extreme loading condition and calibrated by the laboratory experiment. The influence of high temperature on material properties of concrete, reinforcing steel as well as the stiffness and strength of slab structures were investigated.

1. Introduction

"Ferry-free coastal route E39" is a project by the Norwegian Public Roads Administration (NPRA) that aims at designing a coastal route between Kristiansand and Trondheim (1100 km) without ferry connections [1]. The feasibility of submerged floating tunnels (SFT) is being evaluated, see Figure 1. In the unfortunate situation of accidental events, such as an earthquake, the explosion of oil tank truck, the submerged floating tunnel (SFT) reinforced concrete (RC) structure may become damaged by high temperature and blast loads. The present study focuses on the structural performance and risk analysis of the SFT structure.

Figure 1: Proposed submerged floating tunnels (SFT) for the E39 fjord crossing [1].

RC slabs can be a representative component of the concrete structure of SFT and it is important to study if the RC shells can carry the combination of fire and blast load if an accidental explosion occurs. Shock tube can be a helpful equipment for the experiment. Concrete panels could be experimentally tested at the Polytech University of Milan. The shock tube is equipped with a fire burner that can heat the specimen according to different standard fire curves. Once the desired fire exposure time has been reached, the shock test is performed under "hot" conditions.

2. Design of Experiments

Figure 2 shows a sketch of the shock tube, with the driver section on the left and the driven section, which makes up most of the length of the shock tube, in the middle. Several pressure sensors are mounted on the right, close to where the slabs are mounted. A detailed description of the shock tube can be found in the work by Colomb et al. [2].

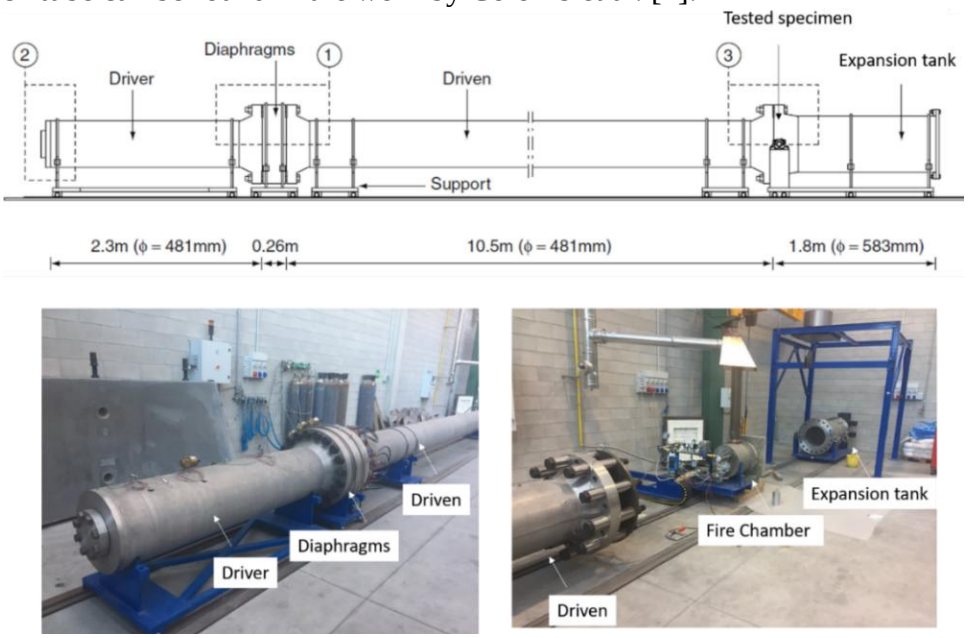

Figure 2: Schematic view of the shock tube including the Fire Chamber [2].

One of the main problems in tunnel accidents is the explosion of a vehicle after a fire exposure; for this reason, proper burner chamber has been designed to simulate fire conditions in the investigated specimen. Different fire curves can be applied, such as hydrocarbon or ISO 834 temperature curves. Once the desired fire exposure time for the specimen is reached, the burner is turned off, the specimen section is connected to the driven chamber and the test is performed. To fasten the slabs to the shock tube-mounting flange, a metal plate is placed on the outside of the concrete slabs.

3. Numerical Prediction

3.1 Numerical simulation approach and solution schemes

According to the experiment scheme, the numerical simulation can be divided into to three phases: (1) Transient heat transfer analysis; (2) Coupled thermal-stress analysis (3) Transient dynamic analysis. Phase (1) aims to simulate the temperature distribution in the RC slab. Phase (2) aims to analysis the performance of RC slab under fire load, including material property and structural deformation. Phase (3) aims to predict the dynamic responses of fire-damaged RC slabs subjected to an explosive load. The influence of high temperature effect on the concrete and steel material is emphasized.

3.2 Finite element model

A finite element model of the tested RC slabs was developed in the commercial software TNO DIANA according to the designed dimension and the solution scheme. Since the slab is axisymmetric, only a quarter of the slab was modelled with 16-node quadratic brick elements, see Figure 3. The average element size is 20 mm. The yellow color area was applied with fire load and following with blast impulse load. The remaining part of the slab was applied with an ambient temperature of 20°C. The temperature time history suggested by ISO 834 was uniformly applied to the exposed area of the slab as flow boundary conditions.

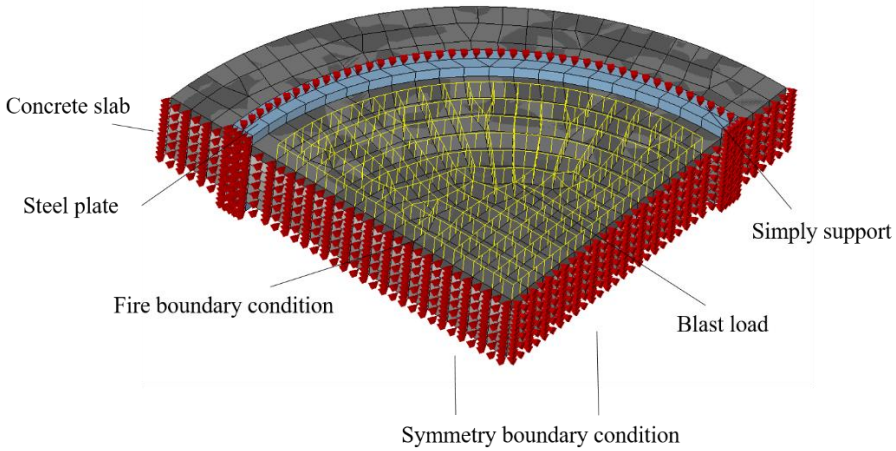

Figure 3: Finite element model of the tested slab, in the TNO DIANA environment.

3.3 Material model and input parameters

Regarding the material model of concrete, the Total Strain rotating crack model with a crack band width approach was used. More information of the material properties for the FE analysis can be found in Shu et al. [5]. The calculated parameters for concrete, steel and boundary interface are listed in Table 1.

Table 1: Calculated input parameters for concrete, steel and boundary interface

	Concrete	Reinforcing steel	Boundary interface
Conduction coefficient	1.32 W/m°C		48 W/m°C
Thermal capacity	7.5×10^{-6} 1/°C		
Density	2400 kg/m^3	7800 kg/m^3	
Poisson's ratio	0.2	0.3	
Heat capacity	2.3×10^{6} J/m^3°C		
Mode I Fracture Energy	65 Nm/m^2		

The material mechanical properties of concrete after fire can be calculated according to EN 1992-1-2; see Figure 4, where $f_{c.\theta}$, $f_{ct.\theta}$ and $E_{c.\theta}$ denote the compressive strength, tensile strength and Young's modulus of concrete after fire exposure, respectively.

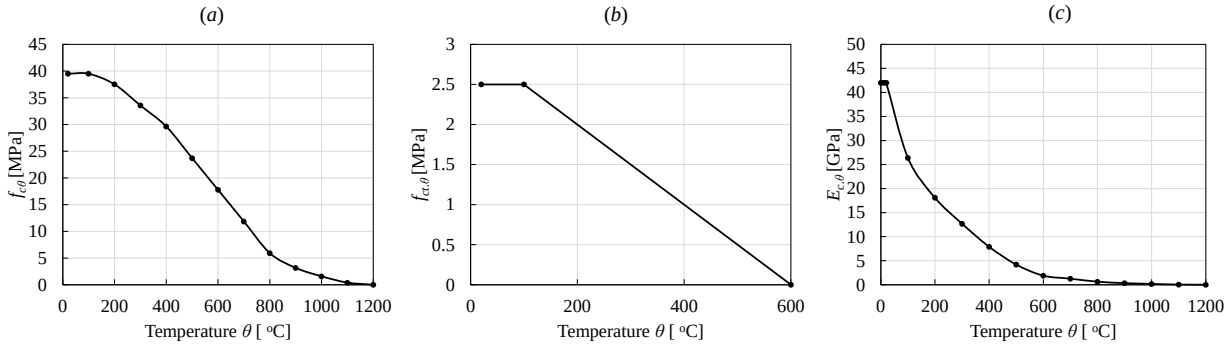

Figure 4: Material properties of concrete after exposed to fire (*a*) Compressive strength (*b*) Tensile strength (*c*) Young's modulus.

4. Numerical Results and Discussion

The fire load was applied to the exposed surface of the slab as the boundary conditions, and a total heat transfer process of 15, 30 and 60 minutes were calculated with a step length of 2 minutes. Figure 5 (*a*) (*b*) (*c*) and (*d*) show the simulation results of the slab under the fire duration of 15 minutes, 30 minutes and 60 minutes, plus the cooling phase of 30 minutes. It is observed that the temperature distribution was different between the heating phase (before 60 min) and cooling phase (after 60 min). During the heating phase, the heat transferred from the boundary to the inner part. On the contrary, the heat emanates from the inner part during the cooling phase. Figure 5 (*e*) presents the temperature-time histories at different depth of the slab. It indicates the variation of the temperature inside the slab model is reasonable.

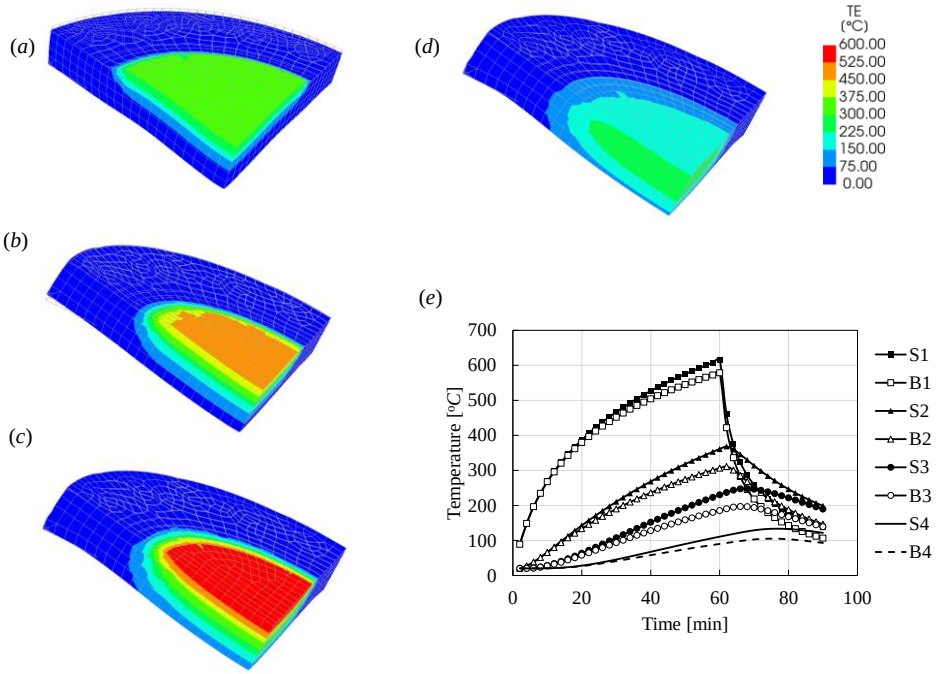

Figure 5: The temperature distribution under the fire duration of (*a*) 15 minutes (*b*) 30 minutes and (*c*) 60 minutes, (*d*) 90 minutes; (*e*) Temperature-time histories at different depth of the slab.

Figure 6 (*a*) presents the deflection-time history after the blast load was added to the surface of the RC slab. When the exposure time increased from 0 minute to 30 minutes and 60 minutes, the deflection was largely increased. It indicates that the mechanical property of the concrete and reinforcement was degraded due to the high temperature. However, one interesting observation is for the case of 15 minutes of exposure time, the average deflection was not influenced but the oscillation was largely decreased. However, the decrease of the oscillation shows the possibility of an increase of the damping, which needs to be studied further. Figure 6 (*b*) presents the total strain based crack pattern of the slab. It shows the crack pattern was extensively distributed at the surface. However, the discrete crack was not shown here because the element size is not small enough.

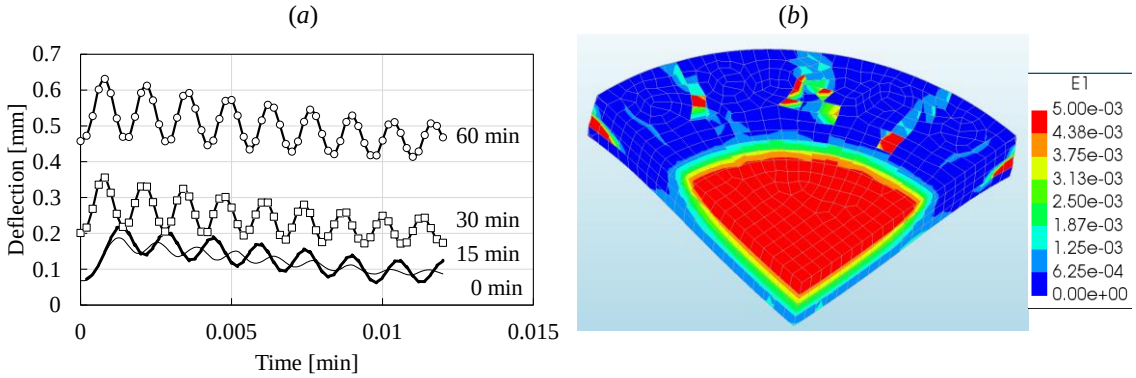

Figure 6: (*a*) Deflection-time history after the blast load (*b*) Strain based crack pattern after the blast load.

5. Summary and Conclusions

Through the study, the following conclusions can be drawn: (*a*) The mechanical property of concrete, reinforceing steel and the structural behaviour of the RC slab under variable extreme temperature environment can be modelled accurately using the developed modelling strategy. (*b*) The stiffness of the RC slab can be decreased considerably by the accumulative fire exposure time. (*c*) A short exposure time may not decrease the stiffness of the slab, but instead, increase the damping related property of the structure. The achievement of this study would help the engineers to have a better understanding of the structural behaviour, and validate the structural safety of the submerged floating tunnel (SFT) considering fire and explosion accidents occur inside the tunnel.

Acknowledgments
This project is funded by NTNU, Department of structural engineering and the Norwegian Public Roads Administration as a part of the Ferry-free coastal route E39 project. The authors would like to express his outmost gratitude to the financers and colleagues at NTNU.

References

[1] StatensVegvesen, Overview of the E39 Coastal Highway Route, Norway (2016)
[2] Colombo, M. et al, A New Shock Tube Facility for Tunnel Safety, Exp. Mech. 51(7), (2011) 1143-1154
[3] Cornelissen, H. W. et al, Experimental Determination of Crack Softening Characteristics of Normalweight and Lightweight Concrete, Heron 31(2), (1985) 45-56
[4] Thorenfeldt, E. et al, Mechanical properties of high-strength concrete and applications in design, In Proc. Symp. Utilization of High-Strength Concrete, Norway (1987)
[5] Shu, J. et al, Numerical prediction of punching behavior of RC bridge deck slabs using 3D continuum non-linear FE analysis, Maintenance, Monitoring, Safety, Risk and Resilience of Bridges and Bridge Networks - Proc. 8th International Conference on Bridge Maintenance, Safety and Management, Brazil (2016), 1607-1611

SynerCrete'18 International Conference on Interdisciplinary Approaches
for Cement-based Materials and Structural Concrete
24-26 October 2018, Funchal, Madeira Island, Portugal

THE IMPACT OF C-S-H NANOSTRUCTURE ON AUTOGENOUS SHRINKAGE AND SORPTION ISOTHERMS

Enrico Masoero [(1)], Giovanni Di Luzio [(2)], Gianluca Cusatis [(3)]

(1) Newcastle University, Newcastle upon Tyne, United Kingdom
(2) Politecnico di Milano, Milano, Italy
(3) Northwestern University, Evanston, IL, United States of America

Abstract

The hydration and durability of cementitious materials are largely determined by the interaction between solid hydration products and water in the pores. This paper shows that drying shrinkage and sorption isotherms during early hydration can be explained by a progressive densification of the cement hydrates at sub-micrometre length scales. A simple conceptual model is presented to support this statement. The model predicts the evolution of self-desiccation during early hydration. The model predictions also align with recent results on C-S-H densification from proton nuclear magnetic resonance experiments. Overall, this indicates how nanoscale modelling can inform the current macroscopic models of concrete hygro-mechanics. This goes beyond the current state of the art, in that self-desiccation and sorption isotherms can now be predicted from the mix design, without other empirical inputs.

1. Introduction

Autogenous shrinkage is the volume contraction of a cement paste hydrating in sealed conditions. It can be explained as the results of a decrease of internal humidity (h), experimentally measured with a humidity sensor placed inside a cavity that is created and kept within a hydrating sample. The decrease of h typically starts after *ca.* 1 day of hydration, when the degree of hydration α is 0.4-0.5 [1,2], and is the combined result of: (i) a progressive desaturation of the pores, due to the consumption of water during the precipitation of hydration products (*e.g.* calcium-silicate-hydrate C-S-H gel and calcium hydroxide CH), (ii) chemical shrinkage, *i.e.* the negative difference in molar volumes between products (C-S-H, CH, etc.) and reactants (dry cement powder and water), and (iii) filling of pore space by hydration product. Three main humidity-dependent mechanisms are usually invoked to

explain autogenous shrinkage [3,4]: (i) capillary pressure due to curved vapour-liquid interfaces, (ii) changes in pore-vapour interfacial energy as a function of the thickness of the layer of adsorbed water, and (iii) disjoining pressure due to hindered adsorption of water in sub-nanometric pores. The internal pressures generated by each of these mechanisms can be expressed as direct (logarithmic) functions of *h*.

Predicting the autogenous shrinkage of a hydrating cement paste is a current challenge for continuum-based models of chemo-mechanics at the macroscale. Their typical approach is the following [5]: (i) autogenous shrinkage is computed from poromechanics, considering the above-mentioned *h*-dependent pressures; (ii) *h* is obtained from the saturation degree, *S*, using a sorption isotherm function *S(h)* which is an empirical input that depends on the chemical composition of the cement paste and on the degree of hydration α; (iii) the saturation degree *S* is a function of the cement paste composition and of α, whose temporal evolution $\alpha(t)$ is usually expressed as a differential equation (in the so-called "affinity" approach) with empirical parameters that depend on the composition of the cement paste.
The just-described macroscopic modelling approach has limited predictive ability, because *S(h)* and $\alpha(t)$ rely on empirical parameters to be obtained experimentally. Recent work has shown that $\alpha(t)$ can instead be parametrised using state-of-the-art simulations of the chemical and microstructural evolution of a cement paste during hydration, *e.g.* CEMHYD3D [2,6]. In principle, the same could be done for *S(h)*, because simulators such as CEMHYD3D also predict the temporal evolution of *S(t)* and of the 3D evolution pore structure, and these two are in principle sufficient to compute the corresponding *h*. However, such a bottom-up prediction of *S(h)* has not been achieved yet. The reason is that a drop of *h* below 99% (autogenous shrinkage typically entails *h* between 75% and 92%) requires the liquid-vapour interface to sit in pores with diameter $\leq$100 nm. This is at least one order of magnitude below the resolution of the above-mentioned microstructural simulators. Therefore, to predict the evolution of *S(h)*, simulators such as CEMHYD3D must be complemented with information about the chemistry-dependent evolution of the pore structure below the micrometre scale. In typical portland cement pastes, this nanoscale porosity is intrinsic to the C-S-H gel phase.
This manuscript presents a simple conceptual model of the co-evolution of hydration degree α and C-S-H gel nanopore structure. This is a simplified version of another recently published model [7], whose key feature is to allow for the C-S-H to: (i) initially precipitate as a low-density high-porosity phase, with pores in the 10-100 nm range, and (ii) subsequently get denser with a progressive reduction of pore sizes towards 1-10 nm. The results shows that the nanopore structure of the C-S-H gel and its densification are essential to predict the onset of self-desiccation (decrease of *h* during hydration) and a realistic evolution of the sorption isotherm *S(h)*. This model provides a starting point to complement the current simulators of microstructure development, such as CEMHYD3D, and eventually to enable continuum-based macroscopic models that can predict autogenous shrinkage starting directly from the chemical composition and curing conditions of the cement paste.

2. Conceptual model

The aims of the conceptual model presented here are to highlight the importance of nanostructure on self-desiccation and sorption isotherms, and to indicate a possible approach

to include information about nanostructure in chemo-mechanical models of cement hydration. A more detailed development of the same concept has recently been published recently [7].

The model considers the hydration of pure tricalcium silicate, C_3S, to produce C-S-H and CH:

$$(CaO)_3SiO_2 + 3.1H_2O \rightarrow (CaO)_{1.7}SiO_2(H_2O)_{1.8} + 1.3Ca(OH)_2 \quad (1)$$

The C-S-H in Eq. (1) refers to the solid part of it only, *i.e.* it does not consider the amount and size of nanopores in the C-S-H gel phase. Considering the molar volumes of the various elements in Eq. (1) [8], one can express the evolutions of C_3S, C-S-H, CH, and water volumes as a function of the degree of hydration α and per unit volume or original paste at $\alpha = 0$. This leads to the plots of volume fractions *vs.* α in the next section of this manuscript. Furthermore, the balance of molar volumes associated to Eq. (1) indicates *ca.* 8.1% of chemical shrinkage [8], *i.e.* a negative difference in volume between products and reactants.

Most of the models of cement hydration to date assume that the C-S-H gel forms immediately with a nanostructure that is similar to the one observed in mature paste. This means an average volume fraction of solid C-S-H per unit volume of gel of $\eta \approx 0.655$, *i.e.* a 34.5% volume fraction of nanopores [8]. Water sorption experiments and computer simulations estimate the average nanopore width in this dense C-S-H gel to be about 3 nm [9, 10]. However, recent results from ^{1}H nuclear magnetic resonance [1] confirmed the already widespread idea that the C-S-H gel initially forms as a low-density phase and significantly larger nanopores. A simple way to model this is to assume a low initial η_0 of the gel, here $\eta_0 = 0.22$ [7], and a linear increase of η with hydration time towards the final above-mentioned $\eta_f = 0.655$. During early hydration (first day or two, with α reaching 0.4 to 0.7 depending on the cement type and curing conditions) one can reasonably approximate $\alpha(t)$ as proportional to $t^{1/2}$, therefore the linear evolution of $\eta(t)$ can be replaced by $\eta(\alpha) = \eta_0 + (\eta_f - \eta_0)\,\alpha^2$. Parallel to this densification, the model should incorporate some information about the evolution of nanopore sizes. A possibility, consistent with nanoparticle models of cement hydrates [10], is to assume an initial average nanopore size $D_0 = 45$ nm at $\alpha = 0$ which decreases linearly with η until a final $D_f = 3$ nm. A similar, but more thorough, model of C-S-H densification is available in the literature.

At equilibrium, the Kelvin equation relates the internal humidity h to the diameter D of the largest saturated pore (for water in cylindrical pores with perfectly hydrophilic surface):

$$D = -4\frac{\gamma_w MV_w}{RT\ln h} \quad (2)$$

In Eq. (2), $\gamma_w = 0.073$ N/m and $MV_w = 18.02 \times 10^{-6}$ m^3/mol are the liquid-vapour interfacial energy and the molar volume of water. In the next section, Eq. (2) will be used to predict self-desiccation and to discuss implications of the presented model for sorption isotherms.

3. Results

Fig. 1 shows the evolution of volume fractions of different phases during the hydration of a pure C_3S paste, as per Eq. (1). The paste has w/c = 0.42, which is the value that, when $\alpha = 1$ and if the gel has $\eta_f = 0.655$, leads to the complete consumption of C_3S and filling of capillary pores by C-S-H gel, while the nanopores inside the gel remain fully saturated with water. This is shown in both Fig. 1a and Fig. 1b at $\alpha = 1$. Both the subfigures also display the same amount of solid phases (C_3S, CH, solid part of the C-S-H) and of chemical shrinkage (the white-coloured complement to volume fraction = 1): this is expected because all these quantities are directly controlled by Eq. (1), which is the same for both the subfigures.

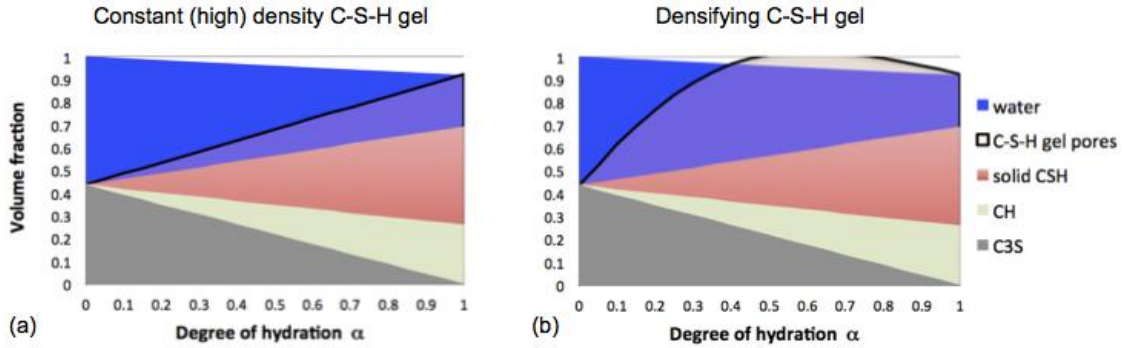

Figure 1: Model results for the evolution of volume fractions of various phases in a C_3S paste during hydration. (a) assumes C-S-H gel with constant volume fraction of pores 0.345 independent of α. (b) assumes a C-S-H gel that gest denser with α^2.

The difference between Fig. 1a and b is in the evolution of the nanoporosity and solid fraction η of the C-S-H gel with α. Fig. 1a considers a constant $\eta_f = 0.655$, independent of α, which is the common assumption in current microstructural simulators of cement hydration, such as CEMHYD3D. Under such an assumption, until $\alpha = 1$, there will always be more water than is necessary to fill all the C-S-H gel nanopores. This water will sit in leftover spaces between the hydration products and the still anhydrous C_3S, and these spaces are typically in the micrometre range. In such a scenario, where the larges saturate pore diameter D is in the micrometre range, Eq. (2) always predicts internal humidity $h > 99\%$, only except for $\alpha = 1$. This clearly contrasts with the experimental observation of self-desiccation starting already at $\alpha = 0.4$-0.5, as shown in Fig. 2 (the impact of considering $w/c = 0.4$, as in the experiment, instead of 0.42, as in the simulation, is very limited, simply reducing the α triggering the humidity drop from 1 to *ca.* 0.9, which is still far from the experiment). Fig. 1b considers a progressive densification of the C-S-H gel with η scaling as α^2 (see rationale in the previous section). This implies that the volume fraction of gel pores increases reapidly at low α and soon, already at $\alpha = 0.4$, all the remaining water in the paste is within the gel (nano)pores. Any further reaction causes the gel nanopores to partially desaturate, leading to a decrease of h predicted by Eq. (2). This is reflected by the drop of h in Fig. 2 starting already at $\alpha = 0.4$, in agreement with the experiment.

Fig. 1b and Fig. 2 display two unphysical features that are due to the strong approximations in the presented conceptual model: these limitations have been already overcome in a more detailed version of a similar model that has been recently published [7]. The first problematic

feature is that the sum of solid phases and gel porosity in Fig. 1b, at some point during hydration ($0.4 < \alpha < 1$) is greater than one. This means that the paste, overall, should swell in that range of α. This unphysical prediction can be (and has been) overcome considering that the precipitation of new C-S-H gel is only possible within capillary pores that contain water (some of them instead empty out during hydration) [7]. The second problematic feature is that the internal humidity in Fig. 2 shows a sudden drop a $\alpha = 0.4$ for the case of a densifying gel, whereas the experiments show a continuous trend of progressively decreasing h with α starting from $\alpha = 0.4$. The reason for the unphysical discontinuity is that the model considers only one single characteristic width for all the pores in the C-S-H gel. In reality, the gel has a wider distribution of nanopore sizes. It has been show that the discontinuity in Fig. 2 indeed disappears if one takes nanopore size distributions from nanoparticle models of the C-S-H gel, and expresses these pore distributions as functions of the gel solid fraction η [7,10].

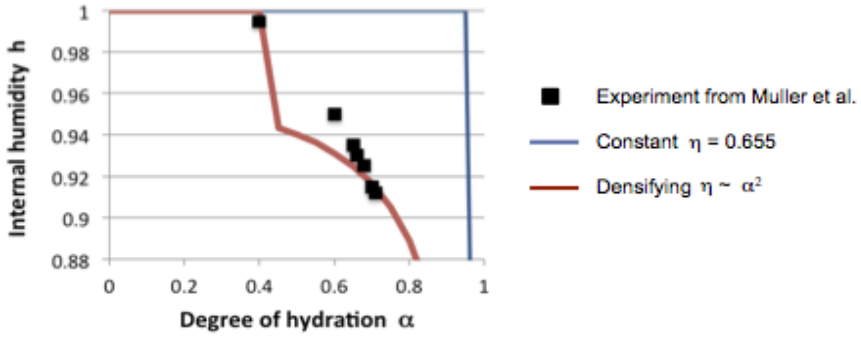

Figure 2: Model and experimental results of self-desiccation (decrease of h) as a function of degree of hydration. The experiment from Muller et al. (cite) refer to a low-alkali cement paste with $w/c = 0.4$. The model results correspond to the two cases in Fig. 1.

4. Conclusion

The simple model presented here has shown that the prediction of self-desiccation in a hydrating cement paste relies on two key features that a model must incorporate:

(i) A progressive densification of the C-S-H gel, which forms initially with a very low density. This is critical in order for the gel to fill the pore volume in the paste and enable the desaturation of nanopores already at low degrees of hydration ($\alpha = 0.4$-0.5, as shown by the experiments). Only when the nanopores starts to desaturate, the Kelvin equation predicts a drop of internal humidity (self desiccation);

(ii) A progressive reduction of the average nanopore size as the gel gets progressively denser. This is necessary in order to predict the progressive decrease of h with α once the nanopores have started to desaturate.

Incorporating these two features in the current model of microstructure development during cement hydration and then, in turn, in the macroscopic models of cement hygro-mechanics, is the way forward to obtain genuine predictions of self-desiccation and autogenous shrinkage based only on the chemical composition, degree of hydration, and curing conditions of the cement paste. This would remove the current reliance of macroscopic models on empirical

sorption isotherms *S(h)*; indeed, coupling the presented model with a more detailed description of the nanopore gel size distribution, has been show to yield realistic predictions of the sorption isotherms too [7]. To this end, a detailed description of how the nanostructure of the gel evolves, as a function of the chemical composition of the cement and on the curing time and conditions, is needed. This level of detail can be obtained from state-of-the-art nanoparticle simulations of cement hydration [11]. This opens to a truly multi-scale predictive modelling approach of self-desiccation, sorption isotherm, and autogenous shrinkage, in line with the vision of a simulation-guided design of future nano-engineered cements.

References

[1] Muller, S. et al, Use of bench-top NMR to measure the density, composition and desorption isotherm of C—S—H in cement paste, Microporous Mesoporous Mater, 178 (2013), 99 – 103
[2] Pathirage, M. et al, A Multiscale Framework for the Prediction of Concrete Self-Desiccation, Proceedings of the EURO-C 2018 Conference - Computational Modelling of Concrete and Concrete, Austria (2018)
[3] Jennings, H.M., et al, Water isotherms, shrinkage and creep of cement paste: hypotheses, models and experiments. In Mechanics and Physics of Creep, Shrinkage, and Durability of Concrete: A Tribute to Zdeňk P. Bažant (2013), 134-141
[4] Bažant, Z.P., Interaction of concrete creep, shrinkage and swelling with water, hydration, and damage: Nano-Macro-Chemo. Proceedings of the 10th International Conference on Mechanics and Physics of Creep, Shrinkage, and Durability of Concrete and Concrete Structures (2015), 1-12
[5] Di Luzio, G. and Cusatis, G., Hygro-thermo-chemical modeling of high performance concrete. I: Theory. Cem Concr Res 31 (2009), 301-308
[6] Bentz, D.P., CEMHYD3D: A three-dimensional cement hydration and microstructure development modelling package. Version 2.0. US Department of Commerce, National Institute of Standards and Technology (2000)
[7] Masoero, E., et al, C–S–H gel densification: The impact of the nanoscale on self-desiccation and sorption isotherms, Cem Concr Res 109 (2018), 103-119
[8] Masoero, E., et al, A Reaction Zone Hypothesis for the Effects of Particle Size and Water- to- Cement Ratio on the Early Hydration Kinetics of C3S. J Am Ceram Soc 97 (2014), 967-975
[9] Baroghel-Bouny, V., Water vapour sorption experiments on hardened cementitious materials: Part I: Essential tool for analysis of hygral behaviour and its relation to pore structure, Cem Concr Res 37 (2007), 414-437.
[10] Ioannidou, K., et al, Mesoscale texture of cement hydrates. Proc Natl Acad Sci 113 (2016), 2029-2034
[11] Shvab, I., et al, Precipitation Mechanisms of Mesoporous Nanoparticle Aggregates: Off-Lattice, Coarse-Grained, Kinetic Simulations. Cryst Growth Des 17 (2017), 1316-1327

BIM AND STRUCTURAL CONCRETE

SynerCrete'18 International Conference on Interdisciplinary Approaches
for Cement-based Materials and Structural Concrete
24-26 October 2018, Funchal, Madeira Island, Portugal

BIM FOR PRECAST

Peter Karlsson [(1)]

(1) StruSoft AB, Malmö, Sweden

Abstract
The precast process is divided into three sub-processes; design, erection and production. Design is giving birth to the precast process with a rough 3D model. When planning the process is reversed so that it starts with the planning of the erection on site and step backwards to the time for production and the time for delivery of detailed shop- drawings.
By doing this planning in a shared Building Information Modelling (BIM) platform in real time all three sub-processes get the correct priority for the main process the project on site.
The site project planners use the 3D model when they make the rough planning on the design structure. They start by setting the planned erection date and then step backwards through the planned delivery date, planned storage date, planned production date and planned drawing delivery date.
The planned production date gives production the time frames when they need to deliver the manufactured elements and the planned drawing date gives design the information when the shop-drawings needs to be ready so that the production can produce the elements in time.

1. Introduction

Building Information Modelling (BIM) means different things for different people. I will not try to define BIM in this article as too much time has been spent on that already, but we prefer to think that there is a silent M after "BIM(M)" that is read out as "Management". Because BIM is about managing multi-disciplinary processes (companies/people), that connect and sometimes overlap, and share data on a high level.
When discussing BIM, it´s of course hard to narrow down and focus on precast but I think that's the first step to a successful implementation of BIM for a precast company ("Precaster"). To look at "what's in it for me"? The precast structure is of course only a part delivery of the whole building project. But if you see that as a process that you bring data into and at the end delivers more high level out from, you can start to make the Precast process

fully BIM so that within in that process, which sometimes is controlled by one company (different departments) or several companies, all the people share their data in a real time environment. Maybe the parties involved have different interfaces or applications, but they are all having the same source of information.

2. The precast process and BIM

BIM is a way of working not a software. That's why the software should support the way of working and not the other way around. To get to a high implementation of BIM you absolutely need to adopt to a new way of working and have a software that supports that new path.
We think that the precast process (once the project is won by a precast company) has three main legs/sub processes. The three legs of precast is design, production and erection. The different legs have different priorities and needs. If you can expose the information of those sub processes for all the other parties involved (in the precast process), in real time, so that for instance the production can see the planning of the erection and vice versa there is a lot of time and effort to save.

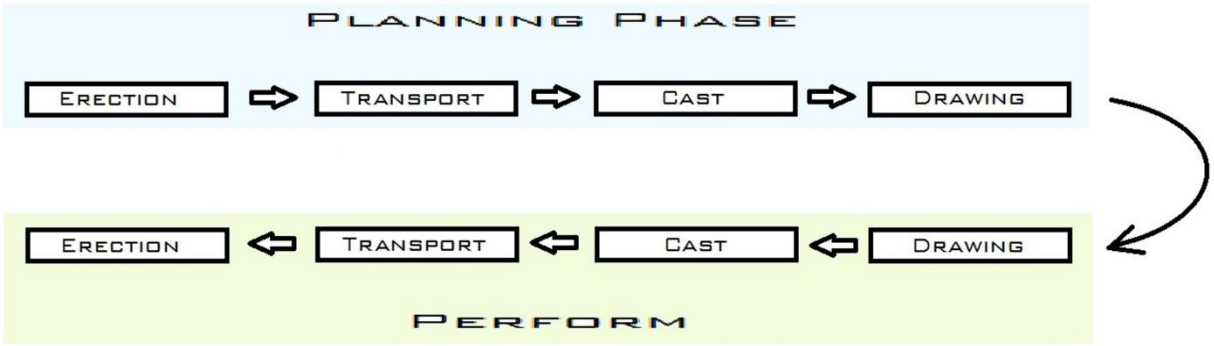

Figure 1: The planning and perform process of precast.

The design is giving birth to the structure of the precast process with the 3D model. First on a rough level and later on a more detailed one. by reversing the process so that we start with the planning of the erection on site and step backwards to the time for production and the time for delivery of detailed shop drawing all three legs get the correct priority for the main process the project on site. By doing this you can setup your production to "just in time delivery" and then the design to deliver precast detailed design (finalizing production drawings) in time to fulfil the needs from production. To come to this doesn't require the same mindset for all legs of precast; it does however require "BIM for precast".
The input for the "Precasters" today (if it´s digital) comes from many different formats produced in software packages like ArchiCAD, AutoCAD, Revit, Tekla etc. Industrial Foundation Classes (IFC) is a great format for the exchange of BIM data. But there is one weakness by using it as the only technical format for the contract of the building: the object information in it needs to be converted to objects of the software it shall be represented in. When doing that there is a great risk that this conversion will make something different with the data than it was originally. To be able to take that type of data in at a high level with less

risk of conversion problems it's better to make plugins into the different software were the information was initially created and then with user control import the data from the origin platform to the BIM database. This is the only reasonable way to deal with the problem today.
The Precast process could be illustrated like a relay race with parallel teams that run towards a common goal (the completed structure of the building on site). Handover of the stick (information) is done within the teams as well as between the different teams. The information provided with the stick changes constantly. Good logistics is the key to success and if things are not in the right place in the right time, the work becomes more complicated not only within the own team but for all the other teams as well.
In the light of that, we see a common storing of data and exchange in real time as the base of BIM for Precast. The change of data happens so frequently during the precast process and if manual (snapshot) exchange of data should be the way of communicating you will lose time and quality. The precast process is iterative: that's why you need to have all the corresponding data updated all the time to make the right decisions.
In the precast world outsourcing has come to stay. In that view the need of a common language between the different stakeholders in the project, whether they are in the homeland of the project or abroad, is the key to success for the "Precasters". The base structure in that language is the 3D model. We can then bind all information needed to the model throughout the process. Then you can sit on the other side of the planet and understand the priorities of the project.
Another important thing when we talk about BIM is that the output is relevant and present for each person involved ("right information at the right time") in the process. That, for instance, means that the production picks the material take off data directly from the BIM database based on their own selection (maybe the planned molds of the week) not based on what design pass on in their offline Excel report delivery. To have the production and design to operate on the same data (real time BIM database) is essential for a successful BIM integration for Precast.

3. Building Information Modelling platform

Our customers today use a mix of taking the information in as reference AutoCAD or on a higher level through our Revit and Tekla interfaces. We have AutoCAD, BricsCAD, Revit and Tekla plugins that interacts in real time with our BIM database.
Inside the precast process our customers interact between their departments by using different interfaces to our BIM database.
Design starts by making a rough 3D model in AutoCAD, BricsCAD, Revit or Tekla with our plugins. Rough means that not all element connections are solved (yet) and no shop drawings are produced.
The erection planners then continue to make the rough planning on the design structure. They start by setting the planned erection date (erection sequence) and then steps backwards through the planned delivery date, planned storage date, planned production date and planned drawing date. They have functionality to simulate time and check against cranes. This they do on a model-based software (Project Manager) that interacts directly with the BIM database. The Project Manager is a common platform for both design, erection and production.

The planned production date gives Production the time frames they need to deliver the manufactured elements and the planned drawing date gives the Design the information when the drawings needs to be ready so that the Production can produce in time.
Production then starts the detailed planning based on the erection planning data. They plan their molds and beds to be as effective as possible and coordinate this with storage and transportation. As a support they use both the Project Manager (Project focus) and the Resource Manager (Factory focus). Throughout the whole process the status chain on the elements gives an instant visible feedback for all the stakeholders in the project of the current situation.

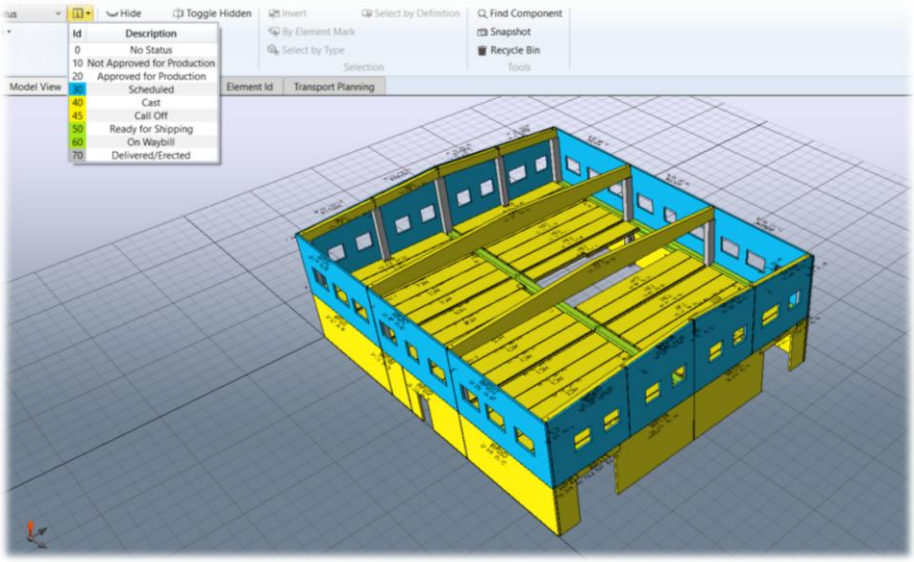

Figure 2: The real time status of the project.

Mobile apps (also connected to the BIM database) gives a remote connection to the BIM database for people working out in the storage or at the erection site. With that application in their phones they can, in real time, add information to the database such as storage location, transport information etc.
The most common output from our customers today to parties in the bigger outer process of the project is IFC models for clash control (clashes in space).

4. Future and the precast process

Different perspectives need different interfaces/apps. We see a future where an extended toolbox of apps for different needs will be joined together with multi-linked cloud-based databases. "The internet of precast" if you like.
With that online functionality the designer that makes the detailed design can for instance directly communicate with the mesh welding machinery (like the Progress Group PTS service application) and check the producibility for the reinforcement mesh and then in real time receive the response in his 3D model for correction.

Talking about clash control the obvious thing is to detect clashes in space, but the future is to use BIM to see clashes in time as well. Sharing time information between different systems will be possible by communicating cloud databases. The IMPACT BIM Cloud database directly communicates with real time interfaces to the main process time schedule.
The Precast manufactures can outsource and let their consultants connect directly to their data (manufacture) in an environment controlled by the precast manufacturer in the cloud. With this the precast manufacturer will be able to check the progress of their consultants and let them see the data needed for making the right decisions.
With environmental data connected to the BIM model the footprint of the precast concrete structure will be visual for everybody in the project. The customer (of the precast manufacturer) will be able to see the result, follow the progress and see the planning ahead in a cloud-based BIM environment.

Figure 3: Real time environmental IMPACT of the Precast structure.

Ask the reinforcement vendor for price and time to deliver reinforcement stirrups or reinforcement mesh for the whole project (or parts of a project) by online communication with the vendor cloud-based system (like the Celsa Steel Service application QR). Instantly let your vendors system give you the expected delivery time and check the producibility of your data. If the vendor fulfils your expectations (including price), accept and place the order directly. Ask the vendor of steel plates in the same way.
Mixed reality where the real environment co-exist with the virtual reality creates a platform for better understanding and implementation of the engineered solutions in the real world. Microsoft HoloLens glasses projection in the mould combined with "naked eyes" can be used to place and control the cast in items in the mould. Mixed reality has already successfully been used in the aerospace and car industry and it will for sure create advantages for the building industry as well. By using mixed reality in the precast production, we will speed up and increase the quality of the manufacturing process and make the production paperless. We can combine the design element model with step by step procedures (data displayed in sequence not all at once) on how to manufacture and assemble an item like for instance a reinforcement cage. This will make it easier to produce advanced components with a less

experienced workforce. When more of the workforce can do complicated task, it will be easier to remove bottlenecks in the production. The data used in the mixed reality environment collect the data in real time from the BIM database information and is always updated and the risk for producing on an outdated paper drawing will be avoided.

Figure 4: Digital element in the mould at SCF Betongelement AB factory in Strömsund Sweden picture from Information Experience.

5. Conclusions

In the future the process at building sites will be more an assembly process than a manufacture process. This will make advance logistics even more important for success. Exchange and visibility of real time data that describes all dimensions (3D, time, cost and environmental impact) to all the stakeholders of the process will reduce the cost and delivery times for the building industry and make the work more attractive for the new generations.

SynerCrete'18 International Conference on Interdisciplinary Approaches
for Cement-based Materials and Structural Concrete
24-26 October 2018, Funchal, Madeira Island, Portugal

COST-OPTIMAL ANALYSIS OF CONCRETE SOLUTIONS FOR SINGLE-FAMILY NZEBS APPLYING AN OPEN BIM WORKFLOW

Afonso Miguel Solak [1,2], Javier Pereiro-Barceló [2]

(1) University of Alicante, Alicante, Spain
(2) CYPE Ingenieros S.A., Alicante, Spain

Abstract

In this study, Building Energy Simulations (BES) have been performed to check the impact of concrete-based building materials as part of the building envelope on the primary energy consumption of a single-family nearly Zero Energy Building (nZEB) to be built in Spain. The aim of this study is to evaluate different concrete solutions and determine which configurations combine the lowest primary energy consumption and the lowest cost by analyzing the building's energy performance throughout its life cycle. An Open BIM workflow, proposed by CYPE Software, was used for the achievement of these objectives. An architectural model was developed using the freeware application IFC Builder and synchronized though the online platform, BIMserver.center, where its project data was available for the energy simulations performed later in CYPETHERM HE Plus. Although the results refer to a Spanish-Mediterranean residential reference, the methodology applied in this study is applicable in other cases and can be useful to support nZEBs design and decision making.

1. Introduction

Cement-based products must play a key role in the transition towards a more sustainable construction, replacing traditional forms of construction with more advantageous, economic and durable ones. In Spain, in 2016, 11.08 million tons of cement were used, with 46% destined to the buildings construction sector [1]. Concrete buildings can provide substantial energy savings during their lifetime. The high level of thermal mass in concrete constructions means that indoor temperatures remain stable, regardless of external fluctuations [1]. In the following years, across the European Union, every new building must fulfill the requirements of the nearly Zero Energy Buildings (nZEB) concept, as it is stated by the Directive 31/2010 -

Energy Performance of Buildings Directive (EPBD) [2]. The deadline, 2020 targets the reduction of the primary energy consumption, but there are no general requirements for the application of the nZEB concept in all countries. In Spain, the basic document outlining Energy Savings, part of the national construction normative "Technical Building Code (CTE-DB-HE)", published in 2013, will be updated during 2018 as the Directive 31/2010 establishes in its Article 4 that "minimum energy performance requirements shall be reviewed at regular intervals which shall not be longer than five years". Cost optimal levels can be seen as a first step towards the achievement of the nZEB target. They refer to the energy performance in terms of primary energy leading to the minimum life cycle cost, and according to the EPBD Guidelines, must include the initial investment and running, replacement and disposal costs.

Building Information Modeling (BIM) can be a useful tool to evaluate the economical and technical viability of a project. In the past decade, BIM has become widely used in the Architecture, Engineering and Construction (AEC) sector [3]. The use of BIM and its visual programming interface has become an integral tool for building design, not only for the conceptual design stage, but also for optimizing the design for thermal performance [4]. It is a remarkable improvement in terms of cooperation and management of the documentation, since it establishes a common platform between the different subjects involved in a project [5]. The term "Open BIM" appears when we take advantage of this protocol to implement an open collaboration system that does not depend on a specific application. The main property of Open BIM technology is that it is based on the use of IFC standard interchange formats. By using this format, which is also public and not linked to a specific developer, the durability of the work that has been carried out is guaranteed [5].

This study focused on the evaluation of different concrete solutions and configurations which combine the lowest total energy consumption of primary energy of non-renewable origin (Ct,nr) and the lowest cost. This was done by analyzing the building's energy performance throughout its life cycle, including the Costs of Construction (CC), Maintenance/Replacement (CM) and Operation (CO), in the Open BIM Workflow proposed by CYPE Software.

2. Methodology

2.1 The Reference Building

The selected reference building consisted of a two-story, single-family house with a net floor area of 164.97 m², a net floor height of 2.70 m and a net volume of 573.15 m³. The aspect ratio was 1.29:1 and the window-to-wall ratio was 16%. Technical drawings and an isometric view of the building are provided in Fig.1. Since the building is located in Colmenar Viejo (Madrid, Spain), it was designed in compliance with the maximum values of energy consumption required by national regulation (CTE DB-HE). Air permeability of the envelope, considering a reference pressure of 100 Pa, was 16 $m^3/(h.m^2)$ for façades and roofs, 60 $m^3/(h.m^2)$ for doors and 10 $m^3/(h.m^2)$ for the other openings.

The demand for sanitary hot water was 112.0 l/day and the set point temperatures established in CTE DB-HE (17 °C to 28 °C) were conditions of operation and internal comfort, considering a residential profile of use. The efficiency of the heat recovery system of the mechanical ventilation system was 87.1%. The values of infiltrations were obtained the calculation method of Enhanced Model (ASHARAE), with a calculated flow coefficient,

without admission openings and considering that the operational conditions were constant. The total ventilation of the habitable enclosures was 0.63 ren/h. The solution adopted for the air-conditioning-heating system consisted of a set of low temperature under floor radiant system complemented by fan coils of low silhouette ducts, associated with an aerothermal system with air/water heat pump and reversible cycle (total cooling power of 10000 W, energy efficiency ratio of 2.78, total heating power of 11200 W and a coefficient of performance of 4.55).

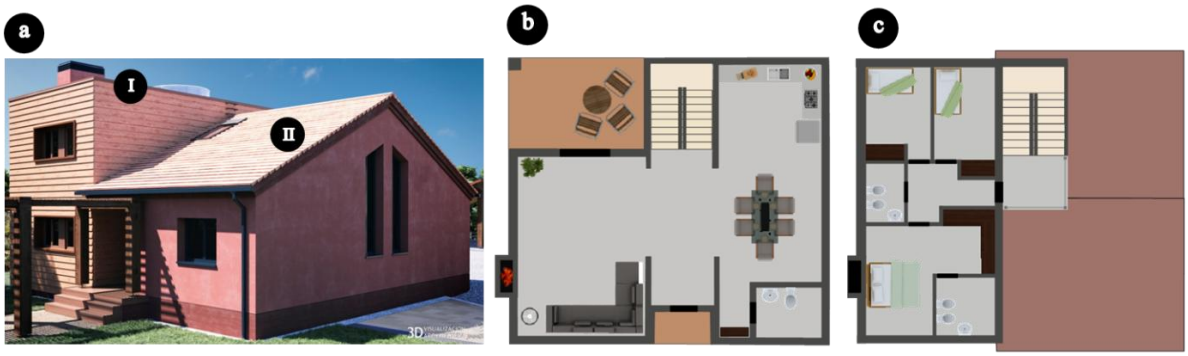

Figure 1: Technical Drawings and Isometric View of the Case Study.

Reinforced concrete slabs (thickness of 15 cm) were used for the horizontal structural system. Its resultant thermal transmittance (U), associated with its insulation layers, were 0.19 W/(m²·K) for the ground floor slab, 0.22 W/(m²·K) for the flat roof slab (I in Fig. 1a) and 0.31 W/(m²·K) for the sloped roof slab (II in Fig. 2a). Windows were composed wood frames (thermal conductivity (λ) of 1.10 W/(m²·K) and solar factor of 0.61) and double low emissivity glass with argon cavity and aluminum spacers (λ = 1.43 W/(m²·K)), resulting in a frame-glass ratio of 22%. Eight additional photovoltaic panels, with a total area of 12.78 m^2, provide 16.92 kWh/m^2 yearly.

2.2 Concrete Solutions Studied

The vertical surfaces (Fig.2) were the main elements evaluated in this work. In all cases, the walls have structural and enclosing function. An External Thermal Insulation Cladding System (ETICS) was considered for the external surface of the façades in order to reduce the losses caused by thermal bridges. ETICS was formed by one layer of a 60 mm rigid expanded polystyrene panel (λ = 0.04W/(m.K)) and four layers, of 4 mm each, of mortar as part of the system, but with no relevant thermal properties. Internal surfaces of the façades were covered by 10 mm plasterboards (λ=0.25W/(m.K)) spaced 10 mm from the structural core.

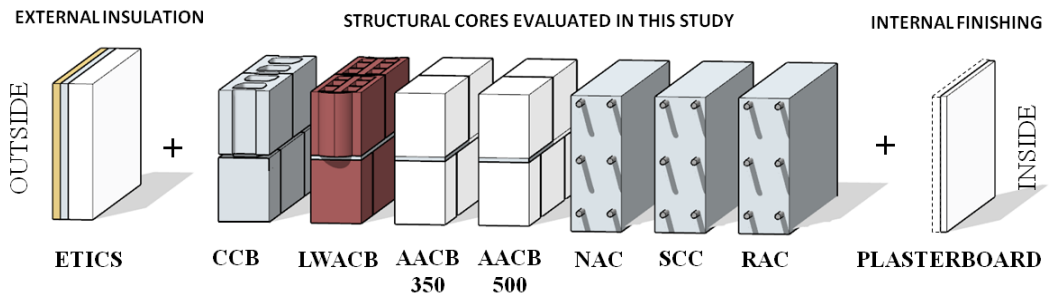

Figure 2: External walls evaluated in this study.

Six different solutions were evaluated as wall-core materials. Three types of cast-in-place concretes were included in the simulations as reinforced concrete walls with materials commonly used in Spain: Natural Aggregate Concrete (NAC), Recycled Aggregate Concrete (RAC) and Self-Compacting Concrete (SCC). In the same way, the structural masonry walls are formed by Conventional Concrete Blocks (CCB), Lightweight Aggregate Concrete Blocks (LWACB) and two different types of Autoclaved Aerated Concrete Blocks (AACB). The thicknesses considered in this study are dimensions commonly used and commercialized by manufactures in Spain (Table 1).

Table 1: Thermal Properties of the Concrete Wall-Cores Evaluated in this Study

		Thickness (cm)											
Material		**10.0**	**12.0**	**15.0**	**20.0**	**22.5**	**25.0**	**30.0**	**34.0**	**35.0**	**36.5**	**40.0**	**42.0**
CCB	λ	0.605	0.670	0.759	0.891	-	1.009	1.117	-	-	-	-	-
	ρ	1337	1247	1201	1112	-	1048	998	-	-	-	-	-
LWACB	λ	-	0.202	0.224	0.256	-	0.285	0.310	-	-	-	-	-
	ρ	-	1066	1001	924	-	868	824	-	-	-	-	-
AACB 350	λ	-	-	-	-	0.090	0.090	0.090	0.090	-	0.090	-	0.090
	ρ	-	-	-	-	350	350	350	350	-	350	-	350
AACB 500	λ	-	-	-	0.125	-	0.125	0.125	-	-	-	-	-
	ρ	-	-	-	500	-	500	500	-	-	-	-	-
NAC	λ	2.300	2.300	2.300	2.300	-	2.300	2.300	-	2.300	-	2.300	2.300
	ρ	2400	2400	2400	2400	-	2400	2400	-	2400	-	2400	2400
SCC	λ	2.300	2.300	2.300	2.300	-	2.300	2.300	-	2.300	-	2.300	2.300
	ρ	2400	2400	2400	2400	-	2400	2400	-	2400	-	2400	2400
RAC	λ	2.300	2.300	2.300	2.300	-	2.300	2.300	-	2.300	-	2.300	2.300
	ρ	2400	2400	2400	2400	-	2400	2400	-	2400	-	2400	2400

λ – Thermal conductivity (W/(m.K)). ρ – density (kg/m^3)

2.3 Open BIM Workflow

The Open BIM Workflow proposed by CYPE Software was employed for the achievement of the objectives (Fig 3).

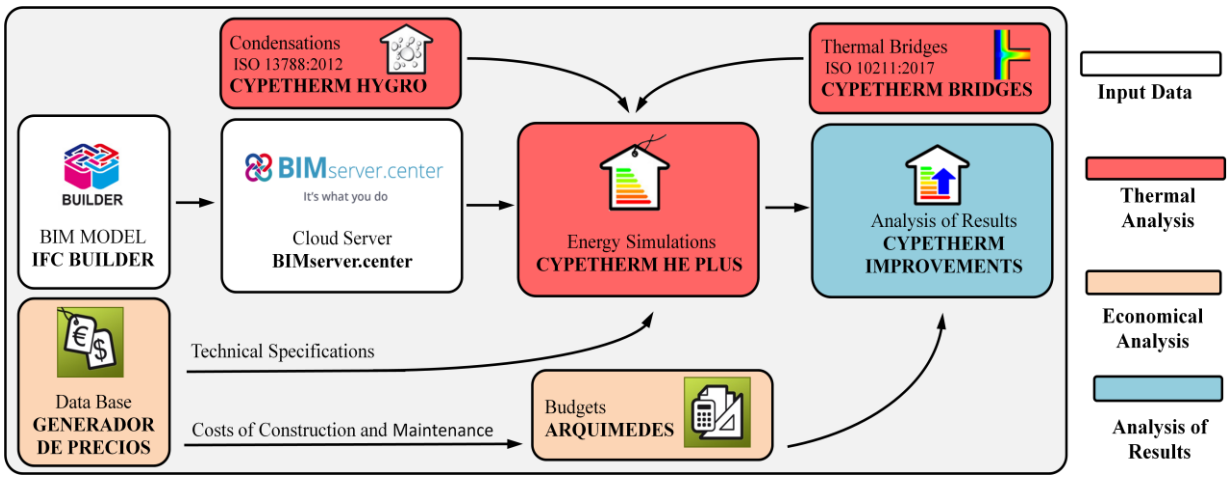

Figure 3: Flowchart of the Methodology Adopted in this Study

First, an architectural model was developed using the freeware application IFC Builder (IFC4 format), where the spaces, orientation and other aspects of the building's geometry were described. Subsequently, the model was synchronized though the online platform BIMserver.center, where its project data became available for the following steps of the workflow. Forty-four energy simulations were performed in CYPETHERM HE Plus employing technical data from CYPE´s data base (Generador de Precios) to characterize the building´s envelope, thickness detail, materials and thermal characteristics of each element. In the same way, the thermal transmittances in linear thermal bridges were evaluated, solving and processing a heat transfer finite element model based on the EN ISO 10211 using CYPETHERM Bridges. The results of each energy simulation were exported to CYPETHERM Improvements, where the budget information related to each hypothesis was also included. Construction and maintenance costs considered were also obtained from CYPE´s data base. The global costs method described by Signes-Orovay et al [6] was adopted considering a 50 year building life-cycle.

3. Results and Discussion

$C_{t,nr}$ was assessed in terms of delivered primary energy, including energy use for heating, cooling and domestic hot water. Primary energy values were calculated using the Spanish primary energy factor (2.368 for electricity). The results for the energy consumption (kWh/m^2.y) versus global cost (€/m^2) were reported for all scenarios in Fig. 4a.

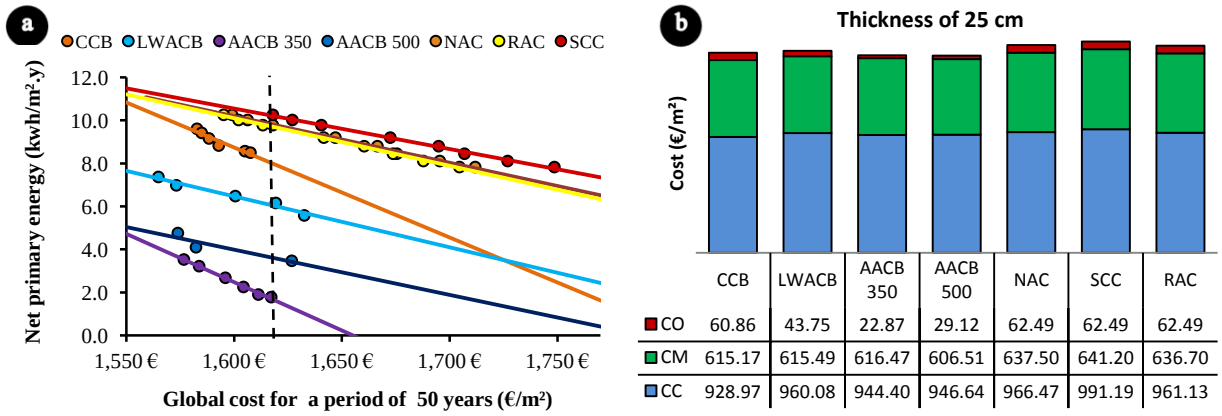

	CCB	LWACB	AACB 350	AACB 500	NAC	SCC	RAC
CO	60.86	43.75	22.87	29.12	62.49	62.49	62.49
CM	615.17	615.49	616.47	606.51	637.50	641.20	636.70
CC	928.97	960.08	944.40	946.64	966.47	991.19	961.13

Figure 4: a) Global Costs versus Net Primary Energy b) Costs Breakdown Analysis for Examples with Thickness of 25 cm

The minimum $C_{t,nr}$ was achieved by the scenario considering AACB350/42cm (1.78 kWh/m^2.y). For comparative purposes (indicated by the vertical dashed line in Fig. 4a) and considering linear interpolated data, the same global cost necessary to implement this solution (1617.19 €/m^2) would increment the $C_{t,nr}$ from 106% to 450% if AACB500 or NAC solutions were respectively employed in substitution of AACB350. Global cost (50 years) ranges from 1564.82 €/m^2 (LWACB/12cm) to 1748.59 €/m^2 (SCC/40cm). Construction Costs (CC) are the most relevant cost, ranging from 57% to 61% of the global cost. Although the initial investments for CCB solutions are lower compared with other solutions, the best results for the whole life cycle of the building were found in AACB solutions, which had their

operational costs reduced due the optimization of the thermal performance of the envelope. The Cost of Operation (CO), related to energy consumptions, could be reduced from 5% (cast in place solutions) to 1% (AACB solutions) of the total overall cost if AACB solutions were employed. Costs of Maintenance/Replacements (CM) are important during construction. The same HVAC and photovoltaic systems were employed for all combinations, and since the calculation period was set to 50 years, replacements occurred twice during the building life cycle. All combinations presented similar results for the Costs of Maintenance/Replacement (CM), ranging from 37 to 39% of the total cost. Fig 4b shows the costs breakdown analysis for examples with thickness of 25 cm.

4. Conclusion

In this study, energy simulations have been performed to check the impact of concrete-based building materials as part of the building envelope on the primary energy consumption of a single-family nZEB. From the results presented, the following conclusions are drawn:

- Since just one architectural model was developed and all scenarios were simulated in specialized applications linked to the workflow, applying the Open BIM method proposed by CYPE led to a compact, but complete, final consolidation of the project.
- Since both masonry and cast-in-place concrete walls can be employed as the building structure, results presented in this work suggest that concrete masonry walls are possible solutions to be used in projects of single-family nZEBs once it presents better energy and economical performances.
- The results also indicate higher energy-economical performances of Autoclaved Aerated Concrete Blocks (AACB), when compared to other structural masonry wall solutions.

References

[1] OFICEMEN - Agrupación de fabricantes de cemento de España. Anuario del sector cementero español - 2016. Madrid: 2016.
[2] EU, Euopean Union. Directive 2010/31/EU of the European Parliament and of the Council of 19 May 2010 on the energy performance of buildings. Off J Eur Union 2010;53:13–35. doi:doi:10.3000/17252555.L_2010.153.eng.
[3] Ma Z, Liu Z. Ontology- and freeware-based platform for rapid development of BIM applications with reasoning support. Autom Constr 2018;90:1–8. doi:10.1016/J.AUTCON.2018.02.004.
[4] Natephra W, Yabuki N, Fukuda T. Optimizing the evaluation of building envelope design for thermal performance using a BIM-based overall thermal transfer value calculation. Build Environ 2018;136:128–45. doi:10.1016/J.BUILDENV.2018.03.032.
[5] Díez Montenegro V. Herramientas de análisis acústico dentro de un flujo de trabajo BIM. 48o Congr. Español Acústica - Encuentro Ibérico Acústica, A Coruña: 2017.
[6] Signes-Orovay J, Miñana-Giner V, Solak AM, García-Hermosa JL, Martínez de los Mozos J, Gilabert-Boronat P, et al. Anexo 6: Análisis Económico y Energético. Proyecto. Cypewood., Alicante: CYPE Ingenieros S.A.; 2018, p. 41.

SynerCrete'18 International Conference on Interdisciplinary Approaches
for Cement-based Materials and Structural Concrete
24-26 October 2018, Funchal, Madeira Island, Portugal

INTEGRATED APPLICATION OF ADVANCED SURVEYING TECHNIQUES AND BIM FOR INSPECTION AND ASSET MANAGEMENT OF REINFORCED CONCRETE BRIDGES

Miguel Azenha [(1)], Gabriel Sousa [(1)], José Matos [(1)], José Sena-Cruz [(1)], Vitor Brito [(2)]

(1) ISISE, University of Minho, Guimarães, Portugal
(2) Betar Consultores, Lisbon, Portugal

Abstract

The aim of the work reported herein was to explore the possibilities of integrating new ways of surveying into RC bridge inspection activities and evaluating the possibility of integrating data into a BIM model, as to allow quick overviews to be obtained after each inspection. Efforts were made in regard to modelling strategies, not only of the RC bridge elements, but also of 'damage' information that required special attention, as to allow non-graphic information to be easily retrievable. Special tools (add-ins to the BIM platform) were also developed in order to allow quick introduction of inspection data into the BIM model through Excel spreadsheets. The concepts/methods proposed were put to test in an extensive inspection to a bridge located in the north of Portugal. This work results from a collaboration of the University of Minho with Betar, a consulting office with more than 20 years of experience in Bridge inspection, which has authored a managing system for road infrastructure and actively applies it.

1. Introduction

Bridges and viaducts are very important and fundamental assets for road/railway infrastructure managers, who need to manage the information of each structure in an organized manner as to perform timely reactions and maintenance activities to ensure safety, adequate service levels and durability. Most countries in the world have national infrastructure strategies for inspection, with Portugal having issued their latest inspection manual in 2015 [1]. Several types of inspection are envisaged (as well as their timing), from the simplest routine ones, to the most complex, the special inspections that intend to gather extensive information on the entire asset or specific aspects of it. In spite of the well-structured activities in such manuals, they are still lacking explicit references to the

integration of the inspection information into Building Information Modelling (BIM) frameworks, particularly taking into account the opportunities brought about by new/emerging surveying inspecting techniques (e.g. laser scanning, GPR, thermography, 360 photography). This is not necessarily a ground-breaking activity in view of the extensive recent developments occurring in BIM at the '*facilities management*' discipline (BIM-FM) [2]. However, very little has been done in applied discussion of the challenges and opportunities brought about by BIM-FM in the particular scope of reinforced concrete bridges that incorporate a set of specificities. This was therefore the main aim of the present work, that focused in the application of BIM methodologies to the extensive survey/inspection of a reinforced concrete bridge located in the North of Portugal. The work carried out was closely monitored and supported by the company Betar, which has authored a widely-used system for infrastructure management in Portugal, named GOA (focus on bridges/viaducts) [3], but does not incorporate yet BIM-based technology in their inspection/management processes. It is also noted that the work reported herein is more extensively described in the MSc dissertation of the second author [4].
This paper is structured in two main parts in Sections 2 and 3: Section 2 presents the case study of the Saltadouro Bridge and a global overview of the survey/inspection actions that were carried out. Section 3, in turn discusses the processes and methods for producing the corresponding BIM model, with adequate incorporation of the inspection data. Final conclusions of the work are presented in Section 4.

2. Saltadouro Bridge: the case study

2.1 Description of Saltadouro Bridge

The Saltadouro Bridge is located in the North of Portugal, within the Natural Park of Gerês (Ruivães). It has been built in the 1950's, but the owner did not have any drawings or written records of the bridge design. The bridge, whose recent photo is shown in Figure 1, has two free spans of approximately 16.8m each, supported in a central column and two lateral abutments. The cross-section of the bridge is a double "T", with two longitudinal ribs supporting the top slab (all monolithically connected to each other). As seen in Figure 1, the water height is different in both spans of the bridge. For that reason, and taking into account the similar apparently similar state of both spans, the detailed inspection has been focused on the leftmost span according to Figure 1 (South side), which was made accessible by a specifically assembled scaffolding.

Figure 1: Overall view of Saltadouro Bridge (left side: North abutment; right side: South abutment).

2.2 Surveying and inspection actions

The surveying and inspection actions needed to be rather extensive in view of the total lack of information about the bridge. In terms of geometry, both manual processes (handheld laser distance meter, measuring tape) and laser scanning techniques were applied for mutual validation. The laser scanning was carried out with a Leica ScanStation P40 with the following main features: survey of 1.000.000 points per second, range of 240m, 1.2mm precision (+/-10 ppm) and integrated digital camera. The equipment was placed at 8 different measuring stations in order to cover the entire structure, as identified in Figure 2a. The resulting global point cloud has more than 170 million points. One view of such point cloud is shown in Figure 2b. From a structural point of view, it was interesting to note that the accuracy of the obtained point cloud, allowed to compare the actual shape of the bottom surface of the beams, to the hypothetical straight line that connects the supports, and therefore infer the deformation. As shown in Figure 2c, a deformation of 2.6cm could be assessed in regard to the fictitious straight line, and the noise level of the point cloud is compatible with the 1.2mm precision mentioned above. This level of accuracy brings laser scanning to a great degree of usefulness in accompanying the deformational behaviour of structures, indeed. It is also remarked that, as expected, all tape measurements have validated the measurements that could be made directly on the point cloud.

a) b) c)

Figure 2: Laser scanning: a) location of stations; b) view of the point cloud; c) deformed shape in comparison to reference line.

The inspection has also involved several inspection techniques that are briefly addressed here. Visual inspection (together with photographic record) allowed the traditional identification of biological colonization, corrosion, surface delamination and suchlike (e.g. corrosion and delamination in Figure 3a). Infrared thermography was also applied with a FLIR E50bx camera, that allowed recording several barely perceptible delamination processes to the naked eye (Figure 3b). In order to assess the rebar diameter, position and type, several minor destructive inspection activities were made, by opening cavities up to the reinforcement (here termed as inspection windows), and even gathering a few rebar samples for lab testing. Two steel rebar detectors were used together in order to get a global picture of all reinforcement distribution within the ribs and the deck: a Hilti PS200 detector and a Hilti PS1000 GPR based scanner. An example of the GPR imaging obtained can be seen in Figure 3c. Seven concrete cores (with ~10cm diameter) were obtained from the bridge and tested in laboratory (Figure 4a). Schmidt hammer assessment of compressive strength was also assessed at 24 distinct locations. Cracks were marked with a felt pen and photographed, whereas a set of representative crack widths were measured with a handheld USB Microscope VEHO VMS-004D, that could accurately pinpoint widths to the hundredth of millimetre (Figure 4b).
The photographic record of the bridge was also taken through 360º photography at 7 locations with a Ricoh Theta camera. An example of a flattened spherical panorama can be seen in

Figure 4c. These spherical photos can be of great utility due to the quickness in which they are obtained and the embedded richness of context.

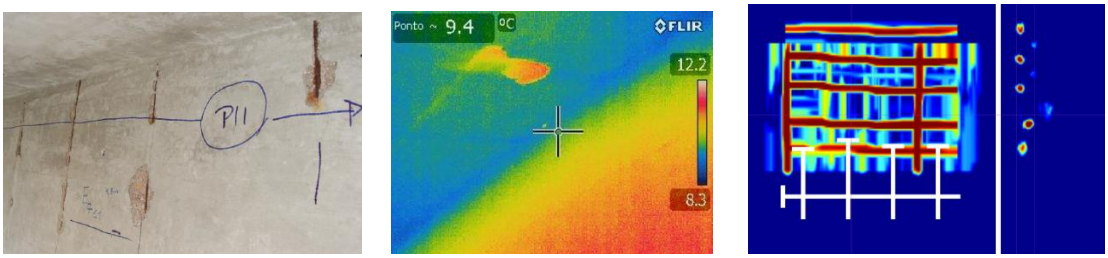

a) b) c)

Figure 3: Inspection techniques: a) photography record of corrosion and delamination; b) infrared thermography image; c) GPR image obtained with a steel rebar detector.

a) b) c)

Figure 4: Inspection techniques: a) core extraction; b) crack width; c) 360º photography.

3. BIM Model and data organization

The selected application for modelling was Autodesk REVIT, following a structural template that encompasses native object classes for such purpose. The point cloud was embedded as a reference in the BIM model and used to support the geometry definition throughout the entire process. In regard to the level of information/detail/development to be included in the model, it was decided to follow similar prescriptions to those provided by BIMFORUM/AIA for LOD400 [5], which means that reinforcement was explicitly modelled. Warping/deformations of the structure's geometry were not explicitly modelled, with the idealized undeformed geometry being considered sufficient for the intended use of the model. The final BIM model is shown in Figure 5a, with a specific comparison of the idealised geometry of the model with the point cloud being shown in half cross-section in Figure 5b. A view of the modelled reinforcement is shown in Figure 5c.

The modelling of inspection information can be made either explicitly, as shown for the cores exemplified in Figure 6a (which incorporate core objects that embed the relevant information of compressive strength, laboratory test sheets, carbonation depth, etc.) or in an implicit manner through 'patch' objects, such as the green patches shown in Figure 6b, which stand for the observed biological colonization. The mentioned patches are BIM objects themselves with relevant fields that characterize the information considered relevant (e.g. type of colonization, extent, link to photo, etc.) in such a way that it remains interoperable and exportable in a specific IFC '*property set*'. The authors consider that, for the sake of BIM-FM purposes, damages and inspection information (including cores, cracks, inspection windows, etc.) are well represented through the 'patch' strategy, that allows embedding all the necessary

information in an easy to systematize/query manner, and indexed to the relevant date of inspection. Furthermore, scripts have been developed within Autodesk REVIT (Dynamo-Python) that allow that inspection data can be inputted or analysed directly in Microsoft Excel, under a natural interface for people that have no expertise in BIM (e.g. an inspector). More details on these contexts can be found in [4].

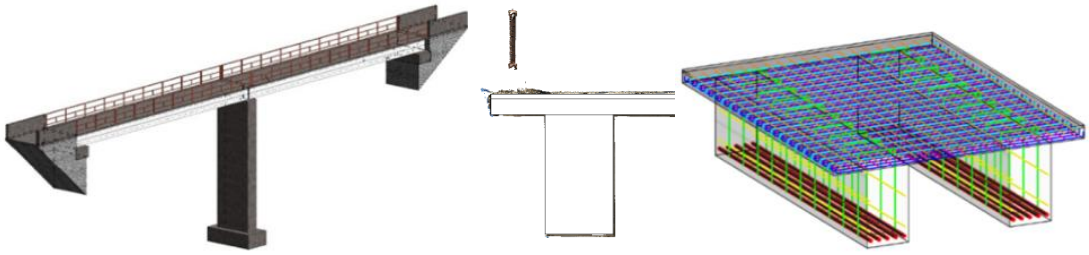

a) b) c)

Figure 5: BIM Modelling: a) global overview of the model; b) comparison of BIM model and laser scanning at cross-sectional level; c) part of modelled reinforcement.

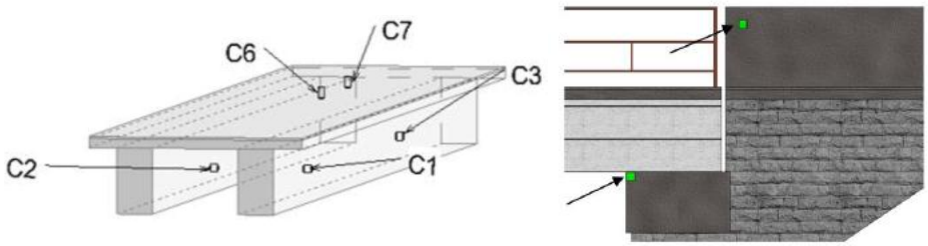

a) b)

Figure 6: BIM Modelling: a) explicit modelling approach for cores; b) patch modelling approach for biological colonization.

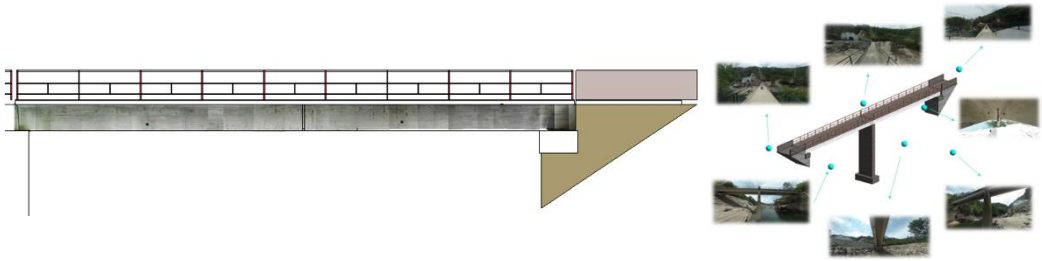

a) b)

Figure 7: BIM Modelling: a) photogrammetry stitching on the surfaces of objects; b) sphere objects to host spherical panoramas.

Another important aspect to preserve is the visualization of inspection/damage data. Not only is the point cloud of each inspection preserved in the BIM model, but also photogrammetry-composed images of beam surfaces can be embedded into the model's surfaces (see Figure 7a), and spherical panoramas can be embedded into specific 'sphere' objects located at the exact spot where each 360 photo was taken in the inspections, as shown in Figure 7b. This has important benefits in the perception of evolution of damages by an experienced user that wants to navigate the model and observe the evolution of surface damages/aspect. Finally, the work reported herein has also tackled with success aspects related to semi-automatic

inspection report generation (drawings) and exporting the model to BIM viewers (including through the use of the open IFC format) that allow the observation of the model and all its data to be made by stakeholders that might not hold licensing for BIM Software.

4. Conclusions

This paper addressed a proposed methodology to gather/register information pertaining operation and maintenance in reinforced concrete bridges, based on BIM modelling. The proposed methodology has been presented and discussed with support on the inspection of a Bridge located in the North of Portugal, for which no data was available before inspection. An extensive surveying inspection has been carried out including: classical measuring tape techniques; laser scanning; standard photography/photogrammetry; spherical panoramas; concrete core extraction; obtaining reinforcement samples; magnetic/GPR reinforcement detection; thermography; crack width measurement, among others. A BIM model has been established with specific action being taken in order to incorporate data that is not normally taken into account in design or 'facilities management' context, due to its specificity for structural inspection of reinforced concrete bridges. A proposal for simplified 'patch' representation of damage objects has been forwarded, and the layout of information in the model (including exporting to other stakeholders) has been address.
Based on the case study reported herein, it is considered that the proposed framework and corresponding workflow are feasible for implementation of bridge management systems.

Acknowledgements
This work was financially supported by: project POCI-01-0145-FEDER-007633 (ISISE), funded by FEDER funds through COMPETE2020 - Programa Operacional Competitividade e Internacionalização (POCI), and by national funds through FCT - Fundação para a Ciência e a Tecnologia. FCT and FEDER (COMPETE2020) are also acknowledged for the funding of the research project IntegraCrete PTDC/ECM-EST/1056/2014 (POCI-01-0145-FEDER-016841).
The financial support of COST Action TU1404 through its several networking instruments is also gratefully acknowledged. The collaboration of Eng. Luís Santos from Leica GeoSystems Portugal is gratefully acknowledged, in view of his participation by carrying out the laser scanning survey of the bridge. The participation of the former MSc student of UMinho, João Rodrigues, in the inspection and early BIM modelling activities is also acknowledged.

References

[1] EP, Manual de Inventário, Rotina, Principal, Especificações Técnicas, Estradas de Portugal, S.A. (2015)
[2] Pärn, E. et al, The building information modelling trajectory in facilities management, Automation in Construction (2017), 45-55
[3] Mendonça, T. Et al, Aplicação de Gestão de Obras de Arte - GOA - Nova Geração, BETAR Consultores Lda. (2010), 1-10
[4] Sousa, G., 'Implementação BIM no contexto de inspeção e gestão da manutenção de Obras de Arte em betão armado: proposta de metodologia e aplicação piloto, MSc Thesis, Universidade do Minho (2017)
[5] BIMForum, Level of Development Specification, Available: http://bimforum.org/wp-content/uploads/2017/11/LOD-Spec-2017-Part-I-2017-11-07-1.pdf (2017)

SynerCrete'18 International Conference on Interdisciplinary Approaches
for Cement-based Materials and Structural Concrete
24-26 October 2018, Funchal, Madeira Island, Portugal

STRUCTURAL DESIGN WITH OPENBIM: FROM THE ARCHITECTURAL MODEL TO THE STRUCTURAL ANALYSIS WITH A STATE-OF-THE-ART CALCULATION ENGINE

Javier Pereiro-Barceló [(1)], Afonso Miguel Solak [(1,2)]

(1) CYPE Ingenieros S.A., Alicante, Spain
(2) University of Alicante, Alicante, Spain

Abstract
OpenBIM is a universal approach to collaborative design, construction and maintenance of buildings. This technology allows a transparent and open workflow, facilitating the participation of all intervening technicians in a coordinated and simultaneous way, regardless of the software tools they use. The process of calculation and structural design can be integrated into the OpenBIM workflow without complicating or modifying the way of working that has traditionally been carried out. To this end, CYPE has recently created applications integrated in the OpenBIM flow to analyze and design structures such as StruBIM Analysis, in addition to adapt the existing ones. StruBIM Analysis is a new software to calculate the structure, that is to say, it obtains nodal displacements, sectional forces of one-dimensional elements and shell forces by means of FEM analysis. StruBIM Analysis integrates OpenSees as its calculation engine. OpenSees is a well-known framework developed by University of California: Berkeley, which performs complex calculations efficiently. This calculation engine has the data entry through code and the result output without graphical interface. However, thanks to the integration of OpenSees in an OpenBIM workflow, calculating non-linearly building structures with a dynamic analysis with integration over time will be possible in a user-friendly and reliable way.

1. Introduction

Open BIM is a global proposal to achieve user collaboration in the design, execution and maintenance of buildings, based on an exchange of information using standard formats (IFC) and an open workflow. By using IFC format, which is standard and public, and not linked to a specific developer, the durability of the work that has been carried out is guaranteed, since it

does not depend on the applications that have been used. Even the own data files of these applications, from a durability point of view of the project, are set aside as auxiliary files, because the generated IFC provides the final information of the project. At the same time, it allows real and efficient communication amongst users, since these formats can be read and generated by the vast majority of applications used in project development.
Cype has recently integrated OpenSees [1] within Open BIM workflow. OpenSees [1] is a well-known framework to perform linear or non-linear analysis, developed at University of California, Berkeley. Its use is widespread all over the world mainly to simulate seismic behavior in structures. Cype has integrated OpenSees [1] as calculation engine for StruBIM Analysis, StruBIM Design and StruBIM Foundations. These programs are in charge of analyzing, designing and checking structures, including their foundations. To fulfill this, Cype has extended OpenSees [1] in some ways and one of them is creating two new finite elements, which will be explained in the following sections.

2. Open BIM workflow

The phases of Open BIM workflow are displayed in Figure 1. A BIM Project starts with an IFC file which must be generated based on a 3D geometrical model produced by any architectural modelling software. This geometrical model is uploaded to a web platform called BIMserver.center which allows direct communication between all the users and applications that participate in a project. Next, all the applications that are compatible with the Open BIM workflow import the IFC model. All intervening agents receive the same geometry and architecture. Each specialized application imports the geometrical model and exports an IFC file with the results. This way, the BIM project is enriched and completed. Thus information of the BIM model increases using the IFC files generated by all the applications and defines the complete BIM project. This process is called consolidation of the BIM project. This information consolidation allows for the complete project to be generated, as a whole, and therefore detect, any possible interferences between the solutions that have been adopted. Besides, during the whole process, if any changes are made to the initial model, all the applications can undergo an updating process. This guarantees that no information is lost.
The IFC format files do not include specific information that makes up the project; all the data is generated and stored in the specialized applications. In other words, each member only shares the results and adopted solutions, whilst the data that has been introduced, the work methodology and intermediate results remain in the private domain of the specialist. By working in this way, the size of the files is significantly reduced, since each member is only in charge of the part of the project which he/she is responsible for. The information in IFC format, which forms the project, exclusively defines the project, and therefore, the specific tools and programs used to create it are auxiliary elements that can be changed or eliminated during the life span of the project.
When the project designer is faced with a design problem, he/she usually has to evaluate different solutions or proposals. As alternative options are rejected and decisions are made, more detailed work is carried out on them, to achieve greater definition. In the Open BIM flow, each analysis model is independent from the rest, so different solutions for the same field can be proposed and defined, since the other models are not affected no matter what decision is made.

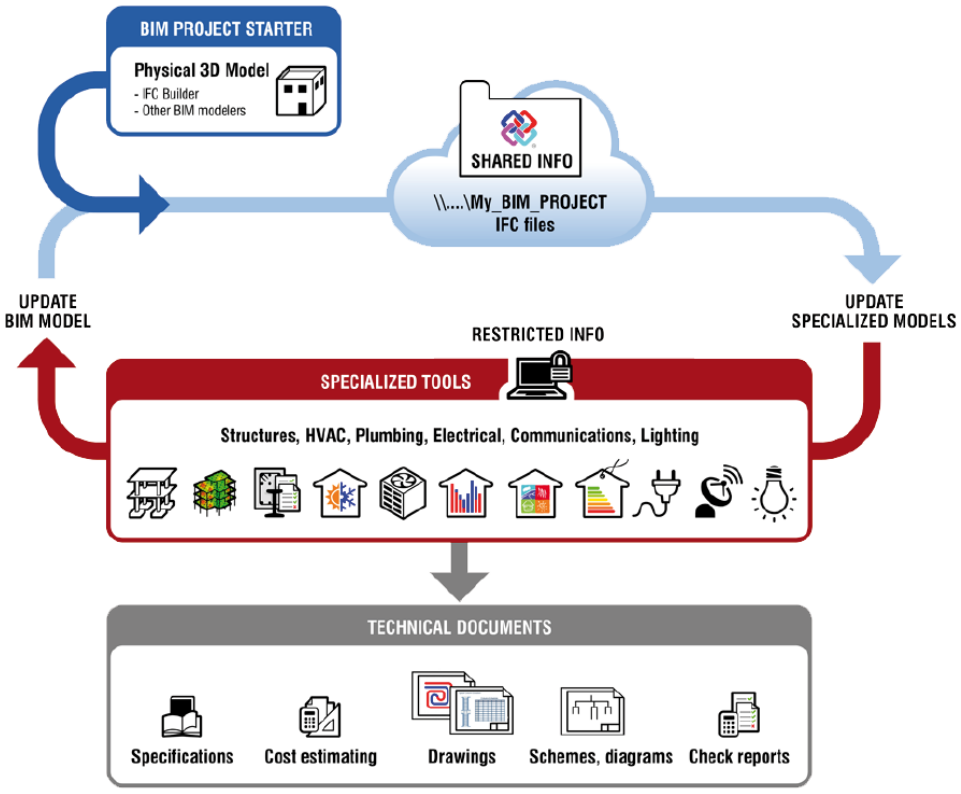

Figure 1: Open BIM workflow.

3. Structural analysis and design in open BIM flow

The stages to carry out the analysis and design of structures are perfectly delimited (Figure 2): (1) create the structural model (based on the architectural o geometrical model); (2) generate the analytical model based on the structural model; (3) solve de analytical model; (4) design and check of structural elements; (5) generate layouts and reports.

3.1 Generation, edition and analysis of analytical model

Cype has developed a program to generate, edit and perform structural analysis: StruBIM Analysis. This program forms part of StruBIM suite, which is a group of structural programs, each one related to one stage of structural design. Sequential version of OpenSees [1] has been used as calculation engine in StruBIM analysis (Figure 3). For this purpose several extensions have been implemented in OpenSees [1]: two new finite elements (one-dimensional and shell) [2-4], a new constraint manager, a new solver called MUMPS (Multifrontal Massively Parallel Sparse Direct Solver) [5], etc. Besides, multiple instances of sequential OpenSees [1] are used to solve several load cases at the same time.

Regarding the generation of the analytical model based on the structural model, StruBIM Analysis transforms automatically entities such as columns, beams or slabs, into one dimensional and two dimensional elements. Problems with this conversion may come up, for instance, when structural elements with different depths are connected. In this case, axes of the structural elements do not coincide and, consequently, neither the finite element nodes of

the analytical model. In order to solve these problems, kinematic constraints are added to assure analytical model behaves as the structural model.

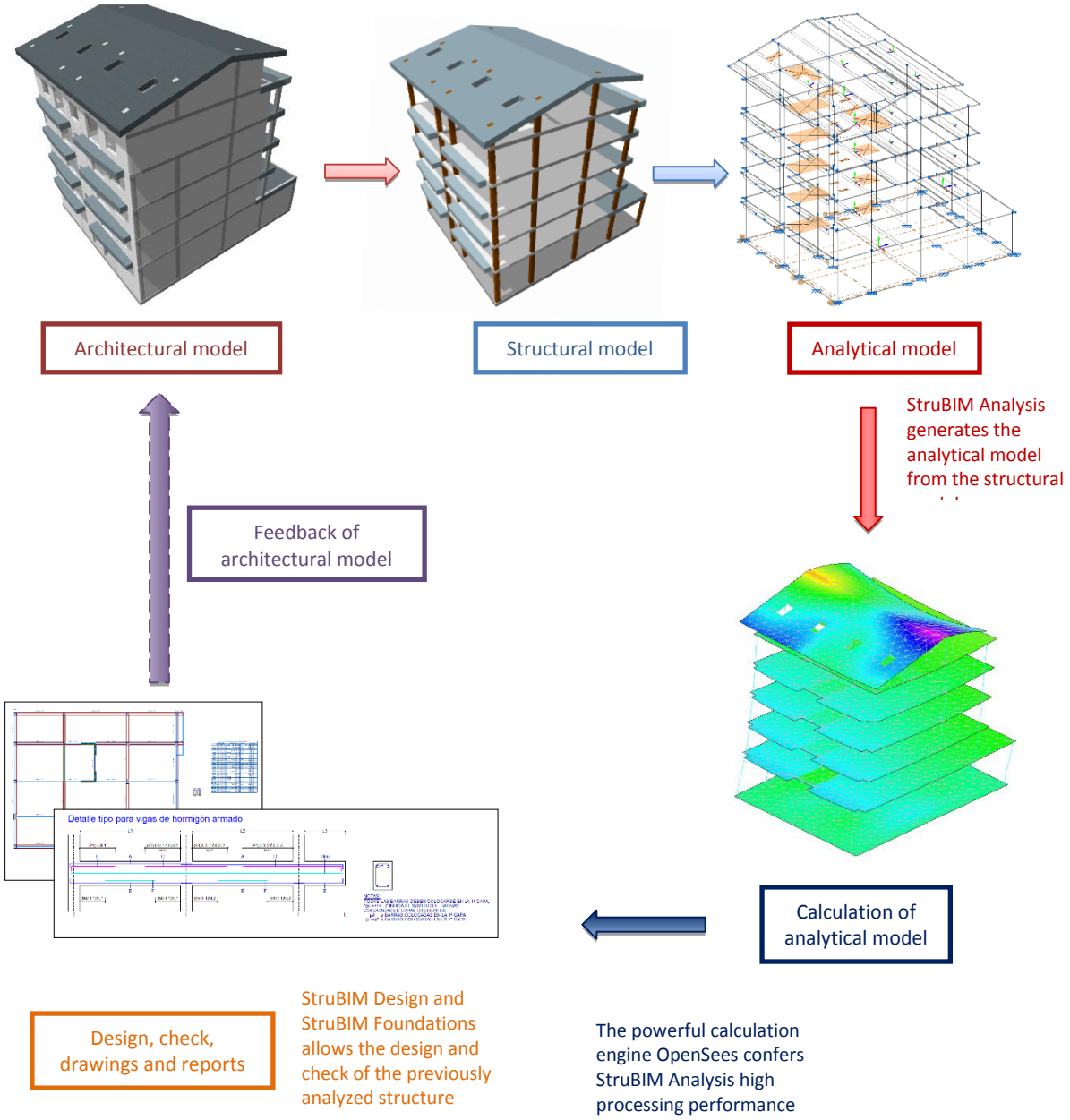

Figure 2: Structural analysis and design integrated in an Open BIM workflow.

The main benefits that users can take from the workflow displayed in Figure 2 is that they will be able to use all the functionality of OpenSees [1] just importing the structural model into StruBIM. The structural model which derives from the architectural model can be made with any modelling commercial tool available on the market. User will be able to perform a

complex non-linear analysis of an actual structure with OpenSees [1] with a minimum effort. This is unthinkable by coding the data input as OpenSees [1] itself requires.

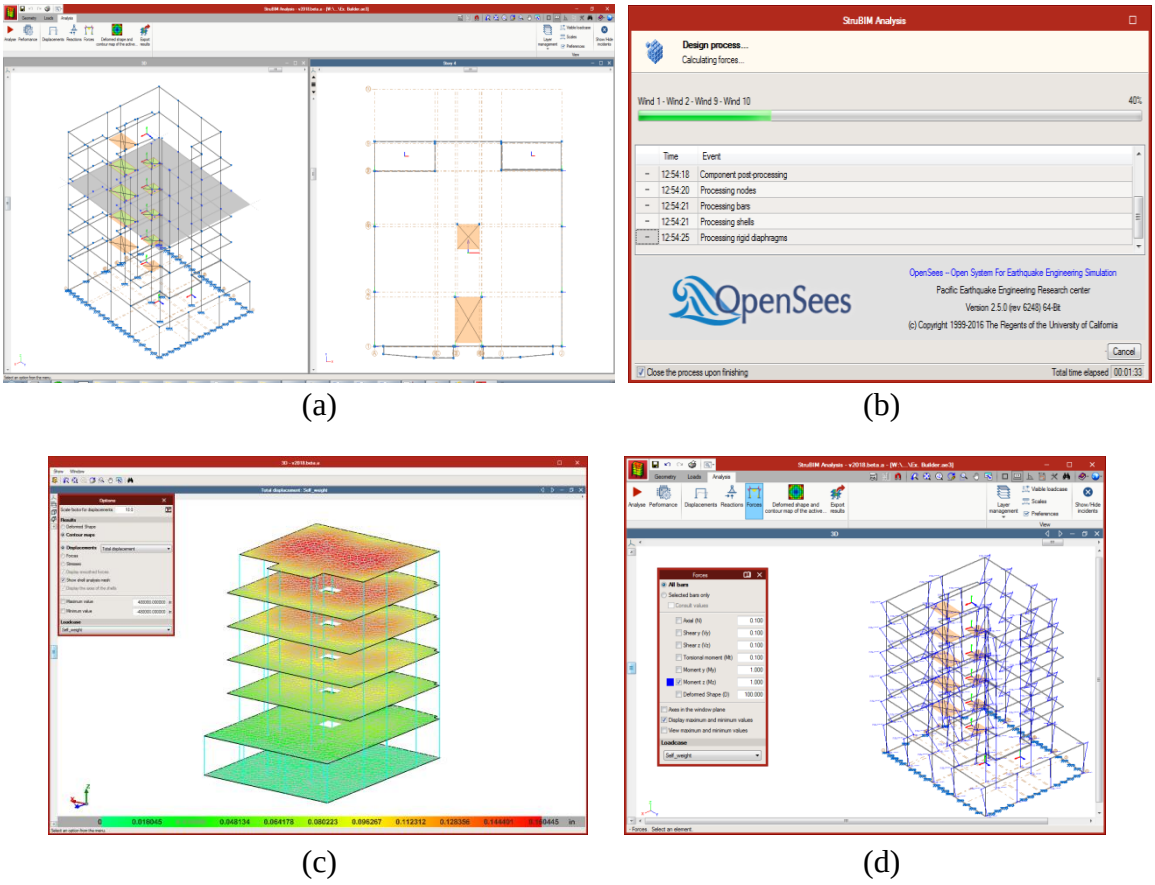

Figure 3: Structural analysis with StruBIM analysis plus OpenSees [1]: (a) Analytical model, (b) Calculating with OpenSees [1], (c) Deflections results, (d) M_z moments in columns.

3.2 Design and check of structural elements

StruBIM Design is responsible for designing and checking columns, beams, slabs and walls according to ACI Codes. It imports the analytical model results from StruBIM Analysis or from an xml file with a specific format. Besides, it is able to manage a local analytical model of each floor to design tendons, slabs and beams. Analogously to StruBIM Design, Cype has created StruBIM Foundations to design foundation elements.

4. Conclusions

The following conclusions are drawn:

- In the Open BIM flow, users work with specific and highly specialized applications to solve each aspect of the project in detail. The relationship and interaction amongst all

the applications is solved via including and integrating the BIM model composed of all the solutions adopted for each project area (consolidation process).

- Using open format interchange files, the applications are capable of reading all the information of the project and show it in an integrated way. Furthermore, with the consolidation process, users are able to detect any possible interferences between the adopted solutions.
- In the Open BIM flow, open formats are used at all times, which implies that any tool of any manufacturer can be part of the workflow in a simple way and, therefore, does not oblige users to have to modify their current working habits,
- Cype has recently integrated OpenSees [1] as calculation engine in its new suite StruBIM which is part of an Open BIM workflow. To fulfill this, Cype has extended OpenSees [1] in some ways and one of them is creating two new finite elements.
- OpenSees [1] itself requires the data input by coding. The main benefits that users can take from the integration of OpenSees [1] in an Open BIM workflow is that they will be able to use all the functionality of OpenSees [1] just importing the structural model into StruBIM. The structural model which derives from the architectural model can be made with any modelling commercial tool available on the market. User will be able to perform a complex non-linear analysis of an actual structure with OpenSees [1] with a minimum effort.

References

[1] McKenna F, Fenves GL, Filippou FC. OpenSees. University of California, Berkeley.
[2] E. Oñate, *Cálculo de Estructuras por el Método de Elementos Finitos, 1th Edition*, Centro internacional de Métodos Numéricos en Ingeniería, Universitat Politècnica de Catalunya, Barcelona, 1992.
[3] C.A. Felippa *Introduction to Finite Element Methods*, Department of Aerospace Engineering Sciences and enter for Aerospace Structures, University of Colorado, USA, 2004.
[4] C.A. Felippa *Finite Element Methods in Dynamics*, Department of Aerospace Engineering Sciences and enter for Aerospace Structures, University of Colorado, USA, 2004.
[5] Multifrontal Massively Parallel Solver (MUMPS), *Users's guide,* March 21, 2017.

SynerCrete'18 International Conference on Interdisciplinary Approaches
for Cement-based Materials and Structural Concrete
24-26 October 2018, Funchal, Madeira Island, Portugal

THE ROAD TO SENSOR-DRIVEN CLOUD-BASED INFRASTRUCTURE MANAGEMENT

Carlos G. Berrocal [1,2], Ignasi Fernandez [1], Rasmus Rempling [1,3]

(1) Chalmers University of Technology, Gothenburg, Sweden
(2) Thomas Concrete Group AB, Gothenburg, Sweden
(3) NCC AB, Gothenburg, Sweden

Abstract

Today, the accelerated degradation of many concrete structures poses a major challenge for the proper maintenance of the transport infrastructure. Therefore, inspection and maintenance operations constitute an important part of the recurrent costs of infrastructure. Furthermore, the increasing migration of population to urban areas has made sustainable development an imperative need. This need has become a driving force for innovation and new challenges such as the concept of smart cities and infrastructure. The successful utilization of newly available technologies will enable a whole new range of possibilities such as sensor driven cloud-based strategies for infrastructure management, which will promote an upgrade of the current infrastructure network to a new generation of safer, more efficient and more sustainable smart infrastructure: the infrastructure 2.0. The aim of this paper is to review the state-of-the-art of the different key technologies comprising a smart monitoring system, focusing on the aspects that are required to ensure a successful implementation of such system. The main result of the study is a scientific roadmap that can serve as a guide for traffic administrations and academic institutions in their task to develop and create a new infrastructure management strategy based on emerging technologies and innovative processes.

1. Introduction

Infrastructures are the fundamental facilities and systems required to support societal activity within a certain region. In particular, the transport infrastructure consisting of mainly roads, bridges and tunnels, is one of the oldest and most crucial elements for society as it embodies the physical platform for the transportation of passengers and goods [1]. Since deterioration of the transport infrastructure poses a serious public safety issue and has a negative impact on

the nation's economy, to effectively maintain the performance of the transport infrastructure is of utmost importance. Nevertheless, the accelerated degradation of structures caused by prolonged exposure to harsh environments added to the advanced age of many structures and the ever-increasing level of demands in terms of traffic loads, volume and vehicle speeds [2], represents an enormous challenge for the effective management of the transport infrastructure, which is often translated into an increased frequency of inspections and maintenance operations. Due to the conservative nature of the construction industry relying on traditional methods and lagging behind in innovation compared to other sectors, these inspections are today very inefficient and, together with maintenance operations, constitute a major part of the recurrent costs of infrastructure, which represent a significant share of the annual budget in developed countries [3].

New management methodologies must, therefore, be developed based on newly available technologies and new ways of thinking, to deliver smart systems that could minimize the number of interventions in the transport infrastructure as well as their extent and duration. Along these lines, current technological development is taking society to a new era where an unprecedented type of knowledge will be accessible through the combination of: (i) extensive wireless sensor networks; (ii) ubiquitous and remote access to cloud-stored data and services; (iii) constantly increasing computational power and more efficient calculation algorithms; and (iv) novel tools to visualize digital information. The successful utilization of the aforementioned technologies will enable a whole new range of possibilities such as a sensor-driven cloud-based strategy for infrastructure management. The main aim of this paper is to investigate the feasibility of combining emerging technologies to create an integrated system that enables an upgrade of the current infrastructure network through a new generation of smart structures. The study focuses on the aspects that are required to ensure that such a system could be successfully implemented in practice.

2. Review of emerging technologies

In order to create a system that minimizes the need for structural inspections, some sort of Structural Health Monitoring (SHM) system must be implemented. A SHM system is a technology based on the continuous condition assessment of a structure through the analysis of data acquired on-site by a distributed network of sensors [4]. If properly implemented, SHM systems could extend the service life of structures by ensuring the early identification of deterioration and/or damage, thereby allowing relatively minor corrective actions to be taken before the damage grows to a state where major actions are required [5]. For a SHM to be effective a streamline of data must undergo four different steps: acquisition; management; analysis; and visualization. In the following section, a review of the different existing technologies enabling these four steps is presented.

2.1 Data acquisition – Sensor networks

Sensors are critical elements in SHM systems, which must be chosen adequately to serve the intended purpose under the expected conditions and for a certain time span. Sensors can be subdivided according to various features, e.g. wired/wireless, embedded/external or active/passive. Each type of sensor possesses its own advantages and drawbacks, which must

be considered with care. Regarding the measured properties, the most commonly used sensors in SHM applications include sensors measuring kinematic parameters, such as displacements, strains and accelerations, dynamic quantities, such as vibrations and forces and environmental factors, such as temperature or relative humidity (RH), some of which are commercially available for concrete applications, see e.g. [6]–[8]. Conventional sensors often present difficulties to perform stable and reliable readings in the long term. Many sensors can be easily affected by changes in temperature, humidity, cable length, magnetic or electric fields, etc, whereas other sensors need to be powered, which requires the use of batteries, thus limiting the service life of the sensors [9]. Nevertheless, the common problems that are often encountered with conventional sensors today will most likely be overcome in the future as new sensing technologies are developed for bridge monitoring and other large structure applications. Two examples of novel sensor applications, currently under development, which possess great potential for the long-term monitoring of reinforced concrete structures are smart cement-based sensor [10] and polymeric optic fibre [11].

2.2 Data management – Cloud services

In large infrastructures with distributed sensor networks containing tens or hundreds of sensors measuring continuously, the amount of generated data can easily surpass the storage capacity of any modern computer. To manage such data volumes and enhance accessibility to the content, a series of cloud-based platforms exists, which provide a wide range of services for users with the only requirement of an internet connection. These platforms are referred to as PaaS (Platform as a Service) and can be defined as a cloud computing model in which a third-party provider delivers hardware and software tools (usually those needed for application development) which can be accessed anywhere via a web browser. One of the main advantages of a PaaS providers is that they host the hardware and software on its own infrastructure, thereby freeing users from having to install in-house hardware and software to develop or run new applications. Some of the best-known PaaS include Microsoft Azure, Google App Engine or Amazon Web Services.

2.3 Data analysis – Machine learning

Another of the key steps towards the implementation of an effective SHM system is the analysis of the measured data. Individual data values by themselves are meaningless. They need to be situated in a context, relativized to other parameters and combined with a certain set of assumptions to extract relevant information. This information must be placed within a theoretical background and used in conjunction with a model to obtain knowledge. Lastly, this knowledge can eventually be turned into expertise, i.e. the required parameters for decision making, through experience and training. The first two steps are relatively easy to automate but for the last one, an experienced and trained operator is still required. This could change in the near future through the implementation of artificial intelligence, i.e. machine learning algorithms, which could not just become a decision support tool for engineers but also unlock the path towards predictive structural assessment.

Machine Learning is currently being used in many existing fields of research to develop countless applications, some of which are fully operational in everyday situations such as spam filters or face recognition systems. For structural health monitoring applications, two main anomaly detection approaches, which may classify as precursors of today's machine

learning, have been previously used for damage identification: model-driven methods and data-driven methods. The former rely on high-fidelity physical models to detect deviations of the measured data whereas the latter usually adopt a statistical representation of the system where data appearing in regions of very low density may indicate deviation from normality [12]. In civil engineering, the application of machine learning has been also attempted, particularly for vibration-based damage assessment of steel bridges, see e.g. [13]–[16]. However, owing to the large size and one-of-a-kind nature of the transport infrastructure elements, the development of effective and generic machine learning algorithms for structural health monitoring have not yet been developed.

2.4 Data visualization – BIM

Effective data visualization is another crucial aspect for the successful implementation of an integrated SHM system. The information, whether it is raw measured data or a sophisticated damage index, needs to be conveyed in a clear, efficient and intuitive way to the operator. Building Information Modelling (BIM), combining 3D computer-aided design visualization with integrated data, is a process originally intended to improve the performance of building projects during their construction phase and service life. Due to the high complexity of the transport infrastructure elements, BIM stands out as a very promising alternative for its integration within a SHM system. Today, a variety of BIM software is available, including both more user-friendly and intuitive commercial packages and more flexible, free open-source programmes. Perhaps, one of the major technical challenges is to find a suitable interface that enables the effective integration of real-time measured data with a 3D design model. A very promising solution to this technical challenge is provided by Autodesk FORGE [17], a connected cloud platform comprised of web services, and technical resources that allows for the development of customized and scalable solutions.

Augmented Reality (AR) also possesses a great potential for the visualization of data on-site, which could represent a giant leap in the efficiency of structural inspections. By visualizing information regarding the real condition of the structure as an overlay displayed on the actual structure, inspection operators could easily spot the location of deficient elements and focus on critical elements, notably reducing the time and extent of the inspection and subsequently minimizing the cost and disruption to the infrastructure users.

3. A scientific roadmap to sensor-driven cloud-based infrastructure management

Based on the four steps constituting a SHM system and the different reviewed technologies, a roadmap towards sensor-driven cloud-based infrastructure management has been drafted. This roadmap, referred to as SensIT and presented in Fig. 1 as an infographic, identifies the critical areas where further research is required and how these areas are interrelated.

- Sensor technology: the first obstacle to overcome in the creation of an integrated SHM system is the deployment of a sensor network that measures different kinematic and physicochemical parameters to form the basis for remaining steps. Ideally, robust and stable sensors which are not affected by external stimuli and can surpass the service life of the parent structure should be developed. This data should be then combined with

environmental information as well as previous damage report in the case of existing structures to offer a holistic view of the structural condition.

- Cloud-based services: the integration of existing cloud platforms is a key aspect to ensure the efficiency, flexibility and scalability of the system. Cloud platforms play multiple roles as: a means to obtain the necessary storage; a platform to carry out remote calculations; and a tool to manage, share and access data from virtually any place in the world.
- Machine Learning: with the steady gain in computational power, these types of algorithms have shown their immense potential for pattern recognition and anomaly detection in multiple areas. Novel algorithms need to be developed focused specifically in the needs of the construction industry and particularly for structural health monitoring of concrete structures. Moreover, these algorithms might benefit from reciprocal data retrofitting with detailed finite element analyses.
- Real-time BIM: a digital twin of the physical structure created through BIM can become a very suitable channel to convey the information related to the structure condition of the transport infrastructure. Interactive BIM applications with an intuitive, user-friendly and cross-platform interface should be developed to offer an effective and versatile decision support tool for the owner/manager/operator of the structure.

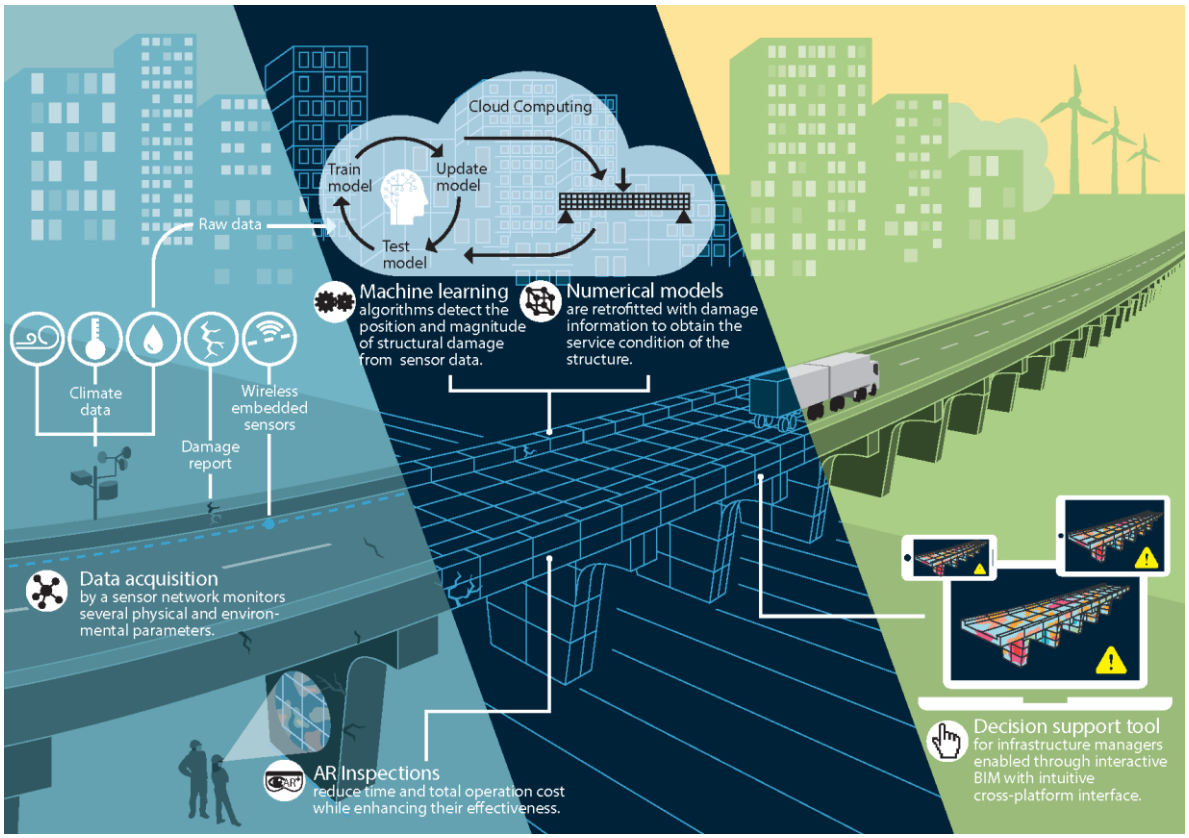

Figure 1: Schematic representation of the SensIT monitoring system.

It is worthwhile mentioning that the approach discussed in this paper presents two main limitations that hinder its full applicability as of today. The first limitation is the absence of sensors specifically developed for concrete applications, which can provide accurate, stable

and reliable measurements during the entire service life of the infrastructure. The second is the lack of advanced numerical models that can describe the various multi-physics phenomena involved in the deterioration mechanisms of concrete, including corrosion of reinforcement, alkali-silica reaction, etc. to support the development of machine learning algorithms.

References

[1] J. Fulmer, "What in the world is infrastructure?," *PEI Infrastruct. Invest.*, vol. July/Augus, pp. 30–32, 2009.
[2] J. Leander, A. Andersson, and R. Karoumi, "Monitoring and enhanced fatigue evaluation of a steel railway bridge," *Eng. Struct.*, vol. 32, no. 3, pp. 854–863, 2010.
[3] OECD - Organization for Economic Co-operation and Development, "Infrastructure investment (indicator) - [Accessed on 18 October 2017]." 2017.
[4] J. M. W. Brownjohn, "Structural health monitoring of civil infrastructure," *Philos. Trans. R. Soc. A Math. Phys. Eng. Sci.*, vol. 365, no. 1851, pp. 589–622, Feb. 2007.
[5] B. M. Phares, T. J. Wipf, L. F. Greimann, and Y.-S. Lee, "Health Monitoring of Bridge Structures and Components Using Smart Structure Technology - Vol. 1," Center of Transportation Research and Education, Iowa State University, 2005.
[6] Giatec, "SmartRock2," 2017. [Online]. Available: https://www.giatecscientific.com/concrete-sensors/smartrock2/.
[7] Electrotech, "Themisto," 2017. [Online]. Available: http://www.electrotech.se/Produkter/BetongsensorThemisto/tabid/1768/Default.aspx.
[8] H. Arup, O. Klinghoffer, and J. Mietz, "Long term performance of MnO2-reference electrodes in concrete," in *Corrosion97*, 1997, no. 243, p. Paper 243.
[9] H. Ceylan, K. Gopalakrishnan, P. Taylor, P. Shrotriya, S. Kim, M. Prokudin, S. Wang, A. F. Buss, and J. Zhang, "A Feasibility Study on Embedded Micro-Electromechanical Sensors and Systems (MEMS) for Monitoring Highway Structures," 2011.
[10] F. Azhari and N. Banthia, "Cement-based sensors with carbon fibers and carbon nanotubes for piezoresistive sensing," *Cem. Concr. Compos.*, vol. 34, no. 7, pp. 866–873, Aug. 2012.
[11] Shute, "Optical Fibre Sensor System," 2017. [Online]. Available: http://shute.dk/?page_id=107.
[12] C. R. Farrar and K. Worden, *Structural Health Monitoring - A Machine Learning Perspective*. 2013.
[13] H. Hao and Y. Xia, "Vibration-based Damage Detection of Structures by Genetic Algorithm," *J. Comput. Civ. Eng.*, vol. 16, no. 3, pp. 222–229, Jul. 2002.
[14] K. Worden and G. Manson, "The application of machine learning to structural health monitoring," *Philos. Trans. R. Soc. A Math. Phys. Eng. Sci.*, vol. 365, no. 1851, pp. 515–537, Feb. 2007.
[15] S. Soyoz and M. Q. Feng, "Long-Term Monitoring and Identification of Bridge Structural Parameters," *Comput. Civ. Infrastruct. Eng.*, vol. 24, no. 2, pp. 82–92, Feb. 2009.
[16] A. C. Neves, I. González, J. Leander, and R. Karoumi, "Structural health monitoring of bridges: a model-free ANN-based approach to damage detection," *J. Civ. Struct. Heal. Monit.*, vol. 7, no. 5, pp. 689–702, Nov. 2017.
[17] Autodesk, "Autodesk Forge," 2017. [Online]. Available: https://forge.autodesk.com/.

DIGITAL FABRICATION

AND

ROBOTICS

SynerCrete'18 International Conference on Interdisciplinary Approaches
for Cement-based Materials and Structural Concrete
24-26 October 2018, Funchal, Madeira Island, Portugal

A 3D PRINTER OF CEMENT MORTARS BASED ON INITIAL DEPOSITION OF DRY MATERIALS

Miguel Azenha [(1)], Caetano Monteiro [(2)], Ricardo Morais [(1)]

(1) ISISE, University of Minho, Guimarães, Portugal
(2) Dep. Mechanical Engineering, University of Minho, Guimarães, Portugal

Abstract
The paper presents the studies of implementation of an equipment for producing mortar elements through a 3D printing process, aiming to demonstrate feasibility and challenges, with the intent of a future upscaling to actual concrete production. The technique for 3D printing is based on the additive method, with an innovative approach in regard to the deposition of materials. Indeed, the cement/sand are deposited by layers into their final positions. After the deposition of each layer, water is sprayed in a controlled manner. When a given set of layers is deposited, compaction is applied to the entire part. This technique has the interesting feature of allowing to differentiate mortar composition at different regions of the produced elements, with possibility of structural optimization of the spatial use of cement. The feasibility of the developed equipment and produced parts is demonstrated, and discussions are held in regard to challenges and future developments.

1. Introduction

The term Construction 4.0, in direct connection with Industry 4.0 concepts, has gained significant attention and momentum in recent years. Amongst the former, one of the most promising fields seems to be the use of 3D printing techniques for digital fabrication of construction elements, or even for entire constructions. An extensive and very up to date recent literature review has been made by Ghafar *et al.* [1], with particular focus on the use of additive manufacturing (AM) technologies, which are defined in such review *as procedures that form layers to create three-dimensional (3D) solid objects from digital models, allowing creatives, engineers, architects and designers to make customised designs in one-step process*.

Several processes have been devised for construction with AM techniques based on extrusion of pre-mixed cement based blends, such as the contour crafting [2], the 'concrete printing' method by the team at Loughborough University [3], amongst other initiatives based on similar principles and applied at laboratory and construction scale by the industry (review in [1]). Even though this is a very interesting idea, the fact that the mix is 'wet' at the stage of deposition, brings many challenges regarding the fresh state material problems, and concerns about printable shapes without the need for specifically tailored support material. However, much less research has been focused on 'dry' deposition of binders, with very few works known on the subject, except for a conceptual discussion by Pegna [4], and the efforts initiated by Enrico Dini with the D-Shape method that relies on such principle with use of binders that require activators [5]. Except for a brief reference at the website of D-Shape [6], and an alternative method based on extrusion of pastes to sand packings [7], no scientific works written in English were found to focus on dry deposition of cement-based materials for 3D printing efforts, which seems to be an important research gap. However, the research team at the Civil Engineering Department at UMinho has dedicated attention to this matter since 2012, with a line of research based on a 3D printer of cement based materials through the dry method. A MSc thesis has been initially developed by Sepúlveda in late 2012 [8], followed by a national conference paper, written in Portuguese [9]. The work has then been continued in a further MSc thesis by Morais [10], which delved further within the acknowledged limitations and challenges. In view of such efforts, the present paper aims to provide an integrated view of the developments achieved, identifying opportunities and challenges.

2. The concept and implementation

2.1 Concept

The concept behind the proposed printing process is relatively straightforward. It relies on the principle that the element to be printed can have an absolutely arbitrary geometry within the printing bounds, and the mixing proportions of the cement-based material can be changed at any given position of the element under construction. In order to materialize these two important performance requirements, the concept is based on mortar printing (cement, graded sand and water) through a dry method. The explanation of the printing method can be understood by observation of the schemes in Figure 1. Three separate containers are attached to the movable printing head: one for cement, one for graded sand, and another for water. The containers of cement and graded sand have their bottom extremity controlled by a computer controlled valve, that allows continuous feed at known rates of sand and cement, which are in turn gathered in a mixing funnel and deposition head. The principle is that this movable deposition head can deposit controlled quantities of each material, allowing to create regions of different mixing proportions in the printed element, according to performance requirements (e.g. structural, tightness or any other). In the regions that are to become hollow, or merely support the printed layers to be placed above (e.g. cantilevered portions), deposition of sand alone is made, so that it can be washed away and reused after the printing process is finished. On the right side of Figure 1, it is possible to see a layer of deposited materials, surrounded by a confining boundary, having respectively: sand deposited in the vicinity of the confining boundary, mortar 1 in the outer regions of the solid to be printed, and mortar 2 (potentially less rich in cement) in the core region. At the present stage of the description, mortars 1 and 2

are not yet watered, so they are mere blends of cement/sand. The controlled watering of these mixtures is then done through an additional printing head, as shown in the left part of Figure 1, which allows finishing the mixing proportions defined by the user, by judiciously spraying water in a potentially differentiated manner throughout the entire layer of dry materials that had previously been deposited. Afterwards, the conceptual principle includes the application of a controlled static compaction weight over the entire recently watered layer, as to promote better final density and material properties.

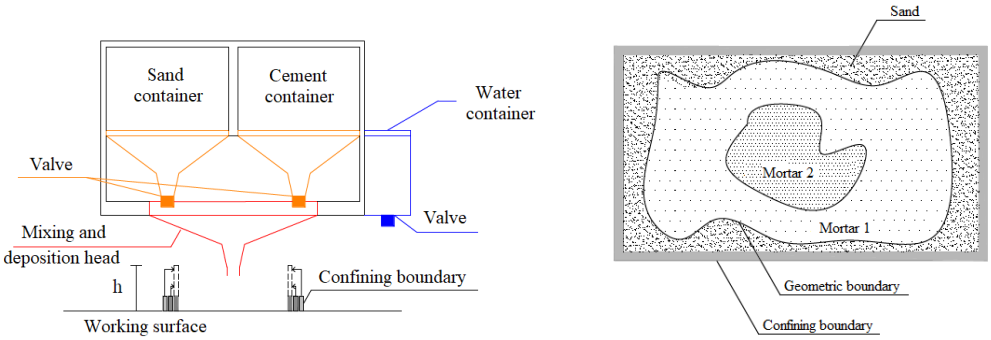

Figure 1: The basic concept of the proposed 3D printing process: cross-sectional view (left); plan view of resulting printing (right). Adapted from [9].

2.2 Implementation

In order to prepare a prototype, the requirements stated above were mostly satisfied, except for the fact that the sand and cement containers were not separated. Instead of that, a single reservoir containing a predefined blend of sand and dry cement was considered. The prototype printer that was developed has a potential field for printing of 1.2 m × 0.6 m in plan, and maximum potential printing height of 0.3m. The frame is depicted in Figure 2a, where the necessary linear guides for the 3 active axes (x, y, z) and corresponding computer controlled step motors can be seen. The dry material dispenser is shown in Figure 2b: it basically consists of a funnel with bottom dispensing diameter of 9 mm, which in turn is filled up to its bottom by a threaded bar. The dry mix for printing (sand and cement) is placed in the funnel, and the threaded bar is acted by a rotary engine (seen in the top part of Figure 2b) that allows controlled deposition of the mix (Archimedes screw principle). The water spraying is made through a standard aerograph, as show in Figure 2c, which is controlled by the central processing unit of the system. For more details on the mechanics and electronics of the system, the reader is directed to [8].

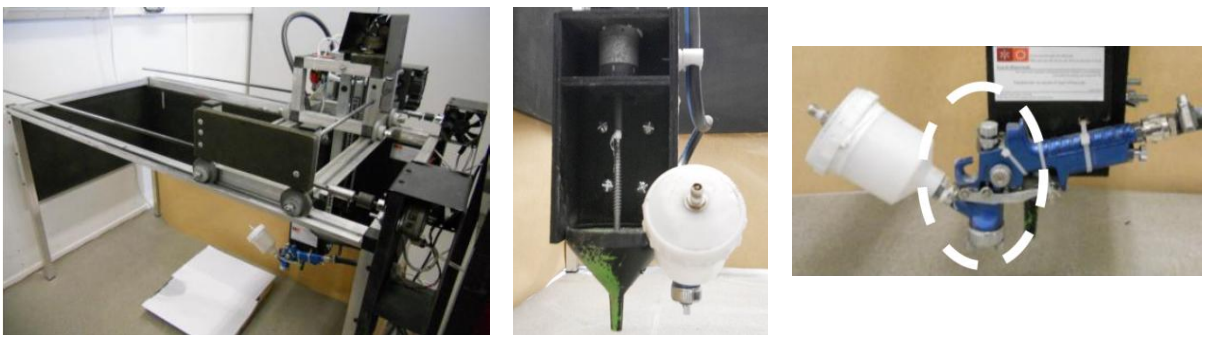

Figure 2: a) The printing frame; b) The dry material dispenser; c) The water dispenser [8].

3. Use of prototype printer and results

3.1 Procedure in effect

The setup described above has been put under test in a small confined region of 5 cm × 5 cm, which in turn was used to produce test cubes of 5 cm edge. At this point, it was also decided to solely print a single proportion of cement/sand, whereas not allowing the possibility of depositing sand only. This means that the single deposit description of Section 2.2 above also applies here. The lateral confinement for pressure application was guaranteed by wooden moulds of 1.25 cm height, that were cumulatively added to the system as needed for lateral confinement of subsequent printing layers. The process is described with support of Figure 3.

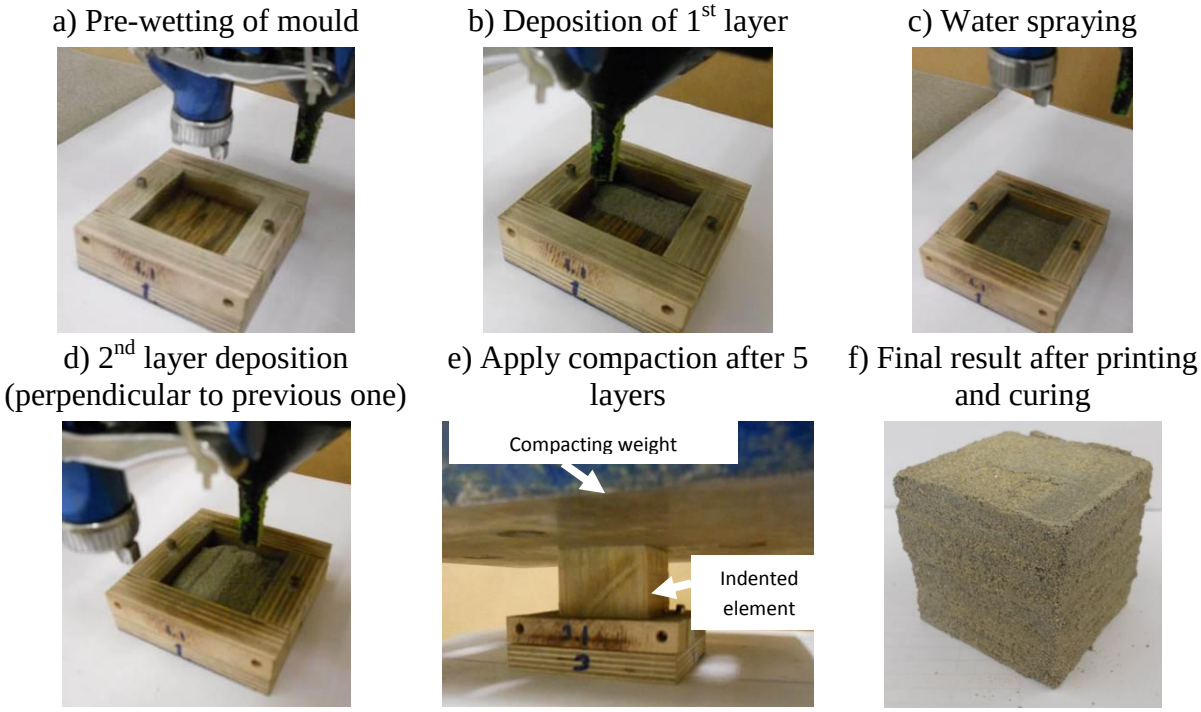

Figure 3: The procedure adopted for printing test mortar cubes.

Initially, the mould is pre-wetted with water spraying (Fig. 3a), followed by the deposition of the 1st layer in a sequence of parallel lines of deposition (Fig. 3b). Immediately afterwards the 1st layer is finished, controlled water spraying is started, as to attain the desired water-to-cement ratio (pre-calibrated timings of valve opening of water – Fig. 3c). The process is then continued in a similar fashion for the subsequent layers (Fig. 3d). However, every subsequent layer that is deposed, is placed on a perpendicular direction of deposition, as compared to the previous one (attempt to avoid excessive accumulation of fragilities in the interfaces of deposition). The process is followed by water spraying, as done for the 1st layer and sequentially repeated up to the 5th layer. At every five layers, a compacting weight is placed on top of a compacting interface which comes into contact with the specimen (Fig. 3e). This compacting interface is slightly indented at its bottom, as to improve connection between this layer after compaction and the layers that follow. As mentioned before, the lateral confinement parts are added as needed, and the final result of the process described is shown in Figure 3f.

3.2 Systematic experimental program and results

A systematic program of testing has been applied to test both the robustness of the mechanical and electronical parts, as well as the feasibility of the obtained specimens in terms of density and compressive strength. CEM II/B-L 32.5 N was used for the test mortars with fine river sand (maximum grain size ~1 mm). In terms of weight, the following mixing proportions were selected: sand/cement=2:1 and water/cement=0.23. A total of 9 specimens have been prepared with the 3D printing process, with the nomenclature and information provided in Tab.1: 3 specimens compacted with 25 kg weigh and tested perpendicularly to the plan of layer deposition; 6 specimens compacted with 50 kg and tested both in parallel (3) and perpendicular direction (3) to the plan of layer deposition. Additionally, 3 more specimens have been prepared and mixed in a Hobart mixer with the same raw materials and mix proportions (except for the addition of superplasticizer to ensure adequate workability).

All specimens were cured at 20 ºC (sealed conditions) up to the age of testing, at 7 days, in which density and compressive strength were assessed sequentially.

The 3D printer was able to produce all specimens without malfunctioning and exhibiting an apparently robust capacity for repetition of the test procedure.

The results are cumulatively shown in Table 1. It was noticed that the density of specimens made with standard mixing had an average of 2069 kg/m^3, as opposed to the average density of 1720 kg/m^3 for printed specimens compacted with 50 kg and 1660 kg/m^3 for printed specimens compacted with 25 kg. These are significant reductions of ~20% with impact on the average compressive strength. In fact, not only is the f_c of 3D printed specimens significantly lower than the traditionally mixed ones, but it also exhibits a significant dispersion, as shown in Tab.1. This is an indication that the process needs improvements, as to allow, at least a better consistency of the quality of produced specimens. Additionally, to the results shown below, more experiments have been made further to try to increase strength and decrease dispersion [10]. In spite of such efforts, no significant improvements were attained yet. Further studies with potentially better performing mixes (e.g. higher w/c ratio) might pave the way for new developments.

Table 1: Systematic experimental programme.

Name	Size [mm]	Compacting weight [kg]	Test direction	Density [kg/m^3]	Compressive strength [MPa]
P1_25_PER	50×50×50	25	Perpendicular to the plan of the layers	1632.24	4.15
P2_25_PER		25		1682.24	***
P3_25_PER		25		1680.22	6.50
P4_50_PER		50		1725.63	7.66
P5_50_PER		50		1730.86	4.80
P6_50_PER		50		1698.47	8.64
P7_50_PAR	50×50×50	50	Parallel to the plan of the layers	1756.57	3.39
P8_50_PAR		50		1721.83	7.44
P9_50_PAR		50		1733.34	4.05
P10_Standard	50×50×50	-	-	2091.28	11.32
P11_Standard		-	-	2074.48	12.25
P12_Standard		-	-	2041.89	10.75

*** Invalid test result.

3. Conclusions

This paper has presented the underlying concept and development of a fully working prototype of a 3D printer for mortars (additive manufacturing), based on the deposition of dry material (sand and cement) and subsequent spraying of water, followed by compaction. The concept may extend further to allow differentiated mixture deposition and creating arbitrary geometry, without having problems of material support of overhangs (satisfied by printing sand to be removed after printing). The working prototype has demonstrated robustness of its mechanical and electronic parts, but the quality of the produced mortar is still inferior to that which can be obtained with the same raw materials through traditional mixing of constituents. The attained results have demonstrated viability to justify further works following the same line of thought of dry-material deposition in 3D printing of cement-based materials.

Acknowledgements

This work was financially supported by: project POCI-01-0145-FEDER-007633 (ISISE), funded by FEDER funds through COMPETE2020 - Programa Operacional Competitividade e Internacionalização (POCI), and by national funds through FCT - Fundação para a Ciência e a Tecnologia. FCT and FEDER (COMPETE2020) are also acknowledged for the funding of the research project IntegraCrete PTDC/ECM-EST/1056/2014 (POCI-01-0145-FEDER-016841).
It is also fundamental to acknowledge the fundamental contribution of João Marcelo Sepúlveda and João Rodrigues, who were fundamental for the initial devising and testing of the 3D printer reported herein during their MSc theses development, but were unfortunately unavailable to assist in the preparation of the present draft.

References

[1] Ghaffara S. et al, Additive manufacturing technology and its implementation in construction as an eco-innovative solution. Aut. Const. 93 (2018), 1-11
[2] Khoshnevis B. et al, Mega-scale fabrication by contour crafting, Int. J. Ind. Syst. Eng. 1 (2006), 301–320,
[3] Lim S. et al, Developments in construction-scale additive manufacturing processes, Autom. Constr. 21 (2012), 262–268
[4] Pegna, J., Exploratory investigation of solid freeform construction. Automation in Construction 5 (1997)
[5] Cesaretti G. et al, Building components for an outpost on the lunar soil by means of a novel 3D printing technology, Acta Astronaut. 93 (2014), 430–450
[6] https://d-shape.com/materials/d-shape-materials/ Acessed in June 2018
[7] Pierre, A. et al, Penetration of cement pastes into sand packings during 3D printing: analytical and experimental study. Materials and Structures 51(1) (2018), 22
[8] Sepúlveda, J., Bio-inspiração aplicada a estruturas de betão: desafios e possibilidades associados às técnicas de impressão 3D, MSc Dissertation, University of Minho (2012)
[9] Sepúlveda, J., et al, Bio-inspiração aplicada a estruturas de betão: desafios e possibilidades associados às técnicas de impressão 3D, Proc. BE2012, FEUP, Porto, Portugal (2012)
[10] Morais, R., Desenvolvimento de técnica de impressão 3D para produção de peças de matriz cimentícia, MSc Dissertation, University of Minho (2014)

SynerCrete'18 International Conference on Interdisciplinary Approaches
for Cement-based Materials and Structural Concrete
24-26 October 2018, Funchal, Madeira Island, Portugal

RESEARCH AND DEVELOPMENT OF INFRASTRUCTURE DIAGNOSTIC ROBOT SYSTEM (ALP) BY CONCRETE WALL MOVING MECHANISM USING VACUUM SUCTION PAD

Junichiro Nojima [(1)], Toshiaki Mizobuchi [(2)]

(1) J-POWER DESIGN (JPD), Kanagawa, Japan
(2) HOSEI University, Tokyo, Japan

Abstract
In this paper, the authors describe the construction of an inspection diagnostic system applying robot technology in detailed investigation of infrastructure such as concrete walls at high places. ALP uses a vacuum suction pad improved by testing with a real structure as a moving mechanism at a high place. In addition, a measurement mechanism uses a high-definition camera, an electromagnetic wave radar, a hammering sound diagnostic device.

1. Introduction

Damage due to aged deterioration of infrastructure has a big influence on safety and security of people's living. In order to prevent such an accident, it is necessary to conduct an appropriate inspection in the maintenance and management of infrastructure. However, in high places where it is difficult for people to access, there are problems such as time and expense are required by using scaffolding etc., danger is involved in inspection works. Therefore, in recent years, various infrastructure diagnosis robots are being developed.
Inspection at high positions on the walls are made by investigations by people applying climbing technology and UAV (Unmanned Aerial Vehicle). (Fig. 1 shows) However, these methods have problems such as human error problems and difficulty in obtaining detailed data. Therefore, as shown in Tab. 1, the authors carried out research and development of infrastructure diagnostic robot system (ALP) which stably adsorbs on the wall surface and can conduct detailed investigation. The ALP can be moved while adsorbing to the wall with a vacuum suction pad installed in the movement mechanism unit. In addition, by acquiring data near the surface of the wall, it is possible to safely conduct surveys of the same accuracy as human inspections. The ALP is composed of two mechanisms. The first is a moving

mechanism that moves the vacuum suction pads. The second is a measurement mechanism that acquires data by horizontally moving various measuring machines.
In this paper, the excellent functions possessed by ALP are introduced and the possibility of investigating the deterioration of concrete in place where measurement is difficult such as downstream surface of structure of dam is reported by using ALP.

Figure 1: (Left photo) Climbing survey, (Right photo) UAV.

Table 1: Comparison of inspection methods at high places.

	Climbing survey	**UAV**	**ALP**
Nearness survey	◎：It is possible	×：It is impossible	◎：It is possible
Inspection item	◎：Something which can be carried	▲：Only picture Photography	○：Something which can be installed
Accuracy of result	○：Depending on the skill of the person	▲：It's bad because an object distance is far	◎：High accuracy, and no human error
Carrying power	○：Basically the lightest one	▲：Very light one	○：About 10 kg can be installed
Reaction force for wall	▲：The reaction force is small	×：It isn't possible to touch	○：It's possible to get the reaction force in plenty
Safety	×：There is a danger of people falling	▲：There is fear of a fall	○：It's possible to secure safety
Cost of inspection	▲：A considerable cost are needed	◎：Very cheap.	○：The cost performance can be expected
Proficiency in operation	×：Lack of experienced technicians	▲：Lack of skilled pilots	○：Easy to use

2. Moving mechanism

The size of ALP is 1.8 m in length × 1.75 m in width × 0.75 m in thickness, the weight is 80 kg. This size is determined by a measurement mechanism that can continuously measure in the lateral direction 1 m. As a moving mechanism of ALP, 3 units are installed on the upper side of the measurement mechanism, and 2 units are installed on the lower side. This unit possesses an improved vacuum suction pad for concrete walls and can be stabilized against shear force of 60 kg per unit. When moving the robot, first a vacuum suction pad remove from concrete surface, move and suction each unit one by one in the moving direction (up, down, left and right), and then move the all robot frame. Fig. 2 shows the outline of ALP and Fig. 3 shows the outline of vacuum suction pad.

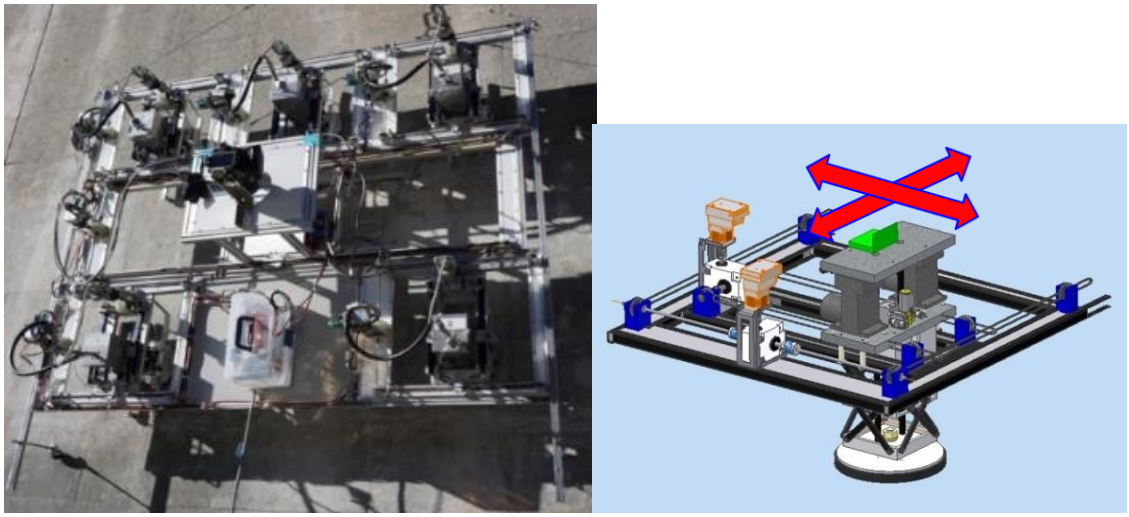

Figure 2: ALP and movement mechanism unit.

Figure 3: Vacuum suction pad for ALP.

3. Measurement mechanism

The measuring mechanism is possible to move the measuring machine in the horizontal direction 1 m and to press the measuring device against the wall surface. At the time of measurement, it is possible to acquire data in a state of being stably adsorbed on the wall surface.

As shown in Fig. 4, the measurement mechanism is equipped with "high-definition camera", "hammering device" and "electromagnetic wave radar". "High-definition camera" mounted a camera with 51.5 million pixels so that cracks of 0.2 mm in width can be judged. Moreover, it is possible to create a highly accurate three-dimensional model by SfM (Structure from Motion). [1] "Hammering device" [2] uses a solenoid magnet to hit the wall surface, acquires the sound generated by the striking with a microphone, and judges the concrete flaking. "Electromagnetic wave radar" can estimate the position of the re-bar and the depth of cover concrete. Moreover, it is possible to estimate the chloride contents in the cover concrete by using the attenuation rate of the electromagnetic wave from re-bar. [3]

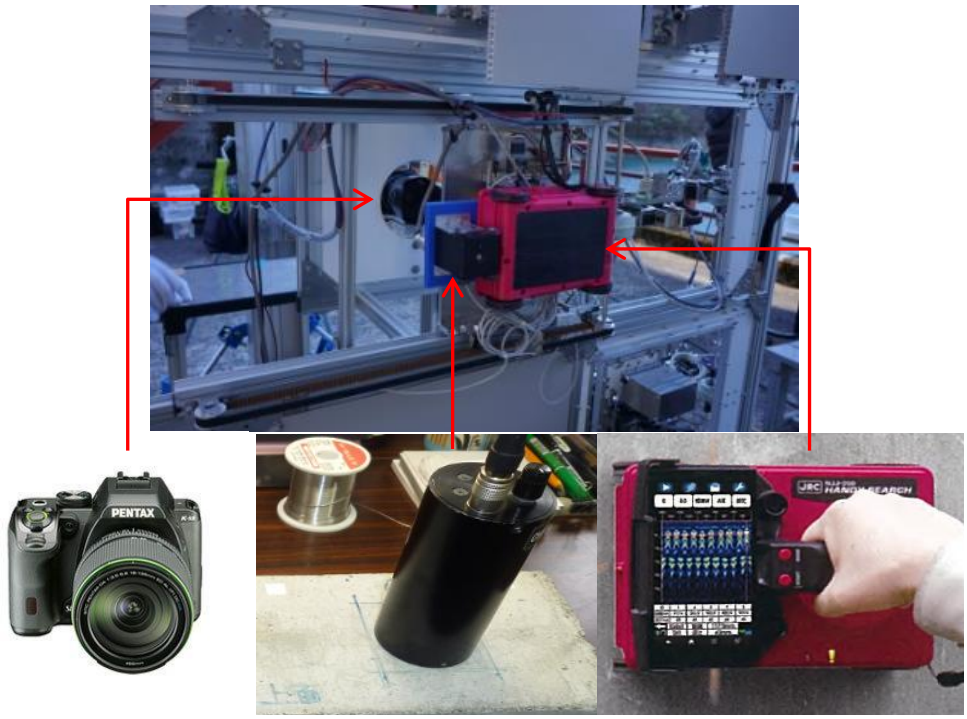

Figure 4: ALP registered measuring instruments.

4. Experimental results on actual structure

The ALP demonstration experiment was carried out on the side wall of the intake gate concrete pier of the arch type dam. Because the ALP is heavy, it moved from the vehicle to the wall of the target using a lifter. Thereafter, the ALP self-moved the wall and acquired data by remote control. The power supply to the ALP was supplied by the power cable, and it was able to drive sufficiently with 0.9 kVA supply by the gas cylinder type small generator. In the demonstration experiment, data was acquired over five hours, and then a three-dimensional model was generated by analysis by SfM. Fig. 5 shows the high-resolution three-dimensional model acquired by the ALP, data by hammering device and electromagnetic wave radar. In addition, the measurement and movement time to acquire the data of fig.5 (about 1 m^2) was 2 hours.

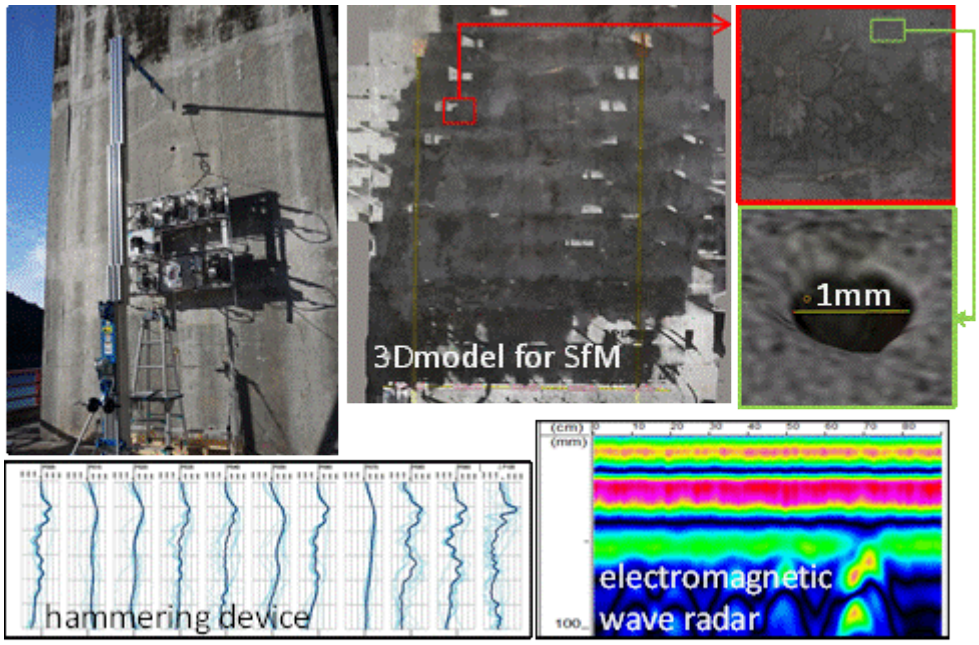

Figure 5: ALP registered measuring instruments.

5. Conclusions

ALP has inferior access function compared with UAV, stable contact investigation is possible, construction of precise three-dimensional model and non-destructive inspection for confirming the progress of deformation etc. are possible. In addition, since diagnosis by a plurality of measurement devices also includes information other than images, it can be expected that the accuracy of judgment of deformation and progressiveness will be higher when AI is applied.

Main issues confirmed in demonstration experiments of actual structures are as follows.

- Moving speed on the wall is slow
- Reflection of shadows on images
- Difference in data acquired by hitting devices when conducted by people

The authors plan to solve these problems and to put ALP in practical use.

Finally, This ALP practical development project was obtained by the subsidy of New Energy and Industrial Technology Development Organization (NEDO).

References

[1] Nishiyama, S. et al, A study on photogrammetric algorithm for crack width measurement, Computer Methods and Recent Advances in Geomechanics - Oka, Taylor & Francis Group (2014)
[2] http://nihonites.co.jp/product/doc/CHES%EF%BC%8DPEA%E2%85%A1.pdf
[3] Nojima, J., Study on Accuracy Improvement and Practical Application for Estimation of Chloride Content in Concrete Structures Using Electromagnetic Wave Method, PhD thesis, Hosei University of Japan (2014)

SynerCrete'18 International Conference on Interdisciplinary Approaches
for Cement-based Materials and Structural Concrete
24-26 October 2018, Funchal, Madeira Island, Portugal

THE ROLE OF VARIOUS AGGREGATES ON RHEOLOGY OF FRESH 3D PRINTING CONCRETE

Martin Boháč [(1)], Bohdan Nešpor [(1)], Theodor Staněk [(1)]

(1) Research Institute for Building Materials, Brno, Czech Republic

Abstract

The improvement of rheological properties of fresh 3D printing concrete by partial replacement of fine aggregate by fine recycled concrete was studied. The fineness and shape of the aggregate and sand content affects the rheological parameters of fresh mixture. Testing on rotational rheometer was carried out using coaxial cylinders. Testing was carried out in flow regime to evaluate shear and time-dependent rheological properties of fresh printing concrete. The role of packing density of various printing concrete mix designs on rheological parameters were discussed. Small addition of recycled concrete can improve rheological parameters of fresh printing concrete. The proper combination of recycled concrete and sand is the key in optimization of flow properties of 3D concrete.

1. Introduction

The rheology of fresh 3D printing concrete is crucial in terms of print quality, shape stability and printability window [1]. Mix design of the concrete, using right proportions of sand and cement blended with admixtures together with proper dosage of superplasticizer, should be balanced to achieve a material with relatively high yield stress and low plastic viscosity to meet the requirements for both pumpability and buildability [2]. The particle shape of aggregate strongly affected the plastic viscosity than the yield stress [3,4]. The type of aggregate influences the workability of concrete by packing density and surface morphology [5-9]. The smooth surface of rounded aggregates or natural aggregates reduces the inter-particle friction and results in an increase in the flowability. The flat and elongated particles can increase the particle collision due to their shape leading to a significant increase in plastic viscosity and yield stress [9]. Recycled aggregates are characterized by the higher water absorption due to the higher porosity of the adhering mortar. Kenai et al. [10] stated that the substitution of natural aggregates by recycled concrete aggregates gave SCC excellent

rheological properties comparable to that of the reference SCC. Güneyisi et al. [11] revealed that the rheological properties and fresh properties of SCC were remarkably improved by the replacement levels of fine recycled concrete aggregates due to their smoother surface. The larger the maximum particle size is, the smaller the specific surface area is and the less the amount of mortar requirement is needed, thus the lower the values of rheological parameters of concrete [12], the weaker the shear thickening behavior [8].

2. Materials and Methods

2.1 Materials

The binder of the printing concrete consists of Portland cement (PC) CEM I 52.5 R (cement Hranice, CZE), silica fume (SF) ELKEM 971 and fly ash (FA) (Dětmarovice, CZE) in proportions 40:40:20 wt. %. Two combinations of fine aggregate - quartz sand Bzenec (B) and Střeleč (S) with fine recycled concrete (R) (fraction below 0.355 mm) were tested. In the mix design, the fine aggregate was replaced by 0% (ref), 2%, 4% and 6% of recycled concrete. Water to solids (PC+SF+FA) ratio was 0.4 for B mixtures and 0.44 for S mixtures. The ratio of binder to aggregates was 1:1.7.

Table 1: Printing concrete mix design.

Sample	**Binder**	**Aggregate**			**Water**	**SP**
		B	**S**	**R**		
		Weight (g, ml)				
B ref	100	170	-	0	40	1
B 2% R	100	166.6	-	3.4	40	1
B 4% R	100	163.2	-	6.8	40	1
B 6% R	100	159.8	-	10.2	40	1
S ref	100	-	170	0	40	1
S 2% R	100	-	166.6	3.4	40	1
S 4% R	100	-	163.2	6.8	40	1
S 6% R	100	-	159.8	10.2	40	1

Superplasticizer (SP) based on PCE (Glenium ACE 40) was used in amount of 1 wt.% (binder). The mix designs are given in Tab. 1. The binder was homogenized for 30 min and then the mixture with aggregates was homogenized again for 1 min in mixer. Liquid SP was added to water and stirred and then the water with SP was added to dry mixture which was then mixed for 3 min.

2.2 Methods

Measurement of particle size distribution (PSD) was carried out by a laser diffraction method using CILAS 920L laser particle size analyzer. In laser diffraction particle size analysis, a representative cloud or ensemble of particles passes through a broadened beam of laser light which scatters the light onto Fourier lens. This lens focuses the scattered light onto a detector array and, using an inversion algorithm, a particle size distribution is inferred from the

collected diffracted light data. Size range of particle size analyzer is 0.3 – 400 μm, dispersing medium was isopropyl alcohol. Before the measurement, every sample was treated with ultrasound (60 s). The particles of sands and recycled concrete were studied in reflected light on an optical microscope. Samples were mounted in epoxy resin and then ground and polished to prepare cross sections.

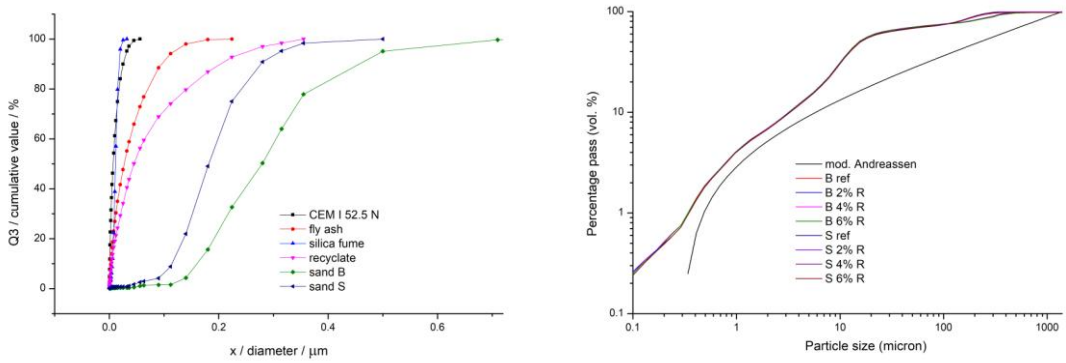

Figure 1: PSD of constituents (right) and cumulative curves (left)

Rheological parameters of printing concrete were determined by means of rotational rheometry (rheometer DHR1). All rheological tests were done at 25 °C. The coaxial cylinders (DIN) geometry. Flow curves were monitored in rage of 1-150 1/s using standard DIN coaxial cylinders geometry. Before each measurement of flow properties, the sample was pre-sheared for 10s with 10 rad/s. To achieve equilibrium conditions at each shear rate, the sweep regime (stepwise measurement) was chosen for flow tests. Yield stress and plastic viscosity were calculated as a linear approximation of descending branch of flow curves using Bingham model eq. (1). Where τ_0 is yield stress, μ is plastic viscosity and $\dot{\boldsymbol{\gamma}}$ is shear rate.

$$\tau = \tau_o + \mu\dot{\gamma} \quad (1)$$

To quantify the thixotropy (Pa/s), the area between ascending and descending curve was calculated by TRIOS software.

3. Results and Discussion

Cumulative particle size distribution was evaluated and curves of all samples were correlated to modified Andreassen model for ideal packing density with q-value 0.35. Cumulative curves of 3D printing mortar binder show only slight difference among mixtures that vary in the content of fine recycled concrete with fraction below 0.355 mm (Fig. 1). The hump around 10-100 microns resulting in gap-gradation is caused by large amount of silica fume with more uniform gradation in the mix (Fig. 1). With increasing content of recycled concrete, the cumulative curve gradation becomes more continuous both in the region of tenths and hundreds of microns. Previous study [2] confirmed positive role of continuous sand gradation on rheological properties, especially on high yield stress and low plastic viscosity. Light microscopy examination showed that particles of recycled concrete compared to B and S sand are often non-spherical or irregularly shaped showing variety of shapes including rectangle, ellipse or random shapes with sharp edges. B sand shows broader distribution of quartz

particles compared to narrower distribution of S sand. Lower circularity of particles of recycled concrete should influence the flow properties and stability of fresh mixtures.

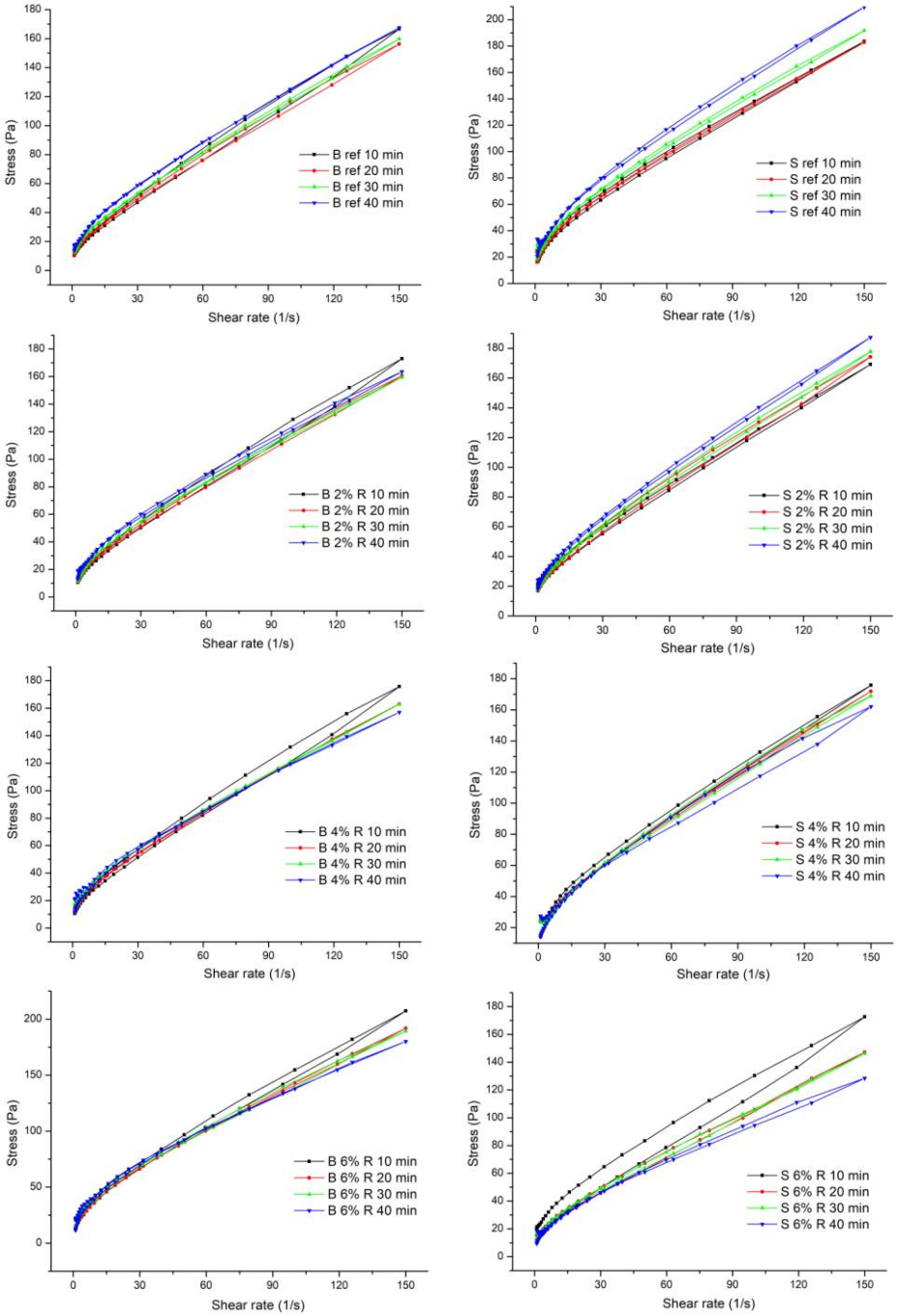

Figure 2: Flow curves of fresh printing concrete with recycled concrete

The role of various content of recycled concrete (R) with quartz sand B or S on rheological parameters was studied. Yield stress and plastic viscosity of fresh mixtures after 10, 20, 30 and 40 min of hydration were calculated from descending branches of flow curves (Fig. 2) using Bingham model (Fig. 3).

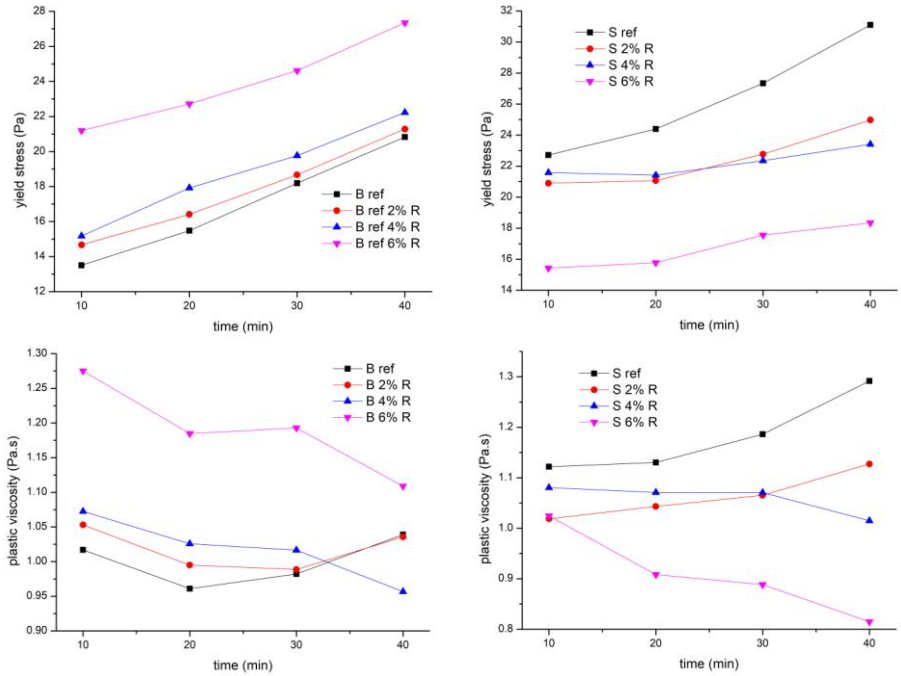

Figure 3: Rheological parameters: yield stress and plastic viscosity of fresh printing concrete

The goal was to find fresh mixture with high yield stress and low plastic viscosity that are needed for good buildability and pumpability. Yield stress increases with increasing content of R in B samples but opposite trend was found for S samples. Plastic viscosity is low up to 4 % of R for B samples and comparable with reference sample. 6% of R considerably increases both yield stress and plastic viscosity in mix with B sand. Addition of R in S samples caused the decrease of values of both yield stress and plastic viscosity. During dormant period, linear increase of the yield stress was confirmed. The increase of yield stress within first 40 minutes is slow showing no signs of initial setting [13,14]. Thixotropy decreases with time of hydration but no clear trend was found between thixotropy and content of recycled concrete. The reason of this fact may be related to combination of thixotropy as a reversible build-up and workability loss as permanent change in rheological properties of the material [15]. An alternative technique of thixotropic build-up quantification calculating critical shear strain measured at low shear rates was proposed by Perrot et al. and Wangler et al. [16,17] giving more insight in what happens when material builds-up after its deposition during printing and defining open time between two deposits.

4. Conclusions

The role of recycled concrete on rheology of fresh 3D printing concrete was studied. Flow parameters of printing concrete can be improved by addition of small amount of fine recycled concrete with irregular shape of particles and proper grading. Replacement of sand by fine recycled concrete up to 4 wt.% can improve rheological parameters related to pumpability and buildability of fresh printing concrete. When using recycled concrete for 3D printing concrete, not only the replacement level of recycled concrete but also the combination with proper sand is crucial.

Acknowledgements
This paper was elaborated with the institutional support for the long-term development of research organizations by the Ministry of Industry and Trade of the Czech Republic.

References

[1] Kazemian, A., Yuan, X., Cochran, E., Khoshnevis, B., Cementitious materials for construction-scale 3D printing: Laboratory testing of fresh printing mixture Construction and Building Materials 145 (2017), 639-647
[2] Weng, Y., Li, M., Tan, M.J., Qian, S., Design 3D printing cementitious materials via Fuller Thompson theory and Marson-Percy model, Construction and Building Materials 163 (2018), 600-610
[3] Westerholm, M., Lagerblad, B., Silfwerbrand, J. et al., Influence of fine aggregate characteristics on the rheological properties of mortars, Cem. Concr. Compos 30 (4) (2008) 274-282
[4] Tattersall, G.H., Workability and Quality Control of Concrete, E & F N Spon, London, 1991.
[5] Hu, J., Wang, K., Effects of size and uncompacted voids of aggregate on mortar flow ability, J. Adv. Concr. Technol. 5 (1) (2007) 75-85
[6] Harini, M., Shaalini, G., Dhinakaran, G., Effect of size and type of fine aggregates on flowability of mortar, KSCE Civ. Eng. 16 (1) (2012) 163-168
[7] Hu, J., A Study of Effects of Aggregate on Concrete Rheology, Iowa State University, Iowa, 2005
[8] Feys, D., Verhoeven, R., De Schutter, G., Why is fresh self-compacting concrete shear thickening, Cem. Concr. Res. 39 (6) (2009) 510-523
[9] Aïssoun, B.M., Hwang, S., Khayat, K.H., Influence of aggregate characteristics on workability of superworkable concrete, Mater Struct. 49 (1-2) (2016) 597-609
[10] Kenai, S., Menadi, B., Debbih, A., et al., Effect of recycled concrete aggregates and natural pozzolana on rheology of self-compacting concrete, Key Eng. Mater 600 (2014) 256-263
[11] Güneyisi, E., Gesoglu, M., Algın, Z., et al., Rheological and fresh properties of self-compacting concretes containing coarse and fine recycled concrete aggregates, Constr. Build. Mater 113 (2016) 622-630
[12] Ba, H., Zhang, W., Influence of aggregate on the rheological parameters of high-performance concrete, Concr (06) (2003) 7-8 (In Chinese).
[13] Struble, L.J., Lei, W.-G., Rheological changes associated with setting of cement paste, Adv. Cem. Based Mater. 2 (1995) 224–230
[14] Lei, W.G., Struble, L.J., Microstructure and flow behavior of fresh cement paste, J. Am. Ceram. Soc. 80 (1997) 2021–2028
[15] Feys, D., Cepuritis, R., Jacobsen, S., Lesage, K., Secrieru, E., Yahia, A., Measuring rheological properties of cement pastes: most commontechniques, procedures and challenges, RILEM Technical Letters (2017) 2: 129- 135
[16] Perrot, A., Rangeard, D., Pierre, A., Structural built-up of cement-based materials used for 3D-printing extrusion techniques, Materials and Structures (2016) 49:1213–1220
[17] Wangler, T., Lloret, E., Reiter, L., Hack, N., Gramazio, F., Kohler, M. Bernhard, M., Dillenburger, B., Buchli, J., Roussel, N., Flatt, R., Digital Concrete: Opportunities and Challenges. RILEM Technical Letters 2016 1:67–75

ON-SITE MONITORING

AND

STRUCTURAL CONDITION ASSESSMENT

SynerCrete'18 International Conference on Interdisciplinary Approaches
for Cement-based Materials and Structural Concrete
24-26 October 2018, Funchal, Madeira Island, Portugal

AN INVESTIGATION ON APPROPRIATE CURING REGIMES FOR PRECAST CONCRETE STRUCTURAL ELEMENTS WITH GGBS USING MATURITY FUNCTIONS

Fragkoulis Kanavaris[(1)*], Marios Soutsos[(2)], Jian-Fei Chen[(2)], Sreejith Nanukuttan[(2)]

(1) Formerly at Queen's University Belfast, currently at Advanced Technology & Research, Arup, London, UK
(2) School of Natural and Built Environment, Queen's University Belfast, Belfast, UK

Abstract

Nowadays, it has been an increasing demand for reducing the carbon footprint of concrete. In several construction projects, new, blended cements are required; not only for being more environmental friendly compared to neat Portland cement but also due to their enhanced durability performance. Precast concrete manufacturers have been traditionally using concretes with high cement content to achieve early compressive strength in order to safely lift structural elements as early as 16 hours after casting and maintain a particular production schedule. However, and regardless of the urge for environmental friendlier construction materials, precast concrete manufacturers are still sceptical with respect to using supplementary cementitious materials, such as ground granulated blast-furnace slag (GGBS), in their concretes due to a potentially slower strength gain of concrete of blended cements compared to conventional ones; which in return causes difficulties to the manufacturer if such cements are specified. In this study, it is demonstrated that using maturity functions for the estimation of the expected compressive strength of concrete is an effective tool towards deriving appropriate curing regimes for precast structural elements containing GGBS without necessarily affecting the production schedule and consequently promoting environmentally friendlier concretes.

1. Introduction

Concrete is arguably the most widely used material worldwide mainly due to its versatility, durability and relatively low production and construction costs. Although it has been used in "countless" projects, from residential buildings to marine and high security structures, the

primary drawback of the material is that its production contributes 5% of total annual anthropogenic global CO_2 production [1]. With Portland cement production being responsible for the higher carbon footprint of concrete, over the past decades the incorporation of cement additions, also known as replacement materials (CRMs) is encouraged, such as ground granulated blast-furnace slag (GGBS).

The need to reduce the carbon footprint of concrete together with the required blended cements for durability performance (CEM II, CEM III, CEM IV and particularly CEM III/B which contains 66-80% GGBS based on EC2 and BS8500) has led to increased demand for innovative and environmental friendlier cement-based materials to be used in the construction industry, including major railway and tunnelling projects. However, precast concrete contractors are faced with barriers regarding the adoption of such cements, especially with high replacement levels of GGBS and they may subsequently fail to comply with the project's regulations or the environmental impact of the project is compromised. These barriers are mostly related with the traditionally preferred CEM I from precast concrete manufacturers and have a direct impact on major construction projects' carbon footprint when precast elements such as structural walls, slabs and tunnelling segments are involved.

One of the main reasons that GGBS has not gained popularity in precast concrete applications, regardless of the need to reduce the carbon footprint of modern concrete, is the fact that the strength development of GGBS concretes at room temperature is slower compared to that of neat Portland cement. A precast concrete contractor is interested in achieving high early age compressive strength in order to enable safe lifting of structural elements within few hours after casting, as this will result in accelerated construction schedules; hence CEM I concrete is generally preferred. However, it has been demonstrated elsewhere that high curing temperature results in greater early age strength enhancement for GGBS rather than for CEM I concrete [2-5]. It is therefore necessary to investigate and optimise curing regimes for GGBS concretes so that early strength lifting criterion of 15 MPa, as specified by PD CEN/TR 15728:2016, is met within a specific time frame. Usually, based on the desired production schedule of precast concrete manufacturers, this time frame lies between 16 and 18 hours after casting (as shown in Figure 1), which enables sequential casting, curing and lifting of precast elements.

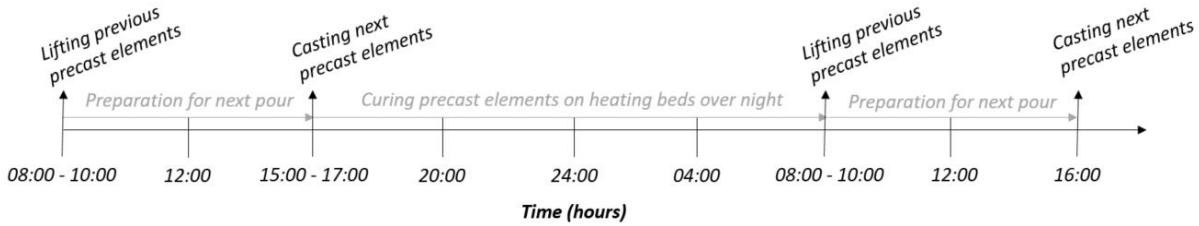

Figure 1: Preferred construction/production schedule of precast concrete manufacturers.

To the authors' best knowledge, such investigation has not been previously evaluated, either experimentally or analytically. However, it is a common in the construction industry which impacts the production efficiency of precast concrete manufacturers, but most importantly, a problem which contributes to ongoing relatively high CO_2 emissions. A solution to this problem will be attempted herein through the use of maturity functions, whilst a brief description of the latter will be provided in the following section. Furthermore, through

combining the curing temperature profile and time required to meet the lifting strength criterion, an indication of the energy consumption required is derived.

2. Maturity functions for concrete

Maturity functions for concrete, initially developed by Nurse and Saul in the early 1950s [5], aim to account for the combined effect of temperature and time on concrete strength. Although several maturity functions exist, as outlined in [5], the most frequently used are the Nurse-Saul and the Arrhenius [5] ones, also due to their inclusion in ASTM C1074-11. While the Nurse-Saul function considers that strength varies linearly with temperature, the Arrhenius function implies an exponential variation of strength with temperature. This, together the temperature sensitivity factor (known as activation energy) inherent in the Arrhenius function, resulted the latter to be deemed as more appropriate for mixes containing CRMs, such as GGBS:

$$t_e = \sum_0^t e^{-\frac{E_a}{R}\left[\frac{1}{273+T}-\frac{1}{273+T_r}\right]}\Delta t \quad (1)$$

Where, t_e is the equivalent age of concrete (hours), E_α is the activation energy (kJ/mol), R is the universal gas constant (J/mol·°K), T is the average concrete temperature (°K) at time internal Δt (hours) and T_r is the reference concrete temperature (°K) which is most frequently taken to be equal to 20 °C. Apart from the maturity function to be used, strength-maturity (or strength-age) is also required in order to relate maturity to compressive strength development. A frequently used one is that developed by Carino [2-5] which is also recommended by the ASTM C1074-11 standard:

$$S = S_u * \frac{k * (t - t_0)}{1 + k * (t - t_0)} \quad (2)$$

Where, S is the concrete strength (MPa), k is the rate constant (hours^{-1}), t is the concrete age (hours) and t_0 is the age at which the strength development is assumed to begin (hours). Although there are several maturity functions, as mentioned before, for this particular investigation, the combination of Equations (1) and (2) produced the most reliable results, hence used herein (detailed information can be extracted from [7]; however, it is thought that further elaboration on the accuracy of different maturity functions does not fall within the scope of this study).

3. Materials and experimental procedures

The materials and experimental methods implemented in this study are briefly explained in the following sections and in detail in [5].

3.1 Materials, mix proportions and number of mixes considered

In order to elucidate the potential of using GGBS in precast concrete applications for structural concrete, appropriate curing regimes for three medium to high replacement levels of cement with GGBS were considered. The mixes were designed to have a 47 MPa target mean

cube compressive strength at 28 days, whilst the GGBS replacement levels (by weight) were 35, 50 and 70% of total binder [5].

3.2 On-site temperature monitoring of precast concrete walls

The temperature evolution in various locations within a precast concrete wall (at Creagh Concrete Products Ltd.) was monitored with the use of thermocouples. The 4.86 × 2.47 × 0.150 m, precast concrete wall was cast (CEM I concrete mix with 420 kg/m^3 cement content) on the so called "heating beds" and prescribed heat was supplied to concrete through the bottom surface (Figure 2). Temperatures were recorded at various locations in the slab and the monitoring was subsequently terminated few hours after lifting.

Figure 2: From left to right – Thermocouples attached on the reinforcement bars, temperature logging system, concrete wall casting on heating bed, wall lifted [photographs: F. Kanavaris].

4. Results and discussion

4.1 Parametric study on appropriate curing regimes for precast concrete

The recorded temperature histories of the investigated precast concrete wall in various locations are shown in Figure 3(a). As it can be seen, the temperature reached up to approximately 37 °C at the heating bed and bottom of slab; however, due to heat dissipation through the lateral and top boundaries the temperature achieved was lower in these regions. However, as the original precast mix contained solely CEM I, such temperatures were ample for the wall to achieve the required strength at 16-18 hours. Therefore, this temperature profile, together with modified ones for GGBS concrete should be investigated and proposed, as shown in Figure 3(a). The "original" curing regime ("CR-org" in Figure 3(b)) is taken as the simplified version of "long side/lifting anchor" in Figure 3(a) as this location is considered to be the critical one for safe lifting, i.e. the concrete region around the lifting anchor.

The predicted strength development for precast concrete walls containing different levels of GGBS and based on the hypothetical temperature histories in Figure 3(b) are shown in Figure 4. The parameters needed for Equations 2 and 3 (E_a, S_u, k, and t_0) to enable a strength prediction were previously determined and shown in detail in [5]. It is rather evident that as the GGBS content increases and the temperature remains relatively low, then the early age strength gain is penalised and the required curing time to enable safe lifting is prolonged to a considerable extend. However, due to the temperature sensitivity of GGBS mixes, in the cases where high curing temperature is applied at early ages, strength develops much faster and the lifting criterion can be met as soon as 9 hours after casting, as also shown in Table 2. In this case, the effect of temperature becomes more pronounced as the percentage of GGBS in the mix increases; a behaviour that is particularly beneficial and can be exploited in precast

concrete manufacturing for the production of greener structural elements. It is therefore suggested that the barriers in the adaptation of GGBS from the precast concrete industry could be potentially overcome if appropriate curing is applied, which includes high temperature curing starting from very early ages.

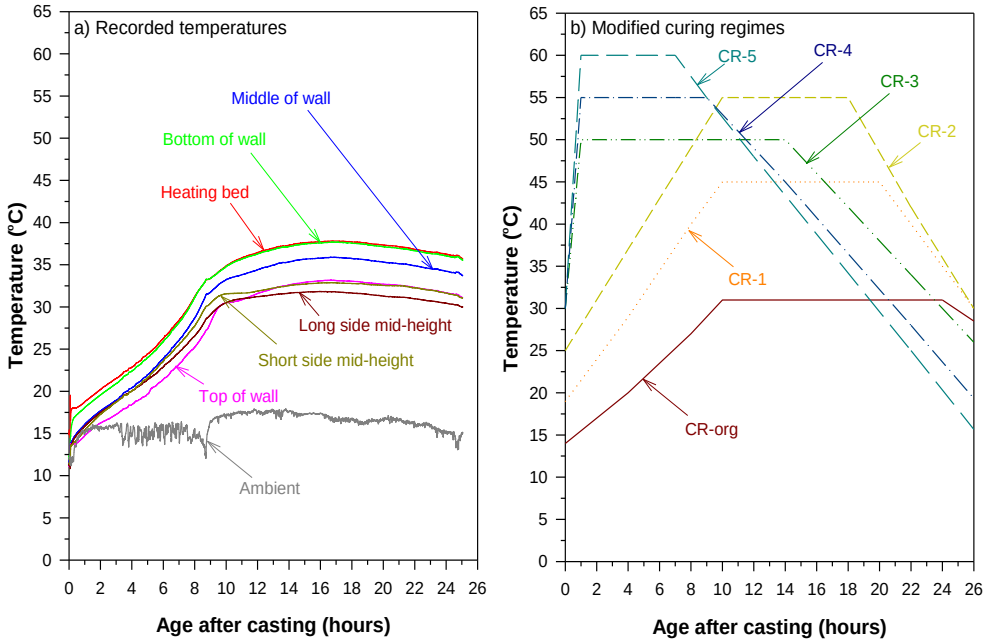

Figure 3: Recorded (a) and investigated (b) temperature profiles

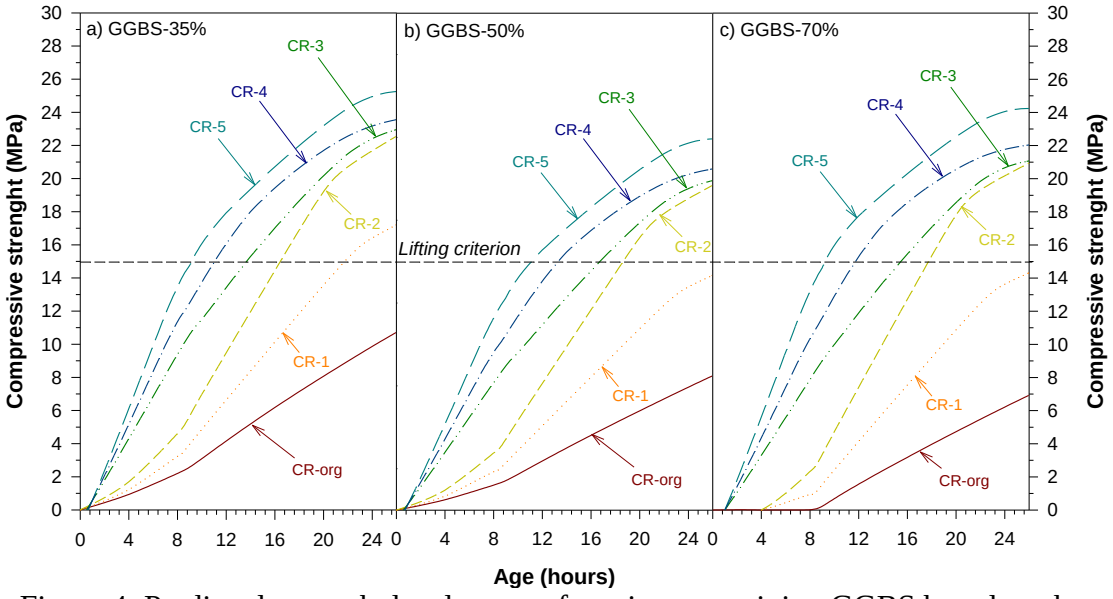

Figure 4: Predicted strength development for mixes containing GGBS based on the temperature histories in Figure 3(b).

4.2 Indication of energy demand

Another issue that should be taken into consideration whenever accelerated curing is investigated is the energy demand of the curing process. Although its accurate calculation in this case may not be possible, it is proposed that indication of energy demand could be

roughly provided through an energy consumption factor (ECF), as shown in Table 2. This ECF can be easily calculated from Figure 3(b) as the area under each curing regime graph whilst the end of curing age is taken to be equal to the time at which the lifting criterion is met. As it can be seen, there is an increase is energy demand for all hypothetical curing regimes when compared to the original ones; however, it may be more environmental friendly to cure GGBS concrete at high temperature for a relatively short period of time rather than at a lower temperature for prolonged periods of time.

Table 2: Calculated potential lifting times and energy consumption factors for the investigated curing regimes and GGBS mixes.

Material	**GGBS-35%**		**GGBS-50%**		**GGBS-70%**	
	Lifting time [hours]	*ECF [C·hours^2]*	*Lifting time [hours]*	*ECF [C·hours^2]*	*Lifting time [hours]*	*ECF [C·hours^2]*
CR-org	36	275	42	315	54	380
CR-1	22	565	28	621	27	616
CR-2	17	530	19	605	18	587
CR-3	14	480	16	530	15	503
CR-4	11	429	13	479	12	454
CR-5	9	454	10	499	9	454

5. Summary and outlook

In this study a preliminary investigation of appropriate curing regimes for precast concrete structural elements containing GGBS was conducted. It was found that is possible to obtain similar to PC concrete strengths when concretes with GGBS are considered, however, higher curing temperature must be applied to satisfy the lifting criterion at 16 hours after casting, whilst to obtain an indication of the energy demand based on the curing regime applied and mix considered, an energy consumption factor (ECF) may be implemented.

References

[1] Crow, J. M., The concrete conundrum, Chemistry World (2008), 62-66.
[2] Soutsos, M., Hatzitheodorou, A., Kwasny, J. and Kanavaris, F., Effect of in-situ temperature on the early age strength development of concrete with supplementary cementititous materials, Con Build Mat (2016), 103, 106-116.
[3] Soutsos, M., Hatzitheodorou, A., Kanavaris, F. and Kwasny, J., Effect of temperature on the strength development of mortar mixes with GGBS and fly ash, Mag Con Res (2017), 69(15), 787-801.
[4] Barnett, S.J., Soutsos, M., Millard, S.G. and Bungey, J.H., Strength development of mortars containing ground granulated blast-furnace slag: Effect of curing temperature and determination of apparent activation energies, Cem Con Res (2006), 36(3), 434-440.
[5] Kanavaris, F. Early age behaviour and cracking risk of concretes containing GGBS, Ph.D. Thesis, Queen's University of Belfast, UK (2017).

SynerCrete'18 International Conference on Interdisciplinary Approaches
for Cement-based Materials and Structural Concrete
24-26 October 2018, Funchal, Madeira Island, Portugal

DETECTION, ASSESSMENT AND MONITORING OF COMMON ANOMALIES IN CONCRETE DAMS

João Conde Silva [(1)]

(1) National Laboratory for Civil Engineering (LNEC), Lisbon, Portugal

Abstract
The current document compiles some of the most relevant information concerning the symptoms and respective causes of common anomalies observed in concrete dam bodies. These include physical degradation phenomena, like abrasion, cavitation and freeze-thaw cycles, and chemical reactions, such as expansive reactions and leaching. The methodologies available to detect, assess and monitor these are addressed as well, with a special focus on cracking.

1. Introduction

Portland cement is an inherently durable material. Nonetheless, even the most well designed and built concrete structures have a life time limited by the cement itself. The degradation of a concrete structure is always a concern, with the situation becoming even more serious when the risk of failure jeopardizes people's lives and properties, which is the case of dams with populations downstream [1, 2]. Given the importance of this topic, some of the most frequently observed anomalies in concrete dam bodies, along with their respective causes as well as procedures developed to identify and evaluate them, are presented here.

2. Most common anomalies

Some of the most common symptoms of pathologies observed in concrete dams are cracking, unexpected displacements, water seepages and degradation of the exposed concrete, mainly in upstream and downstream faces as well as around spillways and outlets [2].
The causes of these anomaly signs can be divided into two main categories, the ones with origin in physical phenomena and the ones caused by chemical reactions. The first ones include abrasion, cavitation, shrinkage, mechanical and thermal loads and freeze-thaw cycles.

In what concerns to the chemical reactions, the most frequent ones in concrete dams are leaching of the cement matrix by seepage water, alkali silica reactions (ASR) and internal sulfate attack (ISA). The dam design, concrete manufacture and construction process are also within the main reasons for the appearance of anomalies in concrete dams [1, 3, 4].
Despite being a symptom, cracking is addressed separately due to its remarkable relevance.

2.1 Physical phenomena

2.1.1 Abrasion

Mirza *et al.* [2] define abrasion in concrete dams as the wear of the concrete surface due to the flowing water carrying solid particles (e.g. sand, gravel and even larger particles), resulting in a smooth surface (smoother than the one produced by cavitation). The extension of the damage is dependent on the speed and turbulence of the water transporting the abrasive material, the hardness of this material as well as the quality of the surface submitted to the abrasion action. Stilling basins (Fig. 1a**)**) and bottom outlets are particularly susceptible to abrasion and the most effective way to detect it is through visual inspection [5].

2.1.2 Cavitation

The erosion by cavitation is one of the most common causes of deterioration in high head spillways and outlet works. It occurs due to a sharp reduction of water pressure during the flow, which may change the state of the water from liquid to vapor. When the pressure drops under a certain limit, the vapor cavities formed inside the liquid become unstable and blow up, which may produce damage to the concrete structure. The damaged surface is more likely to be eroded by cavitation, which often result in a snow ball effect. In hydraulic structures, with high-speed flows, this reduced pressure is typically due to irregularities in the flowing concrete surface, with the most vulnerable zone being the one where the water changes to free flow, e.g. the spillway surfaces, immediately downstream of a floodgate or a valve. The most efficient way to detect damage by cavitation is also through visual inspection [2, 5].

2.1.3 Freeze-thaw cycles

Once saturated, the concrete cracks when exposed to freezing temperatures. The saturation degree is a function of its capillarity and amount of air in its pores. The water expands around 9% from the liquid to the solid state and this volume increase cannot be absorbed by the saturated concrete without damage, normally resulting in cracking or scaling. When there are dissolved salts in the water, the potential damage is even higher. The greater the difference between the thermal expansion coefficients between the aggregates and the cement paste, the higher is the chance of damage due to the freeze-thaw cycles. It can also be easily detected by visual inspection and is mostly observed in the downstream face and in the crest of dams [6].


a) Abrasion in stilling basin

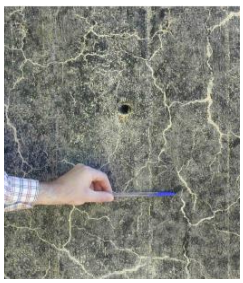
b) Map cracking [8]


c) Crushed joints [8]


d) Relative displacements [8]

Figure 1 - Common anomalies in concrete dams.

2.2 Chemical reactions

The anomalies caused by chemical reactions are also very recurrent in concrete dams, with the expansive reactions (ASR and ISA, which may appear in a combined form) standing out. The ASR needs three ingredients to occur: reactive aggregates, alkalis and external water. The reaction product is a gel, which gradually absorbs external water, resulting in an expansion of concrete and, consequently, introducing internal stresses. Concerning the ISA, the sulfates, soluble in water or in the aggregate, may react with the aluminates in the cement paste. The product, ettringite, absorbs water, which may eventually cause expansion and cracking of the concrete. This reaction is relatively common in massive structures like dams, due to the high temperatures achieved at early ages (over 70^{o}C), which delay the formation of ettringite. This mineral also expands by water absorption, hence this late reaction results in swelling of concrete after hardening, with similar consequences as for the ASR [6, 7, 8].

The current state-of-the-art regarding these swelling reactions is already sufficient to avoid its occurrence in new dams, as long as appropriate measures are taken. The methods to prevent the manifestation of ASR and ISA in new constructions are mostly based on controlling and minimizing the variables that contribute to the development of these chemical reactions. Concerning the ASR, the reaction potential of the aggregates may be assessed by a petrologist, whereas the alkalis present in the cement can be controlled. Regarding the ISA, the recommended procedures are to limit the maximum temperature achieved during the hydration reaction of the binders (e.g. replacing part of the cement by pozzolanic materials) and limiting the amount of aluminates and sulfates in the binder (e.g. using high sulfate resistant cements). Accelerated tests are usually efficient in detecting the concrete potential for developing ISA. Keeping the concrete relatively dry is another relatively common solution to mitigate these expansive reactions (e.g. waterproofing the upstream face), although this solution is mostly used in existing dams [4, 6, 7, 9].

When dealing with operating dams, there are several ways to detect the symptoms resulting from ASR and ISA in concrete dams. The most direct one is through visual inspection, with cracking (Fig. 1b)) and ASR gel being among the most frequent manifestations. Further information on crack assessment can be found in 2.3.1. The other key signs are abnormally closed contraction joints (which may eventually start crushing against one another) (Fig. 1c)), relative displacements between adjacent blocks (Fig. 1d)), elevation of the dam height (crest rising) and horizontal permanent displacements (often upstream drift). The dam apertures may also be affected, e.g. ovalization of the ducts and warping of the floodgates. The most effective way for detecting most of these manifestations is through surveillance instrumentation installed in the structure, whose complexity depends on the dimension and safety risk of the dam [6, 8, 10].

The surveillance methods that can be used to monitor the dam behavior and consequently assess the above mentioned symptoms are: a) internally embedded and external joint meters (axial/radial, planar or 3D measurement) for measuring the joint displacements; b) mechanically isolated extensometers embedded in the concrete, to assess the stress-independent extensions, such as the ones resulting from ASR and ISA; c) geometric levelling, for measurement of vertical displacements of the dam crest; d) plumb lines, global navigation satellite systems (GNSS) or geodetic planar system, for measuring the horizontal displacements. However, the interpretation of the data obtained by most of the above mentioned surveillance methods should include a statistical analysis, in order to estimate the weight that distinct variables have on the dam behavior. Thus, statistical models to

quantitatively interpret the collected data are usually utilized. One of the most used methods is the separation of the effects caused by the variables hydrostatic pressure (which is proportional to the reservoir level), temperature (air and reservoir water) and ageing (such as creep or swelling caused by expansive reactions). The first two variables are usually known (by direct measurement) and their effects are assumed to be reversible, whereas ageing effect is presumed to be a non-elastic phenomenon solely time dependent [6, 10, 11, 12].
The other frequently occurring chemical reaction in concrete dams, i.e. leaching, consists on the dissolution of material from the cement matrix (calcium and magnesium hydroxide crystals) by reservoir water, with the dissolving potential being enhanced by the pureness of the water. This often leads to formation of crystalline salt deposits known as efflorescence (Fig. 2a)). This loss of solids from the cement matrix reduces the strength and the permeability, which will eventually facilitate the penetration of harmful substances into the concrete, namely water. Hydrochemical analyses of the reservoir water, such as temperature, pH, electrical conductivity, redox potential and total dissolved solids are undertaken to evaluate the water aggressiveness [1, 5].

2.3 Cracking

Cracking may have origin on loads (e.g. hydrostatic pressure, self-weight) or on volumetric changes (e.g. thermal, shrinkage, expansion, creep) and should be faced as a potential deficit which needs to be evaluated. The most common causes of cracking in concrete dams are drying shrinkage, temperature changes, expansive reactions (namely ASR and ISA), design or construction defects, ageing, freeze-thaw cycles, foundation settlement and occasional mechanical loads. Understanding the cause of cracking is indispensable for the repair to have effective and long lasting effects. For instance, if cracking is due to drying shrinkage, it will stabilize, so crack repair is more likely to be successful. On the other hand, for the progressive phenomena, such as differential foundation settlements, the treatment of the cracks have more limited effects. Cracking may be the first symptom indicating other issues in concrete. Thus, the structure evaluation, including a detailed crack assessment, should be undertaken when a crack is detected [1, 6, 13].

a) UAV (drone) visual inspection of dam with efflorescence ($CaCO_3$) b) Crack meter in gallery [10]

Figure 2 - Crack assessment in concrete dams.

2.3.1 Assessment of cracking

The surveying of cracks is one of the main tasks involved in the monitoring plan of a concrete dam. It includes a general structure inspection, identifying and describing the cracks as well as, eventually, deducing their origin. Crack meters may also be used to monitor their movement (see Fig. 2b)). If, by chance, the reservoir is emptied, a detailed visual inspection should be undertaken in upstream face, even if no crack signs have been detected. Differential settlements, spalling, seepage and leaching deposits (see Fig. 2a)) are common consequences of cracking [6].

New technologies based on digital image processing are very useful for visual inspections (Aided Visual Inspections) of cracking and its consequences (see Fig. 3). Unmanned Aerial Vehicles (UAV) (see Fig. 2a)) are also extremely convenient for visual inspections [14].

The surface cracking might be mapped using the detailed surveying, photos and pathology maps (see Fig. 3). If necessary, underwater inspections may be undertaken by divers. All the openings (such as tunnels) related to the structure should be inspected as well. When possible, the external signs of cracking should be correlated with internal cracks. The internal cracks may be detected through soft hammering, as a hollow sound usually indicates the presence unsound concrete, e.g. internal cracks. Several tests to identify the internal cracking degree are at one's disposal, such as lab tests on concrete core extracted from the dam. Non-destructive tests (NDT) are also available for this purpose, namely sonic and ultrasonic waves, geo-radar (based on the changes of magnetic permeability and dielectric constant), video cameras, optic fibers, permeability tests and controlled injection of fluids [6, 15].

Numerical damage models, such as finite element models (FEM) and discrete element models (DEM), are often used as a supplement to the above mentioned methods. These models are very helpful at predicting the locations where cracking is probably occurring. FEM and DEM may even indicate the directions in which cracks are most likely to develop.

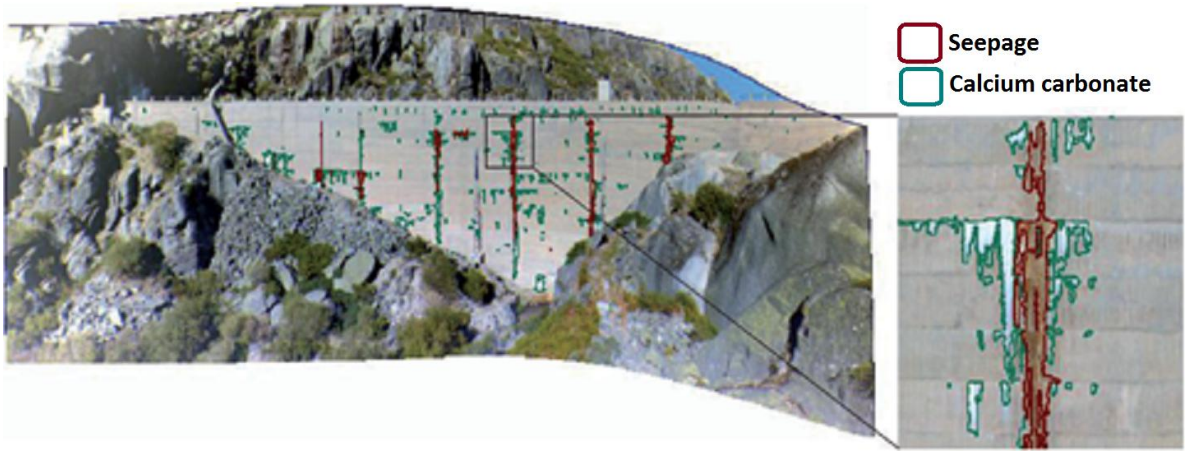

Figure 3 - Pathologies map obtained in the sequence of Aided Visual Inspection [14].

The methods utilized for surface mapping of cracks are relatively simple and relatively inexpensive. On the other hand, the methods to assess the internal cracking degree are usually sophisticated and need specialized workers with adequate training, namely for the processing and interpretation of data [6].

4. Final remarks

The most frequent anomalies in concrete dams may be divided in two main groups, as function of their origin: physical and chemical phenomena. The first ones include abrasion, cavitation and freeze-thaw cycles, and the most adequate way to detect these is through visual inspections. The most relevant chemical reactions are the expansive ones (ASR and ISA) and leaching of the cement matrix. The swelling due to the expansive reactions has numerous typical symptoms, such as abnormally closed contraction joints, distinct displacements and cracking. Instrumentation along with visual observation play a key role in providing early warnings for these unusual behaviors, hence contributing to avoid any subsequent incidents.
Cracking is a common symptom for different causes, so it should be thoroughly evaluated, as an accurate diagnosis is crucial for a successful repair. Several methods for assessing surface and internal cracking have been developed, with their own advantages and limitations.

References

[1] Corns, C.F. et al, Advanced dam engineering for design, construction and rehabilitation, Van Nostrand Reinhold Company (1988)
[2] Mirza, J. et al, Influence of structural parameters on abrasion-erosion resistance of various repairing mortars, Canadian Journal of Civil Engineering 17(1) (1990), 12-18
[3] Sims, G.P., The rehabilitation of dams and reservoirs. In Water Storage, Transport and distribution - Vol 1. Encyclopedia of Life Support Systems, Japan (2009), 126-153
[4] Custódio, J. et al, Concrete structures affected by internal expansive reactions, 3rd National Congress on Safety and Conservation of Bridges (2013)
[5] ICOLD bulletin 119: Rehabilitation of Dams and Appurtenant Works (2000)
[6] ICOLD bulletin 107: Control and Treatment of Cracks (1997)
[7] Taylor, H.F.W., Cement Chemistry, London: Academic Press (1997)
[8] Santos Silva, A., Degradation of concrete due to alkali-silica reaction. The use of fly ash and metakaolin for its prevention (in Portuguese), PhD thesis, University of Minho (2006)
[9] Divet L. et al, Optimization of the choice of binder to reduce the expansion of concrete due to the delayed formation of ettringite (in French), Proceedings 7th CANMET/ACI International Conference on Durability of Concrete, Montreal, Canada (2006), 331-342
[10] Amberg, F., Performance of dams affected by expanding concrete, V-0009401EN/1021-R-237, Switzerland (2011)
[11] Batista, A.L. et al, Models for safety control of concrete dams, Proceedings 3rd International Conference on Dam Engineering, Singapore (2002)
[12] Gomes, J.P. et al, Evaluation of the effects of the deterioration process of Fagilde concrete dam: Analysis of observed behavior and mitigation recommendations (in Portuguese). Proceedings 2nd Encontro Luso-Brasileiro de Degradação de Estruturas de Betão, LNEC, Portugal (2016)
[13] Delatte, N., Failure, distress and repair of concrete structures, CRC Press (2009)
[14] Fonseca, A.M. et al; Visual inspection automation with image processing, Proceedings 7th International Conference on Engineering Surveying (INGEO), LNEC, Portugal (2017)
[15] McDonald J.E. and Curtis N.F., Repair and rehabilitation of dams: case studies, Technical Report REMR-CS-63 US Army Engineer Research and Development Center (1999)

SynerCrete'18 International Conference on Interdisciplinary Approaches
for Cement-based Materials and Structural Concrete
24-26 October 2018, Funchal, Madeira Island, Portugal

DETERIORATION DIAGNOSIS TECHNIQUE OF POLYMER CEMENT WATERPROOFING MEMBRANES BY DIFFERENCE IN THERMAL CHARACTERISTICS OF CONSTITUENT MATERIALS USING ACTIVE THERMOGRAPHY

Masayuki Tsukagoshi [(1)], Hiroki Toyoda [(1)], Takao Ueda [(1)], Masashi Ishikawa [(1)]

(1) Tokushima University, Tokushima, Japan

Abstract
An accelerated degradation test of polymer modified cement waterproofing membrane was carried out. The change in mechanical properties and gloss of the surface was measured. Polymer modified cement waterproofing membranes were prepared according to set polymer to cement ratio parameters, and then applied on concrete surface. These specimens were exposed to 3 types of accelerated deterioration conditions: light irradiation in a quantity of 18.2 W/m^2 by UV lamp; ambient conditions of a temperature of 70 °C and 50 %R.H.; and 70 °C hot water. After exposure test, the surface of the test pieces were heated by a halogen lamp for about 20 seconds and cooled at room temperature. The temperature change during same period was observed with an infrared camera.
For all the test pieces exposed under deterioration conditions the elongation rate tended to gradually decrease as the exposure period increased and the tensile strength increased. And the surface temperature increased as P/C was higher. As the polymer deterioration progressed the lower the observed increases in temperature became. The decrease of the elongation rate due to degradation and the rate of increase in temperature showed a relatively good correlation, but the tensile strength varied greatly.

1. Introduction

Waterproofing materials, of course, must provide waterproof performance and must be able to resist fracturing even when they receive crack bridging tension. Therefore, the polymer cement modified waterproofing membrane is made by polymer-rich formulation, and mixing amount of polymer to cement ratio is 100 to 200 %. Generally, organic materials are degraded by things such as ultraviolet rays, water, oxygen, heat or a combination of these effects during

service period. The organic material is inferior in durability and resistance to weather when compared to the concrete, which is an inorganic material, and because of this it is repaired or modified in a cycle of 10 to 20 years [1]. Generally, in order to evaluate the degree of deterioration of waterproofing materials, the following tests are normally carried out: surface observation, elongation performance test, and component analysis. Any of these existing methods though, require a certain degree of knowledge and high cost. Especially then, when the waterproofing membranes are applied to a large area, there is a need for evaluation methods that can be easily conducted and are non-destructive.
In the field of construction, the active thermography method is a non-destructive and non-contact inspection technique utilized for detection of defects such as peeling of tiles on wall and cavities in concrete. At this point, polymer modified cement is a composite material composed of organic material and cement as an inorganic material, and the thermal characteristics of both materials are greatly different. To this purpose, the degradation condition of the polymer modified cement waterproofing membrane was examined using active thermography method in this study.

2. Experimental program

2.1 Test pieces

For polymer modified cement materials, ordinary Portland cement (Density: 3.16 g/cm^3), crushed sand (Density: 2.56 g/cm^3, Grain diameter <200 μm) acrylic acid ester copolymer (Density: 1.0 g/cm^3, Re-emulsifiable resin powder) were used. The aqueous emulsion was prepared by mixing re-emulsified resin with water in advance. The emulsion, cement, and sand were mixed to produce the test pieces. The preparation of the test pieces largely followed the Guideline for polymer-modified cement waterproofing membrane work [2] and specification. The coating thickness was adjusted to 1.0 mm by controlling the applied weight. These test pieces were cured for 7 days in an environment of 20 ± 2 °C, 60 ± 6 %R.H.. After the polymer cement was fabricating into a film, it was punched out into a dumbbell shape and used as a tensile test piece. The tensile test was carried out at 500 mm/min in the environment of 20 °C and 60 %R.H. according to JIS K 6251. The mix proportion of the test pieces is shown in Tab. 1. The number of test pieces was 3, and the test results showed the average. The test condition and the shape of the dumbbell test piece are shown in Fig. 1.

Table 1 : Mix proportion of polymer cement.

W/B (%)	P/C (%)	S/C (%)	W (kg/m^3)	B (kg/m^3)		S (kg/m^3)
				P	C	
70	100	200	401	572		572
				286	286	
	150		403	575		460
				345	230	
	200		405	405		385
				365	193	

For the thermography test pieces, a polymer modified cement waterproofing membrane was applied on one surface of the substrate concrete (100×100×100 mm) of W/C = 55 %. These were sealed with epoxy resin except for the surface where the polymer modified cement waterproofing membrane was applied.

2.2 Accelerated weathering test

The three main factors of degradation to polymer materials in the outdoors (ultraviolet, heat and moisture) were tested. The distance from the test piece to UV lamp was adjusted so that the irradiation intensity was 18.2 W/m^2 in ultraviolet degradation test. The test pieces were exposed under the atmosphere of 70 °C and 50 %R.H. in the thermal degradation test, and the test pieces were immersed in hot water at 70 °C for heat and water degradation test. The accelerated degradation test time was 500 and 1,000 hours. After exposure, the test pieces were placed in the laboratory for more than 48 hours (20 ± 2 °C, 60 ± 6 %R.H.), then the temperature and moisture content were adjusted for estimating degree of degradation.

2.3 Active thermography test

The test condition of the active thermography test is shown in Fig. 2. Active thermography test method is composed of 1,000 W halogen lamp, thermography camera, and PC for image display and data processing [3]. The temperature resolution of the camera was 0.05 °C, resolution of the picture was 640×480 pix, and the sampling frequency was 3.75 Hz. The resolution of 1 pix image is approximately 0.8 × 0.8 mm, due to the size of the specimen, the camera installation position and resolution. The surface of the specimen was naturally cooled for 40 seconds after 20 second irradiation with the lamp.

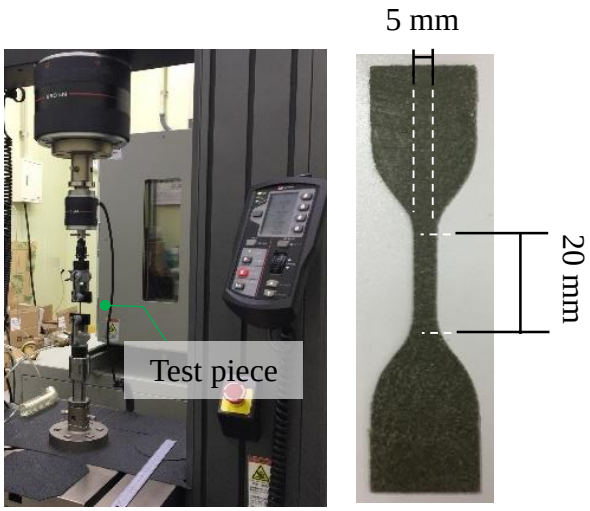

Figure 1 : Tensile test

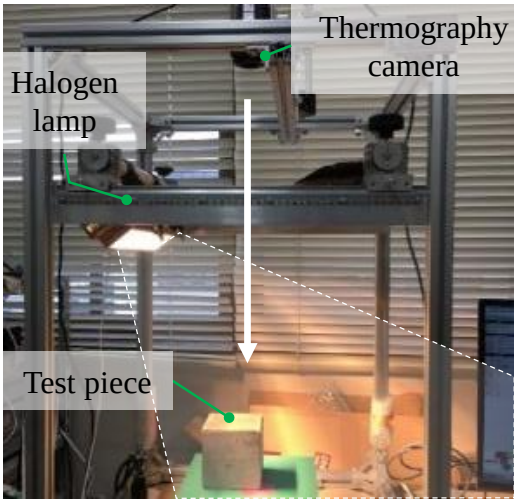

Figure 2 : Active thermography test

3. Test results and discussion

3.1 Mechanical properties

Fig. 3 shows the rate of change in tensile strength and elongation rate for each deterioration condition. With the test pieces made with the materials used in this experiment in sound

condition, the higher the P/C ratio the higher tensile strength and elongation. Tensile strength tended to increase and elongation rate decreased due to weathering degradation, and the mechanical property of polymer modified cement gradually became brittle. In all the test pieces, after the accelerated deterioration tests the rate of change in tensile strength and elongation tended to increase as P/C was higher. Among all these test conditions, the change of mechanical properties of the test piece exposed under hot water degradation was especially remarkable. The strength of the test piece exposed to the hot water degradation test appeared to be due to the increased promotion of the hydration of cement. This, it seems, led to the formation of a cement material with an especially brittle mechanical property.

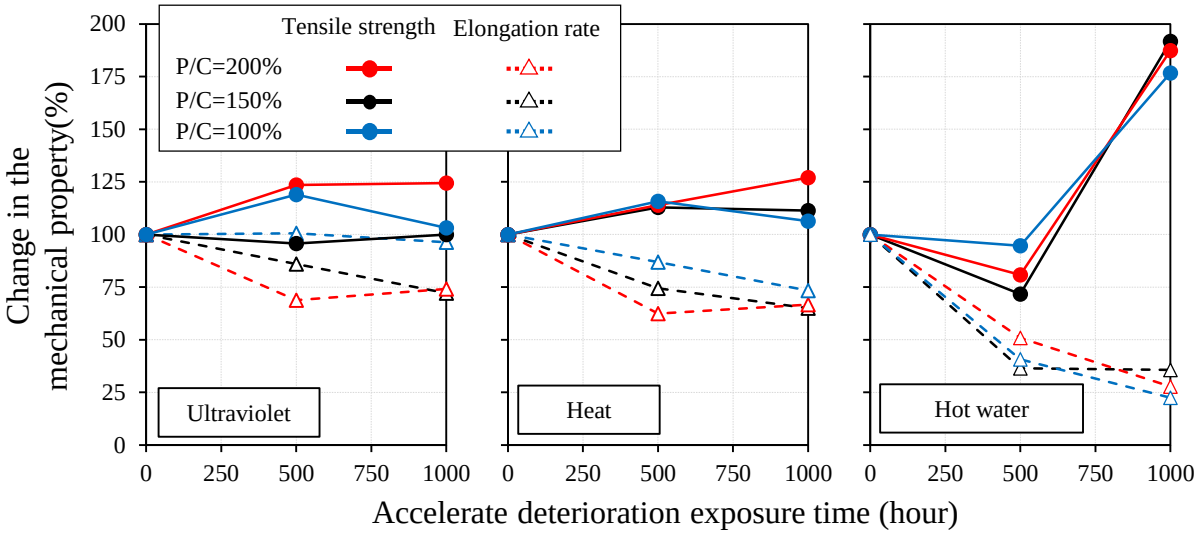

Figure 3 : Change in the mechanical properties of the polymer modified cement due to the accelerated deterioration test

3.2 Active thermography test result

Fig. 4 shows the active thermography test results of the test pieces of P/C = 150 %. The rate of changes in surface temperature during heating decreased as the degradation period increased under all accelerated degradation conditions. Here, the difference of the rate of increase in surface temperature before and after the deterioration test was defined as ΔT.

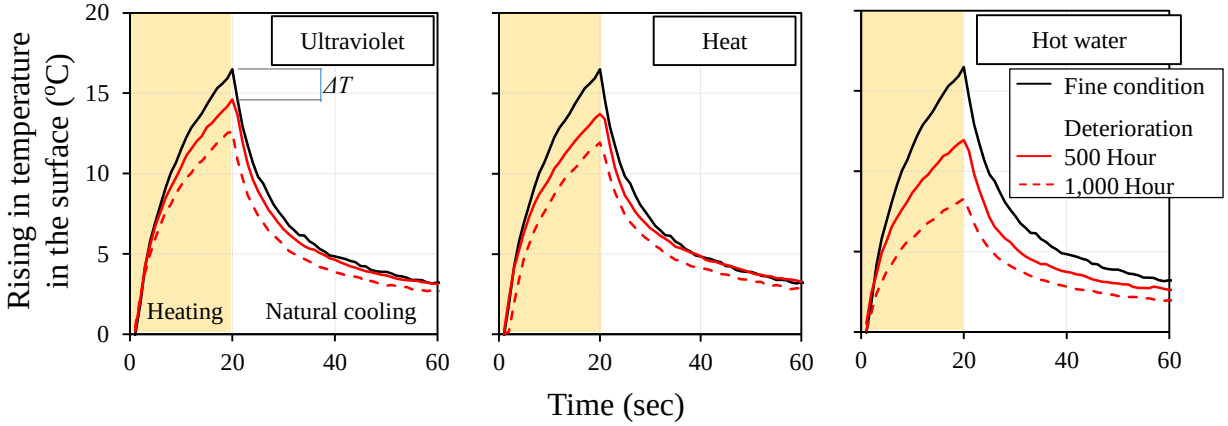

Figure 4 : Changes in surface temperature during heating of specimens exposed to accelerate deterioration condition (P/C=150 %)

Fig. 5 shows the value of ΔT for each degradation test condition. The changes in surface temperature during heating decreased with the progress of deterioration, and the higher the P/C, the lower the temperature and the lower the value of ΔT. In general, dark-color with low reflectance tend to absorb heat and become high temperature. However, the rate of change in temperature during heating decreased despite of the decrease in the reflectivity of the test pieces with deterioration test. It is assumed that the effect of the exposure of cement and aggregate, whose thermal conductivity is much higher than the polymer, is greater than the effect of changes in reflectivity. This result suggests that the measured changes of thermal characteristics recorded by thermography, are not merely the effect of the discoloration of the polymer modified cement waterproofing membrane, but rather a measure of the deterioration of the components constituting the polymer cement.

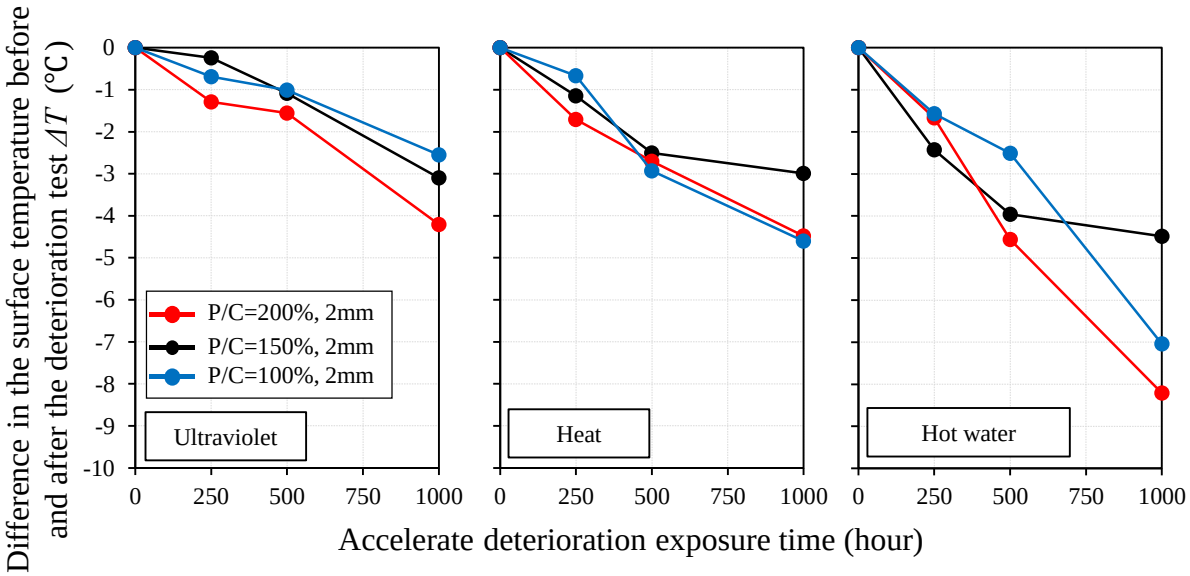

Figure 5 : Difference in the surface temperature before and after the deterioration test

The relationship between the change in the mechanical properties and the value of ΔT is shown in Fig. 6. Although the relationship between elongation rate and ΔT is relatively good, there is great variations in the tensile strength and ΔT. In particular, the greatest deviated value was found in the most deteriorated test pieces subjected to the heat and motion condition. In the deterioration condition of heat and moisture, the deviation seems due to the effect of the promotion of the hydration of cement components in addition to the degradation of polymer components. In addition, the loss of polymer components and numerous small cracks are also observed. This seems to indicate a brittle fracture behaviour similar to cement material caused by the progress of hydration of cement. However, the effect of progress of the hydration of cement is negligible on the thermal properties of polymer cement. As mentioned earlier, the effect of deterioration of the glossiness of the surface due to degradation on ΔT is smaller than the effect of deterioration of the polymer component for changing of thermal conductivity. All this suggests the possibility of estimating the rate of degradation of polymer cement by active thermography.

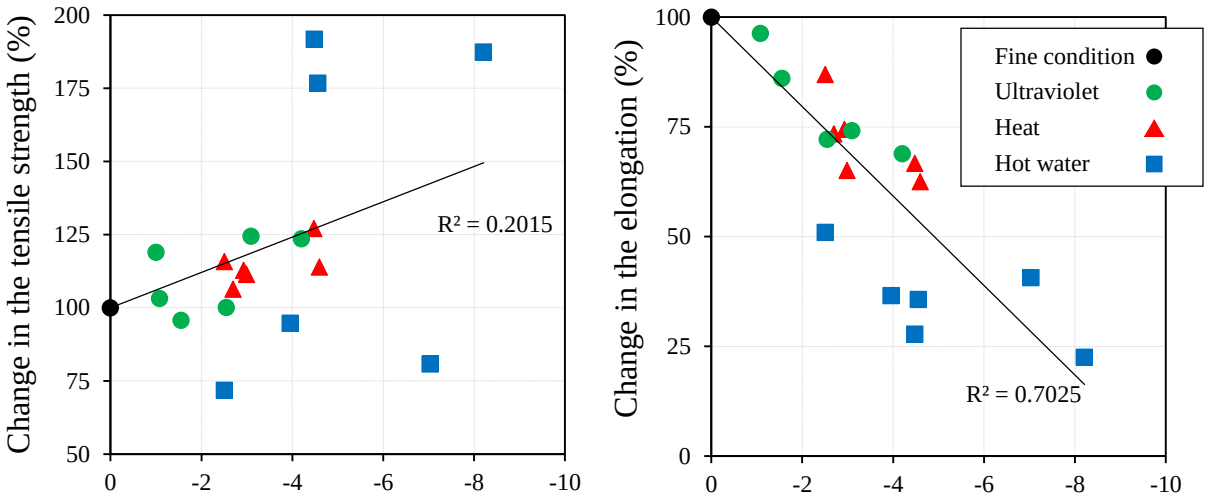

Figure 6 : The relationship between the elongation rate and the difference of surface temperature of ΔT

4. Conclusion

As the degradation of the polymer modified cement test pieces progressed, the elongation rate decreased gradually, and the tensile strength tended to increase.
The higher the P/C test piece, the higher the temperature of the surface during heating. Degradation caused decomposition and discoloration of polymer components. And, the glossiness of the surface was lowered because the cement or aggregate were exposed and the surface became uneven. However, the rate of increase in surface temperature of the deteriorated test piece with weathering became smaller. This result implies that the change in thermal properties due to deterioration of polymer modified cement is more significant than the effect of merely the changes on the surface.
The active thermography method can possibly be used to estimate the reduction of the elongation performance of polymer modified cement waterproofing membrane caused by weathering of polymer component.

References

[1] Naoki Matsuno, Follow-up capability for the substrate cracking and fatigue test results of Polymer-modified cement waterproofing membrane after accelerated deterioration, Summaries of technical papers of Annual Meeting Architectural Institute of Japan, pp863-864, 2005
[2] Architectural Institute of Japan, Guideline for Polymer-modified Cement Waterproofing Membrane Work, Vol.1, 20064
[3] Masashi Ishikawa, Hatta Hiroshi, Habuka Yoshio, Fukui Ryo and Utsunomiya Shin, Detecting deeper defects using pulse phase thermography, Infrared Physics & Technology, Vol.61, pp.216-223, 2013

SynerCrete'18 International Conference on Interdisciplinary Approaches
for Cement-based Materials and Structural Concrete
24-26 October 2018, Funchal, Madeira Island, Portugal

EVALUATION OF THE MATERIAL EMBEDDED IN CONCRETE BY ULTRASONIC AND GPR IMAGES

Sofia Aparicio [(1)], José Vicente Fuente [(2)], Dalmay Lluveras [(1)], Miguel A.G. Izquierdo [(3)], Margarita Gonzáles Hernández [(1)], José Javier Anaya Velayos [(1)]

(1) Instituto de Tecnologías Físicas y de la Información "Leonardo Torres Quevedo", ITEFI (CSIC), Madrid, Spain
(2) Geozone Asesores SL, Paterna, Valencia, Spain
(3) ETSI de Telecomunicación (UPM), Madrid, Spain

Abstract
The evaluation of cementitious materials by images from non-destructive techniques has gained prominence during the last years. Ultrasonic Tomography and Ground Penetrating Radar are two non-destructive techniques that are particularly well suited for the inspection of cementitious structures and materials using ultrasonic and electromagnetic waves, respectively. In this paper, these two techniques were used to generate images for the identification of embedded objects in concrete specimens.
A set of concrete specimens were manufactured in which cylindrical bars and pipes of different materials have been embedded, covering a wide range of acoustic and electromagnetic impedances representative of the most common materials found in concrete. For that purpose, three different types of inclusions were inserted in the concrete specimens: PVC tubes, and aluminium and steel tendons.
The experimental ultrasonic images have been obtained using a portable tomographic inspection system, which has the advantage of needing only two ultrasonic transducers to carry out the inspections. The same mechanical system was used with a commercial GPR using a 2 GHz antenna to generate the GPR images. The positions and diameters of the inclusions have been visualized using tomographic images and the results are discussed.

1. Introduction

In recent years, ultrasonic imaging, and tomographic imaging in particular, has gained increasing prominence in the evaluation of cementitious materials by using different

techniques, equipment, frequencies, and wave types [1]. Tomographic images allow the visualization of the cross section of structures, thus enabling better detection of defects, cracks or discontinuities in the material [2-3]. A tomographic image is obtained from projections through the object. These projections consist of velocity or attenuation measurements of ultrasonic pulses transmitted through the specimen. The most popular methods of tomographic reconstruction are the algebraic techniques, such as the algebraic reconstruction technique (ART) and the simultaneous iteration technique (SIRT), which are based on the resolution of the system of linear equations generated by the projections [4].
The techniques based on the use of the georadar, also known as GPR (Ground Penetrating Radar) are based on the use of the pulse-echo technique using electromagnetic waves. The potential of this technique to generate maps of fractures and discontinuities is well known in the literature [5-6]. These maps can allow early detection of internal fractures and other defects such as inclusions or make a detailed map of the extent and orientation of the fracture in the structure, [7-8].
This study presents the results of ultrasonic tomographic and GPR images used to identify embedded objects in concrete specimens. Several concrete specimens were manufactured in which cylindrical bars and pipes of different materials have been embedded: PVC tubes, and aluminium and steel bars. The results of ultrasonic tomographic reconstruction are based on attenuation measures to obtain information about the positions and sizes of inclusions in concrete specimens. The tomographic images are obtained by an immersion ultrasonic tomography system that operates in transmission mode [9], which has the advantage of needing only two ultrasonic sensors. The same system was used to obtain the radargrams of concrete specimens coupling the antenna to the mechanical system of ultrasound tomography.

2. Experimental setup

The main objective of this work is by means of tomographic and GPR images identify embedded objects in concrete specimens. In the following sections, both inspection systems are presented as well as the set of concrete specimens used in the inspections.

2.1 Ultrasonic tomography

A portable inspection system for immersion ultrasonic tomography was developed by the authors [9]. The system is easy to transport and allows in situ ultrasonic inspections in transmission for specimens with cylindrical symmetry or cores, see Fig. 1. A detailed description can be found in [10].
The procedure used to generate tomographic images consists of three movements. The first movement is a vertical displacement along the height of the specimen, carried out with a step 2 mm in height. The second movement establishes the relative position between the emitter and the receiver. In this case, the inspection angle is 220º and, accordingly, the restriction angle is 70º. The last movement is the rotation of the specimen, which is equivalent to the motion of the emitter transducer. The programmed movement is equivalent to having 100 emission positions. Therefore, each revolution of the specimen generates A-scans coming from 100 emitter positions times 220 receiver positions, resulting in 100 B-scan images of 220 signals taken at 2 mm each, or 22000 A-scans. The diameter between the transducers is 242 mm.

Figure 1: Portable inspection system for immersion ultrasonic tomography.

SENDAS equipment system (CSIC; Madrid, Spain) is used for the emission, amplification, and reception of signals [11]. Two v413 500 kHz wideband transducers (Panametrics, Waltham, MA, USA) are used. A 1 μs and 400 V rectangular pulse is applied as excitation signal, and a variable gain receiver amplifier of between 20 and 60 dB is used. The sampling frequency is 10 MHz. The reconstruction algorithm used to generate the tomographic images is SIRT. This algorithm allows to obtain better solutions at the expense of a lower convergence speed [10].

2.2 GPR

For the GPR measurement the Subsurface Interface Radar SIR 3000 device, of GSSI, was used with the GSSI PALM antenna of 2GHz that reaches tightly spaces as corners and rounded objects. The tests were made using antenna configurations in reflection mode. The GPR techniques measures the time of flight of electromagnetic waves which are reflected and backscattered at interfaces with different dielectric permittivity. The antenna was placed in the mechanical structure of the ultrasonic inspection system. The inspections were made in three different zones of concrete specimens, inferior, medium and upper that corresponds to 0, 1 and 3 inclusions, Fig. 2.

2.3 Concrete specimens

Concrete specimens with different sizes and inclusion materials (aluminium, steel tendon, and PVC tubes) were made. Three inclusions of same diameter (∅20 mm), except the tendons (∅14 mm), and different heights, 200mm, 150mm and 100mm, were placed in each mold before fabrication (Fig 2). The PVC tubes were sealed to prevent their being filled with concrete during the manufacturing process. Three cylindrical specimens (∅150 mm x 300 mm) were moulded according to the UNE 12390-2 and were kept in a laboratory environment for 1 day. After that, the specimens were removed from the molds and stored in water over a 28 days curing process until the inspections were carried out.

Table 1: Concrete mix proportion.

Material	**Cement (kg/m^3)**	**Sand (kg/m^3)**	**Aggregates (kg/m^3)**	**Water (kg/m^3)**	**Superplasticizers (% of cement weight)**
amount	433	983	1000	177.53	1

The materials used to make the concrete specimens were Portland white cement type CEM I 52.5R, normal sand, crushed limestone aggregates, and ViscoCrete 5980 superplasticizer to improve workability. Table 1 shows the mix proportion.

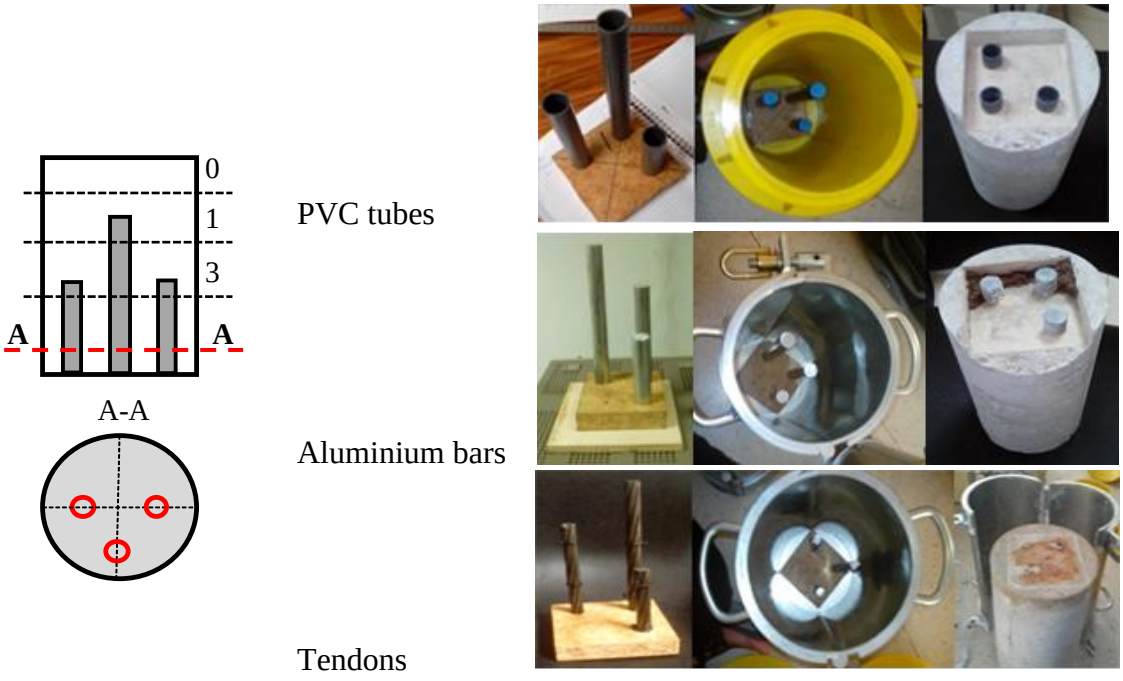

Figure 2: Cylindrical concrete specimens to inspect.

3. Experimental Results

Figure 3 shows the experimental ultrasonic tomography reconstruction images of the concrete specimens. All the images are 80×80 pixels in size. Each side of the image is physically equivalent to the external diameter of the ring of the inspection system, which means that each pixel represents a 3 mm length. Thus, the concrete specimens, as shown in the reconstructed tomographic images, are 50 pixels in diameter. A blue external ring can also be observed in the experimental reconstruction images. This ring is composed by the multiple echoes produced in the aluminium ring of the inspection system. The bars/tubes inserted in concrete modify the ultrasonic image in different ways depending on the material; in all cases it is possible to correctly locate different inclusions from the reconstruction tomographic images. Since the material of the inclusions was known it is possible to determine their size [10].

From the radargrams we have built three tomograms using the usual geometric transformation than correspond to three zones previously mentioned of each concrete specimen, Fig. 4. The inclusions at each zone are identified for all embedded materials. The PVC tubes show lower contrast that aluminium and steel tendons. Therefore, metallic objects are very well identified using GPR techniques, but other materials are not so well detected.

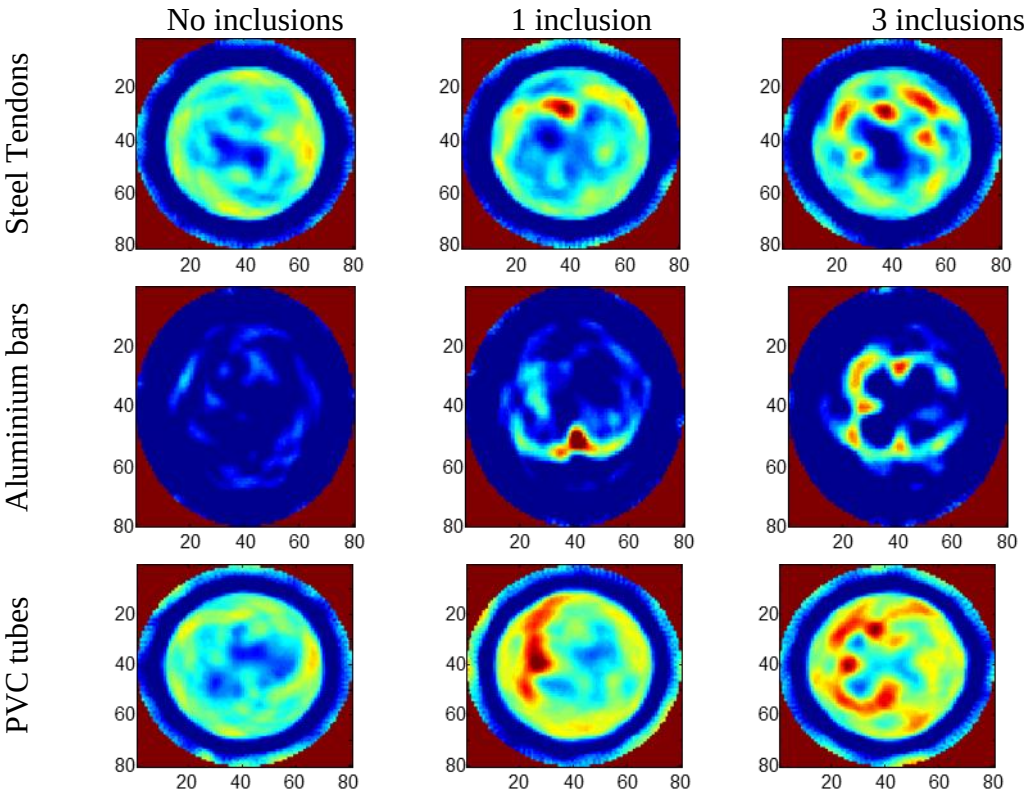

Figure 3: Ultrasonic tomographic reconstruction images of the concrete specimens.

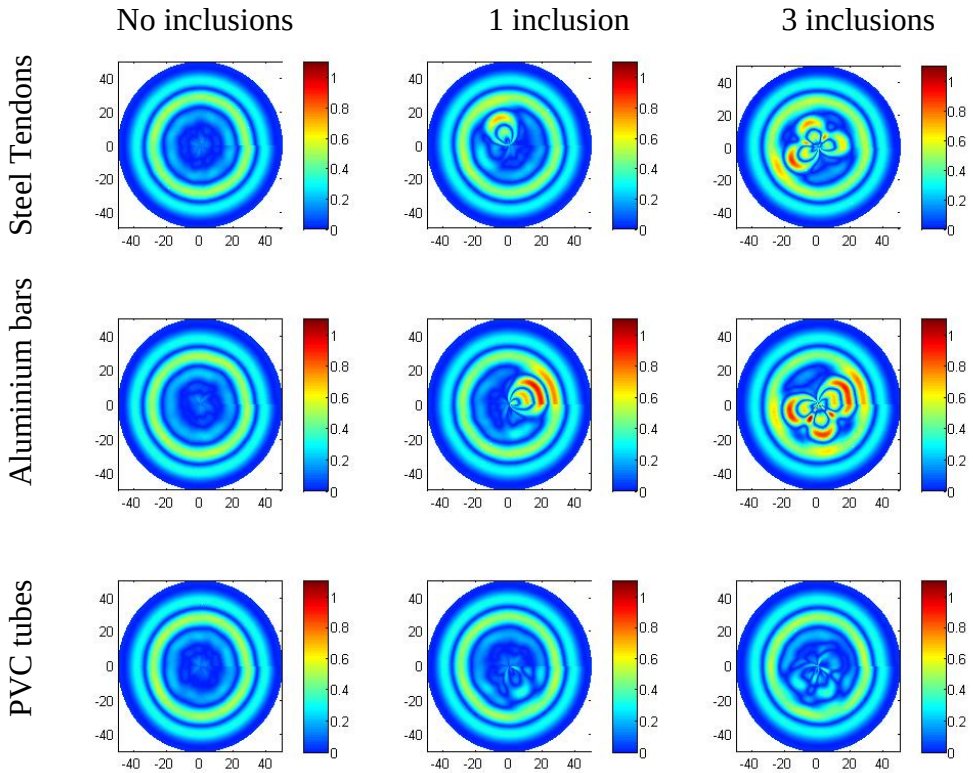

Figure 4: Tomographic images from GPR of the concrete specimens.

4. Conclusions

This study explores the feasibility of using ultrasonic tomographic and georadar images to detect and estimate the most common materials that are embedded in concrete, reinforcements and natural and artificial voids. A limited set of concrete specimens has been made in which bars/tubes of steel, PVC and aluminium have been embedded to analyse the effect of size, material and multiplicity of the inclusions.
The embedded inclusions of different materials have been identified by tomographic and GPR images. Both techniques are complementary. Ultrasonic tomography is better to detect discontinuities of the material. Knowing previously the position and material of the inclusion, the ultrasonic tomography allowed to determine its size very well. GPR technique is better to detect metallic inclusions but it is not well suited to detect their size. The fusion of GPR and ultrasonic tomographic images could to identify material, size and position of the inclusions.

Acknowledgements
The Spanish Ministry of Economy, Industry and Competitiveness supported this research under grants numbers BIA2016-77992-R (AEI/FEDER, UE) and RTC-2015-3185-4 (MAPMIT), co-funded by the European Union through FEDER funds under the objective of promoting the technological development, innovation and high quality research.

References

[1] Schabowicz, K., Ultrasonic tomography – The latest non-destructive technique for testing concrete members – Description, test methodology, application example, Arch Civil Mech Eng 14 (2014), 295-303
[2] Haach, V. G., Ramirez, F. C., Qualitative assessment of concrete by ultrasound tomography, Constr Build Mater 119 (2016), 61-70
[3] Choi, H. et al, NDE Application of Ultrasonic Tomography to a Full-Scale Concrete Structure, Ultrason Ferroelectrics Freq Control IEEE Trans 62 (2015), 1076-1085
[4] Kaks, A. C., Slaney, M. G., Principles of Computerized Tomographic Imaging, New York: Society of Industrial and Applied Mathematics, 2001
[5] Loperte, A. et al, Ground Penetrating Radar in Dam Monitoring: The Test Case of Acerenza (Southern Italy), Int J Geophys 2011 (2011), 1-9
[6] Yehia, S. et al, Investigation of concrete mix variations and environmental conditions on defect detection ability using GPR, NDT & E Int 65 (2014), 35-46
[7] Arosio, D. et al, Quality control of stone blocks during quarrying activities. 14th International Conference on Ground Penetrating Radar (2012), 822-816
[8] Deparis, J. et al, On the potential of ground penetrating radar to help rock fall hazard assessment: A case study of a limestone slab, Gorges de la Bourne (French Alps), Eng Geol 94 (2007), 89-102
[9] Molero, M. et al, Portable non-destructive testing system for cementitious samples with axial symmetry by using ultrasonic imaging and associated procedure. Patent PCT/ES2011/070499
[10] Lluveras, D. et al, Ultrasound transmission tomography for detecting and measuring cylindrical objects embedded in concrete, Sensors 17 (2017), 1085
[11] Fritsch, C. et al, SENDAS: An approach to modular digital processing for automated NDE, Proc. of 2nd Conference on NDE Applied to Process Control on Composite Fabrication, St. Louis, USA (1996)

SynerCrete'18 International Conference on Interdisciplinary Approaches
for Cement-based Materials and Structural Concrete
24-26 October 2018, Funchal, Madeira Island, Portugal

INCREASE CONCRETE QUALITY DURING DESIGN AND EXECUTION PHASE

Stefan Scheuchelbauer [(1)], Massimo Maffezzoli [(1)], Alexander Reinisch [(1)]

(1) Doka GmbH, Amstetten, Austria

Abstract
Amidst the different options in concrete construction, there is one goal at the top of the list: producing a concrete structure faster/better/cheaper. Although the objective is formulated with utmost simplicity, the solutions for getting there are no less challenging.
The combination of formwork experience and concrete expertise of Doka allows the customer a 'scenario gaming' in the design phase of a construction project. During execution phase the 'Concremote Value Engineering Methodology' offers the possibility to use the most economic concrete mixture and to monitor the evolution of the temperature gradients in the concrete. The resulting benefits are a higher productivity during construction, higher concrete quality and financial savings during execution and the service life of a concrete structure.

1. Introduction

The durability and service life of a concrete structure is designed in an early stage of the planning phase. In order to achieve the planned target of concrete quality, monitoring during execution is one of the keys of quality management. For instance, in case of mass concrete structures one of the most important aspects is the monitoring of the temperature gradient and appropriate actions on site to avoid cracking and simply guarantee the concrete quality already during construction.
The ambition is to emphasize the importance how to optimize the combination of formwork expertise with superior material technology enabling a well-defined construction sequence between all relevant parties resulting in increased quality management and enhanced durability of the designated concrete structure.

2. Understanding the building material concrete

Already in the project tendering and work preparation phase, the early strength development of individual concrete mixtures with different performance will be simulated with respective calibration and temperature assumptions. Therefore, the maturity method (e. g. De Vree [1] or Saul [2]) will be applied. Maturity methods are described in different standards (such as ASTM C1074 [3]) and the topic of various research papers ([4] [5]). Necessarily, the intended concrete formulations can be re-adjusted.
For this purpose, the early strength development of the intended concrete type is used as a performance indicator that can be planned, measured and controlled with Concremote (= real-time concrete monitoring system). Doka Concremote is used as a method to optimize the construction process and thus significantly increase productivity on the job site resulting in secured cycle time and optimized concrete costs in the execution phase (= 'Concremote Value Engineering Methodology', Fig. 1).

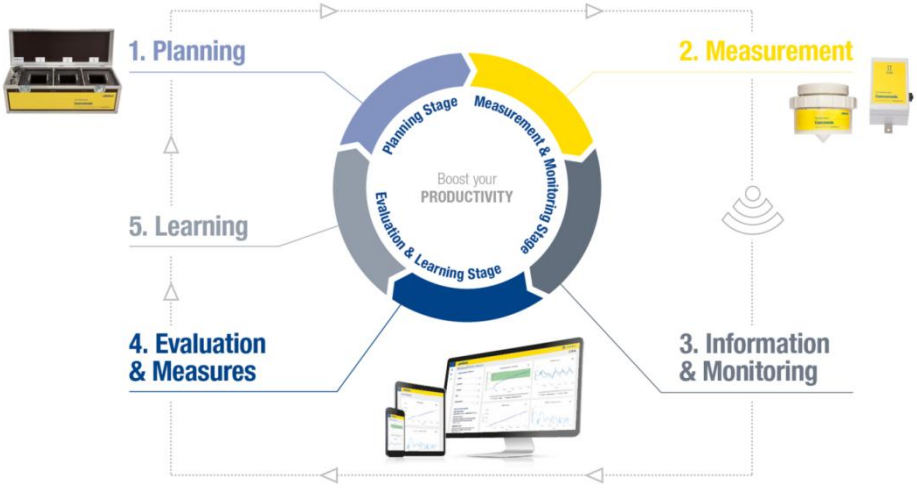

Figure 1: The Concremote Value Engineering Methodology.

Ideally a construction company defines a concrete mix portfolio for example to consider ambient temperature changes (e.g. winter, summer, …) and other influences already before construction. In order to be able to create a portfolio of concrete mix designs a final design strength of specific structure member has to be defined by design engineers. To meet the requirements a wide set of scenarios for possible concrete mix designs are proposed for specific concrete structure ('scenario gaming').
Once the optimized concrete mix portfolio is defined the project can go into the execution phase (transfer to real-time). Before the start of the construction phase each concrete mix design has to be calibrated in order to define correlation between compressive strength and maturity.
In the construction phase, the monitoring of the temperature and strength development by Concremote takes place in each critical concreting section. The reusable devices will be installed before pouring and the result will be monitored with the Concremote web portal (Fig. 2).

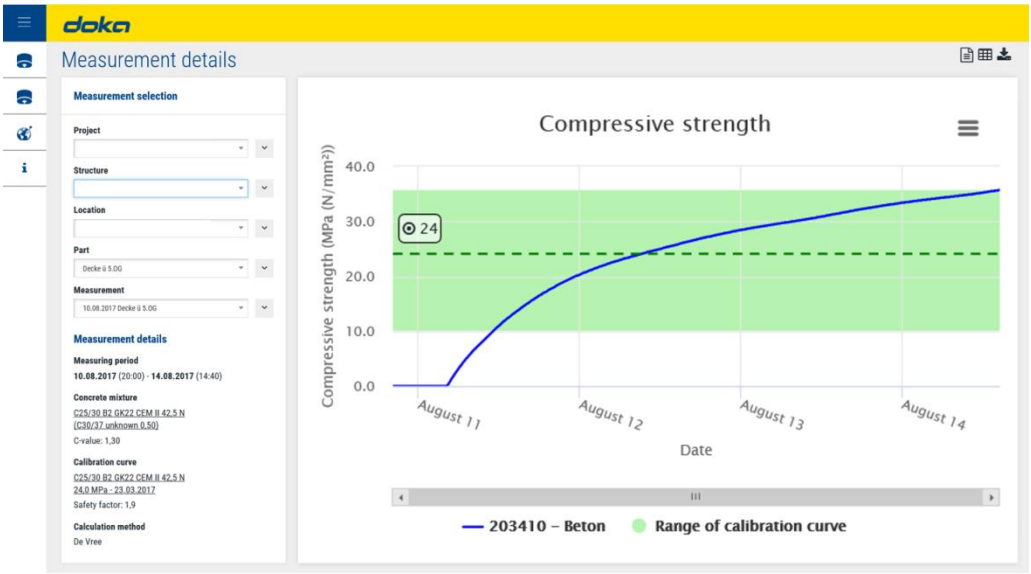

Figure 2: Concremote web portal – Real-time information (e. g. strength).

To enhance the quality of the concrete the curing is monitored and documented. As soon as a certain target value of compressive strength is reached formwork removal takes place. According to that, cycle times and commissioning quantities are reduced and the most optimized curing is obtained at the same time.
Beside the benefits during design and construction phase, Concremote provides easy access for all stakeholders to the measurement data and a digital backup of all measured data.
In addition to the benefits of the Concremote Value Engineering Methodology, the combination with Doka´s formwork expertise will positively impact the durability and the service life of the designated concrete construction.

3. Understanding the formwork design

Understanding, the building and job site requirements as well as the clients' intention of the construction method, is one of the main subjects to discuss before talking about an optimized formwork solution. Different to the common procedure on standard projects, the construction method and the corresponding formwork solution for concrete constructions shall be defined already in the design phase of a project in order to optimize the processes during execution phase.
The optimized formwork solution – for example at a dam construction – can be influenced by the geology, the geometry of the structure, the construction method as well as the construction schedule (Fig. 3). Vice versa an optimized formwork design can influence the geometry of the structure (e.g. increased block size resulting in less construction and block joints), improve the construction method and speed up the construction schedule resulting in increased productivity and ideally reduced construction costs.

Figure 3: Bykle Dam, Norway – influence of geology and geometry.

4. Understanding jobsite requirements and construction methods

At the beginning of a planning phase of a project we need to understand two main subjects:

- What is being built?
- How is it being built?

4.1 Understanding – What is being built?

Already in the project tendering and work preparation phase, the early strength development of individual concrete mixtures with different performance will be simulated with respective calibration and temperature assumptions with the real-time monitoring system Concremote (= 'Concremote Value Engineering Methodology'). A temperature simulation of the critical structural members shows the temperature gradient of various points in the current pouring section and also the influence to the following building parts (= 'scenario gaming').

In the construction phase, the monitoring of the temperature and strength development by Concremote sensors takes place in each critical concreting section. A systematic analysis shows whether the selected concrete mixture matches the requirements or any adjustments has to be made. This ensures compliance with the desired cycle time and concrete costs.

Based on the project's unique requirements ("what is being built", Fig. 4) a tailor-made formwork solution in combination with an optimized construction method between all main structures (e.g. dams) shall be the target of the communication between 'formwork solution provider' and the 'contractor'.

Figure 4: Influencers for optimized formwork solution (what is being built?).

4.2 Understand – How is it being built?

Understanding the building and job site requirements (Fig. 5) is the basis to achieve an optimized working solution. A formwork solution can be influenced by the geometry of the structure, the construction method as well as the construction schedule. Vice versa a formwork design can influence the geometry of the structure (increased block size) resulting in less construction and block joints, improve the construction method and construction schedule to increase productivity and reduce the construction costs.

Just the 'big picture', considering the impact from the formwork and the superior material technology, is providing the possibility to optimize the construction method resulting in increased concrete quality in concrete constructions.

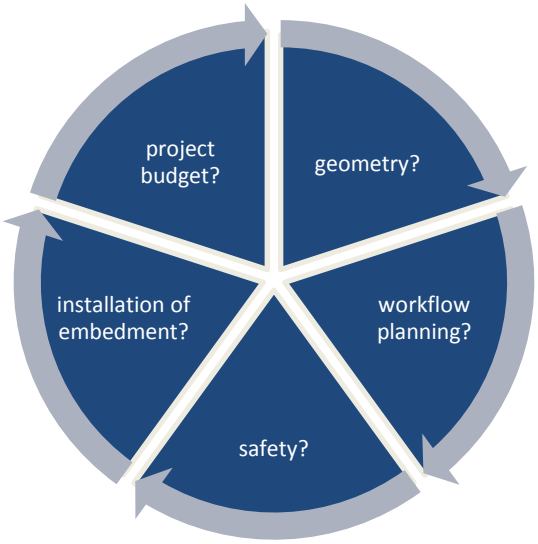

Figure 5: Influencers for optimized formwork solution (how is being built?).

5. What does it mean in practice? (project procedure)

The project success does not only depend on selecting the right material. Guidance for the 'big picture' (= products, concrete, logistics and on-site services) from an expert (consultant) can help to enable target oriented processes and assure to meet the demanded result. Consultancy from the very beginning produces a comprehensive solution for the entire production cycle of the concrete structure.
Professional coordination (Project Management) in all involved processes and along the entire project – for example at ESO Supernova (Fig. 6) – is the foundation of having an influence on the concrete result. Just the sum of all involved processes and the learning of the monitoring is creating and assuring the final concrete result.
To sum up, the 'big picture', considering the influences from the concrete and concrete temperature & strength development in combination with an effective and efficient formwork solution, is providing the possibility to optimize the construction method resulting in increased concrete quality in constructions.

Figure 6: ESO Supernova, Germany.

References

[1] De Vree, R.T. and Tegelaar, R.A., Gewichtete Reife des Betons – Kontinuierliche, zerstörungsfreie Ermittlung der Betondruckfestigkeit, Beton 48(11) (1998), 674-678
[2] Saul, A., Principles underlying the steam curing of concrete at atmospheric pressure, Magazine of Concrete Research 6 (1951), 127-140
[3] ASTM C1074-17, Standard Practice for Estimating Concrete Strength by the Maturity Method, ASTM International, West Conshohocken, USA, 2017
[4] Reinisch, A. et al, Confirmation of real time concrete strength in construction projects, Tagungsband 11th CCC Congress Hainburg (2015)
[5] Zitzenbacher, A. et al, Increase concrete quality in dam construction during design and execution phase, ICOLD 2018 Vienna (2018)

SynerCrete'18 International Conference on Interdisciplinary Approaches
for Cement-based Materials and Structural Concrete
24-26 October 2018, Funchal, Madeira Island, Portugal

INSPECTION AND MAINTENANCE OF CONCRETE BRIDGES: INVESTIGATION OF MOST SIGNIFICANT DAMAGE MECHANISMS VS. LOCATIONS

R.M. Chandima Ratnayake [(1)], Yousef Saad [(1)], Kamshan Karunaharan [(1)], Samindi M.K. Samarakoon [(1)]

(1) Department of Mechanical Structural and Material Sciences, University of Stavanger, Stavanger, Norway

Abstract

This manuscript demonstrates a methodology that has been developed to support bridge inspection planning. The methodology has been demonstrated using a case study performed to investigate significant damage mechanisms and locations on concrete bridges. The case study and analysis have been carried out using the concrete bridge inspection data available in the Norwegian Public Roads Administration (NPRA) database. This manuscript presents the significant damage mechanisms that were identified, the frequency of occurrence of the identified major damage mechanisms, and the typical locations of each type of damage. The developed guideline has been verified using the actual inspection data of a randomly selected reinforced concrete bridge.

1. Introduction

Reinforced concrete bridges are inspected to detect harmful deterioration and other types of deficiencies, as well as to reduce unnecessary maintenance costs. In general, inspection and maintenance procedures are not consistent [1] (e.g. the Norwegian Public Roads Administration (NPRA) handbook [2] provides guidelines and methods for the inspection and maintenance activities of bridges in Norway). Hence, it is important to develop consistent approaches, to perform optimal inspection and maintenance.

Visual inspection is the starting point of any inspection procedure, which enables the prioritization of areas for detailed inspection. In this context, identification of the potential damage mechanisms in a structure vs. locations is vital for developing optimal inspection procedures/guidelines [3]. The damage in concrete bridges is mainly due to discoloring,

scaling, spalling (i.e. because of steel corrosion) and surface cracks. This damage occurs at different locations (i.e. the structural members/joints) of a concrete bridge. Therefore, it is important to figure out the most vulnerable locations prone to damage. Hence, the classification of concrete bridges into different groups that have similar characteristics is essential to enhance the inspection program. This paper discusses how to enhance the existing inspection NPRA guidelines by applying the group technology (GT) concept to bridges, to group those with similar characteristics and prioritize the damage locations.

2. Methodology

It is essential to have inspection guidelines to support inspection planners in developing an optimal inspection program. To develop inspection guidelines, it is vital to identify locations that experience the main degradation mechanisms. For a selected geographical region, it is possible to use the GT concept to group concrete bridges (i.e. bridges with similar characteristics) into families [4], based on type of supports (i.e. continuous, cantilever, simply supported), function and construction methodology (e.g. pre-stressed, in-situ, pre-cast, etc.). This study has selected 30% of the highest damage frequency of a particular damage mechanism (Note: this percentage shall be based on the inspection philosophy) as the cutoff level. Locations with a greater damage frequency than the cutoff frequency are recommended as locations that need to be prioritized in the inspection planning (i.e. as guidelines to support inspection-planning activities). A case study has been carried out to investigate the damage mechanisms vs. where they occur, using the historical inspection data available in the bridge inspection database (BIDB) at the NPRA. Fig. 1 illustrates the overall methodology that has been used to develop the inspection guidelines.

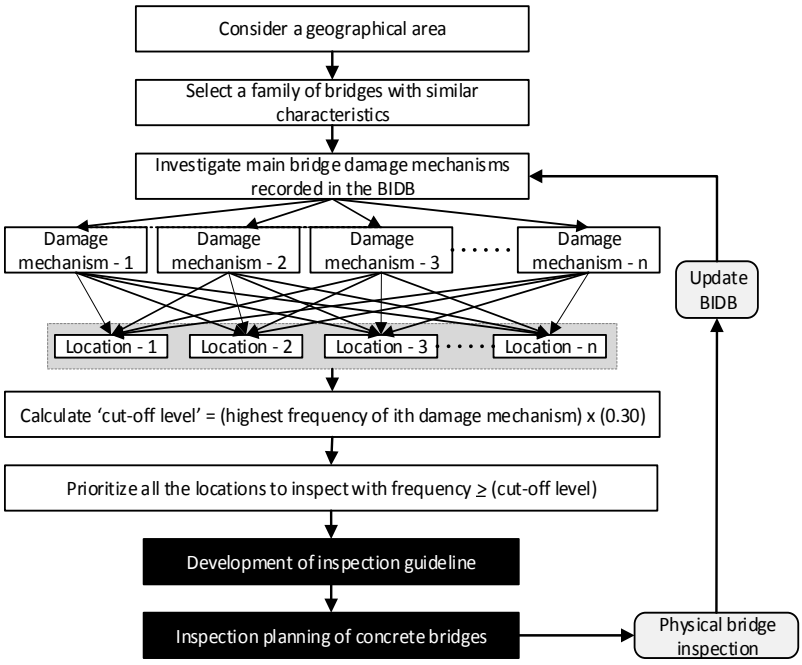

Figure 1: Development of an inspection guideline.

2.1 Development of inspection guidelines

It is important to identify the most common damage mechanisms, as well as damage mechanism vs. location, in order to develop inspection guidelines. The aforementioned enables damage mechanisms vs. most vulnerable locations to be investigated, in order to

prioritize inspection that will optimize inspection planning and the utilization of inspection task-related resources.

2.1.1 Damage analysis

Using the BIDB at the Norwegian Public Road Authority in Norway (NPRA) (i.e. *Staten Vegvesen*, in Norwegian), 34 bridges with similar characteristics (i.e. bridge family BFx) located in a particular geographical area (i.e. region code RGXA1) have been selected to investigate the most common damage mechanisms and the frequency and locations of the damage. Fig. 2 illustrates the bridge element details of a representative bridge in the selected bridge family [2].

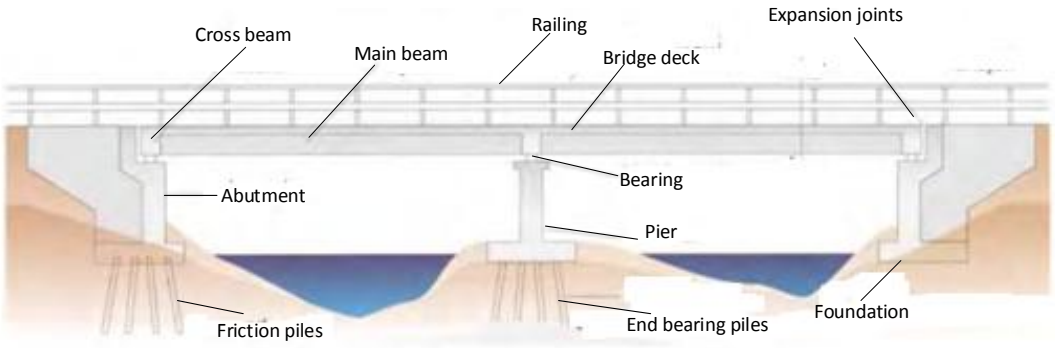

Figure 2: The typical elements of a bridge [2].

The results of the damage analysis of 34 bridges revealed 133 cracks; 53 areas of corrosions; 42 instances of discoloring; 85 incidences of scaling; and 67 leakages. Fig. 3a illustrates damage mechanism vs. frequency plot and Fig. 3b illustrates discoloring damage on concrete, which has not been taken into further analysis (i.e. due to less seriousness in relation to the structural damage) for developing inspection guidelines to carry out inspection prioritizations.

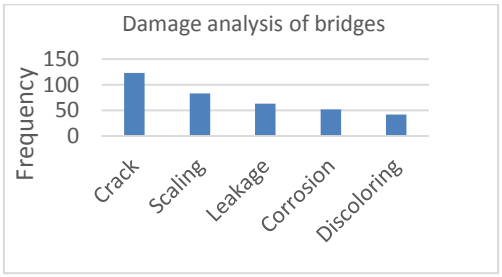

a. Damage vs. frequency

b. Discoloring

Figure 3: Damage mechanism analysis.

Fig. 4a illustrates an example of cracks appearing on a bridge element, while Fig. 4b illustrates the frequency of cracks vs. location. In this case, the cutoff limit is calculated as 13 x 0.3 ≈ 4. Fig. 4b reveals that most of the cracks have appeared (i.e. in relation to the cutoff limit 4) in piers, the main beam, abutments, parapet systems and expansion joints. Hence, it is possible to develop a guideline for inspection planning as follows: bridge elements such as piers, main beam, abutments, parapet systems and expansion joints shall be inspected to examine whether there are any cracks.

a. Cracks

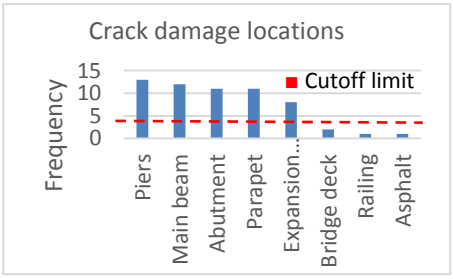

b. Crack location vs. frequency

Figure 4: Crack damage analysis.

Fig. 5a illustrates an example of scaling, and Fig. 5b illustrates the frequency of scaling damage vs. location. In this case, the cutoff limit is calculated as 13 x 0.3 ≈ 4. Fig. 5b reveals that most of the scaling damage has appeared (i.e. in relation to the cutoff limit 4) in the main beam, parapets, abutments, expansion joints, and piers. Hence, it is possible to develop a guideline for inspection planning as follows: bridge elements such as the main beam, parapets, abutments, expansion joints and piers shall be inspected to examine whether there is any scaling damage.

a. Scaling

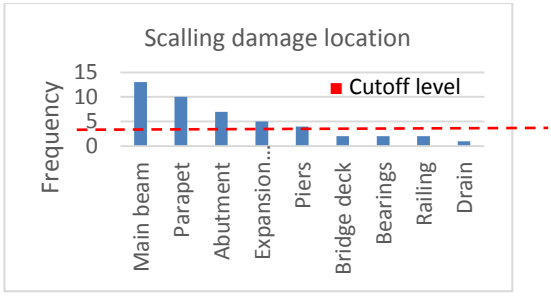

b. Location vs. scaling damage frequency

Figure 5: Scaling damage analysis.

Fig. 6a illustrates an example of leakage, while Fig. 6b illustrates the frequency of leakage damage vs. location. In this case, the cutoff limit is calculated as 17 x 0.3 ≈ 5. Fig. 6b reveals that most leakages have appeared (i.e. in relation to the cutoff limit 5) in expansion joints, abutments, the main beam, and the bridge deck. Hence, it is possible to develop a guideline for inspection planning as follows: bridge elements such as expansion joints, abutments, main beam, and bridge deck shall be inspected to examine whether there is any leakage damage.

a. Leakage

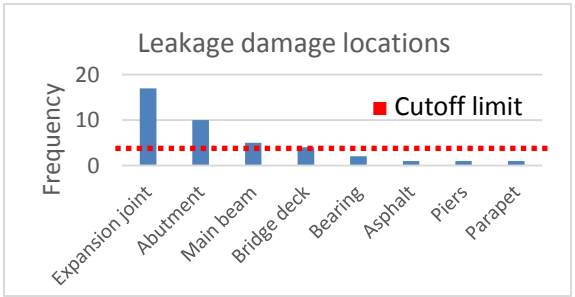

b. Location vs. leakage damage

Figure 6: Leakage damage analysis.

Fig. 7a illustrates an example of corrosion damage and Fig. 7b illustrates the frequency of corrosion damage vs. location. In this case, the cutoff limit is calculated as 11 x 0.3 ≈ 3.3. Fig. 7b reveals that most of the corrosion has appeared (i.e. in relation to the cutoff limit 3.3) in railings, bearings, piers, parapets and the main beam. Hence, it is possible to develop a guideline for inspection planning as follows: bridge elements such as railings, bearings, piers, parapets and main beam shall be inspected to examine whether there is any corrosion damage

a. Corrosion

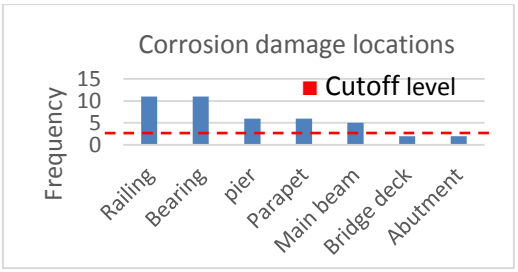

b. Location vs. corrosion damage

Figure 7: Corrosion damage analysis.

Tab. 1 illustrates the summary of the guidelines that have been developed, based on the damage analysis.

Table 1: Guidelines for concrete bridge inspection.

Region – RGXA; bridge family - BFx	
Damage mechanisms	**Guidelines for inspection planning**
Cracks	• Focus on piers, main beam, abutments, parapet systems and expansion joints
Scaling	• Focus on main beam, parapets, abutments, expansion joints, and piers
Leakage	• Focus on expansion joints, abutments, main beam, and bridge deck
Corrosion	• Focus on railings, bearings, piers, parapets and main beam

2.2. Verification study

In order to investigate the validity of the suggested guidelines, a verification study was performed, choosing a bridge at random. The chosen bridge is 207.1m long. It was built in 1967 with a remaining life of 49 years (i.e. built of reinforced concrete) and located over a fjord with seawater (i.e. exposed to chloride ingestion). Therefore, the focus was reinforcement corrosion and spalling. Furthermore, two other common types of damage, cracks and leakage, were taken into consideration. Based on the developed inspection planning guidelines, employing a 30% cutoff limit for corrosion, it is possible to conclude that bridge elements such as railings, bearings, piers, parapets and main beams should be inspected for corrosion. Similarly, bridge elements such as main beam, parapets, expansion joints and piers should be inspected for scaling. The focus locations for cracks should be on piers, main beam, abutments, parapet systems and expansion joints. Tab. 2 illustrates the results revealed by the actual inspections.

Table 2: Actual inspection results- H-0676 Hafrsfjord bridge.

Bridge	**Damage type and frequency**			
	Corrosion	**Scaling**	**Cracks**	**Leakage**
11-0676 - Hafrsfjord	8	8	5	0

Furthermore, we have established a bar chart that graphically illustrates the greatest occurrence of corrosion and scaling for 11-0676 Hafrsfjord.

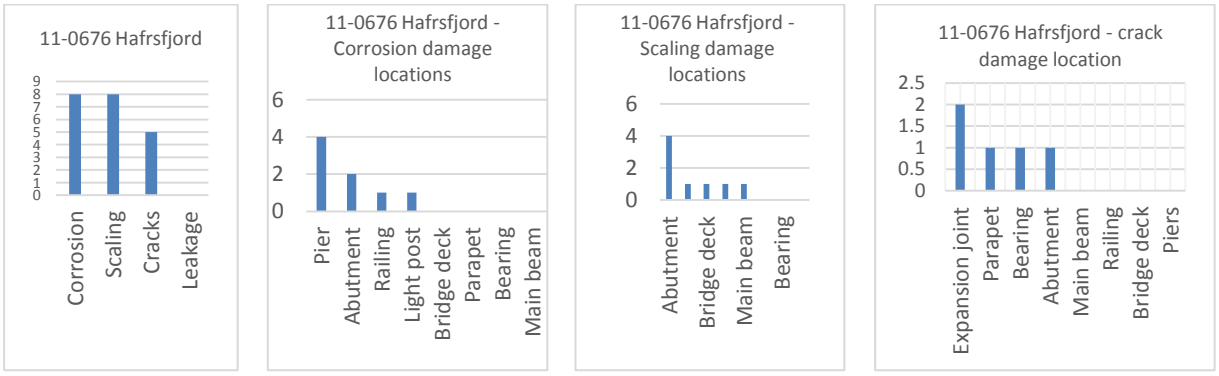

a. Mechanism b. Corrosion c. Scaling d. Cracks

Figure 8: Actual inspection results of '11-0676 – Hafrsfjord' bridge.

Although there are differences, the results (see Fig. 8) reveal that inspection guidelines developed at the 30% cutoff limit provide significantly accurate results.

3. Conclusion

The methodology and resulting guidelines presented in this manuscript are important when a new engineer (or inspection planner) starts inspection planning. It is possible to follow the same methodology and develop a set of guidelines for all the possible groups of bridge families. It is also possible to use the output of the damage analysis to develop a comprehensive risk based inspection (RBI) planning approach.

Future research shall be carried out to investigate the optimal cutoff level and to group bridges into families using the GT approach. Then, these studies shall be continued to develop an RBI planning approach.

References

[1] Vogel, T. and Schellenberg, K., Design for inspection of concrete bridges, Mater Corros 63 (12) (2012)

[2] SVV, Inspeksjonshåndbok for bruer, håndbook V441 (2014), https://www.vegvesen.no/_attachment/69833/binary/964063?fast_title=H%C3%A5ndbok+V441+Inspeksjonsh%C3%A5ndbok+for+bruer+%2836+MB%29.pdf, accessed on 16.05.2018

[3] Samarakoon, S. M. S. M. K. and Ratnayake, R. M. C., Risk-based in-service inspection framework for offshore concrete wind turbine structures and application of Fuzzy Inference System, paper number: OMAE2018-78264, Proceedings of 37th Int. Conf. on Ocean, Offshore and Arctic Engineering (OMAE2018) in Madrid, Spain (2018)

[4] Sacchetti, J. F. et al, A group technology based classification and coding system for reinforced concrete structures, Comput Aided Civ Inf 7 (4) (1992), 307-322

SynerCrete'18 International Conference on Interdisciplinary Approaches
for Cement-based Materials and Structural Concrete
24-26 October 2018, Funchal, Madeira Island, Portugal

OVERVIEW ON THE MULTI-DECADE DATABASE OF PORTUGUESE LARGE CONCRETE DAMS MONITORING DATA

António Tavares de Castro [(1)], José Barateiro [(1)], Carlos Serra [(1)]

(1) National Laboratory for Civil Engineering, Lisboa, Portugal

Abstract
Monitoring is a key activity to ensure the structural safety of dams and is used for detection of deterioration, including local degradation issues and more extensive deterioration scenarios, such as the development of internal expansion reactions which, in the worst case scenario, can lead to severe cracking and even to the abandonment of the dam.
This paper presents an overview of an information system that includes a monitoring database, which includes the records of the main actions (water level, air and water temperatures and temperature inside the concrete) and of the main structural responses (radial and tangential displacements measured in inverted plumb-lines and using geodetic techniques, displacements measured in rod extensometers and by precision levellings in target points, joint displacements measured in joint meters, bi- and tridimensional strain fields measured in sets of strainmeters). The hydraulic behaviour of the foundation is also monitored, including the measurement of water discharges along the drainage gallery and the water pressure in the foundation (uplift). The database has monitoring data since the construction period of each dam until this date through periodic readings over the years.
Different measurements in some dams, with and without identified deterioration processes, are presented and compared in order to showcase the importance of monitoring activities over the structures lifetime.

1. Introduction

The Portuguese Regulation on the Safety of Dams (RSB) [1] determines that the National Laboratory for Civil Engineering (LNEC) must create and maintain updated a digital archive of the monitoring data of the higher risk Portuguese large dams during their lifetime. Based in this determination, LNEC developed an information system that includes the referred database as well as several tools for the numerical and graphical presentation and for processing of all the data. According to this regulation, large dams are considered dams with maximum height larger than 15.0 m or dams that create a large reservoir (with volume larger than 100 000 m^3) [1].

The paper describes the main features of the information system and of the type of dams, devices and the multi-decade results available in the database. It also showcases two examples which represent an overview of the type of results and the comprehensiveness of the information system. The goal of this work is to present the importance of a comprehensive and systematic monitoring system for dam safety assessment, from the planning and installation of each device to the management and storage of the collected data over several decades.

2. Description of the information system and of the monitoring database

2.1 Importance of monitoring

In general, dam surveillance is the assessment of the performance, safety and operability of dam and reservoir [2], which includes monitoring of the dam, foundation and appurtenant structures, visual physical inspections and maintaining the operational facilities. Monitoring of the main actions and of the main structural effects is key for the safety assessment, not only in a short-term period but also for a long-term evaluation of, for example, deterioration scenarios [3]. Additionally, monitoring must result in the analysis and interpretation of the data and, in case of abnormal behaviour, in proper and timely decisions. According to [4], the main goals of monitoring are: i) checking the expected structural behaviour; ii) giving a warning of a potential problem ; iii) Aiding in the identification, definition and analysis of a problem ; and, iv) evaluating the proper remedial actions.

2.2 Type of monitoring devices and data and information system

According to the RSB [1], the type and number of devices and measured quantities is related to the type and height of the dam. Small dams require just the measurement reservoir's water level, of water discharge rates and water pressure in the interface between dam and rock foundation. Large dams, with height larger than 100 m, must have a more complete monitoring system which includes the records of the main actions: water level, air and water temperatures and temperature inside the concrete; and of the main structural responses: radial and tangential displacements measured in plumb-lines and by geodetic methods; displacements measured in rod extensometers and by precision level surveys in target points; joint displacements measured in jointmeters; bi- and tridimensional strain fields measured in sets of strainmeters. The hydraulic behaviour of the foundation is also monitored, including the measurement of water discharges along the drainage gallery and the water pressure in the foundation. RSB also defines the reading frequency for each type of structure and for each stage of the dam: during construction; during the first filling of the reservoir; and during the dam's exploitation.

The Portuguese information system, Gestbarragens [5] includes the results obtained from concrete dams of all types, like double curvature arch and gravity structures, including dams with more than 50 years and structures under construction. In the last years the database has been extended to include also monitoring data of embankment dams and some concrete bridges. Fig. 1 presents the evolution of the number of results included in the database throughout the years obtained from manual and automated monitoring systems and presents an example of a time-series radial and tangential displacement in an inverted plumb-line base of Alto Rabagão dam. The use of automated monitoring systems since 2000 significantly increased the amount of data in the information system.

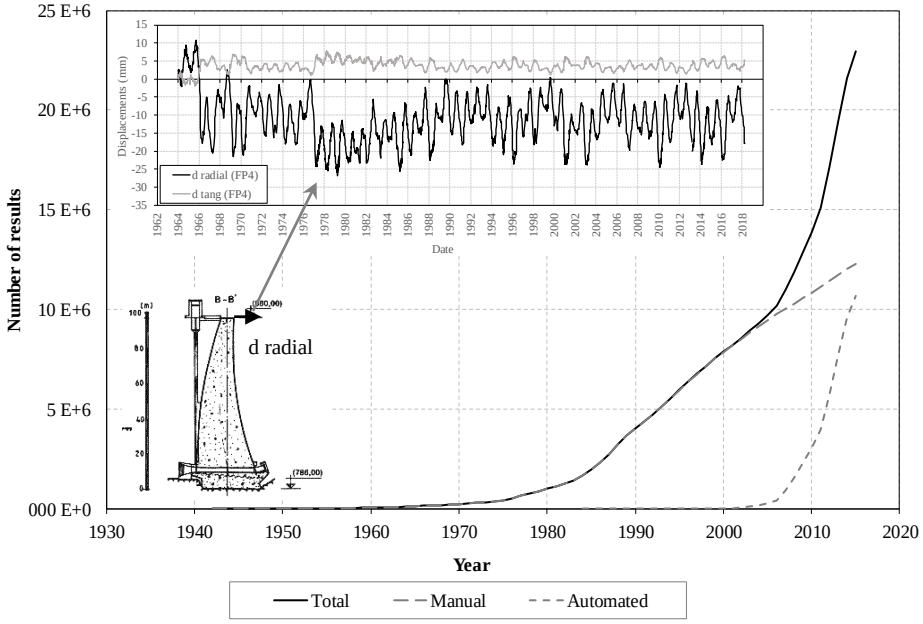

Figure 1: Evolution of the number of total results available in the database collected throughout the years obtained from manual and automated monitoring systems. Example of the development of a radial displacement (d_{radial}) in Alto Rabagão dam.

3. Alto Lindoso and Alto Ceira dams

3.1 Brief description of the dams

In order to illustrate the type of information provided by the monitoring systems, two examples are presented. The first example is the Alto Lindoso dam, a double curvature arch dam with an height of 110,0 m above the rock mass foundation, a crest development of 296,8 m and a crest thickness of 4,0 m [6]. The Alto Lindoso dam's body cast ended in July, 1990 and the first filling started in January, 1992 after the forced cooling and the grout of the vertical contraction joints. Fig. 2 shows the elevation and a central cross section of Alto Lindoso dam. The other example is the Alto Ceira dam which was abandoned and demolished due to severe damage as a results of alkali-silica reactions [7]. This dam was a double curvature arch dam with a height of 33,5,0 m above the rock mass foundation, a crest development of 85,0 m and a crest thickness of 1,5 m. The Alto Ceira dam's construction was completed in 1949.

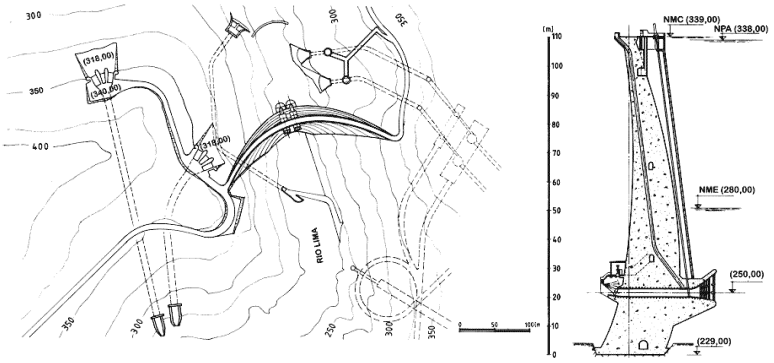

Figure 2: Elevation and cross section of Alto Lindoso dam.

3.2 Examples of dam monitoring data

Fig. 3 and 4 show a set of monitoring data regarding the structural behaviour of Alto Lindoso e Alto Ceira dams, respectively. Alto Lindoso dam has a complete monitoring system which includes the record of all quantities (actions and effects) mentioned before and large reading frequencies. Alto Lindoso dam presents a good behaviour throughout the years and it is possible to observe the influence of the annual temperature variations, which is the main action during the exploitation period. Fig. 3 show the comprehensiveness of the Alto Lindoso dam database, since casting (for temperatures inside the concrete) and since the beginning of the first filling.

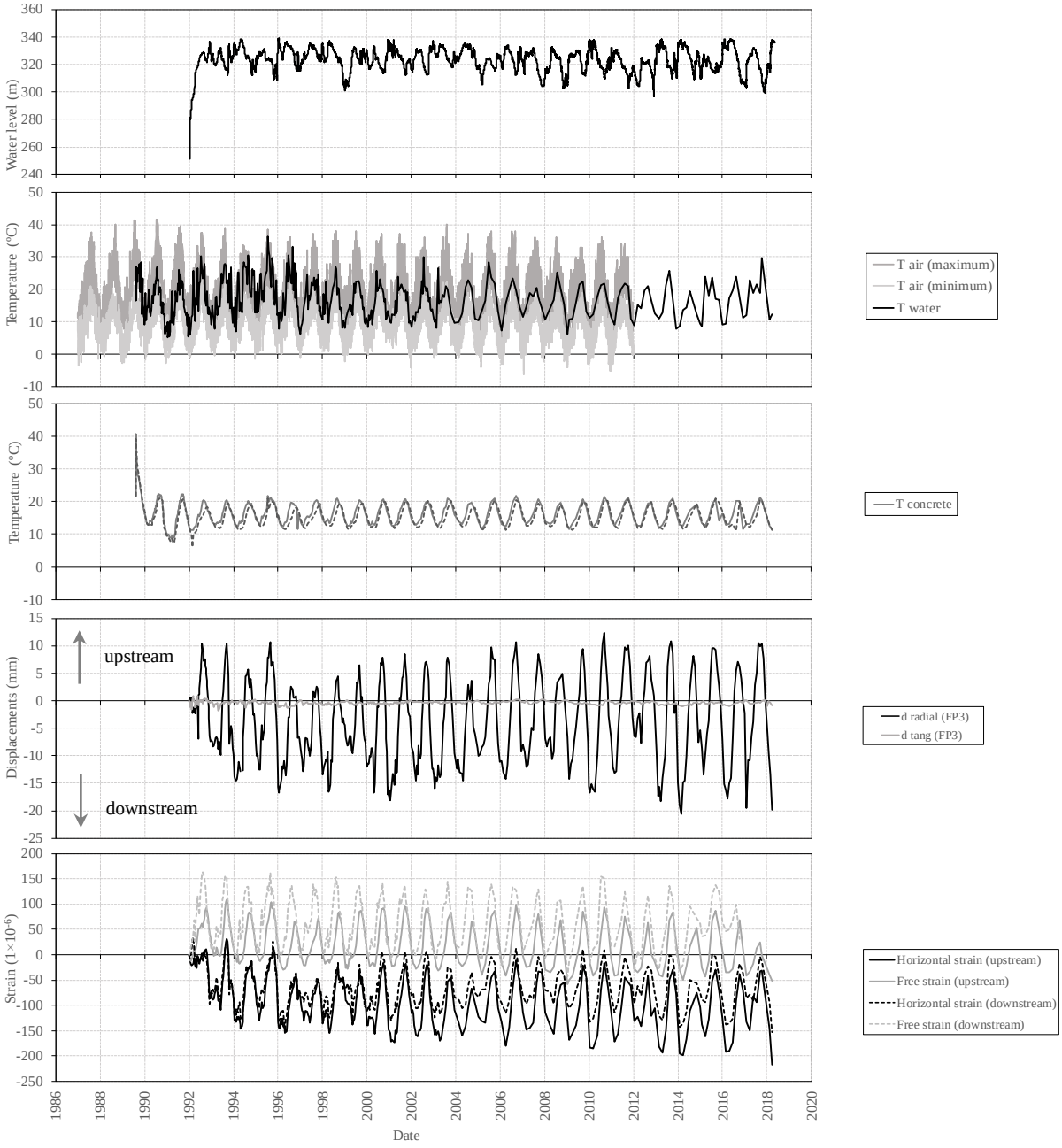

Figure 3: Set of monitoring data of Alto Lindoso dam.

The results show the effect of the upstream water pressure and of the annual temperature variations on the radial and tangential displacements in an inverted plumb-line, on the compressive strains measured in horizontal strainmeters placed in the central cantilever. The free strains are also measured in non-stress specimens in order to separate the effects of temperature and of the water level.

During several years, the behaviour of Alto Ceira dam was mainly monitored using geodetic techniques, namely precision level and triangulation surveys to evaluate the vertical and horizontal displacements, respectively (Fig. 4). Over the years a continuous significant upward displacement was detected, indicating the existence of expansive reactions.

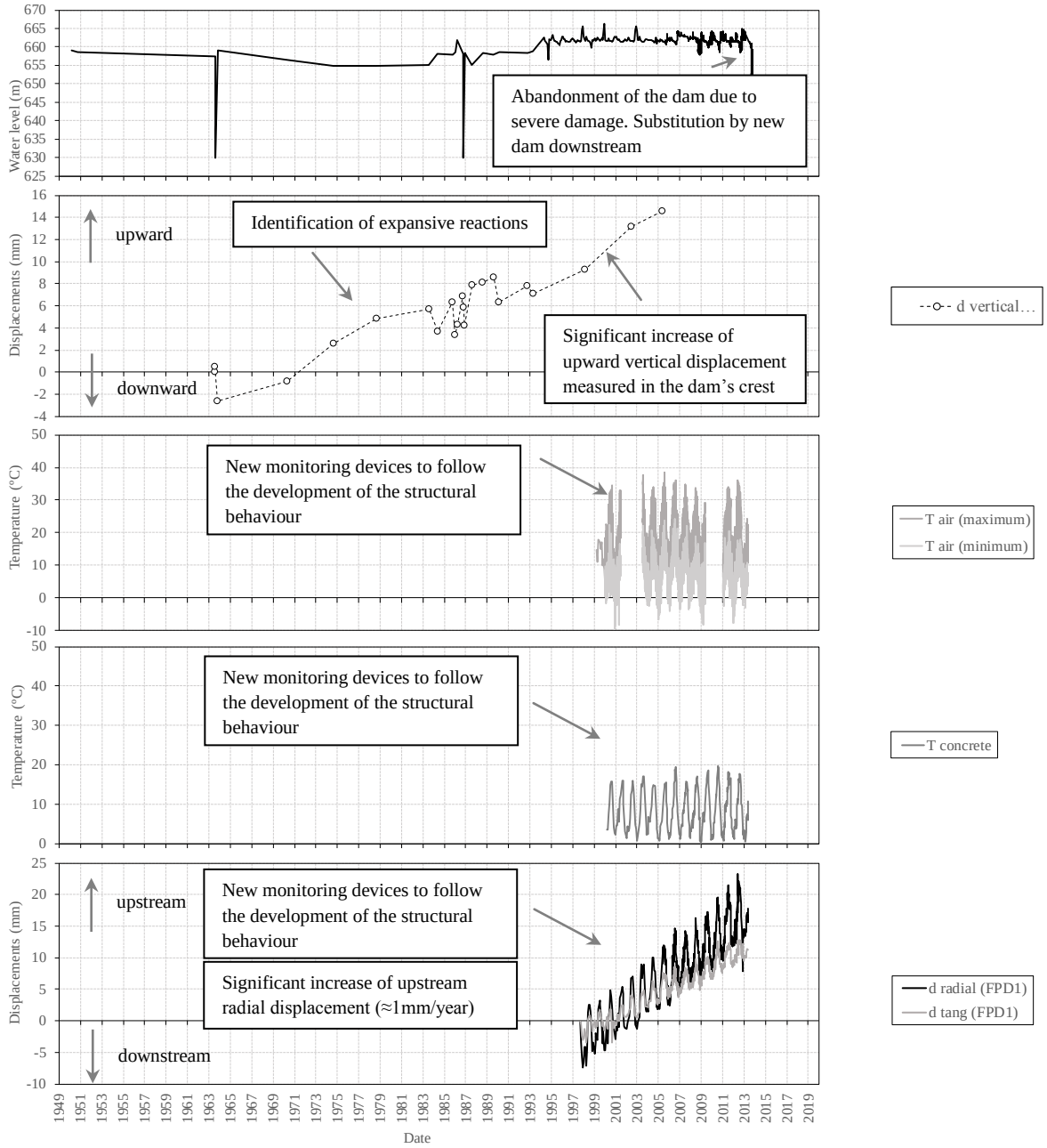

Figure 4: Set of monitoring data of Alto Ceira dam.

In the 1990's new monitoring devices were installed to follow the development of the structural behaviour. These new devices showed that the dam was moving upward and upstream compatible with a generalized increase of the dam's size, despite the main actions remained almost constant over several years. This behaviour was accompanied by severe structural damage in the dam's body which led to the its demolishing and substitution downstream in 2013.

4. Conclusions

The presented paper discusses the importance of dam monitoring system, including the planning, installation of instrumentation and collection and storage of data throughout several years. The National Laboratory for Civil Engineering (LNEC) has developed the GestBarragens system, which stores, organizes and maintains the multi-decade database of Portuguese large concrete dams.
Two examples are presented in order to showcase the type of dams, devices and comprehensiveness of the available data. The examples illustrate the importance of monitoring and of an operational monitoring system for evaluating the expected structural behaviour and for the assessment of deterioration scenarios.

Acknowledgements
Thanks are due to EDP for permission to publish data related to the monitoring of Alto Rabagão, Alto Lindoso and Alto Ceira dams.

References
[1] RSB, "Regulation on Dam Safety". Decree-Law n.º 344/2007, Lisboa, 2007 (in Portuguese).
[2] J. Mata, N. Schclar Leitão, A. Tavares de Castro, and J. Sá da Costa, "Construction of decision rules for early detection of a developing concrete arch dam failure scenario. A discriminant approach", Comput. Struct., vol. 142, pp. 45–53, Sep. 2014.
[3] ICOLD, "Monitoring of dams and their foundations - State of the art (Bulletin 068)", Paris, 1989.
[4] E. Almog, P. Kelham, and R. King, "Delivering benefits through evidence. Modes of dam failure and monitoring and measuring techniques", Bristol, UK, 2011.
[5] A. Tavares de Castro, J. Mata, J. Barateiro, and P. Miranda, "Information management systems for dam safety control. The Portuguese experience". in Dam World, 2012, p. 13.
[6] LNEC, "Alto Lindoso dam. Behaviour analysis report", Lisboa, 2009 (in Portuguese).
[7] A. L. Batista and J. Piteira Gomes, "Practical assessment of the structural effects of swelling processes and updated inventory of the affected Portuguese concrete dams", in Dam World 2012, 2012.

SynerCrete'18 International Conference on Interdisciplinary Approaches
for Cement-based Materials and Structural Concrete
24-26 October 2018, Funchal, Madeira Island, Portugal

LOAD-BEARING PERFORMANCE SIMPLE EVALUATION SYSTEM OF RC BRIDGE DETERIORATED CAUSED BY SALT DAMAGE

Hitoshi Ito [(1)], Toshiaki Mizobuchi [(2)]

(1) Yachiyo Engineering Co., Ltd., Tokyo, Japan
(2) Hosei University, Tokyo, Japan

Abstract

For small bridges managed by municipalities, in order to apply to a large number of bridges than precision, we construct the structural performance simple assessment system that emphasis is placed on simplicity. This system can evaluate the structural performance of bridges in a certain area by obtaining deterioration data from the representative bridge by non-destructive testing. This system does not require a lot of cost and time, because of the less amount workload of survey and analysis. As the structural performance, we evaluate load-bearing performance from the incubation period to the deteriorated period based on structural performance and deterioration factors. However structural performance and deterioration progression have uncertainly factors. Therefore we apply probability method to the system. Since the system of this research is a simple and doesn't require a lot of cost and time, it is possible to periodically update the assessment results. Therefore, we propose efficient maintenance method using this method, such as utilization of area maintenance method.

1. Purpose of the research

In Japan, it is necessary to implement effective maintenance, in order to maintain the good condition of bridges, because the safety of bridges changes by structural performance degradation due to deterioration [1-3]. The structural performance (load-bearing performance) of RC road bridges descend by the deterioration of reinforcement bars. As the result, the traffic of some bridges are closed. In the future, as the number of the aging bridge increasing, the traffic restricted bridge number and the maintenance cost will increase [4]. In addition, human resources of maintenance work have been decreasing. Therefore, the shortage of budget and time are problems in bridge maintaince. As the result, it is required to reduce the maintenance cost and improve the efficiency [5]. Especially, municipalities in Japan have

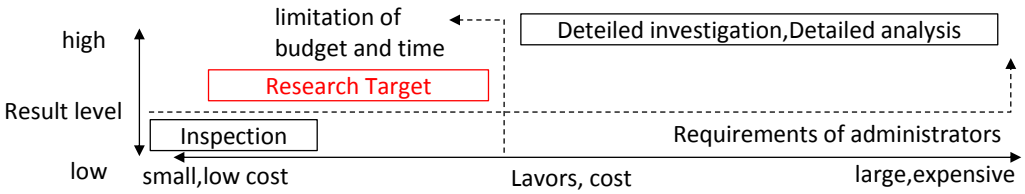

Figure 1: Labors, cost and the result level.

many bridges in need of maintenance, but budget and human resources are limited. However, accidents, caused by insufficient maintenance, are serious problem (safety level requirements are same as national roads). As the result, efficient maintenance is required (preventive maintenance, choice and concentration of maintenance work).

In the bridge maintenance, we evaluate the degree of the bridge safety as part of the structural condition assessment, prior to planning appropriate maintenance items. We collect the information about the degree of deterioration by surveying corrosion of rebars, salt damage. After that, we predict the current structural performance and structural performance degradation based on the obtained surveying results.

Municipalities do inspection for bridge maintenance, and municipalities are difficult to apply the data other than inspection results due to limitation of budget and time. However, we cannot evaluate the individual bridge situation and safety based on only inspection results. As a result, only inspection results are insufficient as evaluation results required by administrators (Fig. 1). Therefore, we propose the method (the structural performance assessment method without much cost and time), to compensate for the insufficient. In addition, the method does not require cost and time for data collection, analysis and update, for continuous implementation. We define it as the "simple" structural performance assessment system.

2. Performance simple assessment system

2.1 Outline of Performance simple assessment system

It is possible to assess the structural performance with high accuracy by carrying out enough

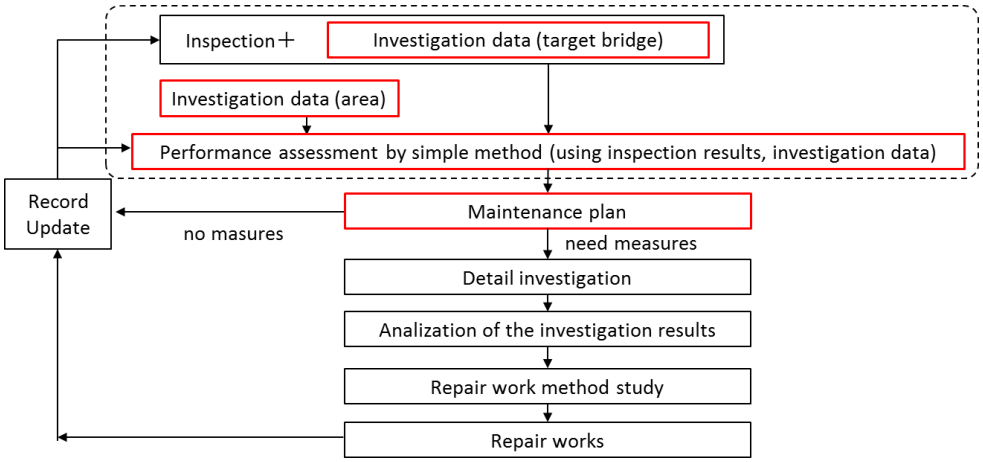

Figure 2: Flow of bridge maintenance.

Table 1: Comparison between conventional and purpose method, *( ) shows example

Item	Conventional method	Proposed method
Investigatin	Detail (Chemical analysis, natural potential etc)	Simple(electromagnetic wave radar, fluorescent X-ray etc)
Analysis	Precise model (FEM etc)	Simple model (based on Specification)
Lavors, Cost	Large, expensive	Small, low cost

Table 2: Applicable condition

Item	Applicable condition
target	small reinforced concrete road bridges
structural type	slab bridge
deterioration factor	complex deteriorationdue to salt damage and carbonation
Structural performance	bending strength

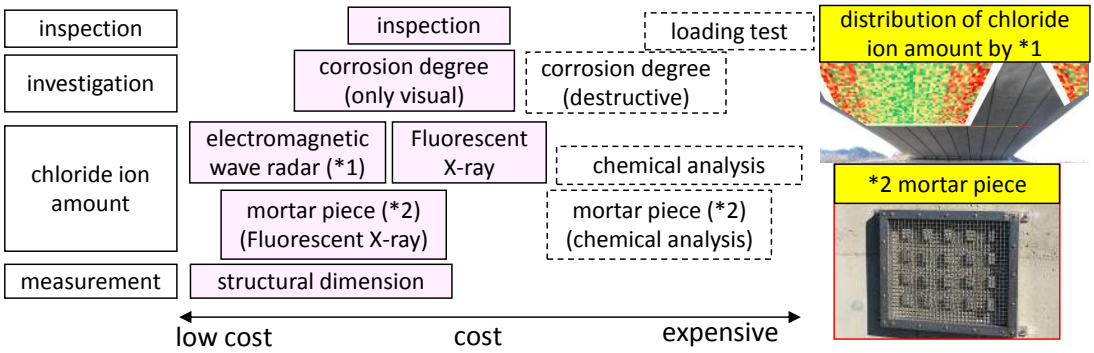

Figure 3: Cost of investigation.

surveys and analysing the condition using an elaborated model. However, that requires a lot of cost and time. Therefore, in this paper, for small bridges managed by municipalities, in order to apply to a large number of bridges than precision, we construct the structural condition simple evaluation system that emphasis is placed on simplicity. In the maintenance flow (Fig. 2), the system provides quantitative evaluation results, they are useful for the maintenance plan. Tab. 1 shows the comparison between the propose method and the conventional method. In this paper, applicable conditions to the system are limited (Tab. 2), and assumption values are applied to a part of data.

2.2 Data of the system requirements

Existing structural data (chloride ion amounts etc.) is necessary for assessment of structural performance. Cost is different for each investigation (Fig. 3). Our proposal system applies low cost investigation data (chloride ion amounts investigation by electromagnetic wave radar method [6], fluorescent X-ray method [7] etc.). These investigation are taken about 1 hour per place including preparation time. The distribution of deterioration can be assessment combining investigation result by these investigations. In addition, the investigation using mortar pieces can be assessment the tendency of salt damage in the area. These investigations are effective in municipality's bridges investigation, because a lot of cost and time is not required.

2.3 Method of performance assessment

The system can evaluate the structural condition of bridges by the deterioration condition. The evaluation is based on specification for highway bridges [8]. As the structural condition, we evaluate load-bearing performance from the incubation period to the performance deteriorated period based on structural condition and deterioration factors. However structural condition and deterioration progression have uncertainly factors. For example, initial performances of structures depend on the material performance, structural dimensions and reinforcement position. In addition, the deterioration progression is affected by various conditions, and also estimation results are depended on the way of evaluation. Furthermore, the thickness of covering concrete is not uniform, so progressions of deterioration depend on the location of the structure. Therefore we apply probability method (Monte Calro method) to the system. Tab. 5 shows specific procedures.

3. Trial assessment result about existing structure

3.1 Target structure

This chapter shows a trial calculation example using proposal system. The target area has a temperate climate with an average annual temperature of 16 ° C or more, and two sides of this area face the sea. Coastal roads are important, because many citizens live in the coastal area. Target structures are 2 bridges (Tab. 3) located in the coastal area. The deterioration condition of salt damage is set as shown in Tab. 4 from investigation results of the representative bridge in each area (3 samples). Nos.1 to 3 are the results of applying the equation of Fick's second law to investigation results. Nos. 4 to 6 are the results of applying the method considering complex deterioration [9]. As described before, the deterioration status depends on the part of the structure, so we varied deterioration conditions according to the distance from the outer surface. The limit value of the bending strength is calculated by the live load shown in Tab. 3. In this case, we set deterioration condition based on the representative investigation result of

Table 3: Bridges condition.

Bridge No	55 (area A)	62 (area B)
Years after construction	56	87
Width,Height,Span length (mm)	W=10000,H=500,S=5400	W=4000,H=300,S=4000
re-bar	D19,n=80	D16, n=32
Strength of concrete	21N/mm2	21N/mm2
Strength of re-bar	235	235
Live load	200kN*2	88kN*1

Table 4: Deterioration condition.

	No	No.1	No.2	No.3	No.4	No.5	No.6
the apparent diffusion coefficient(mm2/year)	Bridge 55	530.99	29.64	105.91	530.99	17.54	67.14
	Bridge 62	55.15	2.23	28.01	20.66	3.19	6.94
the values of surface concentration(kg/m3)	Bridge 55	9.91	22.35	9.83	9.91	27.44	11.85
	Bridge 62	7.57	2.02	3.97	9.14	1.26	10.50

Table 5: Evaluation procedure.

STEP	Implementation content
1	set parameters using random numbers (uniform, normal distribution etc) [10]
2	caluculate time of corrosion occuring, crack occuring, and caluculate reduction of rebar sectional area, based on parameters and data from investigation
3	predict rebar sectional area for trial (1,000 case)
4	based on predicted values, trial cases they match corrosion status are selected.
5	set parameters, for each rebar, to assess performance in assuming that selected trial cases uniformly occurs.
6	assess performance for trial 1,000 case of Monte Carlro method
7	before cracking occur : caluculate probability occur corrosion , cracking after cracking occur : calculate probability of risk index
8	aggregate in t=1~100year

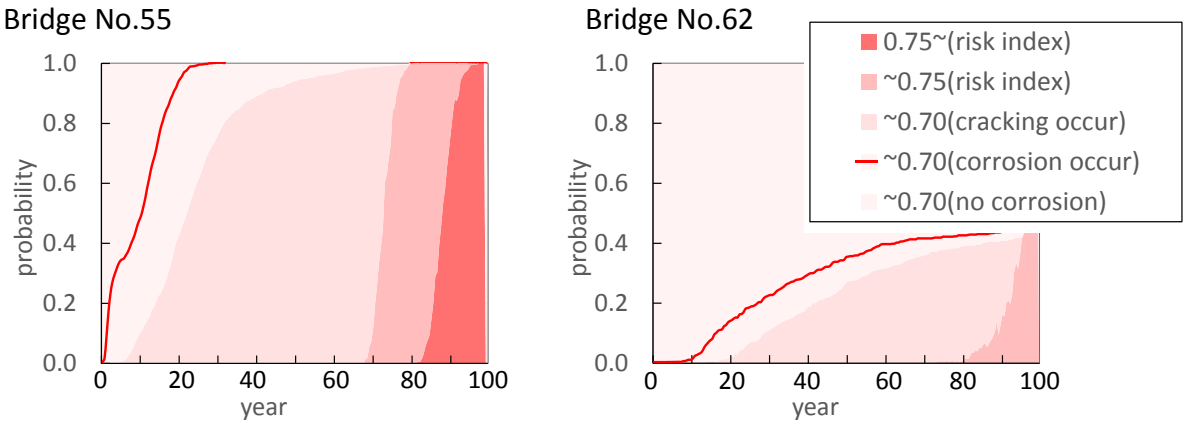

Figure 4: Probability

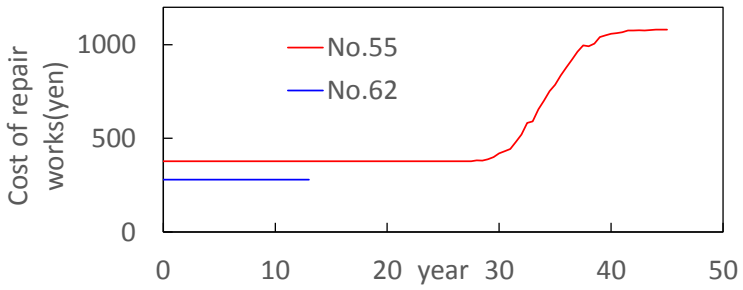

Figure 5: Cost prediction of repair works

each area. However, in the future, we plan to reflect the deterioration distribution assessment result based on investigation result of using mortar pieces, electromagnetic wave radar and X-ray fluorescence.

3.2 The result of the trial assessment

We assessed structural performance according to the procedure shown in Tab. 5. Next we calculate varies in the probability due to progression of deterioration. Fig. 4 shows the result. According to Fig. 4, bridge administrator can quantitatively grasp varies performance

degradation, for example, the risk index expresses safety degradation due to repair works delay, as probability increasing. Fig. 5 shows the repair cost estimation (using the probability by this system). As a result, it is possible to decide the timing and necessity of repair works, such as doing repair at No55 bridge within 30 years before the cost changes greatly.

4. Conclusions

We constructed a framework of the system capable of assessing the current and future performance of structure, in limited budget and time. The results of this paper are below.

- It is possible to construct the system that can assess a series of processes from evaluation of deterioration to structural safety.
- Assessment results (bending strength) include structural characteristics and environmental conditions, in addition, assessment results include from incubation period to deteriorated period (difficult to assess by inspection results).
- The performance simple assessment system does not require significant increasing cost and time relative to the bridge inspection, as the result, updating is easy.
- The system is possible to apply investigation results by simple method (chloride ion amounts investigation using electromagnetic wave radar, mortar piece etc.), as the result, accuracy improvement will be expected.
- The risk index (limit value to structural performance) is effective to set due timing to repair works, and the risk index expresses safety degradation due to repair works delay, as probability increasing.
- The maintenance cost estimation (reflect the result of structural characteristics and deterioration progress assessment) using proposal system is effective as the decision-making basis for repair works timing and repair necessity.

References

[1] Yuji, N., Decaying infrastructure, Nikkei publishing, Inc., (2011)
[2] Toshiaki, M., Concrete collapse, PHP publishing, Inc., (2013)
[3] Satoshi, F., Country resilience theory, Bungeishunju Ltd., (2011)
[4] MLIT, Current status of road structure maintenance, http://www.soumu.go.jp/main_content/000497036.pdf (2013)
[5] MLIT, Measures of road aging, http://www.mlit.go.jp/road/sisaku/yobohozen.html (2016)
[6] Junnichiro, N. et al, Future prediction method of salt damage progression using estimation of chloride ion amounts by electromagnetic wave, Concrete Research and Technology, Vol.35, No.1 (2013)
[7] Ruiko, W. et al, Prediction of chloride ion amounts using fluorescence X-ray, 2017 JSCE annual meeting (2017)
[8] Japan road association, Specification for highway bridges, part3 concrete bridges (2012)
[9] Hitoshi, I. et al, Prediction of complex deterioration and evaluation of RC structural performance, fib symposium (2017)
[10] Shinichi, K. et al, Degradation prediction method on bending strength of RC members in splash zone, Concrete Research and Technology, Vol.33, No.1 (2011)

SCIENTIFIC INSIGHTS

VS.

STANDARDIZATION

SynerCrete'18 International Conference on Interdisciplinary Approaches
for Cement-based Materials and Structural Concrete
24-26 October 2018, Funchal, Madeira Island, Portugal

A COMPARISON OF TWO MAJOR APPROACHES USED FOR CONCRETE STRENGTH PREDICTION FOR DIFFERENT CONCRETE TYPES

Seda Yesilmen [(1)], Sinan Kefeli [(1)]

(1) Cankaya University, Ankara, Turkey

Abstract
Predicting concrete strength has been a popular topic for the last decade and several methods were proposed by researchers each claiming to increase accuracy of predictions. Two methods were selected namely linear regression, and artificial neural networks and their predictive performances were compared using data for different concrete types. Data for high performance concrete (HPC), self-compacting concrete (SCC) and ordinary concrete (OC) were implemented in selected prediction models.

1. Introduction

Compressive strength is arguably the most important mechanical property of concrete. Consequently, prediction of concrete compressive strength has been a popular area for a while. The major factor determining the compressive strength of concrete is mix design the components of which widely used in concrete compressive strength (CCS) prediction. There are lots of other contributing factors such as age, curing, and handling practices, etc. Most common methods predicting the strength of concrete are based on the linear and nonlinear regression methods [1,2] and artificial neural networks [3,4].
Although it was claimed that [5,6] regression analysis is usually less accurate than that Artificial Neural Networks (ANN) method, regression can be more advantageous because it is faster and more effective since it does not require model training. Additionally non-linear regression (NLR) models were proved to be more accurate than linear models [7].

2. Strength prediction methods

Predicting CSS using mix design parameters is a widely researched topic [5,8]. When the popularity of the deep learning was renewed, CSS prediction methods evolved accordingly.

Although several hybrid methods were offered, ANN is still one of the most used methodologies for strength prediction mostly owing to very high accuracy of results.
Regression methods also maintained their popularity because of their simple implementation specifically nonlinear regression was reported to predict CSS with high accuracy [7]. Method of CSS prediction is also important for different concrete types, because concrete ingredients can profoundly affect prediction accuracy.

2.1 Nonlinear regression

Concrete compressive strength (CCS) can be predicted using linear or non-linear regression (NLR) methods. Eq. (1) is known as multivariable power equation and it is used in several studies [2,7,9,10] for CCS prediction. It was reported to be the regression model with the highest accuracy.

$$\ln Yi = b + w_i \ln x_{ij} \quad (1)$$

where Yi is predicted CCS for i^{th} mix design at a certain age, b and w_i are regression coefficients and x_{ij} is the j^{th} input parameter for the i^{th} mix design.

2.2 Artificial neural networks

Artificial neural networks (ANNs) are used to construct mapping functions for predicting CCS [11,12]. Notably, researchers have applied or evaluated the capability of ANNs to predict strength and other concrete behaviors [13-15]. The ANN is a powerful tool for solving very complex problems and it has been used commonly for CCS prediction [14,15]. Multilayer perception (MLP) neural networks are standard neural network models with an input layer representing concrete mix design components, hidden layers with computation neurons, and an output layer containing one neuron representing CCS.
Two hidden layers were used in the ANN model for this study. ANN model was implemented using Tensorflow library and python. Activation function was selected to be sigmoid for all layers except output layer. Adam Optimization algorithm was used since it became a popular algorithm recently which enables learning rate decay using exponential moving average of the gradient. Training and testing data were separated using train test split function of sklearn library. This function also shuffles the data before splitting which can be critical during training. Validation data was not used instead cross validation was performed for hyper parameter tuning.

3. Results

A total of 108 different mix designs for ordinary concrete (OC) mixtures are obtained from various sources [14,16-19]. Ordinary concrete mix design only included 5 parameters namely; cement content, water content, coarse aggregate content, fine aggregate content and superplasticizer content. All the parameters were defined in kg/1m^3 of concrete.
Self-compacting concrete mix design included an additional parameter of Fly Ash content with units of kg per 1m^3 of concrete. Accordingly 6 features were considered in the ANN model. A total of 203 different mix designs were extracted from literature [14,20-27].SCC

mixtures can contain different types of water reducers in addition to superplasticizers, in this study SCC mixtures with only one type of superplasticizers are included as input data (Fig. 3). High performance concrete (HPC) mix design included both blast furnace slag content, and Fly Ash content, so a total of 7 input parameters were included in the model. A total of 426 different mix designs were extracted from literature [14,16-19,28-32].

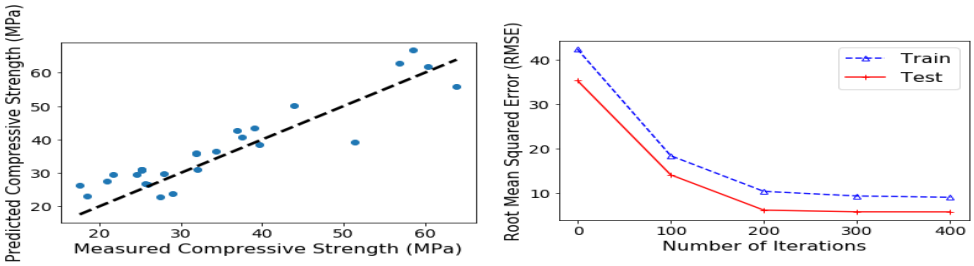

Fig. 1 Predicted strength versus actual strength values for test data and the reduction in RMSE during iterations for both training and test data in ANN model for OC.

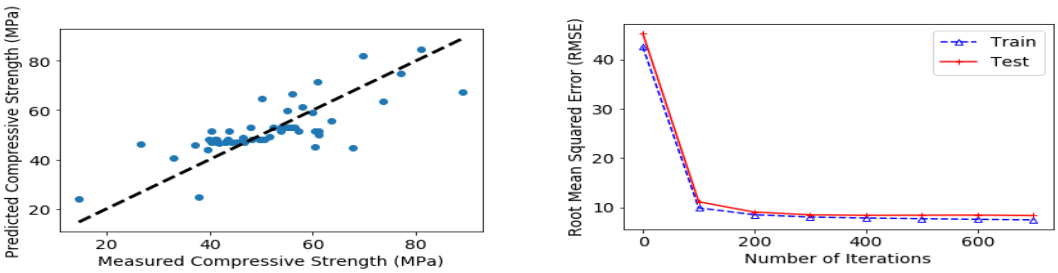

Fig. 2 Predicted strength versus actual strength values for test data and the reduction in RMSE during iterations for both training and test data in ANN model for SCC.

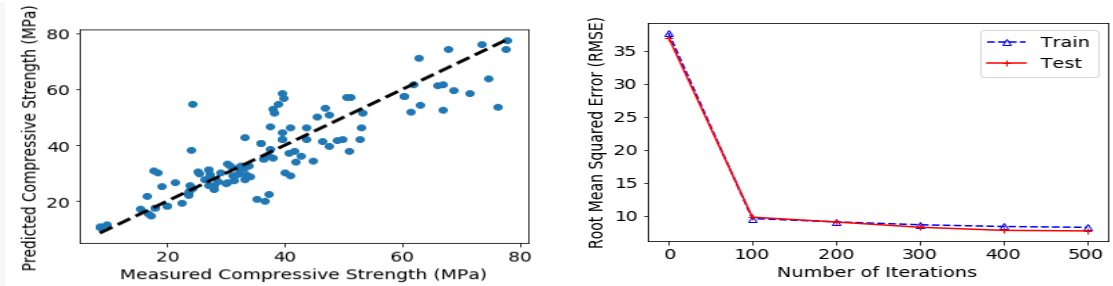

Fig. 3 Predicted strength versus actual strength values for test data and the reduction in RMSE during iterations for both training and test data in ANN model for SCC.

Regression coefficients for NLR and ANN modeling are shown in Tab 1 and Tab 2 respectively. For both analysis methods ordinary concrete has the highest correlation coefficient among other concrete types. However correlation coefficients are low and root mean squared error values are higher than acceptable ranges especially for self-compacting concrete (SCC). The same behavior can be observed from graphs illustrating the relationship between predicted and tested strength values in Fig 4.

Table 1: Nonlinear regression modeling results for test data.

	OC	**SCC**	**HPC**
MSE	39.06	46.79	123.31
RMSE	6.25	6.84	11.10
R^2	0.84	0.53	0.70

Table 2: ANN modeling results for test data.

	OC	**SCC**	**HPC**
MSE	36.48	43.83	59.92
RMSE	6.04	6.62	7.74
R^2	0.91	0.67	0.84

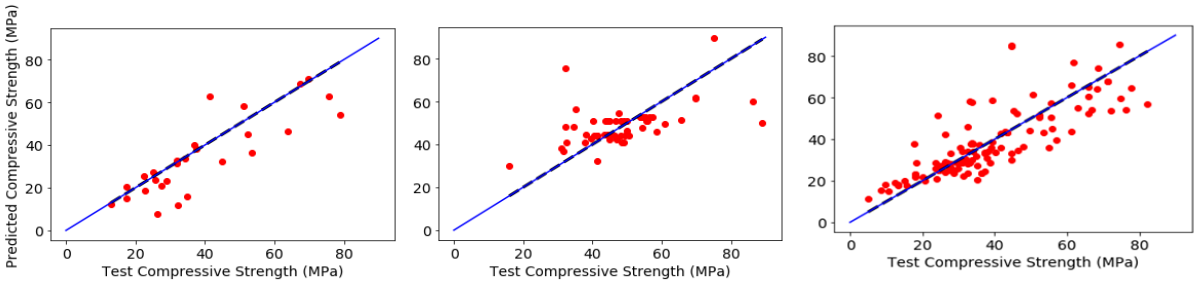

Fig. 4 Predicted strength versus actual strength values for test data in NLR model for OC, SCC and HPC respectively.

4. Conclusion

High accuracy of Ordinary concrete can be attributed to the absence of pozzolans. Among the pozzolanic materials, properties of fly ash known to spread a very wide range and they are dependent on the properties of burned coal in thermal plants. A large percentage of SCC specimens contain fly ash which would be expected to increase the variance of the distribution.

Comparing the two methodologies accuracy of ANN models are slightly higher. Much higher correlation coefficients reported when ANN is used for CSS prediction but most of the literature on CSS prediction uses mix design data from the one or two batches of concrete. Data from several papers with very different sources for ingredients were used in this study which introduced a considerable variance. Addition of certain features such as calcium and silica content of pozzolanic materials should increase the accuracy of ANN predictions. It must be noted that an ANN model needs to be trained on more data and more features in order to claim high accuracies globally. However considering the implementation ease of regression, it might be acceptable to use nonlinear regression for CSS approximation.

Specifically for applications that does not need high accuracy nonlinear regression can stay as a viable option.

References

[1] Tsivilis, S. and Parissaki, G., A mathematical model for the prediction of cement strength, Cem Concr Res 25(1) (1995), 9–14.
[2] Zain, M.F.M. and Abd, SM., Multiple regression model for compressive strength prediction of high performance concrete, J Appl Sci 9(1) (2009), 155–60.
[3] Oztas, A., Pala, M., Ozbay, E., Kanca, E., Caglar, N. and Bhatti, M.A., Predicting the compressive strength and slump of high strength concrete using neural network, Constr Build Mater 20(9) (2006), 769–75.
[4] Hong-Guang, N. and Ji-Zong, W., Prediction of compressive strength of concrete by neural networks, Cem Concr Res 30(8) (2000), 1245–50.
[5] Atici, U., Prediction of the strength of mineral-addition concrete using regression analysis, In: Concrete Research. Thomas Telford Ltd. (2010), 585–92.
[6] Chitra, S., Kumar, SRRS., Chinnaraju, K. and Ashmita F.A., A Comparative Study on the Compressive Strength Prediction models for High Performance concrete Containing Nano Silica and Copper Slag Using Regression Analysis and Artificial Neural Networks, Const and Build Mat 114 (2016), 528-535
[7] Jin, R., Chen, Q. and Soboyejo, A.B.O., Non-Linear and Mixed Regression models in predicting sustainable concrete strength, Const and Build Mat 170 (2018), 142-152
[8] Bhanja, S. and Sengupta, B., Investigations on the compressive strength of silica fume concrete using statistical methods, Cem Concr Res 32(9) (2002), 1391–4.
[9] Kheder, G.F., Al-Gabban, A.M. and Suhad, M.A., Mathematical model for the prediction of cement compressive strength at the ages of 7 and 28 days within 24 hours, Materials and Structures 36 (2003), 693-701
[10] Chopra, P., Sharma, R.K. and Kumar M., Predicting Compressive Strength of Concrete for Varying Workability Using Regression Models, IJEAS (2014)
[11] Dantas, A.T.A., Batista Leite M., Nagahama, K.J., Prediction of compressive strength of concrete containing construction and demolition waste using artificial neural networks, Constr Build Mater 38 (2013), 717–22.
[12] Uysal, M. and Tanyildizi, H., Predicting the core compressive strength of self compacting concrete (SCC) mixtures with mineral additives using artificial neural network, Constr Build Mater 25(11) (2011), 4105–11.
[13] Yeh, I.C., Analysis of strength of concrete using design of experiments and neural networks, J Mater Civ Eng 18(4) (2006), 597–604.
[14] Yeh, I.C., Modeling of strength of high-performance concrete using artificial neural networks, Cem Concr Res 28(12) (1998), 1797–808.
[15] Ni, H.G. and Wang, J.Z., Prediction of compressive strength of concrete by neural networks, Cem Concr Res 30(8) (2000), 1245–50.
[16] Jiang, L.H. and Malhotra, V.M., Reduction in water demand of non-air-entrained concrete incorporating large volumes of fly ash, Cem. Concr. Res., 30(11) (2000), 1785–1789
[17] Bouzoubaa, N. and Fournier, B., Optimization of fly ash content in concrete: Part I: Non-air-entrained concrete made without superplasticizer, Cem. Concr. Res., 33(7) (2003), 1029–1037

[18] Pala, M., Ozbay, E., Oztaş, A. and Yuce, M. I., Appraisal of long-term effects of fly ash and silica fume on compressive strength of concrete by neural networks, Constr. Build. Mate.r 21(2) (2007), 384–394
[19] Demirboga, R., Turkmen, I. and Karakoc, M.B., Relationship between ultrasonic velocity and compressive strength for high-volume mineral-admixtured concrete, Cem. Concr. Res. 34(12), (2004), 2329–2336
[20] Dinakar, P., Sethy, K.P. and Sahoo, U.C., Design of self-compacting concrete with ground granulated blast furnace slag Mater. Des. 43 (2013), 161–169, 2013.
[21] Liu, M., Self-compacting concrete with different levels of pulverized fuel ash, Constr. Build. Mater. 24(7) (2010), 1245–1252
[22] Almeida Filho, F.M., Barragán, B.E., Casas, J.R. and El Debs, A.L.H.C., Hardened properties of self-compacting concrete — A statistical approach, Constr. Build. Mater., 24(9) (2010), 1608–1615
[23]Abu Yaman, M., Abd Elaty, M. and Taman, M., Predicting the ingredients of self compacting concrete using artificial neural network, Alexandria Eng. J. 56(4) (2017), 523–532
[24]Vivek, S.S. and Dhinakaran, G., Fresh and hardened properties of binary blend high strength self compacting concrete, Eng. Sci. Technol. an Int. J. 20(3) (2017), 1173–1179
[25] Mahalingasharma, S.J., Prakash, P., Vishwanath, K.N. and Jawali, V., Effect of mineral admixtures on kinetic property and compressive strength of self compacting concrete, IOP Conf. Ser. Mater. Sci. Eng. 216(1) (2017), 120-126
[26] Ramanathan, B., Baskar, I., Muthupriya, P. and Venkatasubramani, R., Performance of self-compacting concrete containing different mineral admixtures, KSCE J. Civ. Eng. 17(2) (2013), 465–472
[27] Gesoğlu M. and Özbay, E., Effects of mineral admixtures on fresh and hardened properties of self-compacting concretes: binary, ternary and quaternary systems Mater. Struct. 40(9) (2007), 923–937
[28] Proske, T., Hainer, S., Rezvani, M. and Graubner, C.A., Eco-friendly concretes with reduced water and cement content – Mix design principles and application in practice, Constr. Build. Mater. 67 (2014), 413–421
[29] Bharatkumar, B., Narayanan, R., Raghuprasad, B. and Ramachandramurthy, D.S., Mix proportioning of high performance concrete 23 (2001)
[30] Oner, A. and Akyuz, S., An experimental study on optimum usage of GGBS for the compressive strength of concrete, Cem. Concr. Compos. 29(6) (2007). 505–514
[31] Durán-Herrera, A., Juárez, C.A., Valdez, P. and Bentz, D. P., Evaluation of sustainable high-volume fly ash concretes, Cem. Concr. Compos. 33(1) (2011), 39–45
[32] Bilim, C., Atis, C.D., Tanyildizi, H. and Karahan, O., Predicting the compressive strength of ground granulated blast furnace slag concrete using artificial neural network Adv. Eng. Softw., 40(5) (2009), 334–340

SynerCrete'18 International Conference on Interdisciplinary Approaches
for Cement-based Materials and Structural Concrete
24-26 October 2018, Funchal, Madeira Island, Portugal

A SIMPLIFIED 1D STRESS APPROACH FOR CRACKING RISK PREDICTION

Luis Ebensperger [(1)]

(1) Construtechnik Ltda, Concrete Technology Consultant, Santiago, Chile

Abstract

Cracks in concrete structures during early ages occur more often than expected. It affects adversely the concrete structure, especially serviceability and durability. The effect of internal concrete volume changes in absence of loads, such as the effect of temperature changes caused by heat of hydration and the chemical/drying shrinkage, is normally not included during design stages. This occurs despite specific recommendations in Codes for situations when these volume changes are significantly restrained.

This work addresses the development of a simple 1D assessment tool that considers the cement´s heat of hydration, the thermal and viscous-elastic properties of young concrete, and the degree of external restraint. By performing an iterative calculation procedure for seven days, the model graphically shows the expected core and surface temperature, the corresponding stress development, and the Cracking Index for different heights of the concrete member. The tool allows to consider parameters, such as mix design, thermal properties including the heat transfer coefficient, placement conditions such temperature during pouring and curing, demoulding time, geometry of the member, and consideration of chemical and drying shrinkage. Its applicability is discussed for a cast-in-place beam with registered temperature measurements and for a high-cracked wall foundation system of a liquid containing structure.

1. Concrete Cracking at Early Ages

The left side of Figure 1 shows schematically the global situation that occurs at an early age, including the effect of daily variations in temperature, identifying two periods of high risk of cracking [1]:

- From day 1 to 7 approximately, due to the effects of the heat of hydration
- After approximately 3 weeks, due to the effects of hydraulic shrinkage.

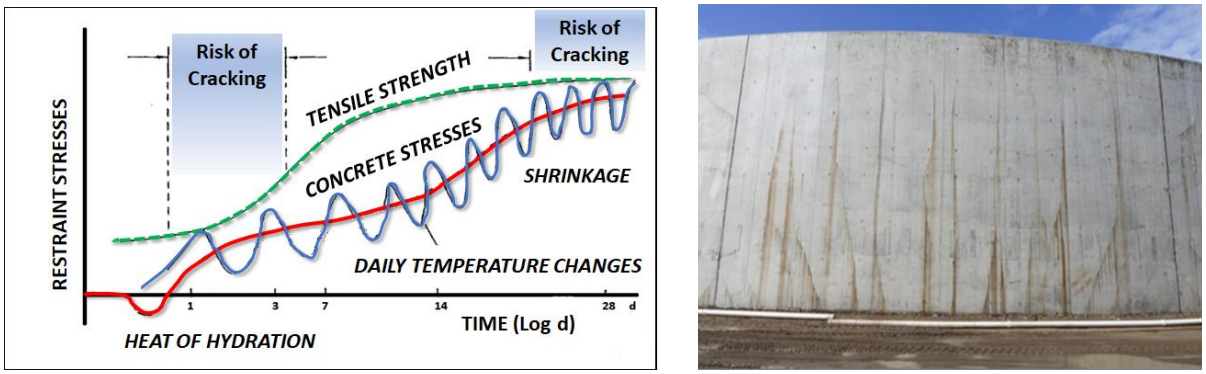

Figure 1: Periods of higher cracking risk and a typical thermal cracking pattern.

2. Modelling Concrete Properties

2.1 Temperature Development

Through the use of the semi-adiabatic Langavant method [2] the heat generation curve $\Delta QHyd(t)$ and the seven days value of $QHyd(7d)$ are determined. This allows to calculate the adiabatic development of temperature T_{ad} in concrete. The cement content cem, the specific heat C_{con}, and the density of the concrete ρ_{con} have to be known (Eq. (1)).

$$\Delta THyd(t) = \frac{cem \cdot \Delta QHyd(t)}{C_{con} \cdot \rho_{con}} \quad (1) \qquad m = \frac{U \cdot S}{c_{con} \cdot \rho_{con} \cdot V} \quad (2)$$

Due the fact the concrete member stays under certain environmental conditions, usually at a lower temperature than the concrete, it will cool down to equilibrium with the ambient temperature. The speed will depend on the capacity or Cooling Index *m*, which depends on the Coefficient of Heat Transfer *U* on the concrete surface (insulation conditions), and on the relation between exposed surface *S* and volume of concrete *V* (Eq. (2)).
The following equation adopted from [3] allows to estimate the Core (Nucleus) Temperature T_{Nu} of the member, considering the Ambient Temperature T_a in each time interval Δt:

$$T_{Nu,i+1} = T_{a,i} + \Delta T_{Hyd,i} + \left(T_{Nu,i} - T_{a,i}\right) \cdot \exp(-m \cdot \Delta t) \quad (3)$$

To characterize the internal heat flow within the concrete, the Biot Number *Bi* is used (Eq. (4)), which is the ratio of the heat transfer resistances inside of (Thermal Conductivity λ) and at the surface of a body (Coefficient of Heat Transfer *U*). This ratio determines whether or not the temperatures inside a body will vary significantly, while the body heats up or cools down over time since a thermal gradient is applied in the surface. With this number it is possible to estimate the Surface Temperature T_{Su} (Eq. (5)).

$$Bi = \frac{U \cdot L}{\lambda} \quad (4) \qquad \frac{T_{Nu} - T_{Su}}{T_{Nu} - T_a} = \frac{Bi}{Bi + 2} \quad (5)$$

With the information provided by the model, two temperature differentials may be calculated (Fig. 2):

- ***ΔT° Section*** = $T_{Nu} - T_{Su}$ (temperature gradient → Tensile stresses at the surface of the concrete, minor cracks that tend to close when the temperature equilibrium is reached).

- ***ΔT° Axial*** = $T_{Max} - T°7d$ (contraction of the member → Tensile stresses in the concrete due to the cooling of the whole member, through-cracks that cross the thickness).

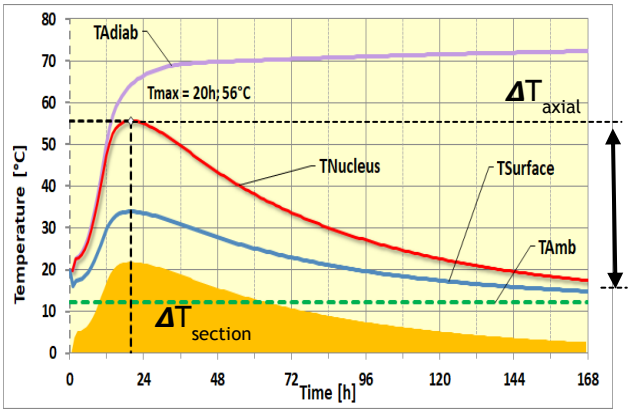

Figure 2: Temperature development in a concrete member.

The amount of heat of hydration lost from the core depends mainly on four factors:

- **Type of element and its dimensions**: the model recognizes the wall-type and the foundation-beam type element. The difference lies in the procedure to determine the L/H ratio (length / height) and the exposed surface. In the wall type, the heat loss occurs sideward of the wall, in both exposed sides, and upper surface. In the case of the foundation or beam, the heat loss occurs upwards and normally only in the exposed upper surface.
- **Placement conditions**: the time of placement and temperature of fresh concrete have a high effect in the expected temperature development in the concrete, as well as the ambient temperature and wind conditions. The latter can be incorporated in 3 ways:
  - Constant value during the seven days.
  - Sinusoidal curve, which requires the average temperature of the period, the daily variation and the time when the maximum daily temperature is reached.
  - Real ambient data measured on-site conditions.
- **Insulation conditions**: the model calculates according to type of material and wind conditions the *U*-value, while the concrete is in the formwork and after demoulding.
- **Steam Curing**: the model allows to enter the complete cycle, from start to end with time and temperature profile.

The temperature deformation is calculated using the CTE of concrete, according to:

$$\varepsilon_T = CTE \cdot \Delta T \qquad (6)$$

2.2 Chemical and Drying Shrinkage Deformations

For the consideration of Chemical Shrinkage, the model uses the methodology of the European standard EN 1992-1-1 [4], which takes the characteristic resistance of the concrete to estimate the ultimate deformation $\mathcal{E}_{asu}$. The model considered the period of the 7 first days.

$$\varepsilon_{asu} = 2.5 \cdot (f'_c - 10) \qquad (7) \qquad \varepsilon_{as}(t) = \{1 - \exp(-0.20 \cdot t^{0,50})\} \cdot \varepsilon_{asu} \qquad (8)$$

For the consideration of the Drying Shrinkage, the model uses the methodology of the Australian AS 5100.5 standard [5], according to the environmental humidity and the effective thickness subjected to the superficial drying conditions. The ultimate deformation ε_{su} is

defined and the shrinkage at any time ε_s is estimated according to the environmental condition (40% to 70% r.h.) by the factor k_1, which is calculated for the period of 7 days.

$\varepsilon_{su} = 850\mu s \pm 30\%$ (9) $\varepsilon_s = k_1 \cdot \varepsilon_{su}$ (10)

2.3 Development of Mechanical Properties

The concrete begins its hardening about 8 hours, at which time it begins to take tensions. This period is known as "dormant phase". The model considers the existing experience in the current update work of Eurocode 2, Annex D [5].

The development of the mechanical properties depends directly on the temperature conditions of the concrete member. This effect is considered in the model by the concept of "Equivalent Age" t_{eq}, which includes the Activation Energy E_{AC} of the cement.

$$t_{eq} = \sum H(Ti) \cdot \Delta ti \quad (11) \qquad H(Ti) = exp\left[\frac{E_{Ac}}{R} \cdot \left(\frac{1}{293} - \frac{1}{273 + Ti}\right)\right] \quad (12)$$

For the determination of the development of the mechanical properties referred to the Equivalent Age, the 28-day values of each property are considered with the factor β, which depends on the factor s, the dormant time, type of cement and class of concrete.

$$\beta = \exp\left[s \cdot (1 - \sqrt{\frac{28 - t_{dor}}{t_{eq} - t_{dor}}})\right] \quad (13)$$

The corresponding development of the compressive strength f_c, the tensile strength f_t and of Elasticity Modulus E_c is considered as follows [6]:

$f_c(t_{eq}) = \beta \cdot f_{c,28}$ (14) $f_t(t_{eq}) = \beta^{0.5} \cdot f_{t,28}$ (15) $E_c(t_{eq}) = \beta^{0.3} \cdot E_{c,28}$ (16)

3. Stress Calculation

3.1 Degree of Restraint

The possibility of concrete members to deform freely due to the action of volumetric changes depends on the degree of restriction of this member. For most cases this condition is not known, which makes it difficult to estimate the generated stresses. The Degree of Restraint can vary from a totally free state $\gamma_R = 0$, in which the member moves freely, to a totally restricted state $\gamma_R = 1.0$, in which all the deformation turns to stresses. In the height of a wall the degree of restraint changes according to the geometry of the member (Fig. 3 left).

3.2 Stress Relaxation Function

As the deformations are generated and these are transformed into stresses, the stress relaxation begins, due to the viscous properties of concrete. The stresses relax in time, which is very strong in the early hours while the concrete is still fresh (Fig. 3 right). The above is represented through a Relaxation Function ψ, which depends mainly on the degree of hydration of the cement. The following function taken from the work of van Breugel [7]

allows precise modeling of this situation:

$$\psi(t,t') = \exp\left[-\left\{\left(\frac{E(t)}{E(t')} - 1\right) + \nu \cdot t'^{-\mathrm{d}} \cdot (t-t')^{n} \cdot \frac{E(t)}{E(t')}\right\}\right] \quad (17)$$

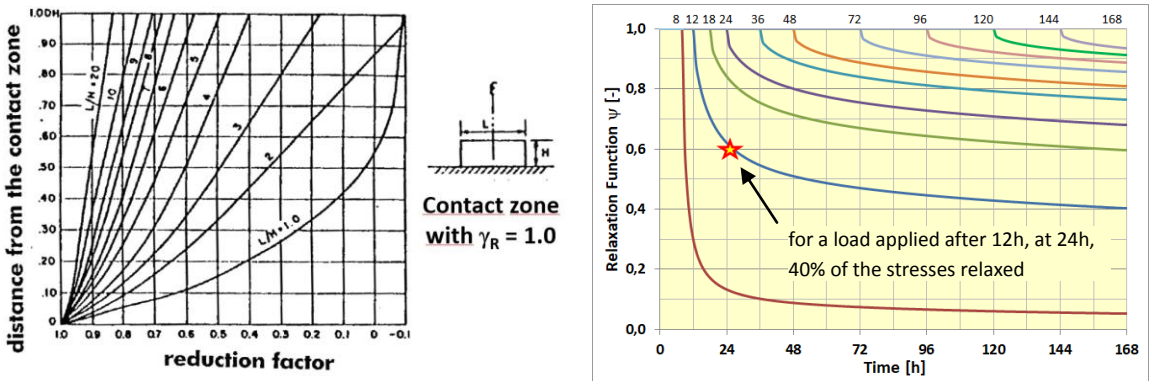

Figure 3: Effect of external restraint in the height and relaxation function.

3.3 Estimation of Stresses

The main difficult in estimating stresses in concrete at early age, due to volumetric changes, lies in the impossibility of knowing precisely the development of the different properties of concrete. Through the following equations the model calculates, considering all the factors mentioned previously, in an hourly step by step procedure, the estimated stresses in the concrete member.

$$\Delta\sigma_t = \left(\varepsilon_{as,t} + \varepsilon_{T,t} + \varepsilon_{s,t}\right) \cdot E_t \cdot \psi_{t,t'} \cdot \gamma_R \quad (18) \qquad \sigma_t = \sum \Delta\sigma(t,t') \quad (19)$$

3.4 Cracking Index

This index corresponds to the ratio between the concrete tensile stress σ_t and tensile strength f_t. It varies in the height of the concrete member, due to the fact of decrease of the internal restraint with height (Fig. 3 left). A value of 1.0 means a crack will occur.

$$I_{cr(t)} = \frac{\sigma_{t(t)}}{f_{t,t(t)}} \quad (20)$$

4. Case Studies

Case I Temperature measurements on-site: a 7.6 m long concrete beam, 4.9 m width, 0.9 m height. Input values: f'_{c28} = 35 [MPa] - Cement content: 380 [kg/m^3] HE - Q_{7d} = 314 [kJ/kg] - U = 25 [kJ/m^{2}h°K]. In Fig. 4 measured values (continuous lines) are compared to estimated values (dotted lines) for Core and Surface temperature. Ambient temperature is also plotted.

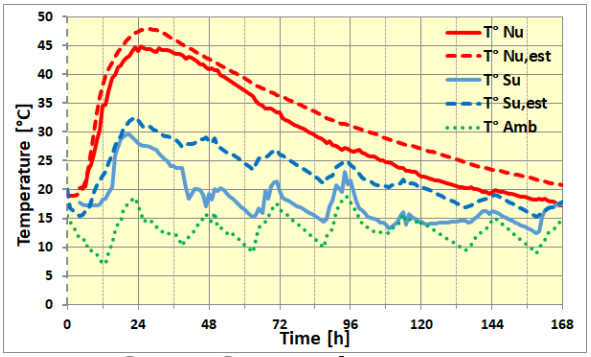

Figure 4: Case I: Concrete beam temperatures.

Case II Cracking observed at early age: a cylindrical water tank, poured in 20 sectors, each 20 m long, 10 m height and 0.65 m width. Input values: f'_{c28} = 55 [MPa] - Cement content = 425 [kg/m^3] HE+8% SF - Q_{7d} = 300 [kJ/kg] – E_a = 35,000 [kJ/mol] – Conductivity = 5.12 [kJ/(mh°K)] – U = 20 [kJ/m^{2}h°K]
Fresh Concrete T° = 18 [°C] / Mean Ambient T° = 10 [°C] / Degree of Restraint = 85 [%].

The predicted temperatures are shown in Fig. 5a, including the *ΔT° Section* in the shadow area. The dotted line correspond to the measured ambient temperature. Figure 5b shows the predicted stresses for a constant elastic, an elastic time dependent and a real elasto-plastic Young´s Module, including the tensile strength development with the dotted line. Figure 5c shows the Cracking Index development for 5 different sections in the height of the wall. The real structure (Fig. 1 right) presented cracks till 1/3 of the height.

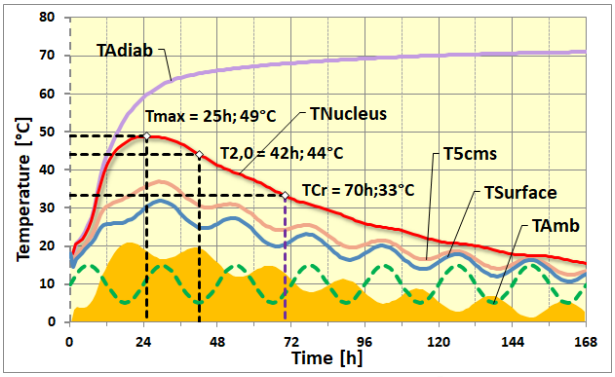

Figure 5a: Temperature Development.

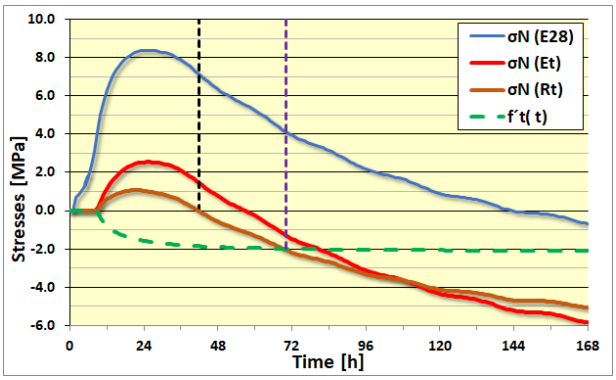

Figure 5b: Stress Development.

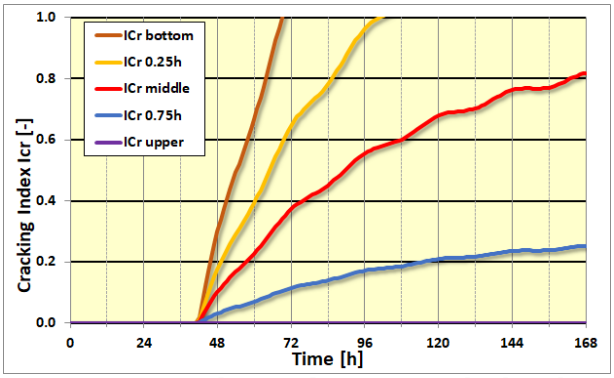

Figure 5c: Crack Development in the height.

5. Conclusions

Despite its simplicity, the model predicts temperature and stress development together with a reliable crack assessment. Sensitivity analysis are easy to perform due to the consideration of technological, pouring, curing and ambient conditions.

References

[1] Ebensperger, L., Wirksamkeit von Quellzusätzen im Beton zur Kompensation von Zwangspannungen infolge Hydratationswärme, PhD Thesis, TU München (1991)
[2] EN 196-9: Methods of testing cement. Part 9: Heat of hydration - Semi-adiabatic method (2010)
[3] Informations Zentrum Beton, Zement-Merkblatt, Massige Bauteile aus Beton (2006)
[4] EN 1992-1-1: Eurocode 2: Design of concrete structures. Part 1-1: General rules and rules for buildings (2004)
[5] AS 5100.5: Australian Standard. Bridge Design – Concrete, Section 6.1.7 (2004)
[6] Kanstad, T., Annex D for Eurocode 2 - 2020: Guidance to limit early age cracking (2017)
[7] van Breugel, K, Development of Temperature and Properties of Concrete as a Function of the Degree of Hydration, RILEM Int. Conf. on Concrete at Early Ages, Paris (1982)

SynerCrete'18 International Conference on Interdisciplinary Approaches
for Cement-based Materials and Structural Concrete
24-26 October 2018, Funchal, Madeira Island, Portugal

EXPERIMENTAL SETUP FOR CHARACTERIZATION OF LONG TERM BOND AND CRACK WIDTHS IN RC TIES UNDER CONSTANT AXIAL FORCE

Carlos Sousa [(1)], Mário Pimentel [(1)], Amin Abrishambaf [(1)], Rui Faria [(1)], Miguel Azenha [(2)]

(1) CONSTRUCT, University of Porto, Porto, Portugal
(2) ISISE, University of Minho, Guimarães, Portugal

Abstract
Crack openings in reinforced concrete (RC) ties are usually calculated as the integral of the relative strains between steel and concrete along the transfer length. The contribution of shrinkage strains (of concrete within the transfer length) to the long-term crack openings is, still today, an unsolved issue. In this context, this paper starts by summarizing common procedures for calculating crack openings in thin RC ties or tensile chords. Then, a short parametric analysis is shown to illustrate the relevance of shrinkage strains in crack openings calculations. Finally, a new test setup, developed for characterization of long-term crack widths and bond stresses between steel and concrete (taking into account the shrinkage influence), is presented.

1. Code formulas for crack width calculations

The procedure for calculation of crack openings, in European codes for RC concrete, is under discussion [1]. In previous Eurocode and Model Code versions, the formulas for determining the maximum crack width, w_{max}, are of the type:

$$w_{max} = 2\, l_{s,max}(\varepsilon_{sm} - \varepsilon_{cm} - \eta_r\, \varepsilon_{sh}) \quad (1)$$

where $l_{s,max}$ is the transfer length; ε_{sm} and ε_{cm} are the steel and concrete average strains along such length; ε_{sh} is the concrete shrinkage (therefore ε_{cm} does not include the shrinkage component); η_r is a coefficient to consider the shrinkage contribution. The coefficient η_r takes the value 1 in fib Model Codes (MCs) 1978 [2] and 1990 [3], and 0 in Eurocode 2 [4]. In fib MC 2010 [5], η_r is 1 for long-term loading of members in the stabilized cracking stage

and 0 in the remaining cases. From a theoretical point of view, considering different η_r values depending on the cracking stage (crack formation or stabilizing cracking) is not justified. The adoption of such η_r value seems to be the result of an effort to calibrate code expressions against experimental results. However, MC background documents do not discuss this important topic [6].

2. Crack width calculations based on the local bond stress-slip relationship

As an alternative to the use of Eq. (1), the maximum crack width can be calculated based on equilibrium and compatibility conditions applied to the transfer length and constitutive relationships for concrete, steel and for the steel-concrete interface (i.e, the local bond-slip relation). The crack opening is equal to twice the slip between steel and concrete at the crack mouth, s_{max}:

$$w_{max} = 2\, s_{max} = 2 \int_0^{l_{s,max}} \varepsilon_s(x) - \varepsilon_c(x)\, dx \tag{2}$$

where $\varepsilon_s(x)$ and $\varepsilon_c(x)$ are the local steel and concrete strains. The coordinate x is the distance to the section of zero slip. The local bond-slip relation is paramount in this type of calculation. The one proposed by the fib MC 2010 [5], for good bond conditions, long-term loading and small slip values (range of values of interest for serviceability calculations), is:

$$\tau(s) = 2.5 \sqrt{f_{cm}} \left(\frac{s}{(1 + k_t)\, s_1} \right)^{0.4} \tag{3}$$

where τ is the local bond stress in MPa, s is the local slip, s_1 is a reference slip value (1mm), f_{cm} is the average concrete compressive strength and k_t is a coefficient to account for the influence of time. This problem can be solved analytically in particular cases (crack formation stage, neglecting the influence of shrinkage) [7]. In the remaining cases, the solution can be calculated using numerical methods, as explained in [8]. It becomes evident that, for long-term calculations, concrete shrinkage strain shall be included in $\varepsilon_c(x)$.

3. Parametric analysis to show the relevance of shrinkage in crack width calculations

Two rectangular RC ties were selected for illustration of the relevance of shrinkage strains in crack width calculation, covering a wide and recurrent range of bar diameters and effective reinforcement rations. Each tie has a rectangular cross section with dimensions B=1 m and H=5 (c + ϕ/2), where c is the clear concrete cover (equal to 40 mm) and ϕ is the bar diameter. The reinforcement consists of two layers of ϕ10 // 100 mm in the first tie and ϕ20 // 100 mm in the second one. The steel cross section, A_s, and the effective area of concrete, $A_{c,eff}$, are shown in Tab. 1. The transfer length, according to the MC 2010 [5] provisions for the stabilized cracking stage, is shown in the same table. The calculation was performed using the numerical framework described in [8], as outlined in §2. The concrete properties correspond

to the strength class C25: f_{cm} = 33 Mpa and tensile stregth f_{ctm} = 2.6 Mpa. The effective modulus of concrete was taken as 12 GPa and the coefficient k_t is 1.8. Besides the amount of reinforcement, the following parameters were varied in the parametric analysis: steel stress at the crack (150 MPa or 250 MPa) and shrinkage strain (0 or 500 μ). Tab. 2 shows representative analysis results, where β is the calculated ratio between the average value (along $l_{s,max}$) of the normal stress in concrete and f_{ctm}; and τ_{bms} is the average bond stress along the same length. The calculated diagrams of local bond stresses are shown in Fig. 1 for the members reinforced with ϕ20 // 100 mm.

Table 1: Characteristics of the analysed RC tensile chords.

	Reinforcement ϕ10 // 100 mm	Reinforcement ϕ20 // 100 mm
A_s (cm^2)	15.8	62.8
$A_{c,eff}$ (m^2)	0.225	0.250
$l_{s,max}$ (mm)	238	150

Table 2: Results of the parametric analysis.

	ϕ10 // 100 mm				ϕ20 // 100 mm			
	σ_s = 150 MPa		σ_s = 250 MPa		σ_s = 150 MPa		σ_s = 250 MPa	
	ε_{sh} = 0	ε_{sh} = 500μ	ε_{sh} = 0	ε_{sh} = 500μ	ε_{sh} = 0	ε_{sh} = 500μ	ε_{sh} = 0	ε_{sh} = 500μ
w_{max} (mm)	0.12	0.24	0.24	0.39	0.14	0.27	0.27	0.40
β	0.25	0.36	0.36	0.49	0.38	0.49	0.49	0.59
τ_{bms} / f_{ctm}	0.54	0.85	0.85	1.09	0.82	1.09	1.09	1.29

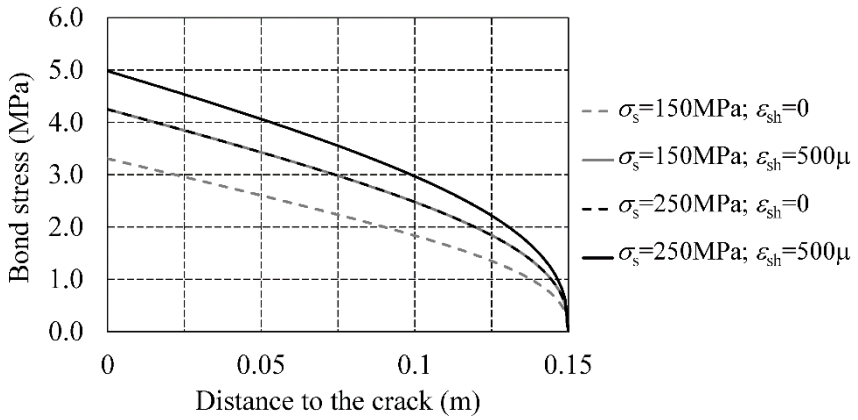

Figure 1. Calculated bond stresses along the transfer length,
for the tensile chord reinforced with ϕ20//100mm.

Note that fib MC2010 [5], as well as the other codes mentioned before [2-4], propose specific values for the parameters β and τ_{bms}/f_{ctm} (explicitly or implicitly, in the adopted formulas). The values shown in Tab. 2, on the other hand, are the result of the analytical calculations.

These results show that shrinkage strains are responsible for an important increase of crack width. Two effects are responsible for an equal crack width variation (because they give rise to the same average deformation): concrete shrinkage equal to 500μ; and steel stress variation equal to 100 MPa. Local bond stresses undergo a moderate increase as a consequence of shrinkage.
This analytical approach provides a sound basis for the derivation of formulas for crack with calculation. However, the calibration of the bond-slip relation and the experimental validation of the analysis methodology is paramount.

4. Tests to assess the bond-slip behaviour

The standard tests to assess the bond behaviour of steel bars embedded in concrete, proposed by RILEM, are described in EN10080 [9]: the pull-out test and the beam test. Even though these tests provide important information regarding the bond behaviour, their results do not provide a true local bond stress-slip relationship to be used in crack width calculations, because: the concrete is loaded differently from what happens in tensile chords; the bond stress and the slip are not measured locally.
A different alternative has been used in the past to assess the bond behaviour [10, 11]: the so-called 'transfer type' test. It consists in a tensile test of an RC tie, with measurement of steel strains in various positions throughout the transfer length. These measurements provide the diagrams of steel strains and, based on that, the bond stresses can be indirectly determined. The main advantage of this test alternative is the fact that it replicates the steel-concrete interaction in a real RC tie or tensile chord. The main difficulty is the steel strain measurement without disturbing the bond action. In the past, electrical resistance strain gages were installed in channels. This technique was pioneered by Mains [10] and improved by Scott [11], among others. More recently, optical Fibre Bragg Grating (FBG) sensors have been used to measure steel strains in closely spaced positions, with a negligible interference in the steel bar and bond action [12, 13]. This technique offers new possibilities for the characterization of the long-term bond stress-slip relation.

5. Developed test setup

The proposed test system applies a tensile force, which can be adjusted to be kept constant throughout time. The test specimen is an RC tie with a single, centred, steel bar. Upon casting of the RC element, a crack is pre-induced, at mid-length, by using a 3 mm thick plate which covers all the concrete cross section. The plate is removed before loading the specimen, in order to create the crack. The initial (~3 mm thick) crack width ensures that the concrete stress in that cross section is zero, even if the system is not perfectly symmetric (small eccentricities are common in test systems to induce axial tension). The length of the concrete element is (in the performed tests) 120 cm. It has to be greater than four times a conservative estimate of the maximum transfer length, so that the transference of bond stresses, near the central crack, can be captured.
Bond stresses are indirectly quantified by measuring the steel strains in 13 positions along the bar length, at the vicinity of a crack (1 at the crack, 6 for each side). For this purpose, an array

of FBGs (made with through-the-coating technology, with a 155 μm thick polyimide continuous coating) is installed in a thin grove (1 mm wide and 1 mm deep) milled in the rebar. The experimental characterization of the slip is carried out using the measured crack opening and transfer length values. In turn, the transfer length is assessed by analysing the diagram of steel strains measured through the FBGs.
Fig. 1 shows the proposed setup. The main components of the load application system are: a rigid frame, two adaptors (couplers), a load cell (capacity of 50 kN), and a hinge. The load is applied simply by tightening a loading nut. The average tie deformation is recorded by four LVDTs (one per lateral face of the RC member), with accuracy of 0.001 mm, held by an aluminium frame. The crack width evolution is measured by a USB digital microscope with a 2Mp camera. For this purpose, two SIM chips (phone SIM cards with known width engravings that act as relative scales) were glued on the pre-induced crack lips, in each of the four sides of the specimen. At some instants of time, the images are captured and processed to determine the crack opening variation.

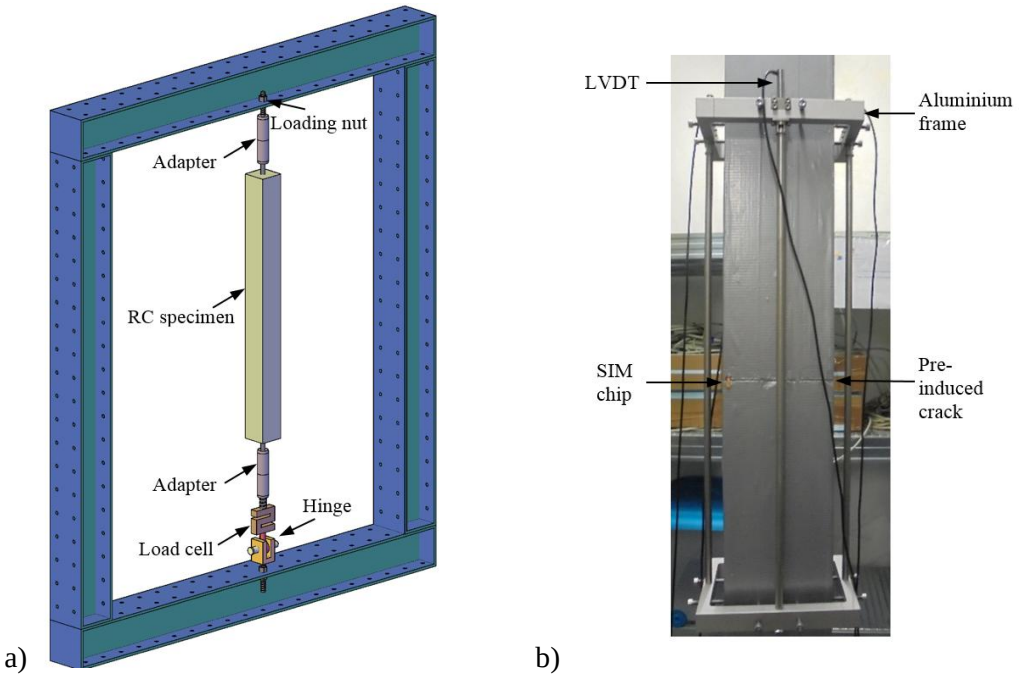

Figure 1. Developed setup: a) three-dimensional image and b) LVDTs to measure the average deformation.

In the ongoing test campaign, two series of tests are performed: a first series of tests on sealed specimens (a sealing membrane is used to prevent drying and, consequently, minimize drying); a second series, with identical specimens, but unsealed. In both series, companion concrete specimens, with the same cross section, are used to measure the free concrete shrinkage. Two bar diameters are tested: 8 and 12 mm. The concrete cross section is chosen so that it corresponds to a reinforcement ratio of 1,1%. FBG sensors are used only in the second series (the one where higher variation of bond stresses are expected throughout time). The results of the first series of tests revealed that the setup is able to record, with good resolution, the specimen long-term deformation and crack opening under a sustained tensile load.

6. Final remarks

The necessity of a new test setup for assessment of the influence of shrinkage on bond stresses and crack width in RC was justified. The developed setup was presented. The experimental results of the ongoing test campaign are expected to provide a contribution to: the understanding of the long-term evolution of crack openings, calibration of constitutive models for long-term finite element analyses; calibration of empirical formulations for calculating long-term crack widths.

Acknowledgments
This work was financially supported by: Project POCI-01-0145-FEDER-007457 (CONSTRUCT) and by project POCI-01-0145-FEDER-007633 (ISISE), funded by FEDER funds through COMPETE2020 - Programa Operacional Competitividade e Internacionalização (POCI), and by national funds through FCT-Fundação para a Ciência e a Tecnologia. FCT and FEDER (COMPETE2020) are also acknowledged for the funding of the research project PTDC/ECM-EST/1056/2014 (POCI-01-0145-FEDER-016841). The financial support of COST Action TU1404 through its several networking instruments is also acknowledged.

References

[1] Caldentey, A., Proposal of new crack width formulas in the Eurocode 2, background, experiments, etc., Proceedings from the miniseminar Crack width calculation methods for large concrete structures, Norway (2017), 17-20
[2] CEB-FIP, Model Code for concrete structures (1978)
[3] CEB-FIP, Model Code 1990. Design code (1993)
[4] CEN, EN 1992-1-1 - Eurocode 2: Design of concrete structures - Part 1-1: General rules and rules for buildings. (2004)
[5] fib, Model Code for Concrete Structures 2010. Wilhelm Ernst & Sohn (2013)
[6] Balázs, G.L. et al, Design for SLS according to fib Model Code 2010, Structural Concrete 14 (2013), 99-123
[7] Balázs, G.L, Cracking analysis based on slip and bond stresses, ACI Materials Journal 90 (1993), 340-348
[8] Sousa, C., Calçada, R. and Neves, A., Numerical evaluation of the non-linear behaviour of cracked RC members under variable-amplitude cyclic loading, Materials and Structures 48 (2015), 2815-2838
[9] CEN, EN 10080 - Steel for the reinforcement of concrete - Weldable reinforcing steel - General (2005)
[10] Mains, R.M., Measurement of the distribution of tensile and bond stresses along reinforcing bars, ACI Journal 23 (1951), 225-252
[11] Scott, R.H., Intrinsic Mechanisms in Reinforced Concrete Beam-Column Connection Behavior, ACI Structural Journal 93 (1996), 1-11
[12] Nellen et al, High strain and high strain gradients measured with fiber Bragg gratings in structural engineering applications, 15th Optical Fiber Sensors Conference TD (2002)
[13] Kenel, A. et al, Reinforcing steel strains measured by Bragg grating sensors, Journal of Materials in Civil Engineering 17 (2005), 423-431

SynerCrete'18 International Conference on Interdisciplinary Approaches
for Cement-based Materials and Structural Concrete
24-26 October 2018, Funchal, Madeira Island, Portugal

INFLUENCE OF CARBONATION AND CONCRETE SPECIMEN SIZE ON GAS DIFFUSION COEFFICIENT

Mouna Boumaaza[(1)], Bruno Huet[(1)], Philippe Turcry[(2)], Christoph Gehlen[(3)], Abdelkarim Aït-Mokhtar[(2)], Detlef Heinz[(3)]

(1) LafargeHolcim research center, 95 rue du Montmurier, 38291 Saint Quentin Fallavier, France
(2) Laboratoire des Sciences de l'Ingénieur pour l'Environnement (LaSIE), UMR 7356 CNRS, Université de La Rochelle, Avenue Michel Crépeau, 17042 La Rochelle, France
(3) Centre for building materials (cbm) Technical University of Munich, Arcisstraße 21, 80333 Munich, Germany

Abstract
This paper investigates the effect of accelerated carbonation on the oxygen-effective diffusion coefficient ($D_{e,O2}$) of dry hardened cement pastes, non-carbonated and carbonated, at different hydration durations (for 1 day to 8 months); the influence of concrete specimen size (discs of 5, 10 and 50mm thickness) on $D_{e,O2}$ and compares $D_{e,O2}$ against oxygen permeability for 14 concrete mixes. The effect of concrete specimen size on oxygen diffusion coefficient is investigated on four concrete mixes hydrated for 90 days. Measurements are made after drying the specimens at 95%RH and 105°C. For each concrete mix: nine replicates of 5mm and 10mm thickness are tested at the dry state and after equilibration at 95%RH and three specimens of 50mm thickness are tested at the dry state only. Carbonation is found to influence $D_{e,O2}$ differently depending on the binder type. $D_{e,O2}$ varies slightly with the concrete specimen thickness, and no clear correlation is found between $D_{e,O2}$ and oxygen permeability.

1. Introduction

Experimental determination of concrete transport properties is required to understand the level of gas tightness of concrete structures in order to limit the ingress of gaseous aggressive species through cementitious materials. Furthermore, the gas diffusion coefficient is a key-parameter for service life prediction models of concrete structures in real environment [1]. In

the case of carbonation which is widely recognized as a significant cause of corrosion of reinforcement in concrete [2], atmospheric carbon dioxide (CO_2) penetrates the concrete by means of a diffusion process through its porous network where it dissolves in the pore water and reacts with different calcium-based phases of the cement paste. Carbonation kinetics depend on how fast the carbon dioxide moves through the concrete carbonated and non-carbonated layers [3]. Thus, it is necessary to determine concrete transport parameters for both carbonated and non-carbonated states in order to model the phenomenon under site conditions. The carbonation reaction modifies the microstructure, changes the porosity of the concrete containing Portland cement [4] and, consequently, could affect the gas transport properties [5]. This brings up the reason why this paper investigates the influence of carbonation on the gaseous oxygen diffusion coefficient of cement paste mixes tested at three different ages, and cast at a volumetric W/C ratio of 1,6. This investigation is carried out at the dry state.

Usually, when concrete transport properties are experimentally determined, common practice is to test specimens of a thickness equal to at least three times the maximum size of the aggregate present in the sample. A major limit in testing these concrete specimens is the long time required to reach water equilibrium. In this work, an experimental campaign is carried out on 4 different concrete mixtures with a main focus on the influence of concrete specimen thickness on gas diffusivity. For each concrete mix, nine discs of 5mm and 10mm thickness are sawn and used to measure oxygen diffusivity at the dry state (oven at 105°C) and after equilibration at 95%RH. Three discs of 50mm thickness that respect the criteria of a thickness 3 times the maximum aggregate size are also tested to oxygen diffusivity but only at the dry state. Finally, the oxygen diffusion coefficient is compared to the oxygen gas permeability for 14 concrete mixes and a correlation between the two transport properties is discussed, as gas permeability is the transport property commonly measured [6].

2. Materials and methods

2.1 Cement pastes

Three cement pastes are tested: Ordinary Portland Cement (OPC) and two paste mixtures prepared by replacing OPC with 50% slag and 10% silica fume (labelled OPC_Slag and OPC_SF, respectively). Additional information on the chemical composition, fineness and specific surface of these materials is given in [7]. These samples are cast at a constant volumetric water-per-cement ratio 1,6. All pastes are tested at three different hydration durations: two months, eight months, 1 day (only for OPC) and 7 days (OPC_SF and OPC_Slag). The latter is achieved by means of an organic solvent, i.e isopropanol. First, the cement pastes are oven dried at 80°C for a month until hydric equilibrium is reached, then they are stored under vacuum for 24h to cool down to laboratory temperature without any mass gain. Then, the diffusion tests are done at the dry non-carbonated state. The paste samples are water saturated under vacuum for 24h, equilibrated for 3 weeks in a relative humidity (RH) of 57%, placed in a storage chamber with a carbon dioxide concentration of 3% by volume for one month and finally oven dried at 80°C to be tested to oxygen diffusivity.

2.2 Concrete

In order to investigate the influence of concrete specimen size on oxygen diffusivity, four concrete mixes are prepared using three cement types as shown in Tab.1. The aggregate volume fraction of these concrete mixes is 70%, the air content 2% and the maximum aggregate size is 22mm. Water porosity of these specimens is determined following the French standard NF P18-459. The mixtures are cast into 11*22cm moulds, demoulded after 24h and stored at 100% relative humidity for 90 days. For each concrete mix, nine replicates are sawn to 5 and 10mm thickness and three replicates to 50mm thickness. First, 5mm and 10mm thickness specimens are dried at 95%RH in a climate chamber. At this relative humidity the water equilibrium was reached after six months. The sides of the specimens are sealed using an epoxy resin to retain oxygen diffusion in one direction. After the determination of the oxygen diffusion coefficient of these samples at 95%RH, they are gradually dried: stored for a week at 60%RH, then at 30%RH, oven dried at 80°C to be finally dried at 105°C until mass equilibrium. This drying process takes around five weeks. Once the mass equilibrium is reached, the samples are placed in a vacuum desiccator 24 hours prior to the diffusion tests to prevent moisture gain when the temperature decreases. As for concrete samples intended to measurements of both oxygen diffusivity and oxygen permeability, 14 mixes are cast and cured for 90 days, then gradually dried at 105°C.

Table 1: Cement type, W/B mass ratio and total porosity of the tested concrete

Concrete label	Cement type	W/B	Water porosity (%)
C1	CEM I	0.65	14.1
C2	CEM III/A	0.4	11.2
C3	CEM III/A	0.65	14.1
C4	CEM IV/A	0.4	11.8

2.3 Transport properties test methods

The oxygen diffusion coefficient is measured using an experimental setup developed during our previous works [7,8]. The test method relies on the accumulation of gaseous oxygen inside the cell. Oxygen diffusion coefficient is determined by the numerical fitting of the accumulation curve to Fick's second law. For cement paste samples, the tested specimens are discs of 4cm diameter and 3mm thickness. Concrete specimens have a diameter of 11cm and a thickness that varies between 5 and 50mm. Oxygen permeability is determined for 14 concrete mixes following the French Standards XP P18-463. For each concrete, three replicates of 5cm thickness and 15cm diameter are tested after being dried at 105°C. These specimens are then cored into discs of 11cm diameter to be tested to oxygen diffusivity.

3. Results and discussion

3.1 Cement pastes

Fig.1 shows results of the oxygen diffusion coefficient of non-carbonated (NC) and fully carbonated cement pastes (C) at three hydration durations (early age = 1 day for OPC and 7

days for OPC_SF and OPC_Slag). These results show that carbonation seems to induce different effects on the three mixes. First, we note that the oxygen effective-diffusion coefficient ($D_{e,O2}$) decreases for OPC pastes by a factor of 9 at two months and 2 at eight months of hydration, and by a factor of 50 at early age. This strong decrease of $D_{e,O2}$ for OPC pastes hydrated only for 1 day could be explained by a possible restart of hydration of these samples during the 24h water saturation under vacuum, the conditioning at 57% RH or during the accelerated carbonation. Carbonation is known to lower the total porosity [4] which could affect the transport properties. However, the decrease of $D_{e,O2}$ with carbonation is not a consequence of the total porosity variation only, since previous works [8] showed that blended cement pastes have lower diffusivity than Portland pastes even though their total porosity was higher. These works also revealed that oxygen-effective diffusion coefficients display a somewhat linear trend with respect to the mean pore diameter. Meanwhile, carbonation impact on blended cements is less consistent: $D_{e,O2}$ decreases by a factor of 3 at the most at early age and slightly increases at two months hydration. Previous works showed that accelerated carbonation of hardened cement pastes containing slag increases gas diffusivity [9,5]. Still, further investigations including XRD/TGA and pore size distribution of the carbonated samples are required for a deeper interpretation of these results.

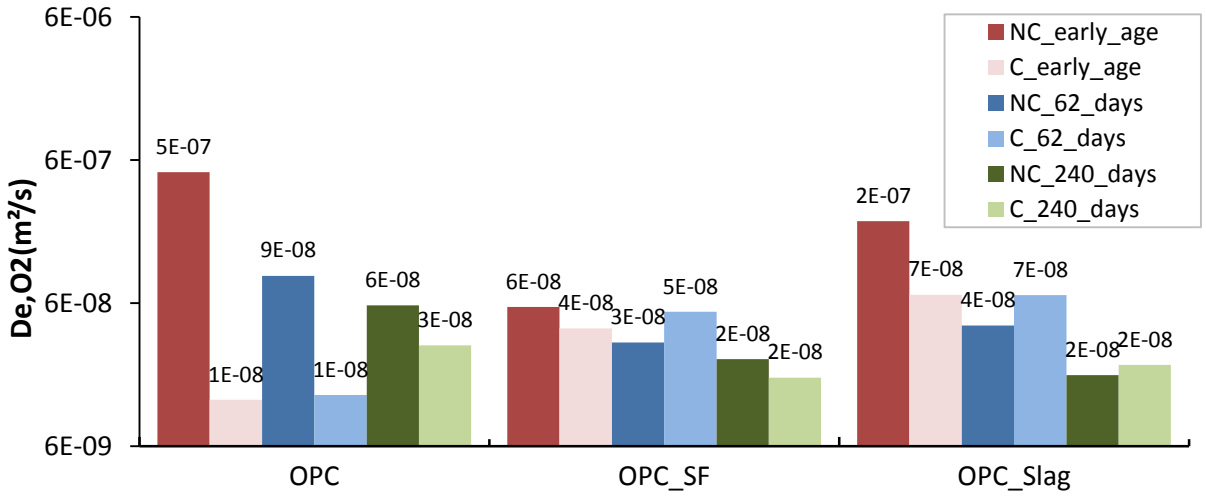

Figure 1: Oxygen diffusion coefficients for carbonated and non-carbonated cement pastes.

3.2 Concrete

Fig. 2 shows that the oxygen diffusivity increases slightly with the specimen thickness (by a factor of 3 at the most) for both dry samples and samples equilibrated at 95%RH (the water saturation degree of the latter samples is found to vary between 65% and 70%). It is suggested that this is a result of cracks induced by oven drying at 105°C. For thin samples, the thermal gradient leads to a lower thermal stress, hence less cracking would appear [10]. Note that $D_{e,O2}$ of specimens equilibrated at 95%RH (i.e high water saturation degree ~70%) is three orders of magnitude lower than $D_{e,O2}$ of dry specimens (example : concrete C4).

Fig.3 shows the oxygen permeability as a function of the oxygen diffusivity in log-scale. For each mix, values of $D_{e,O2}$ and oxygen permeability are computed as the average value of three replicates. Markers on Fig. 3 indicate the cement type used for the tested concrete and colours indicate the W/B ratio value. For example, a red circle is used for a CEMI concrete of a 0.4

W/B. Our results show a very poor correlation between the two transport properties. This could be explained by the fact that drying induced microcracks influence highly the oxygen permeability, while they only vary $D_{e,O2}$ by a factor of 2 at the most [11]. Note that previous works have found a rather good correlation between the two transport properties [11-12]. Nevertheless, their results were established only for few concretes (4 to 6 mixes).

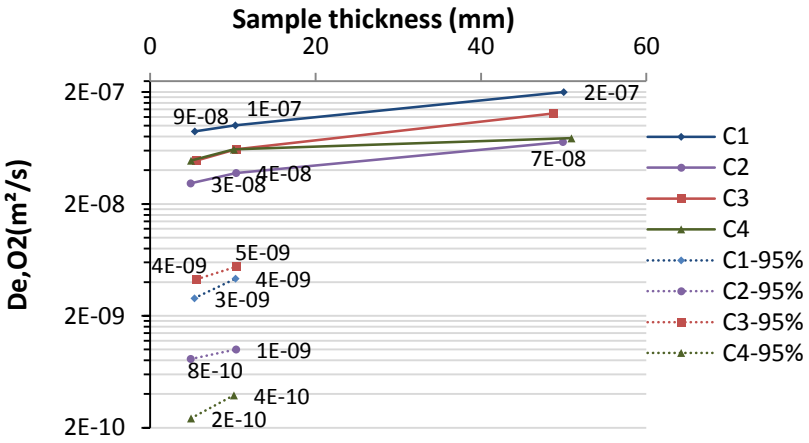

Figure 2: Oxygen-effective diffusion coefficient as a function of sample thickness for concretes at the dry or equilibrated at 95%RH.

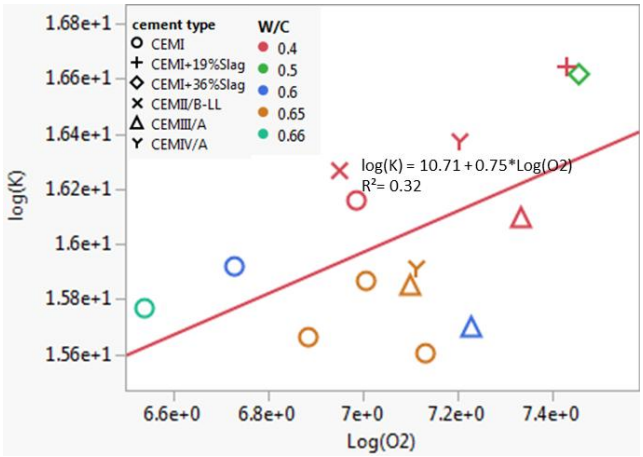

Figure 3: Average (n=3) oxygen effective diffusion coefficient vs oxygen permeability.

4. Conclusion

Even though carbonation decreases highly the oxygen-effective diffusion coefficient ($D_{e,O2}$) of OPC pastes, it slightly varies $D_{e,O2}$ of blended cement pastes. We cannot presently assess these results and further research has to be carried out, especially on pore size distribution variation after carbonation. Using our diffusion test, $D_{e,O2}$ is found to vary by a factor of 3 at the most with the concrete specimen thickness. This is a rather encouraging result since

testing thin concrete samples is of a high convenience: water equilibrium and gas diffusion steady state are reached much faster for thinner concrete samples. Still, these results are only established for 4 concrete mixes and further tests are necessary. No clear correlation is found between $D_{e,O2}$ and oxygen permeability for 14 concrete mixes, oven-dried at 105°C.

References

[1] S. Von Greve-dierfeld, C. Gehlen, Performance based durability design , carbonation part 1 – Benchmarking of European present design rules, 17 (2016) 309–328.
[2] B. Huet, V. L'hostis, G. Santarini, D. Feron, H. Idrissi, Steel corrosion in concrete: Determinist modeling of cathodic reaction as a function of water saturation degree, Corros. Sci. 49 (2007) 1918–1932.
[3] W. Ashraf, Carbonation of cement-based materials: Challenges and opportunities, Constr. Build. Mater. 120 (2016) 558–570.
[4] G. Villain, M. Thiery, Impact of carbonation on microstructure and transport properties of concrete, in: 10DBMC Int. Conférence Durab. Build. Mater. Components, Lyon , France, 2005.
[5] M. Bertin, Impact du séchage au jeune âge sur la carbonatation des matériaux cimentaires avec additions minérales, PhD thesis, Université Paris-est marne la vallée, 2017.
[6] J.S. Andrade, U.M.S. Costa, M.P. Almeida, H.A. Makse, H.E. Stanley, Inertial Effects on Fluid Flow through Disordered Porous Media, (1999) 5249–5252.
[7] M. Boumaaza, B. Huet, G. Pham, P. Turcry, A. Aït-Mokhtar, C. Gehlen, A new test method to determine the gaseous oxygen diffusion coefficient of cement pastes as a function of hydration duration , microstructure , and relative humidity, Mater. Struct. 51 (2018).
[8] M. Boumaaza, B. Huet, P. Turcry, C. Gehlen, A. Ait-Mokhtar, D. Heinz, Gas diffusion coefficient of cement paste and con- crete : effect of water saturation degree and specimen thickness, in: 12th Fib Int. PhD-Symposium Civ. Eng., 2018: pp. 1–8.
[9] P. Turcry, F. Gendron, A. Ait-Mokhtar, CO2 diffusion in cementitious materials : experimental investigations, in: 2nd Int. RILEM/COST Conf. Early Age Crack. Serv. Cem. Mater. Struct. EAC2, ULB-VUB, Brussels , Belgium, (2017).
[10] T. Gardner, Chloride transport through concrete and implications for rapid chloride testing, PhD thesis, University of Cape Town, 2006.
[11] H.S. Wong, M. Zobel, N.R. Buenfeld, R.W. Zimmerman, Influence of the interfacial transition zone and microcracking on the diffusivity, permeability and sorptivity of cement-based materials after drying, Mag. Concr. Res. 61 (2009) 571–589.
[12] C. Villani, R. Loser, M.J. West, C. Di Bella, P. Lura, W.J. Weiss, An inter lab comparison of gas transport testing procedures: Oxygen permeability and oxygen diffusivity, Cem. Concr. Compos. 53 (2014) 357–366.

SynerCrete'18 International Conference on Interdisciplinary Approaches
for Cement-based Materials and Structural Concrete
24-26 October 2018, Funchal, Madeira Island, Portugal

INFLUENCE OF PRESTRESS LOSSES ON THE DYNAMIC OVER STATIC CAPACITY RATIOS OF RAILWAY CONCRETE SLEEPERS

Chayut Ngamkhanong [(1),(2)] and Sakdirat Kaewunruen [(1),(2)]

(1) Department of Civil Engineering, School of Engineering, University of Birmingham, Birmingham B152TT, United Kingdom
(2) Birmingham Centre for Railway Research and Education, School of Engineering, University of Birmingham, Birmingham B152TT, United Kingdom

Abstract
Railway sleeper, which is placed underneath the rail, is one of the main components of railway track. Railway sleepers can be made of timber, concrete, composite materials etc. Prestressed concrete sleeper is one of the most popular types which can be seen in railway track all over the world. However, loss of prestress is a significant concern as it can affect strength of member and its serviceability including stresses in concrete, cracking etc. In prestressed concrete applications, the most important variable is the prestressing force. It was observed that the prestressing force can be reduced with time because of several factors such as creep and shrinkage of concrete, steel relaxation, friction loss, anchorage slip etc. RESPONSE2000 was used to evaluate the static and dynamic capacities based on the modified compression field theory. The study results exhibit that the losses of prestress have significant effects on the overall strength of prestressed concrete sleepers. It is recommended to take into account the effect of prestress losses in standard design of prestressed concrete sleepers.

1. Introduction

Railway sleepers are a main part of railway track structures. Railway sleepers embedded in ballasted railway tracks are laid to support the rails. The main functions of sleeper are to redistribute loads from the rails to the underlying ballast bed, to secure rail gauge and to enable safe passages of rolling stocks. It should be noted that railway sleepers are a structural and safety critical component in railway track systems [1-6]. The sleepers can be typically

made of timber, concrete, steel, composites etc. Remarkably, railway prestressed concrete sleepers have been used in railway industry for over 50 years [7, 8]. Prestressed concrete sleepers would have an improved structural capacity and/or serviceability as compared to conventional reinforced concrete sleepers. However, they are prone to deterioration issues as cracks may occur and expand during operation. Moreover, losses of prestress are a serious concern since it affects the strength of prestressed concrete member. In fact, the prestressing force in prestressed concrete can be reduced due to the initial losses and long-term losses [9, 10]. Initial prestress losses occur when the prestress is transmitted to the concrete, there is contraction due to prestress. This contraction causes a loss of stretch in the wire. Loss can be expressed as percentage or in terms of stress or in terms of total deformation or in terms of strain. According to the literature [11], it is interesting to note that prestrain in steel has a significant effect on the strength of steel. The strength increases with the increasing of pre-strain in steel but the elongation decreases.

Generally, railway track structures often experience impact loading conditions due to wheel/rail interactions associated with abnormalities [12] in either a wheel or a rail. Wheel/rail irregularities induce high dynamic impact forces along the rails that may greatly exceed the static wheel load. Although, the dynamic behaviour of railway sleepers has been studied [13-17], the considerations of its behaviour when the sleepers undergo prestress losses, have not been fully studied. This paper investigates and presents an advanced railway concrete sleeper modelling capable of parametric analysis into the effect of prestress loss on the dynamic behaviors of railway sleepers. This paper considers the wide range of prestress loss in order to cover all the possible behaviours as the railway sleeper may experience higher time dependent losses [18]. The dynamic factors are highlighted. The emphasis of this study has been placed on the impact capacity of the sleepers. The improved understanding in this paper will help update the practical maintenance issues in railway industry. The understanding of the dynamic capacity of railway concrete sleepers will also help improve technology for track condition monitoring [19].

2. Methodology

2.1 Modified compression field theory

The ultimate moment has been used to represent the capacity of prestressed concrete sleepers. In general, concrete sleepers would fail in bending or shear bending mode. The moment capacities are predicted by the adaptation of modified compression field theory using Response-2000 [20]. This software is a nonlinear sectional analysis for the analysis of concrete elements. The theory is capable of predicting the behaviour of reinforced concrete subjected to in-plane shear and normal stresses. The concrete stresses in principal directions along with prestressing steel are considered in only axial direction and uncracked portion will carry on to sustain a load in the analysis [21]. The assumptions of this theory are that the deformation plane section remains plane after loading and there is no transverse clamping stress across the depth of the section. It is also assumed that prestressing wires and concrete are bonded perfectly. The section can be failed in only pure bending or shear-bending modes. The dimension of prestressed concrete sleeper is shown in Figure 1. There are 4 layers with 22 tendons. The ultimate strength of 1860MPa and elastic modulus of 200000MPa are

considered. The high strength concrete with the cylinder compressive strength of 55MPa is taken into account.

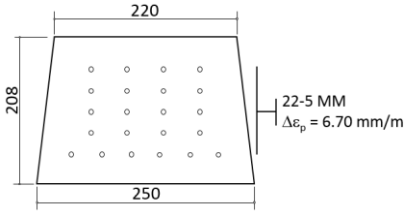

Figure 1: Prestressed concrete sleeper dimension.

2.2 Effect of strain and loading rates

In this study, it is assumed that prestressing wires and concrete are bonded perfectly. It should be noted that the strain rate plays a role in material strengths. The prediction of moment capacity has been carried out using the data obtained from the previous experiments [22, 23]. It should be noted that the average total duration of impact forces is about 4 ms. In this study, the strain rate of concrete used is 2 s^{-1} as recommended by previous studies. It is known that the dynamic ultimate strain of prestressing steel is about 0.02, and the total duration of impact force influencing the steel fibre is roughly from 6 ms. This is because the impact stress wave delays during the stress propagation and will be impeded through concrete [24]. Hence, the strain rates of prestressing wires are estimated to be 6 s^{-1}. The dynamic strength of materials can be obtained as the input for the sectional analysis using Eqs. (1) and (2) as follows.
Concrete:

$$\frac{f'_{c,dyn}}{f'_{c,st}} = 1.49 + 0.268 \log_{10} \dot{\varepsilon} + 0.035[\log_{10} \dot{\varepsilon}]^2 \quad (1)$$

Prestressing wires:

$$\frac{f_{y,dyn}}{f_{y,st}} = 10^{0.38 \log_{10} \dot{\varepsilon}^{-0.258}} + 0.993 \quad (2)$$

Where $f_{y,dyn}$ is the dynamic upper yield point stress, $f'_{c,st}$ is the static upper yield point stress of prestressing wires (about 0.84 times proof stress), and $\dot{\varepsilon}$ is the strain rate in tendon.

3. Results and Discussions

Figure 2 show the static moment capacities of prestress concrete sleepers with the consideration of prestress loss. It is clearly seen that prestress losses play a significant effect on prestressed concrete strength especially at first crack. The moment at first crack decreases with the increasing of prestress loss. They are observed as linear trends in both positive and negative directions. The trends of results are quiet similar to the strength of steel [11] with the consideration of pre-strain as it highly effects the moment at first crack rather than ultimate strength. It is also interesting to note that the difference between moment at first crack and ultimate strength of prestressed concrete sleepers slightly increase with the increase

percentage of prestress losses as prestress loss has a little effect in ultimate moment capacity. Dynamic capacities of prestressed concrete sleepers are shown in Figure 3.

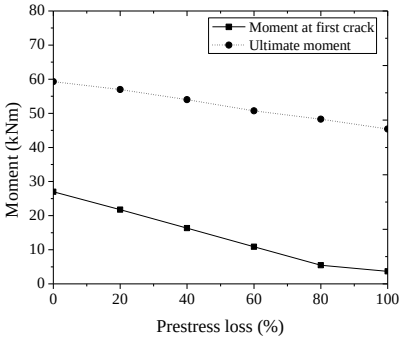

a) Positive moment

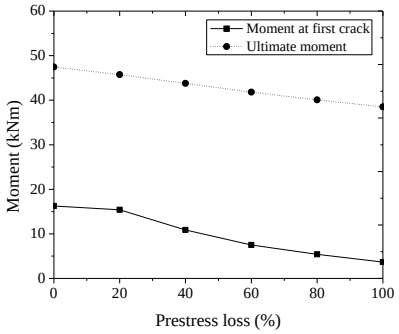

b) Negative moment

Figure 2: Static capacities of prestressed concrete sleepers at various prestress losses.

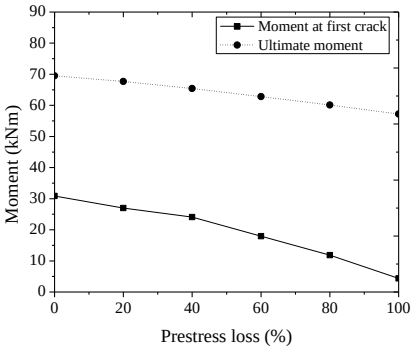

a) Positive moment

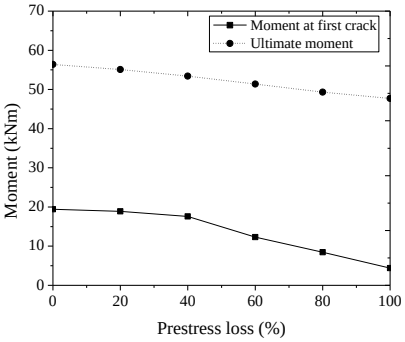

b) Negative moment

Figure 3: Dynamic capacities of prestressed concrete sleepers at various prestress losses.

Figure 4 shows dynamic over static ratios at various prestress losses. It can be seen that the dynamic factors of both positive and negative ultimate moment are in the range of 1.15-1.25. As for the dynamic factor of moment of first crack, it is observed that the dynamic factors of positive and negative moments are in the range of 1.15-2.17 and 1.19-2.26. However, it should be noted that when the huge losses of prestress are applied, the moment at first crack cannot be predicted accurately. This is because the moments observed are at very low range and software cannot provide the appropriate step of results.

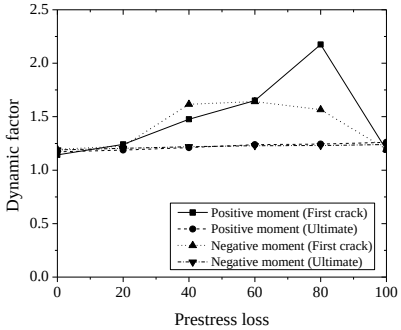

Figure 4: Dynamic factors

4. Conclusions

This study presents the dynamic factor of railway concrete sleepers considering the effects of prestress losses. Dynamic factors are presented in term of the ratio between dynamic and static capacities. The results obtained show that the dynamic factors of ultimate moment are in the range of 1.15-1.25. Moreover, the ranges of 1.15-2.26 are also observed as the dynamic factor of moment at first crack. Nevertheless, it should be noted that the moment at first crack cannot be predicted precisely when the huge losses of prestress are considered. It is interesting to note that the prestress losses have more significant effects on moment at first crack rather than ultimate moment since it shows the variation of dynamic factors associated with prestress losses. The results show that the losses of prestress have crucial effects on the overall strength of prestressed concrete sleepers.

Acknowledgements
The authors are sincerely grateful to European Commission for the financial sponsorship of the H2020-MSCA-RISE Project No. 691135 "RISEN: Rail Infrastructure Systems Engineering Network," which enables a global research network that tackles the grand challenge of railway infrastructure resilience and advanced sensing in extreme environments (www.risen2rail.eu) [25].

References

[1] Fryba, L., Dynamics of railway bridges, Thomas Telford Czech Republic (1996)
[2] Gamage, E., Kaewunruen, S. and Remennikov, A.M., Design of holes and web openings in railway prestressed concrete sleepers, Railway Engineering Conference, Edinburgh, UK (2015)
[3] Kaewunruen, S. and Remennikov, A.M., Structural safety of railway prestressed concrete sleepers, Aust. J. Struct. Eng 9(2) (2009), 129–140
[4] Kaewunruen, S. and Remennikov, A.M., On the residual energy toughness of prestressed concrete sleepers in railway track structures subjected to repeated impact loads, Electronic Journal of Structural Engineering 13(1) (2013), 41-61
[5] Remennikov, A.M., Murray, M.H. and S. Kaewunruen, S., Conversion of AS1085.14 for railway prestressed concrete sleeper to limit states design format, AusRAIL Plus 2 (Dec 2-6, Sydney, Australia) (2007)
[6] Remennikov, A.M., Murray, M.H. and S. Kaewunruen, S., Reliability based conversion of a structural design code for prestressed concrete sleepers, Proceedings of the Institution of Mechanical Engineers: Part F Journal of Rail and Rapid Transit 226(2) (2012), 155-173
[7] Kaewunruen, S. and Remennikov, A.M., Sensitivity analysis of free vibration characteristics of an in-situ railway concrete sleeper to variations of rail pad parameters, Journal of Sound and Vibration 298(1) (2006), 453-461
[8] Kaewunruen, S. and Remennikov, A.M., Investigation of free vibrations of voided concrete sleepers in railway track system, Proceedings of the Institution of Mechanical Engineers Part F: Journal of Rail and Rapid Transit 221(4) (2007), 495-507

[9] Li, D., C. Ngamkhanong, C. and Kaewunruen, S., Time-dependent topology of railway prestressed concrete sleepers, IOP Conference Series: Materials Science and Engineering 245 (3) (2017)
[10] Li, D., C. Ngamkhanong, C. and Kaewunruen, S., Influence of Surface Abrasion on Creep and Shrinkage of Railway Prestressed Concrete Sleepers, IOP Conference Series: Materials Science and Engineering 245 (3) (2017)
[11] Zulfi, F.R. and Korda, A.A., Effect of pre-strain on mechanical properties and deformation induced transformation of 304 stainless steel, J. Phys.: Conf. Ser, 739 (2016)
[12] Remennikov, A.M. and Kaewunruen, S., A review on loading conditions for railway track structures due to wheel and rail vertical interactions, Structural Control and Health Monitoring 15(2) (2008), 207-234
[13] Ngamkhanong, C., Li, D. and Kaewunruen, S., Impact capacity reduction in railway prestressed concrete sleepers with vertical holes, IOP Conference Series: Materials Science and Engineering 236(1) (2017)
[14] Ngamkhanong, C., Kaewunruen, S. and Remennikov, A.M., Static and dynamic behaviours of railway prestressed concrete sleepers with longitudinal through hole, IOP Conference Series: Materials Science and Engineering 251(1) (2017)
[15] Kaewunruen, S. and Remennikov, A.M., Dynamic flexural influence on a railway concrete sleeper in track system due to a single wheel impact, Engineering Failure Analysis 16(3) (2009), 705-712
[16] Kaewunruen, S. and Remennikov, A.M., Dynamic properties of railway track and its components: recent findings and future research direction, Insight-Non-Destructive Testing and Condition Monitoring 52(1) (2010), 20-22(3)
[17] Ngamkhanong, C., Li, D. and Kaewunruen, S., Impact capacity reduction in railway prestressed concrete sleepers with surface abrasions, IOP Conference Series: Materials Science and Engineering 245(3) (2017)
[18] Ngamkhanong, C., Kaewunruen, S. and Costa, B.J.A., State-of-the-Art Review of Railway Track Resilience Monitoring, Infrastructures, 3(1) (2018), 3
[19] Ngamkhanong, C., Li, D., Remennikov, A. and Kaewunruen, S., Dynamic capacity reduction of railway prestressed concrete sleepers due to surface abrasions considering the effects of strain rate and prestressing losses, International Journal of Structural Stability and Dynamics (2018), DOI: 10.1142/S0219455419400017
[20] Bentz, E.C., Sectional analysis of reinforced concrete members, University of Toronto, Department of Civil Engineering (2000)
[21] Remennikov, A.M. and Kaewunruen, S., Experimental load rating of aged railway concrete sleepers, Engineering Structures 76(1) (2014), 147-162
[22] Kaewunruen, S. and Remennikov, A.M., Impact capacity of railway prestressed concrete sleepers, Engineering Failure Analysis 16(5) (2009), 1520-1532
[23] Li, D., C. Ngamkhanong, C. and Kaewunruen, S., Influence of vertical holes on creep and shrinkage of railway prestressed concrete sleepers, IOP Conference Series: Materials Science and Engineering 236(1) (2017)
[24] Wakui, H. and Okuda, H., A study on limit-state design for prestressed concrete sleepers, Concr Lib JSCE 33 (1999), 1–25
[25] Kaewunruen, S., Sussman, J.M. and Matsumoto, A., Grand Challenges in Transportation and Transit Systems, Frontiers in Built Environment, 2(4) (2016)

SynerCrete'18 International Conference on Interdisciplinary Approaches
for Cement-based Materials and Structural Concrete
24-26 October 2018, Funchal, Madeira Island, Portugal

THE INFLUENCE OF SLAG CHEMISTRY ON BLENDED CEMENTS MADE WITH IRON-RICH SLAG

Vincent Hallet [1, 2], Jos Denissen [1], Remus Ion Iacobescu [1], Yiannis Pontikes [1]

(1) Department of Materials Engineering, KU Leuven, Leuven, Belgium
(2) Magnel Laboratory for Concrete Research, Faculty of Engineering & Architecture, Ghent University, Ghent, Belgium

Abstract

Ordinary Portland cement is often substituted by ground granulated blast furnace slag (GGBFS) in order to adjust the properties and decrease the CO_2 emissions of the cement binder. GGBFS is rich in Ca and Si and poor in Fe. On the contrary, non-ferrous metallurgy slags are rich in Fe and Si and poor in Ca. Nonetheless, it is known that Fe^{3+} could develop hydration products at the expense of Al^{3+}. Therefore, this paper investigates the pozzolanic activity of 3 iron-rich slags with varying content of major oxides, as single components and in blended cements. Slag reactivity was assessed through dissolution tests in 0.1M NaOH solution and by thermogravimetric analysis. Additionally, blended cements with 30 wt% substitution of Portland cement were produced and investigated for the phase assemblage and mechanical strength using quantitative X-ray powder diffraction and compression tests, respectively. Following the characterisations, slags with low $(CaO+MgO)/SiO_2$ weight ratio showed pozzolanic activity, whereas the slag with high $(CaO+MgO)/SiO_2$ weight ratio exhibited more latent hydraulic behaviour. Furthermore, after 90 days of curing, all slag blend formulations had higher compressive strengths than those without slag. This work therefore shows that the Fe-rich slags used in this study are suitable candidates for OPC substitution.

1. Introduction

Currently, the only slag type specified in the European EN197-1 norm [1] is ground granulated blast furnace slag (GGBFS), originating from iron production. On the other hand, non-ferrous metallurgy produces high volumes of slags as well. If these slags would exhibit cementitious properties, they could be considered as supplementary cementitious materials (SCMs) in the future. In this way they may contribute to decreased CO_2 emissions for the

cement and concrete industry, although the environmental loads of the metallurgical processes should also be taken into account. These non-ferrous slags are nowadays only scarcely investigated as viable SCMs and are mostly considered for lower-value applications, such as aggregate. Research on typical non-ferrous slags, such as copper slags [2], ferronickel slags [3] and lead/zinc slags [4], has shown that the use of such slags as SCM often leads to lower compressive strengths with respect to pure ordinary Portland cement (OPC), especially at early age, thereby limiting the viable replacement volumes. These lower compressive strengths are a consequence of the chemistry of non-ferrous metallurgy slags. Since GGBFS originates from iron production, they have typically low iron and high calcia contents [5]. On the contrary, non-ferrous metallurgy slags usually have high iron and moderate/low calcia content. Iron is often reported to yield silicious hydrogarnets after hydration in typical OPC hydration environments [6], which do not lead to strength increases due to their low specific volume. Therefore, the high iron content appears to be non-beneficial to their use as SCMs. However, another factor might be the low dissolutions rates, leading to low iron release in the pore solution, also resulting from the high iron contents of these slags [7]. In this work, in order to improve the dissolution rates of the slags, and thus also their reactivity, the slags were water quenched to obtain a high amount of amorphous phase, as it has been shown that this increases the slag dissolution rates [8]. Moreover, the slags with either increased Al_2O_3/SiO_2 or increased $(CaO+MgO)/SiO_2$ weight ratios with respect to a reference slag were produced, as it has been reported that these factors can increase the dissolution rate, the former due to weaker Al-O bonds with respect to Si-O bonds[9] and the latter by acting as additional network modifier [10].

2. Materials & methods

Slags used in this study were a reference slag (B-slag) and slags with either increased Al_2O_3/SiO_2 weight ratio (A-slag) or $(CaO+MgO)/SiO_2$ weight ratio (M-slag) with respect to the reference slag. All slags were characterized by X-ray fluorescence (PW2400, Philips) to determine the chemical composition (Tab. 1) and by quantitative X-ray powder diffraction (QXRD;D2 PHASER, Bruker), for the phase assemblage (Tab. 2). The chemical composition of the amorphous phase was measured using electron probe microanalysis with wavelength dispersive spectroscopy (JXA-8530F, JEOL;Tab. 1). Slags, as well as the inert quartz filler used as a reference, were milled to a specific surface of 4500 ±200 cm^2/g, as determined using the Blaine method described in EN196-6 [11], for all experiments.
Reactivity was investigated by means of dissolution tests and a $Ca(OH)_2$ consumption test. Dissolution tests were conducted by immersion of slags in 0.1 M NaOH (pH = 13) solutions with a liquid-to-slag ratio of 100 to avoid precipitation. Stirring was not used in order to avoid particle abrasion. After filtration, elemental concentrations of Al, Ca and Si were measured at specific times over 7 days with inductively coupled plasma optical emission spectroscopy (ICP-OES). In the $Ca(OH)_2$ consumption test, pastes containing 20 wt% $Ca(OH)_2$ and 80 wt% slag or quartz (as inert material), with water in a water/solid (W/S) ratio of 0.4, were prepared and $Ca(OH)_2$ consumption was determined by thermogravimetric analysis (TGA). TGA was conducted from 20 to 900 °C, with a temperature step of 10 °C/min and under inert (N_2, 100 ml/min) atmosphere.

Finally, blended cements with 30 wt% slag, 70 wt% cement (CEM I 52.5N) and water over solid weight ratio (W/S) of 0.4 were prepared. Phase assemblage over time was investigated using QXRD and compression strength was determined in accordance with EN196-1 [12]. Before QXRD analysis, hydration was stopped by immersion of crushed paste in isopropanol, followed by shaking for 2 hours and finally drying at 40 °C for 1 hour. For QXRD, zincite (95% purity) was used as an internal standard, and quantification was done with normalized Rietveld analysis using TOPAS Academic V5 software.

Table 1: Composition of the slags, where A, B and M refer to the different slags. Subscripts "b" and "am" represent the bulk and amorphous content, respectively and ratios are weight ratios. Relative estimated error of 10% for bulk composition.

Element	**B_b (wt%)**	**A_b (wt%)**	**M_b (wt%)**	**B_{am} (wt%)**	**A_{am} (wt%)**	**M_{am} (wt%)**
FeO	40	38	30	37 ± 0.9	23 ± 0.9	25 ± 0.9
SiO_2	27	24	24	26 ± 0.4	32 ± 0.7	25 ± 0.5
CaO	18	16	22	18 ± 0.2	21 ± 0.3	22 ± 0.6
Al_2O_3	7	13	8	7 ± 0.1	11 ± 0.3	7 ± 0.1
MgO	2	2	10	2 ± 0.0	2 ± 0.0	10 ± 0.1
Other	6	7	6			
Al_2O_3/SiO_2	0.26	0.54	0.33	0.27	0.34	0.28
FeO/SiO_2	1.48	1.58	1.25	1.42	0.72	1
$(CaO+MgO)/SiO_2$	0.74	0.75	1.33	0.77	0.72	1.28

Table 2: Phase assemblage of the slags where A, B and C refer to the different slags.

Phases	**Chemical formula**	**B (wt%)**	**A (wt%)**	**M (wt%)**
Wüstite	FeO	8	4	0
Spinel	$Mg_xAl_yFe_zO$	3	9	8
Periclase	MgO	0	1	9
Trace phases (Quartz, Corundum)	(SiO_2, Al_2O_3)	(<1, 0)	(1, 2)	(< 1, <1)
Others/Amorphous	/	89	83	82

3. Results & discussion

3.1 Reactivity tests

The dissolution behaviour of slag B and A (Fig. 1) in the 0.1 M NaOH solution is very similar, with a slightly higher fraction of the A-slag dissolving after 7 days, most likely due to

the higher Al-content in combination with more easily broken Al-O bonds with respect to Si-O bonds [9]. Additionally, Fig. 1 (left) shows the % of the element dissolved with respect to the amorphous phase content, but taking into account the higher Al-content of the A-slag, the total absolute release difference is even higher. Similarly, total Si-release from slag A was higher as well, and both elements are crucial in pozzolanic reactions. Slag M on the other hand shows increased Ca^{2+} release, both in absolute amounts as well as relative to the amount in the amorphous phase. This is most likely related to the presence of additional Mg^{2+} and Ca^{2+} in the slag, both acting as a network modifier, increasing the dissolution rate [10]. Mg^{2+} ions could not be detected, as they are probably precipitating. The enhanced release of Ca^{2+}, and most likely also Mg^{2+}, will lead to more latent hydraulic behaviour.

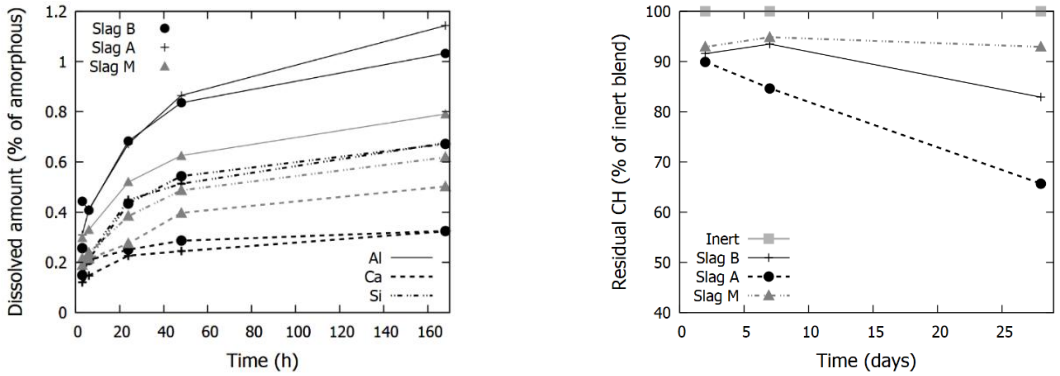

Figure 1: (left) Percentag of the amorphous content of the slags dissolved in 0.1 M NaOH solution over time. (right) CH ($Ca(OH)_2$) remaining as percentage of remaining CH in the inert-CH blend.

$Ca(OH)_2$ consumption is used to determine whether the slags take part into pozzolanic reactions, and thus consume $Ca(OH)_2$. However, since the experiment was carried out with distilled water rather than lime-saturated water, some dissolution of $Ca(OH)_2$ into the water will occur even if there is no pozzolanic reaction. This effect has been taken into account by normalizing to the remaining amount of $Ca(OH)_2$ in an inert-$Ca(OH)_2$ blend (Fig. 1, right). Over time, the amount of consumed $Ca(OH)_2$ increases in the order M < B < A, with the ratio for the M-slag blend staying roughly constant over the entire time. This is a strong indication of either latent hydraulic or inert behaviour. However, considering the increased release of Ca^{2+} from the slag in the dissolution tests (Fig. 1, left), it is most likely that this slag exhibits latent hydraulic behaviour. Strong $Ca(OH)_2$ consumption for the A-slag probably results from pozzolanic reactions or reactions of $Ca(OH)_2$ with the Al^{3+} which is released to the solution to a high extent for this slag, as discussed before.

3.2 Blended cements

The compressive strengths of the slag-blended cements (Fig. 2) are lower than pure OPC at early curing times (2-28 days). However, after 90 days there is a strength increase of 2.5%, 4% and 11% with respect to pure OPC for blends with the B, A and M-slag, respectively. These increased strengths can be attributed to the pozzolanic and latent hydraulic behaviour of the slags. The more latent hydraulic behaviour of slag M yields slightly higher strength gain at late ages whereas the higher Al_2O_3/SiO_2 weight ratio of the A-slag leads to faster strength gain

at early age. This is most likely due to higher Al- and Si-release seen in the dissolution tests, leading to faster pozzolanic reactions.

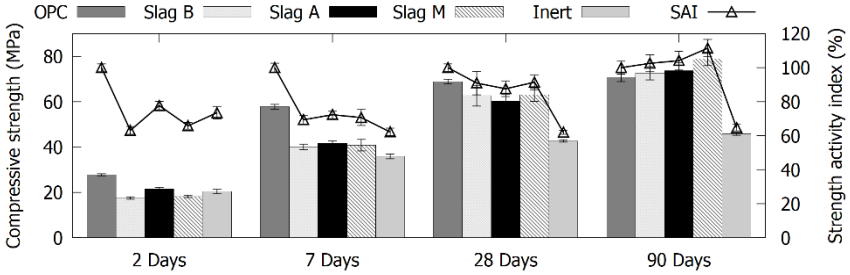

Figure 2: Compressive strength (bars) and corresponding strength activity index (lines) of the hydrated (blended) cements (70 wt% OPC + 30 wt% as indicated in the key). Error bars indicate the standard deviation.

The phase assemblage, as determined by QXRD, (Fig. 3) clearly shows the consumption of clinker phases, with more alite dissolution for slag- and inert-blended cements in comparison to pure OPC hydration at early age. The amount of unreacted alite after 28 days is higher for M-slag blended cement than for the other blends or even pure hydrated cement. This is most likely caused by higher release rate of Ca^{2+} from this slag at later times, leading to lower alite dissolution and is thus another indication of the more latent hydraulic behaviour of this slag. The main crystalline reaction products are ettringite, portlandite and, at later times, monocarboaluminate (Mc). It should be noted that in the M-slag blended cement there was also a presence of hydrotalcite, due to the higher Mg-content of the slag. However, brucite ($Mg(OH)_2$) was not detected, so even though a part of the periclase had reacted, as determined by XRD, no expansive effects were recorded. The amorphous reaction product, C-S-H, could not be investigated properly for the slag-blended cements as it is impossible to distinguish in XRD between amorphous C-S-H and unreacted slag. It is clear that all the slag-blended cements have a higher amount of Mc, most likely caused by aluminium release from the slag at later times as higher Al-availability has been shown to lead to enhanced calcite reactivity and subsequent carbonate-AFm formation [13]. However, it should be mentioned that the high $CaCO_3$ contents indicate carbonation of the samples, thereby hindering the deduction of more definitive conclusions.

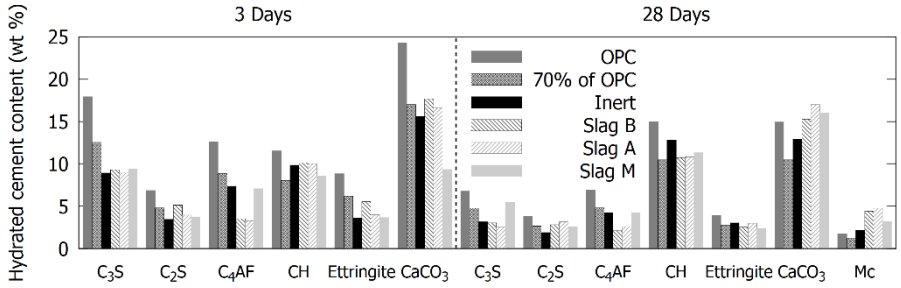

Figure 3: Phase assemblage of hydrated blended cements with different slags after 3 and 28 days, as determined by QXRD. $CaCO_3$ includes both vaterite and calcite while Mc represents monocarboaluminate. Other phases are represented using typical cement chemistry notation.

4. Conclusions

This work shows that iron-rich slags can be used as supplementary cementitious materials in blended cements, mainly contributing to late strength although all slags enhance alite dissolution at early age. Slag chemistry determines the type of behaviour, with high $(CaO+MgO)/SiO_2$ weight ratios leading to more latent hydraulic behaviour and low $(CaO+MgO)/SiO_2$ weight ratios yielding pozzolanic behaviour. Furthermore, early strength gain can be improved by a higher Al_2O_3/SiO_2 weight ratio, whereas a higher $(CaO+MgO)/SiO_2$ weight ratio yields higher final strength, showing that slag chemistry engineering is an important tool in modifying the properties of blended cements with these slags, such as compressive strength.

References

[1] EN197-1, Cement - Part 1: Composition, specifications and conformity criteria for common cements, European committee for standardization , Belgium (2011)
[2] Shi, C. and Meyer, C. and Behnood A., Utilization of copper slag in cement and concrete, Resour Conserv Recycl 52 (2008), 1115-1120.
[3] Rahman, M.A. and Sarker, P.K. and Shaikh, F.U.A. and Saha, A.K., Soundness and compressive strength of Portland cement blended with ground granulated ferronickel slag, Constr Build Mater 140 (2017), 194-202.
[4] Benkendorff, P.N., Potential of lead/zinc slag for use in cemented mine backfill, Miner Process Extr Metall (Trans Inst Min Metall C) 115 (2006), 171-173.
[5] Piatak, N.A. and Parsons, M.B. and Seal II, R.R., Characteristics and environmental aspects of slag: A review, Appl Geochem 57 (2015), 236-266
[6] Dilnesa, B.Z. and Wieland, E. and Lothenbach, B. and Dähn, R. and Scrivener, K.L. Fe-containing phases in hydrated cements, Cem Concr Res 58 (2014), 45-55
[7] Paul, A. and Youssefi, A., Alkaline durability of some silicate glasses containing CaO, FeO and MnO, J Mater Sci 13 (1978), 97-107.
[8] Pontikes, Y. and Machiels, L. and Onisei, S. and Pandelaers, L. and Geysen, D. and Jones, P.T. and Blanpain, B., Slags with a high Al and Fe content as precursors for inorganic polymers, Appl Clay Sci 73 (2013), 93-102.
[9] Oelkers, E.H. and Gislason, S.R., The mechanism, rates and consequences of basaltic glass dissolution: I. An experimental study of the dissolution rates of basaltic glass as a function of aqueous Al, Si and oxalic acid concentration at 25°C and pH = 3 and 11, Geochim Cosmochim Acta 65 (2001), 3671-3681.
[10] Snellings, R. and Paulhiac, T. and Scrivener, K., The Effect of Mg on Slag Reactivity in Blended Cements, Waste Biomass Valor 5 (2014), 369-383.
[11] EN196-6, Methods of testing cement - Part 6: Determination of fineness, European committee for standardization , Belgium (2010)
[12] EN196-1, Methods of testing cement - Part 1: Determination of strength, European committee for standardization , Belgium (2016)
[13] Steenberg, M. et al, Composite cement based on Portland cement clinker, limestone and calcined clay, XIII International Congress on the Chemistry of Cement, Spain (2011), 97-103

FIBRE-REINFORCED CONCRETE AND NON-METALLIC REINFORCEMENT

SynerCrete'18 International Conference on Interdisciplinary Approaches
for Cement-based Materials and Structural Concrete
24-26 October 2018, Funchal, Madeira Island, Portugal

A NUMERICAL MODEL FOR PREDICTING CRACKING OF FIBRE REINFORCED CONCRETE RINGS IN RESTRAINED SHRINKAGE TEST

Wei Dong [(1)], Xiaoyu Zhao [(2)], Xiangming Zhou [(3)], Wenyan Yuan [(4)]

(1) Dalian University of Technology, Dalian, China
(2) Dalian University of Technology, Dalian, China
(3) Brunel University London, Uxbridge, United Kingdom
(4) Dalian University of Technology, Dalian, China

Abstract
In practice, short discrete fibres in concrete can effectively reduce the cracking potential of concrete caused by the restrained shrinkage. In the present study, a fracture mechanics-based numerical model was developed to predict the cracking of fibre reinforced concrete rings in restrained shrinkage test tailored for assessing cracking potential of fibre reinforced concrete. With the proposed model, some remarkable features on the shrinkage cracking such as the age of crack initiation and crack evolution process can be predicted accurately, as well as the crack width for plain and fibre-reinforced concretes. The findings are helpful to move forward the ring test from an index test to be more meaningful that potentially provides quantitative results for interpreting cracking of restrained concrete in the field.

1. Introduction

Restrained shrinkage cracking is of critical concern in concrete elements with a large surface area-to-volume ratio such as highway pavements, industrial floors and slabs, bridge decks etc. Cracks enable the entrance of water and other corrosive ions into concrete, further leading to steel corrosion, which jeopardizes the serviceability and durability of concrete structures. One of the effective methods to reduce the adverse effects of cracking due to restrained shrinkage is the use of short discrete fibres as reinforcement for concrete [1]. Many researchers have conducted restrained ring test to evaluate the cracking resistance of fibre reinforced concrete [2-4]. In ring test, usually strain gauges are attached on the inner circumferential surface of the central restraining steel ring to continuously monitor its circumferential strain over

concrete shrinkage process. The age corresponding to the sudden drop in the measured steel strain is the cracking age of the ring, in which the crack would also propagate throughout the concrete ring cross-section. It is because that a crack once initiates, it can propagate throughout the whole cross-section of the ring in a short period (usually less than 1day). While for fibre reinforced concrete, the existence of fibres will bridge cracks and restrain them to open, which may cause several cracks occurring in the ring, delay the age of crack through-going, and cause significant drop in strain [2]. Thus it is difficult to determine the age of initial cracking and through-going cracking from the measured strain in the ring test in case of fibre reinforced concrete.

In this study, a fracture mechanics-based numerical model was developed, from which some remarkable features of the shrinkage cracking such as the ages of crack initiation and through-going can be determined accurately, as well as the crack width for plain and fibre-reinforced concretes. It is expected that such a fracture mechanics-based numerical model would be useful in exploring the cracking mechanism of plain and fibre reinforced concretes.

2. Experimental program

The mix proportion of the concrete was: 240:750:1150:186:60 (cement: sand: coarse aggregate: water: fly ash) by weight, which was similar to that investigated by Zhang et al. [5, 6]. The physical and mechanical properties of steel fibres for reinforcing concrete are as follows: length 25 mm; diameter 0.5 mm; tensile strength 1000 Mpa; and modulus of elasticity 210 GPa, respectively. The fibre volume fraction was 0.5% in concrete.

2.1 Mechanical and fracture properties of fibre reinforced concrete

Elastic modulus, E (in GPa), and splitting tensile strength, f_t (in MPa), of the concrete were measured from 100×100×200 mm^3 prisms and 100×100×100 mm^3 cubes, respectively. They can be represented by Eq. (1) and (2) by fitting the experimental data at various ages into a continuous expression as following:

$$f_t(t) = 0.487 + 0.314\ln(t) \quad (t \leq 28) \tag{1}$$

$$E(t) = 10.017 + 5.161\ln(t) \quad (t \leq 28) \tag{2}$$

Fracture properties of concrete, i.e. the initial fracture toughness, K_{IC}^{ini}(in MPa·mm$^{1/2}$) and the fracture energy, G_f (in N/m), were determined from three-point bending test of prismatic concrete beams of 100×100×500 mm^3, with a pre-crack length of 30 mm. The experimental results were curve-fitted leading to the following continuous equations:

$$G_f(t) = 39.219 + 12.622\ln(t) \quad (t \leq 28) \tag{3}$$

$$K_{IC}^{ini}(t) = 6.180 + 2.657\ln(t) \quad (t \leq 28) \tag{4}$$

In all these equations, t is the age of the concrete (in days).

2.2 Free shrinkage

Free shrinkage tests were conducted using prisms with the dimensions of 300×75×37.5 mm^3 but with only one 300×75 mm^2 surface was exposed to the environment and the other surfaces were sealed by two layers of aluminum tapes. The drying condition of the free shrinkage specimens was the same as that of the concrete rings in the test. The evolution of shrinkage strain with respect to concrete age from experiment is presented in Fig. 1(a).

2.3 Restrained ring test

The restrained circular ring test was performed conforming to ASTM C1581/C1581 M-09a to evaluate the cracking resistance of plain and fibre reinforced concretes subject to restrained shrinkage. The restrained ring test setup is illustrated in Fig. 1(b). The inner radius of the concrete ring *R* was 150 mm, and the wall thickness of the restraining steel ring and concrete ring were 12.5 mm and 37.5 mm, respectively. Four rings were prepared, including two plain concrete rings and two fibre reinforced concrete rings. In ring tests, concrete was cast directly around the steel ring, and after demoulding, these rings were sealed with double-layer aluminum tapes on their top and bottom surfaces immediately to allow drying from their outer circumferential surface only. They were then moved into an environment chamber of 23 °C and 50% relative humidity (RH) for curing. The number and width of cracks occuring in rings were detected by a DJCK-2 Creuice Width Finder.

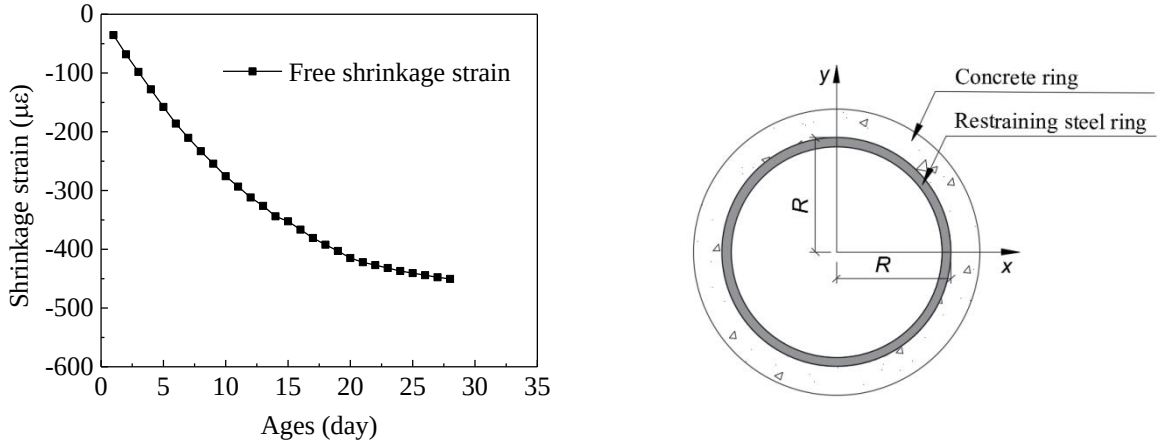

(a) Free shrinkage strains (b) Restained ring test setup

Figure 1: Free shrinkage strains and the schematic of restrained ring test setup

3. Numerical simulations

The numerical simulation was carried out using ANSYS FE code with a two-stage process: thermal analysis and structural analysis. In thermal analysis, the shrinkage of concrete was simulated by applying a fictitious temperature drop to the concrete. The shrinkage caused by the fictitious temperature drop was the same as the magnitude of shrinkage that measured in the free shrinkage test. In structural analysis, through introducing the fictitious crack model and the constitutive model of the bond between fibres and concrete, a fracture mechanics-based method was utilized to investigate the whole process of crack initiation and propagation with respect to the plain and fibre reinforced concretes in the restrained shrinkage ring test.

3.1 Moisture distribution and fictitious temperature field

In this research, an integrative model proposed by Zhang et al. [6, 7] was introduced to calculate the moisture distribution for the concrete ring under drying from outer circumferential surface, and the results are shown in Fig. 2(a). It has been verified that, in the case of RH>50%, the relationship between moisture distribution and shrinkage strain is linear. Applying a fictitious temperature field in the simulation which is the same as the moisture distribution of the concrete prismatic specimen to calculate the shrinkage strain, by comparing the shrinkage strain with those measured in the free shrinkage test, a fictitious temperature field can be determined, which is illustrated in Fig. 2(b).

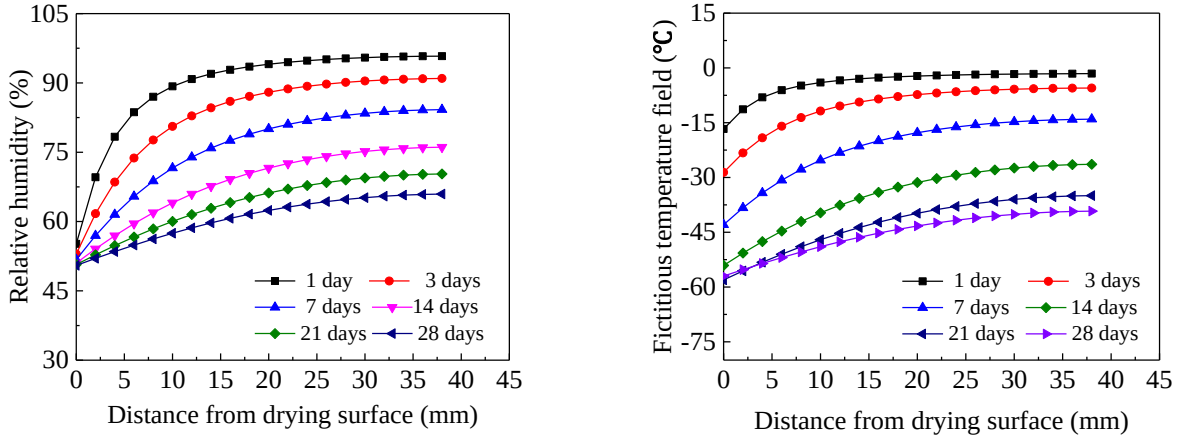

(a) Moisture distributions (b) Fictitious temperature fields

Figure 2: Moisture distributions and fictitious temperature fields in the concrete ring

3.2 Fictitious crack model and the constitutive modelling

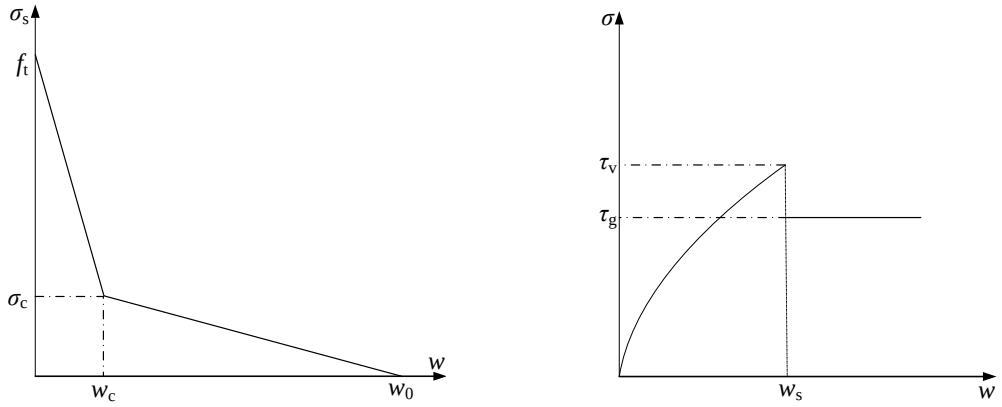

(a) Bilinear softening curve (b) The constitutive law σ-w for fibre

Figure 3: Bilinear softening curve of concrete and the constitutive law σ-w for fibres

The fictitious crack model [8] was introduced to characterize the softening behavior of concrete in micro-cracks, as represented by a relation between the softening stress (σ_s) and the crack opening displacement (w). A bilinear stress-crack opening displacement relation (σ_s-w) was chosen and illustrated in Fig. 3(a). The interfacial bond behavior between the matrix and

fibres can be featured from a pullout test of the fibre, and the constitutive law between the pullout force (σ) of the fibre per unit area and crack width (w) is schemed in Fig. 3(b).

3.3 Crack initiation and propagation

A crack propagation criterion [9, 10] based on initial fracture toughness was employed to analyze crack initiation and propagation, and predict the whole fracture process of concrete. The criterion can be described as: a crack would propagate if the value of the difference between $K_{\mathrm{I}}^{\mathrm{F}}$ and K_{I}^{σ}, which are the stress intensity factor (SIF) caused by the applied fictitious temperature field and the cohesive stress, respectively, is greater than $K_{\mathrm{IC}}^{\mathrm{ini}}$.

4. Results and discussion

Through the above-mentioned simulation technique, the variation of $K_{\mathrm{I}}^{\mathrm{F}} - K_{\mathrm{I}}^{\sigma}$ and $K_{\mathrm{IC}}^{\mathrm{ini}}$ at various ages for the plain concrete and fibre reinfroced concrete are illustrated in Fig. 4(a) and (b), respectively. It can be seen that, from Fig. 4(a), the crack in plain concrete initiated at the age of 16 days while that in fibre reinforced concrete at the age of 17 days.

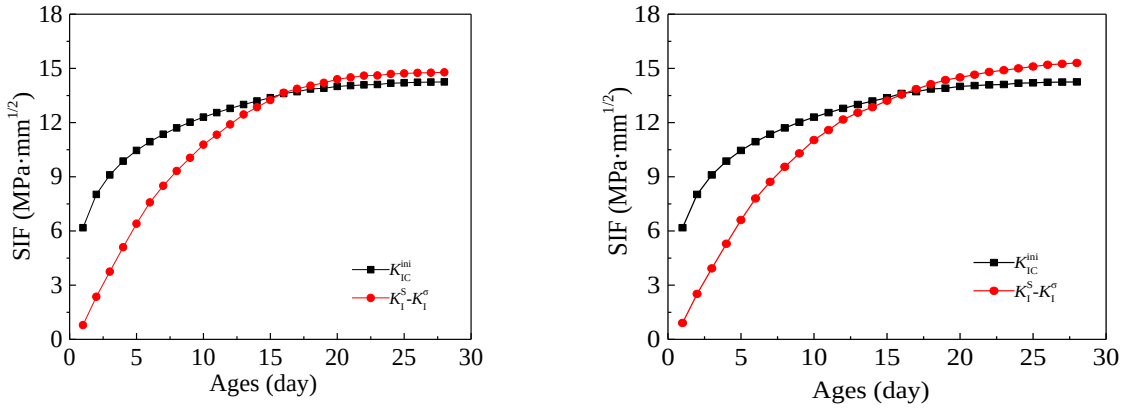

(a) SIF for plain concrete (b) SIF of concrete with 0.5vol.% fibres

Figure 4: Evolution of $K_{\mathrm{I}}^{\mathrm{F}} - K_{\mathrm{I}}^{\sigma}$ and $K_{\mathrm{IC}}^{\mathrm{ini}}$ under various concrete ages

Table 1: Comparison of the results from experimental and numerical

Concrete type	Experimental results				Simulation results			
	Num.	C-T (d)	T-T (d)	Width (mm)	Num.	C-T (d)	T-T (d)	Width (d)
Plain	1	18	18	0.17	1	16	16	0.19
With 0.5% fibre	1	19	-	0.04	1	17	17	0.085

*Num. denotes the total number of crack at the age 28 days, C_T denotes the age of initial cracking, and T_T denotes the age of the through-going cracking.

In addition, the number of cracks and crack width, as well as cracking age and crack through-going age from experiment and simulation are listed in Table 1. It can be seen that the

addition of 0.5% by volume fibres can substantially reduce the width of cracks. Besides, the age of through-going cracking for the concrete reincorced with 0.5% by volume fibres was the same as that of cracking initiation, which were at the age of the 17th day because the amount of fibre was relatively low. Thus, if the addition of the amount of fibre in concrete is less than or equal to 0.5% by volume, once crack initiates, it will continue to propagate throughout the whole cross-section of the concrete ring.

5. Conclusions

Based on the experimental and numerical investigations in this study, the following conclusions can be drawn: (1) the addition of small amount of fibres (0.5% by volume in this study) can substantially reduce crack width in the restrained concrete rings; (2) Once the crack initiates in the concrete reinforced with less than or equal to 0.5% by volume fibres, it will continue to propagate throughout the whole cross-section of the concrete ring.

References

[1] Yousefieh, N., Joshaghani, A., Hajibandeh, E., Shekarchi, M., Influence of fibres on drying shrinkage in restrained concrete, Construction and Building Materials 148 (2017), 833-845.
[2] Grzybowski, M., Shah, S. P., Shrinkage cracking of fibre reinforced concrete, ACI Materials Journal 87 (1990), 138-148.
[3] Shah, S. P., Grzybowski, M., Model to predict cracking in fibre reinforced concrete due to restrained shrinkage, Magazine of Concrete Research 41 (1989), 125-135.
[4] Seung, H. K., Shah, S. P., Prediction of early-age cracking of fibre-reinforced concrete due to restrained shrinkage, Aci Materials Journal 105 (2008), 381-389.
[5] Zhang, J., Hou, D. W., Chen, H., Experimental and Theoretical Studies on Autogenous Shrinkage of Concrete at Early Ages, Journal of Materials in Civil Engineering 23 (2011), 312-320.
[6] Zhang, J., Gao, Y., Han, Y. D., Evaluation of Shrinkage Induced Cracking in Early Age Concrete: From Ring Test to Circular Column, International Journal of Damage Mechanics 26 (2015), 771-797.
[7] Zhang, J., Hou, D. W., Gao, Y., Sun, W., Determination of Moisture Diffusion Coefficient of Concrete at Early Age from Interior Humidity Measurements, Drying Technology 29 (2011), 689-696.
[8] Hillerborg, A., Modéer, M., Petersson, P. E., Analysis of crack formation and crack growth in concrete by means of fracture mechanics and finite elements, Cement & Concrete Research 6 (1976), 773-781.
[9] Dong, W., Wu, Z. M., Zhou, X. M., Calculating crack extension resistance of concrete based on a new crack propagation criterion, Construction and Building Materials 38 (2013), 879-889.
[10] Dong, W., Zhou, X. M., Wu, Z. M., On fracture process zone and crack extension resistance of concrete based on initial fracture toughness, Construction and Building Materials 49 (2013), 352-363.

SynerCrete'18 International Conference on Interdisciplinary Approaches
for Cement-based Materials and Structural Concrete
24-26 October 2018, Funchal, Madeira Island, Portugal

BRITTLENESS OF HIGH-STRENGTH LIGHTWEIGHT AGGREGATE CONCRETE

Jelena Zivkovic [(1)], Mladena Lukovic [(2)], Jan Arve Øverli [(1)], Dick Hordijk [(2)]

(1) Department of Structural Engineering, Norwegian University of Science and Technology (NTNU), NO-7491 Trondheim, Norway
(2) Department of Engineering Structures, Delft University of Technology (TU Delft), 2628 CN Delft, The Netherlands

Abstract

Modern society and infrastructure are facing an increased demand for fast construction. A number of viaducts are aged and will need to be replaced in near future. When considering this replacement task, lightweight, slender bridge is the solution. Dead load reduction and high-strength to weight ratio are the main advantages when using the lightweight aggregate concrete (LWAC). Still, structural applications of LWAC are lacking. The main disadvantage of LWAC compared to regular concrete, which refrains its wider structural application, is its brittleness and uncontrolled crack propagation, especially when LWAC is exposed to compression. One of the ways to improve brittleness and increase the ductility of concrete is by addition of fibers. In this research, preliminary study is performed where fiber reinforced LWAC mixture was designed and tested. The mix consisted of lightweight aggregate Stalite, leading to high-strength LWAC and polyvinyl alcohol fibers (PVA) providing reduced brittleness and explosive failure. Results on fracture behavior and compressive strength with the increased amount of fibers were investigated and showed promising behavior. In future, structural tests (e.g. compression tests on prisms and beams) will be performed to further verify the benefits of combining aggregate Stalite with PVA fibers for structural applications of high-strength LWAC.

1. Introduction

Nowadays, the demand for fast construction increases. A special task is that a majority of the bridges and viaducts are aged and will need to be replaced in the near future. Many countries worldwide face a similar problem and a solution for dealing with it is urgently needed. In this

context, new materials and techniques can provide cost-effective solutions thereby minimizing the construction time and reducing the traffic hinder. When considering replacement task high-strength lightweight, slender bridge can be an optimal solution [1].
Lightweight aggregate concrete (LWAC) has been used successfully for structural purposes for many years. The preferable structures are floating offshore platforms, marine structures and bridges [2,3]. The main advantage that classified lightweight concretes as a desired material for use is reduced dead weight of a structure, and in long-span bridges and high-rise buildings, dead load is a significant portion of the design load. By reducing the weight of the structure, lightweight concrete also reduces bearing, substructure and foundation design loads that may contribute to cost savings in the structure. For the projects where seismic events must be considered in design, reduction of weight is especially significant since it lead to reduction in seismic design load [4,5]. Another important application for the reduced density of lightweight concrete is its use for concrete elements that are prefabricated (precast) to facilitate easier handling and faster construction [2]. High strength lightweight aggregate concrete, i.e. having 28-day characteristic compressive strength in the range 60-80 N/mm^2 with oven dry density equal or less than 2000 kg/m^3.
Apart from many foreseen benefits and advantages when using LWAC, structural applications is still lacking. The main reason for that compared to normal weight concrete (NWC) is its brittleness and uncontrolled crack propagation, especially faced when LWAC is exposed to compression. The brittleness of concrete is characterized by sensitivity to stress concentrations and a rapid crack/fracture development. This is attributed to the difference in fracture behaviour of two types of concretes: in regular concrete, cracks are formed around the aggregates, following aggregate-paste interface zone whereas in LWAC cracks propagate through the aggregate. As a result, more tortuous cracking route is made in regular concrete leading to more stable crack propagation and higher fracture energy. For structural analysis, it is essential to know the complete stress-strain curve under uniaxial compression including the descending branch. The main concern for designers when using LWAC is steep and short descending branch, since concrete behave in a brittle manner. Therefore, additional brittleness introduced by LWAC should be certainly avoided. In order to improve this disadvantage of the LWAC concrete, a case study on several LWAC mixes was performed, whereby lightweight aggregate Stalite was combined with polyvinyl alcohol fibers (PVA) [6].

2. Future replacement task

In the past, many cast in-situ reinforced concrete plate bridges were built. The main advantage of this bridges were higher slenderness because of multiple intermediate supports over a single span bridge. At the time when cast in-situ plate bridges were built, the construction time and traffic hindrance was not a serious issue as today. Keeping in mind that many of these bridges and viaducts are constructed for a design service life of 50 years, the replacement is needed. Nowadays, with expansion of the road network and serious implications due to traffic hindrance, the main replacement requirements become more demanding. Rebuilding of cast in-situ plate bridges is due to its impact on traffic, undesirable solution and should be avoided. In this context, new materials and techniques can provide cost-effective solutions thereby minimizing the construction time and reducing the traffic hinder. The main requirements for the replacement of the existing structures are: to keep the

same traffic profile without additional ground work, to minimize the work on existing foundations and to ease transportation during the construction process and provide joining of separate elements of the bridge. Having in mind all aspects mentioned above, high-strength lightweight, slender bridge can be an optimal solution. With this type of bridge it is possible to keep or reduce bridge height, where traffic profile stays the same of increase. Using of the prefabricated LWAC box girders reduce the weight of concrete elements, making the use of precast elements more feasible by reducing requirements for shipping, handling and erection. In addition traffic impact is reduced to a minimum during construction time.

3. Case study - LWAC with fibres

3.1 Lightweight aggregate concrete (LWAC)

Structural lightweight aggregate concrete is made when normal weight aggregate (NWA) is replaced with lightweight aggregate (LWA). That is simply lighter a rock, produced using shale, clay or slate, so the same batching and admixtures are used for preparation of lightweight aggregate concrete like the same procedures and equipment as a for conventional concrete. Typical LWAC mixtures that use coarse LWA and conventional sand have a oven-dry density of 1750 to 2000 kg/m3, followed by compressive strength up to 70 MPa (based on cylinder strength). Water absorption of LWA is higher than the absorption of NWA, in the range from 6 % to 25 %. Because LWA has a higher absorption, lightweight concrete typically loses mass with time as excess absorbed water migrates out of the concrete. The oven-dry density as the density achieved after moisture loss has occurred is used for design criteria. As a result of lower density of aggregate, density of LWAC is reduced in range from 25-30% compared with NWA. That is significant in areas where dead load is one of the largest determinative factor, especially in seismic areas. This feature allows the reduction of cross sections, improve structural efficiency and economy.

Density of the LWA is lower than density of the cementitious paste, which require extra care during the production of LWAC. Control of absorption and moisture during production is necessary to produce concrete with consistent properties. LWAC generally requires more cementitious material and lower water-cement (w/c) ratio to achieve higher compressive strength. The porous nature of lightweight aggregate reduces its stiffness. In hardened LWAC, strength and rigidity of the aggregate is lower than that of the paste, leading to crack distribution through aggregate, lower strength development and lower ductility. As a result of that phenomena, fracture energy, tensile strength and E-modulus are lower for LWAC [2-5]. In addition, LWAC have brittle nature, uncontrolled crack/fracture development followed by an explosive failure. Together with the main stress-strain curve under uniaxial compression, where the descending branch is steep and short, this is main concern for the designers when using LWAC as preferable material. One of advantages when using lightweight concrete is improved fire resistance. This feature is significant for building construction where structural elements are often required to provide a certain resistance to fire exposure. The insulating properties of lightweight concrete allow a smaller (and also lighter) thickness of concrete to provide the same resistance as for NWA [2,5]. The significant benefit with respect to durability when using the lightweight concrete is reduced shrinkage. This is provided due to internal curing from the water that is absorbed and stored in aggregate itself [5].

3.2 Tensile strength and shear capacity of LWAC with Stalite as aggregate

Previous experimental investigation dealt with the tension behaviour of LWAC with Stalite as aggregate. Behaviour and ductility of beams with and without shear reinforcement were observed in 4-point bending test. The main test parameters that were varied in those tests were the shear span length to effective height ratio (a/d) and amount of shear reinforcement. All the tested beams showed ductile behaviour because they were able to withstand significant increase of load after formation of shear splitting cracks. Crack formation in the tested beams were similar as for normal weight concrete. By qualitative visual inspection for all the tested beams without shear reinforcement it was observed explosive, loud and brittle failure [7]. When observing the cracked area, propagation of cracks goes through and around LWA, leading to higher tensile strength and fracture energy [5,7]. High-strength LWAC with Stalite as aggregate showed promising behaviour.

3.3 Polyvinyl alcohol fibres (PVA)

Polyvinyl alcohol fibers (PVA) is mostly use to improve the inherent brittleness of cementitious materials and to control cracking. They have very little effect on the flexural strength and deflection capacity. The compressive capacity is slightly reduced while concrete surface of the elements become extremely ductile [8].

3.4 Experimental program, results and discussion

Small experimental program have been created in order to create non brittle and ductile high-strength LWAC. The main concern was to deal with brittleness, explosive failure and to improve ductility of LWAC. Because of that PVA fibres was introduced in range 0.5 to 1 % at volume fractions. PVA was type "Kuralon RSC15", 8 mm long with E-modul of 36 MPa. All the concrete mixes have been prepared from the same batch of LWA Stalite, argillite slate from North Carolina.

Stalite was completely saturated to avoid water exhaustion from the paste and in addition have been controlled moisture and absorption of the aggregate just before the mix preparation. One concrete mix (LWAC 65) was prepared as a reference one without addition of the fibres, while three mixes contain fibres. Tab. 1 shows all the concrete mixes and fresh concrete characteristics. All the mixes have been prepared in laboratory controlled conditions, in a mixer with vertical pedals and capacity 25 liters. In order to provide good distribution of the fibres in FLWAC, first was prepared paste where were added fibres and later was introduced aggregate with continuous mixing. From the LWAC and FLWAC mixes have been casted several cubes and cylinders for the testing and following of compressive strength at 7, 14, 28, 38 and 46 days. At age of 28 days cylinders from all the prepared concretes were tested under compression to get E modulus [9]. From that test it was plotted stress-strain diagram, see Fig. 1. It can be noticed that LWAC65 showed brittle behaviour, when failure happened load immediately failed down, while all other mixes with fibres showed ductile behaviour with very smooth peak load where load goes slowly down and samples can sustain additional loading .

When testing lightweight aggregate concretes it was noticed that by adding the fibres, even in small amounts, workability of the concrete mix was significantly reduced. Concrete like this is very tough to cast, especially in sections that contain a lot of reinforcement is tough to embed this concrete. Mix FLWAC 65* contain more fine sand, fraction 0-2mm, in order to provide more stable paste and concrete, but still workability was very low. That happens

because fibres arrest water which is wrapped around them. From the other side through qualitative visual inspection of the fracture, all tree FLWAC concretes did not showed any brittleness and explosive failure compared to LWAC 65. It was surprising that all the FLWAC cubes and cylinders kept together afterwards and can sustain additional loading. By adding the fibres in amount of 0.5% compressive strength is very slightly reduced while effect on the brittleness is the same like for mix with 1% of the fibres. For the FLWAC mix that contain 1% of the fibres compressive strength is significantly reduced, almost 18%.

Table 1: Concrete mix compositions (kg/m3) and fresh concrete properties.

Constituent	**LWAC65**	**FLWAC65 with 0.5 % fibres**	**FLWAC65* with 0.5 % fibres**	**FLWAC65 with 1% fibres**
Cement (Norcem Anlegg FA)	431.1	414.4	397.5	435.5
Silica fume (Elkem Microsilica)	22.7	21.8	20.9	22.9
Water (free)	177	170.1	163.2	206.3
Absorbed water *sand+aggregate	53.6	49.3	46.7	45.6
Sand (Ramlo 0-8 mm)	552.6	559.1	531	517.5
Sand (Ramlo 0-2 mm)	236.8	239.6	377.3	221.8
Aggregate (Stalite ½″)	530.5	536.72	493	496.8
Superplasticizer	5.4	5.1	6.2	6
Synthetic fibres (% of volume)	-	6.5	6.5	13
Fresh concrete properties				
Matrix volume [l/m^3]	360	360	360	400
Slump [mm]	240	35	40	10
Fresh density [kg/m^3]	2013	1900	2011	1663

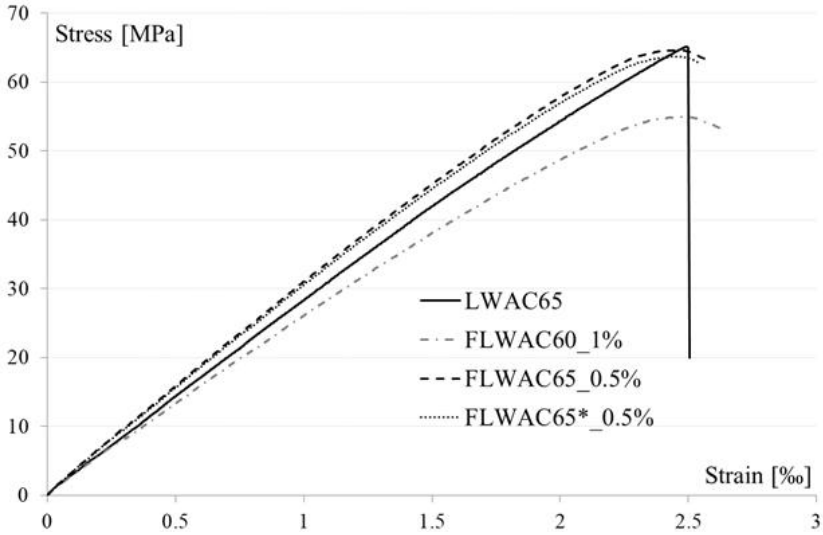

Figure 1: Stress-strain diagram for all the tested mixes at age 28 days

4. Conclusions

When using the LWAC the weight of the structure can be reduced for the 25-30 %. Having this in mind, like all the other mentioned advantages, LAWC seems to be a promising material for any structural applications, especially for the replacement bridge task. By introducing a small amount of PVA fibres, just 0.5%, the lightweight concrete became non brittle and without an explosive behaviour. In addition small amount of fibres did not influenced the compressive strength of concrete. In the future, structural tests (e.g. compression tests on prisms and beams) will be performed to further verify the benefits of combining aggregate Stalite with PVA fibers for structural applications of high-strength LWAC.

Acknowledgement
The work presented in this paper is part of an ongoing PhD studies in the DACS project (Durable Advanced Concrete Solutions). The DACS partners are Kværner AS (project owner), Norwegian Research Council, Axion AS (Stalite), AF Gruppen Norge AS, Concrete Structures AS, Mapei AS, Multiconsult AS, NorBetong AS, Norcem AS, NPRA (Statens Vegvesen), Norwegian University of Science and Technology (NTNU), SINTEF Byggforsk, Skanska Norge AS, Unicon AS and Veidekke Entreprenør AS.

References

[1] A. Reitsema, M. Lukovic, D. Hordijk, Towards slender, innovative concrete structures for replacement of existing viaducts, fib Symposium 2016 Performance-based Approaches for Concrete Structures Cape Town (2016).
[2] Castrodale, R. W. et al, High-performance lightweight concrete bridges and buildings, Eleventh High Performance Concrete (11th HPC) & the Second Concrete Innovation Conference (2nd CIC), Tromsø, Norway (2017).
[3] Sandvik, M. and Hammer, T. A., The development and use of high performance lightweight concrete in Norway, International Symposium on Structural Lightweight Aggregate Concrete, Sandefjord, Norway (1995), 617-627
[4] ACI 213R-03, Guide for Structural Lightweight Aggregate Concrete, American Concrete Institute, ACI Committee 213, Farmington Hills, MI, USA (2003).
[5] Castrodale, R. W., Zivkovic, J. et al., Material properties of high performance structural lightweight concrete, Eleventh High Performance Concrete (11th HPC) & the Second Concrete Innovation Conference (2nd CIC), Tromsø, Norway (2017)
[6] Kuraray Co, Characteristics of KURALON (PVA fibres), PVA fibres-application, available: http://kuralon-frc.kuraray.com/product-application
[7] Zivkovic, J. and Øverli, J. A., Behavior and capacity of lightweight aggregate concrete beams with and without shear reinforcement. Nordic Concrete Research. Volume 57(2) (2017), 59-72
[8] Savija, B. et al., Development of ductile cementitious composites incorporating microencapsulated phase change materials, International Journal of Advances in Engineering Sciences and Applied Mathematics, Volume 9, Issue 3, (2017), 169-180
[9] NS 3676, Norwegian standard, Concrete testing-Hardened concrete-Modules of elasticity in compression. NSF, Oslo, Norway (1987)

SynerCrete'18 International Conference on Interdisciplinary Approaches
for Cement-based Materials and Structural Concrete
24-26 October 2018, Funchal, Madeira Island, Portugal

COST-OPTIMAL DESIGN OF FLEXURAL CONCRETE BEAM REINFORCED WITH FRP REINFORCEMENTS

Sigbjørn Tveit [(1)], Martin Wilhelmsen [(1)], Vlad Aleksander Lundeland [(1)], Mahdi Kioumarsi [(1)]

(1) OsloMet – Oslo Metropolitan University, Oslo, Norway

Abstract

Because of the non-ductile nature of FRP reinforcement, the convention of designing cross-sections with the flexure strength limited by reinforcement yield, as for steel, is not adequate. Although ACI 440.1R-15 gives easily fetched explanations on how to design FRP-reinforced concrete (FRPRC) sections for flexure, an understanding of the different parameters economic influence is required for FRP to be a competitive alternative to steel. In this paper, an analytical tool for cost-optimally analyzing and designing FRPRC-cross-sections according to ACI 440.1R-15 is presented. To this aim, by optimizing the functions for flexural strength and for the approximated price pr. meter of a cross-section – with respect to both fiber cross-section area and effective depth of concrete cross-section – a formula for the most economical ratio of these parameters in regard to flexural strength is presented. For a given FRP and concrete type, the optimal ratio proves to be the same for all desired flexural capacities, and can for rectangular cross-sections be presented as a function of the cross-section width.

1. Introduction

Along with higher initial costs - the lack of experience, standards and guidelines may scare many engineers from entering the unknown landscapes of fiber reinforced polymer (FRP) reinforcement [1]. Despite providing durable concrete structures, free of deterioration caused by corrosion [2], FRP bars as reinforcement has not yet managed to become a major competitor to steel in Europe [3]. Chloride initiated corrosion on steel reinforcement is the number one cause of reinforced concrete (RC) bridges not being serviceable, making up 2/3 of all recorded failures on German bridge constructions [4]. Regardless - the low weight, high tensile strength, superior resistance to deterioration from aggressive environments [5] and

significantly smaller environmental impact [6] has not been sufficient to penetrate the European mainstream market.
Depending on the matrix, as well as the fiber type and their alignment, some important properties of FRP products are generally associated with a drawback in comparison to those for steel [4]. Considering design for flexural strength of rectangular FRP-reinforced concrete beams, the relatively low modulus of elasticity of the reinforcement and its lack of ductility in many cases sets limitations for the possibility to exploit its high tensile strength.
Because of FRPs resistance to electrochemical corrosion, the total life cycle cost of a non-metallic reinforced structure is nevertheless likely to be lower than those for steel-reinforced structures when situated in corrosion-aggressive environments [7], taking realistic costs of repairs and traffic delay in to consideration [3]. This long-term economical viewpoint is part of the reason for an increase in the use of non-metallic reinforcement for new bridge structures in North America. As of 2015 more than 200 Canadian concrete bridges have been designed and built using FRP in slabs, barriers or girders, without showing any signs of deterioration after 10 years [8]. Meanwhile the corresponding marked in Europe is gradually growing importance, and the expanding and extensive construction of new concrete structures reinforced with FRP is motivating research on ways to design FRP structures more efficiently [10]. Because of this, the European Committee of Standardization (CEN) in 2016 published *Prospect for new guidance in the design of FRP: Support to the implementation, harmonization and further development of the Eurocodes* [9], as a step in the direction of a Eurocode governing guidelines for the design and construction of structural concrete reinforced with FRP.
With the industry's concerns of non-metallic reinforcements high first costs, the significance of developing ways to optimize costs is crucial to encourage further use for the future. According to authors' knowledge, there is no guiding to obtain cost-optimal FRP-reinforced concrete cross sections. In this paper, a method for determining the cost-optimal ratio of reinforcement to concrete area in a cross section is therefore presented.

2. Flexural design of FRP reinforced concrete (FRPRC) beams

Designing traditional steel RC beams, it is desirable to take advantage of the ductile nature of the steel reinforcement to obtain a non-brittle failure of the RC element [10]. This is done by designing RC beams so that the strain level in the reinforcement is beyond what is the yield strain of steel, when concrete crushing occurs. This limits an engineer's needs and possibilities to experiment with different reinforcement ratios. FRP reinforcements on the other hand does not inherent this ductile behavior [10]. Instead, the stress/strain of FRP reinforcement bars develops linear elastically, with sudden termination by brittle failure [10].

2.1 Reinforcement ratio and reduction factor for flexural design

Because of the non-ductile behavior of FRP, shown in Fig. 1, the conventional way of designing cross-sections with flexure strength limited by the reinforcement, as for steel, is not adequate [10]. ACI 440.1R-15 [10] refers to researches [11-12] proving failure by FRP-reinforcement rupture to be sudden and catastrophic, with compression-controlled cross-sections being marginally more desirable, exhibiting some inelastic behavior prior to failure.

To compensate for the lack of ductility using FRP, ACI [1] introduces a reduction factor to the nominal flexure strength, ϕ, which is reliant on which limiting state is controlling.

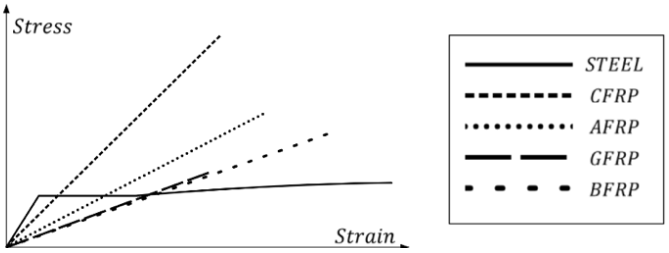

Figure 1: Stress-strain diagrams for steel, GFRP, CFRP, AFRP and BFRP, showing linear-elastic strain development with sudden failure for FRP reinforcement.

$$\phi M_n \geq M_u \tag{1}$$

where ϕ is strength reduction factor, M_n is nominal flexural capacity (kNm) and M_u is factored moment at section (kNm). Comparing a beams reinforcement ratio to a balanced reinforcement ratio, one can determine whether its failure will be controlled by FRP-rupture or concrete crushing, giving a corresponding reduction factor.

$$\rho_f = \frac{A_f}{b \cdot d} \tag{2}$$

where ρ_f is FRP reinforcement ratio, A_f is area of FRP reinforcement (mm^2), b is width of rectangular cross-section (mm) and d is effective depth of cross-section (mm). In ACI 440.1R-15 [10] is presented an equation for the balanced reinforcemenet ratio – the ratio where concrete crushing and FRP rupture will occour simultaniously. The equation does not include any geometric parameters and is along with Eq. (2) also valid for T sections as long as the depth of the compression zone is not larger than the thickness of the flage of the section. If the reinforcement ratio from Eq. (2) is greater than the value of the balanced reinforcement ratio, ρ_{fb}, the section will theoretically be controlled by the concrete crushing limit state. However, for a section with $\rho_{fb} < \rho_f < 1.4\rho_{fb}$ a linearly reduced value of ϕ is imposed in case the member as constructed does not fail accordingly, see Fig. 2.

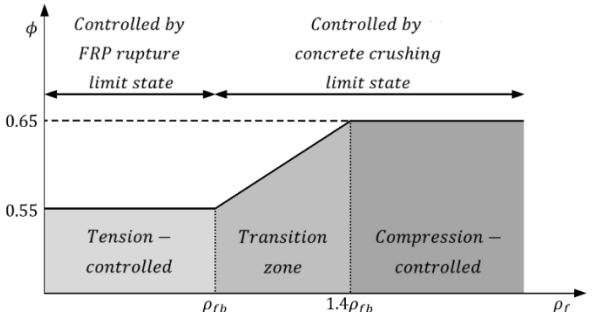

Figure 2: Strength reduction factor as function of reinforcement ratio, showing values for tension-controlled ($\rho_f < \rho_{fb}$), compression-controlled ($\rho_f > 1.4\rho_{fb}$) and a linear transition zone ($\rho_{fb} < \rho_f < 1.4\rho_{fb}$) [10].

3. Cost-optimization method

Having the option to design a cross-section to be controlled by different limit states creates a demand for determining the most economically optimal design with respect to reinforcement ratio. Based on methods from ACI 440.1R-15 the factored nominal flexural strength of a FRP reinforced concrete cross-section can be presented as a function of FRP reinforcement area and effective depth. This is obtained by locking the width of the cross-section, looking at a specific type of FRP.

3.1 Price of cross-section per meter

To consider the material costs of a rectangular FRP reinforced beam, a function of the same variables can be approximated based on the geometry of the cross-section. For the same specific width, the function representing price pr. meter beam can be presented as follows.

$$P(A_f, d) = P_{FRP}A_f + P_c(b(d + d_{c,m}) - A_f) \quad (3)$$

where P is price of cross-section per meter (price/m), P_{FRP} is average price of specific FRP type (price/mm^2/m), P_c is price of concrete (price/mm^2/m) and $d_{c,m}$ is thickness of concrete cover measured from extreme tension fiber to collective center of reinforcement. Since the price of FRP bars varies within the different available diameters, the expression is based on an average price of the most current diameters. Not knowing how many lateral layers of reinforcement will be necessary, an approximated distance from extreme tension fiber to collective center of reinforcement is assumed.

3.2 Minimizing by Lagrange multiplier

According to the method of Lagrange multipliers [13] the price function is minimized by analyzing the dot product of the two functions' associated gradients, when the factored nominal flexural capacity is constrained to a desired value. The pair of input values giving parallel gradients, is the most economically optimal.

$$\nabla\phi M_n(A_f, d) = \lambda \cdot \nabla P(A_f, d) \quad (4)$$

$$\phi M_n(A_f, d) = i \quad (5)$$

where ∇ is the del operator giving the functions gradients [14], λ is the Lagrange multiplier scalar [13], and i is the equality constraint which can be set to any current factored moment at section, M_u [1], or any desired flexural capacity.
Plotting the optimal pairs of input when varying the equality constraint, i, the nature of the two functions gives a straight line, proving a fixed ratio (A_f/d) minimizing the price function for all flexural capacities, see Fig. 3.

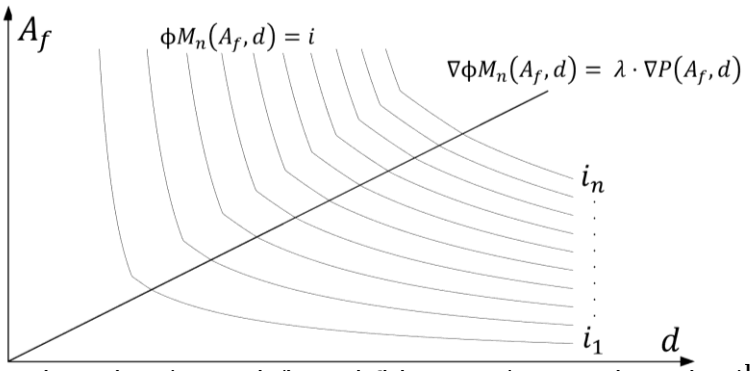

Figure 3: Price optimal combinations of A_f and d for a section reinforced with a specific FRP type, with fixed width. The straight line is obtained by plotting every optimal A_f and d pair which satisfies a flexural capacity $M(A_f, d) = i$, varying i continuously.

With a fixed cost-optimal reinforcement to effective depth ratio for a given width, we can easily generalize the concept to all cross-section widths. Repeating the operation of the optimization, varying the cross-section width discretely, the cost-optimal reinforcement to effective depth ratio as a function of the width, $\Lambda_{FRP}(b)$, is obtained by regression analysis.

$$\Lambda_{FRP}(b) = \frac{A_{f,opt}}{d_{,opt}}(b) \tag{6}$$

where $A_{f,opt}$ over $d_{,opt}$ represents the fixed relationship of values that together fulfills Eq. (4) and Eq. (5). Note that $A_{f,opt}$ and $d_{,opt}$ does not exist independently.
In the case of a GFRP-reinforced cross-section of C45 concrete with the width b, the cost-optimal ratio of A_f over d is presented in Eq. (7). The specific GFRP reinforcement has a modulus of elasticity of 46 000 MPa, guaranteed tensile strength of 724 MPa and price of 0,03 Euro/mm^2/m. The calculation is based on 142 Euro/m^3 as the price of C45 concrete.

$$\Lambda_{GFRP}(b) = 0{,}405b - 0{,}367 \tag{7}$$

4. Conclusion

This paper presents an analytical method to minimize material costs of rectangular FRP reinforced concrete beams designed for flexural strength. Establishing a function for price per meter beam, the cost-optimal relationship between FRP reinforcement area and the cross-sections effective depth is derived. This function, Λ_{FRP}, proves to be invariant of demanded flexural capacity, and can for a specific FRP and concrete type be presented as a function of the cross-section width, b. The high first costs associated with FRP makes this method very useful - specifically when material costs in a project are significant.
Further research will be concerned around generalizing the results and looking into the possibility of an appliance to deflection limit state.

References

[1] Guadagnini, M. et al, FRP reinforcement for durable concrete structures, Proc. 11th annual International fib Symposium. Concrete: 21st Century Superhero: Building a sustainable future, London, UK (2009), 1-8
[2] Erki, M.A. and Rizkalla S.H., FRP reinforcement for concrete structures. Concrete International 15 (1993), 48-53
[3] Balafas, I. and Burgoyne, C.J., Economic viability of structures with FRP rebar and prestress, Magazine of Concrete Research 64(10) (2012), 885-898
[4] Sonnenschein, R. et al, FRP Composites and their Using in the Construction of Bridges. Procedia Engineering 161 (2016), 477-482
[5] International Federation for Structural Concrete (*fib*), FRP reinforcement in RC structures, Lausanne, Switzerland (2007)
[6] Katz, A., Environmental Impact of Steel and Fiber-Reinforced Polymer Reinforced Pavements, Journal of Composites for Construction 8(6), (2004) 481-488
[7] Pearson, C. et al, An Investigation into the Sustainability of FRP Reinforcement Bars, CDCC-11 4th International Conference on Durability and Sustainability of Fibre Composites for Construction and Rehabilitation, Quebec City, Canada (2011), 71-80
[8] Mufti, A. et al, Field Study of Glass-Fibre-Reinforced Polymer Durability in Concrete, Canadian Journal of Civil Engineering 34(3) (2007), 355-366
[9] Ascione, L. et al, Prospect for new guidance in the design of FRP: Support to the implementation, harmonization and further development of the Eurocodes, Publications Office of the European Union (2007)
[10] American Concrete Insitute, ACI 440.1R-15: Guide for the Design and Construction of Structural Concrete Reinforced with Fiber-Reinforced Polymer (FRP) Bars, Farmington Hills, USA (2015)
[11] Nanni, A., Flexural behavior and design of RC members using FRP reinforcement. Journal of Structural Engineering 119(11) (1993), 3344-3359
[12] Jaeger, L.G. et al, The concept of the overall performance factor in rectangular-section reinforced concrete members. Proc. 3rd International Symposium on Non-Metallic (FRP) Reinforcement for Concrete Structures, Sapporo, Japan (1997), Vol. 2, 551-559
[13] Bertsekas, D.P., Constrained optimization and Lagrange multiplier methods, Academic press (1982)
[14] Ghorpade, S. and Limaye, B.V., A course in multivariable calculus and analysis, Springer, New York, USA (2010), 346-361

SynerCrete'18 International Conference on Interdisciplinary Approaches
for Cement-based Materials and Structural Concrete
24-26 October 2018, Funchal, Madeira Island, Portugal

DURABILITY OF HEMP FIBRE REINFORCED CEMENTITIOUS MORTARS BY MEANS OF FIBRE PROTECTION AND CEMENT SUBSTITUTION WITH METAKAOLIN

Bojan Poletanović [(1)], Katalin Kopecskó [(2)], Ildiko Merta [(1)]

(1) TU Wien, Vienna, Austria
(2) Budapest University of Technology and Economics, Budapest, Hungary

Abstract

The aim of this research was to investigate the influence of protection of hemp fibres (with linseed oil) and of partial substitution of cement in matrix with metakaolin (in mass ratio 10wt% and 15wt%) on the durability of hemp fibre mortars under severe environmental conditions of freeze/thaw cycles.Cementitious mortars reinforced with discrete short hemp fibres (*Cannabis sativa L*) were exposed to accelerated aging of 51 freeze/thaw cycles under laboratory conditions and by mean of the composites compression strength, flexural strength and energy absorption capacity in bending its durability assessed.

The results showed that the fibre protection with linseed oil effectively prevents the degradation of the composite after freeze/thaw cycles in term of its compression- and flexural strength, whereas still a significant loss in flexural toughness occur.

In case of partial substitution of cement with metakaolin the results are more promising, the degradation of the composites compression strength under freeze/thaw cycles was completely prevented. The loss in composites flexural strength was prevented only in case of higher substitution rate of cement with metakaolin (15wt%), whereas its flexural toughness still markedly decreased after freeze/thaw cycles.

1. Introduction

Recently cellulose fibres have been widely used for cementitious materials as fibre reinforcement. Their worldwide availability, biodegradability, low density, favorable mechanical properties make them attractive alternatives to the traditional synthetic fibres [1]. Natural fibres such as hemp, flax, coir, sisal, jute, cotton, bamboo are already proved to positively affect the mechanical properties of cementitious composites, such as their tensile

strain capacity, post- cracking toughness, impact- and abrasion resistance, and crack resistance [2-3]. However, the main challenge in broader application of natural fibre composites is their long term durability. Natural fibres within the alkaline environment of cement matrix are found to undergo degradation caused by two main mechanisms, i.e. alkaline attack and fibre mineralization [4]. As a consequence, cementitious composites reinforced with natural fibres undergo significant reduction in mechanical properties – especially in composites toughness [5,6].
It has been found that matrix modification (decrease of the alkalinity of the matrix by adding pozzolanic materials) [7, 8] and impregnation of fibres prior to addition into the matrix [9, 10] are efficient methods in improving the durability of natural fibres in cementitious composites.
The aim of this research was to investigate the influence of fibre protection with linseed oil [10] and of partial cement substitution in matrix with metakaolin (mass ratio of 10wt% and 15wt%) on the durability of hemp fibre mortars under severe environmental conditions of freeze/thaw cycles.

2. Materials and experimental procedure

2.1. Raw materials and specimens preparation

For fibre reinforcement primary bast hemp fibres (*Cannabis sativa L*) with a diameter of 16–50 μm was used. The tensile strength of fibres is between 300-1100 N/mm^2 according to the literature [1] and their density is 1.5 g/cm^3. In all fibre reinforced mortar mixtures the length of the fibres was 10 mm and the dosage 1% by volume.
The ratio of cement:sand:water in mortar mix designs was 1:2:0.5 by weight with the size of aggregate 0-4 mm and with cement CEM I 42,5 N. The first mixture referred as "plain mortar" contained no fibres. The second mixture referred as "non treated fibres" contained hemp fibres which were added in water saturated condition to the matrix. The third mixture referred as "oiled fibres" contained impregnated fibres. Prior to the addition of fibres into the matrix, the fibres were immersed in linseed oil for one hour, then slightly squeezed by hand and wiped. The last two mixtures contained hemp fibres and the cement was partially substituted with metakaolin by 10 wt% and 15 wt% respectively. These mixtures are referred as "10% metakaolin" and "15% metakaolin" respectively. The chemical composition of metakaolin used was SiO_2 52-54 wt%, Al_2O_3 42-44 wt%, Fe_2O_3 < 1wt%, TiO_2 < 2 wt%, K_2O < 0.1 wt%.
The mortars were mixed in a laboratory drum-mixer. Specimens with dimensions of 40x40x160 mm^3 were cast and demolded after 24 hours.

2.2 Aging condition

The demolded specimens were cured in water for 28 days followed by storage of 3 months in a climate chamber (relative humidity 60% and temperature 20°C) in order to undergo self desiccation. The specimens were exposed to 51 freeze/thaw cycles (FTC) from -20°C to +20°C alternately. The individual freeze (and thaw) cycle lasted 4 hours, which resulted in 17 days of total aging.

2.3. Mechanical tests

Three point bending tests (3PBT) and compressive tests were conducted first on specimens at 28 days of age and second after FTC cycles according to the norm ÖNORM EN 1015-11

[11]. The bending tests were done on 6 identical prisms specimens of dimensions 40x40x160 mm^3. The compressive tests were carried out on one half of the split specimens by applying the compressive force on 40x40 mm^2 area on 3 identical specimens.
The flexural toughness (absorbed energy) of the material was calculated from the force-mid span deflection curve of the 3PBT as the area under the curve till the deflection in post-peak part corresponding to 90% drop of the maximal force.

3. Results and Discussion

3.1. Compressive strength

The specimens with oil impregnated fibres and cement substitution showed after FTC no decrease in strength when compared to their counterparts tested at the age of 28 days.
After FTC cycles the specimens with 10 wt% and 15 wt% cement substitution with metakaolin showed 30% and 36% higher compressive strength respectively compared to specimens without metakaolin substitution. The increase could be related to the fact that the fine metakaolin particles fill the pores within the specimens resulting in denser material with higher strength. However, in case if the fibres are impregnated with oil the compression strength of the composite after FTC decrease up to 23%.

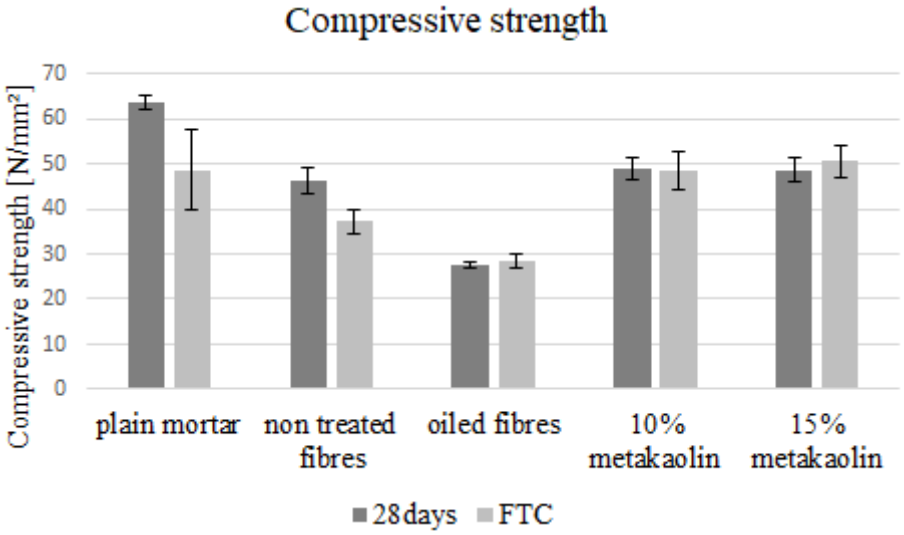

Figure 1. Compressive strength of specimens at the age of 28 days and after freeze-thaw cycles

3.2. Flexural strength

Both the impregnation of fibres and the substitution of cement with 15 wt% metakaolin, efficiently prevented the decrease of the materials flexural strength after FTC when compared to their counterparts tested at the age of 28 days.
The fibres impregnation or cement substitution with metakaolin did not improve the specimens flexural strength after FTC when compared to the specimens with non treated fibres.

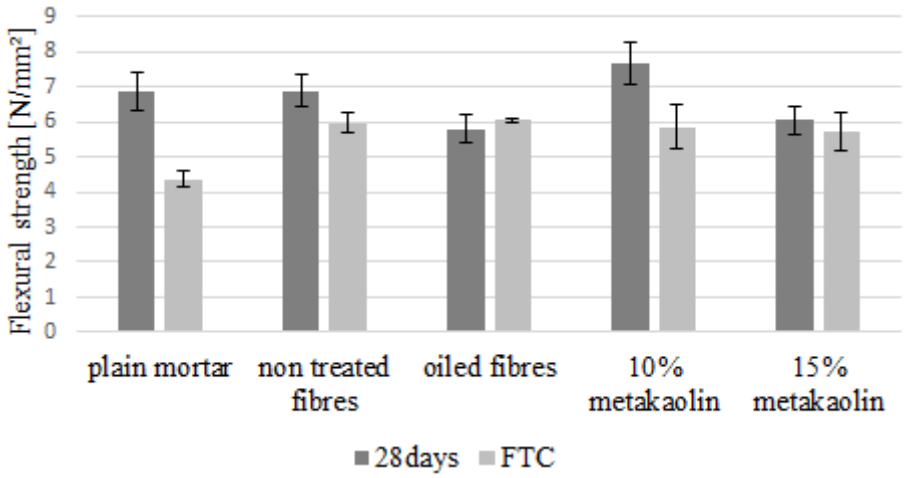

Figure 2. Flexural strength of specimens at the age of 28 days and after freeze-thaw cycles

3.3. Flexural toughness

All specimens after FTC showed decrease in flexural toughness compared to their counterparts tested at the age of 28 days. The most significant loss is observed in case of oiled impregnated fibres.

It seems that fibre impregnation with linseed oil is not so effective in preventing the toughness loss of the material after FTC. In contrary, cement substitution with metakaolin significantly improved the flexural toughness after FTC when compared to the specimens with non treated fibres. In case of 10 wt% and 15 wt% cement substitution with metakaolin, the toughness increased up to 61% and 50% respectively.

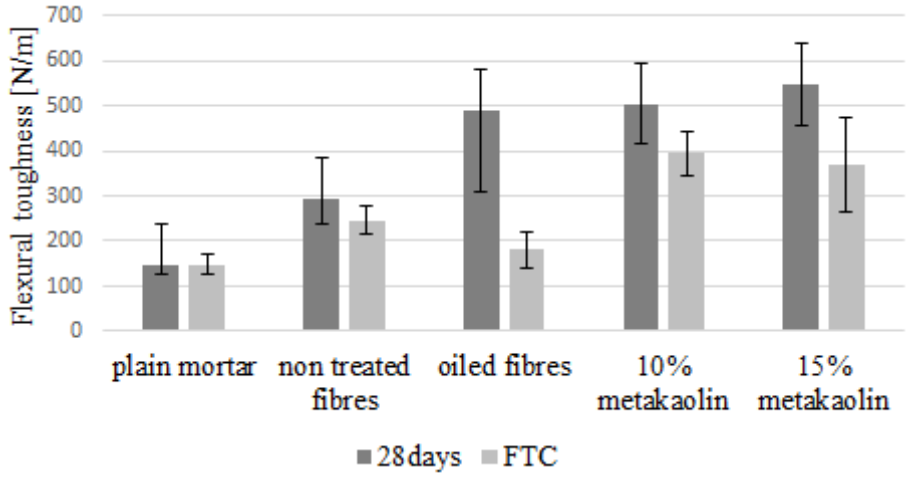

Figure 3. Flexural toughness of specimens at the age of 28 days and after freeze-thaw cycles

4. Conclusion

Based on this research it could be concluded that in term of flexural strength of the composite both applied method, the fibre protection with linseed oil and partial substitution of cement with metakaolin, are effective in preventing the degradation after freeze/thaw cycles. Besides,

the fibre protection with linseed oil proved to be effective also in term of compressive strength of the composite after freeze/thaw cycles, whereas in case of the cement substitution only higher substitution rate of cement with metakaolin (15wt%) was effective.
Neither the fibre protection with linseed oil nor partial substitution of cement with metakaolin proved to be effective in term of flexural toughness of the composites after freeze/thaw cycles.

Acknowledgement
The research is supported by the Stiftung Aktion Österreich-Ungarn in the frame of a bilateral research cooperation project Nr. 95öu6, and in the framework of a visiting student fellowship of the first author at the Budapest University of Technology and Economics. Additionally, the second author acknowledges the support by the Hungarian Research Grant NVKP_16-1-2016-0019 "Development of concrete products with improved resistance to chemical corrosion, fire or freeze-thaw". The authors greatly acknowledge the support of Meselia Hungária Kft for providing metakaolin for the research.

References
[1] Yan, L. et al, A review of recent research on the use of cellulosic fibres, their fibre fabric reinforced cementitious, geo-polymer and polymer composites in civil engineering, Composites Part B (2016)
[2] Merta, I. et al, Fracture energy of natural fibre reinforced concrete, Original Research Article Construction and Building Materials 40 (2013), 991-997
[3] Merta I., et al, Fracture Mechanics of Concrete Reinforced With Hemp, Straw and Elephant Grass Fibres, Composite Materials: Key to the Future, 18th International Conference on Composite Materials, Jeju Island, Korea (2011)
[4] Tolêdo Filho, R. et al, Durability of compression molded sisal fiber reinforced mortar laminates, Constr. Build. Mater. 23 (2009), 2409–2420
[5] Merta, I. et al, Influence of natural fibres on mechanical properties and durability of cementitious mortars, CoMS - 1st International Conference on Construction Materials for Sustainable Future (2017), 1 - 8
[6] Wei J., Meyer C., Degradation mechanisms of natural fiber in the matrix of cement composites, Cement and Concrete Research 73 (2015), 1-16
[7] Merta, I. et al,: Durability of natural fibres within cement-based materials - Review, Concrete Structures, Journal of the Hungarian Group of fib 18 (2017), 10-15
[8] Silva F., A. et al, Physical and mechanical properties of durable sisal fiber–cement composites. Constr Build Mater 24 (2010), 777–785.
[9] Ferreira S., R., et al, Effect of fiber treatments on the sisal fiber properties and fiber-matrix bond in cement based systems. Construction and Building Materials 101 (2015), 730-740
[10] Merta, I., et al, Durability of hemp fibres in the alkaline environment of cement matrix, BEFIB2012 - Fibre reinforced concrete (2012)
[11] ÖNORM EN 1015-11: 2018 01 01, Methods of test for mortar for masonry - Part 11: Determination of flexural and compressive strength of hardened mortar

SynerCrete'18 International Conference on Interdisciplinary Approaches
for Cement-based Materials and Structural Concrete
24-26 October 2018, Funchal, Madeira Island, Portugal

INFLUENCE OF MICRO-CRACKING ON CAPILLARY WATER ABSORPTION OF AN UHPFRC

Ana Mafalda Matos [(1)], Sandra Nunes [(1)], José L. Barroso Aguiar [(2)]

(1) CONSTRUCT-LABEST, Faculty of Engineering, University of Porto, Portugal
(2) University of Minho, School of Engineering, Guimarães, Portugal

Abstract
The aim of this research was to investigate the influence of cracking on water transport by capillary suction in UHPFRC. Specimens were firstly pre-loaded under four-point bending up to a wide range of pre-defined crack open displacement. Crack pattern created was characterized (width, number of cracks) before capillarity testing. Test results showed that micro cracks induced by previous loading significantly increased the sorptivity comparing with non-cracked specimens. However, increasing the damage (COD of 200 up to 400 μm), did not significantly compromise the absorption capillary suction of UHPFRC, as compared to good quality conventional concrete or engineered cementitious composites (ECC).

1. Research Scope

The emergence of Ultra-High Performance Fibre Reinforced Cement-based Composites (UHPFRC) provided the structural engineer with an unique combination of extremely low permeability and very high strength, namely, compressive strength higher than 150 MPa, tensile strength over 7 MPa and with considerable tensile strain-hardening behaviour (multiple micro-cracking formation stage). A promising field of application is the rehabilitation and/or strengthening of reinforced concrete structures, in which a new layer of UHPFRC replaces the deteriorated concrete (cracked, carbonated, chloride attack, etc.). The combination of the UHPFRC as protective layer, which can be reinforced, provides a simple and efficient way of increasing the durability (prolonging the service life), the stiffness and structural resistance capacity while keeping compact cross sections [1], [2], [3].
In those applications, UHPFRC is exposed to severe environmental conditions (as de-icing salts, marine environment, chemical attack) and/or high mechanical loading (e.g. concentrated forces, wear, fatigue, impact) for extended periods. Under applied loads in service conditions,

a progressive multiple micro-cracking is achieved in UHPFRC due to the addition of a significant amount of short steel fibres. Higher number and finer cracks generally characterize the crack pattern of UHPFRC, which might affect the transport mechanisms rates. The water transport through cracked UHPFRC is possibly driven by pressure gradient water permeation or capillary absorption. Very fine cracks can be quickly filled by water due to capillary action, thus the structural element is not protected against aggressive aqueous solutions. Since resistance to water penetration may be considered as a criterion for durability of cementitious-based materials, an investigation on the influence of cracking on transport properties of water is necessary.

In order to improve knowledge on water transport by capillary action in UHPFRC, a research was launched to study the absorption of UHPFRC submitted to pre-defined deformations. The objective was to assess admissible deformations for which the material presents satisfactory transport properties and to evaluate the existence of correlation between certain crack pattern parameters and water absorption by capillary.

2. Experimental program

2.1 UHPFRC tested mixtures

Materials used to prepare UHPFRC in this study were: Type I 42.5R Portland cement, dry micro silica fume, limestone filler, siliceous sand, a polycarboxylate type superplasticizer and short steel fibres (ϕ_f=21mm; l_f=13mm; f_{yk}=2750MPa). In addition, a waste generated by the Portuguese oil refinery industry, the spent equilibrium catalyst (ECat) was introduced in the matrix as partial aggregate replacement. UHPFRC mixture compositions, incorporating 1.5% and 3.0% of steel fibres (in volume), are presented in Figure 1. The UHPFRC self compactability was assessed using the mini-slump flow test [4] (D_{flow}). After the fresh state test, several prismatic (40x40x160 mm) specimens were casted following the procedure prescribed by the standard NP EN 196-1 [5] except the compaction step. In addition, cube specimens (50mm) were casted to assess compressive strength. All specimens were demoulded in the following day and then wet cured in controlled environment chamber at 20±2 ºC and HR≥95%. At 28 days, four-point bending and compressive strength were assessed, as well as, several cracking levels were induced in the prismatic specimens. Main fresh and hardened properties of UHPFRC mixtures are listed in Table 1.

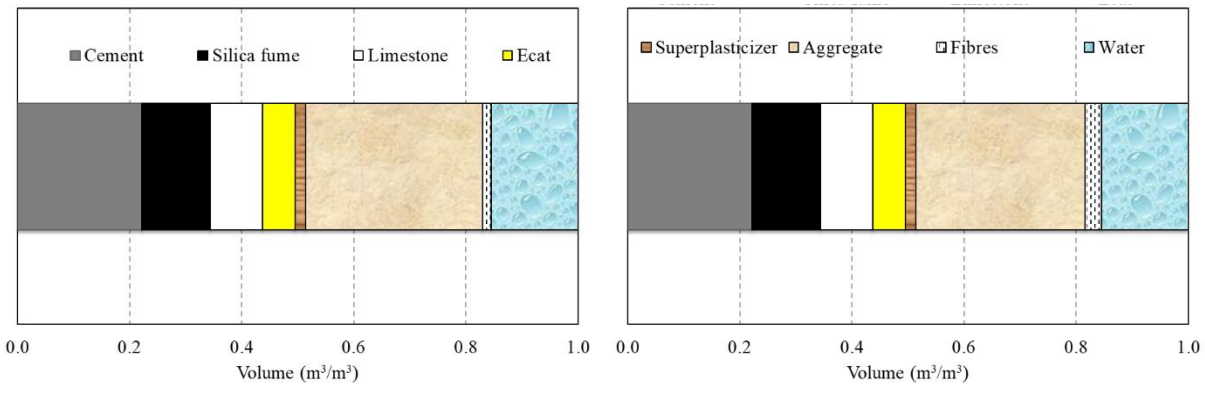

a) b)

Figure 1 – Mixture composition of UHPFRC with a) 1.5% and b) 3.0% fibres content.

2.2 Specimens cracking methodology

UHPFRC specimens were pre-cracked by imposing different crack open displacements (COD) between 200 and 400µm, in steps of 50 µm, to obtain different crack patterns. Predefined COD, were produced through four-point bending loading where the loading span is 1/3 of the support span. The test was performed as displacement-controlled (displacement rate = 0.003 mm/s) and carried out by means of a 300 kN Instron testing machine. Two LVDTs were fixed on each sides of the specimen, perpendicular to loading direction, to monitor the COD. When the target COD was achieved, the specimen was unloaded and the residual COD was recorded. Load-displacement curves obtained during cracking procedure are presented in Figure 2, along with the complete load-displacement curves obtained when the test was conducted until the end (grey lines). For each mixture, non-cracked prisms were also tested for control purposes. As it can be observed from Figure 2, some specimens reached the peak load, in which a macro crack develops (approximately between COD 300-400 micron).

Table 1 – Main fresh and hardened properties of tested UHPFRCs mixtures

		UHPFRC-1.5%	UHPFRC-3%
D_{flow}	[mm]	302	283
Final setting time (NP EN 196-3)	[hh:mm]	02:00	02:00
Compressive strength (ASTM C109/C109M)	7 days [MPa]	104 ± 5.1	118 ± 2.6
	28 days [MPa]	121 ± 4.4	147 ± 2.3
Flexure Strength (4-point bending) (prisms 40x40x160 mm)	28 days [MPa]	23 ± 2.5	36 ± 1.6

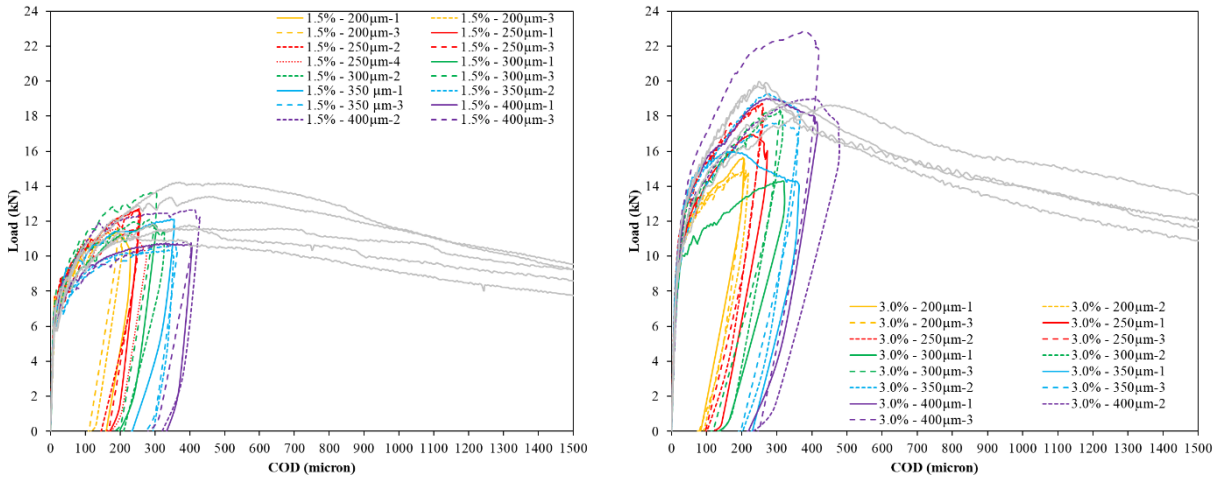

a) b)

Figure 2 – Obtained load-displacement curves in four-point bending test: a) UHPFRC 1.5%; b) UHPFRC 3%.

2.3 Characterization of the crack pattern produced by bending

For each specimen a mesh was drawn in the zone of maximum tension strain (in between the two applied forces) (Fig. 3-a). After imposing the target COD, a 40×40×40 mm^3 cube was cut

from the central portion of each beam specimen. The widths of cracks observed in the tension face of each specimen were measured using a Microscope Multizoom Nikon AZ100 in the unloaded state. Measurements were taken from cracks crossing the three lines A, B and C, as shown in Figure 3.

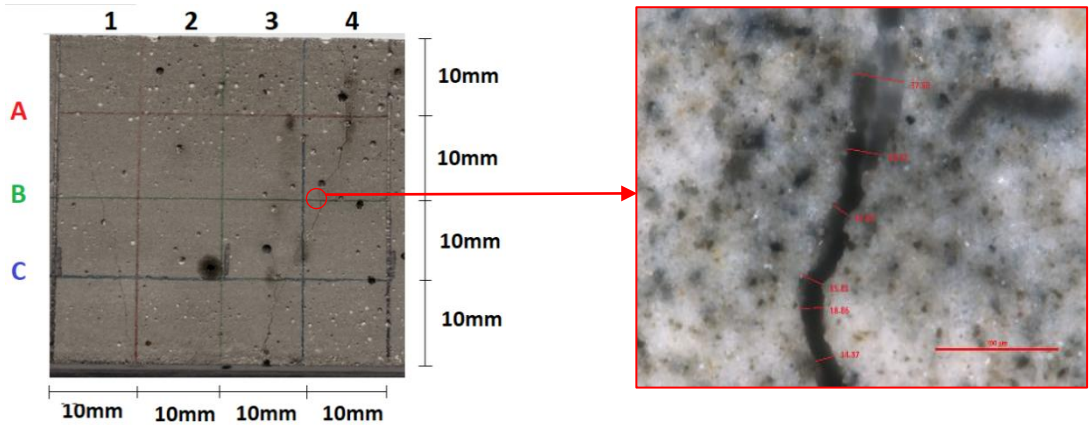

a) b)

Figure 3 – a) Scheme for measuring of the crack number and widths; b) Typical photo made from a measurement.

2.3 Capillary water absorption test

The sorptivity test was carried out according to RILEM TC 116-PCD [6] and it was undertaken on cubic specimens (40 mm), after curing for 28 days plus 12 days drying in an oven at 40°C, until constant mass was achieved. The absorption of water under capillary action is dependent on the square-root of time and may be modelled [7] following Equation 1, where A (mg/mm^2) is the water absorption by unit area of a specimen surface since the moment the specimen was dipped in water, S is the sorptivity of the material (mg/(mm^2.min$^{0.5}$), t is the elapsed time (minutes) and A_0 (mg/mm^2) is the water absorbed initially by pores in contact with water. The slope of the obtained line defines the sorptivity of the specimen during the initial four hours of testing. For all specimens (cracked and uncracked), this slope is obtained by using linear regression analysis of the plot of the rate of absorption versus the square root of time. Equation (1) was found to provide a very good fit to the data with correlation coefficients of over 0.96.

$$A = A_0 + S \times t^{0.5} \quad (1)$$

3. Results and Discussion

Figure 4-a illustrates the relationships between the COD before unloading the specimen (COD_{load}) and COD after unloading (COD_{res}). The COD_{res} increases nearly linearly with the COD_{load}, representing the higher level of damage. Generally, the COD_{res} values decrease when the dosage of steel fibres increases under the equivalent damage, since the cracking severity is reduced by the higher dosage of steel fibres.

The relation between sorptivity values and COD_{res} is depicted in Figure 4-b, including non-cracked specimens. The sorptivity of control specimens was 17.8 and 7.6 (mg/(mm^2.min$^{0.5}$))x10^{-3} for 1.5% and 3% fibres content, respectively. These results are

corroborated with previous research works [8], [9], [10], [11] also illustrated in Figure 4-b. When compared to good quality conventional concrete (w/c=0.40), exhibiting sorptivity above 0.09 (mm/min$^{0.5}$) [12], or even with sorptivity of engineered cementitious composite (ECC) with indicative values around 0.028 (mm/min$^{0.5}$) [13], UHPFRC presented a very low water absorption in a non-damage state. This may be attributed to the very low water content, the absence of coarse aggregates and the dense cementitious matrix that provide a significantly lower capillary porosity and thus capillary sorption capacity of UHPFRC.
The main mechanisms responsible for fluid transport during the absorption test are hydrostatic pressure due to the gravity effect and capillary suction. Since the test was performed at atmospheric pressure, the key mechanism in this study was the suction. The effect of crack width on capillary absorption is reversed compared to permeability under pressure gradients: finer cracks lead to higher capillary absorption. When the first target COD (200µm) is achieved, it corresponds to a multiple cracking stage with cracks below 80µm and 10µm for 1.5% and 3% fibres content, respectively. For these cases, the sorptivity value increased 60% and 300% compared to non-cracked specimens. By increasing the damage, the number of cracks and the crack widths increased with no substantial effect on sorptivity, even when a macro crack develops for target CODs of 350 and 400 µm. Therefore, the measured sorptivity for the cracked UHPFRC specimens (< 44 x10^{-3} mg/(mm^2.min$^{0.5}$)) was not particularly high when compared to that of conventional concrete. Moreover, the sorptivity values of cracked UHPFRC specimens presented in Figure 4-b possibly represent an upper limit of sorptivity in actual structures or elements, since the effect of self-healing was not considered due to the short experiment duration. These features provide UHPFRC with distinct barrier qualities proving that even when cracked it can act as protective layer increasing the durability (and service life) in the rehabilitation of structures or elements.

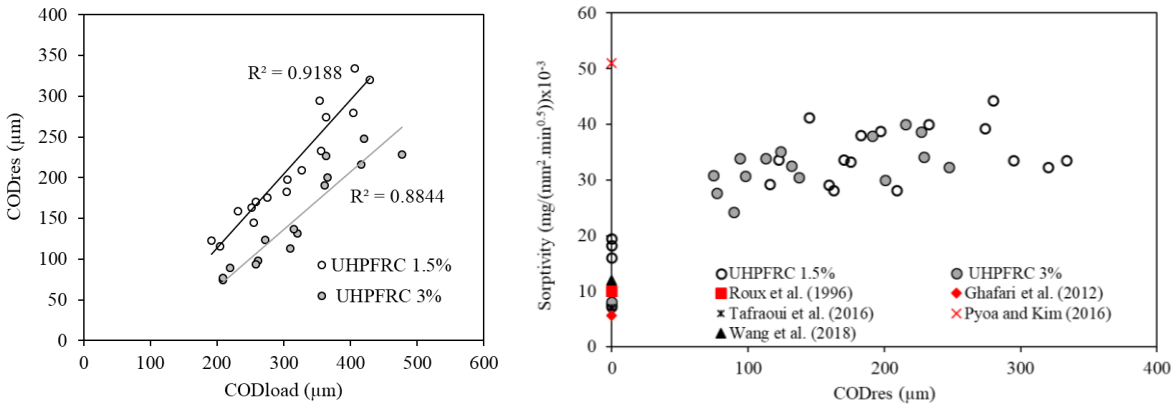

a) b)

Figure 4 – a) COD_{load} and COD_{res}; b) Sorptivity of UHPFRCs as a function of COD_{res}.

4. Conclusion

The results revealed that the very low water content in addition with no coarse aggregate and a dense cementitious matrix provided extremely low sorptivity to non-cracked UHPFRC. Even though UHPFRC cracking increased the sorptivity results, the capillary absorption is still very low when compared to conventional concrete. This feature provides UHPFRC with distinct barrier qualities, which can be beneficial for rehabilitation applications, proving an

improved durability, as well as, increased service life of structures or elements. The influence of cracking patterns on other durability indicators, such as, resistance to chlorides ingress is also under evaluation within the current PhD project.

Acknowledgments

This work was financially supported by: Project POCI-01-0145-FEDER-007457 - CONSTRUCT - Institute of R&D In Structures and Construction and by project POCI-01-0145-FEDER-007633 (ISISE) funded by FEDER funds through COMPETE2020 - Programa Operacional Competitividade e Internacionalização (POCI) – and by national funds through FCT - Fundação para a Ciência e a Tecnologia through the PhD scholarship PD/BD/113636/2015, attributed within the Doctoral Program in Eco-Efficient Construction and Rehabilitation (EcoCoRe). Acknowledgements are also due to Secil, EUROMODAL, Omya-Comital, Dramix and Sika for supplying constituent materials.

References

[1] B. A. Tayeh, B. H. A. Bakar, M. A. M. Johari, and Y. L. Voo, "Utilization of Ultra-high Performance Fibre Concrete (UHPFC) for Rehabilitation – A Review," *Procedia Eng.*, vol. 54, pp. 525–538, 2013.

[2] Emmanuel Denarié and Eugen Brühwiler, "Cast-on site UHPFRC for improvement of existing structures – achievements over the last 10 years in practice and research," in *HPFRCC7: 7th workshop on High Performance Fiber Reinforced Cement Composites*, 2015.

[3] M. Bastien-Masse and E. Brühwiler, "Ultra high performance fiber reinforced concrete for strengthening and protecting bridge deck slabs," in *7th International Conference on Bridge Maintenance, Safety and Management (IABMAS)'*, 2014, pp. 2176–2182.

[4] H. Okamura, K. Ozawa, and M. Ouchi, "Self-compacting concrete," *Struct. Concr.*, vol. 1, no. 1, pp. 3–17, Mar. 2000.

[5] Instituto Português da Qualidade, "NP EN 196-1. Methods of testing cement. Part 1: Determination of strength." IPQ, Lisbon, pp. 1–37, 2006.

[6] RILEM, "RILEM TC 116-PCD: Permeability of concrete as a criterion of its durability.," *Mater. Struct.*, vol. April, pp. 174–179, 2008.

[7] C. Hall, "Water sorptivity of mortars and concretes: a review," *Mag. Concr. Res.*, vol. 41, no. 147, pp. 51–61, Jun. 1989.

[8] N. Roux, C. Andrade, and M. A. Sanjuan, "Experimental study of durability of reactive powder concretes," *J. Mater. Civ. Eng.*, vol. 8, no. 1, pp. 1–6, 1996.

[9] A. Tafraoui, G. Escadeillas, and T. Vidal, "Durability of the Ultra High Performances Concrete containing metakaolin," *Constr. Build. Mater.*, vol. 112, pp. 980–987, Jun. 2016.

[10] S. Pyo and H.-K. Kim, "Fresh and hardened properties of ultra-high performance concrete incorporating coal bottom ash and slag powder," *Constr. Build. Mater.*, vol. 131, pp. 459–466, Jan. 2017.

[11] Y. Chen, R. Yu, X. Wang, J. Chen, and Z. Shui, "Evaluation and optimization of Ultra-High Performance Concrete (UHPC) subjected to harsh ocean environment: Towards an application of Layered Double Hydroxides (LDHs)," *Constr. Build. Mater.*, vol. 177, pp. 51–62, Jul. 2018.

[12] A. M. Neville, *Properties of concrete*, Fifth. Longman Group Limited, 2011.

[13] H. Liu, Q. Zhang, C. Gu, H. Su, and V. C. Li, "Influence of micro-cracking on the permeability of engineered cementitious composites," *Cem. Concr. Compos.*, vol. 72, pp. 104–113, 2016.

SynerCrete'18 International Conference on Interdisciplinary Approaches
for Cement-based Materials and Structural Concrete
24-26 October 2018, Funchal, Madeira Island, Portugal

INFLUENCE OF THE ALKALINE TREATMENT ON THE TENSILE PROPERTIES OF JUTE FIBERS AND ON THE FIBER-MATRIX BONDING

Yasmim Gabriela dos Santos Mendonça [(1)], Bartosz Zukowski [(1)], Romildo Dias Toledo Filho [(1)]

(1) Federal University of Rio de Janeiro, Brazil

Abstract

This work presents the influence of alkaline treatment on the fiber tensile properties and cementitious matrix bond for jute fibers. The reference group of fibers was washed for 3 hours in water at 80 °C, then cooled at 40 °C for 5 hours. This process was applied to remove residues and impurities from the fiber's surface. The group of alkaline treated fibers, after washing and cooling, was additionally submerged in a saturated solution of calcium hydroxide, $Ca(OH)_2$ for 50 minutes. Both groups were dried for 24 hours at 40 °C. The tensile stress-strain behavior of the fibers was determined for the two groups at a microforce testing system using the gage length of 20 mm. The cross-sectional area of the fiber was measured using scanning electron microscope (SEM) micrographs and image analysis. The Young's modulus, force at rupture, maximum stress and strain were calculated from the collected data to evaluate the influence of alkaline treatment on fiber's tensile properties. Pullout tests for embedment length of 7 mm were realized to evaluate the effect of the alkaline treatment on the fiber-matrix bond. The alkaline treatment improved the mechanical behavior of the jute fibers and the fiber-matrix bond.

1. Introduction

The mechanical properties of natural fibers present a lot of variation and depend on some factors: diameter of the fiber, the degree of polymerization, crystalline structure, origin (stem, leaf, fruit, and seed) and growth conditions [1]. The area of jute is smaller than the area of some other fibers as sisal or curauá. The tensile strength of the jute (249 MPa) is less than curauá (543 MPa) and sisal (484 MPa), but Young's modulus is not so distant from it, 43,9, 19,5 and 63,7 GPa to jute, sisal and curauá, respectly [2]. The physical and mechanical

properties of the fibers are influenced by their composition, mainly cellulose, hemicelluloses, and lignin. Fiber treatments can promote a better interaction between lignin, cellulose, and hemicellulose, resulting in a stronger fiber, with a higher crystallinity and modulus. The natural fibers tensile strength increase with the application of hornification treatments, because of the change in the cellulose crystallinity and possible bonds created between different polymer chains in the microfibrils. Alkaline treatment promotes changing in cellulose chemical bonds, as well as the reduction of fiber-water absorption capacity. The jute is the fiber that presents a higher interaction with the calcium hydroxide. Jute contains cellulose of high crystallinity, which collaborates well with $Ca(OH)_2$ [3].It is reported in the literature that the alkaline treatment improved the interaction between jute fibers and cementitious matrix, providing a better frictional phase [3]. This work presents the results of the study of stress-strain behavior and the fiber-matrix bond of alkaline treated jute fibers.

2. Materials and methods

2.1 Jute fiber and treatment applied

The jute fiber is extracted from the plant stem in a process based on the following steps: cutting, hardening, crushing, drying and classification [2]. The jute from Amazon region is combed and then cut in a guillotine. The chemical composition of jute fiber was verified on two sets of samples at the COPPE/UFRJ by calorimetric determination of hexuronic acids. The percentage values showed the amount of cellulose 74.4%, hemicellulose 15.0%, lignin 8.4%. The fibers were first washed in water at 80 °C for 3 hours to remove residues and impurities. Then they were cooled at 40 °C for 5 hours. After the washing process, the fibers were separated into two groups, namely untreated and alkaline. The untreated group was not submitted for treatment and for this reason this group was considered the reference group. The alkaline group was submerged in a saturated solution of $Ca(OH)_2$ with water for 50 minutes, and then dried for 24 hours at the temperature of 40 °C.

2.2 Fiber microstructural analysis

The fiber's microstructure was investigated using a SEM (TM 3000) at 25kV of accelerating voltage. The images obtained were processed using the software package ImageJ for measuring the cross-section of each fiber.

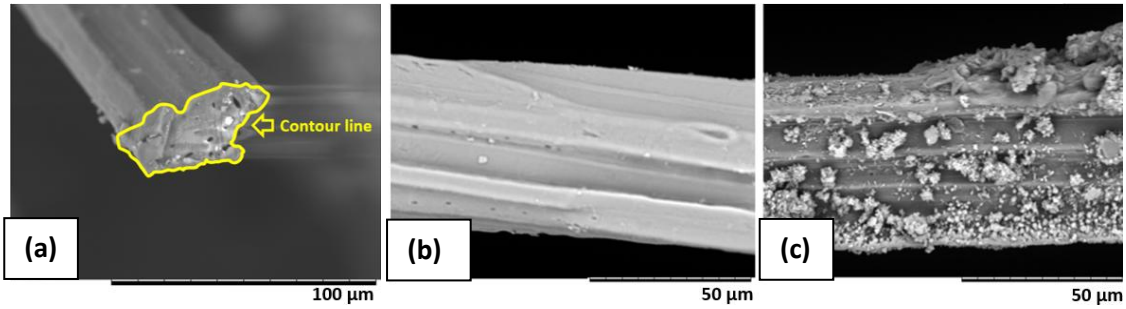

Figure 1: Micrographs of jute fibers at SEM: (a) area calculation using ImageJ, (b) surface of untreated jute fiber, (c) surface of alkaline treated jute fiber.

A contour line was interactively drawn to delineate the fiber's cross-section and then the area was measured, as illustrate the Fig.1. The visual analysis of fiber surface was carried at SEM. The fibers were covered with an approximately 20 nm layer of gold before the visual investigation under the microscope.

2.3 Fiber tensile test

The jute fibers were investigated at the gage length of 20 mm. The groups untreated and alkaline were tested. Before the test fibers were dried for 24 hours at 40 °C. The preparation of the test was performed according to ASTM C1557 [4]. The tensile tests were performed in a microforce testing machine Tytron 250 (Fig.2) at the strain rate of 0.4 mm/min.

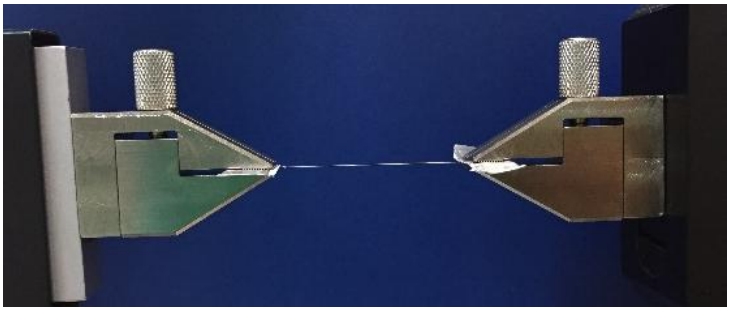

Figure 2: Setup of the tensile according to ASTM C1557 with the detail of clamps and specimen.

2.4 Cementitious matrix composition

The cement matrix was produced with 33% of cement Portland CPII F-32, 27% of metakaolin, 40% of fly ash, sand with maximum diameter of 250 μm, water, superplasticiser Glenium 51, and viscosity agent, in a proportion of 1:0.5:0.4 (cementitious materials: sand: water/cementitious materials). The high dosage of fly ash is justified because of the mechanical behaviour and high deformation capacity [5].

2.5 Fiber-matrix bond

Verification of the fiber-matrix interface was performed through pull-out tests. To ensure an adequate coating of the fiber in the matrix, PVC molds were used. The PVC mold is a tube with a depth of 7 mm corresponding to the fiber embedment length and 25 mm of diameter. The Fig.3a shows the sequence of pull-out specimen preparation.

The matrix was poured inside the PVC mold, and the paper tape closed the specimen providing the straight and central position of the fiber in the mold. After 27 days of curing in a room of 100% RH and 21°C ± 1 °C additional 1 day of drying at 23°C ± 1 °C, to provide conditions similar to composite's curing, the fibers were tested to verify pull-out behavior in microforce machine Tytron 250 at the strain rate of 0.4 mm/min with 50 N load cell.

The pull-out test starts with the tube placed in the iron ring and clenched by screws to prevent specimen's movement during the test. The fiber is pulled out from the specimen and the data of force and displacement are collected by Tytron 250 (Fig.3b). Then the collected data was analyzed according to the modified model of Lin [6] adapted to the vegetal fiber using the perimeter and the area of the surface calculated in ImageJ. According to this model, the values

of chemical debonding energy (G_d) and the maximum bond strength (τ_{max}) were calculated (Eq. (1) and Eq. (2)).

$$G_d = \frac{(P_a - P_b)^2}{2E_f A_f Perimeter} \quad (1)$$

$$\tau_{max} = \frac{P_{max}}{l_f Perimeter} \quad (2)$$

where P_a is the peak load of single fiber pullout curve, P_b is the load after sudden drop fallowing P_a, E_f is the fiber modulus of elasticity, A_f is the fiber area measured in ImageJ software, $Perimeter$ is the perimeter measured in the same software, P_{max} is the maximum force in the frictional region, and l_f is the embedment length.

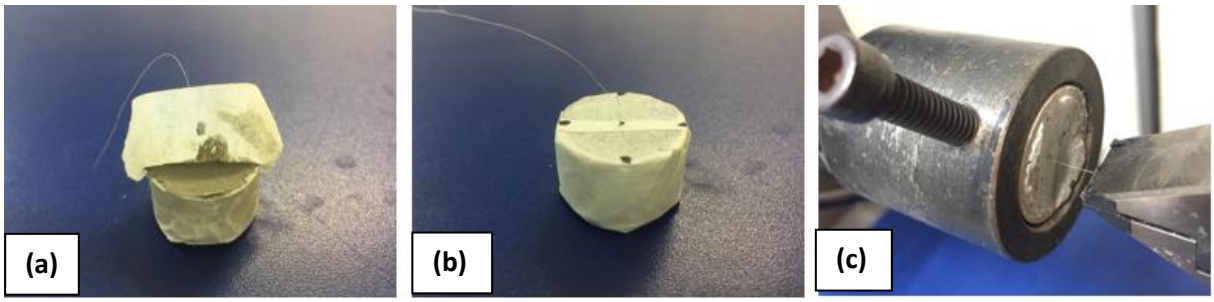

Figure 3: Pull-out test: (a), (b) specimens preparation, (c) completed test.

3. Results and discussion

In the Tab.1 and in the Fig. 4 are presented the results of the tensile test of jute fibers for the two groups (untreated and alkaline). It is possible to note that the alkaline treatment reduced the area of the fibers in comparison to the untreated group, and the treated fibers presented higher tensile strength values than untreated fibers. Moreover, the alkaline treatment increased the value of the elastic modulus. The untreated jute fiber ruptured at 0.89 N (0.35) when the alkaline treated fibers ruptured at 1.37 N (0.15). The higher value of force at rupture of treated fibers was followed by the higher tensile strength 689.77 MPa (74.80) versus 244.34 MPa (95.20) for untreated fiber. The increased value of strength was also a result of the area difference 3660 µm² (57) for untreated fibers versus 1990 µm² (50) for alkaline treated fibers.
The pullout tests (Tab.2 and Fig.05) provided information on the fiber-matrix bond for untreated and alkaline treated jute fibers. The debonding force (P_a), the force required to disconnect the fiber from the matrix and begin the frictional phase was higher after alkaline treatment 0.92 N (0.34) versus 0.85 N (0.08) for untreated fiber suggesting the higher chemical fiber-matrix bond. The latter is confirmed by the higher chemical bond energy needed to disconnect the fiber from the matrix (G_d), 13.31 J/m² (3.45) for alkaline treated fiber versus 6.88 J/m² (0.56) for untreated fiber. The alkaline treatment improved the frictional phase of fiber-matrix interaction, which is visible by the maximum frictional bond strength 0.47 MPa (0.10) for treated fiber versus 0.44 MPa (0.05) for untreated fiber.

Table 1: Summary of average tensile test results and standard deviation for untreated jute fibers and alkaline jute fibers.

Jute fiber	N° of specimens	Area	Diameter		Strain to failure	Force at rupture	Tensile strength	Young's modulus
			Major	Minor				
		(μm²)	(μm)		(%)	(N)	(MPa)	(GPa)
Untreated	11	3660 (570)	95.32 (20.31)	50.01 (9.31)	1.06 (0.40)	0.89 (0.35)	244.34 (95.20)	22.17 (7.89)
Alkaline	7	1990 (500)	74.52 (14.72)	34.87 (10.97)	2.06 (0.77)	1.37 (0.15)	689.77 (74.80)	35.94 (10.83)

*Parenthesis number: standard deviation.

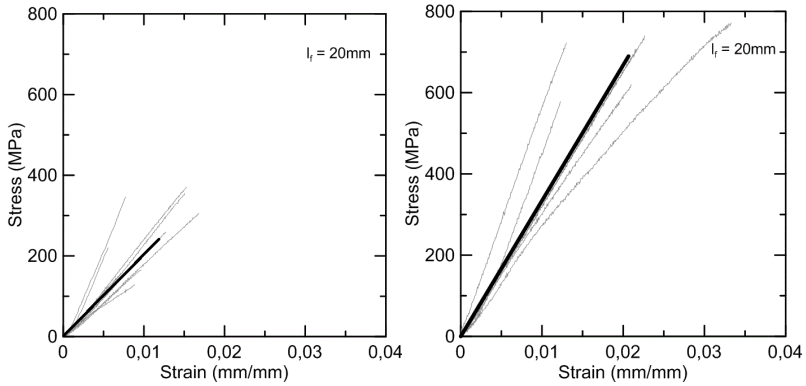

Figure 4: Tensile test results for untreated jute fibers (left) and for alkaline jute fibers (right).

Table 2: Summary of the results of pullout test for untreated jute fibers and alkaline jute fibers.

Jute fiber	l_f	Area	Perimeter	P_a	P_b	$P_{máx}$	G_d	τ_{max}
	(mm)	(μm²)	(μm)	(N)	(N)	(N)	(J/m²)	(MPa)
Untreated	**7**	4401 (248)	290 (35.61)	0.85 (0.08)	0.44 (0.10)	0.89 (0.05)	6.88 (0.56)	0.44 (0.05)
Alkaline	**7**	4391 (1067)	280 (46.92)	0.92 (0.34)	0.50 (0.17)	0.93 (0.33)	13.31 (3.45)	0.47 (0.45)

*Parenthesis number: standard deviation.

The treatment applied to the jute fibers was effective to promote a better interaction between the fiber and the matrix, improving the frictional phase. After the treatment, the modified fiber surface promotes a better chemical and mechanical adhesion improving the interaction, giving it a frictional phase promoted by the surface products.

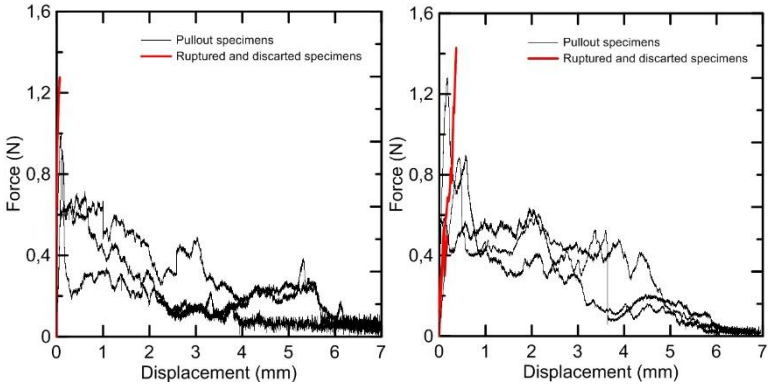

Figure 5: Pullout test results for untreated jute fibers (left) and for alkaline jute fibers (right).

4. Main conclusions

From the results, the alkaline treatment improved the mechanical properties of the fibers, and this can be because of the removal of non-cellulosic materials and impurities that distributed in the interfibrilar region of the fibers. After treatment alkaline, as the fibers become more capable of rearranging over the tensile arrows, since the region is interfibrilar is less dense and all rigid due to removal of hemicellulose. The results presented in this work encouraging the application encouraging their application as a reinforcement in cement-based composites.

References

[1] Thomas, S., Paul, S. A., Pothan, L. A., Deepa, B., "Natural Fibres: Structure, Properties and Applications", in Cellulose Fibers: Bio and Nano Polymer Composites – Green Chemistry and Technology. Springer-Verlag. Edited by Kalia, S., Kaith, B. S., Kaur, I, (2011).

[2] Fidelis, M.E.A., Desenvolvimento e Caracterização Mecânica de Compósitos Cimentícios Têxteis Reforçados com Fibras de Juta. PhD thesis, Federal University of Rio de Janeiro, (2014).

[3] Ferreira, S.R, Effect of surface treatments on the structure, mechanical, durability and bond behavior of vegetable fibers for cementitious composites. PhD thesis, Federal University of Rio de Janeiro, (2016).

[4] ASTM.C1557 /2014 - Standard Test Method for Tensile Sntrength and Young's Modulus of Fibers. West Conshohocken, PA, USA: American Society for Testing and Materials.

[5] Wang, S., Li, V. C., "Engineered Cementitious Composites with High-volume Fly Ash", ACI Materials Journal, Vol. 104, Nº. 3, pp. 233-241, 2007.

[6] Lin, Z., T. Kanda, and Victor C. Li. "On Interface Property Characterization and Performance of Fiber Reinforced Cementitious Composites." Concrete Science and Engineering 1: (1999), 173–184.

SynerCrete'18 International Conference on Interdisciplinary Approaches
for Cement-based Materials and Structural Concrete
24-26 October 2018, Funchal, Madeira Island, Portugal

NUMERICAL SIMULATION OF REINFORCED CONCRETE CUT-OFF WALL WITH STEEL FIBERS UNDER DAM

Homa Kazemi [(1)], Mohammad Mahdi Kioumarsi [(2)], Mohsen Zarghani [(3)], Hamed Sarkardeh [(4)]

(1) Taha Institute of Higher Education, Tehran, Iran
(2) Oslo Metropolitan University, Oslo, Norway
(3) Iran University of Science and Technology, Tehran, Iran
(4) Hakim Sabzevari University, Sabzevar, Iran

Abstract

One of the main components of dams is the cut-off wall, which any damage to this concrete structure could encounter the dam with danger. Flexural behavior of concrete is an important factor in view of creating and growing cracks in the cut-off wall. Few researches have been done on properties and application of fibers in the cut-off walls, but the advantages of using this type of concrete in other hydraulic structures have been proved. In the present research, numerical simulation of a reinforced concrete cut-off wall with steel fibers was performed and its behavior under hydrostatic and earthquake loads were studied using Finite Element Method (FEM). Results showed that by increasing the volume of fibers, the fracture strain of the cut-off wall becomes larger and more energy was absorbed. It can be concluded that using fibers in the concrete cut-off wall improve its flexural behavior.

1. Introduction

The stored water behind the dam is always looking for a way to escape because of its high potential, and therefore penetrates into the porous mass of foundation and bodies of earth dams and leaks to the downstream [1]. One of the most important points in the design and construction of earth dams is the leakage of the body and foundation of the dam [2]. Therefore, evaluation of methods for controlling or reducing water leakage in earth dams is necessary [3]. In the recent years, the concrete cut-off wall, which is one of the anti-seepage structures, has been widely used in the reinforcement of dam projects. For the earth-rock dams where the covering layer of the dam foundation was not thick, the closed cut-off wall

was usually built in the dam, and directly embedded in the rock, usually extends deeply underground and affected by the surrounding formation and the construction process, so its own stress state is very complex [4,5]. Dopant performed tests on 28 beams with the actual size and examined the load-deflection values of the beam by changing the volumetric ratio of the fiber [6]. Pine et al. [7] also considered 1-2% volumetric percentage of fiber as the most suitable amount of fiber to achieve the best mechanical properties of concrete, which is almost confirmed by other researchers. Olivito and Zocarlo indicated that increasing the volumetric percentages and the length of the steel fibers increases the ductility and durability of the concrete [8]. Johnston and Zamap examined the effect of length to diameter ratio and fiber type on fatigue strength under flexural loading [9]. Researches on the concrete structures were recently focused on effect of using fibers and other additives [10-14]. In the present study, effect of using fibers in concrete cut-off wall on its behavior was compared the plain concrete cut-off wall in the dam using a numerical model.

2. Materials and Methods

The dimensions of this wall are 70×50×5 m in y, z and x directions, respectively. All simulations were performed in three dimensional (3D) and ductile form. The Abaqus software was used based on Finite Element Method (FEM). Geometry, mesh and boundary conditions of arches are shown in Figure 1. Cell size is considered cubic as 1×1×1 m in the model regarding the mesh sensitivity analysis. To assign boundary conditions, the cut-off wall bases were considered fixed with zero displacement in three directions.

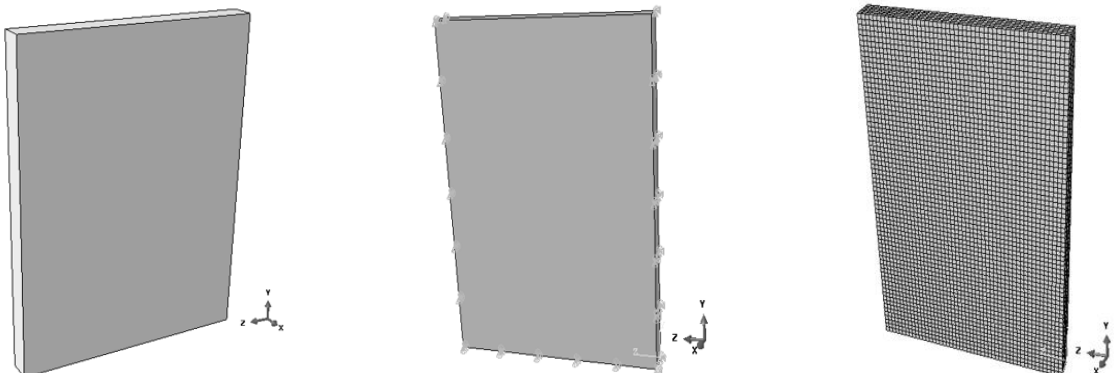

Figure 1: Geometry, mesh and boundary conditions.

To verify the numerical model, results of research by Ben Cardiou et al. on cylindrical and cubic samples of plain concrete and reinforced concrete with steel fibers and fiber content of 1%, 1.6% and 3% were used. Physical characterizes were used according Table 1 [15].

Table 1: Properties of steel fiber and concrete

	Portland cement of ASTM type I	**aggregate**	**silica fume**	**superplasticizer**	**steel fibers (length of 22 mm)**
Density (g/cm3)	3.15	2.65	2.2	1.15	7.85

The hydrostatic pressure load in collaboration with equal soil load on both sides of the cut-off wall which counterbalances each other were considered. The amount of applied load on the structure as a hydrostatic pressure is equivalent to a water pressure to an altitude of 50 m. Moreover, the cut-off wall with the same dimensions and the same volume of fiber was simulated under dynamic load of a recorded earthquake of Tabas as a significant earthquake. Using SAP software the 5% attenuation spectrum response was determined. After that, the response spectra were combined using a root sum square method. Moreover, a single combined spectrum was also constructed which was then compared at the next stage in the range of frequency times of 0.2T and 1.5T with the standardized design spectrum curve. The acceleration scale factor of the structure was found to be such that these mean values are by no less than 1.4 times the value of the standard spectrum. The terrain of Type II structure was assumed with a moderate relative risk and the main time of the fluctuations of the structure was considered to be equivalent to the structures with other systems [16].

$$T = 0.05H^{\frac{3}{4}}$$

$$B = 1 + S\left(\frac{T}{T_0}\right) \qquad 0 \le T \le T_0$$

$$B = S + 1 \qquad T_0 \le T \le T_s$$

$$B = (S+1)\left(\frac{T_s}{T}\right)^{\frac{2}{3}} \qquad T \ge T_s$$

where, B is the reflection coefficient of the structure represents the response of the structure to the motion of the earth, T is the time of the main frequency of the structure oscillation in seconds (s) and T_s and S are parameters that depend on the terrain and the seismicity of the region. The boundary conditions for this modeling are intended with the assumption that the wall at the bottom of its height Z = 0 is immersed in impermeable soil layers and is thus considered to be completely stuck. Boundary conditions for earthquake loading are intended as wall conditions in hydrostatic loading, and the loading is in the horizontal direction of the earthquake in x direction. The type of analysis for hydrostatic loading was selected in one step as dynamical implicit for nonlinear analysis of the structure, and the type of analysis in dynamic loading is considered as dynamic explicit analysis. The aim of this research is to provide a preliminary result including stress-strain behavior and displacement in a cut-off wall under dam. Because the area under the curve of the concrete with fiber volume of 1.6% and 3% is approximately equal, results of 3% and 1% fibers concretes are compared with plain concrete.

3. Results and Discussions

3.1 Under Hydrostatic Load

Since the loading conditions were symmetric in the y direction, evaluation of the results were conducted in the direction of the thickness and height of the cut-off wall (Figures 2 and 3). According to the Figure 2, it was observed that concrete with a 3% volume of fiber at the zero level, due to the greater length in the softening region, has the highest strain value in defining the materials and is 75% higher than that of plain concrete. Figure 3 shows that the total stress

in plain concrete and concrete with 1% volume of fiber at the level of 16.67 m is about 30% larger than concrete with 3% volume of fiber. Due to the smaller strength and modulus of elasticity, the materials behavior for 3% volume of fiber in concrete should have a smaller stress and a greater strain. Figures 4 and 5 show the stresses in x direction and deformations in z direction, respectively.

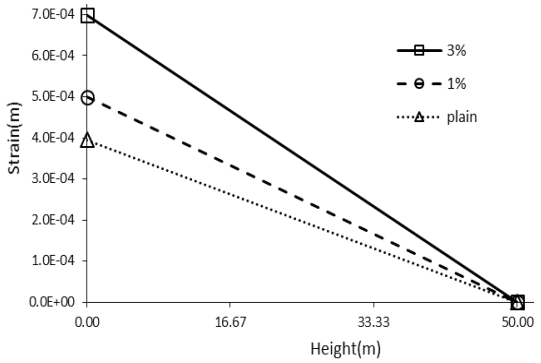

Figure 2: Comparison strains in z direction

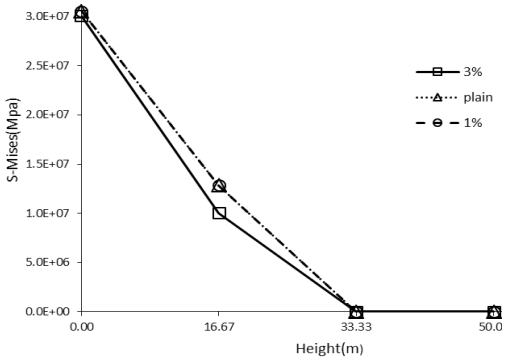

Figure 3: Comparison stresses in z direction

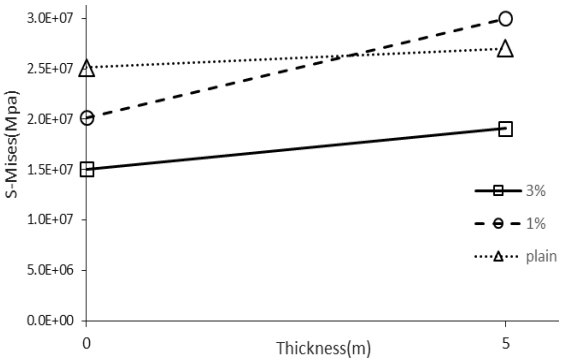

Figure 4: Comparison stresses in x direction

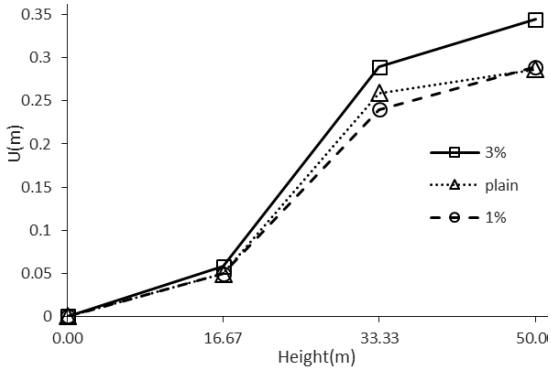

Figure 5: Comparison deformations in z

As can be seen from Figure 4, the minimum of stress is was occurred in concrete with 3% volume of fiber. In Figure 5 by comparing the deformations, concrete with 3% volume of fiber at the level of 50 m, had 19% more deformation compared to the plain concrete, which seems reasonable according to the small modulus of elasticity in concrete with 3% volume of fiber.

3.2 Under Earthquake Load

In the interpretation of the earthquake loading results, stress changes at height and in the direction of wall thickness were compared in Figures 6 and 7, respectively.

Figure 6 shows that the maximum stress in cut-off wall is related to the plain concrete at the level of 16.67 m, which is 66% more than the stress value in concrete with 1% volume of fiber. The behavior of the fiber concretes in the dynamic loading is softer than the plain concrete, and concrete with 1% volume of fiber, in spite of its compressive strength, is almost the same as the behavior of 3% concrete. Moreover, in direction of wall thickness, variations in stress are approximately equal. The strain and deformation changes are also compared to the height of the cut-off wall in Figures 8 and 9, respectively.

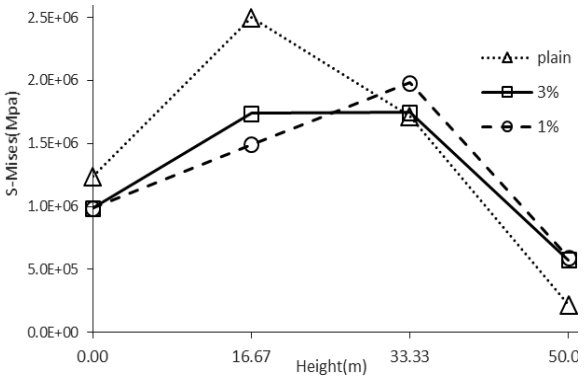

Figure 6: Comparison stresses in height

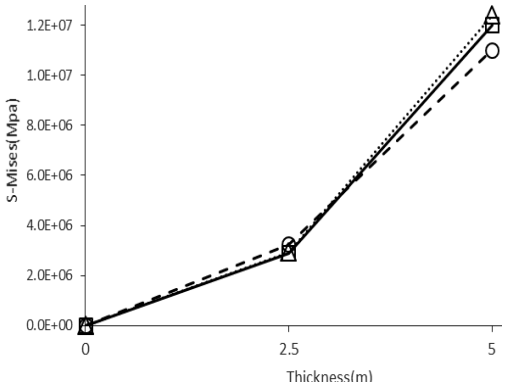

Figure 7: Comparison stresses in x direction

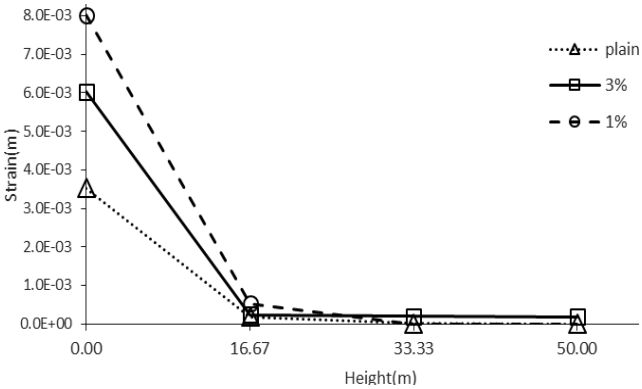

Figure 8: Comparison strains in z directions

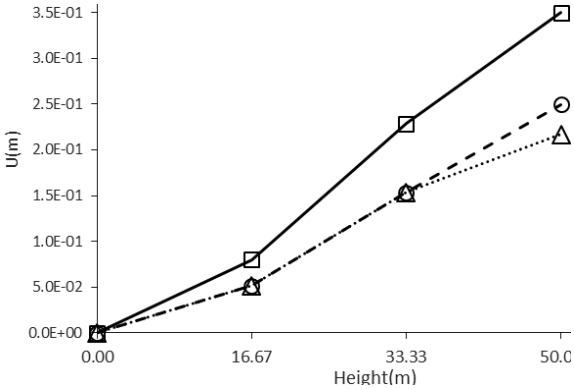

Figure 9: Comparison deformations in z

Figure 8 shows that the maximum value of the strain at the zero level is related to the concrete with 3% volume of fiber, which is different from the lowest value for the plain concrete of 128%. Figure 9 shows that concrete with 3% volume of fiber has the most deformation values, and only at the height of 50 m, the plain concrete has a deformation of 13% less than concrete with 1% volume of fiber.

Table 1: Amount of absorbed energy at the end of the analysis under earthquake loading.

Concrete type	**Plain**	**1%**	**3%**
The amount energy at the end of the analysis	0.1	0.25	0.5

The total energy related to the concrete cut-off wall with 3% volume of fiber is more in comparison with two other types and this means that the energy absorption to the structure in this type is larger than cut-off wall with plain concrete and 1% volume of fiber.

4. Summery and Conclusions

In this study, the concrete behavior of concrete cut-off wall was examined by adding different percentages of fiber to the total volume of materials under hydrostatic and earthquake loads. To do so, simulations were performed using the stress-strain curve obtained from the experimental results of Ben Cardiou et al. [14] for verification. Results of simulations of concrete cut-off wall with 1% and 3% volume of fiber show that the zero level of the wall, the minimum stress created in the structure related to the concrete with 3% volume of fiber,

which is about 30% less than the concrete cut-off wall with 1% volume of fiber and plain concrete. In the direction of wall thickness, the minimum stress value is related to the concrete cut-off wall with 3% volume of fiber. Maximum deformation was for concrete cut-off wall with 3% volume of fibers and 19% with the other two other types. Moreover, the energy absorption at the end of the analysis time, absorption of the energy in concrete cut-off wall with 3% volume of fibers was more in comparison to the concrete cut-off wall with 1% volume of fibers and plain concrete. Strength of concrete against crack increased by adding steel fibers but effect of steel fibers decreased with increasing friction. Maximum deformation and strain under earthquake load was occurred in concrete cut-off with 3% volume of fibers.

References

[1] Hosainy, E., Siosemarde, M. (2015). Seepage analysis in body and foundation of Sang Siah Dam using the Seep/W. Science Journal (CSJ), 36(4), 1697-1701.
[2] Da Silva, J. (2006). Optimization of concrete gravity dams foundation systems. 22nd International congress on large dams-ICOLD, 18 June, Barcelona, Spain.
[3] Soleymani, S., Akhtarpur, A. (2011). Seepage Analysis for Shurijeh Reservoir Dam Using Finite Element Method. Geo-Frontiers, 3227-3234.
[4] Qingyou, W., Wangong, S., Huan, X. (2008). Plastic Concrete Cutoff Wall. China Water Power Press.
[5] Nawy, G. (2000). Fundamentals of high performance concrete, New York: John wiley.
[6] Dupont, V.L. (2002). Bending capacity of steel fiber reinforced concrete (SFRC) beams, Proceeding of the international congress on challenges of concrete construction. P.81-90.
[7] Paine, KA., Elliott, KS., Peaston CH. (2002). Flexural toughness as a measure of shear stress strength and ductility of prestressed fiber reinforced concrete. University of Dundee.
[8] Olivito, RS., Zuccarello, FA. (2010). An experimental study on the tensile strength of steel fiber reinforced concrete, Composites Part B: Engineering, 41(3): 246-255.
[9] Johnston, C.D., Zemp, R.W. (1991). Flexural fatigue performance of steel fiber reinforced concrete-Influence of fiber content, aspect ratio, and type, ACI Materials J., 88(4): 374-83.
[10] Shahrabadi, H., Sayareh, S., Sarkardeh, H. (2017). Effect of natural zeolite-pozzolan on compressive strength of oil-polluted concrete marine structures, Civil Engineering Journal, 2(12): 623-636.
[11] Barkhordari Bafghi, M.A., Amini, F., Safaye Nikoo, H., Sarkardeh, H. (2017). Effect of Steel Fiber and Different Environments on Flexural Behavior of Reinforced Concrete Beams, Applied Sciences, 7(10): 1011.
[12] Shahrabadi, H., Sayareh, S., Sarkardeh, H. (2017). Effect of silica fume on compressive strength of oil-polluted concrete in different marine environments, China Ocean Engineering, 31(6): 716-723.
[13] Sarabi, S., Bakhshi, H., Sarkardeh, H., Safaye Nikoo, H. (2017). Thermal stress control using waste steel fibers in massive concretes, European Physical Journal Plus, 132(11):491
[14] Barkhordari Bafghi, M.A., Amini, F., Safaye Nikoo, H., Sarkardeh, H. (2018). Strength of Different Fiber Reinforced Concrete in Marine Environment, Materials Science, 24(2):204-211.
[15] Bencardino, F., Rizzuti, L., Spadea, G. (2008). Stress-strain behavior of steel fiber-reinforced concrete in compression, ASCE.
[16] Housing and Building Research Center (2010). Regulation Building Designs Against Earthquakes, Third Edition.

SynerCrete'18 International Conference on Interdisciplinary Approaches
for Cement-based Materials and Structural Concrete
24-26 October 2018, Funchal, Madeira Island, Portugal

PERFORMANCE OF RECYCLED AND COMMERCIAL FIBRE REINFORCED CONCRETE BEAMS IN COMBINED ACTION WITH CONVENTIONAL REINFORCEMENT

Katerina Bernhoft [(1)], Samindi Samarakoon [(1)], Luis Evangelista [(1)], Bjarne Mikalsen [(1)]

(1) University of Stavanger, Stavanger, Norway

Abstract

Reuse of recycled steel fibres recovered from tire recycling is a sustainable solution to contribute to the reduction of the waste disposal burden. In addition, commercially available steel fibres are widely used in the construction industry, especially mixed with concrete to enhance flexural strength, toughness, ductility and cracking resistance. Various researchers have found that there is an opportunity to replace commercially available steel fibres with recycled steel fibres from tire waste. However, there are few studies on the behavior of reinforced concrete beams with recycled fibres. Therefore, laboratory experiments have been carried out to study the behavior of reinforced concrete beams cast with recycled fibres and commercially available fibres, which comprise a fibre content of 0%, 0.5% and 1% by volume. The results indicate that the load versus the displacement behavior of the reinforced concrete beams with recycled fibres is similar to that for commercial fibres. Moreover, a numerical analysis was performed, using finite element tool, ATENA, to study the behavior of recycled fibre reinforced concrete, and to compare the performance with commercial steel fibre reinforced concrete. ATENA simulates real structural behavior, such as cracking, crushing and reinforcement yielding, by using non-linear finite element analysis. Moreover, the load-displacement diagrams computed in ATENA were compared to the experimental load-displacement diagrams.

1. Introduction

Used tires are considered the most challenging type of waste to handle, due to the huge quantity of production and their non-biodegradability. Currently, there is a trend towards innovative material recycling and sustainable buildings. The recycling of the used tire is one of the attractive solutions which results in three by-products: crumb rubber/rubber powder,

steel wires and fibre. The aforementioned steel wires have irregular shapes and variable lengths and are further processed into steel fibres. Many studies in the literature have proposed the use, in concrete, of granulated rubber and steel fibres recovered from waste tires [1-2]. Moreover, the addition of recycled steel fibres, instead of their commercially available steel counterparts, gave good post-cracking behavior [3]. However, few studies have been carried out to study the behavior of concrete beams reinforced with recycled steel fibres.
The behavior of concrete beams reinforced with steel fibres can be studied experimentally, as well as numerically, using software like ATENA [4]. Moreover, the numerical models are widely used to simulate/verify the structural performance of the beams, which are observed during experiments. Hence, this study focuses on the development of finite element models of the tested beams with different fibre contents and compares them with the experimental behavior.

2. Experimental testing of beams

Concrete beams reinforced with recycled fibres (RFRC) and commercially available fibres (SFRC) (i.e. fibre content: 0%, 0.5% and 1% by volume) have been tested using the four-point bending test, set up as shown in Fig. 1. The RFRC was supplied by Ragn-Sells Dackåtervinning AB, Sweden. The load vs. displacement behaviors from the experimental study [5, 6] are shown in Fig. 2, and the results are given in Tab. 1.

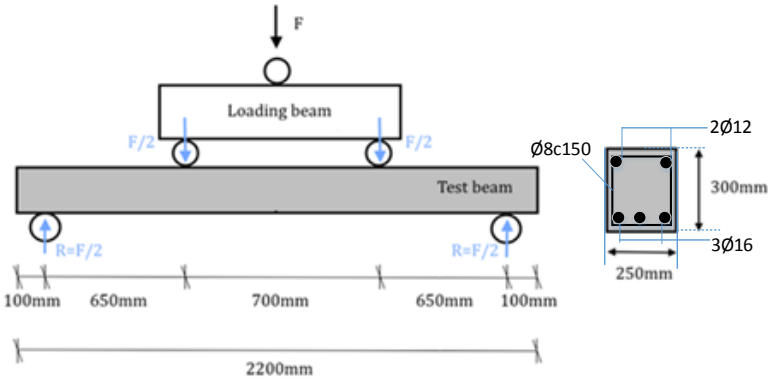

Figure 1: Test setup for four-point bending test [5].

Table 1: Results of the beam tests [6].

	0.0%	**0.5% RFRC**	**1.0% RFRC**	**0.5% SFRC**	**1.0% SFRC**
First peak load [kN]	236.1	228.0	237.8	248.4	243.4
Displacement at first peak load [mm]	10.1	11.7	11.3	11.4	12.7
Maximum load [kN]	251.20	245.3	238.4	259.6	251.5
Displacement at maximum load [mm]	29.6	36.6	13.3	21.8	20.3
Failure at displacement [mm]	≈54.7	≈84.8	≈91.6	76.9	97.7

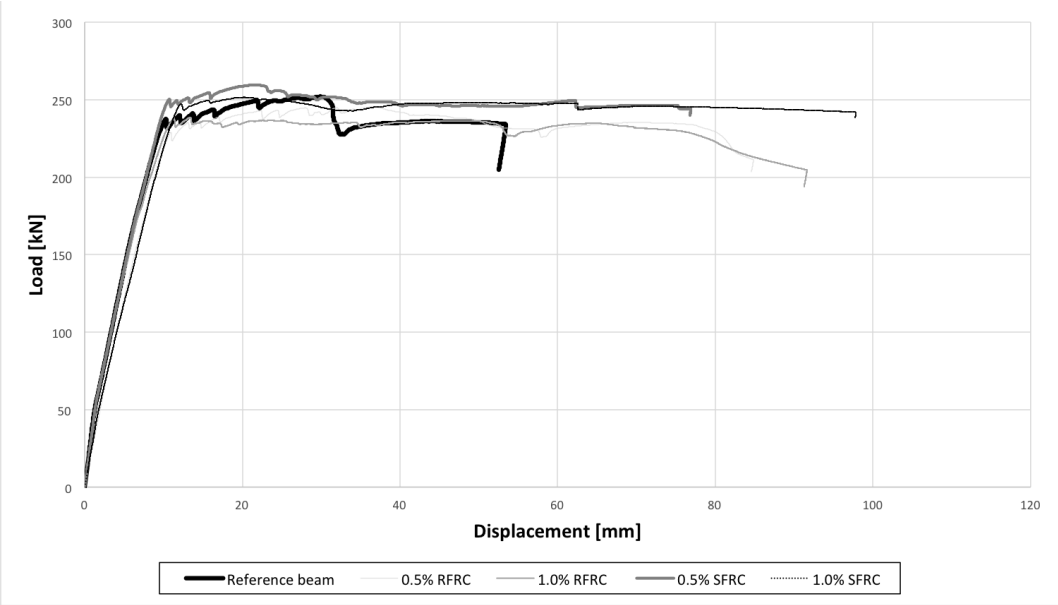

Figure 2: Load vs. displacement of reinforced concrete beams [6].

3. Numerical modeling of reinforced concrete beams with steel fibres

Numerical modeling and analysis were carried out using the software, ATENA and GiD. ATENA-GiD is a finite element-based software, specifically designed to analyze both plain and reinforced concrete structures. Basically, GiD is used for the data preparation and mesh generation, while ATENA is used for the analysis part itself. GiD is a general-purpose pre- and post-processing tool for a variety of numerical problems. ATENA can simulate real structural behavior, such as cracking, crushing and reinforcement yielding, by using non-linear finite element analysis (NFEA). Fracture mechanics and plasticity theories lay the foundation for the non-linear material models implemented in the software [4].

3.1 Modeling of the four-point bending test in ATENA

GiD is used to develop models of the four-point bending test shown in Fig. 1. The model is derived from the software manuals and theory documentation developed by Cervenka Consulting [4]. Since the beam is symmetric about its mid-point, only half of the 3D concrete beam is modeled in GiD. The beam is simply supported by steel roller bearings, in the physical experiments. To avoid local concrete crushing, the load is applied through steel plates of square cross-section of 1.5mm·1.5mm. Steel bars (3Ø16 and 2Ø12) are modeled as discrete elements, and stirrups (Ø8) are modeled as smeared. Quadratic hexahedral isoparametric elements are used, as well as 0.025m mesh size. The Newton-Raphson method is used as a solution method. Fig. 3 shows a geometric model of the beam.

The top surface of the beam is assigned a fixed contact surface to the top steel plate, and the bottom beam surface is assigned a fixed contact surface to the bottom steel support. Displacement-controlled analysis is used, by applying a prescribed vertical displacement at the middle point on top of the loading plate in constant increments of 0.001m. From the

experimental results [5], it has been found that the beams failed at deflection between 0.06 and 0.08m, as given in Tab. 1. The predefined displacement therefore has be multiplied approximately 80 times, to reach failure.

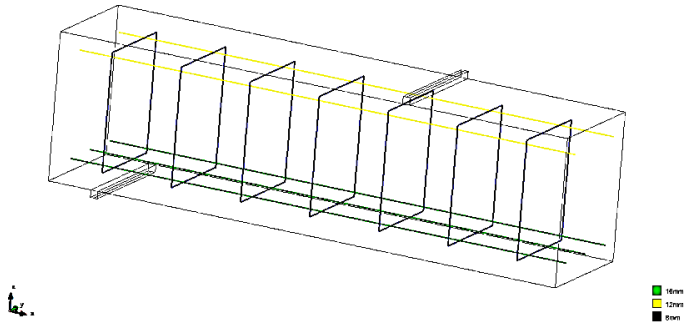

Figure 3: Geometric model of the beam.

3.2 Material models

The steel plates which are used as the support to the beam are modeled as an elastic and isotropic material, using SOLID Elastic material type given in ATENA, where Young's modulus is 200GPa and Poisson's ratio is 0.3. When modeling the reinforcement as discrete bars, the predefined material, Reinforcement from 1D Reinforcement, is selected. The characteristic yield strength of steel reinforcement and stirrups is taken as 500MPa, and E_s is 200GPa. Ultimate strain of steel is used as 7.5%. The bilinear material law is chosen for the steel bars. Moreover, there are several ATENA fracture–plastic constitutive models given in the manual for structural concrete. In this study, the material model, CC3DNonLinCementitious, is used. To input the properties of fibre-reinforced concrete to the material model given in ATENA, the mechanical properties were found experimentally. For example, the average value of compressive strength, modulus of elasticity, splitting tensile strength, and fracture energy (using the wedge splitting test) were found experimentally [5, 6] and are given in Tab. 2. Poisson's ratio of concrete is chosen as 0.2.

Table 2: Input values for the material model for concrete from experimental findings.

Fibre content	**0%**	**0.5% RFRC**	**1% RFRC**	**0.5% SFRC**	**1% SFRC**
Modulus of elasticity (GPa)	25.45	26.7	25	26.7	26.6
Compressive strength (MPa)	29.2	30.6	32.9	34.3	35.1
Splitting tensile strength (MPa)	2.18	2.58	2.49	2.87	2.97
Fracture energy (N/m)	132	592	1096	2616	1726

4. Comparison of results from ATENA and experimental testing

4.1 Reference beam (0% fibres)

To determine the best fit curve for the load vs. displacement behavior of the experimental results, variables, such as different methods of input of shrinkage strain and influence of

dowel action, are considered. In this study, the dowel effect of lower longitudinal reinforcement is taken into account, as well as shrinkage, which is applied as initial strain to the concrete volume by recommended value of $-5.5 \cdot 10^{-5}$[4]. Furthermore, the crack pattern and crack widths are also taken into consideration when determining the best fit curve. Moreover, the reinforcement is monitored to make sure no rupture occurs in the bars before failure is reached. Based on the best fit model, the first peak for the ATENA models is reached earlier than that of the experimental test for the both mesh size; 0.025m and 0.05m. There is a difference in the maximum loads of about 8% (232kN/252kN) for the mesh size; 0.025m.

4.2 Reinforced concrete beams with different fibre contents

When modeling recycled fibres recovered from tire waste, Young's modulus is used as 200GPa, and average yield strength is estimated from laboratory testing as 870 MPa. According to the ATENA Theory manual, the fibres can be represented in the material model by simply increasing the fracture energy of the concrete or fibres is to define them as smeared reinforcement, pointing in six different directions, i.e. three in the principal axes and three in the middle of the octants.

In the case of increasing the fracture energy of the concrete, a higher peak load is predicted for the ATENA model, with 7.6% relative difference of peak loads for the beam with 0.5% RFRC. Moreover, when representing the fibres with smeared reinforcement, the ATENA model predicts a greater capacity of the beam, i.e. a 9.6% difference in maximum loads, as shown in Fig. 4. Similar analysis is performed for the beam with 1% RFRC, and the difference in maximum loads is found to be about 4%.

As regards the beams with 0.5 % SFRC, the difference between the maximum loads for the ATENA model and the experimental beam is about 1%. For the beams with 1% SFRC, the ATENA model with smeared fibres is somewhat overestimated, with the difference in maximum loads between the experimental results and the model with smeared fibres being about 5%.

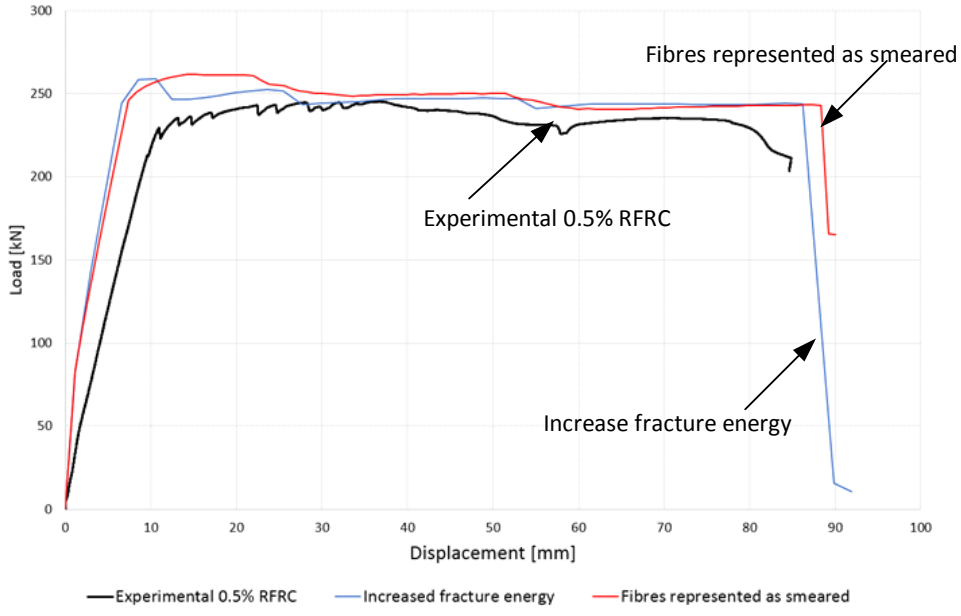

Figure 4: Load-displacement diagram for beam containing 0.5% recycled steel fibres.

5. Discussion and Conclusions

This paper studies the behavior of concrete reinforced with recycled fibre and compares the structural performance of concrete reinforced with commercial steel fibre. It mainly focuses on the load vs. displacement behavior of beams with different fibre content. During the study, the load vs. displacement diagrams using ATENA were compared to the experimental load-displacement diagrams. An equivalent performance of the recycled steel fibres compared to commercially available steel fibres can only be found in the loading phase before yielding of the conventional reinforcement. Moreover, a 1% – 9.6% difference in the maximum load in the load vs. displacement behavior has been found. However, the results were very dependent on the parameters adjusted to create load-displacement diagrams, e.g. representing the fibres as smeared or by simply increasing the specific fracture energy. It should also be noted that several simplifications and assumptions were made along the way, which may also have influenced the results.

References

[1] Aiello, et al, Use of steel fibres recovered from waste tyres as reinforcement in concrete: Pull-out behavior, compressive and flexural strength, Waste Manage, 29 (2009), 1960-1970
[2] Bignozzi, M. C. and Sandrolini, F., Tyre rubber waste recycling in self-compacting concrete, Cem Conc Res, 36 (2006), 735-739
[3] Centonze, M. L. and Aiello, M. A., Steel fibres from waste tires as reinforcement in concrete: A mechanical characterization, Constr Build Mater, 36 (2012), 46-57
[4] Červenka, V., Jendele, L. and Červenka, J., (2016). ATENA Program Documentation Part 1: Theory. Retrieved from http://www.cervenka.cz/assets/files/atena-pdf/ATENA_Theory.pdf
[5] Bernhoft, K., Numerical modelling of recycled fibre reinforced concrete beams and comparison with experimental findings, Master thesis, University of Stavanger, Norway (2017)
[6] Hovind, P. R., Pedersen, J. W. and Mikalsen, B., Behaviour of recycled tyre fibre reinforced concrete, Bachelor thesis, University of Stavanger, Norway (2107)

SynerCrete'18 International Conference on Interdisciplinary Approaches
for Cement-based Materials and Structural Concrete
24-26 October 2018, Funchal, Madeira Island, Portugal

PROBABILISTIC NUMERICAL MODEL FOR DESIGNING STEEL FIBRE REINFORCED CONCRETE STRUCTURES

Pierre Rossi [(1)], Jean-Louis Tailhan [(1)]

(1) Paris-Est University, IFSTTAR/MAST, France

Abstract
This paper enumerates the reasons that motivate the use of finite elements simulations for the design of SFRC structures for the analysis of their cracking behaviour. Those reasons are mainly the consequences of the irrelevancy of the actual design recommendation to take into account adequately some loading conditions of SFRC structures.
The mean criteria to be respected for a relevant numerical model of cracking behaviour of SFRC are also proposed.
Finally, an example of these relevant models is presented with its validation.

1. Introduction

Steel fiber reinforced concrete (SFRC) is increasingly used in structural applications. One of the principal reasons of its gain in popularity is due to the existence of national and international recommendations for the design of structures using this type of material.
These recommendations are efficient for designing simply supported structural elements subjected to bending. However, they do not possess a sufficient physical base to propose relevant solutions for more complex structures such as statically indeterminate or for others types of failure modes such as beam shear and pushing-shear. In certain cases, the proposed methods are too conservative and lead to an over consumption of material, which is not good in the frame of sustainable development. In some other cases, the non-homogeneity of SFRC properties is not considered adequately which could lead to overestimate the strength provided by SFRC.
In addition, cracking control in serviceability limit state is one of the main interests of using SFRC. Crack control is very important for durability aspects, and is certainly an advantage of SFRC compared to structures using traditional reinforcement bars.

Nowadays, existing design recommendations are not able to give enough relevant information regarding cracking in serviceability limit state (cracks openings and spacing). Hence, the most efficient approach for designing structures with respect to both safety and sustainable development is to use finite element analysis.
IFSTTAR, formerly known as LCPC, has been developing and using numerical models in order to achieve this objective.
In order for SFRC to be fully accepted in industrial applications, a cracking model has to be relevant to:

- determine the cracks opening, especially in the service state situation;
- analyze the non-linear behaviour of concrete structures under loadings as shear and punching and of statically indeterminate concrete structures.

2. Numerical Modelling of the SFRC Tensile Cracking Process

IFSTTAR has been developing a probabilistic discrete cracking model to simulate the cracking process of concrete 1987 [1]. In this model, cracking is explicitly treated through the creation of random kinematic discontinuities, which provides access to quantitative information on the cracking state (number of cracks, opening and spacing). Numerically speaking, these cracks are represented by interface elements.
The criterion for the crack creation is very simple: the interface element opens when the normal tensile stress at the centre of the interface element reaches a critical value. This critical value is probabilized through a Weibull distribution function [2]. This means that the rigidity of the interface element becomes equal to zero (perfect brittle behaviour). The value of this critical value depends on the total volume of the two volumetric elements interfaced by the considered interface element.
After the crack creation, which only depends on the cement matrix, the influence of the fibres has to be taken into account. The following modelling approach is considered:

- Normal and tangential stresses in the interface element linearly increase with normal and tangential displacements when a "broken" interface element re-opens to take into account the elastic effect of the fibres inside the crack. Physically speaking, the rigidity of the fibres (inside the cracks) is more important in tension than in shear. Thus, the interface element rigidity is considered different for normal and tangential displacements. In 2D, normal and tangential rigidities of the interface element are K_n' and K_t' respectively. The post-cracking elastic behaviour exists until it reaches a limit, δ_0, related to the normal displacement. Once this limit value is reached, the mechanical behaviour of the interface element changes. As a matter of fact, the normal stress is considered as ***linearly decreasing*** with the normal displacement in order to take into account the damage of the bond between the concrete and the fibre. The decreasing evolution is obtained by a damage model.
  Finally, the interface element is considered definitively broken and its rigidity (normal and tangential rigidities) is equal to zero when the normal displacement occurring during the damage step reaches a critical value, δ_C. This value corresponds to the state where the effect of fibres is considered negligible.

- The post-cracking total energy dissipated during the linear increase and followed by the linear decrease of the normal stress is considered randomly distributed on the mesh elements as for the material tensile strength. The random distribution is a log-normal distribution function with a mean value independent of the mesh elements size and a standard deviation increasing with the decrease in the mesh elements size, which is physically logical. In practice, to model a given structure, the distribution function is determined in the following manner:

    - The mean value is directly obtained by uniaxial tensile tests on notched specimens. It has been previously shown [3] that this mean value is not affected by scale effects.
    - The standard deviation, which depends on material volume tested and so of the mesh elements size, is determined by an inverse analysis approach that consists of simulating the uniaxial tests with different element mesh sizes.

Remark
It is also required to know the values related to δ_0 and δ_C to perform numerical simulation with the above model. δ_C is directly obtained by the uniaxial tensile tests and δ_0 is obtained by the inverse analysis approach assuming that it is a mesh independent parameter.

The numerical mechanical behaviour adopted for the post-cracking step is illustrated in Figure 1. Only the normal stress - normal displacement curve is considered in this figure.
To conclude this part about the adopted numerical modelling approach, it can be said that it is considered a deterministic approach with probabilized parameters. Hence, it is necessary to perform a large number of computations to statistically validate the results following a Monte Carlo method.

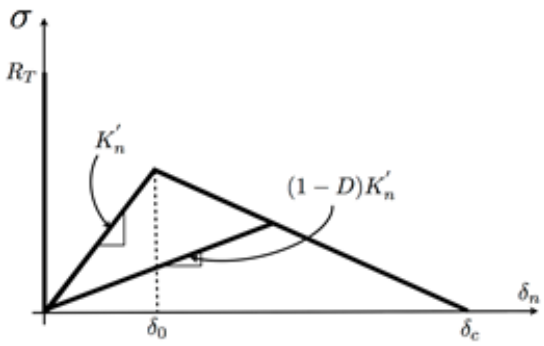

Figure 1: Modelling of the post-cracking behaviour

3. Numerical Simulations of the shear behaviour of a large SFRC beam

The shear behaviour of a large reinforced beam [4] was analyzed by using the above numerical model. This beam contained traditional rebars for the bending strength and only steel fibres as shear reinforcement. The beam was designed to fail in shear.
The beam geometry, its reinforcement, the boundary conditions, and the test apparatus are presented in Figure 2. A normal-strength SFRC containing 100 kg/m^3 of steel fibres with a length of 30 mm and a diameter of 0.5 mm was used. Its compressive strength was 40 MPa.

Uniaxial tension tests on notched cylindrical specimens were performed to evaluate its tensile behaviour (and to determine all the values of the model parameters). These specimens had a diameter of 120 mm and a height of 100 mm, with a 2 mm width and a 20 mm depth circumferential notch.
Two types of measurement were recorded during the shear test:

- evolution of the beam deflection,
- shear crack openings and evolution by using stereophotogrammetry technique.

A single beam was tested during this experimental study.

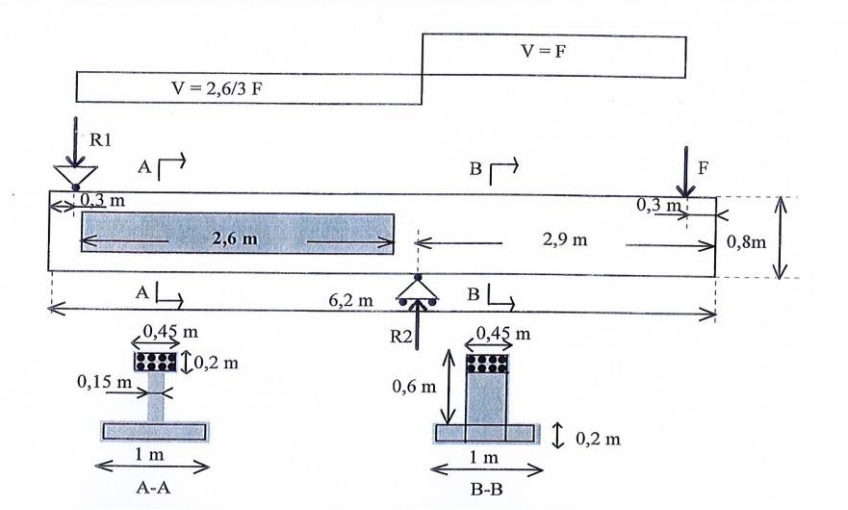

Figure 2: Beam geometry and test set-up

The finite element mesh and the boundary conditions are presented in Figure 3.

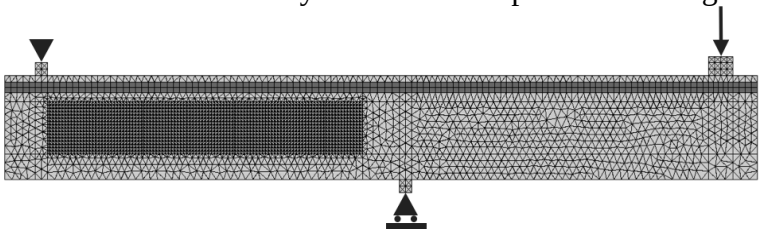

Figure 3: Mesh of the beam and boundary/loading conditions.

The values of the model parameters used in the numerical simulations of the beam behaviour were the followings:

- Means tensile strength: **4.5 MPa**
- Standard deviation: **0.7**
- Mean post-cracking energy: **3.25 MPa.mm**
- Standard deviation of the post-cracking energy: **1.18 MPa.mm**
- δ_0 = **100 µm**
- δ_C = **3 mm**

Figure 4 shows the global responses (load - displacement) of the numerical simulations and the experimental test. It can be noticed that the numerical mean curve is very close to the experimental one. Moreover, the experimental response is clearly located in the scattering of the set of the numerical responses.

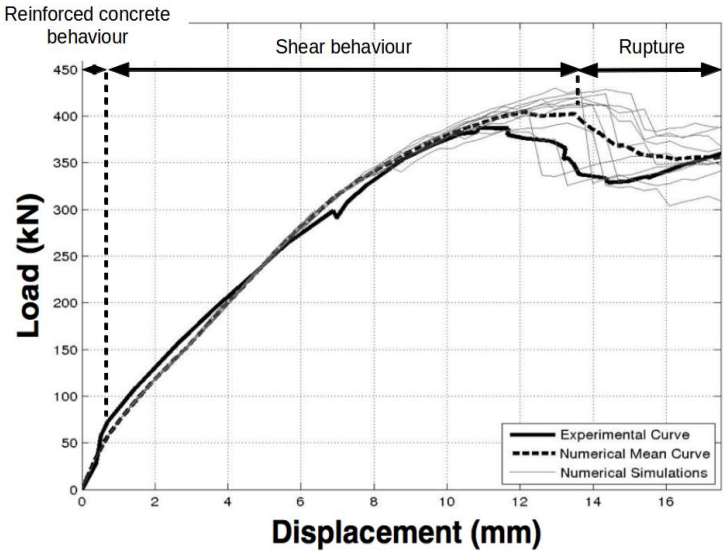

Figure 4: Comparison between simulations and experiment: load vs. deflection curve.

An example of a numerical crack pattern can be observed in Figure 5. On this same figure, the numerical crack pattern is compared to the experimental one at the peak load.
Numerical values of crack openings were computed and were found to be comparable in magnitude with the experimental values. Furthermore, numerical and experimental cracks at a loading step just before the peak load exhibit openings of about 1 mm (see Figure 5).

4. Conclusions

This paper enumerates the reasons that motivate the use of finite elements simulations for the design of SFRC structures for the analysis of their cracking behaviour.
These reasons are mainly the consequences of the irrelevancy of the actual design recommendation to take into account adequately some of the technical problems such as:

- the evaluation of the crack openings in SFRC structures under serviceability loads;
- the analysis of the non-linear behaviour of SFRC structures under complex loadings.

In this paper, the mean criteria to be respected for a relevant numerical model of cracking behaviour of SFRC, is also proposed.
Finally, an example of these relevant models with its validation in the frame of the shear behaviour of a large beam is presented.

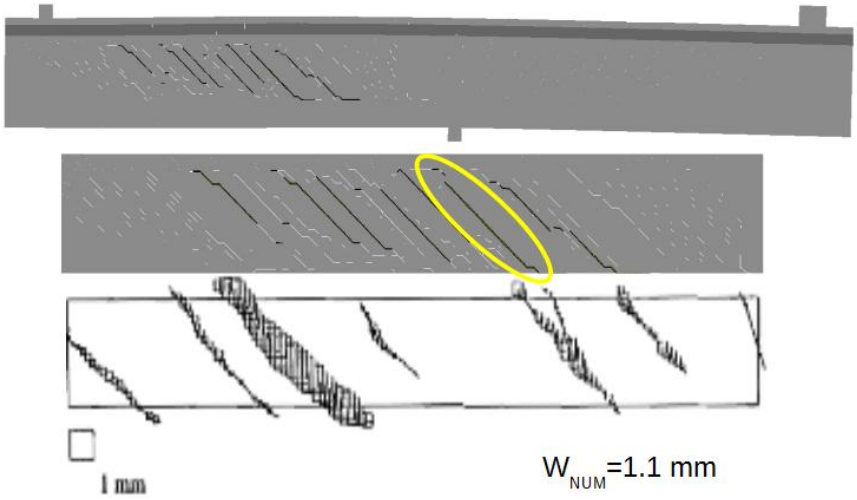

Figure 5: Example of crack pattern at the peak load

References

[1] Rossi, P. and Richer S., Numerical modelling of concrete cracking based on a stochastic approach, Materials and Structures, vol. 20 (1987), 334-337.

[2] Tailhan J.L., Dal Pont S. and Rossi P., From local to global probabilistic modelling of concrete cracking, Ann. Solid. Struct. Mech., vol. 1 (2010), 103-115.

[3] Rossi, P., Experimental study of scaling effect related to post-cracking behaviours of Metal Fibres Reinforced Concretes, European Journal of Environmental and Civil Engineering, Vol.16(10) (2012), 1261-1268.

[4] Casanova, P. and Rossi P., Can steel fibers replace transverse reinforcements in reinforced concrete beams, ACI Materials Journal, vol. 94, n°5 (1997), 341-354.

SynerCrete'18 International Conference on Interdisciplinary Approaches
for Cement-based Materials and Structural Concrete
24-26 October 2018, Funchal, Madeira Island, Portugal

RHEOLOGICAL BEHAVIOUR OF FLEXIBLE FIBER-REINFORCED CEMENTITIOUS MATERIALS

Fariza Sultangaliyeva [(1)], Hélène Carré [(1)], Christian La Borderie [(1)], Nicolas Roussel [(2)]

(1) Université de Pau et Pays de l'Adour, Anglet, France
(2) Navier Laboratory, IFSTTAR, Champs-sur-Marne, France

Abstract
Polypropylene fibers are accepted in many studies as an effective preventative measure against concrete spalling due to fire exposure. A high dosage of the fibers enhances this effect but reduces the flowability of fresh concrete. Due to a lack of literature, it is hard to identify optimal fiber dosage and geometry. This paper is aimed at understanding the influence of polypropylene fibers on the rheology of fresh cementitious materials. Slump flow tests that ensure an isotropic flow of the material are conducted in order to assess the yield stress of cement pastes containing flexible fibers. The results present the influence of fiber dosage and geometry (fiber length and diameter) on the yield stress of fresh cementitious materials. Using predictive scheme for the yield stress of the cementitious materials with rigid fibers, it is seen that the rheology of cement pastes with flexible fibers is more complex compared to the rheology of paste with rigid fibers.

1. Introduction

Numerous studies have been conducted by researchers presenting a positive effect of polypropylene fibers for a reduction of concrete spalling risk due to fire [1], [2]. Higher dosage reinforces this effect but leads to the loss of concrete's workability [3]. In order to reach a compromise between fire resistance and fluidity, it is essential to identify an optimal fiber dosage and geometry. Current state of knowledge concerning the influence of flexible fibers on the rheology of fresh cementitious materials is not sufficient to respond to this question. This paper is aimed at understanding the effect of flexible fibers on the rheology of fresh concrete. Initially, we study the influence of fiber dosage and geometry on the yield stress of cement paste. Then, using prediction for the yield stress of cementitious materials

with rigid fibers, we prove the complexity of the rheology of flexible fiber reinforced cementitious composite.

2. Influence of rigid inclusions on the yield stress

The biphasic approach used for describing the rheology of fresh concrete suggests that concrete is composed of a continuous phase of the suspending fluid (a cement paste assumed to be homogeneous) and a dispersed phase (the inclusions such as sand, gravel and fibers) [4]. Using the extrapolation for Krieger-Dougherty relation for apparent viscosity [5], the yield stress of concrete can be presented as the function of the yield stress of the suspending fluid and the function of the volume fraction of its inclusions [4]:

$$\tau_0^c \approx \tau_0^p f\left(\frac{\phi}{\phi_m}\right) \tag{1}$$

where τ_0^c is the yield stress of concrete, τ_0^p is the yield stress of cement paste, ϕ is the volume fraction of the inclusions, ϕ_m is the dense packing fraction of the inclusions. Packing regimes may influence the interactions of rigid inclusions in the suspending fluid. Change in the interactions, consequently, leads to the change in the yield stress of the material. We therefore need to define different packing regimes. A comprehensive explanation of various packing regimes based on spherical inclusions is given in [4]. It is important to note here that dense packing fraction is characterized by direct contacts between the inclusions. These contacts are a dominant force in the material flow.

3. Rheology of cementitious materials with rigid fibers

3.1 Distinction between flexible and rigid fibers

At high dosage of fibers, direct contacts between fibers provoke significant dissipation of the energy leading to the increase of the yield stress and the decrease of the workability of fresh cementitious material [4]. Since packing of the inclusions influences the interactions and, consequently, the yield stress, we should be able to define it for both rigid and flexible fibers. We expect different packing tendencies for flexible and rigid fibers. Rigid fibers are prone to change a granular skeleton thanks to their rigidity they can move the aggregates that are relatively large compared to fiber length and increase the void space. To compare, flexible fibers tend to bend around aggregates and to occupy the empty spaces between them [6].
In order to distinguish flexible fibers from rigid ones, the rigidity criterion for the fibers in cementious materials was developed by Martinie et al. [4]. She has identified that the order of the deflection of fibers is estimated as:

$$\frac{f}{L} \cong \frac{\tau_0}{E} R^3 \tag{2}$$

where f is the deflection, L is the length of the fiber, τ_0 is the yield stress of the fresh cementitious material, E is Young's modulus of fiber, R is the aspect ratio (the ratio between

the length and the diameter of the fiber). Depending on the properties of the fiber and the nature of the suspending fluid, different flexure responses can be obtained. For example, in case of steel fibers with an aspect ratio of 50, the Young's modulus of 210 GPa in SCC mix (the yield stress of approximately 50 Pa) this value is around 0.003 %, whereas for carbon fibers of the aspect ratio of 500 and the Young's modulus of 190 GPa in regular concrete mix (the yield stress of 1000 Pa), the magnitude of deflection is around 66% [4].

3.2 Dense packing fraction of rigid fibers

We are interested in evaluating dense packing fraction of rigid fibers. Dense packing fraction of rigid fibers was determined experimentally in [4] from the measurements of the apparent volume occupied by fibers before vibration Ω_{before} and after vibration Ω_{after} of the known mass of fibers. Using Philipse's approach for slender bodies with a range of aspect ratios between 50 and 100 [7], a relation between dense packing fraction ϕ_m and aspect ratio R for rigid fibers was determined as:

$$\phi_m = \frac{4}{R} \tag{3}$$

In case of rigid fibers, it is possible to measure dense packing fraction as their flexure in air is comparable to the flexure in cement paste (less than 1%). In case of flexible fibers, dense packing fraction cannot be measured directly due to the fact that their flexure depends on the nature of the suspending medium.

3.3 Yield stress prediction

Yield stress of rigid fiber reinforced cement paste can be predicted as a function of the relative packing fraction of fibers. The yield stress evolves as a function of ϕ/ϕ_m equal to $\phi R/4$ [4]. This means that for the yield stress prediction in case of rigid fibers two parameters are sufficient: fiber volume fraction ϕ and aspect ratio R. Returning back to flexible fibers, we have stated that dense packing fraction is impossible to measure experimentally. Nevertheless, we shall still verify whether the evolution of the yield stress of cementitious material with flexible fibers could be described using framework for rigid fibers, i.e. the yield stress should evolve a function of relative packing fraction ϕR.

4. Rheology of cementitious materials with flexible fibers

4.1 Materials and experimental procedure

All cement pastes for experiments were prepared using Portland cement CEM I 52.5 N Brest. Cement paste with w/c = 0.5 is tested using nine different geometries of fibers at various fiber dosages (0 %, 0.25 %, 0.5 %, 1 %, 2 % and 3 % vol. of cement paste). Tested fiber geometries are presented in Table 1.

Cement is mixed with water by rotating mixer for 2 minutes. It is then left for rest during 20 minutes and remixed again for 2 minutes. The fibers are added and mixed by hand for 2 minutes. The sample is then tested using slump flow test described in [6]. For each dosage and geometry, a new sample is prepared. Samples that presented any signs of instability were not taken into account.

Table 1: Tested fiber geometries.

Aspect ratio, R	Length, L (mm)	Diameter, D (μm)
176	6	34
188	6	32
300	6	20
333	6	18
353	12	34
400	6	15
529	18	34
588	20	34
706	24	34

4.2 Experimental results

The results were obtained from the slump flow test on cement pastes with nine various fiber geometries tested at different dosage. We present our experimental results in terms of the relative yield stress (a ratio of the yield stress of cement paste with fibers and cement paste without fibers) in order to study the influence of fibers as rigid inclusions.

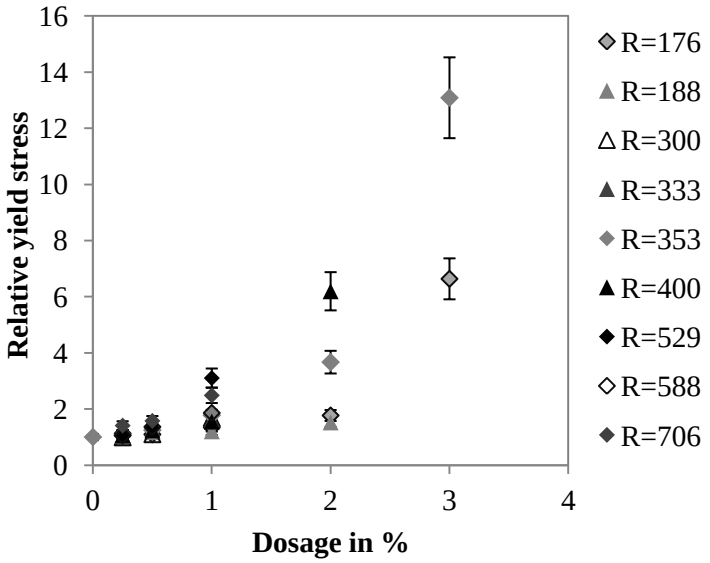

Figure 1: Relative yield stress as a function of fiber dosage. Triangles: fibers of the same length L = 6 mm, rhombus: fibers of the same diameter D = 34 μm.

In Fig.1 the relative yield stress of fresh cement pastes with fibers is plotted as a function of the dosage of fibers. The error bar of 11% is found by repeating the experiment five times on the fibers with an aspect ratio R = 353 (L = 12 mm, D = 34 μm) at 1 % vol. of fibers. This value is assumed as an error for all the results presented here.

4.3 Discussion

The relative yield stress is presented in Fig.1 as a function of fiber dosage for different fiber geometries. As expected, the relative yield stress increases with the increase of fiber dosage. It could be suggested that after a certain critical fiber concentration direct frictions appear and the relative yield stress increases rapidly as seen in Fig.1. In terms of geometry influence, it can be seen that the yield stress does not increase proportionally to aspect ratio of fibers. We plot Fig. 2.a and Fig 2.b in order to study the effect of the length and the diameter of fibers on the relative yield stress accordingly. We observe that the increase of the length of fibers appears to lead to the increase of the yield stress. Even though it seems that fibers with L = 12 mm may have the highest yield stress values, there is insufficient data for longer fibers (18, 20 and 24 mm) due to the instability of the mix. In Fig 2.b we observe that fiber diameter increase, on the contrary, leads to the decrease of the yield stress.

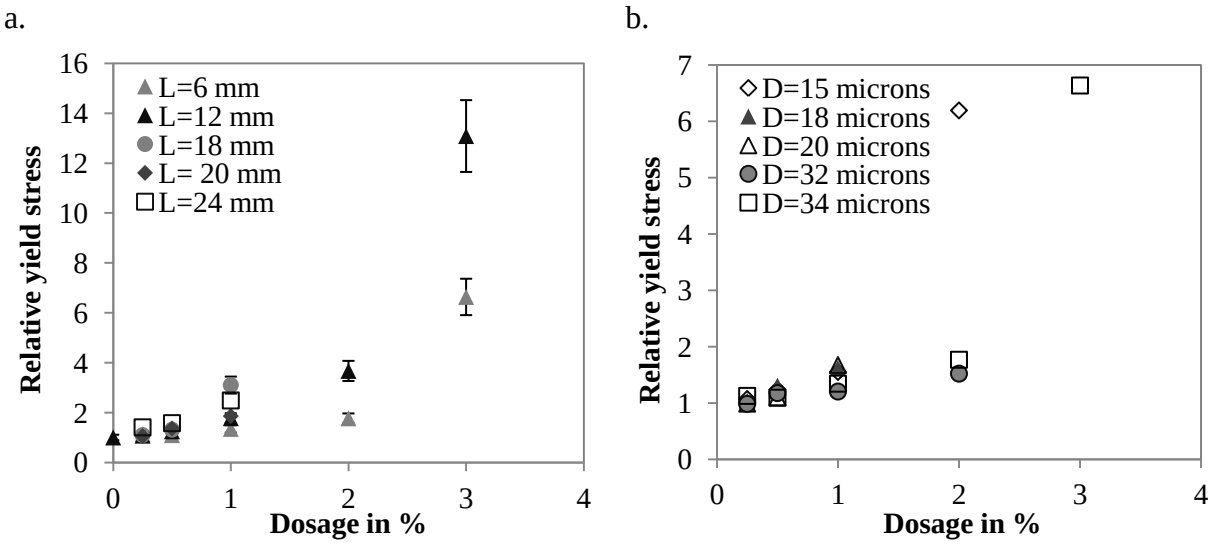

Figure 2: Relative yield stress as a function of fiber dosage. a. Fibers with D =34 μm and L=6, 12, 18, 20 and 24 mm. b. Fibers with L=6 mm and D=15, 18, 20, 32 and 34 μm.

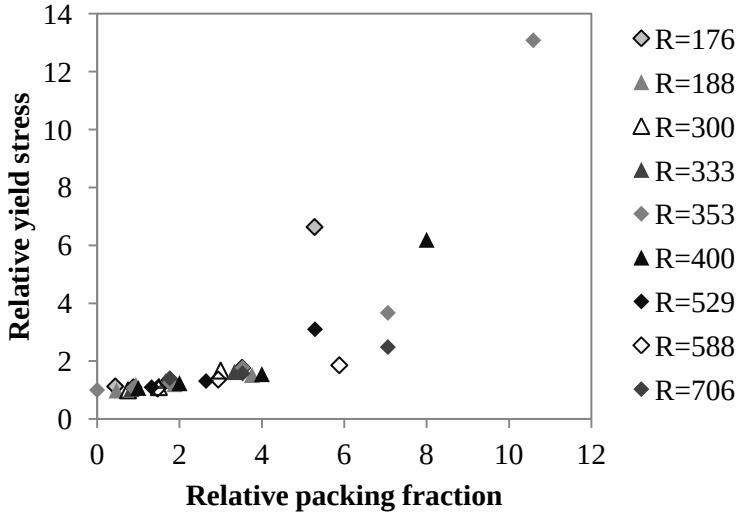

Figure 3: Relative yield stress as a function of relative packing fraction ϕR for rigid fibers.

In this part we verify whether we can predict the yield stress of the fresh cementitious materials with flexible fibers based on the existing scheme for material with rigid fibers. In Fig. 3 we have plotted our results of the Fig. 1 using the predictive scheme for rigid fibers described in Section 3.3. It can be seen that the scheme is valid at low dosages of fibers when the yield stress of the material with fibers is dictated by the yield stress of the cement paste. With an increase of fiber dosage, after formation of a connected network, direct frictional contacts start to be dominant in the system. Therefore, it is logical to observe that data is more scattered with an increase of fiber dosage. From the analysis using predictive scheme for the yield stress of rigid fiber reinforced materials we can conclude that the influence of the flexible fibers is far more complex than that of rigid fibers due to their bending.

5. Conclusions

The aim of this work was to study the impact of flexible fibers on the rheology of the fiber reinforced cementitious materials. In order to accomplish this, slump flow tests were conducted on fresh cement pastes containing polypropylene fibers of various geometries at different dosage. The influence of fiber dosage and geometry was presented and analyzed. From the results, it was possible to conclude that the rheology of flexible fiber reinforced material cannot be characterized the same way as the rheology of rigid fiber reinforced

Acknowledgements
This work is carried out using the financial assistance from the program of the Investments for the Future of the French government managed by ANDRA.

References

[1] Shuttleworth, P., Fire protection of precast concrete tunnel linings on the Channel Tunnel Rail Link, Concrete 35(2001), 12-22
[2] Bilodeau, A., Kodur, V.K.R. and Hoff, G.C., Optimization of the type and amount of polypropylene fibres for preventing the spalling of lightweight concrete subjected to hydrocarbon fire, Cement and Concrete Composites 26 (2004), 163-174
[3] Szwabowski, J. and Ponikiewski,T., Rheological properties of fresh concrete with polypropylene fibres, Proceedings from the 3rd International Conference on Concrete and Concrete Structures, Slovakia (2002), 331-338
[4] Martinie, L., Rossi, P. and Roussel, N., Rheology of fiber reinforced cementitious materials: classification and prediction, Cem Concr Res 40 (2010), 226-234
[5] Krieger, I.M. and Dougherty, T.J., A mechanism for non-Newtonian flow in suspensions of rigid spheres, Trans.Soc.Rheol. 3(1959), 137-152
[6] Roussel, N., Understanding the rheology of concrete, UK (2011)
[7] Philipse, A.P., The random contact equation and its implication for (colloidal) rods in packings, suspensions and anisotropic powders, Langmuir 12 (1996), 1127-1133

SynerCrete'18 International Conference on Interdisciplinary Approaches
for Cement-based Materials and Structural Concrete
24-26 October 2018, Funchal, Madeira Island, Portugal

STRAIN HARDENING CHARACTERISTICS OF BLENDED ALKALI ACTIVATED BINDERS CURED AT AMBIENT TEMPERATURES

M. Talha Junaid [(1)], Mohamed Maalej [(1)]

(1) Department of Civil and Environmental Engineering, University of Sharjah, UAE

Abstract

Micro fibers are extensively used to reduce the brittle response of concrete and alkali activated matrix in tension and flexure. Such composites, if designed correctly, can offer stain hardening characteristics both in flexure and axial tension, which are characterized by large deformations, multiple cracking and high energy absorption during loading. This study looks at characterizing the strain hardening properties of ambient cured alkali activated binders during direct tension and flexural tests at 7 and 28 days. Three-point bending test was performed for flexural evaluation while direct tension test with dog-bone samples were performed to evaluate the axial tensile behavior. A combination of sodium silicate and sodium hydroxide is used to activate a blend of Fly ash and slag to form binders. A high aspect ratio polyethylene (PE) fiber was used in this study. Strength and ductility properties of all samples improved with age of the matrix. The results indicate that the introduction of fibers induced strain hardening response in all samples during flexure and direct tension tests. The load deflection response was significantly improved with high deformations and multiple cracking observed in all tested samples. A significant increase in the flexural toughness for all samples was also witnessed. The results indicate that highly ductile strain hardening alkali activated composites can be obtained at ambient temperatures without the need for heat curing, with properties comparable to both OPC based and heat cured alkali activated composites.

1. Introduction

The brittle response of concrete is of major concern in structural engineering applications. One way of reducing this brittle behavior is the introduction of short discrete fibers, which may be metallic or non-metallic. Practical dosage of fibers varies by volume and has been reported to reduce the brittle response of such composites [1, 2]. Nevertheless, the use of macro fibers in case of fiber reinforced concrete (FRC) results in a quasi-brittle response with increased fracture toughness. More recently over the past few decades the use of micro fibers

has been reported for the development of cementitious composites commonly referred to as engineered cementitious composites (ECC). Such material is characterized by multiple cracking and strain hardening properties. Despite the advantages, such composites utilize a large amount of cement per unit volume thus are deemed unsustainable with a relatively large environmental footprint. To reduce the environmental footprint, alternate binders have been used in the recent past to develop strain hardening composites. Among these is the use of alkali activated binder or geopolymer, which have come to the forefront as an alternate binder to ordinary Portland cement. Alkali activated binders are formed when an alumina and silica-rich source material is activated with a strong metallic alkaline. The source material is usually fly-ash (class F or C), naturally occurring clays, and furnace slag from the production of metals. Generally, sodium, potassium and calcium hydroxides or silicates, or a combination of these is used as activator solutions. Such binders are highly sustainable and cost-effective, since they are manufactured from industrial waste materials. Researchers have found that such binders could be a possible replacement of conventional concrete [3-10]. Past studies [1, 11] on strain hardening alkali activated binders have used extrusion and/or heat curing methods resulting in limited practical applicability for such composites.

In the current work, the alkali activated binder was made using a combination of Class F Fly Ash (FA) and ground granular blast furnace slag (GGBFS) and activated with a combination of sodium hydroxide and sodium silicate solutions. A high aspect ratio polyethylene (PE) fiber in 1.5% by volume was used. The current research aims at studying the flexural and direct tensile behavior of ambient cured alkali activated engineered cementitious composites (AAECC). This works reports on the deflection hardening and multiple cracking behavior of such composites.

2. Materials

Commercially available fly ash class-F and ground granular blast furnace slag (GGBFS) was used in equal proportion as a binder for making the matrix. 10 molar sodium hydroxide solution was prepared by dissolving sodium hydroxide pallets with tap water 24 hours prior using. An extra pure sodium silicate solution was used with chemical compositions of 27.2% SiO_2, 8% Na_2O, and 64.8% water. The sodium hydroxide to sodium silicate ratio was kept constant at 1.0. The mix proportions of the composite are shown in Table 1. The Polyethylene (PE) Fiber had a dia of 38 μm and length of 12.7mm with an elastic modulus of 120 GPa. The fiber tensile strength and density were 2700 MPa and 0.98 g/cm^3, respectively.

Table 1: Mix proportions of the AAECC

NaOH(10M/12M): Sodium Silicate	FA: GGBFS	Fiber Volume
1:1	1:1	1.0%; 1.5% and 2.0%

3. Methodology

Rectangular beam samples were used for flexural testing, while dog-boned samples were used for direct tensile tests. Beam samples has a 25mm by 55mm cross-section and a length of

300mm and a clear span of 250mm. The dog bone sample dimension are shown in Figure 1. All beam specimens were tested under three-point bending static test at a loading rate of 1.5mm/min. The loading rate for the dog-bone sample was 1.5mm/min up to first cracking and then increased to 3mm/min thereafter up to failure. The test setup for the flexural and direct tension test are shown in Fig. 1.

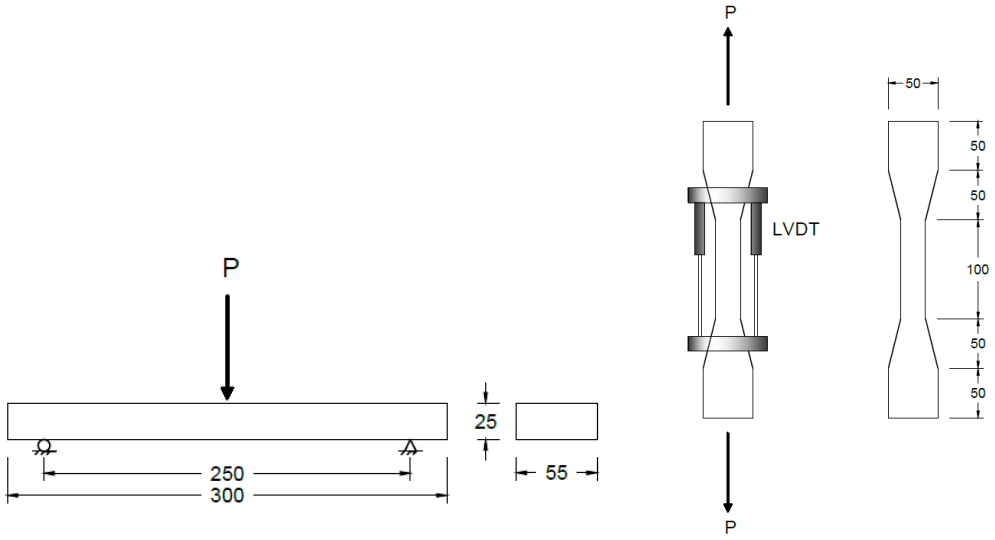

Figure 1: Test set up and sample details (dimensions are in mm)

4. Results and Discussion

The flexural response of the samples made using 10 and 12 M sodium hydroxide solutions at 7 and 28 days is given in Figure 2, while the characteristic properties of these curves are given in Table 2. LOP is the limit of proportionality while, MOR is the modulus of rupture which is defined as the maximum stress after LOP. As per ASTM C1609 the point L/600 and L/150 are defined when the deflection is equal to these values. Since the span of the samples is 250mm these deflection values are 0.417mm and 1.667mm respectively. Other values are defined as; d5 when the deflection is 3 times deflection at LOP, d10 when the deflection is 5.5 times deflection at LOP and d20 when the deflection is 10.5 times deflection at LOP. The toughness, found using the area under the load-deflection curve, at all these key points is also calculated and tabulated in Table 2. As is evident from the results presented in Figure 2, the 7 day behavior for the 10 and 12M specimen is very similar with both samples exhibiting substantial strain hardening response. The toughness properties of these samples is also similar as can be seen from Table 2. At 28 days, the 10M sample gained slight strength as compared to the 7 day samples, while the post peak behavior of this sample exhibited lesser strain softening as compared to samples at 7 days. However, the 28 day response for the 12M sample is much different from all other samples. This sample not only showed increase in LOP and MOR values as well as substantial increase in the toughness at all points of interest, but also had a much better deflection hardening response. This can be attributed to the fact that with time the 12M hydroxide solution was able to form a much denser and stronger binder, resulting in better bond properties between the fibers and the matrix. This enhanced matrix and bond resulted in a more efficient composite.

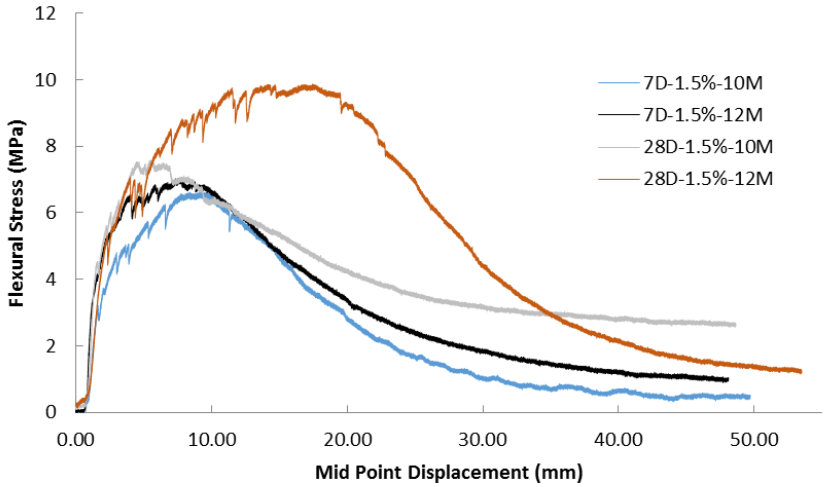

Figure 2: Flexural Response of AAECC with varying Hydroxide Molarity and Time

Figure 3 shows the flexural response of the samples with 1, 1.5 and 2% fiber content at 7 and 28 days for the AAECC with 12M hydroxide solution. As expected, the samples with higher fiber content exhibit better performance in terms of strength and deflection. Also the performance of the samples increased with age of the samples with samples with 2% fiber at 28 days exhibiting the highest strength and a very pronounced deflection hardening response.

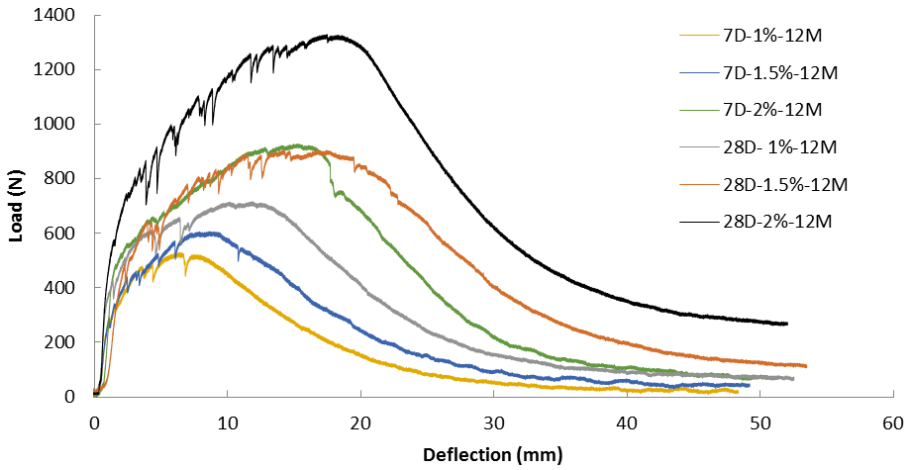

Figure 3: P-Delta curves for AAECC samples with varying fiber content at different age.

The direct tension test results for dog bone samples on 10M samples containing 1.5% fiber by volume at 7 and 28 days is presented in Figure 4. These samples exhibit multiple cracking with significant strain hardening response after first crack with the 28 day sample having a better performance due to increased strength of the matrix, which also positively effects the bond between the matrix and the fiber.

Table 2: Response Quantities of AAECC

Property	**7D-1.5%-R1-10M**	**28D-1.5%-R1-10M**	**7D-1.5%-R1-12M**	**28D-1.5%-R1-12M**
P_{LOP}	286.2 N	409.8 N	328.2 N	459.9 N
δ_{LOP}	1.58 mm	1.49 mm	1.28 mm	2.12 mm
f_{LOP}	3.12 MPa	4.4 MPa	3.58 MPa	5.04 MPa
$Tough_{LOP}$	0.09 N.m	0.215 N.m	0.121 N.m	0.36 N.m
P_{d5}	497.4 N	683.7 N	591.9 N	729.3 N
δ_{d5}	4.74 mm	4.47 mm	3.84 mm	6.36 mm
f_{d5}	5.43 MPa	7.46 MPa	6.46 MPa	7.98 MPa
$Tough_{d5}$	1.38 N.m	1.87 N.m	1.37 N.m	2.92 N.m
P_{d10}	593.7 N	641.7 N	629.4 N	854.4 N
δ_{d10}	8.69 mm	8.195 mm	7.04 mm	11.66 mm
f_{d10}	6.48 MPa	7.0 MPa	6.87 MPa	9.41 MPa
$Tough_{d10}$	3.58 N.m	4.35 N.m	3.28 N.m	7.22 N.m
P_{d20}	363.6 N	478.8 N	493.5 N	746.1 N
δ_{d20}	16.59 mm	15.65 mm	13.44 mm	22.26 mm
f_{d20}	3.97 MPa	5.22 MPa	5.38 MPa	8.16 MPa
$Tough_{d20}$	7.55 N.m	8.45 N.m	7.04 N.m	16.38 N.m
$P_{L/600}$	8.4 N	18.9 N	6.3 N	35.4 N
$\delta_{L/600}$	0.417 mm	0.417 mm	0.417 mm	0.417 mm
$f_{L/600}$	0.1 MPa	0.21 MPa	0.07 MPa	0.39 MPa
$Tough_{L/600}$	0.02 N.m	0.05 N.m	0.01 N.m	0.02 N.m
P_{MOR}	606.3 N	694.2 N	644.1 N	904.8 N
δ_{MOR}	8.4 mm	5.46 mm	7.34 mm	17.43 mm
f_{MOR}	6.61 MPa	7.57 MPa	7.03 MPa	9.8 MPa
$Tough_{MOR}$	3.41 N.m	2.53 N.m	3.47 N.m	12.29 N.m
$P_{L/150}$	259.2 N	388.8 N	393 N	338.1 N
$\delta_{L/150}$	1.667 mm	1.667 mm	1.667 mm	1.667 mm
$f_{L/150}$	2.83 MPa	4.24 MPa	4.29 MPa	3.76 MPa
$Tough_{L/150}$	0.12 N.m	0.29 N.m	0.27 N.m	0.18 N.m

5. Summary and Conclusion

An experimental program was conducted to report on the performance of ambient cured alkali activated engineered cementitious composites in flexure and direct tension. Different dosage of fibers, alkaline activator concentration and curing time were studied as variables and their effect on the response of AAECC was studied. It was found that such composite undergo strain hardening and might be a feasible alternate to ordinary cement based ECC. Based on the current study the following conclusions can be drawn:

- Ambient cured alkali activated engineered cementitious composites offer a viable option for such composite materials and has properties comparable to OPC composites.
- Age of the sample and dosage of fiber have a positive effect on the strength and deformation characteristics of such composites.

- Increasing the molarity of the sodium hydroxide solution does not significantly affect the response at early age, but has a substantial affect at a later age of the sample.
- Bond between the matrix and fiber plays a very important role in the performance of such composites and increasing this bond can substantially enhance the strength and deflection response of AAECC.

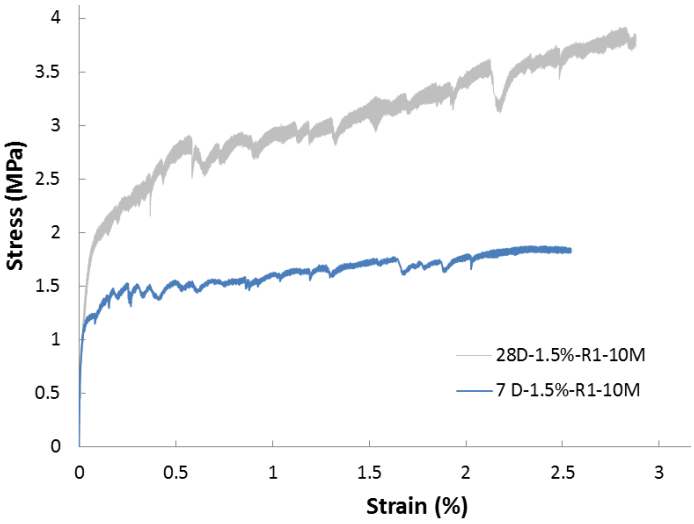

Figure 4: Direct Tensile Response of AAECC at 7 and 28 days

Acknowledgement
The authors appreciate the support provided by the Sustainable Construction Materials and Structural Systems (SCMASS) group at the University of Sharjah. Help provided by Abdallah Elbana is also highly appreciated.

References

[1] SherifEl-Tawil, D.j.A.E.N., Comparative flexural behavior of four fiber reinforced cementitious composites. Cement and Concrete Composites, 2008. 30(10).
[2] Li, M.M.V.C., Flexural/Tensile-Strength Ratio in Engineered Cementitious Composites. Journal of Materials in Civil Engineering, 1994. 6(4).
[3] Elbana, A., Evaluation of flexural behavior of reinforced concrete beams with glass fiber reinforced polymer (GFRP) bars, in Department of Civil and Environmental Engineering2018, University of Sharjah: University of Sharjah. p. 108.
[4] Junaid, M.T., et al., Aspects of the deformational behaviour of alkali activated fly ash concrete at elevated temperatures. Cement and Concrete Research, 2014. 60: p. 24-29.
[5] Junaid, M.T., et al., A mix design procedure for low calcium alkali activated fly ash-based concretes. Construction and Building Materials, 2015. 79: p. 301-310.
[6] Davidovits, J. and J.L. Sawyer, Early high-strength mineral polymer, 1985, Google Patents.
[7] Davidovits, J., Geopolymer cement. A review. Geopolymer Institute, Technical papers, 2013.
[8] Provis, J. and J. van Deventer, Alkali Activated Materials State-of-the-Art Report, J. Provis and J.S.J. van Deventer, Editors. 2014, RILEM.
[9] Junaid, M.T., A. Khennane, and O. Kayali, Stress-Strain Behaviour of Alkali Activated Fly Ash Concrete at Elevated Temperatures, in 2nd International Conference on Advances in Cement and Concrete Technology in Africa2016: Tanzania. p. 301-308.
[10] Rangan, B., Fly ash-based geopolymer concrete. Your Building Administrator, 2008. 2.
[11] F.U.A.Shaikh, Deflection hardening behaviour of short fibre reinforced fly ash based geopolymer composites. Materials & Design, 2013. 50.

SynerCrete'18 International Conference on Interdisciplinary Approaches
for Cement-based Materials and Structural Concrete
24-26 October 2018, Funchal, Madeira Island, Portugal

STRAIN RATE EFFECT ON THE TENSILE BEHAVIOUR OF ULTRA-HIGH PERFORMANCE STEEL FIBER REINFORCED CONCRETE

Veronika Goglin [(1)], Götz Hüsken [(1)], Hans-Carsten Kühne [(1)], H.J.H. Brouwers [(2)]

(1) Bundesanstalt für Materialforschung und -prüfung (BAM), Berlin, Germany
(2) Eindhoven University of Technology, Eindhoven, The Netherlands

Abstract

For the design and application of concrete structures exposed to high-dynamic loading scenarios, e.g. caused by vehicular impact or seismic events, profound knowledge on the rate sensitive changes in the material behaviour is necessary. Based on its ductile behaviour under tensile loading, ultra-high performance steel fiber reinforced concrete (UHPFC) is a suitable material when it comes to high-dynamic mechanical impacts. Therefore, this research investigated experimentally the strain rate effect on the mechanical behaviour of UHPFC under direct tensile loading. The uniaxial tensile tests were performed on small sized dumbbell shaped specimens at different strain rates, ranging from quasi-static to seismic loading conditions of up to 0.5 1/s. Material parameters of single and hybrid steel fiber reinforced UHPFCs were evaluated regarding first and post cracking stresses, strain capacity, as well as energy absorption capacity. The strain rate effect was expressed by the dynamic increase factor (DIF), describing the ratio between dynamic and quasi-static response.

1. Introduction

The strain rate effect on the mechanical response of conventional concrete under tension has been investigated by numerous authors and methods [1-4]. It is assumed that the strain rate dependent increase of the ultimate stress, the elastic modulus, and the peak strain is caused by two different physical mechanisms [5]. These mechanisms comprise the dependence of the rate of crack opening during the fracture process, and the dependence of the viscoelastic deformation of the unfractured cement matrix, respectively [5]. Nevertheless, structures made of conventional concrete or high-strength concrete have a limited protective effect against high-dynamic loading due to its brittle material failure in tension. Based on its improved mechanical properties regarding strength, stiffness and energy absorption capacity, ultra-high

performance steel fiber reinforced concrete (UHPFC) represents an important material advance in the field of protective construction materials [6]. A summary of previously published studies on the influences of the volume fraction and shape of steel fibers on fiber reinforced concrete subjected to dynamic loading can be found in the review of Soufeiani, L. et al. [7]. They concluded that the behaviour of steel fiber reinforced concrete under blast and impact is still insufficient understood as a consequence of limited research in both numerical and experimental.
The objective of this study is to obtain further experimental information on the strain rate sensitive changes of the mechanical response of single and hybrid reinforced UHPFC mixtures under direct tensile loading. The strain rates considered ranged from 0.000025 1/s to 0.5 1/s, representing quasi-static and seismic loading rates, respectively. To compose a consistent experimental data-base, relevant material parameters, such as first and post-cracking stresses, strain capacity, energy absorption capacity, as well as the dynamic increase factor (DIF) were determined and will be discussed.

2. Experimental program

An experimental program was designed to investigate the stress-strain response of two UHPFC mixtures at three different strain rates. The following sections will give a brief description of the materials, mixtures and the test setup.

2.1 Materials and mixtures

The base mix proportions of the plain ultra-high performance concretes (UHPCs) are given in Tab. 1. Single and hybrid reinforcements of the UHPFCs were realized by the addition of normal and high-strength smooth steel fibers, respectively. Tab. 2 summarizes the fiber properties, including fiber diameter, fiber length, length-to-diameter ratio, as well as the tensile strength. The fiber volume fractions for both tested UHPFC mixtures F02_Dx and F02_BlDx were set to two percent, in which the total number of fiber per unit volume increases with a decrease in length-to-diameter ratio. The single reinforced F02_Dx mixture incorporated 100 % Dx fibers, whereas the hybrid reinforced F02_BlDx mixture was composed of 75 % Bl fibers and 25 % Dx fibers, respectively.

Table 1: UHPC base mix proportions in (kg/m³).

CEM I 42.5 R-HS/NA	CEM I 52.5 R LA SR	Micro-silica	Meta-kaolin	Basalt 0.125/2.0	Basalt 2.0/5.0	Water	Super-plasticizer
625	125	37.5	75	916.7	550	180	20.25

Table 2: Properties of steel fiber Bl and Dx.

Notation	Diameter d_f (mm)	Length l_f (mm)	l_f/d_f (-)	Tensile strength (MPa)
Bl	0.30	20	67	> 1200
Dx	0.20	13	65	> 2600

2.2 Test-setup

The direct tensile tests were conducted displacement controlled using a servo hydraulic and a universal testing machine, respectively. The tests were performed on small sized dumbbell shaped specimens at an age of 56 days or older. The geometry of the specimens (cross-section 20x40 mm; gauge length 100 mm) was designed according to the suggestions of Mechtcherine, V. and Schulze, J. [8]. In order to facilitate stable and even crack growth throughout the cross-section, rigid specimen-to-machine connections were generated. For vertical displacement measurements, linear variable differential transformers (LVDTs) were used. A more detailed description of the test-setup can be found in [9]. Three nominal strain rates of 0.000025 1/s, 0.01 1/s, and 0.5 1/s were applied to the corresponding testing series. At least three specimens were tested for each strain rate and UHPFC mixture, resulting in a testing matrix of two mixtures, three specimens, and three loading rates.

3. Experimental outcomes

Four material parameters, including the first cracking stress σ_{cc}, the post cracking stress σ_{pc}, the strain capacity ε_{pc} at post cracking stress, and the energy absorption capacity g_{tc} were evaluated in this study. The first cracking stress is defined as the turning point between elastic and plastic parts, whereas the post cracking stress represents the peak stress within the strain hardening phase. The energy absorption capacity is obtained by integrating the stress versus strain curve up to ε_{tc}, with ε_{tc} describing the point of transition to consistent softening behaviour (Eq. 1 and Eq. 2). Fig. 1 shows a typical interpretation of the generated test results.

$$\sigma(\varepsilon_{tc}) = \sigma_{tc} = \frac{1}{10 - \varepsilon_{pc}} \cdot \int_{\varepsilon_{pc}}^{10} \sigma(\varepsilon)\, d\varepsilon \tag{1}$$

$$g_{\mathrm{tc}} = \int_{0}^{\varepsilon_{tc}} \sigma(\varepsilon)\, d\varepsilon \tag{2}$$

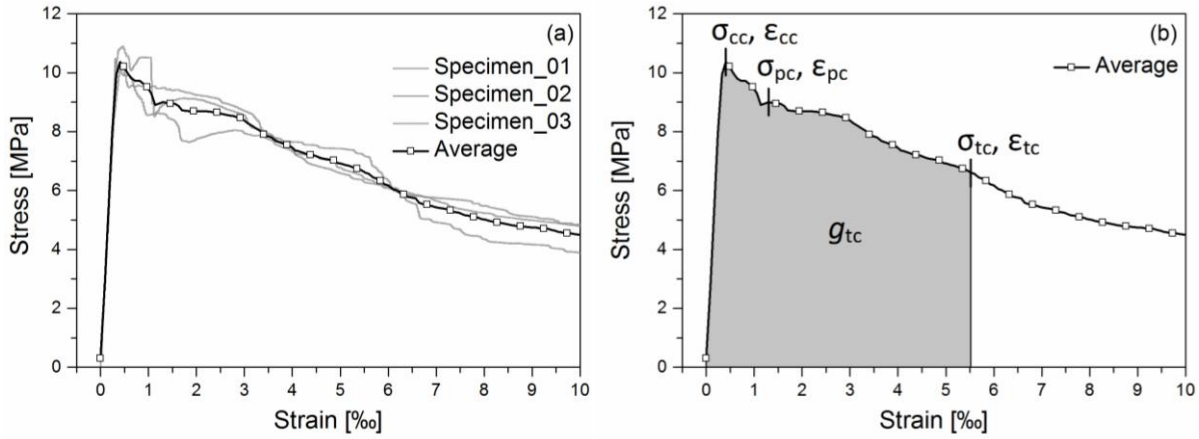

Figure 1: Interpretation of stress-strain results: (a) averaging of the stress-strain curves, (b) material parameters obtained from the averaged stress-strain curve.

3.1 Strain rate effect

Fig. 2 shows the average direct tensile stress versus strain relationship of a single and a hybrid steel fiber reinforced UHPFC subjected to nominal strain rate of 0.000025 1/s, 0.01 1/s, and 0.5 1/s. Corresponding material parameters are summarized in Tab. 3. All given values in Tab. 3 are averaged values from at least three specimens. In general, specimen-to-specimen variability within each tested strain rate was relatively low, although a slightly greater variability was registered at quasi-static testing conditions. The strain rate effect was expressed by the dynamic increase factor (DIF), describing the ratio between dynamic and quasi-static material response. The DIF values are also given in Tab. 3.

An increase in the strain rate led general to an increase of the first cracking stress and associated first cracking strain, although the hybrid fiber reinforced F02_BlDx showed a higher rate sensitivity of first cracking stress than the single reinforced F02_Dx mixture. The first cracking stress of mixture F02_BlDx increased by 54 % at a strain rate of 0.01 1/s and 48 % at a strain rate of 0.5 1/s, whereas the first cracking stress of mixture F02_Dx increased by 32 % for both applied dynamic strain rates. A consistent strain rate dependent increase in post cracking stress was only obtained by the hybrid fiber reinforced F02_BlDx mixture, exhibiting a value of 9.52 MPa at a strain rate of 0.01 1/s and a value of 10.02 MPa at a strain rate of 0.5 1/s. The single fiber reinforced F02_Dx mixture revealed a slight decrease in post cracking stress from 7.82 MPa to 7.01 MPa as the strain rate changed from 0.000025 1/s to 0.01 1/s, even though a value of 9.43 MPa was reached at a strain rate of 0.5 1/s. In contrast to the strain rate effect on the post cracking stress, mixture F02_Dx exhibited a significant strain rate sensitive behaviour for strain capacity which in particular doubled when the strain rate was set to dynamic loading conditions. Mixture F02_BlDx revealed a negligible strain rate effect on strain capacity. For both tested mixtures, not only first cracking stress generally increase as the strain rate increase from quasi-static to seismic loading conditions, but also the energy absorption capacity. The energy absorption capacity of mixture F02_Dx increased from 29.83 kJ/m³ to 34.20 kJ/m³ to 49.01 kJ/m³ as the strain rate increased, resulting in DIF values of 1.15 and 1.64, respectively. Mixture F02_BlDx displayed an energy absorption capacity of 23.01 kJ/m³ at 0.000025 1/s, 44.94 kJ/m³ at 0.01 1/s, and 37.89 kJ/m³ at 0.5 1/s, respectively. Corresponding DIFs were calculated to 1.95 at 0.01 1/s and 1.65 1/s at 0.5 1/s.

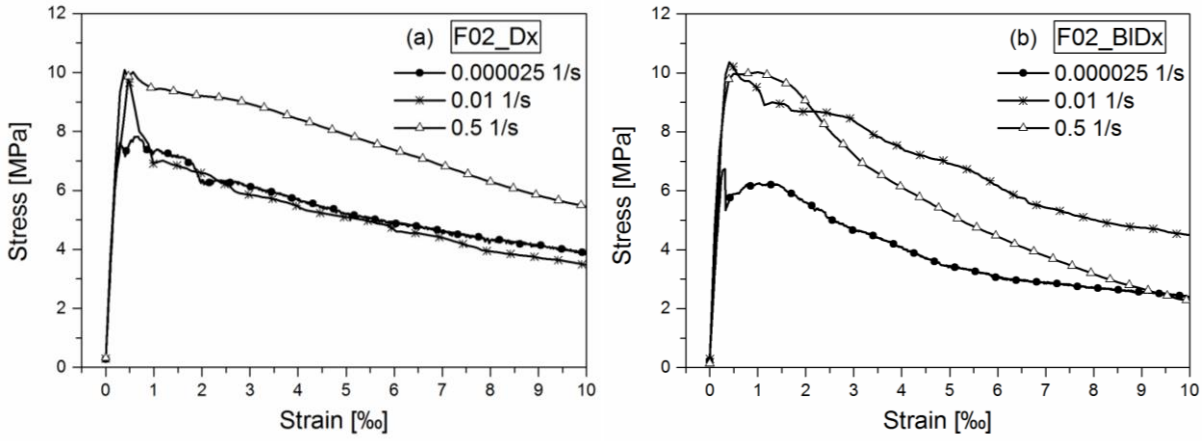

Figure 2: Strain rate effect on the tensile response of single and hybrid reinforced UHPFCs.

Table 3: Average tensile parameters of UHPFC mixtures tested at different strain rates.

Notation	**Strain rate (1/s)**	**First cracking stress σ_{cc} (MPa)**	**DIF (-)**	**Post cracking stress σ_{cc} (MPa)**	**DIF (-)**	**Strain capacity ε_{pc} (‰)**	**DIF (-)**	**Energy absorption capacity g_{tc} (kJ/m³)**	**DIF (-)**
F02_Dx	0.000025	7.62	1.00	7.82	1.00	0.60	1.00	29.83	1.00
	0.01	10.08	1.32	7.01	0.90	1.19	1.98	34.20	1.15
	0.5	10.02	1.32	9.43	1.21	1.22	2.03	49.01	1.64
F02_BlDx	0.000025	6.73	1.00	6.26	1.00	1.03	1.00	23.01	1.00
	0.01	10.36	1.54	9.52	1.44	1.29	1.25	44.94	1.95
	0.5	9.97	1.48	10.02	1.60	0.99	0.96	37.89	1.65

Overall, the single fiber reinforced mixture F02_Dx showed typical strain rate affected behaviour, revealing a log-linear relationship of DIF values. Comparable DIF trends for UHPFC mixtures incorporating two volume percent of high-strength smooth steel fibers were reported by Xu, M. and Wille, K. [10] for moderate strain rates. However, the hybrid fiber reinforced mixture F02_BlDx displayed relative high strain rate sensitivity for all obtained material parameters except the strain capacity, although the increase in DIF values was inconsistent. The high strain rate sensitivity of mixture F02_BlDx might be attributed to the higher fiber-matrix bond of the incorporated long fibers. Furthermore, it can be generally assumed that the embedded fibers are primarily oriented in the longitudinal direction of the specimen, which enhances the mechanical properties of both mixtures under uniaxial tensile loading. The fiber alignment in the direction of the applied load is attributed to the small mold geometry (20 mm x 40 mm) relative to fiber length (13 mm and 20 mm), and hence to the casting method. In case of the hybrid reinforced mixture the incorporated long fibers serve as additional boundaries, which restrict the rotation of the short fibers, and thus maintain a more favorable fiber allegation in the direction of applied load. Nevertheless, for the same volumetric fiber content of two percent the single reinforced mixture F02_Dx generally exhibited better mechanical performance than the hybrid reinforced mixture F02_BlDx. This improvement can be explained by the more efficient fiber dispersion per unit volume, as well as by the effective higher tensile strength of the incorporated steel fibers.

4. Conclusion

The strain rate sensitive changes in the mechanical response of single and hybrid reinforced UHPFCs were investigated experimentally at three different strain rates. Based on the obtained results, the following conclusions can be drawn:

- For both tested UHPFC mixtures first cracking stress and energy absorption capacity generally increased as the strain rate increased from quasi-static to seismic loading conditions. Among all tests, the single reinforced F02_Dx mixture revealed the highest value for energy absorption capacity with 49.01 kJ/m³ at a strain rate of 0.5 1/s.

- The hybrid fiber reinforced mixture F02_BlDx displayed relative high strain rate sensitivity for first and post cracking stresses and energy absorption capacity. The high strain rate sensitivity of mixture F02_BlDx might be attributed to the higher fiber-matrix bond of the incorporated long fibers.
- For the same volumetric fiber content of two percent the single reinforced mixture F02_Dx generally exhibited better mechanical performance than the hybrid reinforced mixture F02_BlDx. This improvement can be explained by the more efficient fiber dispersion per unit volume, as well as by the effective higher tensile strength of the incorporated steel fibers.
- Typical strain rate affected behaviour was only observed for the single reinforced F02_Dx mixture, revealing a log-linear relationship of DIF values.

References

[1] Watstein, D., Effect of straining rate on the compressive strength and elastic properties of concrete, J Am Concrete Inst 49 (1953), 729-744
[2] Mindess, S. and Bentur, A., A preliminary study of the fracture of concrete beams under impact loading, using high speed photography, Cem Concr Res 15 (1985), 474-484
[3] Jawed, I., Childs, G., Ritter, A., Winzer, S., Johnson, T. and Barker, D., A., High-strain-rate behavior of hydrated cement pasts, Cem Concr Res 17 (1987), 433-440
[4] You, J. H., Hawkins, N. M. and Kobayashi, A. S., Strain-rate sensitivity of concrete mechanical properties, ACI Mat J 89 (1992), 146-153
[5] Cusatis, G., Strain-rate effects on concrete behavior, Int J Impact Eng 38 (2011), 162-170
[6] Millon, O., Analyse und Beschreibung des dynamischen Zugtragverhaltens von ultra-hochfestem Beton, PhD thesis, Technische Universität Dresden (2014)
[7] Soufeiani, L., Raman, S. N., Jumaat, M.Z, Alengaram, U. J., Ghadyani, G. and Mendis, P., Influences of the volume fraction and shape of steel fibers on fiber-reinforced concrete subjected to dynamic loading – A review, Eng Struct 124 (2016), 405-417
[8] Mechtcherine, V. and Schulze, J., Testing the behaviour of strain hardening cementitious composites in tension, Paper presented at the int. RILEM Workshop on HPFRCC in Structural Applications, Honolulu (2005)
[9] Goglin, V. et al, Tensile response of ultra-high performance steel fiber reinforced concrete under moderate strain rates, Proc. of the 12th fib International PhD Symposium in Civil Engineering, Prague (2018)
[10] Xu, M. and Wille, K., Fracture energy of UHP-FRC under direct tensile loading applied at low strain rates, Composites Part B 80 (2015), 116-125

SynerCrete'18 International Conference on Interdisciplinary Approaches
for Cement-based Materials and Structural Concrete
24-26 October 2018, Funchal, Madeira Island, Portugal

STRAIN RESILIENT CEMENTITIOUS COMPOSITES MADE WITH CALCAREOUS FLY ASH AND POLYPROPYLENE FIBERS: THE EFFECT OF TEMPERATURE AND FREEZE-THAW ON FLEXURAL TENSION

Souzana Tastani [(1)], Ioannis Savvidis [(2)]

(1) Assistant Professor, Dep. of Civil Engineering, Democritus University of Thrace, Greece
(2) Civil Engineer, Democritus University of Thrace, Xanthi, Greece

Abstract
Strain Resilient Cementitious Composites (SRCC) made by Greek unclassified calcareous fly ash and polypropylene fibers are sustainable materials with adequate mechanical properties, appropriate for structural solutions. They are experimentally studied in the present study in regards to their flexural response with parameters in the composition the high fly ash and fibers contents. Prisms of different geometry were tested in three and four-point bending aiming to explore the effect of the static system on the tensile properties. Accompanied specimens were subjected to elevated temperature (above the fiber's melting point) and freeze-thaw cycling before testing aiming to assess the material tensile vulnerability under these conditions. The experimental results of load and deflection are inversely analyzed for the assessment of the tensile stress-strain law of these materials given the two static systems.

1. Introduction – Scope of the research

Former studies [1,2] on Strain Resilient Cementitious Composites (SRCC) made with Greek unclassified calcareous fly ash and polypropylene fibers (PP) in regards to the compressive behavior (at 28 days, at later age and after being subjected to freeze-thaw conditioning) and to drying shrinkage (in terms of volumetric strain) showed that these materials have adequate strength and resistance against cracking and can be used as sustainable materials for conventional structures. In this accompanying paper, these SRCCs are examined in regards to their flexural tension with parameters in the composition the fly ash share (two and three times the cement weight) and the fibers content (0 as a reference composition, 1.5% and 2% per volume). Specimens of different geometry (prisms and beams) were tested in three and

four-point bending, respectively, aiming to study the effect of the static system on the material mechanical response. Accompanying specimens were subjected to elevated temperature and freeze-thaw cycling before flexural testing aiming to assess any deterioration in the mechanical properties, like as first cracking load, ultimate load, deformation resilience and fracture energy. Three tests were performed for each SRCC and static system. In the second part of the paper, reverse analysis on load – deflection measurements was implemented for both static systems aiming to extract milestone values of the direct tension response of the studied SRCCs. For this purpose the principle of virtual work and cross section analysis along with simplified constitutive relations for compression and tension were adopted.

2. Experimental Program

Cement CEM I 52.5N (C) was used to provide adequate compressive strength at 28 days (over 30MPa) given the later activation of the fly ash. Dried, fine silica sand (S) was also used (100% passed through a sieve with diameter of 0.5 mm). The Greek fly ash (FA) has low sum of pozzolanic components (in the order of 50%) and high content of CaO and CaO_f (38% and 15% respectively). Polypropylene microfibers (PP) had the following characteristics: diameter d_f=25μm, length ℓ_f=12mm, stress and strain at fracture f_{fu}=400MPa, ε_{fu}=0.25, melting/ignition point 160/570^{o}C (ThracePlastics, type TMIX-12). The effective water was kept constant for all mixes (w' is the water to binder ratio). The quantity of the HRWR super-plasticizer (SIKA Hellas, VISCOCRETE-ULTRA 200) was varied in each composite (in Table 1, it is given per binder weight). The composition of the four SRCC mixes is shown in Table 1; the code name FAi-PPj is interpreted as follows: FA2 or 3 denotes the fly ash share per cement weight and PP1.5 or 2 the fibers content per volume. The reference compositions (no fibers) had the same mixing ratios except of the required HRWR (1.33% and 1.5% for FA2 and FA3 respectively). A total of 78 specimens were constructed: 54 prisms of 40x40x160 (height x width x length, in mm) and 24 small beams of 70x60x370 were loaded in three and four point bending, respectively (Fig. 1a). In the case of beams, the absence of shear in the region of constant moment, as opposed to a single cross section of maximum moment in the case of prisms, may mobilize more material in tension. All specimens were cured in chamber (~20°C, 95% RH) for a month from casting. For prisms, 18 specimens were tested in pristine condition (3 specimens x 4 composites + 3 specimens x 2 mixes without fibers, named as FA2 and FA3), 18 accompanied specimens were exposed to 200^{o}C (pre-heated oven) for 2 hours before loading and the remaining 18 were subjected to 34 freeze/thaw cycles (±20^{o}C, cycle duration 48 hours) before testing (simulating extreme winter conditions in Greece). For beams, 12 specimens were served as reference whereas the rest 12 were exposed to 200^{o}C for 3 hours before loading. It is noted that no decaying or cracks were observed after heating or freeze/thaw. A displacement-control protocol was adopted for both tests (0.3mm/min); deflection was recorded by LVDT and digital monitoring (Fig.1a).

Table 1: Mixing ratios of four SRCC composites

Code Name	C	FA / C	S / C	w'	PP (%)	HRWR (%)
FA2-PP1.5	1.00	2.00	1.10	0.37	1.50	4.67
FA2-PP2					2.00	5.33
FA3-PP1.5		3.00			1.50	5.00
FA3-PP2					2.00	6.00

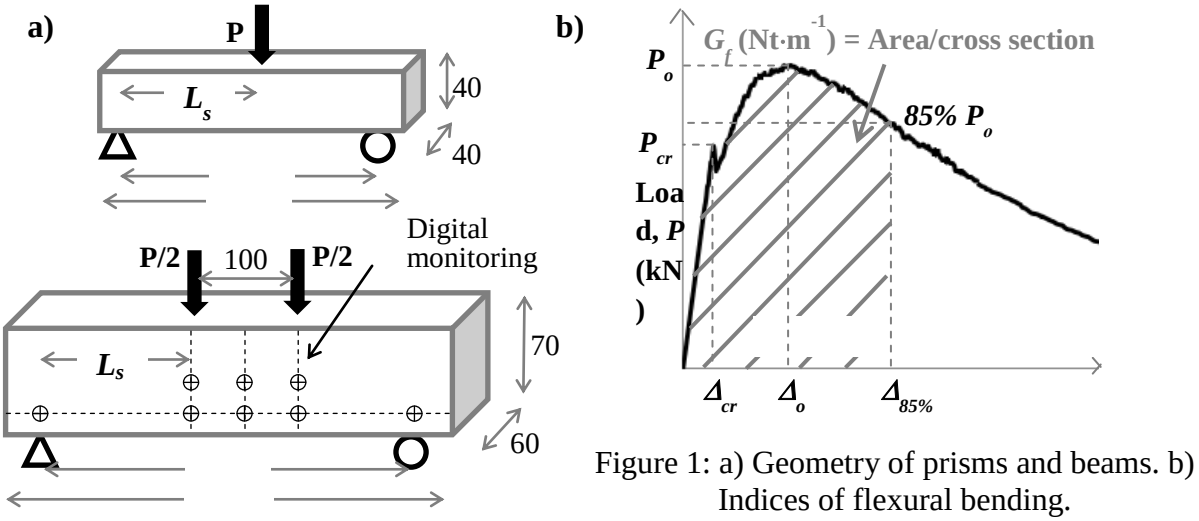

Figure 1: a) Geometry of prisms and beams. b) Indices of flexural bending.

3. Experimental results

The experimental results are presented as average load versus mid-deflection envelopes of three tests for each SRCC. With reference to Fig. 1b, important stages are a) the first cracking (Δ_{cr}, P_{cr}, where the flexural elastic strength $f_{fl,cr}$ is calculated for each test, as $f_{fl,ct}=3P_{cr}L_s/(bh^2)$, where $L_{s,prism/beam}$=70/120mm), at strength (Δ_o, P_o) and at residual resistance ($\Delta_{85\%}$, $P_{85\%}$, with deflection resilience, $\mu_{85\%}=\Delta_{85\%}/\Delta_{cr}$) and b) the apparent fracture energy G_f (ratio of the grey-hatched area up to 85% of residual strength to the specimen cross-sectional area, Fig. 1b).

3.1 Prisms

The reference prisms (denoted at "ref." in Figs. 2, 3) developed only one crack near the point of maximum moment (critical cross section). On the other hand, prisms exposed either to elevated temperature or freeze/thaw cycles (denoted at "t' and "fr-th" respectively in Figs. 2, 3) developed more than two cracks, usually on either side of the critical cross-section. Figure

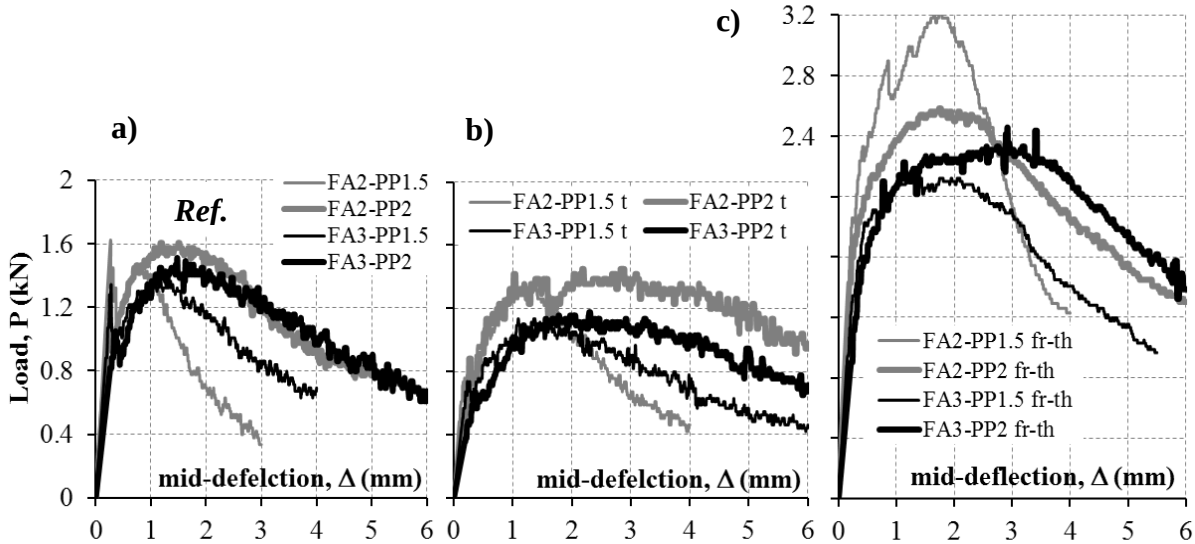

Figure 2: Comparative response of SRCC prisms under conditioning (ref., t, and fr-th).

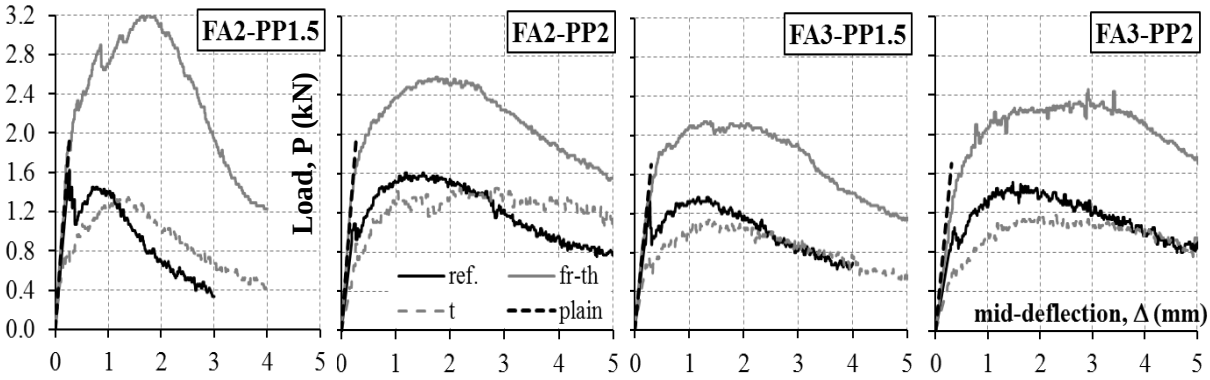

Figure 3: The impact of conditioning (temperature *t*, and freeze-thaw *fr-th*) on each SRCC prism bending response. Also appeared is the elastic response of mixes without fibers (plain).

2 shows the average load-mid deflection curves of the three prism categories, where with grey and black color are denoted the mixes with two and three parts of fly ash respectively (the line thickness is related to the increase in PP content). From Fig. 2a it may be concluded that the most sustainable SRCC (i.e., FA3-PP2) behaved similarly to that of the highest cement content (i.e., FA2-PP2). The fibers' volumetric ratio affected the transition from elastic to post-elastic stage (see also in Fig. 3 the reference curves): in mixes with 1.5% PP, load P_{cr} was instantly reduced by near 35% and fully recovered at strength ($P_{cr}\approx P_o$) whereas in mixes with 2%PP there was a mild transition and $P_{cr}<P_o$. Elevated temperature (Fig. 2b) affected the tensile behavior as follows: there is no distinct first cracking stage (absence of load jump), strength was reduced (it is more pronounced in FA3 compositions, see also Fig. 3), whereas the post-strength response is mildly descending as a consequence of multiple cracking thus attributing the characteristic of strain resilience (i.e., a wide parabolic response, that is stronger in case of FA2-PP2-t, Fig. 3b). Under freeze/thaw conditioning, all SRCCs showed a mild transition from elastic to un-elastic stage, they improved strength (even twice, Fig.2c) as a result of ongoing saturation during conditioning (thus mobilizing the development of late CSH hydrants) as well as strain resilience due to multicracking. Comparing Figs. 2a-c, it is noted that the most sustainable FA3-PP2 is equivalent to the most cementitious FA2-PP2.

3.3 Beams

The reference specimens during loading developed a single crack in the constant moment region despite the fact that a region rather than a cross section is under maximum tension**.** This may be attributed to both the low fiber's stiffness and the strong fiber-to-matrix bond which favors fiber elongation rather than slippage in the cracked cross section resulting in the widening of the crack. Mix FA2-PP2 prevails as per strength, but FA3-PP2 seems to be more resilient demonstrating a broader load – deflection response (Fig. 4a). Heating of beams before loading had the same effect in

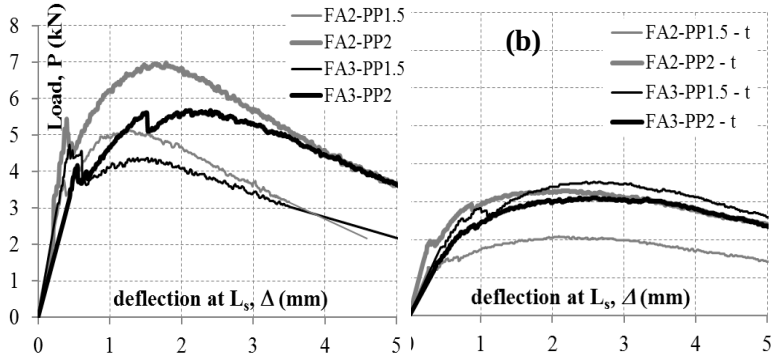

Figure 4: Comparative response of SRCC beams (ref. and t).

respect to cracking and the associated shape of load-deflection response (Fig.4b). The increased duration of heating caused drop of strength about 40 to 60%; to this contributed the elimination of fibers near the outer surfaces of specimens (after inspection of cracked sections).

3.3 The effect of the static system on the flexural response

The comparison of behavioral indices between the two systems is discussed with reference to Fig.5: prisms in three-point bending are indicated in black color and beams in four-point bending in gray. The comparison only refers to the reference specimens:

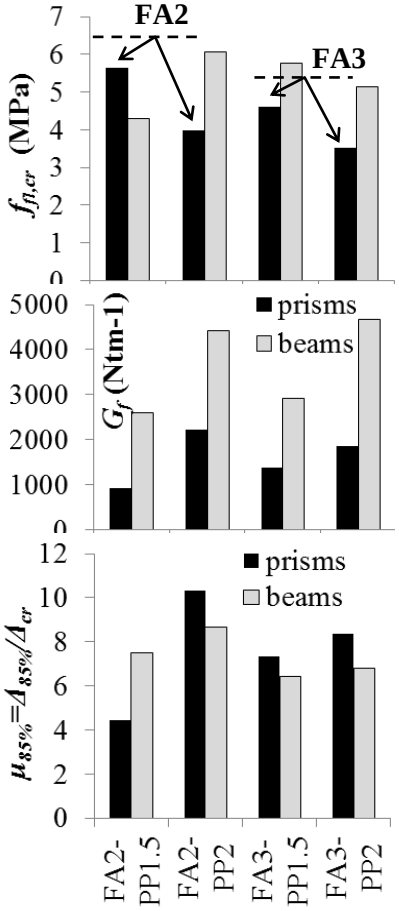

Figure 5: Indices $f_{fl,cr}$, G_f, $\mu_{85\%}$ of reference specimens.

- The elastic flexural strength, $f_{fl,cr}$, is greater in beams for the majority of SRCCs mainly due to the absence of shear in the constant moment area. The associated value for the plain mixes (without fibers) was measured only by prisms and is denoted by dashed lines.
- Apparent fracture energy, G_f, is greater in beams due to the fact that more material is activated in maximum tension (and not a single cross section in the case of prisms); SRCCs with 2% PP fibers (regardless the FA content) have the same magnitudes per static system (plain mixes, G_f =~150Nm^{-1}).
- Deflection resilience $\mu_{85\%}$ at residual resistance of beams is somehow inferior of prisms. Lower bound values of indices $f_{fl,cr}$, G_f, and $\mu_{85\%}$ of SRCCs with PP2% can be considered 5.5MPa, 4500Nm^{-1} and 7 respectively.

4. Analytical tensile stress-strain relation

The following algorithm [3] is implemented in both static systems aiming to determine the axial tensile stress - strain law of the SRCCs; here, only mixes with 2% PP fibers are analyzed (and only the reference tests):

a) First, from load versus deflection the moment – curvature diagram is assessed using the principle of virtual work.

b) Second, a cross-sectional analysis was performed based on force and moment equilibrium and Bernoulli's hypothesis for plane cross section during bending. Necessary tools are the constitutive relations of axial compression and tension. The response in compression is shown in Fig. 6a and it was based on accompanying tests on cubes [1,2]. The response in axial tension is approximated as a tri-linear envelope, in where the stress and strain values are to be the output of the algorithm. The unknown values of the milestone points of the tension law are (Fig. 6b): first cracking (point 1: $\varepsilon_{t,cr}$, $f_{t,cr}$), strength (point 2: $\varepsilon_{t,o}$, $f_{t,o}$) and residual resistance (point 3: $\varepsilon_{t,85\%}$, 85%$f_{t,o}$). The analysis is performed under the conditions that the strains of the extreme fibers of the cross section do not exceed the limits imposed by the compression strain capacity of the SRCC (15% drop of strength, Fig. 6a) and the rupture strain of fiber, ε_{fu}=0.25. Any excess of strain denotes failure. Figure 6.b illustrates the resulting tensile stress-strain law of the considered SRCCs for both static systems. Prism (continuous lines) shows lower strength

but higher strain resilience whereas beam (dashed lines) demonstrates reverse behavior. As lower, safe values for these SRCCs may considered: tensile strength (point 2), $f_{t,o}$=2.5MPa (average of two static systems) while the strain resilience at point 3 is conservatively set to 0.03 (from four-point bending).

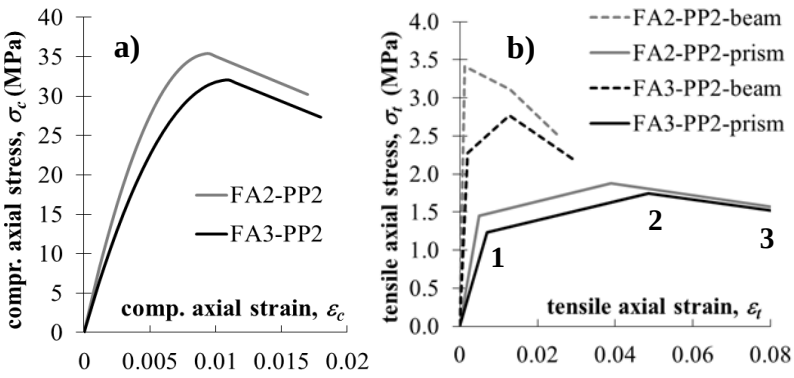

Figure 6: Laws of SRCCs in a) compression and b) tension.

5. Conclusions

Aiming to explore the influence of Greek, calcareous fly ash and the polypropylene fibers contents, as both materials are the list studied ingredients in SRCCs, flexural tests were conducted considering two static systems. Apart from reference specimens, associated coupons, before loading, were subjected to elevated temperature and to freeze/thaw cycling. In general, the experimental curves of load vs. deflection had a wide parabolic shape, with limited load jumps in the post elastic response as a result of the development of few cracks, in where all material's deformation was concentrated. This response is believed to be attributed to the low stiffness of the PP fibers in combination with strong bond at the fiber-matrix interface. The latter promotes fiber elongation rather than controlled slippage promoting the occurrence of early crack stabilization. Comparison between the four SRCCs revealed that the greenest composition (with the maximum fly ash share and 2% PP fibers, FA3-PP2) had equivalent behavior to the one with the higher cement dosage, both in pristine and after freeze-thaw conditioning, and somehow inferior due to heating. This new material is deemed as a sustainable material appropriate for structural use, with axial tensile strength 2.5MPa, strain resilience at least 0.03 and compressive strength over 30MPa.

Acknowledgements
Materials grant: SIKA HELLAS, Thrace Plastics Co S.A., DEI Ptolemais. Funding: SARF DUTh (Project ETAA, ID 81483).

References

[1] Tastani, S. Veneti M., Zapris V. Strain resilient cementitious composites: compressive response and volumetric stability, RILEM/COST PRO from 2nd Int. Conf. on Early Age Cracking and Serviceability in Cement-based Materials and Structures - EAC2, Belgium (2017)
[2] Tastani, S. Ntampanli E., Savvidis I., Veneti M., Zapris V. Strain Resilient Cementitious Composites of unclassified calcareous fly ash and PP fibers: performance by also considering durability effects, RILEM PRO from 4th Int. Conf. SHCC, Germany (2017)
[3] Georgiou, A.V. and Pantazopoulou, S.J., Effect of fiber length and surface characteristics on the mechanical properties of cementitious composites, Constr Build Mat 125 (2016), 1216–1228

SynerCrete'18 International Conference on Interdisciplinary Approaches
for Cement-based Materials and Structural Concrete
24-26 October 2018, Funchal, Madeira Island, Portugal

STUDY ON TEMPERATURE DEPENDENCE OF PROPERTIES OF HIGH STRENGTH MORTAR USING HIGH ALITE CEMENT AND POZZOLANIC FINE POWDER

Hirokazu Kiriyama [(1)], Eiji Maruya [(1)], Kenji Kawai [(2)], Ryoichi Sato[(2)]

(1) Technical Development Center, Construction Materials Co., UBE Industries, Ltd., Japan
(2) Department of Civil and Environmental Engineering, Hiroshima University, Japan

Abstract

A new ultra-high-performance fibre-reinforced concrete (UHPFRC) with a high alite content cement and fine pozzolanic powder matrix, has recently been developed in Japan. This new UHPFRC does not require the heat treatment needed for conventional UHPFRC. The new UHPFRC includes a large quantity of highly reactive binders and fine pozzolanic powder. Moreover, its hydration generates remarkably large heat and the development of its compressive strength is difficult to be evaluated. The objective of this study was to establish a method of estimating the compressive strength of this new UHPFRC. Therefore, the apparent activation energy of the new UHPFRC was estimated to modify the temperature adjusted age. It was found that the temperature dependency of the compressive strength can also be evaluated with high accuracy by using the modified temperature adjusted age. Additionally, it is possible that the apparent activation energy may depend on the reaction of fine pozzolanic powder.

1. Introduction

A new ultra-high-performance fibre-reinforced concrete (UHPFRC), with a high alite content cement and fine pozzolanic powder matrix, has recently been developed in Japan. This new UHPFRC does not require the heat treatment needed for a conventional UHPFRC; therefore, it can be casted on-site. The new UHPFRC has a large quantity of highly reactive binders, whose hydration generates remarkably large heat and results in higher member temperature. Additionally, the new UHPFRC has a low water/binder ratio, which produces high autogenous shrinkage and results in high risk of cracking at early ages.
To reasonably control early age cracking, it is important to properly evaluate the development of physical properties depending on the high temperature thermal history. UHPFRC has a

binders that reacts more actively at high temperatures. Therefore, it is difficult to estimate the properties of UHPFRC, since this depends on the thermal history of high temperatures.
From the abovementioned background, this study estimated the apparent activation energy based on the development of compressive strength, which was normalized by the ultimate strength as an index of the reaction rate, to establish a method of estimating the material properties of ultra-high-strength mortar comprising of high alite content cement and fine pozzolanic powder. Additionally, a modified temperature adjusted age is proposed based on the estimated apparent activation energy. Finally, in order to investigate the factor that the apparent activation is not constant, the relationship between the hydrations of binders and modified temperature adjusted age was studied.

2. Experimental programme

2.1. Materials and proportions of high strength mortar and cement paste

High alite content cement and fine pozzolanic powder were mixed with unreactive inorganic powders as a high strength mortar binder for UHPFRC. Crushed sand (dry density: 2.62 g/cm^3, water absorption rate: 2.5%, fineness modulus: 2.59) was used as a fine aggregate, and a polycarboxylate based superplasticizer was also used. The mixed proportions of high strength mortar for UHPFRC consisted of 230 kg/m^3 of water, 1,830 kg/m^3 of premixed powder, 330 kg/m^3 of fine aggregate, and 31.2 kg/m^3 of superplasticizer content. The cement components were 57.6% C_3S, 21.5% C_2S, 1.1% C_3A and 14.3% C_4AF. The blain surface area was 3,180 cm^2/g. The main component of fine pozzolanic powder was SiO_2, the density was 2.2 g/cm^3, and the BET specific surface area was 18.9 m^2/g.
The mix ratio of cement paste with water/binder was 16%, the replacement ratio of fine pozzolanic powder to cement was 10%, and 1.4% of superplasticizer was used as the binder.

2.2. Specimen preparation and curing

High strength mortar was mixed by mortar mixer for 10 minutes. The fresh mortar was casted into φ50×100 mm cylinder moulds, which were then sealed by plastic sheets and cured at the temperatures listed in Tab.1. The curing temperature exceeded 60 °C. First, the moulds were maintained at a temperature of 20 °C for 8 hours. Then, the heat increase to the set temperature/decrease to ambient temperature was controlled at 20 °C/h. Cement paste was conducted the same way.

2.3. Compressive strength

The compressive strength was measured according to JIS A1108. The ages in the compressive strength experiment are listed in Tab. 1.

2.4. Hydration of cement and fine pozzolanic powder

When the pastes hydrated at the curing temperature (Tab.2), the slices from the cylinders were placed in acetone to stop the hydration reaction, and were then measured hydrations.
The reaction rate of cement was calculated by estimating the area of the unreacted cement particles [1].The specimen was polished to mirror-finish. A scanning electron microscope (SEM) fitted with a backscatter electron detector (BSE) was used for imaging. The microscope was operated at an accelerating voltage of 15Kv, and images were collected per specimen at a magnification of 500 with 20 fields. Image processing was carried out based on

the mode method, such that a binarized image corresponding to the anhydrous particles could be obtained. Subsequently, we estimated the unhydrated area.
The amount of the unreacted fine pozzolanic powder was measured according to the HCl-Na_2CO_3 selective dissolution method [2].

Table 1: Curing temperature and measuring ages of mortar's compressive strength.

T_k *1	Ages of measuring (h: hours, d: days)
80°C	12h, 16h, 18h, 21h, 3d, 7d, 28d
60°C	14h, 23h, 3d, 7d, 28d
40°C	1d, 2d, 3d, 7d, 14d, 21d, 28d
30°C	9.5h, 10.5h, 12h, 14h, 16.5h, 20h, 1d, 2d, 7d, 28d, 56d, 91d
20°C	11.3h, 15.5h, 18h, 20h, 21h, 22h, 1d, 2d, 3d, 6d, 7d, 14d, 21d, 28d, 42d, 56d, 70d, 91d
15°C	16h, 22h, 1.2h, 1.8h, 2.8h
10°C	20h, 1d, 1.2d, 1.3d, 1.4d, 1.9d, 7d, 14d, 21d, 28d, 42d, 56d, 70d, 91d, 182d, 300d

*1: Curing temperature.

Table 2: Curing temperature and measuring age of pastes' compressive strength.

Curing Temperature	Ages of measuring (h: hours, d: days)
	Paste
80°C	2d, 5d
40°C	2d, 7d, 28d
30°C	2d, 7d, 28d
20°C	2d, 7d, 28d

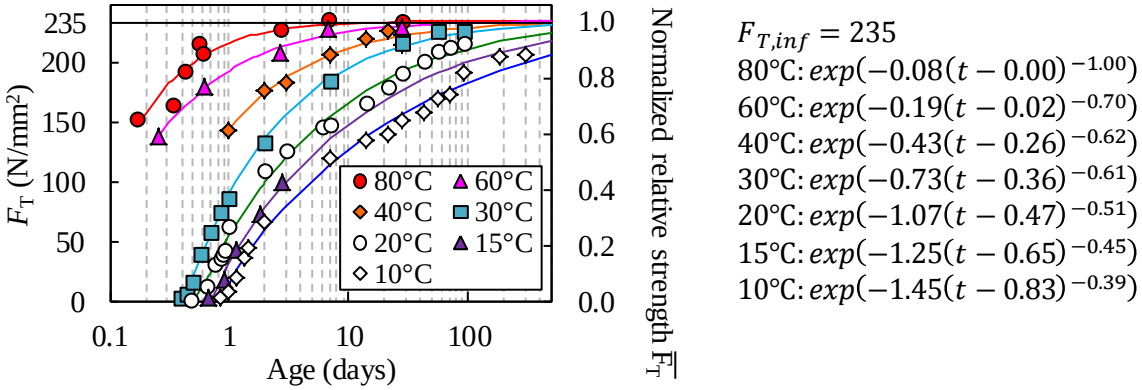

Figure 1: Compressive strength/normalized relative strength at each curing temperature.

3. Result and discussion

Figure 1 shows the compressive strength of mortar at each curing temperature. The compressive strength of the specimens cured at higher temperature was naturally higher. With regard to the specimens cured at 80 °C, their compressive strength peaked at approximately 235 N/mm^2 at the age of two days, which indicates that the compressive strength reached the

ultimate value. The compressive strength of the other specimens appeared to have gained the same ultimate strength, as shown in Fig. 1.

4. Estimation of apparent activation energy

First, the function (Eq. (1)) was applied to estimate the compressive strength development obtained at each curing temperature by using the least-squares method under the assumption that the ultimate compressive strength is constant at 235 N/mm^2, regardless of the curing temperature.

$$F_{\mathrm{T}} = F_{\mathrm{T,inf}} \cdot exp(a \cdot (t - t_0)^b) \tag{1}$$

where F_{T} is the compressive strength at curing temperature T, $F_{\mathrm{T,inf}}$ is 235 N/mm^2, and a and b are constant. At all curing temperatures, the correlation coefficients between the estimated curves and the compressive strength measurements were higher than 0.90.
Eq. (2) was obtained by dividing both sides of Eq. (1) by the ultimate compressive strength. As the reaction rate index, the relative strength expressed by Eq. (2) was adopted.

$$\overline{F_{\mathrm{T}}} = F_{\mathrm{T}}/F_{\mathrm{T,inf}} = exp(a \cdot (t - t_0)^b) \tag{2}$$

Eq. (3) is the Arrhenius Equation, which represents the temperature dependency of the chemical reaction, as follows:

$$k_t = Aexp(-E_a/RT) \tag{3}$$

where k_t is the constant reaction rate, E_a is the apparent activation energy, R is a gas constant, and T is the curing temperature. By substituting Eq. (3) into the chemical reaction rate equation ($d\alpha/dt = k_t f(\alpha)$), Eq. (4) is obtained, which is a reaction rate equation with temperature as an independent variable.

$$d\alpha/dt = k_t f(\alpha) = Aexp(-E_a/RT) f(\alpha) \tag{4}$$

where α is the reaction degree, $f(\alpha)$ is a function of α, and A is constant. Taking the logarithm of both sides of Eq. (4) yields Eq. (5). When the curing temperature and rate of reaction are available, the Arrhenius plot graph is obtained, which indicates the relationship between the log of the reaction rate and 1/T. The slope from the Arrhenius plot gives the activation energy. As the reaction rate index, the development of the compressive strength was adopted, which was normalized by the ultimate strength calculated by Eq. (2).

$$ln(d\alpha/dt) = ln(d\overline{F_T}/dt) = -E_a/RT + ln\left(Af(\overline{F_T})\right) \tag{5}$$

In Fig. 2(a), it can be seen that the Arrhenius plot is only partially plotted as a straight line within the entire range. However, the slope of the Arrhenius plot within the linearly plotted range in the vicinity of 30°C changes depending on the relative strength and curing temperature. Fig. 2(b) shows the apparent activation energy estimated from the linearly plotted range in the vicinity of 30°C. It can be clearly seen that the apparent activation energy increased depending on the development of the relative strength. Additionally, in the case

where the relative strength was more than 0.7, the apparent activation energy at curing temperatures over 30°C had lower values in comparison with the activation energy at temperatures lower than 30°C, which is different to previously reported results [3].

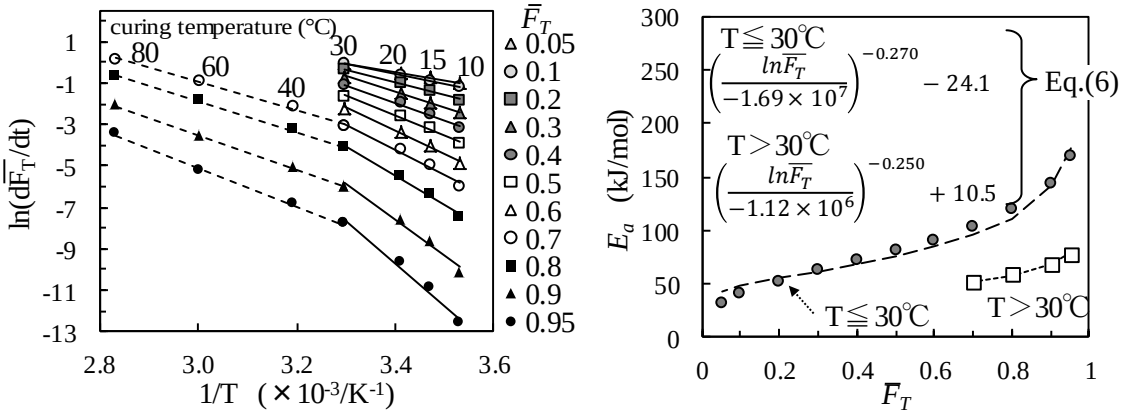

Figure 2: (a) Arrenius plot and (b) relationship between normalized relative compressive strength $\overline{F_T}$ and apparent activation energy E_a.

Eq. (6) in Fig. 2(b) is a function that expresses the apparent activation energy of the high strength mortar, which was obtained from fitting by the least squares method. Eq. (7) shows the temperature adjusted age [4]. The modified temperature adjusted age is derived by substituting the estimated activation energy into the E_a term of Eq. (7).

$$t_e = \sum exp\{E_a/R\,(1/T_0 - 1/T_k)\}\Delta t \tag{7}$$

where t_e is the thermal equivalent age, T_0 is the reference temperature, T_k is the curing temperature during time interval Δt, and t is the age of the concrete. Figure 3 shows the relative strength that was obtained based on the conventional thermally adjusted age (Fig. 3(a)), and that based on the new modified temperature applied to the adjusted age (Fig. 3(b)). Fig. 3(b) shows that the modified temperature adjusted age evaluated the dependency of the developing relative compressive strength at various curing temperatures more appropriately.

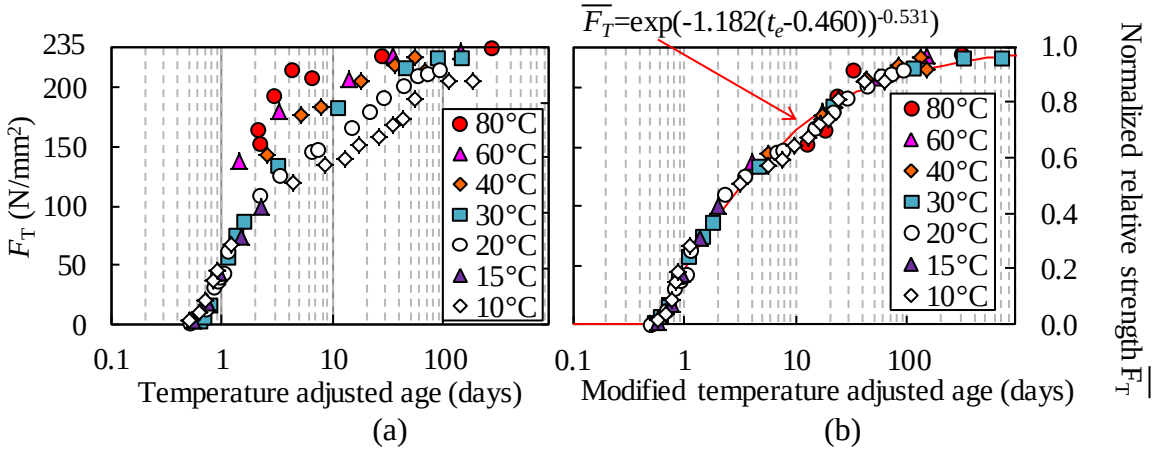

Figure 3: Compressive strength normalized by ultimate compressive strength.

Figure 4 shows the reaction degree of the high alite content cement and fine pozzolanic powder that was applied to the temperature adjusted age shown in Fig. 4(a), and the modified temperature adjusted age shown in Fig. 4(b). Moreover, Fig. 4(b) shows the good relationship between the modified temperature adjusted age and the reaction of the fine pozzolanic powder. Therefore, it is possible that the apparent activation energy was strongly influenced by the fine pozzolanic powder reaction.

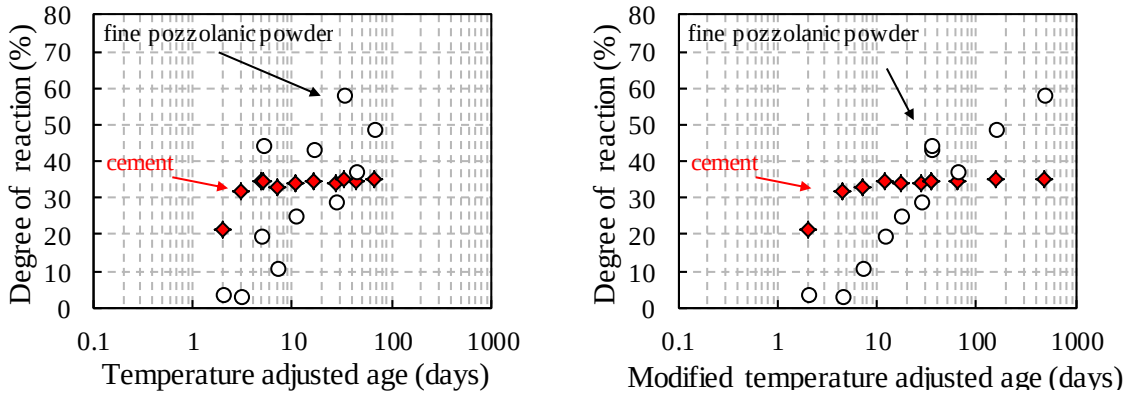

Figure. 4: reaction degree of high alite content cement and fine pozzolanic powder.

5. Conclusion

In this study, the apparent activation energy of a high strength mortar with high alite content cement and fine pozzolanic powder was investigated to establish a method of estimating the compressive strength. The results revealed that the apparent activation energy obtained from the relative strength as an index of the reaction rate was not constant, but rather developed depending on the relative strength and curing temperature. Additionally, the modified temperature adjusted age using the new apparent activation energy was estimated more appropriately in comparison with the conventional temperature adjusted age. Moreover, it was found that the apparent activation energy could have been strongly influenced by the reaction of the fine pozzolanic powder.

References

[1] Inoue, G. and Igarahi, S., Comparison of degree of hydration of cement obtained by several methods, Proceedings of the Japan Concrete Institute 27(1) (2005), 541-546
[2] Asaga, K. et al, Determination of uncombined quartz in hydrothermal reaction of quartz and Portland cement, Journal of the Ceramic Society of Japan 90(1043) (1982), 397-400
[3] Kjellsen, K.O. and Detwiler, R.J., Later-age strength prediction by a modified maturity model, ACI Marerials Journal 90(3) (1993), 220-227
[4] Hansen, P.F. and Pedersen, E.J., Maturity computer for controlled curing and hardening of concrete, Nordisk Betong 1(19) (1977), 21-25

SynerCrete'18 International Conference on Interdisciplinary Approaches
for Cement-based Materials and Structural Concrete
24-26 October 2018, Funchal, Madeira Island, Portugal

TENSION STIFFENING MODEL FOR SERVICEABILITY ANALYSIS OF STEEL AND FRP REINFORCED CONCRETE BEAMS

Gintaris Kaklauskas [(1)], Pui-Lam Ng [(1,2)], Aleksandr Sokolov [(1)]

(1) Vilnius Gediminas Technical University, Vilnius, Lithuania
(2) The University of Hong Kong, Hong Kong, China

Abstract

An improved tension stiffening model is proposed for short-term deformational analysis of reinforced concrete flexural members. The model has been derived by utilising the direct and inverse analysis techniques with the use of layered approach of computation based on experimental moment-curvature relationships of concrete beam specimens. For ease of implementation by structural designers, a simple formulation of tensile stress block with dependence on the reinforcement ratio has been established. The proposal has been verified to have desirable accuracy. In addition to steel reinforced concrete beams, the analytical methodology has been applied to fibre-reinforced polymer (FRP) reinforced concrete beams.

1. Introduction

When a reinforced concrete beam is loaded up to cracking, at the cracked section, the flexural tension is resisted entirely by the reinforcement. Between adjacent cracks, the intact concrete remains to be able to carry tensile stresses transferred via bond between reinforcement and concrete [1]. The tensile resistance of concrete effectively stiffens the member response and this phenomenon is known as tension stiffening. For serviceability analysis of concrete members, the use of a rational tension stiffening constitutive model is of crucial importance.
To model tension stiffening, the tension stiffening stress may be attributed to the reinforcement or to the concrete. The latter allows comparative study of concrete stress-strain relations among smeared crack and discrete crack modelling, thus offering additional advantage for analysts. The tension stiffening stress-stress law reflects the interaction between concrete and reinforcement through bond in the tension zone of member, and is commonly referred to as tensile stress block. It forms a useful tool in combination with sectional analysis for deformational assessment of concrete members [2].

In the current study, an improved tension stiffening model is devised for concrete beams subjected to short-term load. The direct and inverse analysis techniques are employed in the derivation process, with the use of layered approach of computation [1]. A simple formulation of tensile stress block is proposed for practical use. Besides, fibre-reinforced polymer (FRP) has emerged as a corrosion-free reinforcement material. Though its tensile strength can be comparable to reinforcing steel, its elastic modulus is remarkably lower. The flexibility of FRP material would render FRP reinforced concrete members having distinct deformational characteristics from conventional steel reinforced counterparts. In view of this, the authors embark research on the tension stiffening behaviour of FRP reinforced concrete beams.

2. Tension stiffening effect in concrete beams

At the outset, doubly-reinforced concrete beam with uniform cross-section is considered. Plane sections are assumed to remain plane under flexure. The cracks are regarded as smeared over the sections along the longitudinal direction. To conduct analysis, the cross-section is sub-divided into multiple layers (i.e. the layered approach). Governing equations are set up from the force and moment equilibria, and are solved for the concrete stresses at extreme fibres. After establishing the extreme fibre strains, the strain levels of all other fibres can be obtained by linear interpolation, and the corresponding stresses are determined from the materials law. The stress-strain law and the moment-curvature diagram of concrete beam are inter-related. The direct technique enables determination of moment-curvature diagrams from given materials law, whereas the inverse technique enables determination of average stress-strain relationship from known moment-curvature diagrams [1].

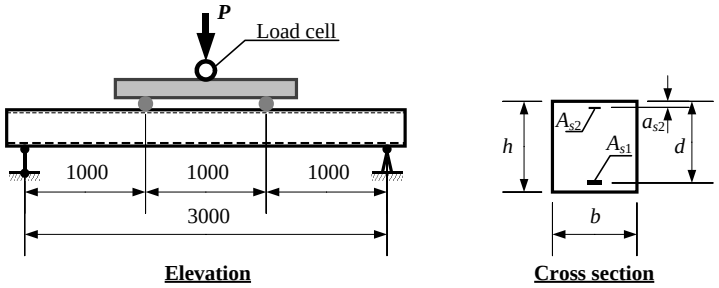

Figure 1: Elevation and cross-section of beam specimen.

The above analytical methodology is applied to a series of steel reinforced concrete beam specimens in the literature [3]. Fig. 1 depicts the elevation and cross-sectional views and Tab. 1 summarises the main characteristics of the specimens. The notations of quantities are graphically annotated in Fig. 1. The beams had uniform rectangular cross-section of 280 mm breadth by 300 mm depth. The reinforcement ratio *p* was varied among 0.3%, 0.6% and 1.0%. The beams had span length of 3.0 m and were subject to symmetrical four-point loading with pure bending zone of 1.0 m and shear span of 1.0 m.

Table 1: Main characteristics of steel reinforced concrete beams.

Beam	***d* (mm)**	a_{s2} **(mm)**	A_{s1} **(mm^2)**	A_{s2} **(mm^2)**	***p* (%)**	f_c **(MPa)**
S1-3	268	23	755	57	1.0	48.2
S2-3	272	29	466	57	0.6	48.1
S3-2-2	274	32	232	57	0.3	52.8
S3-2-3	271	32	232	57	0.3	50.9

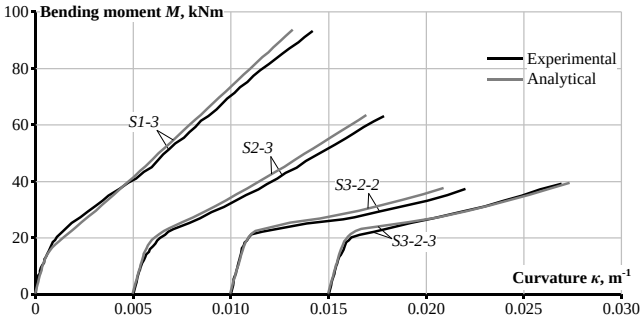

Figure 2: Experimental and analytical moment-curvature response.

The laboratory testing procedures were described in detail in the dedicated study [3]. The experimentally obtained moment-curvature diagrams of the specimens are presented in Fig. 2. By means of inverse analysis technique, the tension stiffening stress-strain curve was obtained from the moment-curvature diagram of each specimen. The stress σ_{ct} and strain ε_{ct} are normalised with respect to the tensile strength f_{ctm} and cracking strain ε_{cr} of concrete, respectively. Fig. 3 shows the resulting normalised stress-strain curves.

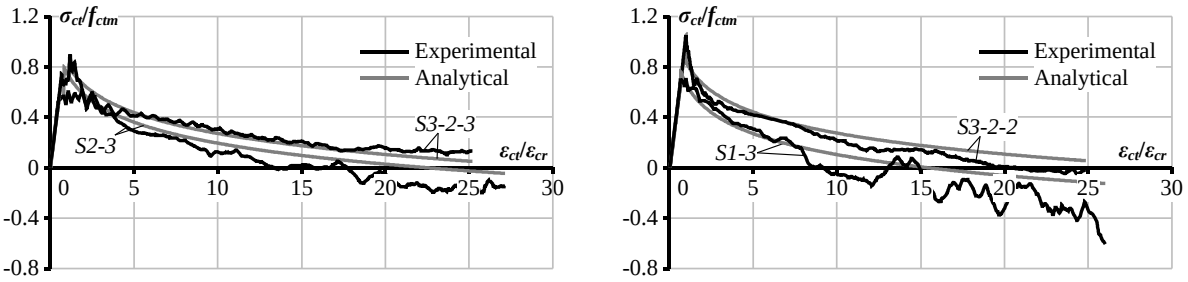

Figure 3: Normalised tension stiffening stress-strain curves.

From Fig. 3, it can be seen that the stress-strain curve typically comprises an ascending branch and a descending branch. Initially, the tensile stress varies linearly with the tensile strain from the origin up to the peak point, which is close to the tensile strength of concrete. Afterwards, the tensile stress decreases gradually with increasing tensile strain. A number of tension stiffening curves in Fig. 3 manifest negative stress portions at large strains, especially for the more heavily-reinforced beam specimens. This could be due to the idealisation of reinforcement-concrete bond as perfect bond, as well as the shrinkage of concrete that had effectively shifted the stress-strain curve towards the negative side. The computational methodology for shrinkage elimination had been studied in detail by the authors' team [4].

3. Derivation and verification of tensile stress block

On the basis of the tension stiffening stress-strain curves, an improved tension stiffening model is devised by curve fitting. The form of equation chosen is a compromise between accuracy and simplicity. In essence, the ascending branch is a straight line passing through the origin, and the descending branch is a logarithmic decay curve. The proposed tensile stress block is depicted in Fig. 4 and its ascending and descending branches are algebraically given by Eq. (1a) and Eq. (1b), respectively. In Eq. (1), p is expressed in percentage. It is apparent that for a more heavily-reinforced beam, the descending branch would be shorter, and vice versa. For cross-comparison, Eq. (1) is plotted for each specimen in Fig. 3 as analytical curve.

$$\sigma_{ct} = (0.9 - 0.25p) f_{ctm} \left(\frac{\varepsilon_{ct}}{\varepsilon_{cr}}\right) \quad \text{for} \quad \varepsilon_{ct} < \varepsilon_{cr} \tag{1a}$$

$$\sigma_{ct} = f_{ctm} \left[0.9 - 0.25p - 0.24 \ln\left(\frac{\varepsilon_{ct}}{\varepsilon_{cr}}\right)\right] \geq 0 \quad \text{for} \quad \varepsilon_{ct} \geq \varepsilon_{cr} \tag{1b}$$

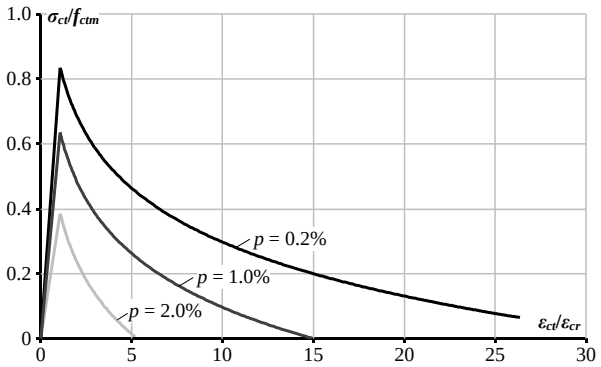

Figure 4: Proposed tensile stress block.

The proposed tensile stress block is verified in the following. By means of the direct analysis technique, the moment-curvature response of concrete beams is evaluated with the stress-strain law of reinforced concrete element taken as Eq. (1). For each specimen, the analytical moment-curvature response is plotted in Fig. 2 for comparison with the experimental data. It is evident that close agreement between the experimental and analytical results is achieved.

4. Tension stiffening behaviour of FRP reinforced concrete beams

To extend the proposed tension stiffening model to concrete beams reinforced with FRP bars, reference is made to the experimental data of five FRP reinforced concrete beam specimens reported in the literature [5-9]. The specimens are labelled F1 [5], FRP1A-HF [6], Group 3 [7], BC2HA [8] and Series 1 [9]. Tab. 2 summarises the main characteristics of the beams, which were all subjected to symmetrical four-point bending loading arrangement.

Table 2: Main characteristics of FRP reinforced concrete beams.

Beam	***b*×*h* (mm)**	***d* (mm)**	***L* (m)**	***p* (%)**	f_c **(MPa)**	f_f **(MPa)**	E_f **(GPa)**
F1	500×185	145	3.40	1.23	30.0	494	42.0
FRP1A-HF	254×184.2	138.2	2.89	1.12	74.3	690	40.3
Group 3	200×260	218	2.70	1.16	31.3	886	43.4
BC2HA	130×180	154	1.50	1.20	57.2	773	38.0
Series 1	200×300	260	3.00	1.10	43.0	690	45.0

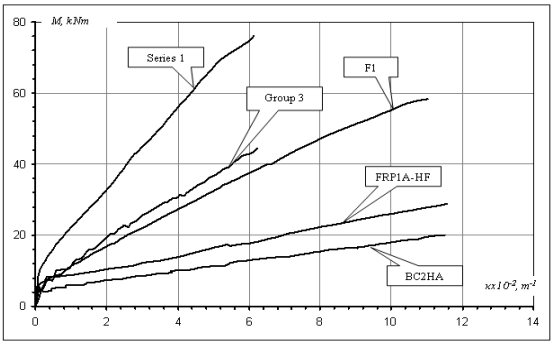

Figure 5: Experimental moment-curvature diagrams of FRP reinforced concrete beams.

The experimentally obtained moment-curvature diagrams for the beams are depicted in Fig. 5. Applying the inverse analysis technique, stress-strain relationship is determined for each specimen. The normalised tension stiffening stress-strain curves are presented in Fig. 6. In comparison with steel reinforced concrete beams, it can be observed that the descending branches in Fig. 6 are significantly longer for FRP reinforced concrete beams. Such difference would be due to the lower elastic modulus of FRP material, and could be reflected in the model by adjusting the coefficient values in Eq. (1). Nevertheless, further research with larger sample size of FRP reinforced concrete beams is necessary to confirm the mathematical formulation of the tensile stress bock. From Fig. 6, it is noted that the ratio of ultimate tensile strain (at which the stress level of the descending branch is zero) to the cracking strain ranges from circa 50 to 135, with an average value of approximately 100.

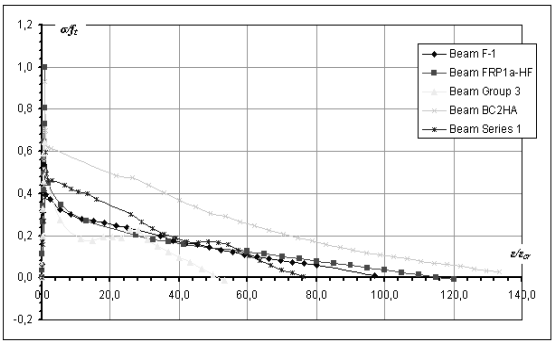

Figure 6: Tension stiffening stress-strain curves of FRP reinforced concrete beams.

5. Conclusions

The tension stiffening effect in steel and fibre-reinforced polymer (FRP) reinforced concrete beams has been studied. An improved tension stiffening model has been formulated with reference to experimental data of beam specimens. The mathematical formulation has accounted for the dependence of tensile stress block on the reinforcement ratio. Good agreement between experimental and analytical moment-curvature response has been attained. Application of the analytical methodology to FRP reinforced concrete beams has revealed longer descending branches. Further research is recommended to confirm the formulation of tensile stress block for FRP reinforced concrete beams.

Acknowledgements
The authors gratefully acknowledge the financial support from the Research Council of Lithuania and the European Union Structural Fund (Project no.: 09.3.3-LMT-K-712-01-0145). The second author wishes to express his gratitude for the support provided by the European Commission Research Executive Agency under the Marie Skłodowska-Curie Actions (Project no.: 751461).

References

[1] Kaklauskas, G., Flexural layered deformational model of reinforced concrete members, Mag Concr Res 56(10) (2004), 575-584
[2] Lam, J. Y. K. et al, Tension stiffening in concrete beams. Part 2: member analysis, Proc ICE Struct Bldgs 163(1) (2010), 29-39
[3] Gribniak, V. et al, Experimental investigation of deformations of lightly reinforced concrete beams, Proc. 9th International Conference Modern Building Materials, Structures and Techniques, Vilnius (2007), 554-562
[4] Kaklauskas, G. et al, Eliminating shrinkage in tension stiffening model of concrete beams by the hybrid approach, Proc. 24th Australasian Conference on the Mechanics of Structures and Materials, Perth (2016), 129-135
[5] Pecce, M. et al, Experimental response and code models of GFRP RC beams in bending, J Compos Constr ASCE 4(4) (2000), 82-90
[6] Yost, J. R. et al, Flexural stiffness of high strength concrete beams reinforced with GFRP bars, ACI SP 210 (2003), 209-224
[7] Almusallam, T. H., Analytical prediction of flexure behaviour of concrete beams reinforced by FRP bars, J Compos Mater 31(7) (1997), 640-657
[8] Thériault, M. and Benmokrane, B., Effects of FRP reinforcement ratio and concrete strength on flexural behaviour of concrete beams, J Compos Constr ASCE 2(1) (1998), 7-16
[9] Benmokrane, B. et al, Flexural response of concrete beams reinforced with FRP reinforcing bars, ACI Struct J 93(1) (1996), 46-55

SynerCrete'18 International Conference on Interdisciplinary Approaches
for Cement-based Materials and Structural Concrete
24-26 October 2018, Funchal, Madeira Island, Portugal

USING INTELLIGENT SYSTEM APPROACH FOR SHEAR STRENGTH FORECASTING OF STEEL FIBER-REINFORCED CONCRETE BEAMS

Ali Kheyroddin [(1)], Masoud Ahmadi [(1)], Mahdi Kioumarsi [(2)]

(1) Semnan University, Semnan, Iran
(2) OsloMet – Oslo Metropolitan University, Oslo, Norway

Abstract

Previous studies have shown that brittle failure in reinforced concrete buildings caused huge losses, both in human and economic terms. The appropriate use of steel fibers to a reinforced concrete beam can change the brittle behavior to a ductile behavior and significantly increase the ductility ratio. The aim of this study is to develop an intelligent system approach for shear strength estimation of steel fiber-reinforced concrete (SFRC) beams without transversal reinforcement using a large number of existing experimental results. The main parameters in this investigation are the steel fiber-volume fraction, the aspect ratio and volume of fiber, compressive strength of concrete, longitudinal reinforcement, effective depth and shear span of beams. The precision of the proposed approach is compared with other existing models for estimating the shear capacity of SFRC beams based on experimental results which showed a reasonable agreement.

1. Introduction

In recent decades different types of fiber, including natural fiber (NF), steel fiber (SF), glass fiber (GF), and synthetic fiber (SNF), were used in various field of the civil engineering concrete construction [1–3]. It is well known that concrete as a material subjected to the tensile stress conditions is brittle. The findings of the previous studies revealed that fibers can significantly boost the post-cracking behavior, flexural toughness, spalling resistance, impact resistance, shear strength, thermal characteristics, and ductility of concrete members under various types of loading conditions [4–6]. SF delays crack propagation in the concrete and noticeably enhances the tensile performance. The brittle failure in reinforced concrete (RC) structures caused huge losses, both in human and economic terms. Thus, it is necessary to

prevent brittle failure and change it to ductile mode. The sufficient amount of SF in a RC beam can alter the brittle mode to a ductile behavior and enhance the ductility ratio. Up to now, many researchers have been studying the use of the steel fibers as replacement of the shear reinforcement, which will ultimately help to improve the behavior of RC beam. It is worth mentioning that the orientation, distribution, and resistance to pull out of fibers play a substantial role in the performance improvement of the steel fiber reinforced concrete (SFRC) beams [7]. Among the steel fibers types, hooked and crimped fibers have acceptable efficiency to prevent premature pull out which affects the load carrying ability. A SFRC beam with hooked/crimped fibers, when design appropriately, has superior ductility in comparison with common RC beams [8].

2. Shear capacity of SFRC beam

Several studies have been carried out to identify the effect of steel fibers on shear strength of SFRC beams without stirrups. Researchers based on the theoretical and experimental studies have been proposed several equations for determining shear strength of SFRC beams. These models are mainly categorized in two groups. In the first group, the independent contribution is assumed for steel fibers and its shear strength is added to the contribution of plain concrete and stirrups.

$$V_{SFRC-Beam} = V_c + V_S + V_{SF} \tag{1}$$

where, V_c, V_S and V_{SF} are the shear strength contribution provided by the plain concrete, transverse reinforcement, and steel fibers. The second group assumes that steel fibers influence on the shear strength of concrete. Narayanan and Darwish (1987) [9] studied the effects the steel fibers on the behavior of RC beams under predominant shear. They proposed empirical formulation for design of SFRC beams without stirrups.

$$v_u = e\left[0.24 f_{spfc} + 80\rho\frac{d}{a}\right] + v_b \tag{2}$$

where, e is arch action factor, f_{spfc} is split tensile strength of concrete, ρ is reinforcement ratio, $\frac{d}{a}$ is effective depth-to-shear span ratio, and v_b is calculated based on average bond stress. The arch action factor is 1.0 for $\frac{a}{d} > 2.8$ and $2.8\frac{d}{a}$ for $\frac{a}{d} \leq 2.8$. Khuntia et al. (1999) [10] developed a design equation for calculating the ultimate shear strength of SFRC beams based on the basic shear transfer mechanisms and large number of experimental results. They proposed the following equation for determining shear capacity of SFRC beams without transverse reinforcement:

$$v_u = (0.167\alpha + 0.25\beta v_f \frac{l_f}{d_f})\sqrt{\acute{f}_c} \tag{3}$$

where, α is arch action factor, v_f is fiber volume fraction, β related to fiber shape and concrete type, $\acute{f}_c$ is compressive strength of concrete, and $\frac{l_f}{d_f}$ is fiber length-to-fiber diameter

ratio. Ultimate shear capacity of SFRC beams without stirrups can be determined according to Sharma (1986) [11] from the following equation:

$$v_u = \frac{2}{3}\acute{f}_t \left(\frac{d}{a}\right)^{0.25} \tag{4}$$

where, $\acute{f}_t$ is split-cylinder tensile strength of concrete, and $\frac{d}{a}$ is effective depth-to-shear span ratio.

3. Group method of data handling (GMDH)

GMDH neural network is a self-organizing black-box learning technique proposed by Ivakhnenko in 1971 [12]. Artificial neural networks is a superior tool in forecasting (any non-linear functions or features) and data mining [13–15]. The discrete form of the GMDH model is given in following equation:

$$\bar{y} = a_0 + \sum_{i=1}^{n} a_i f_i \tag{5}$$

where *a* is coefficient, *f* is the basic function based on different sets of inputs, and *n* is the number of the base function components. The Kolmogorov-Gabor (KG) polynomial is the most popular base function used in GMDH approach. The KG-form of equation 5 based on input vector $X(x_1, x_2, x_3, \dots, x_n)$ can be expressed as following equation:

$$\bar{y} = a_0 + \sum_i^n a_i x_i + \sum_i^n \sum_i^n a_{ij} x_i x_j + \sum_i^n \sum_i^n \sum_i^n a_{ijk} x_i x_j x_k + \cdots \tag{6}$$

where a_i, a_j, and a_k are the weighting coefficients. The GMDH algorithm is considered as a feedforward multilayer network with low-degree polynomial activation function. The outcomes of the first layer is computed based on only two input variables using partial quadratic polynomial function as given in following:

$$z = z(x_i, x_j) = s_0 + s_1 x_i + s_2 x_j + s_3 x_i x_j + s_4 x_i^2 + s_5 x_j^5 \tag{7}$$

The coefficients of partial function are determined utilizing the least squares method to minimize the difference between real and estimated value for each pair of the input vectors.

4. Experimental database

In order to calculate the average shear stress of steel fiber-reinforced concrete beams without transversal reinforcement, 112 experimental results were gathered from the previous studies. A summary range of mechanical-geometric properties of beams is given in Table 1. The

considered parameters include: 1) Shear span-effective depth ratio (a/d), 2) Effective depth of beams (*d-mm*), 3) Longitudinal reinforcement ratios (ρ), 4) Compressive strength of concrete (f_c'-*MPa*), 5) Fiber ratio (F_{SF}). Fiber ratio is determined as follows:

$$F_{SF} = V_{SF}\, {}^{L_{SF}}/_{d_{SF}} \tag{8}$$

where, d_{SF} and L_{SF} are diameter and length of steel fiber, and V_{SF} is volume percentage of fibers.

Table 1. Range of input parameters for network application

Reference	No. of test data	Parameter											
		d (mm)		a/d		ρ (%)		f'c (MPa)		F_{SF}		$v_{exp}(MPa)$	
		Min	Max.	Min	Max	Min	Max	Min.	Max.	Min.	Max.	Min.	Max.
[16]	12	197	197	2	3.6	1.3	2	20.6	33.4	30	60	1.5	3.11
[9]	31	126	130	2	3.5	2	5.72	31.9	63.6	25	200	1.94	7.15
[17]	8	215	215	2	4	2.8	4.58	75.0	79.2	37.5	112.	2.27	7.21
[18]	2	204	204	3	3	2.2	2.2	22.7	26	60	100	3.05	3.05
[19]	4	340	340	2	2.5	3.4	3.44	33	36	30	60	3.78	5.34
[20]	7	265	265	2	4.91	1.5	4.31	33.1	40.9	100	100	2.92	5.51
[21]	9	212	212	2	4	1.5	1.5	30.8	68.6	31.2	46.8	2	5.44
[22]	17	260	305	2.5	4	1.0	3.55	26.5	47.6	11.2	48.7	1.57	3.03
[23]	4	219	219	2	2.8	1.9	1.92	40.9	43.2	60	120	2.93	3.52
[24]	10	381	381	3.4	3.5	1.9	2.67	31	49.2	60	90	2.53	3.77
[25]	8	381	381	3.4	3.5	2	2.7	31	44.9	41.2	82.5	2.6	3.4

5. The GMDH-based equation

In order to construct GMDH network and preventing overfitting, the database was divided randomly in two sets. The overfitting occurs when the error on the training set is driven to a very small value, but when new data is presented to the network the error is large. 74 experimental data were considered for training state and remaining data for testing state. Shear span-effective depth ratio, effective depth of beams, longitudinal reinforcement ratios, concrete compressive strength of standard cylinder, and fiber ratio were utilized as the input variables of the model, and average shear stress of SFRC beam was chosen as the target variable. Shear stress can be obtained using the following equations:

$$\begin{aligned} v_{GMDH} = {} & 2.273 + 4 * 10^{-6} d^2 - (1.92 + 0.26\rho + 0.013\acute{f_c} - 0.38\, {}^{a}/_{d})\, {}^{a}/_{d} \\ & + (0.84 + 0.00185F_{SF})\rho + 0.07\acute{f_c} + (0.025 - 0.0001F_{SF})F_{SF} \end{aligned} \tag{9}$$

In order to verify and quantify the proposed relationship, the predicted values were compared with the three existing models introduced in Section 2 based on a broad range of experimental results. The simulated shear stress compared to the existing equations are plotted in Figure 1. It is found that, the proposed GMDH-based formulation demonstrated the most optimized result compared to all of the other existing formulations. The average absolute error of the GMDH formulation for determining the experimental results is equal to 10% while the

average error for the other three models including Narayanan and Darwish, Khuntia et al., and Sharma are 14.70%, 30.96%,and 22.34% respectively. It should be noted that the best performance of the proposed equation is addressed in the considered ranges of the input parameters.

6. Conclusion

In this paper, a new formulation is developed to determine average shear stress of SFRC beams without web reinforcement. Five input parameters representing shear span-effective depth ratio, effective depth of beams, longitudinal reinforcement ratios, compressive strength of concrete, and fiber ratio were considered as input vectors. In order to overcome overfitting issue, the database was divided randomly in training and testing sets. The results of comparative assessment between existing equations and proposed method reveal that the GMDH model has acceptable ability to determine average shear stress. Finally, it could be concluded that the GMDH-based formulation can be utilized as an alternative method in the pre-design of SFRC beams.

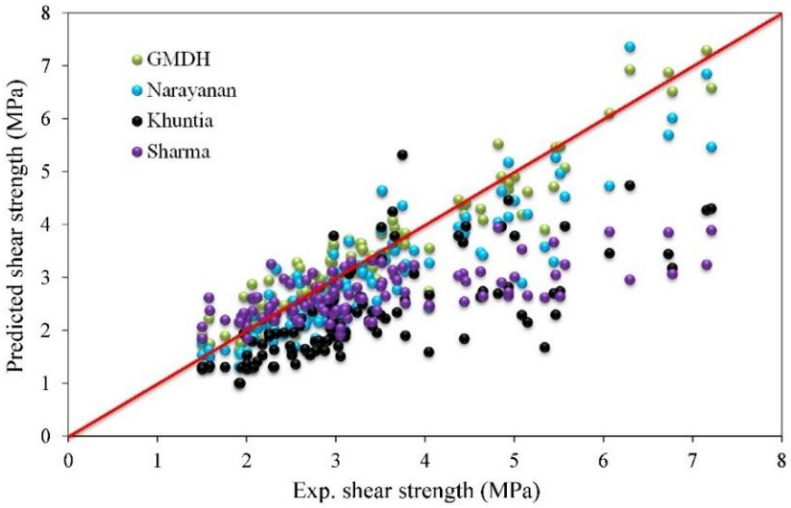

Figure 1. Experimental value against predicted shear strengths

References

[1] M. Shahnewaz, M.S. Alam, Improved shear equations for steel fiber-reinforced concrete deep and slender beams, ACI Struct. J. 111 (2014) 851.

[2] F. Pacheco-Torgal, S. Jalali, Cementitious building materials reinforced with vegetable fibres: A review, Constr. Build. Mater. 25 (2011) 575–581.

[3] C.-C. Chen, C.-Y. Li, Punching shear strength of reinforced concrete slabs strengthened with glass fiber-reinforced polymer laminates, ACI Struct. J. 102 (2005) 535.

[4] E. Cuenca, J. Echegaray, P. Serna, A. Pasetto, Ductility analysis on the post-peak behavior of self-compacting fiber reinforced concrete (SCFRC) beams subjected to shear, in: 8th RILEM Int. Symp. Fibre Reinf. Concr. Challenges Oppor. (BEFIB 2012), 2017.

[5] A. Hemmati, A. Kheyroddin, M. Sharbatdar, Y. Park, A. Abolmaali, Ductile behavior of high performance fiber reinforced cementitious composite (HPFRCC) frames, Constr. Build. Mater. 115 (2016) 681–689.
[6] A. Hemmati, A. Kheyroddin, M.K. Sharbatdar, Plastic hinge rotation capacity of reinforced HPFRCC beams, J. Struct. Eng. 141 (2013) 4014111.
[7] H. Singh, Steel Fiber Reinforced Concrete: Behavior, Modelling and Design, Springer, 2016.
[8] S.-H. Cho, Y.-I. Kim, Effects of steel fibers on short beams loaded in shear, Struct. J. 100 (2003) 765–774.
[9] R. Narayanan, I.Y.S. Darwish, Use of steel fibers as shear reinforcement, Struct. J. 84 (1987) 216–227.
[10] M. Khuntia, B. Stojadinovic, S.C. Goel, Shear strength of normal and high-strength fiber reinforced concrete beams without stirrups, Struct. J. 96 (1999) 282–289.
[11] A.K. Sharma, Shear strength of steel fiber reinforced concrete beams, in: J. Proc., 1986: pp. 624–628.
[12] A.G. Ivakhnenko, Polynomial Theory of Complex Systems, IEEE Trans. Syst. Man. Cybern. SMC-1 (1971) 364–378. doi:10.1109/TSMC.1971.4308320.
[13] M. Ahmadi, H. Naderpour, A. Kheyroddin, Utilization of artificial neural networks to prediction of the capacity of CCFT short columns subject to short term axial load, Arch. Civ. Mech. Eng. 14 (2014) 510–517. doi:10.1016/j.acme.2014.01.006.
[14] M. Ahmadi, H. Naderpour, A. Kheyroddin, ANN Model for Predicting the Compressive Strength of Circular Steel-Confined Concrete, Int. J. Civ. Eng. 15 (2017) 213–221. doi:10.1007/s40999-016-0096-0.
[15] A. Kheyroddin, H. Naderpour, M. Ahmadi, Compressive strength of confined concrete in CCFST columns, J. Rehabil. Civ. Eng. 2 (2014) 106–113.
[16] M.A. Mansur, K.C.G. Ong, P. Paramasivam, Shear strength of fibrous concrete beams without stirrups, J. Struct. Eng. 112 (1986) 2066–2079.
[17] S.A. Ashour, G.S. Hasanain, F.F. Wafa, Shear behavior of high-strength fiber reinforced concrete beams, Struct. J. 89 (1992) 176–184.
[18] V.C. Li, R. Ward, A.M. Hamza, Steel and synthetic fibers as shear reinforcement, ACI Mater. J. 89 (1992) 499–508.
[19] K.H. Tan, K. Murugappan, P. Paramasivam, Shear behavior of steel fiber reinforced concrete beams, Struct. J. 90 (1993) 3–11.
[20] R.N. Swamy, R. Jones, A.T.P. Chiam, Influence of steel fibers on the shear resistance of lightweight concrete I-beams, Struct. J. 90 (1993) 103–114.
[21] Y.-K. Kwak, M.O. Eberhard, W.-S. Kim, J. Kim, Shear strength of steel fiber-reinforced concrete beams without stirrups, ACI Struct. J. 99 (2002) 530–538.
[22] D. Dupont, L. Vandewalle, Shear capacity of concrete beams containing longitudinal reinforcement and steel fibers, Spec. Publ. 216 (2003) 79–94.
[23] C. Cucchiara, L. La Mendola, M. Papia, Effectiveness of stirrups and steel fibres as shear reinforcement, Cem. Concr. Compos. 26 (2004) 777–786.
[24] H.E. Yakoub, Shear stress prediction: Steel fiber-reinforced concrete beams without stirrups, ACI Struct. J. 108 (2011) 304.
[25] H.H. Dinh, G.J. Parra-Montesinos, J.K. Wight, Shear Behavior of Steel Fiber-Reinforced Concrete Beams without Stirrup Reinforcement, ACI Struct. J. 107 (2010).

SELF-HEALING AND REPAIR OF CONCRETE STRUCTURES
(COST CA15202 - SARCOS)

SynerCrete'18 International Conference on Interdisciplinary Approaches
for Cement-based Materials and Structural Concrete
24-26 October 2018, Funchal, Madeira Island, Portugal

A METHOD FOR INDUCING CONTROLLED CRACKS IN CONCRETE AND MEASURING THE EFFICIENCY OF SELF-HEALING AGENTS

Amir Sidiq [(1)], Syed Adil Amzar Bin Syed Amerruddin[(1)], Rebecca Gravina[(1)], Sujeeva Setunge[(1)], Filippo Giustozzi[(1)]

(1) Royal Melbourne Institute of Technology – RMIT University, 376-392 Swanston st., Melbourne, VIC 3000, Australia

Abstract

Durability and mechanical properties of concrete decreases with time due to cracking, resulting in contaminant ingress such as rapid chloride penetration and water particles transferred through these cracks to cause corrosion of the steel in reinforced concrete. The present research presents a method to induce cracking throughout the entire concrete sample's volume homogenously. By placing a cylindrical concrete sample into an ad-hoc steel mould and applying a compressive loading, confined axial and circumferential pressure is generated that induces controlled cracks in the sample. This procedure is used to induce a specific amount of cracks in the concrete sample hence triggering the repairing action of the self-healing agent. This method overcomes common drawbacks of self-healing efficiency measurements where a single crack is usually being generated by a standard flexural test on beams. X-ray tomography analysis was adopted to calibrate the internal state of damage generated into the sample.

1. Introduction

Cracking occurrence in concrete structures is expected at any stage during the life span of the structure typically under tension stresses due to limited tensile characteristics [1]. Due to cracking, the durability and structural capacity of concrete are compromised in an aggressive environment since chlorides and atmospheric water can infiltrates through the cracks and permeate the concrete matrix [2], which will lead to diffusion and enlargement of micro-cracks. Subsequently, corrosion in reinforcement may occur and the risk of failure of the structure increases [3]. To determine the efficiency of self-healing of concrete, research

studies tend to develop artificial cracks in cementitious materials. Conventionally, there are limited techniques available for developing cracks in concrete including four-point bending, three-point bending and split tensile testing. Researchers utilise these test methods to determine the onset of cracking and calculate the crack load capacity for a specific concrete material design and then use this experiment to obtain cracks based on their requirements for self-healing. A few studies utilised split test to generate single cracks in their specimens and further test healing efficiency of the mix [4]. Other studies used the three-point bending test to develop single cracks in the mid-span of a concrete beam [5]. However, the majority of studies on concrete healing use the four-point bending test to initiate cracks [6]. Several methodologies have also been applied to quantify the internal cracking of damaged concrete samples. Researchers utilized non-destructive test methods for crack detection and evaluation, such as ultrasonic methods [7], X-Ray tomography [8], acoustic emission [8] and ground penetrating radar [9]. In this paper an innovative method to induce controlled crack damage in the entire concrete sample was developed. The experiment was conducted by applying various percentage of maximum concrete compressive strength in a specifically-developed steel mould. Measurements before and after sample damaging were taken and comparison related to internal void content, recovery of compressive strength and stiffness were also conducted.

2. Materials and Methodology

The concrete mix consisted of water to cement, sand to cement and aggregate to cement ratio of 0.54, 1.83 and 2.42, respectively. Target compressive strength of the mix was 30-40 MPa although mechanical resistance was not a main focus of the present study, which was instead intended to develop a procedure to generate controlled damage state inside the samples. Cylindrical samples were casted as per AS 1012.8.1-14 [10] with diameter of 100 mm and height of 200 mm. Samples were demoulded after 24 hours and wet cured for 28 days.

2.1 Steel mould fabrication and illustration

A specific steel mould was developed to obtain a controlled internal damage. The designed mould consisted of two semi-circular sections with side plates connected through bolts. Finite Element analysis was used to determine the appropriate thickness of the mould and bolt strength depending on the concrete ultimate strength. The circumference of the mould was 1% larger than the cylindrical sample (with this value depending on the preliminary FE analysis of stresses and strain as well as to accommodate possible small asperities of the sample after demoulding); the height was designed as to accommodate samples of up to 250 mm. Depending on the height of the sample, circular steel plates could be placed at both ends of the mould to provide uniform compression.

2.2 Sample damaging

Concrete cylindrical samples were removed from the water bath after 28 days and dried for two hours at ambient temperature. Samples were then labelled and measured, and Ultrasonic Velocity Pulse (UPV) test was conducted according to ASTM C597-16 [11] to identify the stiffness of concrete before damaging it. Three samples were tested without any confinement to measure the unconfined compressive strength at failure of concrete after 28 days of curing

(e.g. undamaged condition). The remaining samples were then put in the steel mould and incremental loads corresponding to 10%, 15%, 25%, 40%, 55%, 70% and 85% of the maximum strength (unconfined) were applied to generate internal cracking. Four samples were 'damaged' at each loading condition, with one of them being used to evaluate the internal cracking through X-ray testing. UPV measurements were taken after each loading step to obtain the samples' residual stiffness and compressive strength at damaged condition.

2. 3 X-Ray Tomography - µCT scan

In this experiment Bruker Skyscan 1275 X-Ray micro-tomograph was used to determine internal porosity and cracking. Concrete samples with diameter of 55 mm and height of 67 mm were placed on the micro-positioning stage. When the X-ray beam passes through the concrete sample, the intensity is attenuated due to the concrete absorption and the detector receives the residual intensity hence producing the 2D image. At 0.2 degree rotation around its axis and resolution of 1540x1540 a total of 1535 images with thickness of 35 µm were obtained. Porosity and crack development were further investigated.

3. Analysis of Results

3.1 Internal Damage Evaluation

The X-ray tomography was used to determine the porosity induced in the concrete samples; due to differential compression loading and the ad-hoc fabricated mould, an internal damage state was developed. All samples were analysed by separating the internal air phase (e.g. voids and cracks) from the solid phase (e.g. aggregates and cement mortar) for each 2D image. Material with higher density was observed with lighter grey intensity whereas air pores were dark grey coloured due to less attenuation of the translated intensity [12]. To determine the porosity of various concrete samples and controlled cracks, the optimum of 44-255 grey level threshold was used throughout the entire experiment for consistency of results. Global thresholding algorithm to convert the image to binary from the grey-scale image followed by the application of Otsu's method [13] to further separate the pores and solid phases, were applied during post-processing of x-ray results. The results in Fig. 1 show the porosity of different crack-controlled damages in comparison to undamaged concrete sample (average of 8 undamaged samples). Fig. 2-4 depicts the frequency with respect to sphericity and volume of internal pores at 25% and 85% crack controlled damage in comparison to undamaged samples.

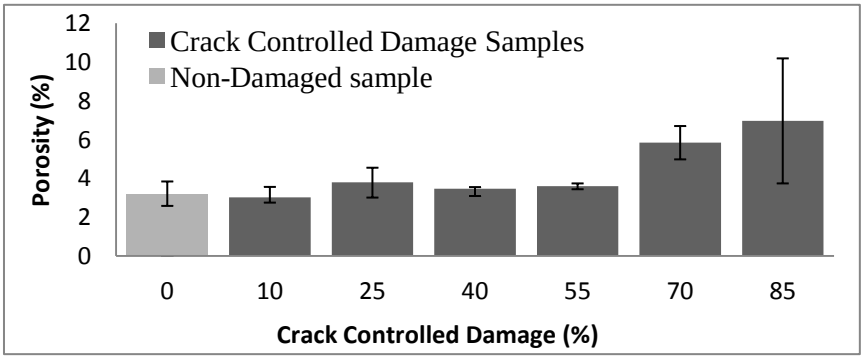

Figure 1: porosity of damaged samples

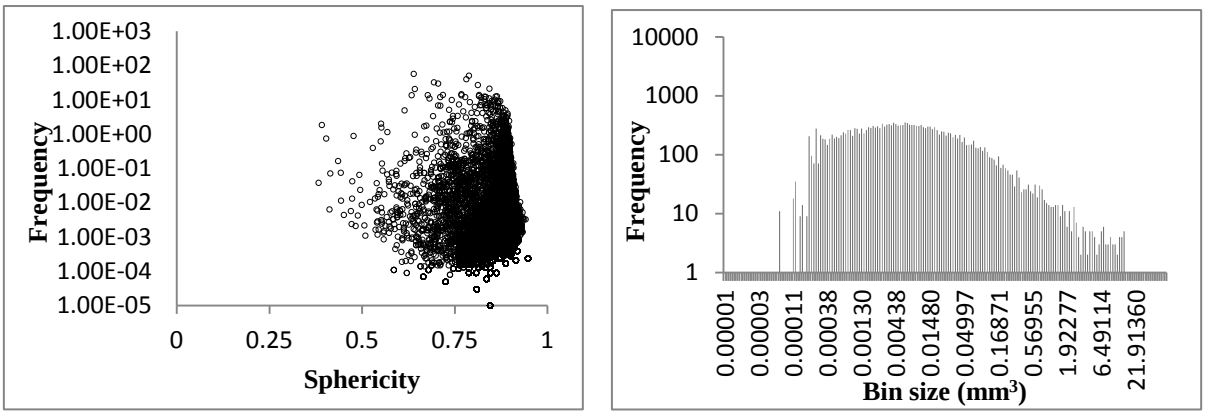

(A) (B)

Figure 2: Frequency of sphericity (A) and bin size (B) of pores for undamaged sample

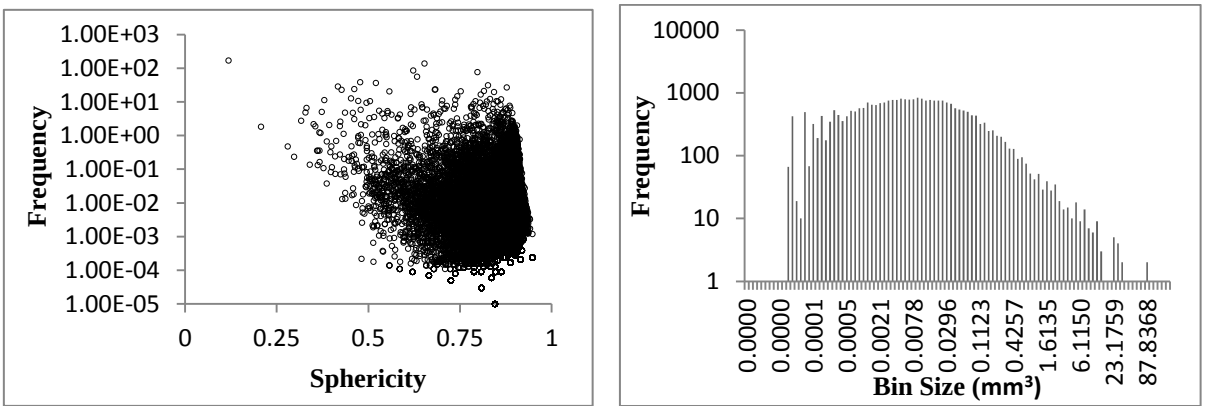

(A) (B)

Figure 3: Frequency of sphericity (A) and bin size (B) of pores for 25% damage

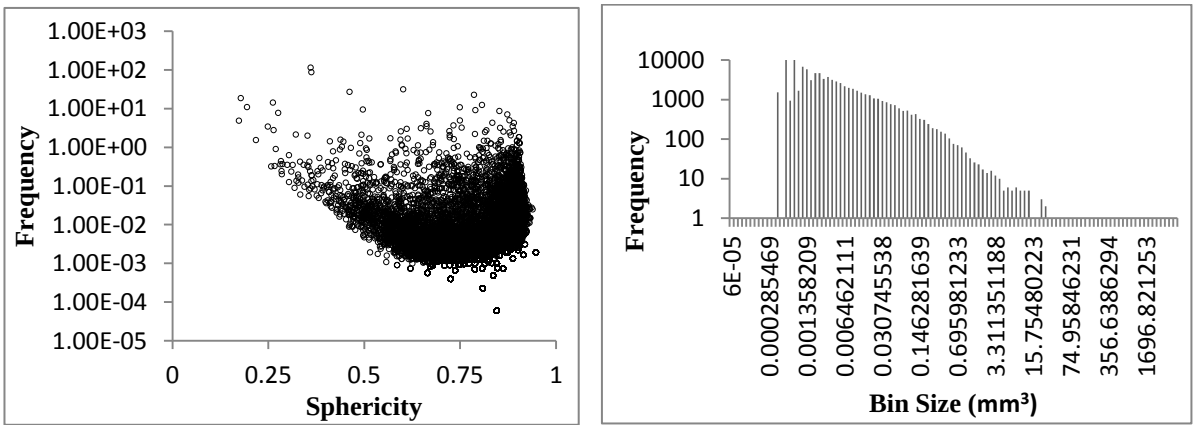

(A) (B)

Figure 4: Frequency of sphericity (A) and bin size (B) of pores for 85% damage

3.2 Compressive strength and stiffness

MTS 1000 kN was used to induce cracks in concrete samples through the steel mould and compressive strength test. After cracks were being induced at different loading levels,

concrete samples were tested under ultimate compressive strength to obtain the residual compressive strength after damage. Fig. 5 shows the compressive strength and residual stiffness modulus at various damage levels in comparison to the control mix. Dynamic modulus of elasticity was measured before and after inducing cracks on the same sample through Ultrasonic Velocity Pulse test.

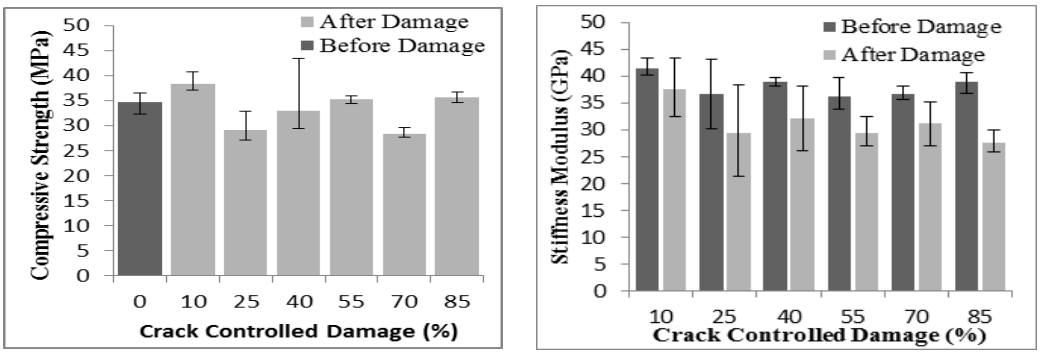

Figure 5: Compressive strength and residual stiffness of concrete after inducing cracking

4. Discussion and conclusions

Compared to common methods that only trigger one single crack (or a few cracks in correspondence to the point of maximum stress), the present approach showed an early possibility to generate cracks of various size and shape inside the entire volume of the sample. The ad-hoc developed steel mould, coupled with X-ray analysis and non-destructive testing, could represent a viable alternative to study the efficiency of healing agents in cementitious materials. The evaluation of the internal damage only based on mechanical testing is in fact a not fully reliable method as depicted in Fig. 5; results showed great variability and very small differences were noticed among different damage levels. The application of loading rates between 10% and 55% proved to generate very small cracking patterns with these being not easy to capture by the X-ray machine; thin capillary cracking (e.g. less than 10-30 μm) can be overlooked due to the equipment resolution. UPV testing was able to capture small variations in stiffness (Fig. 5) before and after damage although variability was slightly high.

Internal porosity was evaluated according to its overall magnitude but also through the study of the distribution of shape and volume of the cracks. From Fig. 2-4, one can observe that the sphericity of the cracks is very close to 1 (perfect sphere) in undamaged samples – bottom right of the graph – and moves to the upper left area of the graph with increasing damage intensity. Sphericity tends to shift from a value of 1 to 0.5 (and lower) thus indicating the change in shape of internal voids due to the formation of the cracks and their geometrical inconsistency. The distribution of the volume of internal voids also follows a clear trend where a greater damage (e.g. 85%) corresponds to bigger voids and the shifting of the volume distribution towards the right side of the histogram scale.

As general representation of results, Fig. 6 shows the 3D visualization of three concrete samples under X-ray at undamaged, 25% and 85% damage conditions.

Based on the results, the fabricated steel mould for developing internal cracks in concrete cylindrical specimens showed to be a viable alternative to generate cracking patterns inside

the sample overcoming common approaches that only simulate single cracks, or a group of cracks in a small specific area of the sample. With proper calibration of the external load to be applied to the sample, the size, shape and volume of the cracks can be modified. Healing agents could achieve different results depending on size and density of the cracks to be filled.

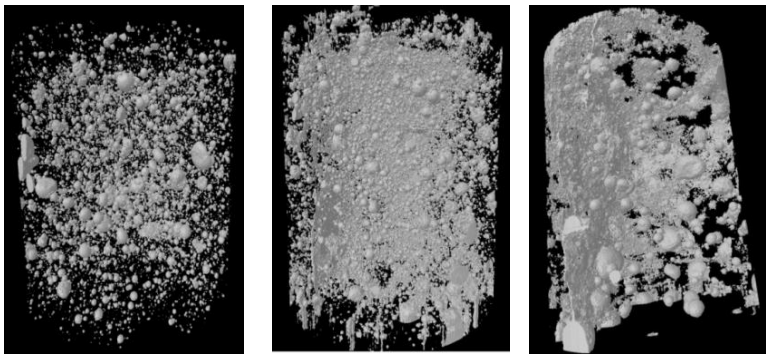

(A) undamaged sample (B) 25% damage (C) 85% damage

Figure 6: 3D visualization of undamaged sample compared to 25% and 85% damage

References

[1] Chahal, N., R. Siddique, and A. Rajor, Influence of bacteria on the compressive strength, water absorption and rapid chloride permeability of fly ash concrete. Construction and Building Materials, 2012. 28(1): p. 351-356.
[2] Picandet, V., A. Khelidj, and H. Bellegou, Crack effects on gas and water permeability of concretes. Cement and Concrete Research, 2009. 39(6): p. 537-547.
[3] Van Tittelboom, K. and N. De Belie, Self-healing in cementitious materials—A review. Materials, 2013. 6(6): p. 2182-2217.
[4] Van Tittelboom, K., et al., Self-healing efficiency of cementitious materials containing tubular capsules filled with healing agent. Cem. Conc. Composites, 2011. 33(4): p. 497-505.
[5] Qureshi, T. and A. Al-Tabbaa. The effect of magnesia on the self-healing performance of Portland cement with increased curing time. in 1st International Conference on Ageing of Materials & Structures. 2014.
[6] Van Tittelboom, K., et al., The efficiency of self-healing concrete using alternative manufacturing procedures and more realistic crack patterns. Cement Conc. Comp., 2015. 57.
[7] Clayton, D.A., et al., Evaluation of Ultrasonic Techniques on Concrete Structures. 2013, Oak Ridge National Laboratory (ORNL).
[8] Suzuki, T., et al., Use of acoustic emission and X-ray computed tomography for damage evaluation of freeze-thawed concrete. Const. B. Materials, 2010. 24(12): p. 2347-2352.
[9] Eisenmann, D., et al. Inspection of a large concrete block containing embedded defects using ground penetrating radar. in AIP Conference Proceedings. 2016. AIP Publishing.
[10] Method for making and curing concrete. Compression and indirect tensile test specimens. 2018.
[11] ASTM C597 - 16 Standard Test Method for Pulse Velocity Through Concrete. 2018.
[12] Fan, S. and M. Li, X-ray computed microtomography of three-dimensional microcracks and self-healing in engineered cementitious composites. Smart Mat. Struc., 2014. 24(1).
[13] Manahiloh, K.N., et al., X-ray computed tomography and nondestructive evaluation of clogging in porous concrete field samples. J. Mat. Civil Eng., 2012. 24(8): p. 1103-1109.

SynerCrete'18 International Conference on Interdisciplinary Approaches
for Cement-based Materials and Structural Concrete
24-26 October 2018, Funchal, Madeira Island, Portugal

A PRELIMINARY STUDY ON THE SELF-HEALING POTENTIAL OF BACTERIA-MODIFIED FIBERS IN CONCRETE

Kira Weise [(1)], Henk Jonkers [(2)], Eddie Koenders [(1)]

(1) Institute of Construction and Building Materials, TU Darmstadt, Germany
(2) Microlab, Delft University of Technology, Delft, The Netherlands

Abstract

Enhancing the self-healing potential of cementitious materials can be achieved in many different ways. An innovative method that gained a lot of attention is to add concrete compatible bacteria to a mixture that reacts when activated with oxygen and water, and produces limestone with the ability to fill up cracks. Most challenging is how to add the bacteria into a concrete so that they survive and are properly positioned with access to the nutrient (lactate). A common way is to add bacteria and precursor together in a porous clay particle, or more recently, adding them as a compressed pill. In this contribution, results of a preliminary study will be presented that show the potential of modifying polypropylene fibres with bacteria and its nutrient. In addition to the bacteria to produce limestone at the crack surfaces, limestone was also formed in the crack opening. This mechanism showed an accelerated self-healing process with the potential to close wider cracks. The study reports first results of various ways to modify the fibres with bacteria with emphasis of the adhesion between fibres and bacteria. The preliminary study showed interesting results and demonstrated the difficulties of getting the bacteria properly coated on fibre surfaces.

1. Introduction

Using self-healing materials cannot only save a lot of maintenance costs but also has the potential to preserve resources and cut back CO_2 emissions. An innovative approach to use bacteria in the concrete mixtures that are activated by oxygen and water after crack occurrence enable to produce limestone as a repair agent for cementitious matrix. With present methods it is possible to heal cracks up to widths of 0.8 mm [1, 2]. However, it turned out that closing these crack sizes with healing agent goes along with a lot of uncertainty. This paper contributes to this issue and presents a preliminary study with the aim to make the healing process for larger crack width more reliable and even more efficient. The conceptual

idea is on the modification of polymer fibres by covering their surfaces by a thin layer of bacteria or blending them in a polymer melt, so that after cracking the limestone will not only be produced on the crack surfaces, but also on the fibres itself, enhancing the healing potential of wider cracks.

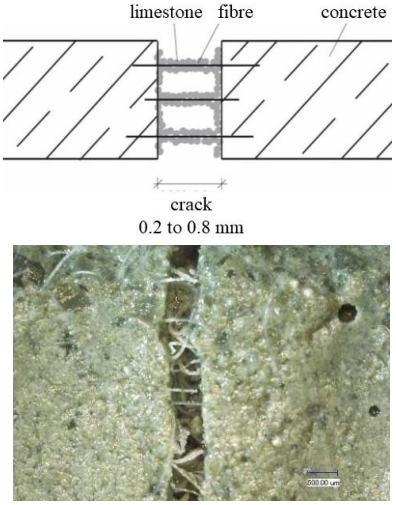

Figure 1: Crack bridging of bacteria-modified polymer fibres.

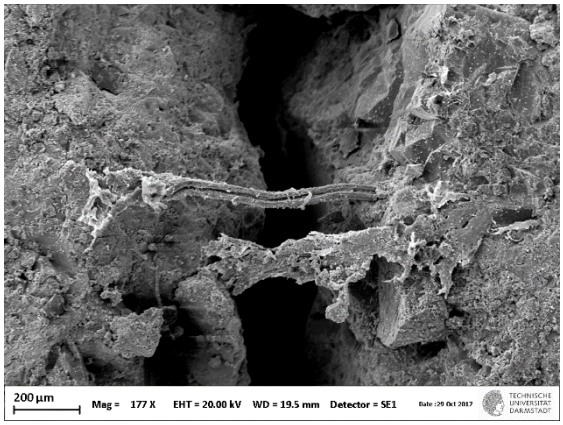

Figure 2: Limestone production on crack bridging polymer fibre.

Fig. 1 and 2 show the basic principles of the mechanism as addressed in this paper. Due to the formation of limestone on the fibres an acceleration of the bio-based self-healing mechanism and its potential to close wider cracks would be very likely. A first step in the development of this method would be on the modification of the fibres, or in this case, on the addition of bacteria on the fibre surfaces. In this paper, four different methods are presented to achieve this, and their performance is evaluated.

2. Materials and methods

The polymer fibres used in this study were received from the company Baumhueter extrusion GmbH [3]. The fibres are made of polypropylene, which is a thermoplastic synthetic polymer. While mixed in a cementitious system, polymer fibres have the potential to bridge micro cracks, reduce shrinkage and enhance the material's fire resistance. In this study, modifying the fibres with a bacteria-nutrient solution was done for a fibre length of 6 mm. In addition to this, uncut fibre strands were used for the modification process, with a liquid polyactide (PLA) granulate and a gluing method. Fig. 3 and 4 show a few grams and a detailed view of polymer fibres used. The bacteria applied for this specific purpose need to be able to produce spores that survive in the high alkalinity of a cementitious system. Researchers from TU Delft [4] found a bacteria type that fulfils these needed criteria. When a crack occurs the bacteria is activated by oxygen and water and produces limestone that fills the crack. For this process, nutrients like for example calcium lactate and yeast extract are required. An impression of the used raw materials are shown in Fig. 5 to 7. For easy handling, storing, transport and preparation, as well as to avoid inhalation of these ultra-fine particles, the bacteria spores were dried on limestone powder. From this, Green-Basilisk B.V. produces concrete resistant PLA granulate that was also used as the healing component in this study [5].

Figure 3: Polymer fibres.

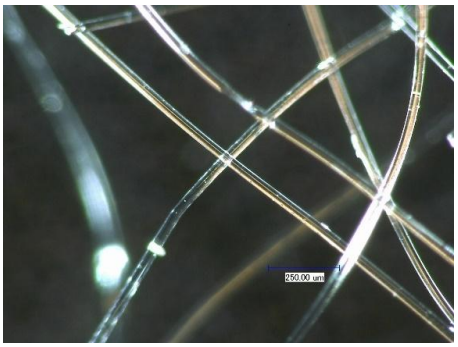

Figure 4: Magnified polymer fibres.

Figure 5: Bacteria spores.

Figure 6: Calcium lactate.

Figure 7: Yeast extract.

Figure 8: PLA granulate 0.25 to 0.5 mm (right) and 0.5 to 1.0 mm (left).

In general, the applied bio-based agent consists of polyactide (PLA), bacteria spores and yeast extract [6]. On one hand PLA protects the bacteria from water and mechanical abrasion, and on the other hand it acts as a nutrient. Fig. 8 gives an impression of the used PLA granulate in two different particle sizes. These materials were used for this study with the main aim to either modify the polymer fibres by producing a blend or to try to cover each individual fibre with a thin layer of it. This was the main difficulty of this approach, namely to find a robust procedure for getting the bacteria and nutrient properly blended in, or on the fibre surface [5]. In order to get an impression about ability to possibilities and their robustness, in this study the adhesion between four different combinations of polymer fibres and bacteria are investigated on their fibre modification potential and their performance. These methods are described in the next sections followed by a systematic evaluation.

a) Bacteria-nutrient solution

A bacteria-nutrient solution was made of water, bacteria spores, calcium lactate and yeast extract. Two different fibre types (multifil and splicing film fibres) with a length of 6 mm were wetted with this solution and dried in an oven afterwards.

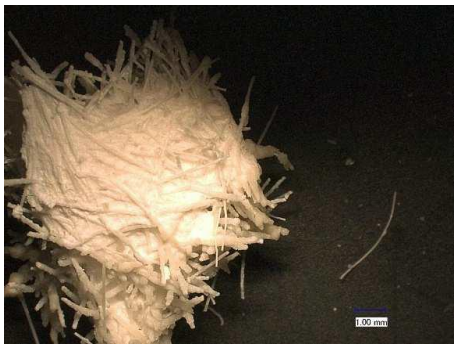

Figure 9: a) Bacteria-nutrient solution.

b) Liquefied PLA granulate

For this modification method, PLA granulate was melted and uncut multifil fibre strands were pulled through it manually. A detailed impression of the final result is provided in Fig. 10, showing the irregularities in the coated fibres.

Figure 10: b) Liquefied PLA granulate.

c) Gluing method

Different types of commercial glues as well as wax and resin were spread over uncut multifil fibre strands. Subsequently, calcium lactate was attached to them.

Figure 11: c) Gluing method (wax).

d) Melted polymer and PLA granulate

Polymer fibres and PLA granulate were melted and stirred together. From this melt fibres were pulled manually. Fig. 12 shows the polymers in a melted situation.

Figure 12: d) Melted polymer and PLA granulate.

3. Results and discussion

All four techniques showed various difficulties in the bacteria-modification process, in particular the adhesion process. To enable an accelerated self-healing process with the potential to close wider cracks by bacteria-modified polymer fibres, the way of properly combining both components is of mayor importance. The bacteria modified polymer fibres need to fulfil various specifications. On one hand, to guarantee an adequate self-healing

process, meaning that the bacteria should to be distributed homogenously in the fibre or over its full surface. On the other hand is it necessary that both components act as a stable system in the cementitious matrix. The bacteria-modified polymer fibres need to be resistant against mechanical abrasion and water, especially with regard to the concrete mixing process, where both influences may occur simultaneously. When modifying the fibres with a bacteria-nutrient solution, agglomerations formed that lumped multiple fibres to an Igel-like configuration. As a result, the modified fibres were not resistant against mechanical abrasion and were soluble in water (Fig. 13). The same issue was observed when gluing the healing components on the fibres` surface (Fig. 15). Distributing the bacteria homogenously in or on the fibre was difficult to achieve for all modification techniques applied (Fig. 11, 13, 14 and 16). When modifying the fibres by adding them in a melt of PLA granulates, and successively pulling fibres from a melt of PLA and polypropylene, a reasonable resistance against mechanical abrasion and water was reached. A more detailed evaluation of the different techniques is outlined in Tab. 1.

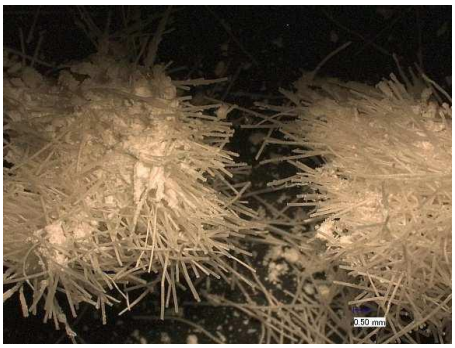

Figure 13: a) Broken agglomeration.

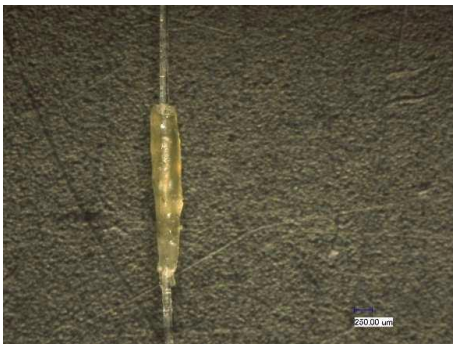

Figure 14: b) No homogenous distribution.

Figure 15: c) No resistance against mechanical abrasion.

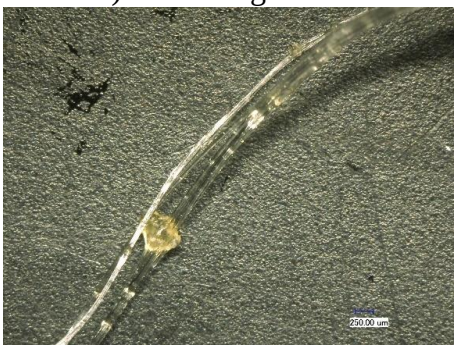

Figure 16: d) No homogenous distribution.

It turned out that for the bacteria-modified polymer fibres the lack of resistance against mechanical abrasion and water was the main issue that could be improved by adding a coating on the fibre surface. From this, the highest potential was identified for the modification with melted PLA granulate and with pulling fibres from a melt of PLA and polypropylene. The fact that the components of the healing agent were not distributed homogenously in or on the fibre surface (Fig. 16) was mainly because of the manual application, as done in this study. This procedure could probably be improved with an automated modification process. In this way, a controlled modification of the fibre, consisting of polymers and the healing agent could be achieved.

Table 1: Evaluation of different modification techniques (- : 1 point, 0 : 2 points, + : 3 points).

	a) Bacteria-nutrient solution	b) Liquified PLA granulate	c) Gluing method	d) Melted polymer and PLA granulate
Homogenous distribution	0	-	0	-
Water resistance	-	+	0	+
Resistance against mechanical abrasion	-	+	-	+
Total	**4**	**7**	**5**	**7**

4. Conclusion

A preliminary study has been conducted that showed conceptual results on modification techniques, and demonstrated the difficulties of getting the bacteria properly attached to the surface, or blended with the polymer fibre. The presented techniques provide a basis for further research by showing main influencing factors as well as potentials and problems whenever developing bacteria-modified fibres. Identified difficulties are on one hand, the lack of resistance against mechanical abrasion and solubility in water, which could be improved with an additional coating on top of the modified fibre. On the other hand, this study shows problems of distributing the bacteria homogenously in or on the fibre surface. This issue could be due to the manual application methods applied. Possibly, this problem could be solved by modifying the fibres by automatic processing. Further research is needed to improve and expand the presented techniques of modifying polymer fibres with bacteria to reach a more efficient self-healing process in cementitious systems.

Acknowledgement
The authors acknowledge support from EU COST Action CA15202-SARCOS, and also from the EU H2020 SUPERCONCRETE Project (H2020-MSCA-RISE-2014 n 645704).

References

[1] Zhang, J. et al., Immobilizing bacteria in expanded perlite for the crack self-healing in concrete, Construction and Building Materials (2017), 610-617
[2] Luo, M. et al., Factors affecting crack repairing capacity of bacteria-based self-healing concrete, Construction and Building Materials (2015), 1-7
[3] Baumhueter extrusion GmbH, https://www.baumhueter-extrusion.de/produkte/pb-eurofiber/funktionsfasern-fuer-moertelmassen/
[4] Jonkers, H.M., Self Healing Concrete: A Biological Approach, Springer Series in Materials Science (2007), vol 100, Springer, Dordrecht
[5] Backes, F., Applikationstechnik, Wirkungsgrad und Mechanismus der Rissschließung faserbewehrter selbstheilender Mörtel, M.Sc. Thesis, TU Darmstadt (2017)
[6] Green-Basilisk B.V., http://www.basiliskconcrete.com/product-healing-agent/?lang=en

SynerCrete'18 International Conference on Interdisciplinary Approaches
for Cement-based Materials and Structural Concrete
24-26 October 2018, Funchal, Madeira Island, Portugal

ACTIVE MINERAL ADDITIVES AND THEIR CONTRIBUTION TO NATURAL SELF-HEALING ABILITY OF CONCRETE

Pavel Reiterman [(1)]

(1) Czech Technical University in Prague, Prague, Czech Republic

Abstract

Reducing of maintenance costs of concrete structures have got into increased professional concern. The protection of existing structures is determined by their primary resistance to the action of the environment, secondarily by additional performance. Concrete is effective material with sufficient structural properties, however the efficiency of its use is essentially dependent on the level of maintenance costs. Present paper is focused on the experimental study dealing with primary resistance of concrete, which is determined by its composition and selection of particular components. The great potential for durability increase of structural concrete have various types of supplementary cementitious materials (SCM), which have beneficial effect on the durability and environment quality. There was studied influence of fly ash, ceramic powder and metakaolin addition. The properties of concrete are evaluated in terms of freeze-thaw resistance and mechanical properties. The experimental program performed confirmed positive impact of active mineral additives on the frost resistance of concrete mixtures with SCMs addition. On the basis of results of residual mechanical properties during cycle freeze-thawing can be assumed, that cycle freeze-thawing could stimulate blended binding system to additional hydration, which led to the partial strengthening. This effect could create reserve leading to the increase of frost resistance.

1. Introduction

Number of relatively new existing concrete structures exhibit significant deterioration due to progressive impact of external environment. It is caused by the limited primary resistance of used concrete, which is determined by its composition. That is why, the development of new concrete mixes is closely related to the assessment of final durability performance. There is also significant simultaneous need to reduce energy consumption, which is related to the production of concrete and Portland cement, respectively, by using various SCMs [1]. Besides positive environmental effect, they considerably contribute to the durability of concrete [2,3].

Increased durability performance of concrete has direct impact on final maintenance costs, which are invested to infrastructure to ensure its service. That is why, technologies able to ensure prolongation of service-life of current concrete structures are concerned through scientific community [4]. Present paper is focused on the assessment of autogenous self-healing ability of concrete exposed to freeze-thaw cycling. Studied technology is closely related to the application of various SCMs, which later hydration after freezing-thawing was monitored. Present work corresponds with focus of COST Action "Self-healing as preventive repair of concrete structures".

2. Experimental program

Performed experimental program was focused on the determination of residual compressive strength of cement based mortars modified by various SCMs, ceramic powder, fly ash, blast furnace slag and metakaolin were used. Studied mineral additives were applied as 10.0% cement replacement by mass. Chemical composition of used additives and Portland cement is introduced in Tab. 1.

Table 1: Chemical composition of used binding components [%].

Component	Cement	Ceramic powder	Fly ash	Blast furnace slag	Metakaolin
SiO_2	18.5	18.5	52.4	36.0	53.1
Al_2O_3	6.5	6.5	35.9	9.0	41.7
Fe_2O_3	2.4	2.4	4.9	0.3	1.08
CaO	64.9	64.9	1.2	43.5	0.13
MgO	1.0	1.0	0.8	8.3	0.18
K_2O	1.2	1.2	1.4	0.5	-
Na_2O	0.1	0.1	-	0.5	-
TiO_2	-	-	2.4	0.3	1.8
SO_3	4.9	4.9	0.2	0.5	0.7

Present binding components were mixed with natural siliceous sand of gradings 0-4mm in mass proportions 1:4, water to binder ratio was set to constant 0.55. Sets of prismatic samples 40×40×160 mm were produced from particular bathes. Samples were cured under standard laboratory conditions for 28 days.
Determination of flexural strength was carried out using three-point bending test with support span 100mm and axial loading. Compressive strength measurement was conducted using fragments left after bending test on loading area 40×40 mm. After 28 days started cyclic freezing-thawing in automatic chamber. Each cycle consisted on freezing phase lasting 4 hours and defrosting period performed by automatic flooding of testing chamber by water. Residual mechanical properties were determined after 25 cycles of freezing-thawing.

3. Results and discussion

Performed experimental program was focused on the determination of residual mechanical properties of cement based mortars modified by partial replacement by various SCMs after cyclic freezing-thawing. Conducted experiments confirmed previous observations during freezing-thawing, where initial increase of mechanical performance was monitored. Residual values of compressive strength after 25 cycles are shown in Fig. 1. It is necessary to note, that values of flexural strength were nearly similar after 25 cycles for all studied mixtures.

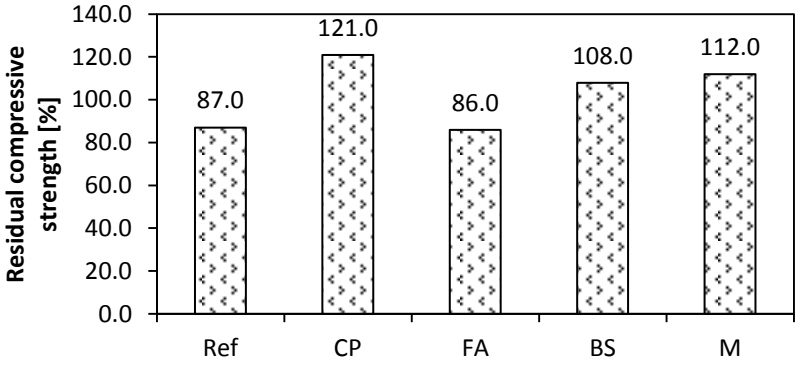

Figure 1: Residual compressive strength [%].

It is evident that 10% replacement by ceramic powder, blast furnace slag and metakaolin led to slight increase of compressive strength by 21%, 8% and 12%, respectively. On the other hand, control mixture as well as mixture with fly ash exhibited decay of mechanical performance by 13% and 14%, respectively. Gradual increase of mechanical performance of concrete mixes with mineral additives replacement during cyclic freezing-thawing was also in [5]. They confirmed additional hydration of binding components induced by action of frost. The positive effect of low temperatures on process of hydration of blended system was confirmed by number of experimental studies [6,7]. Because, the reduced hydration kinetic contributes to the long-term durability performance [8]. Observed mechanism lies in the ongoing hydration, which is positively supported by the presence of water and partial deterioration by micro-cracks propagation, which opens non-hydrated parts of used binding system. It is necessary to note, that present mechanism was observed only in case of mixtures with increased volume of the binder, so concretes with low content of binding components are not able to exhibit the above described self-healing effect. Increase of mechanical performance during freezing-thawing culminates in dependence on the loading regime and used composition, however after initial phases of cycling loading, studied mixtures exhibit gradual decay of mechanical properties. On the other hand, the initial increase create sufficient reserve before following loading induced by external environment.

4. Conclusions

Conducted experiments dealt with the influence of cyclic freezing-thawing on compressive strength of mortars with addition of various SCMs. Realized program confirmed previous

results and observation, that blended binding systems could exhibit increase of mechanical performance during cyclic freezing-thawing, especially in initial phases of loading. Such reached increase create sufficient reserve before additional loading. Laboratory testing related to the simulation of real condition is conducted by accelerated testing, however the effect of external environment is very slow. In Middle Europe the temperature drops below 0°C approximately 35-40 per year, what does not correspond with the kinetic of testing. In real conditions the effect of environment is cumulative, what contributes to the self-healing through stimulated by low temperatures. Controlling of the above described mechanism could significantly contribute the prolongation of service life of current concrete structures and infrastructure. Beneficial of this mechanism in the incorporation of waste materials such as waste ceramics, or materials related to reduced energy consumption such as fly ash, blast furnace slag and metakaolin, which can replace energy demanding Portland cement.

Acknowledgement
This research was supported by project No. LTC18063.

References

[1] Kubissa, W., Jaskulski, R. and Reiterman, P., Ecological Concrete Based on Blast-Furnace Cement with Incorporated Coarse Recycled Concrete Aggregate and Fly Ash Addition, J Renew Mater 5(2017), 53-61
[2] Khodabahshian, A., Ghalehnovi, M., de Brito, J. and Shamsabadi, A. E., Durability performance of structural concrete containing silica fume and marble industry waste powder, J Clen Prod 170 (2018), 42-60
[3] Duan, P., Shui, Z., Chen, W. and Shen, C., Influence of metakaolin on pore structure-related properties and thermodynamic stability of hydrate phases of concrete in seawater environment, Constr Build Mater 36 (2012), 947-953
[4] Ferrara, L., Van Mullen, T., Alonso, M. C., Antonaci, P., Borg, R. P., Cuenca, E., Jefferson, A., Ng, P. L., Peled, A., Roig-Flores, M., Sanches M., Schroefl, C., Serna, P., Snoeck, D., Tulliani, J. M. and De Belie, Experimental characterization of the self-healing capacity of cement based materials and its effects on the material performance: A state of the art report by COST Action SARCOS WG2, Constr Build Mater 167 (2018), 115-142.
[5] Chung, C. W., Shon C. S. and Kim Y. S., Chloride ion diffusivity of fly ash and Silica fume concretes exposed to freeze-thaw cycles, Contr Build Mater 24 (2010), 1739-1745
[6] Soriano, L., Monzó, J., Bonilla, M., Tashima, M. M., Payá, J. and Borrachero, M. V., Effect of pozzolans on the hydration process of Portland cement cured at low temperatures, Cem Concr Comp 42 (2013), 41-48
[7] Hassan, A. A. A., Lachemi, M. and Hossain, K. M. A., Effect of metakaolin and silica fume on the durability of self-consolidating concrete, Cem Concr Comp 34 (2012), 801-807
[8] da Silva W. R. L., Šmilauer, V. and Štemberk, P., Upscaling semi-adiabatic measurements for simulationg temperature evolution of mass concrete structures, Mater Struc 48 (2015), 1031-1041

SynerCrete'18 International Conference on Interdisciplinary Approaches
for Cement-based Materials and Structural Concrete
24-26 October 2018, Funchal, Madeira Island, Portugal

APPLICATION OF LYSINIBACILLUS SPHAERICUS FOR CONCRETE CRACK HEALING USING DIFFERENT CALCIUM SOURCES

Christine Farrugia [(1)], Ruben Paul Borg [(1)], Joseph Buhagiar [(2)], Liberato Ferrara [(3)]

(1) Faculty for the Built Environment, University of Malta, Malta
(2) Department of Biology and Argotti Botanic Gardens & Resource Centre, University of Malta, Malta
(3) Dipartimento di Ingegneria Civile e Ambientale, Politecnico di Milano, Italy

Abstract

Micro-cracks, which develop during the service life of reinforced concrete structures, reduce the durability of concrete through the penetration of fluids. Microbially-induced calcium carbonate precipitation occurs naturally in the presence of ureolytic bacteria which precipitate calcium carbonate ($CaCO_3$) through urea hydrolysis. This deposition leads to the filling of micro-cracks and sealing of pores, reducing ingress of fluids into the concrete. The research aim was to assess the potential of *Lysinibacillus sphaericus* to precipitate $CaCO_3$ on concrete through urea hydrolysis. *Lysinibacillus sphaericus* was cultivated *in vitro* and induction of MICP through urea hydrolysis was tested on cement paste with two different calcium sources. The calcium precipitates where characterised by light microscopy, Scanning Electron Microscopy, Energy Dispersive Spectroscopy and Fourier Transform Infrared Spectroscopy. The study confirmed that MICP is induced successfully on concrete using *Lysinibacillus sphaericus*. Samples exposed to repeated treatment cycles of *Lysinibacillus sphaericus* in the presence of a calcium source exhibited a more extensive and even coating of $CaCO_3$ crystals on the surface confirming that repeated cycles of treatment are more effective in increasing the amount of $CaCO_3$ deposition and therefore increasing crack healing capacity.

1. Introduction

The durability of concrete is greatly reduced by the presence of micro-cracks within the material [1]. Micro-cracks may develop due to various processes and can occur at any time during the service life of the material. They have a negative effect on the concrete as they allow ingress of fluids including liquids, gases and ions into the concrete matrix, causing corrosion of reinforcement and degradation of the cementitious matrix. Therefore crack

widths must be controlled and healing reduces the ingress of fluids. These micro-cracks can heal naturally through autogenous healing which also involves the precipitation of calcium carbonate ($CaCO_3$) inside the crack in the presence of water. However, autogenous healing is only possible in small cracks and takes a long time to occur. Cracks may also heal through a natural microbial process known as microbial-induced calcium carbonate precipitation (MICP). This biological repair by bio-deposition occurs naturally in the presence of ureolytic bacteria which can precipitate $CaCO_3$ in the presence of appropriate nutrients [2]. The process can be induced artificially in the laboratory by adding urea to the medium containing the bacteria. The $CaCO_3$ precipitation allows rapid filling of cracks in concrete and plugging of pores to reduce absorption of fluids. As opposed to autogenous healing, this process can therefore seal cracks a lot quicker and avoid further damage occurring.
Bio-deposition methods as opposed to conventional surface treatments and crack repair methods with synthetic chemicals and formulations are alternative and eco-friendly techniques which merit further investigation. MICP is a natural, non-polluting process which has no damaging effects on the natural environment and therefore can be promoted as a viable alternative to conventional, polluting treatments on concrete. The aim of this research was to assess the potential of *Lysinibacillus sphaericus* to precipitate $CaCO_3$ on concrete through urea hydrolysis in the presence of different calcium sources.

2. Materials and Methods

2.1 Preparation of Medium and Bacterial Inoculum for Bio-precipitation

The strain *L. sphaericus* (LMG 22257) was used in this study. This strain of bacteria is alkaliphilic and was seen to have a continuous formation of dense calcium carbonate crystals from previous studies [3]. Medium 295 agar was prepared using recommended protocol provided by the Belgian Co-ordinated Collections of Micro-organisms (BCCM). The autoclaved medium was poured into sterile petri dishes and later used for surface inoculation. Medium 295 broth was similarly prepared but the addition of agar was omitted. An ampoule of *Lysinibacillus sphaericus* (LMG 22257) was purchased from BCCM in lyophilized form and revived by using 0.5 ml of the recommended Medium 295 broth. The contents of the ampoule were allowed to re-hydrate for a few minutes before transferring onto a Medium 295 agar plate and streaked to obtain individual colonies after incubation. Two drops were also plated but were left untouched to preserve a concentrated inoculum at the centre of the plate. The remaining drops hydrated *L. sphaericus* were added to Medium 295 broth to prepare a liquid culture. The inoculated agar plates and the broth were incubated for 48-72 hours in an incubator (CERTOMAT BS-1, Sartorius) set at 30°C. The bacterial colonies were repeatedly sub-cultured over a period of time using the same procedure of spreading a colony over an agar plate and incubated for 48-72 hours at 30°C to increase the volume of bacterial inoculum required for bio-precipitation. Once substantial colony growth was reached, plates with were transferred to a refrigerator set at 4°C to prevent further multiplication of the bacteria. In order to induce sporulation, the same procedure of bacterial subculture was used but the agar medium was further modified by the addition of 10mg/L of $MnSO_4$ to the Medium 295 agar. For the preparation of the bacterial inoculum for the bio-precipitation experiments, a 0.5 McFarland bacterial inoculum in Medium 295 broth was prepared by comparison to barium sulphate standard prepared using standard protocol. The solution was incubated for 24 hours

at 30°C to obtain a one-day old stock culture. This procedure was repeated using a plate containing *L. sphaericus* (LMG 22257) and Medium 295 agar with 10mg of $MnSO_4$.

2.2 Preparation of Calcium Source Solutions

A solution of calcium chloride ($CaCl_2$) was prepared by adding 6.25g of $CaCl_2$ to 250mL of distilled water. A solution of calcium acetate ($Ca(CH_3COO)_2$) was prepared by adding 6.5g of $Ca(CH_3COO)_2$ to 250mL of distilled water. Both solutions were subsequently autoclaved at 121°C for 15 minutes.

2.3 Preparation of Cement Paste Samples

500g of CEM 1 42,5R cement and 140ml of distilled water were mixed for 2.5 minutes at 285r.p.m. in a 5 litre bowl. The cap of a 1mL Eppendorf flask was isolated from the flask so as to obtain a mould which could hold circa 0.15-0.2g of cement paste. The cement paste was placed in the moulds and vibrated on a vibrating table. They were then allowed to cure inside an enclosed container at 20°C±1°C and a relative humidity of 70%.

2.4 Treatment Procedure for Cement Paste Samples

The cement paste samples were placed under an ultraviolet light source at 254nm for 40 minutes so as to sterilize their upper surface. These samples were labelled and placed inside a sterilized container so as to avoid contamination. The other half of the samples were also labelled and placed inside a container. All treatments were applied on the upper surface of the sample as follows. The bacterial inoculum was applied to the surface of the samples using a Pasteur pipette until ponding was achieved on top of the sample. The samples were left to stand in an enclosed container for 24 hours. After this 24-hour period, any remaining bacterial inoculum on the surface of the samples was gently removed using a paper towel so that ureolytic activity would result primarily from bacteria inside the cement paste. The calcium source solution was then applied to the surface of the samples using a Pasteur pipette until ponding was achieved on top. The samples were left to stand in an enclosed container for 72 hours. After this 72-hour period, any remaining calcium solution on the surface of the samples was gently removed using a paper towel. For the set of samples requiring a second repetition of the treatment, this procedure was repeated at the end of the first treatment. The samples were observed using surface visual observation, stereoscopic microscopy, Fourier Transform Infrared Spectroscopy (FTIR), Scanning Electron Microscopy (SEM) and Energy Dispersive Spectroscopy (EDS).

All treatments were applied on the upper surface of the sample. The variables in the treatment procedures were sterilization of the sample, sporulating or active bacteria (with or without $MnSO_4$ respectively), the presence and type of calcium source, drying of the sample in an oven and the number of repetitions of the treatment procedure. All treatment procedures were carried out in duplicate.

3. Results and Discussion

3.1 Stereomicroscopy

The samples were observed under a stereomicroscope to confirm the presence of crystals on the surface. In Figure 1, the surface of a control sample with no treatment and a sample treated with *L. sphaericus* and $CaCl_2$ under a stereomicroscope can be seen. The control

sample on the left exhibits no precipitates while the treated sample on the right exhibits white precipitates on its surface.

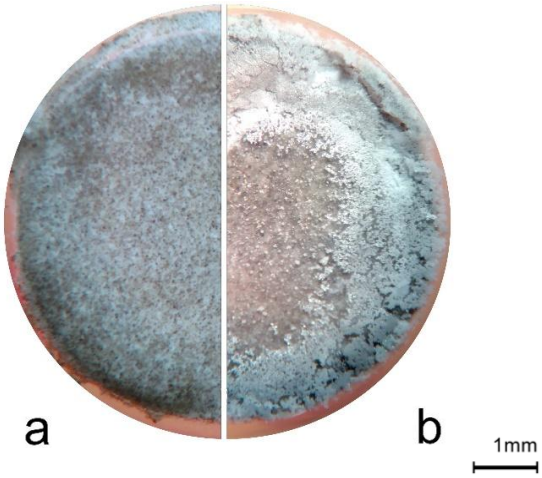

Figure 1: Stereoscopic microscopy images of the surface of cement paste specimens. (a) Control - no treatment (b) treated with *L. sphaericus* and $CaCl_2$.

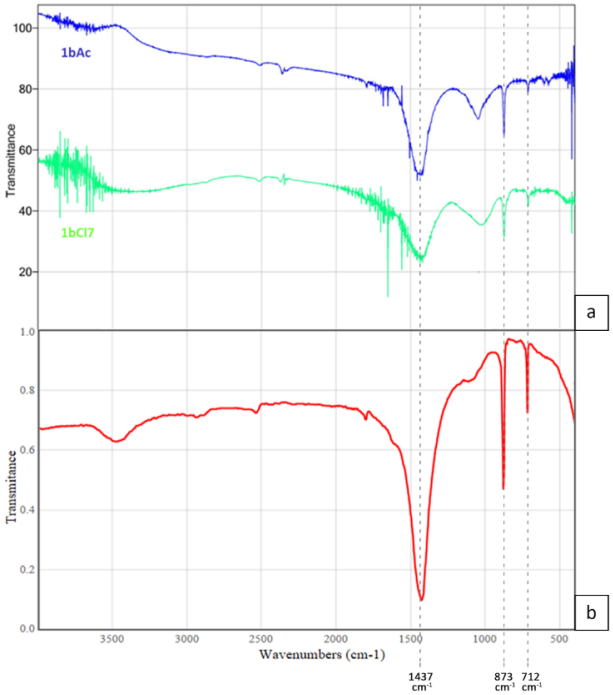

Figure 2: FTIR spectra for (a) scraping from surface of samples 1bCl7 treated with *L. sphaericus* and $CaCl_2$ (bottom) and 1bAc7 treated with *L. sphaericus* and $Ca(CH_3COO)_2$ (top), (b) reference spectrum for calcite [4].

3.2 FTIR

The FTIR spectra in the range of 4000-500cm-1 for the scraping of crystals from the surface of sample 1bCl7 (treated with *L. sphaericus* and $CaCl_2$) and 1bAc7 (treated with *L. sphaericus* and $(Ca(CH_3COO)_2)$ can be seen in Figure 2. The shape of the spectrum indicates the presence of $CaCO_3$. When compared to the typical FTIR spectrum for calcite (Figure 2b), major vibrational bands with peaks at 1437cm-1, 873 cm-1 and 712 cm-1 are comparable. This confirms that the precipitate obtained on the surface of the cement paste samples is calcite ($CaCO_3$).

3.3 SEM and EDS

Sample 1bAc7 treated with *L. sphaericus* and $(Ca(CH_3COO)_2)$ exhibited numerous clusters of crystals on its surface (Figure 3). At a magnification of 5,000X, the crystals were clearly observed to be rhombohedral with sharp edges and with a size ranging from 10µm-15µm. Within these rhombohedral crystals, bacterial cells were observed. This confirms that the crystals are a product of the bio-deposition process induced using *L. sphaericus* and a calcium source. Sample 2/1bCl7 treated with two rounds of treatment of *L. sphaericus* and $CaCl_2$ also exhibited clusters of crystals on its surface similar to those precipitated on sample 1bAc7.

These crystals were also observed to be rhombohedral with sharp edges (calcite) and bacterial cells could be observed within the crystals (Figure 4).

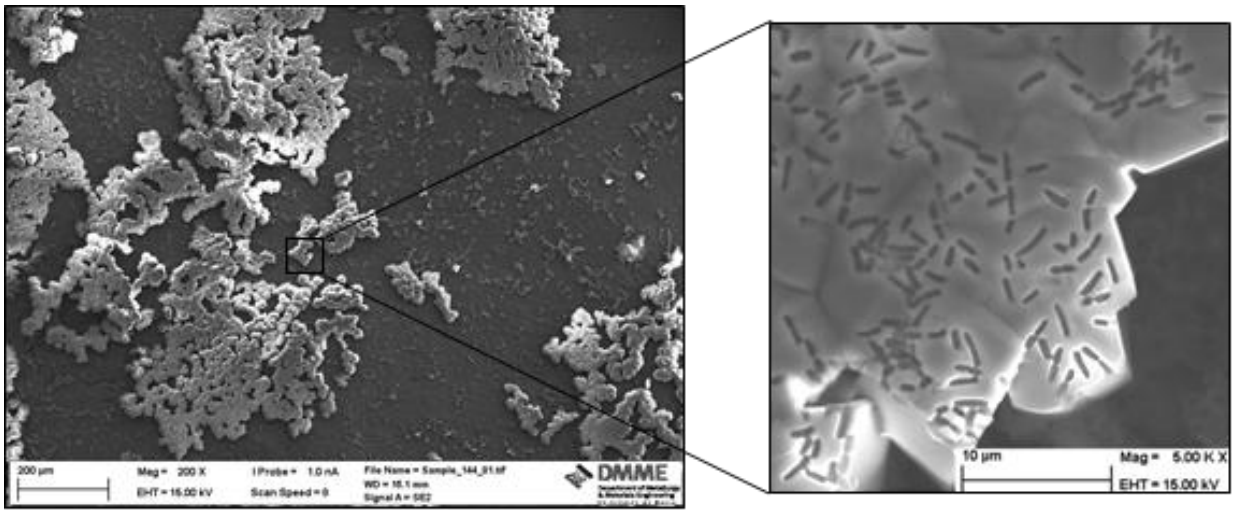

Figure 3: SEM image for sample 1bAc7 (treated with *L. sphaericus* and $Ca(CH_3COO)_2$) at 200X and 5000X magnification.

As opposed to the crystals precipitated on sample 1bAc7, the crystals precipitated on sample 2/1bCl7 covered the whole surface of the cement paste. This was confirmed through EDS analysis of the surface of the sample (Figure 5) as the EDS analysis did not show peaks for Mg, Si, Al and S, indicating that the surface of the cement paste was entirely covered in crystals produced through MICP. Also, various different sizes of crystals were observed on the surface. On average, the size of the crystals ranged from 2µm-50µm.

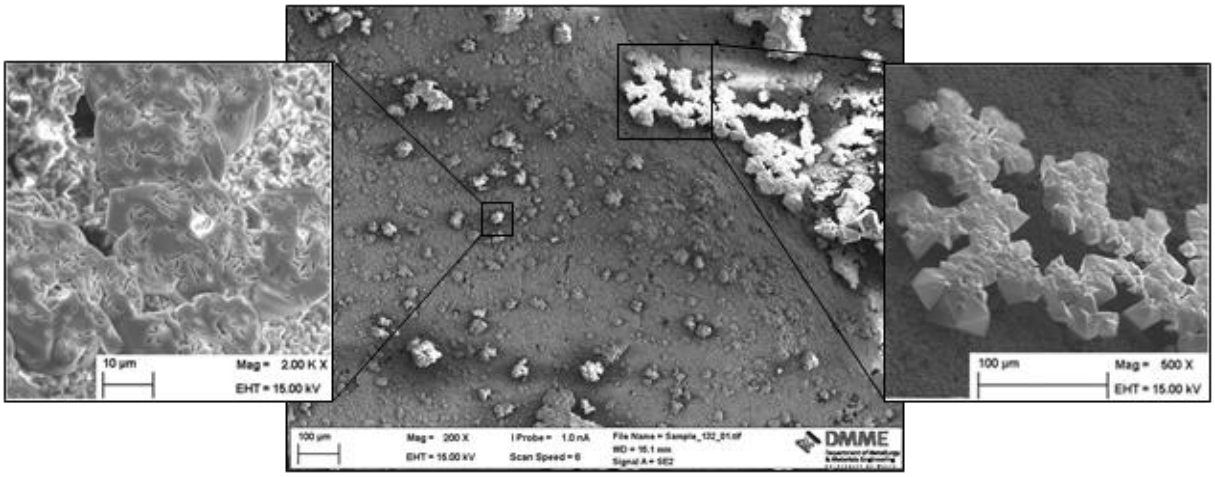

Figure 4: SEM image for sample 2/1bCl7 (two rounds of treatment of *L. sphaericus* and CaCl2). Image magnification: centre 200X, right enlargement 500X and left enlargement 2000X.

These differences between sample 1bAc7 and sample 2/1bCl7 were attributed to the fact that the latter received 2 rounds of treatment of *L. sphaericus* and a calcium source. This resulted in a more even coating on the surface and larger crystal depositions.

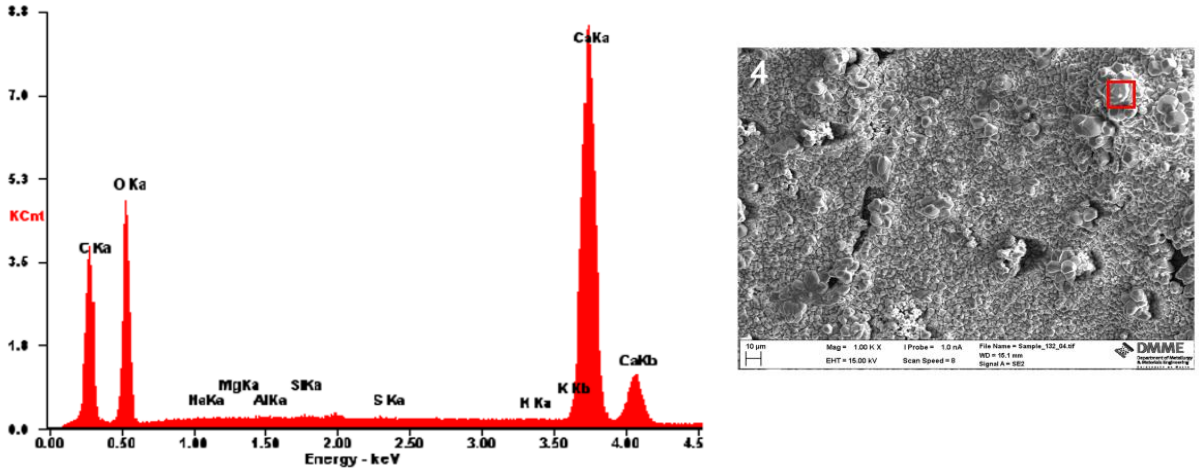

Figure 5: EDS for crystals on surface of sample 2/1bCl7.

4. Conclusion

First and foremost, it was confirmed that MICP could be induced successfully on concrete using *L. sphaericus* and $CaCl_2$ or *L. sphaericus* and $(Ca(CH_3COO)_2)$ in the presence of urea. Furthermore, the characterisation of the precipitates from the MICP process confirmed that the crystals precipitated on these samples were $CaCO_3$ crystals. No difference in the amount of crystal precipitation was observed between samples treated with *L. sphaericus* and $CaCl_2$ or *L. sphaericus* and $(Ca(CH_3COO)_2)$. It was also noted that samples exposed to 2 rounds of treatment of *L. sphaericus* and a calcium source exhibited a greater and more even coating of crystals on the surface. This proves that repeated cycles of treatment are effective in increasing the amount of $CaCO_3$ deposition.

Acknowledgements
ERDF (Malta) testing equipment: "Developing an Interdisciplinary Material Testing & Rapid Prototyping R&D Facility" (Ref. No. 012); Ing. J. Camilleri University of Malta for technical support.

References

[1] Newman, J., and Seng Choo, B., Advanced Concrete Technology: Concrete Properties. Burlington: Elsevier Ltd. (2003)
[2] De Belie, N., et al, Microbial carbonate precipitation in construction materials: A review. Ecological Engineering 36 (2010), 118-136
[3] Chahal, N., and Siddique, R., Effect of ureolytic bacteria on concrete properties. Construction and Building Materials 25 (2011), 3791-3801.
[4] Calcium carbonate (calcite) (2016). Retrieved from National Institute of Standards and Technology (NIST): http://webbook.nist.gov/cgi/cbook.cgi?ID=B6004659&Mask=80

SynerCrete'18 International Conference on Interdisciplinary Approaches
for Cement-based Materials and Structural Concrete
24-26 October 2018, Funchal, Madeira Island, Portugal

BIOTREATED CONVENTIONAL CONCRETE AND CDW-CONCRETE BY USE OF MICROBIAL MIXED CULTURES BIOPRODUCTS

Julia García-González [(1)], André Freches [(2)], Pedro Vaz [(3)], Paulo C. Lemos [(2)], Alice S. Pereira [(4)], Andrés Juan-Valdés [(1)], Paulina Faria [(5)]

(1) Escuela de Ingeniería Agraria y Forestal, University of Leon, León, Spain
(2) LAQV-REQUIMTE, Department of Chemistry, Faculdade de Ciências e Tecnologia, Universidade NOVA de Lisboa, Caparica, Portugal
(3) Department of Civil Engineering, Faculdade de Ciências e Tecnologia, Universidade NOVA de Lisboa, Caparica, Portugal
(4) UCIBIO-REQUIMTE, Department of Chemistry, Faculdade de Ciências e Tecnologia, Universidade NOVA de Lisboa, Caparica, Portugal
(5) CERIS and Department of Civil Engineering, Faculdade de Ciências e Tecnologia, Universidade NOVA de Lisboa, Caparica, Portugal

Abstract

Cracks form in all concrete constructions shortening the life of concrete elements, particularly in exposed concrete. They provide a path for transport of moisture, chlorides, and various other deleterious substances. The aim of this study was to assess the protection and consolidation effect of eco-friendly healing biotreatments on water absorption of conventional and recycled concrete, with 50% substitution of natural coarse aggregate by CDW aggregate. Concrete were treated with bioproducts obtained using waste biomass from a microbial mixed culture process for polyhydroxyalkanoates production. Results showed that the reference samples, with application of tap water, presented an increase in water drop permeability, being the absorption time shorter than in the control (untreated) samples. The biotreatment with the non-sonicated bioproduct increased significantly the water absorption time, more evident in conventional concrete samples than in recycled ones. In the case of the sonicated bioproducts, the behaviour was similar for both types of concrete specimens, but the healing effect was higher. When the biotreatment was performed with three applications, the healing effect was not so effective. This observation may be associated with the formation of a hydrophobic film of organic material from the bioproduct, which detached from the concrete surface after outdoors exposure.

1. Introduction

The quality of concrete surface plays an important role in the concrete service life [1], particularly in exposed concrete. Its quality is impacted by the water/cement ratio of the fresh concrete [2] and affects spreading processes but also hardened concrete properties [3-6]. That is even more important in the case of concrete with recycled aggregates. Due to phenomena such as the wall effect [7], contact with formworks [8] or segregation [9], the exterior layer of exposed concrete often has a different composition from the internal one and its porosity is higher than in the core of the concrete element [10]. Several studies have tested the surface healing effect of organic and inorganic treatments on cement-based materials [11,12], showing improvements on permeability, resistance to moisture diffusion and filling of surface cracks and voids. Leung et al. [13] tested neat epoxy and neat silane as well as epoxy/organoclay and silane/organoclay nanocomposites and stated that the incorporation of organoclay into silane could improve its resistance to moisture diffusion. Pigino et al. [14] applied ethyl silicate by brushing onto the surface of concrete, penetrating up to a depth of about 3-5 mm into the concrete, induced a substantial decrease in water absorption, despite the low quantity of the absorbed product. Amidi and Wang [15] tested other types of surface treatments, using calcium carbonate deposition by hydrolysis of dimethyl carbonate (DMC) to fill the surface cracks and voids of concrete elements. A reduction in water absorption was achieved. Sodium silicate has also been used [16,17].
The search for a suitable bioproduct compatible with the existing cementitious substrate and able to improve the concrete surface quality by biotreatment of incipient cracks and porous structure may be an appropriate technique. Healing, helping the external repair, decreasing maintenance costs of aged concrete structures and increasing sustainability in the construction industry would be some of the advantages of this technology.

2. Materials and methods

Conventional and recycled concrete samples were prepared to assess the protection and consolidation effect of an eco-friendly healing biotreatments on water absorption. For the manufacture of the concrete mixtures, the following materials were employed. Commercially available Portland blended cement (CEM III/A 42.5 N/SR) was conformed to the Spanish [18-19] and European [20] standards. Natural aggregates presented a siliceous nature and complied with the requirements of the EHE-08 [21] and EN 12620+A1 [22]. Recycled mixed aggregates (RMA) were obtained through a mechanical treatment of construction and demolition wastes (CDW) in a recycling plant located in the Autonomous Community of Madrid (Spain). The composition of the RMA, determined according to EN 933-11 [23], is presented in Tab. 1. Physical and mechanical properties of RMA and natural aggregates such as D/d ratio [24], fines content [24], flakiness index [25], Los Angeles coefficient [26], were within the suitable parameters established by EHE-08 [21] for the concrete manufacture. Nevertheless, results obtained for RMA water absorption [27] showed a greater variation compared to the natural aggregates. The presence of attached mortar and ceramic materials in the recycled aggregates caused a significant water absorption, higher than the one of the natural aggregates. The use of aggregates with high water absorption could result in a workability drawback. Consequently, the RMA were pre-saturated: a technique that showed

to be a suitable method to manufacture inexpensive recycled concrete with low strength requirements and maintain a suitable workability [28]. Tab. 2 shows the detailed composition of the different raw components used in the manufacture of the conventional concrete (CC) and recycled concrete (RC). The w/c ratio and f_{ck} of both concretes is 0.5 and 25 MPa, respectively.

Table 1: Non-floating components of recycled aggregates.

Component	**% (w/w)**
Unbound aggregates (natural aggregates without cement mortar attached)	44.1
Ceramics (bricks, tiles, stoneware and sanitary ware, …)	33.6
Concrete and mortar (natural aggregates with cement mortar attached)	17.5
Asphalt	0.4
Glass	0.8
Gypsum	3.5
Other impurities (wood, paper, metals, plastic, …)	0.2

Table 2: Mix composition per cubic metre of conventional and recycled concrete.

Material	**CC**	**RC**
Water (l)	165	155
Cement (kg)	333	313
Sand 0/4 mm (kg)	103	97
Sand 0/5 mm (kg)	470	442
Gravel 4/10 mm (kg)	516	242
Gravel 6/12 mm (kg)	172	81
RMA 4/20 mm (kg)	0	323

The test samples were cubes cut from concrete specimens that were molded, and had a cut surface with 50 mm x 50 mm. The bioproducts used as healing agents were obtained using waste biomass from a microbial mixed culture (MMC) for polyhydroxyalkanoates production using pine wood bio-oil as substrate. MMC cell walls were disrupted by sonication (MMC-P_S) or not (MMC-P). Samples were treated with 2 mL of each bioproduct suspensions by using a pipette, covering the top surface. Half of the samples were biotreated with a single application, whereas on the other half, three applications were made (one application every 24 h).The effect of each bioproduct on surface treatment was evaluated and compared with untreated samples (control) and treated with the same volume of tap water (reference).
For each biotreatment and concrete, three samples were tested. The test room conditions were 20±2°C and 40±5% relative humidity (RH). Two days after the last application, the bio-healing capacity was assessed by water-drop absorption test in the air, in order to simulate real conditions. This test allows evaluating the permeability variation of the biotreated surfaces by monitoring the time required to absorb a water drop under open air conditions. The test was video recorded and the absorption time was then defined for each concrete,

number of applications and treatment. After this test the samples were placed outdoors for natural aging.

3. Results and discussion

Figure 1 shows the treated samples. When the treatment included three applications, a layer of organic material from the bioproduct deposited on the surface of the concrete samples, changing its color, and the healing effect decreased. After 1 month in outdoors exposure the samples were visually observed, and the layer was no longer visualized: it was washed off or, in case of three applications of the bioproducts, it cracked and separated from the concrete surface without spotting (treated samples looked like control and reference samples, without the brownish layer).

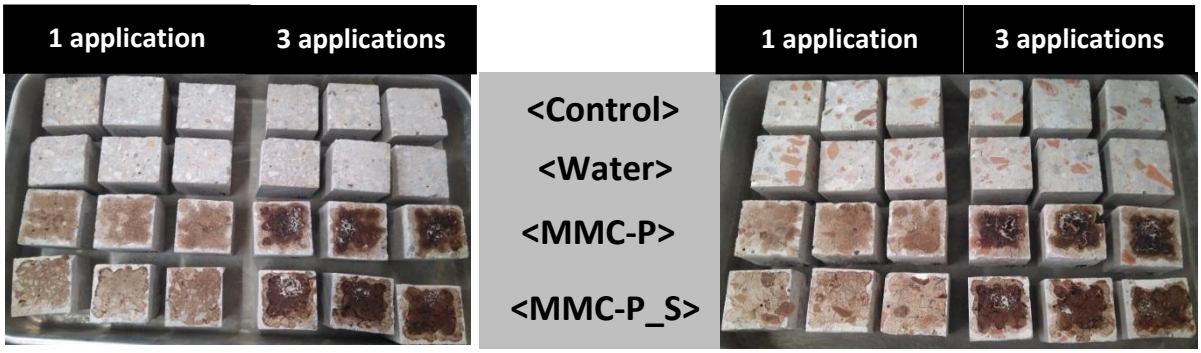

Figure 1: Conventional concrete (left) and recycled concrete (right) samples after treatment.

Figure 2 shows the time of water drop absorption for each biotreated concrete samples, the control (untreated) and the reference (with water application) samples.

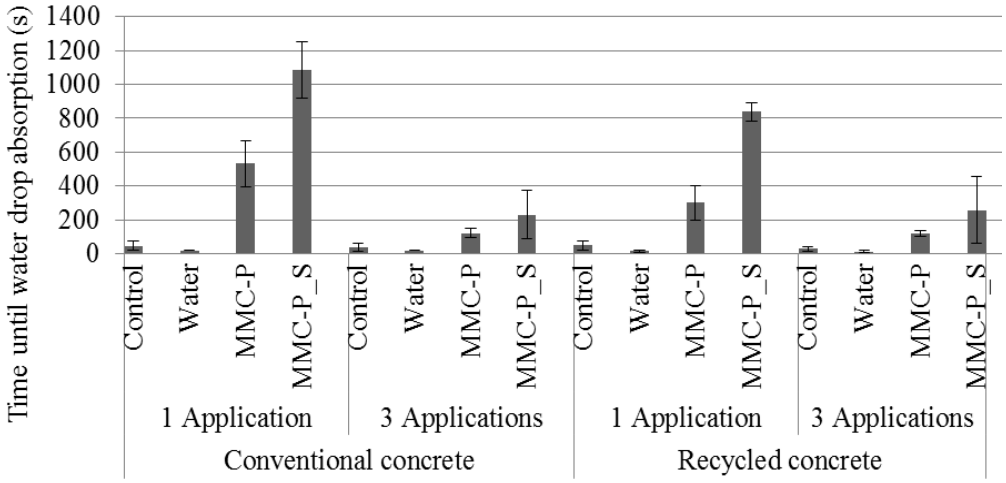

Figure 2: Results of water drop absorption test.

Results have shown that the reference concrete, with tap water, presented an increase in water drop permeability, being the absorption time shorter than in the control concrete in all cases. The biotreatment MMC-P increased the water absorption time significantly, more evident in

conventional concrete than in recycled one. In the case of the sonicated bioproducts (MMC-P_S), the behavior was similar regarding the different kinds of concrete, but the healing effect was even higher.
A comparison of results of the biotreatments with studies from other researchers is presented in Tab. 3. In the short term, the good efficiency of the biotreatments tested in the present study is clearly evident. Further studies will allow to justify this effect and if it will be durable.

Table 3: Water ingress decrease due to concrete surface treatments.

Study	Type concrete	Treatment	Reduction (%)
Woo et al. [11] - permeability	With PVA Fibers	Neat silane and silane/clay nanocomposite	29-57
Chandra et al. [12] - water absorption	Portland	Extract of cactus	83
Present - water drop ingress in comparison with control	Portland	MMC-P - 1 application	996
		MMC-P_S - 1 application	2130
	With CDW	MMC-P - 1 application	521
		MMC-P_S - 1 application	1622

4. Conclusion

The biotreatments with bioproducts from a microbial mixed culture for polyhydroxyalkanoates production process produced a decrease of the permeability on both conventional and recycled concrete. Besides, the sonicated bioproduct achieved a greater healing effect when compared with the non-sonicated MMC one. Multiple applications of biotreatment cause the formation of a hydrophobic film of organic material from the bioproduct, which detached from the concrete surface, cracking with time passed even between applications and decreasing the healing effect. Therefore, a single application of the sonicated MMC bioproduct was the most efficient tested biotreatment to increase concrete durability to water access.

Acknowledgements
This work was supported by a STSM Grant from the COST Action CA15202. (http://www.sarcos.enq.cam.ac.uk). This work was also supported by the Associate Laboratory for Green Chemistry-LAQV and Applied Molecular Biosciences Unit-UCIBIO which are financed by national funds from FCT/MCTES (UID/QUI/50006/2013; UID/Multi/04378/2013) and co-financed by the ERDF under the PT2020 Partnership Agreement (POCI-01-0145-FEDER – 007265; POCI-01-0145-FEDER-007728).

References

[1] Gandhi, G. K., et al, Quantifying changes in surface characteristics of concrete due to progressive deterioration, J Mater Civ Eng 29 (2017), 1-10.
[2] Rizzo, P. et al, Detecting the presence of high water-to-cement ratio in concrete surfaces using highly nonlinear solitary waves, Appl Sci 6(104) (2016), 1-16
[3] Mors, R. and Jonkers, H., Effect on concrete surface water absorption upon addition of lactate derived agent, Coatings 7 (2017), 1-10

[4] Huang, Y., Modeling moisture transport at the surface layer of fatigue-damaged concrete, Constr Build Mater 151 (2017), 196-207
[5] Williams, M. et al, Non-destructive study of the microstructural effects of sodium and magnesium sulphate attack on mortars containing silica fume using impedance spectroscopy, Appl Sci 7 (2017), 1-21
[6] Salvoldi, B. G., Oxygen permeability of concrete and its relation to carbonation, Constr Build Mater 85 (2015), 30-37
[7] Zheng, J.J., Aggregate distribution in concrete with wall effect, Mag Concrete Res 55 (2003), 257-265
[8] De Caro, P., Influence of the nature of the demoulding agent on the properties of the formwork-concrete, Mag Concrete Res 59 (2007), 141-149
[9] Safawi, M. I., The segregation tendency in the vibration of high fluidity concrete, Cem Concr Res 34 (2004), 219-226
[10] Weber, S. and Reinhardt H.W., A new generation of high performance concrete: concrete with autogenous curing, Adv Cem Based Mater 6 (1997), 59-68
[11] Woo et al., Barrier performance of silane-clay nanocomposite coatings on concrete structure, Compos Sci Technol 68 (2008), 2828-2836
[12] Chandra, S. et al., Use of cactus in mortars and concrete, Cem Concr Res 28 (1998), 41-51
[13] Leung et al., Use of polymer/organoclay nanocomposite surface treatment as water/ion barrier for concrete, J Mater Civ Eng 20 (2008), 484-492
[14] Pigino, B., Ethyl silicate for surface treatment of concrete – Part II: characteristics and performance, Cement Concr Compos 34 (2012), 313-321
[15] Amidi, S. and Wang, J., Surface treatment of concrete bricks using calcium carbonate precipitation, Constr Build Mater 80 (2015), 273-278
[16] Jia, L. et al., Effects of inorganic surface treatment on water permeability of cement-based materials, Cement Concr Compos 67 (2016), 85-92
[17] Li, J., et al., Progress of silane impregnating surface treatment technology of concrete structure, Mater Rev 26 (2012), 120-125
[18] Royal Decree 256, Cement Reception Instruction (RC-16) [In Spanish], Ministry of Public Works, Madrid, Spain (2016)
[19] UNE 80303-1, Cements with additional characteristics. Part 1: Sulphate resisting cements [in Spanish], AENOR, Spain (2013)
[20] EN 197-1, Cement. Part 1: Composition, specifications and conformity criteria for common cements, CEN, Spain (2011)
[21] Permanent Commission on Concrete, Code on Structural Concrete (EHE-08) [in Spanish]. Spanish Ministry of Public Works, Spain (2008)
[22] EN 12620+A1, Aggregates for concrete, CEN, Brussels (2008)
[23] EN 933-11, Tests for geometrical properties of aggregates – Part 11: Classification test for the constituents of coarse recycled aggregate, CEN, Brussels (2009)
[24] EN 933-1, Tests for geometrical properties of aggregates – Part 1: Determination of particle size distribution - Sieving method, CEN, Brussels (2012)
[25] EN 933-3, Tests for geometrical properties of aggregates – Part 3: Determination of particle shape - Flakiness index, CEN, Brussels (2012)
[26] EN 1097-2, Tests for mechanical and physical properties of aggregates – Part 2: Methods for the determination of resistance to fragmentation, CEN, Brussels (2010)
[27] EN 1097-6, Tests for mechanical and physical properties of aggregates – Part 6: Determination of particle density and water absorption, CEN, Brussels (2013)
[28] García-González, J. et al., Pre-saturation technique of the recycled aggregates: solution to the water absorption drawback in the recycled concrete manufacture, Materials 7 (2014), 6224-6236

SynerCrete'18 International Conference on Interdisciplinary Approaches
for Cement-based Materials and Structural Concrete
24-26 October 2018, Funchal, Madeira Island, Portugal

CHARACTERIZATION AND MONITORING OF THE CRACK SELF-HEALING ABILITY OF BIO-MORTAR

Bojan Miljevic [(1)], Francesco Lo Monte [(2)], Snezana Vucetic [(1)], Olja Sovljanski [(1)], Ivan Ristic [(1)], Branka Pilic [(1)], Sinisa Markov [(1)], Liberato Ferrara [(2)], Jonjaua Ranogajec [(1)]

(1) University of Novi Sad, Faculty of Technology, Novi Sad, Serbia
(2) Politecnico di Milano, Department of Civil and Environmental Engineering, Milan, Italy

Abstract

It is known that bacteria can promote self-healing of the cracks in concrete structures, but the elevated pH value of the cement-based concrete matrix affects negatively the life span of bacteria and consequently, the self-healing effect. Therefore, a method for encapsulation of bacteria healing agent in a polymer hydrogel system has been successfully established to protect the bacteria from surrounding environment. In order to investigate the healing capacity of the employed bacterial colony and the effectiveness of the proposed encapsulation methods, three groups of mortar specimens were systematically prepared: standard reference samples, samples with hydrogel and bio-mortar samples (with bacteria species encapsulated in the hydrogel system surrounded with nutrition). Microstructure and texture analysis were performed before and after the healing treatment. The mortar specimens were notched at mid-span and pre-cracked by means of 3-point bending tests performed in CMOD-control mode. Water sorption tests were performed periodically in order to ascertain the effects of healing on the recovery of durability performance. The healing ability was also measured by crack opening displacement change by optical microscopy. The specimens were tested in 3-point bending up to failure, to assess the effect of the healing, if any. A cross-comparison analysis of the obtained results was provided.

1. Introduction

Innovative and sustainable solutions for self-healing concrete structures are at the highest demand in these days as their repair and maintenance can reach very high costs [1]. It is known that bacteria promote a self-healing phenomenon in the existing cracks in a concrete structure [1,2]. However, an elevated pH value of the cement-based concrete matrix affects

negatively the life span of bacteria and consequently, the self-healing effect. Therefore, a method for encapsulation of bacteria healing agent in a polymer hydrogel system is needed in order to protect the bacteria from surrounding. The ureolytic bacteria especially *Sporosarcina pasteurii* have generated a lot of interest in the field of crack repair in concrete and calcareous materials, and have been studied extensively. The use of these bacteria leads to accumulation of insoluble $CaCO_3$ in a calcium rich environment through the hydrolysis of urea; this produces dissolved ammonium, inorganic carbon and CO_2, and the ammonia released in the surroundings subsequently increases pH [3].
In order to investigate the healing capacity of the employed bacterial colony and the effectiveness of the proposed encapsulation methods, systematically varied mortar specimens were prepared. The prepared samples were characterized by X-ray diffraction (crystal phases revealed), X-ray fluorescence analysis (chemical content), mercury intrusion porosimetry (pore size distribution) as well as examined by scanning electron microscopy (surface morphology). Microstructure and textural analysis were performed.
The mortar specimens were notched at mid-span and then pre-cracked in 3-point bending in CMOD-control mode (Crack Mouth Opening Displacement). After unloading, the water sorptivity test was performed and then the specimens were kept in a moisture room (90% RH). Their healing ability was measured by crack opening displacement change examined by optical microscopy immediately after the crack formation and after two months of healing. Moreover, at the end of the scheduled exposure periods (one and two months) the water sorption test was performed and the specimens were finally tested in 3-point bending up to failure, in order to assess the effect of the healing. The obtained results were compared with those of the reference samples.

2. Experimental procedures

2.1 Polymer encapsulation of bacterial spores

The carbonate precipitating bacteria *Sporosarcina pasteurii* DSM 33 was used in this experiment. Living cells were cultured on Trypton Soya Agar (HiMedia, India) with the addition of 20% urea (Difco, USA). The culture was aerobically incubated at 30 °C for 5 days, in order to achieve a high yield of spores. The suspension of *S. pasteurii* spores was formed in sterile distilled water and was exposed to the thermal treatment at 80 °C for 10 minutes to remove vegetative cells. The number of spores was determined after the incubation at 30 °C for 48 h on TSA with the addition of 20% urea.
The hydrogel used in the experiment was synthesised by the method of microwave polymerisation. Acrylic acid and acryl amide, in molar ratio of 1: 1, were mixed with a curing agent (N,N'-methylene bisacrylamide) and polymerised in microwave reactor for 2 minutes. The resulting hydrogel was postpolymerised for 24 hours at room temperatures, and then dried to constant mass. The obtained xerogel (dried hydrogel) was mechanically ground and passed through a sieve <0.5 mm. The equilibrium swelling degrees of the xerogel was previously experimentally determined (22.7 g of liquid for 1 g of xerogel).
The obtained quantity of the xerogel particles was divided into three parts, in order to form: (1) hydrogel with nutrients, (2) hydrogel with spores and (3) pure xerogel. The first part of xerogel was hydrated with nutrients, a solution of urea (20 g/L) and calcium lactate (40 g/L). The second part of xerogel was hydrated with a suspension of spores ($4.1 \cdot 10^8$ cfu⁄g of

xerogel). In both cases, the maximum amount of fluid for hydration was 80 % of the equilibrium degree of swelling (~18 ml). After drying, the both types of hydrogels (with nutrients and spores) were mechanically ground. The final concentration of bacterial spores after the complete procedure was $1.1 \cdot 10^8$ cfu/g of xerogel.
The obtained xerogels (gel with nutrients and gel with spores) were encapsulated as follows. The xerogel particles were coated with an elastomer, dissolved in dichloromethane, at a solvent evaporation temperature (~40 °C). These particles were sprayed from both sides in order to achieve a uniform encapsulation.

2.2 Preparation of mortar specimens

The mortar specimens with the dimensions of (160×40×40) mm were prepared, according to the EN 196-1 standard. Three groups of specimens were made systematically as follows: S (standard reference mortar samples), B (bio-mortar samples based on standard mortar mixture with the addition of encapsulated bacterial culture and separately encapsulated nutrition in the hydrogel) and G (mortar samples with addition of hydrogel of the same amount and type as in bio-mortars). All specimens were cured in the same way: firstly kept in a climate chamber at t = 20 °C and relative humidity (RH) of 90 % for 24 h, then demolded and for the next 3 days kept in a tap water (t = 20 °C). The next 24 days of investigation they were kept in laboratory at room temperature and RH of 60 %.

2.3 Characterization

CMOD-controlled 3-points bending tests

The mortar specimens were notched at mid-span (6.2 mm deep) by wet sawing, prepared for the test (gluing knife edges for clip-gauge over the gap with 10 mm spacing) and then pre-cracked in CMOD-controlled (Crack Mouth Opening Displacement) 3-points bending with the target value of 200 μm for the crack opening. For the CMOD 3-points bending tests an *Instron 8562* machine was used with a clip COD gauge and *Instron 8800* control unit. The same set-up was used to monitor and to control the crack opening. The specimens were tested on a 100 mm span. The displacement rate used in the experiment was 0.3 μm/s.

Water sorption tests

The specimens were kept in water with a depth of 10 mm (at room temperature) and their weight was measured manually at time intervals of 10, 20, 30 minutes and 1-8 hours with the step of 0.5 h. The removal of water from the sample surface was done gently by wiping.

Mercury intrusion porosimetry

Pore size distribution of the specimens aged 28 days was measured with a mercury porosimeter (AutoPore IV 9500, *Micromeritics*). Prior to the measurements, the samples were dried in oven at 105 °C for 2 h in order to remove the residual water contained in the samples. Maximal intrusion pressure used was 228 MPa.

X-ray diffraction/ X-ray fluorescence

The X-ray diffraction measurements of the 28 days aged specimens were carried out using a *Philips* PW 1710 XRD instrument, with the Cu $K\alpha_{1,2}$ radiation, and a step scan mode of 0.02° in the angular range 2θ = (5–60)°. The exposition time at each point was 2 s. The X-ray fluorescence measurements were performed by a portable μ-XRF spectrometer ARTAX 200 (*Bruker-Nano*) using the Rh source (25 kV, 1.5 mA) under the He atmosphere with the acquisition time of 100 s.

Optical microscopy / Scanning electron microscopy

The crack mouth opening displacement of each pre-cracked specimen was monitored by optical microscopy using a mobile digital microscope Dino-Lite Pro AM-413ZT (*ANMO Electronics Co.*) at the magnification of ×200. The obtained pictures were evaluated by the software *DinoCapture 2.0*. The study of localization of the used bacterial culture in the newly developed material (bio-mortar) was investigated by Low Vacuum Scanning Electron Microscopy (*JEOL*, JSM-5500LV) at the pressure of 18 Pa and the voltage of 20 kV. All systems had been previously frozen using a liquid nitrogen and subsequently fractured (fresh cross-sections were studied). The imaging was conducted in the first 15 minutes after the samples freezing.

3. Results and discussion

3.1 Microstructure and textural characteristics of the mortar specimens

The results of the XRF analysis of the standard mortar prism show a relatively high content of calcium (35.7 %), followed by the content of silicon (13.7 %), aluminium (2.3 %), sulphur, potassium, iron (~1 %) and the rest elements (Ti, Mn, Zn, Sr) in traces. Expectedly, the results of XRD analysis confirmed no difference between the different specimens. All of the measured mortar specimens consist of alite, belite, portlandite and calcite beside quartz from the sand aggregates. Different pore size distribution between the standard mortar specimen and the specimen with hydrogel can be seen in Fig. 1. The mortar with hydrogel features higher content of pores with a diameter between 32 nm and 64 nm.

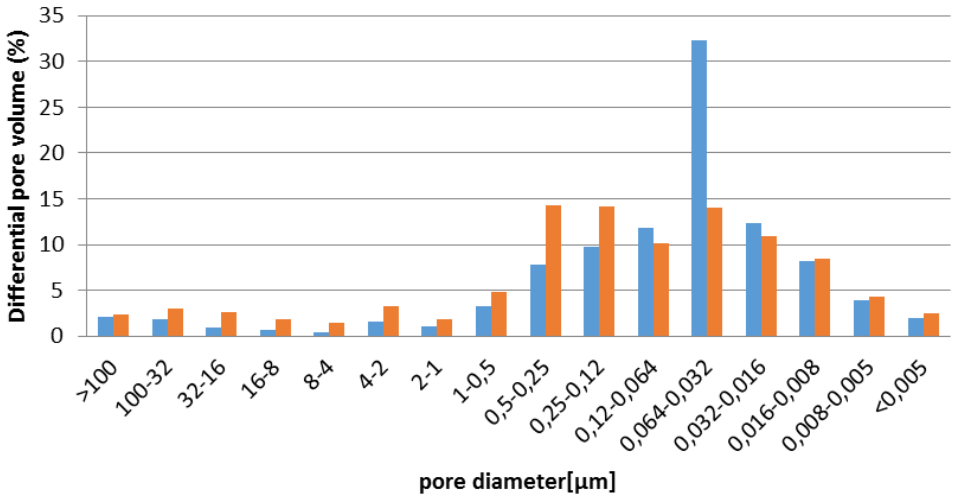

Figure 1: Pore size distribution of mortar specimen with hydrogel – G (blue) in comparison to the standard reference mortar specimen – S (orange)

3.2 CMOD-controlled pre-cracking

Fig. 2a) shows the load force as a function of crack mouth opening displacement measured for different specimens. There is a different relaxation between the samples. For the mortar specimens with hydrogel (G) and for bio-mortar specimens (B) the nature of fractures is less brittle, which is the characteristic of the standard reference specimens.

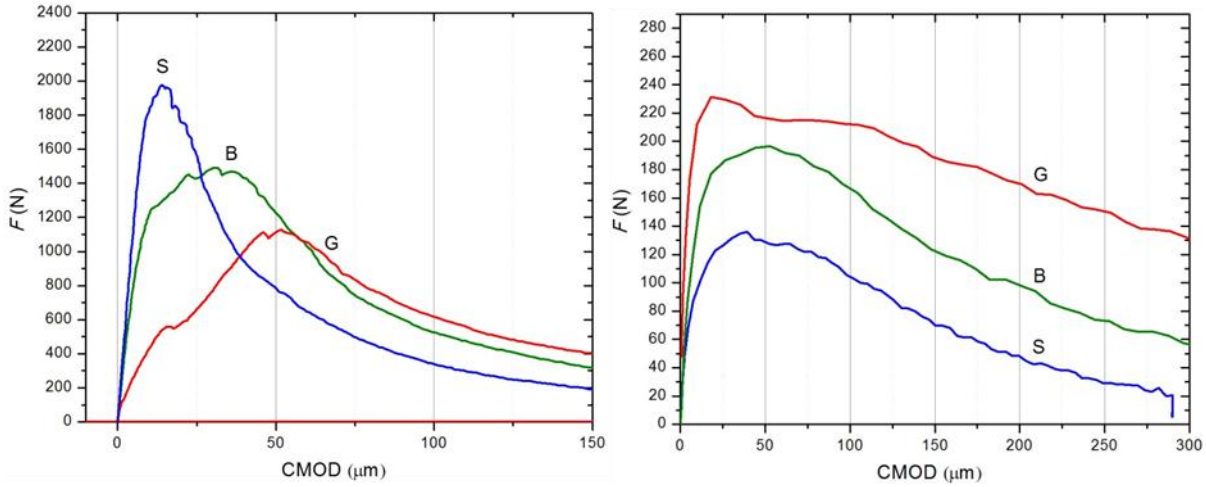

Figure 2: Load force *F* as a function of crack mouth opening displacement (CMOD) measured for different samples, a) during the crack formation b) after two months of curing

The maximum loading force was around 2000 N for the reference sample (S), less than 1500 N for the bio-mortar (B), while it was only about 1100 N for the specimen with hydrogel (G).

After the curing in the moisture room at 20 °C and RH 90 %, the specimens behaved differently. Partially healed specimens were again tested in 3-points bending test. Fig. 2b) showed a much lower maximum load force (between 120 N and 240 N) than the one that specimens could endure, in comparison to the load applied for the crack formation (1100 N – 2000 N, Fig. 2a). Also, the order of specimens regarding the maximum load force changed in the opposite direction. This fact could be attributed to different residual strength values obtained during the crack formation. However, the values of the maximum load force are considerably closer to each other in comparison to the crack formation values. The externally healed specimen unfortunately broke apart at very low load.

3.3 Water sorption

The difference between the weights of the sample kept in water and the dry sample was plot as a function of the square root of time. In fig. 3, the values, averaged over three samples of the same kind, of such a function were plot. The mortar specimens with hydrogel (G) absorb absolutely more water than other two, bio-mortar (B) and standard reference (S). This was expected as hydrogel uptakes water as much as it can and in bio-mortar there is about 30 % less hydrogel substituted with bacteria and nutrition. However, after the initial water uptake the increase of water sorption was steepest for the standard (S), than less steep for bio-mortars (B) and finally,

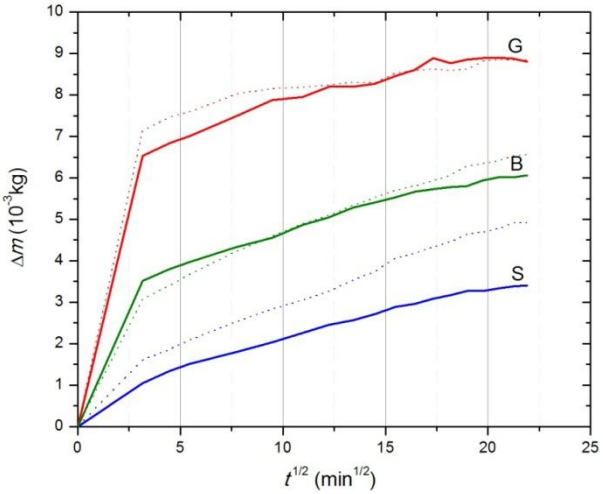

Figure 3: Water sorption of measured mortar specimens after pre-cracking (dashed lines) and after two months of curing (solid lines)

this function was the most flat for the mortars with hydrogel (G). After two months of healing process the water sorptivity of the measured specimens remained almost the same or a bit lower. However, the steepness became lower.

3.4 Scanning electron microscopy of bio-mortars

The results obtained by Low Vacuum SEM showed that the used bacterial culture was successfully encapsulated in the hydrogel (Fig. 4). The obtained results explained the behaviour of bio-mortars regarding textural and mechanical characteristics.

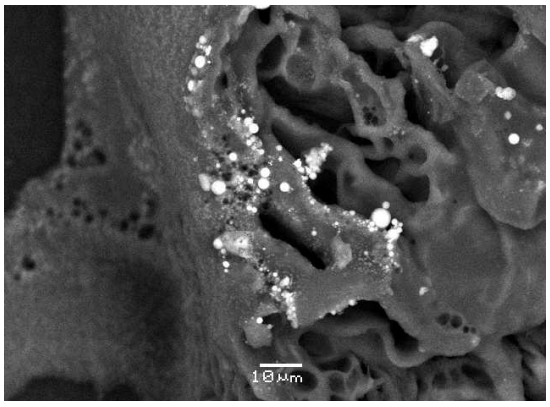

Figure 4: SEM micrograph of the encapsulated bacterial culture (white spheres) in the hydrogel

4. Conclusion

The presence of microorganisms encapsulated in hydrogel particles inserted in the cement matrix, proved by SEM investigation, shows a positive effect on mechanical characteristics and water sorption of the mortar specimens. The CMOD mechanical test of the fresh mortar specimens designed with hydrogel and the specimens with bio-mortar show less brittle behaviour in comparison to the standard ones. After two months of curing, the resistance to the maximum load force changed in favour of the specimens with hydrogel and bio-mortar. The mechanical characteristics of the two months cured specimens could be directly related to the water sorption values. Evidently, the hydrogel ability to retain water affects positively the self-healing phenomenon of the bio-mortar specimens.

Acknowledgment

The authors are grateful for the support of the Ministry of Education, Science and Technological Development of the Republic of Serbia (project number: III 45008) and for the support of COST CA 15202 for the Short-term scientific mission (reference no. 39833) and for the Conference grant no. COST-ITCCG-CA15202-494. The authors would also like to thank Luca Brambilla and Isabella Fisogni, students at Politecnico di Milano for the help during the experiments.

References

[1] Van Tittelboom, K. and De Belie, N., Self-Healing in Cementitious Materials – A Review, Materials 6 (2013), 2182-2217; doi:10.3390/ma6062182
[2] De Belie, N. et al, A Review of Self-Healing Concrete for Damage Management of Structures, Adv Mater Interfaces 5 (2018), 1800074; doi: 10.1002/admi.201800074
[3] Okwanda, G.D.O. and Li, J., Optimum conditions for microbial carbonate precipitation, Chemosphere 81 (2010), 1143–1148; doi: 10.1016/j.chemosphere.2010.09.066

SynerCrete'18 International Conference on Interdisciplinary Approaches
for Cement-based Materials and Structural Concrete
24-26 October 2018, Funchal, Madeira Island, Portugal

EFFECT OF FLY ASH AND SUPERABSORBENT POLYMER OPTIMIZATION ON SELF-HEALING CAPABILITY OF CONCRETE

Pattharaphon Chindasiriphan [(1)], Hiroshi Yokota [(1)], Paponpat Pimpakan [(1)]

(1) Hokkaido University, Sapporo, Japan

Abstract

Concrete with self-healing capability realizes sustainable structures by reducing life cycle cost and extending service life. Many self-healing techniques proposed so far are limited because of requiring prolonged water exposure. This paper investigates the potential of using fly ash and superabsorbent polymer (SAP) as concrete admixtures from the self-healing point of view. Fly ash concrete is characterized by pozzolanic reaction which results in a greater long-term strength. SAP contributes to water accumulation around damaged areas. The effect of both admixtures is examined with varying fly ash and SAP replacement ratios. Cylindrical cement mortar specimens were prepared and PVC jacketed. A uniaxial splitting pre-load was applied at the top edge to generate a crack in the range of 0.02 - 0.5 mm wide. The cracked specimens were water immersed for 28 days. The self-healing performance was evaluated based on crack width mitigation and water-flow through the crack.

1. Introduction

Concrete is a well-known material that is widely used in construction industry. Due to its versatility, durability, and cost saving, the majority of national infrastructure is made of concrete. It is estimated that around US$ 2.7 trillion is invested annually to build new infrastructure [1], but some of them are suffered from inevitable degradation of their performance, especially those exposed to severe environment conditions. Once a crack occurs in concrete, it accelerates transportation of harmful agents into concrete, such as chloride ion and carbon dioxide, and as a consequence, those agents accelerate steel corrosion. Structural maintenance is a time- and cost-intensive process. To prolong service life of concrete structures and overcome the limitation of maintenance budget, concrete with self-healing capability has been developed based on many techniques such as those integrate with calcite-

precipitating microorganism, expansive polymer including second hydration of cement and pozzolanic reactive admixture. This study investigates the potential of using fly ash and superabsorbent polymer (SAP) as concrete admixtures. The effect of both admixtures is examined with varying fly ash replacement ratios and SAP replacement ratios.

2. Methodology

2.1 Specimen preparation

The experiment was conducted by preparing cement mortar specimens that were divided into 2 groups. The first group was focused on optimization of self-healing capability by varying fly ash replacement ratios. The second group was investigated the effect of fly ash and SAP contents with 2 environmental exposure conditions. Table 1 lists the mix proportions of mortar. The mixing started with ordinary Portland cement (OPC), sand, fly ash along with a half of total SAP and lasted for 1 minute. The remaining SAP was mixed for another 1 minute to achieve a uniform distribution of materials. The dry-mix was conducted to minimize potential of adhesive effect and reduction of workability provoked by swollen SAP after exposed to water. Water was then gradually added and mixed with all powders for 3 minutes.

The fresh mortar was casted in cylinder mold that measures 100 mm in diameter and 200 mm in height. The specimens were demolded and cured in tap water for 28 days. Then, three of them were used for determining compressive strength conducted according to ASTM C39. The remaining specimens were spilt into 4 disks having 50 mm thick each. The top and the bottom most disks were disposed, and only the middle disks were fitted into a PVC pipe. A splitting crack was achieved by laid the specimen longitudinally on the concrete compression testing machine. The steel pins were placed on both sides of the specimen to keep it in place. One-point load was gradually applied along the steel plate which attached at the top of the specimen to create a concentrate point load. Under the splitting load, the PVC pipe deformed along with the specimen until the load reached its maximum. When the specimen started to crack, it was spontaneously confined with a lateral support. Crack widths were marked at 6 locations (three locations on the top surface and another three locations on the bottom surface), and were averaged to evaluate the crack closing ratio [2] that can be obtained by Eq. (1)

$$Crack\ Closing\ Ratio = 1 - \frac{Final\ Crack\ width}{Initial\ Crack\ width} = 1 - \frac{\omega_{28}}{\omega_0} \prec 0 \quad (1)$$

ω_0 = Average initial crack width [mm] measured at pre-cracking
ω_{28} = Average final crack width [mm] measured at 28 days of healing period

2.2 Water-flow through crack

An initial water-flow rate after pre-cracking was measured by flow test apparatus. It is specifically designed to achieve a constant hydrostatic pressure adequate to inject water throughout the crack. The inflow was supplied by the tap water which has an inlet located at the top of the apparatus. The excess water was drained out at the overflow outlet which allows water head to be controlled at 320 mm from the top of the specimen. The water-flow through the crack was measured at the measurement outlet.

2.3 Exposure conditions

Once the initial water-flow was investigated, the specimens were cured in the separate water tank for 28 days with the following conditions:

- FXX (specimen with fly ash): continuously immersed in water at 40 ℃.
- F45SX (specimen with fly ash and SAP): continuously immersed in water at 40 ℃.
- F45SX_WD (specimen with fly ash and SAP): immersed in water at 40 ℃ for 1 day and left in the air for 1 day. The procedure was done repeatedly.

Table 1: Mix proportion of mortar

Type	**Cement** (kg/m^3)	**Fly ash** (kg/m^3)	**Water** (kg/m^3)	**Sand** (kg/m^3)	**SAP** (% weight cement)
F00	525	0	237	1459	0
F15	466	79	237	1459	0
F25	394	131	237	1459	0
F35	341	184	237	1459	0
F45	289	236	237	1459	0
F45S4	289	236	237	1459	4
F45S6	289	236	237	1459	6
F45S8	289	236	237	1459	8

3. Results and Discussions

3.1 Effect of fly ash and SAP content on compressive strength

The compressive strengths are listed in Table 2. In the previous research, the authors investigated specimens with SAP replacement ratio between 0%-4%, and found that the SAP has a negligible effect on compressive strength of mortar specimen [3]. However, it is clearly noticeable that compressive strength fairly decreases when the SAP replacement ratio is higher than 4%. The reduction in compressive strength was also confirmed by Lee et al. [4] and Hasholt et al. [5]. They revealed that a sudden water exposure provokes SAP swelling and results in increase in porosity of specimens. At 28 days, the results showed that fly ash mortar encounters the reduction in compressive strength. The reduction is significant when fly ash content is increased. However, it is well known that pozzolanic activity in fly ash attributes to gradual development of strength and to greater final strength. It promotes self-healing behavior, which results in crack closure and mechanical properties recovery.

Table 2: Compressive strength at 28 days of curing

Type	**Compressive Strength**			
	Strength (MPa)	Standard deviation (MPa)	Coefficient of variation (%)	Strength reduction (%)
F00	55.36	0.35	0.63	0
F15	54.17	0.64	1.19	2.16
F25	54.79	1.52	2.78	1.03
F35	52.15	1.34	2.57	5.79
F45	49.11	1.23	2.50	21.28
F45S4	40.02	2.2	5.50	27.70
F45S6	35.26	2.62	7.42	36.31
F45S8	36.65	0.87	2.38	33.79

3.2 Effect of fly ash replacement ratio and SAP content on cracking behaviour and self-healing performance

Crack widths reductions of healed specimens and the load required to achieve crack widths range between 0.43-0.17 mm are presented in Table 3. Crack closure performance was determined by crack closure ratio. The calculation of crack closure was made via the method explained in equation (1). The results revealed that less load is necessary for mortar with higher fly ash content to achieve the designate crack widths.

Table 3: Cracking strength and crack closure ratio at 28 days

Type	**Initial Crack width (mm)**	**Final Crack width (mm)**	**Cracking load (kN)**	**Crack closing ratio**
F00	0.32	0.18	50.6	0.45
F15	0.26	0.07	50.9	0.73
F25	0.22	0.03	47.1	0.86
F35	0.2	0.04	48.8	0.80
F45	0.21	0.01	49.3	0.95
F45S4	0.2	0.03	37.1	0.84
F45S4_WD	0.18	0.06		0.67
F45S6	0.19	0.05	40.8	0.76
F45S6_WD	0.19	0.05		0.75
F45S8	0.18	0	40.3	1.00
F45S8_WD	0.19	0		0.98

On the other hand, a smaller crack width was achieved at higher fly ash content whereas the load was slightly lower. The crack widening was mitigated by newly form products generated by calcium carbonate crystallization [6]. The healing product is clearly noticed as carbonate-like white sediment which is primarily consolidated along the crack area. It was observed that, for the specimens subjected to wet-dry cycle (F45SX_WD), the amount of calcite deposition and crack closing ratio was accountable at the lower average value. The facts confirmed that water and moisture are essential to promote the self-healing mechanism [2]. Narrower cracks have higher potential to be closed completely as they need less volume of calcite. Furthermore, other newly formed hydration products bridge an interconnecting surface. Specimens with the crack widths between 0.15-0.25 mm show the most satisfactory crack closure performance at 28 days of healing. However, the healed specimens show high dispersion in crack sealing performance particularly those exposed to the wet-dry condition. The higher SAP content slightly mitigated variations in crack sealing performance in all the mixes. The phenomenon was characterized by the extensive internal curing due to the discharge of water entrapped by SAP.

3.3 Effect of fly ash replacement ratio and SAP content on water-flow through crack.

Water-flow through crack is plotted in Figures 1 and 2. The SAP specimens show the significant initial water-flow reduction compared to the non-SAP having the same crack width. It was explained by Lee et al. [4] that the swollen SAP gel acts as flow barrier sealing an opening crack. In case of continuously immersed in water, the rate of water-flow gradually decreases as healing time increases due to the maximum expansion of SAP gel, whereas in the wet-dry exposure, specimens reviewed an inconsistent trend of water-flow reduction which caused by insufficient water supply during air curing and shrinkage of SAP. After 12 days healing in wet-dry exposure, the specimens showed a constantly decreasing in water-flow through the crack.

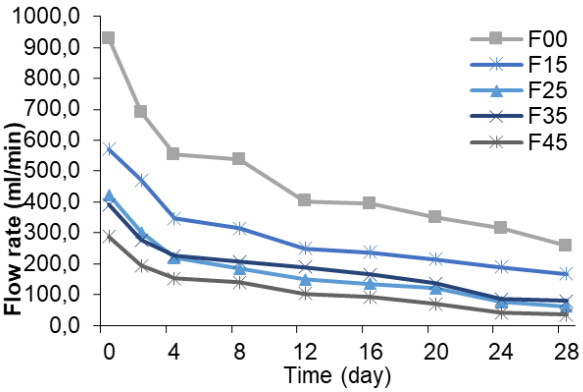

Figure 1: Waterflow through crack of F00-F45

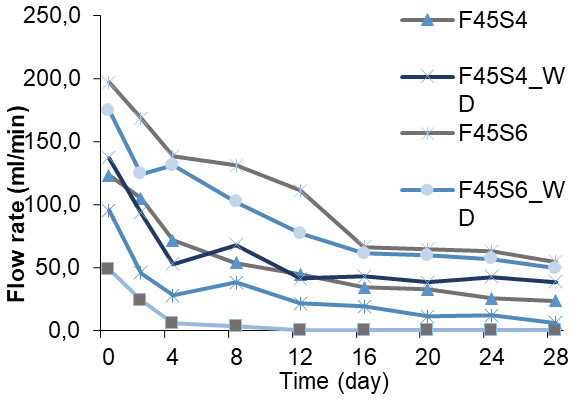

Figure 2: Waterflow through crack of cast-in SAP

The non-SAP-containing specimen showed gradually decreasing in water-flow through the crack. Initial water-flow measurements indicate that the water-flow reduction of the following cases could be attributed from rehydration of cementitious materials and pozzolanic reaction. In the non-SAP-containing specimens, increase in fly ash replacement ratio shows better water-flow rate reduction. F45 achieved the most efficient water-flow reduction, while F45S8 yielded the completely watertight crack around 12 days of healing. The increase in SAP

content accounts for a better water-flow reduction despite of exposure conditions, whereas the effect of fly ash on the recovery of water tightness was not clearly observed. However, as mentioned earlier, higher replacement ratio of fly ash obtained a finer crack under the same pre-crack condition. The advantage of fly ash as damage prevention and self-healing performance were confirmed.

4. Conclusions

This study investigated the effect of fly ash and SAP as concrete admixtures on the self-healing capability. The following conclusions can be drawn:

1. The compressive strength development is interfered by SAP and fly ash at 28 days.
2. Increasing the SAP replacement ratio enhances the efficiency of crack sealing performance which featured in higher crack closure and water-flow reduction. The contribution is attributed by an extensive moisture supply from SAP.
3. The presence of water and moisture is essential to provoke self-healing activity which is characterized by crack width mitigation of the swollen SAP and deposition of newly form cementitious materials.
4. The initial water-flow rate of SAP specimens is significantly decreased resulting from impermeable gel expanding to seal a crack patronized swollen SAP.
5. The continuous immersion in water at 40 ℃ promotes the best healing efficiency, which contributes to a rapid water-flow reduction and crack closure.
6. A significant impact on crack closure is found when the initial crack width is smaller than 0.25 mm. The development of calcium carbonate-like substance along the cracked area is generally found in healed specimens.

Acknowledgements
The authors wish to express our sincere gratitude and appreciation to Professor Minoru Kunieda of Gifu University and his team for all their support and collaboration. The SAP used in this study was sponsored by Nippon Shokubai, Co., Ltd.

Reference

[1] "The Global Infrastructure Gap." Web. 2018 http://reports.weforum.org/strategic-infrastructure-2014/introduction-the-operations-and-maintenance-om-imperative/the-global-infrastructure-gap/
[2] Roig-Flores, M. et al, Effect of crystalline admixtures on the self-healing capability of early-age concrete studied by means of permeability and crack closing tests, Constr Build Mater 114 (2016), 447-457
[3] Chindasiriphan P. and Yokota H., Self-healing ability of concrete made with fly ash and superabsorbent polymer, The 2nd ACF Symposium 2017 from Innovations for Sustainable Concrete Infrastructures, Thailand (2017)
[4] Lee, H. X. D. et al, Self-sealing of cracks in concrete using superabsorbent polymers, Cem Concr Res 79 (2016), 194-208
[5] Hasholt M.T. et al, Mechanical properties of concrete with SAP Part 1: Development of compressive strength, RILEM Proceedings PRO 74 from the International RILEM Conference on Use of Superabsorbent Polymers and Other New Additives, Denmark (2010), 117–126
[6] Snoeck, D. et al, The effects of superabsorbent polymers on the microstructure of cementitious materials studied by means of sorption experiments, Cem Concr Res 77 (2015), 26-35

SynerCrete'18 International Conference on Interdisciplinary Approaches
for Cement-based Materials and Structural Concrete
24-26 October 2018, Funchal, Madeira Island, Portugal

EFFECTIVENESS OF SELF-HEALING TECHNOLOGIES IN CEMENT BASED MATERIALS: CONCEPT FOR AN INTER-LABORATORY EXPERIMENTAL EVALUATION BY MULTIPLE TEST METHODS. A PROPOSAL BY COST ACTION CA 15202 SARCOS

Liberato Ferrara [(1)], Tim Van Mullem [(2)], Estefania Cuenca [(1)], Henk M. Jonkers [(3)], Francesco Lo Monte [(1)], Mercedes Sanchez [(4)], Nele De Belie [(2)] and Antony Jefferson [(5)]

(1) Politecnico di Milano, Italy
(2) Ghent University, Belgium
(3) Delft University of Technology
(4) University of Cordoba, Spain
(5) University of Cardiff, United Kingdom

Abstract

The use of self-healing cement-based materials has been recognized as a viable pathway to enhance the durability of reinforced concrete structures and contribute to increase their service life. Research activities have provided enlightening contributions to understand the crack-healing mechanisms and have led to the blooming of stimulated and engineered self-healing technologies, whose effectiveness has been proven in the laboratory and, in a few cases, also scaled up to field applications, with ongoing performance monitoring. Nonetheless, the large variety of methodologies employed to assess the effectiveness of the developed self-healing technologies makes it necessary to provide a unified framework for their validation. This is also instrumental to pave the way towards a consistent incorporation of self-healing concepts into structural design and life-cycle analysis codified approaches and promote their diffusion into the construction market. COST Action CA15202 SARCOS (www.sarcos.eng.cam.ac.uk) has revealed that a reliable assessment of a healing technology has to rely upon multiple measurements, encompassing all the issues recalled above and establishing correlation between the measured crack closure and recovery of the engineering properties of interest. In this paper the concept for a multi-laboratory evaluation of self-healing technologies is presented.

1. Introduction

The implementation in the construction industry of self-healing cement based materials has been recognized as a pathway worth being travelled with the aim of improving the durability and long-term performance of structures made of and/or retrofitted with the aforementioned category of construction materials, able to extend their lifespan, also through the incorporation of new advanced functionalities to traditional materials. The variety of materials and techniques to either stimulate the autogenous healing capacity of concrete or engineer it [1], also through the incorporation of advanced functionalities, has been validated, in a much needed effort to assess their efficiency, through a multi-fold set of experimental tests and methodologies [2].
As a matter of fact, the experimental characterization of the durability of construction materials in real structure scenarios is quite a challenging task, which requires "tailored" experimental capabilities and consists of several tasks. These range from creating a controlled "damage state" (a crack) in the material to the implementation of "healing conditions" suitably representing the intended functional and structural service scenario, to the evaluation of the sealing of the crack and of the related performance recovery, supported by the comprehension of the underlying mechanisms through the characterization of the healing products.
In this paper the proposal developed in the framework of the same COST Action for a multi-laboratory evaluation of self-healing technologies is presented. Besides the proposed types of tests, the most important experimental variables governing the healing phenomenon and also discriminating about its successful and physically sound experimental evaluation will be discussed, including, e.g., the method to produce the initial crack and control its width, the selection of exposure conditions replicating true structural service scenarios. The selection of experimental properties to be measured will be also discussed in a modelling-oriented framework, in which such properties play the role of model input parameters [3].

2. Experimental variables governing the healing of cement-based materials

In defining the tasks for the inter-laboratory testing activities the concept of the experimental plan has been based on a few fundamental governing variables, while leaving to each participating partner the choice of one or more healing methodologies of its own interest. These may include either autogenous healing stimulated by tailored additions, including, *e.g.*, supplementary cementitious materials, crystalline admixtures, superabsorbent polymers, or autonomous healing, engineered by means of encapsulated minerals or polymers (micro- and macro-encapsulation) or through bacteria. In the planned activities all these techniques can be employed in combination with plain concrete and mortars as well as with high performance fibre reinforced cementitious composites (HPFRCCs).
Mortars can be employed both "per se", as for example local repair materials [4], or be designed with a concrete equivalent composition, In the last case, with main reference to a preliminary validation of the potentials of a healing technology, the use of smaller material quantities than necessary with a conventional concrete would be feasible, even if a dilution effect in the quantity of the healing agent when scaling up to concrete has to be considered.
With reference to HPFRCCs, which are characterized by a mix composition highly conducive

to self-healing [5,6], it is extremely interesting to investigate the synergy between the aforementioned autogenous healing capacity and healing stimulating/engineering constituents. The choice of the material to be investigated has a twofold outcome. First of all it will affect the size of the specimen which has to be employed, with reference to the material heterogeneity scale. Moreover, it will govern the choice of the experimental methods to be employed for the creation of the "controlled state of damage", i.e. a crack with a controlled width, which has to be healed. Additionally, the type of material and the specimen size will influence the test methods which can be used to evaluate the sealing/healing behaviour.

As a matter of fact, since plain mortar and concrete are inherently brittle, closed-loop crack-opening controlled tests are needed in order to produce a crack through bending, splitting tensile or direct tensile tests, in order of difficulty. A few authors [7,8] have proposed to "pre-damage" the specimens by means of compression tests, pre-loading them at a fraction of the compressive strength, either in the pre- or post-peak regime. Though this approach induces a diffused state of damage which can be, *e.g.*, quantified by means of comparative ultrasonic pulse velocity tests, it can hardly be employed to produce a crack whose controlled width has also to stand as a governing variable for the healing processes to be investigated.

In view of this the SARCOS group has recommended the use of prism specimens:

$L \times b \times h = 160 \times 40 \times 40$ *mm* in the case of mortars, and

$L \times b \times h = 500 \times 100 \times 100$ *mm* in the case of plain concrete.

The preferential pre-cracking technique would be in such cases the three-point bending test. In case, a notch could be prearranged through cast-in inserts at the specimen mid-span in order to pre-determine the crack-site formation and ease the crack opening measurement. In all cases, this would provide, *e.g.* through a clip-gauge suitably attached at the beam specimen tension side (Figure 1a), the opening of the crack at its mouth, the true tip opening in the case of notched specimens being even lower, with no information neither on the trend of the crack opening along its length nor on its internal structure. While the former information could be obtained by micro-imaging the crack and processing the images through suitable image analysis tools [9], the latter can only by obtained through advanced experimental techniques such as Computer Tomography [10,11], even if so far no quantitative information has been garnered on the topic.

In the case of HPFRCCs the same mix composition recognized as highly conducive to self-healing yields a signature tensile behaviour, characterized by an extended stable multiple cracking phase after the formation of the first crack and before the onset of unstable crack localization. This makes it possible to stably perform, even under displacement control, three- and four-point bending tests and even direct tension tests. Moreover, at least four-point bending tests need to be performed in order to usefully develop the aforementioned multiple cracking. For this reason, the SARCOS group has recommended for HPFRCCs prism specimens $L \times b \times h = 500 \times 100 \times 20$ *mm* to be pre-cracked in four-point bending, e.g. under a third-point loading scheme.

It is anyway worth remarking that, through such a test, where multiple cracks are expected to develop in the central "between the loads" portion of the specimen, the deformation measured, *e.g.*, at the beam tension side through LVDTS across a gauge length (Figure 1b), represents the sum of the surface openings of all the cracks and is thus only representative of an overall damage level. The quantification of the opening of each single crack would require, e.g., image analysis of crack micrographs as above.

Figure 1: examples of crack measurement via a clip-gauge at specimen mid-span in a three-point bending test (left) and via LVDTs across gauge-length in a four-point bending test (right).

The three-point bending test, recommended for plain concrete and mortar, and the four-point bending test, selected as the most suitable for HPFRCCs, feature a common artefact as far as their use to "pre-crack a to-be healed specimen" is concerned. In most of the investigations, after being cracked the specimen has to be unloaded before being exposed to the healing conditions representative of the structural service scenario. This results in a partial back-closure of the crack, due to the elastic regain of the specimen, unless active crack control techniques are enforced. The amount of crack closure depends on the type of test and pattern of the crack(s), which makes it hardly predictable. This leaves the only option to perform the test up to a prescribed crack opening under load, accepting the elastic regain and anyway measuring the residual opening of the crack upon complete load removal, both through the employed measuring instruments as well as through micro-imaging of the cracks to be further processed. This implies that a range of residual crack openings can be obtained, which have to be duly taken into account when assessing the efficiency of different healing techniques. Crack opening ranges can be defined *e.g.* in accordance with current code prescriptions for serviceability and durability limit states.

The initial crack opening is surely one of the governing parameters which represent the structural service scenario under which the healing has to occur and which has to be replicated in the experiments. Such a scenario also encompasses, as expectable, the environmental exposure conditions but also the age of cracking. In the case of autogenous (stimulated) healing, the age of cracking will be first of all directly related to the amount of un-hydrated binder particles, and hence on the autogenous self-healing capacity, also discriminating between the prevalence between the autogenous mechanisms and the action of the stimulating agent. In the case of autonomous healing, *e.g.* engineered through encapsulated chemicals, the age of cracking is also likely to affect the efficiency of the mechanism, related as it is to the concrete fracture toughness. The formation of a crack at an earlier age is likely to be associated to a lower energy release rate, which is hence likely to be less effective in rupturing the intercepted capsules.

In view of this the SARCOS group has decided in the planned inter-laboratory activity to foresee two different ages of cracking: an earlier one (< 7 days) which highlights the autogenous healing potential and a later one (> 28-56 days, also depending on the presence of pozzolanic mineral additions) to highlight the effects of any stimulating agents. In the case of healing engineered through encapsulated polymers, for which generally quite large crack openings are studied, the combination with the very short healing duration (<7days) allows only for a very limited autogenous healing and then may require only one age of cracking.

The reproduction of structural service scenario is then complemented with the exposure conditions. The availability of water being essential for stimulated autogenous and some engineered healing mechanisms to occur, the proposal is to investigate, besides a continuous

immersion condition also wet/dry cycles, in case in the presence of aggressive substances in the water to broaden the representativeness of the investigation (involved partners may select the aggressive scenario of interest).

3. Measuring the healing through the recovery of the material performance

Once the experimental testing framework, representing the intended structural service scenario, has been defined as above, the healing evaluation methodology through the measurement of the crack sealing and of the recovery of the material durability and mechanical performance has to be specified. Tab. 1 presents the summary of the healing evaluation procedures currently available in the literature [2]. Healing related indices of performance reported in the table stand as the first step for the quantification of the healing efficiency. The inter-laboratory testing activity will consist of:

- the measurement of the crack closure at least by means of optical methods;
- the recovery of one durability related property and a (set of) mechanical properties;
- the assessment of the correlation among the aforesaid parameters, for consistency.

With reference to the connection between index of crack sealing and indices of performance recovery, it is worth remarking that the former, computed from visual measurements of crack closure, only does account for the crack sealing which is taking place on the surface of the specimen, whereas the recovery of any performance, mainly mechanical, is also the outcome of the internal through crack reconstruction of the matrix continuity. This, besides contributing to better understand the trend of the established correlation may also call for the concept and implementation of methods to indirectly estimate the amount of crack closure from the amount of recovered performance. Some attempts in this sense have been proposed in [6] from cross-wise comparison of pre-crack vs. post-healing load vs. crack-opening curves and from damage vs. crack opening curves as built from the evaluation of the stiffness recovery. This implies a modelling concept to be incorporated into the healing evaluation approach.

4. Modelling

The experimental characterization of the self-healing capacity of any material requires the investigation to span along a time frame whose extension could hardly match with the needs of an effective and market oriented technology transfer. In this respect the availability of sound and reliable predictive modelling tools becomes of the utmost importance, since only they would allow to extrapolate the results of performed experimental characterization of the durability performance of cement-based materials to real structure service scenarios [4].

In this respect, the availability of test data from tests on companion undamaged specimens undergoing the same curing history as the cracked/healed ones, will provide the necessary calibration of the evolution of mechanical fracture parameters of the material allowing to discriminate between healing-induced recovery and aging evolution of the property of interest.

As a mere example, it may be worth remarking that, definition of damage evolution curves as a function of crack opening, healing time and exposure may be for example interpreted in this framework, whenever damage mechanics based models are going to be employed. Similarly,

the establishment and validation of correlation between permeability recovery and crack closure may be instrumental, in the case of smeared crack models, to establish a link between the mechanical part of the modelling, which has at least to describe the pre-cracking, and the transport one, the models being linked by a mutual input parameter feeding.
Microstructural models will require likewise microstructural related parameters to be experimentally identified also with the aim of deeper understanding the nature of the healing mechanisms as well as the intrinsic signature properties of the healing products, in a multiscale comprehension effort of the outcomes of the healing.
A survey recently published by the SARCOS consortium [4] has revealed that many papers do not review experimentally observed material behaviour in advance of presenting model theory.
There are probably a number of reasons for this state of affairs. One could be that there is a paucity of experimental data suitable for properly validating numerical models. Another reason might be that there has been insufficient interaction between relevant numerical and experimental research teams. The inter-laboratory activity planned by the SARCOs consortium would hence stand as a one-of-a-kind opportunity in this sense.

Table 1: healing index from recovery of durability related and mechanical properties

	Recovered property	Healing Index	Quantities of interest
Durability properties	Crack closure	Index of Crack Sealing ***ICS*** $\frac{w_{pre-cracking} - w_{post-healing}}{w_{pre-cracking}}$ $w_{pre\text{-}cracking}$ *crack opening at pre-crack* $w_{post\text{-}healing}$ *crack opening after healing*	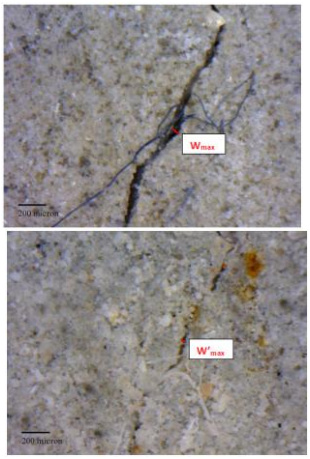
	Permeability	Index of permeability recovery $ISH_{permeability,1}$ $\frac{W_{unhealed,t} - W_{healed,t}}{W_{unhealed,t}}$ $ISH_{permeability,2}$ $\frac{W_{initial} - W_{final}}{W_{initial}}$	$W_{unhealed,t}$ *:amount of water passing through the specimen's unhealed crack at time t* $W_{healed,t}$*: amount of water passing through the specimen's healed crack at time t* $W_{initial}$ *: amount of water passing through the target specimen before healing* W_{final}*: : amount of water passing through the target specimen after healing.*

Table 1 (ctd.): healing index from recovery of durability related and mechanical properties

	Recovered property	Healing Index	Quantities of interest
Durability prop.	Sorptivity	Index of Sorptivity Recovery $ISH_{sorptivity} = \frac{S_{unhealed} - S_{healed}}{S_{unhealed,} - S_{uncracked}}$	$S_{unhealed}$: *sorptivity index for the cracked and unhealed specimen* S_{healed} *: sorptivity index for the cracked and healed specimen* $S_{uncracked}$*: sorptivity index for the uncracked specimen*
Mechanical properties	Residual post-cracking strength	***Index of Strength Recovery*** ISR $\frac{f_{peak,post-conditioning} - \sigma_{unloading,pre-cracking}}{f_{peak,pre-cracking} - \sigma_{unloading,pre-cracking}}$	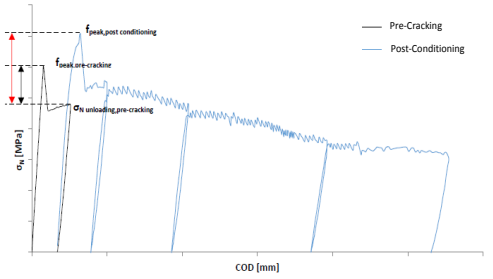
	Stiffness	***Index of Damage Recovery*** IDR = $\frac{K_{loading,post-conditioning} - K_{unloading,pre-cracking}}{K_{loading,pre-cracking} - K_{unloading,pre-cracking}}$	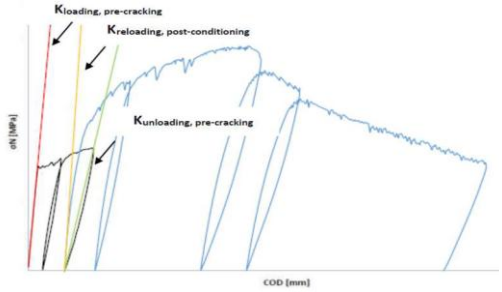

5. Conclusions

In this paper the concept has been presented for an inter-laboratory experimental activity which is going to be performed by the consortium of the COST Action CA 15202 SARCOS. The activity will include both autogenous/stimulated and autonomous healing, investigating both plain concrete and mortar and HPFRCCs. The action will be based on the assessment of the selected healing technique(s) under the exposure conditions of choice (common to all: immersion in water and wet/dry cycles; optional: one aggressive condition) through:

- measurement of the crack sealing through visual micro-imaging of the cracks
- measurement of the recovery of one durability property and mechanical performance

with establishment of mutual correlation between the measurements garnered as above.
The choice of the material of interest will dictate the specimen geometry as well as the method of pre-cracking. This has anyway to take into account the experimental capabilities of the partners as well as the selected method of performance recovery assessment.
Particular care has to be dedicated to the measurement of the crack opening in the pre-cracking stage both because of experimental artefacts inborn in such a procedure (elastic regain upon unloading) but also in view of the representativeness of a "surface garnered"

measure of the crack opening to described a 3D structure such as a crack. In view of this, correlation between surface crack measurements and observation on the internal crack structure through advanced methods, though not mandatory, could be pursued.
The experimental activity as a whole will also be targeted to provide a broad enough database for the calibration and validation of numerical predictive models, thus standing as a one of a kind research also intended to pave the way towards incorporation of self-healing concepts and outcomes into durability-based design approaches.

Acknowledgements
The authors acknowledge the support from EU COST Action CA 15202 "Self-healing as preventive repair of concrete structures – SARCOS" (http://www.sarcos.enq.cam.ac.uk).

References
[1] De Belie, N. Gruyaert, E., Al-Tabbaa, A., Antonaci, P., Baera, C., Bajare, D., Darquennes, A., Davies, R., Ferrara, L., Jefferson, T., Litina, C., Miljevic, B., Otlewska, A., Ranogajec, J., Roig-Flores, M., Pain, K., Lukowski, P., Serna, P. Tulliani, J.M., Vucetic, S., Wang, J., Jonkers, H.M., A review of self-healing concrete for damage management of structures, Advanced Materials and Interfaces, accepted (2018).
[2] Ferrara, L. Van Mullem, T., Alonso, M.C., Antonaci, P., Borg, R.P., Cuenca, E., Jefferson, A., Ng, P.L., Peled, A., Roig, M., Sanchez, M., Schroefl, C., Serna, P., Snoeck D., Tulliani, J.M. and De Belie, N., Experimental characterization of the self-healing capacity of cement based materials and its effects on the material performance: a state of the art report by COST Action SARCOS WG2, Construction and Building Materials, 167 (2018), 115-142.
[3] Jefferson, T., Javierre, E., Lee Freeman, B., Zaoui, A., Koenders, E. and Ferrara, L., Research progress on numerical models for self-healing cementitious materials, Advanced Materials and Interfaces, accepted (2018).
[4] Sanchez, M., Faria, P., Ferrara, L. Horszczaruk, E., Jonkers, H.M., Kwiecien, A., Mosa, J., Peled, A., Pereira, A.S., Snoeck, D., Stefanidou, M. and Stryszewska, T., External treatments for the preventive repair of existing constructions: COST Action CA15202 framework", Construction and Building Materials, submitted (2018).
[5] Ferrara, L., Krelani, V., Moretti, F., Roig Flores, M. and Serna Ros, P., Effects of autogenous healing on the recovery of mechanical performance of HPFRCCs: part 1, Cement and Concrete Composites, 83 (2017), 76-100.
[6] Ferrara, L., Krelani, V. and Moretti, F.: "Autogenous healing on the recovery of mechanical performance of HPFRCCs: part 2 – correlation between healing of mechanical performance and crack sealing, Cement and Concrete Composites, 73 (2016), 299-315.
[7] De Nardi, C., Bullo, S., Ferrara, L., Ronchin, L. and Vavasori, A., Effectiveness of crystalline admixtures and lime/cement microcapsules in engineered self-healing capacity of lime mortars, Materials and Structures, 50(4) (2017), 191.1-191.12
[8] De Nardi, C., Cecchi, A., Ferrara, L., Benedetti, A. and Cristofori, D., Effect of age and level of damage on the autogenous healing of lime mortars, Composites-Part B: Engineering, 124 (2017).
[9] Snoeck, D., Dewanckele, J., Cnudde, V., and De Belie, N., X-ray computed microtomography to study autogenous healing of cementitious materials promoted by superabsorbent polymers, Cement and Concrete Composites, 65, (2016), 83-93.
[10] Van Tittelboom, K., Wang, J., Araujo, M., Snoeck, D., Gruyaert, E., Debbaut, B., Derluyn, H., Cnudde, V., Tsangouri, E., Van Hemelrijk, D. and De Belie, N., Comparison of different approaches for self-healing concrete in large-scale lab tests, Construction and Building Materials, 107 (2016), 125-137.

SynerCrete'18 International Conference on Interdisciplinary Approaches
for Cement-based Materials and Structural Concrete
24-26 October 2018, Funchal, Madeira Island, Portugal

EXTENDING THE SERVICE LIFE OF POLYMER INDUSTRIAL FLOOR COATINGS BY IMPROVING THEIR ADHESION TO CEMENT-BASED SUBSTRATES

Łukasz Sadowski [(1)], Agnieszka Chowaniec [(1)]

(1) Wroclaw University of Science and Technology, Wroclaw, Poland

Abstract
The study focuses on extending the service life of polymer industrial floor coatings by improving their adhesion to cement-based substrates. The purpose of the study is to evaluate the possibility of using waste glass powder in polymer industrial floor coatings made with the use of epoxy resin. The chemical composition and particle size of waste glass powder make it an attractive additive for the durable and sustainable epoxy resins used in industrial floors systems. Waste glass powder is used in epoxy resin coating as a filler. Samples were stored in air curing conditions. Pull-off tests were performed in order to study the effect of adding waste glass powder on the adhesion between modified polymer industrial floors and cement-based substrates. The results were compared to reference samples without waste glass powder.

1. Introduction

State-of-the-art epoxy resins are very popular in civil engineering for producing a full range of floor coatings [1]. These kinds of resins are more and more frequently playing a special role. They need to be, e.g. heavy-duty, conductive, decorative or chemically resistant. In civil engineering they are usually laid on cement-based substrates. It is required that these resins are characterized by high adhesion to the substrate [2, 3].
In order to obtain adequate adhesion of the epoxy resin to the substrate, two technological treatments must be carried out. First, the substrate is required to be processed by grinding, sand- or shot-blasting with thorough cleaning and vacuuming of the surface. There is then a need to apply a bonding agent on the previously treated substrate. After these two actions, the epoxy coating can be applied. It should be noted that there is a risk of making mistakes during the implementation of these technological actions. In addition, they are expensive and time-

consuming. Therefore, in recent times solutions have been sought to reduce or eliminate one of these drawbacks.
It was noted in [4] that recent innovations in civil engineering cannot be done without considering sustainable development. Thus, mineral industrial wastes have recently become more popular as the additives in cement-based composites [5]. To the best of our knowledge, there is no study related to the adhesive properties of epoxy resins modified using waste glass powder. The chemical composition and particle size of waste glass powder make it an attractive additive that can be used in the sustainable epoxy resins used in industrial floor systems.
Bearing the above in mind, the paper presents studies on coatings made of epoxy resins modified with the addition of waste glass powder. The purpose of the tests was to check whether it is possible to obtain the required adhesion of the epoxy resin coating without the use of a bonding agent. According to the authors, this will be possible with the addition of glass powder, which is a by-product from the production of glass microspheres. The aim of the research is also to determine the optimal ratio between the base material and the additive.

2. Materials and methods

A coating containing an epoxy resin based on bisphenol A in an amount from 64.5 to 74.1% by weight, a glass powder filler with a proportion of at least 60% of a plurality of grains of less than 63 μm in diameter and hardener based on aliphatic polyamines in the amount from 16.1 to 8.5% by weight was used. The resin contains bisphenol A with a molecular weight <700. The bisphenol A was mixed with the hardener in weight proportions of 100:25. The composition contains a quartz powder filler that has a mass composition of about 71% SiO_2, 1% Al_2O_3, 9% CaO, 4% MgO, 14% $Na_2O + K_2O$ and a maximum of 0.1% TiO_2 in an amount from 7.4 to 9.4% by weight. The glass powder used is a waste material from the production of glass microspheres. It is successfully used, among others, as a flux, conditioner and as a very good filler, e.g. for cement-based and ceramic materials.
The epoxy resin is ready for use after thorough mixing of the bisphenol A and the glass powder filler. After mixing, a fluid consistency is obtained, and the hardener is added immediately before applying the coating to the surface of the substrate. An indicator of a sufficiently thorough mixing of three components that have a different colour in their initial state is the obtaining of a uniform colour and consistency of the whole mass.
As a substrate for the coating, a cement substrate with a thickness of 40 mm was used. This substrate was made of a ready mix cement screed with self-levelling properties. A total of 11 cement substrates with a compressive strength ranging from 8.7 to 16.5 MPa and a tensile strength ranging from 1.4 to 3.0 MPa were prepared. The letter R indicates the control sample, which was coated with an epoxy resin without the addition of glass powder, and the numbers from 10 to 100 indicate the weight proportions of the content of glass powder X in a weight ratio to the coating components (100:25:X).
The surface of the substrate was cleaned, grinded and then vacuumed. As a result, a dry, (mass humidity of about 4%) hard and stable surface was obtained. The epoxy resin was then spread on the surface of the cement substrate by means of a serrated trowel and deaerated using a paint roller. The application and curing period of the coating took place at room temperature (about 20ºC). Pull-off adhesion (f_b) measurements were made after 7 days, after obtaining the full mechanical load capacity for the epoxy coating (Fig. 1a). The f_b of the

coating to the substrate was tested at three points for each sample using the pull-off method (Fig. 1b).

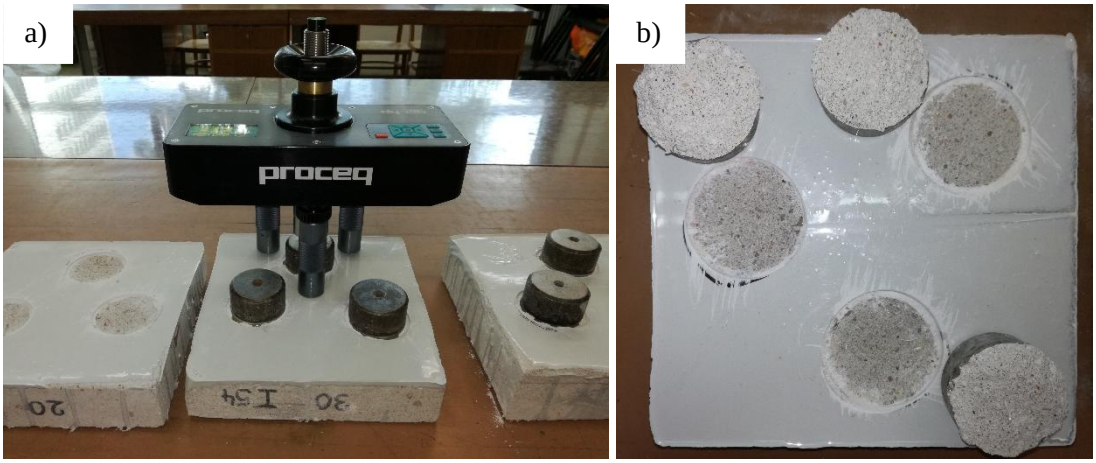

Figure 1: The view of: a) testing the pull-off adhesion using the pull-off method, b) the surface of the sample after the testing

3. Test results and analysis

The summary of the obtained research results is presented in Table 1. The results of the tests are also visualized in Fig. 2 in the form of graphs of functions of three variables.
During the research it was observed that along with the increase in the amount of added glass powder, it was also necessary to extend the mixing time and increase its diligence in order to obtain a uniform mass. A greater amount of powder caused an increase in the density of the mixture, and thus an increase in the force needed for mixing, especially for samples 80, 90 and 100. It was also observed that the absorptivity of the roller decreased with an increasing content of the waste glass mineral powder.
It was also observed that the increase in the content of glass powder resulted in a reduction in the self-levelling ability of the epoxy resin coating. For samples from 10 to 40, the resin still spread very well over the surface of the substrate and self-levelled. However, for subsequent samples, there was a gradual increase in surface irregularities. Even coverage of the undercoats with 80, 90 and 100 coatings was not feasible.
While testing the adhesion of the coating to the substrate using the pull-off method, the failure of the measuring disk was most often at the interface between the coating and the cement substrate (or partially in the substrate).

Table 1: Summary of the obtained research results.

Composition (100:25:X)	**Average value of pull-off adhesion f_b (MPa)**	**Average value of the compressive strength of the substrate f_c (MPa)**	**Average value of the tensile strength of the substrate f_t (MPa)**
0	2.71	14.2	1.7
10	2.31	12.5	1.8
20	2.43	16.5	1.4
30	1.78	10.3	1.4
40	3.07	14.0	1.5
50	2.79	15.7	1.6
60	2.20	15.5	3.0
70	2.53	14.9	2.3
80	2.44	8.7	2.1
90	2.61	10.9	3.0
100	2.12	13.0	2.9

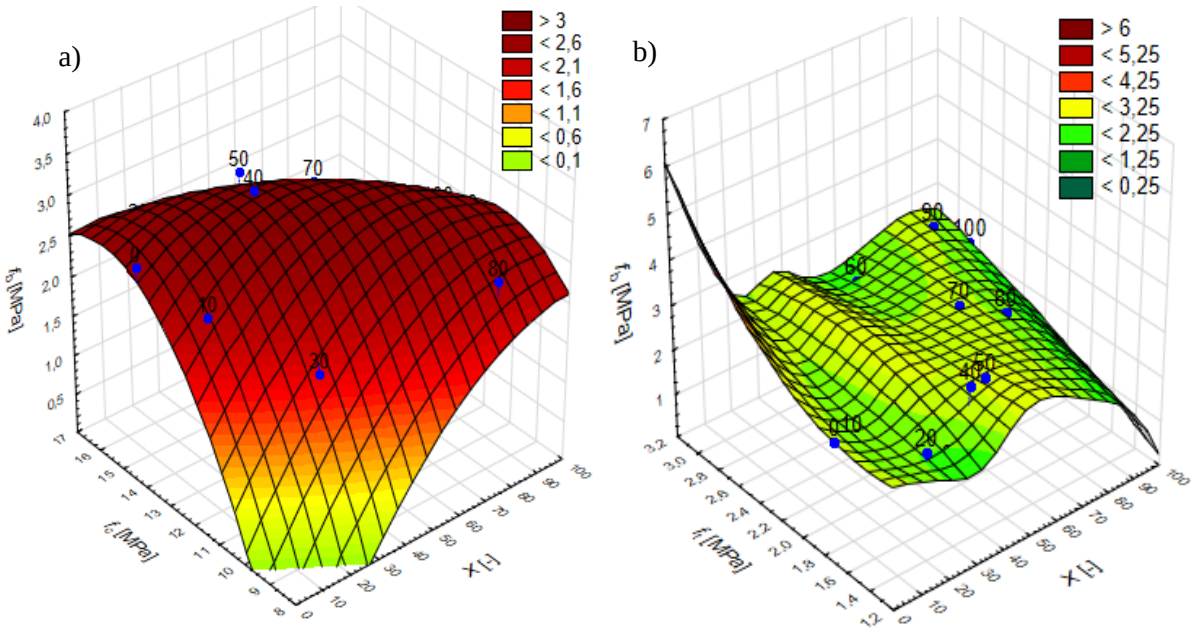

Figure 2: Graphs of functions of three variables for: a) the compressive strength of the substrate, b) the tensile strength of the substrate

In general, it can be seen from Figure 2 that the increase of the value of the pull-off adhesion corresponds with the increase of the compressive and tensile strength and also the amount of glass powder. It should be noted that the plane visible in Figure 2 was determined by the least squares method. It can be concluded from Figure 2a that for the substrates with a compressive strength f_c lower than 10 MPa and a very low value of the amount of waste glass powder, the delamination is expected ($f_b = 0$). This could be due to the lack of mechanical compatibility of the material of the coating and the substrate [6]. This is caused by too high difference in compressive strength between epoxy resin and such a low-strength cement substrate.

4. Conclusions and perspectives

The study was focused on extending the service life of polymer industrial floor coatings by improving their adhesion to cement-based substrates. The performed research results show that in some configurations the addition of glass powder improved the adhesion of the epoxy resin coating. This research proved that it is possible to obtain the required value of pull-off adhesion without prior application of the bonding agent. An additional advantage is the increase in the efficiency of the coating, which is caused by the decrease in the absorptiveness of the roller.

Based on the obtained results, it was found that the optimal weight ratio between the components of epoxy coating A and B, and the content of glass powder X, is A: B: X = 100: 25: 40. The higher content of the additive makes it difficult to obtain a smooth surface.

The presented epoxy resin is convenient to use and can be used in a very wide range of industrial conditions. It may be applied for the manufacturing of epoxy resin coatings. Thanks to the application of the developed coating, it is possible to obtain the required adhesion of the coating to the substrate without the need of applying the bonding agent.

References

[1] Mays, G. C., Hutchinson, A.R., Adhesives in civil engineering, Cambridge University Press (2005)
[1] Sadowski, Ł., Czarnecki, S., & Hoła, J., Evaluation of the height 3D roughness parameters of concrete substrate and the adhesion to epoxy resin. International Journal of Adhesion and Adhesives, 67 (2016) 3-13
[3] Garcia, J., De Brito, J. Inspection and diagnosis of epoxy resin industrial floor coatings. Journal of Materials in Civil Engineering, 20-2 (2008), 128-136
[4] Czarnecki, L., van Gemert D., Innovation in construction materials engineering versus sustainable development. Bulletin of the Polish Academy of Sciences Technical Sciences 65(6) (2017), 765-771
[5] Nagrockienė, D., Girskas, G., & Skripkiūnas, G., Properties of concrete modified with mineral additives. Construction and Building Materials 135 (2017), 37-42
[6] Bissonnette, B., Courard, L., & Garbacz, A., Concrete surface engineering. CRC Press (2015)

SynerCrete'18 International Conference on Interdisciplinary Approaches
for Cement-based Materials and Structural Concrete
24-26 October 2018, Funchal, Madeira Island, Portugal

IMPROVEMENT OF SELF-HEALING EFFICIENCY IN ENGINEERED CEMENTITIOUS COMPOSITES BY ADDITION OF FOREST BIOMASS ASH

Gloria Perez [(1)], José Luis García Calvo [(1)], Pedro Carballosa [(1)], Ana Guerrero [(1)]

(1) Institute of Construction Science Eduardo Torroja (CSIC), Madrid, Spain

Abstract
Self-healing efficiency of an Engineered Cementitious Composite (ECC) in which fly ash is partially substituted by a forest biomass ash was studied in the present work. Prismatic specimens were fabricated with a ratio of fly ash to biomass ash content of 70/30 (material A) and 30/70 (material B). After 28 days of curing in a humidity chamber, some specimens were cracked and left back in the same previous conditions for self-healing during more than 8 months. The results from capillary water absorption tests suggest a higher initial tightness for the uncracked material with a higher content of fly ash, while after the healing period, a higher healing efficiency is inferred for the ECC matrix with higher content of biomass ash. The study of the self-healing mechanism by electron microscopy with compositional analysis indicates that sealing is promoted by reaction products deposited on the fibres bridging the cracks and by crystalline phases incorporating sulphur. The higher content of this element in the composition of biomass ash, as compared to fly ash, explains the higher crack healing efficiency in material B.

1. Introduction

Self-healing Engineered Cementitious Composite (ECC) is a special type of high performance fibre-reinforced cementitious composite designed on a micromechanics base to obtain a high tensile ductility and a tight crack width under mechanical loading [1]. The typical main components of these composites are type I Portland cement, fine silica sand, class F fly ash and poly-vinyl-alcohol (PVA) fibres [2,3], although some works have analysed ECCs incorporating other supplementary cementitious materials [4,5]. The present work studies the self-healing efficiency of an ECC material in which fly ash is partially substituted by a forest biomass ash from the combustion process of a paper Spanish company. The availability of

this by-product and the interest of its valorisation imply economic and environmental benefits from this substitution.

2. Materials and methods

Specimens of the ECC were produced with a composition similar to that described by other authors [2,4]. A CEM I 42,5R Ordinary Portland Cement (OPC), a mix of fly ash (FA) and biomass ash (BA) in a proportion of 1.2 relative to OPC content and siliceous aggregate in a proportion of 0.8 relative to OPC content were used. The water to binder ratio was 0.35 and a 1.5% of weight of superplasticizer, together with a 2% of weight of PVA fibres, were added to the solid.
The chemical composition of OPC, FA and BA used in this work is shown in Tab. 1 in terms of percentage of main oxides (percentage content higher than 0.3%), as obtained by X-ray fluorescence. It is important to indicate that, in addition to the oxides shown in Tab. 1, a 2.8% of Cl was measured in the composition of the biomass ash. In order to minimize the matrix fracture toughness, standard siliceous sand was sieved to stablish a maximum aggregate size of 400 µm. Finally, commercial PVA fibres incorporated to the matrix had a length of 8mm and a diameter of 39µm.

Table 1: Percent chemical composition of cement (OPC), fly ash (FA) and biomass ash (BA) used for the specimens preparation. L.I. stands for Loss on Ignition.

	CaO	**SiO_2**	**Al_2O_3**	**Fe_2O_3**	**MgO**	**SO_3**	**K_2O**	**Na_2O**	**TiO_2**	**P_2O_5**	**MnO**	**L.I.**
OPC	59.6	20.0	6.0	2.6	1.6	4.6	1.5	0.6	< 0.3	< 0.3	< 0.3	3.3
FA	5.4	44.7	26.1	5.5	1.1	0.7	2.6	0.3	1.4	0.9	< 0.3	10.9
BA	39.9	18.0	6.0	4.5	3.4	3.0	6.2	0.8	0.7	1.2	1.3	11.7

Prismatic specimens of 4 cm x 4cm x 16 cm were fabricated with a ratio of fly ash to biomass ash content of 70/30 (material A) and 30/70 (material B). The solid materials (CEM I 42.5R, aggregate and mix of ashes) were first mixed for 2 min at low speed. Water and superplasticizer were then added and mixed at low speed for 1 min, followed by high speed mixing for 2 min. Finally, fibres were added at low speed and mixed at high speed for another 2 min.
The specimens were demoulded after 24 hours and cured for 28 days at 98±2% RH and 20±2ºC. At that age, one set of specimens were cracked by means of the three point bending test using an INSTRON 8801 universal testing machine with a loading velocity of 0.03 kN/s, up to a specified strength value (around 5kN). After the test, the presence of cracks on the specimens' surface was confirmed and the set was left back, together with the uncracked set, in the same previous conditions for more than 8 months for self-healing until the testing date.
In order to study the influence of the biomass ash addition on the self-healing efficiency of the ECC material, capillary water absorption test according to UNE 83892 was conducted in the two uncracked and three cracked specimens of each material previously dried at 50 °C for several days until constant weight. In addition, samples obtained from the cracked area of each specimen were analysed by backscattering electron microscopy with compositional

analysis to characterize the sealing mechanism with a scanning electron microscope Hitachi S-4800 equipped with an energy dispersive analyzer BRUKER 5030. The samples were embedded in resin and polished for the analysis.

3. Results and discussion

3.1 Capillary water absorption

Fig. 1 shows the mean curves of mass increase of the specimens during the capillary water absorption test and Fig. 2 collects the values of the mean capillary water absorption coefficient with corresponding error bars. The uncracked specimens of material A showed a slower mass increase, with a lower final mass increase value during the test than those of material B. Accordingly, the mean capillary absorption coefficient (K) of 0.061 kg/m^{2}min$^{0.5}$ was significantly lower than the value obtained for uncracked material B (K equal to 0.085 kg/m^{2}min$^{0.5}$). This result suggests a higher initial tightness for the uncracked material with a lower content of biomass ash.

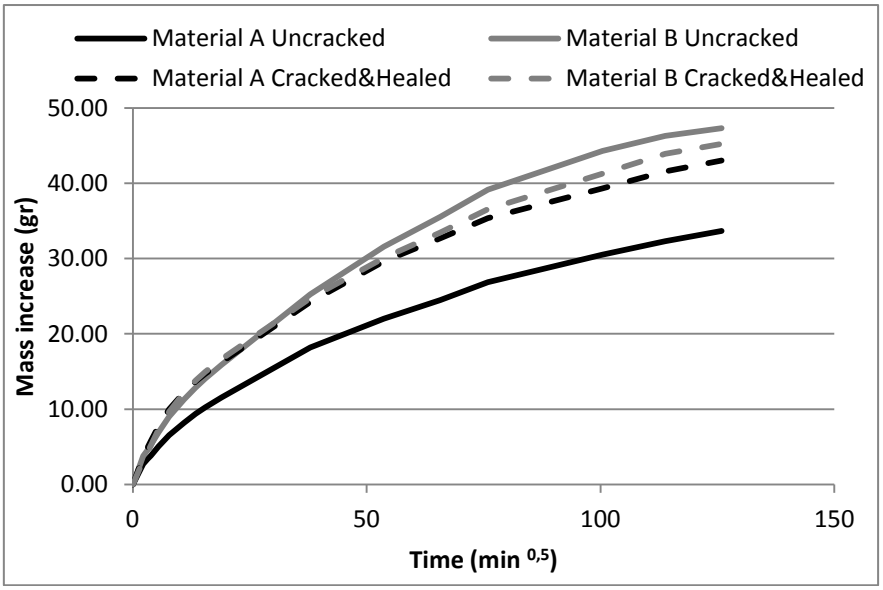

Figure 1: Mean mass increase of ECC specimens during the capillary water absorption test.

Regarding the results of cracked samples after the healing period, in the case of material A a higher water absorption was obtained in the test as compared to the uncracked samples, indicating that tightness recovery was not complete. On the contrary, in the case of material B the mean mass increase curve was very similar in the uncracked and the cracked and healed specimens. Moreover, the mean K value of cracked specimens after the healing period was almost equal to that of uncracked specimens, indicating a practically complete tightness recovery. Consequently, a higher healing efficiency may be inferred from the results for the ECC matrix with higher content of biomass ash.

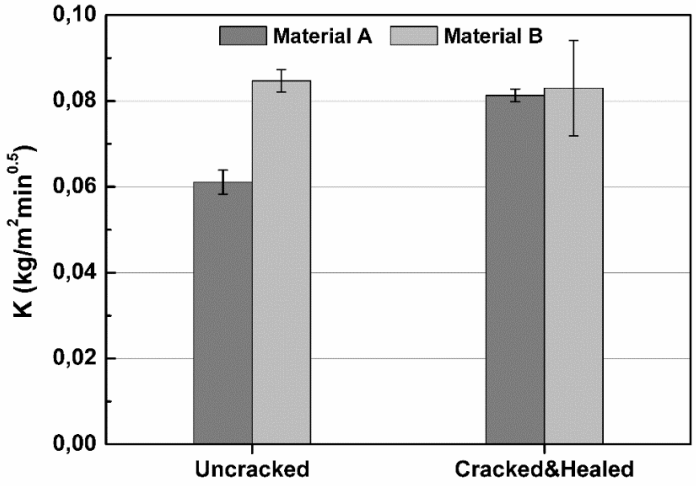

Figure 2: Capillary water absorption coefficient of the ECCs.

3.2 Crack sealing mechanism

The analysis by electron microscopy of the sample from the cracked area of material A, with lower content of BA, showed not sealed wide cracks that appeared filled with the resin used for sample preparation. This is the case of the representative crack in the left side of the top left image in Fig. 3, marked with a star symbol. Thinner cracks, like that in the right side of the top left image (marked with a triangle symbol and zoomed in the bottom left image) were also observed that were at least partially sealed by hydration products. On the contrary, no broad open cracks were observed along the surface of the sample of material B (right side images in Fig. 3). These results confirm the higher healing efficiency in the case of higher BA content within the matrix.

The detailed analysis of the representative crack in the case of ECC specimen prepared with higher content of BA showed healing products growing from both faces of the crack towards the middle, as previously observed by other authors [4]. A smooth surface was observed in areas more separated from the crack (point marked as 1 in Fig. 4) in which the composition was coherent with that expected for the cementitious matrix of the ECC. Silicon and calcium were the predominant elements, with significant contribution from C, Al and K and incorporation of Mg, Na, S and Cl as minor components. On top of the surface, separated cubic structures were clearly observed along the sample, as those surrounding number 1 in Fig. 4. The composition of these structures was coherent with calcium carbonate compound.

Approaching the remaining crack aperture, a less dense morphology was observed with structures clearly oriented perpendicular to the crack (point 3). In fact, perpendicular structures were seen to connect both sides of the remaining crack aperture that may be related to fibres bridging the crack sides on which hydration products precipitate. According to the results of compositional analysis, the precipitate in this case contained a clearly lower amount of silicon than the ECC matrix, with a higher content of aluminium and, especially, a significantly higher content of sulphur. The higher content and the availability of this element in the composition of BA, as compared to FA (see Tab. 1), may explain the higher crack healing efficiency in material B with a higher content of biomass ash.

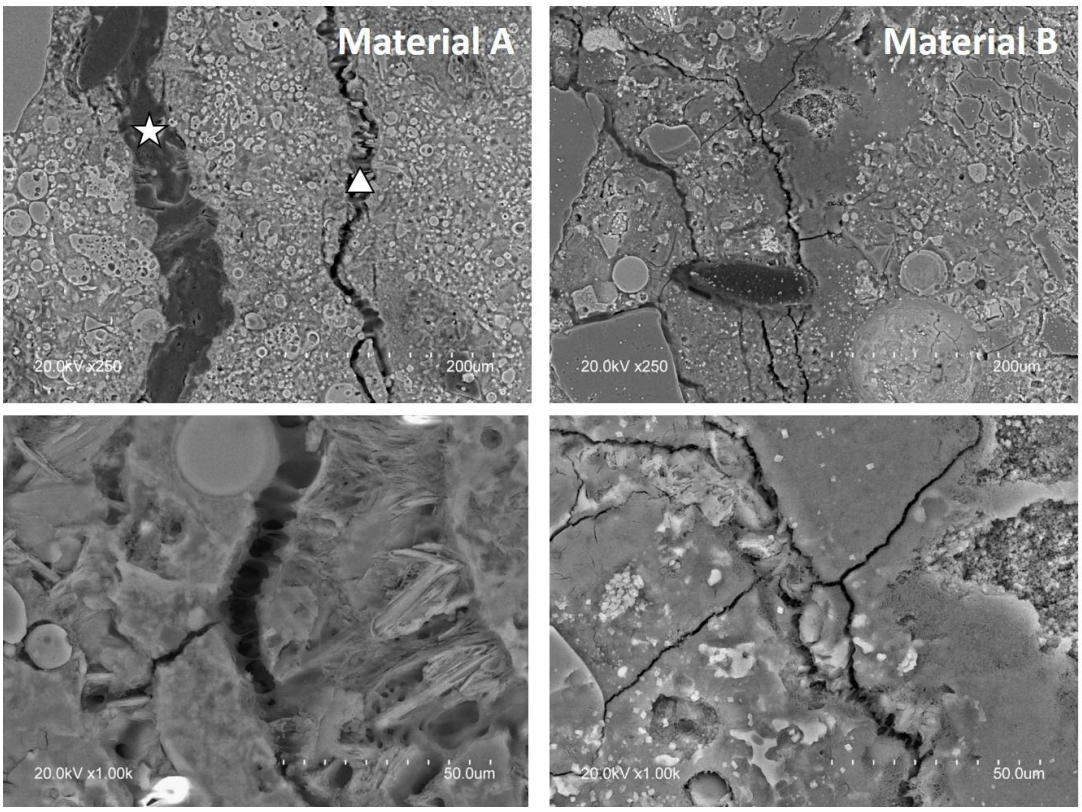

Figure 3: Backscattering electron microscopy images of representative cracks within the crack area of ECC specimens.

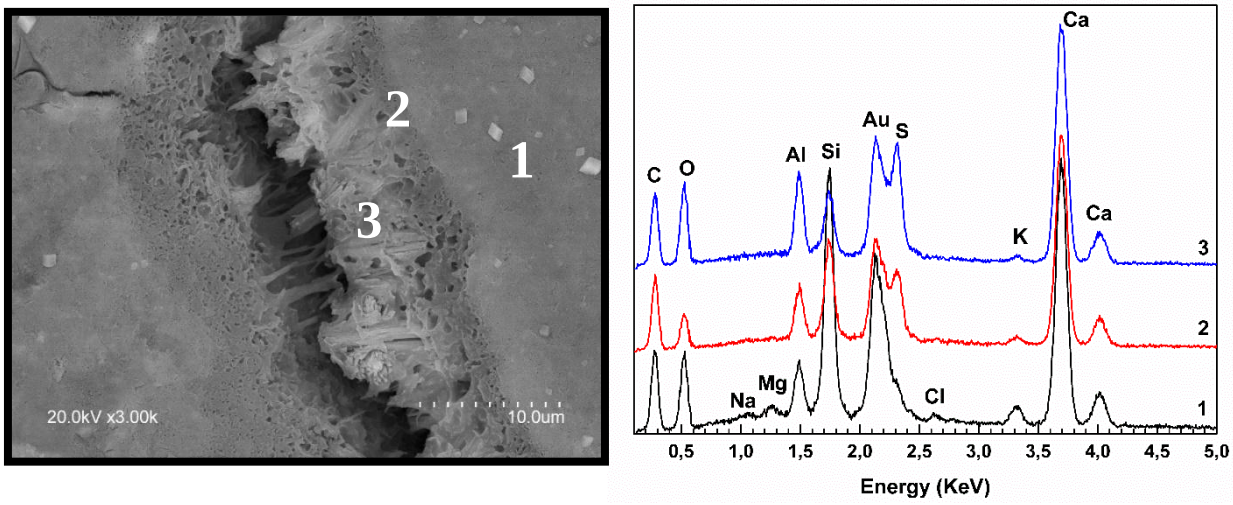

Figure 4: Zoomed backscattering electron microscopy image with compositional analysis of a representative crack within the cracked area of ECC specimen prepared with Material B.

4. Conclusion

The results of the present work confirmed an improvement of the self-healing efficiency of ECC specimens upon partial substitution of a conventional fly ash by a biomass ash. Sealing of cracks was promoted by reaction products deposited on fibres bridging the cracks and by crystalline phases incorporating sulphate ions from the biomass ash composition.

Acknowledgements
Thanks are due to Jose A. Sanchez and to the Physical-Chemical Analysis Unit of IETcc-CSIC for their help in experimental work.

References

[1] Li, V.C., On Engineered Cementitious Composites (ECC). A review of the material and its applications, J Adv Concr Technol 1 (2003), 215-230
[2] Sahmaran, M. and Li, V.C., Durability properties of micro-cracked ECC containing high volumes fly ash, Cem Concr Res 39 (2009), 1033-1043
[3] Liu, H. et al, Influence of microcrack self-healing behaviour on the permeability of Engineered Cementitious Composites, Cem Concr Com 82 (2017), 14-22
[4] Qian, S. et al, Self-healing behavior of strain hardening cementitious composites incorporating local waste materials, Cem Concr Comp 31 (2009), 613-621
[5] Sahmaran, M. et al, Self-healing capability of cementitious Composites incorporating different supplementary cementitious materials, Cem Concr Comp 35 (2013), 89-101

SynerCrete'18 International Conference on Interdisciplinary Approaches
for Cement-based Materials and Structural Concrete
24-26 October 2018, Funchal, Madeira Island, Portugal

NANO-SCALE TAILORING OF ENGINEERED CEMENTITIOUS COMPOSITES FOR SIMULTANEOUS ACHIEVEMENT OF ENHANCED SELF-HEALING AND SELF-SENSING ATTRIBUTES

Oğuzhan Öztürk [(1)], Gürkan Yıldırım [(2)], Anıl Kul [(3)], Ülkü Sultan Keskin [(1)], Mustafa Şahmaran [(3)]

(1) Konya Technical University, Konya, Turkey
(2) Kırıkkale University, Kırıkkale, Turkey
(3) Hacettepe University, Ankara, Turkey

Abstract

Autogenous self-healing can be a handy tool for concrete material to self-repair its own damage. On the other hand, to keep infrastructures in a serviceable state, it is also important to identify and assess any structural damage (cracks) as early as possible, before losing complete and/or sectional integrity. In this regard, efforts can be made to make concrete material work like a sensory material by making its nature electrically conductive (i.e. self-sensing) and responsive to any changes in applied strains. Engineered Cementitious Composites (ECCs) are new-generation ductile concretes capable of favouring autogenous self-healing through the formation of micron-size cracks upon straining. ECCs are also characterized by piezoresistive (self-sensing) response meaning that they exhibit strong dependence of electrical resistivity to the applied loading. Within this context, an attempt has been made here to further nourish both autogenous self-healing and self-sensing capabilities of ECCs by tailoring the matrix properties with different nanomaterials. With the purpose of improving self-healing and self-sensing attributes of ECC material, nano-silica and carbon nanotubes were simultaneously incorporated in mixture compositions, respectively. Tests were performed on sound and pre-loaded (almost-failed) prismatic ECC specimens under four-point bending loading. Both self-sensing and self-healing properties were evaluated before/after the introduction of microcracking and upon exposure to further curing. Results revealed that proposed nano-modification of ECC mixtures significantly improved the autogenous self-healing and self-sensing capabilities simultaneously. Outcomes of this study are believed to make a marked impact on true infrastructural sustainability by not only reducing the frequency of repair/maintenance applications but also making infrastructures much smarter to easily track their own damage.

1. Introduction

As an emerging material, Engineered Cementitious Composites (ECCs) with inherent tight microcracking behaviour under excessive tensile loading were introduced to the construction market by Li V.C [1]. ECCs-based studies have grown in number for the past 20 years. In addition to their superior mechanical/durability properties, ECCs were also tailored to possess additional structural and non-structural functionalities [2-3]. Many efforts were made on investigating the autogenous self-healing performance of ECCs under various conditions [4-5]. Although they are scarce, studies aiming at the self-sensing behaviour of ECCs can also be encountered in the current literature [6-7].

To multiply the benefits of ECC-material utilization in infrastructures, here, efforts were made to nourish autogenous self-healing and self-sensing ability of ECCs simultaneously by tailoring the mixture designs with different nano-materials. Characterization of self-sensing (piezo-resistive) behaviour was made via carbon nano tubes (CNTs) incorporated in ECC systems while intrinsic (autogenous) self-healing attribute was tried to be promoted by the inclusion of nano silica (NS) particles in ECC matrices. According to wide literature review, this study which aims at achieving self-healing and self-sensing functionalities concordantly in ECCs is the first of its kind and is believed to make a significant impact on sustainability of infrastructures not only by reducing the frequency of repair/maintenance applications but also making infrastructures much smarter to easily track their own damage.

2. Experimental Program

2.1 Materials and mixtures

The experimental studies were performed on four ECC mixtures produced with different nano materials. The mixtures were produced using Class-F fly ash (FA), CEM I 42.5 Portland cement (PC) silica sand (with maximum aggregate size of 0.4 mm), polyvinyl-alcohol (PVA) fibres, water and high range water reducing admixture (HRWRA). Carbon nano tubes (CNT, used by 0.55% of the total weight of cementitious materials) and nano silica (NS, used by 3% of the total weight of cementitious materials) were used to achieve self-sensing and self-healing attributes simultaneously.

Two different ECC mixtures were produced with a water to cementitious materials (CM=FA+PC) ratio (W/CM) of 0.27 and a pozzolanic material to Portland cement (PM/PC) ratio of 1.2. PVA fibres were used on a volumetric basis by 2%. HRWRA was used considering the reasonable fresh properties of ECC mixtures. The proportions for ECC mixtures were given in Table 1. Reference ECC mixture (ECC-Ref.) was produced as follows; i) raw materials were first mixed together at 100 rpm for a minute, ii) total water amount and HRWRA was then poured into the dry mixture and mixing was continued at 150 rpm for a minute and later at 300 rpm for additional 2 minutes, iii) PVA fibres were added into fresh mixture and mixing was continued 3 minutes more at 150 rpm for reference mixtures. Nano modified ECC mixture (ECC-CNT-NS) were produced as follows; i) CNTs were mixed with half of the total water and 75% of total HRWRA amount in another blender for 15 min at 3000 rpm [6]. During the preparation of the CNT solution, NS particles were mixed with another half of the mixing water and 25% of the total HRWRA amount for 5

minutes by using ultrasonic mixer [8]. Both nano solutions were added gradually into ongoing raw material mixing after a minute and rest of procedure was similar to ECC-Ref. mixing as mentioned earlier.

Table 1: Proportions of ECC mixtures.

Mix ID	PC/PC[1]	Sand/PC[1]	FA/PC[1]	W/CM[1]	HRWRA[2]	PVA[2]	NM/CM[3]
ECC-Ref.	1	0.36	1.2	0.27	5.1	26	-
ECC-CNT-NS	1	0.36	1.2	0.27	6.1	26	0.55-3

[1] by mass; [2] in kg/m^3; [3]NM/CM stands for nano material to cementitious materials ratio, by mass (i.e. CNT/CM=0.55; NS/CM=3)

2.2 Experimental setup and methods for self-healing/self-sensing evaluation

For the main purpose of the study, prismatic ECC specimens (360x75x50 mm^3) were produced and after one day in their molds, specimens were cured in plastic bags for six days at 95±5% RH, 23±2 °C. Additionally, 50 mm cubic specimens were fabricated for the determination of compressive strength at 7 and 28 days. Prismatic ECC specimens were preloaded up to 75% of their ultimate deformation capacities at the age of 7 days for crack generation. Preloaded specimens were cured in water and tested again after 7 and 28 days. Mechanical tests were conducted by using a loading machine with a computerized data recording system and loading points were insulated for accurate resistivity readings.
Electrical resistivity measurements were executed before and after crack formations by the use of a concrete electrical resistivity meter following procedures explained in [9]. The moisture states of the specimens were standardized by oven drying of specimens for 24 hours at 60 C° before electrical measurements to avoid any variations. ER (electrical resistivity) measurements were evaluated by the use of Eq. (1). Self-sensing of initial pre-loading was determined by calculating the fractional change in electrical resistivity (FCR) as demonstrated in Eq. (2). The self-healing degree was evaluated by comparing the ER values calculated at 7 and 28 days with the initial ER results recorded after pre-loading (Eq. 3). Cracks of all ECC specimens were also tracked by using a video microscope.

(1) ER=Z *cos(θ)* x A/L, where ER is the electrical resistivity (Ω.m), Z is the impedance measured by resistivity meter (Ω), A is the cross-sectional area of the specimen (m^2), L is the length of the specimen (m) and θ is the phase angle (˚).

(2) FCR = ((ER_0 – ER)) / ER) x 100, where ER and ER_0 are electrical resistivity values of sound and preloaded ECC specimens at 7+0 days, before and after pre-loading, respectively.

(3) Self-healing rate in terms of ER = ((ER_n - ER_0)/ER_0) x 100, where ER_n and ER_0 electrical resistivity measured at n_{th} day and initial day of self-healing age, respectively.

3. Results and Discussion

3.1 Compressive strength

Table 2 presents the compressive strength results of 50 mm ECC cubes tested at 7 and 28 days. Incorporation of nano materials into ECCs increased the compressive strength both at 7

and 28 days. Compared to ECC-Ref., 7-day-old cubic specimens modified with nano materials exhibited 22.6% higher compressive strength on average. Similar increment was recorded as 21.4% for 28 days. In ECC-CNT-NS mixtures, NS particles may have acted as a media to improve the interaction between CNTs and C-S-H products so that denser interface could have formed. In addition, CNTs may have provided nucleation sites for additional C-S-H formation together with NS. For this reason, improved microstructure of nano modified ECC specimens resulted in higher compressive strength at 7 and 28 days.

Table 2: Compressive strength results of nano modified ECC specimens (results are in MPa).

Mix ID	**7 days**			**28 days**		
ECC-Ref.	28.96	29.95	30.66	53.84	58.08	59.91
ECC-CNT-NS	36.20	36.08	37.45	69.79	70.36	69.44

3.2 Self-healing and self-sensing performance

Table 3 presents the ER results of sound and preloaded specimens at 7+0, 7+7 and 7+28 days. According to Table 3, average of ER results of sound ECC-Ref specimens were 17% higher than the average of ER results of sound ECC-CNT-NS specimens which was attributed to the presence of CNTs in ECC-CNT-NS mixture creating more electrically conductive paths.

Table 3: ER results of nano modified prismatic ECC specimens (Ω m), *Sound, **Preloaded.

Mix ID	**7+0 days (S)***	**7+0 days (PL)****	**7+7 days (PL)****	**7+28 days (PL)****
ECC-Ref.	21.34	22.68	32.20	36.80
	23.72	24.15	33.42	40.00
	22.40	25.48	33.39	40.80
	24.60	25.77	35.77	38.90
ECC-CNT-NS	19.87	26.84	45.60	61.50
	21.30	27.90	45.10	65.20
	22.12	28.00	43.40	65.40
	15.03	24.15	41.50	64.80

Fractional changes in electrical resistivity were 6.6% and 36.5% for ECC-Ref., and ECC-CNT-NS mixtures at 7+0 days, respectively. These results confirm the efficiency of CNT utilization to improve electrical conductivity, i.e. self-sensing capability. Nano-sized CNT particles provided continuous electrically conductive paths in ECC matrix and favoured the through movement of electrons. When pre-loaded, CNT particles may have debonded from the mixture and crack bridging mechanism of CNT could have been worsened so that increased fractional changes in ER results were recorded.

The further curing of preloaded specimens (7+7 and 7+28 days) caused ER results to increase irrespective of ECC mixture compared to ERs evaluated after preloading at 7+0 days. Self-healing rates (ER results compared to initial preloading at 7+0 days) were 37% and 56%, 59% and 140% for the ECC-Ref., and ECC-NS-CNT mixtures at 7+7 and 7+28 days, respectively. Increased ER results of both mixtures is due to high volume C-S-H reducing overall porosity and conductivity of pore solution leading to increase in ERs. However, increases of ER results were clearly more pronounced in ECC-NS-CNT specimens in both 7+7 and 7+28 days. This

finding is in line with the results of [10] which concluded that use of carbon-based materials increases the self-healing rate of ECCs. The faster and greater self-healing rates of CNT bearing specimens (ECC-CNT-NS) can be attributed to the tendency of CNTs to provide nucleation sites for additional C-S-H formation in self-healing reactions together with NS. This rate of increase indicates that self-healing products are probably the formation of C-S-H and $CaCO_3$ through ongoing cement hydration and pozzolanic reaction. Moreover, only 0.55% of CNT incorporation by weight of total cementitious materials resulted in reduced crack widths in ECC-CNT-NS specimens which is indicative of enhanced self-healing ability. Since crack widths are more decisive than crack numbers on ER measurements [5], increased recovery rate of ECC-CNT-NS specimens can be explained by the reduced crack widths conforming [11]. Video microscope observations also support the above findings. Reductions in crack numbers and widths can be seen for ECC-Ref specimen in Figure 1. However, incorporation of CNT and NS into ECC-Ref. seems favour self-healing more. It can be seen that 100% self-healing of cracks can be achieved in a very limited time due to efficiency of CNTs to lower crack widths together with NS helping create denser C-S-H gels and triggering more stable self-healing products in tight microcracks.

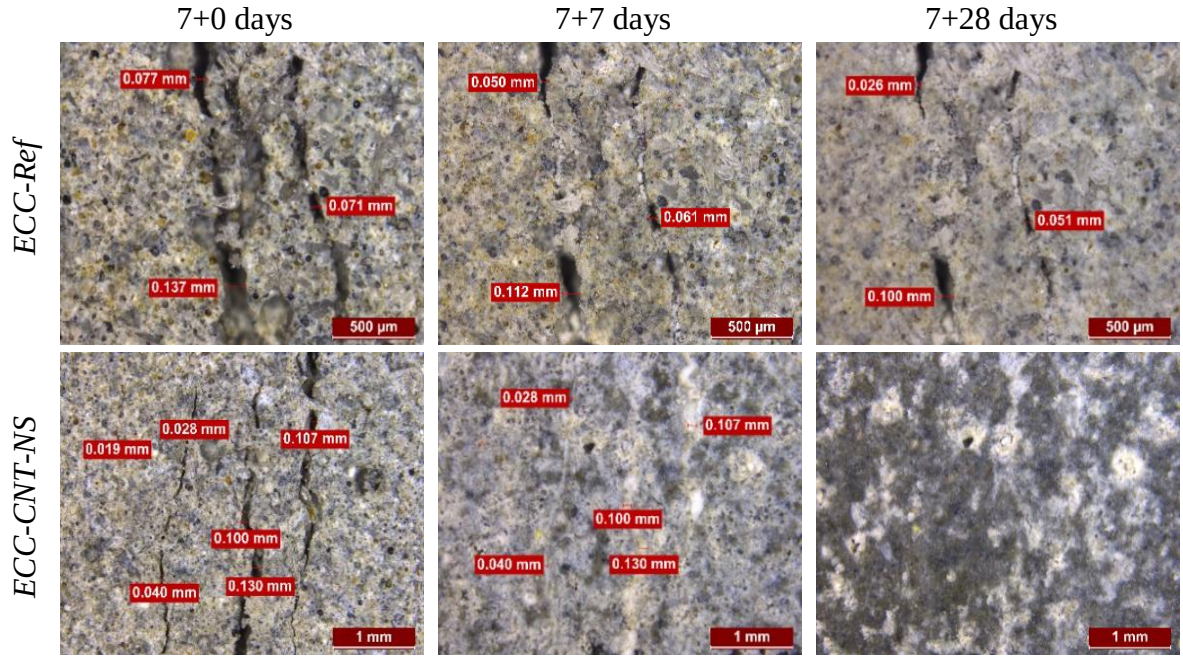

Figure 1: Self-healing of cracks in four different ECC specimens.

4. Conclusions

This study investigated the development of multifunctional ECCs with self-sensing and self-healing efficiency. Below are the conclusions that can be drawn from this study;

- Incorporation of nano materials improved the compressive strength of ECC specimens. More than 20% of increment can be obtained in the presence of CNT and NS compared to reference ECCs after 7 and 28 days.

- After initial pre-cracking, ECC-CNT-NS specimens showed an increased number of cracks and reduced crack widths favouring enhanced self-healing.
- Greater self-healing rates (140%) were registered for ECC-CNT-NS specimens in comparison with ECC-Ref specimens (59%) in terms of ER measurements.
- Microanalysis indicated that ECC-CNT-NS specimens exhibited a full self-healing behaviour after 7 and 28 days of further curing. Moreover, 100% self-healing can be possible when multiple tight cracks form in ECC-CNT-NS specimens. Confirming the possibility to develop multifunctional ECCs having self-sensing and self-healing attributes simultaneously by the inclusion of 0.55% CNT and 3% NS in mixtures.

References

[1] Li. V.C. ECC-tailored composites through micromechanic modelling. In: Banthia N., editor. Proceeding fiber reinforced concrete: present and the future conference. Montreal: CSCE Press; (1998), 64-97.
[2] Sakulich, A.R., Li. V.C., Nanoscale characterization of engineered cementitious composites (ECC), Cement Concrete Research, 41:2, (2011), 169-175.
[3] Han. B., Sun, S., Ding S., Zhang, L., Yu, X., Ou, J., Review of nanocarbon-engineered multifunctional cementitious composites, Composite Part A: Applied Science 31:70, (2015), 69-81.
[4] Ferrara L., Krelani V., Moretti, F., Flores M.R., Ros, P.S., Effects of autogenous healing on the recovery of mechanical performance of HPFRCCs: Part 1, Cem. Concr. Compos., 1:83, (2017). 76-100.
[5] Sahmaran, M., Yıldırım, G., Aras, G.H., Keskin, S.B., Keskin, Ö.K., Lachemi M., Self-healing of cementitious composites to reduce high CO_2 emissions, ACI Mater. J. 1, (2017)-114.
[6] Al-Dahawi, A., Öztürk, O., Emami, F., Yıldırım, G., Sahmaran, M., Effect of mixing methods on the electrical properties of cementitious composites incorporating different carbon-based materials, Constr. Build. Mater. 1. 104 (2016), 160–168.
[7] Han B., Sun S., Ding, S., Zhang, L., Yu, X., Ou, J. Review of nano-carbon-engineered multifunctional cementitious composites, Compos. Part A: Appl. Sci. Manuf. 31 70, (2015) 69–81.
[8] Yeşilmen, S., Al-Najjar, Y., Balav, M.H., Şahmaran, M., Yıldırım, G., Lachemi, M. Nano-modification to improve the ductility of cementitious composites, Cem. Concr. Res.; 76 (2015), 170-179.
[9] Al-Dahawi, A., Öztürk, Ö., Emami, F., Yıldırım, G., Sahmaran, M. Assessment of self-sensing capability of Engineered Cementitious Composites within the elastic and plastic ranges of cyclic flexural loading. Constr. Build. Mater. (2017), 1-10.
[10] Siad, H., Lachemi, M., Sahmaran, M., Mesbah, H.A., Hossain, K.A. Advanced engineered cementitious composites with combined self-sensing and self-healing functionalities. Constr. Build. Mater., (2018), 313-322.
[11] Yildirim, G., Aras, G.H., QaiS, S.B, Sahmaran, M., Lachemi M. Estimating the self-healing capability of cementitious composites through non-destructive electrical-based monitoring, Ndt & E Int., 76 (2015) 26-37.

SynerCrete'18 International Conference on Interdisciplinary Approaches
for Cement-based Materials and Structural Concrete
24-26 October 2018, Funchal, Madeira Island, Portugal

SELF-HEALING AND STRENGTH RECOVERY EVALUATION OF SUPER ABSORBENT POLYMERS CONCRETE MIXES UNDER CONTROLLED DAMAGE

Amir Sidiq[(1)], Rebecca Gravina[(1)], Sujeeva Setuge[(1)], Filippo Giustozzi[(1)]

(1) Royal Melbourne Institute of Technology – RMIT University, 376-392 Swanston st, Melbourne VIC 3000, Australia

Abstract

The durability of concrete is invariably a challenge for engineers and material technologists due to the frequent maintenance and service required on concrete structures and infrastructures hence resulting in economical deficiency. Concrete healing innovations have been developed over the past decade; these various technologies for concrete self-healing include biotechnological, polymeric and chemical compounds. Super absorbent polymers are considered as a progressive method to deliver the water content into the cementitious matrix and stimulate hydration and in situ carbonation of cementitious materials. This study investigates the effect of super absorbent polymer addition into the cementitious materials and the efficiency of concrete crack healing and recovery of mechanical properties from cracks.

1. Introduction

Concrete is the most favourable material used in the construction industry due its production process, raw material availability, affordability and recyclability [1]. Divergently, it is the tensile characteristics of concrete that causes cracking probability [2] which compromises the durability of concrete [3]. The development of micro-cracks in the cementitious matrix is the result of hydration and volumetric variation (i.e. thermal contraction, shrinkage in fresh and hardened concrete), environmental conditions (freezing and thawing) and mechanical loadings (static or dynamic). The formed micro-cracks are extremely difficult to be detected and can lead to the formation of macro-sized cracks [4]. In reinforced concrete, undesirable fluid and gas transport through these cracks can lead to corrosion of steel reinforcement and potential failure of concrete structures [5, 6]. Repairing micro-cracks in a cementitious matrix using the conventional methods could be extremely difficult and expensive. Concrete self-healing is one of the most promising methods for repairing these cracks, autonomously.

Super Absorbent Polymers (SAPs) is a technological material also utilized for concrete self-healing purposes. SAPs are cross-linked polymers and can absorb significant amounts of liquid in the surrounded environment and expand up to 500 times of their size [7]. This swelling capacity property proposes SAP as an additive in cementitious materials that carries water into the cementitious matrix and stimulates the cement hydration and in situ carbonation; however, during the release of the absorbed water, the dry SAP shrinks and reverses to its original dimension [4]. This mechanism of liquid provision and self-shrinkage of SAPs influences crack sealing and crack filling [8].

Researchers have used super absorbent polymers in various methods to propose crack healing and partial recovery of mechanical properties in cementitious materials. Kim and Schlangen [9] deployed SAPs with PVA-based ECC in the mortar mixture for crack width reduction and healing; SAPs content of 0.5% and 1.0% to the weight of cement were considered. After curing for 28 days, the four-point bending test was adopted to develop cracks and an average of 17.3 μm and 15.67 μm in crack width was obtained with respect to the SAP content (0.5 and 1%, respectively) compared to 22.3 μm for the control mix. After additional 28 days, samples were tested to failure by using a four-point bending test and it was concluded that the healing samples developed additional flexural strength and less deflection compared to the control samples. Sneok et al. [8] used SAP (cross-linked Potassium salt polyacrylate, particle size of 476.6 ± 52.9 μm) of 1%, 2% and 4% with respect to the cement weight and 2% by volume of PVA for all mixes. After 28 days, cracks were again developed by using the four-point bending method with crack width of 100-150 μm. Samples were cured under wet and dry cycles for additional 28 days and a four-point bending test to failure was finally conducted. It was observed that cracks' width up to 138 μm was healed for all SAP contents with 100% healing for SAP content of 2% and 4%; a strength reduction of 50% for 4% SAP and strength increment of 20% for 2% SAP was also observed. Gruraert et al. [10] added the in-house fabricated SAP with particle size less than 400 μm and 0.5% and 1% content by weight of cement, and achieved an increment of flexural strength of 8% and 6%, respectively; a general reduction of compressive strength for all SAP mixes was also noticed.

The present study investigates the effect of Super Absorbent Polymers in the concrete mix without the addition of superplastizer, micro-fibres and excessive water content. The analysis was carried out using X-Ray tomography for internal micro-porosity and cracking evaluation as well as standard mechanical tests and non-destructive tests for recovery assessment of mechanical properties.

2. Materials and Methodology

2.1 Materials

General purpose cement (equivalent to CEM-I-42.5R) and local aggregates with nominal size of 7.0 mm, 10.0 mm, sand and water were used for the mixing process. Super absorbent polymers (Floset^{TM} 27CS) with particle size less than 500 μm were purchased from SNF Pty Ltd Australia.

2.2 Sample preparation and curing

Concrete specimens were fabricated with addition of SAPs; the concrete mix consisted of water to cement and sand to cement ratio of 0.54 and 1.83, respectively and nominal

aggregate size of 7 mm and 10 mm with ratio of 0.8 and 1.61 to the weight of cement (PC CEM-I-42.5R) with addition of 1% (by cement weight) of SAPs. Cylindrical samples were casted as per AS 1012.8.1-14 [11] with diameter of 100 mm and height of 200 mm and a vibrating table was used for concrete compaction at 50Hz. Sample were kept at controlled conditions for 24 hours before de-moulding; they were then immersed in water for 28 days. Later, samples were cured in water to the completion of the experiment.

2.3 Crack development

After 28 days of wet curing, samples were removed and dried at ambient conditions for two hours. Three replicates were tested to obtain the maximum compression strength at 28 days. A self-synthesised steel mould was used to generate internal crack patterns; the mould consisted of two halved semi-circular sections with open ends at top and bottom sections. The semi-circular sections were connected by bolts and nuts. Cracks were developed by placing the concrete specimens into the self-synthesised mould and locating cylindrical steel plates at both opened ends. The steel mould with the concrete sample was positioned in the MTS-1000 kN machine between loading platens and an axial force was applied to induce axial circumferential pressure on the samples. Cracks were thus developed throughout the entire volume of the sample. Cracks were triggered by applying 40% and 70% of the maximum compressive strength as per initial measurement at 28 days.

2.4 Methods of testing

Ultrasonic Velocity Pulse and compression tests were conducted on concrete samples with SAPs for mechanical properties recovery while X-ray micro-tomography was undertaken for healing efficiency and change in porosity due to cracking. The three test types were performed at various time intervals after damaging the sample, including the 0, 3, 7, 14 and 28 days post 28 days of curing. All samples were labelled and Ultrasonic Velocity Pulse (UVP) was used to determine the dynamic modulus of concrete before the damaging procedure occurred as well as for each individual time interval (e.g. after being damaged).
Bruker SkyScan 1275 X-Ray micro-tomograph was used to obtain the porosity variation due to the formed cracks as well as to evaluate cracks development during healing. Concrete samples with diameter of 55 mm and 67 mm in height were placed on the micro-positioning stage of the instrument. The X-ray micro-tomograph was set to its maximum capacity with X-ray source of 100 kV tube voltage and 100 µA tube current; for a superior transmission of x-ray through concrete and to obtain minimum noise level, a 1 mm copper film was placed between the x-ray source and concrete sample. The intensity of the x-ray beam transferred through concrete sample is attenuated due to concrete density and the detector receives the residual intensity hence the 2D image is produced [12]. At 0.2-degree rotation around its axis and resolution of 1540x1540 a total of 1535 images with 35 µm thickness were obtained. Based on the 2D images, a 3D object reconstruction was obtained and data on internal porosity and crack development were collected.

3. Results and analysis

3.1 Dynamic Stiffness

In this experiment, non-destructive tests were conducted to obtain the dynamic modulus of concrete. Ultrasonic Velocity Pulse was used to determine the pressure wave velocity passing

through concrete samples. Then, according to ASTM C597-16 [13], Poisson's ratio of 0.15 and obtained average density of 1878.4 kg/m^3 the stiffness of concrete was calculated. In figure 1, the dynamic modulus of the concrete with SAPs is shown at different curing times in comparison to the dynamic modulus of the concrete before cracking development.

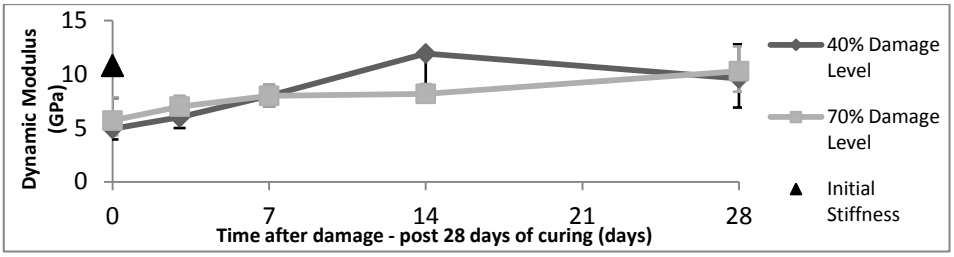

Figure 1: Dynamic modulus of samples after damage and healing effect with time.

3.2 Compressive strength

After internal micro-cracks were generated in all concrete samples, MTS-1000 kN compression machine was used to obtain the maximum axial force at failure; three replicates for each data set were measured. Figure 2 shows the compressive strength at each time interval after damage for 40% and 70% controlled crack development in comparison to the maximum compression strength prior to crack generation.

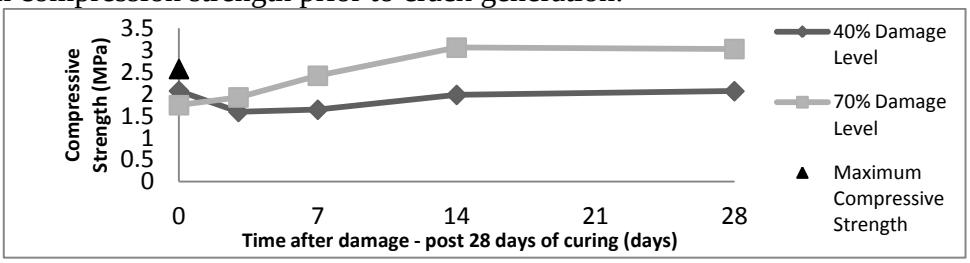

Figure 2: Residual and regain of compressive strength due to healing.

3.3 Micro CT-scan analysis

Micro CT scan tomography was used to analyse the induced porosity in the concrete samples due to damage. The operation involves analysing each 2D image based on the possible grey levels of intensity and the separation of air (voids and cracks) and solid phases. Air pores are dark grey due to lighter density hence less attenuation in translated intensity[14]. To determine the porosity of damaged samples by 40% and 70% in comparison to the control samples, the optimum of 44-255 grey level was applied throughout the entire campaign for consistency of results. Noise was reduced to the minimum level by applying global thresholding algorithm to convert the image to binary grey-scale image followed by the application of Otsu's method [14] to further separate the pore and solid phases. Also, black speckles smaller than 60 voxels were removed to obtain minimum noise level. Figure 3 shows the porosity at each time interval of 40% and 70% crack control damaged samples in comparison to control samples.

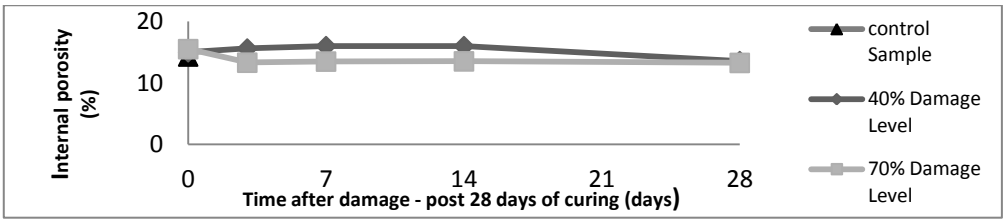

Figure 3: Porosity at various damage levels with respect to time.

4. Discussion

The efficiency of the addition of SAPs solely in a concrete mix for the purpose of crack healing and mechanical properties recovery was evaluated by utilizing non-destructive test methods and standard mechanical testing. It should be noted that the overall mechanical performance of the mix itself was not of interest to this research but rather was the effect of SAP on triggering concrete healing. Figure 1 shows the trend in stiffness of the concrete with SAPs. Prior to damage (and after 28 days of curing), the dynamic modulus of concrete was 10.8 GPa while right after being damaged at 40% and 70% of the maximum compressive strength, samples showed reduced stiffness of 5.44 GPa and 5.87 GPa, respectively. A regain in stiffness, thus increase in the velocity of ultrasonic pulses, was observed in both cases with almost full recovery (10.3 GPa for 70%-damage specimens and 9.6 GPa for 40%-damaged specimens) as per UPV assessment.

In this experiment the compressive strength and dynamic modulus results are generally lower than the standard concrete due to the inclusion of SAPs – absorbing water - without any extra water in the mix; hence less hydration in the cementitious matrix. Though the analysis of compressive strength results has suggested a partial strength regain with greater variability was observed among replicates. Both damaged samples exhibited an upward trend in the capacity of regaining strength with time although the 40%-damage specimens were not capable of fully recover from damage to their initial strength. This may be due to the different crack size generated by the damaging procedure.

Porosity content determination and crack healing efficiency was also estimated by utilizing X-ray tomography. Prior to damage, internal void content was 14.3%, which is generally higher than standard concrete although this could have been expected since no extra water or superplasticiser were used at this stage. Their addition is part of an ongoing research.

After being damaged, samples experienced an initial increase in porosity up to 15% and 15.5% for 40% and 70% damage, respectively. However, in both cases, a reduction of the internal void content was found with time although this was more gradual in the 40%-damaged samples.

Generally, 40%-damaged specimens needed more time to recover after being damaged; this suggests that there could be a close relationship between the healing efficiency of SAP and the size of the crack, which deserves more investigation.

5. Conclusion

The addition of super absorbent polymers in concrete proved to be beneficial in promoting healing phenomena; the efficiency of healing, though, followed different trends depending on

the internal damage being generated in the samples. Non-destructive methods, such as UPV and X-ray, showed to capture well the internal micro-structure before and after damage.
Compared to other studies where healing efficiency is evaluated on a single crack generated by different form of flexural tests (or by a small group of cracks within a restricted area in the proximity of the maximum stress point), the present research developed a methodology to induce cracking patterns inside the entire volume of the sample. This approach, although still at an early stage, can prove to fit well in the assessment of healing.
Finally, the swelling capacity of super absorbent polymers enable them to be used in cementitious materials for delivering stored water into cementitious matrix hence stimulating cement hydration and crack healing.

References

[1] Pelletier, M.M., et al., Self-healing concrete with a microencapsulated healing agent. Cem. Concr. Res, 2011.
[2] Karaiskos, G., et al., Performance monitoring of large-scale autonomously healed concrete beams under four-point bending through multiple non-destructive testing methods. Smart Materials and Structures, 2016. 25(5): p. 055003.
[3] Joseph, C., A. Jefferson, and M. Cantoni. Issues relating to the autonomic healing of cementitious materials. in First international conference on self-healing materials. 2007.
[4] Yang, Z., et al., Laboratory assessment of a self-healing cementitious composite. Transportation Research Record: Journal of the Transportation Research Board, 2010(2142): p. 9-17.
[5] Aldea, C.-M., S.P. Shah, and A. Karr, Permeability of cracked concrete. Materials and structures, 1999. 32(5): p. 370-376.
[6] Mignon, A., et al., pH-sensitive superabsorbent polymers: a potential candidate material for self-healing concrete. Journal of materials science, 2015. 50(2): p. 970-979.
[7] Snoeck, D., et al., Visualization of water penetration in cementitious materials with superabsorbent polymers by means of neutron radiography. Cement and Concrete Research, 2012. 42(8): p. 1113-1121.
[8] Snoeck, D., et al., Self-healing cementitious materials by the combination of microfibres and superabsorbent polymers. Journal of Intelligent Material Systems and Structures, 2014. 25(1): p. 13-24.
[9] Kim, J. and E. Schlangen. Super absorbent polymers to simulate self healing in ECC. in 2nd International Symposium on Service Life Design for Infrastructures, RILEM Publications SARL, Delft. 2010.
[10] Gruyaert, E., et al., Self-healing mortar with pH-sensitive superabsorbent polymers: testing of the sealing efficiency by water flow tests. Smart Materials and Structures, 2016. 25(8): p. 084007.
[11] Method for making and curing concrete_Compression and indirect tensile test specimens. 2018.
[12] Fan, S. and M. Li, X-ray computed microtomography of three-dimensional microcracks and self-healing in engineered cementitious composites. Smart materials and structures, 2014. 24(1): p. 015021.
[13] ASTM C597 - 16 Standard Test Method for Pulse Velocity Through Concrete. 2018.
[14] Manahiloh, K.N., et al., X-ray computed tomography and nondestructive evaluation of clogging in porous concrete field samples. Journal of Materials in Civil Engineering, 2012. 24(8): p. 1103-1109.

SynerCrete'18 International Conference on Interdisciplinary Approaches
for Cement-based Materials and Structural Concrete
24-26 October 2018, Funchal, Madeira Island, Portugal

SELF-HEALING OF CEMENT SLURRY FOR OIL WELLS CONTAINING CRYSTALLINE ADMIXTURE: EARLY RESULTS

Aline de Souza Oliveira [(1)], Romildo Dias Toledo Filho [(1)], Eduardo de Moraes Rego Fairbairn [(1)], Otávio da Fonseca Martins Gomes [(2) (3)]

(1) COPPE – The Graduate Institute of the Federal University of Rio de Janeiro, Brazil
(2) CETEM, Centre of Mineral Technology, Brazil
(3) National Museum, Federal University of Rio de Janeiro, Brazil

Abstract
In this paper we present the early results of the self-healing analysis of an oil well cement slurry containing 1% by weight of cement of crystalline admixture. The specimens cured in a bath at 60°C were pre-cracked at 7 days by splitting test until crack width of 200 µm. The healing process lasted 66 days in a 60°C water bath to reproduce pre-salt temperature conditions. The effectiveness of the healing process was verified by the mechanical recovery of the specimens after reloading. The analysis indicated that self-healing can be useful to improve the performance of the cement sheaths in oil wells.

1. Introduction

During the drilling of an oil well, primary cementing is the process of placing cement slurry in the annulus between the steel casing and the geological formation. After hardening, this hollow cylinder is called cement-sheath [1]. In Brazil, pre-salt oil and gas reserves have been discovered in 2006. In order to explore these reservoirs in ultra-deep water, many scientific and technological challenges had to be overcome. Total depth of the well can reach 7,000 meters. Layers are formed by water, followed by rocks and salt. The upper limit of pressure can reach around 90 MPa, while temperature range varies between 60-70°C [2], [3]. These extreme service conditions may result in crushing or cracking that may cause the lack of zonal isolation. This can lead to contamination of the crude oil or even catastrophic accidents if gas could escape from the well [4]. Therefore, considering the various factors that tend to damage the cement sheath, it would be worthy if the cement slurry had self-healing properties.

In view of the high environmental aggressiveness and loading conditions of the pre-salt, the crystalline admixture (*CA*) used in this research corresponded to those classified as PRAH (Permeability-reducing admixtures for concrete exposed to hydrostatic conditions) as described by the ACI [5].
According to Sisomphon et al. [6] the main healing mechanism on the external surface of the crack is the precipitation of calcium carbonate, since the presence of *CA* boosts the dissolution of ions (Ca^{2+}) and increases the environmental alkalinity. Thus, the region close to the crack would have the optimal concentrations of the ions: (i) Ca^{2+} (released from the matrix); (ii) carbonate (CO_3^{-2}); (iii) bicarbonate (HCO_3^{-}). Kishi et al. [7] explain that the calcium carbonate is the product of the reaction between bicarbonate ions (HCO_3^{-}) or carbonates ions (CO_3^{2-}) solubilized in water, originating from the crystalline additives, and Ca^{2+} ions from the concrete.
From the perspective of internal healing, which results in increased mechanical properties, Sisomphon et al. [8] found that the predominant mechanisms are further hydration and the expansion of anhydrous grains. In view of this, the hydrates produced in greater quantity were $CaCO_3$, C-S-H and ettringite. Jiang et al. [9] classified the action of *CA* into three types: (i) crystallization-precipitation, in which the admixture can supply CO_3^{-2} (carbonate ions) and accelerate the reaction with Ca^{+2} originated from the cement system, forming $CaCO_3$; (ii) expansive formation associated with the presence of new hydrates with higher volume, such as AFt due to hydration of the calcium sulfo-aluminate; (iii) pozzolanic reaction with the formation of C-S-H.
No reference can be found in the use of crystalline admixture as healing agent for oil well cement slurries. Ferrara *et al.,* [10] investigated the interaction between crystalline admixtures and disperse fiber reinforcement. They found that the material could have a better mechanical behavior after the self-healing process. De Nardi *et al.,* [11] realized that the presence of crystalline admixtures in lime mortars enhanced self-healing. They also found that the phenomenon is more evident for specimens exposed to open air. Roig-Flores *et al.,* [12], [13] used a high content of crystalline admixture in concretes, which reached different healing performances according to the exposure conditions. Sisomphon *et al.,* [8] reported how the mechanical recovery of mortars is related to the chemical properties of healing products. Ferrara *et al.,* [14] conclude that crystalline admixture accelerated the healing process and the recovery of mechanical properties. However, in accelerated exposure conditions, under high relative humidity and cycling temperature, the high dispersion of the results did not allow to draw any definitive conclusion. Jiang *et al.,* [15] reported that crystalline admixtures combined with chemical expansive agents can accelerate the healing process.
In this paper we investigated the use of crystalline admixture as healing agent in cement slurries for oil well applications. The effectiveness of the healing process was verified by the response of the specimens after reloading. The analysis indicated that self-healing can be useful to improve the performance of the cement sheaths in oil wells.

2. Experimental program and methodology

2.1 Materials and mixture proportions of cement slurries

Cement slurry was produced with crystalline admixture, in powder form, with content of 0% and 1% by weight of cement. The water/cement ratio was fixed in 0.44. The cement used was

high sulfate-resistant (HSR) class G well cement, with defoamer admixture at a dosage of 0.25% by weight of cement. Discontinuous polypropylene microfibers were added to the mixtures with 0.4% in fiber volume fraction (*Vf*). This low fiber content was added to guarantee cohesion between the two sides of the samples after crack opening. Proportions are shown in Table, where DE stands for defoamer admixture, PP stands for polypropylene microfibers, and CA stands for crystalline admixture. The former is commercially known as Sika WT-200P and its purpose is to seal cracks up to 400 µm and to reduce water penetration under hydrostatic pressure.

Table 1: Mixture proportions with 0.44 of w/c ratio.

Mix code	Cement (kg/m³)	Water (kg/m³)	DE (kg/m³)	PP (kg/m³)	CA (kg/m³)
0%CA	1330	585	3.3	4.0	0.0
1%CA	1307	575	3.3	3.9	13.1

Figure 1: Molds with notch.

2.2 Sample preparation

The mixing procedure was carried out in accordance to API-S-10A standard. The mixture passed the stability requirement of API-10B-2 standard. The slurry was poured in cylindrical moulds (Ø50 x 100 mm) that had notches positioned in two opposite diametrical positions as showed in Figure 1. They were cured in water immersion at 60°C up to 7 days in such a way that the hydration is almost complete as reported by [16] for a similar slurry. The specimens were then cut on the top, middle and bottom resulting in 3 discs (Ø50 x 25 mm), here called samples.

2.3 Pre-cracking by feedback-controlled splitting test

Pre-cracking corresponding to a single and localized crack was induced by a splitting tensile test based on ASTM C496M. The test is controlled in a twofold manner: (i) loading is controlled by the stroke displacement; (ii) a clip gage placed closed to the crack controls the end of the test for a given crack width (*w*). The test was carried out in a Shimadzu press with load cell of 100 kN, in constant rate of 0.5 µm/s. The preloading was automatically stopped until the crack width reached the imposed value of 200 µm.

2.4 Exposure and evaluation of healing properties

After pre-cracking, the samples were left in continuous immersion in water at a temperature of 60°C for 66 days. For this early study, we decided to submit the samples only to the typical temperature of the pre-salt wells in order to separate the various effects of this application such as pressure and salt content. After the healing period, the samples were again submitted to the splitting tensile test. The clip gage was zeroed and the end of the test was set to w = 200 µm.

The following parameters were defined for the load-crack width curves, as displayed in Figure 2: the load at first crack (P_{fc}); the load at a crack width of 200 µm (P_{200}); the residual crack width (w_r); the load corresponding to the crack width of w_r + 200 µm (P'_{200}). The self-healing capacity was computed by means of the Index of Load Recovery (*ILR*) as defined in reference [14] and presented in (1). *ILR*=1 corresponds to total healing and *ILR*=0 indicates

that there was no healing. Besides theses values, *ILR*<1 would indicate that the exposure could have further damaged the cracked region, while *ILR*>1 corresponds to an increase of the tensile strength of the healed crack.

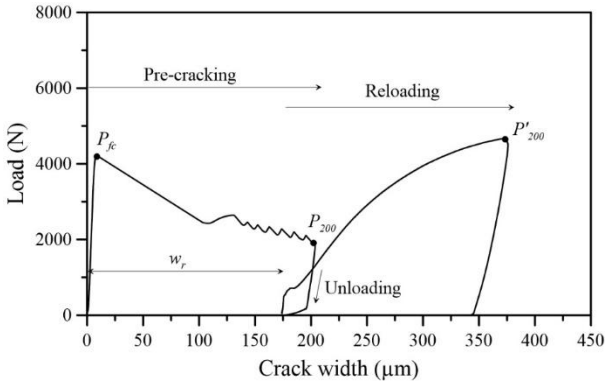

Figure 2: Typical load-crack width curve for self-healing analysis.

$$ILR = \frac{P'_{200} - P_{200}}{P_{fc} - P_{200}} \quad (1)$$

3. Results and discussion

The samples obtained from the top of the specimens were rejected because they presented discrepant *P* – *w* curves, with values of load much lower than the samples obtained from the medium and the bottom of the specimens. Considering that the specimens passed the stability test, a first interpretation of this phenomenon indicates that there was segregation of the PP fibers. Further investigation of the positioning and fiber content will be performed to confirm this hypothesis.

Figure 3 and Figure 4 present the *P* – *w* individual curves (with lower and upper limits) and average curves for both mixtures with 0% and 1%CA contents, respectively. For the pre-cracking branch of the curve, an initial softening region can be observed after the elastic range. It is followed by a sawtooth portion indicating that the fibers are bridging the two faces of the crack. For reloading, it appeared that the samples became much more compliant after healing. Since the clip gage measures the relative displacement in a very tight region close to the crack mouths, this seems to indicate that the healed crack has elastic properties quite different from the initial ones.

The samples with 0%CA had *ILR* equal to 0.8, it means that the mechanical strength was not completely recovered. In contrast, the mixtures with 1%CA had average *ILR* equal to 1.1, which corresponds to complete healing with a slight increase in strength.

To illustrate the evolution of the healing process, we show in Figure 5 a panoramic view of a crack before and after healing assembled from micrographs obtained by a stereo microscope.

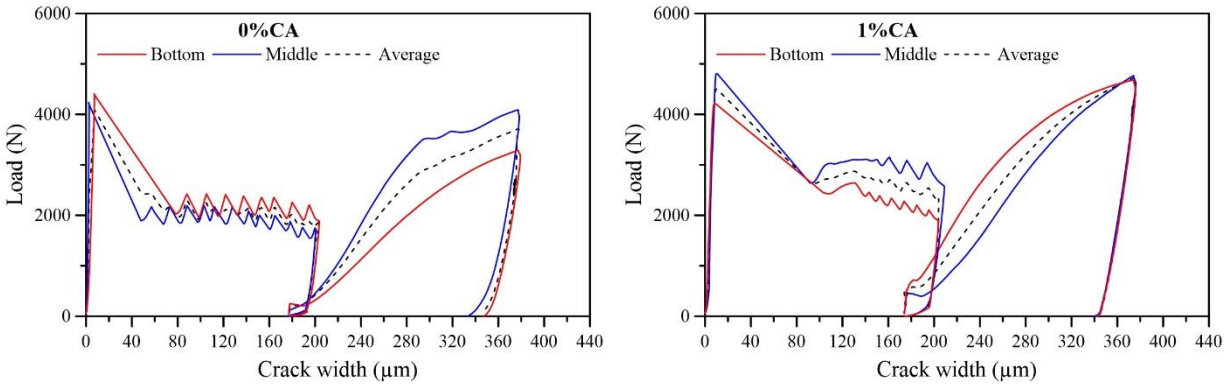

Figure 3: Load-crack width curves for specimens with 0% and 1%CA submitted to pre-cracking and post-conditioning splitting tensile test: bottom, middle and average.

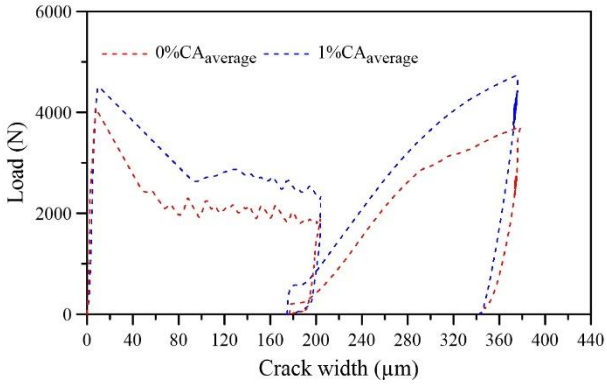

Figure 4: Load-crack width averages curves for specimens with 0% and 1%CA submitted to pre-cracking and post-conditioning splitting tensile test.

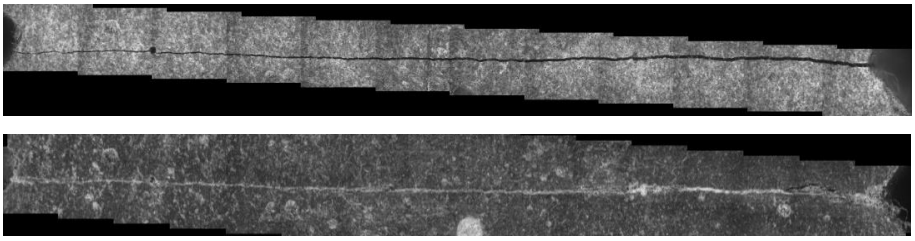

Figure 5: Panoramic view of a crack before and after self-healing.

4. Concluding remarks

The early results for self-healing of the cement slurry for oil well with 1% CA studied in this paper, indicated better mechanical recovery than mixtures with 0% CA. It should be noted that the hydration of the samples was almost completed when they have been submitted to pre-cracking and exposure. Therefore, the healing process was not facilitated by the presence of unreacted anhydrous grains and it can be considered that the conditions for the onset of healing were not the most favorable.

We can then consider that these early results are very promising and that self-healing of oil well cement sheaths may become an important research topic in the coming years.

References

[1] J. D. Mangadlao, P. Cao, and R. C. Advincula, "Smart cements and cement additives for oil and gas operations," *J. Pet. Sci. Eng.*, vol. 129, no. April 2010, pp. 63–76, 2015.
[2] J. Formigli Filho, A. Pinto, and A. Almeida, "Santos Basin's Pre-Salt Reservoirs Development—The Way Ahead," *Offshore Technol. Conf.*, no. May, pp. 4–7, 2009.
[3] J. O. D. S. A. Pizarro and C. C. M. Branco, "Challenges in implementing an EOR project in the Pre-Salt province in deep offshore Brasil," *Soc. Pet. Eng. - SPE*, vol. 2, pp. 954–966, 2012.
[4] A. L. Martins, P. E. Aranha, M. G. Folsta, C. A. Simão, N. A. Batalha, and G. H. V. P. Pinto, "Integrated cementing hydraulics design for massive salt zones," *SPE Lat. Am. Caribb. Pet. Eng. Conf. Proc.*, vol. 1, no. April, pp. 93–101, 2012.
[5] A. 212.3R, "ACI 212.3R-10: Report on Chemical Admixtures for Concrete," 2010.
[6] K. Sisomphon, O. Copuroglu, and E. Koenders, "Self-healing of surface cracks in mortars with expansive additive and crystalline additive," *Cem. Concr. Compos.*, vol. 34, pp. 566–574, 2012.
[7] T. Kishi, T. Ahn, A. Hosoda, S. Suzuki, and H. Takaoka, "Self-Healing Behaviour By Cementitious Recrystallization of Cracked Concrete," *First Int. Conf. Self Heal. Mater.*, no. April, pp. 1–10, 2007.
[8] K. Sisomphon, O. Copuroglu, and E. Koenders, "Effect of exposure conditions on self healing behavior of strain hardening cementitious composites incorporating various cementitious materials," *Constr. Build. Mater.*, vol. 42, pp. 217–224, 2013.
[9] Z. Jiang, W. Li, Z. Yuan, and Z. Yang, "Self-healing of cracks in concrete with various crystalline mineral additives in underground environment," *J. Wuhan Univ. Technol. Sci. Ed.*, vol. 29, no. 5, pp. 938–944, 2014.
[10] L. Ferrara, V. Krelani, and F. Moretti, "On the use of crystalline admixtures in cement based construction materials: From porosity reducers to promoters of self healing," *Smart Mater. Struct.*, vol. 25, no. 8, 2016.
[11] C. De Nardi, S. Bullo, L. Ferrara, L. Ronchin, and A. Vavasori, "Effectiveness of crystalline admixtures and lime/cement coated granules in engineered self-healing capacity of lime mortars," *Mater. Struct.*, vol. 50, no. 4, p. 191, 2017.
[12] M. Roig-Flores, S. Moscato, P. Serna, and L. Ferrara, "Self-healing capability of concrete with crystalline admixtures in different environments," *Constr. Build. Mater.*, vol. 86, pp. 1–11, Jul. 2015.
[13] M. Roig-Flores, F. Pirritano, P. Serna, and L. Ferrara, "Effect of crystalline admixtures on the self-healing capability of early-age concrete studied by means of permeability and crack closing tests," *Constr. Build. Mater.*, vol. 114, pp. 447–457, 2016.
[14] L. Ferrara, V. Krelani, and M. Carsana, "A 'fracture testing' based approach to assess crack healing of concrete with and without crystalline admixtures," *Constr. Build. Mater.*, vol. 68, pp. 535–551, 2014.
[15] Z. Jiang, W. Li, and Z. Yuan, "Influence of mineral additives and environmental conditions on the self-healing capabilities of cementitious materials," *Cem. Concr. Compos.*, vol. 57, pp. 116–127, 2015.
[16] C. A. A. Rocha, "Influência da pressão e temperatura de cura e da adição de NaCl e KCl no comportamento de pastas para cimentação de poços de petróleo," Universidade Federal do Rio de Janeiro (UFRJ), 2015.

SynerCrete'18 International Conference on Interdisciplinary Approaches
for Cement-based Materials and Structural Concrete

24-26 October 2018, Funchal, Madeira Island, Portugal

STRESS REDISTRIBUTION MECHANISM IN CONCRETE ELEMENTS WITH POLYMER FLEXIBLE JOINT: EXPERIMENTAL RESULTS

Łukasz Zdanowicz [(1)], Marcin Tekieli [(1)], Arkadiusz Kwiecień [(1)]

(1) Cracow University of Technology, Cracow, Poland

Abstract

This paper describes the application of a Polymer Flexible Joint (PFJ) as a method of repairing concrete members. Prismatic specimens were concreted and tested in four-point bending up to failure to simulate damage. After failure they were repaired with PFJ with PT-type polymer and tested in flexure again. The aim of the research was to assess the repair effectiveness regarding load bearing capacity and strain capacity before and after repair and to show the stress redistribution phenomenon. Furthermore, during the tests two methods of measurements were applied – conventional measurements with extensometers and Digital Image Correlation (DIC) method. Results of load – crack mouth opening displacement (CMOD) and load – displacement obtained from both methods were compared and their compliance is presented. Moreover, it is shown that the DIC method is capable of presenting the developing crack pattern even before the maximum force is achieved. Failure mode can be thus better described and understood. Finally, the repair effectiveness was calculated as 87% in terms of load-bearing capacity and 278% in terms of strain capacity. The phenomenon of stress redistribution in concrete was explained and described.

1. Introduction

Cracking of concrete is a common problem in civil engineering, which demands a lot of effort during repair [2, 8]. However, not all typical repair methods are effective in the long-term. In this paper we aim to present a method of repairing concrete members with Polymer Flexible Joint (PFJ), based on PT-type polyurethane polymer. Our research is focused on repair of prismatic concrete specimens subjected to flexure and assessing the repair effectiveness in terms of load-bearing and strain capacities. Furthermore, we compare two methods of

measurements – conventional measurements using extensometers and Digital Image Correlation (DIC) method. PFJ allows repairing such structures as concrete floors [5].

2. Experimental program

2.1 Materials

CONCRETE. Specimens were made from normal-weight concrete based on Portland cement with *w*/*c* = 0.45 and a maximal aggregate size of 16 mm. The compressive strength of concrete, calculated from results of compressive test (AV – average value, CV – coefficient of variation - CV), is AV = 68.9 MPa (CV = 5.2%; according to EN 12390-3) and tensile strength obtained from uniaxial tensile test described in [6] is AV = 3.76 MPa (CV = 8.0%).
POLYMER. A two-component PT-type polyurethane polymer was used in the research programme. This polymer has elastic properties. According to EN ISO 527-1, tensile strength of the polymer was equal to AV = 18.8 MPa (CV = 7.2%) [7]. Here only short-term investigation was conducted, nevertheless it should be noted that rheology of the polymer might influence the results. If the tests are performed under long-term or sustained loading, the deflections tend to increase [1].

2.2 Methods

The experimental program contains 63 four-point bending (4PB) tests, here only one series (3 specimens: S01 to S03) is presented.
Prismatic concrete beams with cross-section of 100 x 100 mm and total length of 400 mm were used in 4PB. Each specimen was cut with a 30 mm deep notch in the middle of its bottom surface. The plain concrete elements, before repair, were called "original specimens" and tested in flexure. After failure the specimens were repaired with PT-type polymer with joint thickness 10 mm. Such bonded elements were called "repaired specimens". The repaired elements were tested in flexure about 16-20 hours after polymer application as after this time the full stiffness and strength of the polymer are achieved. All bonded concrete surfaces were cleaned and covered with a primer layer.

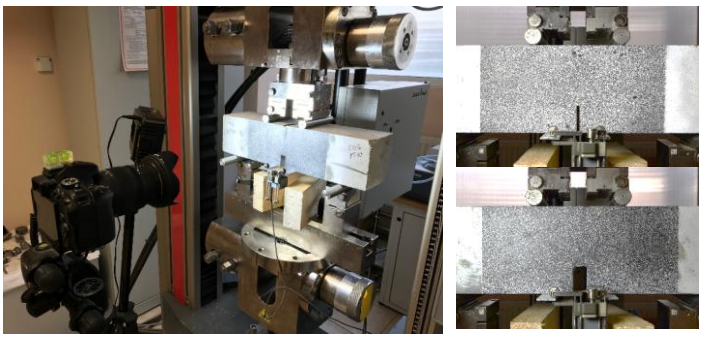

Figure 1: Test setup for four-point bending test (left) with DIC field of original (top right) and repaired specimen (bottom right).

Four-point bending tests were conducted using Zwick/Roell Z100 testing machine. The following test parameters were applied: initial force of 800 N, displacement rate of 0.10 mm/min, span length of 300 mm, distance between loading forces of 100 mm and temperature of 20°C (laboratory conditions). To measure selected values in 4PB tests, three

methods were used: (1) clip gauge with base of 50 mm (extensometer for the crack mouth opening displacement – CMOD), (2) extensometer for vertical displacement of the bottom surface, (3) DIC for measuring the strain field on side surfaces of the specimens (Fig. 1).

2.3 Digital Image Correlation

Optical measurements during the described test have been carried out using CivEng Vision system developed by Tekieli at Cracow University of Technology [3, 4]. System is based on DIC method with subpixel measurement resolution. The main procedure of the iterated measurements is based on the correlation of the digital images obtained during the test. Non-contact measurements during the tests have been conducted using digital single lens cameras equipped with 24 Mpx matrices and low-distortion zoom lenses. Barrel and tangential distortion have been corrected using calibration patterns.

3. Experimental results

3.1 Load response

The load response in 4PB tests using two methods (extensometer and DIC with the same base distance of 50 mm) is presented in Figure 2. Based on the load – CMOD curves, it can be observed that pre-critical phase (before cracking) for both types of specimens, i.e. original and repaired, is typically linear. After achieving F_{max}, a post-critical phase with softening was observed. Stiffness of the original specimens is higher in the linear-elastic phase than of the repaired ones, hence the CMOD values for the repaired specimens were higher than for plain concrete. The original elements showed usually higher load-bearing capacity (F_{max}) than the repaired specimens in presented series (specimens S01 to S03). It was noticed that extensometer and DIC have a good compliance for deflection and CMOD results.

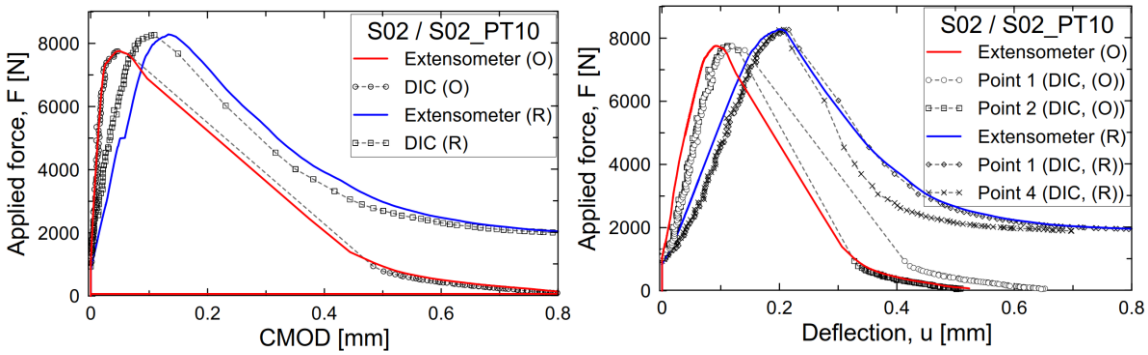

Figure 2: Load response of the notched beam in 4PB for specimen S02: applied load – CMOD (left) and load – deflection (right); (O) – original and (R) – repaired specimens.

3.2 Failure mode

Similar failure mode was observed for all specimens. A main crack ran through cement matrix and aggregates, from the notch up to top surface (Fig. 3). The main crack in the repaired elements ran also through concrete, at 1-3 mm distance from the crack of original specimen. It is considered to appear in the weak zone caused by previous crack.

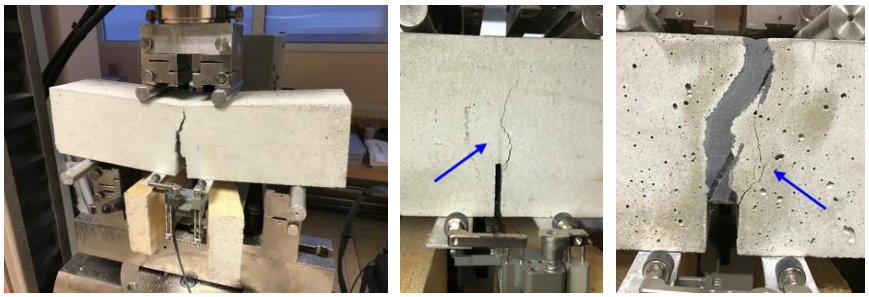

Figure 3: Failure of an original specimen (left), main crack in an original (middle) and a repaired specimen (right).

3.3 Results obtained from Digital Image Correlation

DIC allows to record the sequence of initial micro-cracks, before the peak load is achieved. Figure 4 shows the crack development, the colour-scale designates the horizontal strains. This method can present the whole cracking process in concrete. In original specimen (Fig. 4, top row) initial cracks occurred on the left side of the notch. These cracks developed up to the moment, when some of them linked into one main crack just before failure, and the rest were closed. The main crack selected the easiest path (the lowest energy requirements) through the micro-cracks in the cross-section and no more cracks were observed in DIC, because of micro-cracks closing in the damage area. Contrary to original elements, the failure mechanism of repaired specimens was slightly different (Fig. 4, bottom row). Due to previously damaged cross-section, the initial crack(s) occurred much earlier (at 32% of F_{max}) in the same location.

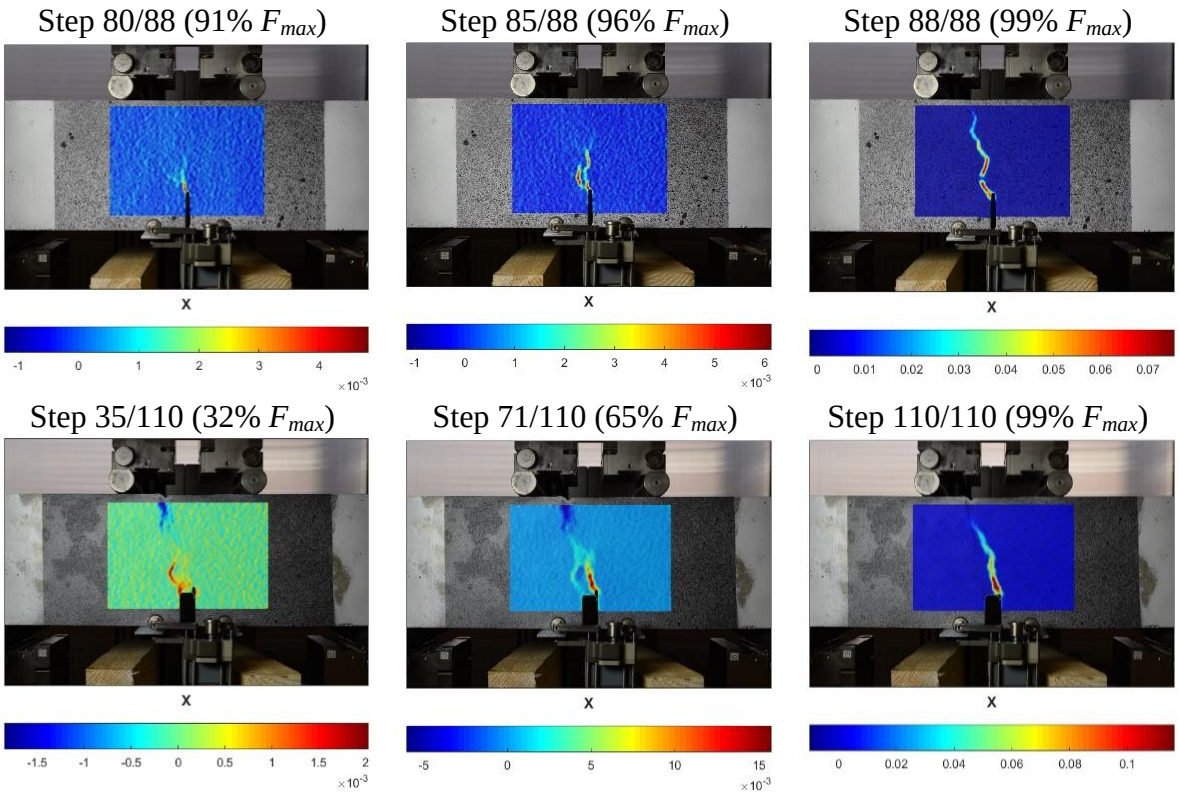

Figure 4: Crack development under applied load for the original specimen S02 (top) and the repaired one S02_PT10 with PT-type polymer joint of 10 mm (bottom).

However, the presence of PFJ after repair allowed protecting the weak, previously damaged zone (surrounding the main crack) by reduction of stress concentrations (responsible for micro-cracks formation) and redistribution of them to larger area. This phenomenon is what is called stress redistribution. As the consequence, the micro-cracks in the weak zone were closed (mechanical healing of the concrete) and a new crack developed on the other side of the notch (at 65% of F_{max}), where micro-cracks required the lowest energy for the main crack formation. From that moment, the previous cracks stopped developing and the new one on the right side caused failure. It was noticed that maximum strain values (DIC measure) of the repaired specimens were 1.5 to 3.0 times higher than of the original ones. Similarly, increase of maximum load and CMOD was observed for this specimen (Figure 2).

3.4 Results comparison

Table 1 presents the results obtained from 4PB tests for the specimens S01, S02 and S03. The average values of maximal load are 8.63 kN for original and 7.52 kN for repaired elements, and the average value of CMOD at failure is equal to 0.0477 mm and 0.1327 mm, respectively. Figure 5 presents a comparison of all tested original and repaired elements. The repair effectiveness is measured by ratios of load-bearing capacity and strain capacity of specimens after and before repair. The load capacity ratio was between 71-107% (AV = 87%). Anyway, in the post-critical phase (after F_{max}) the load-bearing capacity of the repaired elements was significantly higher than of the original ones (Fig. 2). Regarding the deformability, the strain capacity ratio achieved value of 2.78.

Table 1: The results of four-point bending tests.

Specimen	F_{max} [kN]		CMOD [mm]	
	Original specimen	Repaired specimen	Original specimen	Repaired specimen
S01 / S01_PT10	8.47	7.45	0.0481	0.1337
S02 / S02_PT10	7.76	8.28	0.0482	0.1328
S03 / S03_PT10	9.66	6.81	0.0469	0.1316
AV (CV) of S01 – S03	8.63 (11.1%)	7.52 (9.8%)	0.0477 (1.5%)	0.1327 (0.8%)

where: AV – average value, CV – coefficient of variation

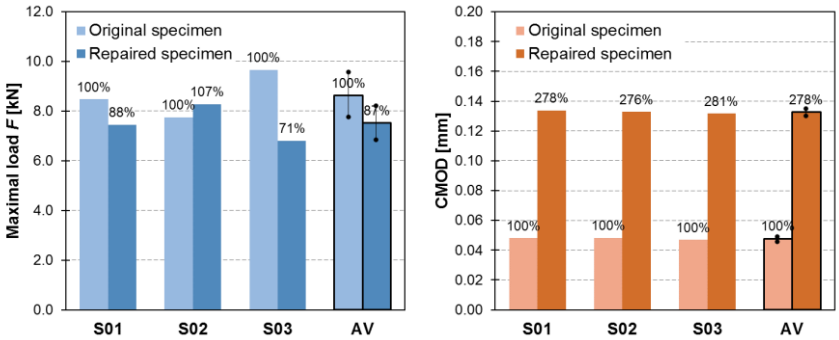

Figure 5: Comparison of the original and repaired specimens in terms of maximal load (left) and CMOD values (right).

4. Summary and Conclusions

This paper presented the experimental results of four-point bending tests of original and repaired specimens. The possibility of using DIC system CivEng Vision was proven. On the basis of presented results, the following conclusions can be drawn:

- Load-bearing capacity of original specimens (100%) was usually higher than the repaired ones (87%); contrary, in post-critical phase the load-bearing capacity of repaired elements was higher than original ones,
- Deformation capacity of the repaired specimens was significantly higher than of the original ones,
- Contrary to the original specimen, the repaired specimen showed that the weak zone around the first main crack does not determine the path of failure (micro-cracks were mechanically healed), it is possible to rearrange failure path under applied load,
- Comparison of traditional equipment (extensometer) and the DIC method shows a good compliance of results of deformation and CMOD; when using DIC method it is possible to register original phenomenon which cannot be observed using ordinary methods,
- It is needed to conduct more research with various parameters and specimens' geometry to confirm the stress redistribution phenomena. Further, the behaviour of polymer at elevated temperatures needs to be investigated. Moreover, it is desirable later to adjust the geometry to real field application setups to confirm the practical application of PFJ method.

References

[1] Kwiecień, A., Polymer Flexible Joints in Masonry and Concrete Structure, Monograph 414, Series: Civil Engineering. Wyd. PK, Cracow, Poland (2012), (in Polish)
[2] Pröbster, M., Baudichtstoffe. Erfolgreich Fugen abdichten, Springer, Wiesbaden (2016)
[3] Tekieli, M. et al., Application of Digital Image Correlation to composite reinforcements testing, Compos. Struct. 160 (2017), 670–688
[4] Tekieli, M. and Słoński, M., Particle filtering for computer vision-based identification of frame model parameters. Comput. Assist. Methods Eng. Sci. (2014), 39–48
[5] Zdanowicz, Ł. Et al, Stress redistribution in concrete floor on ground due to application of polymer flexible joint to fill expansion joint, Procedia Eng. 108 (2015), 467-474
[6] Zdanowicz, Ł. et al, Interaction of polymer flexible joint with brittle materials in four-point bending tests, Procedia Eng. 193 (2017), 517-524
[7] Zdanowicz Ł. et al, Interaction of Polymer Flexible Joint with Concrete Elements in an Uniaxial Tensile Test, High TechConcrete: Where Technology and Engineering Meet, Editors: D.A Hordijk, M. Lucović – Proc. fib Symposium, Maastricht (2017) 1049-1057
[8] Zilch, K. et al, Experimental investigation of reinforced glued joints, Proc. Hipermat, Kassel University Press (2012)

SynerCrete'18 International Conference on Interdisciplinary Approaches
for Cement-based Materials and Structural Concrete
24-26 October 2018, Funchal, Madeira Island, Portugal

SURFACE TREATMENTS AS REPAIR METHODS FOR PROTECTING REBARS FROM CORROSION

Mercedes Sánchez [(1),(2)], Fabiano Tavares [(2)]

(1) Institute of Construction Sciences "Eduardo Torroja", Madrid, Spain
(2) University of Córdoba, Córdoba, Spain

Abstract
In the present work two different solutions based on the application of electrochemical removal chloride treatments for the decontamination of the concrete cover are proposed for improving the treatment effectiveness. After a first stage of the electrochemical extraction of the chloride from the concrete cover until non-active corrosion current values are measured, two different methods are proposed:

1. Application of colloidal nanosilica treatment for sealing the concrete cover avoiding further chloride penetration.
2. Application of silane-based inhibitor for avoiding a further corrosion of the rebars.

The application of both types of treatments promote a significant increase in the resistivity of the treated concrete cover, while similar values of corrosion current density are registered, confirming that no further action of chloride is occurring within the treated samples. The visual analysis of the rebars showed the presence of a more extended corrosion damage on the non-treated samples, and almost no-presence of corrosion in the case of the electrochemical treatment with a further stage of sealing by colloidal nanosilica.

1. Introduction

The electrochemical removal of chlorides has been reported as alternative for repairing reinforced concrete affected by corrosion. It is a highly interesting solution as the removal of the aggressive agent is proposed instead of the removal of the local area affected by the corrosion damage [1]. The application of protective solutions is also interesting for improving the service life of the reinforce concrete, using corrosion inhibitors for protecting the rebar against the action of corrosive agents such as chloride [2], or applying surface methods for sealing the concrete cover for avoiding the penetration of aggressive agents such as chloride.

During the last years the development of innovative corrosion inhibitors which are able to migrate to the rebar surface protecting appear as an alternative for protecting reinforced concrete [3], even considering the simultaneous application of the inhibitor during the electrochemical removal chloride treatment [4]. The penetration of nanoparticles by electrokinetic treatments has been also proposed as an efficient method for improving the durability of reinforced concrete [5-6].
Although different studies have been reported concerning the improvement of performance in reinforced concrete after these types of treatments, no studies have been found about the behaviour of the repaired concrete exposed to a further penetration of the aggressive agent. Thus, in the present work, a comparative study on the real effectiveness of repair treatments based on the electrochemical chloride removal and a further protective surface treatment has been carried out by assessing the electrochemical behaviour of the repair specimens against the action of chloride.

2. Experimental procedure

2.1 Materials

Prismatic concrete samples with a steel rebar (10 mm in diameter) in the centre were fabricated for the study, as shown in figure 1-left. Lime sand (0-4 mm) and aggregates (4-12 mm) were used to produce a low-quality concrete, with water/cement ratio 0.81 and 250 kg/m3 of CEM I 42.5 R. The samples were cured for 28 days in controlled conditions of temperature (21ºC) and relative humidity (95%) before testing. After curing, the prismatic samples were cut to decrease the concrete cover in the treatment side, as schemed in figure 1-right.

Figure 1: Left – Concrete sample dimensions after casting. Right – Concrete samples prepared for testing.

2.2 Corrosion initiation procedure

In order to promote an accelerated corrosion initiation, the reinforced samples, with an age of 30 days, were submitted to a pre-drying period in oven at 50ºC until a constant weight was registered. Then, the dried samples were immersed in a 0.5 M NaCl solution to favour the entrance of chloride to the rebar level. The end parts of the rebar were isolated (Figure 1) for avoiding the exposure to chloride. During this immersion period, the corrosion potential (E_{corr}) and the corrosion current density (i_{corr}) were periodically measured to detect the corrosion initiation by a sharp drop of E_{corr} and/or a sharp increase of i_{corr}.

The part of the specimens without rebar obtained after the cut procedure were also immersed in the chloride solution and were used for analysing the chloride concentration at the same depth at the same time than the corrosion initiation in the reinforced samples was detected.

2.3 Electrochemical chloride removal treatment

Once the corrosion of the rebar was detected, an electric field was connected between the rebar and an external anode located on the concrete surface and consisting in a stainless steel mesh to promote the migration of the chloride ions from the concrete bulk to the surface. For the decontamination procedure the rebar was connected as cathode and a constant current of 0.1 $\mu A/cm^2$ was applied [7].

The corrosion current density was obtained at the end of each cycle of 5 days of electric field connection and 2 days with the electric field stopped for rebar depolarization. The polarization resistance technique [8] was used for obtaining the i_{corr} values by the Stern and Geary equation: $I_{corr} = B/R_P \cdot A$, where B is a constant, R_P is the polarization resistance and A is the exposed area. A compact potentiostat/galvanostat PGSTAT204 was used for the linear polarization measurements. Attending to the literature [8], a B value of 26 mV has been used for I_{corr} estimation. The cycles were repeated until corrosion current density values (i_{corr}) below 0.2 $\mu A/cm^2$ were registered, associated to a low level of corrosion according to [9].

2.4 Protection methods after the chloride removal was finished

A second stage for the protection of the decontaminated samples was considered. Two different situations were studied:

a) Application of colloidal nanosilica treatment for sealing the concrete cover avoiding further chloride penetration (P3).
b) Application of silane-based inhibitor for avoiding a further corrosion of the rebars (P2).

After the surface treatment with the nanosilica or with the corrosion inhibitor, applied by fixing a ponding with the solution on the surface of treatment, a period of 7 days for curing in high humidity conditions was carried out to consolidate the formation of the silica layer. Before exposing the sealed samples to a further chloride penetration, the corrosion current density was measured to confirm that the rebars were not suffering from corrosion anymore. A reference case without further treatment (P1) was also tested as control situation.

2.5 Effectiveness of the treatments

At the end of the treatment, the reinforced samples were broken for confirming the treatment effectiveness through the visual inspection of the rebar with an optical microscope.

3. Results and discussion

3.1 Corrosion initiation

The evolution of the E_{corr} and i_{corr} values during the exposure of the reinforced concrete specimens to the chloride penetration is shown in figure 2. The electrochemical data registered the corrosion initiation after the 3rd day of exposure in two of the samples (P1 and P2) and after the 9th day of exposure in the other (P3).

The corrosion initiation is associated to a sharp drop of the E_{corr} (figure 1-left) reaching values below -400 mV vs SCE, and to a sharp increase of i_{corr} (figure 1-right), with values up to 0.5

$\mu A/cm^{-2}$, reaching even 1.5 $\mu A/cm^{-2}$, which are associated to a high loss of material due to the corrosion process.

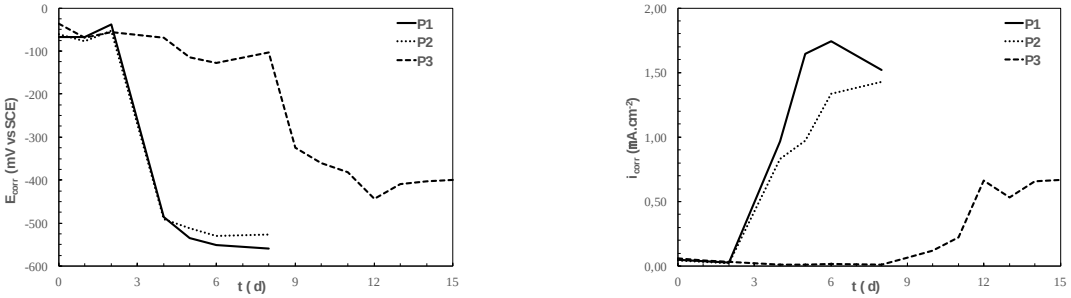

Figure 2: Evolution of E_{corr} (Left) and i_{corr} (Right) values during the chloride penetration for initiating the rebar corrosion.

The analysis of the total chloride content was made in the specimens without rebars but exposed to the same conditions following RILEM recommendations [10]. Three power samples were obtained in each specimen; the average value measured was 1.32±0.20 % total chloride per cement weight.

3.2 Electrochemical chloride removal treatment

During the electrochemical chloride removal treatment, the E_{corr} and the i_{corr} values were measured during the periods of disconnection of the electric field, as has been summarized in the experimental section of the present work. In Figure 3 the evolution of both parameters is shown for the three specimens treated. It can be observed from the figure that both parameters are indicating values of negligible corrosion at the end of the test, after 150 days of treatment. E_{corr} (figure 3-left) around -100 mV vs SCE, and i_{corr} (figure 3-rigth) below 0.2 $\mu A/cm^2$.

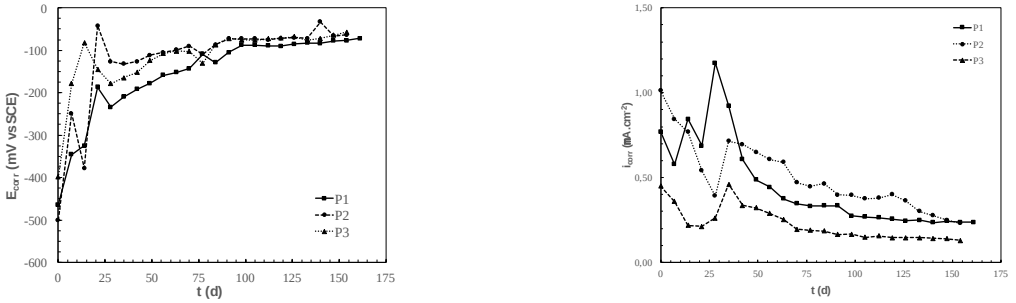

Figure 3: Evolution of E_{corr} (Left) and i_{corr} (Right) values during the electrochemical chloride removal treatment.

3.3 External surface treatment for improving the effectiveness of the repair

After finishing the treatment for the electrochemical removal of the chloride, a further treatment based on applying colloidal nanosilica (P3) or a corrosion inhibitor (P2) on the concrete surface was carried out. After a 7-days curing period in high humidity conditions, the treated samples were exposed to the penetration of chloride. A sample without further surface treatment has been used as control (P1). The evolution of the electrochemical parameters

appears represented in figure 4, E_{corr} (left) and i_{corr} (right). A quick depassivation of the non-treated sample (P1) is observed, as expected due to the chloride penetration.
In the case of the specimen after the treatment with the corrosion inhibitor, a slight decrease of E_{corr} and a slight increase of i_{corr} are detected during the exposure to chloride, while in the case of the treatment with colloidal nanosilica no change associated to the presence of chloride can be observed.

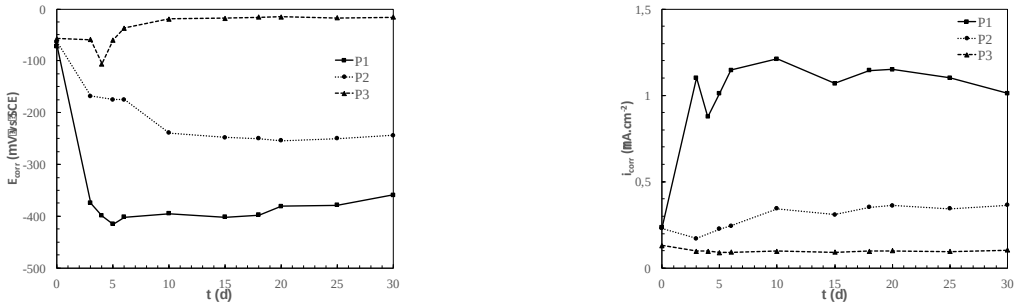

Figure 4: Evolution of E_{corr} (Left) and i_{corr} (Right) values of the treated samples exposed to chloride penetration.

As no sealing effect is expected by the corrosion inhibitor, the chloride in this case should be able to penetrate to the rebar where the competition with the inhibitor avoids the development of a fast corrosion process like in the case of the non-treated rebar. The sealing effect of the treatment with colloidal nanosilica avoids the chloride penetration through the concrete cover, and thus the i_{corr} values are not affected as the chloride is not present at the rebar level. E_{corr} values increase probably due to the extra ohmic drop associated to the presence of the sealing layer of silica.

3.4 Treatment effectiveness assessment

At the end of the test, the samples were broken for the visual observation of the rebar with the optical microscope. In figure 5 the surface of the non-treated rebar (figure 5-left) with an extended presence of corrosion products can be observed. The rebar treated with the corrosion inhibitor (P2) can be observed in figure 5-right. The presence of local spots of corrosion products was observed along the lateral area of the exposed rebar. No corrosion products were observed in the rebar after the treatment with colloidal nanosilica.

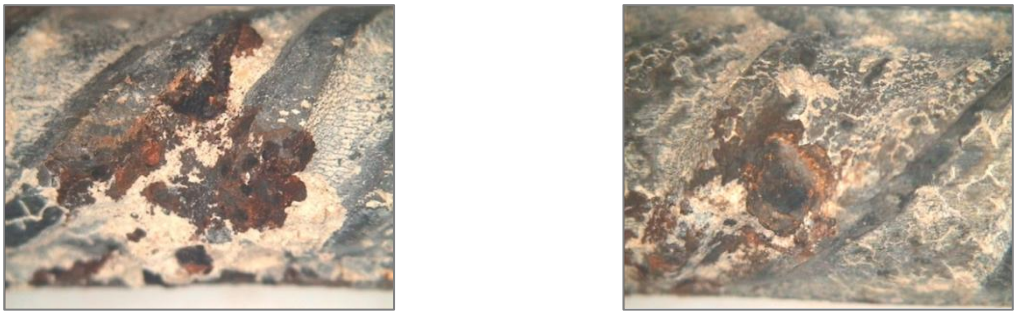

Figure 5: Images form the optical microscope of corrosion points at the end of the test. Left: sample without surface treatment after. Right: sample treated with the corrosion inhibitor.

4. Conclusions

From the present study it can be concluded that the application of an electric field for the electrochemical removal of chloride allows repassivating the corroding rebars. However, the decontaminated specimens are susceptible of further penetration of chloride promoting fast processes of corrosion. It has been confirmed that a further treatment on the concrete cover surface is interesting in order to improve the protection of the rebar against chloride action. The most effective has shown to be the sealing of the surface with colloidal nanosilica, although the application of a corrosion inhibition on the concrete surface also improve the performance of the treated specimen against the corrosion due to the presence of chloride.

Acknowledgements
Authors acknowledge the financial support from COST Association (CA15202) and from the Spanish Ministry MEIC (BIA2014-56825 JIN and RYC-2016-21422).

References

[1] Bertolini, L. et al, Electrochemical methods, Corrosion of Steel in Concrete: Prevention, Diagnosis, Repair, Wiley-VCH Verlap GmbH&Co, Weinheim (2004), 345-380.
[2] Bertolini, L. et al, Corrosion Inhibitors, Corrosion of Steel in Concrete: Prevention, Diagnosis, Repair, Wiley-VCH Verlap GmbH&Co, Weinheim (2004), 217-230.
[3] Zheng, H., Li, W., Ma, F. and Kong, Q., The effect of a surface-applied corrosion inhibitor on the durability of concrete, Constr. Build. Mater. 37 (2012) 36-40.
[4] Sánchez, M. and Alonso, M.C., Electrochemical chloride removal in reinforced concrete strucutres: Improvement of effectiveness by simultaneous migration of calcium nitrite, Constr. Build. Mater. 25 (2011) 873-878.
[5] Kupwade-Patil, K., Cárdenas, H.E., Gordon, K. and Lee, L.S., Corrosion mitigation in reinforced concrete beams via nanoparticle treatment, ACI Mater. J. 109 (2012) 617-626.
[6] Sánchez, M., Alonso, M.C. and González, R., Preliminary attempt of hardened mortar sealing by colloidal nanosilica migration, Constr. Build. Mater. 66 (2014) 306-312.
[7] Technical Specification CEN/TS 14038-2:2011. Electrochemical realkalization and chloride extraction treatments for reinforced concrete. Part 2: Chloride extraction (2011).
[8] Andrade, C. and Alonso, C., Corrosion rate monitoring in the laboratory and on-site, Construction and Building Materials 10 (1996) 315-328.
[9] COST 521. Corrosion of steel in reinforced concrete structures, final report. Cigna R., Andrade C., Nürnberger U., Polder R., Weydert R. and Seitz E., editors. European Communities. Luxembourg Publication (EUR) (2003) p. 20556.
[10] Andrade, C. and Castellote, M., Recommendation of RILEM TC 178-TMC: "Testing and modelling chloride penetration in concrete: analysis of total chloride content in concrete", Materials and Structures 35(2002) 583-585.

SynerCrete'18 International Conference on Interdisciplinary Approaches
for Cement-based Materials and Structural Concrete
24-26 October 2018, Funchal, Madeira Island, Portugal

THE EFFECTS OF CONTINUED HYDRATION OF UNDAMAGED MATERIAL ON APPARENT HEALING INDICES IN CEMENTITIOUS MATERIALS

Robert Davies [(1)], Cristina De Nardi [(2)], Anthony Jefferson [(1)]

(1) Cardiff University, Cardiff, United Kingdom
(2) University IUAV of Venice, Venezia, Italy,

Abstract

This paper addresses the effects of continuing hydration in undamaged material on reported healing for cementitious materials. Numerical simulations show how the increase of strength in self-healing test specimens can be due to a combination of ageing material properties and healing. A numerical model framework combines a hydration model, used to predict material property changes, and a damage mechanics approach, to simulate the cracking and then healing. An experimental study using natural hydraulic lime base mortars is used to illustrate the simulation capability and to examine the contribution to strength increase after healing. The lime mortar cube specimens have a first damage range of between 14 and 84 days old and then are healed for two different periods, 14 and 28 days, in water. The insight gained from this one dataset, on the composition of the strength increase due to either continued hydration or healing, will be useful to other researchers investigating self-healing behaviour in cementitious materials.

1. Introduction

Self-healing materials are being developed in many fields of material science as an alternative to the traditional damage prevention methods. A material is classed as self-healing when there is an inbuilt mechanism for recovering one or more of its initial properties following an occurrence of damage [1]. In general, the measurement of recovery involves a comparison between an initial and a post-healed material property. When the material properties of a material do not change over time, it is relatively straightforward to evaluate the degree of recovery of a material property from a self-healing experiment. However, evaluating the degree of recovery in materials, such as cementitious composites or lime mortar, with

changing properties over time is altogether more complex. The difficulty is further compounded by the fact that the degree of change in any one property varies considerably with the type of cementitious material, the degree of damage, the age of the material when damage occurs, the duration of the healing period and the environmental conditions during healing [2].

2. Essential components of the micro-mechanical model

A cementitious material with aggregate particles and cement paste is represented using a two phase composite with inclusions (Ω) and a matrix (M) phase. A detailed description of the basic micromechanical model can be found in [3] and [4]. The essential components of the micro-mechanical model are shown in the following constitutive equation (1):

$$\bar{\boldsymbol{\sigma}} = \mathbf{D}_{M\Omega} : (\bar{\boldsymbol{\varepsilon}} - \boldsymbol{\varepsilon}_{\mathbf{a}}) \tag{1}$$

$\bar{\boldsymbol{\sigma}}$ is the average stress and $\bar{\boldsymbol{\varepsilon}}$ is the total strain in the composite. $\mathbf{D}_{M\Omega}$ is the composite elastic tensor whose properties are computed using the classical Eshelby solution and the Mori-Tanaka homogenization scheme for non-dilute inclusions. $\boldsymbol{\varepsilon}_{\mathbf{a}}$ is the total additional strain resulting from anisotropic micro-cracking using the approach of Budiansky and O'Connell. A local stress-strain relationship for the micromechanical model is defined in equation (2), in which the added strain is taken to be the equivalent of a micro-cracked band in the material.

$$\mathbf{s}_L = (1-\omega)\mathbf{D}_L\boldsymbol{\varepsilon}_L \tag{2}$$

$\mathbf{s}_L$ is the equivalent local stress tensor and $\boldsymbol{\varepsilon}_L$ is the equivalent local strain tensor, both of which are expressed in a reduced vector form that considers only those components that are non-zero. $\mathbf{D}_L$ is a 3x3 matrix containing the non-zero components of the local stiffness tensor. ω is the micro-crack variable for each direction, taking the values between 0 for uncracked and 1 for the fully micro-cracked state. The elastic local strain can be subtracted from the local strain within the micro-crack band $(\boldsymbol{\varepsilon}_{\mathbf{L}})$ to give the additional strain resulting from the crack in one direction.

This micromechanical model is taken forward to establish a framework for instructing healing, as described in [5]. This work shows that the local constitutive relationship presents itself as a convenient form for including healing. The healing allows the stiffness of a proportion of the damaged component of material to be recovered. An offset or 'solidification' strain is included to ensure that the healing material solidifies in a stress-free state. The healed local stress is given in equation (3).

$$\mathbf{s}_{Lh} = (1-\omega)\mathbf{D}_L\boldsymbol{\varepsilon}_{Lh} + (1-\omega_h)\,h\omega_{th}\mathbf{D}_{Lh}(\boldsymbol{\varepsilon}_{Lh} - \boldsymbol{\varepsilon}_s) \tag{3}$$

The healing proportion is defined by the parameter *h*, which takes the values between 0 for no healing and 1 for fully healed. A subscript *h* is added to the terms to show the healing equivalent terms. $\mathbf{s}_{Lh}$ is the equivalent local stress tensor after healing, $\boldsymbol{\varepsilon}_{Lh}$ is the local

equivalent strain tensor after healing and ω_{th} is the micro-cracking parameter at the time of healing. $\mathbf{D}_{Lh}$ is the local stiffness of the healed material and $\boldsymbol{\varepsilon}_s$ is the 'solidification' strain. Since this newly healed material can also undergo micro-cracking, a term is also included to simulate this further micro-cracking, where ω_h is the healed micro-cracking variable. The degree of micro-cracking is controlled by an effective strain parameter according to the following standard exponential relationship (4);

$$\omega = 1 - \frac{\varepsilon_t}{\zeta} e^{-c\left(\frac{\zeta - \varepsilon_t}{\varepsilon_0 - \varepsilon_t}\right)} \tag{4}$$

in which ζ is the effective strain parameter, c is a constant equal to 5, $\varepsilon_t = f_t / E$, where f_t is the uniaxial tensile strength. ε_0 is the strain at the effective end of the uniaxial softening curve.

A new thermodynamically consistent component is added to this model, which allows for the change in an effective strain parameter over a curing period in an undamaged component of material that undergoes no healing. This means that the effect of hydration on the undamaged ligament of the material can be evaluated and therefore the actual degree of healing can be evaluated. In this work the material is simulated using a model which shows the relative effect of strength recovery for different levels of initial damage and different healing periods.

3. Self-healing experiments on lime based mortar

Natural hydraulic lime-based mortars exhibit promising autogenous self-healing capabilities. The effect of age and damage level on the recovery performance of compression strength and ultrasonic pulse velocity in cube samples of natural hydraulic lime mortars have been investigated [6]. Specimens in this study were pre-cracked (loaded) at ages ranging between 14 and 84 days old and then cured in water, to promote healing, for two periods of 14 and 28 days. These experimental results are used to illustrate the simulation capability of the micromechanical model and to provide an insight into the composition of the continued hydration and autogenous healing.

4. Results

A parametric study was carried out on the lime mortar cube specimens [6]. The micromechanical model was calibrated using a limited number of mechanical parameters. An example is shown in Fig. 1, where the stress against strain response is plotted comparing the experimental data and the resulting output from the micromechanical model. This process was repeated for whole data set and it was found to have excellent correlation. The mechanical properties derived at different material ages were used to evaluate the change in the effective strain parameters. This meant that the undamaged component of the lime mortar can be evaluated over time.

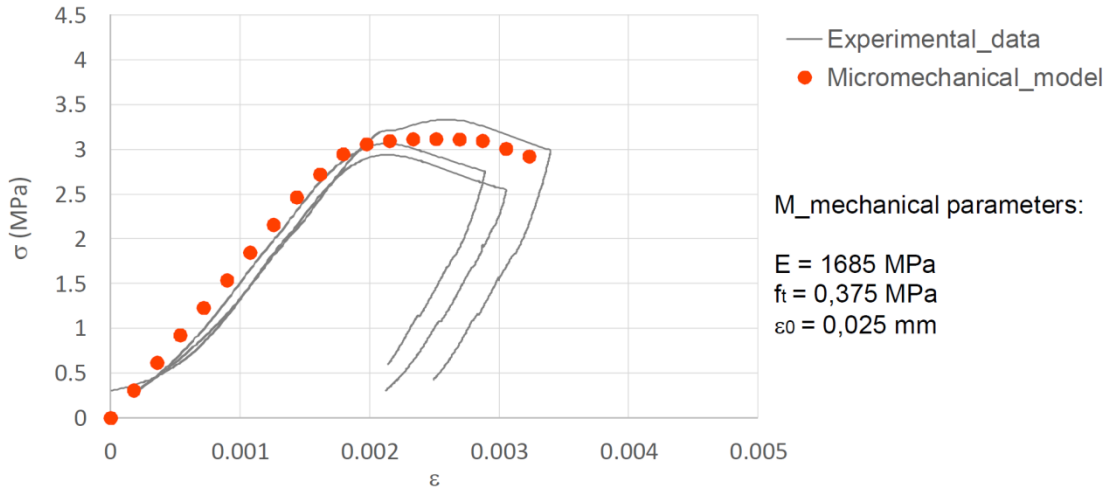

Figure 1: Comparison between experimental data and micromechanical model alongside the key mechanical properties chosen

The behaviours of the compressive strength (derived from the experimental data) and the tensile strength (derived from micromechanical model parameters) were evaluated. However, only the results of the compressive strength analysis is shown in Fig 2 below.

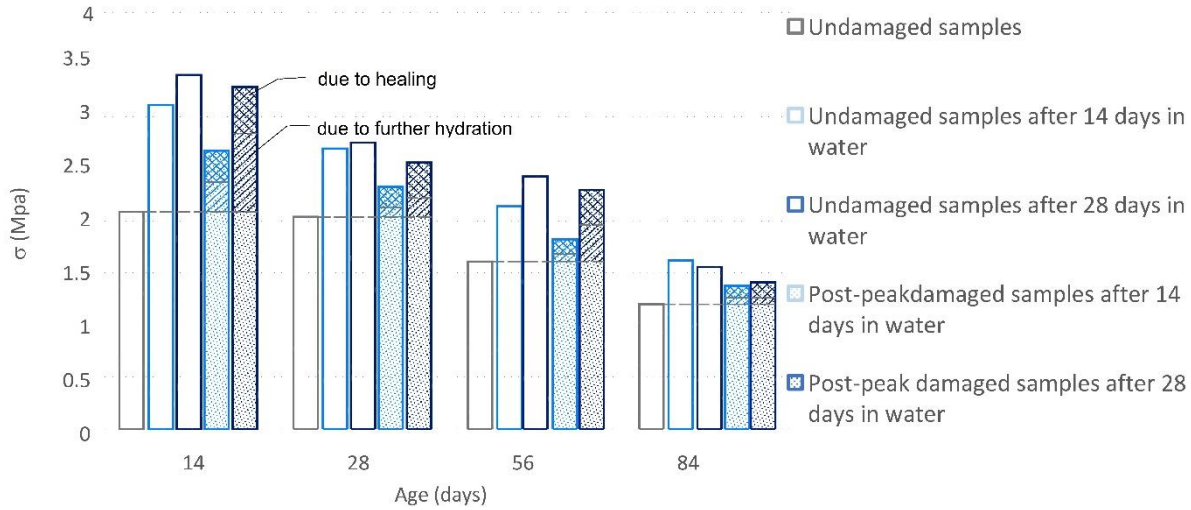

Figure 2: Variation in compressive strength after 14-28 days in water immersion, derived from experimental data, with contribution of strength increase attributed to further hydration and healing

In Fig. 2 the undamaged sample strength, at first test, is shown for an increasing age of sample. As the age of first test increases there is a decrease in strength, which is due ambient curing conditions of lime mortar. After placing undamaged samples in water for 14 and 28 days there is significant increase in strength. Specimen that were damaged into the post peak regime also exhibit an increase in strength after curing in water. The composition of this strength increase is estimated using the micromechanical model and the figure shows the contribution due to continued hydration and autogenous healing. Interestingly, it was found that the older the specimen on first damage the lower the contribution of strength recovery

due to the ageing of undamaged material. This means that healing is contributing more to the strength increase, than continued hydration, for older lime mortar specimens. This work shows that the micro-mechanical self-healing model can represent the characteristic mechanical response of self-healing cementitious materials and provide an insight into the composition of the strength increase.

5. Conclusion

A two-phase composite micro-mechanical constitutive model, that includes anisotropic micro-cracking, provides an excellent basis for the development of a model for cementitious materials, such as hydraulic lime-based mortars, that exhibit self-healing behaviour. The relative simplicity of this micromechanical healing model, combined with the fact that it requires a small number of physically meaningful parameters, shows that it can manage the complex time dependant processes. Numerical simulations have shown how the increase of strength in the self-healing test specimens can be due to a combination of ageing material properties and healing. This study showed that the older the specimen on first damage the higher the contribution of strength recovery is due to healing rather than the ageing of undamaged material.

Acknowledgements
Thanks must go to the EPSRC for their funding of the Materials for Life (M4L) project (EP/K026631/1) and the follow on programme grant Resilient Materials for Life (EP/P02081X/1) http://www.RM4L.com. This conference contribution was supported by a STSM Grant from the COST Action CA15202. http://www.sarcos.enq.cam.ac.uk

References

[1] S. van der Zwaag, Self Healing Materials - An Alternative Approach to 20 Centuries of Materials | Springer. 2007.
[2] K. Van Tittelboom and N. De Belie, 'Self-Healing in Cementitious Materials—A Review', Materials, vol. 6, no. 6, pp. 2182–2217, May 2013.
[3] I. C. Mihai and A. D. Jefferson, 'A material model for cementitious composite materials with an exterior point Eshelby microcrack initiation criterion', Int. J. Solids Struct., vol. 48, no. 24, pp. 3312–3325, Dec. 2011.
[4] R. Davies and A. Jefferson, 'The simulation of inelastic matrix strains in cementitious materials using micromechanical solutions', Eng. Fract. Mech., 2014.
[5] Davies, R., Jefferson, A., 2017. Micromechanical modelling of self-healing cementitious materials. International Journal of Solids and Structures 113–114, 180–191. https://doi.org/10.1016/j.ijsolstr.2017.02.008
[6] De Nardi, C., Cecchi, A., Ferrara, L., Benedetti, A., Cristofori, D., 2017. Effect of age and level of damage on the autogenous healing of lime mortars. Composites Part B: Engineering 124, 144–157. https://doi.org/10.1016/j.compositesb.2017.05.041

SynerCrete'18 International Conference on Interdisciplinary Approaches
for Cement-based Materials and Structural Concrete
24-26 October 2018, Funchal, Madeira Island, Portugal

THE ROLE OF NANO-PARTICLES IN SELF-HEALING PROCESS OF CEMENTITIOUS MATERIALS

Maria Stefanidou [(1)], Eirini-Chrysanthi Tsardaka [(1)], Evangelia Tsampali [(1)]

(1) Laboratory of Building Materials, School of Civil Engineering, Aristotle University of Thessaloniki, Greece

Abstract

The importance of producing materials that can heal their flaws is easily understood as the performance of those materials is high in terms of durable structures with low maintenance cost. The construction section, the last decades, is characterized by efforts to produce high performance rather than high strength materials. To that direction, self-healed concrete has an important role.

On the other hand, the addition of nano-particles in cement-based materials has been proved beneficiary in terms of pozzolanic reaction and early strength gain. The possibility to explore the role of nano-particles to heal the cracks in cement pastes is presented in this article. For that purpose, nano-SiO_2 and nano-CaO were incorporated in cement pastes in different proportions. The produced pastes were tested in terms of mechanical, physical and microstructure properties. The formation of secondary crystals into the nano-modified structure resulted in: porosity refinement, strength increase and the most important, dense structure by the presence of fully compatible products that reinforce the material's structure.

1. Introduction

Despite its numerous advantages, cement is vulnerable to cracking, which limits both its potential uses as well as its structure service life [1]. In the case of concrete and other cementitious products, attention has been directed mainly at the development of composite materials capable of self-healing [2-7]. The advantages of using self-healing materials, on the one hand is the treatment of early-cracks, and on the other the reduction of penetration of harmful agents [5,6]. The research that has already been conducted on old-lime based mortars, which exhibit self-healing properties was very useful to understand the mechanism [8,9]. These studies have revealed that fine-grained lime has the inherent capacity to react with the

environment and produce secondary crystals deposited in empty spaces into the mortar's structure [10]. This results in a compact, continuous structure, which heals cracks and restricts the absorption capacity of damaging substances (i.e. moisture with diluted ions).
Drawing inspiration from this, different ways of healing approaches have been developed during the last decade focusing mainly on adding particles in the binding system generating autogenous healing [11-13]. The combination of this concept of autonomous self-healing and of nanotechnology, resulted in a new class of nano-modified cement, where nano-materials are selected as an alternative particle choice [14-16]. These efforts have produced mortars with upgraded properties such as increased durability and high mechanical stresses and improved performance at environmental conditions in which non-modified cement would degrade rapidly.
In this study, a self-healing system is proposed and evaluated. More specifically, the use of nano-SiO_2 and nano-CaO was investigated. Both of the two possible choices offer distinct advantages. Nano-silica particles contribute to an increased formation of calcium silicate (CSH) gel in cementitious systems due to the reaction of nano-silica with $Ca(OH)_2$ produced from the hydration of tricalcium silicate (C_3S) [17,18].

2. Materials and methods

The Portland cement used for the needs of the experimental work was CEMII32.5N, classified by the EN 197-1. This is a blended pozzolanic cement with major constituents natural pozzolan, fly ash and limestone and it is commonly used in construction. Aerial lime CL90 (according to EN 459-1:2001) and the nanoparticles (commercially available by Sigma Aldrich) that were used are given in Table 1. The addition of superplasticizer (SP) was necessary in the nano-modified mixtures for keeping stable the consistency that was determined according to EN 196-3:2005. To evaluate the consistency, Vicat Needle tests (VNT) according to EN 196-3:2005 were conducted.
Pastes 2.5x2.5x5cm and 2.5x2.5x10cm were formed and cured in a humid environment (85-90% humidity and 20±2°C). Compressive strength and porosity were tested at 7 and 28 days of hydration, according to EN 1015-1 and RILEM CPC 11.3 under vacuum, respectively.
Capillary absorption coefficient tests were determined after 28 days of curing according to EN 1015-18:2002. The microstructure of the samples was characterized, using SEM (Jeol JSM-840A), 28 days. Simultaneous DTA-TG (Differential Thermal- Thermogravimetric Analysis), SDT 2960 TA Instruments, was used for the determination of calcium hydroxide ($Ca(OH)_2$) and calcium carbonate ($CaCO_3$), under N_2 atmosphere from 10^o to 1000^oC.

3. Results and Discussion

3.1 Physic-mechanical properties

Compressive strength of cement pastes is given in Fig. 1. The addition of NS is increasing compressive strength by 13.5% and 23.4% at 7 and 28 days respectively in R_A. The NS doesn't improve the strength in the RL system as the hydration and the carbonation mechanism act in parallel. The addition on NCaO in R_B is also assisting strength while the combination of nano-particles (Rc) results in small strength reduction.The addition of NCaO does not significantly modify this property, either in R_B, or in R_C along with NS. The aerial

lime incorporation in cement affected the mechanical properties of the pastes, so as RL series have slightly reduced strength values in respect to the R series. Cement-lime systems present a similar behavior of the strength development in relation to the nanoparticle inclusion. The only differentiation relies on RL_B strength increase at early age strength by 11.5% comparing to RL, which might be connected to the action mechanism of NCaO in the presence of lime.

Table 1: Content of cement based pastes.

	CEM II32,5N (g)	Aerial Lime (g)	H_2O (mL)	Nano-Silica (NS) %	Nano-CaO (NCaO) %	SP %	Vicat (mm)
R	2000	-	650	-	-	-	6
R_A	2000	-	650	1.5	-	2	6
R_B	2000	-	650	-	1.5	2	0
R_C	2000	-	650	1	0.5	2	7
RL	1600	400	720	-	-	-	6
RL_A	1600	400	720	1.5	-	2	7
RL_B	1600	400	720	-	1.5	2	0
RL_C	1600	400	720	1	0.5	2	7

The comparison between the nano-modified systems and the reference samples at open porosity measurements are displayed in Fig. 2. At both, cement pastes and cement-lime pastes, the addition of NCaO influences impressively the open porosity. At early age, porosity reduction reaches 55% in R_B. and 46% in RL_B. NCaO contributes in porosity reduction and this advantage can be considered as a potential of healing factor. Also, it is worthy to annotate that the filling of porosity is not accompanied by simultaneous compressive strength increase. The latter is connected to the nature of crystals originated from NCaO, as at this early ages they are very small.

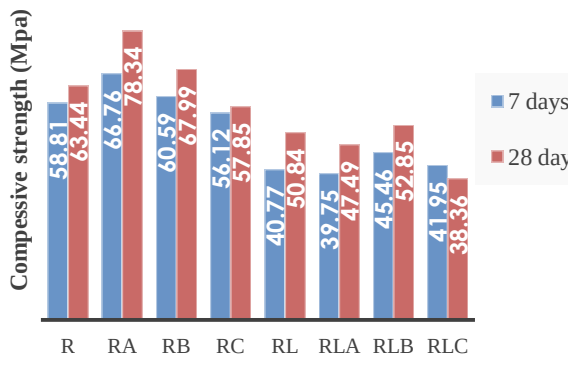

Figure 1: Compressive strength of cement pastes.

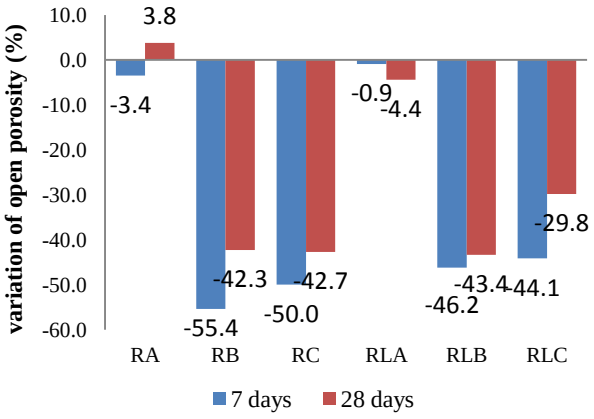

Figure 2: Variation of open porosity (%) of cement pastes, in respect to the reference paste.

Capillary water absorption is given in Fig. 3. The capillarity of nano-modified cement pastes was measured lesser than reference (R). In specific, sorptivity of R_B is 40% smaller than R

and is in agreement to open porosity. The presence of lime in RL series affects capillary absorption but also the addition of NCaO favours capillarity of cement-lime pastes by reducing the water absorption capacity. The water absorption of RL_A, RL_B and RL_C is alike and smaller than RL by approximately 25%.

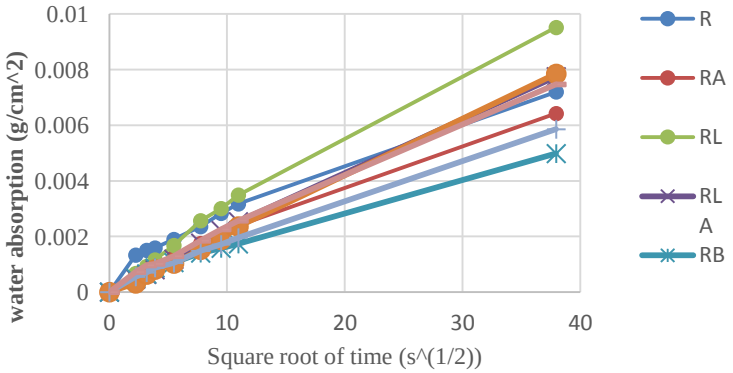

Figure 3: Capillarity of cement pastes at 28 days.

3.2. Differential Thermal and Thermogravimetric Analysis

DTA-TG analysis is used to quantify the portlandite and calcite content of the samples. As given in Fig. 4 and 5, the differentiation of each nano-modified sample from the reference displays the behavior due to NS and NCaO incorporation.

The addition of NS reduced the portlandite by 35% and 32% at 7 and 28 days, respectively. The action of NS initiated further consumption of portlandite in C-S-H compounds. On the other hand, the incorporation of NCaO, both in R_B and R_C, maintained portlandite quantity at early age. At 28 days, R_B and R_C present a smaller proportion of $Ca(OH)_2$, probably due to calcite or C-S-H formations. In cement-lime pastes the addition of NCaO increases the portlandite content (RL_B), as the hydration of nanoparticles contributes in $Ca(OH)_2$ content. On the contrary, NS conduces to the decrease of portlandite. Calcite content is approximately stable in R_A samples, in comparison to R system at 7 and 28 days. The values of R_B and R_C though, indicate higher calcite precipitation from the early age. The acceleration of carbonation is related to NCaO presence. When NCaO particles carbonate, they turn to pure $CaCO_3$ and aid the precipitation of calcite. RL_B and RL_C calcite content at 7 days is higher than the reference and enforced by lime carbonation. RL_A samples have the highest calcite content at 28 days.

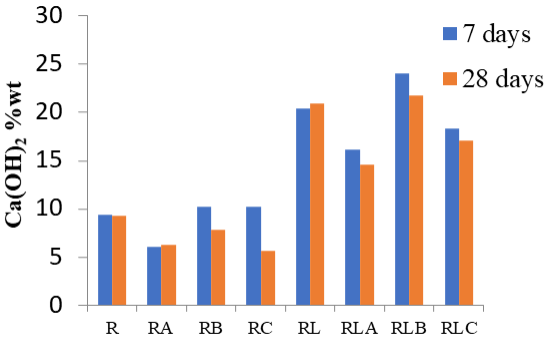

Figure 4: Portlandite content of samples as a percentage by mass, at 7 and 28 days.

Figure 5: Calcite content of systems as a percentage by mass, at 7 and 28 days.

3.3. SEM observation

Observation of the microstructure by scanning electron microscope (SEM) verifies the efflorescing structure of pastes containing NCaO (Fig.6). The presence of nano-CaO was beneficiary in all cases studied as precipitation of small calcitic crystals was observed in openings in the structure, during the first 28 days of curing. Black arrows, in Fig. 6, highlight the flourished microstructure, calcite precipitation and healing "bridges" on cracks.

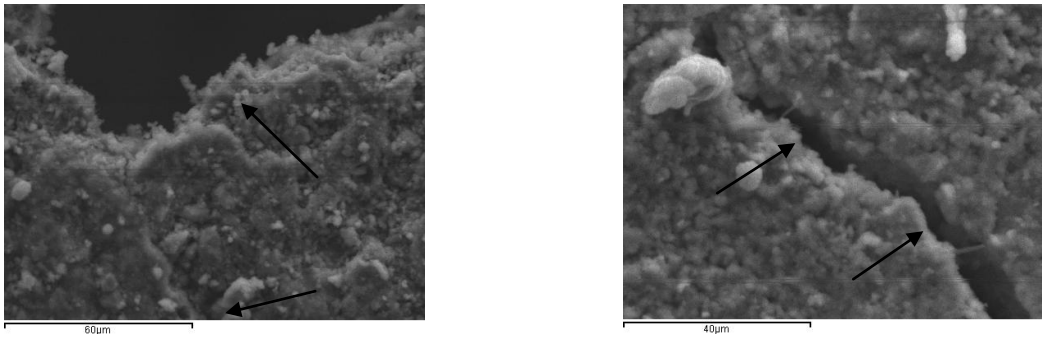

Figure 6: Microstructure of R_c (left) and RL_c (right), where development of secondary crystals filling small and bridging larger cracks have been observed, at 28 days.

4. Conclusions

Cement pastes with incorporated nanoparticles present dense structure and improved mechanical properties. A 13.5% and 23.45increase in compressive strength was recorded at 7 and 28 days respectively when NS was added in cement pastes. In pastea where cement-lime was combined, NS had lower influence due to different mechanisms acting in parallel. NCaO on the other hand had a positive role in strength in both pastesas 7% and 4% in cement-lime pastes at 28days was recorded. In R_B and RL_B pastes the porosity reduction was also impressive. The physical properties such as porosity and capillary absorption have been reduced. CaO nanoparticles not only benefit cement properties, but also the mechanism of their action favors calcite precipitation. Nano-CaO has vital role in terms of healing through secondary calcite formation at very early ages, which even in low percentage (0.5%w/w of binder) is very active.

Lime-cement pastes with nanoparticles contain a considerable amount of available portlandite which at later ages can contribute to further calcite precipitation. Even at 28days, healing crystals seem to be formed in wide cracks. Portlandite content increase and healing "bridges" on cracks enforce that claim.

Despite the encouraging results, the phenomena need to be further studied. The proportion of nanoparticles and the preferable curing environment are some of the issues that need further consideration.

Acknowledgement

The authors would like to express their acknowledgments to the COST Action 15202 "Self-healing as preventive repair of concrete structure - SARCOS"
(http://www.sarcos.eng.cam.ac.uk) for the mobility support to present the research

References

[1] Ferrara L. et al, Experimental characterization of the self-healing capacity of cement based materials and its effects on the material performance: A state of the art report by COST Action SARCOS WG2, Construction and Building Materials 167 (2018), 115-142
[2] Roig-Flores M. et all, Effect of crystalline admixtures on the self-healing capability of early-age concrete studied by means of permeability and crack closing tests, Construction and Building Materials 114 (2016), 447-457
[3] Polat R. et al, Effects of nano and micro size of CaO and MgO, nano-clay and expanded perlite aggregate on the autogenous shrinkage of mortar, Construction and Building Materials 81 (2015), 268-275
[4] Huang H. et al, Effect of blast furnace slag on self-healing of microcracks in cementitious materials, Cement and Concrete Research 60 (2014), 68-82
[5] Min Wu et al, A review: Self-healing in cementitious materials and engineered cementitious composite as a self-healing material, Construction and Building Materials 28 no. 1 (2012), 571-583
[6] Mihashi H. et al, Development of Engineered Self-Healing and Self-Repairing Concrete-State-of-the-Art Report, Journal of Advanced Concrete Technology 10 no. 5 (2012), 170-184
[7] Perez Z. et al, Characterisation of cement pastes with innovative self-healing system based in epoxy-amine adhesive, Cement & Concrete Composites 60 (2015), 55-64
[8] Papayianni I., Stefanidou M., Durability aspects of Ancient Mortars of the archeological site of Olynthos, Journal of Cultural Heritage 8 no. 2 (2007), 193-196
[9] Papayianni I., Stefanidou M, The role of fines in lime-based mortar's technology, Romanian Journal of Materials 41 no. 1 (2011), 26-29
[10] Papayianni I., Stefanidou M., Re-crystallization phases in ancient mortars, from the 9th Euroseminar on Microscopy Applied to Building Materials, Trondheim Norway (2003)
[11] Termkhajornkit P. et al, Effect of fly ash on autogenous shrinkage, Cem Concr Res 3 (2005), 473–82
[12] Mihashi H., Nishiwaki T., Development of engineered self-healing and self-repairingconcrete-state-of-the-art report, J. Adv. Concr. Technol. 10 (2012), 170–184
[13] Ferrara L., Albertini I., Gettu R., Krelani V., Moscato S., Pirritano F., Theeda S., Self-healing of cement based materials engineered throughcrystalline admixtures: experimental results form a multinationaluniversity network, ACI Special Publication 305 (2015), 13.1-13.10. ISBN13:978-1-942727-44-6
[14] Stefanidou M., Nano-modified lime-pozzolan pastes, Romanian Journal of Materials 43 no. 2 (2013), 223-226
[15] Nunes C., Slížková Z., Stefanidou M. and Němeček J., Microstructure of lime and lime-pozzolan pastes with nanosilica, Cement and Concrete Research 83 (2016), 152-163
[16] Stefanidou M., Modification of lime-based pastes by the addition of nano-SiO2, from the 4th International Symposium on Nanotechnology in Construction NICOM4, Crete (2012)
[17] Stefanidou M. Papayianni I., Influence of nano-SiO2 on the Portland cement pastes, Composites: Part B 43 (2012), 2706–2710
[18] Sobolev K. Z. et al, Performance of Cement Systems with Nano- SiO2 Particles Produced Using Sol-gel Method, Advanced Structural Materials 3 1276 (2010), 139-145

SynerCrete'18 International Conference on Interdisciplinary Approaches
for Cement-based Materials and Structural Concrete
24-26 October 2018, Funchal, Madeira Island, Portugal

UTILIZATION OF QUARTZ QUARRY DUST IN ENGINEERED CEMENTITIOUS COMPOSITES PRODUCTION

Olkan İlter Taş [(1)], Süleyman Bahadır Keskin [(1)], Özlem Kasap Keskin [(1)], Mustafa Şahmaran [(2)]

(1) Muğla Sıtkı Koçman University, Muğla, Turkey
(2) Hacettepe University, Ankara, Turkey

Abstract

Engineered Cementitious Composites (ECC) is a type of high performance fiber reinforced cementitious composites characterized by tight micro cracking under mechanical loading, high ductility, hence high durability. Moreover, ECC has been shown to exhibit intrinsic self-healing behaviour. ECC design requires the use of abundant supplementary binding materials especially fly ash together with Portland cement. As aggregate, only micron sized quartz sand is used in order to provide homogeneity and restrict the matrix fracture toughness. Polyvinyl alcohol type synthetic fibers, high range water reducing admixtures and water are the other ingredients of ECC. Tight micro cracks together with abundant binding materials bring about intrinsic self-healing as an important feature for ECC. In this study, a successful ECC mixture is produced with local available fly ash and quartz sand; mechanical and self-healing properties of this mixture are determined. In addition to this control mixture, another ECC mixture is also produced by using quartz quarry dust, which is a waste of a local quartz quarry, as aggregate. The effect of using quartz quarry dust as aggregate for ECC on mechanical and self-healing properties are investigated by comparing with the properties of control mixture.

1. Introduction

Although conventional concrete is a widely used material, it has many disadvantages which shorten its service life and cause economic loss [1]. Engineered Cementitious Composites (ECC) which have similar mechanical properties to concrete under normal service conditions promote sustainability through enhanced tensile and self-healing behavior. Under excessive mechanical tensile and bending loads ECC exhibit strain hardening and deflection hardening

behaviors as a result of multiple tight micro cracking, respectively [2, 3]. ECC not only prevent sudden failure under impact loading such as earthquakes due to its ductile behavior, but also possess self-healing property in multiple micro cracks formed after loading due to abundant binding material content. Although initial cost of ECC is much higher than that of ordinary concrete, dimensional compatibility, low cracking and high self-healing potential put ECC forward as a class of sustainable construction materials [4, 5]. Self-healing property obtained due to controlled tight cracking together with high amount of binding materials is an intrinsic property of ECC. Through self-healing mechanism, the material can heal itself by filling the cracks and regain its properties over time. It is possible to design materials to provide the self-healing characteristics. This feature may avoid costly solutions such as maintenance and renewal and does not require any human intervention [1, 6, 7].
In this study, quartz quarry dust obtained as a waste material from quartz mines located in Muğla region was used for the production of ECC. The effects of utilizing this waste material on self-healing properties and mechanical properties of ECC were investigated. Quartz quarry dust is stacked in nature in wet and dry conditions. Both forms of waste storage lead to environmental pollution and health problems.

2. Experimental Study

2.1 Materials

The aim of this study is to produce ECC by using the fly ash obtained from Yatağan Thermal Power Plant in Muğla region and replacing the commercial quartz sand used in production with quartz quarry dust of a local mine. For this reason, keeping all other ingredients same, an ECC is produced with local fly ash (FA 1.2) with the same proportions reported in the literature which also serves as a control mixture. In addition, another mixture is also produced in which the silica sand is replaced with the quartz quarry dust (FA 1.2 W). The chemical compositions of quartz sand and quartz quarry dust are shown in Tab. 1 together with the chemical compositions of the other ingredients. Due to high SiO_2 content of quarry dust, potential alkali aggregate reactivity test was also conducted on mortar bars and the expansion was found to be innocuous 16 days after casting.

Table 1. Chemical composition and physical properties of powder materials

	Cement	Fly Ash	Quartz Sand	Quartz Quarry Dust
Chemical Composition (%)				
SiO_2	18.69	50.04	99.37	91.98
CaO	61.87	11.21	0.14	0.12
Al_2O_3	4.74	22.85	0.16	4.94
Fe_2O_3	3.37	8.02	0.03	0.08
MgO	3.36	2.23	-	0.02
Na_2O	0.19	0.27	0.03	2.77
K_2O	0.63	2.50	0.03	0.04
SO_3	2.93	0.78	-	-
Physical Properties				
Specific Gravity	3.15	2.28	2.60	2.60
Blaine fineness	3420	2845	-	-

Mixture proportions of ECC used in this study is also provided in Tab. 2.

Table 2. Proportioning of ingredients of ECC mixtures (kg/m^3)

Ingredient	**Cement**	**Fly ash**	**Water**	**Sand**	**HRWRA**	**PVA fiber**
Amount (kg/m3)	560	672	333	442	8.4	26

2.2 Test Methods

Two sets of experiments were carried out on ECC specimens to determine the mechanical and self-healing properties. For mechanical properties, specimens were tested under compression and four-point bending at 7, 28 and 90 days after casting. Compressive strength was determined on 50 mm cubic specimens while for the determination of flexural strength and mid-point deflections 50x75x360 mm beam specimens were used. Flexural tests were carried out on deformation controlled universal testing machine.

For self-healing test specimens were preloaded to 60% of their deflection capacities at 28 days. Self-healing capabilities were tested in terms of four-point bending test, ultrasonic pulse velocity (UPV) test and rapid chloride permeability test (RCPT). UPV and bending tests were conducted on beam specimens while for RCPT tests 100 mm diameter and 50 mm thick puck specimens were cut from ECC cylinders as described in ASTM C 1202 [8]. Results obtained from the virgin specimens were compared with the preloaded specimens for self-healing assessment.

3. Test Results and Discussions

3.1 Mechanical Properties

The compressive strength, flexural strength and mid-point deflection capacities of the specimens determined as average of 3 specimens at ages of 7, 28 and 90 days are provided in Tab. 3.

Table 3. Mechanical Properties of ECC Mixtures

	Compressive Strength (MPa)		**Flexural Strength (MPa)**		**Mid-Point Deflection (mm)**	
Age (Day)	**FA1.2**	**FA1.2W**	**FA1.2**	**FA1.2W**	**FA1.2**	**FA1.2W**
7	39.3	40.0	8.84	11.28	5.16	5.58
28	63.3	64.9	11.10	11.49	3.84	4.88
90	75.2	78.6	11.97	12.33	3.32	3.41

Mixtures which contains fly ash obtained from Yatağan Thermal Power Plant shows similar mechanical properties to the mixtures given in the literature [9]. It is clear that it is possible to produce ECC with the locally available materials around Muğla region. Under bending loads, the specimens show high amounts of deflections as expected in ECC specimens. Test results also indicate the performance of quartz quarry dust as aggregate in ECC production. Mechanical properties observed in FA1.2W is slightly better than that observed in FA1.2. Compressive strength, flexural strength and deflections under four-point bending test are all

higher in case of quartz quarry waste usage. The improved mechanical properties may be attributed to the change in particle size distribution of the aggregates [10, 11] or activation potential of fly ash by higher alkali content of quartz quarry dust [12]. According to the mechanical test results, it is obviously clear that ECC can be produced by using quartz quarry dust waste as replacement of silica sand.

3.2 Self-Healing Properties

Self-healing capacities of ECC mixtures produced by locally available materials were investigated by three different test methods; four-point bending test, UPV test and RCPT test. At 28 days, preloading was applied on some specimens. Preloaded (PL) specimens were moisture cured until the test ages. The rest of the specimens were kept as sound specimens (S), and they were also tested at the same ages. The comparison of the test results for the PL and S specimens is expected to indicate the level of self-healing development in ECC mixtures. Flexural strength and mid-point deflection results are listed in Tab. 4.

Table 4. Flexural properties of the mixtures

Age (Day)	Property	FA 1.2 S	FA 1.2 PL	FA 1.2 W S	FA 1.2 W PL
28+0	Flexural Str. (MPa)	11.10	8.44	11.49	6.58
	Mid-Point Defl.(mm)	3.84	2.07	4.88	2.66
28+30	Flexural Str. (MPa)	11.88	10.5	12.41	8.42
	Mid-Point Defl.(mm)	3.35	3.30	4.58	3.78
28+60	Flexural Str. (MPa)	12.25	10.99	12.46	9.83
	Mid-Point Defl.(mm)	3.27	3.41	4.13	4.27
28+90	Flexural Str. (MPa)	12.56	11.27	12.49	11.52
	Mid-Point Defl.(mm)	3.05	3.69	3.92	4.58

As seen in Tab. 4, with the age of the specimen, flexural strength increased and the deflection capacity decreased as expected for both ECC mixtures. Preloading process caused a significant decrease both in the maximum flexural load carrying and mid-point deflection capacities. In PL specimens, the flexural properties improved with time which was an indication of self-healing of the cracks in the specimens. For both FA1.2 and FA1.2W mixtures, flexural strength of specimens reached the 28-day values of sound specimens in 90 days after preloading process.

UPV is a non-destructive test method which allows to observe the changes in the properties of the same specimens with time. Monitoring the changes in the UPV results provides information about the crack closure because in the presence of cracks. Cracks extend the path for the ultrasonic waves to travel and result in an overall decrease in UPV. The difference between the UPV values of sound and preloaded specimens are shown in Fig. 1. In both mixtures UPV increased with time which indicated the continuation of hydration process in sound specimens and development of self-healing in preloaded specimens. UPV values were decreased in ECC mixtures after the crack formation by preloading. However, as time passes the difference between the sound and pre-loaded specimens decreased. This reduction in the

difference between sound and preloaded specimens showed that the cracks were closed with time.

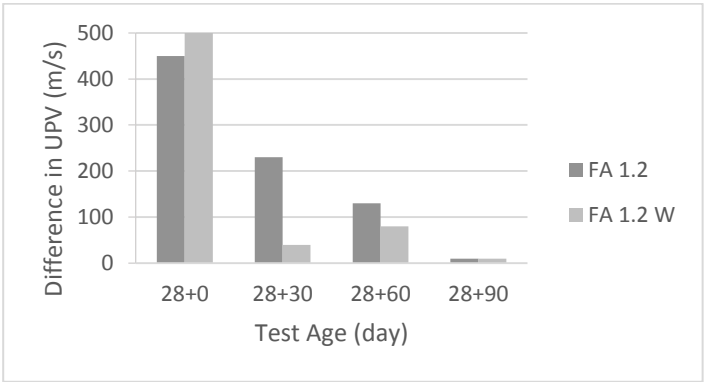

Figure 2. Difference in UPV test results

RCPT is also a non-destructive testing method which shows the transport properties of the specimens. Higher RCPT test result means higher permeability and hence higher pore content, especially in case of precracked specimens with larger or more cracks. Therefore, preloaded specimens are expected to show larger RCPT results. RCPT results decreased with time as hydration continued and the permeability decreased. Preloading application lead to an increase in RCPT results due to increase in permeability as a result of crack formation. However, as seen from Fig. 3 the difference in the results of sound and preloaded specimens decreased with time as in the case of UPV test. Reduction in difference is an evidence of crack closure which indicates that the preloaded specimens self-healed.

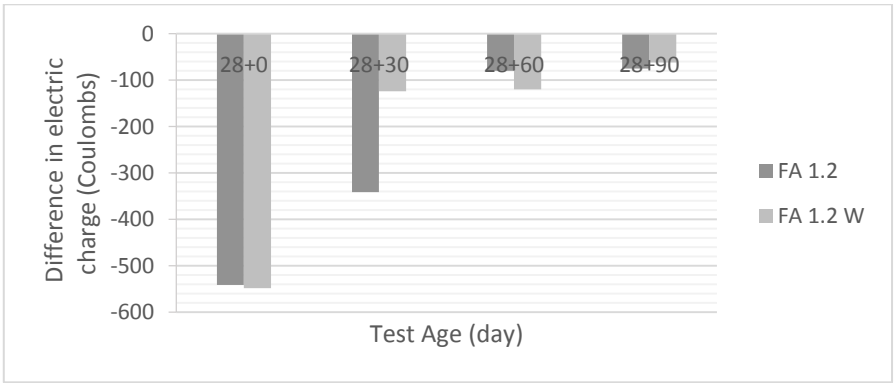

Figure 3. Difference in RCPT results

4. Conclusion

This paper represents the results of an experimental study which aims to produce ECC with locally available waste materials around Muğla region in Turkey. The results revealed that it is possible to produce cementitious composites having high compressive strength, high deflection capacity under bending and self-healing capability by using the locally available

materials. Additionally, it is also possible to reduce the initial cost of ECC mixture by using waste quartz quarry dust as aggregate instead of quartz sand.

Acknowledgement
This paper has been granted by the Mugla Sitki Kocman University Research Projects Coordination Office. Project Grant Number: 17/006 and title "Usability of Industrial Wastes of Muğla Region in Cementitious Composite Production".

References

[1] Yıldırım, G., Kasap Keskin, Ö., Keskin, S.B., Sahmaran, M., Lachemi, M., A review of intrinsic self-healing capability of engineered cementitious composites: Recovery of transport and mechanical properties, Construction and Building Materials (2015), 101: 10–21.
[2] Gohil, B.D. & Parikh, K.B., Study on engineered cementitious composites with different fibres: a critical review, International Journal of Innovations in Engineering and Technology (2016), 6:366-370.
[3] Deshpande, U.L. & Murnal, P.B., Ductile concrete using engineered cementitious composites. International Journal of Engineering Research (2016), 5:756-760.
[4] Sahmaran, M., Yıldırım, G., Erdem, T.K., Self-healing capability of cementitious composites incorporating different supplementary cementitious materials. Cement and Concrete Composites (2013) 35:89–101.
[5] Keskin, S.B., Sahmaran, M., Yaman, I.O., Lachemi, M., Correlation between the viscoelastic properties and cracking potential of engineered cementitious composites. Construction and Building Materials (2014), 7: 375–383.
[6] Schlangen, E., Jonkers, H., Qian, S., Garcia, A., Recent advances on self-healing of concrete. Fracture Mechanics of Concrete and Concrete Structures (2010), 291-298
[7] Li, V.C., On engineered cementitious composites (ECC) - a review of the materials and its applications, Journal of Advanced Concrete Technology (2013), 1:215–230
[8] ASTM C1202, Standard Test Method for Electrical Indication of Concrete's Ability to Resist, Chloride Ion Penetration, ASTM International (2017)
[9] Keskin, S.B., Dimensional stability of engineered cementitious composites, PhD thesis, Middle East Technical University, Ankara, Turkey (2012)
[10] Yang, Y.Z., Yao, Y., Zhu, Y., Effects of Gradation of Sand on the Mechanical Properties of Engineered Cementitious Composites, Advanced Materials Research (2011), 250-253: 374-378.
[11] Tian, L., Chen, J.R., Zhao, T.J., Ding, Z., Influence of Aggregate Gradation on Mechanics Performance of Strain-Hardening Cement-Based Composites (SHCC), Advanced Materials Research (2009), 79-82: 207-210.
[12] Fraay, A.L.A., Bijen, J.M., de Haan, Y.M., The reaction of fly ash in concrete a critical examination. Cement and Concrete Research (1989),19:235-246.